VOLUME 1

TREATISE ON
PROCESS METALLURGY
Process Fundamentals

VOLUME 1

TREATISE ON
PROCESS METALLURGY
Process Fundamentals

Editor-in-Chief

SESHADRI SEETHARAMAN
Royal Institute of Technology
Stockholm, Sweden

Co-editors-in-Chief

ALEXANDER McLEAN
Department of Materials Science and Engineering
University of Toronto,
Toronto, Ontario, Canada

RODERICK GUTHRIE
McGill Metals Processing Centre,
Montreal, Quebec, H3A 2B2, Canada

SEETHARAMAN SRIDHAR
Royal Academy of Engineering / Tata Steel Research Chair
in Low Carbon Materials Technologies
University of Warwick
Coventry, UK



Amsterdam • Waltham • Heidelberg • London • New York • Oxford
ELSEVIER Paris • San Diego • San Francisco • Sydney • Tokyo

Elsevier
The Boulevard, Langford Lane, Kidlington, Oxford OX5 1GB, UK
225 Wyman Street, Waltham, MA 02451, USA

Copyright © 2014 Elsevier Ltd. All rights reserved.

No part of this publication may be reproduced, stored in a retrieval system or transmitted in any form or by any means electronic, mechanical, photocopying, recording or otherwise without the prior written permission of the publisher.

Permissions may be sought directly from Elsevier's Science & Technology Rights Department in Oxford, UK: phone (+44) (0) 1865 843830; fax (+44) (0) 1865 853333; email: permissions@elsevier.com. Alternatively you can submit your request online by visiting the Elsevier web site at http://elsevier.com/locate/permissions, and selecting *Obtaining permission to use Elsevier material*.

Notice
No responsibility is assumed by the publisher for any injury and/or damage to persons or property as a matter of products liability, negligence or otherwise, or from any use or operation of any methods, products, instructions or ideas contained in the material herein. Because of rapid advances in the medical sciences, in particular, independent verification of diagnoses and drug dosages should be made.

British Library Cataloguing in Publication Data
A catalogue record for this book is available from the British Library

Library of Congress Cataloging in Publication Data
A catalog record for this book is available from the Library of Congress

ISBN: 978-0-08-096986-2

For information on all Elsevier publications
visit our website at store.elsevier.com

Printed and bound in United Kingdom.
14 15 16 17 10 9 8 7 6 5 4 3 2 1



This book is dedicated to the Memory of former Chief Co-editor Professor Masanori Iwase, Kyoto University, Japan



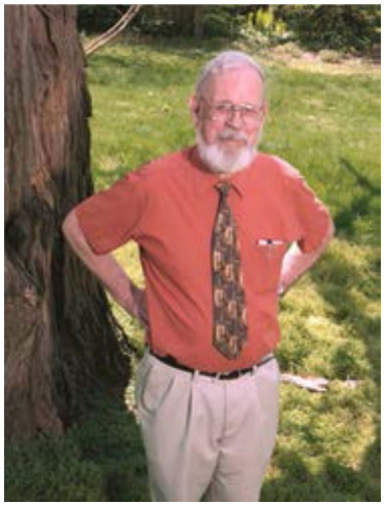
January 10, 1948 to September 29, 2011

Professor Masanori Iwase, known to his friends as "Masa," was a beacon of knowledge with respect to the thermochemistry of metallurgical systems. He graduated from Kyoto University with his Bachelor's Degree in 1971, obtained his Master's Degree in 1973, and his Doctor of Engineering Degree in 1979, by which time he had already published 14 papers. From 1979 through 1981, he was a Post-Doctoral Fellow with Professor Alexander McLean's Group within the Department of Metallurgy and Materials Science at the University of Toronto. He was appointed Associate Professor in the Department of Ferrous Metallurgy, now the Department of Energy Science and Technology, at Kyoto University in 1985 and became Full Professor in 1996. On several occasions he served as Department Chair. He held visiting Professorships at the University of Toronto, the University of New South Wales, and the Royal Institute of Science and Technology in Stockholm and was granted the title of Honorable Professor by North Eastern University in China. He was a member of the International Editorial Board of "Transactions of the Iron and Steel Society of AIME" and "High Temperature Materials and Processes." He presented numerous courses on metallurgical chemistry to steelmaking engineers and researchers in Japan and countries overseas. He published over 200 technical papers and 2 books and obtained over 30 patents. He had a strong interest in the development of electrochemical sensors for the measurement of the chemical potentials of species in

molten copper as well as in molten iron and steel and steelmaking slags. He was the inventor of a "Silicon Sensor" and an "FeO Activity Determinator" both of which are manufactured commercially and currently utilized by a number of steel companies in different parts of the world. In the area of slags, he made a number of major contributions by combining excellent experimental measurements with a sound knowledge of thermodynamics. During his later years, he was deeply engaged in the environmental problems associated with the metallurgical industries and conducted studies on waste incineration in the blast furnace. His research findings on the reduction of steelmaking slag volume and fluorspar consumption have been applied within several steel plants in Japan. In recognition of his many achievements, he received the Silver Medal Award from the Japan Institute of Metals in 1991 and the Nishiyama Memorial Award from the Iron and Steel Institute of Japan in 1993. During his last days, he was Co-Editor-in-Chief for this Treatise on Process Metallurgy. May it serve as a tribute to his numerous contributions.

David R. Gaskell, (1940 – 2013)

A Memorial Tribute



David Robert Gaskell was born in Glasgow, Scotland where he attended Glasgow University and The Royal College of Science and Technology. He received his B.Sc. and A.R.C.S.T. with First Class Honors in Metallurgy and Technical Chemistry in 1962 after which he spent two years working in England with the chemical industry. He married Sheena Morrow in 1964 and they had three children, Sarah, Claire and Drew. Shortly after their marriage they immigrated to Hamilton, Canada where David

conducted graduate studies at McMaster University under the supervision of Professors R. G. Ward and A. McLean. His Ph.D. degree was awarded in 1967 with a thesis entitled: "The Densities of Liquid Silicates Containing Iron Oxide at 1410°C." Following his Doctoral studies, David joined the University of Pennsylvania as an Assistant Professor where he worked closely with Professor Geoff Belton. In 1982 he moved to Purdue University as a Professor of Metallurgical Engineering. During his career, Dr. Gaskell served as a Visiting Professor working with Dr. Charles Masson at the Atlantic Regional Laboratory of the National Research Council of Canada in Halifax, Nova Scotia (1975–1976) and as a Visiting Professor at the G.C. Williams Co-operative Research Centre for Extraction Metallurgy at the University of Melbourne (1995).

Professor Gaskell was gifted with an exceptional combination of intellect and curiosity and particularly enjoyed his teaching, his research and his discussions with students. He served as thesis advisor for numerous graduate students as well as faculty mentor for dozens of undergraduate student projects. He was the recipient on several occasions of the Schuhmann Best Teaching Award in Materials Engineering. Dr. Gaskell was a prolific writer with numerous publications in journals and conference proceedings. He was known internationally for his classic textbooks "Introduction to Metallurgical Thermodynamics", "An Introduction to the Thermodynamics of Materials", and "An Introduction to Transport Phenomena in Materials Engineering". He was also involved in professional activities, including the Metallurgical Society of AIME, Alpha Sigma Mu (President, 1985–1986) and the Iron and Steel Society Transactions International Advisory Board. In 1977 Dr. Gaskell was named a Distinguished Alumnus of McMaster University and in 2000 was the recipient of the John F. Elliott Memorial Lectureship Award from the Iron and Steel Society of AIME. At the time of his death, David was serving as one of four distinguished reviewers for this Treatise on Process Metallurgy. He will be remembered with great fondness by many friends around the world not only for his intellectual achievements, and they were many, but also for his laughter, his sense of fun and his ability to play the bagpipes.

PREFACE

This book, "Treatise on Process Metallurgy", consisting of three volumes, aims to provide a comprehensive work that is intended to be a reference source for industrial and academic researchers and to provide material for teachers of process metallurgy. This effort was inspired by the successful series on Treatise for Physical Metallurgy by Robert Cahn and Peter Haasen published by Elsevier that has become a standard text found on the shelves of most academics and industrial metallurgists. We hope to mirror this success in the field of Process Metallurgy. This work is intended to provide the most pertinent contemporary developments within process metallurgy and offer a single complete collection of information on metal extraction processes from atomic level to industrial production.

The book is an important milestone in the development of technologies in metal extraction and refining that have evolved over the past millennia. After humans discovered fire and started using this energy source for metal extraction, the field of process metallurgy has grown from an art to an area of advanced technology. Growth has been significant over the past 200 years, and over the past five decades it has been exponential. Although there are books available describing well-defined aspects of the subject, it is rather surprising that we do not yet have a comprehensive volume which covers the broad spectrum of topics that constitute "process metallurgy". The current endeavor is aimed at addressing this deficiency.

An important phenomenon that has happened over the years is the separation of the subject of process metallurgy into ferrous and non-ferrous extraction processes. While the underlying principles are the same for both areas, the enormous impact of iron and steel on human civilization has given ferrous metallurgy a special place. Process design in the case of non-ferrous metals such as copper, lead and zinc, has often lagged behind that in iron and steelmaking. Over the course of time, the synergistic effects of the interactions between these two major areas of process metallurgy were lost. The present work is designed to bridge this knowledge gap.

Another development, which has manifested itself especially in Europe, is the division between "Theoretical Process Metallurgy" and "Applied Process Metallurgy". Fortunately, this division is not encountered to the same extent within Northern America. This division between theory and practice can be attributed in large part to the eagerness of industry to solve their immediate problems within tightly defined conditions and within the shortest possible time frame. As a consequence, in the absence of proper theoretical foundations, the solutions tend to be empirical in character and of limited applicability. In this context, it is worth emphasizing that no solution is generally applicable without proper theory, and no theory is particularly helpful, if it cannot be applied.

Another objective of this Treatise therefore, is to provide a bridge between fundamental concepts and practical applications.

The current work aims to present a comprehensive overview of the broad field of process metallurgy, bridging the above-mentioned gaps. It begins with a historical perspective of the development of metal extraction processes from the earliest of times to today's state-of-the art. There are thirteen chapters with about twenty five editors and eighty specialists, who have contributed to particular subject areas within which they

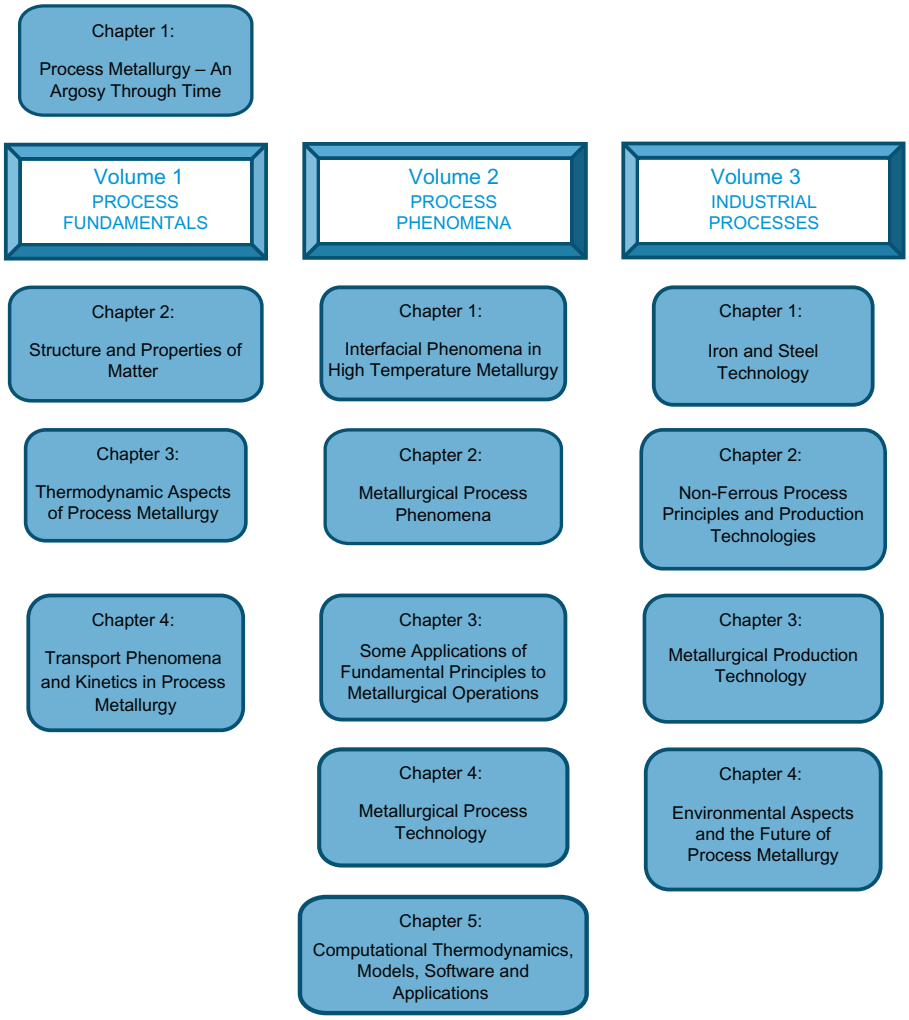


Figure. The flowchart of chapters in the Treatise.

are recognized experts. The development of the subject through these chapters is outlined in the following flow-chart.

The book is divided into three main streams. Following the first chapter which presents a birds-eye view of the history of metal extraction from stone-age to modern times, Chapters 2–4 present the process fundamentals. The second group of chapters on Process Phenomena, *viz*. Chapters 1–5, link the micro-modeling of process phenomena to macro-modeling of industrial processes, reactor technologies and computational models for process simulations. The third group deals with Industrial Processes. Chapters 1 and 2 present details of modern industrial practice for the extraction and refining of ferrous and non-ferrous metals respectively. Chapter 3 describes the design of metallurgical plants including the logistics, economics, intellectual property rights, upscaling and some case studies. The last chapter, Chapter 4, addresses the environmental problems existing today and the directions we should take for a better future. All chapters use the same nomenclature and symbols so that the reader can more readily see the links between related areas.

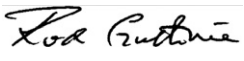
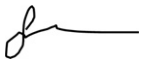
As the subject area is broad, the Treatise was designed as a multi-author work. The editors were asked to choose their contributors so that one red-thread passed through any particular chapter. While the potential problem of different schools of thought in each area had to be resolved, the editors took care that, where necessary, other schools of thought were presented, without causing confusion. The editors and contributors are from all parts of the world and formed a virtual forum of noted metallurgists who have worked in harmony for a period of more than two years. As the Board of Editors-in-Chief, it has been a distinct privilege to bring these leading members of the process metallurgy community together. We were also fortunate to obtain four world-famous metallurgists to review the chapters, so that their views could be implemented before the manuscripts were printed.

The publication of this Treatise is timely, as many of the present younger generation do not perceive Process Metallurgy as a "high-tech" area compared to more recent technologies, such as electronic-, bio- and nano-materials. The work is intended to show to the coming generations that Process Metallurgy is a continuously evolving subject area, like a flowing river, collecting tributaries from adjoining areas: sensor developments, signal processing, physical and mathematical modeling, automation, robotics and business management. It can be said, without exaggeration, that Process Metallurgy has had a major impact on the development of human civilization, and will continue to exert a powerful influence on metals production and the generation of advanced materials, for many decades to come.

The Board of Editors-in Chief expresses its deep gratitude to Staff Members at Elsevier who proposed the concept of a treatise on Process Metallurgy and who encouraged and assisted it throughout this activity. The generous support of Chief Editor, Seshadri Seetharaman, by the Swedish Steel Producers Association is also greatly

appreciated. Finally, the Editors-in-Chief express their sincere thanks to the chapter editors, contributors and reviewers, for providing their valuable time and expertise, in order to bring this endeavor to a successful conclusion.



Seshadri Seetharaman
Stockholm

Alexander McLean
Toronto

Roderick Guthrie
Montreal

Seetharaman Sridhar
Warwick

EDITOR IN CHIEF



Seshadri Seetharaman received his Ph.D. degree in Metallurgy from Indian Institute of Science, Bangalore, India, in the year 1971. He joined the Royal Institute of Technology, Stockholm, in 1973 as Senior Research Associate and became Associate Professor in 1981. Dr. Seetharaman was installed in the Chair of Theoretical Metallurgy in 1990 and he retired from this position at the end of 2010. Professor Seetharaman has about 350 peer-reviewed publications in leading journals in Metallurgy, about 150 conference presentations, and 10 patents. His major scientific interests are the fundamentals of Process Metallurgy that covers thermodynamics, transport phenomena, thermophysical properties of high temperature systems, and interfacial phenomena. He was also involved in the teaching of the above subjects.

Professor Seshadri Seetharaman has been nominated eight times as the best teacher in Materials Design teaching program at the Royal Institute of Technology. He has been awarded the President's Award in 1994 for meritorious contributions in teaching. He was selected as the best teacher of the Royal Institute of Technology in 2004.

Professor Seshadri Seetharaman has been awarded the Brimacombe Prize for the year 2010. He is an Honorary member of the Iron and Steel Institute of Japan, Honorary doctor at the Aalto University in Finland, Honorary Professor at the Metallurgical Academy of Ukraine as well as at The University of Science and Technology Beijing. He also received the Distinguished Alumni Award of the Indian Institute of Science, Bangalore, in the year 2013.

CO-EDITORS-IN-CHIEF



Alexander McLean

Following graduation with degrees in Applied Chemistry and Metallurgy from the Royal College of Science and Technology and the University of Glasgow, Dr. McLean spent 5 years at McMaster University before moving to Jones and Laughlin Steel Corporation in Pittsburgh. He joined the University of Toronto in 1970, and in 1984 the Ferrous Metallurgy Research Group was formed with Professor McLean as Director. He served as Department Chair from 1992 through 1997 and was appointed Professor Emeritus in 2002. He is an Honorary Member and elected Fellow of several organizations including AIME, The Iron and Steel Institute of Japan, the Royal Society of Canada, and the Canadian Academy of Engineering. He is a recipient of the Queen Elizabeth II Diamond Jubilee Medal and received Honorary Doctorates from the University of Miskolc and the University of Strathclyde. He has published extensively in the areas of iron and steelmaking and materials processing.



Roderick Guthrie

Roderick I.L. Guthrie, Ph.D. (Imperial College), ARSM, Eng., is the Macdonald Professor of Metallurgy and Director of the McGill Metals Processing Centre. An Honorary Member of ISIJ, Distinguished Member of AIST, Fellow of the Canadian Institute of Mining and Metallurgy, Fellow of the Royal Society of Canada, and Fellow of the Canadian Academy of Engineering, he is the author of two text books concerning *Engineering in Process Metallurgy* and *The Physical Properties of Liquid Metals*. The winner of the 2006 Killam Prize for Engineering, he was co-inventor of the successful LiMCA process for detecting inclusions in liquid metals, and also of the HSBC process for casting steel and aluminum alloy sheets. As a researcher, he has been keenly interested in the application of fluid flow, heat, and mass transfer phenomena in the description of metallurgical processes. A long-time consultant to the steel industry, Dr. Guthrie has worked in all segments of an integrated steelplant, from blast furnaces through steelmaking and hot rolling mills, to annealing and finishing lines.



Seetharaman Sridhar is currently the Tata Steel/RAEng Joint Chair for Research into Low Carbon Materials Technology. He was until recently the POSCO Professor of Steelmaking at Carnegie Mellon University and the co-director of the Industry–University Consortium, Center for Iron and Steelmaking Research (CISR) of which Tata is a member. He received his Ph.D. from the Massachusetts Institute of Technology and his undergraduate degree from the Royal Institute of Technology in Sweden.

His research and teaching interests lie in the physical chemistry of metal processing. He has published over 125 journal papers in the areas of secondary refining, casting and mold slags, coal gasification, oxidation, and hot-shortness. He has received the following best paper awards: Marcus Grossman Award from ASM, the Herty Award from ISS, The Spriggs Phase Equilibria Award from ACERS, and the Jerry Silver Award from AIST. He has also received the Friedrich Wilhelm Bessel Research Prize from the Alexander Von Humboldt Foundation and the NSF Career Award, both for his general contributions in research. As a teacher, he was recognized by the Benjamin Teare Teaching Award by Carnegie Institute of Technology, the Philbrook Prize by the MSE Department at CMU, and he was the recipient of the 2011 J.F. Elliott Lecturer Award for AIST. He is the editor for *AIST Transactions* and an associate editor for *Metallurgical and Metals Transactions A, B, and E*. He is also on the International Advisory Board for *Steel Research International* and *ISIJ International*.

CONTRIBUTORS TO VOLUME 1

Peter Hayes
School of Chemical Engineering, University of Queensland, Brisbane St Lucia, Australia

Eugene Jak
School of Chemical Engineering, University of Queensland, Queensland, Australia

Yoshio Waseda
Institute of Multidisciplinary Research for Advanced Materials (IMRAM), Tohoku University, Sendai 980-8577, Japan and Research Center for Electron Photon Science, Tohoku University, Sendai 982-0826, Japan

Ivan Egry
Institut für Theoretische Physik, RWTH Aachen, Germany

Kenneth C. Mills
Department of Materials, Imperial College, London, United Kingdom

Miyuki Hayashi
Department of Metallurgy and Ceramics Science, Tokyo Institute of Technology, Tokyo, Japan

Lijun Wang
Department of Physical Chemistry, University Science and Technology Beijing, Beijing, China

Takashi Watanabe
Department of Chemistry and Materials Science, Tokyo Institute of Technology, Tokyo, Japan

Rita Khanna and Veena Sahajwalla
Centre for Sustainable Materials Research and Technology, School of Materials Science and Engineering, The University of New South Wales, Sydney, New South Wales, Australia

Kazuki Morita
Department of Materials Engineering, Graduate School of Engineering, The University of Tokyo

Nobuo Sano
University of Tokyo, Dept. of Metallurgy, Tokyo 113, Japan

Masanori Iwase[‡]
Graduate School of Energy Science, Kyoto University, Japan

Masakatsu Hasegawa
Graduate School of Energy Science, Kyoto University, Japan

Hideki Ono
Division of Materials and Manufacturing Science, Graduate School of Engineering, Osaka University, Japan

[‡] Late Prof.

Takahiro Miki
Metallurgical Process Engineering, Department of Mettallurgy, Graduate School of Engineering, Tohoku University, Japan

Tetsuji Hirato
Department of Energy Science and Technology, Kyoto University, Kyoto, Japan

Viswanathan N. Nurni
Minerals and Metals Research Laboratory (MiMeR), Luleå University of Technology, Luleå, Sweden

N.B. Ballal
Mechanical Engineering Dept, IIT Bombay, Mumbai, India

Bharath N. Ballal
Centre of Excellence in Steel Technology (COEST), Department of Metallurgical Engineering and Materials Science, Indian Institute of Technology Bombay, Mumbai, India

Seshadri Seetharaman
Royal Institute of Technology, Stockholm, Sweden

Seetharaman Sridhar
Tata Steel and Royal Academy of Engineering Joint Chair for Research into Low Carbon Materials Technology WMG, The University of Warwick, Coventry, CV4 7AL, UK

ACKNOWLEDGEMENT

The Editors-in Chief express their sincere gratitude to
"Jernkontoret"- the Swedish Steel Producers' Association

for their generous support to Professor Seshadri Seetharaman towards the production of this book.

The support from the Iron and Steel Institute of Japan is gratefully acknowledged.

THE REVIEW COMMITTEE

The various chapters of the Treatise were distributed for review between the following internationally renowned metallurgists: Professors T. Emi (Japan), D. R. Gaskell (USA), D. C. G. Robertson (USA) and O. Wijk (Sweden). After the sad demise of Professor Gaskell, the review of his assigned material was completed by the Board of Editors-in-Chief and Dr. V.I. Lakshmanan (Canada). The Editors-in-Chief express their gratitude to the Reviewers for their invaluable contributions in improving the quality of the book.

CHAPTER 1

Process Metallurgy—An Argosy Through Time

Seshadri Seetharaman
Royal Institute of Technology, Stockholm, Sweden

Contents

1.1. Introduction to Metallurgical Processing 15

1.1. INTRODUCTION

Metallurgy is a subject evolved over a few millennia, at least the past 3000 years, probably since the dawn of known human history. Old Greek, Hebrew and Hindu scriptures allude to metals like gold, silver, copper, iron, lead, and tin as well as nonmetals like sulfur and carbon [1]. Ancient Greek philosopher Heraclitus among others believed that all substances had a single component. The concept of chemical elements itself has gone through immense changes, from ancient times through Alchemy and Middle Ages to Modern Times. Both Greeks (Empedocles) and Hindus (the Vedas) were in agreement that the basic elements were earth, water, air, and fire, while the Hindus had a fifth component, ether or vacuum. Even the Greek philosopher, Demokritos, had vacuum as the matrix in which particles which were indivisible moved about. Thus, the world of materials had at least four components as described by the illustration given in Figure 1.1, leaving aside the nonmaterial, the ether (Figure 1.1).

The imagination of the modern scientist leads to drawing parallels to ancient thoughts and modern science, obviously a wishful thinking, albeit very fascinating (Figure 1.2).

As we know today, the ancient basic elements are in fact more complex, as for example, air consisting of nitrogen and oxygen apart from other minor gases and earth being most complex of all with mixtures of various compounds.

The ancients had even thought of combinations of these basic elements to form the substances on the Earth, the predecessors to modern chemical equations. The adherents of "Al-Chemie" (the word comes from "Chemia" prefixed by the Arabic definite form "Al") starting from about 300 A.D. were convinced that a base metal such as copper could be converted to a noble metal, gold. Despite the fruitlessness of these efforts, some

Treatise on Process Metallurgy, Volume 1
http://dx.doi.org/10.1016/B978-0-08-096986-2.00026-6
© 2014 Elsevier Ltd.
All rights reserved.

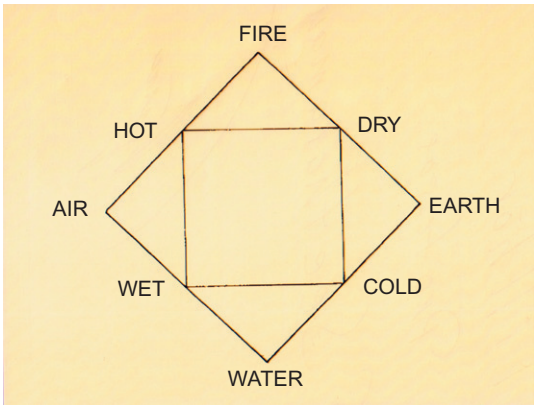


Figure 1.1 The four elements occurring in nature [2].

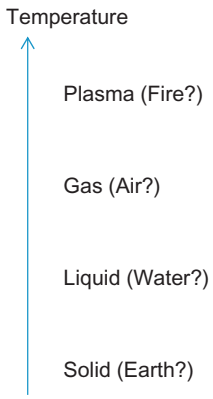


Figure 1.2 An imaginary parallelism between ancient concept of elements and the states of matter according to modern science.

interesting concepts seemed to have evolved. The combinations of the aforesaid four elements, according to the alchemists, can lead to two entirely different "principles": mercury and sulfur, the former standing for the metallic *principle* while the latter for "destruction of metallic principle" [2]. These probably were the forerunners of the modern concept of chemical reactions as represented in Figure 1.3.

Interestingly, Paracelsus from Switzerland (1493–1541) introduced, apart from metallic and nonmetallic principles, the third one, namely *Salt*.

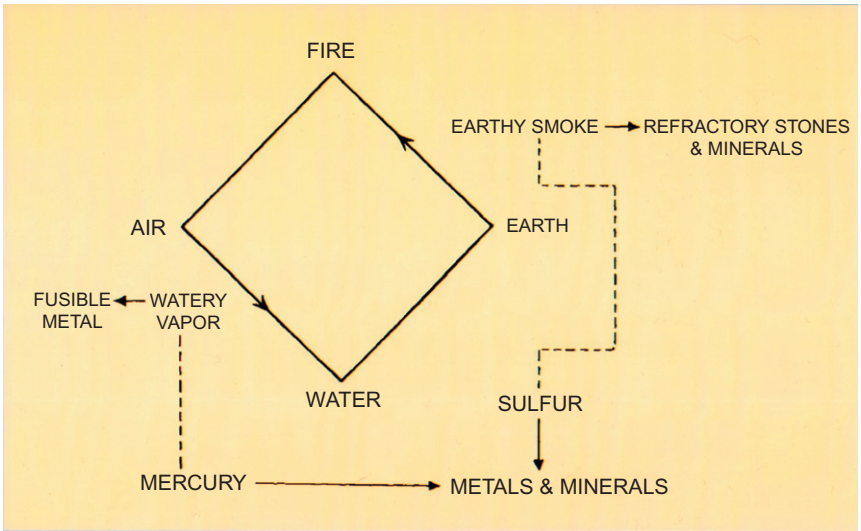


Figure 1.3 Ancient concept of chemical reactions leading to formation of materials [2].

1.2. ALCHEMY AND THE DISCOVERY OF METALS

The alchemists could associate the various metals known at that time with heavenly bodies and these symbols are presented in Figure 1.4.

Later in the seventeenth century, these symbols were elaborated to more fascinating figures representing, at the same time, the properties of the elements as shown in Figure 1.5a–d.

The evolution of human civilization is often conceived as the advancement in human knowledge in using different materials. The first epoch of this kind is often referred to as "Stone Age," where the tools and weapons consisted of stone materials, crudely shaped to serve the purpose. This was followed by the "Bronze Age" or Chalcolithic Period (Greek: chalcos = copper; lithos = stone) when humans were able to produce copper

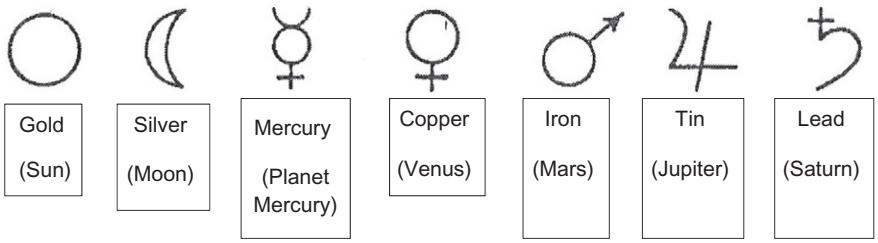


Figure 1.4 The alchemists' symbols for different metals known to them [3].

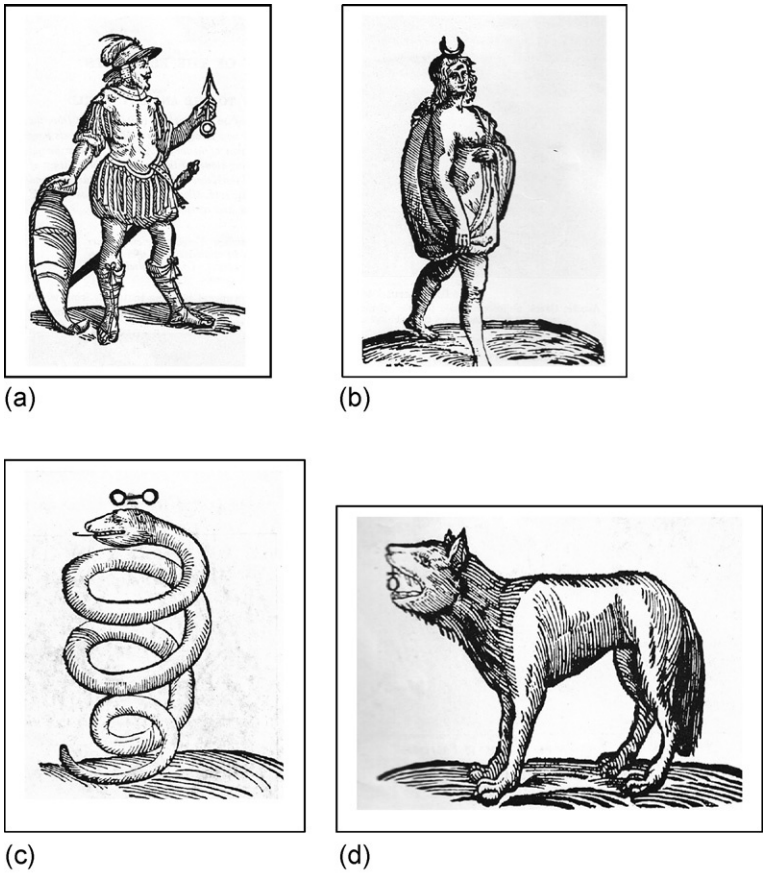


Figure 1.5 Fascinating symbols for a few elements dated to the seventeenth century [1]. (a) Iron, (b) silver, (c) arsenic, and (d) antimony.

metal, followed by the "Iron Age" wherein the humans could master the processing of iron ore and get the metal.

In modern times (1944), Ellingham in England developed [4] a diagram correlating the ability of a metal to form its oxide, which he represented as the Standard Gibbs Energy change (ΔG°), a concept that will be explained in the coming chapters of this book as a function of temperature. While all the metals and their corresponding oxides can be represented in Figure 1.6, it presents a few of the common metals and their corresponding oxides.

Gold is above the zero line which would mean that it would be stable as native metal. The line corresponding to gold is not shown in the figure. The metal silver is expected to be stable above ca. 440.5 K and the oxide Ag_2O is formed below this temperature. This probably explains silver getting blackened at room temperature and needs to be polished.

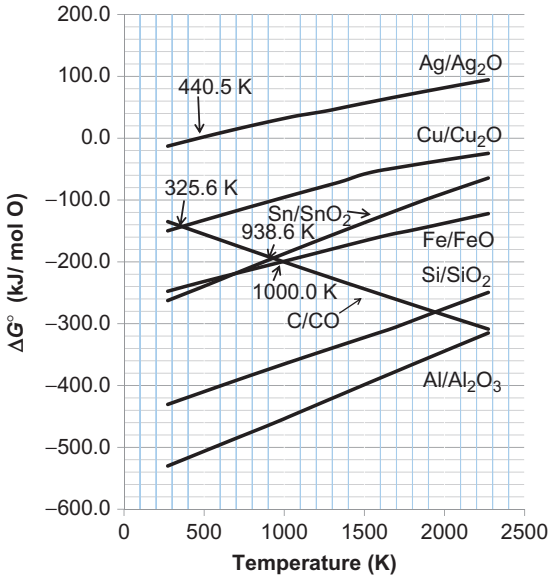


Figure 1.6 The Ellingham diagram for selected elements. *Courtesy: Dr. Lidong Teng.*

Copper is very near the top of the diagram while aluminum is at the bottom. Thus, copper metal would be more stable compared to metallic aluminum and the oxide of copper could be easily reduced to the metal. On the other hand, it is difficult to reduce aluminum oxide to metallic aluminum. The stable oxides such as alumina (Al_2O_3) and silica (SiO_2) which are common components of stone would be the stable materials. These were used during the Stoneage, without any pyroprocessing. With the discovery of fire, clay could be fired to make pottery.

Carbon, produced in ancient days as wood charcoal, was the common reductant used in reducing the oxide to the metal. Figure 1.6 presents even the C/CO line, representing the ease with which carbon forms carbon monoxide. For thermodynamic reasons to be explained in the later chapters, the C/CO line has the opposite slope compared to the M/MO lines (where "M" stands for the metal and "MO" stands for the oxide of the metal "M"). This, in simple words, can be explained as the effect due to the formation of a gas molecule as the product.

Let us consider the reduction of the oxides of the metals. The crossing point between the metal/oxide line and the C/CO line would mark the temperature above which the metal oxide MO would be reduced to metal M by carbon to form CO as carbon monoxide is more stable than MO according to the reaction

$$MO + C = M + CO \tag{1.1}$$

In the case of copper, the crossing point occurs at 325.6 K. In order to increase the reaction rate, the temperature may have to be increased by a couple of hundred degrees.

Even then, the reaction temperature would be relatively low and could easily be achieved during the initial stages of the use of fire. This would perhaps explain the Bronze Age, which is divided into three different evolution stages. Metal tin forms very "stable" alloys with copper (the concept of stability is explained on the basis of Gibbs energy in the later parts of the book) and tin oxide would thus be reduced simultaneously if mixed with copper oxide, leading to the formation of bronze. An interesting experiment was conducted at the Royal School of Mines [5] in London wherein a mixture of 15 lbs (1 lb = 454 g) copper ore (carbonate) containing 30 mass% copper, 10 lbs of cassiterite (tin ore) containing 29 mass% Sn, 7.5 lbs of limestone, and 10 lbs of wood charcoal was heated in a pit furnace of the simplest type. The experimenters could successfully synthesize bronze, thereby confirming the ancient method of bronze production. They also found a certain loss of tin to the slag, which would be expected from thermodynamic considerations.

As the humans started to understand the nature of fire and started finding ways of increasing the temperature, as for example, by the use of blowing into the fire through a pipe, even solid-state reduction of iron oxide to iron could be achieved at a temperature of about 1000 K as shown by the crossing point temperature between Fe/FeO line and C/CO line.

The geographic region in which iron was first produced is very uncertain. As mentioned earlier, there are references to iron in Biblical and Hindu literature. The iron pillar in Delhi, weighing about 6 ton and 7.25 m tall, dated around the first century A.D., has been standing in the open, without rust. This is shown in Figure 1.7.

Pliny the Elder (23–79 A.D.), Figure 1.8, was worried even in those days about the "power" of iron. While he acknowledged the usefulness of iron in construction, tools, etc., he lamented "....as to bring death upon man with still greater rapidity, we have given wings to iron and taught it to fly!.... Nature in her conformity with her usual benevolence, has limited the power of iron by inflicting upon it the punishment of rust..." [1]—How true even today!

In ancient days, the art of sword making was well developed in the Middle East and Europe. An example of the Viking sword from 800 A.D. is shown in Figure 1.9. Iron technology probably came to the Kyushu Island of Japan from Korea. Interestingly, one very learned metallurgist had the following thought regarding the old kanji character for steel, viz.,

- 金 (metal) combined with 夷 (the race living in the east of China, viz., Korean) ⟹ 金 + 夷 = 鋲 (one of the old letters for steel!).

In later years, the Japanese had developed the Tatara steelmaking process which enabled them to make world-famous Samurai swords, an art even today finding an important place in Japanese society.

Beyond the Iron Age, the history of metal synthesis stood still until the English scientist Michael Faraday discovered electricity and electrolysis. It was found that electricity could be used to "break" the metal from its compounds and thus we were able to go



Figure 1.7 The Delhi iron pillar. *Courtesy: Mrs. Yukari Izumi.*

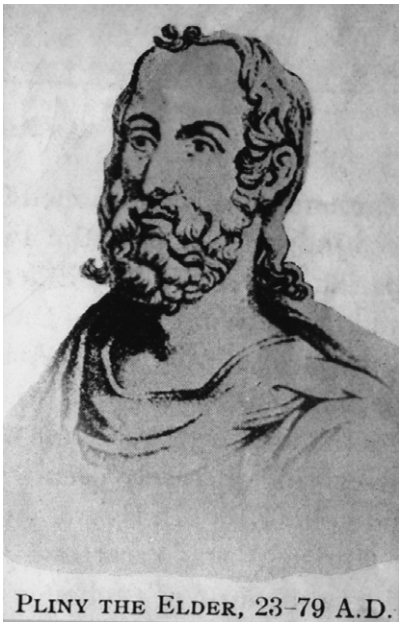


Figure 1.8 Pliny the Elder [1].

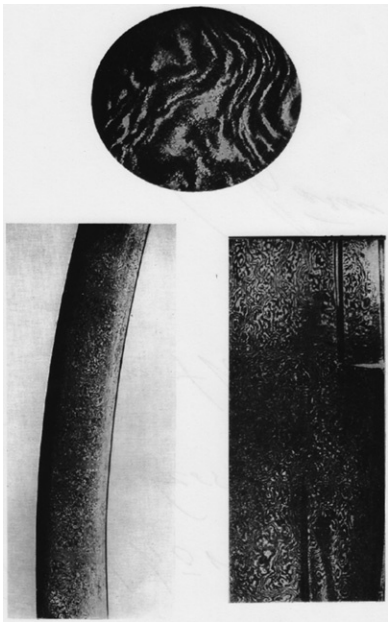


Figure 1.9 A Viking sword from 800 A.D. [2].

further down in the Ellingham diagram in Figure 1.6 to other metals that are produced today. It can also be surmised from this figure that, by increasing the temperature sufficiently high, to 2500 K, even the very stable aluminum oxide could be reduced by carbon. This is the basis for the carbothermic process for aluminum production being developed in recent days.

The stability of the metal compounds as also the similarity of the chemical properties of the metals posed a serious challenge to the chemists in Europe. By careful chemical methods, the elements could be isolated and identified. Most of the metals were discovered in Europe during the sixteenth and seventeenth centuries. A brief summary of the metals discovered and the country that contributed are presented in Table 1.1.

Alkali metals, Na and K, were discovered by Sir Humphry Davy by electrolyzing the hydroxides. Most of the rare earth metals were isolated by Swedish chemists and these metals mostly bear Scandinavian names. The principle of having unified abbreviations, as for example, Au for gold (Latin: Aurum) based on the Latin names of the elements, was suggested by Berzelius [3]. For a complete history of the discovery of various elements, the best source is the book on this subject by Weeks [1]. The most significant milestone is the periodic table developed by Mendeléeff (1869) and at about the same time by Lothar Meyer. The periodic table commonly used today is on the lines of the formulation by Mendeléeff. This is reproduced in Figure 1.10.

Table 1.1 The Discovery of Metals and Metalloids [5]

Nationality of Discoverers	Metals	Metalloids
Swedish	Co, Ni, Mn, Mo, Ta, Ce, Li, Th, V[a], La, Er, Tb, Y, Sc, Ho, Tm, didymium[b]	Se
British	Ti, Nb, Pd, Os, Ir, Rh, Na, K, Ba, Sr, Ca, Mg, Tl	B[a]
French	Cr, Be, Ga, Sm, Dy, Ra, Ac, Eu, Lu, Fr	B[a], Po
American	Np, Pu, Pm, transuranium elements	–
German	Al, U, Cs, Rb, In, Cd, Pa, Zr, Re	Ge
Spanish, Mexican	Pt, W, V[a]	–
Austrian	Pr, Nd	Te
Russian	Ru	–
Italian/American	Tc	–
Dutch, Hungarian	Hf	–

[a]Independent.
[b]Split into Pr and Nd by the Austrian chemist Carl Auer.

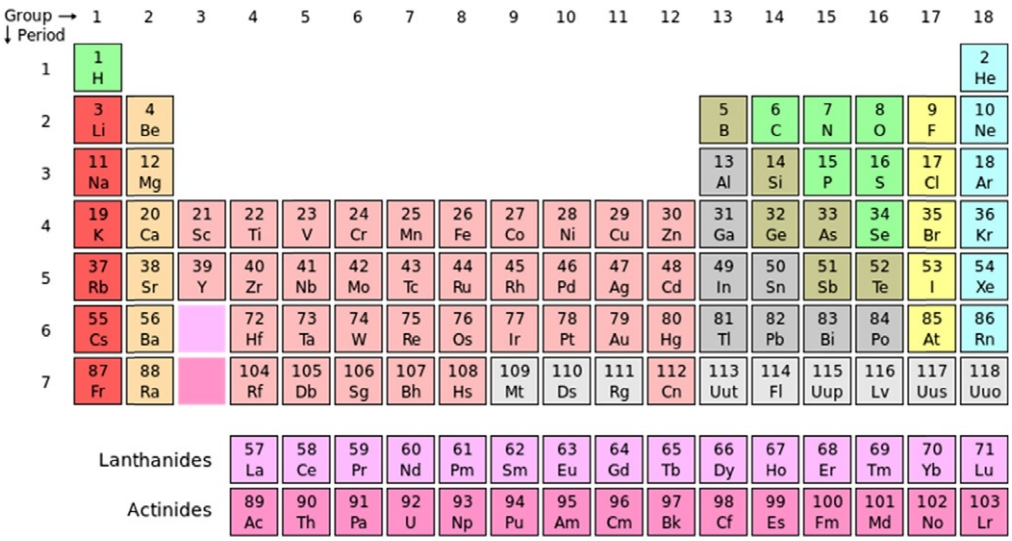


Figure 1.10 The periodic table. *Wikimedia Commons—License free.*

1.3. DEVELOPMENT OF EXTRACTION PROCESSES

Regarding the development of processes for extracting metals, the historical development is even more fascinating. An illustration of the mercury distillation still, one of the oldest metallurgical reactors from 1540, is shown in Figure 1.11. Sulfur was distilled in a similar fashion.

A sketch of an ancient "metallurgical plant" shown in Figure 1.12 with the pyrometallurgical and the forging operations is extremely fascinating.

Earlier pit furnaces were commonly used for the extraction of metals from ores. Such a furnace with air blowing using human power is shown in Figure 1.13.

A shaft furnace from Roman period is shown in Figure 1.14.

With the introduction of bellows powered by water power, the technology improved and higher temperatures could be achieved. A typical furnace of this type from the Middle Ages is shown in Figure 1.15.

In later days, iron making had grown to a big industry with a strong labor-intensive aspect. Figure 1.16 illustrates the situation sketched by an unknown artist [6] of Lassåna Works in Sweden.

The picture depicts the crushing of the ore in the foreground, old timber-clad blast furnace and the new blast furnace on the left, a timber hammer forge in the center, and a sawmill to the right. In the background, ore and charcoal are shoveled. The inscription in the foreground says "The reward is NOT worth the labour!" Even though the details are not very clear in this painting, one gets a broad idea of an iron-making plant in those days.

The evolution of metallurgical processes and reactors has grown today into full-grown science and technology. Metal making was upscaled over the years from backyard mini units to mega plants handling millions of tons per year. Metallurgy has come a long way from the state of art during the early days of Alchemy to the present-day technology-intensive field expanding into a number of areas such as process chemistry, process design,

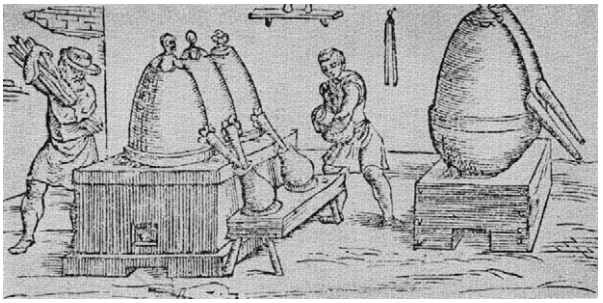


Figure 1.11 Mercury still from the year 1540 [1].



Figure 1.12 An ancient metallurgical plant [2].

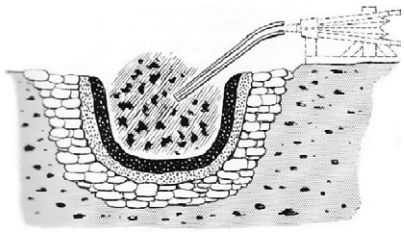


Figure 1.13 A diagrammatic sectional elevation of the simplest form of iron-smelting furnace in antiquity [2].

process technology, process economics, and, most important of all, environmental metallurgy. Metallurgical processes are mostly steered by online computer models, with sensors following the compositional and temperature changes in the reactor. Metal making has attained the status of a high-technology field including the fields of automation and robotics. What was carved out from chemistry, physics, and mechanical engineering

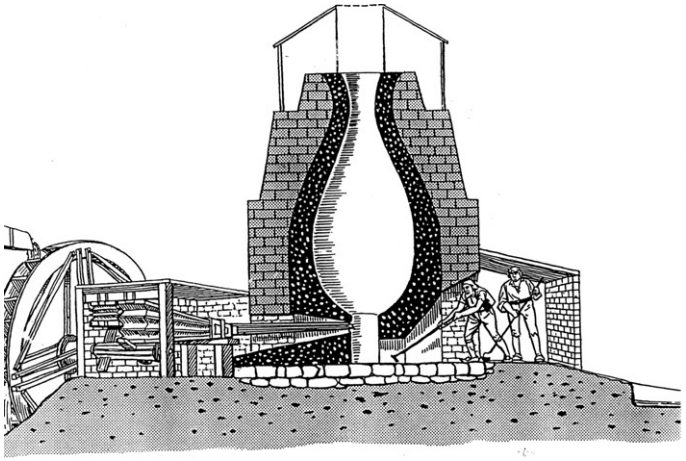


Figure 1.14 A diagrammatic reconstruction of a Roman shaft furnace [2].

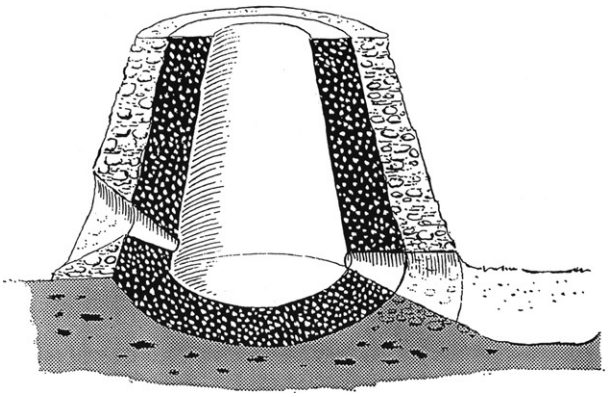


Figure 1.15 A furnace with air blast with water power, predecessor to the blast furnace of today [2].



Figure 1.16 The Lassåna Works in Sweden as conceived by an unknown artist [6] around 1680 A.D.

during earlier days has blossomed into a field that is imperative to the existence and survival of mankind. Developments in metallurgy have led to some of the greatest achievements of mankind including space travel. Some glimpses of the present-day process methods for the extraction of metals are presented in the subsequent subchapter.

ACKNOWLEDGMENTS

The author expresses his gratitude to the Swedish Steel Producers Association, especially to Mr. Göran Andersson and Mr. Yngve Axelsson for providing the author access to the library facilities and fruitful discussions. The author expresses his gratitude to Docént Lidong Teng and Mrs. Yukari Izumi for making available the figure and the photograph much needed for this chapter.

REFERENCES

[1] M.E. Weeks, Discovery of the Elements, Journal of Chemical Education, Easton, PA, USA, 1939.
[2] L. Aitchison, A History of Metals, Interscience Publishers, 1960.
[3] P. Enghag, Jordens Grundämnen. Industrilitteratur AB, Stockholm, Sweden, 1998.
[4] Ellingham, J. Soc. Chem. Ind. London 63 (1944) 125.
[5] W. Gowland, Copper and its alloys in early times, J. Inst. Metals 7 (1912) 43.
[6] F. Habashi, The Discovery of Metals, CIM Bulletin 87 (1994) 69.
[7] J. af Geijerstam, M. Nisser, Swedish Mining and Metalworking-Past and Present, National Atlas of Sweden, Norstedts Förlagsgrupp AB, Sweden, 2011.

CHAPTER 1.1

Introduction to Metallurgical Processing

Peter Hayes and Eugene Jak
School of Chemical Engineering, University of Queensland, Queensland, Australia

1.1.1. RECENT DEVELOPMENT TRENDS

1.1.1.1. Drivers for Change

Although the metallurgical industry is well established, there have been significant changes to the technologies and improvements in the performance of metallurgical processes over time; these improvements continue today with the application of modern scientific and engineering knowledge and the use of advanced design tools. The principle driving forces for technology development, changes in metallurgical practice, and process improvement in recent times stem from the need to

- Improve financial performance,
- Respond to market supply/demand for products,
- Adapt to changing sources of raw materials supply,
- Address environmental issues, including
  - energy efficiency (directly related to the CO_2 footprint),
  - hazardous emissions, and
  - discard materials,
- Improve the occupational health and safety performance of the operations.

In market-driven economies, the lowering of production costs has always been the principal driver for change in processing practice. Production costs include the direct operating and capital costs of operations. These cost reductions have been achieved through a variety of approaches depending on the commodity. For example, the metallurgical industry is capital intensive; the establishment of larger operating plants enables the capital costs/tonne to be reduced.

Improvements to existing technologies bring about incremental changes in the form of improved metal recoveries, increased process efficiencies, and higher productivities. These advances have been achieved through improved design, operation, and control. The impact of increased computing speed and capacity has changed the way we are able to monitor and store information, and with the development of sophisticated software, this provides significant opportunities for systematic analysis of the operational trends, the mathematical simulation of processes, and the consequent optimization of the process

Treatise on Process Metallurgy, Volume 1
http://dx.doi.org/10.1016/B978-0-08-096986-2.00001-1
© 2014 Elsevier Ltd.
All rights reserved.

outcomes. Examples of major improvements in process performance can be found across the range of metallurgical technologies; some notable examples include halving of the coke rate in the iron blast furnace; improving refractory technology, thus reducing downtime; extending furnace lining and campaign life, and improving design and control to reduce the energy requirements for aluminum smelting.

Step changes in technology make it possible to dramatically decrease process costs overcoming the limitations of the conventional technologies of the time. The recovery of fine gold from host rock through improved leaching technologies has replaced placer gold as the major source of this valuable metal. Improved conceptual designs come from deep understanding of process fundamentals from both scientific and engineering perspectives. The use of basic oxygen steel making has led to an order of magnitude increase in the rate in which steel can be produced in a single reactor. The development of freeze linings on furnaces has made possible continuous processes and the use of new process chemistries that could not be previously utilized. The introduction of continuous metal casting technologies has increased energy efficiency and productivity. Advances in coordination and surface chemistry have led to solvent extraction and ion exchange technologies, now enabling the selective separation of solute ions from relatively dilute aqueous process streams.

Financial and environmental drivers have resulted in the geographical redistribution of the operations with a clear trend in preferential development of the primary metallurgical operations in the developing countries and contraction in the developed countries.

Commodity prices are in the main determined by the balance in market supply and demand. This is clearly apparent with the globalization of the world economy that has emerged over the past quarter of a century. In recent times, the strategic needs of individual countries have become less important with changes to the geopolitical scene. Increased population and industrialization have led to increased demand for materials for infrastructure and manufactured goods.

The demand for commodities is determined not only by the quantities of materials required but also in some cases the development of new products. Some examples of this include the development of new steel grades and the need for clean steels; the growth in computer and solar technologies has given rise to improved methods of production of high-purity silicon.

Primary sources of supply are in the process of continuous change. These materials are, by definition, nonrenewable materials. Each ore source has different chemical and physical characteristics. As these finite supplies are exhausted and new sources are used, this must necessarily lead to changes in practice, in some case to changes in technology options. Examples of this are the changes in iron ores from high-grade lump materials to ore fines containing increasing impurity levels, the depletion of nickel sulfide deposits, and the increased sourcing of laterite or oxide-based ores.

The availability of obsolete materials and the decreased energy requirements for reprocessing are driving the changing supply of raw materials; this has resulted in increased materials recycling particularly in industrialized countries.

The past several decades have seen increased community pressure and regulatory requirements to reduce the impacts of industrial operations on the environment and to improve health and safety performance across all industries. In metallurgical industries, this has led to technology developments that, for example, reduce fugitive SO_2 emissions from base metal sulfide smelters, reduce the production of greenhouse gases, and treat process wastes to ensure that they are environmentally benign before disposal or further utilization.

1.1.1.2. Process Trends

The major changes that have occurred in metallurgical processing over the past 50 years involve moves toward

- continuous/semicontinuous processing,
- increased process intensity,
- process integration,
- recycling,
- clean production, and
- flexibility of the processes.

The use of continuous processes offers the possibility of improved throughput, control, efficiency in recovery, and reduced energy and environmental impact.

Increased process intensity has enabled increased production rates to be obtained from reactors and improved utilization of capital.

The integration of processes takes advantage of the potential for energy savings and for the recovery of valuable by-products.

New technologies are being developed for the recycling of obsolete manufactured products. In some cases, these involve the development of new dedicated reprocessing plants, in others the integration of primary and secondary processing operations.

Cleaner production is reflected in the efforts to capture and treat all process streams on site to produce benign or useful products. For example, in pyrometallurgical processes, this has meant enclosure of reactors and capture and treatment of gas and dust in these process streams.

Flexibility in process design enables operations to change and adapt to changing input/output requirements within existing plants.

1.1.2. PROCESS OPTIONS

1.1.2.1. Process Stages and Aims

Increasingly attention is being paid to all the outputs of metallurgical operations; these can be broadly categorized as:

1. The principal value metal
2. Useful by-products, e.g., other metals, compounds, energy
3. Discard/unwanted materials, e.g., wastes and residues

The industry is no longer just about metal production; it is the overall performance, the contributions from all of these outputs, that determines the sustainability or otherwise of the individual processing operations.

A wide range of physical and chemical processes are available for use in modern metal production operations. Due to factors, such as the differences in raw materials, every metallurgical plant has a different combination of processes and different combinations of technologies. Added to this, in complex process operations, the role and sequence of process stages, and interdependence of the various processes, are sometimes hard to determine. One way of looking at this problem is to consider that metallurgical operations typically involve one or more of the following stages:

Separation
Metal compound/solution formation
Crude metal production
Metal purification
Product preparation

Each stage of the operation can be achieved by a single process or a group of processes having the same process aim.

The raw materials or feed stocks for primary or recycling processes are never pure. All metallurgical operations include some form of separation in order to increase the grade or concentration of metal values in particular process streams. In the case of primary metal production, this involves initially size reduction of the ore particles and liberation or partial liberation of the minerals. This is followed by physical separations of the minerals based on differences in the physicochemical properties of the various minerals present in the process stream. In the processing of recycled materials, the simplest separation processes involve the physical sorting of materials, e.g., metals from nonmetals, or separation of different metal alloys.

In both the primary production and the recycling of metals, it is necessary to undertake chemical processing to remove chemically bound elements present in the feed materials and meet product specifications in terms of purity. These chemical process steps necessarily involve the use or formation of more than one phase so that chemical separations also take place.

When seeking to identify the optimum overall process route, from the original raw materials to final product, both physical and chemical processing stages should be considered together. However, for the purpose of the present discussion, which is focused on extractive metallurgy, only the chemical separation steps are considered.

While separation stages involve the physical or chemical removal of unwanted elements or compounds from the source or feed materials, metal compound/solution formation refers to the production of a material that is structurally and/or chemically different from the source material, or the transfer of the value species into solution in another phase that will enable the species to be further processed, for example, dissolving species into aqueous solution.

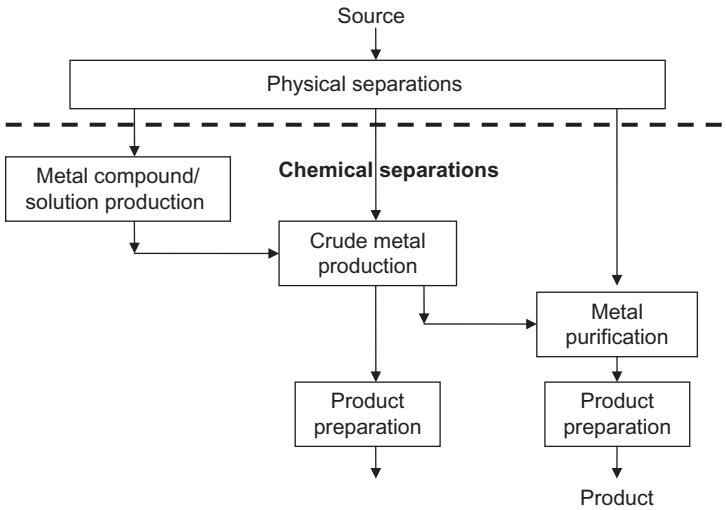


Figure 1.1.1 The hierarchy of stages and process aims in metals production. *Adapted from Ref. [1].*

Metal production refers to the preparation of an impure or crude metal, which may be a saleable product or may be further processed in the metal purification stage in which the final removal of unwanted elements from impure metal is undertaken.

Product preparation includes all processes necessary to ensure that the products are in a form suitable for sale and marketing. This may involve, for example, packaging, blending, compositional adjustments, or the preparation of materials or components having specific shapes and/or physical properties.

The process stages in metallurgical production can then be arranged systematically in the form of a hierarchy or logical sequence that directly reflects the process flow diagrams of the operation. At each of these stages, the aims of the process can be clearly identified. This sequence is illustrated in Figure 1.1.1.

In the case of recycling of metal alloys, following physical separation, the next process step moves directly to metal purification. In contrast, primary production and the treatment of complex raw materials will require combinations of the metal compound/solution formation, metal production, and metal purification stages.

In summary, the process stages of any metallurgical operation follow directly from the definition of both the sources of the raw materials and the products of the operation. Identification of these process stages provides the framework for the initial development of process flow diagram and the aims define the purpose of each stage of processing.

1.1.2.2. Alternative Process Routes

Metal oxides, sulfide, and halides are major sources of metals, and a wide variety of metallurgical processing options are available for the treatment of these materials. Some

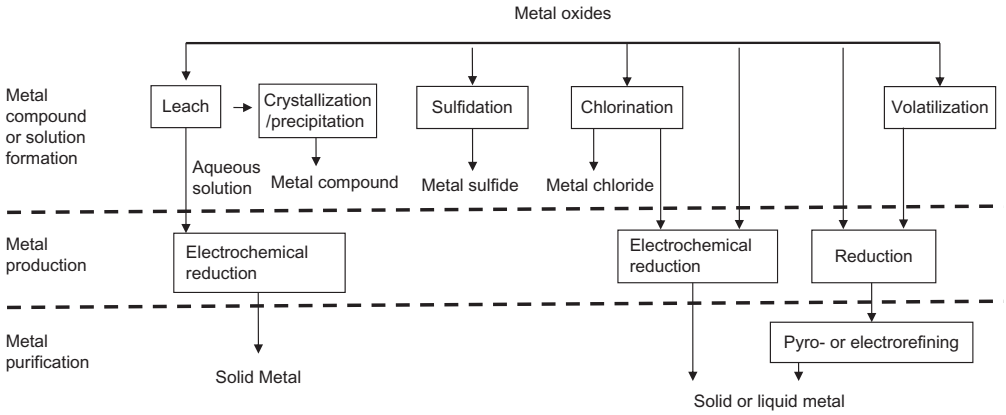


Figure 1.1.2 Alternative process routes for the treatment of metal oxides.

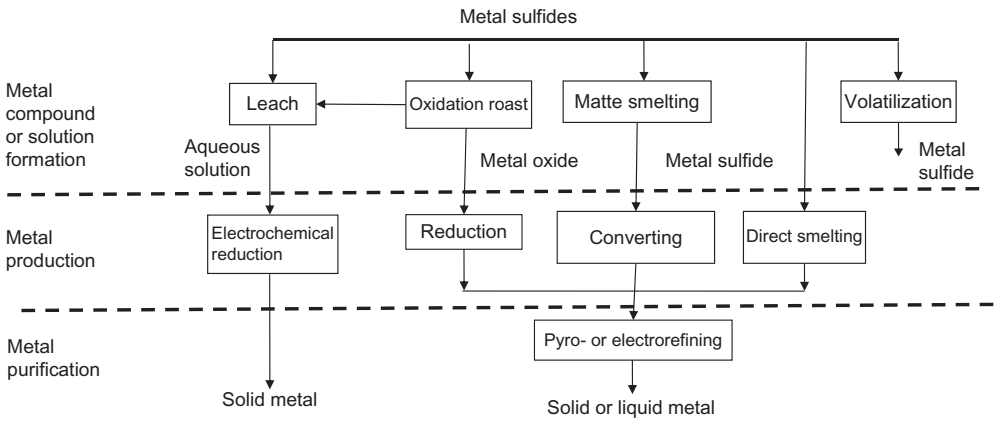


Figure 1.1.3 Alternative process routes for the treatment of metal sulfides.

of the more successful and economically viable processing alternatives used for these metal compounds are summarized in Figures 1.1.2–1.1.4.

The diagrams have been structured so as to clearly demonstrate the process stages, and aims associated with each processing stage, the metal compounds formed at each stage, and, where relevant, the physical states of the products are also indicated.

Another interesting point to note about these alternative processing routes is that often combinations of high temperature, aqueous/organic solution, and electrochemical techniques are used to obtain the desired products. Where new compounds are produced, then the reader should refer to the processing alternatives for the new

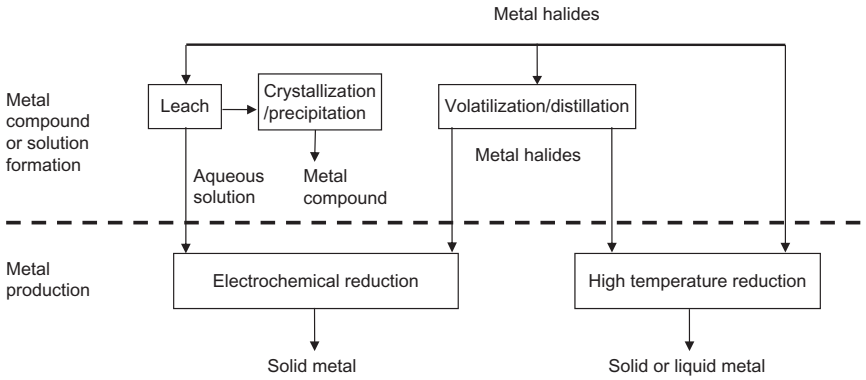


Figure 1.1.4 Alternative process routes for the treatment of metal halides.

compound if further processing is being considered, e.g., if the original material is a metal sulfide and this is transformed to an oxide, the processing options for the metal oxides should then be examined.

1.1.2.3. Alternative Process Routes for Selected Metals

The wide variety of process options and technologies available for a given operation are illustrated in the examples given in Figures 1.1.5–1.1.10. These examples are not intended to cover all process options but merely to highlight some of the more commonly used approaches in current industrial practice. For further details of the reactors used in metallurgical processes and their characteristics (see Section 1.1.3).

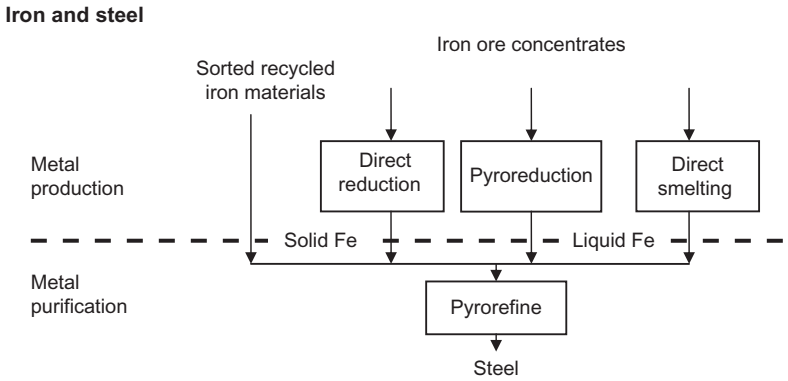


Figure 1.1.5 Alternative process routes for iron- and steelmaking.

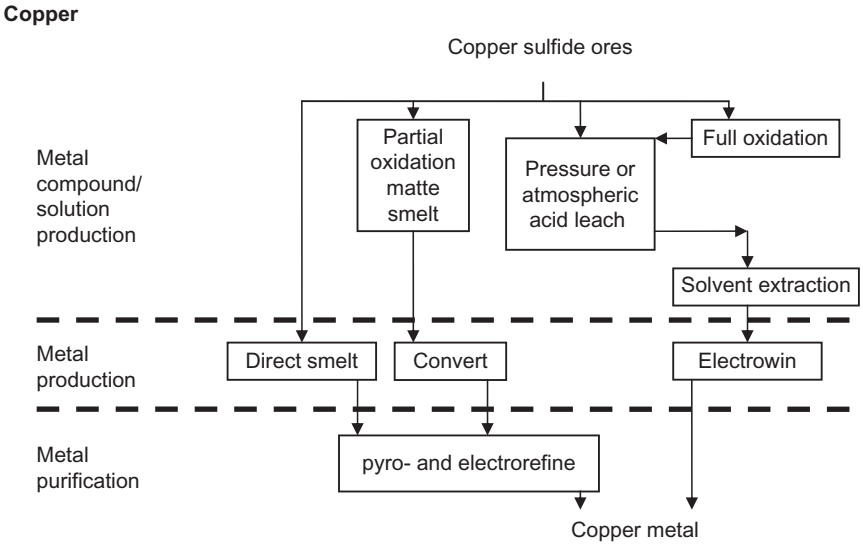


Figure 1.1.6 Alternative process routes for copper production from copper sulfide ores.

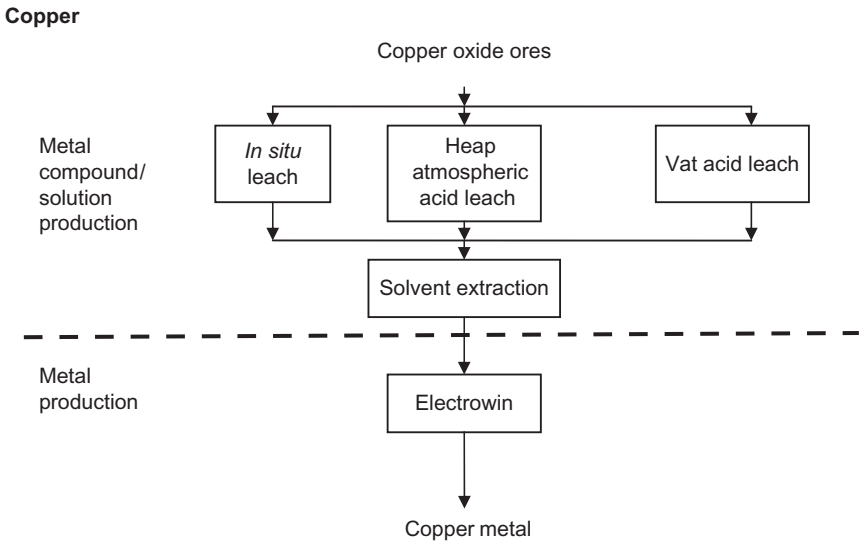


Figure 1.1.7 Alternative process routes for copper production from copper oxide ores.

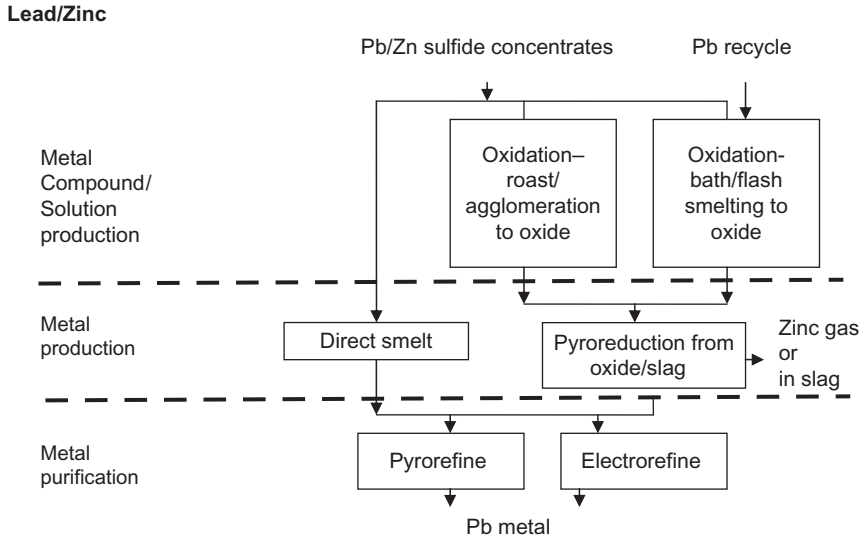


Figure 1.1.8 Alternative process routes for lead metal production from lead/zinc sulfide ores, residues, and recycled materials.

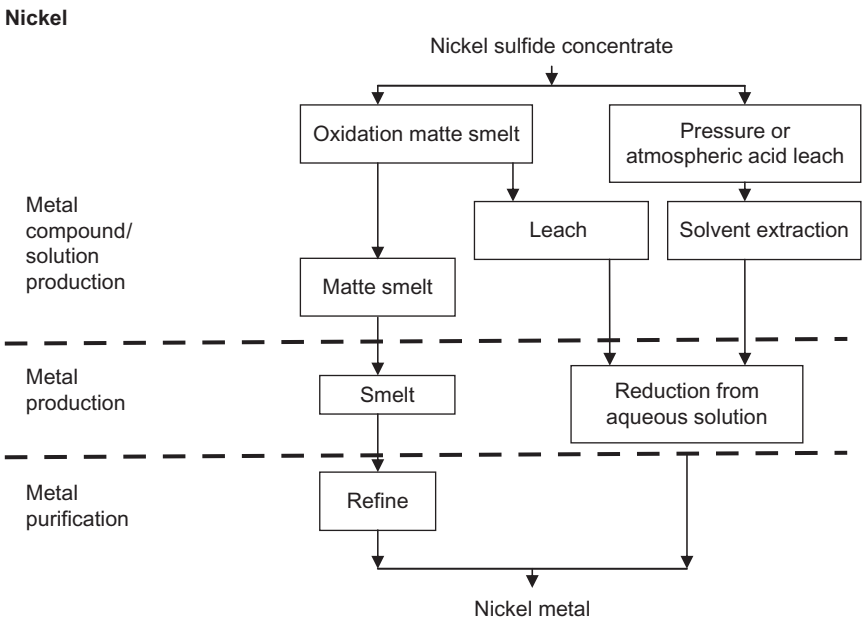


Figure 1.1.9 Alternative process routes for nickel production from nickel sulfide ores.

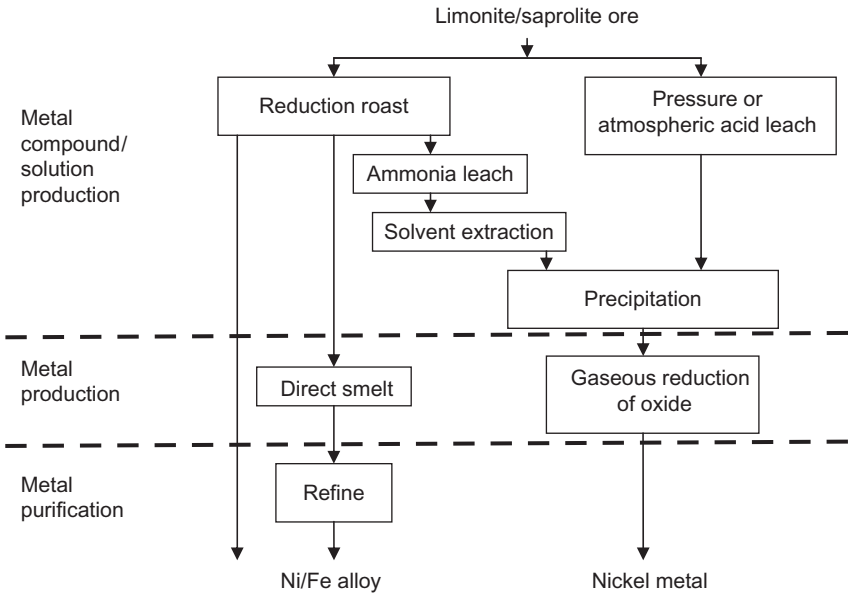


Figure 1.1.10 Alternative process routes for nickel production from nickel oxide-containing ores.

1.1.3. CLASSIFICATION OF METALLURGICAL REACTORS

For ease of analysis, the reactors used in modern metallurgical processes have been first classified in terms of the physical states of the reactants, i.e., gas/solid, liquid/solid, and liquid-phase reactors. These reactors are used as standalone, single-step processes, or combined into multistage or multistep reactor designs.

1.1.3.1. Gas/Solid Reactors

The principal roles of these technologies are to create efficient gas/solid contact to enable rapid mass and heat transfer, and chemical reactions, between these gas and solid phases. Of the many gas/solid reactors used in pyrometallurgical processes, shaft furnaces, rotary kilns, fluidized beds, and combustion reactors are the most representative.

1.1.3.1.1 Shaft Furnaces

The shaft furnace is an excellent countercurrent heat and mass exchanger, consisting essentially of a packed bed of solids through which gases are passed (see Figure 1.1.11). There are, however, important restrictions on the physical characteristics of the feed material. The charge must consist of relatively large, 10–50 mm diameter, particles to avoid elutriation of the solids, i.e., to prevent the particles from being blown out of the bed by the gas. The particles should conform to a narrow size range so as to

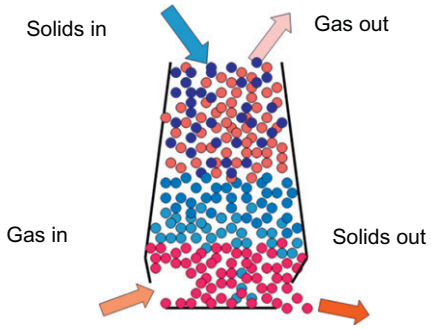


Figure 1.1.11 Schematic representation of a shaft furnace reactor.

provide maximum bed voidage and minimize the resistance to gas flow through the bed. The solids should also be physically strong and abrasion resistant to withstand the weight of the charge at temperature and to avoid the formation of excessive fines. To maximize the rates of the chemical reactions that occur during passage through the reactor, the charge should have a high surface area/unit mass; this is achieved by creating large particles that have high porosity. Since increased porosity also leads to a decrease in strength, the final feed properties must necessarily be a compromise between these conflicting demands.

Applications: direct gaseous reduction (iron ore), MIDREX; reduction roasting of hematite ores to magnetite; limestone calcination, coal gasification.

1.1.3.1.2 Rotary Kiln

The rotary kiln is a cylindrically shaped reactor that is continuously rotated about the major axis of the reactor (see Figure 1.1.12). The reactor is inclined so that the solids

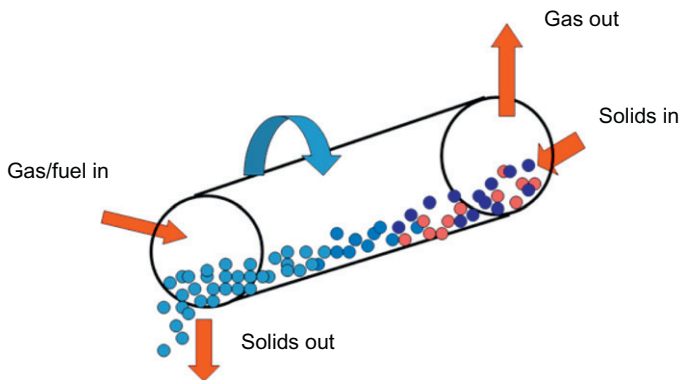


Figure 1.1.12 Schematic representation of a rotary furnace reactor.

charge moves under the influence of gravity from the feed to the discharge end. The process may operate with co- or countercurrent gas streams. Heat is provided primarily by the combustion of hydrocarbon fuel at the discharge end.

The challenge is to improve the utilization of fuel since these reactors are not as thermally efficient as in the shaft furnace, with thermal efficiencies running between 55% and 75% as opposed to 80% and 95% in shaft furnaces. Most of the gas in the kiln is not in direct contact with the charge or the refractory lining; to improve thermal efficiency, kilns are designed with high ratios of length to diameter. The rotation of the kiln gives good mixing of the charge and results in a highly uniform product. The continued abrasion and wear caused by the movement of the solid charge does, however, result in considerable wear of the linings. If the materials become partially molten, then accretion buildup can occur within the reactor.

There is still a restriction on the use of very fine particles in rotary kilns; however, a wide range of feeds can be used. The lack of restrictions on feed characteristics gives high flexibility to the process. Also the elimination of preprocessing of the charge materials considerably reduces both capital requirements and operating expenses.

Applications: drying/reduction kilns, SL/RN; Becher process kiln; cement kilns.

1.1.3.1.3 Fluidized Beds

Fluidized beds operate by balancing the downward gravity forces of the weight of the particles in the charge with the upward forces created by high gas flow. Fluidization or suspension can be carried out on a large range of material densities and particle sizes. In practice, particle sizes from 0.002 to 10 mm have been successfully treated. However, to ensure that a stable fluid bed is maintained, the range of particle sizes that may be used in any one reactor must be within an order of magnitude, e.g., between 0.2 and 2.0 mm. Inside the fluidized bed itself, the particles are highly mobile and this results in relatively uniform bed temperatures and good control over reactions in the bed (see Figure 1.1.13). In fast fluid bed reactors, some fine particles leave the reactor with the gas stream and gas/solid separation is used to recover these solids, and if necessary recycle them if incomplete reaction has occurred. A range of behaviors can be obtained from stable to bubbling beds, to fast fluidized bed behavior depending principally on the gas velocity and particle size and density.

Applications: fluidized bed reduction (iron ores); fluid bed roasting (zinc sulfide); calcination reactors, coal gasification.

1.1.3.1.4 Entrained Flow Reactors

Entrained flow reactors consist essentially of a reaction chamber into which fine particulate solids and gaseous reactants, usually air or oxygen, are injected (see Figure 1.1.14). The chemical reaction between the oxygen and the solids produces heat. The solids may

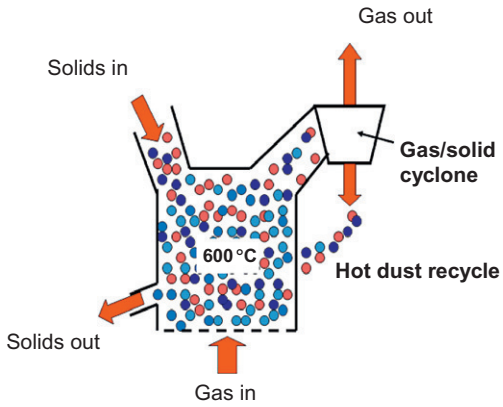


Figure 1.1.13 Schematic representation of a fluidized bed reactor.

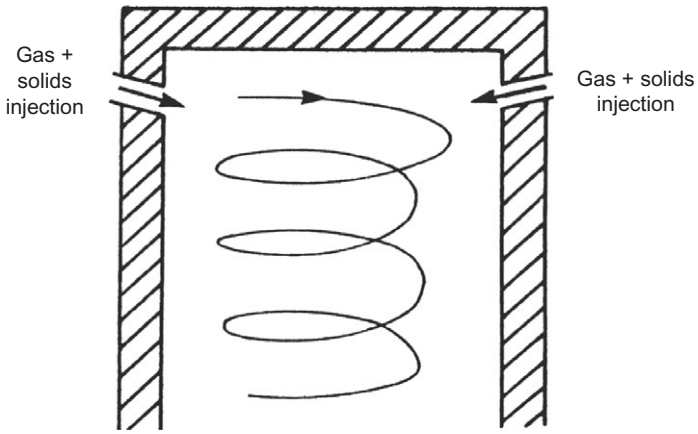


Figure 1.1.14 Schematic representation of an entrained flow reactor.

be fully consumed and converted to gases in the case of combustion or are melted by the enthalpy release as they fall through the reactor.

The reactions are not simply intended to provide heat to the system. Material introduced into the reactor is changed chemically, reacting directly with the coinjected material, e.g., oxygen; or with the other species produced simultaneously in the reactor, e.g., CO produced from combustion of carbon or SO_2 from sulfides. The advantages of such a system are that a fine particulate feed, the product of conventional beneficiation processes, may be used, and the materials are efficiently heated to reaction temperature. The capital expenditure required for such processes is low relative to alternative routes because of the lack of feed preparation necessary. The reactors may also be run on relatively inexpensive fuels, e.g., low-quality coal or sulfide concentrates which are themselves being chemically processed in the reactor.

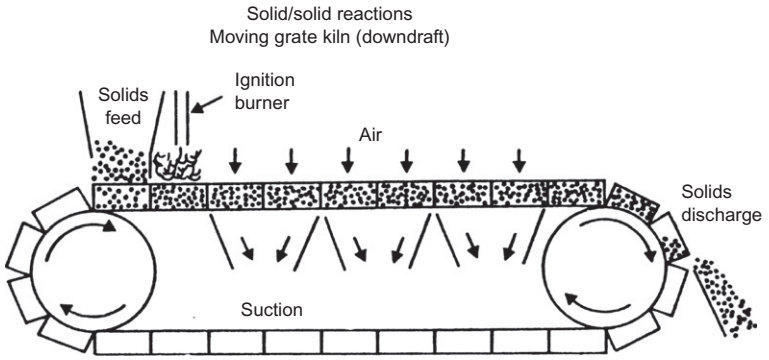


Figure 1.1.15 Schematic representation of a downdraft moving grate reactor.

Applications: continuous sulfide smelting; entrained flow coal gasification; pulverized fuel boilers.

1.1.3.1.5 Moving and Fixed Grate Reactors

The continuous processing of lump or coarse particles can also be carried out in moving or fixed grate reactors (see Figure 1.1.15). This may involve the heating of the solids through the combustion of hydrocarbon fuels or chemical reactions between the gas and solid phases. The gases penetrate through the porous bed and in doing so transfer heat to and from the charge as it moves progressively along the reactor in the case of the moving grate or with time for the fixed bed.

The solids feed may be in the form of briquettes, pellets, or sinter raw materials. Briquettes are formed by pressing together mixtures of the fine particles with various binders to produce large composite particles. Pellets and sinter feed consist of initially spherical-shaped particles made from the agglomeration of fine powders in a drum or disc with water and sometimes an inorganic clay binder. During heating, these materials become partially molten, and on cooling solid state bonds are formed between the particles. In the case of pellets only a small fraction of material becomes liquid and the material retains its spherical shape. The sinter process on the other hand results in a high liquid fraction and significant fusion of the components.

Applications: iron ore and manganese ore sintering, iron ore pelletizing; lead/zinc sulfide sintering, coal gasification.

1.1.3.2. Liquid/Solid Reactors

This class of fluid/solid reactors is principally encountered in hydrometallurgical processes in particular for the selective dissolution of species from the solid phase, a process commonly referred to as leaching. A range of techniques are employed for the leaching of

minerals and metal compounds. These will be discussed in order of the prepreparation required for leaching, starting with the technique requiring least preparation.

1.1.3.2.1 In Situ *Leaching*

In situ leaching refers to directly leaching the ore body while it is still in the ground. The leach solutions are introduced through drill holes above the level of the ore body and are allowed to percolate by gravity through the ore; the resultant liquor containing the dissolved metal is collected at lower levels by a network of sumps. The pregnant leach liquor is then pumped directly to the surface. The technique relies on good permeability of the ore body. One of the difficulties with *in situ* methods is that extreme care has to be taken to avoid loss of the leach liquor to natural groundwater. This is undesirable on two counts. First, it represents the contamination of the water table in the surrounding area, and second, it represents a loss of metal, reducing the efficiency of recovery of the extraction process.

Applications: uranium, gold leaching.

1.1.3.2.2 Heap Leaching

This involves the leaching of mined material that has received little or no size reduction following removal from the ore body. The ore particles typically between 0.01 and 0.1 m diameter are stacked in layers or heaps that are placed on a preprepared impervious base (Figure 1.1.16). Leach times range from weeks to months depending on ore characteristics. The recovery and the rates of leaching of minerals may in some systems be enhanced by the presence of microorganisms. Certain bacteria can withstand the conditions of high acid and high temperature and, either directly or indirectly, contribute to the dissolution of the minerals.

Applications: copper, gold, nickel oxide leaching.

1.1.3.2.3 Percolation Leaching

This term is used to describe a technique in which leach solution is percolated through ore which has been crushed and charged into vats or tanks (Figure 1.1.17). Typical ore particle sizes used are 5–20 mm diameter. Fine particulate matter should be removed

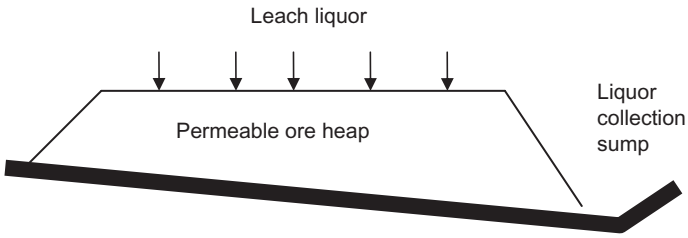


Figure 1.1.16 Schematic representation of a heap leach reactor.

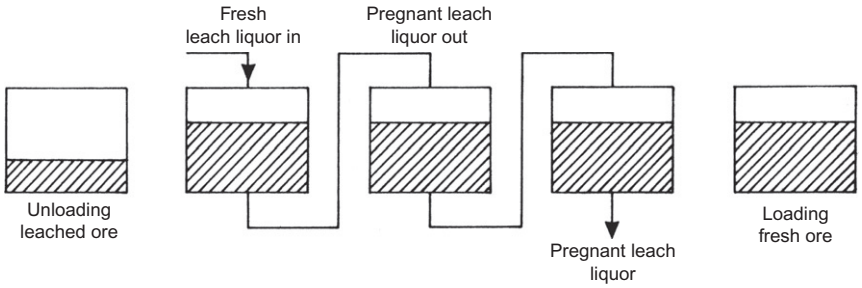


Figure 1.1.17 Schematic representation of a countercurrent percolation leach reactor.

because of its adverse effects on bed permeability. Countercurrent leaching is carried out to ensure high extraction efficiencies (80–90%) with high metal concentrations in solution.

Applications: copper, gold leaching.

1.1.3.2.4 Agitation Leaching

This involves the leaching of fine (200 μm), high-grade concentrates in which slurry or pulp is continuously mixed and stirred to improve the rates of reaction. The four major types reaction vessel used are shown in Figure 1.1.18a–c:

(a) Pachuca (gas lift) tank—This is a simple and inexpensive method of agitation of the pulp. The stirring is achieved by the injection of air under pressure into the bottom of a tall tank. The rising gas draws the surrounding liquid with it to the surface creating bulk liquid flow. The tank may be used with or without the central air lift tube shown in Figure 1.1.18. In some systems, oxygen is consumed during the reactions and this mechanism of agitation provides the additional benefit of aerating the solution.

(b) Low-speed agitators—For systems not requiring high turbulence, large diameter paddles or rakes may be used to mix slurries containing finely ground material.

(c) High-speed agitators—For leaching reactions requiring high turbulence, the agitator should consist of a propeller or turbine; the geometry of the agitator blade determines the extent to which this contributes to bulk flow, or the generation of shear and turbulence in the reaction vessel (Figure 1.1.18).

(d) Agitated autoclaves—In some systems, elevated temperatures (100–300 °C) and high pressures (e.g., up to 3.5 MN m^{-2}) are required to leach the minerals (Figure 1.1.18), in these cases concentrated feed is used and leach times can be relatively short (10 min to 2 h). The complexity and cost of such agitation techniques generally limit their application to use with highly concentrated minerals or high value metals.

Applications: copper, gold leaching.

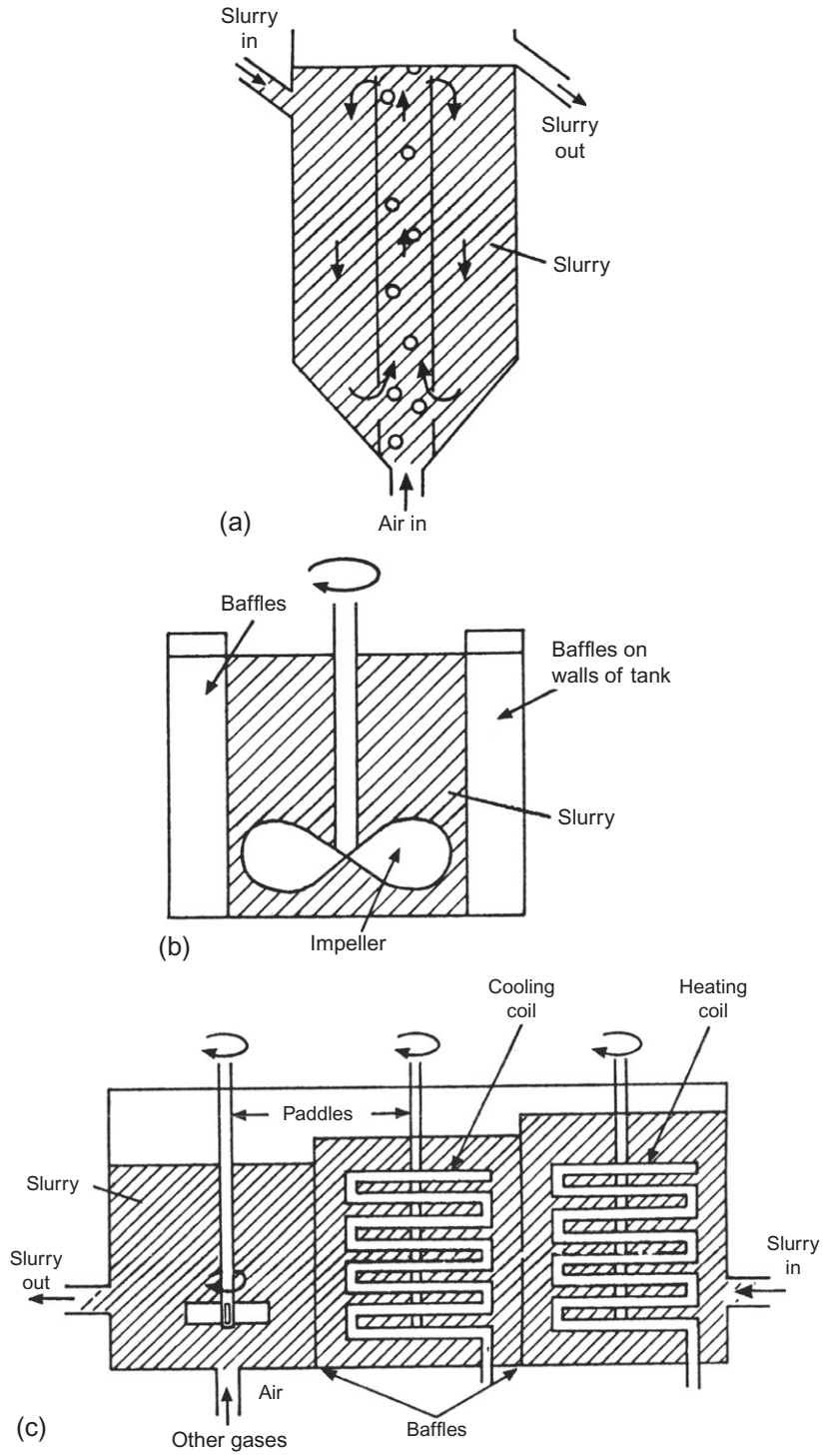


Figure 1.1.18 Schematic representation of (a) a gas lift agitated tank reactor, (b) a stirred tank reactor, and (c) a pressurized/heated/agitated reactor.

1.1.3.2.5 Crystallizers/Precipitation Reactors

The selective formation of inorganic solids from aqueous solutions can be achieved by progressive reduction in temperature of the solution and control of bulk composition of the aqueous solution. These are typically mechanically stirred tank reactors. They can be operated as batch reactors or as continuous processes involving a series of reactors. The particle size distribution can also be controlled through the introduction of fine seed crystals at the start of the process; this can overcome potential difficulties of solids nucleation and avoids the generation of large quantities of fines.

Applications: alumina precipitation; selective precipitation metal hydroxides/sulfides; continuous/batch.

1.1.3.2.6 Electrochemical Production Reactors

Applied electrical potential difference can be used to drive direction and current flow in electrochemical reactors. The reactors used for the recovery of metal ions from solutions (electrowinning) and for the purification of crude metal (electrorefining) in liquid/solid reactors are typically plate-type reactors, and these consist of alternate anode/cathode electrode pairs connected electrically in series (see Figure 1.1.19). Liquid/liquid electrochemical reactions can also be carried out provided there are suitable electrode materials that can conduct the current; in some cases, consumable anode electrodes are used.

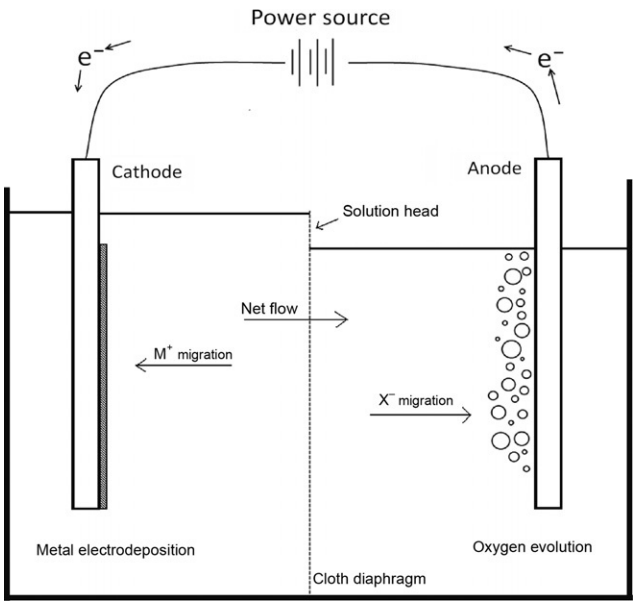


Figure 1.1.19 Schematic representation of a plate-type electrochemical production reactor. Example: Metal deposition from aqueous solution at the cathode. Water decomposition at the anode.

Applications: aluminum, magnesium, sodium production; zinc and copper electrowinning; copper refining; lead refining; sodium hydroxide (chlor-alkali cell), semibatch.

1.1.3.2.7 Ion Exchange Reactors

These reaction systems are designed specifically to treat dilute aqueous process streams; low concentrations of specific elements are selectively adsorbed onto the surfaces of the ion exchange materials and subsequently, in a separate desorption stage, the species are recovered by desorption into a separate process stream. The liquors to be treated can be contacted with the solids in flow-through packed column reactors; alternatively, the liquors can be mixed with the solid ion exchange materials forming a slurry, for example, during leaching reactions. The ion exchange solids have high surface area/unit volume and are designed, through the use of functional groups on the solid surfaces, to be highly selective to different species present in solution. Adsorption/elution of species is controlled through the control of the bulk solution conditions, e.g., pH, Eh, and the presence of complexing species.

Applications: carbon-in-leach, resin-in-leach (RIL) processes for Au, U, minor element recovery; process water treatment.

1.1.3.3. Liquid-Phase Reactors

The feature of modern pyrometallurgical processing is the extensive use of liquid-phase reactors. The reactors may be designed for reaction between the gas phase and a single liquid phase or, as is more often the case, with gas and two immiscible liquids present in the system.

1.1.3.3.1 Gas/Liquid Reactors

1.1.3.3.1.1 Bath Smelting Processes

One of the principal roles of the gas phase in these technologies is to create systems with high interfacial area, high reaction rate, and good mixing. This is achieved through reactant or inert gas injection into the liquid phase at different positions in the bath (see Figure 1.1.20). Particulate solids can also be injected, but usually, the particle sizes are small and the volume fractions low compared to the liquid bath so that these materials rapidly melt or are consumed. The bath temperatures are principally determined through the exothermic heats of reaction between the gas and charge. Fuel injection in the form of gas, oil, or coke can be used to provide necessary temperature control.

A wide range of top-blown reactors are used in industrial practice. The gas is introduced through gas- or water-cooled lances; these can be batch or continuous reactors.

In the case of basic oxygen steelmaking, the injection of tonnage oxygen as a gas jet at supersonic velocity into the melt results in high bath agitation and the creation of a metal/slag emulsion. The mixing intensity and the reaction rate in the bath are controlled by varying the gas injection rate and the lance height. These are operated as batch processes,

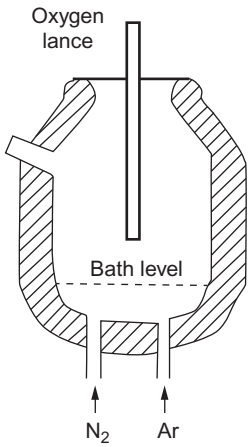


Figure 1.1.20 Schematic representation of a top- and bottom-blown bath steel smelting reactor.

and the reaction vessel is designed to periodically load and tap the reactants and products respectively through rotation of the vessel.

Top submerged lance (TSL) reactors operate on similar principles; however, the reactor position is fixed and the reactors can be operated in batch or continuous mode. The lance, which is immersed in the slag phase, is especially designed so that cooling effect of the incoming reactant gas provides a protective layer of frozen slag on the outer surface of the lance. The gas velocities exiting the lance in TSL reactors are much lower than in the supersonic gas jets used in steel making and result in bubbling flow (IsaSmelt/AusMelt).

Top-blown rotary converters combine the lance injection with continuous rotation of the reaction vessel about a nonvertical axis during processing. The rotation facilitates mixing and heat transfer.

In some applications, it is desirable to ensure uniformity of mixing of the liquid phase and to provide a liquid product within tight specifications. In these cases, greater control over the reactions in the bath reactors can be obtained by combining both top and bottom blowing. The gas introduced through the bottom of the reactor can be reactant or inert gas depending on the needs of the process (see Figure 1.1.21).

Examples of bottom-blown bath reactors include the following designs: Pierce–Smith converter, Noranda, El Teniente converters used in copper production from sulfides.

Applications: oxidation reactions—steelmaking, sulfide bath smelting; reduction reactions—slag fuming, slag cleaning; batch or continuous.

1.1.3.3.1.2 Bath Refining Processes

Gas injection at low gas flow rates results in bubbling flow within the reactor. This enables the removal of low concentrations of dissolved impurities from molten alloy solutions, as the gas principally provides improved stirring of the melt and mass transfer

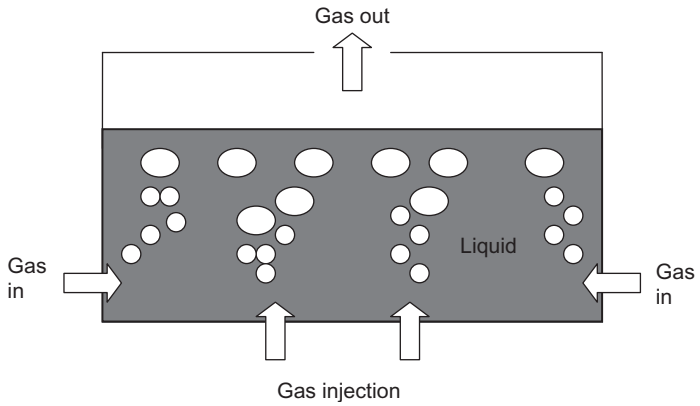


Figure 1.1.21 Schematic representation of a submerged injection reactor.

to the gas and slag phases; the reactions are typically undertaken at atmospheric pressure or in low-pressure systems. Fine particulate solids may also be injected with the gas into the melts to enable chemical refining processes to proceed. Electrical induction or arc furnace heating may be used to maintain the temperatures of the molten metal. These are usually batch processes.

Applications: argon oxygen decarburization; RH (vacuum) degassing; ladle refining and inclusion modification treatments; copper anode furnaces; pyrometallurgical refining.

1.1.3.3.2 Liquid/Liquid Reactions

The principal role of this class of technologies is to enable efficient liquid/liquid separation between immiscible liquids. The principle driving force for separation is density difference between the liquid phases (see Figure 1.1.22). In pyrometallurgical processes, the

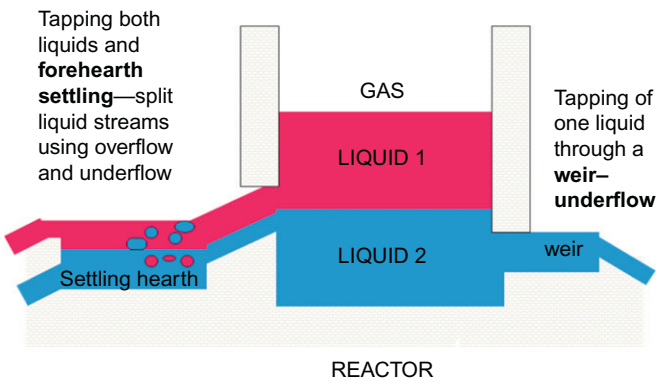


Figure 1.1.22 Schematic representation of a liquid/liquid separation reactor.

liquid phase (molten oxide or molten salt) is also used to protect underlying metal phases from reaction with the ambient atmosphere.

Long residence times and low turbulence are characteristics of these types of reactors. The depth of the bath and the depth/length ratio of the bath are usually low to minimize the time required for the separation of the entrained liquids. In addition, separation times can be controlled through adjustment of the physicochemical properties, e.g., viscosities and densities of the liquid phases.

Applications: tundishes; forehearth and holding furnaces.

1.1.3.4. Multistep Reactors

Multistep reactors combine the features of several different contacting systems with a single reactor.

1.1.3.4.1 Blast Furnaces and Other Counter Current Reactors

This class of reactor is exemplified in metallurgical systems by furnaces that have gravity fed solids charge and liquid metal product. Gas, solid, and liquid phases are present in the reactors.

The iron blast furnace, zinc blast furnace, and lead blast furnace combine the advantages of the packed bed reactor with simultaneous countercurrent gas/solid flow, gas/liquid, solid/liquid and liquid/liquid reaction steps (see Figure 1.1.23). The upper furnace is essentially a gas/solid shaft furnace. In the middle furnace, liquid/solid reactions occur in addition to gas/liquid and gas/solid reactions, and heat transfer takes place from gas to the condensed phases. The lower furnace acts as liquid/liquid reactor with

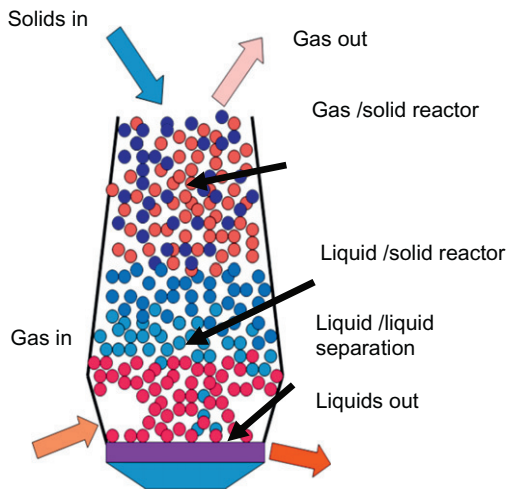


Figure 1.1.23 Schematic representation of a blast furnace reactor.

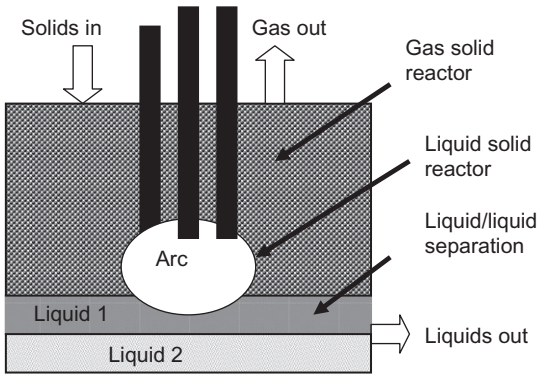


Figure 1.1.24 Schematic representation of a submerged arc reactor.

separation of molten metal and slag phases. Liquid metal and molten slag are tapped from the base of the furnace. In the case of the zinc blast furnace in addition to the production of liquid lead bullion zinc partitions to the gas phase and is subsequently recovered in a gas condensation process.

The cupula furnace is essentially a melting furnace. Materials such as recycled scrap metal are fed into the top of the shaft. The material is heated by the countercurrent gas stream generated by the combustion of coke, which is also charged into the furnace. Liquid metal is periodically tapped from the hearth at the base of the furnace.

Submerged arc electric furnaces have a packed bed of solids consisting of ore feed and coke, countercurrent gas/solid flow take place in the upper furnace, and a liquid/liquid separation step takes place in the high-temperature lower furnace (see Figure 1.1.24). Electrical power is used as a heat source to attain high temperatures and high power densities.

Plasma torches can also be used as additional heat sources to supplement the burning of hydrocarbon fuels in these types of technologies.

1.1.3.4.2 Reverberatory Furnaces

These systems consist of shallow bath melting furnaces. They do have considerable flexibility in the feed charges that can be handled, which can be in the form of large or small solid particles, or liquids. The melting rates of large particles or slabs of material are limited by the thermal conductivities of the materials and their geometries. The rates of heating of small particles, however, are determined by the rates of heat transfer from the surroundings.

Heating may be provided by direct combustion of hydrocarbon fuels over the liquid surface, but direct impingement of the flame on the melt surface is avoided where possible, especially near positions where the products are to be tapped. Electric arc furnaces are also used in some applications to heat the charge. Although direct combustion of fuels in furnaces is usually preferable to electric heating as far as energy utilization is concerned,

the heat transfer between the flame and the charge in this type of reactor is inefficient. Some of the energy in the flue gases may be recovered by the use of waste heat boilers.

Applications: open hearth steel making; glassmaking; matte smelting.

1.1.3.4.3 Flash Smelting Processes

For treatment of fine particulate, base metal sulfide concentrates rapid oxidation of the feed is undertaken in continuous reactors. In the entrained flow or suspended phase combustion (gas/solid) step, the fine particulate feed is partially oxidized. The resulting liquid droplets agglomerate and followed by a matte/slag (liquid/liquid) separation step. Some solid particles remain entrained in the gas and exit the reactor in the off gas stream (see Figure 1.1.25).

In applications, such as, Outokumpu and INCO smelter technologies have been used for the processing of copper sulfide concentrates. The Kivcet process for lead/zinc sulfide smelting consists of an entrained flow step for oxidation and melting of the feed, a packed bed liquid/solid reactor step in which the lead oxide in the liquid slag is reduced by coke to metal, and a liquid/liquid step for the separation of the lead bullion and slag phases. Heat sources are supplied by the exothermic oxidation of sulfide feed and hydrocarbon fuels in the reaction shaft, and by the submerged electric arc in the slag/bullion separation section of the reactor.

1.1.3.4.4 Multistage Smelting Processes

There are several examples of continuous, multistage bath smelting processes, each stage being undertaken with a similar reactor design but under different process conditions. In the case of copper sulfide smelting, for example, this consists of progressive oxidation of the feed with removal of the slag phase at each stage. In the case of lead smelting, this can involve the complete removal of the sulfur through oxidation of the concentrate to produce molten slag in bath smelting processes and subsequent reduction of the slag phase to produce lead bullion.

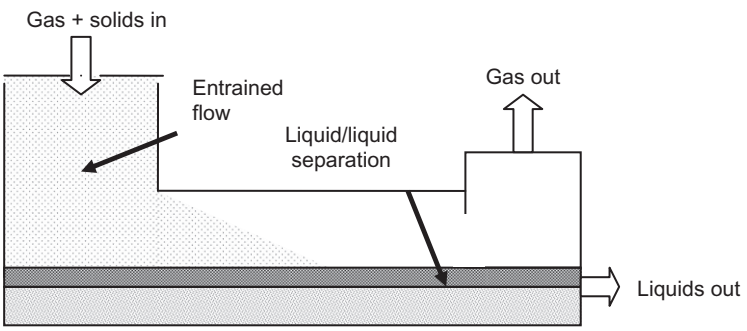


Figure 1.1.25 Schematic representation of a flash smelting reactor.

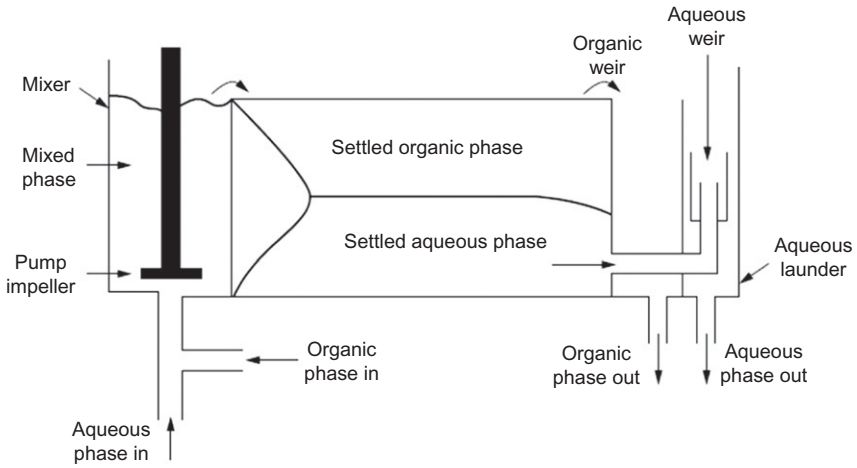


Figure 1.1.26 Schematic representation of a mixer-settler reactor.

Applications: Multistage copper flash smelt/converting (KUCC); Mitsubishi copper smelter; AusSmelt/IsaSmelt copper smelt/convert; QSL lead oxidation/reduction smelting.

1.1.3.4.5 Solvent Extraction

In hydrometallurgical processing, solvent extraction technologies involve the transfer of solute species between aqueous and organic liquid phases. The two-stage process includes a high-shear mixer compartment to obtain high interfacial area and rapid transfer of species across the liquid/liquid interface, and a settling zone to allow for separation of the immiscible liquids under gravity (see Figure 1.1.26).

1.1.4. SUMMARY OF GENERAL CHARACTERISTICS OF METALLURGICAL REACTORS

From a review of the range of processes used in modern metallurgical processing, a number of general observations can be made.

1.1.4.1. Pyrometallurgy

High-temperature processes are best suited to concentrated process streams, for example, the treatment of high-grade ores and recycled materials:

- Reactions at high-temperature approach chemical equilibrium. The use of fluid/solid and fluid/fluid reactions results in high chemical reaction and mass transport rates.
- High specific processing rates, i.e., t h^{-1} m^{-3} and concentrated process streams, mean smaller plant size/ton output, and lower capital cost/ton product.

- Despite the use of high temperatures pyrometallurgical process routes can represent the lowest overall energy option for metal production, through:
  - the utilization of exothermic chemical reactions,
  - the use of hydrocarbon fuels directly in the reactor rather than indirectly through electrical energy generation, and
  - employing energy recovery/secondary power generation systems.
- Modern approaches to reactor and process design enable environmental impacts of these high-temperature processes to be minimized through the capture and treatment of fugitive gases and dusts, and the generation and subsequent utilization of benign solid wastes. Pyrometallurgical routes can then sometimes represent the cleanest of the process options and those having the smallest environmental footprints.

1.1.4.2. Hydro- and Electrometallurgical Reactors

Hydrometallurgical reactions have the potential advantage of high selectivity and can be used to advantage for the chemical separation of metals from low-grade ores and the processing of dilute process streams. Electrochemical methods are used to produce highly reactive metals:

- The extents of metal recoveries from hydrometallurgical leaching reactions are, in the main, limited by the rates or kinetics of the reactions.
- Low specific processing rates, i.e., $t\,h^{-1}\,m^{-3}$ whether chemical reaction or mass transfer limited, and dilute process streams ($<1\ mol\,l^{-1}$) mean:
  - larger plant size/tonne output; the capital cost/tonne product is offset to some extent by the use of more conventional process equipment,
  - potentially greater inventory costs for high value metals.
- Environmental impacts of these processes can be minimized by:
  - treating effluent process streams to remove harmful solute species and suspended solids,
  - ensuring the generation of solid residues that do not break down and result in the release of harmful elements into the environment.

1.1.5. REACTOR AND PROCESS DESIGN METHODOLOGIES

The preceding sections have highlighted the many alternative processes and process routes that can be used for metal production. It is also clear that there exist, and will be in the future, a wide variety of primary and secondary source materials, all of different chemical compositions and physical and chemical characteristics. This will ensure the continued need for new process designs and improvements to existing operations.

How to approach these challenges? The complexities of metallurgical processes are such that it is desirable to develop a framework to enable these problems to be approached

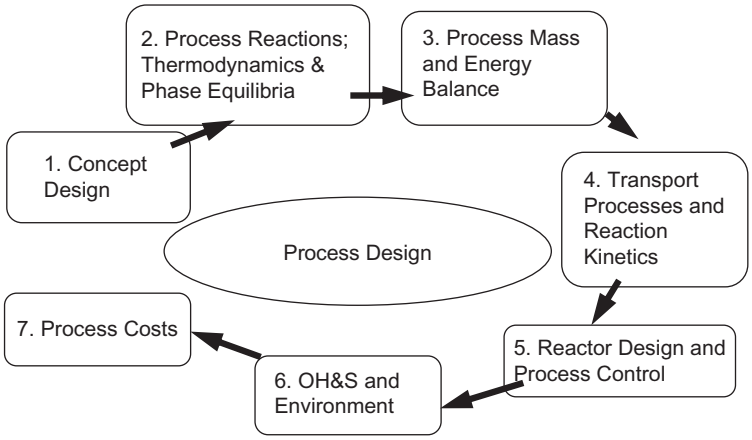


Figure 1.1.27 Potential steps in metallurgical process design and development.

and analyzed in a systematic way. There are many ways this can be done. An example of one of these approaches is illustrated in Figure 1.1.27. This analysis consists of a series of assessments each of which should meet the design criteria.

Step 1: The Concept Design. This step requires the definition of the physical and chemical characteristics of feed and products, the estimation of the potential values of all products and by-products, an initial calculation of likely economic feasibility, and the establishment of the "License to operate" criteria that must be met for a successful project. A conceptual process design to meet these requirements is then proposed.

Step 2: Process Reactions Thermodynamics and Phase Equilibria. The analysis starts by establishing whether or not a process is thermodynamically possible, identifying the process conditions under which the reactions will proceed and the enthalpy changes associated with the reactions. This quantifies the potential reaction and energy yield, the phase assemblages present in the system and the partitioning of elements between phases.

Step 3: Process Mass and Energy Balance. Estimating the material inputs/outputs to the process, the temperatures of the process streams, and the overall energy requirements.

Step 4: Transport Processes and Reaction Kinetics. This stage is focused identifying how fast the processes can take place, examining the potential heat and mass transfer processes and chemical reactions, the rate-limiting reaction mechanisms, and the key process variables.

Step 5: Reactor Design. This involves the development or selection of an appropriate reactor size and geometry; the choice of batch or continuous process and co- or countercurrent material flows; identifying reagent/energy/maintenance requirements, the operability of the process, and how it can be controlled; and specification of any ancillary plant and services required, such as power, water, and transportation.

Step 6: OH&S and Environment. Any industrial process should satisfy requirements for occupational health and safety, and minimizing environmental impact. This includes issues, such as clean production, the capture, treatment and utilization of all process streams, minimizing greenhouse gas emissions, and the achievement of social and sustainability targets.

Step 7: Process Costs. Finally, having satisfied the technical and environmental requirements, the economic viability of the process concept is addressed. Establishing the total revenue (R) of the project from all payments received, the Investment Costs (I) associated with capital costs of plant, ancillary and off-site facilities, and the Production Costs (P), which include direct operating costs and any ongoing payments to be made in the form of capital charges.

The sequence in which the questions might be put in the design process in fact closely resembles the order in which issues are addressed in the different chapters in the present treatise.

1.1.6. SUMMARY

The metallurgical industry has been established for many thousands of years and in technological terms is a "mature industry." As can be seen in this brief summary, there have been major changes over time to the chemical processes and the reactor designs that have been used. Many different process technologies have been developed, and a wide variety of process options are now available for use in metal production. Nevertheless, the process of optimization and new process development continue, and the goal of this treatise is to assist with the development of knowledge so that these further improvements to metallurgical processes can be made.

REFERENCE

[1] P.C. Hayes, Process Principles in Minerals and Materials Production, third ed., Hayes Publishing Co., Brisbane, Australia, 2004.

CHAPTER 2

Structure and Properties of Matter

Yoshio Waseda[a] **and Seetharaman Sridhar**[b]

[a]Institute of Multidisciplinary Research for Advanced Materials (IMRAM), Tohoku University, Sendai 980-8577, Japan and Research Center for Electron Photon Science, Tohoku University, Sendai 982-0826, Japan

[b]Tata Steel and Royal Academy of Engineering Joint Chair for Research into Low Carbon Materials Technology WMG, The University of Warwick, Coventry, CV4 7AL, UK

Contents

2.1. Structure and Properties of Molten Metals 61
2.2. The Structure and Properties of Silicate Slages 149
2.3. Atomistic Simulations of Properties and Phenomena at High Temperatures 287

2.1. STATE AND EQUILIBRIUM

For an isolated system of interest not affected by its surroundings, change may occur within the system. However, this change is observed to cease after a certain period of time as a result of the system reaching the so-called condition of "internal equilibrium," showing no further variation. On the other hand, for a closed system which may exchange energy with its surroundings, the system will eventually reach a condition wherein it is not only internally at equilibrium, but also in "external equilibrium" with its surroundings.

Next, let us consider a system of interest for which we have information about mass, velocity, positional relation, and motion of the constituents in this system. This information is needed for describing the system at a microscopic level. Nevertheless, we frequently use the word "State" which represents the totality of macroscopic properties associated with a system alone. The number of properties, which is arbitrarily set at given conditions to fix the state of a system, depends on the nature of the system and its number is generally small. In other words, one usually requires the limited number of properties selected as independent variables for a particular system. These properties represent one set of thermodynamic coordinates for the system. In other words, if only the macroscopic state of the system of interest is given, the so-called thermodynamics begins with the consideration of the properties of the system without detailed knowledge such as mass, velocity, positional relation, and motion of the constituents. Properties most amenable to

Treatise on Process Metallurgy, Volume 1
http://dx.doi.org/10.1016/B978-0-08-096986-2.00002-3
© 2014 Elsevier Ltd.
All rights reserved.

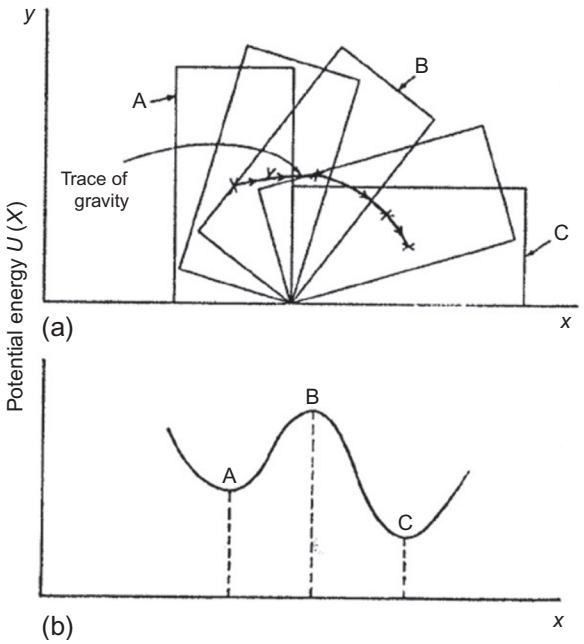


Figure 2.1 Schematic diagram of equilibrium in a simple dynamic system.

control are temperature T and pressure P of the system. Under atmospheric pressure $P = 101{,}325$ Pa (1 atm.), the state of matter is readily explained.

The word "equilibrium" is supplemented for the convenience of the readers. Equilibrium in which the rate of the forward reaction is equal to the rate of the reverse reaction may only be obtained in a closed system. In other words, when a closed system is away from one equilibrium state, it undergoes a process. During this process, the system may exchange heat with its surroundings and the properties change until the equilibrium end state is attained. The concept of equilibrium may be visualized in Figure 2.1 using a simple dynamic system where a box is set on the desk in three different conditions. When tilting the box within the close vicinity of position A (or position C), the box will automatically go back to its original position because the potential energy of the box's center of gravity is at a local minima. Both positions are stable equilibrium states, but the potential energy of the C position is more stable than that of A as seen in Figure 2.1b. Hence, the box set at A position will be called metastable equilibrium, because the box will be expected with sufficiently high reliability to reach the equilibrium end state denoted by the C position. When the box is set at position B, the potential energy of the box's center of gravity is at a maximum, and the box will reach the A or C positions by only slightly tilting the box towards each side. The position of B is frequently called the unstable equilibrium.

2.2. STATE OF MATTER

Matter is known to be made of atoms and individual atoms also combine with other atoms to form molecules. For example, nitrogen and oxygen, which are well known to be the major components of air, consist of diatomic (two atoms) molecules and water denoted by H_2O, is made of two hydrogen atoms and one oxygen atom. Irrespective of the type of molecule, matter can be classified into one of the three common or the two less-common categories of state. The most common states of matter on earth have been referred to as *solid*, *liquid*, and *gas*. In addition to these, the state of plasma is at times encountered. A less common but, in relation to the others, recently found state is the Bose-Einstein condensate, which can be considered to be a super fluid gas where particles are cooled to ultra low temperatures where particles do not move at all [1].

Within a state, the matter can exist in different phases. In the solid state, this is characterized by a variety of phases which give rise to a variety of properties and can be distinguished according to their crystal structures. It should be noted that the glass or amorphous phase is a solid-state phase but retains some structural characteristics of the liquid state. In the liquid state, liquid metal and liquid slag can coexist but these would be two distinct phases. Similarly, there are metallic liquids that separate into distinct phases. In the gaseous state there normally exists a single phase.

What are the characteristic properties of phases in each of the states? Table 2.1 summarizes typical properties of the normal three phases. Some points are illustrated in Figure 2.2, primarily that the constituents of the states are more mobile when going from solid to liquid to gas. Table 2.2 lists some pertinent points concerning glass and plasma.

Table 2.1 Some characteristic properties of solid, liquid, and gas

Solid phase	Liquid phase	Gas phase
Keeps a shape	Assumes the shape of a part of the container	Assumes the shape of the container
Keeps a fixed volume	Keeps a fixed volume	Assumes the volume of the container
Not easily compressible	Not easily compressible Keeps a free surface in a gravitational field	Compressible
The atoms or molecules are closely packed with one another at regular periodicity including a fixed space	The atoms or molecules are distributed with no regular arrangement (at random) close together with a little space between atoms or molecules	The atoms or molecules are distributed at random with a large free space between atoms or molecules

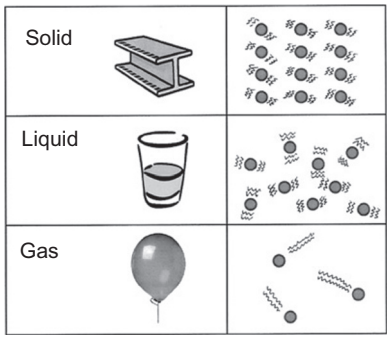


Figure 2.2 Schematic diagram for the most common states of matter, solid, liquid, and gas.

Table 2.2 Some characteristic properties of glass and plasma

Glass (amorphous solid) phase	Plasma (ionized gas) phase
Keeps a shape	Assumes the shape of the container
Keeps a fixed volume	Assumes the volume of the container
Not easily compressible	Compressible
Solid, but thermodynamically in the metastable state, but the conversion rate toward the crystalline counterpart is practically close to zero	Plasma, considering as a gas of highly ionized particles, exists only at temperatures, higher than several thousand degrees Celsius
The atoms or molecules are distributed at random, similar to liquid, but the positional change of atoms or molecules is relatively limited. Oxide glasses and polymers form a random network structure	By heating a gas at higher temperature, electrons leave the atoms and it results in the formation of the mixture of free electrons and protons. Free electric charges make the plasma electrically conductive and then plasma strongly responds to electromagnetic forces

States of matter present the distinct forms that different phases can exist and some typical features of each phase are given next.

2.3. SOLID

The atoms, ions, and molecules in a solid are packed close together at regular intervals to form the long-range order. Since all solids have some thermal energy, the atoms, ions, or molecules in a solid vibrate but their actual movement from one site to another is limited to thermally activated jumps of individual particles and this movement, i.e., diffusion, is in general slow. This makes a solid phase relatively rigid with a definite volume and shape. Solids are usually classified as ionic, covalent, polymeric, and metallic depending on the types of bonding that prevail between the particles that comprises it. In a metallic solid, metal atoms build the regular three-dimensional arrangement

and the valence electrons are free to move from atom to atom without belonging to specific atoms but shared by the whole system. While the densities are usually higher than for fluids, the variation can be quite wide ranging from heavy metals to aerogels. Crystalline solids have both short- and long-range order and thus exhibit sharp peaks in a radial distribution function measured through, e.g., X-ray diffraction [2].

2.4. LIQUID

The atoms, ions, or molecules in a liquid vibrate close together, similar to solid phase. They are, however, able to change their position readily. This produces a liquid property of a definite volume, but the ability of a changeable shape by flowing is given. The shape will be controlled by the container, because the attractive forces between atoms or molecules in a liquid cause a free surface in a gravitational field so as to act as a thin elastic film under tension. In addition, the resistance of a liquid to flow is called "viscosity." Beside viscosity, density and surface tension are pertinent properties that reflect the structure of a liquid. Most liquids lack long-range order and therefore exhibit broad curves rather than peaks in measured radial distribution functions measured through, e.g., X-ray diffraction [3,4]. The commonly encountered liquids in metallurgy are molten metals having metallic bonds and molten oxide slags that are constituted by ions that can be partly polymeric. In some cases like solidification of resulfurized steels, high-temperature ash formation in coals and smelting, a molten matte phase may exist which consists of molten metal sulfides wherein the sulfur exists in an ionic -2 oxidation state. In addition, aqueous processing would involve hydrogen bonding.

2.5. GAS

The atoms or molecules in a gas vibrate and almost freely move by spreading out in a space under very low density, so that a gas phase has no definite volume and shape. This is because the atoms or molecules in a gas are given sufficiently enough energy to overcome attractive forces.

2.6. GLASS = AMORPHOUS SOLID

The atoms or molecules in a glass vibrate close together, similar to solid phase. However, the distribution of atoms or molecules is rather close to the liquid phase where there is no long-range ordering characterized by the periodicity of atoms or molecules unlike those found in a crystalline solid. Typical example of a glass phase is window glass made of silicate with some additives [5]. The glass transition temperature (T_g) is the critical temperature below which a liquid changes to a glass structure which exhibits solid-like

properties but remains in an amorphous state [6]. The transition is accompanied by a smooth increase in viscosity by many orders of magnitude. This transition is a second-order transition and is accompanied by discontinuities in properties such as specific volume, as opposed to an abrupt change, which is observed in first-order transformations such as crystallization. The glass transition temperature is lower than the crystallization (melting) temperature. In polymers, a distinction is made between "rubbery" and "glassy" states. Here, rubbery means elastic and flexible like rubbers and they contrast clearly with "glassy" showing hard and brittle. In other words, when a noncrystalline substance is set at temperature below its T_g, the substance corresponds to the frozen state and large-scale motion of atoms or molecules is not possible. At temperature above its T_g, large-scale motion of atoms or molecules is allowed so as to behave rubbery.

2.7. PLASMA

Under the conditions at the very high temperatures and pressures, the atoms themselves start to break down and electrons are removed from their electronic shell around the nucleus leaving a positively charged ion (proton) behind. The resulting mixture of free electrons and charged ions are referred to as plasma which is rather classified into fluid. Plasma is made of highly ionized particles, so that it responds to the electromagnetic forces which can be analyzed by the Boltzmann equation [7].

Solid and liquid are often referred to as "condensed phases," because the atoms or molecules in these two phases are rather close together under a relatively high density, in comparison to the gas case. On the other hand, liquid and gas are called "fluid," because they are characterized by flow or move. In fluid, the atoms or molecules show random motion colliding with each other as well as colliding with the wall of the container. The motion of fluid and the reaction to external forces are represented by the Navier-Stokes equation, which gives the conservation of mass, momentum, and energy [8]. It may be suggested that the motion of solid and the reaction to external forces are described by the so-called Newton equation of motion and the Boltzmann equation for plasma includes the electromagnetic forces with the normal external forces of the Navier-Stokes equation.

2.8. PHASE TRANSITION

State of matter is also defined in terms of phase transition that is a change in one state of matter to another state and it can be usually distinguished by abrupt variation in properties. This is because state of matter depends upon temperature, pressure and other conditions. Changes in structure (and resulting properties) are cased by changes in conditions.

Distinctions between states are frequently described in terms of differences in the interactions of constituent atoms or molecules of a substance and this, in general, also characterizes the properties in the states. For example, the interactions in solids keep the constituent atoms in fixed spatial relations, whereas gas is the state in which interactions have almost no effect on their respective motions of atoms or molecules. The interactions lie in between the solids and gases in a liquid which keep atoms rather in proximity, but the constituent atoms are not given in fixed spatial relations. Under the atmospheric pressure condition, most substances usually commonly used in structures and devices exist in the solid state at room temperature. Phase transition to another state occurs at the definite temperature when the energy of a substance in a given state exceeds that allowed in the state. In crystalline solids, the atoms or molecules are closely packed with a regular periodicity. There are several different crystal structures, and thus more than one crystal structure is available in the solid phase of the same substance. For example, iron is able to exist in two solid phases (allotropes): a bcc structure, which is stable at low and high temperatures, and a face-centered cubic (fcc) structure, which is stable at intermediate temperatures:

α-Phase: Body-centered cubic (bcc) crystal structure with a lattice parameter $a = 0.28665$ nm exists at temperatures up to 1183 K (910 °C). The maximum solubility of carbon in α-phase is 0.05% in weight, whereas it increases up to 2.0% in γ-phase and these differences are attributed to the difference of vacant space in these two crystal structures.

γ-Phase: Face-centered cubic (fcc) crystal structure with a lattice parameter $a = 0.36469$ nm at temperature region between 1183 K (910 °C) and 1676 K (1403 °C).

δ-Phase: bcc crystal structure with a lattice parameter $a = 0.29323$ nm exists at temperature region between 1676 K (1403 °C) and 1808 K (1535 °C).

It should be noted that iron is considered rather unusual because only one phase exists in the solid state for most pure metallic elements.

Since increasing energy leads to increased motion of atoms, ions or molecules in a substance, a phase transition between solid and liquid state occurs and it is denoted by "melting" and further one obtains phase transition between the liquid and gas state, so-called "vaporization." Phase transition between the solid and gas state is called "sublimation." They are also called "freezing," "condensation" and "deposition". Such relationships are summarized in Figure 2.3. Phase transitions occur at a definite temperature under the atmospheric pressure condition and the point is also mentioned. Figure 2.4 shows schematic diagram of the relation between temperature and energy introduced.

Usually, at lower temperature a substance exists in the solid state. When energy is added to the substance, the atomic or molecular motion is enhanced and then the temperature of solid phase increases. Further, at the temperature of melting point, a substance will begin to undergo phase transition from solid to liquid. At this point, energy

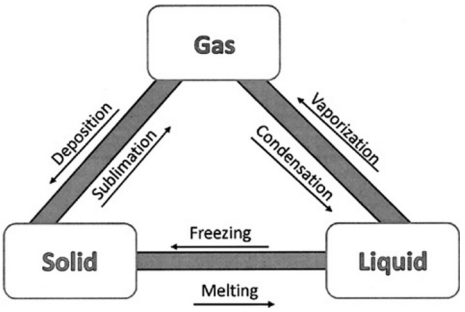


Figure 2.3 Relations of phase transition among solid, liquid, and gas.

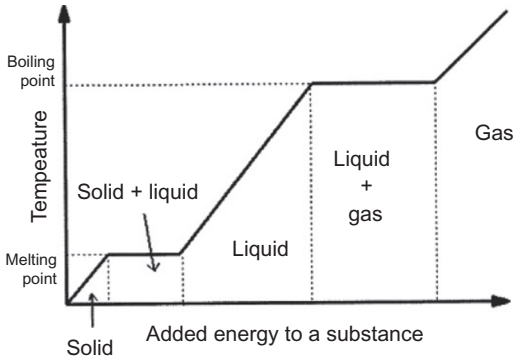


Figure 2.4 Schematic diagram for temperature vs. energy introduced.

introduced into the solid phase will not contribute to increasing its temperature. Added energy is used to shift atoms or molecules to the liquid state. Thus, no matter how high the solid temperature is, the solid phase remains at the same temperature until all of the atoms or molecules have undergone transition to the liquid phase. Although the excess energy introduced will accelerate the solid-to-liquid transition, the temperature is unchanged. The heat curve below illustration given in Figure 2.4 shows schematically the changes in temperature when energy is supplied to cause a substance to undergo phase transition from the liquid to solid state.

As can be seen in Figure 2.4, as one moves from left to right, the temperature of liquid phase increases as energy is continuously added. At a specific temperature, corresponding to boiling point, the liquid phase begins to undergo phase transition from liquid to gas and the temperature again remains constant even as energy is added. The energy that is introduced during this period goes into breaking the interactions of atoms or molecules so that individual atoms or molecules in the liquid phase are able to shift into the gas state. Once the transition is complete and when further energy is introduced to the substance, the temperature of gas phase will again increase.

It should be kept in mind that the same process can be recognized in reverse if we simply look at Figure 2.4 starting from the right-hand side and moving to the left-hand side. For example, let us consider the water (H_2O) case. As water vapor is cooled down, the movement of water molecules in the gas state is suppressed and then the temperature of steam decreases. When the water vapor temperature reaches 373 K (100 °C) and more energy is withdrawn so as to reform the interactions of water molecules, the temperature of the mixed phase of gas and liquid remains constant during the transition, as shown in the flat part of the graph given in Figure 2.4. When condensation is complete, the temperature of liquid phase will again begin to decrease as energy is withdrawn. The Clausius-Clapeyron relation describes the change in vapor pressure in equilibrium with a liquid as the function of the temperature changes [9]:

$$\ln\left(\frac{P_1}{P_2}\right) = \frac{\Delta H_{\text{vap}}}{R}\left(\frac{1}{T_2} - \frac{1}{T_2}\right) \tag{2.1}$$

Here, R is the gas constant and ΔH_{vap} is the enthalpy of vaporization. For simple metals the enthalpy of vaporization can be estimated as $88T_b$ (Trouton's rule), where T_b is the boiling temperature [10].

When the temperature of liquid water reaches 273 K (0 °C), phase transition between liquid and solid water (ice) starts, but the temperature of the mixed phase of liquid and solid remains constant during the transition. When freezing is complete, the temperature of ice (solid water) will again begin to decrease as energy is withdrawn.

2.9. GLASS TRANSITION

One of the typical features of glass or amorphous solid is "glass transition" and supercooling a viscous liquid into the glass state is frequently called "vitrification." The glass transition is not the same as melting or boiling. The glass transition is not at equilibrium, so that the glass sample has no unique value of the glass transition temperature T_g that will depend on the rate of cooling or heating and thermal history. Depending on substances and conditions of the measurement, T_g is not always clearly detected. Nevertheless, the glass transition temperature is always lower than the melting temperature of the crystalline solid. From a thermodynamic point of view, glass transition is classified as "the second-order transition" where there is no heat transfer of system but the heat capacity does change. It is also noted that the volume changes to accommodate the increased motion of atoms, or molecules, but it does not change discontinuously. In comparison, "the first-order transition" is characterized by a transfer of heat between system and surroundings with an abrupt volume change [11]. Such particular feature of glass transition is illustrated in Figure 2.5 using a comparison with the melting case.

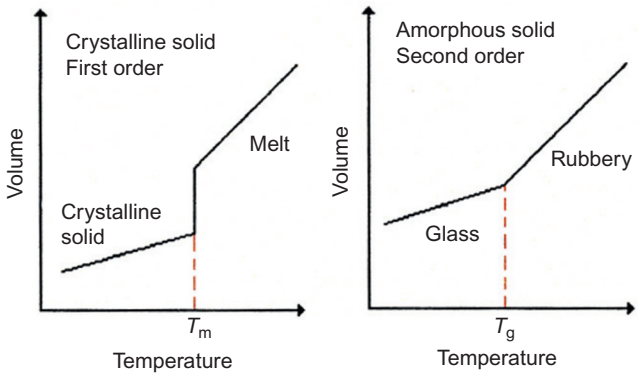


Figure 2.5 Specific volume is given as a function of temperature in two thermodynamic transitions.

The presence of rigidity is frequently used for distinguishing a solid from a fluid and one way is to use the viscosity value, because a given substance is considered rigid if it withstands shear for the time of the measurement. The viscosity coefficient of an amorphous solid is extraordinarily high, such as some of 10^{10} poise. Note that a few centipoise is suggested for the viscosity coefficient of typical liquid metals. In other words, a dramatic change in the shear viscosity value is quite likely observed within a relatively small range of temperature in glass transition. In addition, when increasing the temperature of an amorphous solid very slowly and continuously, the glass phase gradually softens until it becomes a liquid.

2.10. DESCRIPTION OF STRUCTURAL FEATURES OF LIQUID

The three classical states, solid, liquid, and gas of matter, can be distinguished macroscopically in terms of the properties of density, compressibility, and rigidity related to the motion of atoms or molecules. For simplification, let us consider the system consisting of one-component atoms under the atmospheric pressure condition and a solid is equal to the crystalline solid (hereafter referred to as crystal).

In gas, the atoms are distributed randomly and their motions are completely irregular, whereas the atoms in crystal show only a slight vibration about a definite point in the regular three-dimensional lattice. These extremes in the atomic distribution contribute to the construction of simple models for the structure of these two phases. However, the liquid phase appears in a sense to lie midway between these two. The density of a liquid is only slightly (a few percentage expansion on melting) below that of the corresponding crystalline solid. The flow property is important to allow liquid to be designated collectively as fluid and the liquid has to be considered as a collection of atoms which are always sufficiently close to one another in the near neighbor region without any specific regular periodicity. Namely, such ambiguous situation prevents us to construct a perfect model

for the structure of the liquid phase. Thus, the theory of the liquid state has progressed slowly and we have to date no equivalent to the concepts of ideal gas and kinetic theory of gases which allows for unambiguous prediction of gaseous properties. Molecular dynamics offers to some extent the possibility to predict properties and structures of liquids but through simulations based upon a limited set of particles for very short times [12].

All atomic positions in crystal are known and described with a few parameters of distances and angles. Such a simple definition is impossible in noncrystalline systems, liquids, and glasses, because of the lack of long-range periodicity in atomic positions. Nevertheless, the atomic scale structure of noncrystalline systems can be quantitatively described in terms of the radial distribution function (frequently referred to as RDF) indicating the average probability of finding another atom in a specified volume from an origin atom as a function of radial distance [13]. This RDF gives spherically averaged information on the atomic correlations as one-dimensional data. However, it does provide almost undoubtedly unique quantitative information for describing the atomic positions without long-range periodicity [2–4]. For convenience of discussion, only the essential points of the RDF analysis of noncrystalline systems are given below.

In an hypothetical homogeneous noncrystalline system such as liquids and glasses, when taking both over time and space, the radial distribution function, $\mathrm{RDF} = 4\pi r^2 \rho(r)$, may be defined by considering a spherical shell of radius r with thickness dr centered on an origin atom. Here, the quantity of $\rho(r)$ is often referred to as the radial density function corresponding to the average probability of finding another atom as a function of only distance (one-dimensional information). As shown in the schematic diagram of Figure 2.6, the RDF gradually approaches the parabolic function of $4\pi r^2 \rho_o$ at a larger distance, where ρ_o is the average number density of atoms, because the positional atomic correlation disappears with increasing distance. The pair distribution function defined by $g(r) = \rho(r)/\rho_o$ is also widely used in discussion for the structure of liquids and glasses. It is also suggested that there is no atomic correlation within the minimum nearest neighbor distance such as the atomic core diameter due to the repulsion of atomic pairs and then the RDF should be equal to zero in such small distance region of r. The area under the respective peak in the RDF provides information about the coordination number on an average.

It is worth noting how one obtains the RDF of liquid or glass. One option is to carry out experiments, because even in noncrystalline systems with the lack of long-range periodicity, two atoms whose scattered beams coherently interfere with each other, the diffraction intensity depends on the relative positions of the two atoms. Hence, the essential points are given below using X-ray diffraction case as an example [4].

A typical X-ray diffraction set up with a high-temperature chamber for a structural study of high-temperature melts is shown in Figure 2.7 [14,15]. This system consists of a θ-θ type goniometer in the vertical setting where an X-ray tube and a scintillation counter (SC) can rotate in the opposite direction. The high-temperature chamber is

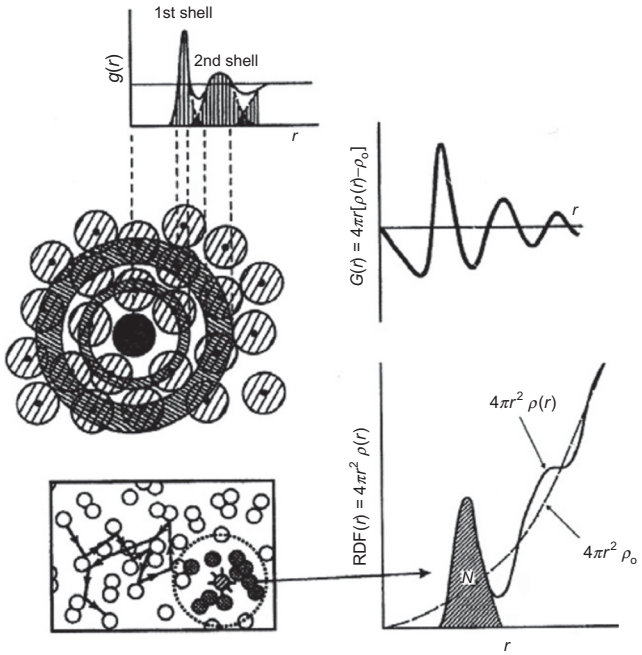


Figure 2.6 Schematic diagram of the RDF for a noncrystalline system with a snapshot of the atomic distribution.

mounted at the center of a goniometer axis and X-ray beams pass a slot with beryllium window through the water-cooled enclosure wall. In the present case, the pyrolytic graphite monochromator is set in the diffracted beam path coupled with a pulse-height analyzer for discriminating the fluorescent radiation from a sample. This configuration makes it possible to measure the scattering intensities from the free surface of a melt sample.

X-ray diffraction intensity is measured as a function of scattering angle 2θ and it is usually converted to the wave vector $Q = 4\pi\sin\theta/\lambda$, where λ is the wavelength of the incident X-rays. As shown in Figure 2.8, the measured intensity $I_{\mathrm{mes}}(Q)$ may be expressed by:

$$I_{\mathrm{mes}}(Q) = PAC[I_{\mathrm{coh}}(Q) + I_{\mathrm{inc}}(Q)] \tag{2.2}$$

where P is the polarization factor, A the absorption factor, C the geometric constant factor including the so-called normalization constant, and $I_{\mathrm{coh}}(Q)$ and $I_{\mathrm{inc}}(Q)$ are the coherent, and incoherent scattering intensities in electron units per atom, respectively.

After correcting polarization and absorption, $I_{\mathrm{coh}}(Q)$ can be obtained by the generalized Krogh-Moe-Norman method [3,4], including the Compton scattering intensity

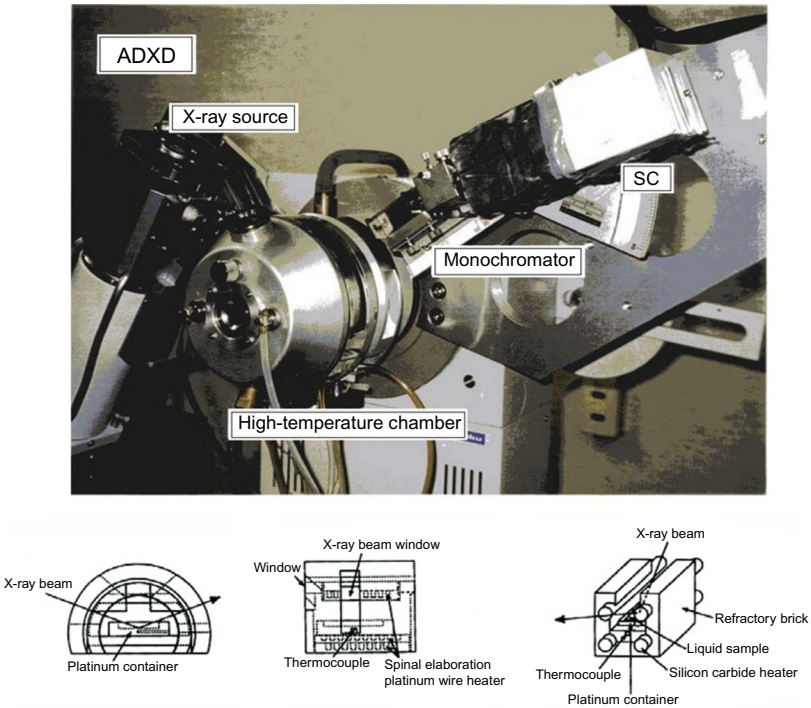


Figure 2.7 Overview of a high-temperature X-ray equipment for structural study of liquid metals and oxide melts together with two typical high-temperature cell assembly.

$I_{\mathrm{inc}}(Q)$ [16]. Then, the so-called interference function $Qi(Q)$ is estimated from the coherent scattering intensity as follows:

$$Qi(Q) = Q\left[I_{\mathrm{coh}}(Q) - \left\langle f^2 \right\rangle\right] / \langle f \rangle^2 \tag{2.3}$$

where $\langle f \rangle$ is the average atomic scattering factor and $\left\langle f^2 \right\rangle$ is average square of atomic scattering factor. By the conventional Fourier transformation of the function $Qi(Q)$, the $\mathrm{RDF} = 4\pi r^2 \rho(r)$ can be readily obtained with the number density value of the sample ρ_{o}:

$$4\pi r^2 \rho(r) = 4\pi r^2 \rho_{\mathrm{o}} + \frac{2r}{\pi} \int_0^{\infty} Qi(Q) \sin Qr \mathrm{d}Q \tag{2.4}$$

To facilitate the understanding of information obtained from X-ray diffraction experiments, the basic features of measured intensity data are also illustrated in Figure 2.9. In crystalline solid, the intensity shows almost zero value everywhere except at certain angles where sharp maxima appear arising from the interference of the regular periodicity in the atomic distribution. In gas, the atoms are distributed with a low average number density and the positional correlation of atoms almost disappears. The resulting intensity pattern

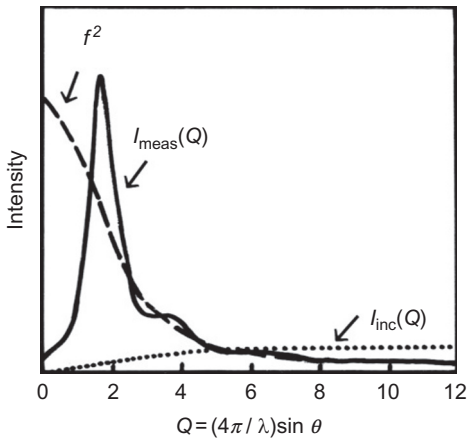


Figure 2.8 Schematic diagram of the measured X-ray diffraction intensity from a liquid sample, in relation to the independent atomic scattering intensity f^2 and theoretical incoherent (Compton) scattering intensity in electron units per atom, $I_{inc}(Q)$.

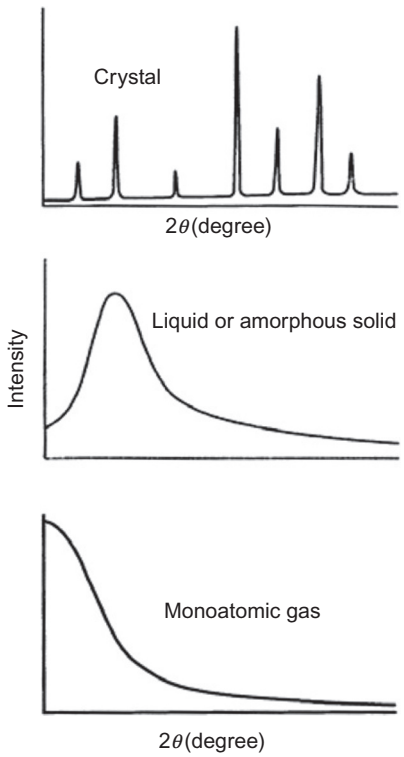


Figure 2.9 Schematic diagram of the X-ray diffraction patterns of crystalline solid, liquid, or glass and monatomic gas. Note that the vertical scales are not equal.

is entirely featureless, characterized by a monotonic decrease with increasing of angle. Contrary to the structure of a crystalline solid, the structure in both liquid and glass is characterized by an almost complete lack of periodicity, but there exists a tendency of the short-range ordering relevant to the atoms fairly tightly arranged together with a relatively high-density value and a statistical preference is found in the near neighbor region. The resulting intensity shows more than one or two broad maxima.

The following points may be suggested. During the course of measurement, numerous changes in the atomic distribution of liquid or gas should occur, such that the resulting intensity is just an averaged value of a changeable atomic configuration. This feature suggests that the averaged structure in both liquid and gas states has homogeneous spherically symmetric character with no preferential orientation. In comparison to such character, it is probable that the positional change of atoms is relatively limited in glass (or amorphous solid). A slight but such a difference contributes to the formation of a characteristic structural feature of glass, although the basic atomic arrangements in glass are essentially similar to those of liquid. For example, homogeneous spherically symmetric character of glass is less distinct than the liquid case, which frequently gives a deformed pattern in the RDF [4,17]. The exception to this is of course an ionic liquid (slag or aqueous) under an electric field.

It is worthy to note that the concept of RDF is applicable to crystals where the atoms occupy the cube corners of a regular three-dimensional lattice. In such cases, the RDF is described by several discrete sharp peaks with fixed coordination numbers. For example, 12 atoms for the first nearest neighbors, 6 atoms for the second nearest neighbors and 24 atoms for the third nearest neighbors in an fcc structure. This means the RDF is quite useful for describing the middle-range ordering in a few nanometer region of a complex system showing the deviation from an ideal crystal structure [18,19].

2.11. STRUCTURAL FEATURES OF METALLIC AND OXIDE MELTS

Figure 2.10 schematically shows the RDFs and their local ordering of liquid metals and oxide melts [15]. General forms of both RDFs for two melts appear to be similar. It may also be noted that such similarity is found in the X-ray diffraction intensity profiles. However, it should be pointed out that the first peak of RDF for oxide melts is almost completely resolved. Such difference in the first peaks implies that the fundamental feature of the structure of oxide melts differs from that of liquid metals. This is attributed to the following reason: the atoms in liquid metals are able to occupy the position of E which is the center of the triangle BCD in the side of the tetrahedron mainly arising from the close packing (see Figure 2.10). In oxide melts such as silica denoted by SiO_2, the silicon atom cannot occupy this E position due to the covalent-like bonding of Si—O—Si to form the SiO_4 tetrahedron and further the atomic configurations are quite likely to involve a large amount of vacant space. From these features, the following points can be given.

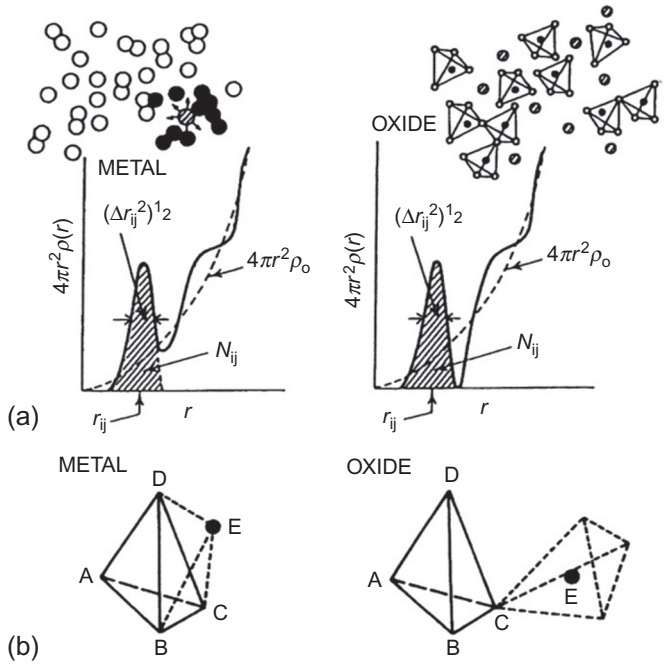


Figure 2.10 Difference of RDFs between liquid metals and oxide melts or glasses: (a) RDF with schematic diagram of the snapshot and (b) atomic positions in the local ordering.

In contrast to the structure of liquid metals, oxide melts, as well as their glasses, display a characteristically distinct local ordering within a narrow region. This results from a strong interaction between cation-oxygen pairs and a complete loss of positional correlation at a few nearest neighbor distance away from any origin. Hence, one of the most important components in the structural study of oxide melts and glasses is to determine such distinct local ordering unit structure and its distribution. The oxygen coordination number for metallic elements is also of interest in discussing the structural aspects of oxide melts and glasses.

There is no unique method for estimating the distance r_{ij} and coordination number N_{ij} in the near neighbor region from the RDF data, but one way is to use the pair function analysis proposed by Mozzi and Warren [17] or a least-squares analysis to fit the experimental RDF or the interference function data proposed by Narten and his colleagues [20,21]. The variations of ± 0.001 nm for r_{ij} and ± 0.2 for N_{ij} are suggested. In the RDF analysis for noncrystalline systems, the root mean square displacements $(\Delta r_{ij})^{1/2}$ corresponding to the magnitude of the peak broadening of the distribution of i-j pairs are also frequently estimated for discussing the structural features [17,20].

Figure 2.11 shows the RDF of a quartz glass [22]. The numerical values in this figure give the coordination numbers of the respective pairs estimated by the pair function

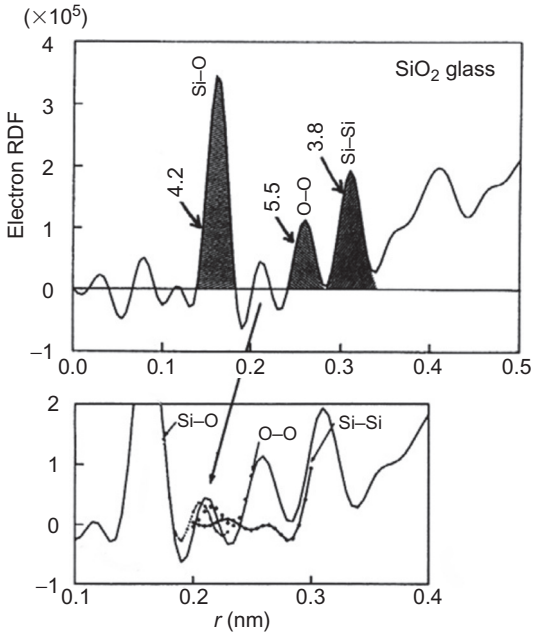


Figure 2.11 Electron RDF of quartz glass in near neighbor region.

method. The first peak assigned to Si—O pair is very sharp and almost completely resolved. However, in the present case, three partial structural functions are superimposed, so that the area under each peak in the RDF might be affected, more or less, by a few kinds of atomic pairs. The peak observed at about 0.21 nm in the RDF of a quartz glass has been considered as a spurious ripple arising mainly from the truncation effect in the Fourier transformation (see Figure 2.11). However, it is now interpreted as a summation of the three-pair correlation tails and their enhancement [22]. Therefore, this point should be taken into account in the RDF analysis, particularly in the determination of the coordination number.

The coordination number for Si—O pairs clearly indicates that each silicon atom is surrounded by four oxygens and that of O—O pairs is consistent with the value expected from the geometry of the SiO_4^{4-} tetrahedral units. The coordination number of Si—Si pairs corresponding to the correlation of SiO_4^{4-} tetrahedral units is estimated to be about four. These results show no significant inconsistency with the atomic arrangements observed in the beta-quartz type crystal structure [23] and the structure of quartz glass consists mainly of SiO_4^{4-} tetrahedral units which are distributed randomly to form the so-called random network structure.

REFERENCES

[1] M.W. Zwierlein, C.A. Stan, C.H. Schunck, S.M.F. Raupach, S. Gupta, Z. Hadzibabic, W. Ketterle, Phys. Rev. Lett. 91 (2003) 250401.
[2] B.E. Warren, X-Ray Diffraction, Addison-Wesley, Reading, MA, 1969.
[3] C.N.J. Wagner, in: S.Z. Beer (Ed.), Liquid Metals, Physics and Chemistry, Marcel Dekker, New York, 1972.
[4] Y. Waseda, The Structure of Non-Crystalline Materials, McGraw-Hill, New York, 1980.
[5] D.R. Uhlmann, N.J. Kreidl, Glass Science and Technology, Academic Press, New York, 1990.
[6] J. Zarzycki, Glasses and the Vitreous State, Cambridge University Press, Cambridge, UK, 1991.
[7] C. Kittel, Introduction to Solid State Physics, sixth ed., John Wiley & Sons, New York, 1986.
[8] N.J. Themelis, Transport and Chemical Rate Phenomena, Gordon and Breach Publisher, Switzerland, 1995.
[9] O. Kubaschewski, A.C. Alcock, Metallurgical Thermochemistry, fifth ed., Pergamon, Oxford, 1979.
[10] D.R. Gaskell, Introduction to the Thermodynamics of Materials, third ed., Taylor & Francis, Bristol, UK, 1995.
[11] J.-P. Hansen, I.R. MsDonald, Theory of Simple Liquids, Elsevier, Amsterdam, 2007.
[12] M.P. Allen, D.J. Tildesley, Computer Simulation of Liquids, Clarendon Press, Oxford, 1987.
[13] T.L. Hill, Statistical Mechanics, McGraw-Hill, New York, 1956.
[14] Y. Waseda, K. Sugiyma, in: H. Aoki, Y. Shona, R.J. Hempley (Eds.), Physics Meets Mineralogy, Cambridge University Press, Cambridge, UK, 2000.
[15] Y. Waseda, J.M. Toguri, The Structure and Properties of Oxide Melts, World Scientific, Singapore, 1998.
[16] V.H. Smith Jr., A.J. Thakkar, D.C. Chapman, Acta Cryst. A31 (1975) 391.
[17] M.L. Mozzi, B.E. Warren, J. Appl. Cryst. 2 (1969) 164.
[18] Y. Waseda, Anomalous X-Ray Scattering for Materials Characterization, Springer, Heidelberg, 2002.
[19] S. Suzuki, M. Saito, M. Kimura, T. Suzuki, H. Kihira, Y. Waseda, ISIJ Int. 43 (2003) 366.
[20] A.H. Narten, H.A. Levy, Science 160 (1969) 447.
[21] A.H. Narten, J. Chem. Phys. 56 (1972) 1905.
[22] K. Sugiyama, E. Mastubara, I.K. Suh, Y. Waseda, J.M. Toguri, Sci. Rep. Res. Inst. Tohoku Univ. A34 (1989) 143.
[23] F.S. Galasso, Structure and Properties of Inorganic Solids, Pergamon Press, Oxford, 1970.

CHAPTER 2.1

Structure and Properties of Molten Metals

Ivan Egry
Institut für Theoretische Physik, RWTH Aachen, Germany

The structure and properties of molten metals are an interesting, important and relevant topic for process metallurgy. Not surprisingly, it has been discussed in several books and review articles. Two excellent books on the subject are written by March [1], and Iida and Guthrie [2]. A completely revised version of the latter is expected to be published in 2014. Review articles by Egry dealing with this subject from slightly different perspectives have been published in Refs. [3–5]. In this contribution, the emphasis is on a comprehensive and detailed presentation of the field.

With respect to temperature, molten metals can be categorized into three different classes: low melting-point metals with melting points below, say, 800 K, high melting-point metals with melting points between 800 and 2000 K, and refractory metals with melting points >2000 K. For low melting-point metals, conventional techniques can be readily applied. For high-temperature and refractory molten metals, containerless techniques, as discussed in the following, are most appropriate.

2.1.1. STRUCTURE

2.1.1.1. Introduction

In comparison to solids and gases, the liquid phase remains the least well understood state of matter. Our microscopic picture of a gas is that of an ensemble of particles moving freely with their thermal velocity in the box in which they are contained and colliding occasionally with other particles, thereby exchanging energy and momentum. The density of particles is rather low and, therefore, collisions are rare events. Based on this picture, the concept of an ideal gas is readily introduced, consisting of structureless, noninteracting particles. Real gases can then be described by starting from the ideal gas and introducing interactions by a perturbation theory with the density as a small parameter. Similarly, we can define an ideal crystal as an assembly of atoms or molecules on a perfectly periodic lattice with translational symmetry. At finite temperatures, the movement of these atoms is constrained to (harmonic) oscillations around their equilibrium positions. A real crystal can then be described by introducing disorder or anharmonicity as a perturbation to the ideal crystal. Unfortunately, we do not have a similar concept for the ideal liquid. The density of a liquid at the melting point is nearly the

Treatise on Process Metallurgy, Volume 1
http://dx.doi.org/10.1016/B978-0-08-096986-2.00007-2
© 2014 Elsevier Ltd.
All rights reserved.

same as that of the corresponding solid (the change in density upon melting is only a few percent) and much higher than that of the gas at the same pressure and therefore collisions and interactions cannot be ignored. However, there is no translational long-range order in the liquid, and the movement of the individual particles is not restricted to small oscillations around a given equilibrium position. In fact, the so-called Lindemann melting criterion [6] is based on the condition that the amplitude of these oscillations reaches a critical value of, say, 1/4 of the interatomic distance.

Given the fact that there is no defined ideal liquid, there is also no way to describe a real liquid by any kind of perturbation expansion. One might then ask whether a liquid is more similar to a solid or to a gas. As mentioned above, a liquid is more solid like, considering its density. However, from a thermodynamic point of view, the opposite may be true: the phase transition between liquid and gas is of second order, exhibiting a critical point, beyond which the two phases become indistinguishable, constituting a so-called supercritical fluid. On the other hand, the liquid-solid phase transition is genuinely first order, with no critical point (even at extreme pressures). This has been attributed to the fact that, at the liquid-solid phase transition, a large number of order parameters have to be established, namely all Fourier components of the density, which vanish in the liquid, but are nonzero in the solid. A first-order phase transition implies that the phase transformation has to occur via nucleation with a finite nucleation barrier. Consequently, there is a range of metastable states, which are not in absolute thermodynamic equilibrium but are kinetically stabilized. A liquid existing below its freezing point is called undercooled, or synonymously, supercooled, whereas a solid above its melting point is superheated. This latter state is rarely ever observed, while an undercooled liquid is a rather common phenomenon. Undercoolings of the order of 20% (i.e., $\Delta T/T_m = 0.2$) can be achieved by containerless [7] or fluxing [8] techniques, which reduce the nucleation sites effectively. Since the undercooled liquid is not in thermodynamic equilibrium, the equilibrium phase diagram does not apply and new, metastable, phases, normally excluded by the phase diagram, may be formed from the undercooled state [9]. In the extreme case the undercooled liquid becomes a glass, i.e., an amorphous solid. Although thermodynamically metastable, such a glass may be practically an extremely stable solid, due to the fact that there is not enough thermal energy left to overcome the nucleation barrier. The transition between the liquid and the glassy state is called glass transition. It is not a thermodynamic phase transition in the strict sense, but rather a kinetic phenomenon. Conventionally, the glass transition temperature is defined as the temperature, T_g, at which the viscosity η of the liquid exceeds 10^{20} Pa s. An alternative, more thermodynamic, definition is due to Kauzmann [10]. The entropy of the liquid phase is always higher than that of the corresponding solid phase, due to the higher disorder. The entropy difference upon freezing at the melting point is therefore finite and positive. However, the entropy of the liquid phase decreases faster than that of the solid. Therefore, at the Kauzmann temperature T_K, the entropy of the undercooled liquid

becomes equal to that of the solid. Undercooling below this temperature would lead to the paradoxical situation that the entropy of the liquid is smaller than that of the solid at the same temperature, despite its higher disorder. This physically inconsistent situation is called entropy catastrophe; consequently, the liquid has to freeze before the Kauzmann temperature is reached. The Kauzmann temperature can be estimated by extrapolating the entropy of the liquid into the undercooled regime. In general $T_K < T_g$. For most metals, the density of the liquid is lesser than that of the solid, but its thermal expansion is larger. Therefore, there might exist a temperature, T_ρ, at which the densities of the solid and the undercooled liquid become equal. It is an interesting open question as to how this temperature is related to the glass transition temperature. The equality of these two temperatures would imply that the glass transition may not only be characterized as an entropy catastrophe, but, equally well, also as a density catastrophe.

The fact that there is no long-range order in the liquid does not imply that there is no short-range order either. As we shall discuss later, short-range order is in fact a distinguished feature of most liquids. The simplest model of a (metallic) liquid is that of hard spheres that can be packed differently: random close packing, hexagonally closed packing (hcp), face-centered cubic (fcc), or icosahedral packing. Due to its fivefold symmetry, the latter is not compatible with translational periodicity and does therefore not exist in any crystalline structure. For atoms interacting via a Lennard-Jones-type potential, the energy of an icosahedral aggregate is about 8% lower than that of aggregates with an fcc or an hcp structure of the same size. At solidification, large structural changes would be required, giving rise to a finite nucleation barrier. Based on this observation, Frank [11] postulated the existence of an icosahedral order in liquids (Figure 2.1.1).

In addition to such topological short-range order, chemical short-range order plays a major role in alloys. This is due to the fact that the interactions between unlike atoms may be different from those between like atoms, leading to a preference of equal or unequal nearest neighbors. If this energy difference is positive (i.e., like atoms are preferred as neighbors) and sufficiently large, it may lead to a genuine liquid-liquid phase transition,

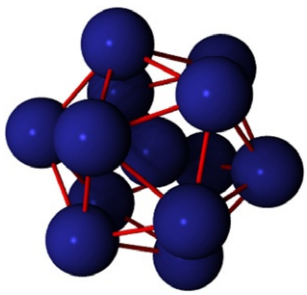


Figure 2.1.1 An icosahedron. *Courtesy DLR-MP.*

namely phase separation. Alloys that exhibit such a transition are called immiscible and they possess a miscibility gap in the liquid part of their phase diagram. Otherwise, these energy differences may lead to clustering effects of like (homo) or unlike (hetero) atoms. It is generally accepted that complex liquids (e.g., water) may exhibit different structures depending on the thermodynamic variables: temperature, pressure, and composition. In analogy with the same phenomenon in the solid state, this effect has been termed polyamorphism [12]. Whether this can also be observed in liquid metals, e.g., iron, is an open question.

Macroscopically speaking, the most pronounced feature of a liquid is its free, and deformable, surface, or, in other words, the existence of a finite surface tension. Capillarity effects are unique to the liquid phase. Therefore, the surface tension is one of the most important thermophysical properties of the liquid phase.

Although there is no satisfying theory of the liquid phase based on statistical mechanics, we can still try to understand its structure by simulations and experiments. Numerical simulations of liquid metals have become quite popular in recent years. In comparison with other liquids, metallic liquids can be considered as "simple," due to the isotropic interaction between the ions. The conduction electrons screen the electrostatic interaction between the ions, and the theoretical approaches differ by the choice of the resulting effective interionic potential. In the simplest approximation, the ions can be treated as hard spheres, modeling only the short-range repulsive interaction by a step function; in a more sophisticated treatment, the interaction can be modeled by a Lennard-Jones-type potential, usually of the embedded atom-type [13]. Once the potential is fixed, numerical simulation, by, e.g., molecular dynamics (MD), can be performed. Phase separation, freezing, and diffusion processes have been successfully simulated using MD [14,15]. We should also mention that there are attempts to describe metallic liquids from first principles, using *ab initio* quantum mechanics. This approach is based on density functional theory and can be extended to finite temperatures [16]. Phase diagrams of a number of pure metals have been calculated from first principles; the liquid phase, however, remains a challenge.

Experimentally, liquid metals are by no means "simple." This is due to the fact that most metals melt at high temperatures only, typically above 1000 K, and are very reactive. Therefore, it is difficult to find chemically inert containers, which are not destroyed during the experiment and, in addition, also do not contaminate the specimen under investigation. A breakthrough in this respect was the advent of containerless methods, based on different levitation techniques. For microscopic structural studies, radiation has to be used with a wavelength comparable to interatomic distances. Therefore, X-rays or neutrons have to be used as microscopic probes. In addition, high intensities of the incoming beams are desirable in order to reduce the measurement time. These are provided by large synchrotron facilities for X-rays; for neutrons, the intensity delivered by nuclear reactors is much less. Progress can be expected by the new spallation sources.

These two methods are in a sense complementary: while X-rays probe essentially the electron density, the neutrons interact mainly with the nuclei of the ions. In principle, the scattered intensity is measured with suitable detectors and absorption or diffraction spectra are acquired. From both methods, information about the microscopic structure can be obtained, e.g., the distance to nearest neighbors and the number of nearest neighbors around the scattering atom (i.e., the coordination number). In addition, quasielastic neutron scattering (Q-ENS) yields information into dynamic processes, like diffusion.

Conventional structural investigations of molten metals by X-rays or neutrons are carried out in suitable containers. As mentioned above, they have to be chemically inert with respect to the investigated specimen, and, at the same time, transparent to X-rays or neutrons. This restricts the choice of suitable container materials rather dramatically. Quite often, sapphire cells are used. The potential for combining containerless processing techniques with synchrotron or neutron sources was recognized and implemented in the 1990s by several research groups worldwide, including R. Weber using aerodynamic levitation [17] and the DLR group, combining electromagnetic levitation (EML) with extended X-ray absorption fine structure (EXAFS) [18]. The state of the art was reviewed recently by Egry and Holland-Moritz [19], as well as Hennet and coworkers [20] and most recently, in a monograph by Price [21]. Since then, this has remained an active research field, with prominent contributions also from Kelton and Price in the USA [22–24], and Japanese groups [25]. In addition to avoiding contamination of the sample by the container, this technique yields access to the undercooled liquid, where all structural properties become more pronounced. Before discussing the basic principles of diffraction experiments, we briefly explain the fundamentals of the different levitation techniques, assuming that the reader may not be familiar with these.

2.1.1.2. Levitation Methods

In order to levitate a massive specimen, the gravitational force must be overcome. This can be achieved by aerodynamic, electrostatic, or electromagnetic forces. Common to all levitation methods is the fact that the sample is not fixed in space, but performs small and slow oscillations about its nominal position, as if it was suspended by very soft springs. We will discuss these three most common techniques shortly in the following. A more detailed account of containerless techniques is given in Ref. [7].

Aerodynamic levitation is a technique based on the use of a gas flow for positioning the sample at a stable position. In this method samples are levitated by controlling a gas stream flowing through a nozzle. The levitation force exerted by the gas stream on the sample is given by:

$$F_A = \int \left(\rho v^2 + p\right) \mathrm{d}f \tag{2.1.1}$$

where ρ, v, and p are the gas density, vertical gas flow velocity, and gas pressure, respectively. Integration is over the specimen's surface. The conical nozzle levitator [26] is the common method to obtain stable aerodynamic levitation of liquids. The sample is supported by a gas flow passing through a diverging conical nozzle. With this method, the sample is usually laser heated from the top. In order to achieve higher temperature homogeneity, sometimes a second laser is aimed at the bottom of the sample, with the beam passing through the levitation nozzle. Temperatures above 3000 K have been obtained with 3-mm-diameter oxide samples. In the configuration of Hennet *et al.* [26] the cone angle is 60°. In side view, two-thirds of the sample can be seen, while the lower third is covered by the cone. The spherical sample is lifted several tenths of a millimeter in an argon flow. This is shown in Figure 2.1.2.

For metallic samples, aerodynamic levitation can be combined with inductive heating, a heating coil replacing the laser. Such a hybrid levitator has been built by Mathiak *et al.* [27] and was used in some of the experiments discussed below. The advantage of such a hybrid levitator is its compact size and its simple operation. The main difficulty stems from the fact that the electromagnetic fields not only provide heating through eddy currents, but also exert forces on the sample. In order to minimize this effect, the Helmholtz configuration is used for the coil geometry, which produces a nearly homogeneous field along the symmetry axis of the coil. Nevertheless, a delicate alignment of the coil with the nozzle is required to match the equilibrium levitation position with the minimum of the electromagnetic field. The heating coils can be either parallel to the levitation nozzle or perpendicular, as required by the beam geometry of either the X-ray or neutron beam. The setup used by Mathiak and coworkers is shown in Figure 2.1.3.

Electrostatic levitation uses a vertical electric field produced by two condenser plates, to which a high voltage is applied. The sample itself must be charged, and levitation is achieved through the Coulomb force

$$F_C = qE \tag{2.1.2}$$



Figure 2.1.2 Aerodynamic levitation of a liquid Al-Ti sample.



Figure 2.1.3 Hybrid aerodynamic-electromagnetic levitation setup. The axis of the heating coils is perpendicular to the direction of the gas stream.

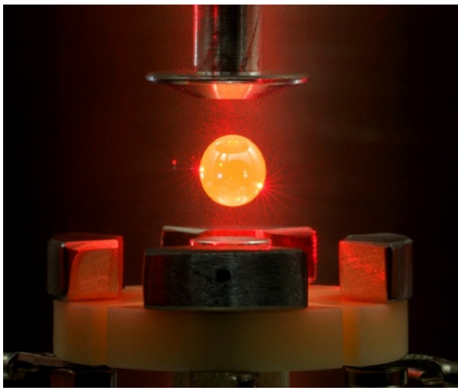


Figure 2.1.4 Electrostatically levitated liquid $Ti_{39.5}Zr_{39.5}Ni_{21}$ droplet with a mass of 0.6 g at a temperature of 1150 K [29].

where q is the charge on the sample. Electrostatic levitation is intrinsically unstable, and a fast feedback mechanism is needed to maintain the sample's position [28]. The sample must be charged initially, and the charge must be maintained, i.e., loss of charge by evaporation must be compensated by the photoelectric effect.

Due to the high voltages applied, electrostatic levitation works best under high-vacuum conditions. In contrast to other levitation methods, the sample is fully visible. As an example, this is shown for a TiZrNi alloy in Figure 2.1.4 [29]. A recent review

on ESL, and its use for thermophysical properties of ceramics [30] and metals [31], has been given by Paradis.

Finally, levitation of electrically conducting samples can be achieved by placing the sample into a high frequency alternating inhomogeneous electromagnetic field, produced by a levitation coil with a conical or cylindrical shape. This field B induces a current in the sample, which in turn interacts with the field. Levitation is caused by the Lorentz force, F_L, given by:

$$\vec{F}_L = \int \left(\vec{j}_{ind} \times \vec{B}\right) dV \tag{2.1.3}$$

where j_{ind} is the current induced in the sample by the external electromagnetic field. The integral can be calculated in a multipole expansion [32,33]. The relevant parameter for EML is the skin depth δ, defined as

$$\delta = \sqrt{\frac{2}{\omega \sigma \mu_0}} \tag{2.1.4}$$

Here, σ is the electrical conductivity of the sample, ω is the frequency of the alternating field, and μ_0 is the magnetic permeability constant.

EML is self-stabilizing: a levitated sample is positioned in a potential well generated by the electromagnetic fields. No electronic feedback control is required.

A levitated liquid copper drop is shown in Figure 2.1.5. The levitation coil is inside a process chamber, and the levitated sample is illuminated by a laser beam in order to produce a shadowgraph of the sample for density measurements.

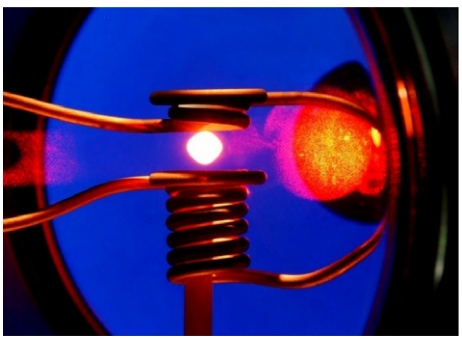


Figure 2.1.5 Electromagnetic levitation of a liquid copper drop. The levitation coil is inside a process chamber, and the levitated sample is illuminated by a laser beam. *Courtesy DLR-MP.*

2.1.1.3. X-ray and Neutron Diffraction—Basics

The principle of diffraction or scattering experiments has been discussed in many textbooks, monographs, and review articles. The standard reference, summarizing the state of the art of the seventies, is a classic text by Waseda [34]. Excellent reviews related to liquids and, in particular liquid metals, can be found in Refs. [35–38]. In a little noted paper, Waseda has summarized structural inhomogeneities in liquid alloys, and their relation to thermophysical and transport properties [39]. Here, we focus on the most important concepts relevant to our topic.

A scattering experiment can be performed in two ways: in absorption, resp. transmission, or in reflection. The geometry of the corresponding setup is shown in Figure 2.1.6. It is customary to denominate the scattering angle by 2θ. It is related to the scattering vector Q and the wavelength of the incoming beam by

$$Q = \frac{4\pi \sin\theta}{\lambda} \tag{2.1.5}$$

As mentioned before, scattering is either due to (valence) electrons for X-rays or nuclei for neutrons. In both cases however, the scattering cross section is related to density-density correlations. This is the basis for structural studies. The measured intensity $I(Q)$ contains contributions from the background, from multiple scattering events, from incoherent, and from coherent single scattering events, which contain the sought information. It is not a simple task to separate this contribution from all other, unwanted terms. When this has been done, the intensity is related to the static structure factor by

$$I(Q) = Nf^2 S(Q) \tag{2.1.6}$$

where N is the number of scatterers, f is the atomic scattering factor, and $S(Q)$ is the static structure factor. A typical example is shown in Figure 2.1.7. For $Q \to 0$, $S(Q)$ tends to

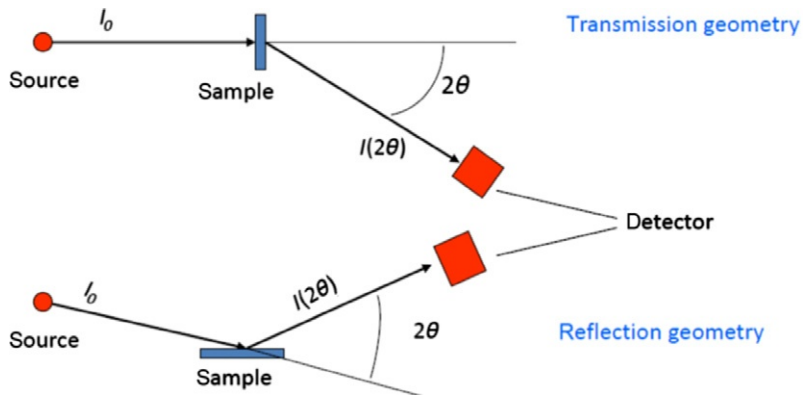


Figure 2.1.6 Scattering geometries.

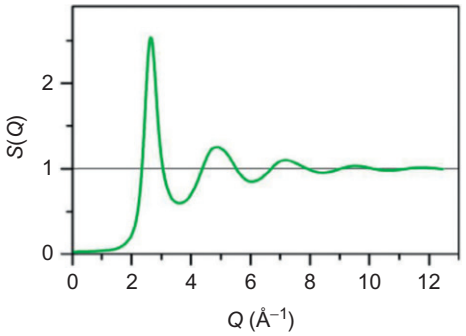


Figure 2.1.7 Typical static structure factor $S(Q)$ for a liquid metal (Ag-Sn).

zero, while for $Q \to \infty$, $S(Q) \to 1$. In contrast to solids, where $S(Q)$ consists of discrete sharp lines, called Bragg peaks, the structure function of liquids is a smooth function, consisting of broad maxima. The first sharp peak around 3 Å^{-1} is called the first sharp diffraction peak (FSDP); its position agrees roughly with the first Bragg peak of the corresponding crystalline structure. One may imagine that upon melting the sharp Bragg peaks broaden and slightly shift in position to account for the thermal and statistical disorder and the new structure of the liquid phase.

The static structure factor contains information about the atomic structure. For isotropic liquids, it depends only on the magnitude of Q, not its direction.

The static structure factor is essentially the Fourier transform of the pair-distribution function $g(r)$:

$$g(r) = 1 + \frac{1}{2\pi^2 n_0 r} \int_0^\infty \mathrm{d}Q (S(Q) - 1) Q \sin Qr \tag{2.1.7}$$

where n_0 is the number density. This function represents the probability of finding an atom at distance r, when there is, at the same time, an atom (i.e., a scatterer) at $r = 0$. For $r \to 0$, $g(r)$ tends to zero, whereas for $r \to \infty$, $g(r)$ approaches unity. A typical pair-distribution function for a liquid metal is shown in Figure 2.1.8. From the position and width of the first sharp peak, distance and number of the nearest neighbors can be determined. Whereas the determination of the nearest neighbor distance is trivial, that of the number of nearest neighbors, the so-called coordination number, Z, is not. It is related to the strength of the signal, i.e., the area under the first peak. Unfortunately, there is the problem that contributions from the second maximum may overlap with the first one. Two different methods are in use which yield slightly different results: Either only the left part of the first maximum is considered, and its value is doubled, or integration is carried out until the minimum between first and second peak:

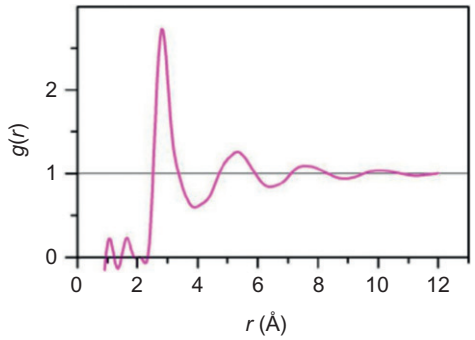


Figure 2.1.8 Typical pair-distribution function for a liquid metal (Ag-Sn).

$$Z^{\mathrm{sym}} = 2\int_{r_0}^{r_{max}} 4\pi n_0 r^2 g(r)\mathrm{d}r, \quad Z^{\mathrm{min}} = \int_{r_0}^{r_{min}} 4\pi n_0 r^2 g(r)\mathrm{d}r \tag{2.1.8}$$

Typically, $Z \approx 12$ for liquid metals, corresponding to close packing. In Figure 2.1.8, small wiggles are visible below the first sharp peak, between 1 and 2 Å. These are artifacts of the Fourier transform, Equation (2.1.7). These effects have been studied in detail by Hoyer et al. [40]. Experimentally, neither $Q = 0$, nor very large Q are accessible, which lead to truncation errors of the Fourier transform. Great care should therefore be taken in interpreting features below the first sharp peak.

So far, we have only discussed the static structure factor, which is obtained from elastic scattering, i.e., when only momentum but not energy is exchanged between the beam and the atoms. For inelastic scattering, the static structure factor $S(Q)$ has to be replaced by the dynamic structure factor $S(Q, \omega)$. As mentioned before, inelastic scattering experiments yield information about time-dependent, dynamic processes, like diffusion.

A further complication arises, when we want to investigate liquid alloys, i.e., liquids with different atoms. In such a case, we are interested in chemical ordering, i.e., we not only want to know where an atom sits but also which kind of atom it is. This leads us to partial structure factors. The formalism has been first worked out by Faber and Ziman [41]. As a first step, we have to generalize Equation (2.1.6), since each kind of atom has a different scattering factor f. For multicomponent systems, the generalized equation reads

$$S(Q) = \frac{I(Q) - \langle |f|^2 \rangle + |\langle f \rangle|^2}{|\langle f \rangle|^2}, \quad |\langle f \rangle|^2 = \left|\sum c_i f_i\right|^2, \langle |f|^2 \rangle = \sum c_i |f_i|^2 \tag{2.1.9}$$

Here, f_i are the different atomic scattering functions and c_i the atomic concentrations of the elements. The total structure factor is an average of the contributions of the different atom pairs to the total scattering intensity:

$$S^{\mathrm{FZ}}(Q) = \sum\sum W_{ij} S_{ij}^{\mathrm{FZ}}(Q), \quad W_{ij} = \frac{c_i c_j f_i f_j}{|\langle f \rangle|^2} \tag{2.1.10}$$

In the above equation, the superscript FZ stands for Faber-Ziman. For a binary system, there are three partial structure factors, namely, S_{AA}, S_{BB}, and S_{AB}, and, correspondingly, three different partial pair-distribution functions $g_{ij}(r)$.

Obviously, one cannot determine three partial structure factors from a single experiment, which only yields the total structure factor. In fact, three independent experiments are required to obtain the three unknowns S_{AA}, S_{BB}, and S_{AB}. One possibility to obtain the partial structure factors is offered by isotopic substitution in neutron diffraction. Different (stable) isotopes have different scattering functions f_i. Therefore, replacing one isotope by another does not change the chemistry, but yields a different total structure factor. Unfortunately, this elegant method is rather expensive. Another possibility is offered by reverse modeling. Defining a topological model, one can calculate its theoretical structure factor for both X-ray and neutron diffraction. By varying the model parameters until both spectra are fitted simultaneously, one can obtain the desired information.

Finally, it should be mentioned that the EXAFS technique is also element specific, as it probes the absorption edge of the scattering atom, which differs from atom to atom. The principle of EXAFS is shortly outlined in the following. The X-ray absorption coefficient of an isolated atom exhibits sharp edges at distinct energies which correspond to the ionization thresholds of the core electrons. If the atom is surrounded by other atoms in a condensed phase, the absorption coefficient at energies of about 50–1000 eV above an absorption edge is observed to oscillate. This structure is called EXAFS (extended X-ray absorption fine structure) and reflects the scattering of the emitted electron by the surrounding atoms. An excellent review of EXAFS can be found in Refs. [42,43]. The EXAFS signal is defined as the difference between the actual absorption $\alpha(Q)$ and the absorption of an isolated atom, $\alpha_0(Q)$, normalized to $\alpha_0(Q)$:

$$\chi(Q) = \frac{\alpha(Q) - \alpha_0(Q)}{\alpha_0(Q)} \tag{2.1.11}$$

where Q is the wave vector of the emitted electron. This quantity is analogous to the structure factor in diffraction experiments. It is related to the pair-distribution function by

$$\chi(Q) = -\frac{3f}{2Q} \int_0^\infty \frac{g(r)}{r^2} \mathrm{e}^{-2r/\lambda} \sin(2Qr + \phi(Q)) \mathrm{d}r \tag{2.1.12}$$

where f is the absolute value of the scattering amplitude, $\phi(Q)$ is the total phase shift of the electron wave function, λ is the electron mean-free path, and $g(r)$ is the pair-distribution function. This formula is similar to the Fourier transform, Equation (2.1.7); note,

however, the presence of the factor 2 in the argument of the sine function. This implies that EXAFS measurements cover twice as much of Q-space as diffraction experiments. The integral cannot be inverted directly; instead parametric models of $g(r)$ are used to fit the experimentally determined function $\chi(Q)$.

When discussing topological versus chemical order, the partial structure factors of the Faber-Ziman formalism are not really suitable. A better way to distinguish between topological and chemical ordering is offered by the so-called Bhatia-Thornton Formalism [44], which can be applied most conveniently to binary systems. In this formalism, three new structure factors S_{NN}, S_{Nc}, and S_{cc} are introduced, corresponding to number-number, number-concentration, and concentration-concentration correlations. The corresponding partial pair-distribution functions g_{NN}, g_{Nc}, and g_{cc} have a direct physical interpretation: $g_{\mathrm{NN}}(r)$ is the probability of finding any particle at position r, while $g_{\mathrm{cc}}(r)$ yields the probability of finding a like ($g_{\mathrm{cc}} > 0$) or unlike ($g_{\mathrm{cc}} < 0$) particle at distance r. Consequently, topological order is described by g_{NN}, while chemical order appears in g_{cc}. In terms of the Faber-Ziman distribution functions, these new entities are defined as

$$\begin{aligned} g_{\mathrm{NN}}(r) &= c_{\mathrm{A}}^2 g_{\mathrm{AA}}(r) + 2c_{\mathrm{A}}c_{\mathrm{B}}g_{\mathrm{AB}}(r) + c_{\mathrm{B}}^2 g_{\mathrm{BB}}(r) \\ g_{\mathrm{Nc}}(r) &= c_{\mathrm{A}}c_{\mathrm{B}}\{c_{\mathrm{A}}g_{\mathrm{AA}}(r) + (c_{\mathrm{B}} - c_{\mathrm{A}})g_{\mathrm{AB}}(r) - c_{\mathrm{B}}g_{\mathrm{BB}}(r)\} \\ g_{\mathrm{cc}}(r) &= c_{\mathrm{A}}^2 c_{\mathrm{B}}^2\{g_{\mathrm{AA}}(r) - 2g_{\mathrm{AB}}(r) + g_{\mathrm{BB}}(r)\} \end{aligned} \tag{2.1.13}$$

while the two sets of structure factors are related by following equations:

$$\begin{aligned} S_{\mathrm{NN}} &= c_{\mathrm{A}}S_{\mathrm{AA}} + 2(c_{\mathrm{A}}c_{\mathrm{B}})^{1/2}S_{\mathrm{AB}} + c_{\mathrm{B}}S_{\mathrm{BB}} \\ S_{\mathrm{Nc}} &= c_{\mathrm{A}}c_{\mathrm{B}}\left\{S_{\mathrm{AA}} + \left[\left(\frac{c_{\mathrm{B}}}{c_{\mathrm{A}}}\right)^{1/2} - \left(\frac{c_{\mathrm{A}}}{c_{\mathrm{B}}}\right)^{1/2}\right]S_{\mathrm{AB}} - S_{\mathrm{BB}}\right\} \\ S_{\mathrm{cc}} &= c_{\mathrm{A}}c_{\mathrm{B}}\left\{c_{\mathrm{B}}S_{\mathrm{AA}} - 2(c_{\mathrm{A}}c_{\mathrm{B}})^{1/2}S_{\mathrm{AB}} + c_{\mathrm{A}}S_{\mathrm{BB}}\right\} \end{aligned} \tag{2.1.14}$$

Bhatia and Thornton have also shown that $S_{\mathrm{cc}}(Q=0)$ becomes very simple for an ideal mixture, namely

$$S_{\mathrm{cc}}^{\mathrm{ideal}}(0) = c_{\mathrm{A}}c_{\mathrm{B}} \tag{2.1.15}$$

Consequently, any deviation from ideal mixing can be detected in $S_{\mathrm{cc}}(0)$.

Sometimes, one does not need the entire spatial information contained in the partial pair-distribution functions. Instead one would like to have a single number, characterizing the degree of chemical ordering. Such a concept was introduced by Warren and Cowley [45] by defining the order parameter α, named after them, from the conditional probability of finding an A atom as the nearest neighbor to a B atom:

$$p_{\mathrm{A|B}} = c_{\mathrm{A}}(1 - \alpha) \tag{2.1.16}$$

For $\alpha = 0$, the distribution is random, $\alpha < 0$ indicates preference of A-B pairs (heteroassociation), while $\alpha > 0$ indicates preference of A-A pairs (self-association, segregation). The Warren-Cowley order parameter can be related to $S_{cc}(0)$:

$$\frac{S_{cc}(0)}{c_A c_B} = \frac{1+\alpha}{1-(Z-1)\alpha} \tag{2.1.17}$$

2.1.1.4. Results

2.1.1.4.1 Pure Elements

The early diffraction experiments on molten metals concentrated on simple systems with relatively low melting points, due to the experimental difficulties outlined above. Typical examples are Rb, Cs, Hg, In, Sn, and Al. The alkali metals offer the additional advantage of being amenable to theoretical treatments due to the small number of conduction electrons and their stable valence. Pioneering work on this group of liquid metals has been performed by Waseda and Suzuki [46]. They were also among the first to report data for the noble and transition metals Ag, Au, Cu, Fe, and Ni [47]. These experiments yielded nearest neighbor distances and coordination numbers close to the respective melting points. As an example, we show the results for liquid Cs in Figure 2.1.9. The density is scaled to the density at the melting point, ρ_{mp}.

Particularly interesting is the more recent work on expanded liquid Hg in the metallic region by Hosokawa *et al.* [49]. They have studied this system at high temperatures and low densities, close to the critical point of the liquid-vapor phase transition. Here, one expects a metal to nonmetal transition due to the diminishing electron density. Liquids in

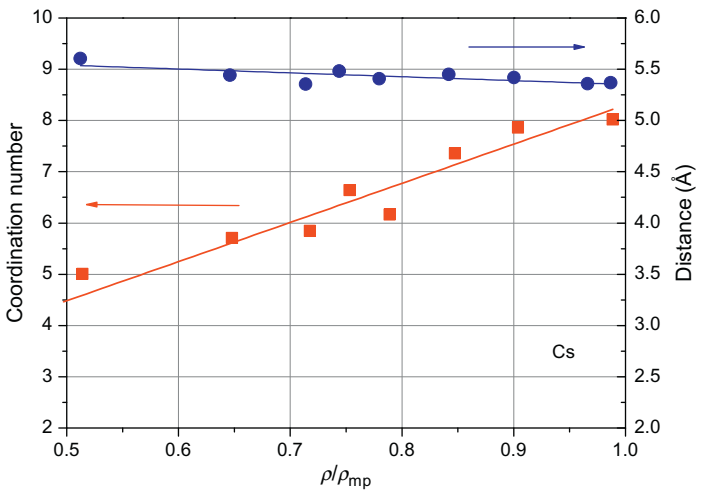


Figure 2.1.9 Coordination number and nearest neighbor distance of Cs as a function of density. *After Ref. [48].*

this region are called "expanded," indicating that a substantial thermal expansion has occurred as compared to the standard room temperature state. Hosogawa *et al.* report the density dependence of the coordination number Z, as well as that of the nearest neighbor distance. The latter is essentially independent of density, whereas the coordination number increases with increasing density. This is shown in Figure 2.1.10. From dimensional considerations, it is clear that the density should scale as $\propto Z/r^3$, where Z is the coordination number and r is the nearest neighbor distance. In addition, as the density scales inversely with temperature in the liquid phase, this implies that the nearest neighbor distance is temperature independent, while the coordination number increases with decreasing temperature. This can be easily understood by noting that the neighbor distances in liquids are essentially determined by the (temperature-independent) atomic radii, while the filling of the first neighbor shell becomes more perfect as the temperature is lowered.

The first observations of short-range order in liquid alloys are due to Ruppersberg for Li-Pb [50] and Ag-Li [51]. In the following, we will however concentrate on more recent experimental results, covering a wide temperature range, including the undercooled regime. They have been mainly obtained by ENS experiments, using a dedicated EML device [52]. In a first set of experiments, the structure factors of the transition metals Fe, Ni, and Zr were determined [53]. Structure factors $S(Q)$ measured by ENS for melts Fe, Ni, and Zr at different temperatures below and above the melting temperature T_L are shown in Figure 2.1.11. All structure factors of the three metals show a characteristic shoulder on the second oscillation, which becomes more pronounced at lower temperatures. The structure factors have been modeled assuming different structures of the melt,

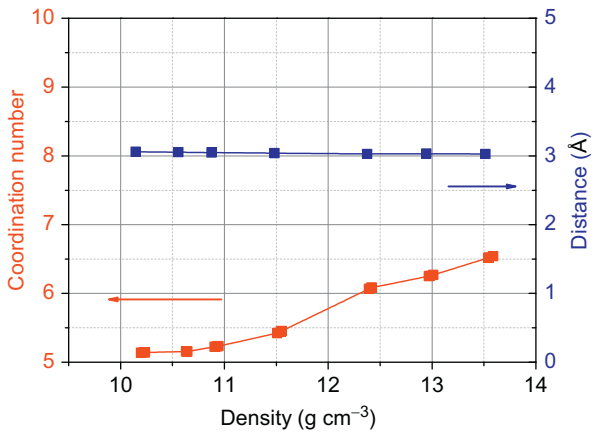


Figure 2.1.10 Coordination number and nearest neighbor distance as function of density for liquid Hg. *After Ref. [49].*

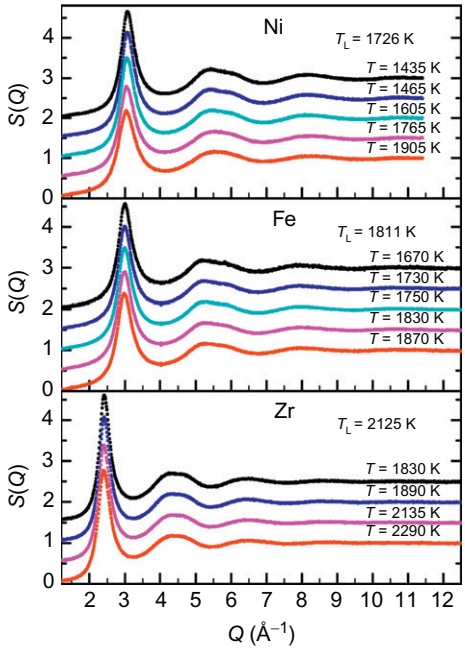


Figure 2.1.11 Structure factors measured by neutron scattering for liquid Fe, Ni, and Zr at different temperatures above and below the melting temperature T_L. *After Ref. [53].*

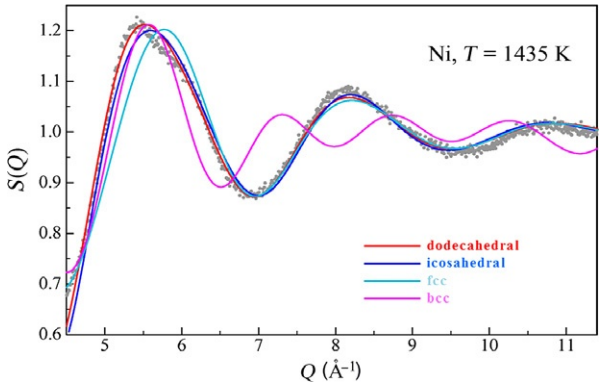


Figure 2.1.12 Fit of the structure factor $S(Q)$ of liquid nickel by different structural models. *After Ref. [53].*

namely fcc, bcc, icosahedral, and dodecahedral order. The fitting was constrained to higher Q-values $Q > 4.5$ Å^{-1}, in order to emphasize the short-range order. The measured structure factors are best described by assuming an icosahedral or dodecahedral order in the melt [53], providing a direct experimental confirmation of Frank's hypothesis [11]. This is shown in Figure 2.1.12 for liquid nickel.

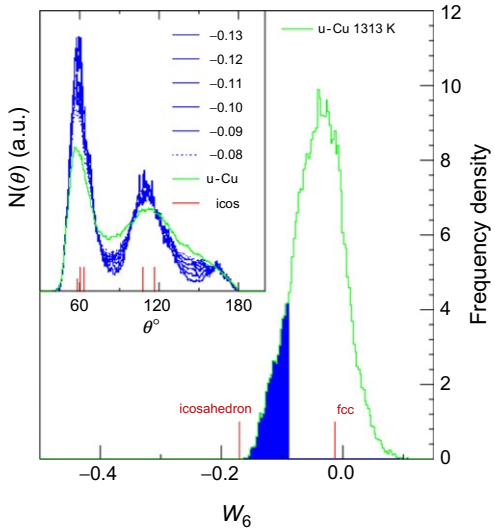


Figure 2.1.13 Cubic invariant, W_6, and bond angle distribution, $N(\theta)$ in undercooled liquid copper. *After Di Cicco and Trapananti [54].*

Using the EXAFS technique, and extending the analysis to three-body correlation functions, Di Cicco and Trapananti [54] have investigated the structure of undercooled liquid copper. Their method also yields, in addition to coordination numbers and distances, bond angle distributions. They find clear evidence for icosahedral order and estimate that about 10% of all atoms are icosahedrally coordinated. Specifically, they have studied the W_6 cubic invariant, introduced by Steinhardt et al. [55] for bond-orientational order. Their result is shown in Figure 2.1.13. The typical values of W_6 for icosahedral and cubic (fcc) order are indicated by vertical bars. Icosahedral order is more evident in $N(\theta)$, the bond angle distribution, with clear maxima at 60° and 110°, and a minimum at 90°, in contrast to cubic systems, where 90° would be most pronounced.

From the structure factors, pair-correlation functions $g(r)$ can be calculated, from which in turn atomic distances and coordination numbers are derived. This is shown in Figure 2.1.14 for Ni, Fe, and Zr as a function of temperature. As in the previous cases, the distances are essentially temperature independent, whereas the coordination numbers decrease with increasing temperature.

Of particular interest is the local structure of liquid silicon. While solid Si—crystalline or amorphous—is a semiconductor, liquid silicon is metallic. Also, the density of silicon increases upon melting, indicating that the atoms in the liquid are more closely packed than in the solid. This is the same density anomaly that we observe in water. As a corollary to this phenomenon, what about the glass transition? It is hardly conceivable that the glass transition should be a first-order phase transition, whereby solidification and

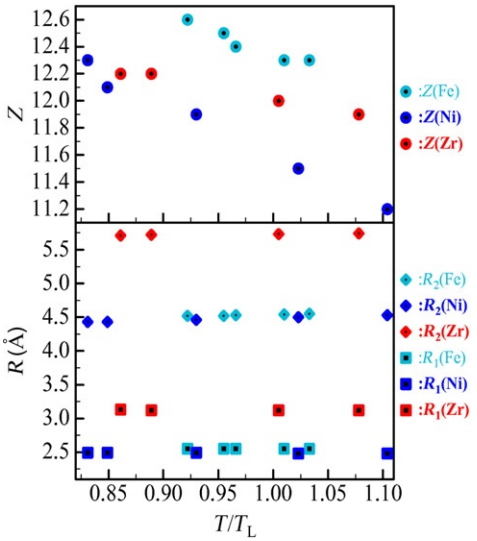


Figure 2.1.14 Coordination number, Z, and neighbor distances, R, as a function of temperature for the three metals Fe, Ni, and Zr. Temperature is scaled by T_L, the corresponding liquidus temperature. *Data from Ref. [53].*

metal-semiconductor transition happen simultaneously. One possible scenario is a liquid-liquid phase transition, accompanied by a metal-semiconductor transition at a slightly higher temperature than the glass temperature, at which the semiconducting liquid solidifies into its final amorphous phase. Recent MD simulations, using either an effective potential [56] or *ab initio* calculations, seem to support this interpretation [57].

A number of research groups have investigated liquid silicon, in particular in its undercooled state [25,58–62], with contradicting results. Stich has also performed an *ab initio* quantum mechanical calculation of liquid silicon at the melting point [63]. Here we summarize the results and discuss in some detail the measurements by Kimura *et al.* [60].

Measurements on undercooled liquids are time critical. Therefore, experimental techniques with short sampling times are preferred. This is the case for energy dispersive X-ray diffraction (EDXRD), where, in contrast to angle-resolved diffraction, an entire spectrum is recorded instantaneously, without waiting for moving parts to reach their position. The difficulty in EDXRD experiments stems from the correction of the energy dependence of incoming intensity, sample absorption, and detector efficiency. This is achieved by taking subsequently spectra at different angles and fitting them simultaneously by a reverse Monte Carlo (RMC) technique. An additional complication arises from the fact that EML works only for electrically conducting specimen. Because solid silicon is not metallic, its EML requires preheating in order to increase its intrinsic

conductivity to a value sufficient for levitation. This is accomplished by using a graphite rod covered by Al_2O_3 simultaneously as sample holder and indirect heater, as suggested by Herlach and coworkers [64]. Once molten, silicon becomes metallic and is very easy to levitate due to its low density. In these experiments, a wide temperature range, including the undercooled regime, was covered and the corresponding structure factors $S(Q)$ were determined. They are shown in Figure 2.1.15, together with the constructed pair-correlation functions. A prominent shoulder of the first peak in $S(Q)$ is clearly visible in the spectra, especially at lower temperatures.

From the pair-distribution functions, the nearest neighbor distances as well as the coordination numbers were obtained as functions of temperature. This is shown in Figures 2.1.16 and 2.1.17, respectively. These results indicate a negligible temperature dependence of the neighbor distance, and a decrease of the coordination number with increasing temperature, consistent with a positive thermal expansion, as discussed above. The data agree with those of Waseda et al. [59], but are at variance with the results of Ansell *et al.* [58] who find that both the nearest neighbor distance and the coordination number increase with temperature. More recent experiments by Kelton *et al.* [61] find a temperature-independent coordination number of $Z=6$ between 1100 and 1500 °C; nearest neighbor distances are not reported.

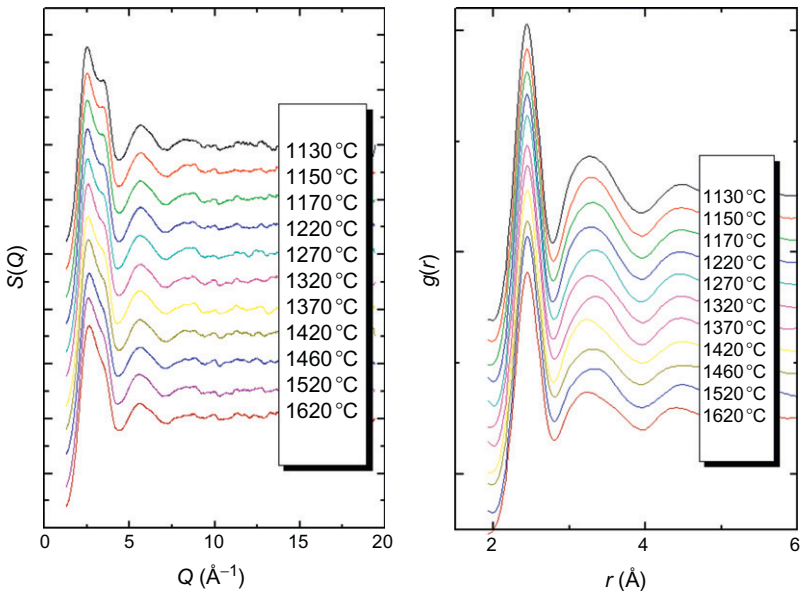


Figure 2.1.15 Structure factor $S(Q)$ (left) and pair-distribution function $g(r)$ (right) of liquid and undercooled silicon at different temperatures. *After Ref. [60].*

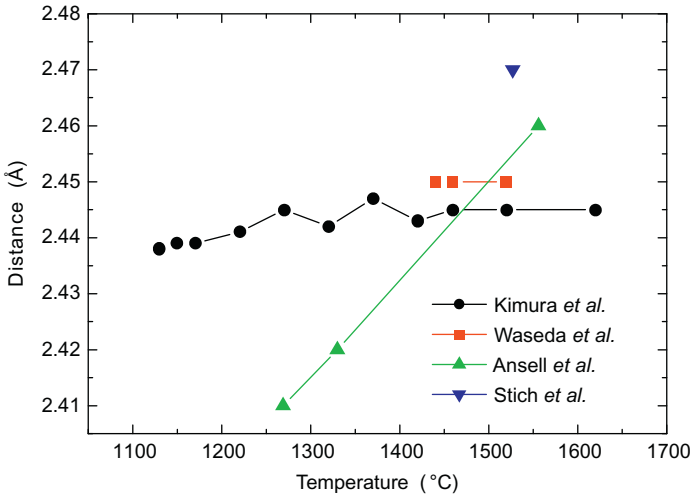


Figure 2.1.16 Nearest neighbor distance in liquid Si by different authors.

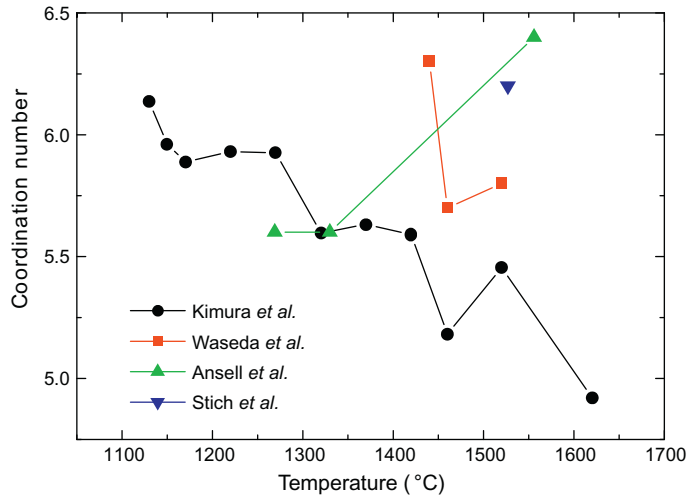


Figure 2.1.17 Coordination number in liquid Si by different authors.

2.1.1.4.2 Alloys

When discussing the structure of liquid alloys, a new category of topics come into play, namely how the different species are distributed, or, in other words, whether there is chemical ordering. Whereas for pure elements topological short-range order, expressed by coordination numbers and distances, is the main issue, we may now address the question of chemical short-range order. The theoretical framework is provided by the partial

structure factors, discussed above. From the experimental point of view, neutron scattering experiments become indispensable. While for monoatomic systems ENS and X-ray diffraction provide, in principle, the same structural information, for alloys the measured total structure factors strongly depend the ratios of the scattering lengths of the alloy components for different types of radiation. Hence, the structural information gained by neutron scattering is complementary to that of X-ray experiments as demonstrated in a recent study on the topological and chemical short-range order of electromagnetically levitated Ti-Fe melts [65]. A special strength of neutron scattering techniques results from the fact that different isotopes of the same element show different neutron scattering lengths. Hence, isotopic substitution techniques allow to vary the neutron scattering contrast of the alloy components and to determine partial structure factors. Isotopic substitution of Ni (using natural Ni, ^{60}Ni, and, ^{58}Ni) has recently been utilized for the determination of the full set of partial structure factors in binary $Zr_{64}Ni_{36}$ melts processed under containerless conditions by EML [66]. It should be noted however, that not all metals have stable isotopes, and some are very expensive. In such cases, when isotopes are not available or are too expensive, partial structure factors of alloys can also be determined by a similar approach, namely the isomorphous substitution of one alloy component by another chemically similar element. Examples of this kind are the investigations on Al-(Co,Fe) melts [53]. Here the assumption is made that substituting Fe by Co does not change the chemistry, as these two elements are very similar (as compared to Al, the other alloying element).

An interesting and much discussed effect in the structural data of liquid alloys is the so-called prepeak [34]. The prepeak appears at smaller Q-values than the FSDP in the structure factor $S(Q)$. If we attribute the FSDP as the Fourier transform of the nearest neighbor distance, then the prepeak corresponds to distances larger than that; therefore the existence of a prepeak is interpreted as a superstructure, or medium-range order. It is also a sign of chemical ordering, and is mainly found in compound-forming alloys, the classical example being Ag-Mg [67]; a more recent one is the work of Hoyer *et al.* on the eutectic system Au-Ge [68].

There is a large amount of structural data for binary alloys, and very little for ternary or multicomponent systems. It is impossible to present a comprehensive overview over all these data. Instead, we will discuss some showcases, which have received some attention recently and which can serve as representing the width of typical applications.

We start our discussion with the work of Hoyer *et al.* on liquid eutectic $Ge_{15}Te_{85}$ [69]. In their analysis they combined X-ray diffraction data with neutron data and modeled both spectra simultaneously by an RMC technique. This allowed them to reconstruct all partial structure factors and partial pair-correlation functions as shown in Figure 2.1.18. As is evident, nearest neighbors are Ge-Te pairs at approximately 2.7 Å, while Ge-Ge pairs can only be found at larger distances at app. 4 Å, as second nearest neighbors. Te-Te pairs appear in both shells, as first and second nearest neighbors.

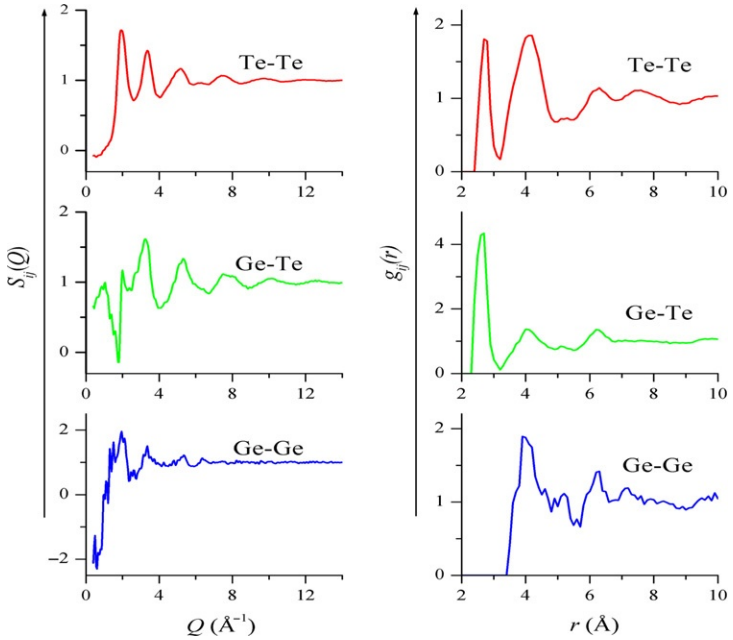


Figure 2.1.18 Partial structure factors $S_{ij}(Q)$ and partial pair-correlation functions $g_{ij}(r)$ for liquid $Ge_{15}Te_{85}$. *After Ref. [69].*

The coordination numbers are as follows: $Z_{Ge\text{-}Te} = 3.7$, $Z_{Te\text{-}Te} = 1.7$. This is consistent with a tetrahedral order in the liquid phase.

We now turn to the system Al-Ni. This is a technologically interesting material, and its phase diagram displays a number of intermetallic phases. Al-Ni can be considered as an example for a compound-forming alloy. Neutron diffraction [70], X-ray diffraction [71], and EXAFS investigations [72] have been reported. Maret and coworkers [70] have investigated $Al_{80}Ni_{20}$ by neutron diffraction. They found a prepeak and could attribute it to Ni-Ni pairs. Distances and coordination numbers are as follows: $r_{Ni\text{-}Ni} = 2.6$ Å, $r_{Ni\text{-}Al} = 2.54$ and 3.5 Å, $r_{Al\text{-}Al} = 2.82$, $Z_{Ni\text{-}Ni} = 1.7$, $Z_{Ni\text{-}Al} = 10.9$, and $Z_{Al\text{-}Al} = 9.6$. From the coordination numbers, the Warren-Cowley order parameter α was determined as $\alpha = -0.09$. A negative α indicates preference for heteroatomic ordering, i.e., a tendency for compound formation. The results of Maret were confirmed by Egry and coworkers [71], using high-energy X-ray diffraction (HEXRD) on levitated Al-Ni alloys. Due to the relatively low melting points of these alloys, a hybrid aerodynamic-EML technique was employed [71]. The HEXRD technique, in combination with data acquisition by an image plate, offers quick acquisition times, suitable for undercooled liquids. This is due to the fact that no parts have to be moved mechanically, and an entire spectrum is taken in a single shot. As pointed out previously, short sampling times are indispensable for

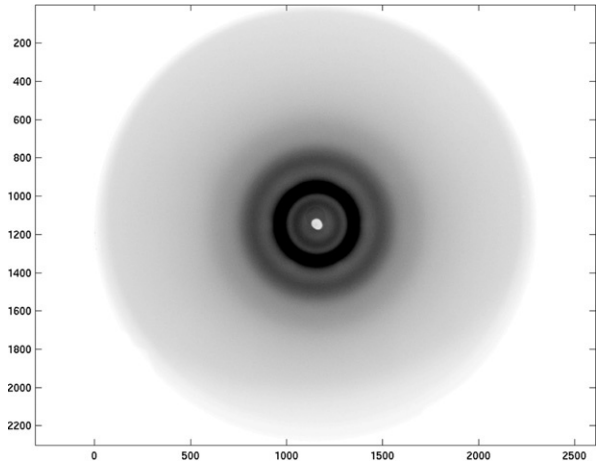


Figure 2.1.19 Diffraction image of a liquid Al_3Ni sample.

experiments on undercooled liquids. A typical image of an experiment run on liquid, Al_3Ni is shown in Figure 2.1.19. As can be seen, the scattering is isotropic; there is no angular dependence. In fact, solidification of the undercooled liquid can be observed as the appearance of sharp Bragg peaks at specific angular positions. An angular integration of the image is performed to obtain the raw intensity $I(Q)$. Subsequent data treatment yields the total structure factor, $S(Q)$. Partial structure factors are not accessible by this technique. In contrast to Maret's work, two different alloys were studied, one with intermetallic (Al_3Ni) and the other with eutectic composition (Al-2.7 at% Ni), in order to study the influence of compound formation on the prepeak. It is believed that such chemical order should be most pronounced in the liquid at compositions where the corresponding solid displays a (stoichiometric) intermetallic phase. Indeed, a prepeak in $S(Q)$ was found for the intermetallic composition (Al_3Ni), while no prepeak exists for the nickel-poor eutectic composition. This is shown in Figure 2.1.20. Alternatively, one can also argue that the amplitude of the prepeak is simply proportional to the nickel concentration of the alloy, since it is due to Ni-Ni correlations. This question is unresolved and would require a series of experiments, scanning through the entire composition range.

In order to shed more light on the chemical ordering and its composition dependence, EXAFS spectra were also taken, using the same hybrid levitator, for six different compositions of the Al-Ni alloy, starting with 5 at% Ni, and increasing it to 30 at% in steps of 5 at%. Spectra were taken at the absorption edge of Ni, probing the local environment of a nickel atom [72]. The obtained spectra were fitted by a two-shell model, one for Al, and one for Ni neighbors. A typical example of the data and the quality of the fit is shown in Figure 2.1.21 for $Al_{70}Ni_{30}$.

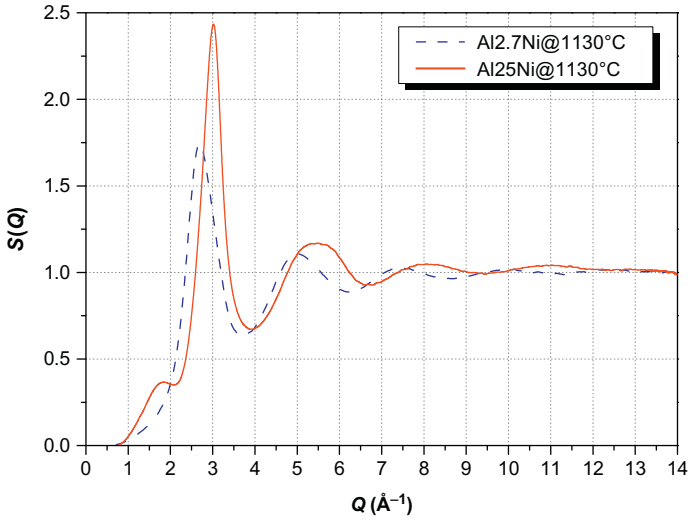


Figure 2.1.20 Structure factor $S(Q)$ of liquid eutectic (Al-2.7 at% Ni) and intermetallic (Al_3Ni) Al-Ni alloys.

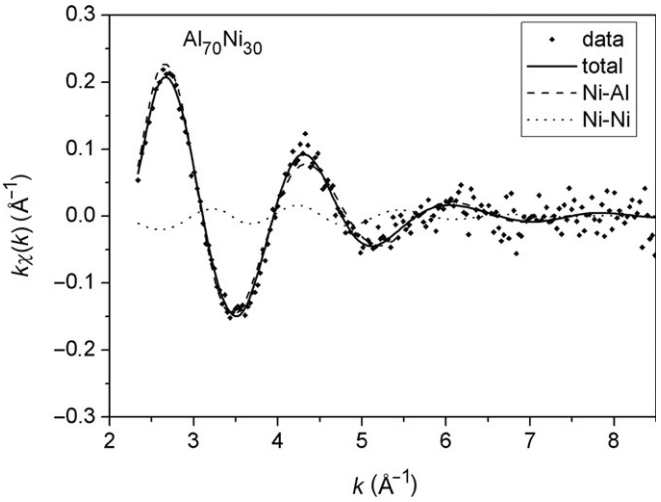


Figure 2.1.21 EXAFS spectrum of $Al_{70}Ni_{30}$ taken at the Ni K edge. Data points are designated by dots, the fit by the full line, the contribution of Al and Ni shells by the dashed and dotted lines, respectively.

As a result of the fitting procedure, the number of nickel neighbors, n_{Ni}, and the number of aluminum neighbors, n_{Al}, was obtained. From these parameters, an order parameter, $\Phi(x)$, can be constructed, where x is the concentration of Ni. It is defined as

$$\Phi(x) = \frac{n_{\mathrm{Ni}}}{n_{\mathrm{Al}}}\frac{1-x}{x} - 1 \tag{2.1.18}$$

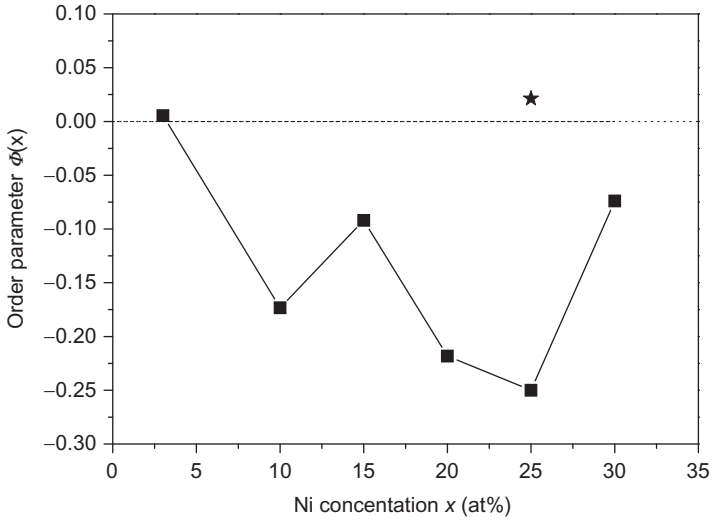


Figure 2.1.22 Order parameter in Al-Ni alloys as a function of composition. Full squares correspond to spectra taken at 980 °C, whereas the star refers to a spectrum at 1150 °C.

This is very similar to the Warren-Cowley order parameter α, adapted to EXAFS data. For a random distribution $\Phi(x) = 0$. $\Phi(x) > 0$ corresponds to homo-atomic association, while $\Phi(x) < 0$ indicates a preference for heteropairs. The experimentally determined $\Phi(x)$ at 980 °C is shown in Figure 2.1.22. For all values of x, $\Phi(x) < 0$, indicating a preference for Al-Ni pairs. This behavior is particularly pronounced at the intermetallic composition Al_3Ni. With increasing temperature, this chemical short-range order is destroyed, as indicated by the star in Figure 2.1.22, obtained at 1150 °C.

We now turn to our last example, Al(Co,Fe). Structural data on this alloy have been obtained with neutron diffraction by isomorphous substitution of Co by Fe. The interpretation of the data is based on the Bhatia-Thornton partial structure factors, in order to complement our previous discussion of the Ge-Te alloy. With this method, the partial structure factors of an $Al_{13}(Co,Fe)_4$ alloy were determined by stepwise replacement of Co by Fe [73]. The total structure factors measured for $Al_{13}(Co,Fe)_4$ melts with different Co/Fe ratio at two different temperatures are shown in Figure 2.1.23. Variation of the scattering length of the transition metal (TM) component results in marked differences of the measured total structure factors depending on the composition, as for instance the intensity of the prepeak at about 1.7 $Å^{-1}$ and the shape of the second oscillation. From three of these total structure factors, measured with different scattering contrast of the components, all three partial structure factors of the quasi-binary Al-TM are calculated and, by Fourier transformation, also the corresponding partial pair-correlation functions, providing information on both chemical and topological short-range order in the liquid. As an example, the Bhatia-Thornton pair-correlation functions of the $Al_{13}(Co,Fe)_4$ melts

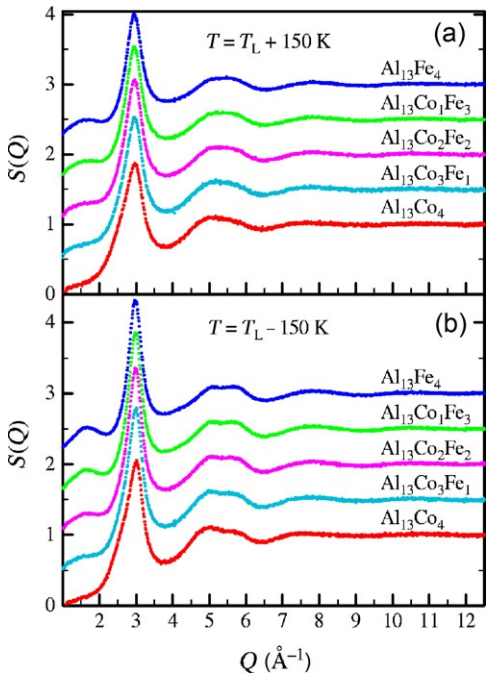


Figure 2.1.23 Total structure factors measured by neutron scattering for different liquids of $Al_{13}(Co, Fe)_4$ at temperatures 150 K above (a) and below (b) the liquidus temperature T_L. *After Ref. [73].*

are shown in Figure 2.1.24 for different temperatures. A deep minimum in $G_{cc}(r)$ is visible at nearest neighbor distance, indicating chemical short-range order, and a preference for heteroatomic pairs. With decreasing temperature, this effect becomes more pronounced.

2.1.2. PROPERTIES

Whereas we have been concerned with microscopic structural properties in the previous chapter, we now turn our attention to macroscopic properties of molten metals. These comprise mechanical, thermal, and electrical properties. Sometimes, a distinction is made between thermodynamic and thermophysical properties or between thermal and transport properties. This may be justified from a rigorous statistical mechanics point of view, but it is not really helpful in applications, and we will not make such distinction.

Specifically, we will first introduce the following properties, and methods to measure them, before we discuss some representative results:

- Emissivity
- Density and thermal expansion
- Specific heat

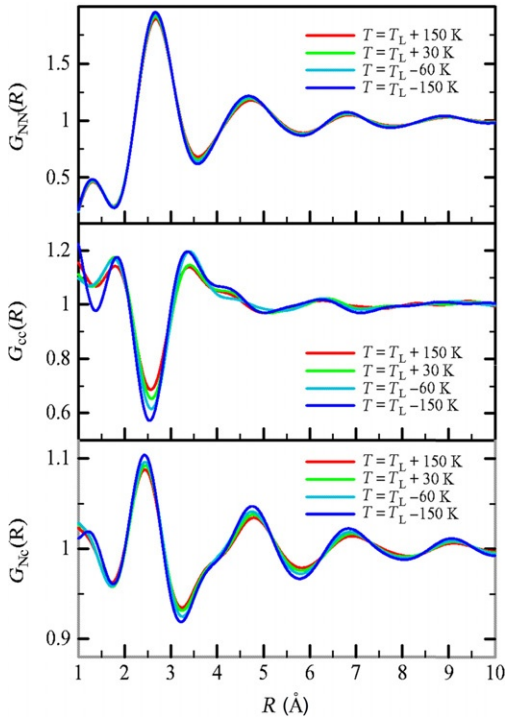


Figure 2.1.24 Bhatia-Thornton partial pair-correlation factors for $Al_{13}(Co,Fe)_4$ for different temperatures obtained by isomorphous substitution. *After Ref. [73].*

- Thermal conductivity
- Thermal diffusivity
- Electrical conductivity
- Mass diffusion
- Viscosity
- Surface tension

Excellent review papers of this topic exist [74–76], and the reader is referred to these articles for more details. A very recent field, namely the utilization of the microgravity environment on board an orbiting spacecraft for thermophysical property measurements, will not be discussed here, as there are corresponding review articles [5,77].

2.1.2.1. Experimental Techniques

2.1.2.1.1 Pyrometry

It is necessary to start our discussion by addressing the question of temperature measurement at high temperatures. At high temperatures, the use of thermocouples for temperature measurement becomes increasingly difficult due to chemical reactions with the

molten metal. For containerless techniques, they cannot be used anyway. Therefore, noncontact temperature measurement techniques, such as pyrometry, have to be employed. Pyrometry is based on Planck's law for blackbody radiation, which relates the emitted power to the true thermodynamic temperature of a black body. In Wien's approximation, the spectral radiance per unit area, J_b, of a black body is given by [78]

$$J_b(\lambda,T)=\frac{c_1}{\lambda^5}\exp\left(-\frac{c_2}{\lambda T}\right),\quad c_1=1.19\times10^8\,\mathrm{W\,\mu m^4\,m^{-2}\,sr^{-1}},\quad c_2=1.44\times10^4\ \mu\mathrm{mK} \tag{2.1.19}$$

where λ is the wavelength and T is the temperature. The total power emitted per unit area into the solid angle of π is obtained by integration over λ and yields the Stefan-Boltzmann law:

$$P_b=\sigma_{S.B.}T^4,\quad \sigma_{S.B.}=5.67\times10^{-8}\,\mathrm{W}\left(\mathrm{m^2K^4}\right)^{-1} \tag{2.1.20}$$

Temperature measurement can be based on both Equations (2.1.19) and (2.1.20), the first being a spectral pyrometer, the latter a total radiance pyrometer, or a bolometer.

Unfortunately, the surface of a molten metal is far from being a black body. To account for this difference, the emissivity $\varepsilon<1$ of a real body has to be introduced into the above equations:

$$J(\lambda,T)=\varepsilon_n(\lambda,T)J_b(\lambda,T) \tag{2.1.21}$$

$$P(T)=\varepsilon_h(T)P_b(T) \tag{2.1.22}$$

where $\varepsilon_n(\lambda,T)$ is the normal spectral emissivity, and $\varepsilon_h(T)$ is the total hemispherical emissivity. (Strictly speaking, the spectral emissivity is also a function of the relative angle θ between surface normal and emission direction: $\varepsilon=\varepsilon(\lambda,T,\theta)$. The normal spectral emissivity is then defined as: $\varepsilon_n(\lambda,T)=\varepsilon(\lambda,T,0)$.) If the emissivity turns out to be independent of wavelength, the specimen is characterized as gray body.

For any material, the emissivity ε is equal to the absorptivity α according to Kirchhoff's law. Consequently, for nontransparent media, like molten metals, the emissivity is related to the reflectivity r by

$$\varepsilon(\lambda,T)+r(\lambda,T)=1 \tag{2.1.23}$$

On the other hand, the normal incidence reflectivity can be calculated from the Beer equation [79]:

$$r_n(\lambda,T)=\frac{(n-1)^2-k^2}{(n+1)^2+k^2} \tag{2.1.24}$$

where n and k are real and imaginary parts of the complex refractive index, respectively. This relation forms the basis for ellipsometric measurements of the normal spectral

emissivity [80]. Alternatively, one can use Equation (2.1.21) to determine this quantity by measuring the spectral radiance of the material and that of a black body at the same temperature simultaneously. This is achieved by using a heated tubular specimen with a carefully designed hole in its wall, serving as blackbody [81]. Originally designed for solid specimen, this technique can also be used for molten metals near the melting point, provided the measurement time is shorter than the time of collapse of the tube, i.e., it is in the μs range. Finally, Righini and coworkers have developed a method based on an integrating sphere [82].

Conventional pyrometers are usually single-color, narrow-band pyrometers based on Equation (2.1.21), operating in a narrow band around a central wavelength λ_0. If the spectral emissivity is known from independent measurements, Equations (2.1.19) and (2.1.21) allow a direct determination of the true temperature [83]:

$$\frac{1}{T}-\frac{1}{T_{\mathrm{P,b}}}=\frac{\lambda_0}{c_2}\ln[\varepsilon(\lambda_0,T)] \tag{2.1.25}$$

where $T_{\mathrm{P,b}}$ is the temperature reading of the pyrometer calibrated with a black body of temperature T. In practice, however, the emissivity is often not known, and the pyrometer is calibrated at a suitable temperature T_{L}, which in most cases is taken to be the melting or liquidus temperature. This temperature is known from thermodynamic data, such as phase diagrams, and is easily recognizable in heating or cooling curves due to thermal arrests at melting. The reciprocal difference between the true temperature, T, and the pyrometer reading, T_{P}, is then given by the difference of the reciprocal calibration temperature and the pyrometer reading at that temperature $T_{\mathrm{L,P}}$:

$$\frac{1}{T}-\frac{1}{T_{\mathrm{P}}}=\frac{1}{T_{\mathrm{L}}}-\frac{1}{T_{\mathrm{L,P}}} \tag{2.1.26}$$

This approximation of course assumes that the emissivity is not strongly dependent on temperature. It has been shown [84] that the emissivity of pure metals depends only slightly on temperature. For alloys, in particular if there is surface segregation, this may not be true. When performing this calibration, it must be made sure that the pyrometer looks at a completely molten surface, because the emissivity of the solid (of the molten metal or alloy or of an oxide thereof) at the same temperature may be notably different.

There are numerous attempts to overcome the problem of the unknown emissivity in pyrometric temperature measurements. A popular approach is the use of the so-called ratio or two-color pyrometer [85]. This instrument measures the radiation at two different wavelengths λ_1 and λ_2 and tries to determine the temperature by taking the ratio of the two radiance signals. In analogy to the derivation of Equation (2.1.25) the following equation for the temperature is derived:

$$\frac{1}{T}-\frac{1}{T_{\mathrm{P,b}}}=\frac{\lambda_1\lambda_2}{c_2(\lambda_2-\lambda_1)}\ln\left(\frac{\varepsilon(\lambda_2,T)}{\varepsilon(\lambda_1,T)}\right) \tag{2.1.27}$$

The argument for ratio pyrometry is that the term containing the logarithm of the two emissivities will be generally small, and, moreover, the temperature dependence of the emissivities at different wavelengths will be similar, so that, by taking the ratio, the logarithm will become temperature independent. In practice, unfortunately, these assumptions often do not hold [86]. The main reason is due to the fact that the effective emissivities also contain the transmissivity of the optical path. If there is some degradation due to evaporation, this will usually affect the longer wavelength more strongly and the ratio temperature will drift away from its original value.

2.1.2.1.2 Thermal Expansion and Density

Density is probably the most important thermophysical property. It enters many dimensionless numbers used in hydrodynamics, like the Rayleigh number, *Ra*, defined as

$$Ra=L^4\nabla T g\frac{\rho\beta}{\kappa\eta} \tag{2.1.28}$$

where L is a characteristic system length, ∇T the temperature gradient, g the gravitational acceleration, ρ the density, β the thermal expansion, κ the thermal diffusivity, and η the viscosity of the liquid. The Rayleigh number characterizes buoyancy effects and the onset of thermal convection. Density also plays a decisive role in our everyday life, as shown in Figure 2.1.25.

Yet, both theory and experiment are not fully developed. Conventional fixed-volume simulations are not sufficient to derive molar volumes and thermal expansions. To calculate such entities from first principles, much more effort is required [14].

The density ρ is defined as

$$\rho=\frac{M}{V} \tag{2.1.29}$$

Here, M is the mass and V the volume of the sample. The temperature dependence of the density of pure liquid metals is linear over a wide temperature range; in other words, the thermal expansion is independent of temperature. Physically speaking, it is more appropriate to consider the reciprocal of the density, i.e., the molar volume V_{m}, since this is an extensive (additive) quantity. We can write:

$$\begin{aligned} V_{\mathrm{m}}(T)&=V_{\mathrm{m}}(T_{\mathrm{L}})+V'_{\mathrm{m}}(T-T_{\mathrm{L}})\\ \rho(T)&=\rho(T_{\mathrm{L}})-\rho'(T-T_{\mathrm{L}}) \end{aligned} \tag{2.1.30}$$

where T_{L} is the liquidus temperature. The molar volume of (binary) alloys is conveniently expressed as

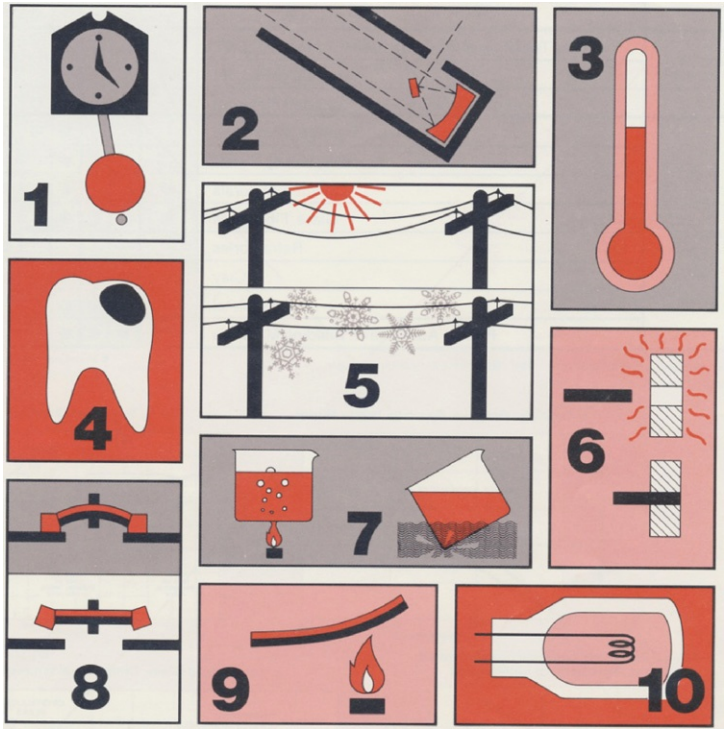


Figure 2.1.25 Examples of everyday density effects. 1, clock pendulum; 2, telescope mirror; 3, thermometer; 4, dental filling; 5, power lines; 6, shrink fit; 7, pyrex glass; 8, bimetal switch; 9, bimetal thermometer; 10, glass-metal seal. *By courtesy of Theta Industries.*

$$V_{AB} = c_A V_A + c_B V_B + V_x \tag{2.1.31}$$

Here V_A, V_B are the molar volumes of components A and B, respectively, and c_A, c_B are their respective mole fractions. The quantity V_x is the so-called excess volume. It can be negative or positive, depending on the details of the atomic interactions [87]. For $V_x = 0$, Equation (2.1.31) reduces to the ideal mixing, or Vegard's law [88].

Experimentally, there are a number of different measurement techniques available, but not all of them are well suited for high-temperature systems, such as metallic melts. Most density measurements are in fact volume measurements of a sample of known mass. The most important techniques are Archimedean, dilatometric, gamma-ray attenuation, levitated drop (LD), maximum bubble pressure (MBP), pycnometric, and sessile drop (SD). An extensive review of the densities of liquid metals and alloys and their measurement has been given by Crawley [89] and later by Iida and Guthrie [2]. As far as available data are concerned, the handbook of physicochemical properties at high temperatures is an excellent compilation [90]. The two most popular techniques are the MBP and the

pycnometric method. The latter has probably the highest accuracy of all techniques, while the former is probably the easiest to use. The pycnometric method has been discussed extensively by Crawley; in principle, the mass M of a liquid filling a container of known volume V is measured. For more details, we refer the reader to his review. In the following, we will discuss briefly the MBP technique, the dilatometric techniques, and the LD technique. The latter is still the least used, but maybe has the highest potential. The SD technique is primarily used for surface tension measurements and will therefore be discussed in Section 2.1.2.1.7.

2.1.2.1.2.1 Maximum Bubble Pressure

In this technique, the liquid metal of unknown density is placed in a thermostated vessel. A capillary tube is immersed into the melt at a depth h and pressurized with an inert gas. The pressure necessary to produce a spherical bubble of radius r is given by

$$p_1 = \rho g h + 2\gamma / r \tag{2.1.32}$$

where γ is the surface tension of the liquid metal. Performing the measurement at two different depths, the unknown surface tension can be eliminated and one obtains

$$\rho = \frac{p_1 - p_2}{g(h_1 - h_2)} \tag{2.1.33}$$

In the derivation of Equation (2.1.33), it is assumed that both γ and r are independent of the immersion depth. This means for γ that the temperature inside the melt must be homogeneous. The radius r is that of the maximum bubble, which is maintained by the capillary tube and is assumed to be determined solely by the geometry of the capillary's tip.

The MBP technique is popular because it is easy to use and allows to determine density and thermal expansion as a function of temperature in a single run, in contrast to the pycnometric method. In addition, once the density is known, Equation (2.1.32) can also be used to determine the surface tension of the liquid metal. In practice, measurements at different heights are performed and the pressure is plotted against height. This yields a linear relation, with the slope being given by ρg, and the intercept being $2\gamma/r$. This technique requires rather large amounts of the liquid metal which may turn out to be a considerable cost factor. Since the probing is carried out sub-surface, the sensitive area is only exposed to the inlet gas and therefore reactive metals and alloys can be characterized.

2.1.2.1.2.2 Dilatometers

In contrast to pycnometers, dilatometers measure volumes and volume changes. This means that an amount of liquid metal of known mass is filled into a dilatometer and the volume it occupies is measured. Two types of dilatometers can be distinguished: capillary dilatometers and push-rod dilatometers.

2.1.2.1.2.3 Capillary Dilatometers

The best known example of a capillary dilatometer for liquid metals is the mercury thermometer. In fact, mercury is often used to calibrate dilatometers, i.e., to determine their volumes. Capillary dilatometers consist of a long, thin capillary tube connected to a reservoir of known volume. If the capillary is exactly cylindrical, i.e., there are no variations of the radius r as a function of height h, the volume V of a liquid column inside the capillary is given by

$$V = V_0 + \pi r^2 h \tag{2.1.34}$$

The sensitivity of the apparatus is given by $\mathrm{d}h/\mathrm{d}V = 1/\pi r^2$, and this is the reason why narrow capillaries are used. Capillary dilatometers are well suited to measure volumetric thermal expansion of liquid metals by observing the height of the meniscus as a function of temperature. Corrections must be made for the thermal expansion of the capillary tube itself, and for the meniscus shape, for liquid metals at high temperatures, transparent tubes cannot be used, and the height of the liquid column cannot be read off by visual inspection. In these cases, the height must be measured by electrical contacts [91].

2.1.2.1.2.4 Push-rod Technique

Most commercially available dilatometers apply the push-rod technique. This method was originally developed for solid samples, but it can be extended to liquids by using piston-cylinder devices as special crucibles. The sample is placed between a plate and a moving piston, the push-rod, and the movement of the push-rod is recorded. Both horizontal and vertical configurations are possible, with the latter being preferred for high-temperature sintering studies. Push-rod dilatometers measure the linear thermal expansion of solid samples, i.e., the change Δl. The accessible temperature range is determined by the furnace used and the crucible material. Dilatometers with a temperature range well over 2000 K are commercially available. One special version of push-rod dilatometers uses an optical interferometric system to detect the movement of the push-rod or of the plates enclosing the specimen. This kind of apparatus has been described in detail by Ruffino [92].

When push-rod dilatometers are used to measure thermal expansion of liquids, some care must be taken in the evaluation of the data, especially at the liquid-solid phase transition. Whereas the linear thermal expansion is measured in the solid, the dilatometers indicate the volumetric thermal expansion in the liquid phase. This is due to the fact that the liquid fills the container, and linear thermal expansions in the directions perpendicular to the push-rod movement are converted into linear movements along the push-rod direction. In the case of isotropic expansion, linear thermal expansion β_l and volumetric thermal expansion β_v are simply related by

$$\beta_\mathrm{v} = -\frac{1}{\rho}\frac{\partial \rho}{\partial T} = \frac{1}{V}\frac{\partial V}{\partial T} = 3\beta_\mathrm{l} = 3\frac{1}{l}\frac{\partial l}{\partial T} \tag{2.1.35}$$

Corrections are needed for the thermal expansion of the container itself, i.e., the change in cross section with increasing temperature, and the increase in piston length.

2.1.2.1.2.5 Levitated Drop

Density measurements of levitated samples can be made using videometry. For this purpose, high-resolution digital cameras, based on CCD or CMOS technology, are used, equipped with telecentric or macro optics.

In terrestrial levitation, samples are not spherical, but slightly elongated due to the action of gravity and the electromagnetic field. However, their static equilibrium shape is, to a good approximation, rotationally symmetrical around the vertical axis (parallel to the gravity vector). Therefore, images are taken perpendicular to this axis, and the volume V of a rotationally symmetrical body is calculated from:

$$V = \frac{2\pi}{3} \int_{-1}^{1} r^3(u) \mathrm{d}u \tag{2.1.36}$$

Here $u = \cos\theta$ with θ being the angle measured from the vertical axis and $r(u)$ is the angle-dependent radius of the sample. The mass M of the sample is known; it is weighed before and after the measurement. The density of the sample is then obtained from Equation (2.1.29). The images are taken at constant temperature and analyzed by a digital image processing system. In a first step, the software detects the edge of the incandescent sample; then an average of approximately 1000 images is performed to remove the potentially asymmetrical dynamic surface oscillations. Finally, the averaged shape is fitted with a series of Legendre polynomials. As has been shown by Hyers [93], the best fit is obtained with the origin of the polynomials chosen off-center of the drop. Once the coefficients of this series expansion are known, the volume can be calculated in pixel units. As a final step, conversion into physical units requires calibration by a body of known dimensions. A detailed description of this algorithm has been given in Refs. [94,95].

It is also essential to confirm that the edge detection algorithm is independent of the brightness of the liquid drop, since this changes with temperature. A very elegant solution is to not take direct images of the incandescent sample but to use backlight illumination and to apply a shadowgraph technique. There are two major advantages: the contrast between shadow and background is temperature independent and the size of the shadow is independent of translational oscillations, if parallel light is used for illumination. A sketch of the optical components is shown in Figure 2.1.26.

2.1.2.1.3 Thermal Properties

In order to characterize the thermal properties of a material, in particular, a molten metal, one needs to know its phase transformation temperatures, e.g., the liquidus temperature, T_L, or the critical temperature for phase separation, T_c, and the associated enthalpy

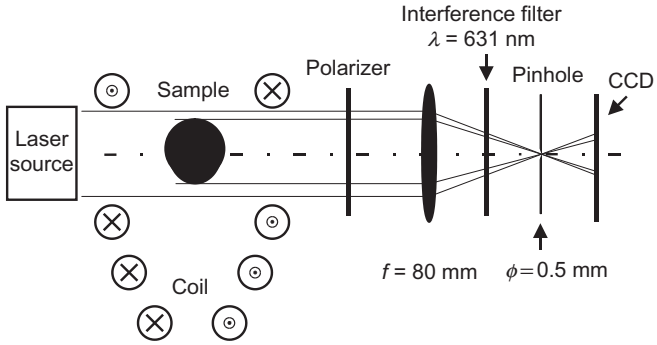


Figure 2.1.26 Optical path for density measurements on levitated samples. Left: Laser source. Right: Polarizer to reduce stray light, optical lens, interference filter for blocking radiation from sample, pinhole to reduce stray light, CCD chip for image capture. *After Ref. [95].*

change, if any, like the heat of fusion ΔH_f. In addition, its specific heat capacity, or shortly, specific heat c_p, must be known. It is defined as

$$M c_p = \frac{dQ}{dT} \tag{2.1.37}$$

where Q is the amount of heat fed (reversibly) into the system under constant pressure.

The heat capacity of simple solid materials can be estimated at high temperatures by the Dulong-Petit rule:

$$c_p = 3R = 25\,\mathrm{J\,(molK)^{-1}} \tag{2.1.38}$$

(Note that in this equation c_p is given per mole, not per mass.) This simple formula does not hold for molten metals. Their heat capacity is higher due to the irregular motion of the ions in the liquid. Nevertheless, the Dulong-Petit rule provides a useful lower bound for the specific heats of (monatomic) liquids.

The heat capacities of alloys can be estimated from the Neumann-Kopp rule [96], assuming ideal mixing behavior. For a binary alloy, AB, with mass fractions m_A and m_B, it reads

$$c_p^{AB} = m_A c_p^A + m_B c_p^B \tag{2.1.39}$$

The Neumann-Kopp rule provides a reasonably good estimate for the specific heat of an alloy, against which experimental data should be checked for plausibility.

Finally, the liquid's capability for heat transport, expressed either as thermal conductivity λ or thermal diffusivity κ, is an important property. The thermal conductivity is defined via Fourier's law:

$$j_Q = -\lambda \nabla T \tag{2.1.40}$$

relating the heat flux j_Q to the temperature gradient. The thermal diffusivity is related to λ by

$$\kappa = \frac{\lambda}{\rho c_p} \tag{2.1.41}$$

Whereas the thermal conductivity is, physically speaking, the fundamental quantity, it is the thermal diffusivity that is generally measured and also mostly needed in applications. The reason is that it appears in the differential equation for the temperature field:

$$\frac{\partial T}{\partial t} - \kappa \Delta T = 0 \tag{2.1.42}$$

Here Δ is the Laplace operator, and the above equation has the same mathematical form as the (mass) diffusion equation, hence the name thermal diffusivity.

Fourier's law, Equation (2.1.40), is just one example of a linear relationship between a flux and a force. Other examples are Fick's law for diffusion, or Ohm's law for the electrical current. In the framework of irreversible thermodynamics, Onsager [97] has generalized these relations by defining

$$j_i = \sum L_{ik} X_k \tag{2.1.43}$$

Here j_i are the currents, X_k are generalized thermodynamic forces, and L_{ik} the Onsager coefficients. It can be shown that the Onsager matrix is symmetric[1] and positive definite, i.e.:

$$L_{ii} > 0, \quad L_{ik} = L_{ki} \tag{2.1.44}$$

This behavior is related to the fact that the rate of entropy production is always positive:

$$\dot{S} = \sum j_i X_i \geq 0 \tag{2.1.45}$$

For the above equation to hold, the thermodynamic forces must be defined correctly. In the case of thermal gradients, the correct generalized thermodynamic force is $\nabla \frac{1}{T} = -\frac{1}{T^2} \nabla T$. If there is only thermal transport, it therefore follows that the heat flux is always opposite to the temperature gradient, i.e., from hot to cold. For the case of mass transport, which we will discuss later, the correct thermodynamic force is given by $-\nabla \frac{\mu}{T}$, where μ is the chemical potential. In addition to the diagonal elements, the Onsager matrix may also contain off-diagonal elements. Note that in such case Equation (2.1.45) only requests that the sum is positive, not the individual terms. In other words, in the case of nonzero off-diagonal

[1] The precise definition of the symmetry relation is somewhat more complicated. It reads: $L_{ik}(B,\omega) = \varepsilon_i \varepsilon_k L_{ki}(-B, -\omega)$, where B is an applied magnetic field, ω any rotation, and ε_i, ε_k are the signs of X_i, X_k upon time reversal.

elements, some of the fluxes may flow against their natural gradient. A well-known example of such an off-diagonal coupling is the Soret effect, also known as thermophoresis or thermomigration [98]. It means that a mass flow is induced by a thermal gradient. The corresponding flow equation for a binary alloy is conventionally written as

$$j_c = -D\nabla c - D_T c_0(1-c_0)\nabla T \tag{2.1.46}$$

where c and c_0 are the actual and initial concentrations of one component, D is the (mass) diffusion coefficient to be discussed later, and D_T is the thermodiffusion coefficient. The Soret coefficient S is defined as

$$S = \frac{D_T}{D} \tag{2.1.47}$$

Due to the symmetry of the Onsager matrix, the opposite effect, namely heat transport by concentration gradients, must also exist. This is the so-called Duffour effect. In most cases, the Soret and Duffour effects are small. Unfortunately, no satisfactory theory exists for these coefficients, and not even the sign of D_T can be predicted from first principles. A similar relation is electrocapillarity where electron transport is coupled to atomic mass transport.

The measurement of transport properties, like the thermal conductivity, is difficult due to the possible presence of convection. Convection is a very effective transport mechanism, and much effort must be spent in preventing it from disturbing transport property measurements, including the use of microgravity platforms [99].

Transition temperatures, enthalpy changes, and specific heats are measured in calorimeters, like DSC (differential scanning calorimeter), while the thermal diffusivity is typically measured in Laser Flash instruments. Thermal conductivities can be measured with transient techniques, like the transient hot wire (THW). We will discuss these instruments in the following.

2.1.2.1.3.1 Differential Scanning Calorimetry

To start with, there is a confusion of naming convention in calorimetry. Many companies and textbooks distinguish between differential thermal analysis (DTA) and DSC. For our purposes, it suffices to say that DTA can be used to identify temperatures of exo- or endothermic reactions, such as phase transformations, while DSC allows to measure the heat capacity and enthalpy changes quantitatively. Very often, the same instrument can be used in both ways. The term *differential* refers to the fact that the sample is measured relatively to a second inert sample of approximately the same heat capacity. The principle of DSC has been described in detail in Ref. [100]. In principle, three different heat fluxes are measured: one from the sample under investigation, one from the reference sample, and one from the empty instrument (baseline correction). The heat capacity of the sample, c_p, is obtained from the following equation:

$$c_p(T) = c_p^r(T)\frac{m^r}{m}\frac{\Delta_3 - \Delta_1}{\Delta_2 - \Delta_1} \tag{2.1.48}$$

where Δ_1, Δ_2, and Δ_3 are the DSC signals with empty pans, of the reference sample and of the sample. m^r, m are the masses of the reference sample and the test sample respectively, and c_p^r is the known heat capacity of the reference sample.

Apart from a correct baseline determination, a fundamental problem of DSC is the smearing of temperature data due to the finite heating or cooling rate and the finite size of the samples. In fact, the measurements are not performed in true thermal equilibrium. Therefore, puristically speaking, the DSC yields apparent specific heats. For example, as is known from thermodynamics, the specific heat diverges at the critical temperature of a second-order phase transition, while the DSC-derived c_p remains finite and shows a peak, smeared out over a finite temperature interval. Also, transition temperatures are usually heating (or cooling) rate dependent. This effect can, in principle, be eliminated by making measurements at different heating rates and extrapolating to zero heating rate. A typical DSC trace for solid Fe is shown in Figure 2.1.27. Due to the sharp and well-defined peaks, Fe is often used as reference sample.

A specific problem of high-temperature DSC is related to the choice of a proper crucible. This not only refers to the problems of chemical reactions between sample and crucible, but also to thermal properties of the crucible. For compatibility reasons, one

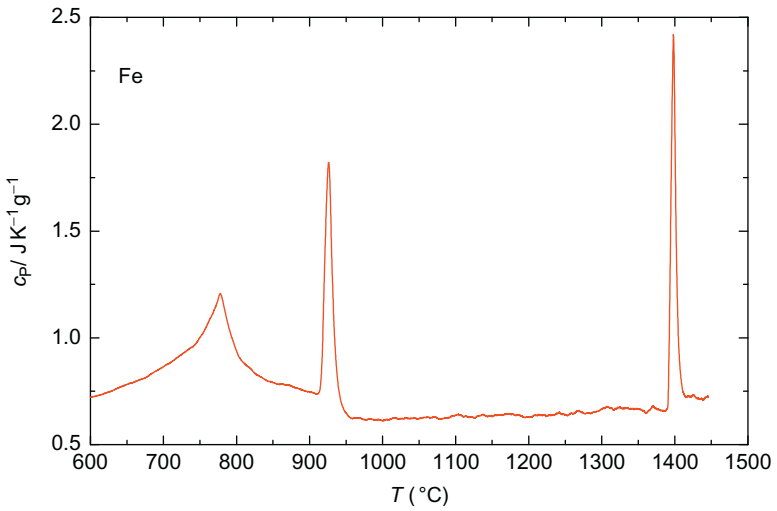


Figure 2.1.27 DSC trace for solid Fe, showing peaks related to phase transformations. The sharp peak at 1394 °C is the δ-γ phase transformation, the one at 912 °C corresponds to the α-γ transition, while the broad peak below 800 °C indicates the ferromagnetic phase transition. Fe is often used as reference sample.

is forced to use ceramic crucibles. In the derivation of the working equation of DSC, Equation (2.1.48), it is assumed that heat fluxes are controlled through the pans and registered by the sensors of the instrument. However, at high temperatures, there is an increasing heat loss due to radiation from the ceramic crucibles, which is not accounted for. As these losses are proportional to surface area rather than volume, the DSC signal becomes no longer directly proportional to the sample mass.

Generally speaking, the use of DSC-type equipment for the study of high-temperature liquid metals is rather restricted. For the reasons discussed above, alternative methods need to be applied. One of them is drop calorimetry, which will be discussed in the following.

2.1.2.1.3.2 Drop Calorimetry

In drop calorimetry, the heat content of a specimen dropped into a calorimeter is determined through the temperature rise of the calorimeter [101]. If the thermal mass of the sample is much smaller than the thermal mass of the calorimeter, the temperature rise is proportional to the heat content Q_K of the sample at the time when it enters the calorimeter:

$$Q_K = C_K \Delta T^* \tag{2.1.49}$$

Here, C_K is the calibration constant of the calorimeter, and ΔT^* is the temperature rise measured at the calorimeter, and corrected for inevitable heat losses, as described in Ref. [100]. The temperature of the drop is measured before it is released. Therefore, one must also account for heat losses Q_f during the fall of the sample:

$$Q_T = Q_f + Q_K \tag{2.1.50}$$

Here Q_T is the heat content of the sample at release, given by

$$Q_T = M[H(T) - H(T_0)] \tag{2.1.51}$$

where $H(T)$ is the enthalpy and M is the mass of the sample. If the drop calorimeter operates under vacuum conditions, the heat loss Q_f is entirely due to radiation, and the falling time t_f is simply given by

$$t_f = \sqrt{\frac{2h}{g}} \tag{2.1.52}$$

In this equation, h is the falling distance, and g is the gravitational acceleration. In most cases, however, the calorimeter is filled with inert gas, such as helium or argon, and there are additional heat losses and a time delay due to drag forces on the falling sample.

Generally, the heat loss Q_f is given by

$$Q_f = \int_0^{t_f} A\alpha(T - T_0)\mathrm{d}t + \int_0^{t_f} A\varepsilon_h\sigma_{SB}\left(T^4 - T_0^4\right)\mathrm{d}t \tag{2.1.53}$$

where α is an empirical heat transfer coefficient of the gas, A is the surface area of the drop, ε_h is the total hemispherical emissivity, σ_{SB} is the Stefan-Boltzmann constant, Equation (2.1.20), T is the sample's temperature at time t, and T_0 is the ambient temperature. If the falling time t_f is short enough, the temperature of the sample does not change much during fall, and the integration may be replaced by a multiplication. In addition, at those high temperatures characteristic for liquid metals, heat loss by radiation is the dominant effect, and the heat losses due to heat conduction can be safely neglected. Furthermore, the sample temperature is always much higher than the ambient temperature, and $T_0^4 << T^4$. With all these approximations, an approximate, but explicit equation can be derived for Q_f:

$$Q_f = \sqrt{\frac{2h}{g}} A\varepsilon_h\sigma_{SB}T^4 \tag{2.1.54}$$

Putting all equations together, we finally obtain

$$H(T) - H(T_0) = \sqrt{\frac{2h}{g}}\frac{A\varepsilon_h\sigma_{SB}T^4}{M} + \frac{C_K\Delta T^*}{M} \tag{2.1.55}$$

If drops are performed at different temperatures, one finally obtains the enthalpy as a function of temperature. The specific heat is then obtained by differentiation:

$$c_p = \frac{\partial H}{\partial T} \tag{2.1.56}$$

Drop calorimetry is a fairly popular technique. In the case of liquid metals, it is often combined with EML [102,103]. A typical setup, as used at the National Physical Laboratory (NPL), UK, is shown in Figure 2.1.28.

A conventional levitation coil is powered by a generator to provide levitation and heating. The sample is contained in a quartz tube within the coil, under a flowing atmosphere of argon and hydrogen, or argon and helium. The calorimeter consists of a copper block with a copper liner to receive the sample, fitted with a platinum resistance thermometer and two heater elements for calibration. This is contained in a chamber immersed in a constant temperature bath and is filled with inert gas also heated through the bath, and separated from the levitation gases by a shutter.

An extensive review of "Thirty years of levitation melting calorimetry" has been published by Frohberg [104]. He also introduced an interesting variant of levitation calorimetry, which he termed levitation alloying calorimetry [105]. This method allows the

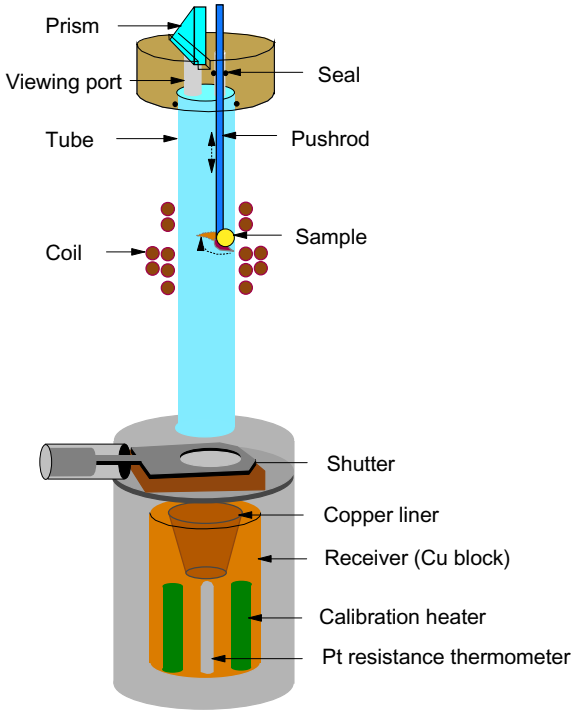


Figure 2.1.28 Drop calorimeter setup. The levitated sample is dropped into a copper receiver. *Courtesy NPL.*

measurement of the enthalpy of mixing of liquid alloys. It works as follows: If one wants to measure the enthalpy of mixing of alloy AB in the A-rich side of the phase diagram, a sample of pure A of mass m_A is levitated and melted. The levitation device is modified in such a way that small samples of pure B of mass m_B can be dropped onto the levitated and molten drop, leading to the formation of a liquid drop of composition A_xB_y. Under the condition of energy conservation, the enthalpy balance of the mixing process can be expressed by

$$-\Delta h_{\text{mix}} = m_B[H_B(T) - H_B(T_0)] + (m_A + m_B)c_p^{AB}\Delta T \qquad (2.1.57)$$

Here T and T_0 are the temperatures of samples A and B before release, and c_p^{AB} is the heat capacity of the alloy, usually approximated through the Neumann-Kopp rule, Equation (2.1.39). Thus the enthalpy of mixing is consumed by two processes: first, sample B must be heated up to the temperature of sample A, and, second, the temperature of the alloyed drop changes by ΔT. If the enthalpy of substance B and the heat capacity of the alloy are known, the enthalpy of mixing can be derived from the measured temperature change. By adding subsequently additional samples of B to the alloy A_xB_y, the

enthalpy of mixing can be obtained as a function of concentration. Of course, eventually, the levitated drop will become too heavy and will drop out of the levitation field.

2.1.2.1.3.3 Modulation Calorimetry

Modulation calorimetry is a well-known method in low-temperature physics. It is based on a (sinusoidal) modulation of heat input into the sample and the analysis of the resulting temperature response. Fecht and Johnson [106] have applied this concept to determine the specific heat of molten metals in levitation experiments. In EML, the heater power is modulated according to $P_\omega(t) = \Delta P_\omega \cos(\omega t)$, resulting in a modulated temperature response ΔT_ω of the sample. A thermal model considering heat loss to the environment and heat conduction within the sample has been developed by Wunderlich and Fecht [107]. It considers heat loss to the exterior (typically by radiation only if the experiment is carried out under vacuum), spatially inhomogeneous heating of the sample, and heat conduction within the sample. For small Biot numbers, $Bi = k_r/k_c \ll 1$, where k_r is the heat loss due to radiation and k_c the heat loss due to heat conduction, adiabatic conditions are realized and quantitative modulation calorimetry is possible. Under such conditions, the following relation for ΔT_ω is obtained:

$$\Delta T_\omega = \frac{\Delta P_\omega}{\omega c_p} \left\{ \left(1 + \left(\frac{\omega}{\lambda_1} \right)^2 \right) \left(1 + \left(\frac{\lambda_2}{\omega} \right)^2 \right) \right\}^{-1/2} \tag{2.1.58}$$

where λ_1 and λ_2 are functions of k_r and k_c. For $Bi \ll 1$, we have $\lambda_2 \ll \lambda_1$. This allows to choose the modulation frequency between λ_2 and λ_1 such that $\lambda_2 \ll \omega \ll \lambda_1$. Under these circumstances, a simple relation for the specific heat, c_p, can be derived as

$$c_p = \frac{1}{\omega} \frac{\Delta P_\omega}{\Delta T_\omega} \tag{2.1.59}$$

The power input into the sample, ΔP_ω, cannot be measured directly. It is related to the current I flowing through the heating coil by a coupling coefficient G_H which has to be determined separately:

$$\Delta P_\omega = G_H I_\omega^2 \tag{2.1.60}$$

It should be noted that a harmonic modulation of the current with ω' leads to components in the power P with $\omega = 0$, $\omega = \omega'$, and $\omega = 2\omega'$. The static and frequency-doubled components can also be analyzed along the lines indicated above.

Recently, Fukuyama *et al.* have modified this approach to levitated samples heated by a laser [108]. They have derived the analogue of Equation (2.1.60) for laser heating and have successfully measured specific heat, total hemispherical emissivity, and even thermal conductivity of liquid Si in an EML device, where a high static magnetic field was superimposed to eliminate convective effects. More details can be found in Ref. [109] (Figure 2.1.29).

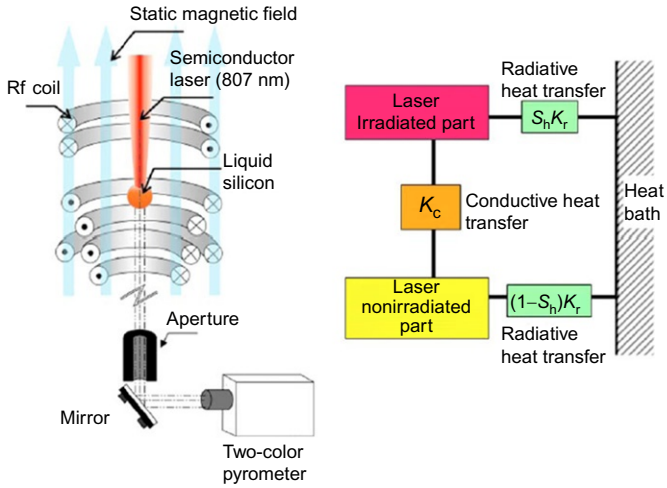


Figure 2.1.29 Schematics of a setup for modulation calorimetry of levitated samples (left) and heat flow model (right). *After Ref. [109].*

2.1.2.1.4 Thermal Conductivity and Thermal Diffusivity

Heat can be transferred by conduction, convection, and radiation. The main difficulty in performing accurate measurements of thermal conductivity or thermal diffusivity of liquids lies in the isolation of the conduction process from the other two mechanisms of heat transfer, as a temperature gradient has to be imposed on the sample, in order to generate fluid flow. The imposition of this temperature gradient in the gravitational field of the earth creates natural convection, which is especially crucial in steady-state methods of measurement and in regions of phase diagrams close to the critical point.

The success of transient methods is based on the fact that the characteristic time for the acceleration of the fluid by buoyancy forces is much longer than the propagation time of the temperature pulse originated by a strongly localized temperature gradient. Therefore, it is possible by a suitable choice of the experimental conditions and geometrical design of the measuring cells to perform, in principle, convection-free measurements [110].

Microgravity experiments can be used to show that convection is also present in thermal conductivity measurements and to demonstrate the best experimental conditions (temperature gradients, transient cells, duration of an experiment, etc.) to study a given system.

If the measurements are performed at high temperatures, heat transfer by radiation becomes important, as its contribution increases as T^4 with temperature.

In molten metals, heat is dominantly conducted by the conduction electrons, rather than the ions, due to the higher mobility of the electrons. Using a Boltzmann equation approach and exploiting the Fermi statistics of electrons, the thermal conductivity λ can be calculated [6], in principle, from

$$\lambda = \frac{k^2}{36\pi\hbar} T \int \Lambda \mathrm{d}S_\mathrm{F} \tag{2.1.61}$$

Here, k is Boltzmann's constant, $\hbar$ is Planck's constant, Λ is the electron mean-free path, and the integration is over the Fermi surface.

The first measurements of the thermal conductivity under microgravity conditions of molten salts and molten semiconductors have been made by Hibiya *et al.* for InSb [99,111], applying the THW technique. More recently, THW was applied to molten Al, Si, and Ni by Fukuyama and coworkers [112]. In this technique, a rod-shaped ceramic probe is used, with a platinum wire in a cylindrical vessel. The heat source can be described by

$$\dot{Q}_\mathrm{ext}(r,t) = \dot{q}\delta(r)\theta(t) \tag{2.1.62}$$

where $\dot{q}$ is the heat rate generated at $r = 0$ and $t \geq 0$. The temperature field is obtained as:

$$\Delta T(r,t) = -\frac{\dot{q}}{4\pi\lambda} Ei\left(-\frac{r^2}{4\lambda t}\right) \tag{2.1.63}$$

Here, $Ei(x)$ is the exponential integral function and λ is the thermal conductivity of the liquid. For $4\lambda t \gg r^2$ it can be expanded to finally yield

$$\Delta T(t) = \frac{\dot{q}}{4\pi\lambda} \ln t \tag{2.1.64}$$

The THW method thus predicts that the temperature increase in the wire generated by a step heat input from time zero, and dissipated by Joule effect, varies linearly with ln t, as expressed by Equation (2.1.64). The constant slope with time permits the calculation of the thermal conductivity of the melt. If convection is present, the experimental temperature rise will not vary linearly with ln t, and the calculated apparent thermal conductivity will increase with time. This is shown schematically in Figure 2.1.30.

In addition to transient methods, like the THW discussed above, thermal conductivity can also be measured by steady-state techniques. Different variants and geometries exist. For example, Sklyarchuk and Plevachuk [113] have developed a steady-state apparatus for thermal conductivity measurements of liquid metals and semiconductors. Their design is based on two concentric cylinders with diameters d_1 and d_2, both of length L, held at temperatures T_1 and T_2, respectively. From the steady-state solution of the heat equation the thermal conductivity is obtained as

$$\lambda = \frac{\dot{q}}{2\pi L(T_1 - T_2)} \ln \frac{d_2}{d_1} \tag{2.1.65}$$

This concludes our discussion of the measurement techniques for the thermal conductivity. As discussed above, an alternative to these measurements is the determination

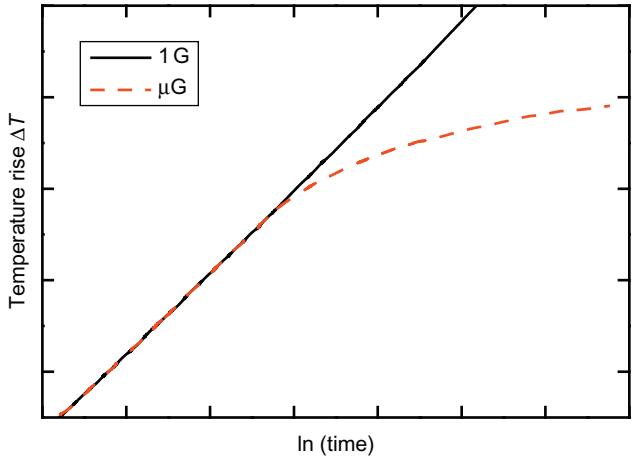


Figure 2.1.30 Temperature response in transient hot wire technique in microgravity (μG) and under 1 G (schematically).

of the thermal diffusivity, κ. Thermal diffusivity measurements in the solid, but also in the liquid, can be performed in a laser flash apparatus (LFA). A schematic of the LFA is given in the Figure 2.1.31. The technique was originated by Parker *et al.* [114], and more details about the technique may be found in Ref. [115].

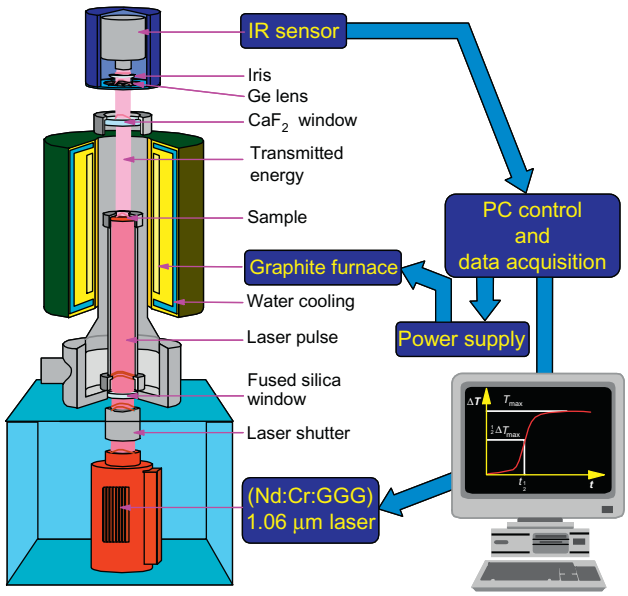


Figure 2.1.31 Schematic of the laser flash apparatus for thermal diffusivity measurement. *Courtesy NPL.*

Briefly, the measurement consists of heating the bottom face of a disc-shaped sample (typically 1-3 mm in thickness depending on the value of thermal diffusivity) using a high-intensity laser pulse and monitoring the temperature rise on the top face using a pyrometer. From the temperature rise, the thermal diffusivity κ can be calculated by

$$\kappa = 0.1337 \frac{l^2}{t_{1/2}} \tag{2.1.66}$$

where l is the thickness of the specimen and $t_{1/2}$ is the time taken for the temperature to reach half the value of the maximum temperature rise. Equation (2.1.66) assumes ideal adiabatic conditions for an idealized instantaneous energy pulse. A more precise result can be obtained by fitting the entire temperature profile according to the procedure proposed by Cape and Lehman [116–118]. A typical temperature profile is shown in Figure 2.1.32.

In principle, LFA can also be applied to molten metals. In addition to the general problem of finding a suitable container material, difficulties arise from possible convective effects. In some of the commercially available instruments, heating is from below which results in a thermally unstable configuration giving rise to buoyancy-driven convection. Also, the thermal analysis assumes flat and parallel surfaces at top and bottom. To provide such conditions, the liquid sample is usually sandwiched between two parallel plates [119].

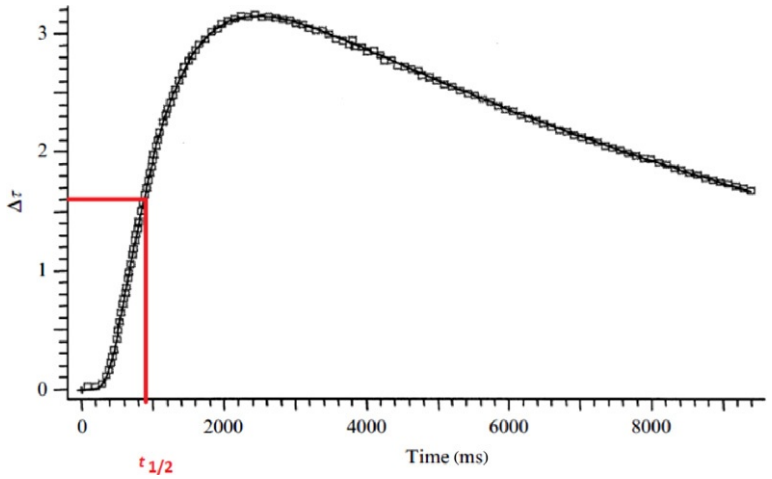


Figure 2.1.32 Recorded temperature history at the top surface of a solid specimen exposed to a laser pulse at $t = 0$ from below. Squares are data points, full line is the Cape-Lehmann fit. Also indicated is $t_{1/2}$, Equation (2.1.66). *After Ref. [118].*

2.1.2.1.5 Electrical Conductivity

Like the thermal conductivity, the electrical conductivity is just another linear transport coefficient. It is defined by Ohm's law, written as

$$j_e = \sigma E \tag{2.1.67}$$

where j_e is the electrical current density, E the applied electric field, and σ the electrical conductivity. Its reciprocal is the electrical resistivity, $\rho_e = 1/\sigma$, with Ω m as the appropriate SI unit. In metals, liquid or solid, electrical transport is dominated by the nearly free electrons. A very simple expression of the conductivity of a nearly free electron gas is provided by the well-known Drude formula [120]:

$$\sigma = \frac{ne^2\tau}{m} \tag{2.1.68}$$

In this equation, n is the electron density, e the electron charge, τ the relaxation time, and m the electron mass. The relaxation time is the consequence of the scattering events to which the electrons are exposed. It is not known *a priori* and must be estimated or calculated, e.g., from quantum mechanics. More elaborate treatments can be based on the Boltzmann equation. In this framework, the electrical conductivity is given by [6]

$$\sigma = \frac{e^2}{12\pi^3\hbar}\int \Lambda \, \mathrm{d}S_F \tag{2.1.69}$$

where the integral is the same as in Equation (2.1.61).

Like in the case of heat and mass transport, there are also off-diagonal elements between heat flow and electrical current. We can write generally

$$\begin{aligned} j_e &= \sigma E - P\nabla T \\ j_q &= SE - \lambda \nabla T \end{aligned} \tag{2.1.70}$$

The off-diagonal elements represent thermoelectric effects, namely the Peltier effect and the Seebeck effect. The Seebeck effect states that a temperature gradient will produce an electric field, $E = \frac{P}{\sigma}\nabla T$, while the Peltier effect denotes the reciprocal effect of establishing a temperature gradient through an applied electric field. When the fluxes are written as functions of generalized forces, the Onsager relation given in Equation (2.1.24) would of course hold.

Generally speaking, the electrical resistivity ρ_e is higher in the liquid than in the solid, due to the stronger disorder. Also, in most cases, the electrical resistivity increases with temperature, i.e., $\frac{\partial \rho_e}{\partial T} > 0$, but there are exceptions. In fact, Mooij [121] has discovered a phenomenological correlation between the absolute value of the electrical resistivity and the sign of its temperature coefficient:

$$(\rho_e - \rho_M)\frac{\partial \rho_e}{\partial T} < 0 \tag{2.1.71}$$

If the electrical resistivity exceeds the Mooij resistivity $\rho_e > \rho_M$, then $\frac{\partial \rho_e}{\partial T} < 0$. The Mooij resistivity is roughly $\rho_M = 150\ \mu\Omega$ cm.

Measurements of the electrical conductivity are relevant *per se*; in addition, they are often used as an alternative to direct measurements of the thermal conductivity, as they are linked by the Wiedemann-Franz law, discussed in Section 2.1.3.2.

The most common method for measuring the electrical resistivity of liquids is the so-called four-probe method. The liquid metal is contained in a long tube or capillary, and four electrodes are in contact with the liquid. Two electrodes provide a constant electric (d.c.) current I, while the second pair is used to measure the potential drop U between them. From Ohm's law, $U = RI$, where R is the resistance, the specific electrical resistivity can be calculated from

$$\rho = R\frac{A}{d} \tag{2.1.72}$$

with the cross section A of the tube, and the distance d between the potential electrodes. Temperature is measured through thermocouples. The principle and its technical realization are described in Ref. [122]. Great care must be taken to avoid contamination of the melt by the electrodes and, vice versa, damaging of the electrodes by the melt. A typical measurement cell is shown in Figure 2.1.33.

At extremely high temperatures, e.g., in the case of molten refractory metals, other techniques must be employed. An elegant method is that of the exploding wire. This is a transient method, where a wire is heated rapidly above its melting point, and its resistance is measured before it collapses. This technique has been widely employed by Pottlacher and coworkers in Graz, Austria. A recent compilation of their work can be found in Ref. [123]. Usually, the samples are resistance heated under water or in argon at pressures in the range of 0.1 MPa to 1 GPa, up to the end of the solid phase in less than 40 μs by a large current pulse from a capacitor bank (540 μF, 10 kV). Current I and voltage drop U are measured as a function of time with μs resolution. The temperature is monitored

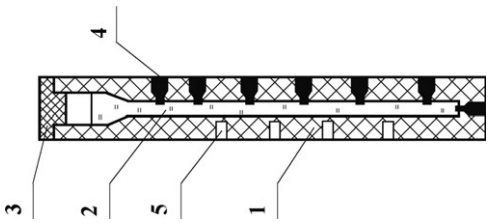


Figure 2.1.33 Measuring cell with cylindrical cavity: 1, ceramic container; 2, liquid sample; 3, filler plug; 4, graphite electrodes; 5, socket for junctions of differential thermocouples.

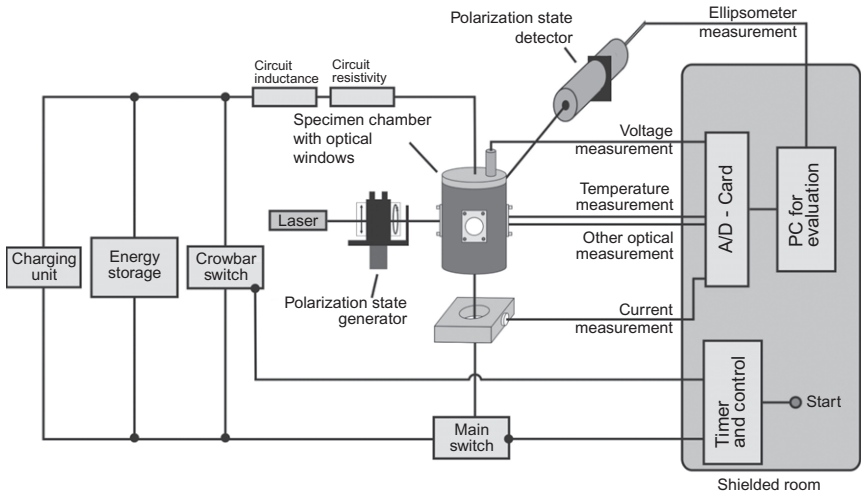


Figure 2.1.34 Experimental setup for pulse-heating experiments at the University of Graz.

pyrometrically. The resistivity is obtained from Equation (2.1.72). Volume expansion of the wire must be taken into account when considering the cross section A. This is accomplished through a high-speed video camera recording the visible cross section of the wire. As a spin-off, this technique also allows to determine the free enthalpy $H(T)$ of the molten metal. The setup at TU Graz is shown schematically in Figure 2.1.34.

In addition to these two classical methods, containerless methods have also been proposed and applied in the past. Enderby et al. [124] have devised a method for electrical conductivity measurements on aerodynamically levitated samples, while Lohöfer performed measurements on electromagnetically levitated samples, both on ground [125] and in microgravity [126]. Both methods are based on an inductive noncontact technique and measure the changes in impedance (resistance and inductance) generated by the presence of the sample in the interior of an induction coil. The impedance of the empty coil must of course be known. As the impedance is a function of the skin depth δ, Equation (2.1.4), the electrical conductivity can be derived from the measured impedance changes. In the following, we briefly describe the principle of this inductive method, as developed by Lohöfer [127].

The complex impedance Z_{coil} of the coil including the sample is a function of the oscillation frequency ω of the electromagnetic field, properties of the empty coil, and properties of the sample:

$$\begin{aligned} Z_{\mathrm{coil}} &= Z_{\mathrm{coil}}\left(\omega,\delta,a_0,\vec{r},\vec{\alpha}\right) \\ &= R_0 + i\omega L_0 + \Delta R_{\mathrm{s}}\left(\delta,a_0,\vec{r},\vec{\alpha}\right) + i\omega\Delta L_{\mathrm{s}}\left(\delta,a_0,\vec{r},\vec{\alpha}\right) \end{aligned} \tag{2.1.73}$$

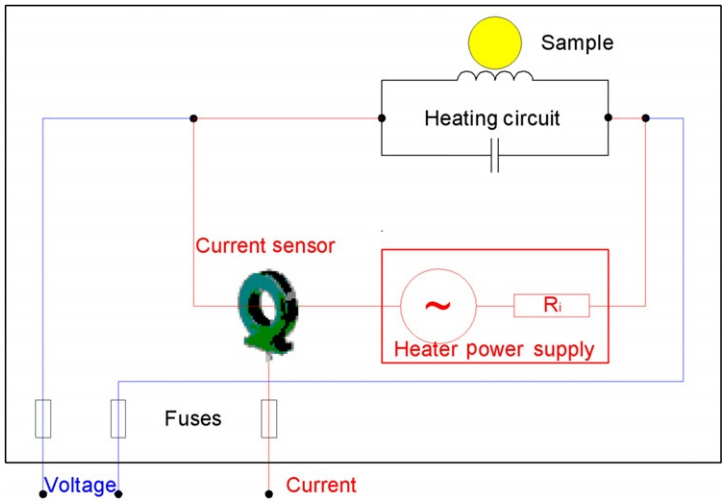


Figure 2.1.35 Schematics of impedance measurement on levitated samples. *After Ref. [127].*

Here, R_0 and L_0 are resistance and inductivity of the empty circuit and ΔR_s, ΔL_s are the changes induced by the sample. These latter functions depend on the skin depth, δ, the radius a_0 of the sample, and its position $\vec{r}$ within the coil. The vector $\vec{\alpha}$ is meant to describe the shape of the sample as given by the coefficients of a series expansion in spherical harmonics. In a homogeneous magnetic field, and for a spherical sample, the dependence on $\vec{r}$ and $\vec{\alpha}$ vanishes. The coil is part of an oscillatory circuit and is connected in parallel to a capacitor of capacitance C_0. This is shown schematically in Figure 2.1.35.

The complex impedance Z_{tot} of the oscillatory circuit is determined by measuring the alternating current I through and the voltage U over the circuit as well as the phase shift ϕ between both quantities. The real and imaginary part of Z_{tot} yield two equations for the two unknowns δ and a_0. For small Ohmic losses in the circuit, these are given by

$$\frac{C_0}{L_0}(R_0+\Delta R_s)=\frac{I}{U}\cos(\phi) \tag{2.1.74}$$

$$\frac{C_0}{L_0}\left\{\frac{L_0}{\omega}\left(\omega^2-(L_0C_0)^{-1}\right)+\omega\Delta L_s\right\}=\frac{I}{U}\sin(\phi) \tag{2.1.75}$$

For small skin depth, $3\delta < a_0$, which is generally realized for liquid metal samples of $a_0 > 3$ mm, and frequencies $\omega > 2\pi$ 300 kHz, ΔR_s has a relatively simple form, and Equation (2.1.74) can be inverted to yield

$$\delta=\frac{a_0}{2}\left(1-\sqrt{1-\frac{A}{a_0^3}\left\{\frac{I}{U}\cos\phi-B\right\}}\right) \tag{2.1.76}$$

Here, A and B are two instrument constants, to be determined by calibration. Equation (2.1.4) finally yields the electrical conductivity σ.

2.1.2.1.6 Mass diffusion

Diffusion is an atomistic and stochastic process, whereby atoms follow a concentration gradient without the presence of external forces. Within the framework of linear irreversible thermodynamics, this is expressed through Fick's law:

$$j_D = -D\nabla c \tag{2.1.77}$$

which is analogous to Fourier's law for heat conduction, Equation (2.1.40), and is a special case of Equation (2.1.46). In this equation, D is the diffusion coefficient (strictly speaking, the generalized driving force is $\nabla\frac{\mu}{T}$ rather than ∇c.) The atomic process underlying diffusion can be quite different in solids and liquids. Whereas hopping along vacancies or interstitials may be dominant in solids, a collective motion is possible in liquids. If diffusion is an activated process, its temperature dependence is best described by an Arrhenius-type formula:

$$D = D_0 \exp\left(-\frac{E_D}{kT}\right) \tag{2.1.78}$$

where k is Boltzmann's constant, T the absolute temperature, and E_D the activation energy for diffusion. This relation is also often used to fit diffusion coefficients in liquids. However, Swalin [128] has employed a fluctuation theory for diffusion in liquids, which yields a different temperature dependence, namely:

$$D = AT^2 \tag{2.1.79}$$

Recent MD simulations have confirmed this power law, with an exponent ranging between 1.7 and 2.3 [129], and also experiments in microgravity seem to agree with this behavior [130].

If one could tag an individual particle (atom), one could follow its individual diffusion. This process is called self-diffusion, D^*. It cannot be determined experimentally, since atoms are indistinguishable. However, it is possible to track the diffusion of radioactive isotopes (if they exist). Their diffusion is characterized by the tracer diffusion coefficient D^T. Assuming Vegard's law [88] for the molar volume of an alloy, they are related by

$$D_i^* = D_i^T \Phi, \quad \Phi = \frac{\partial \ln a_i}{\partial \ln c_i} \tag{2.1.80}$$

where a_i is the activity and c_i the mole fraction of a given component. Φ is the so-called thermodynamic factor. It allows to express the interdiffusion coefficient in terms of the

tracer self-diffusion coefficients. The corresponding relation is called Darken equation and reads for a binary alloy as [131,132]:

$$D = \left(c_A D_B^T + c_B D_A^T \right) \Phi \tag{2.1.81}$$

Here, D_A^T and D_B^T are the individual tracer diffusion coefficients of species A and B, respectively, and c_A and c_B are the corresponding mole fractions.[2] If there is considerable deviation from Vegard's law, the Darken equation has to be modified according to

$$D = \left(c_A \tilde{\nu}_A D_B^T + c_B \tilde{\nu}_B D_A^T \right) \Phi \tag{2.1.82}$$

where $\tilde{\nu}_i$ are the partial molar volumes of component i.

It should also be noted that the thermodynamic factor Φ can be linked to the Bhatia-Thornton structure factor S_{cc} (0) [133]:

$$\Phi = c_A c_B \left(S_{cc}(0) \right)^{-1} \tag{2.1.83}$$

There are two distinct methods for measuring the diffusion coefficient: one is macroscopic and derives the diffusion constant from fitting the diffusion profile, and the other is microscopic and is based on quasi-ENS. We first discuss the macroscopic methods.

Upon combining Fick's first law, Equation (2.1.77) with the continuity equation, one obtains Fick's second law, which is a partial differential equation for the concentration profile $c(r,t)$:

$$\frac{\partial c}{\partial t} = D \Delta c \tag{2.1.84}$$

where Δ is the Laplace operator. Considering only the one-dimensional case and preparing the initial condition such that, at $t = 0$, $c(x) = 0$ for $x < 0$, and $c(x) = c_0$ for $x > 0$, the solution to this equation is

$$c(x,t) = \frac{c_0}{2} \left(1 + \mathrm{erf} \left(\frac{x}{2\sqrt{Dt}} \right) \right) \tag{2.1.85}$$

where erf(y) is the error function. For $t = 0$, erf $(\infty) = 1$, while for $t = \infty$, erf$(0) = 0$. As an example, the diffusion profile for Cu in an Al-Cu alloy at 983 K is shown in Figure 2.1.36 for two different times. The straight lines are fits to Equation (2.1.85).

The diffusion coefficient, D, is obtained by fitting the experimentally obtained diffusion profile to Equation (2.1.85). Consequently, the goal is to determine the diffusion profile. Two methods exist: the shear cell technique, and the long capillary technique. In the shear cell technique, a long tube is segmented into short cells that can be rotated against each other along a common axis. In the beginning, the upper segments contain

[2] Sometimes, the thermodynamic factor Φ is given in a different, but identical form: $\Phi = 1 + \frac{\partial \ln \gamma_i}{\partial \ln N_i}$, $\gamma_i = \frac{a_i}{N_i}$.

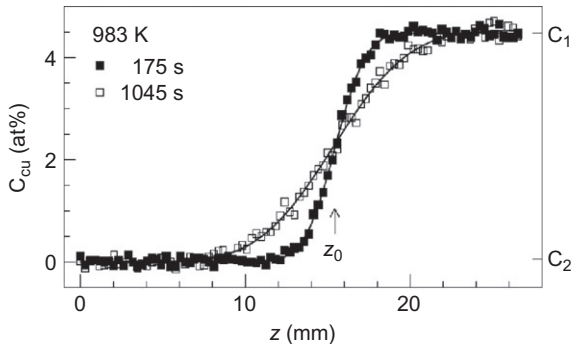


Figure 2.1.36 The diffusion profile of Cu in Al-Cu at 983 K after 175 and 1045 s. The straight lines are fits according to Equation (2.1.85). z_0 is the initial position of the interface. *After Ref. [134].*



Figure 2.1.37 Prototype of a 1600 °C shear cell consisting of 30, 2-mm thick, shear segments. *Courtesy DLR-MP.*

one species, and the lower ones the other. They are sheared against each other so that there is no contact. Then the assembly is heated above the melting temperature of both components. To start diffusion, both parts are rotated (sheared) such that they are in contact. After the well-selected time, t_{end}, all cells are sheared against each other, and the temperature is lowered to initiate solidification. Consequently, each cell contains part of the diffusion profile, which can be analyzed for the concentration. A typical shear cell is shown in Figure 2.1.37.

The second method is that of a long capillary. Here the initial sample is prepared as shown schematically in Figure 2.1.38. The diffusing species is placed in the middle, and can diffuse into two different host melts (left and right). Diffusion is initiated by raising the temperature above the melting point of all components. Diffusion is terminated by

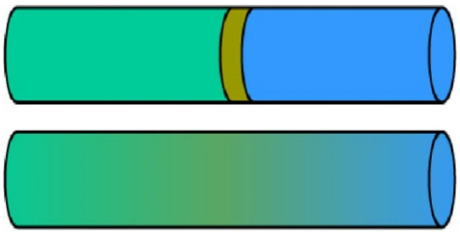


Figure 2.1.38 Long capillary for diffusion experiments. Diffusion of the middle part into two different components (left and right) can be measured simultaneously.

lowering the temperature and initiating solidification. The solidified sample is investigated by metallographic or radiographic methods, if tracer diffusion was studied.

There are a number of difficulties associated with these techniques: first of all, convection must be suppressed as it overwhelms and masks the diffusion process. Second, radial temperature and concentration gradients must be avoided to realize a one-dimensional system. Finally, the shearing process itself and the solidification may introduce additional artifacts. A thorough analysis of these effects can be found in Ref. [130].

Recently, a new variant of the long capillary method has been introduced by Meyer and coworkers [134]. By using X-ray tomography, they observe the diffusion process *in situ*. This eliminates the deficiencies of the *postmortem* analysis of the solidified sample. In addition, the diffusion profile can be observed at different times, thereby improving the fitting quality considerably. Of course, this elegant method only works if the X-ray contrast of the diffusing species is sufficiently strong.

The alternative microscopic method using quasi-ENS is based on the behavior of the dynamic structure factor $S(Q,\omega)$ in the hydrodynamic limit, i.e., $Q \to 0$ and $\omega \to 0$. In this limit, the width Γ of the quasielastic peak of $S(Q,\omega)$ is related to the self-diffusion coefficient, D, of incoherent scatterers through the following equation [1]:

$$D = \frac{\Gamma}{\hbar Q^2} \tag{2.1.86}$$

Such experiments can be performed, e.g., at the time-of-flight spectrometer TOF-TOF of the neutron reactor FRM-II in Munich [135]. Monochromatic neutrons are scattered at the sample. The wave vector Q is determined through the angle of the scattered neutron beam, whereas the energy transfer is related to the time of flight between sample and detector banks. The quasielastic signal can be described with a Lorentzian function convoluted with the instrumental energy resolution. Typical spectra, taken at two different temperatures on levitated liquid nickel [136], are shown in Figure 2.1.39. In contrast to macroscopic techniques, this method is free from the influence of convection, due to the different time scales involved.

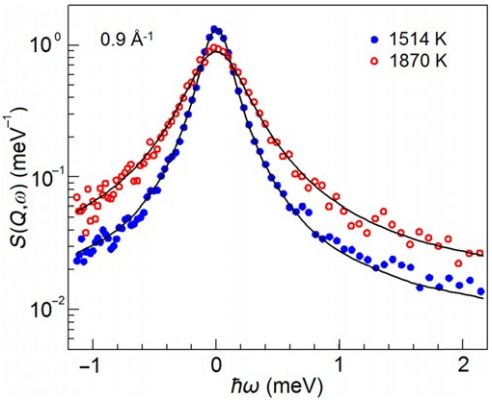


Figure 2.1.39 Dynamic structure factor, $S(Q,\omega)$, of liquid Ni at $Q = 0.9$ Å^{-1} for two temperatures. Open circles correspond to $T = 1870$ K, closed circles represent data at $T = 1514$ K. Lines are Lorentzian fits. *After Ref. [136].*

2.1.2.1.7 Surface Tension

Free deformable surfaces are characteristic of the liquid phase. The physical origin of the associated surface tension, γ, lies in the fact that surface atoms are less tightly bound and have therefore a higher energy than the corresponding bulk atoms. The tendency of the system to minimize its free energy leads to the concept of the surface tension.

The surface tension, or, equivalently, the surface energy, of a liquid can be defined in two different ways, namely mechanically or energetically. The first definition is given by the Young-Laplace equation, describing the pressure drop across a surface with principal radii of curvature R_1, R_2:

$$\Delta p = \gamma \left(\frac{1}{R_1} + \frac{1}{R_2} \right) \tag{2.1.87}$$

In contrast to solids, surface energy and surface tension are identical; consequently, the energetic definition of the work required to create a new surface yields the same result:

$$W = \int \gamma \, \mathrm{d}f \tag{2.1.88}$$

Many classical and quantum statistical models and theories have been proposed for the surface tension in the last century [137–142]. The classical expression is due to Born and Fowler [137] and reads like

$$\gamma = \frac{\pi n^2}{8} \int_0^\infty \mathrm{d}r \, r^4 \frac{\mathrm{d}\phi}{\mathrm{d}r} g(r) \tag{2.1.89}$$

Here n is the number density, ϕ is the pair potential, and $g(r)$ is the pair-correlation function. It is remarkable that the surface tension can be calculated entirely from bulk properties.

Surface tension is an important quantity, both from a physical and a technological point of view. In particular, the knowledge of its temperature dependence is crucial, because it drives Marangoni convection [143]. Many metallurgical processes involve the fluid phase and a free surface. Under such circumstances, Marangoni convection is the dominant mass transport process and must be taken into account. A difference $\delta\gamma$ in the surface tension between two points on the surface provides a driving force for fluid flow toward the region of high γ. Due to mass conservation, the fluid recirculates in the bulk, creating the typical pattern for Marangoni convection. The difference $\delta\gamma$ can be due to temperature or concentration gradients. This driving force must be strong enough to overcome the resistance of the fluid to flow, characterized by the viscosity, η, and fast enough to avoid equilibration of all gradients by diffusion. The dimensionless Marangoni number, *Ma*, expresses this condition. It is defined as [144]

$$Ma = \frac{L\delta\gamma}{\kappa\eta} \tag{2.1.90}$$

where L is a characteristic length, κ is the thermal (or solutal) diffusivity, and $\delta\gamma$ is the difference in surface tension along L. In most cases, $\delta\gamma$ is due to a temperature difference δT along L, and it can therefore be written as

$$\delta\gamma = \partial\gamma/\partial T \cdot \delta T \tag{2.1.91}$$

Therefore, the temperature coefficient $\partial\gamma/\partial T$ of the surface tension has to be determined, which involves the differentiation of the primarily measured surface tension $\gamma(T)$ with respect to temperature. Accurate results can only be obtained if a wide temperature range is covered and the scatter of the original data points is small.

In a wide temperature range around the melting point T_m, the temperature dependence of the surface tension is linear:

$$\gamma(T) = \gamma(T_m) - \gamma_T(T - T_m) \tag{2.1.92}$$

For pure elements $\gamma_T > 0$. This follows from the fact that $\gamma_T = -\frac{\partial\gamma}{\partial T} = S$, where S is the surface excess entropy. A positive S indicates that the surface is more disordered than the bulk, which is generally true. An exception has been reported for Ga [145], but has not been confirmed by others so far. Also, a nonmonotonous temperature dependence of the surface tension with a maximum has been reported for pure metals. This "Boomerang effect" can be explained by adsorption and desorption of an oxide layer on the apparently clean metal surface [146].

At very high temperatures, approaching the critical point T_c of the liquid-vapor phase transition, the surface tension vanishes with a critical exponent:

$$\gamma(T) \propto (T_c - T)^{\mu} \tag{2.1.93}$$

with $\mu \approx 5/4$ [147].

It should also be noted that empirical relations exist, linking the surface tension to the enthalpy of sublimation [148] and to the melting point [2]. They read

$$\gamma \approx 1.8 \times 10^{-9} \frac{\Delta H_s}{V_m^{2/3}} \approx 4.8 \times 10^{-8} \frac{R T_m}{V_m^{2/3}} \tag{2.1.94}$$

where V_m is the molar volume and all quantities are to be expressed in SI units.

In many applications, the processes involve alloys rather than pure metals. It is therefore important to study the surface tension of binary and, possibly, multicomponent alloys. This problem can be tackled by the thermodynamics of mixtures. The overwhelming effect is that of surface segregation. This means that the component with the lower surface tension tends to segregate at the surface, thereby minimizing the surface energy of the system. On the other hand, segregation raises the entropy, and equilibrium is established when the sum of these two contributions is minimized. The resulting concentration profile can be calculated explicitly in the ideal solution model [149]. For a binary alloy with bulk concentrations c_A, c_B, one obtains

$$c_A^s = \frac{c_A}{c_A + c_B/S_0}, \quad c_B^s = \frac{c_B}{c_B + c_A S_0}, \quad S_0 = e^{A(\gamma_B - \gamma_A)/RT} \tag{2.1.95}$$

where c_A^s, c_B^s are the surface concentrations, and S_0 is the surface segregation factor.

$A = A_A = A_B$ is the (average) molar surface area [149]: $A = 1.09 V_m^{2/3} N_A^{1/3}$. N_A is Avogadro's constant: $N_A = 6 \times 10^{23}\,(\text{mol})^{-1}$, V_m is the molar volume, R is the gas constant ($R = 8.3$ N m mol^{-1} K^{-1}), and T is the temperature. This is a large effect for, e.g., Fe-Cu, as shown in Figure 2.1.40.

Using the surface concentrations, Equation (2.1.95), the surface tension of the alloy can be written as

$$\gamma(T) = c_A^s(T)\gamma_A(T) + c_B^s(T)\gamma_B(T) \tag{2.1.96}$$

where $\gamma_i(T)$ are the surface tensions of the pure components. The ideal solution model neglects interactions between the atoms and generally overestimates surface segregation. A more precise description of the surface tension of alloys can be obtained from Butler's equation [150]. Butler derived his expression for the surface tension following Gibbs assumption that the surface is an independent thermodynamic phase, in equilibrium with the bulk phase.

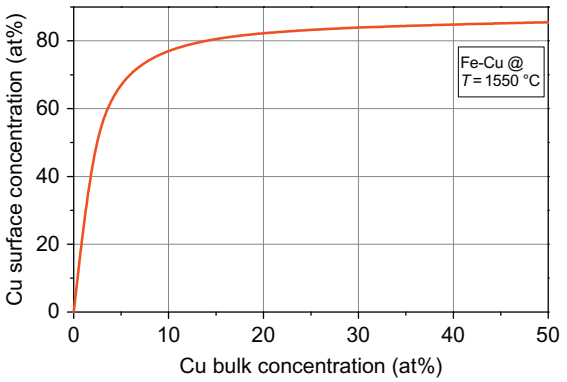


Figure 2.1.40 Surface segregation for Fe-Cu alloy in the ideal solution model.

This leads to following form of Butler's equation for a binary alloy of components A and B:

$$\gamma = \gamma_A + \frac{RT}{A_A}\ln\frac{c_A^s}{c_A} + \frac{\Delta G_A^E}{A_A} = \gamma_B + \frac{RT}{A_B}\ln\frac{c_B^s}{c_B} + \frac{\Delta G_B^E}{A_B} \tag{2.1.97}$$

Here, ΔG_i^E are the differences in the partial excess free energies of component i in the surface and bulk phase:

$$\Delta G_i^E = G_i^{E,s}\left(T, c_i^s\right) - G_i^{E,b}(T, c_i) \tag{2.1.98}$$

While $G_i^{E,b}$ is available from thermodynamic data bases, $G_i^{E,s}$ is not. A central assumption in surface tension calculations based on Equation (2.1.98) is that $G_i^{E,s}(T, c) = \beta G_i^{E,b}(T, c)$ where $\beta \approx 0.8$ [151]. The argument behind this crude approximation is that the main difference between bulk and surface is the number of nearest neighbors, its ratio being approximated by β. Butler's equation is an equation for the surface concentrations. It can only be solved numerically. Once the surface concentrations are known, they can be plugged into Equation (2.1.97) to obtain the surface tension of the alloy. In principle, Butler's equation allows to calculate the surface tension of any multicomponent alloy, provided the surface tensions of the pure elements and the bulk excess free energies are known.

In addition to the theoretical problems, the surface tension is also very difficult to measure, mainly because of the high reactivity of metallic melts at high temperatures as well as due to the extreme sensitivity of surface tension to impurities. Impurities with lower surface tension than the host metal segregate at the surface and reduce the surface tension of the system considerably. For liquid metals, the most prominent and ubiquitous surface active element is oxygen. A few ppm of oxygen can lead to a decrease in surface

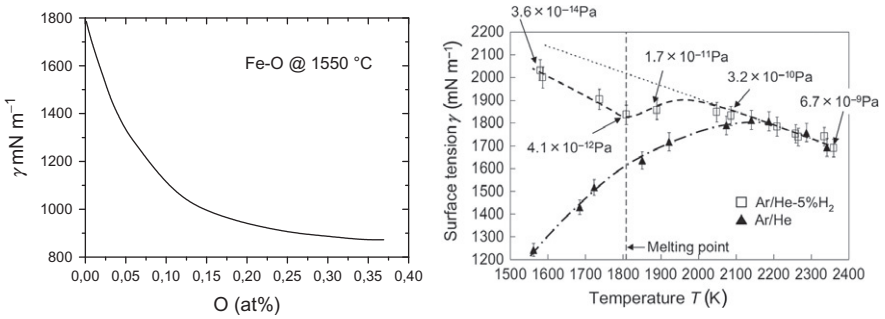


Figure 2.1.41 Left: Surface tension of iron as function of oxygen concentration. Right: Temperature coefficient of iron as function of oxygen concentration. *Left: After Ref. [154]. Right: From Ref. [146].*

tension by several percent, and to a sign reversal of the temperature coefficient, $\partial\gamma/\partial T$ [152,153], as shown in Figure 2.1.41.

A review of the various measurement techniques and a survey of high-temperature tensiometry problems can be found in Ref. [155]. More recently, Eustathopoulos *et al.* have published a monograph on wettability at high temperatures, including a careful discussion of the SD technique [156]. The following methods have generally been used: MBP, maximum drop pressure, capillary rise, SD, pendent drop (PD), LD, and maximum pull (MP). For high melting-point materials, only four of these methods are really relevant, namely MBP, SD, PD, and LD. Among these, SD is by far the most popular method. For a more detailed discussion of the PD technique, we refer the reader to Keene's article [157]. The other three methods are discussed below.

2.1.2.1.7.1 Maximum Bubble Pressure

This method can also be used for density measurements and it has been already discussed in Section 2.1.2.1.2. If it is applied for surface tension measurements, some additional comments must be made. First of all, one major advantage of MBP for surface tension measurements is the fact that for each measurement, for each bubble, a fresh, uncontaminated surface is created. On the other hand, in the derivation of Equation (2.1.32) it was assumed that the bubble is spherical and its size is independent of the immersion depth. This, however, is a too crude approximation for surface tension measurements. The hydrostatic pressure on the top of the bubble is smaller than at the bottom, which makes the bubble non-spherical and leads to a depth-dependent deformation of the bubble. This effect can be minimized by working with small bubbles, i.e., with narrow capillaries, but it cannot be neglected. In other words, the pressure drop across a non-spherical surface is not simply given by $2\gamma/r$, but by $(2\gamma/r)f$, where f is a correction factor. Several authors have given expressions for f; they are discussed in Ref. [158]. A popular correction formula is given below [157]:

$$\gamma = \gamma_{\text{eff}} \left[1 - \frac{1}{3} \frac{r^2 \rho g}{\gamma_{\text{eff}}} - \frac{1}{24} \left(\frac{r^2 \rho g}{\gamma_{\text{eff}}} \right)^2 \right] \tag{2.1.99}$$

where $\gamma_{\text{eff}} = (p_h - \rho g h) r/2$, i.e., the surface tension value, which one would obtain from Equation (2.1.32) directly. Obviously, Equation (2.1.99) is a series expansion in the Bond number, $B_o = r^2 \rho g / \gamma_{\text{eff}}$ and is valid only for $B_o \ll 1$, which is generally well satisfied.

2.1.2.1.7.2 Sessile Drop

The SD technique is very popular for measuring both surface tension and density. The major problem areas are substrate, atmosphere, drop alignment, image processing, and data analysis.

It is important that the substrate does not react with the liquid drop and the drop should not wet the substrate, i.e., the contact angle θ should be larger than 90°. Graphite, BN, ZrO_2, and Al_2O_3 have been used as substrate material. In addition to being inert and nonwet, the substrate should also be microscopically smooth to avoid pinning of the triple line between substrate, drop, and environment. Eustathopoulos *et al.* claim that a surface roughness of less than 0.1 μm should be achieved [156]. Equally important is the clean surface of the drop. If an oxide skin forms, the drop will not acquire its equilibrium shape, and the data analysis will lead to erroneous results. Most groups use a purified helium or argon atmosphere to prevent oxidation; operation under ultra-high vacuum has been attempted, but under such conditions, evaporation from the sample causes additional difficulties. A typical vertical setup for SD measurements using a drop dispenser is shown schematically in Figure 2.1.42.

For calculation of drop shape and volume, a rotationally symmetrical drop is always assumed, and this must be realized experimentally. This means that the substrate must be

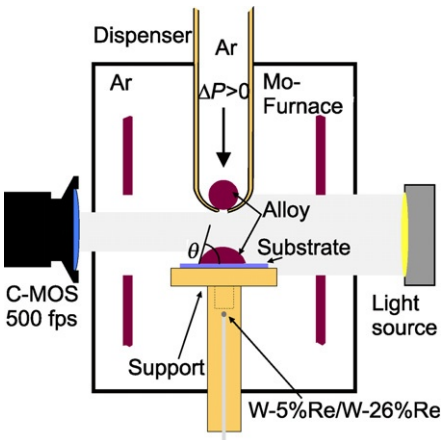


Figure 2.1.42 Typical setup for sessile drop measurements. *After Ref. [159].*

perfectly aligned horizontally, and it should be mounted on a vibration isolation mount. If the substrate is smooth and flat, the positioning of the drop inside the field of view of the observing optics can become a problem. Therefore, sometimes a slightly conical shape of the substrate is preferred, which helps to center the drop [160].

As for the LD, the volume is calculated from the meridional profile of the drop, using Equation (2.1.36). The density then follows from Equation (2.1.29). An example of an SD is shown in Figure 2.1.43.

For surface tension measurements, the meridional profile, as derived from image processing, must be compared with the theoretically predicted shape. This follows from the Laplace equation and is given, in nondimensional form, as follows:

$$b/r_1 + b/r_2 = 2 + B_o z/b \tag{2.1.100}$$

In this equation, b is the radius of curvature at the apex of the drop, r_1 and r_2 are the two principal radii of curvature at point $[z, x(z)]$, where z is the vertical depth measured from the apex. The coordinate system and geometry of the SD are shown schematically in Figure 2.1.44. B_o is the Bond number, in this case defined as

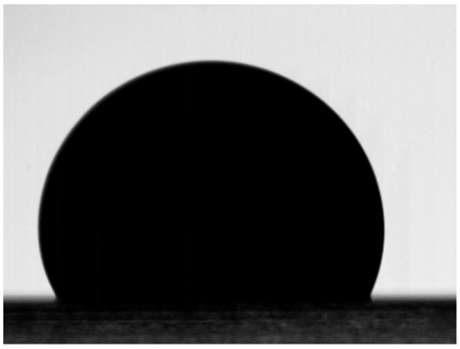


Figure 2.1.43 Picture of a sessile liquid Al-Cu drop. *Picture is taken with backlight illumination.*

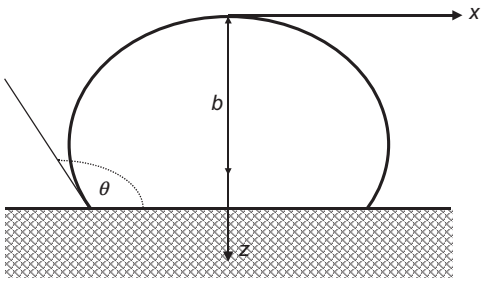


Figure 2.1.44 Schematics of a sessile drop. The contact angle is θ, and the radius of curvature at the apex is *b*.

$$B_o = \rho g b^2/\gamma \tag{2.1.101}$$

The principal radii of curvature can be expressed as second-order derivatives, d^2x/dz^2; consequently, Equation (2.1.100) is a second-order, second-degree differential equation. It does not possess a closed analytical solution, and must be solved numerically with the appropriate boundary conditions. In the past, approximate explicit expressions have been used [156] avoiding the numerical integration of Equation (2.1.100). Since the profile determination is nowadays performed by digital image processing anyway, this approach is no longer necessary. Instead, automatic computerized fitting procedures are used, e.g., by Passerone and coworkers [155,161].

As a result of the fitting procedure, one obtains the meridional profile $x(z)$ as a function of the two parameters b and B_o. The first is only a scaling factor, while the second contains the surface tension γ, however in the combination $\rho g/\gamma$. Since the density can be determined simultaneously by determining the volume as described above, the value of the surface tension can be deduced.

2.1.2.1.7.3 Oscillating Drop

The oscillating drop technique is an elegant way to measure the surface tension of LDs. It employs digital image processing for frequency analysis of surface waves. Neglecting damping, the radius r of a droplet undergoes oscillations of the form:

$$\delta r_{l,n}(\vartheta,\varphi,t) \propto Y_{l,n}(\vartheta,\varphi)\cos\left(\omega_{l,n}t\right) \tag{2.1.102}$$

Here, $Y_{l,n}$ are spherical harmonics. The frequencies $\omega_{l,n}$ are related to the surface tension, being the restoring force for these oscillations. If the equilibrium shape of the droplet is spherical, the formula of Lord Rayleigh can be used to relate frequency ω of the oscillations to the surface tension γ. Rayleigh's formula reads

$$\omega_R^2 = \frac{32\pi}{3}\frac{\gamma}{m} \tag{2.1.103}$$

where m is the mass of the droplet. This expression relates to the fundamental mode of oscillation, which corresponds to $l=2$. For spherical drops, the frequencies do not depend on n ($|n|<2$). Spherical shape is obtained only if the droplet is free of external forces. This situation is well approximated in microgravity. Under terrestrial conditions, the above relations are not valid and corrections have to be made for the external forces. For EML these corrections have been calculated by Cummings and Blackburn [162]. They take into account both the splitting of the peaks due to symmetry breaking and the shifting of the peaks due to magnetic pressure. The Cummings correction reads

$$\frac{32\pi}{3}\frac{\gamma}{m}=\frac{1}{5}\sum_{n}\omega_{2,n}^{2}-1.9\bar{\Omega}_{\mathrm{tr}}^{2}-0.3\left(\bar{\Omega}_{\mathrm{tr}}^{2}\right)^{-1}(g/r)^{2} \qquad (2.1.104)$$

Here, $\bar{\Omega}_{\mathrm{tr}}^{2}$ is the mean of the translational frequencies of the sample in the potential well of the levitation field, and g is the gravitational acceleration. It has been shown that by applying the Cummings correction to surface tension data obtained by the oscillating drop technique on earth, a spurious mass dependence can be eliminated [163].

The surface oscillations are recorded by a high-speed video camera and evaluated by digital image processing. Pictures can be taken from the top (along the symmetry axis of the drop) or from the side. The top view is generally preferred, because it is not obstructed by the windings of the levitation coil. The following parameters are usually determined frame by frame: horizontal radius, vertical radius, area of cross-sectional area, and the center of mass of cross section. Geometrical selection rules allow the identification of the different n-modes [164]. By taking the Fourier transform of sum and difference of two perpendicular radii, some modes disappear from the spectrum. This is shown in Figure 2.1.45.

In contrast to density measurements, only relative changes are important, and edge detection is not a critical issue. On the other hand, the oscillations have usually frequencies of the order of 50–100 Hz, which implies that a frame rate of at least 200 Hz has to be used to avoid aliasing effects.

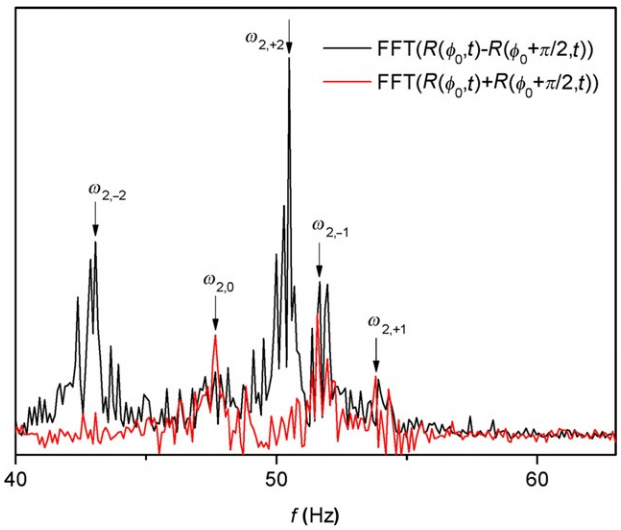


Figure 2.1.45 Oscillation spectrum of a levitated spherical drop. Fourier transform of sum and difference of two perpendicular radii, demonstrating the selection rules. *After Ref. [165].*

The Cummings formula, Equation (2.1.104), is derived under a number of assumptions. It is a linear theory with respect to the amplitude of the oscillations and with respect to the deviation from sphericity of the drop's equilibrium shape. In addition, it also assumes that the magnetic field inside the levitation coil has a linear gradient and that the drop has no viscosity. Corrections for the frequency shift due to viscous effects have been calculated [166], and they are negligibly small for liquid metals. Whether or not the field geometry of the levitation coil meets the assumptions of Cummings' theory can be checked by taking the ratio between the frequency $\Omega_{\mathrm{tr},\perp}$ of the translational oscillations in the plane perpendicular to the symmetry axis of the coil and that along the coil axis, $\Omega_{\mathrm{tr},||}$. It should equal 0.5. If the amplitude of the oscillations increases, the frequency may become amplitude dependent. McLean *et al.* [167] claim an increase in frequency, while Nogi *et al.* find a decrease [168]. On the other hand, a large amplitude improves image processing. As a compromise, amplitudes of about 3–5% should be used.

Finally, the surface tension is obtained from the frequencies by multiplying with the mass m of the drop. Therefore, evaporation losses during processing must be minimized. In view of the total accuracy of the method, mass losses of less than 1% are acceptable.

2.1.2.1.8 Viscosity

The viscosity η is a typical property of a fluid. It expresses its resistance to a fluid flow and is defined by following Gedanken experiment: If one moves a plate of surface A along the x direction, the force F_x to establish a velocity gradient $\partial v/\partial z$ is given by

$$F_x = \eta A \frac{\partial v}{\partial z} \tag{2.1.105}$$

This defines the (shear) viscosity η. It is often denoted as dynamic viscosity and its corresponding SI unit is Pa s. The kinematic viscosity v is defined as

$$v = \frac{\eta}{\rho} \tag{2.1.106}$$

where ρ is the density. This is a useful definition, because this combination appears in many hydrodynamic expressions, like the Rayleigh number, Equation (2.1.28) or the Marangoni number, Equation (2.1.90). The relation between dynamic and kinematic viscosity resembles that between thermal conductivity and thermal diffusivity, Equation (2.1.41). As is evident from Equation (2.1.105), the viscosity is, precisely speaking, a tensor. Not surprisingly, there exists, in addition to shear viscosity, also a longitudinal, or volume, viscosity [169]. This quantity however is only relevant for compressible fluids and can be safely neglected for incompressible molten metals.

From statistical mechanics Born and Green have derived the following equation for the viscosity [170]:

$$\eta = \sqrt{\frac{m}{kT}} \frac{2\pi n^2}{15} \int_0^\infty \mathrm{d}r r^4 \frac{\mathrm{d}\phi}{\mathrm{d}r} g(r) \tag{2.1.107}$$

where m is the atomic mass, and all other symbols are the same as in Equation (2.1.89). An empirical relation for the viscosity at the melting point is due to da Andrade [171]:

$$\eta(T_\mathrm{m}) = 1.6 \times 10^{-7} \frac{\sqrt{MT_\mathrm{m}}}{V_\mathrm{m}^{2/3}} \tag{2.1.108}$$

where M is the molar mass, and all quantities are in SI units.

Many different models have been developed to describe the temperature dependence of the viscosity. In the simplest case, shear flow is treated as an activated process that leads to an Arrhenius-type temperature dependence:

$$\eta = \eta_0 \mathrm{e}^{\Delta E/kT} \tag{2.1.109}$$

Here, ΔE is the activation energy, and k is Boltzmann's constant. Later Cohen and Turnbull [172] developed their free volume model, which leads to the Vogel-Fulcher-Tamman relation:

$$\eta = \eta_0 \mathrm{e}^{\Delta E'/k(T-T_0)} \tag{2.1.110}$$

where T_0 is the ideal glass temperature. This expression is often used to describe the divergence of the viscosity at the glass transition. More recently, theories of viscosity have been based on the idea of mode coupling [173]. These theories lead to a power-law behavior of the form:

$$\eta = A(T - T_0)^{-\alpha} \tag{2.1.111}$$

The exponent α is not universal and is typically of the order of 2.4 [174].

In monotectic systems, i.e., alloys that undergo a liquid-liquid phase separation, like Al-In, a singular contribution due to critical density fluctuations appears near the critical temperature T_c [175,176]. In this region the viscosity η scales as:

$$\eta = B(T - T_\mathrm{c})^{-Z_\eta \nu} \tag{2.1.112}$$

Here Z_η is the critical exponent of the viscosity and ν is the critical exponent of the density correlation length. The generally accepted, not universal, value for the product is $Z_\eta \nu = 0.043$.

It is also interesting to discuss the concentration dependence of the viscosity for alloys. In contrast to, e.g., the density, there is no ideal model for the viscosity. However, a number of phenomenological expressions have been proposed in the past. A good overview on selected models is given for instance in Ref. [177]. The most prominent are the

Moelwyn-Hughes model [178], the Kozlov-Romanov-Petrov model [179], the Hirai equation [180], and the Kaptay equation [181].

In the Moelwyn-Hughes model [178], the viscosity η is given by the following expression:

$$\eta = (c_A\eta_A + c_B\eta_B)\left(1 - 2\frac{\Delta H}{RT}\right) \tag{2.1.113}$$

Here, η_i are the viscosities of the pure elements A or B, c_i the corresponding molar concentration, T is the absolute temperature, R the universal gas constant, and ΔH is the enthalpy of mixing.

The Kozlov-Romanov-Petrov model [179] is derived by expressing the Gibbs free energy in terms of atomic vibration frequencies. For an alloy with N components, $i = 1 \ldots N$, it reads

$$\ln(\eta) = \sum_{i=1}^{N} c_i \ln(\eta_i) - \frac{\Delta H}{3RT} \tag{2.1.114}$$

The Hirai equation [180] estimates the activation energy E from the liquidus temperature T_L. It reads

$$\eta = 1.7 \times 10^{-7} \frac{\rho^{2/3} T_L^{1/2}}{M^{1/6}} \exp\left[\frac{2.65 \times T_L^{1.27}}{R}\left(\frac{1}{T} - \frac{1}{T_L}\right)\right] \tag{2.1.115}$$

where ρ is the density and M the molar mass of the alloy. The great advantage of this equation is that its input parameters are easily accessible. Also, it relates the viscosity directly to the liquidus temperature, T_L, of the alloy, implying that the concentration dependence of the viscosity should follow that of the phase diagram. Such behavior has been observed for a number of systems, as noted by Richardson [182] and Brillo et al. [183].

The Kaptay equation [181] relates the activation energy to the enthalpy of mixing ΔH by introducing a semiempirical parameter, $\alpha = 0.155$, which has been estimated from the properties of pure metals:

$$\eta = \frac{hN_A}{V} \exp\left(\sum_i c_i \ln\left(\frac{\eta_i V_i}{hN_A}\right) - \alpha\frac{\Delta H}{RT}\right) \tag{2.1.116}$$

Here h is Planck's constant, N_A Avogadro's number, η_i and V_i are viscosity and molar volume of the pure components, respectively. For the evaluation of some of these expressions, the enthalpy of mixing, ΔH, and the excess Gibbs enthalpy ${}^{E}G$ are needed. They can usually be found in thermodynamic databases. Brillo et al. [183] have compared the different models to experimental data of ternary Fe-Ni-Cu alloys and finds that the Kaptay equation usually provides the best description.

Note added in proof: In a recent paper, Schick et al. have developed a simple model which seems to fit the data even better. It is shown in Figure 2.1.51 (a).

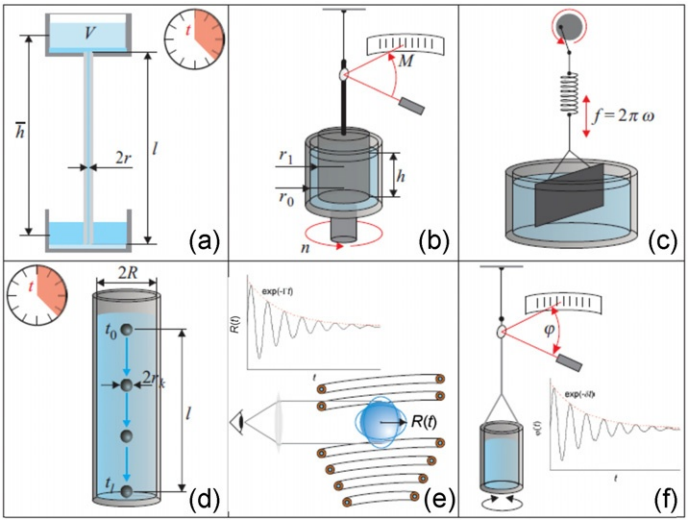


Figure 2.1.46 Different types of viscometers: (a) capillary, (b) rotating cup, (c) oscillating plate, (d) falling sphere, (e) oscillating drop, and (f) oscillating cup. *After Ref. [238].*

Finally, if the molten metal specimen has a free surface, potential effects of a surface viscosity need to be considered [184]. A free surface may exhibit rheological properties different from the bulk liquid. This may be an intrinsic effect due to a different electron density near the surface [185], or an extrinsic effect, due to, e.g., a thin oxide film covering the surface. Surface viscosities are usually discussed in aqueous or organic solutions, like an oil film on water, but have also been observed for molten metals, e.g., Hg [185].

The experimental techniques for measuring the viscosity of molten metals have been reviewed by Brooks *et al.* [186] and Sato [187]. For this class of materials, mainly three different methods are in use: (a) capillary method, (b) rotating cup, and (f) oscillating cup. More recently, viscosity measurements on levitated liquid metal drops have also been attempted (e), using an extension of the oscillating drop technique discussed in Section 2.1.2.1.7. The principles of the different methods are shown schematically in Figure 2.1.46.

2.1.2.1.8.1 Capillary Viscometer

In this technique, a fixed volume V of the test liquid has to pass through a capillary of radius r and height h, and the time t required is measured. The fluid flow can be described by the Hagen-Poiseuille equation and yields for the kinematic viscosity v:

$$v = \frac{\eta}{\rho} = C_1 t - \frac{C_2}{t} \tag{2.1.117}$$

The two constants C_1 and C_2 contain only parameters of the viscometer and need to be determined by measuring viscosities of two known reference fluids. For high-temperature materials, like molten metals, the capillary viscometer must be placed inside a furnace providing a homogeneous temperature profile, and the capillary must be inert to the melt and should have little thermal expansion. It is typically made of quartz glass. Note that the density must be known to obtain the dynamic viscosity.

2.1.2.1.8.2 Rotating Cup Viscometer

In the rotating cup viscometer, the test liquid is placed between two concentric cylinders of radii r_0 and r_1 respectively, and the filling height of the liquid is h. One of the cylinders, usually the inner one, is rotated at a frequency f, and the torque T generated on the other cylinder is measured. The viscosity is then given by

$$\eta = \left(\frac{1}{r_1^2} - \frac{1}{r_0^2}\right)\frac{T}{8\pi^4 f h} \tag{2.1.118}$$

As with all viscometers, the internal friction of the apparatus must be small, such that the effect of viscosity is not masked. This is particularly difficult for the rotating cup viscometer, and, consequently, this type is mainly used for systems with high viscosity, such as slags. For liquid metals with a relatively low viscosity, it is also necessary to make the gap between the two cylinders small, which can lead to jamming.

2.1.2.1.8.3 Oscillating Cup Viscometer

The oscillating cup viscometer consists of a cup, containing the liquid metal. It is suspended on a wire that is excited to torsional oscillations. Frequency and damping of the oscillations are recorded and the viscosity is derived from the corresponding working equation.

The basis for this device is the equation of motion of a damped harmonic oscillator, written for the torsion angle ϕ as

$$I\frac{\partial^2\phi}{\partial t^2} + L(\eta)\frac{\partial\phi}{\partial t} + k\phi = 0 \tag{2.1.119}$$

The moment of inertia, I, and the spring constant, k, are constants of the viscometer, whereas the friction term $L(\eta)$ is due to the sloshing of the liquid inside the oscillating cup. An analytical expression for $L(\eta)$ is obtained by solving the corresponding Navier-Stokes equation [188]. A detailed description of such a device can be found in Ref. [189]. In short, a vacuum furnace with a graphite heater is used to heat the sample. The temperature inside the furnace is controlled by a thermocouple and/or a pyrometer. The sample inside the furnace is placed in a cup made of a temperature-resistant and chemically inert material. The sample is then set in torsional oscillations, which are detected by a reflected laser on a position-sensitive device (PSD). The setup is shown schematically in Figure 2.1.47. The oscillation period T_{osc} and the logarithmic decrement δ are extracted from the oscillation and inserted into the Roscoe equation [188]:

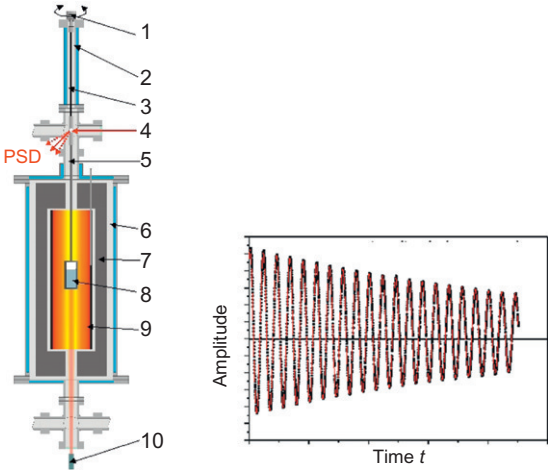


Figure 2.1.47 Left: An oscillating cup viscometer. 1, oscillation excitation; 2, tubing; 3, torsion wire; 4, laser beam; 5, tungsten rod; 6, housing; 7, insulation; 8, sample cup; 9, heater; 10, pyrometer. Right: Measured signal and fit.

$$\eta Z^2(\eta) = \left(\frac{I\delta}{\pi R_{\text{cup}}^3 H}\right)^2 \frac{1}{\pi \rho T_{\text{osc}}} \tag{2.1.120}$$

for calculating the viscosity. In the above equation, Z is a known function of η, R_{cup} is the inner radius of the cup, H is the height of the sample inside the cup, and ρ is the density of the liquid sample. To obtain the viscosity, this equation is inverted numerically. As for the capillary viscometer, the density of the liquid must be known.

It is essential that the cup does not react with the material under study. Generally, alumina, zirconia, or yttria cups are used, similar to a high-temperature DSC (see Section 2.1.2.1.3).

2.1.2.1.8.4 Oscillating Drop

The oscillating drop technique, discussed in Section 2.1.2.1.7, can also be used to measure the viscosity of the liquid drop by extending the mathematical treatment to viscous fluids. This has been done by Lord Kelvin [190]. If damping is included, Equation (2.1.102) has to be generalized as

$$\delta r_{l,n}(\vartheta,\varphi,t) \propto Y_{l,n}(\vartheta,\varphi)\cos\left(\omega_{l,n}t\right)\exp\left(-\Gamma_{l,n}t\right) \tag{2.1.121}$$

indicating that an excited oscillation decays as $\exp(-\Gamma t)$. For spherical, force-free, droplets there is no dependence on the index n, and the damping for the fundamental mode $l=2$ is related to the viscosity by Kelvin's formula:

$$\eta = \frac{3m}{20\pi R_0}\Gamma_2 \tag{2.1.122}$$

where m is the mass and R_0 the radius of the levitated liquid drop.

Like Rayleigh's formula for the surface tension, Equation (2.1.103), this equation is only valid for spherical drops in the absence of external fields. This is hardly realized in terrestrial EML experiments. Consequently, experiments under microgravity may in fact be the only possibility to apply this method. Here the positioning fields can be minimized and magnetohydrodynamic damping effects can be neglected. The situation may however be different for electrostatic levitation where there are essentially no damping effects due to the electric field. In both cases, a short pulse is applied to the levitation coils or electrodes, respectively, resulting in squeezing the liquid drop. The decay of this deformation is then monitored by a high-speed video camera, and the time dependence of the radius is fitted by a damped harmonic oscillation.

2.1.2.2. Results

There exists a large collection of thermophysical property data. First of all, the book of Iida and Guthrie [2] contains these data in tabular form. The handbook of Kawai and Shiraishi [90] is also an excellent source. Mills has compiled thermophysical property data for selected commercial alloys [191]. Surface tension data of pure metals have been reviewed and critically assessed by Keene [157]. He has also reviewed surface tension data of iron and its binary alloys [154]. Recent reviews and recommended values for the viscosity and density of aluminum and iron [192] as well as copper and tin [193] have been published by Assael *et al.* Diffusion data up to 1986 are compiled in Ref. [129]. On the other hand, there is only some data available for thermal properties, i.e., specific heat and thermal conductivity. In this section, we provide data for selected pure metals and binary alloys, using, whenever possible, most recent sources.

2.1.2.2.1 Pure Metals

2.1.2.2.1.1 Emissivity

There is only a little data on the normal spectral emissivity of molten metals, and they have been published mainly by three groups, namely the group of Cezairliyan at NIST, Righini's group in Torino, and Krishnan and coworkers at Containerless Inc. The work at NIST and Torino is summarized in a review paper [194], while the work of Krishnan, based on ellipsometry, is published in Refs. [80,84]. We reproduce their data for $\lambda = 633$ nm in Table 2.1.1.

2.1.2.2.1.2 Density and Thermal Expansion

The density of molten metals measured on levitated droplets by the DLR group has been published in Ref. [195]. They are reproduced in Table 2.1.2 in the form $\rho(T) = \rho_L - \rho_T(T - T_L)$, where T_L is the liquidus temperature.

2.1.2.2.1.3 Specific Heat

Specific heat data of liquid metals have been compiled in the book of Pottlacher [123]. They are reproduced in Table 2.1.3.

Table 2.1.1 Normal spectral emissivities of pure liquid metals at $\lambda = 633$ nm

Metal	ε_n (633 nm)
Ag	0.09
Au	0.30
Cu	0.13
Ni	0.40
Pd	0.38
Pt	0.38
Zr	0.41
Hf	0.52–0.61
Ir	0.30–0.34
Mo	0.45–0.48
Nb	0.48–0.49
Ta	0.48–0.53
V	0.42–0.46

After Refs. [80,84].

Table 2.1.2 Densities of liquid metals

Element	T_L (K)	ρ_L (g cm^{-3})	ρ_T (10^{-4} g cm^{-3} K^{-1})
Ag	1235	9.15	7.4
Al	933	2.35	2.0
Au	1337	17.4	11
Co	1773	7.81	8.85
Cu	1357	7.90	7.65
Fe	1811	7.04	10.8
Ni	1727	7.92	10.1
Si	1683	2.52	3.53

After Ref. [195].

2.1.2.2.1.4 Thermal Conductivity

In an extensive review, Monaghan *et al.* have compiled thermal conductivity data for pure liquid metals [196]. We have not found any more recent collection of data. Therefore, we reproduce an excerpt of their results in Table 2.1.4. Where available, the temperature-dependent data are given in the form $\lambda(T) = \lambda_L + \lambda_T 10^{-2}(T - T_L)$, where T_L is the liquidus temperature (melting point). Thermal diffusivities can be derived from this table by using Equation (2.1.41) and the data from Tables 2.1.2 and 2.1.3.

2.1.2.2.1.5 Electrical Resistivity

Electrical resistivity (denoted as $1/\sigma$ to avoid confusion with density ρ) heat data of liquid metals have been compiled in the book of Pottlacher [123]. They are given mainly as a linear fits in Table 2.1.5.

Table 2.1.3 Specific heats of selected pure liquid metals

Element	C_p (J mol^{-1} K^{-1})
Co	46.734
Cu	33.775
Au	30.924
Fe	43.001
Mo	47.164
Ni	40.819
Nb	43.294
Pd	37.32
Pt	36.48
Re	52.697
Rh	46.102
Ag	28.024
Ta	40.895
Ti	49.925
W	51.291
Va	49.108
Zr	45.274

After Ref. [123].

Table 2.1.4 Thermal conductivities of pure liquid metals

Element	T_L (K)	λ_L (W m^{-1} K^{-1})	λ_T (W m^{-1} K^{-2})
Ag	1235	175	2.0
Al	933	91	0.34
Au[a]	1337	105	3.0
Co	1768	36	
Cu	1358	163	2.0
Fe	1811	33	
Nb	2750	66	
Ni	1728	60	
Pd	1828	87	
Pt	2042	53	
Si	1687	56	
Sn	505	27	
Ti	1941	31	
V	2183	43.5	

[a]Note that the original table lists 1090 K as melting point for Au, which is not correct.
After Ref. [196].

2.1.2.2.1.6 Self-diffusion

Data on diffusion coefficients of molten metals are sparse. Data up to 1988 have been compiled in Refs. [90] and [129]. Results for some low-melting materials Sn, Pb, In, and Sb can be found in Refs. [197,198] and in the article by Suzuki in Ref. [130]. As

Table 2.1.5 Electrical resistivities of selected pure liquid metals

Element	$1/\sigma$ ($\mu\Omega$ m)
Co	$0.858 + 1.738 \times 10^{-4}$ T
Cu	$0.110 + 7.831 \times 10^{-5}$ T
Au	$0.147 + 1.127 \times 10^{-4}$ T $+ 2.0954 \times 10^{-8}$ T^2
Fe	$1.027 + 2.209 \times 10^{-4}$ T
Mo	$0.931 + 3.957 \times 10^{-5}$ T
Ni	$0.667 + 1.043 \times 10^{-4}$ T
Nb	$0.683 + 1.477 \times 10^{-4}$ T
Pd	$0.777 + 2.058 \times 10^{-5}$ T
Pt	$0.832 + 9.604 \times 10^{-5}$ T
Re	$-3.682 + 2.543 \times 10^{-3}$ T $- 3.235 \times 10^{-7}$ T^2
Rh	$0.516 + 1.680 \times 10^{-4}$ T
Ag	$4.592 \times 10^{-2} + 9.856 \times 10^{-5}$ T
Ta	$1.196 + 4.406 \times 10^{-5}$ T
Ti	$1.706 + 1.483 \times 10^{-5}$ T
W	$2.313 - 4.585 \times 10^{-4}$ T $+ 5.65 \times 10^{-8}$ T^2
Va	$1.418 - 1.730 \times 10^{-4}$ T $+ 6.012 \times 10^{-8}$ T^2
Zr	$1.258 + 8.735 \times 10^{-5}$ T

After Ref. [123].

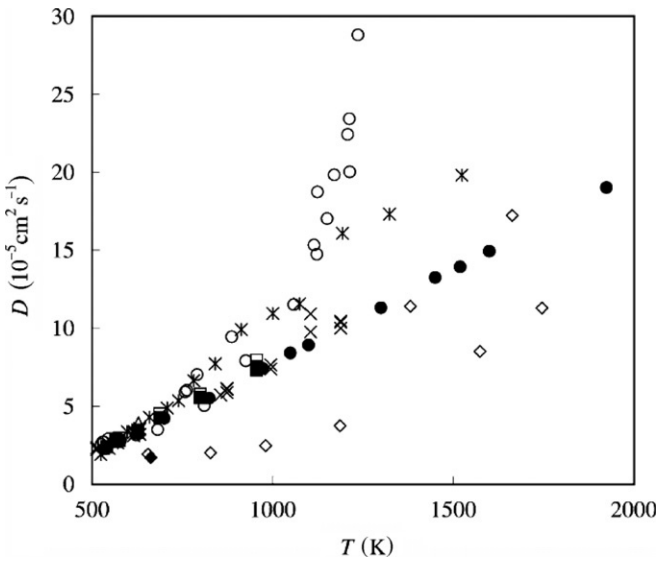


Figure 2.1.48 Self-diffusion coefficient of liquid Sn. Compilation of different publications. *After Ref. [198].*

Table 2.1.6 Self-diffusion coefficients of liquid Cu, Ni, and Ti, obtained by QENS

Element	D (10^{-9}m^2 s^{-1})
Cu	$59\ \exp(-3911/T)$
Ni	$77\ \exp(-5454/T)$
Ti	$87\ \exp(-5597/T)$

Table 2.1.7 Viscosities of selected pure metals

Element	log η (mPa s)	References
Fe	$-0.6074+2493/T$	[202]
Ni	$-0.5695+2157/T$	[202]
Co	$-0.6620+2430/T$	[202]
Sn	$-0.4461+331/T$	[203]
Ag	$-0.3585+1153/T$	[203]
Cu	$-0.3696+1305/T$	[203]
Zr	$-0.1192+1660/T$	[31]
Nb	$-0.2596+2552/T$	[31]
Ru	$-0.2218+2599/T$	[31]
Hf	$-0.3010+25422/T$	[31]

can be seen from Figure 2.1.48, the scatter of data obtained by different authors is quite considerable. The self-diffusion of iron under high pressure has been studied by Dobson [199]. More recent data obtained from quasi-ENS are available for Ni [136], Cu [200], and Ti [201]. The results obtained are given in Table 2.1.6.

2.1.2.2.1.7 Viscosity

The viscosities of the transition metals Fe, Ni, and Co as well as their binary alloys have been measured by Sato [202] using the oscillating cup method; the same method was applied by Kehr et al. [203] to Sn, Ag, and Cu, while those of the refractory elements have been measured by Paradis, using electrostatic levitation [31]. Their results are shown in Table 2.1.7.

2.1.2.2.1.8 Surface Tension

The surface tensions of selected pure liquid metals measured on levitated droplets by the DLR group have been published in Ref. [195]. They are reproduced in Table 2.1.8 in the form $\gamma(T)=\gamma_L-\gamma_T(T-T_L)$, where T_L is the liquidus temperature.

2.1.2.2.2 Alloys

It is impossible to give a complete account of all measured thermophysical property data of metallic alloys, including ternary and multicomponent systems. In the following we will restrict ourselves to binary alloys and recent references. A key to some selected publications is compiled in Table 2.1.9. Typical examples will be discussed below.

Table 2.1.8 Surface tensions of pure liquid metals

Element	T_L (K)	γ_L (N m^{-1})	γ_T (10^{-4} N m^{-1} K^{-1})
Ag	1235	0.91	1.8
Al	933	0.88	2.0
Au	1337	1.12	0.9
Co	1773	1.89	3.3
Cu	1357	1.29	2.34
Fe	1811	1.92	3.97
Ni	1727	1.77	3.3
Si	1683	0.784	6.5

After Ref. [195].

Table 2.1.9 References to thermophysical properties of liquid binary alloys

Alloy	Density	Surface tension	Viscosity
Al-Cu	[204]	[165]	[205]
Al-Ni	[206]	[207]	[208]
Al-Si	[209]	[210]	[211]
Al-Fe	[206]	[207]	
Al-Ag	[204]	[212]	[213]
Ag-Cu	[214]	[215]	[213]
Au-Ag	[214]	[216]	[217]
Au-Cu	[95]	[216]	
Cu-Si	[218]	[218]	[219]
Cu-Ni	[220]	[221]	[183]
Cu-Fe	[220]	[221]	[183]
Cu-Co	[222]	[223]	[224]
Co-Fe	[222]	[223]	[202]
Fe-Ni	[220]	[221]	[202]

The interest, of course, is on the concentration dependence of the thermophysical properties, and their deviation from ideal behavior. We start by comparing the densities, or more precisely the molar volumes, of two copper alloys, namely Al-Cu and Fe-Cu. Their concentration dependence is shown in Figure 2.1.49. Evidently, the excess volume V_x, Equation (2.1.31), is negative for Al-Cu, while it is positive for Fe-Cu.

A similar behavior can also be observed for the surface tension. The surface tensions of Cu-Fe and Al-Ni are shown in Figure 2.1.50a and b, respectively. The phase diagram of the Cu-Fe alloy shows a metastable liquid miscibility gap, indicating a tendency of phase separation for this alloy. As a consequence, surface segregation of copper is much more pronounced as predicted by the ideal solution model, Equation (2.1.95), which leads to a steep decrease of surface tension even for small copper concentrations. By using the appropriate thermodynamic excess Gibbs energies, this behavior is well predicted by

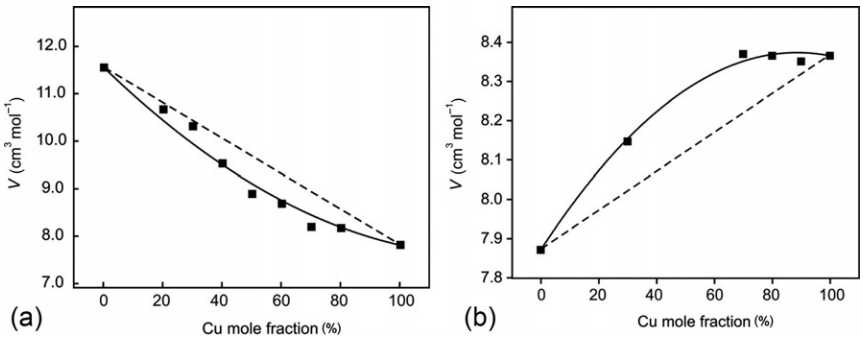


Figure 2.1.49 (a) Molar volume of Al-Cu at $T = 1020$ K (symbols) versus copper concentration with $V_x < 0$ (solid line). (b) Molar volume of Fe-Cu at 1760 K (symbols) versus copper concentration, with $V_x > 0$ (solid line). For comparison, both plots show Vegard's ideal law, $V_x = 0$ (dashed lines). *Panel (a): After [204]. Panel (b): After [222].*

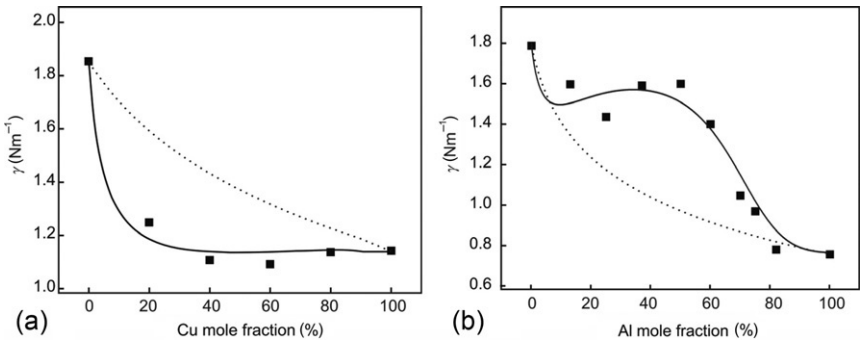


Figure 2.1.50 (a) Surface tension of Cu-Fe at 1970 K versus copper mole fraction (symbols) showing a steep decrease at small concentrations. Shown is also a plot of the solution of the Butler equation, Equation (2.1.97) (solid line) and of the ideal solution model (dashed line). (b) Surface tension of Al-Ni at 1670 K versus aluminum concentration (symbols) with the appearance of a shoulder. The solid line corresponds to a simple model, Equation (2.1.123), for the effect of compound formation [149], the dashed line to the ideal solution model. *Panel (a): After Ref. [221]. Panel (b): After Ref. [207].*

the Butler equation, Equation (2.1.97). In contrast to Cu-Fe, the phase diagram of Al-Ni shows a number of intermetallic solid phases of high stability, indicating a preference for heteroatomic Al-Ni pairs. This behavior is also in agreement with the findings of the structural studies discussed in the previous section. Such compound formation tendency counteracts surface segregation, since the Al atoms that would prefer to segregate at the surface like to stay in the bulk where they find more Ni atoms lowering their binding energy. The concentration dependence of Al-Ni, as shown in Figure 2.1.50b, is typical for compound-forming alloys. The surface tension is higher than predicted by the ideal solution model and shows a shoulder or maximum near the composition of the most stable solid intermetallic phase, which in this case is AlNi. A very simple extension of the ideal solution model, taking into account the binding energy of Al-Ni pairs [149], is

capable of describing this effect quantitatively. In this model, the segregation coefficient, Equation (2.1.95), is modified to account for the compound-forming tendency in the following way:

$$S'_0 = e^{A(\gamma_B - \gamma_A) - f(n+m)c_A^n c_B^m / RT} \tag{2.1.123}$$

where f is a fit parameter describing the strength of the interaction, and n and m are the stoichiometric coefficients of the compound, in the present case of Al_1Ni_1, $n = m = 1$.

Considering the viscosities of alloys, it must be first stated that a homogenization of the melt is absolutely necessary to avoid artifacts due to segregation and sedimentation effects. As a corollary, it is also clear that viscosities of two-phase mixtures, i.e., of immiscible liquids or of solid-liquid mixtures like in the mushy zone during solidification cannot be measured using conventional methods and are, in fact, ill-defined quantities.

In the previous section, we have discussed several phenomenological models trying to describe the concentration dependence of the viscosity of alloys. We have chosen Al-Cu and Al-Ni as examples to compare experimental data with model predictions. Al-Cu has been measured by Schick et al. [205], while the data on Al-Ni are due to Kehr *et al.* [208]. Data and models are shown in Figure 2.1.51a and b, respectively. Generally speaking, the viscosity of alloys is higher than predicted by the ideal mixing rule. This can be attributed to metastable clusters formed in the liquid, which hinder fluid flow.

Finally, we show two examples for the electrical resistivities of alloys in Figure 2.1.52, namely Cu-Ni and Al-Fe. In both cases, the resistivity exceeds that of the ideal mixing rule for the same reasons as discussed above for the viscosity. While Cu-Ni shows a nearly monotonous concentration dependence with a shallow maximum around 80 at% Ni, the Al-Fe system exhibits a pronounced maximum in the region of the equiatomic composition.

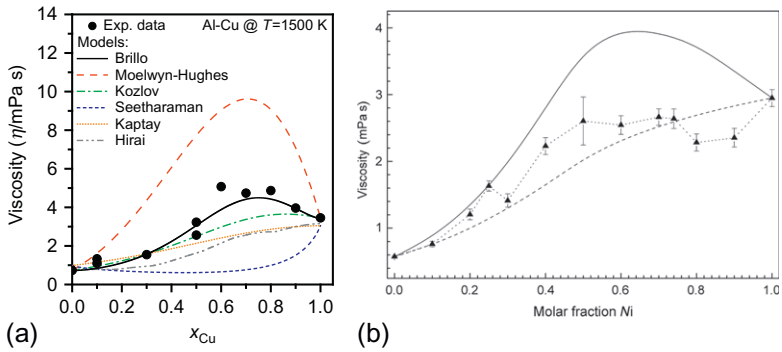


Figure 2.1.51 (a) Viscosity of liquid Al-Cu at 1500 K versus copper concentration. In addition to the experimental data [205] (squares) the results of model calculations are displayed. (b) Viscosity values of Al-Ni at $T = 2073$ K versus nickel concentration. In addition to the measured data [208] (triangles), also the results calculated using the Kozlov model, Equation (2.1.114) (solid line) and the Kaptay model, Equation (2.1.116), (dashed line) are displayed.

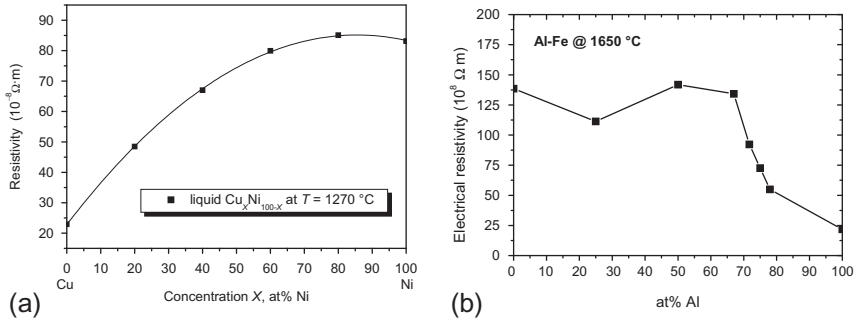


Figure 2.1.52 (a) Electrical resistivity of liquid Cu-Ni alloys at 1270 °C, measured in electromagnetic levitation [125]. (b) Electrical resistivity of liquid Al-Fe alloys at 1650 °C [225].

2.1.3. STRUCTURE-PROPERTY RELATIONS AND INTERPROPERTY RELATIONS

2.1.3.1. Structure-Property Relations

Whereas there are obviously structure-property correlations for the solid phase, the situation may be different for the liquid. The micro- or macrostructure of a crystalline material directly influences such properties as elasticity or brittleness. Structural properties like dendrites, grain boundaries, or defects bear directly on macroscopic properties as well as the crystal structure itself, be it fcc, bcc, or anything else. In liquids, there may be topological or chemical short-range order, and we can discuss their influence on the (thermophysical) properties of the macroscopic liquid. All the data about structure are contained in the structure factor $S(Q)$, or, equivalently, in the pair-distribution function $g(r)$. Consequently, structure-property correlations have to invoke these quantities and link them to macroscopic properties.

We start by recalling the famous compressibility sum rule [1]:

$$K_{\mathrm{T}} = \frac{1}{\rho k T} \lim_{Q \to 0} S(Q) \tag{2.1.124}$$

where $S(Q)$ is the static structure factor, k Boltzmann's constant, and K_{T} is the isothermal compressibility. Due to the fact that liquids are essentially incompressible, $S(0) \ll 1$ for molten metals, typically $S(0) \approx 0.02$. In the case of (binary) alloys, the above equation has to be generalized and it reads as

$$\begin{aligned} \rho k T K_{\mathrm{T}} &= \frac{S_{\mathrm{AA}}(0) S_{\mathrm{BB}}(0) - S_{\mathrm{AB}}^2(0)}{c_{\mathrm{B}} S_{\mathrm{AA}}(0) + c_{\mathrm{A}} S_{\mathrm{BB}}(0) - 2(c_{\mathrm{A}} c_{\mathrm{B}})^{1/2} S_{\mathrm{AB}}(0)} \\ &= \frac{S_{\mathrm{NN}}(0) S_{\mathrm{cc}}(0) - S_{\mathrm{Nc}}^2(0)}{S_{\mathrm{cc}}(0)} \end{aligned} \tag{2.1.125}$$

There is a similar relation for the dynamical structure factor $S(Q,\omega)$ in the quasielastic limit. In fact, it has already been used for the measurement of the diffusion coefficient, Equation (2.1.86). It reads

$$D = \pi \lim_{\omega\to\infty} \omega^2 \lim_{Q\to 0} \frac{S(Q,\omega)}{Q^2} \tag{2.1.126}$$

Here D is the diffusion constant.

There are additional structure-property relations, which involve integrals over the pair-distribution function and the two-body interatomic potential. One example is the Born-Fowler relation for the surface tension, Equation (2.1.89)

$$\gamma = \frac{\pi n^2}{8} \int_0^\infty \mathrm{d}r r^4 \frac{\mathrm{d}\phi}{\mathrm{d}r} g(r) \tag{2.1.127}$$

the other is Born-Green's equation for the viscosity, Equation (2.1.107):

$$\eta = \sqrt{\frac{m}{kT}} \frac{2\pi n^2}{15} \int_0^\infty \mathrm{d}r r^4 \frac{\mathrm{d}\phi}{\mathrm{d}r} g(r) \tag{2.1.128}$$

One would expect a similar equation for the density in terms of the pair-correlation function, but, surprisingly, such an equation does not exist. The (number) density is always an input to such calculations (a scaling factor) rather than an output. Iida and Guthrie [2] present also an equation for the specific heat in terms of the pair-distribution function:

$$c_V = \frac{3}{2}k + 2\pi n \int_0^\infty \left[\frac{\partial g(r)}{\partial T}\right]_V \phi(r) r^2 \mathrm{d}r \tag{2.1.129}$$

Here c_V is the specific heat at constant volume, n the number density, and $\phi(r)$ has been assumed independent of temperature.

2.1.3.2. Interproperty Relations

Interproperty relations are a useful tool to estimate a thermophysical property, which is difficult to measure, from another, more easily accessible quantity. Such relations can also serve as consistency checks for independently obtained data. It should be noted, however, that most of these relations are semiempirical, and their range of validity may be restricted.

Useful interproperty relations between thermal conductivity, viscosity, and self-diffusion coefficient can be derived from statistical mechanics, assuming that the pair potential is of Lennard-Jones type. They are discussed in Ref. [226].

We first discuss the Hagen-Rubens relation [79]. This relation establishes a link between the (d.c.) electrical conductivity σ_0 and the normal spectral emissivity. It reads [79]

$$\varepsilon_n(\lambda, T) = 0.365(\lambda\sigma_0(T))^{-1/2} \tag{2.1.130}$$

In this equation, conductivity is in $(\Omega\ \mathrm{m})^{-1}$ and λ in (m). This relation is only valid at long wavelengths, of the order of 10 μm. For smaller wavelengths, correction terms of the order of $(\lambda\sigma)^{-1}$ must be included.

A relation between surface tension and viscosity has been first noted by Turkdogan [227] and later discussed in greater detail by Egry [228]. These authors have made use of the fact that the integral appearing in Equations (2.1.127) and (2.1.128) is the same. Therefore dividing both equations, one obtains:

$$\frac{\gamma}{\eta} = \frac{15}{16}\sqrt{\frac{kT}{m}} \tag{2.1.131}$$

where m is the atomic mass. This expression has been derived for pure metals and works reasonably well, as can be seen from Figure 2.1.53. It has also been applied to alloys; however, this is somewhat questionable, in view of the atomic mass appearing in the equation.

We now turn to a further, well-known relation between electrical and thermal conductivity. This is the famous Wiedeman-Franz law (WFL). It is obtained by dividing Equations (2.1.61) and (2.1.69)

$$\frac{\lambda}{\sigma} = LT;\quad L = \frac{1}{3}\left(\frac{\pi k}{e}\right)^2 = 2.445 \times 10^{-8}\,\mathrm{W\Omega K^{-2}} \tag{2.1.132}$$

where L is the so-called Lorenz number. This is a rather old result dating back to 1853, and was in fact, already explained by Drude [120] without invoking quantum mechanics.

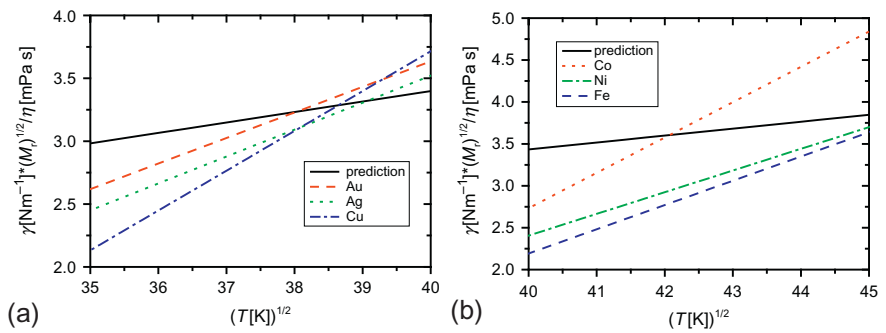


Figure 2.1.53 Interrelation between surface tension and viscosity for molten metals. (a) Noble metals Ag, Au, and Cu. (b) Transition metals Co, Fe, and Ni. The prediction is based on Equation (2.1.131).

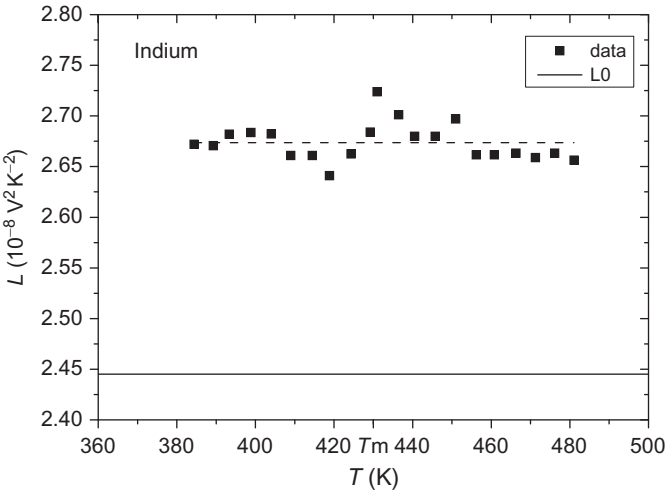


Figure 2.1.54 Lorenz number for solid and liquid Indium. The melting point is marked as T_m, and the solid line indicates the theoretical value of the Lorenz number, Equation (2.1.132). *After Ref. [230].*

The Wiedemann-Franz law is based on two assumptions: (i) heat and electrical current are carried by the same species, electrons in our case, and (ii) the scattering events responsible for a finite electrical resistivity are elastic. Its validity is discussed in some detail in Ref. [229]. The first assumption implies that the contribution of the ions is negligible, the second makes sure that the electrons do not lose their energy on their way. Ionic contributions become relevant for solids at low temperatures, and inelastic scattering events set in at high temperatures. For molten metals, Equation (2.1.132) should hold reasonably well. Data for solid and liquid Indium are shown in Figure 2.1.54 as an example. Whereas the absolute value of the Lorenz number is somewhat too high, the temperature dependence is correct, and the value of L is—within experimental error—the same for the solid and liquid phase. Data on liquid tin and lead have been published by Yamasue *et al.* [231]. Monaghan *et al.* [196] state that for liquid metals, Equation (2.1.132) is accurate within 10%. However, when these conditions are not met, gross violations of the WFL can occur, as recently observed by Wakeham *et al.* [232] in one-dimensional conductors.

Another important interproperty relation links diffusion coefficient with viscosity. This is the Stokes-Einstein relation [233]. It reads

$$D\eta = \frac{kT}{c6\pi a}, \quad c = \begin{cases} 2/3 & \text{slip} \\ 1 & \text{stick} \end{cases} \tag{2.1.133}$$

In this equation, a is an effective (covalent) atomic radius, and the value of the constant c depends on the choice of the hydrodynamic boundary condition in the derivation of this equation. In their study of simple Lennard-Jones fluids, Capelezzo *et al.* have shown that the slip boundary condition holds well for a large range of parameters [234].

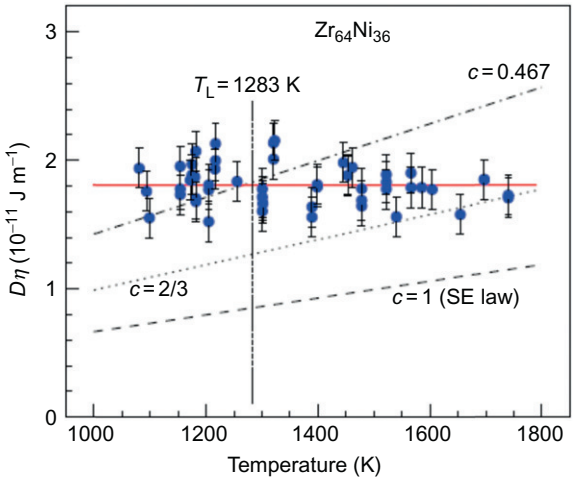


Figure 2.1.55 Stokes-Einstein relation for liquid $Zr_{64}Ni_{36}$, above and below the liquidus temperature of $T_L = 1283$ K. Predictions of the Stokes-Einstein (SE) law for different choices of c with the covalent atomic radius of Ni. *After Ref. [237].*

The difficulty with this relation is the fact that a macroscopic friction force is applied on microscopic scale to describe the movements of atoms. It has also been argued that the Stokes-Einstein relation should break down near the glass transition [235], where the atomic dynamics changes qualitatively. This has been shown for supercooled water by Chen and coworkers [236]. Very recently, Brillo *et al.* [237] have measured viscosity of a liquid Ni-Zr alloy above and below the liquidus temperature. They find that the product $D\eta$ is independent of temperature, contradicting the Stokes-Einstein relation. This is shown in Figure 2.1.55. A theoretical explanation for this unexpected behavior is still missing.

2.1.4. SUMMARY

In this chapter, we have discussed structure and properties of molten metals. We have seen that liquid metals are not void of structure, and the prevailing microscopic short-range order is intimately related to the macroscopic properties of the material. We have discussed a number of structure-property and property-property relations. The latter need to be used with some care, as their validity may be restricted. New experimental techniques, often based on containerless methods, allow a precise determination of thermophysical properties at high temperatures. In addition, numerical simulations, based on MD, Monte Carlo, or even *ab initio* density functional theory, provide a valuable alternative, when the experimental approach proves to be not feasible. The knowledge base thus created is an indispensible prerequisite for any modeling of processes or thermodynamics, as discussed in the following chapters.

REFERENCES

[1] N.H. March, Liquid Metals, Cambridge University Press, Cambridge, 1990.
[2] T. Iida, R. Guthrie, The Physical Properties of Liquid Metals, Clarendon Press, Oxford, 1988.
[3] I. Egry, C. Nieto de Castro, in: T. Letcher (Ed.), Chemical Thermodynamics, Blackwell, Oxford, 1999, p. 171.
[4] A. Goodwin, K. Marsh, W. Wakeham (Eds.), Measurement of the Thermodynamic Properties of Single Phases, Elsevier, Amsterdam, 2003(Chapter 10.3).
[5] H. Fukuyama, Y. Waseda (Eds.), High Temperature Measurements of Materials, Springer, Berlin, 2009(Chapter 7).
[6] J. Ziman, Principles of the Theory of Solids, Cambridge University Press, Cambridge, 1969.
[7] D. Herlach, R. Cochrane, I. Egry, H. Fecht, A. Greer, Int. Mater. Rev. 38 (1993) 273–347.
[8] D. Turnbull, J. Chem. Phys. 20 (1952) 411–424.
[9] D.M. Herlach, Mater. Sci. Eng. R12 (1994) 177.
[10] W. Kauzmann, Chem. Rev. 43 (1948) 219–256.
[11] F.C. Frank, Proc. R. Soc. Lond. A 215 (1952) 43.
[12] P.F. McMillan, M. Wilson, M.C. Wilding, D. Daisenberger, M. Mezouar, G.N. Greaves, J. Phys. Condens. Matter 19 (2007) 415101.
[13] Y. Mishin, M.J. Mehl, D.A. Papaconstantopoulos, Phys. Rev. B 65 (2002) 224114.
[14] C. Woodward, M. Asta, D.R. Trinkle, J. Lill, S. Angioletti-Uberti, J. Appl. Phys. 107 (2010) 113522.
[15] J. Bokeloh, R. Rozas, J. Horbach, G. Wilde, Phys. Rev. Lett. 107 (2011) 145701.
[16] B. Grabowski, T. Hickel, J. Neugebauer, Phys. Rev. B 76 (2007) 024309.
[17] R. Weber, S. Krishnan, P. Nordine, JOM Mag. 43 (1991) 8.
[18] G. Jacobs, I. Egry, K. Maier, D. Platzek, J. Reske, R. Frahm, Rev. Sci. Instrum. 67 (1996) 3683.
[19] I. Egry, D. Holland-Moritz, Eur. Phys. J. (Spec. Top.) 196 (2011) 131–150.
[20] L. Hennet, V. Cristiglio, J. Kozaily, I. Pozdnyakova, H.E. Fischer, A. Bytchkov, J.W.E. Drewitt, M. Leydier, D. Thiaudiere, S. Gruner, S. Brassamin, D. Zanghi, G.J. Cuello, M. Koza, S. Magazu, G.N. Greaves, D.L. Price, Eur. Phys. J. (Spec. Top.) 196 (2011) 151–165.
[21] D. Price, High-Temperature Levitated Materials, Cambridge University Press, Cambridge, 2010.
[22] L. Hennet, I. Pozdnyakova, A. Bytchkov, V. Cristiglio, P. Palleau, H. Fischer, G. Cuello, M. Johnson, P. Melin, D. Zanghi, S. Brassamin, J. Brun, D. Price, M. Saboungi, Rev. Sci. Instrum. 77 (2006) 053903.
[23] K.F. Kelton, G.W. Lee, A.K. Gangopadhyay, R.W. Hyers, T.J. Rathz, J.R. Rogers, M.B. Robinson, D.S. Robinson, Phys. Rev. Lett. 90 (2003) 195504.
[24] G.W. Lee, A.K. Gangopadhyay, K.F. Kelton, R.W. Hyers, T.J. Rathz, J.R. Rogers, D.S. Robinson, Phys. Rev. Lett. 93 (2004) 037802.
[25] K. Higuchi, K. Kimura, A. Mizuno, M. Watanabe, Y. Katayama, K. Kuribayashi, J. Non-Cryst. Solids 353 (2007) 2997.
[26] L. Hennet, D. Thiaudiere, M. Gailhanou, C. Landron, J.-P. Coutures, D.L. Price, Rev. Sci. Instrum. 73 (2002) 124.
[27] G. Mathiak, I. Egry, L. Hennet, D. Thiaudiere, I. Pozdnyakova, D. Price, Int. J. Thermophys. 26 (2005) 1151–1166.
[28] W.-K. Rhim, S.K. Chang, D. Barber, K.F. Man, G. Gutt, A. Rulison, R.E. Spjut, Rev. Sci. Instrum. 64 (1993) 2961.
[29] T. Kordel, D. Holland-Moritz, F. Yang, J. Peters, T. Unruh, T. Hansen, A. Meyer, Phys. Rev. B 83 (2011) 104205.
[30] P. Paradis, T. Ishikawa, S. Yoda, Meas. Sci. Technol. 16 (2005) 452.
[31] T. Ishikawa, P. Paradis, T. Itami, S. Yoda, Meas. Sci. Technol. 16 (2005) 443.
[32] G. Lohöfer, IMA J. Appl. Math. 68 (2003) 1–21.
[33] G. Lohöfer, Quart. Appl. Math. 11 (1993) 495.
[34] Y. Waseda, The Structure of Non-Crystalline Materials, McGraw-Hill, New York, 1980.
[35] J.B. Suck, D. Raoux, P. Chieux, C. Riekel (Eds.), Proceedings of the ILL/ESRF Workshop on Methods in the Determination of Partial Structure Factors (Grenoble), World Scientific, Singapore, 1993.

[36] A.C. Barnes, H.E. Fischer, P.S. Salmon, in: H.E. Fischer, H. Schober (Eds.), Neutrons et Systemes Desordonnes, Journal de Physique IV, vol. 111, EDP Sciences, Les Ulis, 2003, pp. 59–96.
[37] M.-L. Saboungi, W. Geertsma, D.L. Price, Annu. Rev. Phys. Chem. 41 (1990) 207–244.
[38] H.E. Fischer, A.C. Barnes, P.S. Salmon, Rep. Prog. Phys. 69 (2006) 233–299.
[39] Y. Waseda, S. Takeda, Chin. J. Phys. 31 (1993) 225.
[40] W. Hoyer, I. Kaban, Th. Halm, J. Optoelectron. Adv. Mater. 3 (2001) 255.
[41] T.E. Faber, J.M. Ziman, Philos. Mag. 11 (109) (1965) 153–173.
[42] P. Lagarde, in: N.H. March, R.A. Street, M. Tosi (Eds.), Amorphous Solids and the Liquid State, Plenum Press, New York, 1985, p. 365.
[43] B.K. Teo, in: B.K. Teo, D.C. Joy (Eds.), EXAFS Spectroscopy, Plenum Press, New York, 1981, p. 13.
[44] A.B. Bhatia, D.E. Thornton, Phys. Rev. B 2 (8) (1970) 3004–3012.
[45] J.M. Cowley, Phys. Rev. 77 (1950) 669–675.
[46] Y. Waseda, K. Suzuki, Phys. Stat. Sol. (B) 49 (1972) 339.
[47] Y. Waseda, M. Ohtani, Phys. Stat. Sol. (B) 62 (1974) 535.
[48] F. Hensel, W. Warren, Fluid Metals, Princeton University Press, Princeton, 1999.
[49] S. Hosokawa, T. Matsuoka, K. Tamura, J. Phys. Condens. Matter 3 (1991) 4443.
[50] H. Ruppersberg, Phys. Lett. 46A (1973) 75.
[51] H. Ruppersberg, Phys. Lett. 54A (1975) 151.
[52] D. Holland-Moritz, T. Schenk, P. Convert, T. Hansen, D.M. Herlach, Meas. Sci. Technol. 16 (2005) 372.
[53] T. Schenk, D. Holland-Moritz, V. Simonet, R. Bellissent, D.M. Herlach, Phys. Rev. Lett. 89 (2002) 075507.
[54] A. Di Cicco, A. Trapananti, J. Non-Cryst. Solids 353 (2007) 3671.
[55] P.J. Steinhardt, D.R. Nelson, M. Ronchetti, Phys. Rev. Lett. 47 (1981) 1297.
[56] S. Sastry, A. Angell, Nat. Mater. 2 (2003) 739.
[57] P. Ganesh, M. Widom, Phys. Rev. Lett. 102 (2009) 075701.
[58] S. Ansell, S. Krishnan, J.J. Felten, D. Price, J. Phys. C11 (1999) 8167.
[59] Y. Waseda, K. Shinoda, K. Sugiyama, S. Takeda, K. Terashima, J. Toguri, Jpn. J. Appl. Phys. 34 (1995) 4124.
[60] H. Kimura, M. Watanabe, K. Izumi, T. Hibiya, D. Holland-Moritz, T. Schenk, K.-R. Bauchspieß, S. Schneider, I. Egry, K. Funakoshi, M. Hanfland, Appl. Phys. Lett. 78 (2001) 604.
[61] T.H. Kim, G.W. Lee, B. Sieve, A.K. Gangopadhyay, R.W. Hyers, T.J. Rathz, J.R. Rogers, D.S. Robinson, K.F. Kelton, A.I. Goldman, Phys. Rev. Lett. 95 (2005) 085501.
[62] S. Krishnan, L. Hennet, T. Key, B. Glorieux, M.-L. Saboungi, D.L. Price, J. Non-Cryst. Solids 253 (2007) 2975.
[63] I. Stich, M. Parrinello, J.M. Holender, Phys. Rev. Lett. 76 (1996) 2077.
[64] D. Li, D. Herlach, Europhys. Lett. 34 (1996) 423.
[65] D. Holland-Moritz, O. Heinen, R. Bellissent, T. Schenk, D.M. Herlach, Int. J. Mater. Res. 97 (2006) 948.
[66] D. Holland-Moritz, S. Stüber, H. Hartmann, T. Unruh, T. Hansen, A. Meyer, Phys. Rev. B 79 (2009) 064204.
[67] H. Bühner, S. Steeb, Z. Naturforsch. 24a (1969) 428.
[68] W. Hoyer, R. Jödicke, J. Non-Cryst. Solids 192 (1995) 102.
[69] I. Kaban, P. Jovari, W. Hoyer, R. Delaplane, A. Wannberg, J. Phys. Condens. Matter 18 (2006) 2749.
[70] M. Maret, T. Pomme, A. Pasturel, Phys. Rev. B42 (1990) 1598.
[71] G. Mathiak, J. Brillo, A. Bytchkov, I. Egry, L. Hennet, I. Pozdnyakova, D.L. Price, D. Thiaudiere, D. Zanghi, J. Non-Cryst. Solids 352 (2006) 4008.
[72] I. Egry, L. Hennet, M. Kehr, G. Mathiak, S. De Panfilis, I. Pozdnyakova, D. Zanghi, J. Chem. Phys. 129 (2008) 0645081–5.
[73] T. Schenk, V. Simonet, D. Holland-Moritz, R. Bellissent, T. Hansen, P. Convert, D.M. Herlach, Europhys. Lett. 65 (2004) 34.
[74] S. Beer, Liquid Metals, Marcel Dekker, New York, 1972.

[75] P. Quested, R.F. Brooks, in: P. Sahm, P. Hansen, J. Conley (Eds.), Modeling of Casting, Welding and Advanced Solidification Processes IX, Shaker, Aachen, 2000, p. LXXIII.
[76] K. Mills, L. Courtney, R. Brooks, B. Monaghan, ISIJ Int. 40 (2000) S120.
[77] I. Egry, High Temp. High Press. 32 (2000) 127.
[78] D.P. deWitt, F.P. Incopera, in: D.P. deWitt, G.D. Nutter (Eds.), Theory and Practice of Radiation Thermometry, Wiley, New York, 1989.
[79] Y. Touloukian, D. DeWitt, in: Thermal Radiative Properties, Metallic Elements and Alloys, vol. 7, Plenum Press, New York, 1970.
[80] G.P. Hansen, S. Krishnan, R. Hauge, J. Margrave, Appl. Opt. 28 (1989) 1885.
[81] A. Cezairliyan, J. Res. Nat. Bur. Stand. 75C (1971) 7.
[82] F. Righini, J. Spisiak, G. Bussolino, Int. J. Thermophys. 20 (1999) 1095.
[83] G.D. Nutter, in: G.D. Nutter, D.P. deWitt (Eds.), Theory and Practice of Radiation Thermometry, Wiley, New York, 1989, p. 231.
[84] S. Krishnan, G. Hansen, R. Hauge, J. Margrave, High Temp. Sci. 29 (1990) 17.
[85] A.S. Tenney, in: D.P. deWitt, G.D. Nutter (Eds.), Theory and Practice of Radiation Thermometry, Wiley, New York, 1989, p. 459.
[86] M. Khan, C. Allemand, T. Eagar, Rev. Sci. Instrum. 62 (1991) 392.
[87] S. Amore, J. Horbach, I. Egry, J. Chem. Phys. 134 (2011) 044515.
[88] L. Vegard, Z. Phys. 5 (1921) 17.
[89] A. Crawley, Int. Met. Rev. 19 (1974) 32.
[90] Y. Kawai, Y. Shiraishi (Eds.), Handbook of Physico-Chemical Properties at High Temperatures, The Iron and Steel Institute of Japan, Japan, 1988.
[91] A. Keskar, S. Hruska, Met. Trans. 1 (1972) 2357.
[92] G. Ruffino, in: K.D. Maglic, A. Cezairliyan, V.E. Peletsky (Eds.), Compendium of Thermophysical Property Measurement Methods, Survey of Measurement Techniques, vol. 1, Plenum Press, New York, 1984, p. 689.
[93] R.C. Bradshaw, D.P. Schmidt, J.R. Rogers, K.F. Kelton, R.W. Hyers, Rev. Sci. Instrum. 76 (2005) 125108.
[94] E. Gorges, L. Racz, A. Schillings, I. Egry, Int. J. Thermophys. 17 (1996) 1163.
[95] J. Brillo, H. Giffard, A. Patti, I. Egry, Int. J. Thermophys. 25 (2003) 1881–1888.
[96] R. Lin, M.G. Frohberg, High Temp. High Press. 24 (1992) 543.
[97] L. Onsager, Phys. Rev. 37 (1931) 405–426.
[98] J. Platten, J. Appl. Mech. 73 (2006) 5.
[99] S. Nakamura, T. Hibiya, F. Yamamoto, T. Yokota, Int. J. Thermophys. 12 (1991) 783.
[100] G. Höhne, W. Hemminger, H.-J. Flammersheim, Differential Scanning Calorimetry, Springer, Berlin, 1996.
[101] V.Y. Chekhovskoi, in: K.D. Maglic, A. Cezairliyan, V.E. Peletsky (Eds.), Compendium of Thermophysical Property Measurement Methods. Volume 2: Recommended Measurement Techniques and Practice, Plenum Press, New York, 1992ISBN: 0-306-43854-2.
[102] V. Chekhovskoy, in: D.P. deWitt, G.D. Nutter (Eds.), Theory and Practice of Radiation Thermometry, Wiley, New York, 1989, p. 555.
[103] K. Ohsaka, J. Gatewood, E. Trinh, Script. Met. Mat. 25 (1991) 1459.
[104] M.G. Frohberg, Thermochim. Acta 337 (1999) 7.
[105] J. Qin, M. Rösner-Kuhn, K. Schaefers, M.G. Frohberg, Z. Metallkd. 85 (1994) 10.
[106] H. Fecht, W. Johnson, Rev. Sci. Instrum. 62 (1991) 1299.
[107] R. Wunderlich, H. Fecht, Meas. Sci. Technol. 16 (2005) 402.
[108] H. Fukuyama, H. Kobatake, K. Takahashi, I. Minato, T. Tsukada, S. Awaji, Meas. Sci. Technol. 18 (2007) 2059.
[109] H. Kobatake, H. Fukuyama, I. Minato, T. Tsukada, S. Awaji, J. Appl. Phys. 104 (2008) 054901.
[110] M. Assael, C. Nieto de Castro, H. Roder, W. Wakeham, in: W. Wakeham, A. Nagashima, J. Sengers (Eds.), Experimental Chemical Thermodynamics, vol. 2, Blackwell, Oxford, 1991, p. 161.
[111] T. Hibiya, S. Nakamura, Int. J. Thermophys. 17 (1996) 1191.
[112] K. Nagata, H. Fukuyama, K. Taguchi, H. Ishii, M. Hayashi, High Temp. Mater. Process. 22 (2003) 267.

[113] V. Sklyarchuk, Y. Plevachuk, Meas. Sci. Technol. 16 (2005) 467–471.
[114] W.J. Parker, R.J. Jenkins, C.P. Butler, G.L. Abbott, J. Appl. Phys. 3 (2) (1961) 1679.
[115] K.D. Maglic, R.E. Taylor, in: K.D. Maglic, A. Cezairliyan, V.E. Peletsky (Eds.), Compendium of Thermophysical Property Measurement Methods. Volume 2. Recommended Measurement Techniques and Practices, Plenum Press, New York, 1992ISBN: 0-306-433854-24.
[116] J. Cape, G. Lehman, J. Appl. Phys. 34 (1963) 1909–1913.
[117] L. Dusza, High Temp. High Press. 27 (1995) 467.5.
[118] J. Blumm, J. Opfermann, High Temp. High Press. 34 (5) (2002) 515–521.
[119] T. Nishi, H. Shibata, H. Ohta, Y. Waseda, Mater. Metallur. Trans. 34A (2003) 2801.
[120] P. Drude, Ann. Phys. 306 (1900) 566.
[121] J. Mooij, Phys. Stat. Sol. (A) 17 (1973) 521.
[122] Yu. Plevachuk, V. Sklyarchuk, Meas. Sci. Technol. 12 (1) (2001) 23.
[123] G. Pottlacher, High Temperature Thermophysical Properties of 22 Pure Metals, Edition Keiper, Graz, 2010.
[124] J.E. Enderby, S. Ansell, S. Krishnan, D.L. Price, M.-L. Saboungi, Appl. Phys. Lett. 71 (1997) 116.
[125] T. Richardsen, G. Lohöfer, Int. J. Thermophys. 20 (1999) 1029–1039.
[126] G. Lohöfer, I. Egry, in: W. Hofmeister, J. Rogers, N. Singh, S. Marsh, P. Vorhees (Eds.), Solidification 1999, TMS, Warrendale, 1999.
[127] G. Lohöfer, Meas. Sci. Technol. 16 (2005) 417–425.
[128] R. Swalin, Acta Metallur. 7 (1959) 736–740.
[129] M. Shimoji, T. Itami, Atomic Transport in Liquid Metals, Trans. Tech, Aedermannsdorf, 1986.
[130] S. Suzuki, in: H. Fukuyama, Y. Waseda (Eds.), High Temperature Measurements of Materials, Springer, Berlin, 2009, p. 61.
[131] L.S. Darken, Trans. AIME 175 (1948) 184–201.
[132] H. Mehrer, Diffusion in Solids, Springer, Berlin, 2007.
[133] R. Singh, F. Sommer, Phys. Chem. Liquids 36 (1998) 17–28.
[134] B. Zhang, A. Griesche, A. Meyer, Phys. Rev. Lett. 104 (2010) 035902.
[135] T. Unruh, J. Neuhaus, W. Petry, Nucl. Instrum. Methods Phys. Res. A 580 (2007) 1414.
[136] A. Meyer, S. Stüber, D. Holland-Moritz, O. Heinen, T. Unruh, Phys. Rev. B 77 (2008) 092201.
[137] R. Fowler, Proc. R. Soc. A159 (1937) 229.
[138] J. Kirkwood, F. Buff, J. Chem. Phys. 17 (1949) 338.
[139] R. Kumaravadivel, R. Evans, J. Phys. C 8 (1975) 793.
[140] W.H. Shih, D. Stroud, Phys. Rev. B 32 (1985) 804.
[141] M. Hasegawa, J. Phys. F 18 (1988) 1449.
[142] M. Nijmeier, C. Bruin, A. van Woerkom, F. Bakker, J. van Leeuwen, J. Chem. Phys. 96 (1991) 565.
[143] C. Marangoni, Nuovo Cim. 3 (1878) 97.
[144] J. Legros, A. Sanfeld, M. Velarde, in: H. Walter (Ed.), Fluid Sciences and Materials Sciences in Space, Springer, Berlin, 1987(Chapter 3).
[145] V. Kolevzon, J. Phys. Condens. Matter 11 (1999) 8785–8792.
[146] S. Ozawa, K. Morohoshi, T. Hibiya, H. Fukuyama, J. Appl. Phys. 107 (2010) 014910.
[147] S. Fisk, B. Widom, J. Chem. Phys. 50 (1969) 3219.
[148] A. Skapski, J. Chem. Phys. 16 (1948) 389.
[149] I. Egry, Int. J. Thermophys. 26 (2005) 931–939.
[150] J. Butler, Proc. R. Soc. A135 (1932) 348.
[151] T. Tanaka, K. Hack, T. Iida, S. Hara, Z. Metallkd. 87 (1996) 380.
[152] B. Keene, K. Mills, E. Hondros, Can. Met. Quart. 21 (1982) 393.
[153] B. Gallois, C. Lupis, Met. Trans. B 12 (1981) 549.
[154] B. Keene, Int. Mater. Rev. 33 (1988) 1.
[155] A. Passerone, E. Ricci, in: D. Moebius, R. Miller (Eds.), Drops and Bubbles in Interfacial Research, Elsevier, Amsterdam, 1998, p. 475.
[156] N. Eustathopoulos, M. Nicholas, B. Drevet, Wettability at High Temperatures, Pergamon, Oxford, 1999.
[157] B. Keene, Int. Mater. Rev. 38 (1993) 157.

[158] V. Fainerman, R. Miller, in: D. Moebius, R. Miller (Eds.), Drops and Bubbles in Interfacial Research, Elsevier, Amsterdam, 1998, p. 279.
[159] J. Schmitz, J. Brillo, I. Egry, J. Mater. Sci. 45 (2010) 2144–2149.
[160] I. Egry, E. Ricci, R. Novakovic, S. Ozawa, Adv. Coll. Interface Sci. 159 (2010) 198–212.
[161] L. Liggieri, A. Passerone, High Temp. Technol. 7 (1989) 82.
[162] D. Cummings, D. Blackburn, J. Fluid Mech. 224 (1991) 395.
[163] I. Egry, S. Sauerland, Mater. Sci. Eng. A178 (1994) 73.
[164] S. Sauerland, K. Eckler, I. Egry, J. Mater. Sci. Lett. 11 (1992) 330–333.
[165] J. Schmitz, J. Brillo, I. Egry, R. Schmid-Fetzer, Int. J. Mater. Res. 100 (2009) 1529–1535.
[166] P. Suryanarayana, Y. Bayazitoglou, Int. J. Thermophys. 12 (1991) 137.
[167] H. Soda, A. McLean, W. Miller, Met. Trans. 9B (1978) 145.
[168] Y. Asakuma, T. Hirata, T. Tsukada, M. Hozawa, K. Nogi, N. Imaishi, J. Chem. Eng. Jpn. 33 (2000) 861.
[169] R.E. Graves, B.M. Argrow, J. Thermophys. Heat Transf. 13 (3) (1999) 337–342.
[170] M. Born, H. Green, Proc. R. Soc. A190 (1947) 455.
[171] E. da Andrade, Philos. Mag. 17 (1934) 698.
[172] M.H. Cohen, D. Turnbull, J. Chem. Phys. 31 (1959) 1164.
[173] U. Bengtzelius, W. Götze, A. Sjölander, J. Phys. C 17 (1984) 5915.
[174] S. Das, Rev. Mod. Phys. 76 (2004) 785.
[175] F. Herwig, W. Hoyer, Mater. Sci. Eng. A190 (1995) L5.
[176] Y. Plevachuk, V. Sklyarchuk, O. Alekhin, L. Bulavin, J. Alloys Compd. 452 (2008) 174.
[177] I. Budai, M.Z. Benkő, G. Kaptay, Mater. Sci. Forum 473–474 (2005) 309.
[178] E.A. Moelwyn-Hughes, Physical Chemistry, Pergamon Press, Oxford, 1961.
[179] L.Y. Kozlov, L.M. Romanov, N.N. Petrov, Izv. Vysch. Uch. Zav. Chern. Metallur. 3 (1983) 7(russ.).
[180] M. Hirai, ISIJ Int. 33 (1993) 251.
[181] G. Kaptay, in: Proceedings of MicroCAD 2003 Conference, Section Metallurgy, University of Miskolc, 2003, p. 23.
[182] F. Richardson, Physical Chemistry of Melts in Metallurgy, Academic Press, London, 1974.
[183] J. Brillo, R. Brooks, I. Egry, P. Quested, Int. J. Mater. Res. 98 (2007) 457.
[184] L. Scriven, Chem. Eng. Sci. 12 (1960) 98–108.
[185] J. Earnshaw, Philos. Trans. R. Soc. Lond. A356 (1998) 855–856.
[186] R. Brooks, A. Dinsdale, P. Quested, Meas. Sci. Technol. 16 (2005) 354.
[187] Y. Sato, in: H. Fukuyama, Y. Waseda (Eds.), High Temperature Measurements of Materials, Springer, Berlin, 2009(Chapter 2).
[188] R. Roscoe, Proc. Phys. Soc. 72 (1958).
[189] M. Kehr, W. Hoyer, I. Egry, Int. J. Thermophys. 28 (2007) 3.
[190] S. Chandrasekhar, Hydrodynamic and Hydromagnetic Stability, Dover, New York, 1961.
[191] K. Mills, Recommended Values of Thermophysical Properties for Selected Commercial Alloys, Woodhead Publishing, Cambridge, 2002.
[192] M.J. Assael, K.E. Kakosimos, R.M. Banish, J. Brillo, I. Egry, R. Brooks, P.N. Quested, K.C. Mills, A. Nagashima, Y. Sato, W.A. Wakeham, J. Phys. Chem. Ref. Data 35 (2006) 285.
[193] M. Assael, A. Kalyva, K. Antoniadis, R.M. Banish, J. Wu, E. Kaschnitz, W. Wakeham, J. Phys. Chem. Ref. Data 39 (3) (2010).
[194] A. Cezairliyan, A. Miiller, F. Righini, A. Rosso, High Temp. High Press. 23 (1991) 325–332.
[195] I. Egry, J. Brillo, J. Chem. Eng. Data 54 (2009) 2347.
[196] B. Monaghan, K. Mills, B. Keene, High Temp. High Press. 30 (4) (1998) 457–464.
[197] G. Mathiak, A. Griesche, K.H. Kraatz, G. Frohberg, J. Non-Cryst. Solids 412 (1996) 205–207.
[198] T. Itami, T. Masaki, H. Aoki, S. Munejiri, M. Uchida, S. Masumoto, K. Kamiyama, K. Hoshino, J. Non-Cryst. Solids 177 (2002) 312–314.
[199] D.P. Dobson, Phys. Earth Planet. Inter. 130 (3-4) (2002) 271–284.
[200] A. Meyer, Phys. Rev. B 81 (2010) 012102.
[201] J. Horbach, R.E. Rozas, T. Unruh, A. Meyer, Phys. Rev. B 80 (2009) 212203.
[202] Y. Sato, Meas. Sci. Technol. 16 (2005) 363.

[203] M. Kehr, W. Hoyer, I. Egry, Int. J. Thermophys. 28 (2007) 1017.
[204] J. Brillo, I. Egry, J. Westphal, Int. J. Mater. Res. 99 (2008) 162–167.
[205] M. Schick, J. Brillo, I. Egry, B. Hallstedt, J Mater Sci 47 (2012) 8145–8152.
[206] Y. Plevachuk, I. Egry, J. Brillo, D. Holland-Moritz, I. Kaban, Int. J. Mater. Res. 98 (2007) 107–111.
[207] I. Egry, J. Brillo, D. Holland-Moritz, Y. Plevachuk, Mater. Sci. Eng. A 495 (2008) 14–18.
[208] M. Kehr, M. Schick, W. Hoyer, I. Egry, High Temp. High Press. 37 (2008) 361–369.
[209] J. Schmitz, B. Hallstedt, J. Brillo, I. Egry, M. Schick, J. Mater. Sci. 47 (2012) 3706–3712.
[210] J. Goicoechea, C. Garcia-Cordovilla, E. Louis, A. Pamies, J. Mater. Sci. 27 (1992) 5247–5252.
[211] Z. Persion, A. Prigunova, V. Kisunko, A. Romanova, V. Efimenko, V. Mazur, Metallofizika 5 (1983) 107(in Russian).
[212] J. Brillo, Y. Plevachuk, I. Egry, J. Mater. Sci. 45 (2010) 5150–5157.
[213] J. Brillo, R. Brooks, I. Egry, P. Quested, High Temp. High Press. 37 (2008) 371–381.
[214] J. Brillo, I. Egry, I. Ho, Int. J. Thermophys. 27 (2006) 494–506.
[215] R. Novakovic, E. Ricci, D. Giuranno, A. Passerone, Surf. Sci. 576 (2005) 175–187.
[216] B. Gallois, C. Lupis, Met. Trans. B 12 (1981) 679–689.
[217] L. Kozlov, L. Romanov, N. Petrov, Izv. Vuz. Chernaya Met. 3 (1987) 7.
[218] M. Adachi, M. Schick, J. Brillo, I. Egry, M. Watanabe, J. Mater. Sci. 45 (2010) 2002–2008.
[219] A. Shlykov, V. Chursin, Izv. Vuz. Tsvetnaya Met. 4 (1976) 141(in Russian).
[220] J. Brillo, I. Egry, Z. Metallkd. 95 (2004) 691–697.
[221] J. Brillo, I. Egry, J. Mater. Sci. 40 (2005) 2213–2216.
[222] J. Brillo, T. Matsushita, I. Egry, Int. J. Mater. Res. 97 (2006) 1526–1531.
[223] R. Eichel, I. Egry, Z. Metallkde. 90 (1999) 371–375.
[224] M. Schick, J. Brillo, I. Egry, Int. J. Cast. Metals Res. 22 (2009) 82–85.
[225] E.S. Levin, P.B. Gel'd, G.D. Ayushina, Russ. Phys. J. 15 (1972) 1505–1507translated from Izvestiya Vysshikh Uchebnykh Zavedenii, Fizika, No. 10, 135-18, 1972.
[226] D.M. Heyes, N.H. March, Int. J. Thermophys. 20 (1999) 267.
[227] E. Turkdogan, Physical Chemistry of High Temperature Technology, Academic Press, New York, 1980.
[228] I. Egry, Script. Met. Mat. 28 (1993) 1273–1276.
[229] P. Klemens, R. Williams, Int. Mater. Rev. 31 (1986) 197–215.
[230] E. Goldratt, A. Greenfield, J. Phys. F Metal Phys. 10 (1980) L95.
[231] E. Yamasue, M. Susa, H. Fukuyama, K. Nagata, Int. J. Thermophys. 24 (2003) 713.
[232] N. Wakeham, et al., Nat. Commun. 2 (2011) 396.
[233] A. Einstein, Ann. Phys. 17 (1905) 549–560.
[234] M. Cappelezzo, C.A. Capellari, S.H. Pezzin, L.A. Coelho, J. Chem. Phys. 126 (2007) 224516.
[235] J. Hodgdon, F. Stillinger, Phys. Rev. E 48 (1993) 207.
[236] S.-H. Chen, F. Mallamace, Ch.-Y. Mou, M. Broccio, C. Corsaro, A. Faraone, L. Liu, Proc. Natl. Acad. Sci. U. S. A. 103 (2006) 12974–12978.
[237] J. Brillo, A.I. Pommrich, A. Meyer, Phys. Rev. Lett. 107 (2011) 165902.
[238] M. Kehr, 2009. PhD thesis TU Chemnitz. http://archiv.tu-chemnitz.de/pub/2009/0175.

CHAPTER 2.2

The Structure and Properties of Silicate Slags

Kenneth C. Mills[a], Miyuki Hayashi[b], Lijun Wang[c] and Takashi Watanabe[d]

[a]Department of Materials, Imperial College, London, United Kingdom
[b]Department of Metallurgy and Ceramics Science, Tokyo Institute of Technology, Tokyo, Japan
[c]Department of Physical Chemistry, University Science and Technology Beijing, Beijing, China
[d]Department of Chemistry and Materials Science, Tokyo Institute of Technology, Tokyo, Japan

SYMBOLS, UNITS, AND ABBREVIATIONS

$\boldsymbol{A}$ surface area (m^2)
$\boldsymbol{a}$ thermal diffusivity ($m^2\ s^{-1}$)
$\boldsymbol{C}$ concentration ($kg\ m^{-3}$ or $kg\ mol^{-1}$)
$\boldsymbol{C_p}$ heat capacity ($J\ K^{-1}\ kg^{-1}$)
$\boldsymbol{c}$ speed of sound ($m\ s^{-1}$)
$\boldsymbol{D}$ diffusion coefficient ($m^2\ s^{-1}$)
$\boldsymbol{d}$ thickness of slag (m)
$\boldsymbol{f}$ fraction
$\boldsymbol{f}^*$ coefficient of chemical activity
$\boldsymbol{H}$ enthalpy ($J\ kg^{-1}$ or $J\ mol^{-1}$)
$\boldsymbol{k}$ thermal conductivity ($W\ m^{-1}\ K^{-1}$)
$\boldsymbol{N}$ number of available cations
$\boldsymbol{N_{coord}}$ coordination number
$\boldsymbol{n}$ refractive index
$\boldsymbol{q}$ heat flux ($J\ s^{-1}\ K^{-1} = W\ K^{-1}$)
$\boldsymbol{R}$ electrical resistivity ($\Omega\ cm = S^{-1}cm$)
$\boldsymbol{R}^*$ gas constant = $8.31\ J\ K^{-1}\ mol^{-1}$.
$\boldsymbol{S}$ entropy ($J\ K^{-1}\ kg^{-1}$)
$\boldsymbol{r}$ cation radius (m)
$\boldsymbol{T}$ temperature (K)
$\boldsymbol{T_{br}}$ break (solidification) temperature (K)
$\boldsymbol{T_g}$ glass transition temperature (K)
$\boldsymbol{T_{liq}}$ liquidus temperature (K)
$\boldsymbol{V}$ molar volume ($m^3\ mol^{-1}$)
$\boldsymbol{\alpha}$ linear thermal expansion coeff. (K^{-1})
$\boldsymbol{\alpha}^*$ absorption coefficient
$\boldsymbol{\alpha_m}$ mean electronic polarizability
$\boldsymbol{\beta}$ volume thermal expansion coefficient (K^{-1})
$\boldsymbol{\beta_s}$ adiabatic compressibility ($m\ s^2\ kg^{-1}$)
$\boldsymbol{\varepsilon}$ emissivity
$\boldsymbol{\gamma}$ surface tension ($mN\ m^{-1}$)
$\boldsymbol{\gamma_{msl}}$ interfacial tension ($mN\ m^{-1}$)

Treatise on Process Metallurgy, Volume 1
http://dx.doi.org/10.1016/B978-0-08-096986-2.00008-4
© 2014 Elsevier Ltd.
All rights reserved.

$\boldsymbol{\eta}$ viscosity (dPas)
$\boldsymbol{\kappa}$ electrical conductivity (Ω^{-1} cm^{-1})
$\boldsymbol{\lambda}$ wavelength (m)
$\boldsymbol{\rho}$ density (kg m^{-3})
BO bonding oxygen
DSC differential scanning calorimetry
DTA differential thermal analysis
LP laser pulse method
NBO nonbridging oxygen
RDF radial distribution function
scl supercooled liquid
THW transient hot wire method

SUBSCRIPTS

l liquid
m metal
nb network breaker
nf network former
s solid
sl slag

SUPERSCRIPTS

m value at T^{liq}, e.g., k^m.
n number of bridging oxygens, e.g., Q^n
(5) coordination number, e.g., $^{(5)}Si$ = fivefold coordination

In chemical formulae: A = Al_2O_3; B = BaO; C = CaO; F = FeO; Fl = CaF_2; K = K_2O; M = MgO; Mn = MnO; N = Na_2O; P = PbO; S = SiO_2; Sr = SrO; Z = ZnO.

2.2.1. INTRODUCTION

The properties of molten silicates have impact on both the natural world (in the form of volcanic magmas) and the industrial world (as glasses and slags). Their industrial importance is well illustrated by the old adage passed on from one generation to the next in the steel industry "Look after the slag and the metal will look after itself." The physical properties of molten silicates have a significant impact on a wide range of processes and must be optimized to obtain good process control and improved product quality. Mathematical modeling has improved to the stage where models can be used to improve process control and minimize product defects. Reliable property information is required (as input data) for these models. We will show below that these properties are largely dependent upon the structure of the slag and thus it is essential to have a good grasp of the factors affecting the structure of silicates.

It should be noted that, in general, the thermodynamic temperature (K) has been adopted here since it is used directly in thermodynamic properties and in Arrhenius relations used to describe the temperature dependence of viscosity, electrical resistivity, and diffusion coefficient. However, we realize that the Centigrade scale is widely used within industry and consequently, where data have been reported in °C we have indicated this as $T_{°C}$ to differentiate it from the thermodynamic temperature (T or T_K).

Composition is represented here in the form of both weight % and mole fractions; thus a composition value of 0.40 will probably indicate a mole fraction and 18% indicates a value in weight %.

2.2.2. STRUCTURE OF SLAGS AND GLASSES

The first thing that should be said about silicate melts is that they are ionic in nature. Reactions, such as that shown in Equation (2.2.1), are *ionic* (i.e., they involve the transfer of electrons) and are best described in the form of Equation (2.2.2) where the underline indicates that it is in the metal phase

$$4\underline{Al}_{steel} + 3SiO_{2slag} = 3\underline{Si}_{steel} + 2Al_2O_{3slag} \quad (2.2.1)$$

$$4\underline{Al} + 3Si^{4+} = 3\underline{Si} + 4Al^{3+} \quad (2.2.2)$$

2.2.2.1. Structure of Silicates

The building block for silicates is the Si-4O tetrahedron. This consists of a centrally placed Si^{4+} ion surrounded by $4O^-$ ions in a tetrahedral array (Figure 2.2.1). These tetrahedra can join to other tetrahedra through the divalent O^{2-} ions sited at the corners of the tetrahedron. Thus, the Si-4O tetrahedron is the fundamental building block for all silicates and for aluminosilicates. In pure SiO_2 each O^{2-} connects two Si^{4+} tetrahedra and this results in a three-dimensional polymerized network structure (Figure 2.2.1b) [1,2]. Thus, SiO_2 is referred to as a *network former*.

When cations, such as Na^+ or Ca^{2+}, are added (in the form of Na_2O or CaO) to SiO_2 they break some of the Si^{4+}—O^- bonds and replace them with ionic Na^+—O^- (or Ca^{2+}

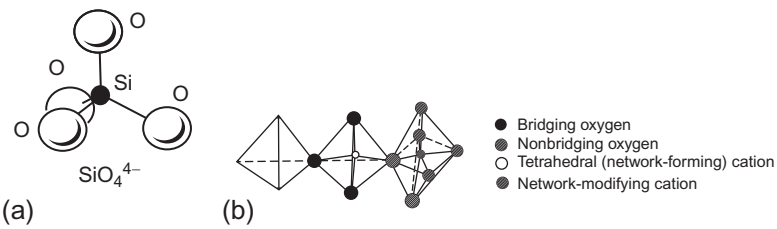


Figure 2.2.1 Schematic diagrams showing (a) Si^{4+}—O^- bonds arranged in form of a tetrahedron and (b) the creation of a network through the connection of each O^{2-} to two Si^{4+} ions.

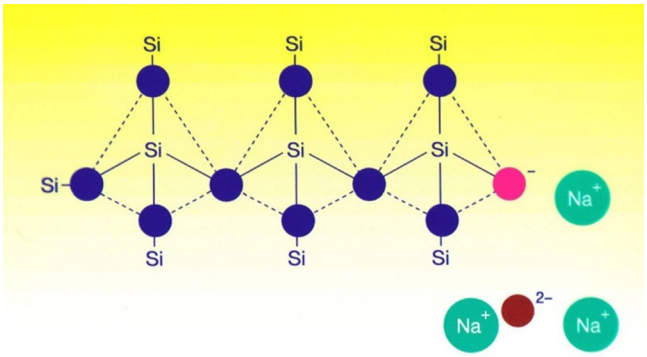


Figure 2.2.2 Schematic drawings and silicate chain with bridging O (O^0) shown in black, nonbridging O (O^-) shown as red and free O^{2-} shown as purple and cations in green.

bonded to two O^- bonds). Further addition of Na^+ ions results in progressively more depolymerization of the melt; the Na^+ cations are referred to as "*network breakers*." The bonds within the tetrahedron and those involved in joining one tetrahedron to another are both covalent. In contrast, a cation (e.g., Na^+)-oxygen bond is ionic. Thus, silicate slags contain both covalent and ionic bonds (Figure 2.2.2) and the thermophysical properties are very dependent upon the level of polymerization in the slag. The different types of bonds are frequently classified in terms of the O bonds formed, namely:

(i) *Bridging O's* (e.g., Si—O) denoted both as BO and O^0.
(ii) *Nonbridging O's* (denoted NBO or O^- e.g., Si—O—Na bond).
(iii) *Free-O's* (i.e., bonded to cations and not to Si) denoted as O^{2-}.

The first structural studies were carried out using X-ray diffraction and provided measurements of the *short-range order* in the sample. However, much of our knowledge of the structure of silicates comes from the work of the geological fraternity. They introduced new techniques to study silicate structures, for instance, Raman and nuclear magnetic resonance (NMR) spectroscopy and these have provided us with considerable insight into the structure of silicates.

Valuable information was obtained by comparing the spectra of crystalline and glassy (or amorphous) samples of similar composition. When liquid slags are cooled they can form either crystalline or supercooled liquids (*scl*). Further rapid cooling of the *scl* produces a frozen glass at the fictive temperature (T_{fic}) which is dependent upon cooling rate (dT/dt), i.e., $T_{fic} \uparrow$ as $(dT/dt) \uparrow$. Thus, faster quenching rates will result in a higher T_{fic}.

Glassy samples are prepared by rapid quenching from the liquid state and it is assumed that these glassy samples (used in room-temperature spectroscopic studies) pertain to the liquid with the ions being frozen into position at the fictive temperature (T_{fic}). It follows

that the structure may be dependent upon the cooling rate of the quench. Consequently, it is customary to characterize the silicate sample (or structure) in terms of the fictive temperature. The fictive temperature (T_{fic}) is the temperature of the melt corresponding to its glass structure. Much of our knowledge has resulted from the assumption that the structure for the "frozen state" is typical of that for the liquid and supercooled states; however, recent work has shown that the bonding characteristics (e.g., coordination) of cations in the frozen state are somewhat different from those for the liquid and supercooled phases [3,4].

The structure of crystalline and glassy silicates is often defined in terms of their *short-range-*, *intermediate-range-*, and *long-range-order*. The *short-range order* in silicates is determined by the Si-4O tetrahedron, so when looking for differences between crystals and glasses it is necessary to examine the *intermediate-range order* (which occurs in the range 0.2–0.3 nm) and the *long-range order*. The arrangement of atoms inside the crystal is determined by the size of the atom and columbic force between ions. Crystalline phases exhibit a periodic and symmetric arrangement of atoms and all atoms within the unit cell are equivalent; thus crystals exhibit periodicity. In contrast, the atoms in molten and glassy silicates do not exhibit periodicity. Thus, the unit cell is infinitely large and no two atoms are equivalent and there is no *long-range order*. This disorder results in a higher entropy and higher stored energy in glasses cf. crystalline phases. Thus, the crystalline phase has a lower free energy than that of the glassy phase; this is due to the higher *configurational entropy* of the glass.

We will see below that the silicate melts contain a variety of structural (silicate) units with different degrees of polymerization (Q^n). Calculations indicate that the ideal mixing of these various Q^n units can account for about half of the energy difference between glass and crystal [5,6].

2.2.2.2. Structure of Aluminosilicates

Many industrial slags contain alumina (Al_2O_3). When Al_2O_3 is introduced into the silicate network the Al^{3+} ions can be absorbed into the silicate structure (i.e., Al^{3+} behaves like Si^{4+} and exhibits fourfold coordination like Si^{4+}). However, there is a charge difference between Al^{3+} and Si^{4+} and consequently, a Na^+ ion must be sited near the Al^{3+} to provide electrical charge balance (i.e., to form ($NaAl^{4+}$)) [1,2,7] (Figure 2.2.3). If M^{2+} (e.g., Ca^{2+}) ions do the charge balancing, the M^{2+} ions must be sited between two Al^{3+} ions. It is considered that a Na^+ ion acting on charge-balancing duty cannot act as a network breaker. Thus, Al_2O_3 additions act principally as *network formers* but when large amounts of Al_2O_3 are added to the slag, the Al^{3+} ions can also act as *network breakers* (i.e., exhibit five- or sixfold coordination) [6] and for this reason Al_2O_3 is often referred to as an "amphoteric."

Aluminosilicates are classified with regard to the cations available to charge balance the Al^{3+} ions present; for compositions of $xCaO \cdot yAl_2O_3 \cdot (1-x-y)\ SiO_2$, where x

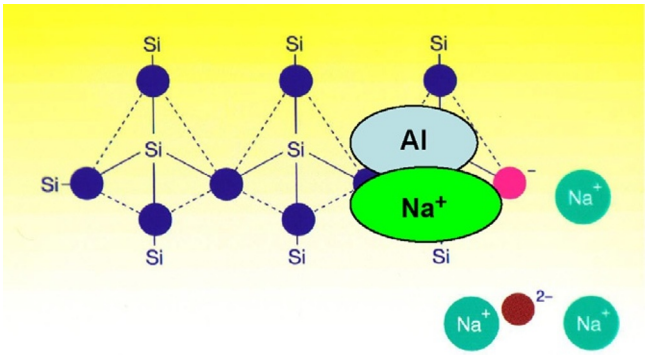


Figure 2.2.3 Schematic drawing showing Al^{3+} incorporated into silicate (Si^{4+}) chain which requires cation (shown here as Na^{+}) to maintain charge balance.

and y denote the mole fractions, the melts are denoted as following (where Q is a measure of the degree of polymerization, see Section 2.2.2.6.2):

Per-alkaline: $x > y$: the melt contains an excess of cations after charge balancing Al^{3+}.
Meta-aluminous: $x = y$; the melt contains just enough cations to charge balance Al^{3+}.
Per-aluminous: $x < y$: the melt has a deficiency of cations for charge balancing and thus has an excess of Al^{3+} ions.

2.2.2.3. The Effect of Fe_2O_3 and Cr_2O_3 on Silicate Structure

It might also be anticipated that Fe_2O_3 and Cr_2O_3 would act like Al_2O_3 in slags and result in absorption of Fe^{3+} and Cr^{3+} into the silicate network. This is largely true in the case of Cr_2O_3 (except when the slag contains a significant Al_2O_3 content) but Fe_2O_3 appears to act as both *network breaker* and *network former* [8]. It is possible to use viscosity data to calculate the fraction of M_2O_3 acting as a network breaker (f_{nb}) and values of f_{nb} for Fe_2O_3 of ca. 0.6 were obtained and for Cr_2O_3 f_{nb} is close to zero except when the slag contains Al_2O_3 also [9].

2.2.2.4. Effect of TiO_2 and ZrO_2 on Silicate Structure

TiO_2 additions would be expected to behave like SiO_2 with Ti^{4+} ions fitting into the Si^{4+} network and thereby further polymerizing the melt. However, TiO_2 has been shown to decrease the viscosities of slags [10–14] which suggests that TiO_2 may act as a weak network breaker.

Structural studies on silicates with low concentrations of ZrO_2 (0.2%) indicated that the Zr^{4+} ions were found to be in sixfold coordination ($^{(6)}Zr$, i.e., acted as a network breaker) but some eightfold coordination ($^{(8)}Zr$) was observed in more polymerized silicates [15].

2.2.2.5. Effect of CaF_2 and B_2O_3 on Silicate Structure

Calcium fluoride and boron oxide have been used extensively to flux slags. However, there are safety concerns concerning HF emissions from slags containing CaF_2 and there has been a recent movement to eliminate, or reduce, the CaF_2 levels used in industrial slags.

Recent work [16–25] has indicated that when a fluoride (e.g., CaF_2) is added to a silicate melt:

(i) there is some competition between cations to bond with fluorine, however, in general, the F ions prefer to bond with those cations with the highest field strength (z/r^2), e.g., $La^{3+} > Mg^{2+} > Ca^{2+} > Ba^{2+} > Na^{+}$.

(ii) Al^{3+} competes with the above cations to form some Al—F bonds but few Si—F bonds (ca. 2%) are formed [25].

If the F is added as additions of CaF_2 to say, a CaO-BaO-SiO_2 slag, the F^{-} ions bond preferentially with Ca^{2+} ions and thus the CaF_2 formed will act primarily as a diluent to the remaining CaO-BaO-SiO_2 slag. However, if CaF_2 just replaces CaO, with the Ca and Si contents remaining constant, then the added F^{-} ions will bond preferentially with Ca^{2+} ions thereby reducing the number of network-breaking cations and thus increasing the polymerization of the melt.

B_2O_3 is also used to flux slags but tends to be used mostly in small concentrations (e.g., <5% in mold fluxes) because of the danger of boron pick-up by the steel. For low concentrations of B_2O_3, the 4 O^{-} ions are arranged around the B^{3+} ion in the form of a tetrahedron (denoted as BO_4). However, at higher concentrations of B_2O_3, threefold bonding of O^{-} ions around three B^{3+} ion occurs (BO_3) which gives rise to a wide variety of structures made up of BO_3 and BO_4 units [26–30].

In summary, the various constituents of slags can be classified as follows:

Network formers: SiO_2, Al_2O_3, and P_2O_5;

Network breakers: CaO, MgO, BaO; FeO, MnO, CrO, Na_2O, Li_2O, and K_2O;

Fluxes: CaF_2 and B_2O_3.

2.2.2.6. Parameters to Represent the Structure of Slags

A variety of different parameters have been used to represent the structures of silicate slags and these are discussed below.

2.2.2.6.1 Basicity

Various basicity indices (e.g., B = % CaO/% SiO_2) have been used to represent slag structure in the calculation of viscosities [31]. Thus, high SiO_2 melts are sometimes referred to as *acidic* and melts with high CaO concentrations are denoted as *basic*. The behavior of acidic and basic melts can be summarized as *acids accept* electrons and *bases donate* electrons (and create, e.g., Ca^{2+}). Thus, network formers are acidic and bases are network breakers. The major problem lies in dealing with oxides which can act as

both *networker formers* and *network breakers* (e.g., Fe_2O_3 and Al_2O_3) which are usually referred to as *amphoteric* oxides. In its simplest form, basicity is taken as (wt% CaO/% SiO_2) which is sometimes referred to as the V-ratio. A variety of other basicity relations have been used and some of these are shown in Equations (2.2.3) and (2.2.4) where X is the mole fraction. The reader is directed to the Slag Atlas, Chapter 2 [7] for a more complete listing of various basicity indices.

$$\text{Basicity} = (X_{CaO} + X_{CaO})/X_{SiO_2} \tag{2.2.3}$$

$$\text{Basicity} = (X_{CaO} + X_{CaO})/(X_{SiO_2} + X_{Al_2O_3}) \tag{2.2.4}$$

2.2.2.6.2 NBO/T and Q

The (nonbridging O/tetragonal O) ratio, which is denoted (NBO/T) is a *measure of the depolymerization* of the melt [1,2] and where T denotes the ions (Si^{4+}, Ti^{4+}, or Al^{3+}) in tetragonal configurations. It is the ratio of the mole fraction of *available* network breaking oxides (where *available* indicates the total number of cations minus those on charge-balancing duties) divided by the mole fraction of the network-forming oxides. Thus, (NBO/T) ratio is a kind of basicity index (Equation 2.2.5) which allows for corrections for cations acting on charge-balancing duties

$$\text{NBO/T} = 2\left(\sum X_{MO} + \sum X_{M_2O} - X_{Al_2O_3}\right)/(X_{SiO_2} + 2X_{Al_2O_3}) \tag{2.2.5}$$

where X is the mole fraction and $X_{MO} = X_{MgO} + X_{CaO} + X_{BaO} + X_{FeO} + X_{MnO} + \cdots$ and $X_{M_2O} = X_{Li_2O} + X_{Na_2O} + X_{K_2O}$.

There has been a long-standing problem on how to deal with the CaF_2 when calculating (NBO/T) for mold fluxes. The Slag Atlas [7] suggests CaF_2 acts as (i) a *network breaker* in polymerized slags and (ii) a *diluent* in basic slags. Recent structural studies (see above) indicate that when fluorine is added the F^- ions bond to Ca^{2+} ions and thereupon remain apart from the slag. This would suggest that mold fluxes be regarded as (slag + CaF_2). Thus, the CaF_2 concentration is ignored here when calculating the NBO/T ratio for the slag component given by Equation (2.2.5), where X is the mole fraction.

Since it is not known whether TiO_2 should be regarded as a *network breaker* or *network former*, it is suggested that TiO_2 and ZrO_2 concentrations should be ignored when calculating the (NBO/T) for the slag component and any effect on properties determined as a function of X_{TiO_2}.

Some people find it easier to visualize polymerization than depolymerization, and thus prefer the parameter, Q; this is a *measure of the polymerization* of the melt and which can be calculated from (NBO/T) using Equation (2.2.6):

$$Q = 4 - (\text{NBO/T}) \tag{2.2.6}$$

The Q value can be considered to the average of the Q^n structural units (see Section 2.2.2.6.4).

The main disadvantages in the use of Q and (NBO/T) lie in:

(i) the inability of these parameters to differentiate between different cations and

(ii) how to deal with constituents like CaF_2.

2.2.2.6.3 Optical Basicity (Λ)

The *optical basicity* was introduced to partially resolve this problem of differentiating between different cations on the structure and then, in turn, on property estimations [7]. The *optical basicity* (Λ) is a measure of the *electron donor power* of different ions relative to that of CaO [32–34]. Measurements were derived from the shift in the frequency absorption band of the UV region (associated with the $6s \rightarrow 6p$ transition) which is related to the basicity of the slag. It was shown that the optical basicity could be calculated from Pauling electron negativity values [33].

It was also used as a measure of the depolymerization of the melt and can be calculated by Equation (2.2.7) where m is the number of O atoms, e.g., 1 for CaO and 2 for SiO_2 and Λ_1 is the optical basicity value for oxide 1. Reported values of Λ for individual oxides are given in Table 2.2.1:

$$\Lambda = \sum (X_1 m_1 \Lambda_1 + X_2 m_2 \Lambda_2 + X_3 m_3 \Lambda_3 + \cdots) / \sum (X_1 m_1 + X_2 m_2 + X_3 m_3 + \cdots) \tag{2.2.7}$$

The composition can be corrected to allow for the cations on charge-balancing duties [35] by subtracting $2X_{Al_2O_3}$ from $\Sigma(X_1 m_1 \Lambda_1) + \Sigma(X_2 m_2 \Lambda_2)$, where 1 and 2 refer to MO and M_2O, respectively; this can be done by assuming that charge-balancing duties are done by the cations with the highest field strength (z/r^2) [36].

Optical basicities for the various constituents of slags are given in Table 2.2.1. The relation between optical basicities for various Group I and Group II oxides and the parameter (z/r^2) (which is used as a measure of bond strength) is shown in Figure 2.2.4.

The principal disadvantages to the use of optical basicities result from:

Table 2.2.1 Values of optical basicity cited in Slag Atlas, Chapter 2 [7]

	CaO	SiO_2	Al_2O_3	MgO	BaO	Na_2O	Li_2O	K_2O	FeO	MnO	CaF_2	B_2O_3	TiO_2
UV shift	1.0	0.48	0.605	0.78	1.15	1.15	1.0					0.42	
Pauling e.n.	1.0		0.60	0.78	1.15	1.15	1.0	1.4	0.51	0.59	0.43, 0.67	0.42	0.61
Electron densities	1.0	0.47	0.66	0.92	1.08	1.11	1.06	1.16	0.94	0.95		0.42	0.65

Values derived from (a) Pauling electron negativities, (b) measurements of UV shift, and (c) electron densities.

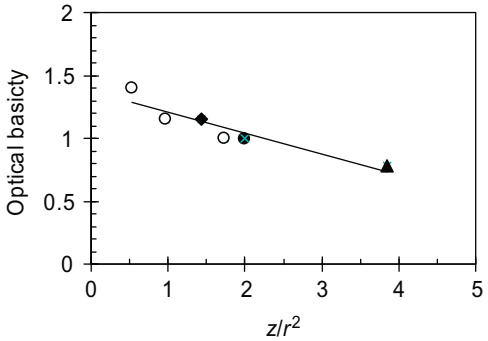


Figure 2.2.4 The optical basicity as a function of the parameter (z/r^2) for Group I and II oxides; ○ = M_2O oxides; ♦ = BaO; ▲ = MgO; ● = CaO.

(i) Uncertainties in the Λ values for some components (e.g., transition metal oxides, e.g., FeO, CrO, and others like CaF_2).

(ii) The optical basicity is a reasonable measure of the M—O bond strength [37] but does not differentiate between the size of cations which affects the coordination number and is also important in electrical resistivity and diffusion.

(iii) The trend in predicted viscosities for different cations is the reverse of that found experimentally; viscosity increases with decreasing Λ so the predicted trend would be expected to be $\eta_{Li_2O} > \eta_{Na_2O} > \eta_{K_2O}$ whereas the experimental viscosities lie in the hierarchy $\eta_{K_2O} > \eta_{Na_2O} > \eta_{Li_2O}$.

The corrected optical basicity has been used to estimate the following properties: viscosity [35,38], density [39], electrical conductivity and resistivity [40], and thermal conductivity of molten slags [37].

2.2.2.6.4 Concentrations of O^0, O^-, and O^{2-}

The structure can be represented in terms of the concentrations in the slag of *bridging O's* (O^0), *nonbridging O's* (O^-), and *free O's* (O^{2-}). The principal limitation to this approach has been that, until lately, it required a mathematical model [41–43] to determine these concentrations. However, recently a method has been developed to calculate these concentrations without the aid of a mathematical model [44–280] and this would appear to be exceedingly useful in predicting properties since it can differentiate between Si—O and Al—O bonds and their effects on specific properties. Recently, the method has been applied to the prediction of viscosities of slags containing CaF_2 [44].

Differences in (i) the nature of the cations present or (ii) the temperature can cause changes in the concentrations of O^0, O^-, and O^{2-}. Furthermore, a reaction can be written for which an equilibrium constant can be derived (Equations 2.2.8 and 2.2.9, respectively):

$$2O^- = O^{2-} + O^0 \tag{2.2.8}$$

$$K = \left(O^{2-}\right)\left(O^0\right)/\left(O^-\right)^2 \tag{2.2.9}$$

2.2.2.6.5 Q^n Values

Within a silicate melt there are a variety of structural units present. The degree of polymerization of these units can vary significantly. Deconvolution of spectroscopic data can provide values for the abundance of the different structural units present in the melt (e.g., in Raman spectroscopy, intensity versus frequency of Raman shift is used, see Figure 2.2.5). These structural units are usually expressed as Q^n, i.e., Q^0, Q^1, Q^2, Q^3, where n is the number of bridging oxygens (BOs); the degree of polymerization increases with increasing n. Thus, a single tetrahedron unit is denoted as Q^0 since it contains no BO, and Q^1 (i.e., a single BO) represents a double tetrahedron, etc.

The Q^n species can interact as shown in Equation (2.2.10) (referred to as "the disproportionation reaction") in which the move to the right-hand side is promoted by increasing cation bond strength (z/r^2) and increasing temperature [6]:

$$2Q^n = Q^{n+1} + Q^{n-1} \tag{2.2.10}$$

where $n = 1$, 2, or 3.

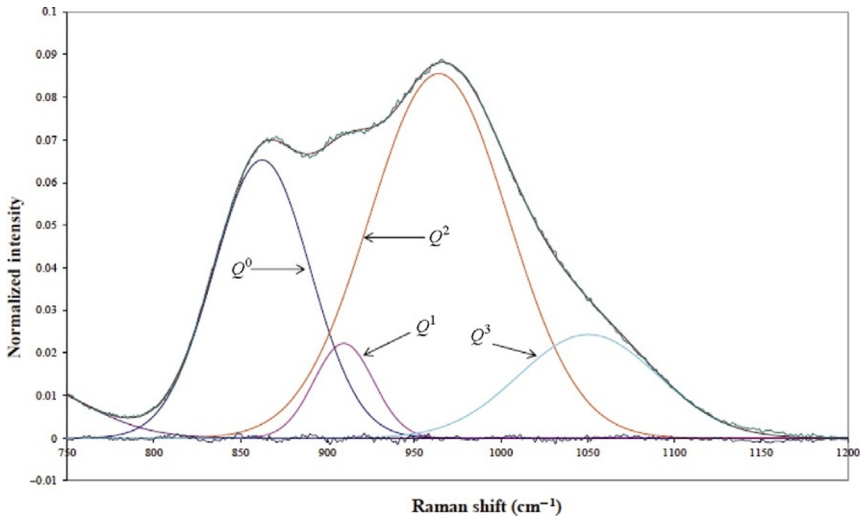


Figure 2.2.5 Intensity as a function of frequency of Raman shift for 54.5% CaO-45.5% SiO_2 showing the Gaussian plots for individual species [30].

2.2.2.6.6 Viscosity

The viscosity represents the resistance to the flow of one layer of molecules over another. The flow will be hindered by both the size and shape of the structural units (of silicates) present (sometimes denoted *steric hindrance*). Properties such as the electrical resistivity (and diffusion coefficient) involve at least two factors, i.e., (i) the *resistance* to movement of the cations through the silicate network when an electric field is applied and (ii) the *mobility* of the cations. The viscosity provides a good measure of the resistance of the silicate network to fluid flow under an applied stress. Consequently, several authors have used the viscosity as a measure of structure in the calculation of electrical resistivity [45,46] and diffusion coefficient [47,48].

2.2.2.7. Effect of Cations on Structure

The silicate network is affected by the nature of the cations present. This can be seen in the hierarchy of cations for properties like viscosity and electrical resistivity for a given SiO_2 content (or Q value). The effect of the cations, on say, the viscosity, could be due to the effect of the cation:

(i) on the *silicate structure* or

(ii) on the *mobility* of the cation and thus on the viscosity (e.g., as shown in Figure 2.2.21).

It has been reported that small highly charged cations tend to favor the disproportionation reaction shown earlier [6] in Equation (2.2.10) (Table 2.2.2).

2.2.2.8. Structural Characteristics

The structure and properties of glassy and crystalline silicates are affected by the *short-range-*, *medium (or intermediate) range-*, and the *long-range order* occurring in the sample. The *short-range order* is principally determined by the Si-O tetrahedron. Thus, there are few differences between the short wave order in crystalline and quenched glasses. However, there are considerable differences in the medium-range-order of crystalline and glassy phases. In crystals there is a periodic and symmetric arrangement of atoms and all atoms within the unit cell are equivalent. In contrast, frozen glasses and molten silicates form different arrangements

Table 2.2.2 Values of the cation radius (r), the relative values of the field strength (z/r^2), and relative cation size $(r_M/r_{Ca})^3$ [49]

	Li_2O	Na_2O	K_2O	MgO	CaO	SrO	BaO	FeO	MnO
$10^{10}r$ (m)	0.76	1.02	1.38	0.72	1.0	1.18	1.35	0.74[a]	0.80[a]
z/r^2	1.73	0.96	0.53	3.85	2.0	1.43	1.1	3.65	3.13
$(r_M/r_{Ca})^3$	0.44	1.06	2.63	0.373	1.0	1.64	2.46	0.405	0.512

[a]From Ref. [34].

of these tetrahedral units (e.g., rings, chains, sheets, etc.) and there is considerable disorder and no periodicity. The specific arrangement adopted by the silicate is determined by the *medium-range* order and this covers the nanometer range. Thus, the differences between crystalline and molten or glassy silicates lie in the differences in the *medium-range* order. The differences in medium-range order result from differences in characteristics such as bond angles, bond strengths, and coordination numbers.

2.2.2.8.1 Nature of Structural Units

The silicate units can join together in different ways (e.g., as rings, chains, sheets, etc.). The resulting structures are shown in Figure 2.2.6 and the nature of these structures will have a significant effect on the property values. Table 2.2.3 summarizes the different forms available for silicate slags and correlates them with the degree of polymerization (i.e., Q). These data are plotted along with the viscosity as a function of Q in Figure 2.2.7; it can be seen that the steep increase in viscosity at $Q > 3$ coincides with the appearance of a three-dimensional structure.

Nonbridging oxygens (NBOs) have been detected in some highly polymeric [52] aluminosilicate melts even in those melts containing insufficient concentrations of cations to charge balance the Al^{3+} ions in tetrahedral coordination (i.e., $Q > 4$).

2.2.2.8.2 Coordination Number of Cations (N_{coord})

The mean coordination of cations (including Si^{4+}, Al^{3+}, Ti^{4+} as well as Ca^{2+}, Na^{+}, etc.) tends to be higher in the crystalline phase than in the molten, glassy phase [4,3]. In general, the coordination is fourfold for cations involved (denoted $^{(4)}Si$) in network forming and sixfold coordination (in octahedral array and denoted $^{(6)}Ca$) for those ions acting as network breakers. As pointed out earlier there are some oxides which can act as

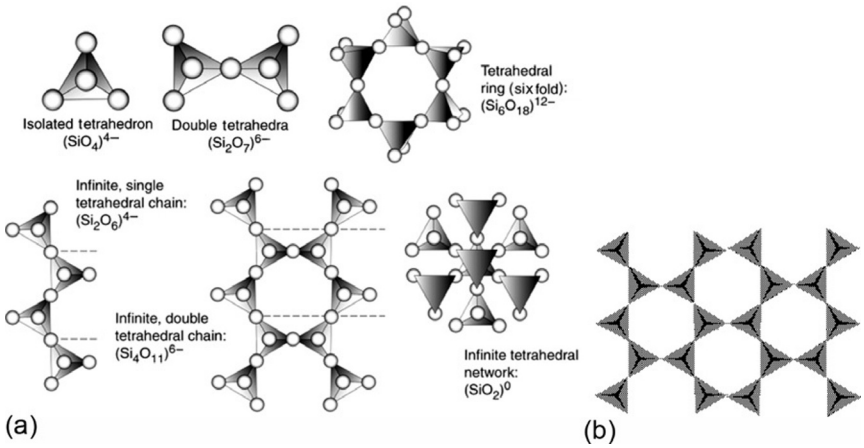


Figure 2.2.6 Schematic diagrams showing (a) various structures formed by silicate tetrahedra [49] and (b) sheet structure [50].

Table 2.2.3 Summary of the different forms of silicate structural units which are available: the typical composition is expressed as a CaO-SiO_2 composition with the silicate unit in parenthesis

Type	Typical composition	NBO/T	*Q*	Examples of industrial slags
Tetrahedra	Ca_2SiO_4 $(SiO_4)^{4-}$	4	0	Fayalite slags (Cu-making) basic-O-steelmaking slag
Double-tetrahedra	$Ca_3Si_2O_7$ $(Si_2O_7)^{6-}$	3	1	
Ring	$(Si_nO_{3n})^{2n-}$ $Ca_3Si_3O_9$ $Ca_4Si_4O_{12}$	2	2	Blast furnace slag
Chain	$(Si_nO_{3n})^{2n-}$ $Ca_3Si_3O_9$	2	2	Blast furnace slag
Double-chain	$(Si_{4n}O_{11n})^{6n-}$ $Ca_3Si_4O_{11}$	1.5	2.5	CC-mold fluxes-slabs
Sheet	$(Si_{2n}O_{5n})^{2n-}$ $CaSi_2O_5$	1	3	CC-mold fluxes-billets
Three-dimensional	SiO_2	0	4	$Q > 3$, some magmas

Note: *Q* for mold fluxes calculated from remaining slag composition, i.e., ignoring X_{CaF_2}.

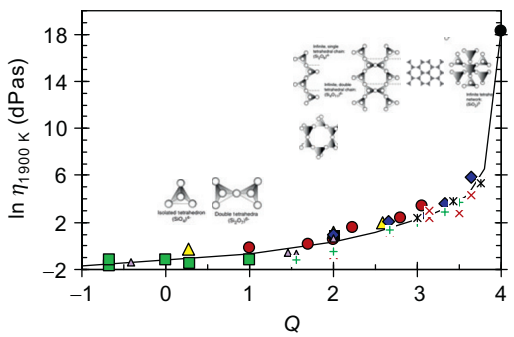


Figure 2.2.7 Viscosity (ln η_{1900K}) for binary MO- and M_2O-silicates as a function of the parameter *Q* showing the structures (shown in Figure 2.2.6) formed at approximate positions of *Q* where the different silicate structures are formed; it should be noted that negative *Q* values have no structural meaning.

both network formers and as network breakers; these are known as *intermediary* (or as *amphoteric* when classifying in terms of acids and bases).

In general, the coordination number (N_{coord}) for cations tends to increase with increasing cation size or decreasing field strength (z/r^2) and an increased N_{coord} will lead

to a lower proportion of NBOs and a higher proportion of BOs [53]; this would lead to higher values of the viscosity and electrical resistivity and a higher diffusion coefficient.

This could account for the apparent increase in viscosity observed with increasing cation size which can be seen in an examination of Figures 2.2.7 (and 2.2.15).

Although the coordination numbers for network formers and network breakers are predominantly 4 and 6, respectively, they are not always so. Some examples are given below:

(i) Some Ni^{2+}, Fe^{2+}, and Zn^{2+} ions can be incorporated into tetrahedral units connected into a polymeric network [3].

(ii) $^{(5)}Si$ and $^{(5)}Ti$ ions (fivefold coordination in silicates and silico-titanates) can coexist, respectively, with $^{(4)}Si$ and $^{(4)}Ti$ ions (in fourfold coordination) [3]; other elements reported to exhibit fivefold coordination are Mg^{2+} [54], Fe^{2+} [55], Ni^{2+} [56], and Al^{3+} and Si^{4+} [57].

(iii) Zr^{4+} ions can occur in sixfold coordination with local charge balancing [58].

(iv) Ca^{2+} maintains a steady coordination of 5 in $Ca_{0\cdot5x}\cdot Al_xSi_{1-x}O_2$ for x values between 0.25 and 0.667 [59].

The same cation may be located at two or more different sites. Furthermore, the cation distribution may not be homogeneous and there is evidence of ordering of the cations and this can lead to cation-rich regions [3].

2.2.2.8.3 Topology, Bond Angles, Bond Energies

As we have seen earlier the structure can be defined in terms of the short-range- and intermediate-range order. However, structure can also be defined in terms of *topology*, i.e., the way in which structural units (i.e., tetrahedra) are joined together as rings, chains, etc. It is usually defined [4,60] in terms of:

(i) *Connectivity* (C), which is the number of atoms in each structural unit which is shared with other units, e.g., in Figure 2.2.8c each corner atom of the two-dimensional structure is completely shared with a neighbor, so $C=3$ but for a three-dimensional structure C would have a value of 4.

(ii) *Connection mode*, which is the number of atoms which two neighboring structural units share, e.g., in Figure 2.2.8c each pair of adjacent triangles share only one corner atom, so the mode has a value of one.

(iii) *Decoration*, which is the ability to use a basic topological structure (such as that in Figure 2.2.8a) which can be decorated so as to represent different silicate melts (e.g., the two-dimensional hypothetical structure can be decorated to give the different structures shown in Figure 2.2.8c [60]).

Ring structures are formed in silicates within a certain compositional range and have been identified in both crystalline and disordered (glassy) phases. Figure 2.2.9 shows a network containing 5-, 6-, and 7-member rings (polygons) with a mean ring size of 6.

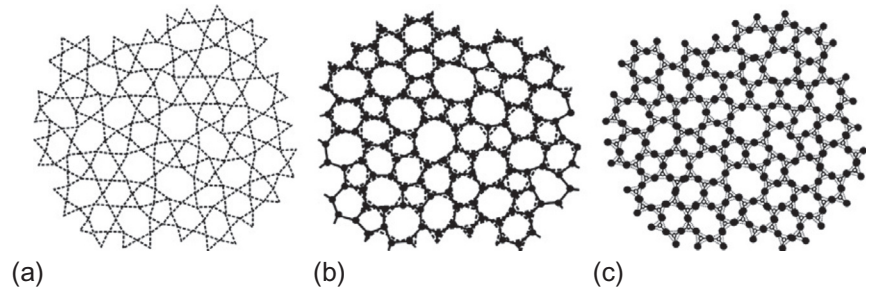


Figure 2.2.8 Schematic diagrams showing two-dimensional structures for (a) hypothetical connected network and (b) and (c) different decorations [4,60].

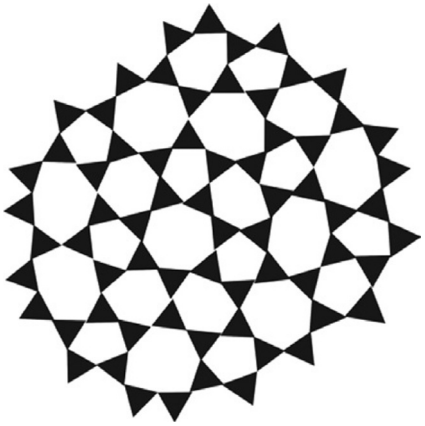


Figure 2.2.9 Schematic drawing showing a two-dimensional network containing different-sized rings [4].

The bond angles shown in Figure 2.2.10 affect the way that structural units are joined (e.g., as rings or chains). There are two bond angles involved: (i) the *tetrahedral angle* (φ in Figure 2.2.10), which is typically 144° but can vary between 120° and 180° (Figure 2.2.11a [61]) and (ii) the *inter-tetrahedral angle* (α in Figure 2.2.10). The variation in bond angle contributes to the configurational entropy and is largely responsible for the absence of long-range order in glassy and liquid silicates.

In aluminosilicates it has been found that the T-O-T inter-tetrahedral angle was affected by (i) the Al content as represented by $f_{as} = X_{Al}/(X_{Al} + X_{Si})$ and (ii) the field strength (z/r^2) of the cation [62]. It was found that the inter-tetrahedral angle went through a maximum at $f_{as} = 0.2$. Furthermore, the distribution of T-O-T inter-tetrahedral angles was affected by the field strength of the cations with the maximum occurring at a lower angle and the peak becoming broader as (z/r^2) decreased (i.e., $Mg^{2+} > Ca^{2+} > Na^{+}$).

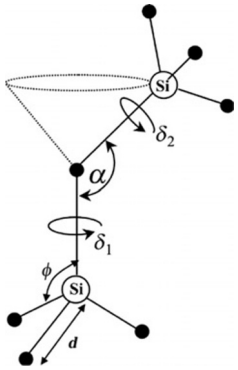


Figure 2.2.10 Schematic diagram showing *tetrahedral* and *inter-tetrahedral* angles; the dotted line indicates the possible trajectory of the upper Si atom [4,60].

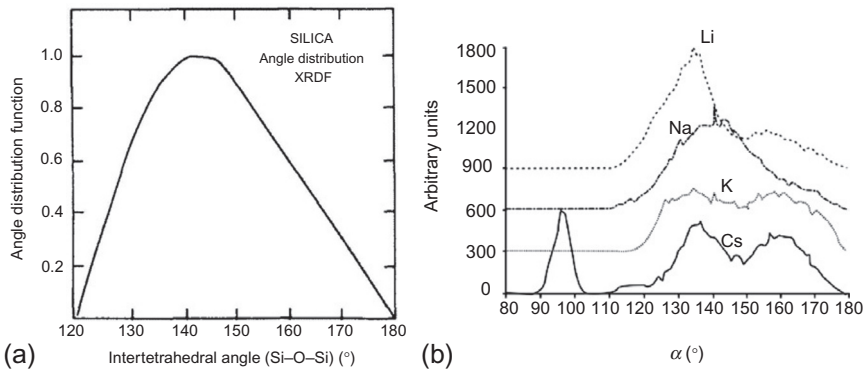


Figure 2.2.11 (a) Schematic diagram showing distribution of Si—O—Si bond angles in SiO_2 reported by Mozzi and Warren from RDF measurements [61]; it should be noted that more recent studies show a slightly different distribution with a narrowing of the peak and a movement to a slightly lower angle [64] and (b) the Si—O—Si bond angle distribution showing the effects of different cations.

The line width of the ^{29}Si NMR spectra can be used as a measure of the disorder in the melt. It was suggested that disorder in a meta-aluminosilicate melt decreases with increasing f_{as} and decreasing (z/r^2) for the charge-balancing cation [63].

The bond strength tends to increase (↑) as:

(i) bond length (d) decreases (↓).

(ii) as the O-coordination number (N) decreases (since $N \downarrow$ as $d \downarrow$)

(iii) as Si—O—Si bond angle (θ) increases (since $N \uparrow$ as $\alpha \downarrow$ or $d \uparrow$ as $\alpha \downarrow$)

The decrease in Si—O—Si bond angle ($\alpha \downarrow$) with increasing coordination ($N_{coord} \uparrow$) arises from the steric hindrance caused by the relatively large Si^{4+} ions. A decrease in Si—O—Si bond angle results in a decrease in the free energy of formation of ring

structures. The Si—O—Si bond angle distribution for M_2O-SiO_2 systems has been reported to be affected by the nature of the cation as can be seen from Figure 2.2.11b [4,65]. Variation in Si—O—Si or Si—O—T (where T = atom in tetragonal configuration, e.g., Ti or Al) leads to higher configurational entropy in the sample.

The bond length for a Si—O bridging O is larger than that of a NBO ($d_{BO} > d_{NBO}$) [66].

2.2.2.8.4 Configurational Entropy

In crystalline solids, the atoms, or ions, are arranged in a regular manner and the level of disorder and thus, the entropy, are both low. In contrast, in both liquids and quenched glasses there is a high level of disorder and thus the entropy is higher than that in the equivalent crystalline phase. This additional entropy is usually referred to as "configurational entropy."

When a quenched glass is heated it undergoes a transition at the glass transition temperature (T_g) from a frozen glass to a *scl*. This transition (glass → *scl*) involves an increase in configurational entropy (ΔS_{config}) which manifests itself as a "*step-like jump*" in $C_p\left(\Delta C_{pT_g}\right)$ since $S = \int C_p/T$. This jump in $C_p\left(\Delta C_{pT_g}\right)$ can vary between 10% and 50% of the C_p value at T_g [67].

In contrast, the crystal does not undergo a transition at T_g so for temperatures between T_g and T_{liq} the crystal exhibits lower C_p and entropy values than the glass. However, it eventually disorders at T_{liq} and the entropy of fusion (ΔS^{fus}) is much higher than that of the glass since S_{config} for the liquid is the same, regardless of the path taken (crystal or glass).

Disorder between BOs and NBOs (or disorder between various Q^n species) makes significant contributions to the configurational entropy and calculations based on ideal mixing of the species indicate that entropy contribution constitutes >50% of the total configurational entropy [3,6]. The remaining contributions to S_{config} come from bond angles, bond lengths, and from the promotion of the reaction shown in Equation (2.2.10) by (i) cations with a high (z/r^2) value and (ii) increasing temperature. Disorder in the cation array will also contribute to the entropy. In aluminosilicates disorder will be increased by the fact that several possible combinations can be formed, namely, Si—O—Al, Si—O—Si, and Al—O—Al bonds. In titano-silicates, disorder will increase with the formation of similar Si—O—Ti, Si—O—Si, and Ti—O—Ti bonds. The disorder in titano-silicates is exemplified by the high value of ΔS^{fus} for $CaTiSiO_5$ [68].

Thus, the configurational entropy affects thermodynamic properties of slags but, more surprisingly, also affects the flow properties (e.g., viscosity) since samples which show a large value of ΔC_{pT_g} were found to exhibit a strong temperature dependence for the viscosity in the supercooled phase (*scl*) [69]. The Adam-Gibbs relation, used to describe the temperature dependence in the *scl* phase, is based on the configurational entropy of cooperative relaxation [70].

2.2.2.9. Structural Information

2.2.2.9.1 Silicates

The silicate melt contains various silicate species; these are denoted as Q^n where n can vary between 0 and 4. The distribution of these Q^n species is mainly determined by the SiO_2 content of the melt but the nature of the cations and the temperature can have some effect on their concentrations. It was pointed out earlier that the trend for reaction (2.2.10) ($Q^3 = Q^2 + Q^4$) is to move to the right (i) for cations with high field strength (i.e., high z/r^2) and (ii) with increasing temperature. Thus, cations like Mg^{2+} will encourage a more varied distribution of structural units but there will be a smaller distribution of structural units with cations like K^+.

There is also evidence of small concentrations (ca. 0.1% of bonds) of 5-coordinated ($^{(5)}Si$) bonding in $K_2Si_4O_9$ [6].

2.2.2.9.2 Aluminosilicates

When Al_2O_3 is added to a silicate melt there are two ways that the Al^{3+} can be incorporated into the network, namely, (i) by the formation of Al—O—Al and Si—O—Si bonds or, alternatively, (ii) by the formation of Al—O—Si bonds. The Al-avoidance (or Lowenstein) Rule states that the formation of Al—O—Si bonds is favored on energy grounds [71]. Lee and Stebbins [62] have shown that the rule is followed in the majority of the cases with the formation of Al—O—Si in ca. 85% and 95% of the bonds formed in Ca- and K-aluminosilicates, respectively. This suggests the rule is followed better with low-field strength cations (low z/r^2) than with highly polarized cations, e.g., Ca^{2+}, Mg^{2+} (i.e., with high z/r^2).

There have been a number of investigations of aluminosilicates and these have been reviewed by Henderson [4]. Starting with the Al_2O_3-SiO_2 system, there is phase separation into Al_2O_3-rich and SiO_2-rich phases. It would appear that, although there is variability in the results, the Al^{3+} ions are predominantly in fourfold coordination ($^{(4)}Al^{3+}$) with some formation of rings and tri-clusters [4].

Investigations of the structure of M_2O-Al_2O_3-SiO_2 systems indicate that Al^{3+} is predominantly in tetrahedral coordination ($^{(4)}Al^{3+}$) [72]. There are two proposals to account for Al coordination in per-aluminous melts (where $X_{M_2O} < X_{Al_2O_3}$, i.e., insufficient M_2O to charge balance Al^{3+} ions), namely (i) that Al assumes a higher coordination ($^{(6)}Al^{3+}$ or $^{(5)}Al^{3+}$) or (ii) tri-clusters are formed to charge balance the Al^{3+} (see Figure 2.2.12) [73]. The consensus seems to be that little $^{(6)}Al^{3+}$ is formed but both tri-clusters [74] and $^{(5)}Al^{3+}$ [75] have been reported. It should also be noted that NBOs have been identified in these highly polymerized, per-aluminous melts [52] and NBOs would be expected if $^{(5)}Al^{3+}$ is formed.

Investigations of the structure of MO-Al_2O_3-SiO_2 systems indicate that Al^{3+} is predominantly in tetrahedral coordination. In more polymerized melts it exhibits a preference to form Al—O—Si bonds in highly polymerized units (e.g., Q^4 or Q^3)

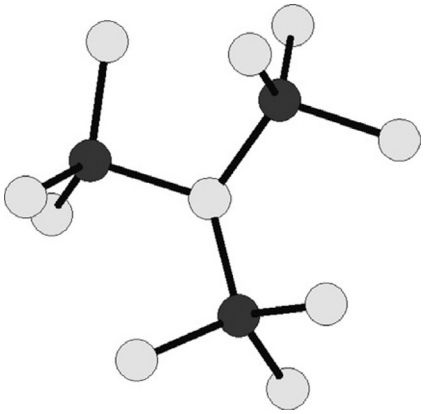


Figure 2.2.12 Schematic diagram depicting a tri-cluster showing the centrally placed oxygen ion (=light gray) shared between 3 Al ions (=black) from 3 tetrahedra (no charge compensation needed with this arrangement) [4].

but in less polymerized melts will enter into less polymerized units (e.g., Q^2). Tri-clusters (shown in Figure 2.2.12) and some $^{(5)}Al^{3+}$ (<2% of Al^{3+}) have been observed in highly polymerized melts [4,74].

Measurements of the viscosity [76,77] and electrical resistivity carried out on melts, where the Al/M ratio ($= X_{Al_2O_3}/X_{M_2O+MO}$) is gradually increased, exhibit a maximum when the ratio has a value of 1.0. This corresponds to a composition of $(\gamma X_{MO+M_2O} + (1-2\gamma)\, X_{SiO_2} + \gamma X_{Al_2O_3})$ and has a value of $Q=4$, i.e., all of the cations are needed to charge balance the Al^{3+} ions held in tetrahedral sites. For melts where $Q>4$ the slag does not have enough cations to fully charge compensate the Al^{3+} ions. This maximum occurs at Al/M ratio slightly below 1. The bonding of the Al^{3+} ions in such melts (with Al/M > 1) has been a topic of considerable debate [73]. As mentioned above, there are two propositions:

(i) that some of the Al^{3+} ions switch from fourfold (tetrahedral) bonding to sixfold (octahedral) coordination.

(ii) that Al^{3+} ions remain tetrahedrally coordinated over the entire range but that there is rearrangement in the topology which results in the formation of *tri-clusters*.

Tri-clusters consist of three BOs (originally in tetrahedral configuration) which are rearranged around an Al^{3+} ion so as to produce a 3-coordinated oxygen (Figure 2.2.12). Tri-clusters have been identified in mullite ($2Al_2O_3 \cdot 3SiO_2$) in $CaAl_4O_7$ and in small concentrations in calcium aluminosilicates [74].

The conventional view is that NBOs cannot be formed in meta-aluminous $CaAl_2Si_2O_8$ (with $X_{CaO} = X_{Al_2O_3}$ and $Q=4.0$) melts. However, Stebbins and Xu [52] have reported that NBOs constituted 3-5% of the total bonds and suggested a mechanism for NBO formation which involves the formation of a tri-cluster. The formation of NBOs is necessary for the formation of 5-coordinated, $^{(5)}Si$. The presence of relatively

weak NBOs and the formation of $^{(5)}Si$ will have important effects on the flow properties (viscosity, electrical resistivity, and diffusion coefficient).

It has been reported that most of the NBOs are associated with Si^{4+} ions and not with the $(MAl)^{4+}$ ions [6]; this is consistent with the finding that most Al ions tend to congregate in highly polymerized Q^3 and Q^4 units (but will inhabit lower Q^n units in less polymerized slags).

The T-O-T inter-tetrahedral angle in aluminosilicates is affected by (i) the Al/Si ratio (i.e., the ratio $X_{Al}/(X_{Al}+X_{Si}) = 2X_{Al_2O_3}/(2X_{Al_2O_3}+X_{SiO_2})$ and (ii) the field strength (z/r^2) of the cation [62]. It was found that the inter-tetrahedral angle went through a maximum at $X_{Al}/(X_{Al}+X_{Si}) = 0.2$. The field strength of the cation has also been found to affect the distribution of T-O-T, inter-tetrahedral angles with the maximum occurring at a lower angle and the peak becoming broader as (z/r^2) decreased (i.e., $Mg^{2+} > Ca^{2+} > Na^{+}$).

The line width of the ^{29}Si NMR spectra can be used as a measure of the disorder in the melt. It was suggested that disorder in a meta-aluminosilicate melt decreases with increasing $X_{Al}/(X_{Al}+X_{Si})$ and decreasing (z/r^2) for the charge-balancing cation [63].

This opens up the question "which cations do the charge-balancing?" when there are two or more cations present in aluminosilicates. The general rule appears to be that charge compensation is done by the cations with the smallest field strength (z/r^2). Thus for a melt $\{K_2O_{0.05}Na_2O_{0.1}CaO_{0.05}(Al_2O_3)_{0.1}(SiO_2)_{0.7}\}$ where the subscript denotes the mole fraction, the charge balancing is performed by the K^+ and by some of the Na^+ ions. This rule appears to be based on the finding that thermodynamic stability (as represented by the enthalpy of mixing) of meta-aluminous, aluminosilicates was in the order $(K > Na > Li \approx Ba > Sr > Ca > Mg)$ as can be seen below (Figure 2.2.29 [36]). This view is supported by the fact that NBOs were found to prefer interactions with Ca^{2+} ions (cf. Na^+ ions) and charge-balancing duties tended to be carried out by Na^+ ions in Na_2O-CaO-Al_2O_3-SiO_2 glasses [78–80].

2.2.2.9.3 Titano-Silicates

There have been a number of studies on the structure of titano-silicates and the results have been reviewed by Henderson [4]. The coordination of Ti has been a subject of dispute with $^{(4)}Ti$, $^{(5)}Ti$, and $^{(6)}Ti$, all having been identified in various investigations [4]. For the TiO_2-SiO_2 system, most investigators indicate that Ti ions are in 4-coordination (i.e., $^{(4)}Ti^{4+}$) especially at higher TiO_2 concentrations but $^{(5)}Ti$ coordination was suggested to occur in glasses containing <3.6% TiO_2 [4].

In M_2O-TiO_2-SiO_2 systems most of the studies indicate $^{(4)}Ti$ and $^{(5)}Ti$ coordination with higher proportions of $^{(5)}Ti$ at high TiO_2 contents [4].

In MO-TiO_2-SiO_2 systems, both $^{(4)}Ti^{4+}$ and $^{(5)}Ti^{4+}$ coordination have been identified with $^{(4)}Ti^{4+}$ observed in both high- and low-TiO_2 contents; it has also been suggested that larger cations (e.g., Sr and Ba) promote $^{(4)}Ti^{4+}$ coordination [4].

The addition of TiO_2 to a $CaO\text{-}SiO_2$ melt results in the following:

(i) an increase in the chemical activity a_{SiO_2}

(ii) a decrease in viscosity [10–14]

(iii) a region where the electrical resistivity remains fairly constant followed by an increase in resistivity [81] (which is surprising because resistivity would be expected to follow the viscosity).

The $CaO\text{-}SiO_2\text{-}TiO_2$ phase diagram [7] shows a large region of phase separation (i.e., immiscibility) and given that TiO_2 additions cause an increase in a_{SiO_2} there is a definite trend for Si- and Ti-species to keep apart. This tendency can be expressed in terms of the dis-proportionation reaction which results in greater configurational entropy because of mixing of Ti—O—Ti and Ti—O—Si and Si—O—Si bonds

$$2\text{Ti} - \text{O} - \text{Si} = \text{Ti} - \text{O} - \text{Ti} + \text{Si} - \text{O} - \text{Si} \tag{2.2.11}$$

However, Stebbins *et al.* [6] have also hinted at phase separation on a nanoscale and it would appear that there is a tendency in titano-silicates toward phase heterogeneity even if phase separation does not physically occur.

Kroeker *et al.* [68] used NMR spectroscopy to compare the various species present in glass and crystal and found glass exhibited more variety in bonding (Si—O—Si and Si—O—Ca + Ti—O—Ti and Ti—O—Si) than that found in the crystal (Ti—O—Ti and Ti—O—Si only). They reported high concentrations of Si—O—Si and Si—O—Ca bonds.

Henderson *et al.* [3] have reported that $^{(5)}$Ti and $^{(4)}$Ti coexist and it could be the $^{(5)}$Ti which is responsible for the gradual decrease in viscosity with TiO_2 additions.

2.2.2.9.4 Silicates Containing Iron Oxides

Slags containing iron oxides (FeO_x) are of great importance to the steel- and copper-making industries. The effect of FeO_x on the structure of silicates has been studied by a number of workers and the results of these studies have been reviewed by Henderson [4]. The situation is complicated by the fact that Fe can exist as Fe^{2+} or Fe^{3+} and that both species are capable of different coordinations $^{(4)}$Fe, $^{(5)}$Fe, or $^{(6)}$Fe, all of which complicates the situation. Henderson [4] points out that the situation is further complicated by the fact that there is a sharp discrepancy between the results obtained with XANES and Mossbauer spectroscopies. The results, in general, indicate that in:

(i) $M_2O\text{-}FeO_x\text{-}SiO_2$ melts, Fe^{3+} adopts fourfold coordination ($^{(4)}Fe^{3+}$) with M = Na or K but $^{(5)}$Fe or $^{(6)}$Fe are found in melts with M = Li [4], whereas Fe^{2+} adopts four- or fivefold coordination (i.e., $^{(4)}$Fe or $^{(5)}$Fe).

(ii) $MO\text{-}FeO_x\text{-}SiO_2$ melts there is more variation in the coordination of Fe^{3+} with $^{(4)}$Fe or $^{(5)}$Fe being formed, whereas Fe^{2+} adopts the coordination of $^{(4)}$Fe or $^{(5)}$Fe.

This is largely consistent with the view (derived from analysis of viscosity data) that Fe_2O_3 acts as both network former and network breaker and Fe^{2+} acts largely as a network breaker.

2.2.2.9.5 Additions of CaF_2

It was noted earlier in Section 2.2.2.5 that:

(i) F bonds preferentially with the cations and prefers cations with the highest field strength [23–25].

(ii) Some Al—F bonds are formed but Si—F bonds (ca. 2% of total F bonds) tend to be rare.

(iii) If F is added as, say, CaF_2 to a $CaO\text{-}SiO_2$ slag, the F ions remain bonded to the Ca ions so the CaF_2 acts predominantly as a diluent [17–20] but if F replaces O (CaF_2 replacing CaO while maintaining X_{SiO_2} constant) the Ca^{2+} ions forming CaF_2 reduce the number of network-breaking cations which results in increased polymerization of the slag [16–20].

Structural studies carried out by Luth [16] and molecular dynamics (MD) studies [17,18,21] showed that the replacement of CaO by CaF_2 did, in fact, result in an increase in Q^3 and Q^4 units and that the replacement of CaO by Na_2O had little effect on the abundance of the various Q^n units. Further structural studies showed that F^- ions bonded preferentially with the cations with highest field strength ($La^{3+} > Mg^{2+} > Ca^{2+} > Ba^{2+} + Na^+$) [25]. These studies also confirmed that some Al—F bonds were formed and that Si—F bond formation was at a low level [25].

Two mechanisms have been proposed recently to account for the way that CaF_2 behaves in silicate melts for (a) when CaF_2 is added to a melt [23] and (b) for the situation where CaF_2 replaces CaO in the melt [19]; these are shown in Figure 2.2.13. In the Hayashi mechanism [23] the two O—Ca—O bonds are replaced by two O—Ca—F bonds, and in the Sasaki mechanism the Ca^{2+} and $2F^-$ ions replace a NBO with a "loosely bonded Ca-2F complex" [19].

These structural findings also have repercussions on the calculation of the parameter (NBO/T). In the past, many investigators were wary about calculating NBO/T for slags (containing CaF_2) because of the uncertainty in chemical bonding arising from the F additions. Consequently, the CaF_2 content was frequently ignored when calculating (NBO/T). In view of the new findings that F^- bonds almost exclusively with Ca^{2+}, it would seem that such caution was well placed and that the best way of calculating NBO/T is to ignore the CaF_2 and concentrate on the other components.

2.2.2.10. Methods of Determining Structure

Our knowledge of slag structure has been derived by using a variety of techniques to extract a wide range of information which is then used to gain insight into slag structure. The information provided by the various techniques is summarized in Table 2.2.4.

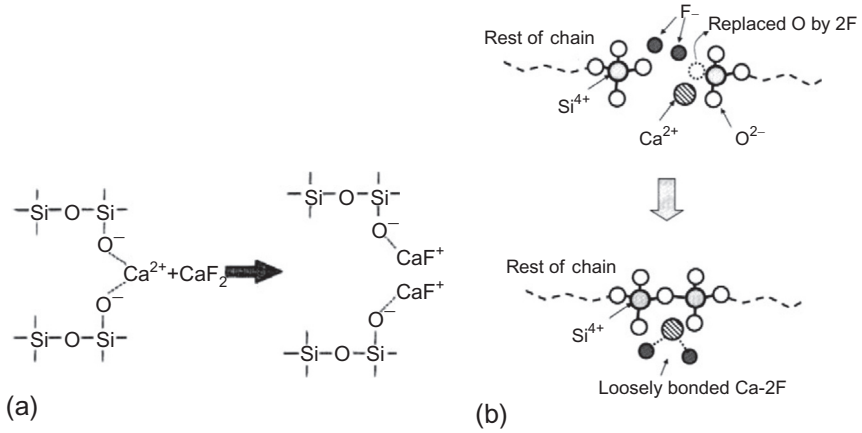


Figure 2.2.13 Proposed mechanisms for the addition of CaF_2 to silicate slag: (a) the mechanism proposed for the case where CaF_2 is added to a $CaO\text{-}SiO_2$ slag [23] and (b) the mechanism proposed for the case CaO is replaced by CaF_2 [19].

Table 2.2.4 Summary of the various methods used to provide information on the structure of slags and glasses (note that T in T-O-T refers to Si or Al exhibiting tetragonal bonding)

Method	Measurement	Structural information obtained
Diffraction X-ray, neutron, electron	Radial distribution function	(1) Bond lengths, (2) coordination numbers, (3) inter-tetrahedral angles T-O-T, (4) overall intermediate structure, (5) local O coordination around large cations
Spectroscopy Raman, infrared, ultraviolet		(1) Bond lengths, (2) bond angles, (3) identification and concentrations of various anionic units Q^0, Q^1, Q^2, Q^3
Nuclear magnetic resonance (NMR)	Chemical shift	(1) Bond lengths, (2) bond angles, (3) identification and concentrations of various anionic units Q^0, Q^1, Q^2, Q^3
Mossbauer	Isomer shift	(1) Valence state, (2) coordination of environment; identification and concentration of Fe^{3+} with four- and sixfold coordination
	Quadrupole splitting	(1) Distortion of O polyhedron, (2) oxidation state Fe^{2+} or Fe^{3+}, (3) coordination of Fe^{3+} (four- or sixfold)
X-ray absorption spectroscopy	EXAFS XANES	(1) Bond lengths, (2) bond angles, (3) coordination of specific atoms or ions
X-ray emission (ESCA or XPS) ESR spectroscopy	K_α: K_β	(1) Coordination of specific atoms or ions, (2) changes in valence state

Table 2.2.4 Summary of the various methods used to provide information on the structure of slags and glasses (note that T in T-O-T refers to Si or Al exhibiting tetragonal bonding)—cont'd

Method	Measurement	Structural information obtained
Luminescence spectroscopy		Coordination of Mn^{2+}, Fe^{3+}, Ti^{3+}, or S (S^{2-} or SO_4^{2-})
Chromatography		Distribution of chain lengths of different polymeric units
Property measurement	Density, molar volume	Packing and coordination
	Molar refractivity	Concentrations of N^{O^0}; N^{O^-}; $N^{O^{2-}}$
	Viscosity	(1) Activation energies related to bond strength, (2) effect of cations on structure
	Enthalpy of mixing, or solution	(1) Measure of bond strength, (2) effect of different cations including structural ordering
	Electrical/ thermal conductivity	(1) Indication of amount of ionic and electronic conduction, (2) information on whether fluorides form Si—F bonds
Molecular dynamics (MD)	Calculations	(1) Bond strengths, (2) T-O-T angles, (3) coordination (e.g., Al is fourfold in $Na_2O + Al_2O_3 + SiO_2$ slags)
Thermodynamic modeling	Calculations	Concentration of various anionic polymeric units in melt

Although all the data provided by these techniques are valuable, the information obtained in Raman and NMR spectroscopy has been particularly useful in expanding our knowledge of slag structure.

Brief descriptions of the experimental techniques are given below and for a full description of these methods the reader is referred to articles presented by Fleet [82] and Wong and Angell [83].

2.2.2.10.1 X-ray, Electron, and Neutron Diffraction

Diffraction methods provide information pertaining to the short-range and intermediate-range order. Values of the radial distribution function (RDF) are usually derived from which a variety of information, such as bond angles, can be derived. Neutron diffraction has some distinct advantages since it is not dependent upon atomic number.

2.2.2.10.2 Infrared, Ultraviolet, and Raman Spectroscopy

Excitation of the sample produces vibrations and rotations and these can be detected directly at IR and microwave frequencies using spectroscopy. However, with Raman spectroscopy these excitations can be detected in the visible region where the detection systems are well developed. When a photon interacts with a bond (or electron cloud) it becomes partially polarized. The vibrations can be classified as (i) *symmetric stretching* (shown in Figure 2.2.14a) which leads to intense and partly polarized Raman lines, (ii) *asymmetric stretching* (shown in Figure 2.2.14b) which produce weak polarized lines, and (iii) *bending* [30].

In crystalline phases the lattice vibrations are dominated by the silicate species and the vibrations produce well-defined Raman lines. However, in both quenched glass and liquids, the vibrations produce broad bands which must be deconvoluted (see Figure 2.2.5) into the various polymeric species (Q^0, Q^1, Q^2, etc.). Individual bands correspond to individual Q species and the concentrations of these species can be determined by calculating the areas under the individual peaks. The attribution of the various bands to structural units is given in Table 2.2.5.

2.2.2.10.3 NMR Spectroscopy

When a sample is placed in a magnetic field there is a change in the energy state of the atom or molecule. This energy change is dependent upon (i) the magnetic field, (ii) the internal field of the sample, (iii) the chemical bond, and (iv) the molecular motion. The outer electrons shield the nucleus and thus there is a minute change in the resonant energy which results in a chemical shift in NMR absorption peak. The structural information is derived from these chemical shifts [84]. These have been determined when

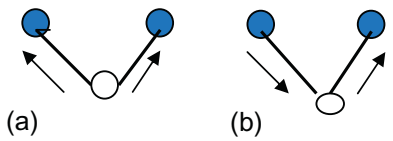


Figure 2.2.14 Schematic drawings showing (a) *symmetric stretching* and (b) *asymmetric stretching*: ○ = Si; ● = O [30].

Table 2.2.5 The various bands in Raman spectrum for silicates and the source of the vibration; pol = polarized [30]

Raman shift (cm^{-1})	**1200**	**1050–1100**	**950–1000**	**900**	**850**	**800**	**430**
SiO_2	Weak	Weak				Medium	Strong pol
Silicates		Strong	Strong	Strong	Strong		
		Q^3	Q^2	Q^1	Q^0		3-Member ring

using a variety of isotopes ^{29}Si, ^{27}Al, ^{17}O, and ^{19}F. In liquids, sharp peaks are obtained but in solids, interactions (e.g., that between chemical shift and the orientation to the magnetic field) cause broadening of the peaks. However, this line broadening can be minimized by rapid rotation of the solid and by using the "magic angle" ($\theta = 54.7°$ to magnetic field) which produces narrow lines [84].

2.2.2.10.4 Electron Spin Resonance

Electron spin resonance (ESpRes) involves the resonant absorption of long wavelength-microwave radiation by electrons with un-paired spins. It is used principally to determine the coordination of specific transition metals (e.g., Fe^{2+}) which are present in the silicate network. However, quadrupole-splitting provides information on the distortion of the cubic symmetry.

2.2.2.10.5 Mossbauer Spectroscopy

Mossbauer spectroscopy involves the emission of γ-rays and their resonant absorption by atoms in the sample; this resonance is associated with allowable nuclear spin states. The chemical isomer shift provides information on the coordination environment and valence state of Fe atoms and the quadrupole shift gives a measure of the distortion from cubic symmetry. Mossbauer spectroscopy has proved extremely useful in differentiating between octahedral and tetrahedral coordination for Fe^{3+}, i.e., the fractions of Fe^{3+} acting as network breakers and network formers, respectively.

2.2.2.10.6 X-ray Absorption Spectroscopy (XANES and EXAFS)

Two forms of X-ray absorption spectroscopy are in common use. These are X-ray near-edge absorption spectroscopy (XANES) and extended X-ray absorption fine structure (EXAFS). The energy threshold (E_o) is the energy required to eject a bound electron; XANES covers the range 0-40 eV and EXAFS from 40 to 1000 eV. EXAFS provides the RDF which when subjected to Fourier transformation provides information on bond lengths, bond angles, and the coordination environment of specific atoms. XANES tends to be more qualitative than EXAFS.

2.2.2.10.7 X-ray Emission Spectroscopy

The wavelength of X-rays shifts slightly with coordination environment and valence state. The shifts in K_α and K_β are calibrated with crystalline silicates and are then applied to frozen melts (glasses).

2.2.2.10.8 X-ray Photon Spectroscopy or ESCA

When X-rays (or UV radiation for a charged particle) strikes the sample electrons are emitted. The energy is determined and the energy levels can be used to determine both the coordination number and the valence state.

2.2.3. EFFECT OF STRUCTURE ON PROPERTIES

It was mentioned previously that the properties of silicate melts are very dependent upon the structure of the melt. The structure is, in turn, affected by:

(i) the degree of polymerization of the melt
(ii) in aluminosilicates by the amount of Al_2O_3 present in the slag or glass
(iii) by the nature of the cations present and
(iv) the temperature

The way that these various factors affect the properties is discussed in detail below.

2.2.3.1. Effect of Silicate Structure on Properties of Slags

The degree of polymerization is the principal factor affecting properties such as the viscosity, electrical conductivity, diffusion coefficient, and thermal conductivity. However, when Al_2O_3 is added to a silicate melt, it effectively increases the degree of polymerization in the melt and hence results in an increase in viscosity. However, these changes in viscosity for aluminosilicates cannot be totally explained in terms of the degree of polymerization. Consequently, silicates and aluminosilicates are treated separately below.

2.2.3.1.1 Silicates

The structure has an important effect on properties such as the viscosity (η), electrical conductivity (κ), and diffusion coefficient (D). The slag structure (i.e., silicate anions) can be seen as a strong resistance to the movement of one layer of molecules over another layer in the case of viscosity and to the movement of cations through the network in the case of electrical conduction and diffusion. The effect of increasing polymerization can be clearly seen in Figure 2.2.15 where ln η_{1900K} and ln R_{1900K} (where $R = 1/\kappa$) are plotted against Q

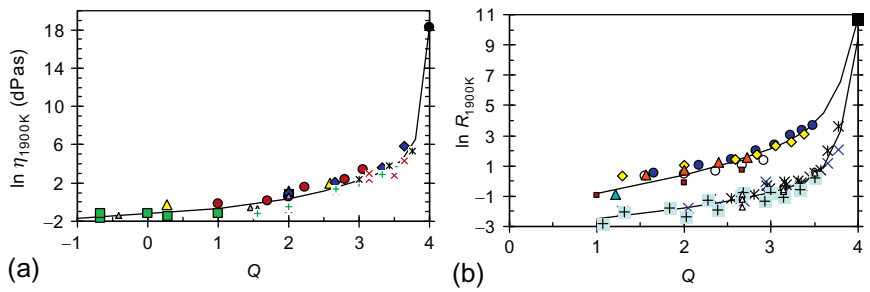


Figure 2.2.15 (a) Viscosities (ln η_{1900K}) and (b) electrical resistivities (ln R_{1900K}) of MO-SiO_2 and M_2O-SiO_2 systems as functions of the parameter Q; + = LS; × = NS; * = KS; ○ = CS; ▲ = MS; ◊ = SrS; ● = BS; ▲ = FS; ■ = MnS; ◆ = MFS; the upper curve = MO and lower curve M_2O [85].

(=4 − (NBO/T)) which is a measure of the polymerization of the melt [85]. Similar curves would also be obtained for temperatures where the sample is in the form of an *scl*.

Looking at the right-hand side of Figure 2.2.15a and b, it can be seen that the addition of network-breaking cations (e.g., Ca^{2+}) to pure SiO_2 causes a sharp decrease in viscosity and electrical resistivity. Increased temperature tends to have a similar effect to cation additions. However, different properties tend to have different temperature dependencies but for those properties which are principally determined by the nature of the silicate structure (e.g., viscosity and electrical resistivity) the temperature dependence of the liquid phase is usually represented in the form of Arrhenius or Weymann relations (denoted by the subscripts A and W) shown in Equations (2.2.12) and (2.2.13), respectively:

$$\eta = A_{A\eta} \exp(B_A/T) \tag{2.2.12}$$

$$\eta/T = A_{W\eta} \exp(B_W/T) \tag{2.2.13}$$

where η is in dPas, T is in K, and A_A and A_W are the preexponential terms and B_A and B_W represent the activation energy (E) term ($B = E/8.314$). It can be seen from Figure 2.2.16 that the parameters B_η and B_R increase with increasing polymerization (i.e., increasing Q). Typical Arrhenius plots are shown in Figure 2.2.17 for the cases where (a) a crystalline phase is formed on cooling and (b) when a *scl* is formed. Throughout this chapter, the temperature dependence of viscosity, electrical conductivity, and diffusion coefficient for the liquid phase will be expressed in the form of an Arrhenius relation.

The viscosity exhibits a much stronger dependence on temperature in the supercooled region than in the liquid; this can be seen in Figure 2.2.17b. Consequently, temperature dependence of the *scl* is usually represented in the form of a Vogel-Fulcher-Tamman relation (Equation 2.2.14) which requires the knowledge of three constants

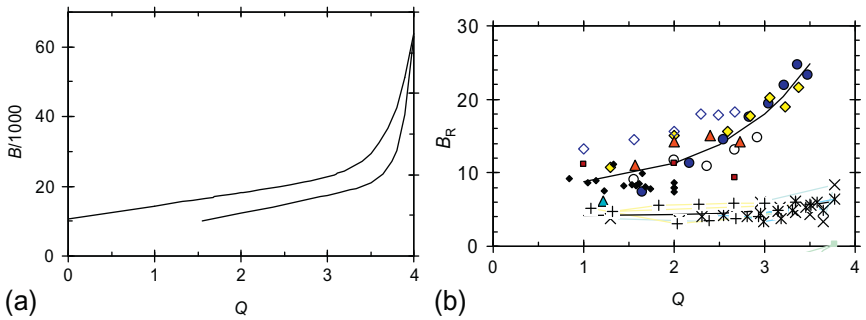


Figure 2.2.16 The activation energy parameter, B_η and B_R for MO-SiO_2 and M_2O-SiO_2 systems as functions of Q. (a) Viscosity (B_η) (upper curve = MO; lower curve = M_2O) and (b) electrical resistivity (B_R); + = LS; × = NS; ∗ = KS; ○ = CS; ▲ = MS; ◊ = SrS; ● = BS; ▲ = FS; ■ = MnS; ♦ = MFS; − = CMS; upper curve = MO; lower curve = M_2O [85].

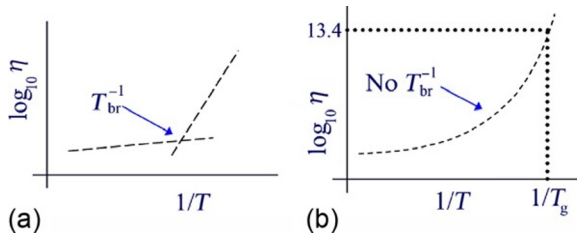


Figure 2.2.17 Plots of $\log_{10}$ viscosity as functions of reciprocal temperature (K^{-1}) for (a) a slag where crystallites are precipitated ($Q = 2$) and (b) glassy slag forming a *scl* ($Q > 2.5$).

A, B, and $T°$. The viscosity has a value of η (dPas) $= 10^{13.4}$ at the glass transition temperature (T_g):

$$\eta = A_V \exp(B_V/(T - T°)) \tag{2.2.14}$$

The Adams-Gibb relation (denoted by subscript AG) is also used for the supercooled phase; it is based on the configurational entropy of cooperative relaxation and is given in Equation (2.2.15) where C_{AG} is a constant [70]:

$$\eta = A_{AG} \exp(B_{AG}/(T \log(T/C_{AG})) \tag{2.2.15}$$

The activation energy terms (B_η and B_R, see Equation 2.2.12) are also sensitive functions of the degree of polymerization, Q. It can be seen from Figure 2.2.16 that the viscosity and electrical resistivity become increasingly sensitive to temperature as the degree of polymerization increases.

2.2.3.1.2 Aluminosilicates

It has been shown earlier that Al^{3+} ions can be integrated into the Si^{4+} network provided that cations are available for charge balancing the Al^{3+} ions (i.e., by forming, e.g., $(NaAl)^{4+}$). The introduction of Al^{3+} ions into the Si^{4+} network results in further polymerization and simultaneously decreases the number of cations available for network breaking (because cations on charge-balancing duties cannot act as network breakers). Consequently, the absorption of Al^{3+} ions into the Si^{4+} network results in an increase in the parameter, Q, i.e., the degree of polymerization. However, it can be seen from Figure 2.2.18 that the viscosities and electrical resistivities are lower than those for equivalent silicate melts [85]. This strongly suggests that the integration of Al^{3+} ions into the Si^{4+} network results in the formation of structural units which exhibit less resistance to the flow of both anions (i.e., viscosity) and cations (electrical resistivity) for polymerized melts where $Q > 2.8$. This may be a reflection of the weakness of the Al—O bond (cf. Si—O) or alternatively, may be due to the increasing concentrations of fivefold-coordinated Al ($^{(5)}$Al) and the associated NBOs in the melt.

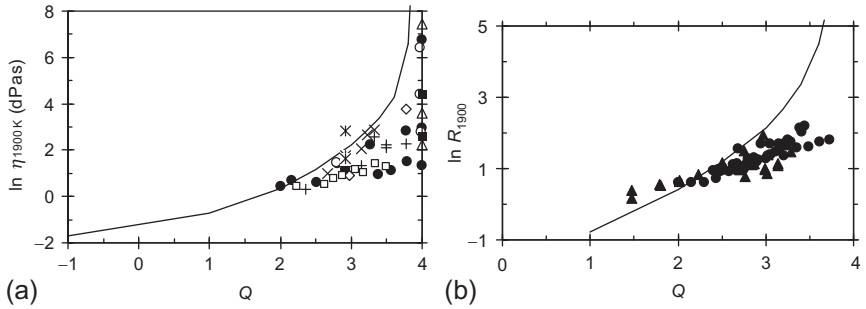


Figure 2.2.18 Comparison of data for aluminosilicates (points) with those for silicates (curve) for the dependence on Q of (a) ln η_{1900K} ● = CAS; ○ = MAS; ■ = BAS; Δ = SrAS; ◊ = MnAS; + = LAS; × = NAS; ∗ = KAS; □ = CMAS and (b) ln R_{1900K} ● = CAS; ▲ = CMAS [85].

The activation energy parameter, B for the viscosity (B_η) and electrical resistivity (B_R) for aluminosilicates is compared with those for silicates in Figure 2.2.19 [85]. It can be seen that the bulk of the B_η values for the aluminosilicates lies below the values for equivalent silicates. In contrast, the B_R values for aluminosilicates are higher than those of the silicates; this will be discussed below.

The underlying cause of the lower viscosity and resistivity for aluminosilicates (cf. silicates) is not known but it is possibly connected to (i) the weakness of the Al—O bond (cf. the Si—O bond), (ii) increasing amounts of $^{(5)}$Al and NBOs associated with $^{(5)}$Al in highly polymerized aluminosilicates, and (iii) the decrease in both the T-O-T inter-tetrahedral angle and the disorder as the Al/(Al + Si) ratio increases.

These possible causes may also explain the lower B_η for aluminosilicates (cf. silicates) but the higher B_R values indicate that the lower number of available cations is probably the principal factor affecting the activation energy for electrical resistivity.

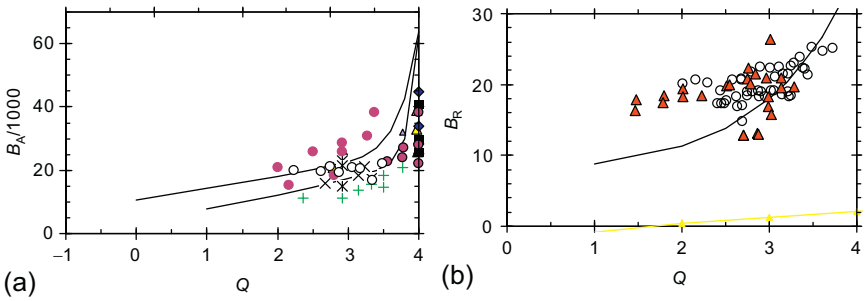


Figure 2.2.19 Comparison of activation energy parameter, B, for aluminosilicates (points) with those for silicates (curve) for (a) $B_{A\eta}$ for viscosity ● = CAS; ♦ = BAS; ■ = SrAS; Δ = MAS; Δ = MnAS; + = LAS; × = NAS; ∗ = KAS; ○ = CMAS; ■ = SiO_2; +, ∗, and × pertain to lower curve all other symbols to upper curve and (b). B_R for electrical resistivity ○ = CAS; ▲ = CMSA [85].

2.2.3.2. Effect of Cations on Slag Properties

Although the degree of polymerization in the silicate network is the dominant factor affecting the properties of slags, the nature of the cations (e.g., Ca^{2+} or Na^{+}) can also affect the properties [86,87]. This can occur by (i) direct intervention (e.g., through cation size or field strength) or (ii) through their effect on the silicate network. The properties can be affected by the following:

2.2.3.2.1 Strength of the Ionic M^{+}—O^{-} Bond

The strength of the M^{+}—O^{-} bond is frequently represented by either the field strength (z/r^2) where z is the charge and r is radius of the cation (M^{+}) or by the optical basicity, Λ. The two properties are related (see Figure 2.2.4) with the bond strength increasing as (z/r^2) increases and as Λ decreases. The field strength decreases with increasing cation size (Figure 2.2.20). It has been reported that the dis-proportionation reaction (Equation 2.2.10) is promoted by cations with high field strength (high z/r^2) [3,6]. It has also been reported that the coordination number and the distribution of T—O—T inter-tetrahedral angles are both affected by the field strength (z/r^2) of the cations [53] (Figure 2.2.11).

The silicate structure is also affected by the field strength of the cation; it has been reported that increasing (z/r^2) for the cation causes:

(i) increased distribution of Q^n units ($2Q^n = Q^{n-1} + Q^{n+1}$)

(ii) decreasing coordination number (N_{coord}) which, in turn, the proportions of BOs and NBOs are affected by N_{coord}.

(iii) a more compact distribution of inter-tetrahedral (Si—O—Si or Si—O—Al in aluminosilicates) bond angles.

(iv) increasing disorder in the melt, and

(v) an increasing attraction for NBOs and a decreased probability of carrying out charge-balancing duties in aluminosilicates.

2.2.3.2.2 Fraction of Ionic Bonding in the M—O Bond

M—O bonds are mostly ionic but also contain some covalence (e.g., the fraction of ionic bonding (expressed as %) has been calculated to be 78%, 48%, and 59% for CaO, FeO, and MnO, respectively [281]).

2.2.3.2.3 Size of the Cations

From a structural viewpoint it has been shown that the cation environments are affected by the size of cation [53]. The coordination number (N_{coord}) increases with increasing



Figure 2.2.20 Schematic diagram showing relative strengths (denoted by thickness of bond) of M^{+}—O^{-} bonds for Li^{+}, Na^{+}, and K^{+} [87].

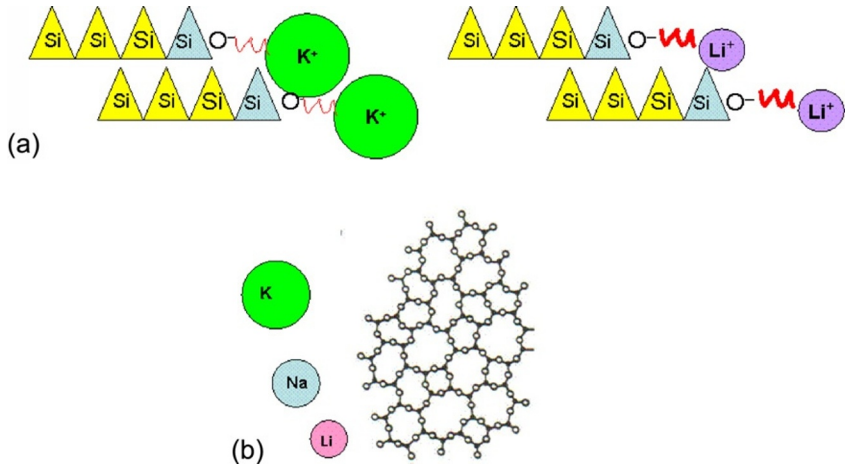


Figure 2.2.21 Schematic diagram showing hindrance caused by large cations in (top) viscosity and (bottom) electrical conductivity [87].

cation size. In mixed alkali silicates it was reported that both the coordination number and the average size of the cation site increased with increasing substitution with a smaller cation (i.e., N_{coord} ↑ and site size ↑ as Na was replaced by Li) and vice versa. Furthermore, smaller cations with higher field strength (z/r^2) tend to have a smaller coordination number and hence result in a higher proportion of NBOs and fewer BOs [4,53].

From a physical viewpoint (Figure 2.2.21), larger cations tend to:

(i) hinder the motion of one layer of molecules over another layer and thereby increase viscosity (Figure 2.2.21a)

(ii) find it difficult to pass through the "holes" in the silicate network which thereby cause a decrease in electrical conductivity (Figure 2.2.21b), or alternatively

(iii) affect the silicate network in such a way so as to cause an increase in viscosity and electrical resistivity.

Thus, any effect of cation size on the physical properties could be due to the effect of its size on (i) the structure or (ii) on the cation mobility.

2.2.3.2.4 The Bridging of Cations

When monovalent cations (M^+, e.g., Na^+) break a chain the M—O bond is complete but with divalent cations (M^{2+}, e.g., Ca^{2+}) the cation must find another Si—O bond to break. Consequently, the Ca^{2+} ions must bridge two sites (Figure 2.2.22). This bridge could lead to increases in viscosity, electrical resistivity, and to a decrease in the diffusion coefficient (D). "Bridging" may be responsible for the gap between the two curves in Figure 2.2.16 (the other possible cause being that structural units formed by M^+ have a lower activation energy than those formed by M^{2+}). Bridging of charge-balancing M^{2+} cations can also occur.

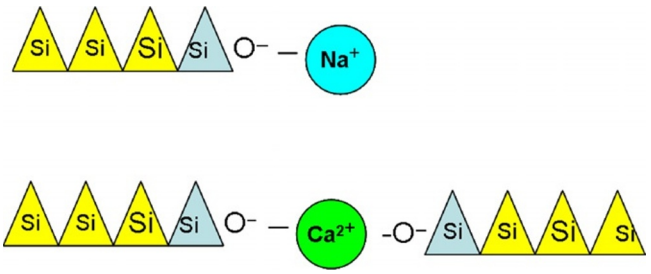


Figure 2.2.22 Schematic representation of the "bridging" with Ca^{2+} ions cf. absence of bridging for Na^{+} ions [87].

2.2.3.2.5 The Number of Cations

Although 1 mol of CaO is equivalent to 1 mol of Na_2O it should be noted that CaO gives rise to one Ca^{2+} cation whereas Na_2O provides two Na^{+} cations. Thus, Na_2O provides twice as many cations as CaO. Both electrical conductivity and diffusion coefficient increase with increasing number of cations (N) [86,87]. The gap between the two curves in Figure 2.2.15b is due to the greater number of cations available for charge transport for M_2O-SiO_2 systems compared with their equivalent in MO-SiO_2 systems.

2.2.3.2.6 Mixed Alkali Effect

For slags containing two (or more) cations with widely different radii (e.g., when K_2O is added to Li_2O-SiO_2) there is a decrease in electrical conductivity (and T_g) which is much greater than that predicted from linear mixing rules. The effect tends to diminish with increasing temperature and is more prevalent in the supercooled phase than in the liquid. Explanations for the mixed alkali effect tend to involve the movement of the cations being hindered by either (i) the blocking of cation sites or (ii) phase separation at a microlevel (resulting from *like-pairing* Li-Li and K-K in M_2O silicates) [4]. However, in M_2O-MO silicates *mixed pairs* (e.g., Li-Ca) seem to form [53].

It has been reported that in mixed alkali melts the cation environment is affected by cation size [53]; both the (mean size of the cation site) and the coordination number (N_{coord}) increase with replacement by a smaller cation (e.g., K^{+} replaced by Li^{+}) [53]. It has been proposed when N_{coord} for one ion decreases there is an increase in the coordination of the other cation [4,53].

2.2.3.3. Effect of Temperature on Properties

Slag properties are very sensitive to temperature and this sensitivity increases with increasing polymerization of the melt. Increasing temperature tends to loosen the silicate structure (akin to the depolymerization caused by the addition of cations). Thus, the effect of increasing temperature on various properties can be predicted since it is equivalent

to depolymerization (i.e., it causes decreasing viscosity, electrical resistivity, and thermal conductivity).

2.2.3.3.1 Solid Slags

Solid slags can exist as *glassy* or *crystalline* phases or, in some cases as mixtures of glass and crystalline phases. The form of the slag is dependent upon (i) composition (glasses are promoted by a high Q value) and (ii) the thermal history of the sample.

Some slags can be produced in the form of a glass by rapid quenching of the melt. If the heat capacity of this glassy mold slag is measured during heating the following sequence of events occurs:

(i) There is a smooth increase in C_p until the temperature exceeds the glass transition temperature (T_g).

(ii) At T_g there is a "step increase" in C_p and a threefold increase in thermal expansion coefficient (α); these events are associated with the transition of the glass to an *scl* (Figure 2.2.23a).

(iii) In the case of some more basic slags an inverted peak in C_p can be observed (starting at about 100 K above T_g); this is due to partial crystallization of the mold slag (Figure 2.2.23b). (Note: crystallization is a first-order, exothermic transition and in differential scanning calorimetry (DSC) measurements, the exothermic, enthalpy of transition manifests itself as an *apparent* decrease in C_p.)

(iv) The mixture of (glass + crystalline) phases undergoes an endothermic transition at the solidus temperature of the slag (T_{sol}) when the crystalline phase starts to melt and this process (crystal → liquid) is complete when the temperature reaches T_{liq}; in contrast, the *scl* undergoes a smooth transition to liquid (Figure 2.2.24a).

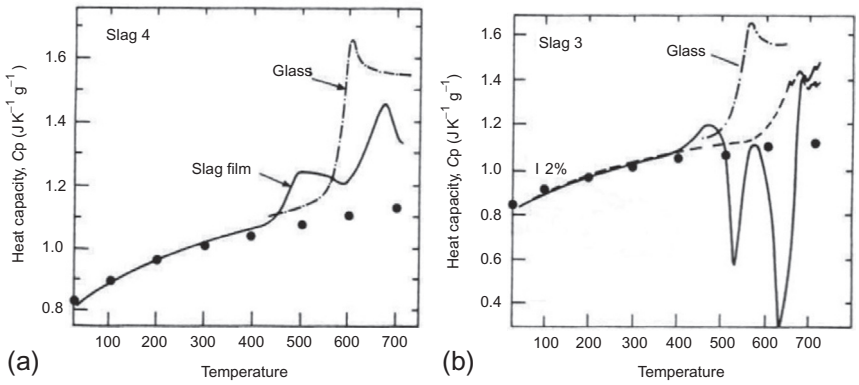


Figure 2.2.23 Apparent heat capacity as a function of temperature (T°C) glassy specimen derived from a partially crystalline slag film; ——= slag film; ---= glassy specimen; •= estimate (a) slag showing step increase in C_p at T_g for glassy and partially crystalline samples; and (b) a slag showing an apparent decrease in C_p resulting from crystallization [88].

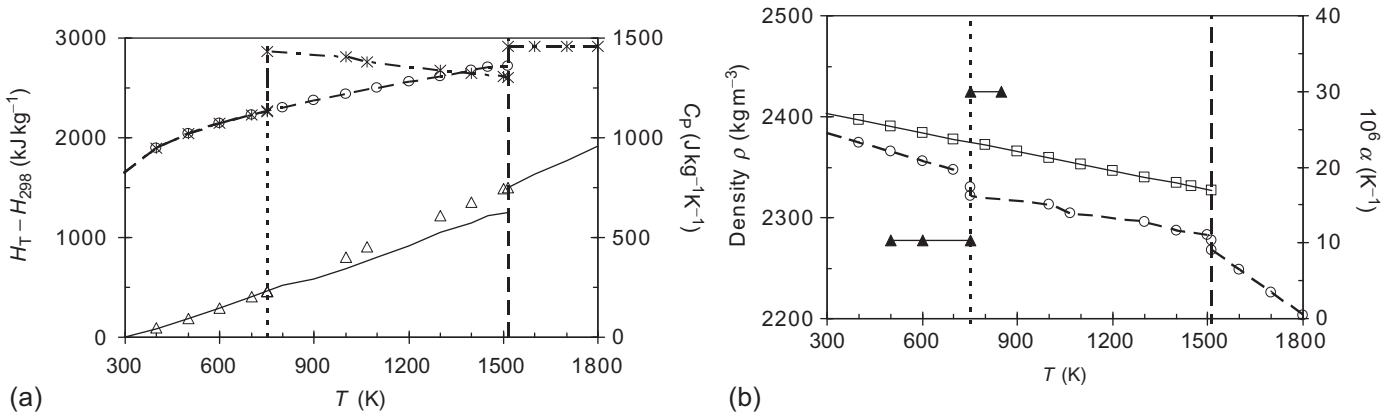


Figure 2.2.24 Schematic diagrams showing the effects of the glass transition on (a) C_p and enthalpy ($H_T - H_{298}$) C_p: —·—·, and × = *scl*; o and solid line = glass and crystalline phase and ($H_T - H_{298}$): solid line = glass, crystalline, and liquid phases; Δ = *scl*; and (b) density and thermal expansion coefficient, α; density □ = crystalline phase; glass and *scl* and liquid phases; α; ▲ = glass and *scl* phases.

(v) As mentioned above in (ii) the thermal expansion coefficient (α) exhibits a threefold increase at T_g when the frozen glass transforms to an *scl* (Figure 2.2.24b); thus, the density of the crystal is higher than that of the *scl* in the temperature range between T_g and T_{sol} (Figure 2.2.24b).

The (crystal → liquid) transition is accompanied by an enthalpy of fusion and a change in volume (or density) whereas the equivalent values (*scl* → liquid) transition are zero or very low.

2.2.3.3.2 Liquid Slags

When a molten slag is cooled below T_{liq} it forms either crystallites or an *scl* depending upon both the slag composition and the cooling rate. If viscosities are measured in the cooling cycle, when solid particles (crystallites) are formed (Figure 2.2.17a) there is a sharp increase in viscosity and the slag exhibits non-Newtonian behavior (i.e., measured viscosities differ for different rotation speeds). In contrast, when a liquid slag transforms to an *scl* it is accompanied by a smooth increase in viscosity (Figure 2.2.17b) until the temperature reaches the glass transition temperature, T_g (at T_g $\log_{10}\eta$ (dPas) = 13.4).

2.2.4. PROPERTIES OF SLAGS BASED ON SILICATE NETWORK

Slag properties have been classified here into the following four groups: (i) thermodynamic properties, (ii) flow and transport properties, (iii) heat transfer properties, and (iv) optical properties.

2.2.4.1. Thermodynamic Properties

In this section on thermodynamic properties, the comments are largely directed toward how these properties are influenced by the structural nature of the slag and how approximate values of the properties can be calculated.

Thermodynamic properties are exceedingly important since the thermodynamics of the system determines the viability of any proposed reaction and provides indications of the optimum conditions for the process. Commercial software packages are available to calculate the thermodynamic properties of multicomponent slags and their databases cover most slag constituents, e.g., [89–91]. These thermodynamic models are powerful tools and thermodynamic properties calculated with these models are more accurate than values derived by partial molar methods described below.

Thermodynamics provides a measure of bond strengths and thus several thermodynamic models can be used to calculate the concentrations of O^0, O^-, and O^{2-} present in the slag [41–43,89–91]. Recently, a simple model based on mass balances has been used to calculate these quantities [44,281–283].

Since thermodynamic models can provide structural information, it is not surprising that one approach to modeling physical properties involves the use of thermodynamic relationships [89–94].

2.2.4.1.1 Liquidus Temperature (T_{liq})

Phase diagram information is essential for the design and optimization of processes and sorting out process problems. There are extensive miscibility gaps in the high-SiO_2 regions of the CaO-SiO_2, MgO-SiO_2, FeO-SiO_2, and MnO-SiO_2 systems and there is an extensive miscibility gap in the TiO_2-SiO_2 system [7].

2.2.4.1.1.1 The Importance of T_{liq} in Industrial Processes

The liquidus temperature of the slag is possibly the most important property to the process engineer since it is essential to maintain a liquid slag in most processes and disasters can occur if the slag freezes in the vessel. Many workers have used the value at T_{liq} as a reference to compare property values, e.g., viscosity at T_{liq} ($\ln \eta^m$) as a function of (NBO/T), Q or optical basicity, etc. One consequence of this practice is that a reliable value for T_{liq} is essential.

2.2.4.1.1.2 Factors Affecting T_{liq}

The liquidus temperature is a thermodynamic quantity. The liquidus temperatures of binary silicate slags are affected by the M^+—O^- bond strength of the NBO bonds (which is referred to here as the field strength (z/r^2)). It can be seen from Figure 2.2.25b that T_{liq} values decrease as (z/r^2) decreases [37,86]. However, T_{liq} values are also affected by the nature of the phase formed.

Liquidus temperatures for MO-SiO_2 and M_2O-SiO_2 systems are shown in Figure 2.2.25. It should be noted that MO-SiO_2 systems tend to exhibit a miscibility gap at SiO_2-rich compositions.

2.2.4.1.1.3 Measurement Methods

A variety of techniques have been used to determine the melting range of slags. These techniques are outlined in Table 2.2.6.

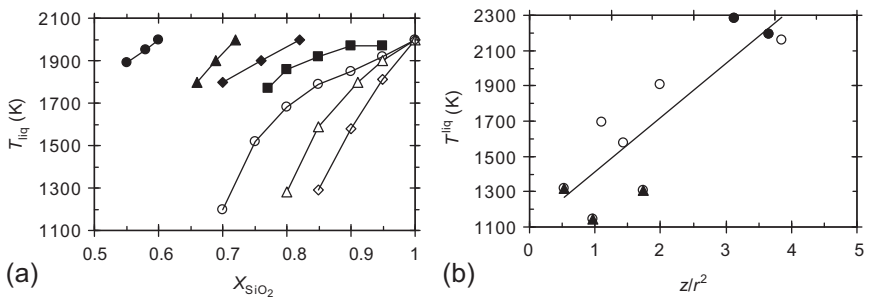


Figure 2.2.25 Liquidus temperatures of MO-SiO_2 and M_2O-SiO_2 systems as functions of (a) mole fraction of SiO_2; ◊ = KS; Δ = NS; ○ = LS; ■ = BS; ◆ = SrS; ▲ = CS; ● = MS and (b) field strength (z/r^2) of the cation, ●, ○ = MO-SiO_2; ▲ = M_2O-SiO_2.

Table 2.2.6 Methods used to determine liquidus temperature

Method	Details of method	Comments
Boat tests	Known mass of decarburized sample placed in combustion boats and then placed in a muffle furnace and allowed to come to thermal equilibrium at set temperature and quenched. Examined metallographically for evidence of melting	
Quench tests	As above but sealed in Pt tubes	Small sample may not be representative of slag bulk
Smith or single-pan calorimeter [94,95]	Two concentric crucibles with thermocouples placed on the walls. The temperature difference between inner and outer crucibles is monitored continuously. The sample is placed in the inner crucible. Measurements are made with the inner crucible (i) empty, (ii) filled with a calibrant of known C_p (e.g., Al_2O_3), and (iii) filled with the sample	Large sample
DTA/DSC	There are two pans, one holding the sample and the other a reference material. The pans sit in a metal block and are heated at a set heating rate and the temperature difference between these two pans is monitored continuously (Figure 2.2.26a). When a sample undergoes an exothermic or endothermic event there is departure from the baseline. For accurate temperature measurements, runs should be carried out with calibrants to (i) check the temperature scale and (ii) correct for heating rate A typical DTA/DSC output is shown in Figure 2.2.26b	Relatively small sample may not be representative of slag bulk Temperature range should be calibrated with materials of known T_{liq} T_{liq} values should be extrapolated to zero heating rate
Hot stage microscope [97]	The melted sample is placed in a loop in the thermocouple (which also acts as heating element) and is allowed to solidify. The sample is then heated at 5 °C min^{-1} and the specimen observed through a microscope. The sample is then cooled at 15 °C min^{-1} and monitored for the signs of precipitation	Tendency for undercooling

Continued

Table 2.2.6 Methods used to determine liquidus temperature—cont'd

Method	Details of method	Comments
Leitz microscope test DIN 51740 [98]	The shape of a pressed cylinder of decarburized powder is monitored as it is heated at a set heating rate. The temperatures where the sample takes up a set shape is determined; values of $T_{softening}$, $T_{hemisphere}$, and $T_{fluidity}$ are measured and subsequently, define the melting range (Figure 2.2.27). The melting temperatures obtained with this test tend to differ from the T_{liq} values measured by DTA/DSC	T_{liq} values tend to differ from T_{liq} values measured by DTA/DSC

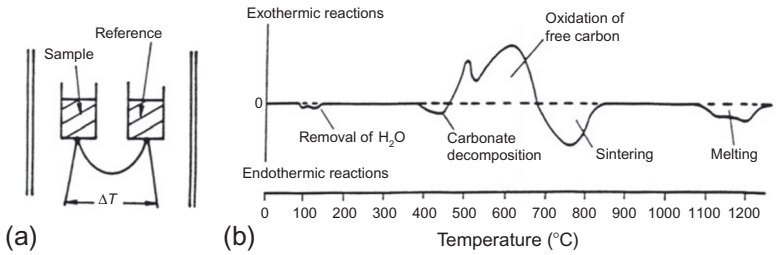


Figure 2.2.26 (a) Schematic diagram showing DTA apparatus and (b) typical DTA/DSC trace for a slag during heating.

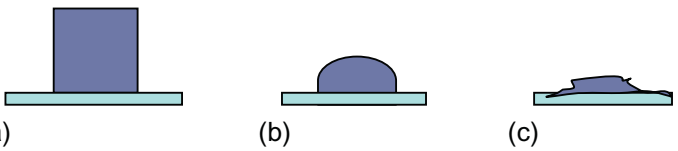


Figure 2.2.27 Schematic drawings showing typical shapes corresponding to (a) just before $T_{softening}$, where rounding of corners occurs, (b) $T_{hemisphere}$, and (c) $T_{fluidity}$ or flow point.

2.2.4.1.1.4 T_{liq} Data for Slags

A large amount of T_{liq} data can be found in the Slag Atlas, Chapter 4 [7] and phase diagrams for ceramists [99].

2.2.4.1.1.5 Calculation of T_{liq}

Commercial, thermodynamic software (e.g., [89–91]) provide reliable values for T_{liq} for multicomponent slags because they contain phase equilibrium data for the various phases formed.

Values of T_{liq} can be calculated by developing a large database of T_{liq} values for given slag compositions and deriving "best-fit" constants. Such methods reveal the trends of the

Table 2.2.7 Summary of methods for calculating liquidus temperatures

Sample type	Models/reference	Details, comments
Slags, glasses	Thermodynamic [100–102]	Reliable calculations for T_{liq}
Slags general	Numerical fit [103]	See Equation (2.2.16): subject to large uncertainty
Mold flux	Numerical fit [104]	$T_{liq}(K) = 1464 + 11.4\%SiO_2 - 11\%CaO + 4.2\%Al_2O_3 + 5.7\%MgO - 10.1\%Na_2O - 15.8\%K_2O + 1.9\%F + 8.3\%Fe_2O_3 + 11.6\%MnO$ (2.2.17) Subject to ±30 K

effects of different slag constituents on T_{liq}. However, they do not take the effects of individual phase fields into account which can lead to considerable errors in the predicted errors.

When these methods are applied to families of slags (e.g., mold fluxes) T_{liq} values with an uncertainty of ±30 K can be obtained because they tend to have similar phase fields. However, when these are applied to a wide range of slag compositions where the slags belong to a large number of phase fields (Equation 2.2.16 [87]) then the uncertainties in the calculated T_{liq} values are ca. ±100 K and in a few cases, several hundred degrees. The methods are summarized in Table 2.2.7:

$$\begin{aligned}\text{Slags in general}: \; T_{liq}(K) &= 958 + 656.9X_{SiO_2} + 1040.7X_{CaO} + 1343X_{Al_2O_3} \\ &+ 137X_{Na_2O} + 408.7X_{Li_2O} - 668X_{K_2O} + 1091X_{MgO} \\ &- 532X_{CaF_2} + 761X_{MnO} + 522X_{FeO} + 1022X_{CrO} \\ &+ 2198X_{Cr_2O_3} + 1768X_{SrO} + 1207X_{BaO} + 844X_{TiO_2} \\ &+ 2234X_{ZrO_2} + 794X_{Fe_2O_3} - 12.6X_{B_2O_3} \end{aligned} \quad (2.2.16)$$

2.2.4.1.2 Activity Coefficients and other Thermodynamic Properties

2.2.4.1.2.1 Why Thermodynamic Property Data are Needed

The viability of various slag/metal reactions is determined by the change in free energies between the products and reactants. Free energies, in turn, are affected by the configurational entropies of the phases involved. Heat capacity and enthalpy data are needed for carrying out heat balance calculations for the process and they provide insight into the nature of the disorder in the silicate melt.

2.2.4.1.2.2 Factors Affecting Activities and Other Thermodynamic Functions

Activity data for silicates and aluminosilicates tend to be scarce but data are available for the M_2O-SiO_2 and MO-SiO_2 binary systems. The data are presented in Figure 2.2.28a where the dashed lines represent the large miscibility regions in the MO-SiO_2 systems. It can be seen from Figure 2.2.28a that the activity coefficient of SiO_2 ($f^*_{SiO_2}$) decreases as [105]:

(i) The mole fraction of SiO_2 decreases.

(ii) The M^+—O^- bond strength (as represented by z/r^2) increases [105].

For further discussion of the activity data, the reader is directed to Mysen and Richet, Chapter 6 [63].

The introduction of Al^{3+} into the silicate network results in a further decrease in the $\ln f^*_{SiO_2}$. It can be seen from Figures 2.2.28b and c that $\ln f^*_{SiO_2}$ for aluminosilicates:

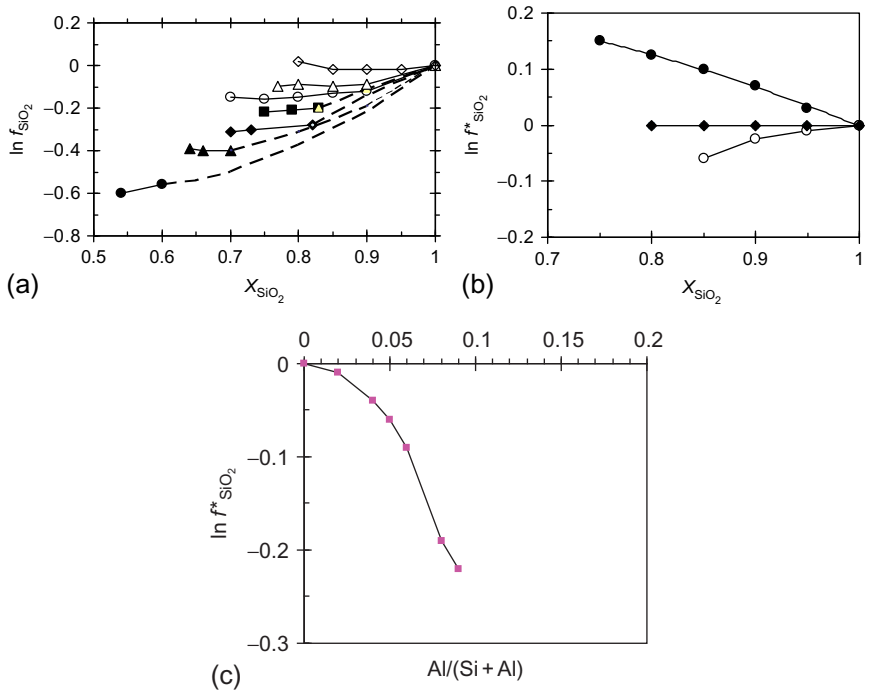


Figure 2.2.28 Logarithm of activity coefficient of SiO_2 ($\ln f^*_{SiO_2}$) for (a) MO-SiO_2 and M_2O-SiO_2 slags at 1823 K [105]; ●=MgO; ▲=CaO; ♦=SrO; ■=BaO; ○=Li_2O; Δ=Na_2O; ◊=K_2O; dashed lines=extrapolations; (b) meta-aluminous M_2O (or MO)-Al_2O_3-SiO_2 systems as a function of X_{SiO_2} ●=CaO; ♦=Na_2O; ○=K_2O [105]; and (c) meta-aluminous M_2O-Al_2O_3-SiO_2 systems as function of (Al/Al + Si) where M=Na or K where $Al/(Al+Si) = 2X_{Al_2O_3}/(2X_{Al_2O_3} + X_{SiO_2})$ [63].

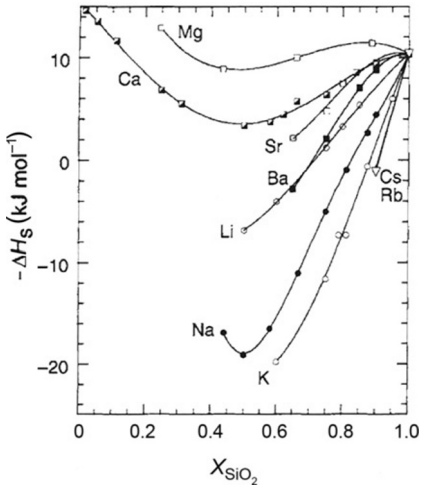


Figure 2.2.29 The enthalpy of solution (in liquid lead borate at 973 K) for meta-aluminous M_2O-Al_2O_3-SiO_2 and MO-Al_2O_3-SiO_2 systems (i.e., where X_{MO} or $X_{M_2O} = X_{Al_2O_3}$) [36,63].

(i) decreases as (z/r^2) increases for the cation doing the charge balancing (Figure 2.2.28b).

(ii) decreases as the ratio $\mathrm{Al}/(Al+\mathrm{Si})\{=2X_{\mathrm{Al_2O_3}}/(2X_{\mathrm{Al_2O_3}}+X_{\mathrm{SiO_2}})\}$ increases for a meta-aluminous M_2O-Al_2O_3-SiO_2 melts, where M = Na or K.; it can also be seen that the activity coefficient is little affected by the nature of the cation.

The enthalpy of solution values for meta-aluminous M_2O-Al_2O_3-SiO_2 and MO-Al_2O_3-SiO_2 systems are shown in Figure 2.2.29 [36,63]. It can be seen that:

(i) the negative enthalpy of mixing indicates that there is strong affinity between the components (note the positive enthalpy for Mg, Ca, Sr at high X_{SiO_2} where phase separation occurs)

(ii) the nature of the cations affects the stability of the melt (K > Na > Li ≈ Ba > Sr > Ca > Mg), i.e., in order of diminishing (z/r^2).

This suggests that the melt becomes more stable when charge compensation is carried out by cations with low values of (z/r^2) (K > Na > Li ≈ Ba > Sr > Ca > Mg).

2.2.4.1.3 Heat Capacity (C_p) ($H_T - H_{298}$), Entropy, Entropy of Fusion (ΔS^{fus})

2.2.4.1.3.1 Factors Affecting C_p and Enthalpy

The C_p of glassy samples of glasses or glassy slags show a "step-like" increase at T_g which is associated with the transformation of a glass to an *scl*; this can be seen in the dashed line in Figure 2.2.23a [88]. The twin valleys in the *apparent* C_p-T curve shown in Figure 2.2.23b indicate that further crystallization of the sample occurs above 500 °C in this sample. The decrease is not a true effect but is the exothermic, enthalpy of crystallization (ΔH_{crys})

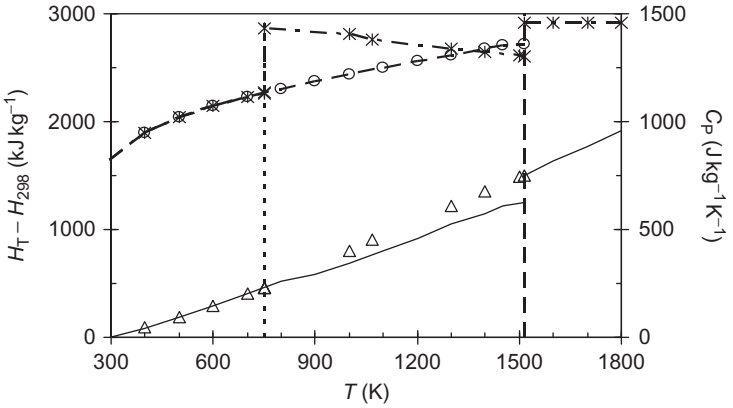


Figure 2.2.30 The C_p (upper curves) and enthalpy ($H_T - H_{298}$) as functions of temperature for glass, *scl*, and crystalline phases; C_p curves: × = *scl* and liquid; ○ and solid line = glass and crystalline phase and ($H_T - H_{298}$) curve: solid line = glass, crystalline, and liquid phases; Δ = *scl*.

which manifests itself as an apparent decrease in C_p. Values for ΔH_{crys} can be derived by integrating the area under the curve.

The different C_p values for *scl* are greater than those for crystalline specimens for the region between T_g and T_{sol} and the C_p and enthalpy values for partially crystalline samples will fall between the two curves (Figure 2.2.30) since the overall C_p will depend upon the fraction of the slag which has crystallized.

It can be seen from Figure 2.2.31 that the entropy of fusion (ΔS^{fus}) of the *crystalline phase* shows the expected result, i.e., that ΔS^{fus} increases with increasing $M^+—O^-$ bond strength (represented by z/r^2) [37]. It is considered here that for the transition, *scl* → liquid, ΔS^{fus} has a zero, or low, value. It is known from structural studies that the disorder (or configurational entropy) in silicate melts is higher for cations with high field strength (z/r^2). Thus, the ΔS^{trans} for *scl* → liquid transition will be lower for melts containing cations with lower (z/r^2) values.

2.2.4.1.3.2 Measurement Methods

Values of C_p and enthalpy can be determined using a variety of calorimeters. However in practice, the principal methods employed are DSC, drop calorimetry (or a combination of both), and Calvet calorimetry since these are available commercially. Experimental uncertainty is about ±2% for the solid phase but may be higher at higher temperatures with these techniques.

2.2.4.1.3.3 Differential Scanning Calorimetry

The principles underlying DSC are similar to those given above (in Table 2.2.6) and Figure 2.2.26. The sample (in the form of a disc or loose powder) is placed in one crucible and the other crucible is kept empty. The instrument is then heated at a set heating rate.

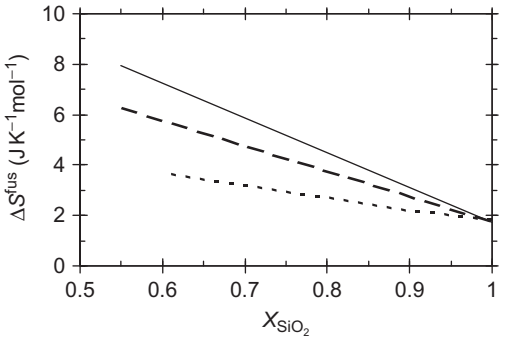


Figure 2.2.31 The effect of mole fraction SiO_2 on (*a*) entropy of fusion; solid line = LS; dashed line = NS; dotted line = KS [37,86].

The sample requires more energy than the empty crucible and thus the temperature of the sample crucible lags behind the empty crucible. This temperature difference is monitored. Three sets of measurement runs are made with the sample crucible: (i) empty, (ii) filled with a known mass of sample (m_{sample}), and (iii) with a sapphire (Al_2O_3) disc of known mass ($m_{Al_2O_3}$). The $C_{p\ sample}$ can be calculated from the difference in signals (S), i.e., ($S'_{sample} - S'_{empty}$) and ($S'_{Al_2O_3} - S'_{empty}$) and m_{sample} and $m_{Al_2O_3}$ [106]. This type of DSC is usually denoted as differential scanning temperature calorimetry. However, there is a second type of DSC in which the power required to keep the two crucibles at the same temperature is monitored (differential scanning power calorimetry) [106].

The enthalpy can be calculated by integration of the C_p values for the solid and liquid phases:

$$(H_T - H_{298}) = \int_{T_1}^{T_2} C_p \, dT \tag{2.2.18}$$

The enthalpy of fusion (ΔH^{fus}) can be derived by extrapolating the ($H_T - H_{298}$) values for both the solid and liquid phases to T_{liq} and determining the difference

$$\Delta H^{fus} = \left\{ (H_T - H_{298})_{liq}^{T_{liq}} - (H_T - H_{298})_{sol}^{T_{liq}} \right\} \tag{2.2.19}$$

The entropy of fusion can be calculated using the following equation:

$$\Delta S^{fus} = T_{liq} \Delta S^{fus} \tag{2.2.20}$$

2.2.4.1.3.4 Drop Calorimetry

The sample, of known weight, is placed in a Pt crucible and heated to the required temperature until the temperature has equilibrated. The gate separating the furnace from the calorimeter is then opened and the sample is dropped into a massive, silver or copper

calorimeter held at constant temperature and then the gate is closed. The temperature rise (<5 K) is then measured accurately and converted into enthalpy ($H_T - H_{298}$) using the mass and heat capacitance of the calorimeter. A series of blank experiments are carried out with the empty crucible and the enthalpy of the blank for the measuring temperature is then subtracted from that for the (crucible + sample). Values of the C_p sample at 25 K are needed to differentiate the enthalpy values to obtain C_p values; the most accurate data are obtained by combining the drop calorimetry data with C_p values obtained by DSC. The enthalpy of fusion (ΔH^{fus}) can be determined using Equation (2.2.19).

However, one problem in using drop calorimetry is that quenching results in the formation of the glassy phase and not the crystalline phase which has a lower entropy and is the reference state. Typical experimental uncertainties are ±2% but these errors associated with the configurational entropy may result in slightly higher uncertainties.

2.2.4.1.3.5 Calvet Calorimetry

Two matched crucibles are placed in an isothermal block. The temperature difference between each crucible and the block is measured accurately by thermopiles (i.e., a collection of thermocouples). Commercial Calvet calorimeters are available. The calorimeter can be operated in two ways: (i) in the *scanning mode* (i.e., similar to that for DSC) or (ii) in the *isoperibol mode* where $T_{sample} - T_{block}$ is kept constant. Usually a calibrant of known C_p is placed in the reference crucible and the temperature differences for both sample and reference pans with the block are monitored (Figure 2.2.32).

2.2.4.1.3.6 Single Pan (Smith) Calorimetry

This technique was developed by Smith [95]. It can be seen from Figure 2.2.33 that a crucible is placed inside a second crucible [96]. Thermal insulation is placed between the outer crucible and the furnace and between the two crucibles. This assembly is placed in a furnace. Thermocouples are sited in the center of the sample (or calibrant) and in the walls of the two crucibles. The calorimeter is run and temperatures are monitored for (i) the crucible empty (T_E), (ii) the crucible filled with a calibrant (T_C), and (iii) the crucible + sample (T_S) as a function of time. When heat is applied for time, dt, the temperature rises dT_E, dT_C, and dT_S are determined from the slopes of dT as

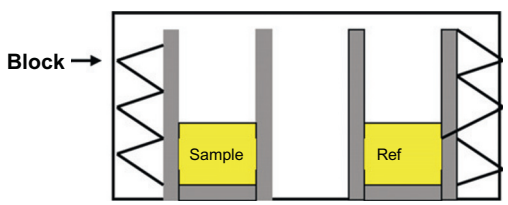


Figure 2.2.32 Schematic diagram showing setup of a Calvet-type calorimeter.

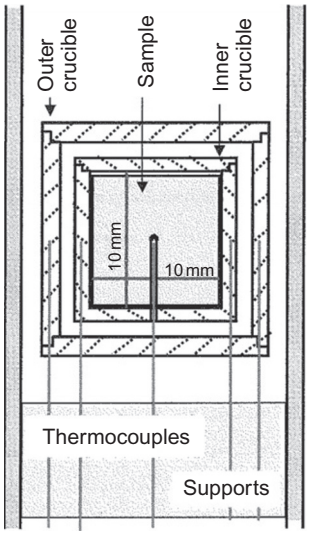


Figure 2.2.33 Schematic drawing showing experimental setup of a single-pan (or Smith) calorimeter [96].

a function of time. The temperature difference between the thermocouples located in the inner and outer crucibles (ΔT_D) is determined for the empty (ΔT_{DE}), calibrant (ΔT_{DC}), and sample (ΔT_{DS}). The C_p of the sample can be calculated from the equation [96]

$$C_{pS}\,dT_S = dH_S = C_{pC}\{\Delta T_{DS} - (\Delta T_{DE}\,dTS/dTE)\}/\{(\Delta T_{DC}/dT_C) - (\Delta T_{DE})/dT_E)\} \quad (2.2.21)$$

2.2.4.1.3.7 C_p and Enthalpy Data for Slags

C_p values have been reported for silicates and compilations of data are given in Table 2.2.8. Examples of the C_p results obtained by DSC are shown in Figure 2.2.23.

2.2.4.1.3.8 Calculation of C_p and Enthalpy

The reported models for calculating heat capacity (C_p) and enthalpy ($H_T - H_{298}$) are outlined in Table 2.2.9.

2.2.4.1.3.9 Entropy of Fusion (ΔS^{fus})

The entropy at temperature, T, is given by Equation (2.2.27) and the entropy of fusion is given by the difference of entropies of the solid and liquid at the melting temperature (Equation 2.2.28):

Table 2.2.8 Details of investigations used to measure C_p and enthalpies of slags; drop cal = drop calorimetry

Specimen/ {phase}	Reference	Method	Comments
Slags Glasses	Kelley [107]	Drop cal	Contains data for a number of slag and glass systems
Magmatic melts	Carmichael *et al.* [108]	DSC	C_p values higher for melts with cations with high field strength (z/r^2) values
Mold flux	Mills *et al.* [109]	DSC+	10 samples
	Monaghan and Brooks [110]	DSC	
ESR fluxes	Gohil and Mills [111]	Drop cal+DSC	Samples high CaF_2 contents
Coal slags	Rhine *et al.* [112]	DSC+drop cal	Data used to develop estimation routines for C_p and $(H_T - H_{298})$

$$S_T = \int_0^T \left(C_p/T\right) \mathrm{d}T \tag{2.2.27}$$

$$\Delta S^{fus} = \left(S_{T_{liq}}\right)_{liq} - \left(S_{T_{solid}}\right)_{liq} = \Delta H^{fus}/T_{liq} \tag{2.2.28}$$

It should be noted that silicates tend to melt over a temperature range, so strictly the above equations should be carried out at a temperature of 0.5 $(T_{liq} + T_{sol})$ where T_{sol} is the temperature where melting begins.

The entropy of fusion relates primarily to crystalline silicates. Glasses disorder into a *scl* at T_g and continue to disorder further between T_g and T_{liq}. In contrast, crystalline silicates do not disorder abruptly at T_g and have a significantly lower C_p than that of the glass between T_g and T_{liq}. The disorder of the crystalline sample occurs suddenly at T_{liq} in the form of entropy of fusion (Figure 2.2.30). The entropy of fusion of Li-, Na-, and K-silicates are plotted in Figure 2.2.31 and it can be seen that ΔS^{fus} increases:

(i) as the SiO_2 content decreases

(ii) in the order Li > Na > K (i.e., $\Delta S^{fus} \uparrow$ as $(z/r^2) \uparrow$)

2.2.4.2. Flow and Transport Properties

This category of properties includes the viscosity, electrical conductivity (or resistivity), and diffusion coefficient. These properties relate to momentum transfer, electrical transfer, and mass transfer, respectively. The three properties are linked here because the silicate structural units (anions) tend to resist, or impede, movement. However, in

Table 2.2.9 Details of published models to calculate C_p and enthalpies ($H'_{T_K}-H_{298}$) of mold?fluxes

Model/reference	Details of model	Uncertainties
Thermodynamic models [89–91,100–102]	Commercial thermodynamic models, such as factsage; MTDATA and thermocalc, provide accurate thermodynamic data for slag systems	
Partial molar model [113,114]	C_p is little affected by the polymerization. Thus, C_p values can be calculated from partial molar C_p's for the slag constituents. The temperature dependence of C_p can be expressed in the form: $$C_p = a' + b' T_K + c'/T_K{}^2 \quad (2.2.22)$$ The constants for the slag, a', b', and c' can be calculated from the values for the various constituent oxides, e.?g., as shown for a' in Equation (2.2.23): $$a' = \sum (X_{CaO} a'_{CaO}) + (X_{SiO_2} a'_{SiO_2}) + (X_{Al_2O_3} a'_{Al_2O_3}) + (X_{CaF_2} a'_{CaF_2}) + \cdots \quad (2.2.23)$$ Values for C_p of the liquid phase can be calculated from the following equation: $$C_{p\ liq} = \sum \left(X_{CaO} C_{p\ liq\ CaO}\right) + \left(X_{SiO_2} C_{p\ liq\ SiO_2}\right) + \left(X_{Al_2O_3} C_{p\ liq\ Al_2O_3}\right) + \left(X_{CaF_2} C_{p\ liq\ CaF_2}\right) + \cdots \quad (2.2.24)$$ Values for a', b', c', and $C_{p\ liq}$ for the various constituents of mold slags given in Ref. [113,114] Values for the enthalpy ?$(H_T - H_{298})$ can be calculated from Equation 2.2.25 where T is in K $$(H_T - H_{298}) = \int_{298}^{T} C_p d'T = a(T_K - 298) + 0.5bT_K{}^2 - 0.5b(298)^2 - (c/T_K) + (c/298) \quad (2.2.25)$$ Enthalpy of fusion (ΔH^{fus}) is calculated from entropy of fusion (ΔS^{fus}) where T is in K $$\Delta S^{fus} = \sum \left(X_{CaO} \Delta S^{fus}_{CaO}\right) + \left(X_{SiO_2} \Delta S^{fus}_{SiO_2}\right) + \left(X_{Al_2O_3} \Delta S^{fus}_{Al_2O_3}\right) + \left(X_{CaF_2} \Delta S^{fus}_{CaF_2}\right) + \cdots$$ $$\Delta S^{fus} = T_{liq} \Delta S^{fus} \quad (2.2.26)$$	±2%
Stebbins *et al.* [115]	Partial molar approach; $C_p = a' + b'T + c''T^{-2} + d'T^{-0.5}$; values or a', b', c', and d' calculated from partial molar quantities	

the case of electrical and diffusion coefficient the properties are also affected by other factors, namely, the *concentrations* and *mobility* of the cations.

2.2.4.2.1 Viscosity (η)

2.2.4.2.1.1 Why Viscosity Data are Needed

The slag viscosity, along with the liquidus temperature, is probably the most valuable property in industrial, high-temperature processes. Slag viscosity is important since it determines the ease of draining the slag from the vessel. In the continuous casting of steels, the slag viscosity is the most important property because it affects [116]:

(i) the lubrication supplied to the newly formed, steel shell which is proportional to $(1/\eta)$

(ii) the SEN erosion rate is proportional to $(1/\eta)$, and

(iii) slag entrapment in the metal where high-viscosity fluxes are sometimes used to minimize this problem.

2.2.4.2.1.2 Factors Affecting Viscosity

The viscosity is very dependent upon the degree of polymerization of the slag. In fact, the viscosity has been used by some workers to represent the slag structure. The principal factor affecting the viscosity is the degree of polymerization (Q) as can be seen from Figure 2.2.7. The viscosity also exhibits a small increase with increasing cation size for ($K^+ > Na^+ > Li^+$) for both liquid and *scl* phases but the hierarchical trend is less obvious for MO silicates (where M = Mg, Ca, Sr, and Ba) [87]. It has been reported that there was less scatter in ln η (at a fixed temperature, e.g., 1900 K)-Q plots than for equivalent plots for values at T_{liq} [86].

The viscosity increases with (i) increasing concentrations of *network formers* (e.g., SiO_2 and Al_2O_3), (ii) decreasing concentrations of both *network breakers* (e.g., CaO, MgO, MnO and FeO, Na_2O, K_2O, Li_2O), and (iii) *fluxes* (e.g., CaF_2 and B_2O_3).

In aluminosilicates the charge balancing of the Al^{3+} by a Na^+ or 0.5 Ca^{2+} is important and since the cation on charge-balancing duties cannot act as a network former, Al substitution leads to more polymerization and hence higher viscosities. A maximum in the viscosity $-Q$ plot occurs at close to $Q = 4.0$ [76] (i.e., where there are just enough Na^+ ions to charge balance the Al^{3+} ions). However, Toplis *et al.* [77] found that this maximum occurred slightly away from the point where $Q = 4$, i.e., at $(X_{Na}/(X_{Na} + X_{Al}) = 0.45$.

2.2.4.2.1.3 Methods Used to Determine Viscosity

Several methods have been used to measure slag viscosities, these are detailed below. Some of the classical methods of measuring viscosity (e.g., capillary viscometry) are rarely used because of the difficulty of obtaining a uniform temperature zone of sufficient length at the required temperatures.

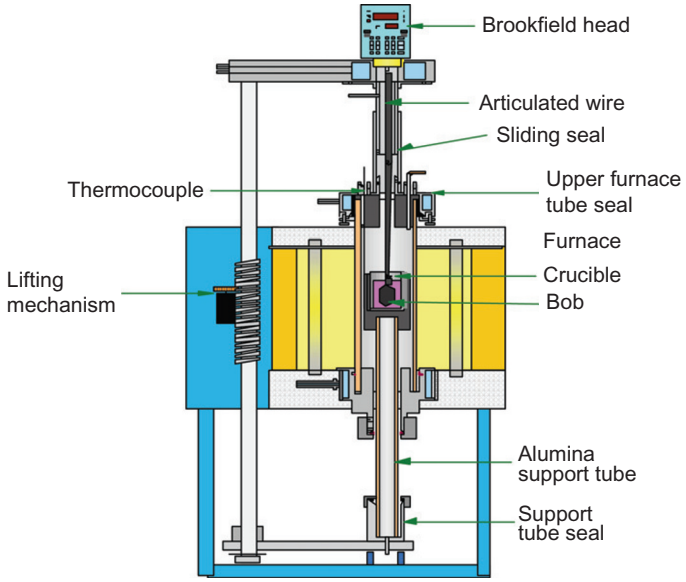


Figure 2.2.34 Schematic diagram showing the rotating bob (or cylinder) method. *Courtesy of P Quested and RF Brooks, NPL.*

2.2.4.2.1.4 Concentric Cylinder Method

These viscometers consist of two concentric cylinders, namely, the crucible (holding the molten sample) and the bob (Figure 2.2.34). When one of these cylinders is rotated at constant speed, the viscosity can be determined from measurements of the torque developed [7,117].

It is difficult to obtain the accurate alignment of the two cylinders but the viscosity of most slags is usually high enough to ensure self-centering of the bob; it is for this reason (i.e., ease of alignment) that the rotating bob (or cylinder) method is the more popular method.

2.2.4.2.1.5 Oscillating Plate Method

The oscillating plate method has been used to measure the viscosities of mold fluxes [118,119]. A plate is immersed in the melt and undergoes vertical oscillations in the fluid (Figure 2.2.35). When steady state has been established the amplitude of the oscillations is determined in both the fluid (φ) and in the gaseous atmosphere (φ_{atm}). Care must be taken to ensure "backwash" from the crucible walls does not affect the results. The method gives values for the product ($\rho \cdot \eta$) and so values of the slag density (ρ) are needed to calculate the viscosity (η).

$$\eta \cdot \rho = G\{(\varphi_{atm}/\varphi) - 1\} \tag{2.2.29}$$

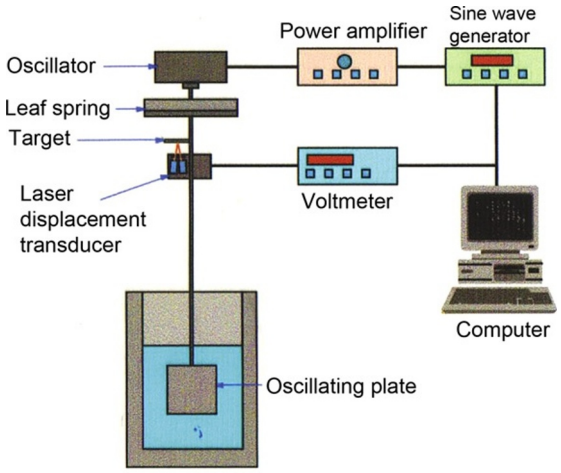


Figure 2.2.35 Schematic drawing of the oscillating plate method [118,119]. *Courtesy of P Quested and RF Brooks, NPL.*

where G is a cell constant which is determined in calibration experiments with liquids of known viscosity.

2.2.4.2.1.6 Falling Ball Method

In this method, the time is measured for a sphere to travel through a known distance in the slag; this can be done by either (i) letting a ball fall or (ii) dragging a wire attached to the sphere vertically through the melt [7]. The principal problem lies in the difficulty of obtaining a zone of uniform temperature of sufficient length at high temperatures. The viscosity is calculated from the following equation where g is the gravitational constant, r_{sph} and v_{sph} are the radius and velocity of the sphere, ρ is the viscosity, and subscript fl refers to the slag sample:

$$\eta = 2g{r^2}_{\mathrm{sph}}\left(\rho_{\mathrm{sph}} - \rho_{\mathrm{fl}}\right)/V_{\mathrm{sph}}. \tag{2.2.30}$$

2.2.4.2.1.7 More Recent Methods

The *draining crucible* (*DrCru*) method [120] and the *SLLS* (*surface laser light scattering* [121–123]) method have not been applied yet to slag systems but would appear to be viable methods for measurements on these systems. In the first technique the sample is allowed to drain through an orifice of known diameter and the rate of mass loss is recorded. The viscosity, surface tension, and density can be derived from hydrodynamic analysis of the data [120].

In the *SLLS* method "ripplons" are monitored [121–123]. The surface of a melt may appear smooth but it is being continually deformed by thermal fluctuations of the

molecules. Capillary waves (*ripplons*) have small amplitudes (ca. 1 nm) and a wavelength of ca. 100 μm which is dependent upon the frequency. Ripplon action depends upon surface tension for restoration and the kinematic viscosity ($v = \eta/\rho$) for oscillation damping. The spectrum of the *ripplons* is derived using a Fourier spectrum analyzer allowing the surface tension and the viscosity to be determined. The method has been successfully used for measurements on liquid silicon [122] and $LiNbO_3$ [123] up to 1750 K. It has been estimated that it can be used for liquids with viscosities in the range 0.005–10 dPas [121] which covers most of the viscosity range for industrial slag systems. However, a value of the density is required to calculate the dynamic viscosity (η).

The advantages of these methods are that they also provide simultaneous values of the viscosity and other properties (density and surface tension with the draining crucible method and surface tension with SLLS method).

2.2.4.2.1.8 Inclined Plane Test

This simple test has been used to measure viscosities as quality assurance tests for mold flux supplies. In this test 10 g of decarburized sample is weighed into a carbon crucible and it is then placed in a muffle furnace at the required temperature for about 15 min for temperature equilibration [124]. It is then removed from the furnace and poured onto a V-shaped inclined plane (usually an incline of 9°) where it forms a slag ribbon. The length (L) of the solidified slag ribbon is then measured and is related to ($1/\eta$) (Figure 2.2.36). It is possible to obtain viscosities of reasonable accuracy with this method by taking suitable precautions and procedures [124]. The method is less successful at higher temperatures (>1700 K) because of the heat losses from the crucible during the pouring procedures.

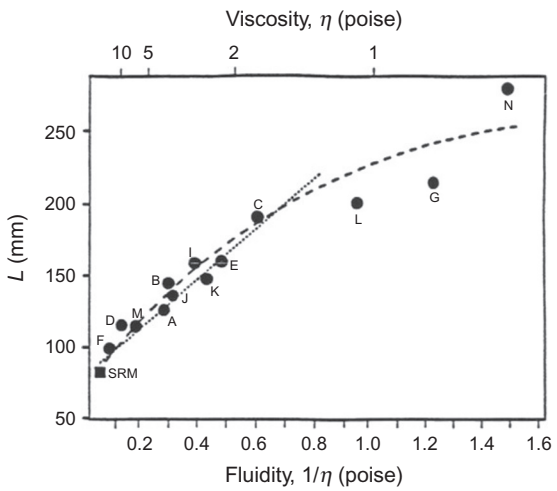


Figure 2.2.36 The length of the slag ribbon (L) as a function of the fluidity for inclined plane test [124]. *Note*: poise = 1dPas.

2.2.4.2.1.9 Viscosity Data for Slags

There have been a large number of determinations of viscosities of silicate slags and glasses. The Slag Atlas [7] contains a large amount of viscosity data at fixed temperatures for binary, ternary, quaternary systems and industrial silicate slags presented as a function of composition. Iida and Shiraishi [125] and Urbain *et al.* [126] have reported viscosity data obtained for a wide range of silicate slags in the form of Arrhenius parameters (A_η and B_η, i.e., Equation 2.2.12). Fluegel [127] reported references for viscosity data of some glass systems in the supercooled state and Dingwell [11,128] and Toplis *et al.* [77] have reported data for magmatic melts.

2.2.4.2.1.10 Methods of Calculating Viscosity Values from Composition

A number of models have been reported to estimate viscosities of slags from their chemical compositions. It is not possible to cover all the published models here but details of some of the models are summarized in Table 2.2.10; these estimated values are subject to uncertainties of *ca.* ±25%. In recent years commercial, thermodynamic models (e.g., [89–91]) have been extended to the calculation of viscosities (see Refs. [42,43,101,102,129]). These powerful tools can express the silicate structure in thermodynamic terms. The accuracy of their predictions lies in how well the selected thermodynamic functions represent the viscosity.

2.2.4.2.2 Electrical Conductivity (κ) and Electrical Resistivity (R)

Electrical conductivity involves the movement of cations through a silicate network when an electrical field is applied. A well-developed network will hinder their movement of these cations (see Figure 2.2.14b). The electrical resistivity ($R = 1/\kappa$) is the reciprocal of the conductivity. The most commonly used units are Ω^{-1} cm^{-1} for κ and Ω cm for R.

Since anions are polymeric they tend to be large and do not move readily, so the electrical conductivity is usually associated with the movement of the cations present, e.g., Na^+, Ca^{2+}, etc. Electrical resistivity ($R = 1/\kappa$) is the measure of the resistance to ionic transport provided by the molten slag.

The specific electrical conductivity (κ) is the conductivity of a 1 m^3 of the sample and is given by the relation:

$$\kappa = F\sum czu \tag{2.2.31}$$

where F is the Faraday constant and c, z, and u are the concentration, charge, and mobility of the ionic species.

The temperature dependence is usually represented by the Arrhenius equation:

$$\kappa = A_\kappa \exp(-B_\kappa/T) \tag{2.2.32}$$

where A_κ = constant; $B_\kappa = (E_\kappa/R^*)$, E_κ = activation energy, and R^* = gas constant = 8.314 J K^{-1} mol^{-1} and T in K.

Table 2.2.10 Summary of some of the models used to calculate viscosities of slags from chemical composition

Reference	Slag type	T-Dep	Details of model and comments	Δ%
Riboud *et al.* [130]	Various	Wey	A_W; B_W functions of five groups "CaO" + "SiO_2" + "Al_2O_3" + "CaF_2" + "Na_2O," where $X_{\text{"CaO"}}$ contains $X_{CaO} + X_{MgO} + X_{FeO} + X_{MnO}$, etc. $\ln A = -19.81 + 1.73X_{CaO} + 3.58X_{CaF_2} + 7.02X_{Na_2O} - 35.76X_{Al_2O_3}$ $B = 31{,}140 - 23{,}896\,X_{CaO} - 46{,}356X_{CaF_2} - 39{,}159X_{Na_2O} - 68{,}833X_{Al_2O_3}$ Works well (30%) for variety of slags	30
Urbain [8]	Various	Wey	A_W; B_W functions of three groups Glass formers: $X_G = X_{SiO_2} + X_{P_2O_5}$ Amphoterics: $X_{Al} = X_{Al_2O_3} + X_{B_2O_3} + X_{Fe_2O_3}$ Modifiers: $X_M = X_{CaO} + X_{MgO} + X_{Na_2O} + 3X_{CaF_2} + X_{FeO} + X_{MnO} + 2X_{TiO_2}$ $B_W = B_0 + B_1X_G + B_2{X_G}^2 + B_3{X_G}^3$ and $Bi = \alpha I + bi\alpha + ci\alpha i^2$ $\ln A_W = 0.2693B_W + 11.6725$. Special B_W values for MnO, MgO	25
Iida *et al.* [31]	Many	Arr	η (Pas) $= A\eta_0 \exp(E/\text{Bi})$, where η_0 is viscosity of hypothetical network-forming melt and Bi = basicity index, $E = 11.11\text{-}3.65 \times 10^{-3}$ T and $a = 1.745\text{-}1.962 \times 10^{-3}$ T $+ 7 \times 10^{-7}$ T^2 and Bi $= \sum(\alpha_i\%_i)_B / \sum(\alpha_i\%_i)_A$, where A = acid oxides and B = basic oxides or fluorides: $\eta = 1.8 \times 10^{-7}(MT^m)^{0.5} \exp(H_i/RT^m)/{V_m}^{0.667} \exp(H_i/RT^m)$, where $H_i = 5.1\ T^m$ and values of α given	25 19
Senior and Srinivasachar [131]	Coal	Wey	$A = a_0 + a_1B + a_2$ (NBO/T), where $a_0 = 2.816$, $a_1 = 0.4634$, and $a_2 = 0.3534$ $(\text{NBO/T}) = X_{CaO} + X_{MgO} + X_{Na_2O} + X_{FeO} + X_{MnO} - X_{Al_2O_3} + X_{Fe_2O3}/\{0.5(X_{SiO_2} + X_{TiO_2}) + X_{Al_2O_3} + X_{Fe_2O_3}\}$ Equations also given for low temperatures	

Continued

Table 2.2.10 Summary of some of the models used to calculate viscosities of slags from chemical composition—cont'd

Reference	Slag type	T-Dep	Details of model and comments	Δ%
Mills and Sridhar [35] Mills *et al.* [9]	Various	Arr	Optical basicity (Λ)—measure of depolymerization Composition adjusted for Al_2O_3 needed for charge balancing $\rightarrow \Lambda_{corr}$ ln A = − 232.7 $(\Lambda_{corr})^2$ + 357.3 (Λ_{corr}) − 144.2 ln $(B/100) = -1.77 + (2.88/\Lambda_{corr})$ ln η (Pas) = ln $A + \exp(B/T)$	34
		Arr	Based on the parameter, Q, a measure of the polymerisation	
Gupta *et al.* [132]	Mold fluxes	Arr	Three groups "Acidic": $Yx = (\%\ SiO_2/60) + \alpha\ (\%\ Al_2O_3/102)$ "Basic" $Y_O = (\%\ CaO/56) + (\%\ MgO/40) + (\%\ Na_2O/63) + (\%\ FeO/72)$ "Fluorides" $Y_F = (\%\ F/19)$: $N_F = Y_F/(Y_X + Y_O + Y_F)$ $N_X = Y_X/(Y_X + Y_O + Y_F)$: $N_O = Y_O/(Y_X + Y_O + Y_F)$ Na^+/Ca^{2+} affected η: values of a_0 to a_5 given for 1573 and 1673 K $\eta = a_0 + a_1(M^+/M^{2+}) + a_2N_X + a_3N_X(M^+/M^2) + a_4(M^+/M^2)^2 + a_5{N_X}^2$	35
Du *et al.* [92], Seetharaman [93,133]	Syn	Arr	$\eta = hN_A\ \rho/M \exp(\Delta G_\eta/RT)$, where h = Planck constant, N_A = Avogadro number Structure accounted for thermodynamics: $$\Delta G^*_\eta = \sum \Delta G^*_\eta(\text{oxides}) + \Delta {G_\eta}^{mix} + 3R^*TX_1X_2$$ $\Delta {G_\eta}^{mix}$ for interactions of cations only Works well for synthetic slags (±15%)	<20
Zhang *et al.* [42,43]	Various	Wey	Structure as N_O; N_{O^-}; $N_{O^{2-}}$ calculated from cell model (thermodynamic) A_W and B_W as functions of—N_O; $N_{O^{2-}}$ Molecular dynamics calculations Works well (20%) several slags	22

Zhang *et al.* [44,281–283]	Ternaries	Arr	Calculates N_O; N_{O^-}; $N_{O^{2-}}$ from mass and charge balances; uses Arrhenius equation and relation between ln A and B_η Applied to silicates, aluminosilicates, and slag systems containing CaF_2	
Tanaka *et al.* [134]	Syn	Arr	X_O; X_{O^-}; $X_{O^{2-}}$ calculated from thermodynamic cell model $N_{MO} = a^*(X_{O^-} + X_{O^2})$, where a^* is a measure of free space available and n is the frequency of the step in MO-SiO_2 system: a^* values: $Al_2O_3 = 0.95$; $MgO = 1.8$; $CaO = 2.0$; and $FeO = 3.8$ Multicomponent slags: $E_\eta = E_o/(1 + \Sigma\, a^* X_{O^-})^{0.5}$, where $E_o = E_\eta =$ for SiO_2	
Kondratiev and Jak [135] Jak [136]	Coal Syn	Wey	Modified Urbain method for $CaO + FeO + Al_2O_3 + SiO_2$ system Modification 1: $-\ln A = mB + Nn$; $n = 9.322$ but m is composition dependent $m = m_1X_1 + m_2X_2 + m_3X_3 + m_4X_4 + \cdots$ and values given for various m values Modification 2: Different B values given for FeO and CaO; constants given to calculate B values	25
Robinson *et al.* [100]	Syn	Arr	Uses thermodynamic software: data for binaries Based on Du and Seetharaman model	
Nakamoto *et al.* [137,138], Hanao *et al.* [139,140]	Syn Fe/Cr slag Mold flux		Neural network model based on experimental data	<22
Fluegel [127]	Glasses	VFT	Statistical "best-fit" model with various component interactions; *scl* and liquid	
Priven [141]	Glasses		Replaces chemical activities with empirical constants	

Arr, Arrhenius relation; Wey, Weymann relation; Emp, empirical relation; Syn, synthetic slag; T-Dep, temperature dependence; BF, blast furnace slags: $\Delta\% = (\Sigma\, \delta_n\%)/N$, where $\delta\% = 100\{(\eta_{meas} - \eta_{calc})/\eta_{meas}\}$ and N = number of measurements.

$$\ln \kappa = \ln A_\kappa - (B_\kappa / T) \tag{2.2.33}$$

and for the resistivity

$$\ln R = \ln A_R + (B_R / R * T) \tag{2.2.34}$$

When a metallic electrode is submerged in a molten electrolyte there is a potential difference across the interface. One phase acquires a positive charge and the other a negative charge. The Helmholtz model assumes a layer of charge at the electrode surface to which ions of the opposite charge in the electrolyte are rigidly held (Figure 2.2.37a) and is equivalent to a simple parallel plate capacitor. In the Stern model, the charges are adsorbed on the electrode surface and are rigidly fixed there by the presence of an immobile layer of oppositely charged ions in the melt (Figure 2.2.37b). The Stern model allows for the thermal motion of ions.

The specific electrical conductivity is also referred to the *ionic conductivity* (denoted κ_{ion}) in order to distinguish it from the *electronic conductivity* (κ_{elect}). The electronic conductivity occurs by a different mechanism and has been identified in silicate melts containing transition metal oxides (e.g., it has been observed in FeO-SiO_2, FeO-CaO, FeO-CaO-SiO_2, FeO-MnO-SiO_2, and FeO-CaO-MgO-SiO_2 systems). Electronic conduction involves a mechanism of "charge hopping." Take, e.g., a FeO-Fe_2O_3-SiO_2 melt, when increasing temperature and thermal excitation frees an electron; this electron can jump from a Fe^{2+} ion to a Fe^{3+} ion [142,143]. Since both Fe^{2+} and Fe^{2+} ions are needed for this mechanism to occur it follows that the mechanism does not occur when one species is missing.

2.2.4.2.2.1 Why Electrical Conductivity and Resistivity Data are Needed

The electrical resistivity is a key factor in determining the design of the power requirements in an electrical slag resistance furnace [144]; typical examples of slag resistance furnace are those used in electrical steelmaking, electro-slag remelting (ESR), and smelting operations.

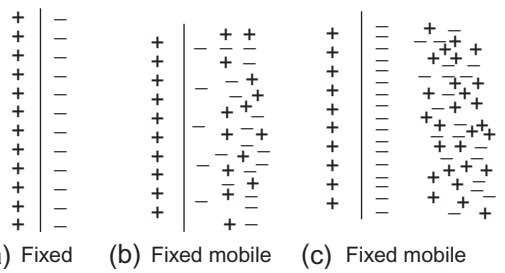


Figure 2.2.37 Schematic drawing of models of double layer (a) Helmholtz and (b, c) Stern.

The electrical conductivity is important because metals such as Al, Mg, and Ti are all produced by electrolytic processes involving a slag and electrical conductivity data are needed to optimize the process. It has also been proposed that the rate-determining step for interfacial reactions (which are electrochemical in nature) is associated with the electronic transfer.

2.2.4.2.2.2 Factors Affecting Electrical Conductivity and Resistivity

2.2.4.2.2.2.1 Ionic Conductivity The electrical (ionic) conductance can be considered to consist of two terms [86,87]:

(i) the concentration and mobility of the cations

(ii) the resistance to movement of cations posed by the silicate network.

The degree of polymerization for the silicate network (i.e., Q) affects both the conductivity ($\ln \kappa^m$) and resistivity ($\ln R^m$); this can be clearly seen in Figure 2.2.38a and b, respectively. The $\ln R^m$-Q curve has the same form (double exponential) as that for the viscosity (Figure 2.2.14). Thus, the resistance to the movement of cations under an applied electrical field can be reasonably represented by the viscosity.

The concentration and mobility effects are affected by the number of cations available (N) and the size of cations (r^3), respectively [85]. It was pointed out that when Na_2O replaces CaO in a slag there are $2Na^+$ cations for every Ca^{2+} and hence the number of available cations (N) increases. Thus, the resistivity of MO-SiO_2 slags (in both the liquid and the *scl* phases) is higher than those for the equivalent M_2O-SiO_2 slags. It should also be noted that when the Al^{3+} is introduced into the Si^{4+} network, a cation is needed to charge balance the Al^{3+} ion; it is assumed that cations on charge-balancing duties are not available for charge carrying. Thus, the introduction of Al_2O_3 brings about a decrease in the number of available cations.

The mobility of the cations also affects the resistivity, where for equivalent compositions values of $\ln R_{1900\ K}$ are in the order $R_{K_2O} > R_{Na_2O} > R_{Li_2O}$. In slags containing

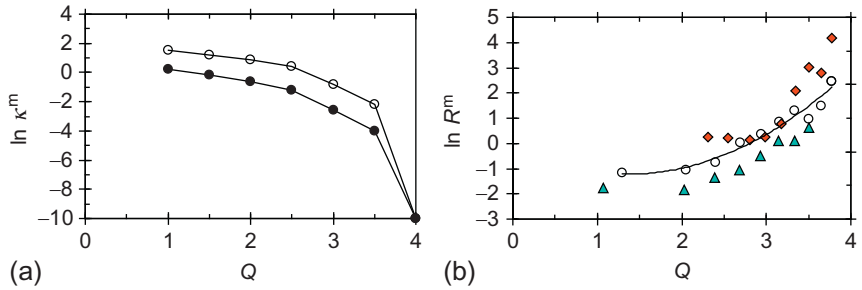


Figure 2.2.38 (a) Logarithm of the electrical conductivity at the melting point ($\ln \kappa^m$) as a function of Q; ○ = M_2O-SiO_2 and ● = MO-SiO_2 and (b) $\ln R^m$ as a function of Q for molten M_2O-SiO_2 slags; Δ = Li_2O; ○ = Na_2O; ♦ = K_2O.

M_2O and MO oxides, it also follows that the electrical resistivity will be affected by which cation takes on the charge-balancing duties (which would be expected to be those cations with the lowest (z/r^2) values).

Increased temperature tends to loosen the network, so increased temperature would be expected to increase the conductivity (or decrease R). The relation between viscosity and electrical resistivity of the liquid indicates that the resistivity can be represented by an Arrhenius equation (or a Weymann equation), e.g.,

$$\ln R = \ln A_R + (B_R/T) \tag{2.2.35}$$

where $B_R = E_R/R^*$ and E_R is the Arrhenius, activation energy for the transfer of ions and R^* = gas constant.

In summary, the resistivity, $\log_{10} R$-Q relation can be represented by a double-exponential relation with adjustments for both the number of available cations and the cation size, i.e., in the form Equation (2.2.36), where γ and the various k and t terms are constants [9]:

$$\log_{10} R = \left\{(\gamma + k_1 \exp(Q/t_1) + k_2 \exp(Q/t_2)\right\} - k_3 N + k_4\left(r^3\right) \tag{2.2.36}$$

These results are consistent with the view that the silicate network restricts the movement of cations and smaller cations can pass through the network easier than larger cations. It is probably easier to visualize this concept in terms of resistance and for this reason the electrical resistivity is used here. Thus, resistivity increases (conductivity decreases) as (i) $Q \uparrow$, (ii) $r \uparrow$, and (iii) the number of available cations, $N \downarrow$. Some workers [45,46] have suggested that the viscosity could be used to represent the resistance to movement of the cations and Figure 2.2.39 shows that $\log_{10} R$ is a linear function of $\log_{10} \eta$ for the *scl* phase.

In silicate melts containing transition metal oxides (e.g., FeO and Fe_2O_3) it has been reported that the ionic conductivity (κ_{ion}) decreases as:

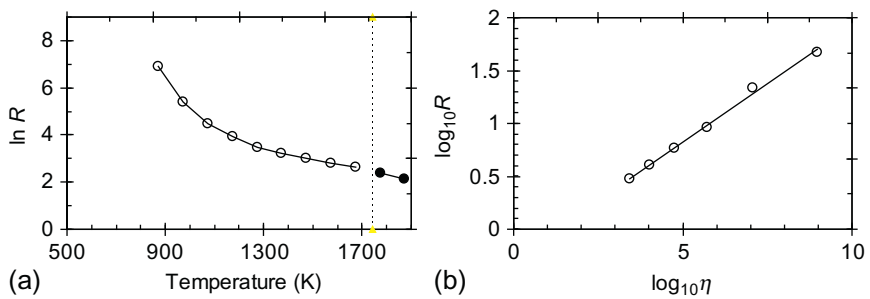


Figure 2.2.39 The measured resistivity logarithm R [145] as functions of (a) temperature ○ = *scl*, ● = liquid and (b) calculated viscosity ($\log_{10} \eta$ (dPas)) [127] for 0.199 Na_2O + 0.801 SiO_2 in the supercooled region.

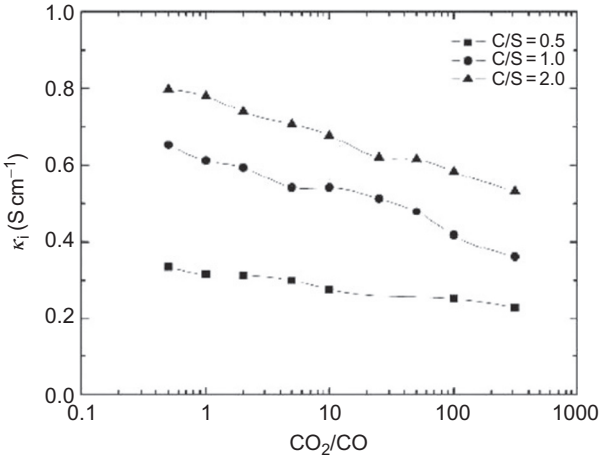


Figure 2.2.40 Ionic conductivity of CaO-SiO_2-30% FeO_x as a function of CO_2/CO at 1750 K [142]; S='Ω^{-1}.

(i) the p_{O_2} (represented as CO/CO_2) increases (Figure 2.2.40), i.e., Fe_2O_3 has a much lower ionic conductivity than FeO.
(ii) the (% CaO/% SiO_2) ratio decreases.

A decrease in (% CaO/% SiO_2) results in (i) an increase in polymerization and (ii) a decrease in the number of available cations, e.g., Ca^{2+} if the FeO_x is kept constant.

Generally, it is assumed that Fe^{2+} is the only type of iron ions which contribute to the ionic conduction in FeO_x containing slags.

2.2.4.2.2.2.2 Electronic Conductivity (κ_{elect}) The electrical conductivities of silicate melts containing transition metal oxides are relatively high since they contain contributions from both ionic and electronic conduction mechanisms:

$$\kappa_{total} = \kappa_{ion} + \kappa_{elect} \tag{2.2.37}$$

Most workers have found that there is a sharp increase in the electronic conductivity when the FeO_x content exceeds 60% FeO_x which is due to the sharp increase in the electronic transference number [142,143] at this composition.

It can be seen from Figure 2.2.41a that the electronic conductivity:

(i) decreases as (% CaO/% SiO_2) decreases (i.e., as the polymerization, Q increases) and
(ii) goes through a maximum at a certain (CO_2/CO) value; this maximum moves to higher (CO_2/CO) values as (% CaO/% SiO_2) decreases.

The maxima occur because the electronic conduction will be at its greatest when there are roughly equal amounts of Fe^{2+} and Fe^{3+} ions (as can be seen from Figure 2.2.41b). At low CO_2/CO values there will be a deficiency of Fe^{3+} ions and beyond the maxima there will be deficiency of Fe^{2+} ions. However, $^{(4)}Fe^{3+}$ occurs more abundantly at low silica contents (high basicity) and $^{(6)}Fe^{3+}$ occurs more abundantly at high SiO_2

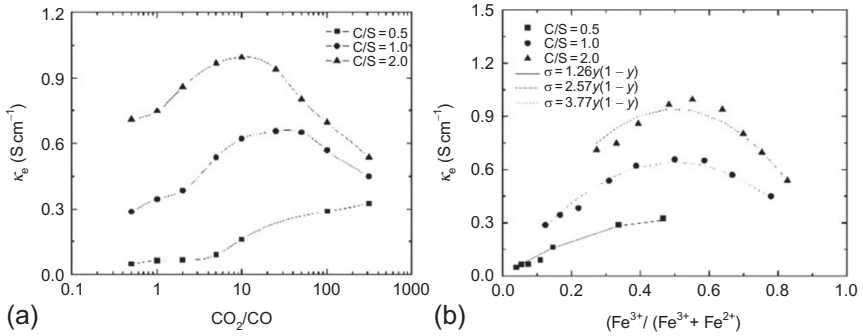


Figure 2.2.41 The electronic conductivity of CaO-30% FeO_x-SiO_2 melts at 1750 K as a function of (a) CO_2/CO [142] and (b) the fraction $(Fe^{3+}/(Fe^{2+}+Fe^{3+}))$ [143]; S='Ω^{-1}.

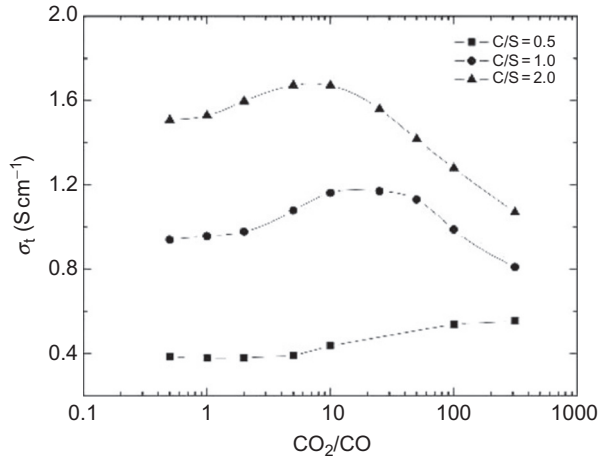


Figure 2.2.42 Total (ionic + electronic) electrical conductivity as a function of CO_2/CO at 1750 K for CaO-SiO_2-FeO_x melts [142]; S='Ω^{-1}.

content (low basicity). Barati and Coley [143] derived the following relation for the $(Fe^{3+}/(Fe^{2+}+Fe^{3+}))$ ratio to describe where the maximum occurs and where $f_{tet} = ({}^{(4)}Fe^{3+})/({}^{(4)}Fe^{3+} + {}^{(6)}Fe^{3+})$:

$$\left(Fe^{3+}/\left(Fe^{2+}+Fe^{3+}\right)\right)_{max} = 0.5(1-f_{tet}) \tag{2.2.38}$$

Thus, a shift in $(Fe^{3+}/(Fe^{2+}+Fe^{3+}))_{max}$ to values >0.5 is expected for more basic slags since f_{tet} increases with increasing basicity.

It can be seen from Figure 2.2.42 that the total (=ionic + electronic) electrical conductivity also shows the same maxima as that shown in Figure 2.2.41 but the peaks are less pronounced.

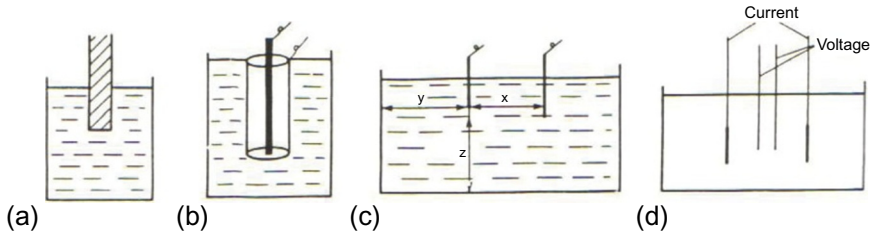


Figure 2.2.43 Cell arrangements for measuring electrical conductivities of molten slags: (a) central electrode, (b) ring cell, (c) two-electrode cell, and (d) four-electrode cell.

The activation energy values for electronic conductivity are very similar to those for ionic conductivity.

2.2.4.2.2.3 Methods Used to Determine Electrical Conductivity and Resistivity

The various methods used to determine electrical conductivity are described below. Methods can be divided into the various two-electrode methods (Figure 2.2.43a–c) and the four-electrode methods (Figure 2.2.43d) with preference being given to the latter since it minimizes problems associated with polarization. In general, it is preferable to have the two electrodes with similar areas (Figures 2.2.43c and d).

Polarization is the principal problem encountered and it arises from concentration gradients arising in the electrolyte and manifests as a *back electro-magnetic force* opposing the normal ionic flow. The four-wire method is used to minimize polarization in which two electrodes carry the current and the other two monitor the potential.

Frequency (f') has been reported to affect κ [7]; some workers assume that the impedance of electrolyte region is a function of f'^{-1}.

The reported values of electrical conductivity are prone to a certain amount of experimental uncertainty.

A high-accuracy, calibration-free, technique to measure the electrical conductivity of molten silicates has been reported [145]. It utilizes coaxial electrodes and the ac impedance is measured. The electrodes are immersed in the melt to an arbitrary initial depth, and ac impedance is measured over a range of frequencies. The electrodes are then immersed to a number of other known depths and the ac impedance is measured (for each depth) over the same range of frequency. The electrical conductivity is calculated from the change in measured conductance with immersion depth [145].

2.2.4.2.2.4 Data for Electrical Conductivity and Resistivity

Compilations of electrical conductivity/resistivity data for slags and glasses are listed in Table 2.2.11.

Table 2.2.11 Summary of the electrical conductivity (κ) and resistivity (R) data for slags

Specimen	Reference	Method	Details of contents
Slags/ liquid	Slag Atlas [7], Chapter 14	Review	κ-Composition at fixed temps: large number of binary, ternary, and quaternary systems covered
	Kozuka and Morinaga [147]	Collected data	κ-T plots for following: ferrites; silicates CS; PS; MPS; NPS; CPS; M PS; LPS; NPS; KPS; BST; LST; NST; KST; CST; MST; SrST; CAST; $CSTFe_2O_3$
ESR fluxes	Mills and Keene [148]	Review	κ-Composition plots for slags with high (>50%) CaF_2 content
Glasses/ *scl*	Fluegel [145]	Review	Evaluated data at 1273, 1473, and 1673 K are given for NS; KS; CNS; CKS; CNKS; LNKS; NKAS; LNKS; NKMS; NMS; NSrS; ZNS systems; references are given

Note: Units for conductivity are Ω^{-1} cm^{-1} and resistivity, Ω cm.

2.2.4.2.2.5 Methods of Calculating Electrical Resistivity Values from Composition

The various models and routines proposed for calculating electrical conductivities of slags and glasses are listed in Table 2.2.12.

2.2.4.2.3 Diffusion Coefficient (D)

Diffusion is the process by which one of the ions in the slag move from point to point within the sample. The diffusing atoms (or ions) are thought to move by a series of jumps from one vacant site to another. Diffusion always occurs from a region of high concentration (C) to a region of low concentration.

2.2.4.2.3.1 Fick's First and Second Laws

Fick's first law refers to steady state conditions; it can be represented by Equation (2.2.39) where J = diffusion flux (mol m s^{-1}), D is the diffusion coefficient (m^2 s^{-1}), and (dC/dx) is the concentration gradient (mol m^{-1}) where x represents the position.

$$J = -D(dC/dx) \tag{2.2.39}$$

Fick's second law deals with the nonsteady state conditions when temperatures are changing with time (t). For one-dimensional flow it can be expressed by Equation (2.2.40):

$$\left(d^2C/dx^2\right) = (dC/dt)/D \tag{2.2.40}$$

For two-dimensional flow it is represented by

$$\left(d^2C/dx^2\right) + \left(d^2C/dy^2\right) = (dC/dt)/D \tag{2.2.41}$$

Table 2.2.12 Summary of published models to calculate the electrical conductivity/resistivity of slags, glasses, and fluxes

Sample (phase)	Model/ reference	Details of model
Glasses (scl and liq)	Fluegel [145]	Multiple regression model with interactions of some constituents; resistivity values calculated for 1273, 1473, and 1673 K; modeled against compositions
Slags (liq)	Jiao and Themelis [149]	Equation involving CaO, MnO, and MgO: does not account for slag structure: $\kappa_{1773}\ (\Omega^{-1}\ \mathrm{cm}^{-1}) = -3.34 + 6.41X_{\mathrm{CaO}} + 6.45X_{\mathrm{MgO}} + 8.06X_{\mathrm{MnO}}$
Ternary—slags	Wang [150]	Ternary values calculated from binaries: κ is linearly related to $r* = \sum(XI)_{M^{2+}}/(XI)_{Si^{4+}}$ MO-SiO_2: $\kappa = 2.2235\ r^* - 0.295$; M_2O-SiO_2: $\kappa = 15.8\ r^* - 0.493$
Liq	Zhang *et al.* [46]	κ as a function of viscosity; MO-SiO_2-systems: $\ln\eta = 0.15 - 1.10\ln\kappa$; M_2O-SiO_2 systems: $\ln\eta = 4.02 - 2.87\ln\kappa$
Liq	Zhang and Chou [40]	κ as a function of corrected optical basicity; CAS and CMAS systems CAS: $E = -4599.2 + 9113.8\Lambda$; CMAS: $E = -4048.7.2 + 7838.4\Lambda$
Liq	Mills *et al.* [85]	Takes into account (1) κ as a function of Q (double-exponential equation), (2) the number of cations available, and (3) cation size on $\ln\kappa_{1900\mathrm{K}}$ and B_{R}

The evolution of C-x curves with increasing time is frequently represented in the form of error function complement (erfc) where C_0 is the initial concentration at x:

$$C(x,t) = C_0\,\mathrm{erfc}\left(x/2\sqrt{\mathrm{Dt}}\right) \tag{2.2.42}$$

Increasing temperature will increase the "excitation" of the ions in the melt which, in turn, will encourage the movement of the ions into other sites. The silicate network can be regarded as a hindrance to the diffusion process. This hindrance to the movement of ions in the case of the diffusion coefficient is equivalent to those for fluidity (i.e., reciprocal viscosity) and electrical conductivity. Thus, the diffusion coefficient can be expressed in the form of an Arrhenius relation

$$D\left(\mathrm{m}^2\ \mathrm{s}^{-1}\right) = A_{\mathrm{D}}\exp(B_{\mathrm{D}}/T) \tag{2.2.43}$$

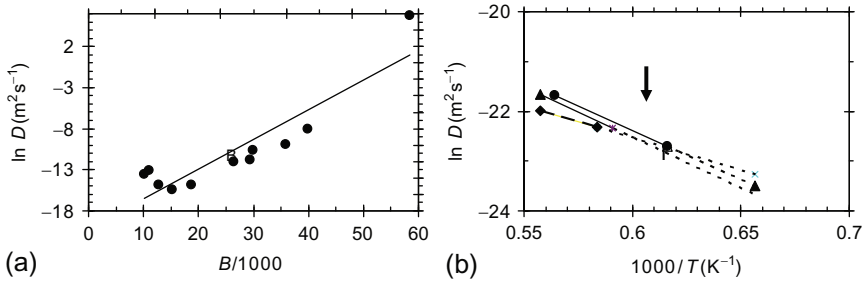


Figure 2.2.44 (a) The preexponential term, ln D_0 as a function of the activation energy term, B for various cations in rhyolite melts and (b) values of ln D as a function of reciprocal temperature for cations in 0.25 CaO 0.25 MgO 0.5 SiO_2 [151]; the arrow denotes crossover point (ca. 1650 K).

where A is the preexponential term (sometimes written D_0) and $B_D = E_D/8.314$ and E_D is the activation energy for diffusion. It has been proposed that ln A_D is a linear function of B_D (Figure 2.2.44a). It has also been reported that experimental values of ln D when plotted against $(1/T)$ (where T is in K) exhibit a constant value at a specific temperature (denoted the "crossover temperature") which occurs around 1650 K (Figure 2.2.44b). This is a result of the *compensation effect*.

For the supercooled liquid the inverse relation between D and the viscosity suggests that the diffusion coefficient can be expressed in the form of a Vogel-Fulcher-Tamman relation:

$$(1/D) = A_D \exp(B_D/(T - T^\circ)) \tag{2.2.44}$$

There are several different types of diffusion and these can be classified as:

2.2.4.2.3.2 Self-diffusion

Random motions in the melt result in the movement of different species present in the slag; there is no (i) net flux and (ii) chemical potential gradients involved in self-diffusion.

2.2.4.2.3.3 Tracer Diffusion

In this form of diffusion, a radioactive isotope is introduced into the melt in order to follow the movement of that species. Consequently, tracer diffusion is a very similar process to self-diffusion. However, in tracer diffusion both a net flux and chemical potential gradients are present but only for the tracer species. Tracer diffusion in solids results from successive jumps of the tracer species which is linked to the movement of vacancies and consequently $D_{tracer} < D_{self}$. However, in liquids the tracer diffusion is considered the equivalent of self-diffusion ($D_{tracer} = D_{self}$). Self-diffusion values are often quoted for impurity elements in the sample which strictly should be classified as chemical diffusion since a chemical potential exists in the melt.

When only one diffusing species (e.g., O) is involved single-component diffusion can be regarded as self-diffusion.

2.2.4.2.3.4 Chemical Diffusion

This occurs when concentration or temperature gradients result in the formation of a gradient in chemical potential which results in the movement of that species. The diffusion occurs in a direction such that it causes a decrease in the gradient for chemical potential. Diffusion can occur as a result of local changes in redox states; such processes are considered to be cases of chemical diffusion. Temperature gradients can also give rise to chemical diffusion; this is usually referred to as *Soret diffusion*.

2.2.4.2.3.5 Inter-diffusion

If the chemical diffusion involves two, or more, species it is known as *inter-diffusion*. Take a process involving a cation and a much more sluggish anion. The anion cannot move as rapidly as the cation, so an electrical field is established which tends to reduce the cation flux and increase the anion flux in order to prevent the formation of a space charge.

For *multicomponent diffusion* it is customary to use the Onsager extension of Ficks first law where D_{ij} is the diffusion coefficient of species, i, developed in response to a concentration gradient in species j

$$J_i = \sum\nolimits_j D_{ij}\left(\mathrm{d}C_j/\mathrm{d}y\right) \tag{2.2.45}$$

Several solutions have been proposed. The approach put forward by Okongawu *et al.* [152] results in Equations (2.2.46) and (2.2.47) when it is assumed that (i) the anion concentration is uniform (i.e., $\mathrm{d}C_k/\mathrm{d}y = 0$) and (ii) there is no build up of space charges:

$$J_i = -D(\mathrm{d}C_i/\mathrm{d}y) \tag{2.2.46}$$

$$J_j = -D\left(\mathrm{d}C_j/\mathrm{d}y\right) \tag{2.2.47}$$

2.2.4.2.3.6 Factors Affecting Diffusion Coefficients

There are several factors affecting diffusion in slags and glasses, namely: (i) the degree of polymerization of the silicate, (ii) the size of the diffusing species, (iii) the number of cations (n) which is related to the valence of the diffusing ion, and (iv) temperature.

2.2.4.2.3.7 Degree of Polymerization

The diffusion coefficient (D) is the equivalent of the electrical conductivity (κ). Thus, we would expect the silicate network to act as a resistance to diffusion in a similar way as it was seen to affect the electrical conductivity above. Thus, if we wish to compare the diffusion coefficient with viscosity and electrical resistivity it is necessary to use the

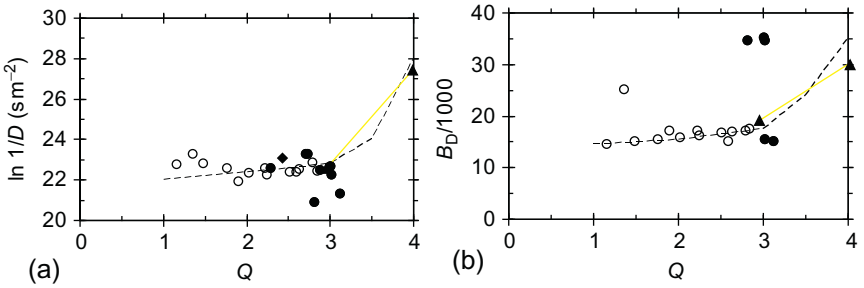


Figure 2.2.45 Ca self-diffusion (a) values of ln (1/*D*) for 1773 K and (b) the activation energy term, B_D, as functions of *Q* (a measure of the polymerization); ○ = CS; • = CAS; ◆ = CMAS [7]; ▲ = magmatic melts [153].

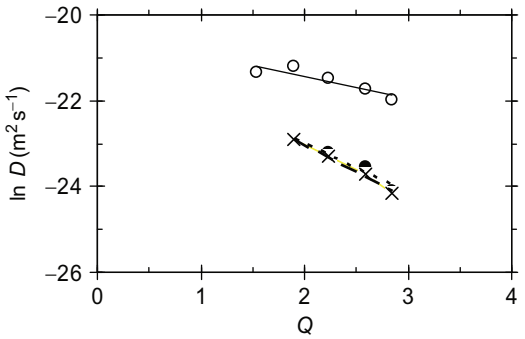


Figure 2.2.46 Values of $\ln_{10} D$ for tracer diffusion coefficients for O, Si, and Ca at 1873 K [154–156] as a function of the parameter *Q* (a measure of the polymerization of the melt); ○ and solid line = Ca, • and dotted line = O, and × and dashed line = Si.

reciprocal diffusion coefficient (D^{-1}). Values of the reciprocal of the diffusion coefficient for Ca self-diffusion ($1/D$) and the activation energy term ($B_D/1000$) are plotted as functions of *Q* in Figures 2.2.45a and b. It can be clearly seen $\ln(D^{-1})$ shows a similar relationship to those shown for (i) viscosity and electrical resistivity (Figure 2.2.14) and (ii) the curve for the activation energy term ($B_D/1000$) as a function of *Q* appears to be similar to those shown in Figure 2.2.15.

The effect of increasing polymerization (represented by *Q*) on the tracer diffusion coefficients of Ca, Si, and O in $CaO\text{-}SiO_2$ melts at 1873 K can be clearly seen in Figure 2.2.46 where *D* values decrease with increasing *Q* [154–156].

2.2.4.2.3.8 Size of Anions

Since the anionic units are much bigger than the cations, thus it would be expected that diffusion coefficients would be much smaller than those for the cations. This can be clearly seen in Figure 2.2.46 where D_{Si} and D_O are much smaller than D_{Ca}. The size

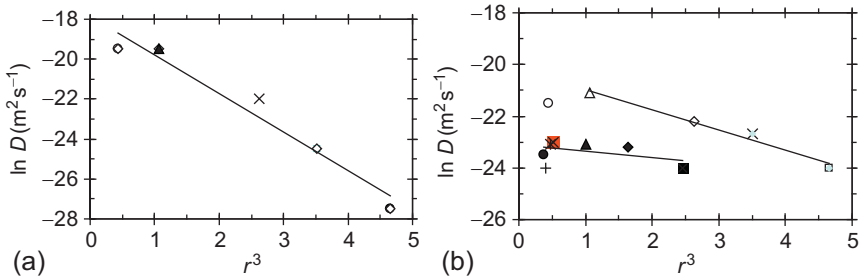


Figure 2.2.47 Values of ln D for tracer diffusion at 1673 K [153] (a) in rhyolite melts shown as a function of cation size relative to Ca ion radius ($r^3 = (r_M/r_{Ca})^3$); from left to right ○ = Li, ▲ = Na, × = K, ◊ = Rb, ○ = Cs [153] and (b) in basalt melts ○ = Li; Δ = Na; ◊ = K; × = Rb; ■ = Cs; ● = Mg; + = Fe; □ = Mn; ▲ = Ca; ♦ = SrO; ■ = BaO.

of the anionic units would be expected to increase with increasing polymerization (i.e., Q) in the melt and consequently, it would be expected that D would decrease with increasing Q.

The effect of cation size for Group I oxides (e.g., Na_2O) on the tracer diffusion coefficient at 1673 K can be clearly seen in Figure 2.2.47 where D decreases with increasing cation size (r^3), i.e., diffusivities Li ≈ Na > K > Rb > Cs. It can be seen that for this group of oxides the effect of cation size is large. This effect on D may be due to either (i) the direct effect of cation size or (ii) the effect of the cation on the slag structure. However, it can be seen from Figure 2.2.47b that the effect of cation size for Group II oxides (e.g., CaO) is much less pronounced. Zhang *et al.* [153] examined the hierarchy of D values for these oxides in various geological melts; they found that (i) the hierarchical order varied from melt to melt and (ii) D tended to increase with increasing cation size (i.e., Ba ≈ Sr > Ca > Mg). The relation between D and cation size will be discussed below.

2.2.4.2.3.9 Number of Cations, Valence

It was pointed out in Section 2.2.4.2.2 that electrical resistivity data for both ln $R_{1900\ K}$ and activation energy term, B_R, were affected by the number of available cations (N) present in the melt. A certain mole fraction of Na_2O produces twice as many cations as the same mole fraction of CaO. Thus for one O atom, the values of N for Na_2O, CaO, Fe_2O_3, and TiO_2 produce 2, 1, 0.667, and 0.5 cations, respectively; this can be expressed as $(2/Z)$ where Z is the valence state. It can be seen from the values given in Figures 2.2.47b and 2.2.48 that D decreases with increasing values of $(2/Z)$. Zhang *et al.* [153] found that diffusivities were in order $M_2O > MO > M_2O_3 > MO_2$, i.e., Groups I > II > III > IV (Figure 2.2.49).

Zhang *et al.* [153] suggested that there were two factors affecting the diffusion process (i) detachment of the diffusing ion (i.e., through breaking of the existing M—O bond)

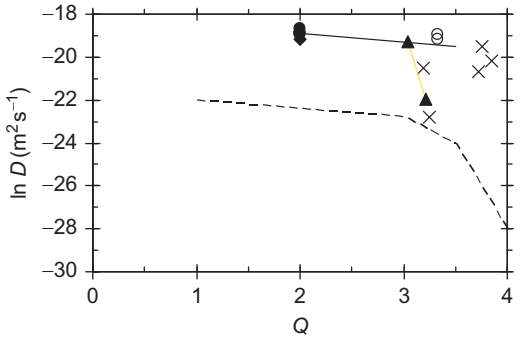


Figure 2.2.48 Values of ln *D* for tracer diffusion of Na at 1773 K as a function of *Q* and showing a comparison of values for Ca (dashed line) with other systems; ○ = NS; ♦ = NMS; ▲ = NCS; ● = CS; × = mineralogical melts [153].

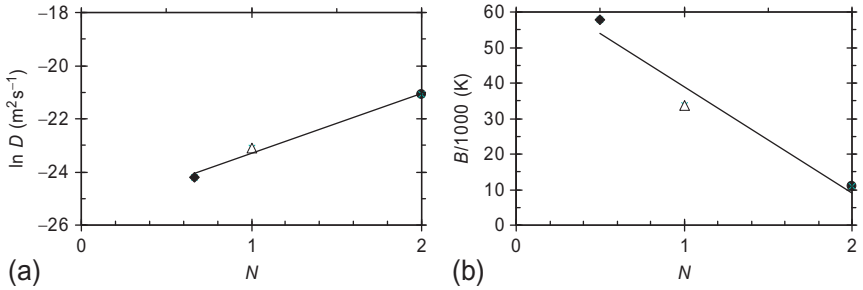


Figure 2.2.49 (a) Values of ln *D* at 1773 K for tracer impurity of Ca (=Δ), Na (=●) and Sc, Eu, and Gd (=♦) in basalt melts as a function of *N* (=number M ions per O in M_yO) and (b) activation energy term (*B*/1000) as a function of *N*; ♦ = Na; Δ = Ca; ● = Ce in solid granites [7].

and (ii) its subsequent movement through the melt. The overall diffusion coefficient will be determined by the slower of these two steps. In the case of M_2O oxides, the M—O bond strength (z/r^2) is low and thus the slow step is the diffusion through the network; hence *D* is principally affected by cation size. For divalent and trivalent cations, the M—O bond strength (z/r^2) is high and the detachment process is the slower step, so *D* increases with increasing size (i.e., with lower z/r^2 values). Zhang *et al.* [153] point out that the variation in hierarchy is also affected by the network structure. For polymerized melts there tends to be more free space available for cations to move and thus detachment (i.e., bond strength, z/r^2) is the more important process and *D* values are in order Ba ≈ Sr > Ca > Mg. In contrast, in depolymerized melts there is less free space and thus *D* is largely determined by cation size (e.g., in basalt Ca ≈ Co > Sr > Ba and in haplobasalt Mg > Ca > Ba).

2.2.4.2.3.10 Relation to other Properties

There have been three approaches to relate the diffusion coefficient to other physical properties for *self-diffusion*.

2.2.4.2.3.10.1 Mean Free Path Approach The diffusing species is assumed to move in a series of jumps where the start and finish of the ion is determined by interaction with other particles and D can be calculated by Equation (2.2.48) where n^* is the number of diffusing particles, $\lambda =$ mean free path, and $\tau =$ mean time per jump:

$$D = n^* \lambda^2 / 2\tau \tag{2.2.48}$$

2.2.4.2.3.10.2 Friction Coefficient Approach In this approach, the friction coefficient of the diffusing species (β^*) is calculated and the diffusion coefficient is calculated by the following relation where m is the mass of the diffusing species, k^* is the Boltzmann constant:

$$D = k^* T / m\beta \tag{2.2.49}$$

2.2.4.2.3.10.3 Absolute Rate Theory Approach For an isotropic medium the absolute rate theory results in the following equation where k^* is the Boltzmann constant, T is the temperature in K, η is the dynamic viscosity, and $\lambda = 2r$:

$$D = k^* T / \eta\lambda \tag{2.2.50}$$

2.2.4.2.3.11 Methods used to Determine Diffusion Coefficients

There are some severe measurement problems when determining the diffusion coefficient. The main problem is convection, like thermal conductivity, but large times are needed to establish concentration profiles and so convection cannot be minimized by using short-duration experiments. Thus, precautions must be taken to minimize convection such as minimizing thermal gradients in the apparatus and designing the furnace to provide a long zone of uniform temperature. Some workers have minimized convection by carrying out experiments in microgravity but even here care must be taken to avoid perturbations like "*g-jitter*" which can affect the concentration profile. It had been suggested that preference should be given to diffusion coefficients measured in more recent years because of the improvement in experimental techniques.

Short descriptions of the principal techniques used to measure diffusion coefficients are given below; for a more detailed account of the methods the reader should consult the reviews of Walls [157], Lundy [158], and also Le Claire [159].

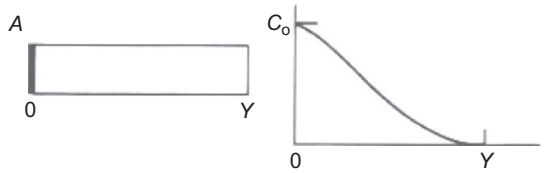


Figure 2.2.50 Schematic drawing showing the instantaneous plane source method and a typical concentration gradient at time, *t*.

2.2.4.2.3.12 Instantaneous Plane Source

The sample is in the form of a long column which can be considered to be infinitely long. Then a tracer (usually a radioactive isotope of the diffusing species) is deposited in thin layer at one end of the sample (Figure 2.2.50). The sample is then maintained at constant temperature for a known time and then quenched. The concentration (C) of the diffusing species is then determined and the diffusion coefficient derived using Equation (2.2.51) (based on error function method) where m = mass of tracer deposited, t is the time, and x and y are distances in x and y directions:

$$C(x,t) = m/(\pi Dt)^{0.5} \exp\left(y^2/4Dt\right) \tag{2.2.51}$$

2.2.4.2.3.13 Capillary Reservoir (CR or Immersion) Method

The diffusing species is held in a capillary which is immersed in the melt. Tracer (or impurity) diffusion occurs from the capillary to the melt for a set time. Then the capillary is removed and the distribution of the species is determined.

2.2.4.2.3.14 Diffusion Couple Method

The diffusion couple (DifC) contains two melts of identical composition except that one contains the tracer element (Figure 2.2.51). The diffusion coefficient can be determined from linear regression of the concentration gradient where the slope is equal to $(0.5Dt)^{0.5}$ or by using the error function method.

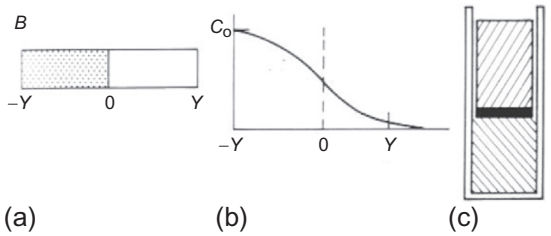


Figure 2.2.51 Schematic drawing showing the diffusion couple method and concentration gradient and typical experimental setup.

2.2.4.2.3.15 Electrochemical Method

An electrochemical cell is established consisting of the slag melt and with the diffusing species being held in the electrode. The electrolysis is carried out with constant current (I). The diffusion coefficient can be calculated from Equation (2.2.52) providing the electrode reaction is controlled by diffusion where Z is the valence and F is the Faraday constant:

$$I = ZFD(\mathrm{d}C/\mathrm{d}y)_{y=0} \tag{2.2.52}$$

2.2.4.2.3.16 Molecular Dynamics Calculations

In these calculations, potential energy functions are used to represent the forces within the Si—O tetrahedron and the effects of the cations. Calculated values of the diffusion coefficient have been found to be in good agreement with experimental values. The drawbacks to the method lie in the absence of key data needed in the calculations. Henderson [4] has pointed out that although MD calculations produce useful information they are calculations and preference should be given to reliable experimental data.

2.2.4.2.3.17 Data for Diffusion Coefficients

There are several compilations of diffusion data and these are summarized in Table 2.2.13.

2.2.4.2.3.18 Methods of Calculating Diffusion Coefficients from Composition

The *Stokes-Einstein relation* is shown in Equation (2.2.53) where k^* is the Boltzmann constant, f is the radius of the diffusing species, and η is the dynamic viscosity:

Table 2.2.13 Summary of sources of diffusion coefficients for silicate melts

Sample type	Reference	Comments, details
Slags,	Slag Atlas [7], Chapter 13	Self-, tracer-impurity, and chemical-diffusion coefficients for various species; inter-diffusion coefficients; tabulated data for oxides, binary–ternary—silicates and geological melts
Slags	Nagata *et al.* [160]	As above; tabulated data
Magmatic melts	Zhang *et al.* [153]	Large amount of self-, tracer-impurity, and chemical-diffusion coefficients diffusion data for geological melts. Inter-diffusion coefficients. Presented in form of ln D versus $(1/T)$ plots with some equations
	Brady [161]	Large amount of tabulated data for geological melts: data for ln D_0; B_D and ln D at either 1073 or 1473 K

$$D = k^* T / 6\pi\eta r \tag{2.2.53}$$

However, this equation does not work well since it assumes the diffusing species (cations) is large whereas we have seen above that the cations are small compared with the silicate anions.

The Eyring relation does provide reasonable estimates of the diffusion coefficient and is given in Equation (2.2.54) where λ = mean inter-atomic difference (=2r)

$$D = k^* T / \eta\lambda \tag{2.2.54}$$

However, it was found [162,163] that values of λ of more than 2r were needed to obtain calculated values in good agreement with experimental values.

Few models for calculating diffusion coefficients have been reported; available models and routines are summarized in Table 2.2.14.

Given the fact that diffusion coefficients and electrical conductivities (κ) of silicates are both dependent upon (i) the degree of polymerization (Q), (ii) the number of available cations, and (iii) cation ion size in M_2O-silicates, it would appear that reasonable values of D could be calculated from κ (electrical conductivity). In fact the Nernst-Einstein equation links the two properties, Equation (2.2.55) where R^* = gas constant, F = Faraday constant, C_i is the concentration of species i, z is the charge, and T is in K

$$D_i = \kappa R^* T / \left(C_i z^2 F^2\right) \tag{2.2.55}$$

Table 2.2.14 Summary of published models to calculate the diffusion coefficients in silicate melts

Sample type	Reference	Comments, details
Slags	Nernst-Einstein	$D_i = \kappa\, R^*\, T/(C_i z^2\, F^2)$
Magmatic melts	Baker [164]	Inter-diffusion coefficients. Uses Eyring relation and calculates D from viscosity. Uses two different calculation (1) for Group I cations and (2) other cations
Magmatic melts	Mungall [47]	$\ln D_i = 16.16 + \{(42.6\ (r_i - 1.03)^2 + 6.63 Y_1 - 1239 Y_2 + 27424\ (r_i - 1.03)^2 + 6975)/T\}$ where $r_i = r$ of ion; $Y_1 = X_M / X_O = \sum X_M \sum X_{MO} + X_{M_2O\,O} + X_{M_2O} + 2X_{MO_2} + 3X_{M_2O_3}$ and $Y_2 = X_{Al_2O_3}/(X_{Na_2O} + X_{K_2O})$
Solid	Fortier and Guiletti [165]	Empirical model for range (773-1073 K). $\log D\ (\mathrm{cm^2\ s^{-1}}) = a + b/T + (c + d/T)Z^*$, where a, b, c, and d are constants and Z^* = total ionic porosity; for O diffusion $a = -2$; $b = -3.4 \times 10^{-4}$; $c = -0.13$; and $d = 640$

2.2.4.3. Density (ρ) and Thermal Expansion Coefficient (α, β) and Ultrasonic Velocity

2.2.4.3.1 Density (ρ) and Thermal Expansion Coefficient (α, β)

2.2.4.3.1.1 Why Density and Thermal Expansion Data are Needed

Density values of silicate slags are important in calculating (i) buoyancy flows in vessels, (ii) the removal of inclusions from the metal by flotation, and (iii) the conversion of thermal diffusivity (a) values to thermal conductivities ($k = C_p \cdot a \cdot \rho$).

Thermal expansion coefficients (α, β) are needed in the calculation of (i) convection in the vessel and (ii) densities at higher temperatures.

2.2.4.3.1.2 Factors Affecting Density and Thermal Expansion

The molar volume (V) is related to the density via Equation 2.2.56 and is only slightly affected by the polymerization of the slag and this can be accommodated by expressing V_{SiO_2} (and $V_{Al_2O_3}$) as polynomials of ($X_{SiO_2} V_{SiO_2}$) where X is the mole fraction [113]. The oxides with higher molecular weight (M) tend to have lower molar volumes (or higher densities), e.g., $V_{K_2O} < V_{Na_2O} < V_{Li_2O}$:

$$V\rho = M \tag{2.2.56}$$

Thermal expansion in slags results from the asymmetry of the thermal vibrations produced when a slag is heated. These asymmetric vibrations are affected by (i) the chemical bonding in the slag and (ii) the thermal history of the specimen (i.e., the cooling rate and thus the configurational entropy). The thermal expansion coefficient can be cited as either the coefficient of *linear thermal expansion* (α) or *volume thermal expansion* (β) which are given by Equations (2.2.57) and (2.2.58), respectively, where $\Delta T = (T - T_{ref})$ and T_{ref} = reference temperature (e.g., 20 °C), α and β pertain to the mean temperature, i.e., 0.5 $(T + T_{ref})$ and V_o is the molar volume at the reference temperature.

$$\alpha = (L_T - L_{ref})/L_{ref}(T - T_{ref}) \tag{2.2.57}$$

$$\beta = (V_T - V_{ref})/V_{ref}(T - T_{ref}) \tag{2.2.58}$$

$$V = V_o(1 + \alpha\Delta T)^3 \tag{2.2.59}$$

The principal factors affecting the thermal expansion are:

(i) the degree of polymerization (α and β decrease as Q increases, i.e., $\alpha \downarrow$ as $Q \uparrow$) and

(ii) the bond strength of the M—O bonds with $\alpha \downarrow$ as $(z/r^2) \uparrow$ where z = cation charge (e.g., 1 for Na^+ and 2 for Ca^{2+}) [87].

The thermal expansion coefficient of a glass undergoes a threefold increase above T_g (as can be seen from the change in slope at T_g in Figure 2.2.52a). This is associated with the increase in disorder accompanying the transformation of a glass to a *scl*. The *scl* sample collapses at the deformation temperature (usually 50-100 K above T_g) and no measurements are possible above this temperature. In contrast, the α-T relation for the crystalline phase exhibits a smooth curve between $< T_g$ and T_{sol} as can be seen from Figure 2.2.52b.

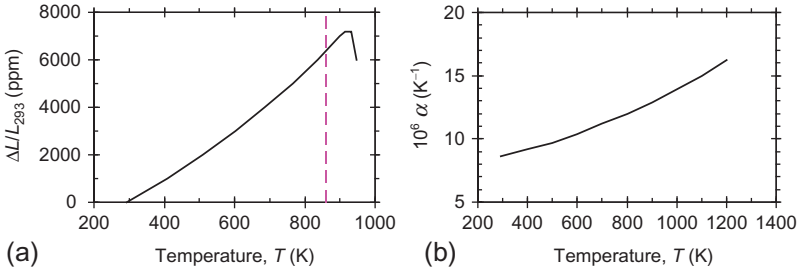


Figure 2.2.52 Thermal expansion as a function of temperature; (a) relative change in length of glassy mold flux sample; dashed line = T_g and (b) linear thermal expansion coefficient of crystalline $CaMgO_3$ [166].

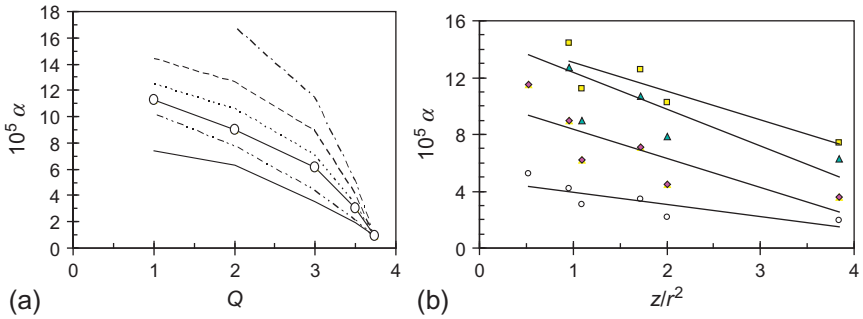


Figure 2.2.53 Thermal expansion coefficient (α) values for liquid MO- and M_2O-SiO_2 slags [167] as a function of (a) the parameter Q, from the bottom; solid line = MgO; CaO; BaO (○); Li_2O, Na_2O, and K_2O; and (b) (z/r^2), i.e., a measure of the M—O bond strength; ○ = Q = 3.5; ◆ = Q = 3; ▲ = Q = 2; ■ = Q = 1 lines are "best-fit" trend lines of data [87].

Crystalline samples exhibit a decrease in the density (or increase in molar volume) between T_{sol} and T_{liq} (Figure 2.2.21b) due to fusion. Thus, the density values in the range (T_g and T_{sol}) will vary according to the degree of crystallization in the sample.

The thermal expansion of the liquid increases as both Q and the field strength of the cation (z/r^2) decrease ($\alpha \uparrow$ as $Q \downarrow$ and $z/r^2 \downarrow$) as shown in Figure 2.2.53 [87].

2.2.4.3.1.3 Methods Used to Determine Density and Thermal Expansion

For solid slags at room temperature, the density is usually measured by the *Archimedian* method. The slag sample of known weight and volume is suspended on a wire from a balance and the weight of the sample is determined in air (W_{atm}) and then in water or dichloromethane (W_{fluid}):

$$\rho = (W_{atm} - W_{fluid})/V \tag{2.2.60}$$

2.2.4.3.1.4 Dilatometry

Thermal expansions of slags are usually measured by machining two parallel faces on a cylindrical sample (usually ca. 30 mm long) and measuring the changes in length as the specimen is heated at a known heating rate. For glassy samples the specimen collapses at the "deformation temperature" which is ca. 50–100 K above the glass transition temperature (T_g) and no further measurements can be made above this temperature.

2.2.4.3.1.5 Liquid Slags

The following methods are frequently used to measure density of molten slags and fluxes; the experimental uncertainty is ca. 2–5%.

2.2.4.3.1.6 Archimedian (or Buoyancy) Method

A bob of known volume is suspended from a balance. The weight of the bob before immersion (W_{atm}) and then again after full immersion (W_{fluid}) in the molten slag is determined. It is necessary to correct the density value for the effect of the surface tension force acting on the wire.

2.2.4.3.1.7 Pyknometry (or Weighing) Method

The slag is melted in a specially designed vessel of known volume and the mass of the slag determined. Corrections must be made for the thermal expansion of the vessel.

2.2.4.3.1.8 Maximum Bubble Pressure Method

The maximum bubble pressure (MBP) method is described in detail below in 2.2.4.4.3.1. The MBP (p_{MBP}) is determined at different heights (h_1, h_2, etc.) and the density calculated by Equation (2.2.61).

$$\rho = (p_{MBP2} - p_{MBP1})/(h_2 - h_1). \tag{2.2.61}$$

2.2.4.3.1.9 Sessile Drop Method

The volume of a sessile drop (SD) of known mass is determined through measurements of the drop dimensions [7]. Recent improvements in software to describe the profile of the drop have improved the accuracy of this method.

2.2.4.3.1.10 Draining Crucible

This has not been used to date on molten slags but would appear to be viable for the measurement of slags. The rate of drainage of slag from an orifice in the crucible is determined by continuous weighing of the crucible. The density is determined through hydrodynamic analysis of the measurements.

2.2.4.3.1.11 Density and Thermal Expansion Data for Slags and Glasses

A considerable amount of density and thermal expansion coefficient data for solid and liquid silicates and fluxes have been published; sources of collected data and reviews are given in Tables 2.2.15 and 2.2.16, respectively. The density and thermal expansion coefficient measurements are shown in Figures 2.2.24b and 2.2.53, respectively.

2.2.4.3.1.12 Methods of Calculating Density and Thermal Expansion Coefficients from Composition

The models reported for the calculation of density and thermal expansion from chemical composition are given in Tables 2.2.17 and 2.2.18, respectively.

2.2.4.3.2 Velocity (c) and Absorption Coefficient (α) of Ultrasonic Waves

Ultrasonics are defined as acoustic waves with frequencies above 20 kHz up to around 1 GHz, while audio frequency falls in the range, 20 Hz to 20 kHz, although, over time, the upper limit has been reduced significantly. Ultrasonic waves are composed of *longitudinal* and *transverse* waves, in which the oscillation is parallel and perpendicular, respectively, to the direction of wave propagation. In fluids, e.g., molten slags, only longitudinal waves can propagate. In this sense, the propagation of bulk waves in liquids and gases is much simpler than that in solids.

2.2.4.3.2.1 Why Acoustic Property Data are Needed

Ultrasonic waves have potential application in refining processes. For example, the size and distribution of nonmetallic inclusions in molten steel and the thickness of refractory walls of a blast furnace can be estimated using instruments based on ultrasonics. The velocity and absorption coefficient of ultrasonic waves have also scientific interest because they are relevant to the thermodynamic and thermophysical properties, such as adiabatic compressibility and volume viscosity. Since ultrasonic waves propagate in materials via phonons, the ultrasonic velocity is regarded as the velocity of phonons. The thermal conductivity (k) of insulators can be expressed by Equation (2.2.62) where C_v is the heat capacity per unit volume, c is the phonon velocity, i.e., the ultrasonic velocity, and l is the phonon mean free path. The phonon mean free path can be evaluated from the ultrasonic velocity:

$$k = C_v c l/3 \tag{2.2.62}$$

2.2.4.3.2.2 Factors Affecting Acoustic Properties

2.2.4.3.2.2.1 Frequency Dependency In many cases, the velocity (c) of ultrasonic waves is assumed to be independent of frequency, i.e., *dispersionless*. Dispersion denotes that the velocity varies with frequency (f'). In fact, dispersion does occur in the following circumstances:

Table 2.2.15 Density values reported for slags, glasses, etc.; in chemical formulae, e.g., CTS = $CaO\text{-}TiO_2\text{-}SiO_2$ system—see "Symbols, units, and abbreviations"

Type/ phase	Reference	Method	Comments
Slags	Slag Atlas [7], Chapter 8	Review	Liquid phase ρ-composition plots at fixed temps Large number of systems, binaries, ternaries, quaternaries, industrial slags
	Watanabe *et al.* [168]	Review	Liquid phase: ρ-composition plots; molten Al_2O_3; B_2O_3; AS; FS; MnS; CFe_2O_3S; BFe_2O_3S; $SrFe_2O_3S$; NFe_2O_3S; CFS; CMnS; CF; $CFFe_2O_3$; CaF_2-slags
Slags, magmas	Ghiorso and Kress [169]	Review	Large database of experimental data to carry out modeling activities
ESR slags	Mills and Keene [148]	Review	Density composition at fixed temperatures for binary and ternary systems containing CaF_2
BOS slags/ liquid	Mills and Keene [113]	Review	Density-composition plots for 1873 K for systems relevant to BOS
Glasses			
Solid	Fluegel [170]		Provides some references of studies of α measurements
Scl and liquid	Fluegel *et al.* [171]		Provides some references of studies of α measurements
	Scholze [172]	Compilation	Collection of density data for glasses
	SciGlass [173]	Database	Database of glass properties
Magmatic liquid	Ghiorso and Kress [169]	Collected data	Collection of experimental data for molar volumes
Slag	Sukenaga *et al.* [174]	Archimedean-double bob	$CaO\text{-}SiO_2\text{-}Al_2O_3\text{-}M_2O$ (M = Li, Na, K) melts, ρ for CALi 2.31-2.34 $\times 10^3$ kg m^{-3}; CAS-Na 2.41-2.44 $\times 10^3$ kg m^{-3}, density of CAS-K is 2.45-2.47 $\times 10^3$ kg m^{-3}

Continued

Table 2.2.15 Density values reported for slags, glasses, etc.; in chemical formulae, e.g., CTS = $CaO\text{-}TiO_2\text{-}SiO_2$ system—see "Symbols, units, and abbreviations"—cont'd

Type/ phase	Reference	Method	Comments
Slag	Muhmood and Seetharaman [175]	Archimedean	$CaO\text{-}SiO_2\text{-}Al_2O_3$ 1683 K, 1783 K
Slag	Lee and Gaskell [176]	MBP	ρ of $CaO\text{-}FeO\text{-}SiO_2$, evaluate effect of temperature, SiO_2 content as well as CaO/FeO on slag structures
Slag	Licko *et al.* [177]		$CaO\text{-}FeO\text{-}Fe_2O_3\text{-}SiO_2$ in the temperature region of 1540-1910 K $V = X_{CaO}V_{CaO} + X_{FeO}V_{FeO} + X_{Fe_2O_3}V_{Fe_2O_3}$
	Monaghan and Brooks [110]		15.51% CaO-15.05% Al_2O_3-69.5% SiO_2: 1000-1700 K
	Dingwell *et al.* [128]		Density of $Na_2O\text{-}FeO\text{-}Fe_2O_3\text{-}SiO_2$ is 2.17-2.88, and average deviation is 0.36%
	Doweidar [179–182]		ρ of $M_2O\text{-}SiO_2 (M_2O/SiO_2 < 1)$
	Hara *et al.* [183]	Archimedean	(1673 K): $10^5/\rho = (1/2.676\%\ CaO) + (1/4.624\%\ FeO) + (1/4.298\%\ Fe_2O_3)$ (1773 K) = (1/2.664% CaO) + (1/4.588% FeO) + (1/4.259% Fe_2O_3) (1873 K) = (1/2.654% CaO) + (1/4.548% FeO) + (1/4.221% Fe_2O_3)
	Henderson [184]	MBP	1255-1410 °C "FeO"-SiO_2, CaO-"FeO"-SiO_2
	Vadasz *et al.* [185]		$CaO\text{-}FeO\text{-}Fe_2O_3\text{-}SiO_2$ $CaO\text{-}FeO\text{-}Fe_2O_3\text{-}Al_2O_3$ $V = A_1x_{CaO} + A_2x_{FeO} + A_3x_{Fe_2O_3} + A_4x_{SiO_2} + B_{13}x_{CaO}x_{Fe_2O_3} + B_{14}x_{CaO}x_{SiO_2} + B_{23}x_{FeO}x_{Fe_2O_3} + C_{124}x_{CaO}x_{FeO}x_{SiO_2} + C_{134}x_{CaO}x_{Fe_2O_3}x_{SiO_2}$
	Aksay and Pask [186]	X-ray	Densities of $SiO_2\text{-}Al_2O_3$ melts, 1800-2000 K

Table 2.2.16 Experimental values reported for the thermal expansion of slags

Specimen	Reference	Comments
Glasses	Scholze [172]	Compilation of thermal expansion data
Solid $< T_g$	Fluegel [187]	Contains collection of data for glasses for α below T_g
	Priven [141]	MDL-SciGlass database
	SciGlass [173]	Database of glass properties
Magmas	Ghiorso and Kress [169]	Data for (dV/dT) of molten minerals
Slags and minerals	Touloukian *et al.* [166]	Thermal expansion-T data for a number of silicates and aluminosilicates

(i) at very high frequencies (e.g., with thermal phonons near the Brillouin zone boundaries) and

(ii) for highly viscous (i.e., *unrelaxed*) melts, where part of the atomic movements cannot follow the high frequencies of ultrasonics and the velocity increases with increasing frequency ($c \uparrow$ as $f' \uparrow$).

If the characteristic relaxation time (τ) of the melt is short, the condition ($f' \ll 1/\tau$) is met and the velocities are (i) essentially independent of frequency and (ii) the value of $\alpha^*/(f')^2$ is roughly constant (where α^* is the absorption coefficient of ultrasonic waves).

If it is assumed that the propagation of ultrasonic waves proceeds adiabatically and that the local fluctuations in liquid density (due to the propagation of ultrasonic waves) are negligibly small, then the *adiabatic compressibility* β_s can be calculated using Equation (2.2.63) where ρ is the density of the sample:

$$\beta_s = \frac{1}{\rho c^2} \tag{2.2.63}$$

2.2.4.3.2.2.2 Temperature Dependency In general, the velocities of ultrasonic waves decrease with increasing temperature (providing the coordination structure does not change). Figure 2.2.54 shows the temperature dependency of the ultrasonic velocity of 0.33 Li_2O-0.67 SiO_2 and 0.5 Li_2O-0.5 SiO_2 in the liquid states. This is because thermal motions of the ions lead to increasing nearest neighbor separation, resulting in an increase in compressibility.

2.2.4.3.2.2.3 Compositional Dependency Rivers and Carmichael [191] have reported two compositional correlation equations for the ultrasonic velocities of molten silicates. The first is based on the proposal by Ernst *et al.* [193] that if a solution mixes without volume change, one can imagine separating the liquid into layers whose thicknesses are proportional to the volume fraction of each component, $x_{i,c}$. The total time for

Table 2.2.17 Details of some published models to calculate densities of slags

Reference	System/ phase	Details of method	Uncertainty
Bottinga and Weill [188]	Slags, glasses/ liquid	$V = \Sigma\ X_1 V_1 + X_2 V_2 + X_{33}$, values of V given Corrections to V values for compositions of Al_2O_3, Na_2O, K_2O, CaO, MgO, FeO Equations for β also corrected for chemical compositions of these oxides	2-3%
Mills and Keene [113]	Slags/ liquid/solid	*Method 1*: ρ (kg m^{-3}) = 2460 + 18 (% FeO + % Fe_2O_3% + MnO + % FeO)	5%
		Method 2: $V = \Sigma X_1 V_1 + X_2 V_2 + X_3 V_3 + \cdots$ at 1773 K. V (10^{-6} m^3 mol^{-1}) values for: CaO = 20.7; FeO = 15.8; Fe_2O_3 = 38.4; MnO = 15.6; MgO = 16.1; Na_2O = 33; K_2O = 51.8; TiO_2 = 24; P_2O_5 = 65.7; $SiO_2 = (19.55 + 7.97 X_{SiO_2})$; $Al_2O_3 = (28.3 + 32 X_{Al_2O_3} - 31.45 X^2_{Al_2O_3})$ $(dV/dT) = 0.01\% K^{-1}$; also constants for solid phase	2%
Robinson *et al.* [100]	Slags/liquid	Use of thermodynamic software: molar volumes stored for oxides and correction based on molar Gibbs energy of system	2%
Hayashi and Seetharaman [93]	Slags/liquid	$V/\Sigma\ X_1 V_1 = (K \Delta H^{mix}/R^* T)$ where ΔH^{mix}= the relative integral enthalpy of mixing (determined with thermodynamic software) and K = constant	2%
Persson [94,178]	Slags/liquid	$V^M = \lambda H^M$. $\Sigma X_i\ V_m/R^* T$, where M and m indicate integral and partial molar volumes, λ is a constant, and H^M is the integral enthalpy of mixing Values of ΔG^M, λ, and interaction coefficients obtained from thermodynamic model	2-5%
Shu [39]	Slags	$V_{mix} = (V_{meas} - V_{ideal})$ where $V_{ideal} = \Sigma X_1 V_1$. Values of correlated with reciprocal optical basicity ($1/\Lambda$). Corrections made for charge balancing and Al in IV and VI-coordination	2%
Priven [141]	Glasses	Solids: $V = \Sigma X_1 V_1 + X_2 V_2 + X_3 V_3$. Values and range of applicability given Special procedures for boro-silicates	
Fluegel [170] Fluegel [127]	Glasses/ solid/scl and liq	Statistical "best-fit" model with interactions. Gives references for other glass models Solid [170]: Best-fit interactive model for density at 298 K based on SciGlass database [] Scl and liquid [130]: Best-fit interactive models; ρ calculated for 1273, 1473, and 1673 K	1%

Table 2.2.17 Details of some published models to calculate densities of slags—cont'd

Reference	System/ phase	Details of method	Uncertainty
Ghiorso and Kress [169]	Slags magmas	Partial molar ($V_{1673K} = \Sigma X_1 V_1$) + interaction between Na_2O and TiO_2 and K_2O and TiO_2. Values given for FeO, $FeO_{1.3}$, and Fe_2O_3; values also given for (dV/dT)	1%

Table 2.2.18 Models to calculate thermal expansion coefficient of slags and glasses

Slag type	Reference	Details of model
Glass	Priven [141]	Covers a large range of oxides
Glass solid	Fluegel [187]	α at 210 °C (483 K). Multiple regression model with interactions. Gives details of other models for glasses. Limited composition range for metallurgical slags
Glass—scl and liq	Fluegel [127]	Multiple regression model with interactions; density values given at 1273, 1473, and 1673 K
Magmatic liquids	Ghiorso and Kress [169]	Partial molar values of (dV/dT) given for constituent oxides: $(dV/dT) = \Sigma X_1 (dV/dT)_i$
Slag	Mills *et al.* [103]	Partial molar values

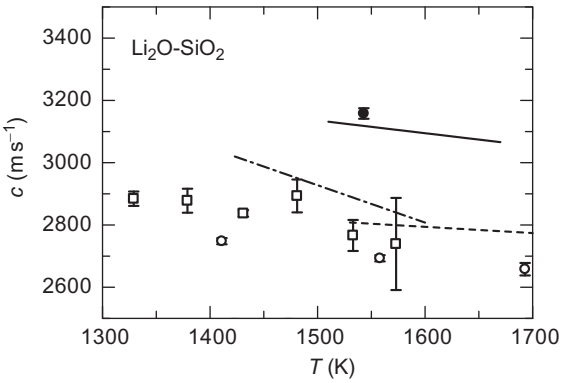


Figure 2.2.54 Temperature dependency of the ultrasonic velocity of 0.33 Li_2O-0.67 SiO_2 and 0.5 Li_2O-0.5 SiO_2 in the liquid states; 0.33 Li_2O-0.67 SiO_2; — — — = Baidov and Kunin [189]; □ = Matsuzono *et al.* [190]; ○ = Rivers and Carmichael [191];— ▪ — = Shiraishi *et al.* [192]; 0.5 Li_2O-0.5 SiO_2; ——— = Baidov and Kunin [189]; • = Rivers and Carmichael [191].

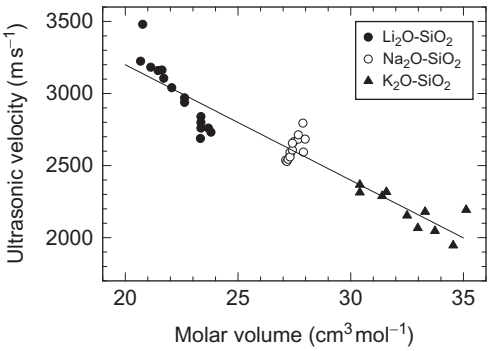


Figure 2.2.55 Ultrasonic velocities of the M_2O-SiO_2 systems (M = Li, Na, and K) at 1573 K as a function of the molar volume.

an acoustic wave to transverse the system is equal to the sum of the times required to pass through each layer, $x_{i,c}/c_i$, where c_i is the speed of sound for layer i:

$$\frac{1}{c} = \sum \frac{x_{i,c}}{c_i} \tag{2.2.64}$$

Here, c_i will be referred to as the sound speed coefficient of component i, which is the definition adopted by Ernst *et al.* [193] for the sound speed in an ideal solution. For instance, the values of c_i for SiO_2, Li_2O, Na_2O, and K_2O are 2524, 4265, 2639, and 1660 m s^{-1}, respectively. It may be surprising that the value of c_i for SiO_2 is relatively small and between the values for Li_2O and K_2O. This means that ultrasonic velocity does not seem to be related to the ionicity or covalency of bonding. In fact, this small ultrasonic velocity (i.e., large compressibility) for SiO_2 is in agreement with the results reported by Laberge *et al.* [195] and Bucaro and Dardy [194].

2.2.4.3.2.2.4 Dependence on Molar Volume Figure 2.2.55 shows the ultrasonic velocities of the M_2O-SiO_2 systems (M = Li, Na, and K) at 1573 K plotted against the molar volumes. There is an identical linear relation between the adiabatic compressibility and the molar volumes. This indicates that the molar volume is one of the most significant factors affecting the ultrasonic velocity value. This is quite reasonable because the adiabatic compressibility, which is related to the velocity by Equation (2.2.63) is strongly relevant to the molar volume; the component with larger molar volume will have more free space between ions for compression.

2.2.4.3.2.3 Methods Used to Determine Acoustic Properties

In most cases, high-temperature ultrasonic measurements are carried out using a pulse technique. An ultrasonic pulse is generated and detected by a piezo-electric transducer of quartz or $BaTiO_3$ crystals at room temperature. It is then transmitted to the high-temperature section of the furnace through a buffer rod made of fused silica, or

polycrystalline or single crystal-alumina. The ultrasonic pulse techniques can be divided into four classes: (i) *pulse echo* technique [191,196], (ii) *pulse transmission* technique [192,197], (iii) *pulse transmission/echo* technique [198], and (iv) *interferometric method*. The pulse transmission/echo technique is best suited to ultrasonic measurements at high pressure. The interferometric method is a derived form of the pulse echo or transmission technique. Some examples of this method have been explained elsewhere [189,191,199]. The principles of pulse echo and transmission techniques are given below.

2.2.4.3.2.3.1 Pulse Echo Technique A schematic diagram of the apparatus is shown in Figure 2.2.56a. Acoustic pulses, generated by the transducer, transmit through a buffer rod and are reflected at the interface between the rod and the sample. The reflected pulses come back though the rod to the transducer where acoustic pulses are converted into electrical pulses. A certain transmission of the pulses takes place from the rod to the sample. The pulses transmitted through the interface are reflected back by the reflector, travel through the rod to the transducer, and generate delayed electrical pulses in the transducer. These are received, amplified, and displayed on the oscilloscope with the first reflected pulses. When the distance between the end of the rod and the reflector is known, the time delay between the pulse reflected at the interface (between the rod and the sample) and the pulse reflected by the reflector gives the desired velocity of ultrasonic waves. The advantage of this technique is that the cell design is simpler than that of the pulse transmission technique. However, the technique has a drawback in that the main pulse is more likely to be affected by the trailing pulse generated by incoherent reflections from the surface of the rod.

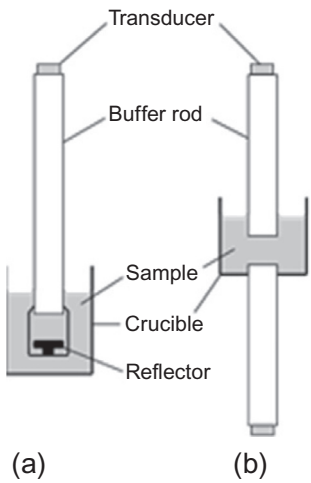


Figure 2.2.56 Cell assemblies of (a) pulse echo technique and (b) pulse transmission technique.

2.2.4.3.2.3.2 Pulse Transmission Technique This technique is employed for liquid samples. In this technique, pairs of buffer rods and transducers are used as shown in Figure 2.2.56b. Acoustic pulses generated from the upper (or lower) transducer travel through the attached rod, the liquid and the other rod in turn, and are received by the lower (or upper) transducer. The upper rod can be moved vertically by a distance Δx, which can be measured very accurately by, for instance, a micro screw gauge or a cathetometer. The time required for a pulse to travel from one transducer to another is precisely measured by an oscilloscope. The velocity of ultrasonic waves (c) can be calculated by dividing the change in the distance between two ends of the rods (Δx) by the change in the time of the travel of the ultrasonic pulses (Δt):

$$c = (\Delta x/\Delta t) \tag{2.2.65}$$

2.2.4.3.2.4 Data for Acoustic Properties

The various systems covered in compilations of acoustic velocity data for silicate melts are summarized in Table 2.2.19.

Figure 2.2.57 shows the velocities of the M_2O-SiO_2 systems (M = Li, Na, and K) at 1573 K as a function of the M_2O content. The data from the various investigations [189,191,200] are in good agreement with the exception of the study due to Bloom and Bockris [199] which may have been affected by the corrosion of the Al_2O_3 buffer rods (thereby increasing the path length and thus decreasing the apparent velocity). The values cited by Shiraishi *et al.* [192] also show a tendency to be higher which may be due to the high frequency used (10 MHz) which is much higher than that used by other workers (<4 MHz). It was pointed out earlier that the acoustic velocity should be independent of frequency (i.e., "dispersionless"). However, dispersion does occur at very high frequencies with high-viscosity melts (ca. >1000 dPas) where relaxation times are very long and the velocity increases with frequency [189]. Thus, the measurements reported by Shiraishi *et al.* [192] are probably affected by the high frequency used.

Table 2.2.19 Systems covered in compilations of acoustic velocity data; see "Symbols, units, and abbreviations" for chemical formulae abbreviations

Reference	Systems covered
Watanabe *et al.* [168]	SiO_2; Al_2O_3; B_2O_3; LS; NS:KS: PS, Na, and Pb borates
Ghiorso and Kress [169]	CS; FS; KS; CFS; CMS; CoNS; FNS; KNS; NiNS; CMNS CAS; KAS; MAS; NAS; CFAS; CMAS; CNAS; NMAS; CKMAS; CMNAS CTS; FAS; KTS; MTS; NTS; CKTS; CNTS; FKTS; CFMAS; CATS; CKATS; CFMNATS; CFMNATS; CFKMNATS

Note: F = FeO_x (i.e., FeO + Fe_2O_3); Co = CoO; Ni = NiO.

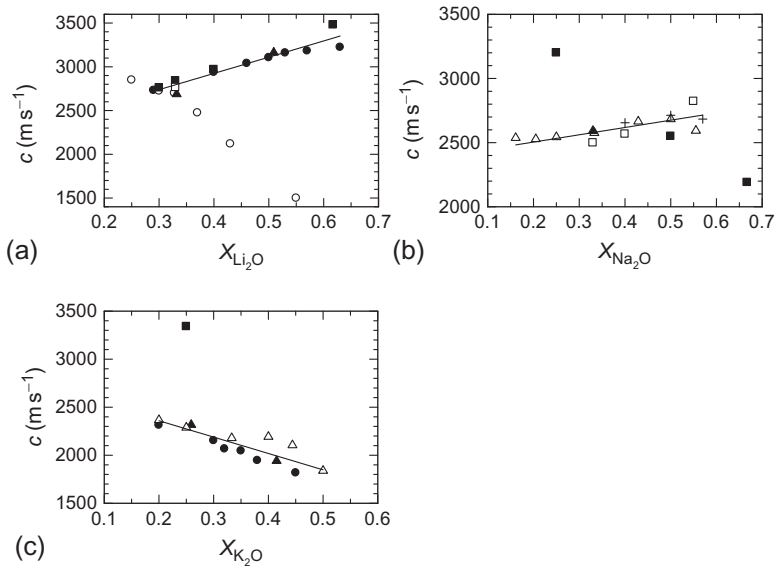


Figure 2.2.57 Velocities of the M_2O-SiO_2 systems at 1573 K as a function of the M_2O content (a) Li_2O: ●=Baidov and Kunin [189]; ○=Bloom and Bockris [199]; ▲=Rivers and Carmichael [191]; ■=Shiraishi *et al.* [192]; □=Matsuzono *et al.* [190]; (b) Na_2O: ▲=Rivers and Carmichael [191] (4-11 MHz); ■=Shiraishi *et al.* [192] (5-20 MHz); □=Matsuzono *et al.* [190] (5 MHz); Δ=Bochris and Kojonen [201] (1 MHz); +=Nagata *et al.* [202] (5 and 10 MHz); and (c) K_2O; ●=Baidov and Kunin [189] (1 MHz); ▲=Rivers and Carmichael [191] (4-5 MHz); Δ=Bockris and Kojonen [201] (1 MHz); ■=Shiraishi *et al.* [192] (10 MHz).

It can be seen from Figure 2.2.57 that:

(i) the velocities are in the hierarchy $Li_2O > Na_2O > K_2O$

(ii) the slope (dc/dX_{M_2O}) is positive for Li_2O and Na_2O but negative for K_2O.

Figure 2.2.58 shows the temperature dependency of the velocity and the parameter $(\alpha^*\lambda)$ values for $0.33Na_2O{\cdot}0.67SiO_2$ and $0.33\ K_2O{\cdot}0.67\ SiO_2$, respectively, where α^* is the absorption coefficient and λ is the wavelength of ultrasonic waves; the term $(\alpha^*\lambda)$ represents the absorption per wavelength. It can be seen from Figure 2.2.58 that

(i) the acoustic velocity (c) decreases with increasing temperature;

(ii) at lower temperatures (where the melt is unrelaxed) the velocity (at that temperature) increases with increasing frequency;

(iii) the term $(\alpha^*\lambda)$ goes through a maximum.

With regard to the maximum in the $(\alpha^*\lambda)$-T relation, at high temperatures the melt is relaxed and the response of the melt to acoustic pressure is instantaneous: when cooling toward the glass transition region, the response of a melt to acoustic pressure is delayed. The absorption of acoustic energy is associated with this delay between acoustic pressure

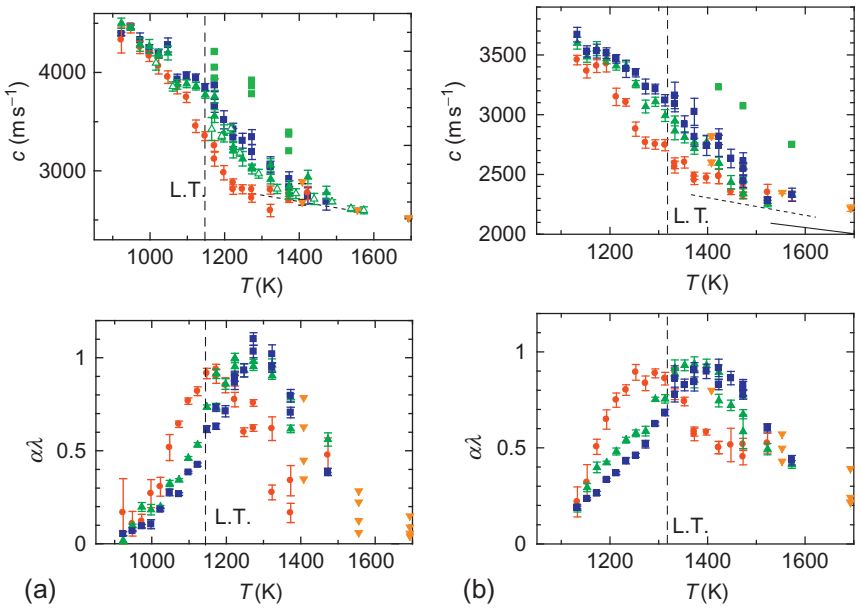


Figure 2.2.58 Temperature dependency of the velocity of sound and values of $\alpha^*\lambda$ for (a) 0.33 Na_2O-0.67 SiO_2; ▲ = Hayashi *et al.* [200] (1.2 MHz); ▲ = Hayashi *et al.* [200] (5 MHz); ◊ = Hayashi *et al.* [200] (6 MHz); Δ = Matsuzono *et al.* [190] (5 MHz); ● = Rivers and Carmichael [191] (4-11 MHz); ■ = Shiraishi *et al.* [192] (6-15.3 MHz); — — = Bochris and Kojonen [201] (1 MHz) and (b) 0.33 K_2O-0.67 SiO_2: ♦ = Hayashi *et al.* [200] (1.2 MHz); ▲ = Hayashi *et al.* [200] (3.6 MHz); □ = Hayashi *et al.* [200] (6 MHz); Δ = Rivers and Carmichael [191] (4-11 MHz).

and the medium response (density or volume change). This delay increases as the temperature continues to decrease, and hence the absorption of acoustic energy becomes greater. However, with further temperature decrease (toward T_g) the structure of the glass becomes frozen. Under these conditions there is less response to acoustic pressure resulting in less absorption of acoustic energy. Consequently, the peak temperature of the $\alpha^*\lambda$ versus T curve corresponds to the glass transition temperature for ultrasonic waves. The peak temperature (1180-1270 K for 0.33 Na_2O-0.67 SiO_2 and 1270-1400 K for 0.33 K_2O-0.67 SiO_2) increases with increasing frequency, as shown in Figure 2.2.58. It has been reported that the conventional "glass transition temperatures" obtained by thermal expansion measurement are 729 K for 33 $Na_2O{\cdot}67$ SiO_2 and 755 K for 33 $K_2O{\cdot}67$ SiO_2 [22]. Thus, there is a large diversion between T_g values recorded for ultrasonic waves and those recorded in thermal expansion studies; these differences are due to the differences in the experimental observation timescale, i.e., microseconds for ultrasonic waves against seconds for thermal expansion.

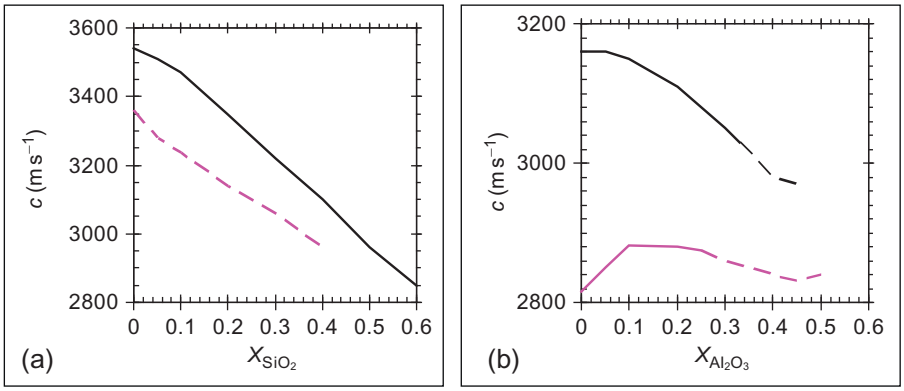


Figure 2.2.59 The acoustic velocity of CaO-Al_2O_3-SiO_2 melts as functions of (a) mole fraction SiO_2; solid curve = $(X_{Ca}/X_{Al}) = 1$; and dashed curve = $(X_{Ca}/X_{Al}) = 2$; and (b) mole fraction Al_2O_3 upper curve = $(X_{Ca}/X_{Si}) = 1$ and lower curve = $(X_{Ca}/X_{Si}) = 0.5$; solid line = peralkaline region (i.e., $X_{Ca} > X_{Al}$) dashed line = peraluminous region (i.e., $X_{Ca} < X_{Al}$).

The acoustic velocity of CaO-Al_2O_3-SiO_2 melts has been determined [203] and the data are plotted in Figure 2.2.59. It can be seen that the acoustic velocity (c):

(i) decreases as the mole fraction of SiO_2 increases (Figure 2.2.59a).

(ii) decreases with increasing mole fraction Al_2O_3 for melts where $(X_{Ca}/X_{Si}) = 1$ but for more highly polymerized melts with $(X_{Ca}/X_{Si}) = 0.5$ there is an initial increase in c followed by a fairly flat region (Figure 2.2.59b).

2.2.4.3.2.5 Methods of Calculating Ultrasonic Velocities from Composition

The published models for calculating based on the chemical composition of the melt are summarized in Table 2.2.20.

2.2.4.4. Surface (γ_{sl}) and Interfacial Tension (γ_{msl})

Surface tension (γ) and interfacial tension (γ_{msl}) differ from other properties in that they are *surface properties* and not *bulk properties*.

2.2.4.4.1 Why Surface and Interfacial Tension Data are Needed

Surface and interfacial tensions (γ) are important because they affect many processes. For instance, gradients in surface tension give rise to Marangoni flows which affect the kinetics of metal/slag reactions and also affect flow patterns in the vessel; Marangoni flow in the fluid always occurs in the direction of low surface tension to high-surface tension. These Marangoni forces can arise from surface tension gradients caused by variations in (i) temperature ("Thermo-capillary"), (ii) composition ("Diffuso-capillary"), and (iii) electrical potential ("Electro-capillary").

Table 2.2.20 Summary of models to calculate the acoustic velocity (m s^{-1}) of silicate melts

Reference	Model	Comment
Rivers and Carmichael [191]	*Method 1*: for 1673 K	±3.8%
	$1/c = \sum (x/c)_i$ (2.2.65)	
	where x = volume fraction. Values of dc/dT can also be calculated	
	$1/c = (X_{Li_2O}/4265) + (X_{Na_2O}/2639) + (1380X_{K_2O}) + (X_{MgO}/5328) + (X_{CaO}/5317) + (X_{FeO}/2200) + (X_{SiO_2}/2524) + (X_{Al_2O_3}/2796) + (X_{TiO_2}/1965)$ (2.2.66)	
	Method 2: for 1673 K	±2.7%
	$\text{Partial molar } c = \Sigma(X_i c_i)$ (2.2.67)	
	$c_{1673K} = (3675X_{Li_2O}) + (2861X_{Na_2O}) + (1660X_{K_2O}) - (129X_{Rb_2O}) - (1149X_{Cs_2O}) + (3472X_{MgO}) + (3994X_{CaO}) + (2949X_{SrO}) + (2453X_{BaO}) + (2361X_{FeO}) + (2381X_{SiO_2}) + (2677X_{Al_2O_3}) + (1492X_{TiO_2})$ (2.2.68)	
	Values of dc/dT can also be calculated	

Ghiorso and Kress [169]	Partial molar values: $c = \Sigma(X_i c_i) + X_{Na_2O} X_{Al_2O_3} \cdot c_{Na-Al} + X_{Na_2O} X_{TiO_2} \cdot c_{Na-Ti} + X_{K_2O} X_{TiO_2} \cdot c_{K-Ti}$ (2.2.69) $c_{1673K}\left(ms^{-1}\right) = (3081 X_{Na_2O}) + (1682 X_{K_2O}) + \left(3350 X_{MgO}\right) + (3967 X_{CaO}) + (2400 X_{FeO}) + (1365 X_{Fe_2O_3}) + (1956 X_{FeO_{1.3}}) + (2400 X_{MnO}) + (2322 X_{SiO_2}) + (2738 X_{Al_2O_3}) + (1694 X_{TiO_2}) + 5801 X_{Na_2O} X_{Al_2O_3} - 1325\, X_{Na_2O} X_{TiO_2} - 994\, X_{K_2O} X_{TiO_2}$ (2.2.70) Partial molar values for (dc/dT) also given	±1.7%
Hayashi *et al.* [200]	Calculate c for M_2O-SiO_2 systems from molar volume: $c_{1573K}\left(ms^{-1}\right) = 4800 - 80\, V_{1573}$ (2.2.71)	±3%

The interfacial tension γ_{msl} (between the metal and slag) affects the following:

(i) The removal of inclusions from the liquid metal by both flotation and argon bubbling.

(ii) Entrapment of slag in metal (or metal in slag) which decreases with increase in γ_{msl} [204].

(iii) The *shape of the meniscus in continuous casting* is affected by γ_{msl}.

(iv) The *adhesion of scale and scum* is dependent on interfacial tension between the mold flux and solid steel [205].

(v) Marangoni forces arising from local changes in electrical potential occurring in slag/metal reactions are thought to increase the kinetics of these reactions.

Values of the surface tension of the slag (γ_{sl}) are needed to calculate the interfacial tension (γ_{msl}), see Equation (2.2.72).

2.2.4.4.2 Factors Affecting Surface and Interfacial Tension

The surface tensions of both metals and slags are dependent upon the concentrations of *surfactants* present. Surfactants tend to be materials with low surface tension; the surface layer of a liquid tends to have a high concentration of surfactants. That is why ppm levels of surfactants can have a significant effect on surface tension since surfactants concentrate in the surface layer. In steels the principal surfactants are *soluble* sulfur and oxygen whereas the principal surfactants in slags are B_2O_3, K_2O and Na_2O and CaF_2; however, their effect on γ_{sl} is much less dramatic than the effect of *soluble* $\underline{S}$ and $\underline{O}$ on γ_m.

The interfacial tension is given by the following equation where γ_m and γ_{sl} are the surface tensions of the metal and slag phases, respectively, and φ is an interaction coefficient [206]:

$$\gamma_{msl} = \gamma_m + \gamma_{sl} - 2\phi(\gamma_m\gamma_{sl})^{0.5} \tag{2.2.72}$$

The parameter, ϕ, was found to have a value of 0.5 for slags free of FeO but increased with FeO additions [134]. It was proposed that the following equation could be applied where the effect of FeO presumably accounted for the fact that FeO in the slag resulted in a higher concentration of soluble $\underline{O}$ in the metal

$$\phi = 0.5 + 0.3X_{FeO} \tag{2.2.73}$$

More recently, Tanaka [207] accounted separately for the effects of soluble oxygen on the metal and the slag when calculating γ_{msl}; the surface tension of the steel is usually expressed in the form of Equation (2.2.74) since most steels contain sufficient Al to keep the soluble O to ca, 4ppm; where k_1 and k_2 are stated constants

$$\gamma_T = 1880 - 0.41(T - T_{liq}) - k_1 T \ \mathrm{In}\{(1 + \exp(k_2/T)) \cdot (\mathrm{wt\%S})\} \tag{2.2.74}$$

Surface tensions of the steel (γ_m) tend to have values between 1500 and 1850 mN m^{-1} whereas the surface tension (γ_{sl}) of most slags has values of ca. 450 mN m^{-1}; thus $\gamma_m \approx 4\,\gamma_{sl}$. Consequently, the most important term in Equation (2.2.72) is γ_m and this is very dependent upon the *soluble* S- and O-contents of the steel [208] (Figure 2.2.60a). In most steels the Al content is sufficiently high to hold the *soluble* O content down to ca. 4 ppm but Al has little effect on the soluble S content. Thus, γ_m is largely determined by the S content of the steel and it can be seen from Figure 2.2.60a that 50 ppm S causes a 25% decrease in γ_m. However, FeO in the mold slag will increase the *soluble* O in the steel and it is probably the latter which causes the apparent increase in the interaction coefficient (ϕ) (Equation 2.2.73).

When there is a reaction between slag and metal (S-transfer or Al transfer, Equations 2.2.1 and 2.2.2) the vigorous mass transfer (Figure 2.2.60) apparently results in a dramatic reduction in the interfacial tension (Figure 2.2.61 [210,211]). When most of the slag/metal reaction is complete and the mass transfer approaches completion and the mass transfer rate is much reduced the apparent interfacial tension increases sharply (Figure 2.2.61). It has been suggested (on the basis of observations on organic systems) that this effect is related to the large differences in volume of the slag and metal ($V_{sl} > V_m$) used in the experiments and that there would be a smooth change in interfacial tension for $V_{sl}/V_m \leq 1$ [212].

The interfacial tension of a mold flux has been reported to increase as (i) Al_2O_3 increased [213] and (ii) the contents of Na_2O, CaF_2, FeO, and MnO decreased [213]. The interfacial tension is usually increased by reducing the Na_2O content of the flux [205].

Measured values of γ_{ms} tend to be in the range 1100-1400 mN m^{-1} and values of the surface tensions of mold fluxes tend to be in the range 300-400 mN m^{-1}.

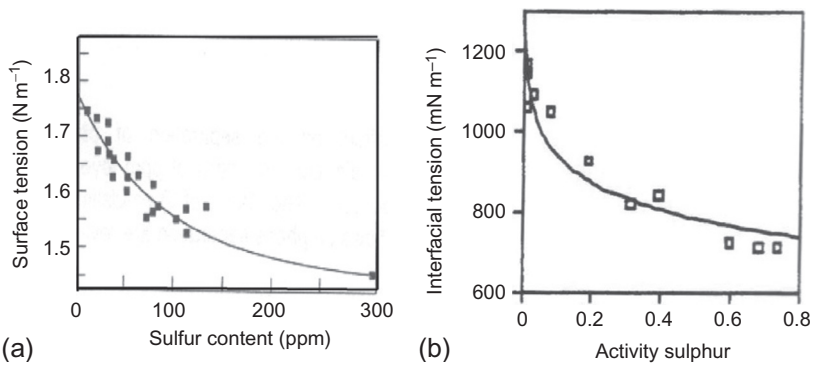


Figure 2.2.60 The effect of *S* on (a) surface tension (γ_m) of steels [208] and (b) interfacial tension [204,209].

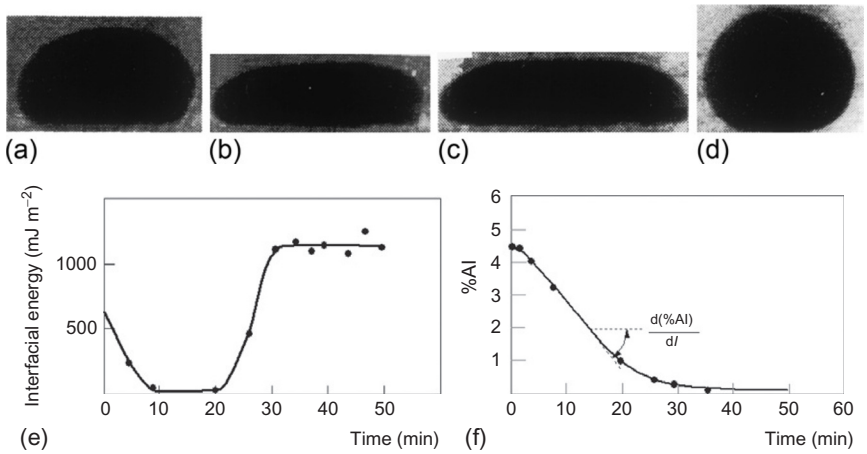


Figure 2.2.61 Transient sessile drop profiles during metal/slag reactions (a) at start of experiment, (b) and (c) during the experiment, and (d) at end of the experiment (when slag/metal reactions are complete) [211] and (e) transient measurements of interfacial tension and (f) mass transfer rate for Al transfer between metal and slag phases (Equations 2.2.1 and 2.2.2) [210].

2.2.4.4.3 Methods Used to Determine Surface and Interfacial Tension

2.2.4.4.3.1 Surface Tension (γ_{sl})

There are several methods available to measure the surface tensions of molten slags and these are detailed below.

2.2.4.4.3.1.1 MBP Method In the MBP method, the gas pressure in a capillary tube is increased continuously until a bubble is formed at the mouth of the tube and subsequently detaches. The capillary radius (r) is made sufficiently small to ensure that the bubble has a spherical contour. The maximum pressure (p_{MBP}) occurs when the bubble formed at the mouth of the capillary is hemispherical. The Laplace equation is used to derive the surface tension (γ) of the melt where $\Delta\rho = (\rho_{sl} - \rho_{gas}) \approx \rho_{sl}$; g = gravitational force and h = depth of immersion [7]. Care must be taken to establish the optimum conditions, e.g., the lifetime of the bubble:

$$P_{MBP} = (2\gamma/r) + \Delta\rho g h \tag{2.2.75}$$

2.2.4.4.3.1.2 SD and Big Drop Methods The shape adopted by a SD (Figure 2.2.62a) represents the balance of surface and gravitational forces. These forces involve the surface tension and the density, respectively, and values of both these properties can be derived with this method. The slag is melted on a metallic plaque and the dimensions and the profile of the drop are measured accurately. Several methods have been used to derive the surface tension and density from the dimensions [7]. In recent years, the accuracy of surface tension and density values has been improved by using software which calculates the "best-fit" values for the parameters affecting the drop profile.

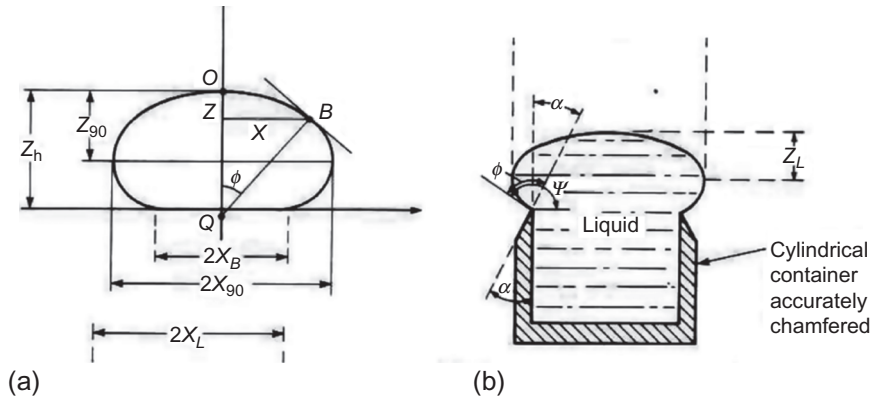


Figure 2.2.62 Schematic drawings showing (a) sessile drop and (b) big drop methods.

The big drop method is a variant of the SD technique (Figure 2.2.62b) where the slag is held in a crucible and the surface profile of the drop is determined.

2.2.4.4.3.1.3 Pendent Drop (PD) and Drop Weight Method A pendent drop (PD) also represents the balance of surface and gravitational forces [7]. Frequently, when this method is applied at high temperatures, the sample is in rod form and the tip of the rod is heated by electron beam or laser heating. For these conditions the surface tension values can only be determined for the liquidus temperature. Software similar to that used in the SD method is used to provide a best fit of the measured drop profile.

The PD method is often used with the drop weight method; since the PD eventually falls and forms a spherical drop; the solidified drops are collected and weighed giving W_{ideal}. The surface tension is calculated from the following equation where r = the radius of the tube or rod:

$$W_{\text{ideal}} = 2\pi\gamma r \tag{2.2.76}$$

However, the measured weight (W_{meas}) of the drops is less than W_{ideal} and so a correction term (f) is usually applied and f' is determined in preliminary experiments using liquids of known surface tension [7]:

$$W_{\text{ideal}} = 2\pi\gamma r f' \tag{2.2.77}$$

2.2.4.4.3.1.4 Detachment Methods In this technique, a tube (or rod, plate or ring) is located just below the surface of the liquid. The probe is attached to a balance and then the mass is measured continuously as the probe is slowly pulled from the melt [7]. The force on the probe is measured; this force is the resultant of surface tension and mass. This force goes through a maximum at the point where the meniscus is about to break and thus

the measured weight also goes through a maximum (W_{max}). The surface tension is calculated by Equation (2.2.78) where r = radius of tube or probe and G is a correction factor

$$\gamma = ((W_{max})g)\,G/4\pi r \tag{2.2.78}$$

2.2.4.4.3.1.5 Other Methods As mentioned earlier in the section dealing with measurement of viscosities, the draining crucible and the SLLS methods are also capable of measuring the surface tension.

In the SLLS method "ripplons" are monitored [121–123]. The surface of a melt may appear smooth but it is being continually deformed by thermal fluctuations of the molecules. Capillary waves (ripplons) have a small amplitude (*ca.* 1 nm) and a wavelength of ca. 100 μm which is dependent upon the frequency. Ripplon action depends upon the surface tension for restoration and the kinematic viscosity ($v = \eta/\rho$) for oscillation damping. The spectrum of the *ripplons* is derived using a Fourier spectrum analyzer allowing the surface tension and the viscosity to be determined. The method has been successfully used for measurements on liquid silicon [122] and $LiNbO_3$ up to 1750 K [123].

2.2.4.4.3.2 Interfacial Tension (γ_{msl})

Two methods have been used to measure metal/slag interfacial tension of slags and steel:

2.2.4.4.3.2.1 X-ray SD Method A cylinder of steel is placed in a MgO crucible and then covered with slag and heated in a tube furnace under an inert atmosphere. When both slag and metal have melted, a SD of steel in molten slag is formed and observed by passing X-rays through the crucible (Figure 2.2.63). The slag is transparent to X-rays whereas the steel is opaque and thus the image of the SD can be observed. The contact angle and the dimensions of the drop are measured and the interfacial tension is determined using software packages based on the Laplace equation. Most of the published data have been obtained with this method.

2.2.4.4.3.2.2 Lens Method In this method mold slag forms are placed on the meniscus of molten steel. The slag melts and forms a lens-shaped drop [7]. The dimensions and contact angle are observed and measured.

2.2.4.4.3.3 Data for Surface and Interfacial Tension

The data sources for the surface and interfacial tension involving silicate melts are summarized in Table 2.2.21.

2.2.4.4.4 Methods of Calculating Surface and Interfacial Tension from Composition

The various methods used to calculate the surface and interfacial tension from chemical composition data are summarized in Table 2.2.22.

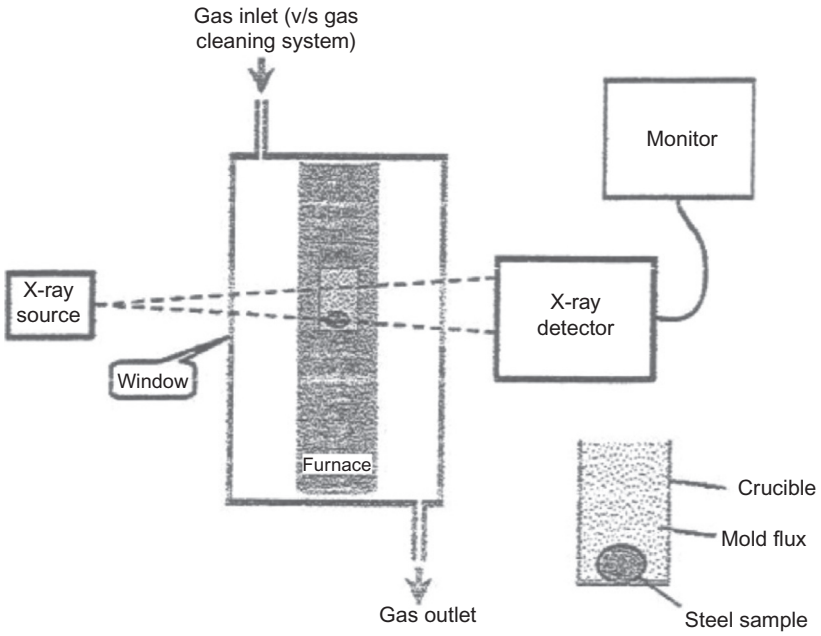


Figure 2.2.63 Schematic drawing showing the X-ray sessile drop method.

2.2.4.5. Heat Transfer and Transport Properties

When an object is heated, the atoms (or ions) become agitated and start to vibrate and these vibrations cause further agitation in neighboring atoms and these, in turn, interact with their neighbors and so heat is transferred in this manner. Thus, heat is conducted by *phonons*, i.e., *lattice waves*.

Glasses, slags, and fluxes are considered to be *semitransparent media* and heat transfer occurs by several mechanisms in these materials, namely by:

(i) *lattice conduction* which involves the transfer of *phonons* (lattice waves)
(ii) *convection* (in liquids)
(iii) *radiation conduction* which involves a process of absorption and reemission of IR radiation (see Section 2.2.4.4.2) which is sometimes denoted *photon conduction*.

These mechanisms can all contribute to the overall conductivity (k_{eff})

$$k_{\text{eff}} = k_{\text{lat}} + k_{\text{conv}} + k_{\text{R}} \tag{2.2.83}$$

where k_{lat} = lattice conductivity, k_{conv} = contribution from convection, and k_{R} = radiation conductivity. The usual approach taken is to determine these contributions individually. However, it will be seen that it is frequently difficult to disentangle the individual contributions from the measurements of k_{eff}.

Table 2.2.21 Sources of surface tension data for slags and glasses (γ_{sl}) and interfacial tension (γ_{ms}) units are mN m^{-1}; for abbreviations in chemical formulae see "Symbols, units, and abbreviations"; *Fl* = CaF_2

Property/ sample	Reference	Comments, systems covered
Surface tension		
Glass	Fluegel [214]	Based on SciGlass database
	Priven [141]	Based on MDL-SciGlass database
Slags—general	Slag Atlas [7], Chapter 10 Ogino [178]	(γ_{sl}-composition) and (γ_{sl-T}) plots for many binary, ternary, quaternary systems
BOS slags	Mills and Keene [113]	Surface tension—composition on ternary diagrams
CaF_2-based slags	Mills and Keene 4 [148]	For slags used in electro-slag remelting (ESR); *Fl* = CaF_2 Binaries: A *Fl*; B_2O_3 *Fl*; B *Fl*; C *Fl*; M *Fl*; S *Fl*; T *Fl*; V_2O_5-*Fl*; ZrO_2-*Fl* Ternaries: CA *Fl*; AS *Fl*; CS *Fl*
Interfacial tension Slag/Fe	Slag Atlas [7], Chapter 11	Values of γ_{msl} between Fe and slags: binary, ternary, and quaternary slags; also slags containing CaF_2 Effect of O and S in metal on γ_{sl}
	Jimbo [206], Chung and Cramb [213]	Fe/slag
	Sharan and Cramb [215]	Fe/Ni alloy and CAS slag
	Sun *et al.* [216]	Fe and CAS slag
Mold flux/ Fe	Cramb and Jimbo [213]	Effect of Al_2O_3; Na_2O on γ_{msl} determined
	Elfsburg and Matsushita [217]	Measured γ_{msl} for mold flux/Fe
	Gornerup [218]	γ_{msl} measured for two mold fluxes

2.2.4.5.1 Why Thermal Conductivity Data are Needed

The thermal conductivities of slags and glasses are very important since it is essential that the processing temperature is sufficient to ensure (i) reasonable draining times for the process and (ii) good glass products. The fact that much of knowledge of radiation conduction comes from work carried out on glasses underlines the importance of heat transfer to the glass industry. In the metallurgical industry, freeze (slag) linings are used to prolong refractory life but also provide valuable thermal insulation. However, it is the continuous

Table 2.2.22 Summary of models to calculate the surface tension of slags and slag/metal interfacial tensions

Slag type (phase)	Reference	Details of model
Surface tension		
Glasses (liquid)	Priven [141]	Thermodynamic approach but equm. constants and chemical activities replaced by empirical constants. Surface tension at 1673 K
-(liquid)	Fluegel [214] (Kucuk *et al.* [219])	Multiple linear regression of data for 1673 K: $\gamma\left(\mathrm{mN\,m^{-1}}\right) = 271.2 + 148X_{\mathrm{Li_2O}} - 222X_{\mathrm{K_2O}} + 196X_{\mathrm{LMgO}} + 334X_{\mathrm{CaO}} + 148X_{\mathrm{Li_2O}} + 128X_{\mathrm{BaO}} + 332X_{\mathrm{SrO}} + 268X_{\mathrm{FeO}} + 292X_{\mathrm{MnO}} + 347X_{\mathrm{Al_2O_3}}$ (2.2.79) Limited compositional range for metallurgical slags
Slags multicomponent	Mills *et al.* [114]	Nonsurface active component $\gamma = \Sigma\, X_1\gamma_1 + X_2\gamma_2 + X_3\gamma_3 + \cdots$ (2.2.80) whereas surfactants are treated (i) as a polynomial ($X_2\,\gamma_2 = a + bX + cX^2$) for $X_2 =$ (0-critical point, N) and (ii) by $X_2\gamma_2 = a' + b'X, \quad \text{for } X_2 > N$ (2.2.81) Overestimates the effect of surfactants when several surfactants present
Slags multicomponent	Mills *et al.* [104]	As above but assumes surface saturation of surfactants occurs when $N = 0.12$ and when $N > 0.12$ remaining surfactants taken as positive contributions of $X_i\,\gamma$
Slags ternaries	Nakamoto and Tanaka [137,138] Hanao *et al.* [140]	1. Butler-Bloom equation uses molar volume data and ionic radii for cations 2. Takes radii of cations and anions into account and the partition of ions between bulk and surface Applied to various ternary systems including systems involving surfactants B_2O_3, CaF_2, and Na_2O

Continued

Table 2.2.22 Summary of models to calculate the surface tension of slags and slag/metal interfacial tensions—cont'd

Slag type (phase)	Reference	Details of model
Ternaries	Wang *et al.* [220]	Geometric model to calculate surface tensions from binary data
	Nakamoto *et al.* [221,222]	Neural network-predicted values in good agreement with measured values for ternaries Also applied to mold fluxes—Hanao *et al.* [140]
Interfacial tension Fe/slag		
Fe/mold flux	Chung [206]	$\gamma_{ms} = \gamma_{ml} + \gamma_{sl} + 2\phi(\gamma_m \cdot \gamma_S)^{0.5}$ (2.2.82)
	Qiao *et al.* [223]	Excess interfacial tension $\gamma^{xs}_{msl} = (\gamma^{meas}_{nsl} - \gamma^{calc}_{msl})$
	Tanaka *et al.* [134]	$\gamma_{ms} = \gamma_{msl} + \gamma_{sl} + \phi\ (\gamma_m . \gamma_S)^{0.5}$: ϕ has value of 0.5 except for systems containing FeO where $\phi = 0.5 + 0.3\ X_{FeO}$
	Tanaka [207]	Approach as above: models for surface tensions of (1) alloys, (2) salts and slags, (3) interfacial tensions, and (4) model of wetting angle metal/oxide

casting of steel (which is used to cast >90% of the world steel production, i.e., >1 billion ton per annum) which is most heavily reliant on the heat transfer characteristics of the slag to minimize product defects and process problems. In this process the steel initially freezes as a thin shell in the water-cooled mold. The heat transfer is controlled by a thin slag film (ca. 2 mm thick) formed between the thin, steel shell and the mold. For medium-carbon steels, excessive heat extraction results in both a thicker, less-uniform, shell and in the formation of *longitudinal cracks* on the product surface which is very undesirable. In high-carbon steels, the shell is weak and it can easily crack if the shell is too thin. Under these conditions cracks in the shell allow steel to escape from the mold (*sticker breakout*). *Stickers* are estimated to cost up to 1 million $ per incident. So control of heat transfer is absolutely essential to the success of continuous casting.

2.2.4.5.2 Factors Affecting Thermal Conductivity and Diffusivity

2.2.4.5.2.1 Lattice (or Phonon) Conductivity (k_{lat})

The lattice conductivity (k_{lat}) is usually determined by making use of *Fouriers first and second laws*.

Fourier's first law was derived by empirical observation and refers to *steady state* conditions; it can be represented by Equation (2.2.84) where Q = rate of heat supplied (J s^{-1}), A = area (m^2), k is the thermal conductivity (W m^{-1} K^{-1}), and (dT/dx) is the temperature gradient (K m^{-1}) where x represents the position:

$$Q = -kA(dT/dx) \tag{2.2.84}$$

Fourier's second law deals with the *nonsteady state* conditions when temperatures are changing with time (t). For one-dimensional flow it can be expressed by Equation (2.2.85) where a is the thermal diffusivity with units of m^2 s^{-1} (the same units as D and kinematic viscosity ($=\eta/\rho$)).

$$\left(d^2T/dx^2\right) = (dT/dt)/a \tag{2.2.85}$$

For two-dimensional flow it is represented by

$$\left(d^2T/dx^2\right) + \left(d^2T/dy^2\right) = (dT/dt)/a \tag{2.2.86}$$

The evolution of T-x curves with increasing time is frequently represented using the error function complement (erfc) where T_0 is the initial concentration at x:

$$T(x,t) = T_0 \,\mathrm{erfc}\left(x/2\sqrt{at}\right) \tag{2.2.87}$$

The thermal diffusivity (a) is related to the thermal conductivity (a) through Equation (2.2.88) where C_p = heat capacity and ρ = density of the sample:

$$a_{eff} = k_{eff}/C_p \cdot \rho \tag{2.2.88}$$

Several factors affect the thermal conductivity value of solid silicate samples, namely:

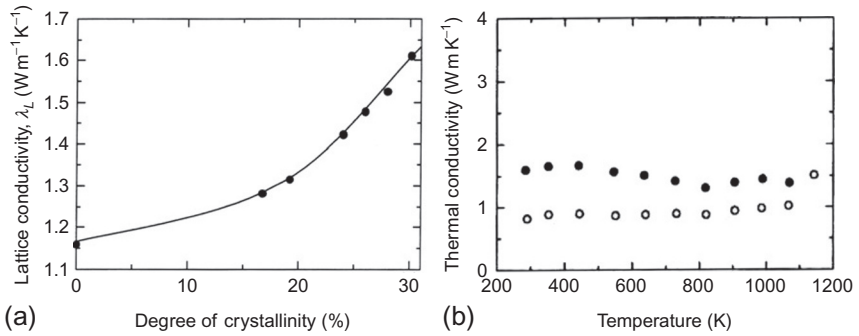


Figure 2.2.64 Thermal conductivity of (a) mold flux as function of fraction crystalline phase (f_{crys}) expressed as % [225] and (b) of $CaO\text{-}Al_2O_3\text{-}SiO_2$ slags as a function of temperature ○ = glassy phase; ● = crystalline phase [224].

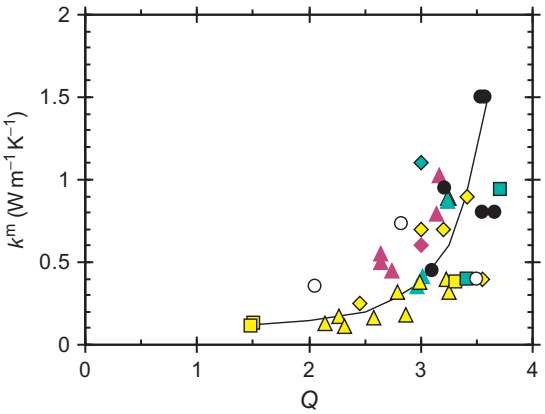


Figure 2.2.65 Thermal conductivity of liquid slags as a function of Q for (a) k^m, ◆ = LS; ◊ = NS; ◆ = KS; ○ = CS; Δ = CNS; ▲ = CLS; ▲ = CKS; ● = CAS; ■ = LAS; □ = NAS [85].

- **(i)** The nature of the sample (i.e., whether it is *crystalline or glassy*) since $k_{cryst} \approx 2\ k_{glass}$ (see Figure 2.2.64b [224]) since the atoms are closer packed in the crystalline phase than in the glass; the effect of gradual crystallization of a mold flux sample on k_{eff} is shown in Figure 2.2.64a [225].
- **(ii)** The *porosity* in the sample since k_{eff} decreases as the porosity increases.
- **(iii)** The *SiO_2 content* (or the degree of polymerization, Q) of the slag increases, with k_{eff} increasing as Q increases (see Figure 2.2.65); note the curve has a similar double-exponential curve to that for viscosity
- **(iv)** The *nature of the cation* with k_{eff} increasing as the field strength (z/r^2) of the cation increases (see Figure 2.2.65) with k_{298}, $k_{T_{crit}}$, and k^m values all increasing with increasing field strength (z/r^2).

2.2.4.5.2.2 Radiation Conductivity (k_R)

In the early 1960s, it was found that the measured thermal conductivity (k_{eff}) values of glass samples (Figure 2.2.66) increased with increasing sample thickness (or depth) [226]. This was ascribed to increasing contributions from radiation conductivity as the sample thickness increased. Consider the glass sample to be made up of a number of layers. When infrared radiation strikes the surface layer, it is absorbed and the temperature ($T_{\text{layer 1}}$) increases. Layer 1 then radiates to layer 2 since $T_{\text{layer 1}} > T_{\text{layer 2}}$ and the radiation is absorbed so that $T_{\text{layer 2}} > T_{\text{layer 3}}$. Then layer 3 radiates to layer 4 and so on. Thus, radiation conduction occurs by a mechanism of absorption of IR radiation and reemission. Values of k_R continue to increase with increasing sample thickness (d) until a critical point is reached whereupon it remains constant. Samples below this critical point are described as *optically thin* and those above as *optically thick*. Optical thickness occurs when the parameter ($\alpha^* d > 3$) where α^* is the absorption coefficient.

Values of k_R can be calculated for optically thick conditions using Equation (2.2.89) where σ = Stefan-Boltzmann constant, n = refractive index, and T is in K providing gray-body conditions apply:

$$k_R = 16\sigma n^2 T^3 / 3\alpha^* \tag{2.2.89}$$

It can be seen that k_R increases sharply with temperature since it is dependent upon T^3.

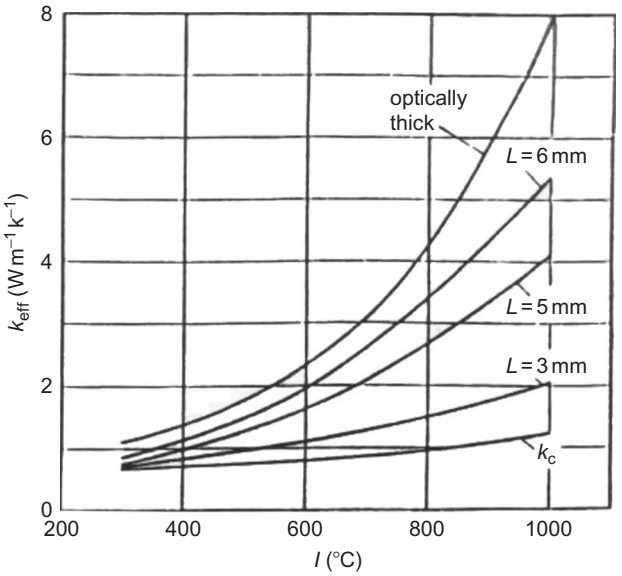


Figure 2.2.66 Effective thermal conductivity (k_{eff}) as a function of temperature, it can be seen that k_{eff} increases with increasing sample thickness [226].

It should be noted that the absorption coefficient is dependent upon both wavelength and temperature (Figure 2.2.74a). It should also be noted that the distribution of emitted energy is also a function of wavelength and temperature (see Figure 2.2.74b).

In practical situations k_R can be reduced by the presence of:

(i) crystallites, grain boundaries, and pores in the sample, all of which *scatter* the IR radiation

(ii) transition metal oxides (e.g., FeO and NiO) which *absorb* the IR radiation [88,226].

2.2.4.5.2.3 Contributions from Convection

Convection can make a significant contribution to the measured thermal conductivity (k_{eff}); in the modeling of the heat transfer in the continuous-casting mold some workers assume that the ratio (k_{conv}/k_{lat}) has values of >10. There are software packages (e.g., k-ε model) which allow the convective contributions to be calculated for the specific experimental conditions.

The measurement of thermal conductivity of molten phases is exceedingly difficult because it is difficult to eradicate all contributions from convection.

2.2.4.5.3 Measurement Problems

There are two major problems encountered when measuring thermal conductivities of slag films, namely, *convection* and *radiation conduction*.

The usual approach taken is to determine a value of the thermal conductivity of the liquid slag free from convection and to calculate the convective contribution using turbulence models (e.g., k-ε model). The main difficulty lies in determining the value of the thermal conductivity of liquid slag which is free from convective contributions. This is achieved by using *transient* methods (i.e., where the measurements are completed before convection has had time to develop, typically around 1 s). *Steady state* methods are unsuitable for these measurements. The two transient techniques in common use are the *laser pulse* (LP) and the *transient hot wire* (THW, sometimes referred to as the line source) methods.

Glasses, slags, and fluxes are semitransparent media and thermal conductivity measurements on both solid and liquid slags are known to contain contributions from radiation conductivity. It is difficult to determine the magnitude of these k_R contributions in the measured thermal conductivity.

2.2.4.5.4 Methods Used to Determine Thermal Conductivity and Diffusivity

2.2.4.5.4.1 LP Method [227–234]

The LP method provides values for the thermal diffusivity (a) from which the thermal conductivity (k) is derived using Equation (2.2.88) (i.e., $k_{eff} = a_{eff} \cdot C_p \cdot \rho$, where C_p and ρ are the heat capacity and the density of the slag, respectively).

The sample is a disc (usually 10-15 mm diam. × 1-2 mm thick) which may be coated on both planar surfaces. Experiments have been carried out in two ways. In the first method (Figure 2.2.67a), a laser beam is directed onto the front face of the specimen

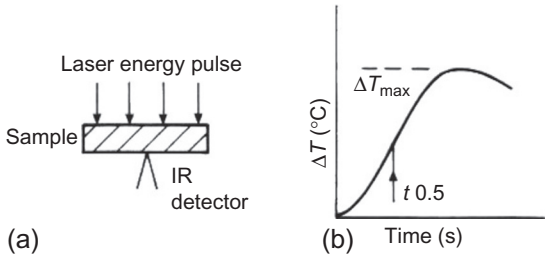


Figure 2.2.67 Schematic diagrams showing laser pulse method used to determine thermal diffusivities of solid specimens (a) sample assembly and (b) typical temperature transient.

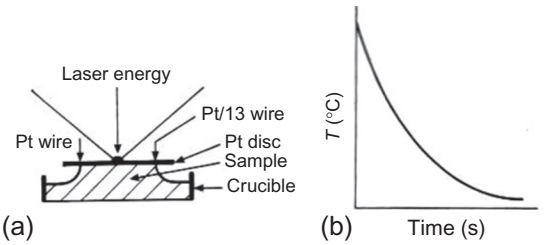


Figure 2.2.68 Alternative laser pulse method used to determine thermal diffusivities of liquids (a) specimen assembly and (b) typical transient of temperature attenuation.

and the temperature of the back face is monitored continuously. The thermal diffusivity is calculated using the relation ($a_{\text{eff}} = 1.37d^2/\pi^2\, t_{0.5}$) where $t_{0.5}$ is the time required to reach $0.5\Delta T_{\max}$ (Figure 2.2.67b). Corrections are usually made to account for radiation losses. The method is used only for measurements on solid samples.

The second method can be used for solid and liquid samples. The sample is in good contact with a Pt disc (Figure 2.2.68a) and the LP is directed onto the Pt disc or the base of a crucible. The temperature transient of the disc (or crucible base) is monitored continuously and the temperature transient data are analysed to provide values of either the thermal diffusivity (a) or effusivity (b). Numerical methods have been used to disentangle k_{R} and k_{c} contributions [230,233,235]. However, when the temperature decay of the Pt crucible is subjected to analytical treatment, it gives values for the *thermal effusivity*, $b = a\,(C_{\text{p}} \cdot \rho)^{0.5}$ [232,234]. The thermal conductivity (k) and diffusivity (a) can be calculated from the thermal effusivity values with values for the density and C_{p} at the measurement temperature.

2.2.4.5.4.2 THW method [234,237]

In this method the sample is placed in a crucible and melted. Then a long thin wire (typically 0.1 mm diam.) is immersed in the molten slag. The thin wire acts as both a heating element and as a temperature sensor (Figure 2.2.69a). When thermal equilibrium is attained, a current is applied for a short duration. The temperature of the wire is monitored continuously for a period of ca. 1 s. The thermal conductivity (k) can be calculated

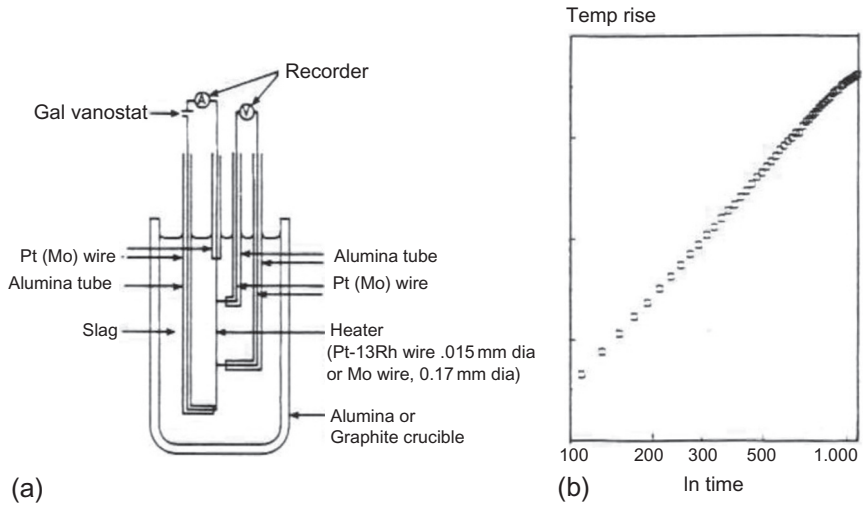


Figure 2.2.69 Transient hot wire method (a) schematic drawing of probe and (b) temperature transient [237,238].

from the following equation where q = heat input per unit length of wire, r = radius of wire, ΔT = temperature rise, and $C = \exp \gamma^*$ where γ^* = Euler's constant:

$$\Delta T = (q/4\pi k)\ln\left(at/r^2 C\right) \tag{2.2.90}$$

However, k is usually determined from the slope ($=1/k$) of the plot of the temperature rise (ΔT) as a function of ln time (Figure 2.2.69b).

2.2.4.5.5 Data for Thermal Conductivity and Diffusivity

Thermal conductivity (k) and diffusivity (a) data for various slag and glass samples are summarized in Table 2.2.23, where entries are grouped according to specimen type.

Table 2.2.23 Summary of thermal conductivity (k) and diffusivity (a) measurements on silicate slags

Type (phase)	Reference	Method	Values	Comments
Slags Binaries, ternaries (solid, *scl* and liquid)	Nagata and Goto [236]	THW		NS; CAS; sharp decrease in k-T when $T > 900$ K
	Susa *et al.* [226] Susa *et al.* [237] Ozawa [239,240]	THW	$k_m = 0.4$-0.8	LS-LiF; NS-NaF; sharp decrease in k-T when $T > 900$ K CAS (300-1270 K) CS, LCS NCS, KCS; sharp decrease in k-T when $T > 1000$ K
	Hayashi *et al.* [238]	THW	Liq: $k < 1$	LS; NS; KS; sharp decrease in k-T when $T > 900$ K

Table 2.2.23 Summary of thermal conductivity (k) and diffusivity (a) measurements on silicate slags—cont'd

Type (phase)	Reference	Method	Values	Comments
	Kang and Morita [241]	THW	Liq: $k > 0.5$	12 Samples CAS (1573-1873 K); k decreases with increasing temperature
Liquid	Ohta *et al.* [232]	LP	Liq: $k = 1.5$-2.8	5 samples CAS; 3 NAS
	Eriksson and Seetharaman [242]	LP	$10^7 a = (4\text{-}8)$	CAS; a-increases with increasing temperature
BF slag/solid and liq	Nagata and Goto [236]	THW	Liq: $k = < 0.3$	Sharp decrease in k-T when $T > 1100$ K
Steelmaking slag	Nagata and Goto [236]	THW	Liq: $k = < 0.8$	Sharp decrease in k-T when $T > 1100$ K
Coal slag/solid	Rhine *et al.* [112,243]	LP		Solid slags (800-1300 K)
Mold fluxes	Nagata and Goto [236]	THW	Liq: $k = < 0.2$	Solid, scl, and liquid; sharp decrease in k-T when $T > 1000$ K
(Liquid)	Powell [244]	THW	$k =$ ca. 0.2	
(Solid, scl)	Taylor and Mills [227]	LP	$10^7 a = (4.5 \pm 0.5)$	10 different mold fluxes a independent of temperature (300 K)
	Shibata *et al.* [229]	LP	$10^7 a = (4\text{-}6.5)$	
	Hayashi *et al.* [238]	LP	$10^7 a = (4.65)$	
	Gornerup *et al.* [218]	LP	Liq: $10^7 a = (4)$	
	Monaghan and Brooks [110]	LP	Liq: $10^7 a = (4)$	Equivalent to $k \approx 1.5$ $\mathrm{Wm^{-1}\,K^{-1}}$
	Waseda *et al.* [228], Ohta *et al.* [231]	LP	$10^7 a = (4)$	Studied effects of TiO_2, ZrO_2, HfO_2 on k_R contribution
Glass	Ohta *et al.* [234]	LP	$10^7 a = (4.5 \pm 0.5)$	Thermal effusivity measured

Note: k ($\mathrm{W\,m^{-1}\,K^{-1}}$) values and ($10^7 a$) values are given in the same column but $10^7 a$ values are denoted in parenthesis, e.g., (4) indicates 4×10^{-7} $\mathrm{m^2\,s^{-1}}$. For abbreviations see "Symbols, units, and abbreviations."

2.2.4.5.6 Analysis of Thermal Conductivity and Thermal Diffusivity Data

Analysis of the data given in Table 2.2.23 indicates that there are significant differences between the values of thermal conductivity derived using the THW and LP methods. A comparison of data for mold fluxes and for Na_2O-CaO-SiO_2 slags of similar compositions (shown in Figures 2.2.70a and b, respectively) indicates that there are large differences between:

(i) k_{THW} and k_{LP} values, especially for the liquid where $k_{LP} \approx 5\ k_{THW}$.

(ii) The shape of the k-T relationships, with k_{LP} remaining fairly constant at high temperatures, in contrast to k_{THW} which shows a marked decrease with increasing temperature above a specific temperature (denoted $T_{crit} \approx 1000$ K in these two cases).

The magnitudes of k_{THW} and k_{LP} and their temperature dependencies are both self-consistent. Two propositions have been put forward to account for the divergence:

(i) k_{LP} values contain much larger k_R contributions in LP studies than those in THW studies due to large differences in the surface areas of the heat sources ($A_{LP} = 10\ A_{THW}$).

(ii) k_{THW} values are low because of electrical leakage from the hot wire into the melt.

At this point of time the problem is unresolved and no values can be recommended for k for temperatures above 970 K.

However, it should be noted that a plot of k_{THW} versus $\log_{10}$ viscosity (dPas) shown in Figure 2.2.71 revealed that T_{crit} always occurred at the temperature where $\log_{10} \eta$ (dPas) = 6 (i.e., between the softening temperature (T_{soft}) where the sample cannot support its own weight and the flow temperature (T_{flow}) [86,87]). This suggests that the magnitude of the thermal conductivity is related to the rigidity of the silicate network, providing that the k_{THW} values prove to be correct.

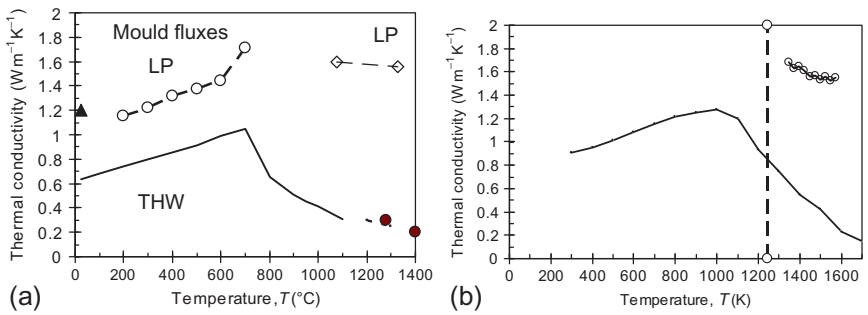


Figure 2.2.70 Comparison of the temperature dependence of thermal conductivity for (a) mold fluxes, k_{THW} values, ——, ● = Nagata and Goto [236] and k_{LP} values (O) calculated from $a = 4.5 \times 10^{-7}$ m^2 s^{-1} due to Taylor and Mills [227] and $a = 4 \times 10^{-7}$ m^2 s^{-1} for the liquid and (b) 0.2 Na_2O-0.1 CaO 0.7 SiO_2 slags; k_{THW} values = line [239] and ○ = k_{LP} values [232].

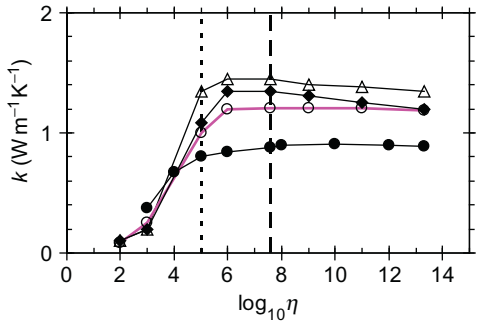


Figure 2.2.71 Values of $\log_{10}$ viscosity for M_2O-SiO_2 slags [240] as a function of calculated viscosity [245]; Δ = NS_4; ◆ = NS_3; o = NS_2, ● = KS_2 in the supercooled phase; --- = T_{soft}; ..... = T_{flow} [87].

Table 2.2.24 Summary of published models to calculate the thermal conductivity of slag films and liquid mold fluxes

Model/reference	Details of model
Mills *et al.* [103]	Accepts k_{THW} data. Calculates values at 298 K, T_{crit} and T_{liq} where T_{crit} is T before the rapid descent with increasing temperature. Assumes linear relations between these points and k values are a function of Q
Mills *et al.* [85]	Two methods based on accepting THW data or LP values. Method 1 (THW): As above Method 2 (LP): Assumes $10^7 a = 4.5$ m^2 s^{-1} for solid for all temperatures and $10^7 a = 4$ m^2 s^{-1} for liquid
Fluegel [245] (Choudhary and Potter [246])	Glass samples, only covers low levels of F. Numerical fit of thermal conductivity data for glasses at ambient temperatures $k = \Sigma(b_{w\%})_1 + (b_{w\%})_2 + \cdots,$ (2.2.91) where b = given constant for constituent 1, 2 etc. and w% = wt%

2.2.4.5.6.1 Methods of Calculating Thermal Conductivity Values from Composition

There are few models available to calculate the thermal conductivity; details of these are summarized in Table 2.2.24.

2.2.4.6. Optical Properties

Since light is a form of electromagnetic radiation, any oscillation in the electrical field will interface with the electrons present in the material. The optical phenomena (transmission and refraction of light) are described as the propagation of the interaction between the oscillation of the electrical field and the electrical dipole in the material.

The various optical properties (refractive index, absorption coefficient, transmissivity, reflectivity, and emissivity) are treated individually below.

2.2.4.6.1 Why Optical Property Data are Needed

The optical properties affect the heat transfer in high-temperature processes where the radiation conductivity (k_R—see Section 2.2.4.4.2 and Equation 2.2.89) is often the biggest factor affecting heat losses from furnaces containing molten glasses and slags; it has been estimated that 90% of the total heat loss from a furnace containing molten glass comes from radiation conduction. The efficiency of freeze linings for thermal insulation will also depend upon the optical properties. The control of k_R in slag films formed between the steel shell and the mold in the continuous casting of steel is essential in minimizing both *longitudinal cracking* and *sticker breakouts* [116]. We have seen earlier (Section 2.2.4.4.2) that radiation conductivity is dependent on the specimen thickness (d) with a sample being described as being *optically thick* when $\alpha^* d > 3$ where α^* is the absorption coefficient.

The refractive index of the slag is important in practical applications, since it provides an index of refining power (i.e., basicity, which is commonly expressed as the ratio {% CaO/% SiO_2} for the slag). The concept of "optical basicity" or "refraction basicity" is derived from the electron polarizability of oxygen and has also been employed to describe the refining power of the slag [32,33,247,248].

2.2.4.6.2 Factors Affecting Optical Properties

2.2.4.6.2.1 Refractive index (n)

The magnitude of optical refraction in a material depends upon its polarizability. The refractive index (n) is directly correlated with the polarizability (via the Lorentz-Lorenz equation)

$$\frac{n^2-1}{n^2+2} = \frac{4\pi}{3} N_A \alpha_m \frac{\rho}{M} \tag{2.2.92}$$

where ρ = density, M = the average molecular weight, N_A = Avogadro's number, and α_m = average electronic polarizability of material.

2.2.4.6.2.2 Effect of Composition

Equation (2.2.92) suggests that the refractive index is determined most strongly by both the packing (i.e., the number of ions per unit volume) and by polarization of the glass. The polarizability, α_m, is calculated as

$$\alpha_m = \sum N_i \alpha_i \tag{2.2.93}$$

where N_i is the concentration and α_i is the electron polarizability of component, i. Values of polarizability have been reported [248–250] and are given in Table 2.2.25.

Table 2.2.25 Values of electronic polarizability, α_i, for various cations and bonding and nonbonding O's

Ion/bond	*T* (K)	α	Ion/bond	*T* (K)	α	Ion/bond	*T* (K)	α
Li^+	298	0.029	Mg^{2+}	298	0.094	Al^{3+}	298	0.052
	298	0.028		298	0.073			
Na^+	298	0.179	Ca^{2+}	298	0.47	BO in Si—O	298	1.467
	298	0.148		298	0.473		1500	1.52
K^+	298	0.83	Sr^{2+}	298	0.86	BO Al(Na^+)—O	298	1.63
	298	0.79		298	0.77		1500	1.70
Rb^+	298	1.4	Ba^{2+}	298	1.55	BO in Al(Ca^{2+})—O	298	1.50
	298	1.34		298	1.50		1500	2.08
Cs^+	298	2.4	B^{3+}	298	0.003	NBO(Na^+)—	298	1.90
	298	2.26					1500	2.17
Be^{2+}	298	0.008	Si^{4+}	298	0.0165	NBO(Ca^{2+})—	298	1.85
	298						1500	1.96

Units of $\alpha_i = Å^3$, where $Å = 10^{-10}$ m.

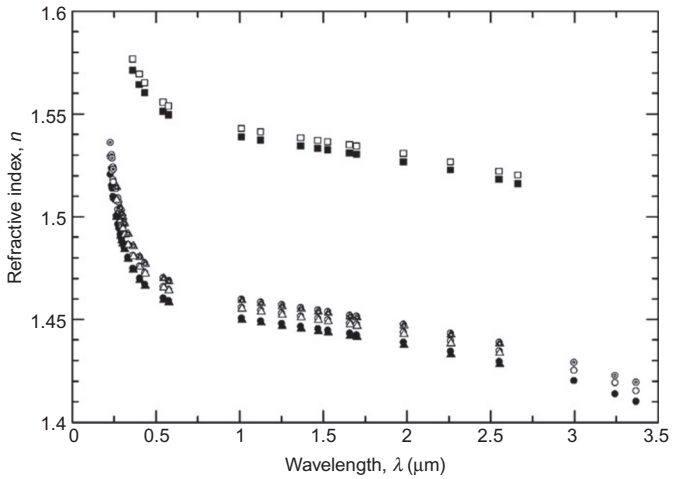


Figure 2.2.72 Refractive index as a function of wavelength: pure SiO_2 ● = at 299 K; o = at 744 K; ○ = at 1100 K; 10% CaO + 7% MgO + 6% BaO + 5% B_2O_3 + 15% Al_2O_3 + 57% SiO_2 ■ = 301 K; □ = 800 K; 3.5% B_2O_3 + 96.5% SiO_2; ▲ = 301 K; Δ = 800 K; ▲ = 1100 K.

2.2.4.6.2.3 Effect of wavelength (λ)

The dependence of the refractive index on wavelength is shown for several commercial glasses and at several temperatures in Figure 2.2.72. It can be seen that the refractive index decreases with increasing wavelength ($n \downarrow$ as $\lambda \uparrow$), the effect being much greater at low wavelengths (<0.5 μm).

2.2.4.6.2.4 Temperature Dependence (d*n*/d*T*)

In general, refractive indices change monotonically with temperature. However, there is some uncertainty as to whether the coefficient (dn/dT) is positive or negative. It is possible to obtain (dn/dT) by differentiating the Lorentz-Lorenz equation with respect to temperature; the result is shown in Equation (2.2.94). It can be seen that the temperature dependence of refractive index can be separated into two terms, namely, a thermal expansion (β) term and a polarization term (φ) (see Equation in 95)

$$\frac{dn}{dT} = \frac{(n^2-1)(n^2+2)}{6n}(\phi - \beta) \tag{2.2.94}$$

$$\phi = \frac{1}{\alpha_m}\frac{d\alpha_m}{dT}, \quad \beta = \frac{1}{V_m}\frac{dV_m}{dT} \tag{2.2.95}$$

where the term V_m is molar volume and α_m is the mean electronic polarizability. Since the term $(n^2+1)(n^2-1)$ is always positive, the positive or negative sign of (dn/dT) is controlled by the magnitude of the β and φ terms. In the case of the Li_2O-SiO_2 system at 1673 K, the critical point is reached when the value of β exceeds that of φ which occurs at X_{Li_2O} = ca. 0.25 and is accompanied by a change in (dn/dT) from positive to negative as shown in Figure 2.2.73 [251,252].

2.2.4.6.3 Absorption Coefficients (α^*)

When IR radiation strikes a glass or liquid some of the energy is absorbed and the remainder is transmitted to other parts of the sample

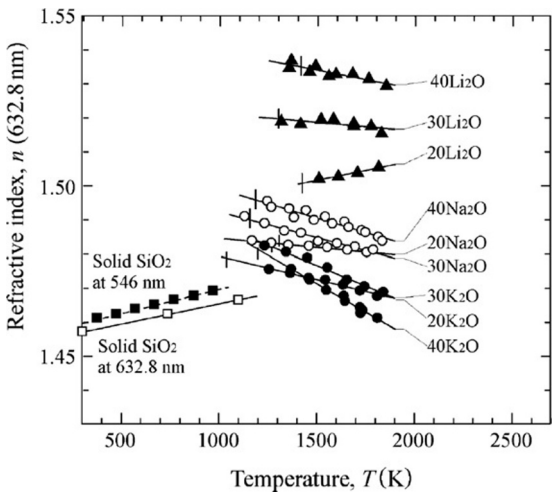


Figure 2.2.73 Refractive indices for binary alkali silicate melts as functions of temperature [251,252]; values refer to mol%.

$$A' + + T' = 1 \tag{2.2.96}$$

where A', and T' are absorptivity and transmissivity, respectively.

The transmissivity is given by the Lambert-Beer law,

$$T' = \exp\{-(\alpha^* d\} \tag{2.2.97}$$

where α^* = absorption coefficient and d = specimen thickness.

The absorption coefficient is very dependent upon wavelength as can be seen from Figure 2.2.74a. It can be seen that the absorption coefficient changes with both wavelength and temperature. When calculating an average absorption coefficient, it should also be noted that the energy emitted is dependent upon both wavelength and temperature (Figure 2.2.74b); the wavelength (in μm) corresponding to peak intensity is given by Wien's law (=2898/T). Thus at 2000 K the peak intensity in emitted energy occurs at ca. 1.45 μm but at 500 K it occurs at ca. 5.8 μm.

The absorption coefficient increases with increasing concentration of transitions metal oxide (e.g., FeO and NiO); this has the effect of reducing k_R and thus the overall heat transfer (Equation 2.2.89).

The absorption coefficient pertains to liquid and glassy phases but for crystalline or partially crystalline materials it is necessary to use the *extinction coefficient*, E (=$\alpha + s$, where s = scattering coefficient). It is not possible to use Equation (2.2.89) for partially crystalline materials since the scattering mechanism is different to that for absorption. In order to use Equation (2.2.89) for crystalline slags, it is necessary to have values for the *albedo* which is used to link scattering to absorption. Unfortunately, we have little data available for the *albedo*.

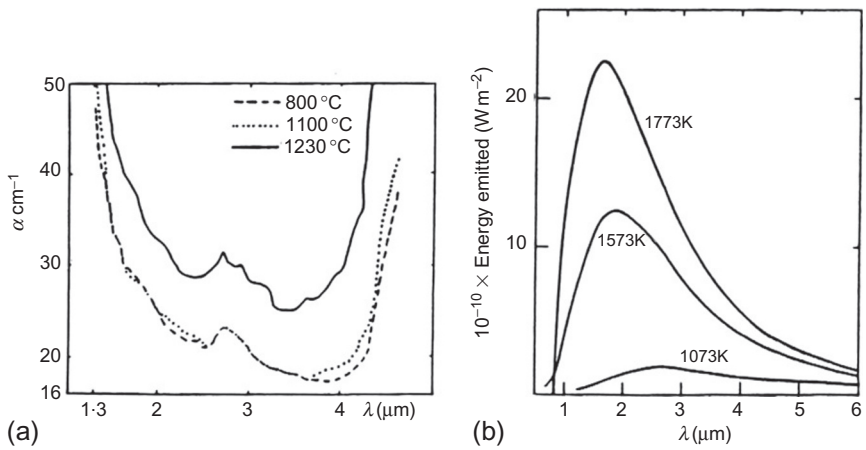


Figure 2.2.74 The effect of both wavelength and temperature on (a) absorption coefficient for a glass (16% Na_2O + 9% FeO_x + 67% SiO_2) and (b) energy emitted by a black body.

When IR radiation strikes a partially crystalline slag film only a fraction of the energy is transmitted since energy is absorbed and reflected; Equation (2.2.98) applies where A', R', and T' are absorptivity, reflectivity, and transmissivity, respectively:

$$A' + R' + T' = 1 \tag{2.2.98}$$

From the Lambert-Beer law, the transmissivity is given by the following

$$T' = \exp\{-(\alpha^* + s)d\} \tag{2.2.99}$$

Susa *et al.* [253,254] measured A', R', and T' for two mold slags and reported that:

(i) transmissivity decreased and reflectivity increased as the fraction of crystalline phase (f_{crys}) increased [253] ($R' \uparrow$ and $T' \downarrow$ as $f_{crys} \uparrow$).

(ii) the addition of 1-2% FeO_x causes A' to increase but R' to decrease [253].

(iii) R' increases and T' decreases with increasing grain size [254] ($R' \uparrow$ and $T' \downarrow$ as $D_{crys} \uparrow$); a grain size of 2-3 μm is recommended for the lowest heat flux, q_{hor} [254].

(iv) in order to reduce the overall heat flux, the use of a sample free of FeO_x is recommended [254].

Values of the absorption coefficient, α, are significantly increased by the presence of transition metal oxides in the slag (α^* (m^{-1}) = $\alpha^{*0} + K\%MO$) where α^{*0} = absorption coefficient with 0% transition metal oxide (MO) where K has values of 910, 5, and 410 m^{-1} for FeO, MnO, and NiO, respectively, and $K_{Cr_2O_3} > K_{FeO}$ [88,226].

2.2.4.6.4 Methods Used to Determine Properties

2.2.4.6.4.1 Reflectivity, transmissivity, and absorption coefficient

The *transmissivity*, T', is determined as a ratio of the intensities of the transmitted and input light (Equation 2.2.100) and is related to the absorption coefficient through the Lambert-Beer law (Equations 2.2.97 and 2.2.99)

$$T' = I_{tranmit}/I_{input} \tag{2.2.100}$$

where $I_{transmit}$, I_{input}, and d are intensity of transmitted and input light and sample thickness, respectively.

The *reflectivity*, R', is determined as a ratio of the intensity of reflected and input light (Equation 2.2.101)

$$R' = I_{reflect}/I_{input} \tag{2.2.101}$$

where $I_{reflect}$ and I_{input} are the intensities of reflected and input light, respectively. Normal incidence reflectivity, R'_{normal}, is also associated with the refractive indices of the medium and material in Equation (2.2.102):

$$R'_{normal} = \left(n_{medium} - n_{sample}\right)^2 / \left(n_{medium} + n_{sample}\right)^2 \tag{2.2.102}$$

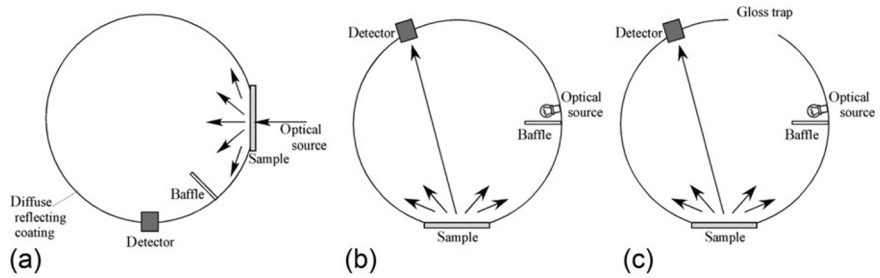


Figure 2.2.75 Schematic diagram showing reflectivity and transmissivity for a partially crystallized, opaque sample when using an integrating sphere (a) transmissivity measurement, (b) reflectivity including specular reflection, and (c) reflectivity without specular reflection (only diffuse reflection).

For opaque samples, like a partially crystallized glass, a portion of the light tends to be diverted from the source axis by the dispersed crystals in the sample; it is necessary to use an integrating sphere device (Figure 2.2.75) to capture both transmitted and reflected light.

2.2.4.6.4.2 Refractive Index (*n*)

2.2.4.6.4.2.1 Optimal Angle Method In this method, the sample is placed on a thin liquid layer and a reference prism. Both the prism and liquid have higher refractive indices than the sample. When a convergent beam of monochromatic light is incident on the sample, some light enters the prism and emerges from another surface of the prism. The critical angle, ϕ_c, can be determined from the light and shade image appearing at the emergent angle, θ_c, in the telescope. The refractive index of the sample can be calculated from the data of refractive index of the prism (n_p), angle of prism, α, and observed θ_c using Equation (2.2.103). It is referred to as the Abbe refractometer:

$$n = \sin\alpha\sqrt{n_p^2 - \sin^2\theta_c} \pm \cos\alpha\sin\theta_c \tag{2.2.103}$$

In the case of the Pelfrich refractometer (Figure 2.2.76), it is only necessary to observe the emergent angle and the refractive index can be calculated from that angle using Equation (2.2.104):

$$n = \sqrt{n_p^2 - \sin^2\theta_c} \tag{2.2.104}$$

2.2.4.6.4.2.2 Minimum Deviation Method In this method, the sample is constructed in the form of a prism with a refracting angle of 60°. The prism is then manipulated so that the beam light will pass through the prism symmetrically (Figure 2.2.77). The prism is said to be in a position of minimum deviation and δ is the angle of minimum

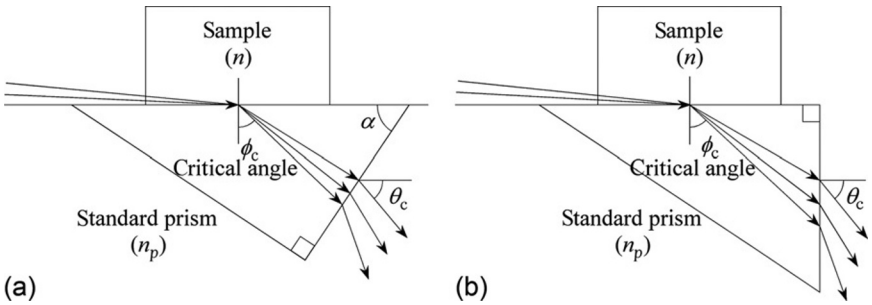


Figure 2.2.76 Principle of (a) Abbe refractometer and (b) Pulfrich refractometer.

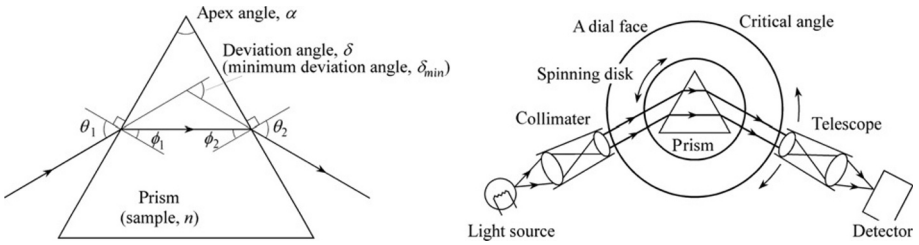


Figure 2.2.77 Schematic illustration of principle of minimum deviation method and arrangement of devices.

deviation. Observing the angle, δ, the refractive index can be calculated from the angle α and δ using

$$n = \frac{\sin\left[\left(\alpha + \delta_{\min}\right)/2\right]}{\sin\left(\alpha/2\right)} \tag{2.2.105}$$

2.2.4.6.4.2.3 Ellipsometry Linearly polarized monochromatic light with a direction of vibration at P to the plane of incidence is directed onto the sample (Figure 2.2.78). The incident light is separated into a *"p"* polarization component and "*s*" polarization components and then are expressed as $\cos p$ and $\sin s$, respectively. The incident angle is expressed as θ_i. Values of the amplitude reflectance are determined as r_p and r_s, respectively. A new parameter, ψ, which is the ratio of amplitude reflectance, is expressed as follows:

$$\frac{r_p}{r_s} = \tan\psi, \quad \Delta = \Delta_p - \Delta_s \tag{2.2.106}$$

Observing the incident angle, θ_i, the ratio and phase difference, Δ, of the amplitude reflectance, refractive index, n, and extinction coefficient, k, can then be calculated using the following equations:

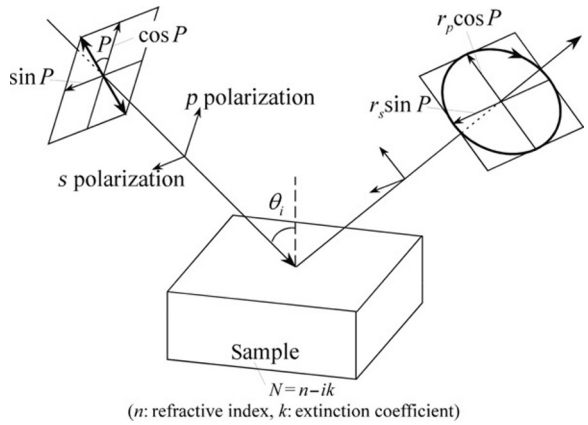


Figure 2.2.78 Schematic illustration of the principle of ellipsometry.

$$n^2 - k^2 = \sin^2\theta_i \left[1 + \frac{\tan^2\theta_i (\cos^2 2\psi - \sin^2 2\psi \sin^2 \Delta)}{(1 + \sin 2\psi \cos \Delta)^2} \right] \tag{2.2.107}$$

$$2nk = \frac{\sin^2\theta_i \tan^2\theta_i \sin 4\psi \sin \Delta}{(1 + \sin 2\psi \cos \Delta)^2} \tag{2.2.108}$$

2.2.4.6.4.2.4 Immersion Method In this method, a ground sample is immersed into a reference liquid, sandwiched between two glass plates and is then observed using a polarization microscope. When there is a difference of refractivity, a *Becke line* can be observed clearly near the boundary between the sample and reference liquid. When $n_{\text{sample}} < n_{\text{reference}}$, the Becke line shifts to the liquid side when the object lens is distanced from the sample. In the case of $n_{\text{sample}} > n_{\text{reference}}$, the reverse phenomena occur. The refractive index of the sample can be narrowed down by using liquids with known $n_{\text{reference}}$.

2.2.4.6.4.3 High-temperature Measurement for Bulk Sample

There are many reports about high-temperature measurement on solid bulk glass, since some of methods are applicable to high temperatures with only minor modifications. For example, Figure 2.2.79 shows the schematic illustration of an experimental setup for high-temperature refractive index measurement used by Wray and Neu [255].

2.2.4.6.4.4 High-temperature Measurement for Molten Sample

There were no published reports of measurements on molten slag until Yagi reported values obtained with an ellipsometry method this was due to the difficulties of maintaining the specimen shape during measurements [250–253]. A He-Ne laser (632.8 nm) was employed as a light source. The probe light was linearly polarized and irradiated the specimen at an incident angle of 60°. The sample was located on a vertical

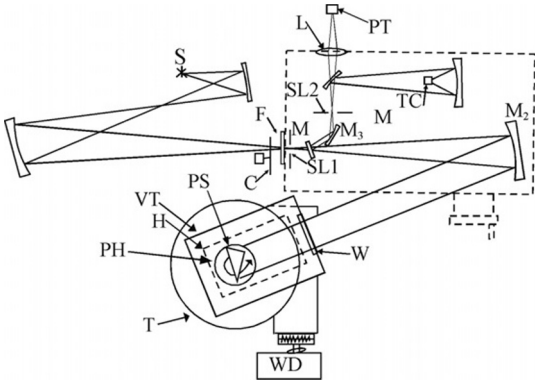


Figure 2.2.79 Schematic illustration of modified Perkin-Elmer 112UG monochromator and rotary table for high-temperature refractive index measurement [255]; C = chopper, F = filter, H = heater core, L = quartz lens, M: P. E. model 112UG monochromator, M1 and M3 = plane mirrors, M2 = parabola mirror, PH = prism holder, PSt = prism sample, PT = phototube, SL1 = entrance slit, SL2 = exit slit, S = source, T = imperial ultra-precision rotary table, TC = thermocouple, VT = vacuum tank, W = fused silica window, WD = wavelength drive.

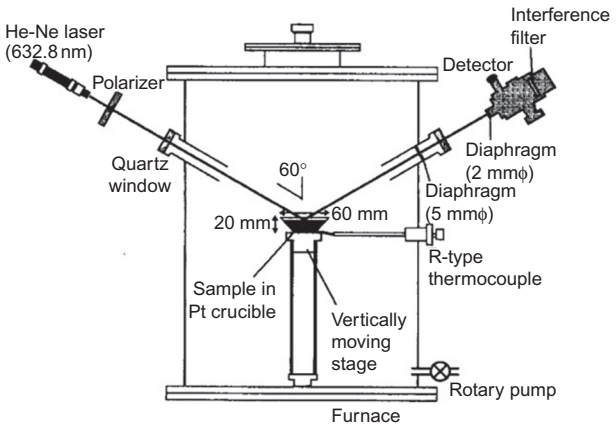


Figure 2.2.80 Schematic illustrations of ellipsometer combined with electric furnace for high-temperature refractive index measurement [250–253].

moving stage surrounded by six $MoSi_2$ heating elements (Figure 2.2.80) and the chamber was evacuated to eliminate probe-light fluctuation.

2.2.4.6.5 Data for Optical Properties

There are a number of compilations of optical property data for glasses [141,172,173,245,256] and for slags [7]. In recent years, there have been a number of publications focused on the optical properties of mold fluxes because of their importance to the heat transfer in the continuous casting of steel; these are summarized in Table 2.2.26.

Table 2.2.26 References for published optical property data for mold flux specimens

Property/(*phase*)	Phase	References
Refractive index (n)	Glass	Susa *et al.* [226,259], Ozawa *et al.* [225]; Ohta []; Mills *et al.* [109]
	Slag film (partially crystalline)	Susa *et al.* [88], Holzhauser *et al.* [257]
Absorption coefficient (α^*)	Glass	Susa *et al.* [88,259], Ohta *et al.* [231]
	Partially crystalline	Susa *et al.* [88,259], Susa [248]
Reflectivity	Partially crystalline	Susa *et al.* [237], Susa [248]
Transmissivity	Partially crystalline	Susa *et al.* [237], Susa [248]
Emissivity	Liquid CaF_2	Keene and Mills [258]

2.2.4.6.6 Calculation of Optical Properties Values from Composition

Some of the published models for calculating optical properties of slags and glasses are summarized in Table 2.2.27.

2.2.5. SUMMARY AND CONCLUSIONS

2.2.5.1. Structure of Silicates

(i) The basic building block in silicate structures is the Si-tetrahedron; this consists of a Si^{4+} ion surrounded by 4 O^- ions in a tetrahedral array. Each of these O^- ions can join either to (i) a Si^{4+} in another tetrahedron thereby creating a BO or (ii) to a cation like Na^+ and thereby creating a NBO.

(ii) Pure SiO_2 consists of a three-dimensional array of BOs in which the O^- ions at the corners of every tetrahedron are connected to other tetrahedra.

(iii) When cations (e.g., Na_2O) are added to pure SiO_2 they break a BO (i.e., O-Si-O) to form 2 *nonbridging Os* (i.e., O-Na + O-Na).

(iv) The *short-range order* is determined by the Si-tetrahedron. Valuable information on the *intermediate-range order* has been obtained by comparing structural characteristics of crystalline materials with those for equivalent glasses. The principal difference in intermediate-range order lies in the configurational entropy (a measure of the disorder present) which is much greater for the glassy phase than that in crystalline materials.

(v) Much of our knowledge on the structural characteristics of melts has been deduced from the study of quenched glasses (representing the structure at T_g); however, recent information suggests that cation arrangements for the melt may differ from that for the quenched glass.

Table 2.2.27 Summary of published models to calculate optical properties

Property/ reference	Details	Comments
Absorption coefficient Susa *et al.* [88,226,259]	$\alpha * \left(\mathrm{m}^{-1}\right) = \alpha^{0} + K\%\mathrm{MO}$ (2.2.109) α^{*0} = absorption coefficient with 0% transition metal oxide (MO): K_{FeO} (m^{-1}) = 910; $K_{\mathrm{MnO}} = 5$; $K_{\mathrm{FeO}} = 410$	
Refractive index (n) Karlsson *et al.* [260]	Li_2O-Na_2O-MgO-CaO-TiO_2-ZrO_2-SiO_2 glasses $n = 1.50303 + 10^{-3}\{2.554(\%\mathrm{MgO}) + 1.854(\%\mathrm{CaO}) + 5.831(\%\mathrm{TiO_2}) + 2.395(\%\mathrm{ZrO_2})\}$ (2.2.110)	$\sigma = 2.997 \times 10^{-3}$; $R^2 = 98.5\%$
Larsen and Berman [261]	Simplified (Equation 2.2.92) by operating Taylor expansion around $n = 1$: $K = (n-1)/\rho = 2\pi N_A \alpha_m / M$ and $K = \Sigma k_i(\%\mathrm{M}_x\mathrm{O}_y)$: k_i values below other oxides available SiO_2 0.207; Al_2O_3 0.214; Li_2O 0.31; Na_2O 0.181; K_2O 0.189; MgO 0.20; CaO 0.225; SrO 0.143; BaO 0.127; FeO 0.187; MnO 0.224; TiO_2 0.397; ZrO_2 0.201	
Doweider [179–181]	Based on Q^n structural units: $N_i = \Sigma N_j f_i$. N_i = no. of structural units mol^{-1}, f_i = "differential refraction"(dimensionless) $x\mathrm{MO} - (1-x)\mathrm{SiO_2}$ system: $x < 0.333$: $x\mathrm{MO} + (1-x)\mathrm{SiO_2} \rightarrow (1-3x)Q^4 + 2xQ^3$: $n = \{(1-3x)f_4 + 2xf_3\}$ (2.2.111) *N:* $0.333 \le x \le 0.5$: $x\mathrm{MO} + (1-x)\mathrm{SiO_2} \rightarrow (2-4x)Q^3 + (3x-1)Q^2$: $n = \{(2-4x)f_3 + (3x-1)f_2\}N_A$ (2.2.112) $0.5 < x \le 0.6$: $x\mathrm{CaO} + (1-x)\mathrm{SiO_2} \rightarrow (3-5x)Q^2 + (4x-2)Q^1$ $n = \{(3-5x)f_2 + (4x-2)f_1\}N_A$ (2.2.113) $0.6 \le x \le 0.666$: $x\mathrm{CaO} + (1-x)\mathrm{SiO_2} \rightarrow (4-6x)Q^1 + (5x-3)Q^0$ $n = \{(4-6x)f_1 + (5x-3)f_0\}N_A$ (2.2.114)	

$x\mathrm{Na_2O}$-$y\mathrm{Al_2O_3}$-$z\mathrm{SiO_2}$ system:

$(x-y)/z \le 0.5$: $x\mathrm{Na_2O} + y\mathrm{SiO_2} + z\mathrm{SiO_2} \rightarrow 2y\mathrm{AlO_4} + 2(x-y)\,Q^3 + \{z-2(x-y)\}\,Q^4$

$$n = [2yf_{\mathrm{Al}} + 2(x-y)f_3 + \{z-2(x-y)\}f_4]N_{\mathrm{A}} \tag{2.2.115}$$

where f_{Al} is for $\mathrm{AlO_4}$ structural unit.

$0.5 < (x-y)/z \le 1$: $x\mathrm{Na_2O} + y\mathrm{SiO_2} + z\mathrm{SiO_2} \rightarrow 2y\mathrm{AlO_4} + \{2(x-y)-z\}\,Q^2 + 2\{z-(x-y)\}\,Q^3$

$$n = [2yf_{\mathrm{Al}} + \{2(x-y)-z\}f_2 + 2\{z-(x-y)\}f_3]N_{\mathrm{A}} \tag{2.2.116}$$

Tabulated data for various systems and cations given [Doweider 4]

Susa *et al.* [262]

$\mathrm{Na_2O}$-$\mathrm{K_2O}$-CaO-MgO-$\mathrm{Al_2O_3}$-$\mathrm{SiO_2}$ system: $X_{\mathrm{SiO_2}} > 0.4$: $X_{\mathrm{M_2O}} + X_{\mathrm{MO}} > X_{\mathrm{Al_2O_3}}$:

Considers various bonds: Si—BO, Si—NBO(R_i), and Al—BO(R_i); calculated from composition

$\pm 0.65\%$ up to 1800 K

$$n = a_{\mathrm{Si-BO}}n_{\mathrm{Si-BO}} + \sum_i b_{\mathrm{Si-NBO}(R_i)}n_{\mathrm{Si-NBO}(R_i)} + \sum_i c_{\mathrm{Al-BO}(R_i)}n_{\mathrm{Al-BO}(R_i)} \tag{2.2.117}$$

	$n_{\mathrm{NBO\text{-}Si(M)}}$					$n_{\mathrm{NBO\text{-}Al(M)}}$				$n_{\mathrm{Si\text{-}BO}}$
$n_{\mathrm{bond}} = aT + b$:	$\mathrm{Li_2O}$	$\mathrm{Na_2O}$	$\mathrm{K_2O}$	MgO	CaO	$\mathrm{Li_2O}$	$\mathrm{Na_2O}$	$\mathrm{K_2O}$	CaO	
$a/\times 10^{-6}$ ($\mathrm{K^{-1}}$)	−20.6	−27.3	−49.2	−3.8	−9.83	1.52	3.3	4.45	0.51	
										3.0
b	1.21	1.17	1.18	1.19	1.27	0.402	0.377	0.375	0.437	0.363

Fluegel [245] Statistical "best-fit" model with various component interactions based on SciGlass database

---

Priven [141] Replaces chemical activities with empirical constants for glasses

(vi) The Si^{4+} cations are mostly in fourfold coordination ($^{(4)}Si^{4+}$) and the network-breaking cations are normally arranged in sixfold coordination in an octahedral array. However, on occasions there may be deviations in the coordination number.

(vii) The principal structural factor affecting the properties is the degree of polymerization which is represented here by the parameter Q (=4-NBO/T); however, the melt contains a variety of different structural units (Q^n where n = number of BOs, e.g., coexisting Q^1, Q^2, and Q^3).

(viii) The structure is also affected by the nature of the cations although the effect is much smaller than that of polymerization. The field strength of the cation (z/r^2) is a principal factor affecting structure; cations with increasing (z/r^2) values have been reported to bring about the following structural characteristics:

- **(a)** increased distribution of Q^n units
- **(b)** decreasing coordination number (N_{coord}) and the proportion of BOs and NBOs is affected by N_{coord}
- **(c)** less distribution in inter-tetrahedral (Si—O—Si or Si—O—Al in aluminosilicates) bond angles
- **(d)** increasing disorder in the melt, and
- **(e)** both an increasing attraction for NBOs and a smaller probability of carrying out charge-balancing duties in aluminosilicates.

2.2.5.2. Effect of Temperature

Solid silicates and aluminosilicates can exist as crystalline or glassy materials; the temperature dependence of these phases is completely different. For crystalline materials there is a smooth change in C_p and thermal expansion coefficient (α) with increasing temperature up to the point where melting occurs after which there are significant changes in the enthalpy and entropy accompanying the fusion process (ΔH^{fus}, ΔS^{fus}). In contrast, in glasses a transition of glass $\rightarrow$ *scl* occurs at the glass transition temperature (T_g) which is accompanied by a significant increase in both C_p and α throughout the *scl* range but exhibits zero, or low, values of ΔH^{fus} and ΔS^{fus} at T_{liq}.

The effect of increasing temperature on the physical properties of silicate melts is very similar to that of adding cations to the melt.

2.2.5.3. Effect of Additions of Al_2O_3, TiO_2, Fe_2O_3, and CaF_2 on Slag Structure

2.2.5.3.1 Aluminosilicates

When Al_2O_3 is added to the silicate melt the Al^{3+} cations are readily incorporated into the silicate (Si^{4+}) network but require a cation (e.g., Na^+ or 0.5 Ca^{2+}) to provide charge balancing (i.e., to form M $Al)^{4+}$; those cations on charge-balancing duties cannot act as network breakers. In *per-aluminous* melts (where there is insufficient MO or M_2O to

charge balance the Al_2O_3) there is evidence of the formation of *tri-clusters* where, effectively, Al^{3+} provides the charge compensation. In highly polymerized, aluminosilicate melts the presence of both $^{(5)}Al^{3+}$ (i.e., Al in fivefold coordination) and of NBOs have been identified which will have impact on the property values. This may account for lower values in viscosity, electrical resistivity, and the reciprocal of the diffusion coefficient values of aluminosilicates (cf. silicates with same Q values) for melts with $Q > 3$.

The rule for cations carrying out charge compensation is that in a melt containing several metal oxides, the charge balancing will be done by the cation(s) with the lowest field strength (i.e., z/r^2); this may be due to the fact that cations with high field strength have a greater attraction for NBOs.

2.2.5.3.2 Titano-Silicates

It might be expected that TiO_2 would be readily incorporated into the silicate network and form Ti—O—Si bonds. Although some of these bonds are formed there is some evidence that they prefer their own company (i.e., preferring to form Ti—O—Ti and Si—O—Si bonds). The coordination of Ti has been a contentious issue and coordinations of $^{(4)}Ti^{4+}$, $^{(5)}Ti^{4+}$, and $^{(6)}Ti^{4+}$ have all been reported and there is general acceptance that Ti is coordinated as both $^{(4)}Ti^{4+}$ and $^{(5)}Ti^{4+}$. It has been observed that TiO_2 additions reduce the slag viscosity and this could be due to the presence of $^{(5)}Ti^{4+}$ ions in the melt.

2.2.5.3.3 The Effect of Fe_2O_3

It might be anticipated that Fe_2O_3 would act like Al_2O_3 but it seems that it acts as both a network breaker and a network former with the fraction of network breaking (f_{nb}) increasing at high SiO_2 (and Q) compositions and vice versa.

2.2.5.3.4 The Effect of CaF_2 Additions

When fluorine is added to silicate or aluminosilicate melts it bonds preferentially with Mg^{2+} or Ca^{2+} ions and more or less does not involve itself with the remainder of the slag. The effect of fluorine can be expressed in two ways:

(i) when CaF_2 is added to a slag the CaF_2 acts principally as a diluent and will cause a gradual decrease in viscosity with increasing CaF_2 content.

(ii) when CaF_2 replaces CaO in the slag, the F^- ions bond preferentially with Ca^{2+} ions and thereby reduce the number of network-breaking cations and thus increase both the polymerization of the melt and viscosity.

2.2.5.4. The Effect of Structure on Thermophysical Properties

2.2.5.4.1 Phase Equilibria and Thermodynamic Properties

(i) The phase diagrams of MO-SiO_2 systems exhibit miscibility gaps at high SiO_2 contents; the width of the miscibility gap increases as the field strength of the cation (z/r^2) increases (i.e., Mg > Ca > Sr).

(ii) The liquidus temperature (T_{liq}) of M_2O-SiO_2 and MO-SiO_2 systems tended to decrease with increasing field strength of the cation (z/r^2).

(iii) The activity coefficients of SiO_2 ($f^*_{SiO_2}$) in M_2O-SiO_2 and MO-SiO_2 systems were also found to increase as the field strength of the cation (z/r^2) decreases ($K_2O > Na_2O > Li_2O > BaO > SrO > CaO > MgO$). In meta-aluminous, aluminosilicates, the order changes with $f^*_{SiO_2}$ increasing (a) in the order ($Ca > Na > K$) (i.e., $f^*_{SiO_2}$ ↑ as (z/r^2) ↑) for the cations carrying out charge-balancing duties and (b) as the ratio, $Al/(Al+Si)$ decreases.

(iv) The enthalpy of solution of meta-aluminous (M_2O-Al_2O_3-SiO_2 and MO-Al_2O_3-SiO_2 systems in lead borate) became more negative (=more thermodynamically stable) as (z/r^2) increased for those cations (doing the charge balancing) (i.e., in the hierarchy $K > Na > Li \approx Ba > Sr > Ca > Mg$).

(v) The entropy of fusion (ΔS^{fus}) for crystalline phases increases with (a) decreasing SiO_2 content and (b) increasing field strength (z/r^2) of the cation.

(vi) The hest capacity (C_p) and enthalpy ($H_T - H_{298}$) for crystal phases can be estimated in most cases to ±2% using partial molar quantities; routines are available to estimate C_p and ($H_T - H_{298}$) for the *scl* phase.

2.2.5.4.2 Flow and Transport Properties (Viscosity, Electrical Resistivity, Diffusion Coefficient)

(i) Two factors affect these properties

(a) the hindrance (or resistance) to movement posed by the large silicate anions.

(b) the number and mobility of the cations.

The resistance term tends to be dominant, especially for polymerized slags and various properties can be expressed as a function of the degree of polymerization (represented here by the term Q but can also be represented by the number of BOs and NBOs). The resistance posed by the silicate anions can be seen in the plots of ln viscosity ($\ln \eta$), ln resistivity ($\ln R$), and ln reciprocal of the diffusion coefficient ($\ln D^{-1}$) for a set temperature as functions of Q; these plots all exhibit similar curves which can be represented as a double-exponential relation.

(ii) The temperature dependencies of viscosity, resistivity, and diffusion coefficient can all be represented by:

(a) the Arrhenius equation (e.g., $\eta = A_A \exp(B_A/T)$) or by the Weymann equation (e.g., $\eta/T = A_W \exp(B_W/T)$) for the liquid where B contains the activation energy term (for viscous flow in this example)

(b) the Vogel-Fulcher-Tamman equation ($\eta = A_V \exp\{B_V/(T - T^\circ)\}$) or by the Adam-Gibbs equation ($\eta = A_{AG} \exp\{B_{AG}/(T \log(T/C_{AG}))\}$), where C_{AG} is a constant for the supercooled phase (*scl*).

(iii) The activation energy term, B_η, also exhibits a "double-exponential" relationship with Q but the data for M_2O-SiO_2 and MO-SiO_2 systems lie on different curves.

(iv) Both $\ln R$ and $\ln(D^{-1})$ at a set temperature along with the parameters B_R and $B_{1/D}$ are also affected by the number of available cations (which is related to valence of the cation).

(v) Values of $\ln \eta$, $\ln R$, and $\ln(D^{-1})$ increase with increasing cation size for M_2O-SiO_2 systems but the relation is less obvious for MO-SiO_2 systems; Zhang *et al.* [153] have suggested that in diffusion there are two steps involved: (a) detachment of the diffusing ion (i.e., through breaking of the existing M-O bond) and (ii) its subsequent movement through the melt with the overall diffusion coefficient being determined by the slower of these two steps.

(vi) When values of both $\ln \eta$ and $\ln R$ at a set temperature are plotted against Q for aluminosilicate melts the values lie significantly below those for the silicates for melts where $Q > 3$; this may be due to the presence of $^{(5)}Al^{3+}$ and the associated NBOs in the melt.

(vii) For melts containing significant concentrations of transition metal oxides (e.g., FeO and NiO), the electrical (*ionic*) conductivity is increased by contributions from *electronic conductivity*; the latter mechanism involves *charge hopping* between Fe^{2+} and Fe^{3+}.

2.2.5.4.3 Density (ρ), Molar Volume (V), Thermal Expansion, and Acoustic Properties

(i) The density (ρ) can be calculated from the molar volume ($\rho V = M$, where M = molecular weight).

(ii) The molar volume (for both liquid and solid) can be calculated from the sum of individual contributions of partial molar volume ($X_i V_i$) for individual oxides but corrections must be applied for the network-forming oxides and it has been reported that these rules break down in per-aluminous melts (i.e., where there is a shortage of charge-balancing cations).

(iii) Thermal expansion data tend to be available only for lower temperatures (<900 K) for glassy specimens because of specimen deformation in the *scl* but are available at higher temperatures for crystalline silicates.

(iv) The thermal expansion coefficient (α) of pure SiO_2 is low but α increases with increasing depolymerization; it has been found that α for silicates increases as (i) the degree of polymerization (Q) decreases and (ii) the field strength (z/r^2) of the cation decreases (i.e., $\alpha \uparrow$ as $Q \downarrow$ and $(z/r^2) \downarrow$).

(v) For glassy samples there is a large increase in thermal expansion coefficient (α) above the glass transition temperature ($\alpha_{>T_g} \approx 3\,\alpha_{<T_g}$) which continues to T_{liq}, whereas crystalline phases exhibit a lower α in the solid but experience a volume change on melting.

(vi) The ultrasonic velocity (c) of molten silicates is a linear, inverse function of the molar volume (i.e., $c \downarrow$ as $V \uparrow$) and can be calculated on a partial molar basis.

2.2.5.4.4 Thermal Properties, Thermal Conductivity (k), Optical Properties

Many silicate samples are considered to be semitransparent media and heat transfer through these media involves several mechanisms, namely (i) *phonon* or *lattice conduction*, (ii) convection, and (iii) radiation conduction (k_R, a mechanism which involves emission and absorption of IR radiation). This complex situation poses severe measurement problems. The problems with convection can be minimized by using transient techniques such as the LP and the THW methods. However, the measured thermal conductivity (k_{eff}) for silicates may contain a k_R contribution of unknown magnitude. For an *optically thick sample* (defined as $\alpha^* d > 3$, where $\alpha^* =$ absorption coefficient and $d =$ thickness of sample) k_R can be calculated ($k_R = 16\sigma n^2 T^3/3\alpha^*$ where $n =$ refractive index and $\sigma =$ Stefan-Boltzmann constant); contributions from k_R rise sharply with increasing temperature (due to the T^3 dependence).

Thus, there is some uncertainty in measured thermal conductivity values since:

(i) At the present time, there are large differences between the values obtained with the LP (k_{LP}) and THW (k_{THW}) methods; reported values for liquid slags of similar composition indicate $k_{LP} \approx 5\, k_{THW}$. At this time no values of k for slags can be recommended.

(ii) Radiation conduction (k_R) contributions are reduced by (a) adding transition metal oxides (e.g., FeO and NiO) to increase the value of the absorption coefficient of solid and liquid slags and (b) by promoting crystallization in solid slags which scatters the IR radiation.

(iii) The temperature dependencies of the thermal conductivities obtained with the two methods are also very different with (a) k_{LP} exhibiting only a gentle rise with temperature up to T_{liq} and showing a small decrease for the liquid and (b) k_{THW} showing little change until a certain critical temperature (denoted T_{crit}) is reached, whereupon, there is a rapid decrease in k_{THW} for $T > T_{crit}$ with increasing temperature. This descent carries on into the liquid.

(iv) It was found that T_{crit} for k_{THW} values occurred at the temperature where the viscosity, $\eta = 10^6$ dPas, i.e., midway between the *softening temperature* (where the sample cannot support its own weight) and the *flow point*.

(v) The measurements of k_{THW} indicate that k_{THW} increases with (a) increasing polymerization (Q) and (b) increasing field strength (z/r^2).

(vi) The magnitude of the thermal conductivity (k_{THW}) of the solid appears to be associated with the *rigidity* of the silicate network.

2.2.5.4.5 Surface (γ) and Interfacial Tension (γ_{msl})

(i) Surface tension and interfacial tension are *surface properties* not *bulk properties* and are affected by the presence of *surfactants*, which are materials with very low surface

tensions which tend to occupy the surface layers of the sample; typical surfactants in silicates are B_2O_3, K_2O, CaF_2, and soluble S and O in the metal phase.

(ii) The temperature dependence ($d\gamma/dT$) tends to switch gradually from a negative value to a positive value with increasing SiO_2 content; the crossover point is ca. $X_{SiO_2} > 0.5$.

(iii) The surface tension for the metal phase tends to be 3 or 4 times higher than the surface tension of silicate melts so the interfacial tension is mostly controlled by the surface tension of the metal phase and hence is sensitive to the *soluble* O and S contents in the metal.

2.2.5.4.6 Modeling of Properties

Many models have been developed to estimate the thermophysical properties of silicate slags and most of these make use of the various parameters employed to represent the polymerization of the melt (e.g., (NBO/T) Q, optical basicity, (O^0, O^-, and O^{2-}), etc.). However, we have seen from the structural studies that the nature of the cations can result in changes in both the coordination number and the disorder (or configurational entropy) which can affect the proportions of BOs and NBOs and hence the properties. Thus, the challenge for the future will be how well the models can describe both the degree of polymerization and the coordination of the cations.

APPENDIX. THERMODYNAMIC PROPERTIES OF SLAGS

In Subchapter 1.2, the structure of slags was discussed and it was described in detail how the slag properties are dependent upon the degree of polymerization of the ionic entities. The thermodynamic properties such as activities and integral molar free energy of mixing are naturally dependent upon the slag structure. Thermodynamic and thermophysical properties are all in one way or another connected to (i) the degree of polymerization and (ii) the size and shape of the polymeric units. Generally, industrial slags and fluxes contain: SiO_2, Me_xO (metal oxides) and depending on the slag additional compounds like Al_2O_3, CaF_2, and P_2O_5. The current appendix to Subchapter 1.2 describes treatments in literature on how to model the thermodynamic properties of molten slags based on reviews available in the literature [263,264].

NOMENCLATURE OF APPENDIX

a_i activity of species i
G^M Gibbs Free energy of Mixing J mol^{-1}
N_i Mole fraction of species i
a fraction of reacted O^-.

A.1. PERTINENT PROPERTIES

The properties that are discussed in this section are those relevant when studying reactions in molten oxides such as crystallization or inclusion formation or reactions between molten oxides and slags and include:

(i) Activities which in ionic/partly ionic solutions is described as the activity of the compound, e.g., oxide such as a_{MO} for an oxide MO dissociated and dissolved into M^{2+} and O^{2-}. The purpose for this is that while individual cannot be experimentally measured.

(ii) The integral molar free energy of mixing:

$$\Delta G^{M} = R^{*}T\sum_{i} N_i \ln a_i \tag{2.2.A1}$$

wherein N is the mole fraction and i refers to the oxide in solution. R and T have their usual meanings. The activity can be split in into, $a_i = N_i \cdot \gamma_i$, where γ_i is the mean activity coefficient ($\gamma_{MX} = \gamma_{M^+} \cdot \gamma_{X^-} = \gamma_{\pm}^2$).

A.2. BONDING, ELECTRONEGATIVITY, AND IDEAL IONIC SOLUTION

If the electronegativity difference in the M-X pairs were large, then the solution would be ionic. Such is the case for molten salts. Further, if the distribution of ions is truly random, then the system can be described by means of Temkin's model [265] wherein activity of MX is described as the product of the ion fractions:

$$a_{MX} = \frac{N_{M^+}}{\sum_{\text{Cations}} N_{i^+}} \cdot \frac{N_{X^-}}{\sum_{\text{Anions}} N_{i^-}} \tag{2.2.A2}$$

Here, N_i refers to the number of ions in a defined volume.

Richardson [266] presented a model for ternary AO-BO-SiO_2 slag systems wherein the free energy of mixing was considered as the sum of the free energies of the pseudo-binary components AO-γSiO_2 and BO-γSiO_2 which are nonideal excess terms and the ideal mixing of the cations similar to Temkins approach:

$$\begin{aligned}\Delta G^{M} &= RT\left[N_{AO}\ln\frac{N_{AO}}{N_{AO}+N_{BO}}+N_{BO}\ln\frac{N_{BO}}{N_{AO}+N_{BO}}\right]\\ &+\frac{N_{AO}}{N_{AO}+N_{BO}}RT\left[\frac{1}{1+\gamma}\ln\ a_{AO}+\frac{\gamma}{1+\gamma}\ln\ a_{SiO_2}\right]\\ &+\frac{N_{BO}}{N_{AO}+N_{BO}}RT\left[\frac{1}{1+\gamma}\ln\ a_{BO}+\frac{\gamma}{1+\gamma}\ln\ a_{SiO_2}\right]\end{aligned} \tag{2.2.A3}$$

The resulting activities are:

$$\begin{aligned}\ln\ a_{SiO_2} &= \frac{N_{AO}}{N_{AO}+N_{BO}}\ln\ a_{SiO_2}(AO-SiO_2)\\ &+\frac{N_{BO}}{N_{AO}+N_{BO}}\ln\ a_{SiO_2}(BO-SiO_2),\\ \ln\ a_{AO} &= N_{AO_\gamma SiO_2}\cdot a_{AO(AO-SiO_2)}\left(\frac{a_{SiO_2}}{a_{SiO_2}(\text{in AO}-SiO_2)}\right)^{\gamma}\end{aligned}$$

and

$$\ln\ a_{BO} = N_{BO_\gamma SiO_2}\cdot a_{BO(BO-SiO_2)}\left(\frac{a_{SiO_2}}{a_{SiO_2}(\text{in BO}-SiO_2)}\right)^{\gamma}$$

A.3. NONIDEAL SOLUTIONS STRUCTURAL MODELS FOR LIMITED DEGREE OF POLYMERIZATION

The model by Flood *et al.* [267] considers nonideality where enthalpy of mixing is nonzero and uses equivalent ion fractions rather than ion fractions to estimate the activities. The models discussed so far would be applicable to the ionic bonds present in molten salts. In the case of oxides, however, the electronegativity differences are less and this results in significant degrees of covalent character in the bonds [268] necessitating the use of models based on the structure of the ion units which results from the types of bonds in the melt.

This brief discussion will be limited to these two properties and primarily for systems wherein oxygen is the sole anion (X) in the individual oxides, although other species such

as F and S would be present in some metallurgical systems. For a more extensive background on this subject, the reader is referred to the comprehensive review by Gaskell [363].

The models developed by Mason [269] and Whiteway *et al.* [270] are based upon the polymerization/depolymerization of silicate network depending on the mole fraction of silica (N_{SiO_2}) in a slag mixture of MO-SiO_2 (with M being a metal cation). The metal oxide MO brings with it a free oxygen (O^{2-}) and as a result of this one of the Si—O—Si bonds is broken and the two O^- are charge balanced by the M^{2+}. If N_{SiO_2} falls below 1/3, then the structure is completely depolymerized and the silicate units are made up of SiO_4^{4-}. In this case, there is no oxygen that would bridge different silicate units (such oxygen species that only bind to a single Si are denoted O^-). The oxygen that is bound to two Si units is denoted as O^0. The polymerization takes place when an MO is removed and thereby N_{SiO_2} increases according to the following equivalent reactions:

$$2O^- \rightarrow O^{2-} + O^0 \tag{2.2.A4}$$

$$SiO_4^{4-} + Si_xO_{3x+1}^{2(x+1)-} = Si_{x+1}O_{3x+3}^{2(x+2)-} + O^{2-} \tag{2.2.A5}$$

A parameter, α, is defined as the fraction of O^- in a melt that have reacted according to Equation (2.2.A4). In the initial polymerization model [5], referred to as the linear chain model, it was assumed that only two of the four O^- can bond through reaction (2.2.A3), the probable distribution of silicate ions of various x-mers is given by

$$N_{Si_xO_{2x+1}^{2(x+1)-}} = \frac{N_{SiO_2}(1-\alpha)^2\alpha^{x-1}}{1-2N_{SiO_2}} \tag{2.2.A6}$$

The anion fraction, $N_{O^{2-}}$, is given by

$$N_{O^{2-}} = \frac{(1-3N_{SiO_2}+\alpha N_{SiO_2})}{1-2N_{SiO_2}} \tag{2.2.A7}$$

As a consequence of the aforementioned assumption in the linear chain model, the equilibrium constant for reaction (2.2.A5) (and standard free energy) becomes independent of x and one obtains (please consult Refs. [1,5] for full derivation):

$$a_{MO} = N_{O^{2-}} \tag{2.2.A8}$$

$$a_{SiO_2} = \frac{\alpha^2(1-2N_{SiO_2})}{N_{SiO_2}(1-\alpha)^2} \tag{2.2.A9}$$

where α is evaluated from the minimization of the free energy for reaction (2.2.A5) when (2.2.A5) and (2.2.A6) are inserted in the equilibrium constant.

When compared to experimental data, the model generally seems to fail when N_{SiO_2} reaches values of around 0.5 and beyond since other types of Si-ions, i.e., rings become

significant. In these cases, models other than polymerization based ones need to be considered.

A.4. NONIDEAL SOLUTIONS STRUCTURAL MODELS FOR HIGHER DEGREE OF POLYMERIZATION

Based on Temkin's model of dividing the cations and anions into subgroupings, there are several models (reviewed, e.g., in Ref. [271]) that propose expressions for the nonideal or excess part of the free energy of mixing in Equation (2.2.A1). This is of course equivalent to describing the deviation from ideality (or developing expressions to describe the activity coefficient, γ_i).

Several models are available in the literature [272–274] but the most extensively used is the cell model. The cell model, first developed by Kapoor and Frohberg [275] was extended to multicomponent slags by Gaye and coworkers [276]. It has been expanded to allow for other anions (sulfur and fluorine) in addition to oxygen. The nonideal interactions caused by bonds between species are represented by symmetric (i-O-i) and asymmetric (i-O-j) cells and certain rules are then applied to determine the energies for forming the cells and energy changes due to the reaction between cells.

Gibbs free energies are then obtained as polynomials and these can then be used to determine Redlich-Kister-Muggiannu coefficients that are used in CALPHAD based software such as ThermoCalc [277] or FactSage [278]. The Gibbs excess energy has also been used to develop chemistry-property relations where there are obvious links between the inter-ion bond types and thermophysical properties. Such as, e.g., the case for the activation energy for viscous flow (see, e.g., [279,280]) of molten industrial slags where the bonds between the ion units and the size of the ion units would be expected to have a relation to the activation energy for viscous flow.

Further progress in multicomponent slag systems could be made through coupling between first-principle predictions and CALPHAD but this is discussed in the chapter by Khanna and Sahajwalla. Slag models are also taken up in Chapter III on thermodynamic aspects as well as Chapter XI, wherein the software based on various models are presented.

ACKNOWLEDGMENTS

The authors wish to thank Prof. Sohei Sukenaga (Kyushu University) and Prof. S. Seetharaman (KTH Stockholm) for their valuable comments.

REFERENCES

[1] B.O. Mysen, Structure and Properties of Silicate Melts, Elsevier, Amsterdam, 1988.
[2] B.O. Mysen, Earth Sci. Rev. 27 (1990) 281–365.
[3] G.S. Henderson, G. Calas, J.F. Stebbins, Elements 2 (2006) 269–273.
[4] G.S. Henderson, Can. Mineral. 43 (2005) 1921–1958.
[5] M.E. Brandriss, J.B. Stebbins, Geochim. Cosmochim. Acta 52 (1988) 2659–2670.
[6] J.F. Stebbins, I. Farnan, X. Xue, Chem. Geol. 96 (1992) 371–385.

[7] Slag Atlas, Stahl u Eisen, VDEh, Dusseldorf, 1995.
[8] G. Urbain, Steel Res. 58 (1987) 111–116, see also Trans. J. Brit. Ceram. Soc. 80 (1981) 139–141.
[9] K.C. Mills, L. Yuan, Z. Li, Estimation of the thermo-physical properties of slags. Part 1: viscosity, to be published.
[10] A. van Bernst, C. Delaunois, Verres Refract. 20 (1966) 435.
[11] D.B. Dingwell, Am. Mineral. 77 (1992) 270–274.
[12] T. Nakamura, K. Morinaga, T. Yanagase, Nippon Kinzoku Gakkaishi 41 (1977) 1300.
[13] A. Shankah, Studies of high-alumina blast-furnace slags, Ph.D. Thesis, KTH, Stockholm, 2007.
[14] S. Yagi, K. Mizoguchi, Y. Suginohara, Bull. Kyushu Inst. Technol. Sci. Technol. 40 (1980) 33.
[15] C.W. Ponader, G.E. Brown Jr., F. Farges, Geochim. Cosmochim. Acta 55 (1992) 935–1217, see also J. Non-Cryst. Solids 201 (1996) 81–94.
[16] R.W. Luth, Am. Mineral. 73 (1988) 297.
[17] Y. Sasaki, M. Iguchi, M. Hino, ISIJ Int. 47 (2007) 638–642.
[18] Y. Sasaki, M. Iguchi, M. Hino, ISIJ Int. 47 (2007) 643–647.
[19] Y. Sasaki, M. Iguchi, M. Hino, ISIJ Int. 47 (2007) 346–347.
[20] Y. Sasaki, M. Iguchi, M. Hino, ISIJ Int. 47 (2007) 1370–1371.
[21] T. Asado, Y. Yamada, K. Ito, ISIJ Int. 48 (2008) 120–122.
[22] J.H. Park, ISIJ Int. 47 (2007) 1368.
[23] M. Hayashi, T. Watanabe, K. Nagata, S. Hayashi, ISIJ Int. 44 (2004) 1527.
[24] J.F. Stebbins, Q. Zeng, J. Non-Cryst. Solids 262 (2000) 1.
[25] T.J. Kiczenski, L.S. Du, J.F. Stebbins, J. Non-Cryst. Solids 337 (2004) 142–149.
[26] S.H. Yun, P.J. Bray, J. Non-Cryst. Solids 27 (1978) 363.
[27] S.H. Yun, S.A. Feller, P.J. Bray, J. Non-Cryst. Solids 33 (1979) 273.
[28] W.J. Dell, P.J. Bray, S.Z. Xiao, J. Non-Cryst. Solids 58 (1983) 1.
[29] S.H. Feller, et al., Phys. Chem. Glass. Eur. J. Glass Sci. Technol. B 53 (2012) 210–218.
[30] J. Klein, Structures of $CaO\text{-}SiO_2$, $CaO\text{-}MgO\text{-}SiO_2$ and $CaO\text{-}Al_2O_3\text{-}SiO_2$ slags and with the addition of B2O£: a Raman spectroscopic study, Ph.D. Thesis, Norw Inst. Natl. Univ., Trondheim, 2013.
[31] T. Iida, H. Sakai, Y. Kita, K. Murakami, High Temp. Mater. Process. 19 (2000) 153–164.
[32] J. Duffy, M.D. Ingram, J. Non-Cryst. Solids 21 (1976) 373–410.
[33] J. Duffy, M.D. Ingram, J. Inorg. Nucl. Chem. 37 (1975) 1203–1206.
[34] T. Nakamura, Y. Ueda, J.M. Toguri, J. Jpn. Inst. Metals 50 (5) (1986) 456–461.
[35] K.C. Mills, S. Sridhar, Ironmaking Steelmaking 26 (1999) 262–268.
[36] B.N. Roy, A. Navrotsky, J. Am. Ceram. Soc. 67 (1985) 606–610.
[37] K.C. Mills, ISIJ Int. 33 (1993) 148–156.
[38] H.S. Ray, S. Pal, Ironmaking Steelmaking 31 (2004) 125–130.
[39] Q. Shu, K.C. Chou, Ironmaking Steelmaking, 40 (2013).
[40] G.H. Zhang, K.C. Chou, Metall. Mater. Trans. B 41B (2010) 131–136.
[41] H. Gaye, J. Welfinger, in: D. Gaskell, H.A. Fine (Eds.), 2nd International Symposium on Metallurgical Slags and Glasses Held Lake Tahoe, NV, 1984, pp. 357–375.
[42] L. Zhang, S. Sun, S. Jahanshai, Metall. Trans. B 29B (1998) 177–186.
[43] L. Zhang, S. Sun, S. Jahanshai, Metall. Trans. B 29B (1998) 187–195.
[44] G.H. Zhang, K.C. Chou, Ironmaking Steelmaking 40 (2013) 376–380.
[45] M. Kato, S. Minowa, Trans. ISIJ 9 (1969) 39–45.
[46] G.H. Zhang, B.J. Yan, K.C. Chou, F.S. Li, Metall. Mater. Trans. B 42B (2011) 261–264.
[47] J.E. Mungall, Geochim. Cosmochim. Acta 66 (2002) 125–143.
[48] H. Eyring, J. Chem. Phys. 3 (1935) 107, see also M.G. Evans, M. Polanyi, Trans. Faraday Soc. 31 (1935) 875.
[49] Wikipedia: www.wikipedia.org/wiki/Ionic_radius.
[50] http://geology.cafe.silicates.jpg.
[51] http://jaeger.earthsci.unimelb.edu.au.
[52] J.F. Stebbins, Z. Xu, Nature 390 (1997) 60–62.
[53] J.F. Stebbins, Solid State Ionics 112 (1998) 137–141.
[54] A.E. George, J.F. Stebbins, Am. Mineral. 83 (1998) 1022–1029.

[55] W.E. Jackson, F. Farges, M. Yeager, P.A. Mabrouk, S. Rossano, G.A. Waychunas, E. Solomon, G.E. Brown Jr., Geochim. Cosmochim. Acta 69 (2005) 4315–4332.
[56] I. Galoisy, G. Calas, Geochim. Cosmochim. Acta 57 (1993) 3613–3626.
[57] J.R. Allwardt, J.F. Stebbins, Am. Mineral. 90 (2005) 1218–1222.
[58] F. Farges, C.W. Ponander, G.E. Brown Jr., Geochim. Cosmochim. Acta 55 (1991) 1563–1574.
[59] V. Petkov, S.J.L. Billinge, S.D. Shastri, B. Himmel, Phys. Rev. Lett. 85 (16) (2000) 3436–3439.
[60] A.C. Wright, J.A. Hulme, D.I. Grimley, R.N. Sinclair, S.W. Martin, D.L. Price, F.L. Galeener, J. Non-Cryst. Solids 129 (1991) 213–232.
[61] R.L. Mozzi, B.E. Warren, J. Appl. Cryst. 2 (1969) 164–172.
[62] S.K. Lee, J.F. Stebbins, Am. Mineral. 84 (1999) 93–945.
[63] B.O. Mysen, P. Richet, in: B. Mysen, P. Richet (Eds.), Silicate Glasses and Melts: Properties and Structure, vol. 10, Elsevier, B.V., Amsterdam, 2005. ISBN 13: 978-0-444-52011-1.
[64] I. Farnan, et al., Nature 358 (1992) 31–35.
[65] I. Yasui, Y. Akasaka, H. Inoue, J. Non-Cryst. Solids 177 (1994) 91–96.
[66] T. Uchino, T. Yoko, J. Phys. Chem. B103 (1999) 1854–1858.
[67] C.A. Angell, K.L. Ngal, G.B. McKenna, P.F. McMillan, S.W. Martin, J. Appl. Phys. 88 (2000) 3113–3157.
[68] S. Kroeker, D. Rice, J.F. Stebbins, Am. Mineral. 87 (2002) 573–579.
[69] C.A. Angell, W. Sichina, Ann. N. Y. Acad. Sci. 279 (1976) 53–67.
[70] G. Adam, J.H. Gibbs, J. Chem. Phys. 43 (1965) 139–146.
[71] W. Lowenstein, Am. Mineral. 39 (1954) 92–96.
[72] J.F. Stebbins, Rev. Mineral. 18 (1995) 141–245.
[73] D.M. Zirl, S.H. Garofalini, J. Am. Ceram. Soc. 73 (1990) 2848–2856.
[74] J.F. Stebbins, J.V. Oglesby, S. Kroeker, Am. Mineral. 86 (2001) 1307–1311.
[75] D.R. Neuville, L. Cormier, D. Massiot, Geochim. Cosmochim. Acta 68 (2004) 5071–5079.
[76] E.F. Riebling, J. Chem. Phys. 44 (1966) 2857–2865.
[77] M.J. Toplis, D.B. Dingwell, K.U. Hess, T. Lenci, Am. Mineral. 82 (1997) 979–990.
[78] A. Pedone, E. Gambuzzi, M.C. Menziani, J. Phys. Chem. C 116 (2012) 14599–14609.
[79] L. Cormier, D.R. Neuville, Chem. Geol. 213 (2004) 103–114.
[80] S.K. Lee, S. Sung, Chem. Geol. 256 (2008) 326–333.
[81] K. Mori, Tetsu-to-Hagane 42 (5) (2009) 633.
[82] M.E. Fleet, in: C.A. Scarfe (Ed.), X-Ray Diffraction and Spectroscopic Studies on the Structure of Silicate Glasses. Short Course in Silicate Melts, Mineralogy Society of Canada, Ottawa, ON, 1986, pp. 1–13.
[83] J. Wong, C.A. Angell, Glass Structure by Spectroscopy, Marcel Decker, New York, 1976.
[84] K.A. Smith, R.J. Kirkpatrick, E. Oldfield, D.M. Henderson, Am. Mineral. 68 (1983) 1206–1215.
[85] K.C. Mills, L. Yuan, Z. Li, G.H. Zhang, Proceedings of 5th International Congress on Science and Technology of Steelmaking, Held Dresden October 2012, Paper 1331 to be published in High Temp. High Press. (2013).
[86] K.C. Mills, L. Yuan, Z. Li, G.H. Zhang, K.C. Chou, Proceedings of 9th International Conference on Molten Slags, Fluxes and Salts (Molten 12), Held Beijing China, May 2012, to be published in Steel Res. Int. (2013).
[87] K.C. Mills, L. Yuan, Z. Li, G.H. Zhang, K.C. Chou, High Temp. Mater. Process. 31 (2012) 301–322.
[88] M. Susa, K.C. Mills, M.J. Richardson, R. Taylor, D. Stewart, Ironmaking Steelmaking 21 (1994) 279–286.
[89] Factsage Web site: www.factsage.com/.
[90] MTDATA Web site: www.npl.co.uk/mtdata/.
[91] Thermocalc Web site: www.thermocalc.com.
[92] S. Du, J. Bygden, S. Seetharaman, Metall. Trans. B 25B (1994) 519–525, 589–595.
[93] M. Hayashi, S. Seetharaman, CAMP-ISIJ 16 (2003) 860–863.
[94] M. Persson, T. Matsushita, J. Zhang, S. Seetharaman, Steel Res. Int. 78 (2007) 102–108.
[95] C.S. Smith, Trans. AIME 137 (1940) 236–245.

[96] H.B. Dong, J.D. Hunt, in: Proceedings of 12th International Conference on Thermal Analysis, Held Copenhagen, August, 2004.
[97] T. Kishi, et al., Nippon Steel Tech. Rep. 34 (1987) 11–20.
[98] Deutsche Inst. Normalung: DIN 51740.
[99] Phase diagrams for Ceramists, Volumes 1 to 8: Am. Ceram. Soc., 1956, 1964, etc.
[100] J. Robinson, A.T. Dinsdale, L.A. Chapman, P.N. Quested, B.J. Monaghan, J.A. Gisby, K.C. Mills, in: Proceedings of 2nd International Conference on the Science and Technology of Steelmaking, Held Swansea, IOM, London, 2001, pp. 149–160.
[101] S. Dectorov, N. Grundy, A. Pelton, in: Proceedings of 8th International Conference on Molten Slags and Fluxes, Held Santiago, Chile, 2009.
[102] A.D. Pelton, in: Proceedings of 9th International Conference on Molten Slags, Fluxes and Salts (Molten 12), Held Beijing, China, May, 2012.
[103] K.C. Mills, L. Yuan, Z. Li, R.T. Jones, J. S. Afr. Inst. Min. Metall. 111 (2011) 649–658.
[104] K.C. Mills, A.B. Fox, R. Thackray, Z. Li, in: Proceedings of 7th International Conference on Molten Slags, Fluxes and Salts, Held Capetown, South Africa, 2004, pp. 713–721.
[105] F.J. Ryerson, Geochim. Cosmochim. Acta 49 (1985) 637–651.
[106] M.J. Richardson, in: K.D. Maglic, A. Cezairliyan, V.E. Peletsky (Eds.), Compendium of Thermophysical Property Measurement Methods, Survey of Measurement techniques, vol. 1, Plenum, New York, 1984, p. 669 (Chapter 17).
[107] K.K. Kelley, in: Contributions to the Data on Theoretical Metallurgy, US Bureau of Mines Bulletin 584, Washington, DC, 1960.
[108] I.S.E. Carmichael, J. Nicholls, F. Spera, B.J. Wood, S.A. Nelson, Philos. Trans. R. Soc. Lond. A286 (1977) 373.
[109] K.C. Mills, A. Olusanya, R.F. Brooks, R. Morrell, S. Bagha, Ironmaking Steelmaking 15 (1988) 257–264.
[110] B.J. Monaghan, R.F. Brooks, Ironmaking Steelmaking 29 (2002) 115–120.
[111] D.D. Gohil, K.C. Mills, Archiv. Eisenhuttenw. 52 (1981) 335–340.
[112] J.M. Rhine, K.C. Mills, F.H. Ponsford, High Temp. High Press. 17 (1985) 173–183, see also Fuel 68 (1989) 193–200.
[113] K.C. Mills, B.J. Keene, Int. Mater. Rev. 32 (1987) 1–120.
[114] K.C. Mills, in: K. Vorres (Ed.), Proceedings of Symposium on Chemistry of Mineral Matter and Ash in Coal, Held Philadelphia (1984), American Chemical Society Monograph Series, vol. 301, American Chemical Society, Washington, DC, 1986, pp. 197–214.
[115] J.F. Stebbins, I.S.E. Carmichael, L.K. Moret, Contrib. Mineral. Geol. 86 (1984) 131–148.
[116] K.C. Mills, A.B. Fox, ISIJ Int. 43 (2003) 1479–1486.
[117] J.D. MacKenzie, in: J.O'.M. Bochris, J.L. White, J.D. MacKenzie (Eds.), Physico-Chemical Measurements at High Temperatures, Butterworths, London, 1959 (Chapter 15).
[118] T. Iida, T. Tanaka, in: Proceedings of 4th International Conference on Metallurgical Slags and Fluxes, Held Sendai, ISIJ, Tokyo, 1992, p. 444.
[119] M. Tokuda, et al., Sumitomo Search 44 (1990) 368–390.
[120] S.J. Roach, H. Henein, Can. Metall. Quart. 42 (2003) 175–185.
[121] A.P. Froba, A. Leipertz, in: Proceedings (Abstracts) of 16th European Conference on Thermophysical Properties, Held London, 2002, pp. 59–60.
[122] N. Kawasaki, K. Watanabe, Y. Nagasaka, High Temp. High Press. 30 (1998) 91.
[123] Y. Kobayashi, Y. Nagasaka, in: Proceedings (Abstracts) of 16th European Conference on Thermophysical Properties, Held London, 2002, pp. 103–104.
[124] K.C. Mills, M. Halali, H.P. Lorz, A. Kinder, R. Pomfret, B.A. Walker, in: Proceedings of 5th International Conference on Metallurgical Slags and Fluxes, Held Sydney, Australia, 1997, pp. 535–542.
[125] T. Iida, Y. Shiraishi, in: Y. Kawai, Y. Shiraishi (Eds.), Handbook of Physico-Chemical Properties at High Temperatures, ISIJ, Tokyo, 1988, pp. 127–144, Special Issue No. 41 (Chapter 4).
[126] G. Urbain, Y. Bottinga, P. Richet, Geochim. Cosmochim. Acta 46 (1982) 1061–1072.
[127] A. Fluegel, Glass Technol. Eur. J Glass Sci. Technol. A 48 (2007) 13–30.
[128] D.B. Dingwell, M. Brearley, J. Dickinson, Geochim. Cosmochim. Acta 52 (1988) 2467–2475.

[129] P. Taskinen, J. Gisby, J. Pihlasalo, T. Kolhinen, in: Proceedings of EMC2009, International Conference, Held Innsbruck, Austria, 2009.
[130] P.V. Riboud, Y. Roux, L.D. Lucas, H. Gaye, Fachber. Huttenprax. Metallweiterverarb. 19 (1981) 859–869.
[131] C.L. Senior, S. Srinivasachar, Energy Fuel 9 (1995) 277–283.
[132] V.K. Gupta, S.P. Sinha, B. Raj, Steel India 21 (1998) 22–29, 17 (1994) 74–78.
[133] S. Seetharaman, S. Du, F.Z. Ji, Metall. Mater. Trans. B 31B (2000) 105–109.
[134] T. Tanaka, M. Nakamoto, J. Lee, T. Usui, in: Proceedings of Science Technology Innovative Ironmaking, Aiming Energy Half Consumption, Held Tokyo November, 2003, 2003, pp. 161–164, see also CAMP-ISIJ 16 (2003) 864–867.
[135] A. Kondratiev, E. Jak, Metall. Trans. B 32B (2001) 1015–1025.
[136] E. Jak, in: Proceedings of 8th International Conference on Molten Slags and Fluxes, Held Santiago, Chile, 2009.
[137] M. Nakamoto, A. Kiyose, T. Tanaka, L. Holappa, M. Hamalainen, ISIJ Int. 47 (2007) 38–43.
[138] M. Nakamoto, L. Forsbacka, L. Holappa, in: Proceedings of 11th International Conference on Ferrochrome Process, INFACON XI, Held South Africa, 2007, see also Nakamoto *et al.*, ISIJ Intl 47 (2007) 1409–1415.
[139] M. Hanao, M. Kawamoto, T. Tanaka, M. Nakamoto, ISIJ Int. 46 (2006) 427–433.
[140] M. Hanao, M. Kawamoto, M. Nakamoto, T. Tanaka, in: Proceedings of 8th International Conference on Molten Slags and Fluxes, Held Santiago, Chile, 2009.
[141] A.I. Priven, Glass Technol. 45 (2004) 244–254, see also Sov. J. Glass Phys. Chem. 14 (1988) 321.
[142] M. Barati, K.S. Coley, Metall. Mater. Trans. B 37B (2006) 41–50.
[143] M. Barati, K.S. Coley, Metall. Mater. Trans. B 37B (2006) 51–60.
[144] M. Kennedy, M. Garcia, F. Olesen, in: J.P. Downey, T.P. Battle, J.F. White (Eds.), TMS Proceedings of International Smelting Symposium, Held Orlando, FL, Wiley2012, pp. 241–249.
[145] A. Fluegel, Electrical Resistivity of Silicate Glass Melts Based on SciGlass Database, http://glassproperties.com, 2007p. 21.
[146] S.L. Schiefelbein, D.R. Sadoway, Metall. Mater. Trans. B 28B (1997) 1141–1148.
[147] Z. Kozuka, K. Morinaga, in: Y. Kawai, Y. Shiraishi (Eds.), Handbook of Physico-Chemical Properties at High Temperatures, ISIJ, Tokyo, 1988, pp. 127–144, Special Issue No. 41 (Chapter 8).
[148] K.C. Mills, B.J. Keene, Int. Metals Rev. 21 (1981) 21–67.
[149] Q. Jiao, N.J. Themelis, Metall. Trans. B 19B (1988) 133–140.
[150] L.J. Wang, Steel Res. Int. 80 (2010) 680.
[151] A. Jambon, J. Geophys. Res. 87 (1982) 10797–10810.
[152] D.A. Okongawu, W.K. Lu, A.E. Hamielec, J.S. Kirkaldy, J. Chem. Phys. 58 (1973) 777.
[153] Y. Zhang, H.W.. Ni, Y. Chen, Rev. Mineral. Geochem. 73 (2010) 311–408.
[154] H. Keller, K. Schwerdtfeger, K. Hennesen, Metall. Trans. B 10B (1979) 67–70.
[155] H. Keller, K. Schwerdtfeger, Metall. Trans. B 10B (1979) 551–554.
[156] H. Keller, K. Schwerdtfeger, H. Petri, R. Holzle, K. Hennesen, Metall. Trans. B 13B (1982) 237–240.
[157] H.A. Walls, in: R.A. Rapp (Ed.), Physico-Chemical Measurements in Metals Research, Interscience, New York, 1970(Chapter 9C).
[158] T.S. Lundy, in: R.A. Rapp (Ed.), Physico-Chemical Measurements in Metals Research, Interscience, New York, 1970(Chapter 9A).
[159] A.E. Le Claire, in: M. McLean (Ed.), The Characterisation of High Temperature Materials: Physical and Elastic Characteristics, Institute of Metals, London, 1989, pp. 139–176 (Chapter 5).
[160] K. Nagata, Y. Ono, T. Ejima, T. Yamamura, in: Y. Kawai, Y. Shiraishi (Eds.), Handbook of Physico-Chemical Properties at High Temperatures, ISIJ, Tokyo, 1988, pp. 181–204, Special Issue No. 41 (Chapter 7).
[161] J.B. Brady, in: A Handbook of Physical Constants, American Geophysical Union, Washington, DC, 1995. Available from:science.smith,edu/~jbrady/papers/diffusion+paper.
[162] T. Dunn, in: C.A. Scarfe (Ed.), Short Course in Silicate Melts, Mineralogy Society of Canada, Ottawa, ON, 1986, pp. 57–92(Chapter 3).

[163] N. Shimizu, K. Kushiro, Geochim. Cosmochim. Acta 48 (1984) 1295–1303.
[164] D.R. Baker, Chem. Geol. 98 (1992) 11–21.
[165] S.M. Fortier, B.J. Guiletti, Science 245 (1989) 1481–1484.
[166] Y.S. Touloukian, R.K. Kirby, R.E. Taylor, T.Y.R. Lee, in: Thermophysical Properties of Matter, Thermal Expansion, vol. 13, IFI Plenum, New York, 1975.
[167] J.O'.M. Bockris, J.A. MacKenzie, J.A. Kitchener, Trans. Faraday Soc. 55 (1955) 1734, see also J.O'M. Bockris, et al., Trans. Faraday Soc. 48 (1952) 75.
[168] S. Watanabe, K. Ogino, Y. Tsu, in: Y. Kawai, Y. Shiraishi (Eds.), Handbook of Physico-Chemical Properties at High Temperatures, ISIJ, Tokyo, 1988, pp. 1–31Special Issue No. 41 (Chapter 1).
[169] M.S. Ghiorso, V.C. Kress, J. Am. Sci. 304 (2004) 679–751.
[170] A. Fluegel, J. Am. Ceram. Soc. 90 (2007) 2622–2625.
[171] A. Fluegel, D.A. Earl, A.K. Varshneya, T.P. Seward III., Eur. J. Glass Sci. Technol. B 49 (2008) 245–257.
[172] H. Scholze, Glass, Nature, Structure and Properties, Springer-Verlag, Berlin, New York, 1991.
[173] SciGlass 6.5 Database and Information System, 2005). http://www.sciglass.info.
[174] S. Sukenaga, S. Haruki, Y. Nomoto, N. Saito, K. Nakashima, ISIJ Int. 51 (2011) 1285–1289.
[175] L. Muhmood, S. Seetharaman, Metall. Mater. Trans. B 41B (2010) 833–844.
[176] Y.E. Lee, D.R. Gaskell, Metall. Trans. 5 (1974) 853–860.
[177] T. Licko, V. Danek, Z. Panek, Chem. Papers 39 (5) (1985) 599.
[178] K. Ogino, in: Y. Kawai, Y. Shiraishi (Eds.), Handbook of Physico-Chemical Properties at High Temperatures, ISIJ, Tokyo, 1988, pp. 145–179, Special Issue No. 41 (Chapters 5 and 6).
[179] H. Doweidar, Phys. Chem. Glass. 41 (2000) 94–99.
[180] H. Doweidar, J. Non-Cryst. Solids 277 (2000) 98–105.
[181] H. Doweidar, J. Non-Cryst. Solids 303 (2002) 387–392.
[182] H. Doweidar, J. Non-Cryst. Solids 240 (1998) 55–65.
[183] S. Hara, K. Irie, D.R. Gaskell, K. Ogino, Trans. Jpn. Inst. Metals vol.29, (1988) 977–989.
[184] J. Henderson, Trans. AIME 230 (1964) 501.
[185] P. Vadasz, M. Havlik, V. Danek, Can. Metall. Quart. 39 (2) (1999) 143–151.
[186] I.A. Aksay, J.A. Pask, J. Am. Ceram. Soc. 62 (1979) 332–335.
[187] A. Fluegel, Thermal Expansion Calculation of Silicate Glasses at 210 °C Based on Systematic Analysis of Global Databases, 2007). http://glassproperties.com.
[188] Y. Bottinga, D.F. Weill, Am. J. Sci. 272 (1972) 438, also Geochim. Cosmochim. Acta 46 (1982) 909.
[189] V.V. Baidov, L.L. Kunin, Sov. Phys. Dokl. Engl. Transl. 13 (1968) 64.
[190] Y. Matsuzono, Y. Kitamura, M. Hayashi, K. Nagata, CAMP-ISIJ 23 (2010) 981.
[191] M.L. Rivers, I.S.E. Carmichael, J. Geophys. Res. 92 (1987) 9247.
[192] Y. Shiraishi, M. Yamashita, Y. Tokunaga, A. Tanaka, et al., in: Proceedings of 8th International Conference on Molten Slags, Fluxes and Salts, Held Santiago, Chile, ISS, Warrendale, PA, 2009, CD-ROM.
[193] S. Ernst, J. Glinski, B. Jezowska-Trzebiatowska, Acta Phys. Pol. Engl. Transl. A 55 (1979) 501.
[194] J.A. Bucaro, H.D. Dardy, J. Appl. Phys. 45 (1974) 5324.
[195] N.L. Laberge, V.V. Vasilescu, C.J. Montrose, P.B. Macedo, J. Am. Ceram. Soc. 56 (1973) 506.
[196] P. Macedo, T.A. Litovitz, Phys. Chem. Glass. 6 (1965) 69.
[197] T. Ejima, T. Yamamura, Int. J. Thermophys. 5 (1984) 131.
[198] K. Takimoto, R. Endo, Phys. Chem. Liquids 12 (1982) 141.
[199] H. Bloom, J.O'.M. Bockris, J. Phys. Chem. 61 (1957) 515.
[200] M. Hayashi, Y. Matsuzono, K. Nagata, ISIJ Int. 51 (2011) 689.
[201] J.O'.M. Bockris, E. Kojonen, J. Am. Chem. Soc. 82 (1960) 4493.
[202] K. Nagata, K. Ohira, H. Yamada, K.S. Goto, Metall. Trans. B 18B (1987) 549.
[203] L.N. Sokolov, V.V. Baidov, L.L. Kunin, Svoistr. Strukt. Shlakovykh Rasplavov 1970 (1970) 94–100.
[204] S. Feldbauer, I. Jimbo, A. Sharan, J. Harman, A.W. Cramb, in: Proceedings of 78th Steelmaking Conference, 1995, pp. 655–667.
[205] H. Nakato, in: Proceedings of 74th Steelmaking Conference, Held Washington, DC, 1991.

[206] Y. Chung, Surface and interfacial phenomena in iron-alloys, Ph.D. Thesis, Carnegie-Mellon University, Pittsburgh, PA, 1999; see also Y. Chung, A.W. Cramb, Metall. Mater. Trans. B 31 (2000) 957–971.
[207] T. Tanaka, in: Proceedings of 5th International Congress on Science and Technology of Steelmaking, Held Dresden October, 2012, 2012, Paper 1302.
[208] K.C. Mills, B.J. Keene, R.F. Brooks, A. Shirali, Philos. Trans. R. Soc. Lond. A A356 (1998) 911–925.
[209] H. Gaye, D. Lucas, M. Olette, P.V. Riboud, Can. Metall. Quart. 23 (1984) 179–191.
[210] P.V. Riboud, L.D. Lucas, Can. Metall. Quart. 20 (1981) 199–208.
[211] A. Jakobsson, M. Nasu, J. Mangwiru, K.C. Mills, S. Seetharaman, Philos. Trans. R. Soc. A 356 (1998) 995–1001.
[212] M. Ferrari, L. Liggieri, F. Ravera, C. Amodio, R. Miller, J. Colloid Interface Sci. 186 (1997) 40–45.
[213] A.W. Cramb, I. Jimbo, Steel Res. 60 (1989) 157–165.
[214] A. Fluegel, Calculation of Surface Tension, http://glassproperties.com, 2007.
[215] A. Sharan, A.W. Cramb, Metall. Mater. Trans. B 26 (1995) 87–93.
[216] H. Sun, K. Nakashima, K. Mori, ISIJ Int. 46 (2006) 407–412, see also 37 (1997) 323.
[217] J. Elfsburg, T. Matsushita, Steel Res. 82 (2011) 84–94.
[218] M. Gornerup, M. Hayashi, C.A. Dacker, S. Seetharaman, in: Proceedings of 7th International Conference on Molten Slags, Fluxes and Salts, Held Capetown, South Africa, SAIMM2004, p. 745.
[219] A. Kucuk, A.G. Clare, L. Jones, Glass Technol. 40 (1999) 149–153.
[220] L.J. Wang, K.C. Chou, Y. Chen, S.A. Chang, Zeitsch. Metallkunde 96 (2005) 715–720.
[221] M. Nakamoto, M. Hanao, T. Tanaka, M. Kawamoto, L. Holappa, M. Hamalainen, ISIJ Int. 47 (2007) 1075–1081.
[222] M. Nakamoto, T. Tanaka, L. Holappa, M. Hamalainen, ISIJ Int. 47 (2007) 211–216.
[223] Z.Y. Qiao, L.T. Kang, Z.M. Cao, B.Y. Yuan, CAMP-ISIJ 16 (2003) 868–871.
[224] K. Nishioka, T. Maeda, M. Shimizu, ISIJ Int. 46 (2006) 427–433.
[225] S. Ozawa, M. Susa, T. Goto, R. Kojima, K.C. Mills, ISIJ Int. 46 (2006) 413–419.
[226] M. Susa, S. Kubota, M. Hayashi, K.C. Mills, Ironmaking Steelmaking 28 (2001) 390–395.
[227] R. Taylor, K.C. Mills, Ironmaking Steelmaking 15 (1988) 187–194.
[228] Y. Waseda, M. Masuda, K. Watanabe, H. Shibata, H. Ohta, K. Nakajima, High Temp. Mater. Process. 13 (1994) 267–276.
[229] H. Shibata, J.W. Cho, T. Emi, M. Suzuki, in: Proceedings of 5th International Conference on Molten Slags, Fluxes and Salts, Held Sydney, ISS, Warrendale, PA, 1997, p. 771.
[230] H. Shibata, H. Ohta, A. Suzuki, Y. Waseda, Mater. Trans. JIM 41 (2000) 1616–1620.
[231] H. Ohta, M. Masuda, K. Watanabe, K. Nakajima, H. Shibata, Y. Waseda, Tetsu-to-Hagane 80 (1994) 463–468.
[232] H. Ohta, H. Shibata, H. Hasegawa, Y. Kawakri, Y. Shinoki, S. Kitamura, Y. Waseda, in: Proceedings of 9th International Conference on Molten Slags and Fluxes (Molten 12), Held Beijing, 2012.
[233] H. Ohta, Y. Shiraishi, in: Proceedings of 2nd International Conference on Metallurgical Slags and Fluxes, Held Lake Tahoe, NV, USA, Metallurgical Society of AIME, Warrendale, PA, 1984, pp. 863–873.
[234] H. Ohta, H. Shibata, A. Suzuki, Y. Waseda, Rev. Sci. Instrum. 72 (2001) 1899–1903.
[235] M. Kishimoto, M. Maeda, K. Mori, Y. Kawai, in: Proceedings of 2nd International Conference Metallurgical Slags and Fluxes, Held Lake Tahoe, NV, USA, Metallurgical Society of AIME, Warrendale, PA, 1984, pp. 891–905.
[236] K. Nagata, K.S. Goto, in: H.A. Fine, D.R. Gaskell (Eds.), Proceedings of 2nd International Conference on Metallurgical Slags and Fluxes, Held Lake Tahoe, NV, TMS-AIME, Warrendale, PA, 1984, p. 875.
[237] M. Susa, M. Watanabe, S. Ozawa, R. Endo, Ironmaking Steelmaking 34 (2007) 124–130.
[238] M. Hayashi, H. Ishii, M. Susa, H. Fukuyama, K. Nagata, Phys. Chem. Glass. 42 (2001) 6–11.
[239] S. Ozawa, M. Susa, Ironmaking Steelmaking 32 (2005) 487–493.
[240] S. Ozawa, R. Endo, M. Susa, Tetsu-to-Hagane 93 (2007) 8–14.
[241] Y. Kang, K. Morita, ISIJ Int. 46 (2006) 420–426.
[242] R. Eriksson, S. Seetharaman, Metall. Mater. Trans. B 35B (2004) 461–469.
[243] J.M. Rhine, K.C. Mills, F.H. Putland, High Temp. High Press. 17 (1985) 173–183, Fuel 68 (1989) 193–200, 904–910.

[244] J.S. Powell, Unpublished experimental measurements on thermal conductivity of a liquid mould flux, NPL, Teddington cited in Slag Atlas [7], p. 598.
[245] A. Fluegel, Calculation of Optical Properties, http://glassproperties.com, 2007.
[246] M.K. Choudhary, R.M. Potter, in: D.L. Pye, A. Montenaro, I. Joseph (Eds.), Chapter 9 in Glass Formation Melts, CRC press, Boca Raton, FL, 2005.
[247] N. Iwamoto, Y. Makina, S. Kasahara, J. Non-Cryst. Solids 68 (1984) 379–388, 389–397.
[248] M. Susa, Y. Kajino, K. Kusano, R. Kojima, Glass Technol. 46 (2005) 55–61.
[249] L. Pauling, Proc. R. Soc. Lond. 114 (1927) 181.
[250] T. Yagi, M. Susa, Metall. Mater. Trans. B 34B (2003) 549–554.
[251] T. Yagi, M. Susa, K. Nagata, J. Non-Cryst. Solids 315 (2003) 54–62.
[252] T. Yagi, T. Kimura, M. Susa, Phys. Chem. Glass. 43C (2002) 159–164.
[253] M. Susa, A. Kushimoto, H. Toyoto, M. Hayashi, R. Endo, Y. Kobayashi, ISIJ Int. 49 (2009) 1722.
[254] M. Susa, A. Kushimoto, R. Endo, Y. Kobayashi, ISIJ Int. 51 (2011) 1587–1596.
[255] J.H. Wray, J.T. Neu, J. Opt. Soc. Am. 59 (1969) 774–776.
[256] G.W. Morey, The Properties of Glass, Reinhold, New York, 1960.
[257] J.F. Holzhauser, K.H. Spitzer, K. Schwerdfeger, Steel Res. 70 (1999) 252.
[258] B.J. Keene, K.C. Mills, Archiv. Eisenhuttenw. 52 (1981) 311–315.
[259] M. Susa, K. Nagata, K.C. Mills, Ironmaking Steelmaking 20 (1993) 272–278.
[260] K.H. Karlsson, G. Liu, J. Non-Cryst. Solids 345–346 (2004) 297–301.
[261] E. Larsen, H. Berman, in: The Microscopic Determination of the Non-opaque Minerals, US Geological Survey Bulletin 848, US Government Printing Office, Washington, DC, 1934.
[262] M. Susa, Y. Kumijo, Kusano, R. Kojima, Glass Technol. Eur. J. Glass Sci. Technol. A 46 (2005) 55–61.
[263] D.R. Gaskell, in: J.K. Tien, J.F. Elliot (Eds.), The Thermodynamic Properties and Structures of Slags, Metallurgical TreatisesMetallurgical Society of AIME, Warrendale, 1981, pp. 59–77.
[264] F.D. Richardson, Physical Chemistry of Melts in Metallurgy, vol. 1, Academic Press, 1974.
[265] M. Temkin, Acta Phys. Chim. USSR 20 (1945) 411.
[266] F.D. Richardson, Trans. Faraday Soc. 52 (1956) 1312.
[267] H. Flood, T. Förland, K. Grjotheim, Z. Anorg. Allg. Chem. 276 (1954) 289.
[268] L. Pauling, The Nature of the Chemical Bond, third ed., Cornell University Press, 1960.
[269] C.R. Mason, Proc. R. Soc. A287 (1965) 201.
[270] S.G. Whiteway, I.B. Smith, C.R. Mason, Can. J. Chem. 48 (1970) 33.
[271] A.C. e Silva, J. Min. Metall. 35 (1B) (1999) 85–112.
[272] J. Lumsden, in: G.R. St. Pierre (Ed.), Physical Chemistry of Process Metallurgy, Metallurgical Society Conference, vol. 7, Interscience, New York, 1961.
[273] M. Hillert, B. Jansson, B. Sundman, J. Agren, Metall. Trans. A 16A (1985) 261.
[274] H. Flood, T. Førland, K. Grjotheim, The Physical Chemistry of Metals, Institute of Mining and Metallurgy, London, 1953, pp. 46–62.
[275] M.L. Kapoor, M.G. Frohberg, in: Theoretical Treatment of Activities in Silicate Melts in Chemical Metallurgy of Iron and Steel, Proceedings of a Conference, University of Sheffield, ISI, London, 1971.
[276] H. Gaye, J. Welfringer, in: Modelling of the Thermodynamic Properties of Complex Metallurgical Slags, Second International Symposium on Metallurgical Slags and Fluxes, TMS-AIME, Lake Tahoe, Nevada, 1984.
[277] J.O. Andersson, T. Helander, L. Höglund, P.F. Shi, B. Sundman, CALPHAD 26 (2002) 273–312.
[278] C.W. Bale, P. Chartrand, S.A. Decterov, G. Eriksson, K. Hack, R. Ben Mahfoud, J. Melançon, A.D. Pelton, S. Petersen, CALPHAD 26 (2002) 189–228.
[279] S. Sridhar, Du Sichen, S. Seetharaman, K.C. Mills, Steel Res. Int. 72 (1) (2001) 3–7.
[280] S. Seetharaman, K. Mukai, Du Sichen, in: Viscisities of Slags—An Overview, VII International Conference on Molten Slags Fluxes and Salts, The South African Institute of Mining and Metallurgy, 2004.
[281] G.H. Zhang, K.C. Chou, G. Xue, K.C. Mills, Metall. Mater. Trans. B 43B (2012) 64–72.
[282] G.H. Zhang, K.C. Chou, K.C. Mills, ISIJ Int. 52 (2012) 355–362.
[283] G.H. Zhang, K.C. Chou, J. Min. Metall. B 48 (2012) 433–442.

CHAPTER 2.3

Atomistic Simulations of Properties and Phenomena at High Temperatures

Rita Khanna and Veena Sahajwalla
Centre for Sustainable Materials Research and Technology, School of Materials Science and Engineering, The University of New South Wales, Sydney, New South Wales, Australia

2.3.1. INTRODUCTION

Atomistic computer modeling and simulations are increasingly being used to determine thermodynamic and structural properties of crystalline/amorphous solids and fluids. These are of significant importance in the study of bulk materials, interfaces, surfaces, and defects. The strength of atomistic simulation lies in probing those length scales where continuum theory breaks down and complex many-body problems need to be solved to understand atomic level processes. They have an invaluable role to play in providing essentially exact results for theoretical problems that could only be solved by approximate methods, or might be quite intractable. In addition, computer simulations can be used as a test of theoretical models and approaches; simulation results are compared with and/or validated against real experiments. Simulations therefore can act as bridge between models and theoretical predictions on one hand, and between models and experimental results on the other hand. Because of this connecting role, computer simulations are often referred to as "computer experiments" opening new avenues of investigations of microscopic origins of material phenomena.

Computer simulation methods alleviate some of the major difficulties of theoretical approaches for complex systems such as large number of degrees of freedom, lack/low level of symmetry, nonlinear response, and complicated multi-body interactions. These can be used as a testing ground for theoretical concepts and be a source of physical/chemical information, which is not accessible to laboratory experiments. For example, molecular modeling and simulation is a particularly useful tool for studying the behavior of high-molecular-weight pitch components, since these very large and irregular compounds are not available in pure form for fundamental experimental studies. Computer simulations of material properties under extreme conditions such as shock waves, high temperature plasma, and earth's core elucidate technologically valuable information that is very difficult to obtain experimentally. A variety of physical phenomena from atomic levels to galactic scales with extremely slow to rapid reaction kinetics can be probed using

Treatise on Process Metallurgy, Volume 1
http://dx.doi.org/10.1016/B978-0-08-096986-2.00009-6
© 2014 Elsevier Ltd.
All rights reserved.

computer simulation investigations. It is currently possible to simulate very large systems (10^7–10^8 atoms) for much longer times (few nanoseconds) with empirical or semi-empirical potentials and investigate problems such as fracture, diffusion, plastic deformation, etc.

Our aim is elucidate the wealth of information about the fundamental mechanisms and processes that govern the response and properties of materials at high temperatures; we have focused on atomistic computer simulations based on realistic interaction potentials/parameters including pair-wise and multi-body interactions on a variety of systems of importance in process metallurgy. This chapter is organized as follows. Basic operating procedures and key aspects of computer simulation techniques are described in Section 2.3.2. These are followed in Section 2.3.3 by a variety of special algorithms that significantly extend the application of basic techniques and latest developments in the field. Section 2.3.4 outlines simulation procedures employed to determine/characterize physical/dynamical properties of the system such as diffusion, computation of free energies, behavior of defects; phase transitions, thermodynamics, wettability, surface tension, etc., from atomistic computer simulations. Fundamentals of atomic interaction potentials, which are at the heart of all atomistic simulations and determine the force fields acting on the atoms in simulation cell, are discussed in Section 2.3.5. A wide variety of interaction potentials for simple and transition metals, covalently bonded materials, binary and ternary alloys and various alloying elements in steelmaking have been presented and critically assessed. Section 2.3.6 provides a comprehensive summary on applications of atomic level simulations on a wide variety of problems of relevance to process metallurgy. Section 2.3.7 concludes this chapter with comments on the status of research in this fast evolving field, current trends, and future directions.

2.3.2. ATOMISTIC COMPUTER SIMULATION TECHNIQUES

Monte Carlo (MC) simulations and molecular dynamics (MD) methods are the two key approaches used in computer simulations of a wide variety of problems. To explain the macroscopic properties of matter, one needs to understand the behavior and interactions of a large number of microscopic constituents. For example, a collection of N ($\sim 10^{23}$) molecules of a gas in a container is characterized by a 6N-dimensional phase space with each molecule requiring 6 (3 position and 3 momentum) co-ordinates; the entire macroscopic system at a given time is represented by a string of $6N$ numbers representing microstates. With the number of microstates being very large, complex and varying with time, a variety of statistical approaches are used to obtain information about the system. Using a probabilistic approach, MC methods generate a stochastic trajectory through phase space to compute thermal averages; MD methods on the other hand use a deterministic approach numerically solving Newton's equations of the interacting system. Both these methods have found widespread application in a variety of problems

in statistical physics. These will be discussed in detail in the following sections along with specific algorithms used to obtain structural/thermodynamical information about the system.

2.3.2.1. MC Method

2.3.2.1.1 Basic Approach

MC method is based on the random sampling of various microstates of the system and was developed during the Second World War at Los Alamos by Metropolis and Ulam [1]; the first simulation on a hard disk fluid was reported in 1953 [2]. Computer simulations in this approach are generally implemented by assuming a system of N particles in a cubic box of length L and volume L^3; N generally ranges between 10^2 and 10^6 atoms depending on the application. To determine probabilities of random motion from one state to another, the Metropolis method uses the Markov property for statistical independence that requires the distribution of future states to be determined only by the present state. In other words, the system is considered to be independent of past (memory effects) and the future processes in a Markov chain depend only on the current state [3]. A particle is selected at random and given a small random displacement; the energy change associated with the move is computed. A random walk in the phase space is constructed such that the probability of visiting a point r^N is proportional to the Boltzmann factor associated with the move: $\exp(-\Delta E/KT)$ where K is the Boltzmann constant, T temperature, and ΔE the change in energy. The particle move is accepted for $\Delta E \leq 0$. For $\Delta E > 0$, the exchange could be accepted with a transition probability $W = \exp(-\Delta E/KT)$. W is compared to a random number η, chosen uniformly between 0 and 1. The move is accepted for $W > \eta$; otherwise the old configuration is counted once more for averaging. Specific aspects of MC simulations including ensembles, sampling procedures, types of movement, boundary conditions, random numbers, and accuracy limitations are discussed next.

2.3.2.1.2 Statistical Ensembles

A statistical ensemble is a collection of various microstates of an equilibrium macroscopic system as determined by the constraints operating on the system. The choice of ensemble is dictated by the nature of the physical system under consideration and properties to be computed. Details of some of the few well-known ensembles and associated criteria are given below:

2.3.2.1.2.1 Micro-Canonical Ensemble for Isolated Systems

Constraints on an isolated macroscopic system in equilibrium are constant energy (E), constant volume (V), and constant number of particles (N). The probability of all microstates of an isolated equilibrium system is considered equal and is given by $1/\Omega$ where Ω is the total number of microstates of the system. This system does not use random numbers

to determine the acceptance of a move. Let U be the potential energy of a system in a given state and E ($>U$) be the total energy of the system. The move is accepted for $\Delta E < 0$ and $\Delta E < (E - U)$ and rejected otherwise. This ensemble has limited application and is used sometimes to evaluate bias, if any, introduced by the random number generator.

2.3.2.1.2.2 Canonical Ensemble for Closed Systems

Consider a closed macroscopic system in thermal contact with a heat bath (temperature T). The volume (V) and number of particles (N) in the system is fixed but the energy (E) is no longer a constant and can be exchanged with the reservoir. This ensemble is also known as the NVT ensemble. Different microstates of the system can have different energies and the probability of finding a closed system in a given microstate "i" with energy E_i is given by exp ($-\beta E_i$) (where $\beta = 1/KT$). The canonical partition function Z is determined by the sum of Boltzmann weights taken over all microstates belonging to the system and is given by

$$Z(\beta, V, N) = \sum_i \exp[-\beta E_i] \tag{2.3.1}$$

Let $O(i)$ be a macroscopic property of the closed system in state "i"; the average of O, $<O>$, is given by

$$\langle O(\beta) \rangle = \frac{1}{Z(\beta, V, N)} \sum_i O(i) \exp(-\beta E_i) \tag{2.3.2}$$

The size of the canonical ensemble is generally taken to be quite large so as to provide adequate representation even to those microstates that are expected to occur with a very low probability. Canonical ensemble is used extensively to investigate a wide variety of problems.

2.3.2.1.2.3 Grand Canonical Ensemble for Open Systems

In an open system, there is exchange of energy as well as particles with the surrounding bath. This system is represented by constant volume (V), temperature (T), and chemical potential (μ). The probability of finding a system in a microstate "i" containing N_i particles and energy E_i is then given by $\exp(-\beta E_i + \mu\beta N_i)$. The grand canonical partition function Q can then be written as

$$Q(\beta, V, \mu) = \sum_i \exp(-\beta E_i + \mu\beta N_i) \tag{2.3.3}$$

and the expectation value of a macroscopic property $<O>$ can be written as

$$\langle O(\beta, V, \mu) \rangle = \frac{1}{Q(\beta, V, \mu)} \sum_i O_i \exp(-\beta E_i + \mu\beta N_i) \tag{2.3.4}$$

Grand canonical ensemble is a natural choice for adsorption studies [4], where the adsorbed gas is in equilibrium with the gas in reservoir. The temperature, volume and chemical potential outside and inside the adsorbent are fixed but the number of gas atoms adsorbed is allowed to fluctuate. This ensemble is also used extensively in phase-diagram simulations and associated applications [5].

2.3.2.1.2.4 Isobaric Isothermic Ensemble

The isobaric isothermic ensemble also referred to as NPT ensemble is one of most widely used ensembles as most of the real experiments are carried out under controlled conditions of temperature and pressure [6]. Here the volume of the system is allowed to fluctuate at constant pressure (atmospheric or otherwise) and the energy is computed for new configurations. In the NPT ensemble, volume is treated as an additional parameter toward reaching the lowest energy configuration. The system is allowed to equilibrate at a given volume; the volume is then changed to a new state and the trial move is accepted or rejected with a certain probability and then the system is allowed to equilibrate at the new volume. This ensemble is being used extensively for investigating phase equilibrium, equation of states and structural phase transitions.

2.3.2.1.3 Sampling Procedures

With the probability of finding a point X in the phase space given by $(1/Z)\exp(-E(x)\beta)$, this point could be selected either randomly (simple sampling) from the phase space or one may need to use "importance sampling" depending on the probability distribution. If the probability distribution is quite uniform, for example, configurations of randomly mixed crystals on a given lattice, simple sampling procedures are used from random numbers distributed uniformly between 0 and 1. Other examples include lattice gas models, diffusion of neutrons in a nuclear reactor, statistical properties of percolation clusters, etc. [7]. A number of techniques such as Fernandez–Criado technique, Box–Muller algorithm, and ones based on the central limit theorem have been developed as random sampling techniques [8,9]. In these schemes, atoms may either be selected randomly or in a sequential manner with equal probability.

In the presence of peaked distributions such as a Gaussian, the use of uniformly distributed random numbers can give poor results/statistics and could also be in small error. Importance sampling helps to predominantly sample from the important regions of phase space. For example, consider an exponential function $f(x) = \exp(-x)$ defined for $x \geq 0$. Consider a score function $h(x) = 0$ for $x < T$ and 1 for $x < T$. The function $f(x)$ has finite values in the region $x < 5$; but the score for this region has been set to zero. On the other hand, the function $f(x)$ approaches 0 for $x > 5$ and this region with score 1 will rarely be sampled. This problem can be overcome by introducing an importance density: $r(a, x) = a \exp(-ax)$ with $x \geq 0$ and parameter "a" lying between 0 and 1 and optimized for

minimum variance. Such weighted distribution helps to maximize the sampling in the important region and enhance statistical accuracy [10].

2.3.2.1.4 Trial Moves and Boundary Conditions

There are two main types of movements associated with atoms/molecules. A large number of MC studies are carried out on what is referred to as "lattice gas" models. In these models, atomic motion takes place on a rigid lattice grid with atoms hopping from one site to another. Simulations can be carried out both in canonical and grand-canonical ensembles; these studies generally use periodic boundary conditions. In the canonical ensemble, atomic pair gets exchanged between neighboring sites; in the grand-canonical ensemble the concentration of atoms gets changed by swapping the nature of atoms on a given site from A to B [11]. This technique can also be applied to the centers of mass movement of rigid molecules.

Alternatively, when atoms are free to move continuously on nonlattice regions, translational motion can occur in $\pm x$, $\pm y$, and $\pm z$ directions. With a random number "r" chosen uniformly between 0 and 1, a move by $(r-0.5)$ can move the particle in both positive and negative directions. Sometimes all three co-ordinates x, y, and z are moved simultaneously, and at times these are moved one by one in a random manner. Three types of boundary conditions are used for these simulations. While periodic boundary conditions are quite common, these sometimes can cause the simulation cell to slide in the phase space without much action within the cell. In the NVT ensemble, the volume can be kept fixed through a rigid outer wall of atoms while the atoms within the cell can move freely. In the NPT ensemble, while the simulation cell is controlled by fixed walls, the location of these walls and the size of the simulation cell are allowed to fluctuate between equilibrium steps. Thirdly in open systems, there is no bounding wall and atoms can relax in all directions. In this scenario, atoms have a tendency to fly apart; sometimes a retaining wall is required to contain constituents.

Thirdly, in the case of extended molecules, the orientation of molecules can also change along with the location of the centers of mass. Close-packed low energy configurations are a general requisite in organic crystallography, and these can be obtained through molecular orientations. In a study on the possible size effect in organic disordered molecular crystals, it was observed that stresses due to molecular disorder could easily be relieved through molecular reorientation and without much movement of centers of mass [12]. Self-avoiding walks on lattices have also been used for generating configurations of polymeric chains good solvents [13].

2.3.2.1.5 Random Numbers and Accuracy Considerations

For MC simulation, one needs random numbers that are uncorrelated and have uniform distribution in the interval 0 and 1. While true random numbers such as produced during radioactive decay cannot be predicted in advance, computer simulations use random

numbers generated through several simple algorithms. A variety of approaches are used to generate random numbers. Using congruential generators, one starts with an integer R_1 and generates successive integers through the recursion relation: $R_{i+1} = aR_i + b(\text{mod } m)$; the constants a, b and m need to be carefully chosen. Other generators include Marsaglia lattice structure, shift register generators, lagged Fibonacci generators, etc. [14]. The existence of nonvanishing triplet or higher degree correlations is a serious concern and testing of random number generators itself is an important component of research [15].

One needs to be aware that both "statistical" and "controllable systematic" errors can occur during simulation. Statistical errors can be minimized through increasing the sample size (N) and by increasing the computing time sufficiently. The standard deviation of the arithmetic mean of N random variables is inversely proportional to $\sqrt{N}$; a reliable prediction of statistical error sometimes becomes difficult due to dynamic correlation. Systematic errors arise from the incomplete randomness of numbers, finite system size, and finite observation times. Truncation errors in the finite step size can also become significant in simulations of transport properties [16].

2.3.2.2. MD Method

2.3.2.2.1 Basic Approach

This method uses Newton's equation of motion for describing the time evolution of atoms at location "r" and momentum "p" and is used to calculate the equilibrium and transport properties of a classical system. A model system of "N" particles is selected and the equations of motion of this system are solved until the system reaches equilibrium and the properties of system no longer change with time. Quantities that need to be observed during simulation are expressed in terms of atomic positions and momenta. The Hamiltonian (total energy) of a system of N particles can be written as

$$H\left(r^N, p^N\right) = A\left(r^N\right) + B\left(p^N\right) \tag{2.3.5}$$

The position and momenta of the system evolve with time in the following manner: $\frac{\partial r}{\partial t} = \frac{\partial H}{\partial p_i}$, and $\frac{\partial p}{\partial t} = -\frac{\partial H}{\partial r_i}$. The initial configuration of the system is chosen by selecting initial positions and velocities of all particles in the simulation cell. Forces on all particles are computed next and the Newton's equations of motion are integrated; these steps form the core of the simulation. Simulation steps are repeated in a loop for a specified length of time and averages of measured quantities are computed from the final configuration.

In MD simulations, the trajectory of a particle takes place in discrete time steps Δt and can be written using Taylor's expansion:

$$r(t+\Delta t) = r(t) + \left(\frac{\mathrm{d}r}{\mathrm{d}t}\right)_t \Delta t + 0.5\left(\frac{\mathrm{d}^2 r}{\mathrm{d}t^2}\right)_t \Delta t^2 + \ldots \tag{2.3.6}$$

The derivatives are computed from the forces operating on various atoms at time t. The truncation of Taylor's expansion to second order indicates constant acceleration, and can introduce approximations in the particle trajectory. Algorithms for MD simulations need to give rise to stable trajectories over extended periods of time, have reversible temporal evolution, and must conserve energy and momentum. "Verlet" algorithm is one of the most commonly used approaches in MD simulations [17]. Approximate equations for a forward and a backward step from a time t can be written as:

$$\begin{aligned} r(t+\Delta t) &= r(t) + v(t)\Delta t + 0.5a(t)\Delta t^2 \\ r(t-\Delta t) &= r(t) - v(t) + 0.5a(t)\Delta t^2 \end{aligned} \tag{2.3.7}$$

where $v(t)$ and $a(t)$ respectively represent the velocity and acceleration at time t. These equations can be solved to yield atomic velocity as

$$v(t) = \frac{r(t+\Delta t) + r(t-\Delta t)}{2\Delta t} \tag{2.3.8}$$

Acceleration can be unambiguously computed from the force acting on the atom. Typical time steps of 10^{-15} s are used. This algorithm has found extensive application for a variety of problems; an upgrade known as velocity Verlet program has also been developed [18]. Using Taylor's expansion, velocity can be written as

$$v(t+\Delta t) = v(t) + \frac{f(t+\Delta t) + f(t)}{2m}\Delta t \tag{2.3.9}$$

where "f" is the force acting on an atom of mass "m." The velocity can be written as

$$v(t) = \frac{v(t+0.5\Delta t) + v(t-0.5\Delta t)}{2} + \frac{\Delta t}{12}\left(\frac{\partial v(t-\Delta t)}{\partial t} - \frac{\partial v(t+0.5\Delta t)}{\partial t}\right) \tag{2.3.10}$$

There are small errors of the order of Δt^4 associated with the computation of velocity. Schemes involving higher order are also being used when longer time steps are required without losing short time memory.

2.3.2.2.2 Ensembles

Most of the MD simulations are carried out in the micro-canonical (NVE) ensemble. A system of N particles is contained in volume V; energy E is a constant of motion. Two approaches have been used to perform MD simulations in other ensembles as well. In Parrinello–Rahman scheme, crystalline solids are placed under constant stress and the volume (and shape) of the simulation cell is allowed to fluctuate [19,20].

2.3.2.2.2.1 Constant Temperature Ensemble

For a statistical system in thermal contact with a large heat bath, the particle velocities and energies are governed by the Boltzmann distribution. Velocity distribution $P(p)$ can be written as

$$P(p) = \left(\frac{\beta}{2\pi m}\right)^{3/2} \exp\left[-\beta p^2/2ma\right] \tag{2.3.11}$$

The kinetic energy per particle is then directly related to temperature as: $K_B T = m \geq \langle v_\alpha^2 \rangle$, where v_α is the αth component of velocity v. It is however important to note that the condition of constant temperature does not imply constant kinetic energy for all particles as it would lead to zero variance. The average kinetic energy per particle in a canonical ensemble of N is known to be inversely proportional to N; and the instantaneous temperature is known to fluctuate with time.

In the constant temperature algorithm developed by Anderson [21], the simulation cell is stochastically coupled to a heat bath that can take the system to a predefined temperature through random collisions with some atoms. Simulation is carried out in three steps. In the first step, equations of motion in the ensemble are integrated using standard MD approach. In the second step, a number of particles are chosen randomly and these undergo collisions with the heat bath as MC moves and modify the system energy from one level to another. The new velocity of particles undergoing collisions will be in accordance with Maxwell–Boltzmann distribution. In the third step, the system evolves at the new (but constant) energy according to Newton's laws. This procedure is repeated several times to obtain properties of interest. Other approaches for constant temperature MD simulations include Nose–Hoover thermostat based on an extended Lagrangian [22].

2.3.2.2.2.2 Constant Pressure Ensemble

Following an approach similar to MC simulations, constant pressure MD simulations are carried out by treating the volume of the simulation cell as a variable that changes dynamically during simulations. While only volume is changed for homogeneous fluids, simulations on nonhomogeneous fluids require changes in both the shape as well as size of the simulation cell. For further details on equations of motion under constant pressure, refer to a scheme by Martyna *et al.* [23]. Simulations have been reported that compared the results obtained at constant pressure and constant temperature with constant energy calculations; results were found to be quite comparable for static properties [24]. However, velocity autocorrelation function and diffusion coefficient were found to be affected by the collision rate used for constraining temperature [25].

2.3.2.2.3 Accuracy Considerations

There can be a number of sources of errors in MD simulations that can affect the accuracy of simulation results. The operational definition of temperature in MD simulation is in

terms of the average kinetic energy of N particles $\left\langle \frac{1}{2}mv_\alpha^2 \right\rangle = \frac{1}{2}KT$; the average kinetic energy is computed by dividing the total kinetic energy by the total number of degrees of freedom N_f (=$3N-3$). Fluctuations in energy cause the instantaneous temperature to fluctuate to the order of $1/\sqrt{N_f}$. With N typically around 100–1000 in MD simulations, statistical fluctuations in temperature are of the order of 5–10%. The trajectory of the system through the phase space is quite sensitively dependent on initializations; two trajectories that are very close initially could diverge with increasing time. The finite step size Δt can modify the dynamics in a systematic way and may also introduce energy drift in some integration schemes. The statistical error decays at a rate proportional to $1/\sqrt{\tau}$ where τ is the simulation time. The truncation error is asymptotically proportional to Δt^r where r is the accuracy of the numerical integrator [26].

2.3.2.3. *Ab initio* Density Functional Theory

2.3.2.3.1 Basic Approach

It is becoming increasingly desirable to probe the electronic structure in the field of nanomaterials and materials science; a number of experimental methods such as scanning tunneling microscopy, photon and electronic spectroscopy, etc., have been developed. Over the past 30 years, density functional theory (DFT) has become a dominant first-principles approach for the quantum mechanical simulation of electronic behavior in periodic systems. The ground state energy of a collection of atoms can be computed using the time-independent nonrelativistic Schrodinger equation:

$$H\psi(r_1, r_2, \ldots r_N) = E\psi(r_1, r_2, \ldots r_N) \tag{2.3.12}$$

The Hamiltonian H of the system is a sum of kinetic energy, interaction with external potential, and electron–electron interaction. Equation (2.3.12) is solved for a set of anti-symmetric eigenvectors ψ; the lowest energy eigenvalue E_0 represents the ground state energy. The probability density of finding an electron with a set of co-ordinates $\{r\}$ is given by $|\psi_0|^2$. A general solution of Equation (2.3.12) is very difficult. For example, consider a simple application to nano-carbons: a C atom has six electrons, which can be represented by 18 co-ordinates in three dimensions; a solution for a collection of 100 C atoms would require operations of the order of 100^{18} that can become quite unmanageable even on supercomputers.

Using Hartree–Fock approximation, the many-electron problem is solved in terms of N-coupled one-electron equations. The basic idea is to solve the N electron problem using a physical quantity, such as electron density, to describe the system uniquely. Basic concepts of DFT theory were developed by Hohenberg and Kohn [27] and Kohn and Sham [28]; these are known as Kohn–Sham equations and state that the total energy of a solid depends only on the electron density in the ground state. The electron density

is a scalar function defined at each point in real space: $\rho = \rho(r)$; the energy density and total energy then depends on the type of atomic nuclei (α) and their spatial arrangements (R_α):

$$E = E[\rho(r), \{R_\alpha\}] \tag{2.3.13}$$

The force acting on each atom is determined by the derivative of total energy with respect to nuclear position. Simulations on the system are carried out under the Born–Oppenheimer approximation that assumes the motion of electrons is much faster than those of nuclei; while this approximation is generally valid for heavy nuclei, it can lead to serious errors for light elements. The motion of atoms is computed according to laws of classical mechanics; and the electronic structure is calculated on an array of fixed atoms. The exact form of exchange-correlation function for which Kohn–Sham equations will lead to a solution similar to many-body Schrodinger equation is not known; a variety of approximations have been developed.

In the local density approximation (LDA), the local exchange-correlation energy density is assumed to be identical to that of a uniform gas of the same density [29]. In the generalized gradient approximation (GGA), energy functional depends on the local gradient of electron density. Meta-GGA functionals use the kinetic energy density as an additional variable; Hyper-GGA functionals use Kohn–Sham wave functions to evaluate the exact exchange; hybrid functionals mix exact and DFT exchange [30]. The length and time scales accessible by DFT calculations are determined by the maximum system size (typically few hundred to thousand atoms) and by the maximum time covered by *ab initio* MD (typically tens of picoseconds). A wide variety of DFT codes such as VASP, ABINIT, CASTEP, CRYSTAL, FLAPW, SIESTA, etc., are available using pseudo-potentials or all electron codes with plane-wave or local basis set. For many applications, DFT codes themselves are not sufficient for calculating material properties; a large number of codes have been developed for the postprocessing of DFT results toward a comprehensive description of dynamics and processes.

2.3.2.3.2 Applications to Materials Science

DFT methods can be seen as a "microscope" to study materials at atomic and electronic levels. These computations allow the prediction of total ground state energy of the system as a functional of nuclear positions without requiring additional system parameters. DFT methods have been used to study solids, surfaces as well as isolated molecules [31]. Surfaces and interfacial phenomena play an important role especially for thin films, wafers, microstructures with very high ratio of surface to bulk atoms. DFT calculations have been used to compute surface relaxation, structure/location of defects, adsorption geometries, etc. [32]. Norskov *et al*. have reported on the quantitative determination of rates of heterogeneous catalytic reactions and on the development of new catalysts [33]. Extensive computations have been carried out on clean surfaces of semiconductors Si and Ge and these have been used for investigating adsorption of atoms/molecules [34].

DFT has been used to aid the development of high strength steels, low-modulus high strength titanium alloys, and for materials with specific properties [35]. Crack propagation in Si has been investigated combining DFT with quantum MD simulations to understand the behavior of atoms near the crack tip and during propagation [36]. As a computer-aided design, DFT calculations were carried out on Fe–Co alloys as promising materials for magnetic data storage with high saturation magnetism and magnetic anisotropy [37]. This theory has made significant contributions to low-dimensional magnetism of surfaces as it can lead to a variety of novel phenomena such as localized electronic surface states, complex magnetic ordering, crystalline anisotropies, etc. [38].

DFT calculations have also been used to investigate oxides of main group elements, alkalis, and alkali-earth elements. These have been used to simulate conditions in the Earth's interior to predict the behavior under extreme conditions of temperature and pressure. Other applications include band-gaps and defect states for semiconductors, the formation of ordered structures through self-assembly, electronic transport in molecular devices, complex processes in biomaterials, energy computations in DNA molecules, etc. [39,40].

2.3.2.3.3 Current Limitations and Future Directions

First-principles total energy computations using DFT methods is one of the fastest growing fields in computational materials science. However, there still remain a number of major obstacles. The simulation of dynamic processes and meaningful comparison with experiments requires time and length scales many orders of magnitude higher than currently feasible. To bridge these gaps, novel approaches involving multi-scale modeling and simulation are being developed through the use of hybrid techniques. Using a two-step process, the configurational free energies of the system are obtained using DFT and cluster variation methods at zero kelvin and then these energies are used in high temperature MC/or MD simulation to achieve the phase or dynamic behavior of system under investigation.

Quasi-random structure approach has been used for the direct calculation of electronic and energetic properties of disordered materials [41]. The formation energy computed from DFT has been treated as input for thermodynamic models using CALPHAD [42]; DFT methods have also been used with phase-field models for investigating microstructures. To overcome issues with length/time scales, DFT component is embedded in to other algorithms such as accelerated MD, quantum MC, meta-dynamic techniques, etc., where quantum calculations using DTF are used to continuously fine tune energies and force fields while operating at much bigger time/length scales [43]. Continual efforts are being made to improve the accuracy of DFT simulations through improved construction of exchange-correlational functionals and postprocessing of simulation results.

2.3.3. SPECIAL TECHNIQUES AND ADVANCED ALGORITHMS

In Section 2.3.2, we have provided a brief description of three basic computer simulation techniques being used for atomistic simulations in materials science. In this rapidly developing field, where the availability, capacity and power of computers is increasing almost exponentially, a large number of new techniques/special algorithms have been developed to solve a variety of problems. These have significantly extended the application of original techniques. Some of the well-known algorithms are presented in this section. Our specific focus in this section is on the novel features of computer algorithms; their application to a variety of metallurgical problems will be presented in later sections.

2.3.3.1. Kinetic Monte Carlo Method

First developed in 1966 by Beeler [44], kinetic Monte Carlo (KMC) method is used for the dynamical evolution of a system from state to state, in contrast to the Metropolis method for equilibrium properties. The dynamical evolution of a system is generally computed through MD simulations solving classical equations of motion in a simulation cell with periodic boundary conditions. The force field is provided by interatomic potentials relevant to the system. While being immensely popular, an accurate integration in MD scheme requires very small time steps ($\sim 10^{-15}$ s) due to lattice vibrations; the overall simulation times are typically in micro-seconds which significantly limits the capacity of MD simulations to study longtime dynamic processes.

KMC method overcomes this limitation by modeling diffusion process through jumps from one state to another (discrete steps as against almost continuous trajectories in MD simulation) over much longer time scales [45]. Consider a collection of atoms in a simulation cell with periodic boundary conditions. Prepare an initial state by moving an atom from one site (interstitial, surface or other configuration) and allow nearby atoms to relax and achieve a lowest energy configuration. Increasing the temperature by a small amount will cause atoms to vibrate but these will eventually return to the same ground state unless it can overcome energy barriers to adjacent states (potential wells) and move to a new state. Through random infrequent events, atoms move their location followed by local area relaxation which in turn moves the entire system to another energy state. As the system vibrates and moves around in a given state for a period of time before moving to the next state, it loses its memory of the preceding state it came from; it therefore satisfies the basic criteria for a Markov process. The probability of finding a path to escape therefore remains identical during every time step resulting in a first-order exponential process. If there are a number of pathways to go from state "i" to state "j" with a rate constant k_{ij}, the probability distribution of escape is given by: $p_{ij}(t) = k_{ij} \exp(-k_{ij}t)$. An exponentially distributed random number is chosen to represent these probabilities;

the configuration of the system is appropriately modified, while continuously updating time and transition probabilities.

KMC simulation can be carried out with atoms/molecules in well-defined positions on regular lattices or not following prescribed locations with average locations determined through lowest energy configurations. Spatial movements during vibrations/relaxations are generally quite slow and the system evolves to lowest energy configuration using Metropolis algorithm. Rejected moves in these trials are labeled as a *null event*. Due to significant differences in timescales between thermal vibrations and lattice jumps over energy barriers (also labeled as *rare events*), a significant amount of computer time is lost computing thermal motion with atoms moving around their equilibrium configuration. Special algorithms have been developed to enhance the efficiency of KMC sampling.

There are a number of challenges facing KMC simulation. First, the timescales in computer simulation do not represent real times; a correspondence needs to be established for validation with experimental results. Basic input to KMC requires the identification of all microscopic processes that are expected to occur and the determination of their transition probabilities. Most KMC algorithms are hampered to some extent by inefficient search and upgrade methods for transition probabilities; a variety of *n*-level search methods, binary search methods, and update algorithms are being developed [46,47]. There are difficulties associated with time-scale separations among various processes such as multiple diffusion paths with different barrier heights and too fast diffusion kinetics along surfaces [48]; multi-scale KMC techniques, probability rescaling, and non-event MC methods are some of the approaches used [49,50]. Challenges on length-scale separation on internal surfaces and chemical potential gradients are being handled through spatial coarse-grained MC methods [51].

2.3.3.2. Reverse Monte Carlo Method

Reverse Monte Carlo (RMC) method is a general method for modeling atomic structures based on experimental data. Developed originally by McGreevy and Pusztai in 1988 [52], this approach has found extensive application in the development of computer models of atomic structures including crystalline, liquids, glasses, polymers, magnetic structures, etc. [53]. The key focus in RMC is to develop structural models based on a set of constraints that are consistent with experimental data. The approach consists of stochastically modifying atomic positions in some initial configuration using Metropolis Monte Carlo algorithm. The changes in atomic configurations (moves) are accepted or rejected on the basis of agreement between the simulated properties and the corresponding experimental target. Most commonly used properties include structure factor, pair correlation function, neutron, X-ray and electron diffraction data [54,55], extended X-ray absorption fine structure, NMR [56], etc. Up to five experimental data sets covering different ranges (and resolutions) from four different experiments have been simultaneously fitted to RMC models [57].

For example, if pair correlation $g(r)$ is being used as a target function, then the quantity to be minimized is given by χ^2:

$$\chi^2 = \frac{\sum_{i=1}^{n_{\exp}} \left[g_{\mathrm{sim}}(r_i) - g_{\exp}(r_i)\right]^2}{\sum_{i=1}^{n_{\exp}} \left[g_{\exp}(r_i)\right]^2} \tag{2.3.14}$$

where $n_{\exp}$ is the number of experimental points, g_{sim} and $g_{\exp}$ are simulated and experimental values of pair correlation functions. After every move, the quantity χ^2 is computed. If the new ${\chi_n}^2$ is less than the old χ_0^2, then the move is accepted. For $\chi_n^2 > \chi_0^2$, the move is accepted with a probability: $\exp(-0.5(\chi_n^2 - \chi_0^2))$ or is rejected otherwise. The model then slowly evolves toward a closer fit to the experimental data within certain error bars, reaching an equilibrium state with small fluctuations.

Key features of RMC approach include the use to periodic boundary conditions to avoid edge effects; typically few thousand atoms are used in a simulation cell. The initial configuration does not play a significant role and its effect can get neutralized fairly quickly in the simulation run. Fitting is generally carried out on the total experimental data instead of functions derived from experiments. As no interatomic potentials are used in the simulation, the application of RMC is quite general and not limited to specific systems. Simulations are carried out within a set of constraints such as distance of closest approach (hard-sphere model), packing and atomic number density, atomic coordination, constraints on bond angles, etc.

There are some limitations regarding the uniqueness of structural models developed using the RMC approach. Diffraction data provide limited, incomplete, and insufficient information about correlations between constituent atoms. While atomic models can be developed to explain certain aspects of structure–property correlation, there is no guarantee on the uniqueness/correctness of the structural model. In the case of a bulk fluid, a structural model developed using RMC by fitting with data on with pair-correlation function may not necessarily have higher-order correlations. According to the uniqueness theorem of statistical mechanics [58], for systems that are governed by pair-wise additive potential, structural model developed using pair-correlation functions uniquely determine higher-order correlation functions. In such cases, RMC modeling would in principle lead to a unique structure. This may not be the case in the presence of many-body interactions and angular distributions. RMC approach has nowadays become an established technique to develop an understanding of a wide variety of materials including single crystals, powders, glasses, fluids, disordered and nano-materials.

2.3.3.3. Hybrid MC Methods

With computer simulation techniques increasingly being applied to study a wide variety of problems, a number of problems currently use two or more of these techniques simultaneously to overcome basic limitations or to extend their range of application. For example, DFT codes are being embedded in MD algorithms; RMC codes are being used

in conjunction with MD [59], constant pressure MD makes use of random movements of atoms for volume fluctuations. Both MC and MD have their advantages and limitations, but these are quite complementary. MD generates kinetic and thermodynamic data through a slow exploration of phase space in many small discrete time steps resulting in a systematic error. MC method, on the other hand, uses random discontinuous trajectories; there are only statistical errors but no time step error. The sequence of steps in MC simulation can lead to a rapid exploration of phase space.

Hybrid Monte Carlo (HMC) method, developed by Duane *et al.* in 1987 [59] combines the features of MD with MC simulation by calculating equations of motion with parallel updates at all lattice sites followed by an accept/reject decision for the whole configuration. Unlike normally discrete integration of differential equation, there are no truncation errors. The step size $\Delta\tau$ in the hybrid method is chosen to be as large as possible keeping the acceptance rate of MC steps reasonably high. Each new trajectory is calculated using short constant MD trajectory with an MC rejection step. Each new trajectory is accepted with a probability after which all momenta are reset. In order to retain dynamic information, the HMC has been generalized to allow for partial momentum updates between MC steps instead of complete replacement of momenta by random samples from the appropriate Boltzmann distribution [60]. New generalized HMC techniques are being developed for applications from physics, biology, and statistics [61].

2.3.3.4. The Gibbs Ensemble Method

The Gibbs ensemble technique is a computational technique developed by Panagiotopoulos [62] for studying first-order phase transitions/equilibria for fluids. The phase behavior of fluids and their mixtures are of significant importance to a large number of chemical and pharmaceutical industries. Using force-field-based simulations, equilibrium properties can be obtained by MD or MC methods. To determine the phase behavior, one requires the knowledge about the chemical potential of all components as a function of density, composition, and temperature. The Gibbs ensemble method overcomes significant limitations caused by the relatively high proportion of interface atoms (as compared to bulk) when two or more phases co-exist in a given simulation cell. Even with a simulation cell containing 10^6 atoms, up to 6×10^4 atoms could be on interfaces with characteristics distinct from the atoms in the bulk. This technique is based on the simultaneous calculations of two co-existing regions coupled through particle transfers and changes in volume. This technique is being used extensively to study vapor–liquid and liquid–liquid equilibria.

Two or more phases are known to co-exist when their pressures (P), temperatures (T) and chemical potentials (μ) become equal, thereby corresponding to a μPT ensemble. All these three variables are intensive parameters and therefore linearly dependent, the system requires at least one fixed extensive variable (volume V or number N) to keep it bounded.

In the Gibbs ensemble technique, the simulations are carried out in two separate microscopic regions bounded by periodic boundary conditions. The difference in chemical potential for two regions is kept fixed (at $\Delta\mu = 0$), and the total volume V and total number of particles N in the overall system are kept constant, that is, if N_1 and V_1 represent the number of atoms and volume in phase 1, the number of atoms N_2 and corresponding volume V_2 are given by $(N - N_1)$ and $(V - V_1)$ respectively. Both regions are also assumed to be in thermal equilibrium with identical temperatures and pressures.

Three sets of MC moves are made either sequentially or randomly in a given MC step. These include random displacements of particles in a given region, fluctuations in volume with the total volume remaining constant, and transfer of atoms from one region to another keeping the total number unchanged. In the original approach, N attempts were made to move all particles in the NVT ensemble, then volume of a region was changed in NPT ensemble and finally particles were transferred from one region to another in μVT ensemble. Detailed balance is maintained in each MC step. Detailed rules for accepting/rejecting various moves can be found elsewhere [63]. Using this approach, the system spontaneously moves toward densities and compositions of co-existing phases. The main limitation of this approach is that it requires a large number of particle insertions from one phase to another. It is very difficult to study phase equilibria in dense solids with this technique, as these have limited access to sites where additional particles could be added. This method has found extensive application in the study of model systems such as binary Lennard–Jones mixtures [64], realistic potential models for pure fluids [65] and mixtures [66].

2.3.3.5. Biased MC Schemes

A number of biased MC techniques have been developed where the natural dynamics of system is too slow for the simulation to reach equilibrium or the probability of random trials/moves is extremely slow. In an extension of Metropolis Monte Carlo methods, the moves are biased to increase the probability of acceptance as compared to random moves. A variety of biased sampling moves including force bias, orientation bias, configuration bias, etc., have been used in a range of algorithms/applications. In the force bias procedure, each move is chosen with enhanced probability in the direction of instantaneous force on the particle [67]. As the particle moves in a direction that lowers net force acting on it, the system is generally moving toward a lower energy configuration; therefore, the move has a higher probability of being accepted. Especially for simulations on disordered molecules with motions of centers of mass as well as molecular reorientation, the system tends to get locked in local energy states with most of the random moves getting rejected. This situation can be relieved to a great extent with small moves made in the direction of force [68]. A similar approach known as Brownian dynamic smart MC method has also been developed with a slightly different choice for transition probability [69]. For

solutions containing strongly interacting solutes, trial moves in the direction of force as well as torque with significant reduction in step sizes were found to significantly enhance the acceptance probability [70].

Configurational bias MC technique is used for the simulation of flexible molecules (e.g., alkanes, polymers) into various configurations. The architecture of the molecule has a significant influence on the acceptance probability and overall simulation time toward equilibrium. The total potential energy at a given site is arbitrarily divided into two parts: first part being internal bonded interaction potential and the second part being external potential to be used to bias the move. The conventional algorithm for generating a trial orientation is to generate a random vector in a sphere, compute internal energy and accept/reject the move according to the transition probability. This algorithm is very inefficient as a large number of trial orientations will be rejected as the probability distribution of allowed states is very narrow and could become a rate-limiting step. The process could be made significantly more efficient by splitting the potential into bond-bending (θ) and torsional components (φ) and making the moves in a sequential manner [71]. Rosenbluth scheme is used to add weights to given moves and to define transition probabilities during configuration biased MC runs [72].

Another approach, known as rotational insertion bias, has been developed for simulating dense phases of structured particles during grand-canonical and Gibbs ensemble MC simulations [73]. In the grand canonical ensemble (μVT), the number of particles is allowed to fluctuate (created as well as removed from the system) and in the Gibbs ensemble new particles are created in one phase with a coupled depletion in a co-existing phase. In dense systems, there are very few places (cavities) where new particles may be inserted which leads to very low acceptance rates for MC moves. In the cavity-bias approach [74], a grid is set up that tests the points at which cavities are bigger than a certain radius and then creations are attempted at random in those cavities. The created grid is updated for each new configuration.

2.3.3.6. Wang–Landau Formalism

A novel multiple range random walk algorithm was developed by Wang and Landau in 2001 [75] to calculate the density of states to directly access the free energy and entropy. This approach known as Wang–Landau (WL) algorithm has been applied to a large number of problems [76–78] and overcomes difficulties associated with critical slowing down near second-order phase transitions, long relation times, and rough energy landscapes for complex systems. Conventional MC approaches can be used to directly generate a canonical energy distribution: $g(E)e^{-E/KT}$, where $g(E)$ is the density of states with energy E. The WL approach can directly determine $g(E)$ with high accuracy through a random walk that produces a flat histogram in energy space. Multiple random walks in different energy regimes can be carried out sequentially or in parallel, and the resultant

density of states joined together to produce canonical averages toward generating thermodynamic behavior.

This algorithm is based on the premise that when a random walk is carried out in energy space with a transition probability proportional to $1/g(E)$; it leads to a flat histogram for energy distribution. The estimated density of states is modified in a systematic manner to converge to the true value after a large number of iterations. Initially $g(E)$ is set equal to 1 for all energies. A spin is then chosen at random and flipped with a probability W (=min(1, $g(E)/g(E')$); the function "min" automatically selects smaller of the two values). E' is the energy of the system with the chosen spin being overturned. The random walk moves in a bounded range of energy so that the moves that go outside the range are rejected. A histogram $H(E)$ records how often a state of energy E is visited. The density of states $g(E)$ is updated continuously in a systematic way during the random walk to produce a flat histogram over the allowed energy range while simultaneously making the density of states converge to the true value. The simulation is terminated after reaching a predetermined level of accuracy. To speed up the simulations, several random walks are performed simultaneously on adjacent energy intervals. Finally, the simulated results on $g(E)$ are normalized to get the absolute density of states using either known values of density of states, the ground state degeneracy, or other constraints for $g(E)$. During the early stages, the algorithm does not satisfy detailed balance as the density of states are getting continuously modified; but detailed balance condition is satisfied as the system rapidly converges to true values.

This algorithm can be used to calculate Gibbs free energy and the entropy that are generally not accessible in standard MC techniques. The internal energy $<E>_T$ of the system can be represented in terms of density of states as

$$U(T) = \frac{\sum_E E \cdot g(E) \mathrm{e}^{-E/kT}}{\sum_E g(E) \mathrm{e}^{-E/kT}} = \langle E \rangle_T \tag{2.3.15}$$

The Gibbs free energy can be written as

$$F(T) = -kT \log\left(\sum_E g(E) \mathrm{e}^{-E/kT} \right) \tag{2.3.16}$$

With an accurate measurement of density of states, the entropy can be calculated as

$$S(T) = \frac{U(T) - F(T)}{T} \tag{2.3.17}$$

and the specific heat of the system is defined by the fluctuation expression

$$C(T) = \frac{\partial U(T)}{\partial T} = \frac{\langle E^2 \rangle_T - \langle E^2 \rangle_T}{T^2} \tag{2.3.18}$$

A significant amount of work has been done to improve the efficiency and accuracy of this algorithm and on its application to a variety of problems including MD [79,80].

2.3.3.7. Parallel Tempering Method

The concept of parallel tampering or replica exchange was first introduced by Swendson and Wang [81]; the replicas of a system were simulated at a series of temperature with a partial exchange permitted between configurations at adjacent temperatures. In the parallel tempering approach, simulations are carried out at a range of temperatures in a canonical ensemble to generate different configurations. Whereas the high temperature simulations will generally span a large volume of phase space, low temperature simulations will generally be sampling local regions and could also get trapped in local energy minima. Parallel tampering then permits exchanges of complete configurations with adjacent temperature configurations. This approach significantly extends the states being sampled at a given temperature and is being used extensively in statistical physics, biomolecules, chemistry, engineering, and materials science [82–84].

The exchange of configurations between two replicas of energies E_1 and E_2 with inverse temperatures $(1/KT)$ β_1 and β_2 is accepted with a probability given by

$$P(E_1,\beta_1 \rightarrow E_2,\beta_2) = \min[1, \exp(\Delta\beta \cdot \Delta E)] \tag{2.3.19}$$

where $\Delta\beta = \beta_2 - \beta_1$ and $\Delta E = E_2 - E_1$ respectively represent differences between inverse temperatures and energies of adjacent states. Each replica is required to spend the same amount of time at each temperature. The choice of optimal temperature intervals is determined from the flow in temperature space; and these are systematically adjusted during the simulation. These swap moves are quite inexpensive as these do not involve additional computations; these moves also do not disturb the Boltzmann distribution corresponding to a given ensemble and represent an equilibrium MC scheme.

For example, consider the motion of a single particle under the influence of an external field. Depending on the temperature, the particle can overcome some of the potential barriers. The entire phase space may only be sampled at high temperatures, whereas at low temperatures the particle could get locked in some low energy wells. Through parallel tempering and swapping between adjacent configurations, significant improvement can be observed even at low temperatures. Other applications include thermodynamic investigations on phase equilibria, polymers, etc. [85].

Bittner *et al.* [86] have extended the power of the parallel tempering algorithm especially near second-order phase transitions where systems with diverging specific heat would give rise to a high density of replicas around the critical temperature. A constant acceptance rate was calculated from the following expression:

$$A(1 \rightarrow 2) = \sum_{E_1, E_2} P_{\beta_1}\left(E_1 P_{\beta_2}(E_2) P(E_1, \beta_1 \rightarrow E_2, \beta_2)\right) \tag{2.3.20}$$

where $P_{\beta i}(E_i)$ represents the probability for replica "i" to have energy E_i at inverse temperature β_i. Using Equation (2.3.20), a set of inverse temperatures can be calculated starting from a given inverse temperature β_1 such that acceptance rate A remains constant. This approach is able to overcome the bottlenecks due to critical slowing down near second-order phase transitions and moves to low temperature phases.

2.3.4. DETERMINATION OF PHYSICAL PROPERTIES

2.3.4.1. Free Energy

Thermodynamic integration is one of the key approaches used to compute differences in thermodynamic properties, for example, free energy between the state of interest and a reference state. In this simulation, the thermodynamic parameters of the system are changed in very small steps to ensure that the path traversed remains reversible and the system remains in equilibrium at all points. While pressure P, volume V and temperature T are typical experimental variables, the influence of additional variables such as interaction potentials can also be investigated in computer simulations [87]. When the path followed is reversible and is characterized by the change in a single parameter, the work done provides a measure of the change in free energy of the system [88]. A brief derivation is given below.

Consider a system in contact with a bath held at constant temperature T and pressure P. If a reversible work ΔW^r is done on the composite system, it can be expressed in terms of changes in internal energies of the system (ΔU) and the surrounding bath (ΔU_B)

$$\Delta U_B = T\Delta S_B - P\Delta V_B \tag{2.3.21}$$

According to the second law of thermodynamics, there is no change in entropy for an isolated system and a reversible process, that is, $\Delta S + \Delta S_B = 0$, and $\Delta V + \Delta V_B = 0$. Total reversible work ΔW^r can then be written as the change in Gibbs free energy:

$$\Delta W^r = \Delta U - T\Delta S + P\Delta V = \Delta G \tag{2.3.22}$$

Work done at constant temperature determines changes in Helmholtz free energy. While this approach can be used to study the phase behavior by changing temperature and pressure infinitesimally as long as the main requirement of reversibility holds good for thermodynamic integration. However, this condition breaks down near first-order phase transitions due to hysteresis effects. Due to large free energy barrier near a first-order phase transition, the transformation to the new phase can occur either irreversibly or well beyond the co-existence point. As a general rule, a qualitative prior knowledge of phase diagram is quite important to avoid first-order phase transitions along the integration

path. Secondly, the reference state and the final state of interest are chosen to be energetically and structurally quite close to minimize hysteresis effects.

To calculate liquid phase free energy, a rarefied ideal gas is used as a reference state. The temperature of the liquid phase "L" is increased continuously till it becomes supercritical. The change in free energy is given by

$$\Delta(\beta F) = \int_L^S U(\beta, V, N)\mathrm{d}\beta \tag{2.3.23}$$

where $\beta = 1/\mathrm{KT}$ is the inverse temperature. Here, F_i the Helmholtz free energy for the ideal gas at the temperature/density corresponding to a supercritical state "S." The integrand in Equation (2.3.23) can be computed at a number of co-existence points along the path using canonical ensemble simulations. The next path takes the system from the supercritical state to dilute state "D" where the gas phase behaves as an ideal gas, with energy computed at a number of coexistence points along this path:

$$\beta(\Delta F)_s = F_s - F^{\mathrm{I}} = \int_D^S \mathrm{d}\rho \left(\frac{P - \rho KT}{\rho^2}\right) \tag{2.3.24}$$

where F^{I} is the Helmholtz free energy for the ideal gas at the temperature and the density of the supercritical gas. The solid phase however cannot be directly connected to the ideal gas state through a reversible path. A nonphysical path therefore needs to be constructed with analytical computation of free energy. Using an Einstein crystal method [89], harmonic springs are used to attach particles to their respective sites with a potential given by

$$\varphi(R) = N\varphi_0 + 0.5K\sum_{i=1}^{N}(r_i - R_i)^2 \tag{2.3.25}$$

where φ_0 is the static lattice energy, K the harmonic spring constant, and r_i and R_i the instantaneous and equilibrium positions of atoms. The free energy of the reference state "F_{E}" defined by the Einstein crystal phase can be determined analytically as

$$F_{\mathrm{E}} = \frac{3N}{\beta}\ln\left(\frac{\beta h\sqrt{K}}{2\pi}\right) + N\varphi_0 \tag{2.3.26}$$

where "h" is the Planck's constant. The free energy of the solid phase is determined by connecting it to the Einstein crystal phase through the following equations

$$\varphi(\lambda) = \lambda\varphi_{\mathrm{S}} + (1-\lambda)\varphi_{\mathrm{E}} \tag{2.3.27}$$

$$\Delta F = \frac{1}{\beta}\int_0^1 \mathrm{d}\lambda \left\langle \frac{\partial\varphi}{\partial\lambda}\right\rangle \tag{2.3.28}$$

The integrand is evaluated numerically at a function of λ using the canonical ensemble to obtain the free energy of the solid phase. These methods can however become highly computationally expensive when attempts are made to compute phase diagrams. Kofke [90] developed a novel approach combining elements of thermal integration and Gibbs ensemble technique for the direct evaluation of phase equilibria. Thermodynamic integration is used to evaluate the chemical potentials of co-existing phases; the path of integration is chosen to coincide with the saturation line. For a pure substance, we can write

$$\mathrm{d}(\beta\mu) = h\mathrm{d}\beta + \beta v\mathrm{d}p \tag{2.3.29}$$

where μ, h, v and p respectively represent the chemical potential, molar enthalpy, molar volume and pressure of the system. This equation can be rewritten for two co-existing phases α and γ and combined as Clapeyron equation:

$$\left(\frac{\mathrm{d}p}{\mathrm{d}\beta}\right)_{\sigma} = -\frac{\Delta h}{\beta \Delta v} \tag{2.3.30}$$

where $\Delta h = h_{\alpha} - h_{\gamma}$ is the difference in molar enthalpies of two phases and $\Delta v = v_{\alpha} - v_{\gamma}$ is the change in molar volumes; the derivatives are taken along the saturation line. Alternatively, a function $f(\beta,p)$ is defined such that

$$f(\beta,p) = \left(\frac{d\ln p}{\mathrm{d}\beta}\right)_{\sigma} = -\frac{\Delta h}{\beta \rho \Delta v} \tag{2.3.31}$$

First-order nonlinear Equations (2.3.30) and (2.3.31) describe how the pressure must change with temperature for two phases to remain in coexistence. Given an initial condition of coexistence with defined pressure and temperature at a point, the equation can be numerically integrated to determine the entire co-existence line using either NPT MC or MD method. In each simulation, the pressure is adjusted to satisfy equality of chemical potentials according to Gibbs–Duhem equation (Equation 2.3.29). A single simulation is required for each simulation point. This method is highly efficient as compared to standard thermodynamic integration approaches; another advantage being that it does not require parameterization of interaction potentials or additional external potentials. However, there exists a possibility of systematic drift from the true coexistence line as the integration proceeds; it is therefore quite important to use very small steps in the predictor–corrector algorithm and to check for accuracy by obtaining two or more coexistence points using thermal integration. In a recent development, Habershon and Manolopoulos [91] have developed a new approach for calculating quantum mechanical corrections to classical free energies, which are numerically stable even in the presence of strong quantum delocalization.

2.3.4.2. Surface Tension

The surface tension for a liquid–vapor interface is calculated as integral over the interface of the difference between the normal and tangential components of the pressure tensor [92].

$$\gamma = \int_{z_l}^{z_v} \mathrm{d}z[p_N(z) - p_T(z)] \tag{2.3.32}$$

where bulk liquid is assumed to be on the left of the interface and bulk vapor on the right. Z_l and Z_v are arbitrary positions in the liquid and vapor phases; p_N and p_T represent normal and tangential components of the thermodynamic pressure in the bulk phases. The components differ from each other in the interface zone. Kirkwood–Buff virial expansion has been the key route to determine planar surface tensions in computer simulations [93]. This equation can be derived from the derivative of Helmholtz free energy "F"

$$\gamma = \frac{\partial F}{\partial A} + L_z P \tag{2.3.33}$$

L_z is the length of the system normal to the interface at the bulk pressure "p." This equation can be written as an ensemble average of an additive pair-wise interaction over all the atoms of the system [94,95]:

$$\gamma = \left\langle \sum_{i>j}^{N} \frac{(x_i - x_j)^2 + (y_i - y_j)^2 - 2(z_i - z_j)^2}{2r_{ij}} u'(r_{ij}) \right\rangle \tag{2.3.34}$$

where $u'(r_{ij})$ is the derivative of the interatomic potential between the ith and jth atoms. Both Equations (2.3.32) and (2.3.34) are used to simulate planar surface tension at the liquid–vapor interface. A number of studies on surface tension of ionic liquids and water have been reported in literature based on Lennard–Jones and other model potentials [96–98]; however, surface tension values were found to fluctuate significantly with the presence/or absence of certain configurations strongly influencing the simulation result.

Lee and Scott [99] computed the excess free energy required to create a surface using the Bennet formula [100].

$$F_1 - F_0 = -kT \ln \frac{\langle M(\Delta U^*) \rangle_0}{\langle M(-\Delta U^*) \rangle_1} \tag{2.3.35}$$

where $M(x) = \min\{1, \exp(-x)\}$ is the Metropolis acceptance probability, $\langle\rangle$ denotes the canonical average over all configurations of system "i," and $\Delta U^{\star} = (U_1 - U_0)/kT$. Another approach [101] uses

$$F_1 - F_0 = -kT \ln \left\langle e^{-\Delta U^*/kT} \right\rangle \tag{2.3.36}$$

Due to the presence of exponential functions, conventional MC sampling is quite inefficient in these algorithms. A sampling technique called "umbrella sampling" was used to make the program more efficient.

Ackland and Finnis [102] developed a new approach to calculate the surface tension γ as distinct from surface energy σ for solid bcc transition metals that go beyond pair-wise interaction potentials. A surface stress tensor was defined for anisotropic materials and surface tension was determined by averaging its diagonal components. An extensive quantity corresponding to the surface energy is referred to as superficial energy, that is, it is surface energy multiplied by surface area: σA. A stress tensor $\tau_{\alpha\beta}$ is defined as the strain derivative of the superficial energy per unit area. Considering only homogeneous strains within the plane of the surface: $\varepsilon_{\alpha\beta}$

$$\tau_{\alpha\beta} = A^{-1} \partial(\sigma A)/\partial \varepsilon_{\alpha\beta} \tag{2.3.37}$$

The surface tension is the average of the x and y tensile surface stresses: $\gamma = 0.5 (\tau_{xx} + \tau_{yy})$. The energy of the surface was minimized by allowing the top 16 interlayer spacings to vary until the forces on each atom fell below 10^{-11} eV/Å using a variable metric algorithm [103]. The structure of the layer was held constant and no lateral movement was permitted. In the final state, the structure of the layer was found to be a minimum with respect to lateral movement in all directions. Once the final layer separations were determined, the relaxed surface tension was determined by differentiating the energy function with respect to area. Simulations have also been reported on surface tension simulations on curved surfaces [104].

2.3.4.3. Wettability

A few studies have been carried on atomic level modeling and simulation of the wetting behavior. In a computer simulation investigation on the dissolution of carbon from alumina–carbon refractories into molten iron [105], carbon dissolution from a model system was compared with experimental results. As a first step, poor wetting between alumina and molten iron was modeled as repulsion between alumina (treated as a composite unit) and iron; this model agreed with the observed trend qualitatively but with significant differences. As a second step, poor wetting was modeled as a surface effect only; the repulsive nature of interaction was restricted to the surface region only. The fit with the experiment was somewhat better. As a third step, poor wetting between alumina and iron led to their mutual exclusion from their neighborhood, that is, no alumina was present around iron atoms and vice versa; this condition led to an almost perfect fit with the experimental data.

Hautman and Klein [106] carried out MD simulations to investigate wetting phenomena on a microscopic length scale. The usual description of the wetting of a solid

surface relates to the contact angle θ of a liquid drop on a planar substrate to the free energies of the three interfaces based on the Young's equation:

$$\cos\theta = (\gamma_{sv} - \gamma_{sl})/\gamma_{ls} \tag{2.3.38}$$

where γ_{ab} represents the surface free energy of the interface a–b: s (solid), l (liquid), and v (vapor). Microscopic studies of a Lennard–Jones liquid in contact with a solid were found to be inconsistent with Young's equation [107]. Hautman and Klein carried out simulation on water molecules in contact with polar and nonpolar surfaces. The simulation cell consisted of 90 water molecules and 90 substrate chains. These were arranged on an experimentally observed triangular lattice with periodic boundary conditions. A constant temperature MD simulation was carried out for a total of 350 ps with a time step of 4.5×10^{-3} ps. The water molecules gradually reorganized to form a cluster in the form of a droplet. The evolution of the center of mass of the droplet ($Z_{c\cdot m}$) in a direction normal to substrate surface was monitored; its average value was directly correlated with the contact angle θ:

$$\langle Z_{c\cdot m}\rangle = (2)^{-4/3} R_0 \left(\frac{1-\cos\theta}{1+\cos\theta}\right)^{1/3} \frac{3+\cos\theta}{2+\cos\theta} \tag{2.3.39}$$

where, $R_0(3N/4\pi\rho_0)^{1/3}$, the radius of free spherical water droplet of N water molecules at density ρ_0. Simulation results were found to be in good agreement with experimental results. The wetting behavior of water nano-droplets on homogenous and phase-separated self-assembled monolayers has also been reported using MD simulations [108]. Atomistic simulations have also been used to investigating spreading and wetting behavior to elucidate fundamental details of reactive wetting [109].

Nakanishi and Fisher [110] have used an Ising lattice-gas model approach toward developing an understanding of the wetting behavior in terms of liquid and liquid-wall short-range interactions. Atoms were represented as spins on lattice points; a semi-infinite very thick Ising slab was used with the top and bottom surfaces so widely separated that each acts as a boundary to the semi-infinite system. Of particular interest is the case of a fluid slab where the two surfaces favor different phases. For the fluid near the gas–liquid existence in the bulk, one surface favors high-density liquid and other wall prefers low-density gas. Another case of such competing walls is realized for a liquid drop on a solid substrate on one wall and free on the other side [111]. The geometry of the system plays an important role in the application of the model to investigate wettability and interfacial phenomena.

2.3.4.4. Phase Diagrams and Critical Phenomena

Extensive studies have been reported in literature on the study of phase transformations using a variety of computer simulations [112–119]. In atomistic computer simulations, one considers a finite system, typically a cubic box of edge length L with periodic

boundary conditions to obtain statistical information on thermodynamics, correlation functions, order parameters, etc. Before preparing the system for computer simulations, the simulation cell size, observation time, order parameter and initial state need to be carefully chosen to minimize some of the fundamental difficulties associated with phase transition investigations. One of the key difficulties is associated with the finite size rounding and shifting of the phase transition; it can become quite difficult to distinguish between second-order and weakly first-order transitions. The use of periodic boundary conditions for a given shape of the simulation cell can sometimes suppress those new structures that do not fit in with the original structure, for example, in phase transitions between structures of different lattice symmetry. Alternatives approaches use nonlattice simulations, fluctuating cell dimensions as in NPT ensembles or using linear dimensions of the cell as an additional simulation variable [120]. Third issue is with the occurrence of metastable states and hysteresis; it is quite possible that the system may get locked in a metastable state with a lifetime longer than the simulation observation time.

For example, the ordering behavior of binary AB alloy such as Cu–Au on a rigid fcc lattice has been examined in the framework of lattice gas Ising model [121]. The local concentration at a site "i" is defined as $c_i = 0$ if occupied by atom A and equal to 1 for atom B. Using pair-wise interaction and neglecting the role of defects, if any, the total energy of the system can be written as

$$V = \sum_{i \neq j} \left\{ (1-c_i)(1-c_j) V_{ij}^{AA} + \left[c_i(1-c_j) + c_j(1-c_i) \right] V_{ij}^{AB} + c_i c_j V_{ij}^{BB} \right\} \qquad (2.3.40)$$

Here various V's represent AA, AB, and BB interactions. In spin notation with $S_i = 1 - 2c_i$, spin up (1) is associated with atom A and spin down (-1) with atom B. The Ising Hamiltonian can be written in terms of spin–spin interaction parameters: $J_{ij} = -(V_{ij}^{AA} + V_{ij}^{BB} - 2V_{ij}^{AB})/4$ and a magnetic field H: $H' = \frac{1}{2}\sum_{j \neq i} \left(V_{ij}^{AA} - V_{ij}^{BB} \right) + \frac{1}{2}(\mu_A - \mu_B)$ where μ's represent various chemical potentials.

$$H = -\sum_{i \neq j} -J_{ij} S_i S_j - H' \sum_i S_i \qquad (2.3.41)$$

Various interaction parameters need to be determined *a priori* through comparison of simulation results with experimental data. In a simulation on Fe–C system by Khanna and Sahajwalla [122], the strength of various interaction parameters was determined from the solubility limit of carbon in molten iron. Interactions are generally assumed to range up to nearest or next nearest neighbors depending on the system geometry [123].

Various order parameters relevant to expected ordered states such as AB, A_3B need to be appropriately defined. Sub-lattice magnetizations in an fcc lattice can be defined as

$$m_v = (1/N)\sum_{i\in v}\langle S_i\rangle \quad v = 1,2,3,4 \tag{2.3.42}$$

where the average is computed over time over one or more MC runs. Order parameter components for AB structure are expressed in terms of m_v as:

$$\begin{aligned} &\breve{m}_{AB}^{(1)} = m_1 + m_2 - m_3 - m_4; \quad \breve{m}_{AB}^{(2)} = m_1 - m_2 - m_3 + m_4; \\ &\breve{m}_{AB}^{(3)} = m_1 - m_2 + m_3 - m_4 \end{aligned} \tag{2.3.43}$$

These m_{AB} will reach a value of 1 in the AB phase and go toward zero otherwise. The order parameter components for A_3B ordering can similarly be defined as

$$\breve{m}_{A_3B}^{(1)} = m_1 + m_2 + m_3 - m_4 \tag{2.3.44}$$

The total concentration can be written in terms of average magnetization m as

$$m = m_1 + m_2 + m_3 + m_4 \tag{2.3.45}$$

$$c_B = (1 - m)/2 \tag{2.3.46}$$

These order parameters can also be related to the long-range order parameter ψ as

$$\Psi = \left(\breve{m} - m\right)/(1 - m) \tag{2.3.47}$$

and short range order parameter $g(R)$ as

$$g(R) = \langle S_i S_{i+R}\rangle - m^2 \tag{2.3.48}$$

During investigations on Fe–C phase diagram simulating the saturation solubility of carbon in molten iron at high temperatures, Khanna and Sahajwalla [122] used a hexagonal close packed structure with carbon and iron atoms distributed randomly on the rigid lattice; a different set of order parameters were defined. It should be noted that the choice of order parameters is not unique and these could be designed carefully as dictated by the system under investigation.

When the transitions from the ordered phase to disorder are of first order, attention needs to be paid to the occurrence of metastable states and hysteresis; there could be significant differences between the location of the phase transition and regimes where the lifetime of metastable states becomes quite small due to the nucleation and growth of second phase. It is also much more difficult to create order from disorder than other way round; metastable effects can be quite significant. It is therefore very important to approach transition from both sides for accurately locating a phase transition. Simulations can be performed both in canonical and grand-canonical ensemble. Another issue near phase transitions is that of "broken ergodicity." Ergodicity requires that any one configuration of a Markov chain during computer simulation be accessible from any other configuration via a finite number of steps [124]. Broken ergodicity is expected

to occur near a phase transition and may itself be an indicator of the change occurring. This is due to difference in simulation (or observation) time scales τ_{ob} becoming much slower than the time scales of relaxation in the system; the simulation experiment then will not represent a true canonical equilibrium.

2.3.4.5. Diffusion

Diffusion is caused by molecular/atomic motion in fluids to smooth out nonuniform concentration distributions. According to Fick's law:

$$j = -D\nabla c \tag{2.3.49}$$

where j is the flux of diffusing species proportional to the gradient of concentration "c" with diffusion constant "D" as the constant of proportionality. The time evolution of the concentration profile can be written as

$$\frac{\partial c(r,t)}{\partial t} + \nabla\cdot(r,t) = 0 \tag{2.3.50}$$

A solution of Equation (2.3.50) for boundary condition: $c(r, 0) = \delta(r)$, where $\delta(r)$ is Dirac delta function, can be written as

$$c(r,t) = \frac{1}{(4\pi Dt)^{1/2}} \exp\left(-\frac{r^2}{4Dt}\right) \tag{2.3.51}$$

Based on a derivation by Einstein, macroscopic diffusion (transport) constant "D" can be written in terms of mean squared distance over which molecular species have moved over time τ:

$$\frac{\partial\langle r^2(t)\rangle}{\partial t} = 2dD \tag{2.3.52}$$

where "d" is the dimensionality of the system. Alternatively, a correlation has also been developed between the diffusion coefficient and velocity autocorrelation function (known as Green–Kubo relation):

$$D = \int_0^\infty \mathrm{d}\tau\langle v_x(\tau)v_x(0)\rangle \tag{2.3.53}$$

Both these equations can be used to compute diffusion coefficients. In addition to predicting diffusion coefficients, atomistic simulation can provide insights into atomic mechanisms and design strategies for control of diffusion rates.

Self-diffusion in metals is known to be mediated by the migration of point defects [125]; the diffusion coefficient can be written as

$$D = a^2 f \gamma \nu x_e^d \exp\left(-\frac{G_m^d}{KT}\right) \tag{2.3.54}$$

where "a" is the jump length, γ a geometrical factor, f a jump correlation factor, ν the jump frequency, x_e^d the defect concentration, and G_m^d the free energy associated with defect migration. Self-diffusion in fcc metals is generally controlled by vacancy mechanism as the self-interstitial formation energy is much larger than the vacancy formation energy. This however may not be the case for bcc metals and these two energies could be quite comparable. Temperature dependence of various parameters and anharmonicity of lattice vibrations can further complicate the issue. Another issue of concern is that lattice diffusion in solids is generally quite slow and is much beyond the time scales accessible by MD simulations. The jump rates of point defects are very slow compared to corresponding rates at grain boundaries/free surfaces. Secondly, the point defect concentrations are generally kept quite low to avoid their probable clustering during very long simulations times and cell sizes are generally required for generating good statistics. Mendelev and Mishkin [126] used a block of 2000 (N) atoms with periodic boundary conditions, introduced a single defect and performed a 20,000 step MD run to equilibrate the system; these were then followed by 2,900,000 MD steps to compute the average energy E_d. A similar calculation was carried out on a block without defects and an energy E_p of the system was computed. The point-defect formation energy was computed as:

$$E_f = E_d - E_p N_d / N \tag{2.3.55}$$

where $N_d = N - 1$ for a vacancy and $N + 1$ for an interstitial.

Alternatively, nonequilibrium molecular dynamics (NEMD) methods are used to compute transport properties [127]; the simulated system is perturbed away from equilibrium and the subsequent response of the system is measured. The perturbation can be either steady state or transient and can be implemented as a boundary condition or an external field or as a nonuniform initial condition. KMC methods are also being used extensively to investigate slow atomic level transport; Paschek and Krishna [128] have applied KMC simulations to investigate the diffusion of binary mixtures in Zeolites. A Languir-type system was used that contained a lattice of equal sites that were occupied by only one molecule at a given time. Particles can hop from one site to another, with the transition probability chosen to reproduce published experimental as well as MD simulation data [129,130]. A hop is made every KMC step and the system clock is updated with variable time steps. A process list containing all possible moves is created with the transition probability depending on the type of move as well as particle type. The rate constant is inversely proportional to the elapsed time and is correlated with diffusivity in the system.

2.3.5. ATOMISTIC INTERACTION POTENTIALS

2.3.5.1. Fundamentals

2.3.5.1.1 Beyond Pair Potentials

To develop a fundamental understanding of materials and to make accurate predictions of their properties, structure and defects, an accurate description of atomic interactions is of utmost importance. Best existing approaches for atomic interactions in the condensed phase are based on quantum mechanics; these are however computationally very expensive and limited to systems of few hundred atoms. For problems that involve large systems or require statistical averages, quantum mechanical calculations are presently not feasible. One solution to the problem is to construct empirical potential functions as an explicit function of a set of particle co-ordinates; then one can perform realistic calculations of the properties of quite large systems. The correspondence between the physical system and the simulation model depends to a great extent on the nature of potential energy function. A real-space description of bonding energetics can be obtained by integrating out a number of degrees of freedom to achieve effective potentials that represent basics more clearly than the complete set of all interactions [131].

In ionic crystals, the attractive coulomb interactions between separated ions is counterbalanced by short-ranged repulsive interactions described either by pair potentials or by density-based theories [132,133]. In rare gases, the dominant attractive term comes from van der Waal's fluctuating dipole interaction [134]. Metallic atoms can be represented as closely packed hard balls with relatively weak attractive forces. For simple metals, uniform electron gas forms the basis for electron–ion pseudo-potentials for perturbative power expansions [135]. For transition metals, while radial forces are consistent with close-packed structures, additional angular forces are required to reproduce advanced features such as energy differences between various structures. In semiconductors, focus is generally on strong covalent bonds with charge accumulation and localization between the atoms. In a system containing N atoms, the potential energy can generally be written as a sum of *n*-body interatomic potentials depending on the co-ordinates of individual atoms [136]:

$$\Phi = \sum_i \phi_i(r_i) + \sum_i \sum_{j>i} \phi_{ij}(r_i, r_j) + \sum_i \sum_{j>i} \sum_{k>j>i} \phi_{ijk}(r_i, r_j, r_k) + \ldots \qquad (2.3.56)$$

The summation notation indicates summation over all distinct pairs without counting any pair twice in pair potentials or in multi-body interactions. The potentials and number of terms retained depend on the nature of system under investigation. The first term represents the effect of external fields including the influence of simulation cell geometry and container walls, etc. [137]. The second term, Φ_{ij}, the pair potential is one of the most important terms in the potential energy and depends only on the magnitude of

pair-separation r_{ij}. Pair potentials can quite adequately describe rare gases and ionic systems [138]. The 6–12 Lennard–Jones potential for rare gases can be represented as:

$$V(r) = 4\varepsilon\left[\left(\frac{\sigma}{r}\right)^{12} - \left(\frac{\sigma}{r}\right)^{6}\right] \tag{2.3.57}$$

When parameters ε and σ are chosen appropriately, the potential $V(r)$ represents a negative well of depth ε, an attractive long-range tail and a steeply rising repulsive wall for distances less than σ. We refer to Allen and Tildeseley's [139] book for further details and potential parameters for a number of systems. For systems characterized by covalent bonding such as Group IV elements carbon, silicon and other semiconductors, one needs to go beyond pair-potentials due to the directionality of charge localization in the bonding region. Using three-body terms, Stillinger and Weber [140] developed a potential for Si with a following form:

$$\Phi_{ij}\left(r_{ij}\right) = A\left[B{\cdot}r_{ij}^{-P} - 1\right]g_{\beta}\left(r_{ij}\right) \tag{2.3.58.1}$$

$$\Phi_{ijk} = U_{jik} + U_{ijk} + U_{ikj} \tag{2.3.58.2}$$

$$g_{\beta} = \exp\left[\frac{\beta}{r-a}\right] \tag{2.3.58.3}$$

$$U_{ijk} = \lambda{\cdot}g_{\beta}(r)\left[\cos\theta_{jik} + 1/3\right]^{2} \tag{2.3.58.4}$$

The parameters of the potential were determined through empirical fits to properties of silicon in crystalline and liquid phases.

For describing the energetics of transition metals, pair potentials have been used extensively to simulate defects such as dislocations, grain boundaries and cracks, and to generate qualitative information regarding the possible local configurations of atoms. It is well-known that cohesive energy of metals contains volume/density-dependent contributions [141]; unless elastic constants in a cubic crystal satisfy the Cauchy relation for elastic constants: $C_{12} = C_{44}$ (seldom the case in real metals), an equilibrium pair potential model cannot reproduce them. It is customary to add a volume-dependent term in the total energy by analogy with perturbation theory [142]. Alternatively, a description of metallic systems is provided by effective medium theory (EMT) [143] or the embedded atom method (EAM) [144], wherein the effect of surrounding atoms is described in terms of average electron density or the embedment of an atom in a homogeneous electron gas.

2.3.5.1.2 Development of Interatomic Potentials/Parameters

Most large-scale atomistic simulations over extended periods of time are performed using empirical or semi-empirical descriptions of interaction potentials as a compromise between computational efficiency, accuracy and generality [145]. Empirical potentials

are obtained by fitting a proposed functional form to available experimental and first-principles theoretical data [146]. Generally, the data may include lattice parameter, cohesive energy, elastic constants, melting point, and vacancy formation energy. Using data from perfect crystals and highly symmetric configurations, application of these potentials has several disadvantages when used to the study defects, high temperature properties and liquids. Approaches have been developed that fit potentials to properties sensitive to a range of atomic separations such as liquid structure factor and formation energies of self-interstitials [147]. A brief description of various approaches is detailed below.

First step in developing a potential requires fundamental details regarding the system under investigation. For molecules, the essential features of intermolecular interaction would require an anisotropic repulsive core to represent the shape, an anisotropic dispersion interaction and partial charges to model electrostatic effects. Short-range site–site interactions can be modeled using Lennard–Jones potential (Equation 2.3.2); the energy parameter ε increases with atomic number due to increasing polarizability and σ also increases down a group of the periodic table but increases across a period with increasing atomic number. Atom–atom interaction parameters of a range of materials have been reported in literature [148–150]. Large molecules are often represented as a single unified site for sake of computations [151]. An angle-dependent term is always included to represent the directionality of covalent bonds. For metals, a volume-dependent term representing band energy is added to the pair potential. For example, in an empirical approach developed by Finnis and Sinclair, a term based on a function of ρ_i is added to the potential [152]. ρ_i is a measure of local density of atomic sites or alternatively it represents the local electronic charge density at site i constructed by a rigid superposition of individual atomic charge densities. The energy of the atom is then approximately the same as if it were in a uniform density of electron gas at that density; a concept very similar to the basic definition of a metallic bond as representing an array of ions embedded in a sea of electrons.

In the second step, the potential is used to calculate a number of properties of the system; comparison of simulation results with experiment is then used to refine the potential, and the cycle is repeated several times till an optimal potential is achieved. A wide range of properties are used in the fitting procedure based on the application. With focus on perfect crystals, thermodynamic data, cohesive energy, lattice constants, phase transitions, elastic constants and vacancy formation energy are some of the typical results used. For the study of defects such as interstitials, dislocations, grain boundaries and dynamic phenomena such as melting, additional properties such as self-interstitial formation energy and liquid structure factor are used. An approach used statistical mechanical correlation between the parameters of interatomic potential and liquid diffraction data [153]; another used fits to atomic forces obtained from first principle calculations in a proposed liquid structure [146].

As an alternative approach, a large number of atomistic MC investigations in binary systems have been carried out using a rigid lattice framework, wherein atoms can only

move from site to site and a continuous variation of interatomic distances is not allowed. Using an Ising lattice gas model, Binder *et al.* investigated the ordering behavior of Cu–Au alloys on a rigid fcc lattice (*AB*) using pair-wise interactions [154]. Khanna and Sahajwalla used a rigid lattice approach to investigate the saturation solubility of carbon in molten iron at high temperatures [155]. These studies were further extended to investigate the retarding influence of sulfur on carbon dissolution and a set of optimum interaction parameters were obtained for Fe–C–S system [156]. Biborski *et al.* used a ternary bcc lattice gas model to investigate the ordering of vacancies in Ni–Al intermetallics [157].

2.3.5.2. Interaction Potentials for Iron

Because of their importance in steelmaking, magnetism and processes taking place in earth's core, iron and its alloys have been investigated extensively. A large number of interatomic potentials have been reported; these will be critically reviewed and their limitations identified. Pair potentials have been used extensively for generating qualitative information such as local atomic configuration around defects, etc.; but this approach is not really appropriate for metals. Potentials developed by Johnson [158], and Osetsky *et al.* [159] are purely pair-wise and cannot adequately describe the defect and elastic properties of metallic Fe. Modeling of Fe is a tough challenge; iron exhibits a phase transition between bcc α-iron and fcc γ-iron at $T_c = 1184$ K, and a transition back to the bcc phase δ-iron at 1665 K before melting [160]. The contribution of ferromagnetic energy to the total energy stabilizes α-iron at low temperatures over γ-iron; the degrees of freedom of magnetic spins make decisive contributions to the entropies of various phases affecting various transitions, while the vibrational contributions play a secondary role [161]. A wide variety of potentials have been used to model iron in various structural forms. Some of the well-known potentials for iron are presented below; the list however is not exhaustive due to the large number of iron potentials and their variants reported in the literature. For ease of cross-referencing and application, original terminology/nomenclature has been retained for various potentials reported below; parameters such as *U*, *V*, and *E* have been used to represent energy/potential.

2.3.5.2.1 Finnis–Sinclair Potential

Finnis and Sinclair developed a multi-ion interaction potential in an attempt to overcome some of the difficulties associated with modeling interactions in transition metals [152]. For computing the energy of transition metals, a volume-dependent term is generally added as a perturbation to pair potentials, and elastic constants adjusted arbitrarily to supply fictitious external pressure to balance Cauchy pressure, $0.5(C_{12} - C_{44})$ [141]. Unless the volume-dependent term is linear in volume, this addition leads to discrepancies in the computation of bulk modulus. The application of special surface forces is also not

desirable while simulating internal cavities or cracks within a metal. Secondly, if the model accepts the absence of surface forces (with $C_{12} = C_{44}$), the vacancy formation energy is found to be approximately equal to the cohesive energy; experimentally it is about one-third [162]. Using a simple model, Finnis and Sinclair attempted to incorporate the essential band character of metallic cohesion to central pair-potential models. In the tight-binding model, cohesive energy per atom varies as $\sqrt{z}$, where z is the atomic co-ordination number that can range from one (diatomic molecule) to about 12 for fcc crystals [163]. In the Finnis–Sinclair model, the total energy of an assembly of atoms at positions R_i is written as

$$U_{\text{tot}} = U_n + U_p \tag{2.3.59.1}$$

where U_n is the n-body term that can be empirically written as a sum over all atoms of a "cohesive function"

$$U_n = -A\sum_i f(\rho_i) \tag{2.3.59.2}$$

where $\rho_i = \sum_j \varphi(R_{ij})$—with R_{ij} representing interatomic separation between atoms at sites "i" and "j." The function $f(\rho)$ was chosen to be of the form $\sqrt{\rho}$ to mimic the tight-binding theory and function φ as a sum of overlap integrals [164]. The cohesive function φ was assumed to have a parabolic form

$$\varphi(r) = (r-d)^2 \text{ for } r \le d; \text{ and } \varphi(r) = 0 \text{ for } r > d \tag{2.3.59.3}$$

The range "d" is a disposable parameter assumed to lie between the second and third neighbors.

U_n represents the band energy that is cohesive in nature. The U_p is the repulsive core–core interaction and can be written as

$$U_p = \frac{1}{2}\sum_{ij} V(R_{ij}) \tag{2.3.59.4}$$

A quadratic polynomial was used to represent the pair potential $V(r)$

$$V(r) = (r-c)^2\left(C_0 + C_1 r + C_2 r^2\right) \text{ for } r \le c; \text{ and } V(r) = 0 \text{ for } r > c \tag{2.3.59.5}$$

The range "c" is assumed to lie between the second and third neighbors. For iron, Equation (2.3.59.3) was modified to account for its anomalously low Cauchy pressure as

$$\varphi(r) = (r-d)^2 + \beta(r-d)^3/d \tag{2.3.59.6}$$

Cohesive energy and elastic constants of bcc iron were used to fit the potential and to determine optimal parameters. In the case of iron, these were determined to be: $d = 3.699579$ Å; $A = 1.889846$ eV; $\beta = 1.8$; $c = 3.4$ Å; $c_0 = 1.2110601$,

$c_1 = -0.7510840$ and $c_2 = 0.1380773$. This potential was considered to be too short-ranged to distinguish between fcc and hcp structures, for which an extension of the model was envisaged to the third-neighbor distance in those structures.

2.3.5.2.2 Embedded-Atom Method

The embedded-atom method (EAM) is a semi-empirical approach for computing the energy of an arbitrary configuration of atoms. In this method, the energy is modeled as having two contributions: the energy to embed an atom in the local electron density provided by the rest of the atoms and an electrostatic interaction by pair potentials [165]. The energy can be written as

$$E_{\text{tot}} = \sum_i F_i(\rho_i) + \frac{1}{2}\sum_{i,j,i\neq j} \varphi_{ij}(R_{ij}) \tag{2.3.60.1}$$

ρ_i represents the electron density at site "i," $\rho_i = \sum_{j\neq i}\rho_j^{\alpha}(R_{ij})$ where $\rho_j(R)$ is the electron density of atom "j" at a distance "R" from its nucleus. The embedding function "F" and pair interactions are determined through fits to the zero-temperature equation of state, the elastic constants and the vacancy formation energies. The requirement regarding the equation of state introduces information about the anharmonicity of the interactions into the potentials. Different basis functions including cubic splines, exponentials, and polynomials have been used in the literature [164]. It is important to note that the Finnis–Sinclair and EAM potentials are essentially identical for single component systems. However these differ in the form of the embedding function used; Finnis–Sinclair used a square root function and a general function was used in EAM potentials. Mendelev *et al.* [164] developed interatomic potentials appropriate for crystalline and liquid iron utilizing a range of fitting procedures including fits to perfect crystal data, interstitial data, and liquid data. The general form of pair-wise potentials is given by:

$$\begin{aligned}
\phi(r) &= \frac{Z^2 q_e^2}{r}\Phi\left(\frac{r}{rs}\right) \text{ for } r < r_1 \\
\phi(r) &= \exp^{(B_0 + B_1 r + B_2 r^2 + B_3 r^3)} \text{ for } r_1 < r < r_2 \\
\phi(r) &= \sum_{k=1}^{n^{\varphi}} a_k^{\varphi}\left(r_k^{\varphi} - r\right)^3 \theta\left(r_k^{\varphi} - r\right) \text{ for } r > r_2
\end{aligned} \tag{2.3.60.2}$$

where Z is the atomic number, q_e is the charge on an electron, $\theta(x)$ is the Heaviside step function, and r_B the Bohr radius. Other functions are defined as follows:

$$r_s = 0.88534\frac{r_B}{2^{1/2} z^{1/3}} \tag{2.3.60.3}$$

$$\phi(x) = 0.1818\exp^{(-3.2x)} + 0.5099\exp^{(-0.9423x)} + 0.2802\exp^{(-0.4029x)} + 0.02817\exp^{(-0.2016x)} \quad (2.3.60.4)$$

The embedding energy is given by

$$\Phi(\rho) = -\rho^{-1/2} + a^{\Phi}\rho^2 \quad (2.3.60.5)$$

Various parameters used for the EAM potential for Fe can be found in the reference [166]. A number of variants EAM potentials and modified EAM potentials have also been developed for a range of materials [167,168].

2.3.5.2.3 Analytic Bond-Order Potential

Muller *et al*. [169] have reported on an angle-dependent bond-order potential for bcc and fcc iron based on experimental data and results from first principle calculations. The key idea of their approach was to mimic the Gibbs free energy difference between the bcc phase and the fcc phase by lattice energy and phonon contributions. This potential attempts to counterbalance the missing electronic degrees of freedom. The total energy is written as a sum over individual bond energies:

$$E = \sum_{i<j} f_{ij}^{c}(r_{ij})\left[V_{ij}^{R}(r_{ij}) - \frac{b_{ij}+b_{ji}}{2}V_{ij}^{A}(r_{ij})\right] \quad (2.3.61.1)$$

The pair-wise repulsive and attractive terms are taken as Morse-like potentials:

$$V^{R}(r) = \frac{D_0}{S-1}\exp\left(-\beta\sqrt{2S}(r-r_0)\right)$$
$$V^{A}(r) = \frac{SD_0}{S-1}\exp\left(-\beta\sqrt{2/S}(r-r_0)\right) \quad (2.3.61.2)$$

Here, S is an adjustable parameter, D_0 the dimer bond energy and r_0 the dimer bond strength, β determined from the ground state oscillation frequency. The interaction range is determined by the cut-off function:

$$f^{c}(r) = \begin{cases} 1 & r \le R - D \\ \frac{1}{2} - \frac{1}{2}\sin\left(\frac{\pi}{2}(r-R)/D\right) & |R-r| \le D \\ 0 & r \ge R + D \end{cases} \quad (2.3.61.3)$$

where R and D are adjustable parameters. Three-body interactions and angularity enter via the bond-order parameter b_{ij}:

$$b_{ij} = \left(1+\chi_{ij}\right)^{-1/2} \quad (2.3.61.4)$$

$$\chi_{ij} = \sum_{k \neq i,j} f_{ik}^{c}(r_{ik}) g_{ik}(\theta_{ijk}) \exp\left(2\mu_{ik}(r_{ij} - r_{ik})\right) \tag{2.3.61.5}$$

$$g(\theta) = \gamma\left(1 + \frac{c^2}{d^2} - \frac{c^2}{d^2 + [h + \cos(\theta)]^2}\right) \tag{2.3.61.6}$$

The parameter set of the analytic bond-order potential for iron was determined to be: $D_0 = 1.5$ eV, $r_0 = 2.29$ Å, $\beta = 1.4$ Å^{-1}, $S = 2.0693109$, $\gamma = 0.0115751$, $c = 1.2898716$, $d = 0.3413219$, $h = -0.26$, $\mu = 0.0$, $R = 3.15$ Å and $D = 0.2$ Å.

2.3.5.2.4 Models for Simulations on Liquid iron in the Earth's Outer Core: Sutton–Chen Potentials

The Earth's core consists of a solid inner core and a liquid outer core consisting mainly of iron [170,171]. Koci *et al.* carried out MD simulations to study the properties of liquid iron under high pressure–high temperature conditions of earth's outer core [172]. They used Sutton–Chen model for interaction potential for liquid iron that is quite similar to the Finnis–Sinclair model [152]. The model can be written as:

$$E_{\text{tot}} = \frac{1}{2}\sum_{i=1}^{N}\sum_{j=1, j\neq i}^{N} \Phi(r_{ij}) + F(\rho_i) \tag{2.3.62.1}$$

where E_{tot} is the total energy of the system, $\Phi(r_{ij})$ represents the interaction between atoms i and j at a distance r_{ij}, $F(\rho)$ is the embedding function, where the density term is given by

$$\rho_i = \sum_{j=1, j\neq i}^{n} \rho(r_{ij}) \tag{2.3.62.2}$$

Other terms in Equation (2.3.62.1) are represented by

$$\begin{aligned} \Phi(r_{ij}) &= \varepsilon\left(\frac{a}{r_{in}}\right)^n \\ \rho(r_{ij}) &= \left(\frac{a}{r_{ij}}\right)^m \\ F(\rho_i) &= -\varepsilon C\sum_{i=1}^{N}\sqrt{\rho_i} \end{aligned} \tag{2.3.62.3}$$

The potential was fitted to energy–volume data [172]. The parameters showing the best fit were: $\varepsilon = 0.017306$ eV, $a = 3.471392$ Å, $n = 8.137381$, $m = 4.7877$, $C = 24.9390$ [173].

2.3.5.3. Interaction Potentials for Other Metals

2.3.5.3.1 Finnis–Sinclair Potentials for Transition Metals

In addition to the interatomic potential for iron, Finnis and Sinclair [152] have also constructed potentials for a number of transition metals. Fitting parameters for a range of metals for the set of equations (Equations 2.3.59.1–2.3.59.6) are given below in Table 2.3.1.

2.3.5.3.2 Modified Embedded-Atom Method Potentials for Cubic Materials and Impurities

In a compressive study, Baskes [168] extended the modified embedded-atom method (MEAM) to 26 elements including ten fcc, ten bcc, three diamond cubic, and three gaseous materials. The materials modeled included metals (Cu, Ag, Au, Ni, Pd, Pt, Al, Pb, Rh, Ir, Li, Na, K, V, Nb, Ta, Cr, Mo, W, Fe), semiconductors (C, Si, Ge), and gases (H, N, O). The key ingredient for all these potentials with a wide variety of bonding arrangements is the common attribute that the interaction between two atoms depends on their local environment. Properties of these materials, including elastic moduli, equation of state, structural energies, lattice constants, defects, and surface behavior were computed. Reader is referred to the original manuscript for further details and list of parameters sets.

2.3.5.3.3 EAM Potentials for Liquid Transition Metals

Foiles [173] applied the EAM method developed by Daw and Baskes [145,174] to describe liquid transition metals. For the determination of embedding functions and the pair potentials, generally information regarding small deviations from the equilibrium solid is used. These may not be able to describe liquids that are qualitatively different from solids in this regard. The motion of atoms in a liquid can bring atoms much closer than the equilibrium distances in a solid. Foiles used the pair-correlation function as a sensitive test for computations at distances less than nearest neighbor distance in the solid. The parameter set for six liquid transition metals (Ni, Pd, Pt, Cu, Ag, and Au) were given in this paper.

Table 2.3.1 Finnis–Sinclair potential parameters for a number of transition metals

Parameters	d (Å)	A (eV)	β	c (Å)	c_0	c_1	c_2
Vanadium	3.692767	2.010637	0	3.8	−0.8816318	1.4907756	−0.397637
Niobium	3.915354	3.013789	0	4.2	−1.5640104	2.0055779	−0.4663764
Tantalum	4.076980	2.591061	0	4.2	1.2157373	0.0271471	−0.1217350
Chromium	3.915720	1.453418	1.8	2.9	29.1429813	−23.397503	4.7578297
Molybdenum	4.114825	1.887117	0	3.25	43.4475218	−31.933298	6.0804249
Tungsten	4.400224	1.896373	0	3.25	47.1346499	−33.766566	6.2541999

Table 2.3.2 Parameters for Sutton–Chen potentials

Parameters	*m*, *n*	ε (K)	C_ε (K)	*a* (Å)	U_c (10^3 K)
Aluminum	7, 6	384.5	7307.9	4.05	38.08
Platinum	10, 8	230.14	7919	3.92	66.3
Gold	10, 8	148.44	5107.7	4.08	42.76
Lead	10, 7	64.44	2949.7	4.95	23.41
Nickel	9, 6	180.29	7187	3.52	50.48
Copper	9, 6	143.644	5663.4	3.61	39.78
Palladium	12, 7	48.49	5250.5	3.89	45.43
Silver	12, 6	29.50	4260.0	4.09	33.73

2.3.5.3.4 Sutton–Chen Potentials

Todd and Linden-Bell [175] have developed potentials based on Sutton–Chen formalism and have reported on parameters for a range of metals. These are given in Table 2.3.2.

2.3.5.3.5 Interatomic Potentials from First-Principles Calculations

Ercolessi and Adams [176] developed a novel scheme, "the force matching method," to extract numerically optimal interatomic potentials from the data produced by first-principal calculations. The potential was obtained by fitting *ab initio* forces for a range of configurations including clusters, liquids, surfaces, and solids at high temperatures. A *glue* potential was developed for aluminum. Mishin *et al.* [177] extended this approach to Ni as well. The potential developed in this model has a formalism that is quite similar to the EAM approach. The embedding energy is a function of the host electron density; a basis set of cubic splines was used to model electron density. A rescaling of interatomic distances was used in an attempt to improve the compatibility between *ab initio* and experimental data used in the fitting procedure. The potentials developed accurately replaced basic equilibrium properties, elastic constants, phonon dispersion curves, the relative stability of alternative crystal structures, the stacking fault energies, and the surface energies.

2.3.5.4. Interaction Potentials for Covalently Bonded Group IV Elements

A general feature of physically reasonable atomic pair potentials is that they favor the formation of close-packed structures, so they are unsuitable for describing covalent systems that assume more open structures. In the formulation of interatomic potentials for covalent systems, it has been recognized that the strength of each bond (bond order) depends on the local environment [178,179]. An atom with many neighbors forms weaker bonds than an atom with fewer neighbors; this dependence of bond strength appears to stabilize low co-ordination number structures. Multi-body interaction potentials for Si and C are detailed below:

2.3.5.4.1 Silicon

Silicon is one of the most investigated materials due to its technological importance. Regarded as a prototype covalent solid, silicon presents significant modeling challenges as it has a number of polymorphs with qualitatively different bonding but similar cohesive energies. A covalent material presents a difficult challenge as quantum-mechanical effects such as chemical bond formation, hybridization, charge transfer, bond bending, bond breaking, etc., need to be described by an effective interaction between atoms wherein electronic degrees of freedom have somehow been integrated out. More than 40 potentials have been reported for Si; we present below three of the most commonly used Silicon potentials.

2.3.5.4.1.1 Stillinger and Weber Potential

Any potential energy function describing interactions between N identical particles can be resolved into one-body, two-body, three-body, etc., contributions (Equation 2.3.1), with the proviso that component functions v_n converge quickly to zero with increasing n. With Silicon crystal being held together with strong and directional bonds, Stillinger and Weber (SW) proposed a potential model in terms of only pair and triplet potentials [180]

$$\begin{aligned} v_2 &= \varepsilon f_2\left(r_{ij}/\sigma\right) \\ v_3\left(r_i,r_j,r_k\right) &= \varepsilon f_3\left(r_i/\sigma, r_j/\sigma, r_k/\sigma\right) \end{aligned} \tag{2.3.63.1}$$

where ε, the energy unit, was chosen to give f_2 a depth of -1, length unit σ is chosen to make $f_2(2^{1/6})$ go to zero. While the function f_2 depends on the scalar distance r_{ij}, the function f_3 possesses full translational and rotational symmetry. These functions had the following form:

$$f_2(r) = \left\{A\left(Br^{-p} - r^{-q}\right)\exp\left[(r-a)^{-1}\right]\right\}, \quad r < a \quad = 0, \quad r \geq a \tag{2.3.63.2}$$

where A, B, p and a are positive with potential and its derivatives automatically cut-off at $r = a$. Extending the same cut-off to three-body interactions, f_3 can be written as

$$f_3\left(r_i,r_j,r_k\right) = h\left(r_{ij},r_{ik},\theta_{jik}\right) + h\left(r_{ji},r_{jk},\theta_{ijk}\right) + h\left(r_{ki},r_{kj},\theta_{ikj}\right) \tag{2.3.63.3}$$

where θ_{jik} is the angle between vectors r_j and r_k subtended at vertex "i." Function "h" has the following form for interatomic distances less than the cut-off distance "a."

$$h\left(r_{ij},r_{ik},\theta_{jik}\right) = \lambda\exp\left[\gamma\left(r_{ij}-a\right)^{-1} + \gamma(r_{ik}-a)^{-1}\right]\cos\left(\theta_{jik} + \frac{1}{3}\right)^2 \tag{2.3.63.4}$$

Otherwise h goes to zero. Most satisfactory parameter set for this potential was determined to be: $A = 7.049556277$, $B = 0.6022245584$, $p = 4$, $q = 0$, $a = 1.8$, $\lambda = 21.0$, $\gamma = 1.20$.

The SW potential captures the directed nature of sp^3 bonds in a simple manner selecting diamond lattice over close-packed structures. This potential provides reasonable description of many experimentally relevant states such as point defects, surface structures, amorphous and liquid states, and is a favorite choice in the literature due to its simplicity [181,182].

2.3.5.4.1.2 Tersoff Potential

A number of approaches using three-body interactions were not successful in describing the wide range of bonding geometries in silicon [183,184]. Tersoff used an alternative approach based on the bond strength (order) being dependent on the co-ordination number, that is, the numbers of neighbors close enough to make bonds [185]. Bond strength decreasing rapidly with co-ordination number will correspond to diatomic molecules as being the most stable structure (top RHS of periodic table); alternatively if the bond strength depends weakly on the co-ordination number, it will correspond to close-packed structures to maximize the number of bonds being formed (a typically metallic behavior at the lower left end of periodic table). This trend suggests that bond order could be a monotonic decreasing function of co-ordination with both aspects playing crucial roles. In the middle of the periodic table, these two effects need to be delicately balanced to get intermediate co-ordination. Silicon can assume a large number of polymorphic structures with modest changes of pressure; the differences in cohesive energies of various phases are generally quite small [184]. An interatomic potential developed by Tersoff has the following form [185]:

$$E = \sum_i E_i = \sum_{i \neq j} f_c(r_{ij}) \left[a_{ij} f_R(r_{ij}) + b_{ij} f_A(r_{ij}) \right] \tag{2.3.64.1}$$

The total energy E of the system is decomposed into site energies E_i's; the function f_R represents a repulsive pair potential of the form: $f_R = A \exp(-\lambda_1 r)$; and f_A represents an attractive pair potential associated with bonding: $f_A = -B \exp(-\lambda_2 r)$. The extra term f_c represents a smooth potential cut-off to limit the range of the potential and has a form similar to that given in Equation (2.3.61.3). Following definitions were used for various functions in the potential:

$$\begin{aligned} a_{ij} &= \left(1 + \alpha^n \eta_{in}^n\right)^{-1/2n} \\ n_{ij} &= \sum_{k \neq i,j} f_c(r_{ik}) \exp\left(\lambda_3^3 (r_{ij} - r_{ik})^3\right) \end{aligned} \tag{2.3.64.2}$$

With α being sufficiently small, "a" is approximately 1 unless η is exponentially large. The form proposed for b_{ij} is

$$b_{ij} = \left(1 + \beta^n \chi_{ij}\right)^{-1/2n} \tag{2.3.64.3}$$

$$\chi_{ij} = \sum_{k \neq i,j} f_c(r_{ik}) g_{ik}(\theta_{ijk}) \exp\left(\lambda_3^3 (r_{ij} - r_{ik})^3\right) \tag{2.3.64.4}$$

$$g(\theta) = \left(1 + \frac{c^2}{d^2} - \frac{c^2}{d^2 + [h + \cos(\theta)]^2}\right) \tag{2.3.64.5}$$

Various optimal parameters for silicon were reported as: $A = 3264.7$ eV, $B = 95.373$ eV, $\lambda_1 = 3.2394$ Å^{-1}, $\lambda_2 = 1.3258$ Å^{-1}, $\lambda_3 = \lambda_2$, $\alpha = 0$, $\beta = 0.3375$, $n = 22.956$, $c = 4.4381$, $d = 2.0417$, $h = 0.0$, $R = 3$ Å, $D = 0.2$ Å. Tersoff [185] further optimized various parameters of the interaction potential reported above to more accurately produce the elastic properties of silicon and properties of liquid Si; however these modifications reduced the accuracy of surface energies. New parameters were determined to be: $A = 1830.8$ eV, $B = 471.18$ eV, $\lambda_1 = 2.4799$ Å^{-1}, $\lambda_2 = 1.7322$ Å^{-1}, $\lambda_3 = \lambda_2$, $\alpha = 0$, $\beta = 1.099 \times 10^{-6}$, $n = 0.78734$, $c = 1.0039 \times 10^5$, $d = 16.218$, $h = -0.59826$, $R = 2.85$ Å, $D = 0.15$ Å.

2.3.5.4.1.3 Other Potentials

In recent years, more than 30 empirical potentials have been developed for silicon and were recently compared to each other [186]. A natural strategy to improve on the SW and Tersoff's potentials is to replace with more complex forms with even more elaborate fitting procedures. The Bolding–Anderson model [187] generalized the Tersoff format with over 30 adjustable parameters to simultaneously describe bulk phase, defects, surfaces, and small clusters. Justo *et al.* [188] developed an empirical potential that showed significant improvement in describing local bonding for bulk defects and disordered phases. Lee [189] has developed a MEAM potential to describe elastic, structural, point defect, surface, thermal and cluster properties of silicon, aiming to apply these formalisms to multi-component materials and not be restricted to diamond-structured materials.

2.3.5.4.2 Carbon

Carbon has a special place among the elements; its uniquely strong bonds and high melting point make it a technological important material. Carbon is also one of the most important alloying elements in steel; a number of different properties have been attributed to strong interactions between interstitial carbon atoms and defects such as vacancies, dislocations and grain boundaries. Some of the most commonly used potentials for carbon are described below:

2.3.5.4.2.1 Tersoff Potential

This empirical potential for carbon has a form similar to the Tersoff potential for silicon (Equations 2.3.64.1–2.3.64.5). The parameters of this potential [190] were chosen

primarily by fitting the cohesive energies of carbon poly-types along with the lattice constant and bulk modulus of diamond. This potential gives a relatively accurate description of the structural properties and energetics of elastic properties, phonons, defects, migration barriers in graphite and diamond. The parameter set for carbon is as follows: $A=1393.6$ eV, $B=346.74$ eV, $\lambda_1=3.4879$ Å^{-1}, $\lambda_2=2.2119$ Å^{-1}, $\lambda_3=\lambda_2$, $\alpha=0$, $\beta=1.572\times10^{-7}$, $n=0.72751$, $c=3.8049\times10^{4}$, $d=4.3484$, $h=-0.57058$, $R=1.95$ Å, $D=0.15$ Å.

2.3.5.4.2.2 Brenner Potential

In an attempt to develop an empirical potential for simulating the chemical vapor deposition off diamond films, Brenner [191] developed an empirical potential-energy function that was expected to fulfill the following criteria: (1) reproduce the inter-molecular energetics and bonding in diamond, graphite as well as a number of essential hydrocarbons, (2) allow for bond-breaking and forming, and (3) yield realistic energetics for other structures as well. The Brenner potential takes care of the chemical environment as well as their geometrical arrangements. The binding energy is written as a sum over bonds as

$$E_{\mathrm{b}}=\sum_{i}\sum_{j>i}\left[V_{\mathrm{R}}\left(r_{ij}\right)-\bar{B}_{ij}\,V_{\mathrm{A}}\left(r_{ij}\right)\right] \tag{2.3.65.1}$$

where the repulsive and attractive pair terms are given by

$$V_{\mathrm{R}}\left(r_{ij}\right)=f_{\mathrm{c}}\left(r_{ij}\right)D_{ij}^{(e)}/\left(S_{ij}-1\right)]x\exp\left[-\sqrt{2/S_{ij}}\beta_{ij}\left(r_{ij}-R_{ij}^{(e)}\right)\right] \tag{2.3.65.2}$$

$$V_{\mathrm{A}}\left(r_{ij}\right)=f_{\mathrm{c}}\left(r_{ij}\right)D_{ij}^{(e)}S_{ij}/\left(S_{ij}-1\right)]x\exp\left[-\sqrt{2/S_{ij}}\beta_{ij}\left(r_{ij}-R_{ij}^{(e)}\right)\right] \tag{2.3.65.3}$$

The cut-off function f_{c} restricts the pair potential to nearest neighbors. The empirical bond-order function is given by the average of terms associated with each atom in a bond plus a correction term

$$\bar{B}_{ij}=\frac{1}{2}\left[B_{ij}^{-\delta_i}+B_{ji}^{-\delta_j}+F_{ij}\left(N_i^{(t)},N_j^{(t)},N_{ij}^{\mathrm{conj}}\right)\right] \tag{2.3.65.4}$$

where

$$B_{ij}=\left[1+\sum_{k(\neq i,j)}G_i\left(\theta_{ijk}\right)f_{ik}(r_{ik})x\exp\left[\alpha_{ijk}\left\{\left(r_{ij}-R_{ij}^{(e)}\right)-\left(r_{ik}-R_{ik}^{(e)}0\right)\right\}\right]\right]^{-\delta} \tag{2.3.65.5}$$

$$G(\theta)=a_0\left\{1+c^2/d^2-c^2/\left[d^2+(1+\cos\theta)^2\right]\right\} \tag{2.3.65.6}$$

Various parameters for C–C interaction have been given as: $R^{(e)}=1.315$ Å, $D^{(e)}=6.325$ eV, $\beta=1.5$ Å^{-1}, $S=1.29$, $\alpha=0.0$, $a_0=0.011304$, $c_0=19$, $d_0=2.5$.

2.3.5.4.2.3 Nonbonded Macro-Molecular Potentials

For many simple organic molecules, nano-carbons, bonding between graphitic layers, etc., the most important quantities in determining their molecular structures are the nonbonded C–C interactions. For nonpolar hydrocarbons, the only nonbonded interactions are the van der Waal's interactions among carbons and hydrocarbons. Based on a macro-molecular potential developed by Lii and Alinger [192], the nonbonded potential for the interaction of two molecules labeled as 1 and 2 can be written as a representative example.

$$E_{12}^{\mathrm{nb}} = \sum_{i,j} A_{ij} \left[2.90 \times 10^5 \exp\left(\frac{-12.5 r_{ij}}{B_{ij}} \right) - 2.25 \left(\frac{B_{ij}}{r_{ij}} \right)^6 \right] \tag{2.3.66}$$

The C–C interaction parameters for saturated hydrocarbons are: $A = 3.8$ kcal/mol, $B = 0.0440$ Å, and for unsaturated hydrocarbons: $A = 3.88$ kcal/mol, $B = 0.0440$ Å.

2.3.5.5. Interaction Potentials/Parameters for Binary and Ternary Systems

2.3.5.5.1 Fe–C System

2.3.5.5.1.1 Interaction Potentials

Carbon is one of the most important alloying elements in steel, and the thermodynamic properties of iron-carbon solid solution have been investigated extensively due to their relevance in steel technology. Carbon is hardly soluble in α-Fe but its solubility is better in γ-Fe due to more favorable geometry. One of the earliest atomistic approaches to Fe–C system were carried out by Johnson *et al.* [193] for carbon in α-Fe using simple pair-wise potentials for metal–metal and the metal–carbon interactions. As simple pair potentials cannot properly reproduce metal cohesion (see Section 2.3.2.2), Rosato [194] introduced non-pair-wise interactions for metal–metal interactions while retaining the pair-wise potentials for carbon–metal interactions. The Fe–C potential reported by Johnson *et al.* had a cubic form

$$\Phi(r) = a(b - r)^3 + cr + d \tag{2.3.67.1}$$

Various parameters were determined as: $a = -3.365$ eV/Å^{-3}, $b = 2.236$ Å, $c = 0.886$ eV/Å, and $d = -2.156$ eV. Rosato further improved these parameters to describe the behavior of carbon in both α- and γ-iron by using: $a = 11.777$ eV/Å^{-3}, $b = 2.236$ Å, $c = 3.101$ eV/Å, and $d = -7.101$ eV. Both these models neglected C–C interactions in their simulations.

Lau *et al.* [195] developed a multi-body potential for point defect clusters in Fe–C alloys for body centered cubic α-Fe supersaturated in C. Adopting a many-body Finnis–Sinclair alloy format, the total energy contribution of atom i is given by

$$E_{\alpha,i} = -A_\alpha \sqrt{\sum_{j\neq i} \rho_{\beta\alpha}(r_{ij})} + \frac{1}{2}\sum_{j\neq i} \phi_{\beta\alpha}(r_{ij}) \tag{2.3.67.2}$$

$$\rho_{\beta\alpha}(r) = t_1\left(r - r_{c,\rho}\right)^2 + t_2\left(r - r_{c,\rho}\right)^3, \quad r \leq r_{c,\rho} \tag{2.3.67.3}$$

$$\phi_{\beta\alpha}(r) = \left(r - r_{c,\phi}\right)^2\left(k_1 + k_2 r + k_3 r^2\right) \quad r \leq r_{c,\phi} \tag{2.3.67.4}$$

These terms are zero for $r > r_c$. Constants for various interactions have been reproduced below to five-decimal accuracy in Table 2.3.3. Units for energy and length used are eV and Å respectively.

This model was successful in calculating energetically favored defects, and predicted formation energies and configurations of multi-carbon–multi-vacancy clusters that were identified previously by methods. Ruda *et al.* [196] reported on a Fe–C pair interaction based on a linear combination of Tersoff's C–C [183,184] potentials and Mendelev's Fe–Fe potentials [147]:

$$V^{\text{eff}}_{\text{Fe-C}}(a + bx) = A\left[V^{\text{eff}}_{\text{C-C}}(c + dx)\right] + B\left[V^{\text{eff}}_{\text{Fe-Fe}}(e + dx)\right] \tag{2.3.67.5}$$

where $A = 0.8$, $B = 0.2$, a, c and $e = 0.75$ Å, $b = 5.3$ Å, $d = 5.76$ Å, $f = 5.67$ Å and $0 \leq x \leq 1$. Energy values are in eV. The quantities used in fitting include dilute heat of solution of C in bcc Fe, lattice stability, cohesive energy and bulk modulus of metastable FeC phase.

In a recent paper, Hepburn and Ackland have focused on the absence of covalent bonding in existing Fe–C potentials and have attempted to resolve these issues within the EAM framework (see Section 2.3.2.2.2 for relevant details) [197]. This potential describes fairly accurately the interaction of carbon and iron across a range of defect environments. Henriksson and Nordlund [198] have developed an analytical bond-order potential (ABOP) for the iron–carbon system for simulating various phases such as ferrite and cementite phases. Using the ABOP formalism reported in Section 2.3.2.2.3, the potential parameters for Fe–C system were reported as: $D_0 = 4.82645134$ eV, $r_0 = 1.47736510$ Å, $\beta = 1.63208170$ Å^{-1}, $S = 1.43134755$, $\gamma = 0.00205862$, $c = 8.95583221$, $d = 0.72062047$, $h = 0.87099874$, $\mu = 0.0$, $R = 2.5$ Å and $D = 0.2$ Å.

For high-temperature applications in the fluid phase, atomistic MC computer simulations use an alternative approach. Using a rigid lattice gas model, atoms can move from

Table 2.3.3 Constants of Fe–C potentials developed by Lau *et al.* [195]

α	β	A_α (eV)	$r_{c,\rho}$	t_1	t_2	$r_{c,\varphi}$	k_1	k_2	k_3
Fe	Fe	1.82899	3.56975	1	0.50424	3.40	1.23712	−0.3592	−0.0386
Fe	C	1.82899	2.54594	10.0240	1.63898	2.4688	8.97249	−4.0864	1.4832
C	Fe	2.95879	2.54594	10.4824	3.78256				
C	C	2.95879	2.89207	0	−7.3292	2.8756	22.0618	−17.468	4.8126

site to site but the continuous motion of atoms is not permitted [199]. Complex distance-dependent potentials are then replaced by interaction parameters with various atoms occupying rigid lattice sites. Simulations can either be carried out in the grand canonical ensemble wherein the concentration of atomic species is allowed to continuously fluctuate, or in the canonical ensemble where the concentration is kept fixed and a pair of atoms are exchanged between various sites with temperature-dependent probabilities and system reaching lowest energy equilibrium after a large number of MC steps (units of time).

2.3.5.5.1.2 Interaction Parameters for High-Temperature Applications

With their focus on the dissolution of carbon from solid graphite into molten iron, Khanna and Sahajwalla [200] developed a theoretical model of the graphite/Fe–C melt interface and carried out a MC simulation of the interfacial region. Representing atoms as magnetic spins ($S=+1$(up) for carbon and $S=-1$(down) for Fe), the Hamiltonian of the system was written as

$$H=-\sum_{i\neq j}^{nn}\left[J_1(\alpha-\beta)S_i^{\alpha}S_j^{\beta}\right]-\sum_{i\neq j}^{nnn}\left[J_2(\alpha-\beta)S_i^{\alpha}S_j^{\beta}\right]-\sum_i S_i \qquad (2.3.67.6)$$

where spin S_i^{α} represents the type of atom (α) occupying the site I and J's are the various interaction parameters. H is the magnetic field. Simulations were carried out using the following set of interaction parameters: J_1(C–C) = J; J_2(C–C) = γJ_1(C–C); J_1(Fe–Fe) = $-J$; J_2 (Fe–Fe) = J_1(Fe–Fe); J_1(Fe–C) = J_2(Fe–C). γ was varied in the range 0.05–0.2 and J_1(Fe–C) was varied in the range 0.4–0.7J. The parameter J has units of energy and is assumed to be positive in magnitude.

The sign and magnitude of Fe–C interaction plays a crucial role in locating the phase boundary between a homogeneous Fe–C solution and a saturated solution containing graphite precipitates. The phase transition was very broad for J_1(C–Fe) $\leq 0.5J$ and became progressively sharper for J_1(C–Fe) $\geq 0.6J$. Apart from slightly broadening the transition, the relative strength of the second neighbor interaction did not appear to have much effect. As the phase boundary is approximately linear in the temperature range of interest, one can also make quantitative comparison with experiment. For simulating Fe–C melt in the temperature range, 1200–2000 °C, on a rigid graphitic lattice, the following set of interaction parameters can be used [201]: J_1(C–C) = J, J_2(C–C) = γJ_1(C–C); J_1(Fe–Fe) = J_2(Fe–Fe) = −J; J_1(C–Fe) = J_2(C–Fe) = $0.5J-0.7J$. γ varies in the range 0.05–0.2.

2.3.5.5.2 Fe–S–O System

An atomistic potential model was developed by de Leeuw *et al.* to investigate the surface structure and reactivity of pyrite (FeS_2) [201]. The short-range interactions between the

iron and sulfur atoms were fitted to the pyrite structure; these were described by an effective Buckingham potential:

$$\Phi_{ij}(r_{ij}) = A_{ij}e^{-r_{ij}/\rho_{ij}} - \frac{C_{ij}}{r_{ij}^6} \quad (2.3.68.1)$$

where A and ρ respectively represent the size and hardness of the ion; an effective pair potential was used in this study. The first term in Equation (2.3.68.1) represents short-range repulsive interaction and the second term the attractive van der Waal's force. The interactions between the sulfur atoms of S_2 dimer were described by a simple bond harmonic function:

$$\Phi_{ij}(r_{ij}) = \frac{1}{2}k_{ij}(r_{ij} - r_o)^2 \quad (2.3.68.2)$$

where k (=8.44 eV) and r_0(=2.23 Å) respectively represent the bond force constant and the equilibrium separation in S–S system. Lennard–Jones potential ($A = 39344.98$ eV Å^{12} and $B = 42.15$ eV Å^6) was used to represent O–O interaction. A bond-bending term was also introduced to account for the directionality of bonding between an iron atom and two sulfur atoms that do not belong to the same dimer. Various pair-potential parameters are given in Table 2.3.4.

Guillermet *et al.* carried out an assessment of the Fe–S system using a two sub-lattice model for the liquid phase [202]. In an attempt to describe the thermodynamic properties of the liquid phase, it was postulated that the liquid phase had an atomic arrangement similar to the ordered phase based on the structure of the pyrrhotite phase (FeS) with one sub-lattice for Fe atoms and another sub-lattice for S atoms. The deviation from stoichiometry was considered by introducing vacancies on two sub-lattices. A large number (up to 10) of parameters were used in developing the thermodynamic properties of Fe–S system over a wide composition range; these were systemically optimized based on the experimental information available in literature using specially developed software packages.

2.3.5.5.3 Fe–C–S System

Ohtani and Nishizawa calculated the Fe–C–S ternary phase diagram on the basis of the thermodynamic analysis of Fe–C and Fe–S and Fe–C–S ternary melts [203]. The Gibbs

Table 2.3.4 Buckingham potential pair parameters for Fe–S–O system

Ion pair	*A* (eV)	*r* (Å)	*C* (eV Å^6)
Fe–S	94813.9	0.18125	0
Fe–O	483.04	0.3084	0
S–S	1777.08	0.3308	97.4915
S–O	1421.67	0.3308	64.104

free energy of individual phases was approximated by the interstitial solution model, assuming both C and S to be interstitial atoms. Calculated results indicated that re-melting reactions occurred during the cooling of Fe–C–S alloy, a result later confirmed through SEM investigations on Fe–C–S (0.02 wt%) alloy.

Sahajwalla and Khanna carried out a MC simulation study of the effect of sulfur on the solubility of graphite in iron melts in the temperature range 1400–1600 °C based on the atomistic model of Fe–C system developed in their group [204]. Atoms in the ternary Fe–C–S system were arranged on a graphitic hexagonal lattice and pair-wise interactions between them were assumed to be short-ranged. It is well-known that C and S atoms are strongly repulsive in the Fe–C–S system and S atoms also repel each other [205]. The attractive bond between Fe and S is very strong and is more or less ionic in nature. This strong Fe–S bond is capable of distorting the electron distribution around the Fe atom and affecting other bonds made by it [206]. In the event of such a distortion taking place, the resulting bond energy will be a fraction $(1-\varepsilon)$ of the energy of the bond made in the absence of a Fe–S bond, with ε ranging between 0 and 1.

Representing atoms as magnetic spins ($S=+1$ for carbon, $S=-1$ for iron and $S=0$ for sulfur), the Hamiltonian H of the system in the spin −1 Ising model can be written as

$$H=-\sum_{i\neq j}^{nn}\left[J_1(\alpha-\beta)S_i^{\alpha}S_j^{\beta}+K_{ij}R_1(\alpha-\beta)\right] -\sum_{i\neq j}^{nnn}\left[J_2(\alpha-\beta)S_i^{\alpha}S_j^{\beta}+K_{ij}R_2(\alpha-\beta)\right]-H\sum_i S_i \tag{2.3.69}$$

where spin $S^{\alpha}{}_i$ represents the type of atom (α) occupying the site i while values of J are the various interaction parameters of the Fe–C system. The constant K_{ij} has a value of 1 if either one or both sites i and j are occupied by S and is zero otherwise. Values of R represent various interactions of S with other atoms. The coefficient Js and Rs have units of energy. H is the magnetic field.

Let J represent the magnitude of the nearest-neighbor C–C interaction strength. Various interaction parameters have been represented in units of J. Simulations were carried out using the following set of interaction parameters: $J_1(\text{C–C})=J$; $J_2(\text{C–C})=\gamma J$; $J_1(\text{Fe–Fe})=J_2(\text{Fe–Fe})=-J$; $J_1(\text{Fe–C})=J_2(\text{Fe–C})=0.5J$ and $0.6J$; $R_1(\text{S–S})=R_2(\text{S–S})=-(0.1–0.5)J$; $R_1(\text{S–C})=R_2(\text{S–C})=-(0.1–0.5)J$; $R_1(\text{Fe–S})=R_2(\text{Fe–S})=(0.2–1)J$. The bonds made by Fe atoms which have at least one bond with a sulfur atom were modulated by a factor $(1-\varepsilon)$ where ε takes on three values: 0.0, 0.5, and 1. Two values of γ (0.02 and 0.2) were used in these simulations. Detailed simulations on the system showed that the strength of the Fe–C interaction ($J_1(\text{Fe–C})=0.5J$ or $0.6J$) did not appear to have much effect on the linear trend of the decrease in graphite solubility with sulfur. It also does not seem to affect the magnitude of the slope to a great extent.

As C and S atoms tended to displace each other to regions of high and low concentrations, it was assumed that this displacement was mediated by an Fe atom [207]. Treating both C and S atoms on an equal basis and assuming electronic distortions around Fe play a significant role in this displacement process, two new parameters (δ's) were defined. δ(Fe–C) represents the modification in the Fe–C interaction parameter, when the Fe atom has an additional bond with S. Similarly δ(Fe–S) represents modification in the Fe–S interaction parameter, when the Fe atom has an additional bond with C. These parameters were varied over a large range in simulations on the Fe–C–S system. δ(Fe–S) ranged from -0.5 to 1.0 with $\delta(\mathrm{Fe-C}) = 1.0$. It was expected that a locally repulsive Fe–S interaction may lead to a displacement of S from C's neighborhood. Simulations results on a homogenous Fe–C–S system showed that the liquid separates into two immiscible regions only for $\delta(\mathrm{Fe-S}) = 1.0$. This indicates that distortion around Fe does not significantly affect Fe–S interaction strength and may be neglected. This separation was, however, most pronounced for $\delta(\mathrm{Fe-C}) = 1.5$. A new result, emerging from these simulations, was the simultaneous displacement of iron from regions of high carbon concentration to regions of high sulfur concentration.

Phase diagram simulations on carbon solubility also led to similar conclusions. Small values of δ(Fe–S) (-0.5 and 0.0), which were found unsuitable in miscibility studies, also showed negligible effect of sulfur on carbon solubility. The parameter, $\delta(\mathrm{Fe-C}) = 0.5$, was found to be completely unsuitable as it led to a slight increase in solubility rather than a decrease. Optimum parameters for this system, which simultaneously simulate the well-known properties of Fe–C–S system are: $\varepsilon(\mathrm{Fe-Fe}) = 1.0$, $\delta(\mathrm{Fe-S}) = 1.0$, $\delta(\mathrm{Fe-C}) = 1.0$ and 1.5. These simulation results on the Fe–C–S system clearly show that distortions around Fe due to a strong Fe–S bond do not play a significant role in the molten state. Even though a slight increase in Fe–C repulsion locally gives optimum results, this atomic model with zero distortions, with all local modification parameters equal to unity, also brings out key features of the Fe–C–S system.

2.3.5.5.4 Fe–Cr System

Chromium is a common alloying element in steel, having a strong impact on the mechanical properties of alloys. Due to their superior thermal, corrosion and radiation resistance, high chromium (9–12 at.%) ferritic–martensitic steels are used in high-temperature applications in aggressive environments and are a material of choice in advanced nuclear and fusion reactors. Radiation damage from high-energy neutrons can create a large number of point defects, defect clusters, displacement cascades that can lead to microstructure evolution resulting in performance limiting deleterious effects. A number of Fe–Cr binary potentials have been developed to describe such steels in a modeling framework with focus on defect properties.

Konishi *et al.* constructed a *N*-body potential for Fe–Cr alloy system by mixing Finnis–Sinclair (FS) potential for Fe and Cr, while realizing some of the physical

parameters of the alloy system [208,209]. The FS potential consists of a many-body term related to the charge density supplied by the surrounding lattice points and a pair term:

$$U_{\text{tot}} = -A\sum_i \sqrt{\sum_j \phi(r_{ij})} + \frac{1}{2}\sum_{i\neq j} V(r_{ij}) \tag{2.3.70.1}$$

The many-body terms for each system can be extended to the alloy system as follows:

$$\phi_i^{\text{Fe}} = \sum_{j=j_{\text{Fe}}} A^{\text{Fe}^2}\phi^{\text{FeFe}}(r_{ij}) + \sum_{j=j_{\text{Cr}}} A^{\text{Fe}}A^{\text{Cr}}\phi^{\text{CrFe}}(r_{ij}) \tag{2.3.70.2}$$

$$\phi_i^{\text{Cr}} = \sum_{j=j_{\text{Cr}}} A^{\text{Cr}^2}\phi^{\text{CrCr}}(r_{ij}) + \sum_{j=j_{\text{Fe}}} A^{\text{Fe}}A^{\text{Cr}}\phi^{\text{CrFe}}(r_{ij}) \tag{2.3.70.3}$$

$$U_{\text{many}} = \sum_{i=i_{\text{Fe}}} -\sqrt{\phi_i^{\text{Fe}}} + \sum_{i=i_{\text{Cr}}} -\sqrt{\phi_i^{\text{Cr}}} \tag{2.3.70.4}$$

$$\phi_{\text{FeCr}} = \alpha\sqrt{\phi_{\text{FeFe}}\phi_{\text{CrCr}}} \tag{2.3.70.5}$$

The pair terms are expressed as a linear combination of individual terms:

$$V^{\text{Fe-Cr}} = \frac{\beta}{2}\left\{\frac{\phi^{\text{CrFe}}(r_{ij})}{\phi^{\text{FeFe}}(r_{ij})}V^{\text{Fe-Fe}} + \frac{\phi^{\text{FeCr}}(r_{ij})}{\phi^{\text{CrCr}}(r_{ij})}V^{\text{Cr-Cr}}\right\} \tag{2.3.70.6}$$

While Equations (2.3.70.4) and (2.3.70.5) were used for computing alloy potentials, these were further scaled by factors α and β with magnitudes 1.035 and 1.18 respectively to improve fit with experimental results. Other scale factor sets (1.0, 1.25) and (0.94, 0.90) have also been used by Shim *et al.* to describe the extremes of binding between substitutional Cr atoms and self-interstitial Fe atoms [210].

Farkas *et al.* used EAM approach to develop potentials for Fe–Cr alloy system [211]. While a number of EAM potentials are available for bcc iron, it is known that EAM technique is not able to exactly reproduce the elastic constants of Cr due to the negative value of the Cauchy pressure (C_{12}–C_{44}) for this material. Pasianot *et al.* developed an interatomic potential for Cr using an additional term to the standard EAM method to overcome this difficulty [212]. Focusing on alloys with relatively low Cr contents and neglecting angular terms for both Cr and Fe–Cr interactions, an effective pair interaction potential was written in the following form:

$$\begin{aligned} V(r) &= \left\{(r-d)^2(a_3r^3 + a_2r^2 + a_1r + a_o)\ r \le d \right. \\ V(r) &= \left\{(r-d)^2(a_3r^3 + a_2r^2 + a_1r + a_o)\ r \le d \right. \\ V(r) &= 0\ r > d \end{aligned} \tag{2.3.70.7}$$

Parameters for these potentials are given in Table 2.3.5. While energies in eV, the distances are in units of nearest neighbor distances.

Table 2.3.5 Potential parameters for effective pair potentials

Material	a_3	a_2	a_1	a_0	d
Cr	−0.2796	10.0123	−21.6681	11.4988	1.65
Fe–Cr	0.0293	11.297	−27.447	15.597	1.575

While these EAM-based potentials can reproduce Fe–Cr's heat of mixing and the complexity of ferromagnetic phase in an effective manner, they are not able to capture temperature-dependent effects attributed to magnetic transitions. DFT calculations have shown that mixed enthalpy for Fe–Cr system is negative below a critical concentration (∼10 at.%) and positive above it [213,214]. A negative enthalpy of mixing indicates solubility and tendency toward partial ordering, and a positive magnitude indicates clustering of Cr atoms. Bonny *et al.* [215] used an extra s-band embedding term in the EAM potentials for the system.

$$E=\frac{1}{2}\sum_{i,j(j\neq i)}V_{t_it_j}\left(r_{ij}\right)+\sum_i F^{\mathrm{d}}_{t_i}\left(\rho^{\mathrm{d}}_i\right)+\sum_i F^{\mathrm{s}}_{t_i}\left(\rho^{\mathrm{s}}_{t_i}\right) \tag{2.3.70.8}$$

F^{s} and F^{d} respectively represent the embedding terms from s-band and d-band electrons; t_i denotes the type of atom in site "i." The electron densities ρ are calculated as

$$\rho^{\lambda}_i=\sum_{j(j\neq i)}\varphi^{\lambda}_{t_it_j}\left(r_{ij}\right) \tag{2.3.70.9}$$

Various functions φ satisfy the following relations: $\varphi^{\mathrm{d}}{}_{AA}=\varphi^{\mathrm{d}}{}_{BA}=\varphi^{\mathrm{d}}{}_{A}$; $\varphi^{\mathrm{d}}{}_{BB}=\varphi^{\mathrm{d}}{}_{AB}=\varphi^{\mathrm{d}}{}_{B}$; $\varphi^{\mathrm{s}}{}_{AA}=\varphi^{\mathrm{s}}{}_{BB}=0$; $\varphi^{\mathrm{s}}{}_{BA}=\varphi^{\mathrm{s}}{}_{AB}$. Fe potential parameters were taken from the potential developed by Mendelev *et al.* [153].

A simple Thomas–Fermi screening function was used for Cr potentials, which was smoothly truncated between the third and fourth neighbor distance on a bcc lattice:

$$\phi(x)=\phi_0\left(\frac{\exp(-\beta x)}{x}-\frac{\exp(-\beta x_{\mathrm{cut}})}{x_{\mathrm{cut}}}\right)f_{\mathrm{cut}}(x) \tag{2.3.70.10}$$

$$\begin{aligned} f_{\mathrm{cut}}(x)&=1 \quad x\leq 1\\ &=1-\frac{(x-1)^3}{(x_{\mathrm{cut}}-1)^3} \quad 1<x\leq x_{\mathrm{cut}}\\ &=0 \quad x_{\mathrm{cut}}<x \end{aligned} \tag{2.3.70.11}$$

where $x=r/r_0$; r and r_0 are the distance and the equilibrium nearest neighbor distance respectively; $\varphi_0=0.0676504617$ is a normalizing factor and $\beta=5$. The pair interaction V was characterized using a cubic spline expansion:

$$V(r) = \sum_{k=1}^{N} a_k (r_k - r)^3 \Theta(r_k - r) \tag{2.3.70.12}$$

where N denotes number of atoms, a_k the fitting parameters, and Θ the heavyside unit step function.

For the Fe–Cr potential, the square of 4s-type Slater function was chosen for the s-electron density function [216]:

$$\varphi^s_{\mathrm{FeCr}}(r) = Kr^6 \exp(-2\zeta r) g_{\mathrm{cut}}(r) \tag{2.3.70.13}$$

where $K = 20.34075425$ is a normalizing constant, $\zeta = 2.5001$ and g_{cut} is a cut-off distance that provides a smooth cut-off between fifth and sixth neighbors:

$$\begin{aligned} g_{\mathrm{cut}}(x) &= 1 \quad r \le r_c^i \\ &= \frac{1}{2}\left\{1 - \sin\left[\frac{\pi(r - r_m)}{2d}\right]\right\} \quad r_c^i < r \le r_c^f = 0 \quad r_c^f < r \end{aligned} \tag{2.3.70.14}$$

r_c^i(=5.1 Å) and r_c^f (=5.3 Å) are inner and outer cut-offs respectively, $r_m = (r_c^i + r_c^f)/2$ and $d = (r_c^f - r_c^i)/2$. The mixed pair interaction has a cubic spline form (Equation 2.3.70.12) and s-embedding function F^s is written in terms of parameters A_1 and A_2 as

$$F^s(\rho) = A_1\sqrt{\rho} + A_2\rho^2 \tag{2.3.70.15}$$

The parameters of s-embedding function for Fe are: $A_1 = -0.217009784$; $A_2 = 0.388002579$; for Cr, these are: $A_1 = -0.00977557632$; $A_2 = 0.374570104$.

2.3.5.5.5 Fe–Ni–Cr System Equivalent Atom Approach

Grujicic used an "equivalent atom approach" to investigate Fe–Ni–Cr system, which was assumed to be completely disordered, that is, using, all the atoms in the system were considered to be identical with average mass and chemical identity [217]. This approach makes the system pseudo-monoatomic and was justified because of minor differences in the atomic masses and electronegativity of these elements. The embedding energy and the electron density for the effective atoms were defined as weighted averages of corresponding functions for Fe, Ni, and Cr.

$$F_{\mathrm{eff}} = \sum_{i=\mathrm{Fe,Ni}} \gamma_i F_i(\rho) \tag{2.3.71.1}$$

$$\rho_{\mathrm{eff}} = \sum_{i=\mathrm{Fe,Ni}} \gamma_i \rho_i(r) \tag{2.3.71.2}$$

The effective pair potential was also defined as a weighted average of the pair potentials between Fe, Ni and Cr and their average neighbors.

$$\phi_{\text{eff}} = \sum_{\text{Fe,Ni,Cr}} \gamma_i \phi_{i\alpha}(r) \tag{2.3.71.3}$$

where

$$\phi_{i\alpha} = \sum_{j=\text{Fe,Ni,Cr}} \gamma_i \phi_{ij}(r) \quad i \equiv \text{Fe,Ni,Cr} \tag{2.3.71.4}$$

which can be further simplified as

$$\phi_{\text{eff}}(r) = \sum_{i=\text{Fe,Ni,}Cr} \sum_{j=\text{Fe,Ni,Cr}} \left(2 - \delta_{ij}\right) \gamma_i \gamma_j \phi_{ij}(r) \tag{2.3.71.5}$$

Grujicic and Yang [218] have reported an EAM potential for Fe–Ni system and investigated fcc → bcc martensitic transition in Fe–Ni alloys containing 20–40 at.% Ni. Johnson's EAM interaction potentials for Fe and Ni were used for bcc structures [219,220].

2.3.6. PROPERTIES AND PHENOMENA AT HIGH TEMPERATURES: COMPUTER SIMULATIONS AND OTHER RESULTS

2.3.6.1. Carburization of Molten Steel

2.3.6.1.1 Carburization of Solid and Molten Iron

Bartocha and Janerka [221] have reported a computer simulation study on the dissolution of carburizing material (anthracite, petroleum coke, and graphite) particulates in molten iron. The kinetics of relative movements of C and Fe was investigated along with the influence of thermo-physical properties such as thermal conductivity coefficient, specific heat, thermal diffusivity, density, etc. A simplified 2D model of bath sector was used in calculations based on CFD (computational fluid dynamics) software. The diameter of the particle was chosen such that the mass fraction of the inserted carbon amounted to 3.1 wt %. The cast iron temperature was kept at 1723 K; the initial temperature of the carbonaceous particle was 300 K. The highest density material, graphite, was found to have minimal relative motion, which coupled with the heating process indicated that the carburization process was fastest for graphite and slowest for anthracite. The relative motion of the carburizer particle and metal bath (local stirring) had a strong influence on carbon dissolution; increases in surface area were also found to enhance various carburization rates.

Mass transport (diffusion) is known to play an important role in carburization. With a source of carbon placed at the surface of low carbon steel, carbon slowly diffuses into iron over a long period (few hours to a day) at high temperatures (1144–1255 K) producing a carbon gradient. Kula *et al.* [222] have reported computer simulations on low-pressure (and vacuum) carburization which was characterized by rapid saturation of carbon atoms

on the steel surface layer. Computer simulations were used for process control due to the lack of intrinsic equilibrium conditions. A detailed analysis of the flux of carbon atoms delivered to the metal surface showed that the process becomes effective when the overall process is divided into two stages: (1) a boost stage, when a significant amount of carbon is delivered to the surface, and (2) a diffusion stage holding the charge at a given temperature without a further supply. Such a partitioning was found to be advantageous due to the limited solubility of carbon in austenite, and that excess carbon atoms created a solid carbonaceous layer on the metal surface. Experiments were carried out at 1193 and 1223 K with experimental results showing gray carbonaceous deposits on the metal surface when the carbon potential exceeded the maximum solubility in austenite.

Goldstein and Moren [223] have developed mathematical models for simulating the carburization process in low carbon steels as a function of temperature, time, surface carbon content and diffusion coefficient using a two-step and vacuum carburization conditions. During the pack/gas carburizing process, the CO/CO_2 ratio in the gaseous atmosphere, the temperature and the carbon solubility in steel were found to be three key factors of significant influence. Thermodynamic aspects of heat treatment of low carbon and alloy steels in CO/CO_2 mixtures have also been investigated [224,225]. The carburization process can be described by the diffusion equation:

$$\frac{C_C - C_S}{C_0 - C_S} = \mathrm{erf}\left(X/2\sqrt{Dt}\right) \tag{2.3.72}$$

where C_S is the surface concentration of carbon, C_0 the initial carbon level in iron, D the diffusion coefficient for carbon, and C_C the carbon concentration as a function of distance and time. Volume was assumed to remain constant during diffusion of carbon in iron. There were several limitations to this approach. Diffusion constant was found to increase with increasing carbon levels [226]; the saturation value of surface concentration C_S was found to vary with time and the presence of ternary impurities (Mn, Cr, Si, Ni, etc.) had a significant impact on carbon diffusion during the carburization process. Goldstein and Moren [223] carried out numerical analysis of binary diffusion based on finite difference technique employing a 1D space grid. The composition distribution of carbon in the γ phase was represented as C_i at any grid point i; the diffusion problem was bounded spatially by a constant carbon concentration at the surface and zero at the mass transfer boundary. The diffusion equation

$$\frac{\partial C}{\partial t} = \frac{\partial}{\partial x}\left(D\left(\frac{\partial C}{\partial X}\right)\right) \tag{2.3.73}$$

reduces to $\frac{\partial C}{\partial t} = D\frac{\partial^2 C}{\partial X^2}$ when D is independent of concentration. Following finite difference equations were used to solve concentration gradients in a given phase:

$$\frac{\partial C}{\partial t} = \frac{C_i^{n+1} - C_i^n}{\Delta t} \tag{2.3.74}$$

$$\frac{\partial^2 C}{\partial X^2} = \frac{1}{2}\left\{ \frac{C_{i+1}^{n+1} - 2C_i^{n+1} + C_{i-1}^{n+1}}{(\Delta X)^2} + \frac{C_{i+1}^{n} - 2C_i^{n} + C_{i-1}^{n}}{(\Delta X)^2} \right\} \tag{2.3.75}$$

Results from the solution of these computer models predicted that a variation of surface carbon content during the diffusion cycle caused decarburization close to the surface and prevented any significant increase in the penetration depth. Vacuum carburization was modeled as consisting of two steps: carburization with a supply of gas into the chamber and the computation of diffusion profile as the initial carburization gets redistributed in the melt.

MC simulations on the dissolution of carbon from graphite into molten iron were reported by Sahajwalla *et al.* [227]. Two identical blocks with regular lattice sites were placed in contact with each other. All sites on the first block representing solid graphite were occupied by carbon. Sites on the second block representing Fe–C system were occupied by Fe, C atoms distributed randomly. The relative concentrations of Fe, C atoms were governed by the carbon content of the melt under consideration. Using a lattice gas model, atoms were allowed to hop from one site to another; atomic motion in between lattice sites was not permitted. The dissolution rate of graphite was defined in terms of the number of carbon atoms that dissolve in the melt as a function of time. With N_c representing the total number of C atoms that transfer into the melt at time t and N_t the total number of MC steps: $dC/dt = N_c/N_t$. The dissolution rate was computed throughout the duration of the dissolution process; the simulation time was measured in units of MC steps. As the focus was on identifying various simulation trends, no attempt was made to quantitatively compare simulation results with the experimental results.

The computed magnitudes of energy, dissolution rate, interfacial profile, and widths were found to depend on simulation variables such as lattice size, contact area, relative interaction strengths, etc. Figure 2.3.1a shows a plot of the initial atomic profile of the graphite/Fe–C system across the basal plane. The initial carbon concentrations in the melt were chosen to be 0.0 and 2 wt%. The layer $Z = 80$ indicates the initial boundary between the solid and the melt. Figure 2.3.1b shows the atomic distribution after simulation. Fe atoms appeared to have moved by up to 40 layers into graphite. On the other hand, C atoms moved right up to the melt boundary. The midpoint of C profile in graphite also moved back from $Z = 80$ to $Z = 55$, indicating significant dissolution of graphite.

Once a C atom gets dissociated from graphite, it can propagate easily in the melt. Fe atoms, however, find it difficult to penetrate solid graphite due to energy considerations. The movement of a C atom in the melt involved the replacement of a repulsive Fe–Fe bond with a less repulsive Fe–C bond or an attractive C–C bond in place of a repulsive Fe–C bond. This process lowers the energy of the system and is therefore energetically

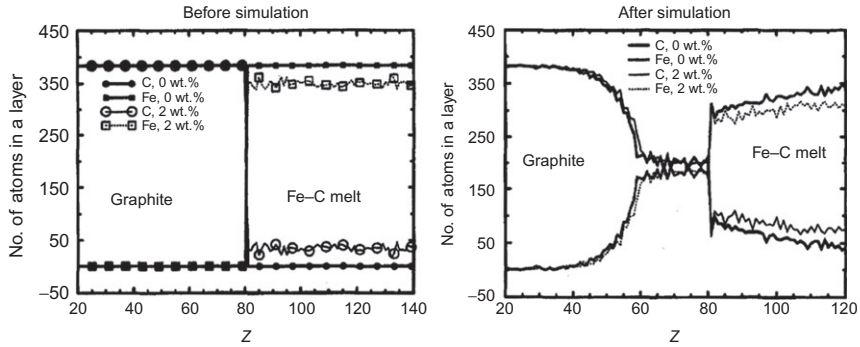


Figure 2.3.1 Atomic distribution profile across graphite/Fe–C interface before and after simulation. *Z* corresponds to the layer number normal to the interface [227].

favorable. On the other hand, the movement of Fe atom replaces an attractive C–C bond with a repulsive Fe–C bond, a move not favored energetically. At $T=0$, there should be no movement of Fe into graphite. However, a carbon atom once released from the graphitic substrate can dissolve into the melt at all temperatures. Figure 2.3.1b also shows a slight reduction in the width of the interfacial region with increasing carbon content of the melt.

Graphite dissolution rates across the basal plane were computed as a function of time for temperatures ranging from 1300 to 1600 °C. Simulation results could clearly be divided in two regions. A sharp increase in dissolution rate was observed during the initial stages of contact between graphite and melt (Region I); the dissolution rate of graphite was controlled by the slow reactions at the interface ($k < K_m$). The dissociation of C picked up after a short time. Increasing temperature also made the dissociation of C atoms easier and pushed region I to shorter times. In region II, the dissolution was controlled by the mass transfer in the melt, which now becomes the slower process ($K_m < k$). This represents the typical behavior observed in graphite dissolution experiments. The influence of temperature in region I was more significant as compared to region II. Due to generally higher activation energies, chemical reactions are more sensitive to temperature than mass transfer. This result supports the hypothesis that dissolution process is controlled by interfacial reactions in region I and by mass transfer in region II. Region I was not observed during dissolution across prismatic planes as there was no hindrance to C dissociation at the interface and the reactions at the interface were quite fast. The dissolution rates, which were much higher in the initial stages, were completely controlled by mass transfer in the melt.

A MC simulation study was also carried out on the dissolution of a single graphite particulate in Fe–C (0–4 wt%) melts in the temperature range 1400–1600 °C [228]. Using canonical ensemble, simulations were carried out as a function of particle size, carbon content of the melt and temperature. The overall particle dissolution profile as a

function of particle size, temperature and *C* concentration in the melt showed a good agreement with theoretical and experimental results. Simulation results showed that the dissolution of a graphitic particle did not take place layer by layer. Even as carbon dissolution neared completion on a given surface, small islands of graphite could still be seen in a sea of melt. The C atoms in the basal plane dissolved preferentially from the edges and iron liquid slowly moved in toward the center. The atoms on a prismatic plane on the other hand dissolved all across the particle surface. Iron liquid penetrated deep in the particle and led to the formation of a broad interfacial region containing high concentrations of both C and Fe.

2.3.6.1.2 Effect of Ternary Impurities on Iron Carburization

The effect of sulfur on the solubility of graphite in iron melts was investigated in the temperature range 1400–1600 °C based on the atomistic model of Fe–C system. It is well known that C and S atoms are strongly repulsive in the Fe–C–S system, and S atoms also repel each other [229]. It was expected that a locally repulsive Fe–S interaction may lead to a displacement of S from C's neighborhood. Initially sulfur atoms were distributed randomly and uniformly in the Fe–4 wt% S melt. Atomic distribution profiles for Fe, C, and S atoms are plotted in Figure 2.3.2 as number of atoms in a given layer before and after simulation. $Z = 50$ represents the initial graphite/melt contact surface. When this melt was brought in contact with a block of graphite, various atoms started diffusing across the interface. While C atoms dissociated from the graphite block and dissolved in the iron melt, some Fe atoms also penetrated the graphite block [206].

However, there was no indication of S atoms penetrating the graphite block or blocking up the interfacial region. Instead, these tended to move away from the interface and penetrate deep in the iron melt. This result is in excellent agreement with the EDS results of Wu *et al.* [230] as they also did not find any evidence of a sulfur peak in the interfacial region in the initial stages of contact. There appeared to be well-defined regions of high C and low S close to the interface and low C and high S deep in the melt. In Figure 2.3.3, the dissolution rate of graphite is plotted as a function of time for a range of C and S concentrations of the melt. These results are for the basal plane of graphite in contact with hot melt. Due to strong covalent bonds between C atoms in the basal plane, dissociation of C atoms was quite slow and interfacial effects were rate controlling in the initial stages of contact. Dissociation rate picked up after some time and the carbon dissolution rate-controlling mechanism changes over to mass transfer in the melt. However the presence of sulfur in the melt appeared to affect both these mechanisms.

The presence of sulfur in the melt affected the overall carbon dissolution rate adversely. This reduction takes place in the initial stages of contact and also when carbon concentration in the melt is close to saturation. In the initial stages of contact when interfacial effects were rate controlling, the presence of S led to a lowered carbon dissociation

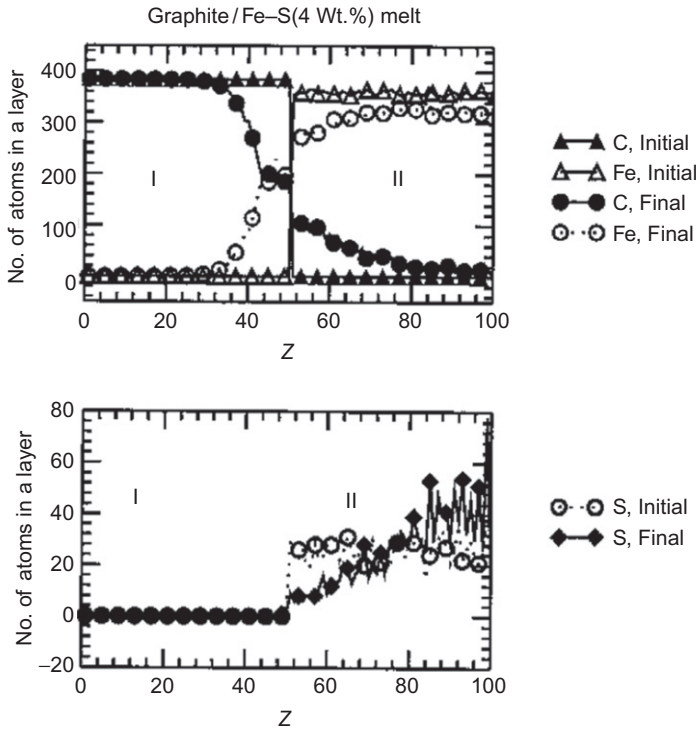


Figure 2.3.2 Atomic distribution profile across graphite/Fe–S interface before and after simulation. *Z* corresponds to the layer number normal to the interface [206].

rate. This decrease was attributed to bond energy considerations and was not due to any interface blockage by sulfur atoms.

The presence of ternary solute impurities such as Ni, Mn, Cr, and Si is also known to influence the solubility limits of carbon in austenite. Dunn *et al.* [231] investigated the carburization of manganese steel assuming a negligible Mn concentration at the surface. The practical implication of such a configuration is to increase the effective surface concentration of carbon by up to 20 pct., which allows much more carbon to enter the steel than from binary considerations alone. A gradient of ternary impurities can influence the diffusion of carbon. Another mechanism through which ternary steel additions may redistribute during carburization is oxidation. Both surface and internal oxidation can occur resulting in the formation of oxides such as SiO_2, Cr_2O_3 and MnO. Both Cr and Si have large cross-section coefficient effects and are expected to have significant influence on carburization. The formation of a surface oxide layer may however complicate carbon control and exchange of carbon from gases to the solid. Segregation of solute atoms to interfaces in metallic systems is also a common phenomenon during heat treatment.

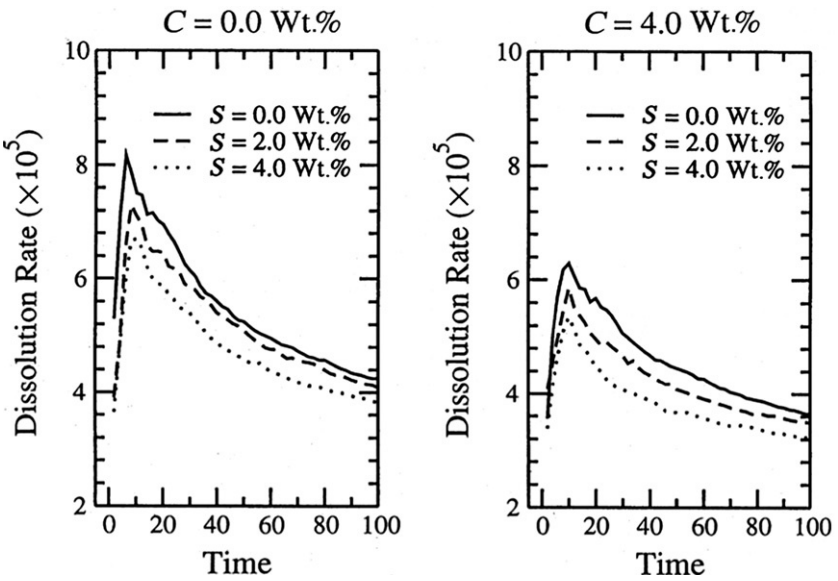


Figure 2.3.3 Carbon dissolution rate as a function of time, across basal plane for a range of carbon and sulfur concentrations in the melt [227].

2.3.6.2. Decarburization Reactions in Molten Fe–C–S System

Carbon levels in steel are controlled carefully through decarburization and refining processes [232,233]. During decarburization of continuously carbon-saturated liquid iron by CO_2 between 1280 and 1600 °C, the presence of small amounts of sulfur (0.01–1 wt%) was found to significantly slow down the decarburization rate [234]. It was also found that during the decarburization of iron melts; an oxide film was consistently observed on the metal droplet surface. Increasing sulfur contents generally increased the tendency of surface oxide formation under otherwise similar conditions. Gao *et al.* [235] investigated the influence of sulfur content on the carbon boil phenomena and CO generation in Fe–C–S droplets (C = 4.2 wt%, S = 0.005–0.4 wt%, 1370–1450 °C). During these decarburization studies, sulfur levels remained fairly unchanged throughout the duration of the experiment. Carbon boil occurs when the internal pressure of CO gas exceeds the surface energy of the metal drop. Times for carbon boil were found to range between 5 and 20 s; these were independent of sulfur up to a certain level and then decreased with a further increase in the sulfur content. Existing theories were found to be inadequate in explaining key experimental results on the decarburization of steel, a very important aspect of steelmaking. Using ideal monolayer adsorption isotherms, Sain and Belton [236] had assumed that the surface activity effects of sulfur could to be due to its occupying a majority of the surface sites thereby blocking the reaction. For high sulfur levels in the melt (~0.02 wt% S), these models predicted a complete coverage of the surface with sulfur and zero decarburization of the melt.

2.3.6.2.1 Atomistic Computer Modeling of Decarburization

Computer simulations on thin films have reported that surface effects extend up to the top three atomic layers, where the surface characteristics are significantly different from the bulk [237]. It is quite likely that the surface of molten steel was multi-layered instead of a monolayer and could include several neighboring layers close to the liquid surface. If sulfur atoms were present on a number of surface layers instead of the top monolayer, there is a strong likelihood for elements other than sulfur to be present on the surface thereby pointing to additional reaction pathways. Atomistic computer simulations were carried on molten Fe–C–S system; free surfaces were characterized by a missing layer of atoms. Simulations were carried out as a function of melt carbon and sulfur concentration, temperatures of the simulation cell. Simulations were based on the bulk interaction parameters; surface interactions parameters between Fe, C, and S atoms were assumed to be identical in magnitude to the corresponding bulk interaction parameters. Turbulence in the liquid at high temperatures allowed a continuous/sporadic movement of atoms within the liquid. Another key difference between the surface atoms and those in the bulk was in the form of absent atomic planes/bonds, which could in turn result in major differences in overall interaction energies.

The size L of the simulation cell was chosen to be quite large, ranging from 24 to 36; depth M was chosen to range between 10 and 300 to investigate bath configurations with different surface/volume ratios. Computer simulations were carried out at 1400 and 1500 °C for melt carbon contents of 3.2 and 4.2 wt%. Sulfur concentration in the melt typically ranged from 0 to 1.5 wt%. Simulation results for the configuration: $24 \times 24 \times 15$ lattice, $C = 4.2$ wt%, 1500 °C, are shown in Figure 2.3.4. Sulfur was found to predominantly concentrate in the top few layers with very little sulfur found in the interior of the melt. The sulfur concentration was found to be highest in the second layer; this result was observed for all sulfur concentrations under investigation.

With 1.25 wt% average sulfur concentration in the bulk melt, S atoms occupied 118 sites out of the 384 sites available on the top surface layer. This result clearly shows that a complete surface coverage with sulfur does not take place even when the number of available sulfur atoms far exceeds the number of surface sites available. Instead, these are distributed in a 3–5 atomic layer thick surface region leaving plenty of sites available for other atomic species. This trend appears to be a fundamental characteristic of the system. This finding is significantly different from the monolayer theory for the surface proposed by Sain and Belton [236].

The system was investigated further to probe the influence of temperature and carbon concentration. Temperature was varied from 1400 to 1600 °C, and the carbon concentration in the melt from 1.2 to 5.2 wt%. Total S was maintained at 0.5 wt%. Sulfur was found only in the surface region with very small levels sulfur detected in the bulk region at all temperatures and carbon levels under investigation. In the surface region, there was not much influence of temperature or of carbon concentration on sulfur levels. No

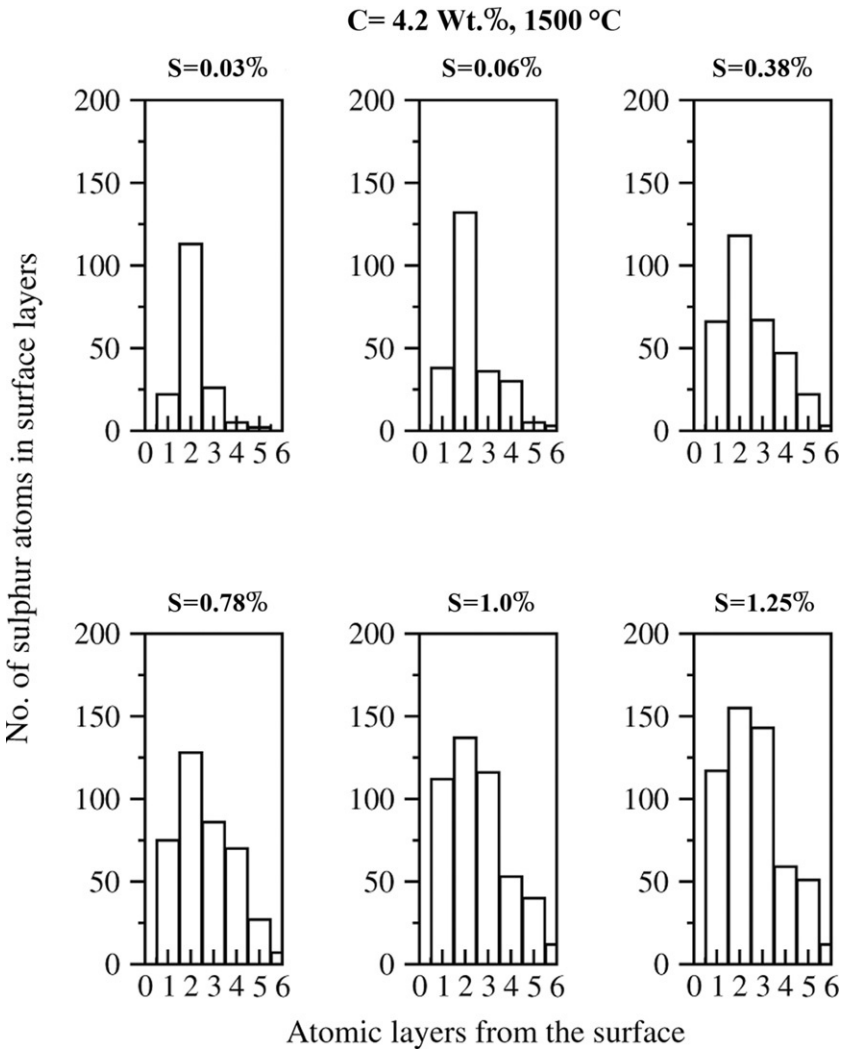


Figure 2.3.4 Concentration of sulfur in the top five surface layers in a liquid bath configuration ($24 \times 24 \times 15$) [237].

well-defined trends were observed. Carbon level in the surface region was however significantly lower than the corresponding bulk values. For a 5.2 wt% C bulk concentration, the surface region showed ~2% carbon and the bulk region showed a slightly higher value of 5.6 wt%. Temperature once again had only a marginal influence. Iron levels in the bulk region were marginally higher than their corresponding levels in the surface region, which was caused by several of the surface sites being preferentially occupied by sulfur atoms. Iron concentration was higher than 94% across the entire simulation zone.

This result indicates that the liquid surface was not completely depleted of iron; iron present in the surface region could participate in a number of surface-based reactions previously considered to be blocked by the sulfur monolayer. There was little influence of temperature. The continuous decrease in iron levels observed with increasing carbon was probably due to overall changes in the bulk metal composition; the presence of free surfaces did not have any role in this decrease.

The influence of sulfur on the redistribution of carbon within the liquid is an important result. A high surface accumulation of sulfur automatically resulted in low surface concentrations of carbon. As sulfur was concentrated in the top few layers, the concentration of carbon was significantly reduced in the surface region, and was slightly higher in the bulk region. For 3 wt% C in the bulk, ~1 wt% C was observed in the surface region along with ~3.5 wt% C in the bulk region. Surface decarburization and carbon boil phenomena will depend strongly on the carbon concentration in the bulk and in the surface regions. Another important result was finding up to 99% surface sites being occupied by Fe atoms. Fe–Fe interaction parameters are repulsive in nature with iron being in the molten state at these temperatures. The system tends to lower its energy by concentrating repulsive bonds on free surfaces; both C and S had moved away from the outermost layer. However since S is a surface-active element and has a strong attractive interaction with Fe, S tended to concentrate in the second layer. Another key finding was on the influence of sulfur on the redistribution of carbon within the liquid. Carbon and sulfur atoms tend to displace one other in molten steel; a high surface accumulation of sulfur will automatically result in low surface concentrations of carbon. As sulfur was concentrated in the top few layers, the concentration of carbon was significantly reduced in the surface region, and was correspondingly higher in the bulk region. The presence of free surfaces therefore resulted in a major redistribution of various atomic species.

Observed simulation findings are consistent with the formation of iron oxide layer on Fe–C–S droplets in oxidizing atmospheres. Iron needs to be a major reacting species present on the surface for oxidizing reactions to take place. Secondly, since a major proportion of sulfur was present in the second layer and not in the top outermost layer, it would significantly reduce its direct interactions with oxidizing gases. This would help minimize loss of sulfur to the environment and could account to a certain extent for the negligible loss of sulfur observed experimentally.

For decarburization reactions under CO_2 atmospheres, the addition of small amounts of sulfur resulted in a significant reduction of decarburization rate. This experimental result was explained by Sain and Belton [233] by assuming that S atoms blocked most of the surface sites and only 1.4% active sites were available for other reactions. These simulation results point to an alternative mechanism. Due to mutual displacement between C and S, the presence of S in the surface region would automatically move C away from the surface thereby significantly reducing its direct contact with CO_2 gas. The reduction in decarburization rate can also be explained by C atoms moving away

from the surface; a complete blockage of surface by sulfur may not be necessary for slowing down the reactions. Secondly, it was observed that the top layer always contained small amounts of carbon as well. This finding could account for the observed residual decarburization without the need for arbitrarily blocking reactive sites through atomic misfit or orientation considerations.

Simulation results suggest a novel approach is required to enhance current understanding on the influence of surface-active elements. Theoretical models using the concept of reactive sites suggest that surface activity effects of sulfur may be due to its occupying a majority of surface sites; a complete coverage of surface with sulfur has been suggested for sulfur levels ~0.07 wt%. Although simulations indicate sulfur concentrating close to the surface, these atoms are present in several top layers instead of a monolayer. Simulations indicate that a complete surface blockage by sulfur is not likely and opens up the possibility for surface reactions with other atomic species such as Fe.

2.3.6.2.2 Theoretical Models of Decarburization

Theoretical models have been developed for an argon-oxygen decarburization (AOD) converter that also incorporated a thermodynamic description of the process [238]. The decarburization in an AOD converter is made in a series of steps with distinct oxygen/inert gas ratio, which is progressively decreased with increasing decarburization; this approach has been found to minimize chromium loss during the decarburization of stainless steel scrap. Asai and Szekely [239] developed a mathematical model of system that prevented the reaching of equilibrium by balancing an equilibrium driving force and an opposing resistant driving force. Fruehan [240] focused on the mathematical modeling of the tuyere zone. Chromium was found to react with oxygen and the oxide thereafter getting transported to the upper parts of converter and its subsequent reactions with carbon. Ohno and Nishida [241] developed a model focused on reactions involving gas bubbles; Reichel and Szekely [242] claimed the existence of critical carbon content, where the decarburization rate is controlled by kinetic factors instead of oxygen supply.

Andersson *et al.* [238] used a mathematical model of gas injection in a 3D AOD converter accounting for steel, slag and gas phases. They used the PHOENICS software to solve two separate sets of Navier–Stokes equations for the liquid and the gaseous phase. The model was augmented to account for bubble swarms. Following assumptions were made in modeling the fluid flow. Due to the symmetry along the middle layer, only a half 3D grid was used in calculations. Free surface was assumed to be flat and gas bubbles were allowed to leave the domain through the free surface. Gas bubbles were introduced through nozzles located on side walls with flow rates of 20 $Nm^3\ min^{-1}$. An interface friction coefficient describes the force between the gas and the liquid phase. Temperatures are time-dependent functions of the industrial charge under consideration. The slag phase is assumed to be homogenous and in the form of spherical liquid droplets.

Transport equations for the 3D three-phase fluid flow model for gas injection in AOD converter were solved using mass conservation equations for steel, gas and slag phases as well as equations for the conservation of momentum in three directions for all three phases. Frictional forces between the gas and the liquid phases and turbulent transport equations were also investigated. Thermodynamic investigations on the system were carried out using a Thermo-Calc [243] software package. The system was defined with five elements Fe, C, Cr, Ni and O which could take the form of the following stoichiometric oxides: FeO, Fe_2O_3, Fe_3O_4, Cr_2O_3, NiO. The gas species transported were O_2, CO, and CO_2. Equilibrium was assumed to be reached for every simulation cell at every time step. Thermodynamic software was directly coupled with the fluid flow software; reaction products within a solution sequence were directly inserted in the fluid flow transport. The partial pressure of carbon monoxide gets lowered with increasing fraction of inert gas resulting in increasing decarburization ratio. Such a change is generally brought about in a step-wise manner. The temperature profiles in the main reaction zone need to be determined by solving energy equation to high precision for bringing calculated chemistry closer to the tuyeres. The locations for Cr_2O_3 formation around the tuyeres as well as in refractories need to be examined for temperature measurements.

Jiang *et al.* [244] have developed a mathematical model based on the reaction kinetics and mass balance to investigate the decarburization rate in UHP electric arc furnace in order to describe the sequence of decarburization process and to provide a means of calculating the control of endpoint operations. A number of assumptions and simplifications were used in the model. The decarburization reaction was assumed to follow the general rule of reaction kinetics. At high carbon contents, the decarburization content was proportional to the extent of oxygen supply and was considered to be independent of the carbon content. At much lower carbon values, the decarburization rate was assumed to decrease with carbon content. While a proportion of oxygen was consumed to cut scrap, the remainder is used to oxidize C, Si, Mn, and P. A parabolic relationship was assumed between the decarburization rate and the carbon content [C]. The effect of flow rate of oxygen on decarburization rate, decarburization time, and total oxygen consumption was determined. The decarburization rate was found to increase with increased oxygen supply, resulting in shorter decarburization times. When carbon transfer became the rate-controlling step, the increase in the decarburization rate was found to be independent of oxygen flow rate. A large oxygen flow rate also led to an over oxidation of molten steel. It was possible to compute the evolution of carbon content dynamically; calculated results were found to have good agreement with the production data.

Shukla *et al.* [245] have reported on the decarburization reaction in the middle blow period of BOF. It has been suggested that decarburization takes place in the slag-metal emulsion directly under the jet, on the refractory walls as well as within the CO gas bubbles in the bulk metal [246]. The decarburization was assumed to proceed through the following intermediate steps. The metal droplets were injected into the slag phase due to

impinging oxygen jet and by CO gas bubbles carrying a thin film of metal into the slag phase. Despite high carbon content, the surface of metal droplets was supersaturated with oxygen; the presence of dissolved Si prevented the nucleation of gas bubbles to some extent. Homogeneous nucleation also occurred at high oxygen super saturation. For high carbon melts at low partial pressures of oxygen, the decarburization rate was found to be independent of gas flow rate and was a linear function of oxygen partial pressure. Decarburization was controlled by dissociative adsorption of oxygen; oxygen activity was close to equilibrium. Both sulfur and nitrogen were found to retard decarburization. For high carbon melts under high partial pressure of oxygen, the rate of carbon removal varied linearly with gas flow. Changes in temperature and the presence of sulfur and nitrogen had a negligible influence on decarburization rate. The rate-controlling step was the chemical reaction: $C + FeO = Fe + CO$. For low carbon melts, the critical carbon below which the rate of carbon oxidation was affected by mass transfer was determined to lie between 0.7% and 0.3%; and was found to be independent of partial pressure of oxygen, temperature and other elements. Thermodynamic models were developed to predict all the practically observed features of BOF process. Effects of heat and mass transfer were coupled in the integration of the scrap dissolution module.

2.3.6.3. Depletion of Carbon from Alumina–Carbon Refractories

An atomic model of the graphite–alumina/liquid iron system was developed based on the experimental observations in the system [247]. The aim was to use the atomistic model with optimum interaction parameters to systematically investigate the effect of various operating conditions such as temperature, melt turbulence, composition, on carbon depletion from refractories into molten metal. Alumina was represented as an inert, rigid unified group of five atoms, masking the fine detail regarding aluminum and oxygen constituents. This approach is quite common in computer simulation studies on complex molecules. As the molar volume for alumina is nearly five times the molar volume for graphite, a molecule of alumina was allocated five neighboring lattice sites as against a single site for a carbon and iron atoms. The atomic size differences between C and Fe atoms were neglected. Two identical blocks of dimensions $L \times L \times L_d$, with regular lattice sites, were placed in contact with each other. Sites on the first block, representing alumina–graphite refractory were occupied by alumina and carbon distributed randomly. The relative concentrations of alumina and carbon atoms were governed by the refractory composition under consideration. All sites on the second block representing liquid steel were occupied by Fe atoms.

The alumina–carbon interactions were assumed to be attractive in nature and the strength of the alumina–carbon interaction was varied over a range in an attempt to simulate the effect of binders. The alumina–iron interaction was assumed to be repulsive in nature due to their generally nonwetting behavior. While signs of these interaction

parameters were estimated from fundamental considerations, their magnitudes were optimized and determined during these simulations. The interactions were chosen to be isotropic throughout the simulation lattice except for the C–C interactions, which were anisotropic due to weak van der Waal's interactions along *c*-axis.

The nonwetting between alumina and graphite was modeled through strong but finite repulsion between alumina and iron (Figure 2.3.5a) and also by modifying the nature of interactions on the solid/liquid interface (Figure 2.3.5b). Both approaches proved to be unsuccessful. A third attempt was then made to simulate nonwetting behavior in terms of mutual exclusion of alumina and iron from their immediate neighborhood (Figure 2.3.5c). This approach coupled with the immobility of alumina showed a good fit to experimental results on the graphite–alumina/liquid iron system and helped in developing an atomistic model of the system.

Turbulence in the melt was generated through additional atomic motion on melt sites. With increased turbulence, there was an increase in the rate of carbon dissolution in the initial stages of contact for high carbon refractory mixtures (90% C and 70% C). However, there was no significant change in their steady-state carbon content. This result can be understood in terms of increased rates of mass transfer in the melt caused by the melt turbulence leading to an improvement in the overall carbon dissolution rates. Melt turbulence did not have any effect on carbon dissolution from the refractory mixture containing 50% C. The effect of temperature on carbon dissolution was also investigated in the range 1400–1600 °C. While there was no noticeable change observed in carbon

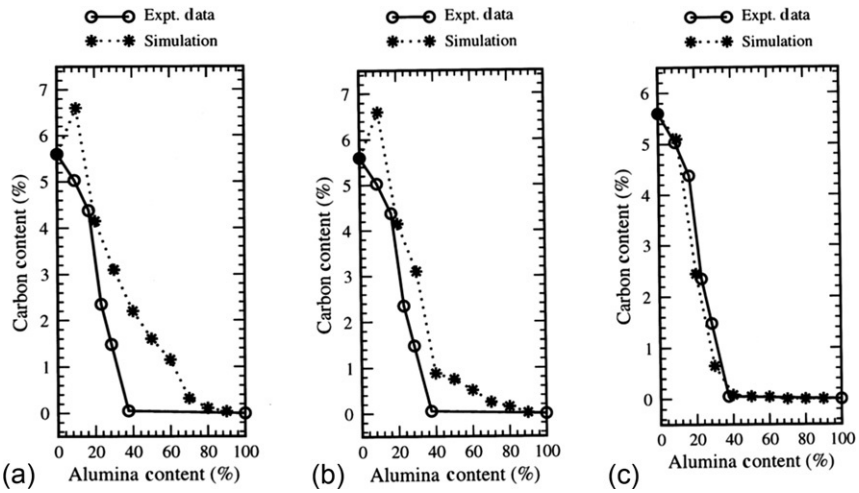


Figure 2.3.5 Atomistic simulation results on graphite–alumina/liquid steel system. The nonwetting between alumina and liquid iron modeled as (a) strong but finite repulsion, (b) a modification of the nature of interactions on the solid/liquid interface, (c) mutual exclusion of alumina and iron from their immediate neighborhood [248].

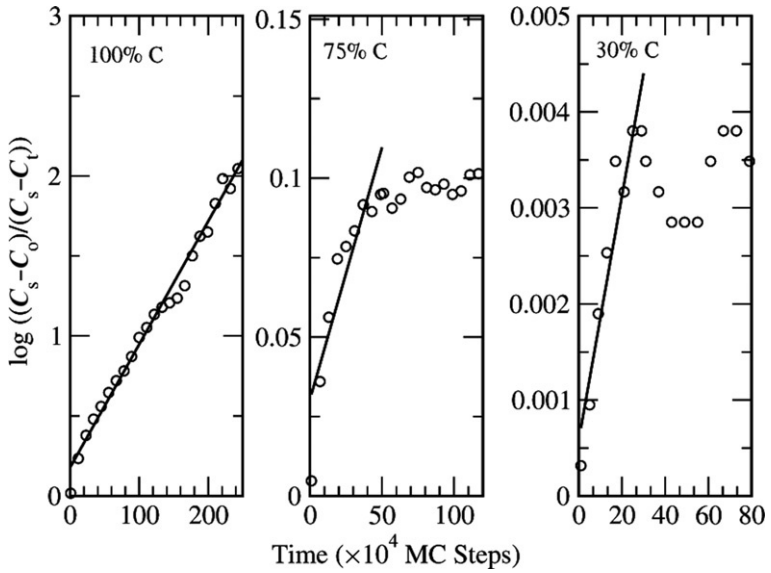


Figure 2.3.6 Simulation results on $\log((C_s - C_t)/(C_s - C_o))$ plots as a function of time for alumina–carbon refractories in contact with liquid iron at 1600 °C [249].

dissolution from refractory mixture containing 50% C, a substantial increase in carbon dissolution was observed for the mixture containing 90% C. A marginal improvement in carbon dissolution rates was observed for 70% C. Both temperature and melt turbulence had a significant influence on high carbon systems, these results clearly indicate that for refractory mixtures containing alumina in excess of 50%, carbon depletion from the refractory was not affected by the increased levels of melt turbulence or higher temperatures.

In Figure 2.3.6, $\log((C_s - C_t)/(C_s - C_o))$ have been plotted as a function of time for three substrates [249]. While a linear trend was observed for synthetic graphite (100% C), simulations from refractories containing 75% C and 25% C respectively did not show a linear correlation between $\log((C_s - C_t)/(C_s - C_o))$ and time. Simulation results indicate that carbon dissolution in refractory mixtures was not governed by a first-order kinetic process. Atomistic simulations and experimental results on these three systems have shown similar trends.

These results indicate that mass transfer in the melt was not a dominant rate-controlling mechanism for alumina–carbon refractories. Poor wettability of alumina with liquid iron and its significant influence on inhibiting the penetration of liquid iron in the refractory matrix, and consequently a very limited contact between carbon and liquid iron was found to the dominant mechanism through which carbon dissolution from refractories gets strongly suppressed. This study has important implications for a fundamental understanding of refractory behavior at high temperatures.

2.3.6.4. Phase Behavior

2.3.6.4.1 Phase Equilibria of Fluids

In order to link the atomic-scale macroscopic description of a system to its equilibrium thermodynamic/macroscopic properties such as heat capacity, compressibility, free energy, etc., it is important to investigate the phase behavior to determine conditions under which solid, liquid or gas phases become stable. The corresponding regions of the phase diagram are marked by phase boundaries where a transition occurs from one phase to another; other features include a triple point where three phases meet or a liquid–gas critical point to terminate the liquid–gas phase boundary. A phase with lowest free energy will be favored thermodynamically; two co-existing phases have the same energy at the phase boundary. A common problem during computer simulations is the existence of hysteresis where the simulated transition point depends on the thermodynamic history of the system under investigation. Mixed phase configurations generally possess higher free energy than pure fluids due to the free energy associated with the interface. The transition temperature can depend on the initial state of the sample, the direction and the rate at which the phase boundary is approached; it is therefore important to approach the phase boundary from both directions at a range of speeds.

Phase equilibria between two co-existing fluid phases require the establishment of an interface; direct simulations can be performed by MC and MD approaches. Some of the difficulties experienced include large number of particles, long equilibration times, and a significant proportion of atoms near the interface with characteristics different from those in the bulk [250]. Investigations have been reported on model systems including spherically symmetric and Lennard–Jones potentials for simple fluids, mixtures and multicomponent systems. Some of these are detailed below.

Square-well fluids were investigated over a wide range ($\lambda = 1.5$, 2, and 3) using histogram methods and fluids in the Gibbs ensemble [251,252]. The critical points of Lennard–Jones potentials were obtained under hyper-spherical and periodic boundary conditions; gas–liquid nucleation was also investigated [253,254]. Other model potentials investigated include the hard core Yukawa fluid, exponential-6 fluids, three-body Axilrod–Teller interactions; both vapor–liquid and liquid–liquid equilibria were investigated [255,256]. Liquid-vapor phase of symmetric binary Lennard–Jones mixture was investigated using histogram approach [257]; the phase diagram showed the existence of a critical point for a certain range of unlike pair interaction strength. A number of studies have been reported on one component systems such as the phase behavior of infinitely thin poly-disperse platelets and rod-like colloids; segregation of large particles in the nematic phase was observed [258]. A system with highly directional interactions was found to lack liquid–vapor co-existence.

In addition to model systems, a large number of complex realistic potential models have been developed for fluids aimed at reproducing energetic and structural properties of the liquid state near room temperature. Two-body potentials have been reported for

water, alkanes, and hydrogen fluoride [259,260]; three body forces have been reported for argon to investigate gas–liquid co-existence [261]. Small nonpolar hydrocarbon molecules have been used to develop model potentials; critical properties of *n*-alkanes have been investigated through computer simulations. The phase behavior of C_{60} has been investigated to probe the formation, if any, of a stable liquid phase [262]. Some studies indicate a narrow liquid region, whereas others indicate that the liquid–vapor critical point is in the metastable part of the phase diagram [263]. Studies have been reported on polar fluids including alkanols, hydrogen sulfide, carbon disulfide, water, and alkali fluids [264,265]. The phase behavior of quantum fluids based on H_2 and Neon have been investigated using Gibbs and grand canonical MC methods [266]. An important goal in this field will be to develop pure component-based potentials and combining rules for realistic mixtures; higher-order interactions and polarizability need to be accounted for.

Oxtoby and Evans [267] investigated the homogeneous nucleation of the gas to liquid transition using DFT approach. It took the work of Cahn and Hilliard on nucleation in two-component incompressible liquids as the starting point [268]. One of the limitations of the classical theory is the prediction of a finite barrier to nucleation as the spinodal is approached, whereas a spinodal decomposition is defined by a vanishing of this barrier as the liquid passes to an unstable state. In their nonclassical theory of nucleation, the grand potential of a single phase was chosen to be a functional of inhomogeneous density. The hard sphere chemical potential and pressure were calculated using Carnahan–Starling form [269]. The co-existence curve was calculated by finding the solutions to liquid and gaseous density at the same temperature, pressure and chemical potential. In an inhomogeneous liquid, the energy becomes a functional of the varying density. Predictions from simulations were found to be consistent with experimental data from cloud chambers; it was suggested that the gas bubble formation in a liquid subjected to tensile stress could nucleate at a significantly higher rate than predicted classically.

2.3.6.4.2 Phase Behavior of Binary Alloys

A few representative examples of computer simulations and phase transformations in binary alloys are presented in this section.

2.3.6.4.2.1 Structural and Magnetic Phase Transformations in the Fe–Al System

Fe–Al is regarded as the prototype binary magnetic alloy with a bcc structure. Experimental research has shown evidence for a complex phase diagram with phases A2, B2, and DO_3 symmetries appearing in both the paramagnetic and ferromagnetic states [270]. At 30% Al, the system is seen to transform from paramagnetic to ferromagnetic state at low temperatures, then revert to the paramagnetic phase and eventually transform to a spin glass state [271]. Extensive theoretical studies have been carried out on the Fe-rich end of the phase diagram; Bragg–William (BW) treatments of free energy, cluster variation method (CVM), and MC simulations have been used in these investigations

[272–274]. While simulation results from both CVM and MC were found to be in good agreement, results from BW were found to be significantly different.

Schmid and Binder derived interaction parameters for the Fe–Al system from the experimental data within the framework of the Ising–Heisenberg model [275]. The ordering tendencies were found to depend strongly on the underlying magnetic structure, local magnetic moments as well as the Wigner–Seitz radius. Various energy parameters were found to depend strongly on the concentration of alloy under investigation [276]. Dorfman *et al.* investigated the stability of the disordered Fe–Al phase and the phase transformation in the B2 phase at 1068 °C [277]. The free energy of ordering was evaluated using static concentration wave (SCW) theory combined with first-principles calculations of atomic interactions to determine concentration and temperature dependence of interaction strengths. These computations showed that energy parameters were closely linked with interaction potentials and their concentration dependence reflected the corresponding dependence in interaction potentials. A good agreement was observed in short-range order properties of Al-transition metal alloys [278].

Allen and Cahn pointed out that magnetic interactions were not required to reproduce the tri-critical point in the phase diagram [279]; whereas Sagane and Oki indicated that a two-phase region lies between a ferromagnetic ordered phase and the paramagnetic B2 phase ending at an apparent bi-critical point [280]. Contreras-Solario *et al.* recalculated the phase diagram of Fe–Al system using BW approach as well as CVM approach under tetrahedron approximation including nearest and next-nearest chemical and magnetic interactions [281]. Although these reproduced most of the general features of the phase diagram, BW results were found to be in error by as much as 30%. Interactions up to third neighbors were required to produce the tri-critical point in the phase diagram. The chemical environment was found to play an important role in determining the local magnetic moment of Fe in Fe–Al alloys. A reliable description of the local environment required an accurate treatment of chemical short-range order to simulate the sensitivity of magnetic moment of iron.

2.3.6.4.2.2 Order–Disorder Transformations and Phase Separation in the Al–Li System

Cahn and Hilliard developed a classical continuum model to study the composition profiles of a critical nucleus with concentration close to spinodal decomposition; the composition of the nucleus was found quite similar to that of the matrix [282]. Legoues used a discrete model of a critical nucleus during isostructural transformations and observed that their model agreed well with Cahn–Hilliard model at high temperatures and low supersaturation [283]. In Al–Li (and also in Ni–Al) system, the precipitate phase is an ordered intermetallic and the matrix is a disordered phase; both have different compositions and structures. The critical nucleus needs to be characterized both by the composition as well as by the long-range order parameter. Poduri and Chen [284] developed a nonclassical

theory of ordered intermetallic precipitates and showed that only when the composition of the initial disordered matrix is near the phase boundary of the disordered phase, the composition and order parameter inside the critical nucleus become close to the equilibrium ordered phase. Critical profiles become increasingly diffuse as the composition of the disordered phase approaches the ordering stability line. The size of critical fluctuations, the critical free energy change and the nucleation rate were estimated for the precipitation of $\delta(Al_3Li)$ ordered phase from the disordered Al–Li matrix.

The atomistic behavior of various micro-alloying elements during low-temperature precipitation in Al–Li alloys has been investigated using a MC computer simulation [285]. Simulation parameters derived from known thermodynamic quantities were found to reproduce the phase decomposition of Al–Li alloys involving simultaneous reactions of clustering and ordering processes. The spatial and temporal evolution of the simulated microstructures provided information on the nucleation and growth of precipitates, the change in the degree of order and the preferential partitioning of micro-alloying elements.

Khachaturyan *et al.* [286] proposed that when the Li composition is above 0.12, the disordered phase undergoes a congruent ordering reaction without any compositional changes followed by spinodal decomposition into Li-rich and Li-lean regions. Low Li regions were found to spontaneously become disordered. This analysis required the kinetic argument involving atomic diffusion of the order of atomic lattice spacing that was assumed to occur much faster than phase separation over typical distances of precipitate size. Poduri and Chen applied microscopic diffusion equations in combination with thermal noise in different compositional regimes within the two-phase field [287]. These computer simulations showed that for average compositions below but near the ordering stability line, thermal noise led to a smaller size of ordered domains initially; however, congruent ordering was found to occur and domain sizes were comparable with or without noise at later times. The formation of critical nucleus could not be described by compositional fluctuations alone and required fluctuations in order parameter as well. The size of the critical nucleus was characterized by nonclassical nucleation mechanism. Zhang *et al.* [288] applied a diffuse interface model to predict the morphology of critical nuclei during solid to solid phase transformations in both two and three dimensions. The influence of elastic energy on the morphology of critical nucleus and shape bifurcations was demonstrated with increasing contributions of strain energy.

2.3.6.4.2.3 Martensitic Transformations in Fe–Ni System

Bonny *et al.* [289] developed a Fe–Ni many-body potential specifically for metallurgical applications that was capable of describing both the ferritic and austenitic phases. The Fe–Ni system exhibits two stable ordered intermetallic phases, namely, $L1_0$ FeNi and $L1_2$ $FeNi_3$. A procedure, based on a rigid lattice Ising model and the theory of correlation functions space, was developed to address all possible ground states of the system; the

mixing enthalpy and defect properties were fitted. Both bcc and fcc defect properties were compared with DFT calculations and other potentials found in the literature. The potential was thermodynamically validated by constructing the alloy phase diagram which was reasonably well reproduced.

Grujicic and Dang [290] carried out MD simulations of the fcc → bcc martensitic transformations in Fe–Ni alloys containing between 20 and 40 at.% Ni. EAM potentials were used for iron with interactions extending up to second neighbors. The role of crystal defects such as free surfaces and grain boundaries on martensitic transformation was investigated. EAM potential parameters were used to compute various material properties including equilibrium lattice parameter, second-order elastic constants, stacking fault energy, enthalpy and free energy differences between the fcc and the bcc phase. This research was focused on developing a material structural change through the nucleation and growth of a bcc phase within the parent fcc phase. Fe–Ni system was considered to be completely disordered; all atoms (both Fe and Ni) were assumed to have an average mass and chemical identity based on an equivalent atom approach. Marginal differences in their atomic masses and electronegativity were ignored.

EAM functions correctly predicted the relative stability of the fcc and the bcc structures and their relative dependence on the nickel content. The Bain strain was applied continuously along one of the cubic directions of fcc lattice, and the resulting lattice relaxed by minimizing the energy with respect to the aspect ratio (c/a). Simulation results on a cylindrical computational crystal showed that the fcc to bcc martensitic transformation was heterogeneous in nature and was dependent on the presence of defects such as free surfaces, grain boundaries, etc. These results are consistent with the experimental findings of Cech and Turnbull [291] that showed an absence of phase transformation in Fe–30% Ni system despite extensive undercooling. A lattice invariant deformation by twinning or slip was required for accommodating transformation strain.

Yu and Clapp [292] have investigated Fe–30% Ni system with specific focus on the mobility of the martensitic interface and associated structure using MD simulation. The effect of strain conditions on the growth rate of the martensitic transformation was investigated by varying the average atomic density in the simulation box. These computer simulations indicated that increasing strain conditions resulted in a decrease of the growth velocity during transformation. Simulations also pointed toward the highly anisotropic mobility of the interface associated with its orientation that favored a sharp transition instead of a glassy transition. The structural changes were found to be shear-like cooperative movement of atoms. The temperature dependence of the growth velocity was found to be of secondary importance. The simulated phase transition appeared to favor a direct contact of two phases without any transition region. Shibata and Fujita [293] investigated the serrated plastic flow in Fe–Ni binary austenitic steels in some coolants such as liquid helium. The simulation was carried out by dividing the specimen into small elements and repeatedly calculating basic equations for thermally activated

movement of dislocations and thermal balance to obtain the amount of strain during each time increment. The simulated results showed good agreement with experimental tensile test results.

Grujicic and Du [294] carried out atomistic simulation of the transformation toughening in Fe–Ni austenite and followed the progress of the fcc to bcc martensitic transformation surrounding a crack, structural orientation between the parent structure and product structure. The amount of Ni was varied to examine the effect of thermodynamic instabilities. The results showed that the structural transformation was accompanied by a twinning deformation, which gave rise to the relaxation of lattice mismatch stresses. The transformation took place along with the emission of dislocations from the crack tip that caused the crack tip to blunt, stop crack propagation, and hence enhance material toughness. The twin density was noticeably lower in Fe–40Ni and the twinning dislocations were emitted into the transformed region behind the crack tip causing the crack faces to move apart. For Fe–20Ni and Fe–30Ni systems, such a region had completely transformed into the bcc structure. As the crack propagates, the fcc to bcc transformation continues within two fin-like regions emanating from the crack tip. The force acting on the crack gets considerably reduced when the material ahead of the crack tip undergoes martensitic transformation.

Engin and Urbassek [295] investigated the fcc to bcc martensitic transformation in pure iron to study the influence of internal and external constraints on the dynamics of the phase transformation. Metallic iron shows a bcc structure below 911 °C and an fcc structure above it. A number of iron alloys (Fe–Ni and stainless steel) are used in the metastable austenitic (fcc) phase and may transform under load to the martensitic bcc phase with catastrophic results [296]. Fe has quite a complex phase diagram mainly due to its magnetic properties that influence the behavior of conduction electrons and hence binding characteristics. MD and thermodynamic integration investigations were carried out to calculate the free energy differences between the two phases (typically several 10 meV/atom). The temperature-induced homogeneous decay of the fcc phase was made possible by the monotonic decrease of free energy along the Bain path. The system was found to become tetragonally distorted; the transformation required the system to change its volume in at least two directions. No transformation was observed if the system was constrained to a constant volume under periodic boundary conditions. The availability of free volume in the specimen provided the requisite space for the phase transformation to occur.

2.3.6.5. Diffusion

Diffusion plays an important role in the kinetics of a number of material processes [297]; computer simulations have been used extensively to complement experimental studies and to probe regions that are difficult to access experimentally [298]. A few representative case studies are presented in this section.

2.3.6.5.1 Self-Diffusion in bcc Iron

Self-diffusion in metals is generally mediated by migration of point defects. Under this mechanism, the diffusion constant "D" can be expressed by

$$D = a^2 f \gamma \nu x_e^d e^{-G_m^d/kT} \tag{2.3.76}$$

where a is the jump length of atoms, γ a geometrical factor, f the jump correlation factor, ν the attempt frequency, G the free energy associated with the barrier of point-defect migration, and x the equilibrium defect concentration. The self-diffusion is generally controlled by the vacancy mechanism in fcc metals as the vacancy formation energy is much smaller than the interstitial formation energy. This however may not be the case for bcc metals [299]. The interstitial formation energy for bcc metals is only slightly higher than the vacancy formation energy; with the interstitial migration energy being much lower than the vacancy migration energy, interstitial diffusion rates may become quite comparable to corresponding rates for vacancy diffusion [297]. Defect characteristics required for diffusion calculations are generally based on zero kelvin data; it is however important to take into account the temperature dependence of the defect formation and migration energies. Some corrections such as quasi-harmonic approximations to atomic vibrations have been used.

Although MD simulations have been extensively used to investigate diffusion, there are some difficulties/issues associated with this approach. Firstly, an investigation of lattice diffusion is currently beyond the time scales accessible through MD simulations with empirical potentials. The jump rates of point defects are very slow compared to typical jump rates in grain boundaries. Simulation blocks need to be large enough to create sinks and sources of equilibrium concentration of defects. The defect migration would generally require very long MD times. To overcome some of these issues, Mendelev *et al.* [300] considered a simulation cell where a large number of defects were simultaneously present initially and average diffusivity per defect was computed.

Two mechanisms of self-diffusion in bcc iron were investigated, one mediated by the migration of interstitials and other through vacancy migration. Self-diffusion was found to be controlled by vacancy diffusion at all temperatures. This was attributed to the much higher vacancy concentrations as compared to equilibrium interstitial concentrations; even though the vacancy migration energy was much higher than the interstitial migration energy. The vacancy formation energy is low at low temperatures; however an increase in the vacancy formation energy at high temperatures is off-set to a great extent by the changes in vacancy formation entropy. These simulations showed a good agreement with the experimental data. Computer simulations have also shown that the temperature dependence of point-defect formation/migration energies can be significant and need to be taken into account. This specific result for bcc iron

cannot be extended to all bcc metals, for example, *ab initio* calculations predict much closer vacancy and interstitial formation energies for bcc vanadium [301].

2.3.6.5.2 Carbon Diffusion in bcc Iron

Iron–carbon system has been investigated extensively due to its importance in steel technology. It has been known experimentally that the interaction of carbon interstitials with lattice defects can significantly affect the mechanical properties of ferritic steels [302]. The diffusivity of vacancy (V) gets significantly reduced due to trapping by carbon (C) atoms. Vehanen *et al.* [303] determined the energy of V–C complex to be ~0.85 eV, which when added to the vacancy formation energy of 0.55 eV is consistent with the vacancy migration energy of 1.35 eV. The role of self-interstitial (I) atoms in the trapping of C atoms is not very clear; binding energies ranging from 0.1 to 0.4 eV have been quoted [304]; *ab initio* calculations quoted negative energies for the C–I complex are in the range −0.2 to −0.4 eV [305]. Domain *et al.* [305] investigated the properties of C atoms in α-Fe and their interactions with intrinsic point defects and small clusters using density-functional theory. The carbon atom was found to occupy the octahedral site and the activation energy of atom jumps between the octahedral and tetrahedral sites was determined to be 0.9 eV, which was about 0.05–0.1 eV higher than experimental values.

Tapasa *et al.* [306] investigated thermally activated diffusion of carbon atoms in bcc iron and V–C interactions using MD simulations. Potential by Johnson *et al.* was used for Fe–C interactions [193] and Ackland potential was used for Fe–Fe interactions [164]. Two atomic-scale techniques were used to study static and dynamic properties of C atoms and V–C complexes. Firstly, MD simulations were used to model thermally activated motion of an interstitial atom and secondly statics relaxation was carried out using potential energy minimization to study different configurations at 0 K and to calculate energies of formation, binding and migration. The simulations were carried out in an NVT ensemble with periodic boundary conditions.

The pre-exponential factor in the diffusion coefficient of a C atom was determined to be 1.89×10^{-7} m^2/s, which compares well with the *ab initio* value of 1.44×10^{-7} m^2/s [307], and the experimental value of 1.67×10^{-7} m^2/s (243 K $< T <$ 347 K) [308]. An analysis of C atom jumps shows that C diffusion may be described as a random walk on a lattice of octahedral interstitial sites. MD simulations also showed that V–C complexes were immobile and have dissociation energy higher than the C atom migration energy. A rate theory analysis of the annealing temperatures was performed; the results of *ab initio* calculations for the vacancy migration energy (0.65 eV), the binding energy of V–C pair (0.47 eV), and the binding energy of additional C atoms with a V–C pair (0.8 eV) can satisfactorily reproduce various recovery stages.

Ishii *et al.* [309] have reported an accelerated MD method to model atomic-scale rare events. When there are large activation barriers involved, many macroscopic events in

solids such as diffusion may have a typical waiting time of few seconds or more; typical MD simulations are limited to a few nanoseconds. Several approaches such as local elevation, conformational flooding, umbrella potential, hyperdynamics, metadynamics, bond boost, strain boost, etc., have been used [310–315]. Ishii *et al.* applied adaptive boost technique to evaluate carbon diffusion in bcc iron that is known to occur through carbon movement on adjacent octahedral interstitial sites. Carbon diffusivity at room temperatures is $\sim 10^{-20}$ cm^2/s [316]; monitoring of diffusion with conventional MD simulations is therefore quite difficult.

One C atom was inserted in a $6 \times 6 \times 6$ supercell of α-Fe in a canonical ensemble; the supercell's dimensions were adjusted for zero internal stress and were kept fixed during simulations. The activation potential barrier for a C jump was calculated to be 0.86 eV; the collective variable was set to be the projected distance of C along [100] direction relative to the center of mass of all Fe atoms. The hopping of C atoms to the adjacent site would be accelerated by factors up to 10^{17}; the diffusivity will be computed based on the jump frequency ν of the C atom ($D = 1/6\nu d^2$; where $d \approx 1.44$ Å is the distance between adjacent O sites). Simulations were carried out at a range of temperatures and in several crystallographic directions. A C atom at a certain O site tends to move within the plane in the direction of four equivalent and adjacent O sites and not in a direction perpendicular to the plane.

This method was also applied to the carbon atom diffusion inside the edge dislocation core in bcc Fe. A 3960 atom-simulation cell was used containing six atomic layers with periodic boundary conditions in $[11\bar{2}]$ direction having an edge dislocation at the center of the cell and one interstitial atom at a stable site in the dislocation core. The temperature was set at 200 K and 100,000 MD steps were used. Several long-stay sites were observed along with several short-stay sites in-between. The average time for C migration between long stays was found to be 0.53 s with typical activation energies to be 0.3–0.4 eV; the corresponding energies for the short-stay sites was determined to be 0.1–0.2 eV. These studies have shown that single particle displacement is a sufficient collective variable for boosting carbon interstitial diffusion. Even with a moderate dislocation density in a ferritic steel grain, there could be a critical temperature below which C transport by dislocation cores could be the dominant diffusion mechanism.

Evteev *et al.* [317] have carried out a kinetic and MD analysis of carbon diffusion in fcc austenite. A 10-frequency model was developed for interstitial diffusion via octahedral interstices. The specific role played by the transition probabilities during association and dissociation of the nearest-neighbor pairs via the second-neighbor sites was investigated. MD simulations were carried out for low C contents with the assumption that C atoms can only interact via neighboring Fe atoms; simulation results were compared with experimental data at 1273 K. There was a clear indication of repulsion between nearest-neighbor C pairs and indirect repulsive interaction between second-neighbor pairs that was mediated by Fe, resulted in significantly low concentrations of both first- and

second-neighbor C–C pairs. The concentrations of third- and fourth-neighbor pairs were close to a random distribution.

2.3.6.5.3 Oxygen Vacancy Diffusion in Alumina

Understanding diffusion in alumina is a longstanding challenge in ceramic science. Oxygen diffusion is generally believed to be slower than aluminum diffusion under most conditions and is expected to be rate-controlling [318,319]. Theoretically calculated migration energies are of the order of 1–2.5 eV, whereas experiments have determined migration energies to be ~5 eV [320]. This discrepancy has not yet been explained adequately; the possible presence of AlO bivacancies could be an important factor.

The formation of oxygen vacancies through Frenkel and Schottky defects has been investigated in computer simulations [321–324]. Reported formation energies for Frenkel defects range between 3.79 and 8.27 eV and for Schottky defects between 4.18 and 5.86 eV; this variation is attributed to various interaction potentials used. Such high formation energies will in turn result in a very small number of defects. Jacob and Kotomin [321] identified five possible anion migration paths in the unit cell through interpolation between discrete ion positions. Jumps located between two octahedral aluminum ions were labeled as small triangles (migration energy 0.34 eV) and those in the vicinity of octahedral interstitial site as large triangles (migration energy 2.5 eV). There are significant differences in the values of migration energies reported in the literature. A value of 3.7 eV has been reported for the vacancy migration energy based on density functional methods [324] as one of the lowest energy jumps. Some of the uncertainties in anion diffusion are regarding the significance of experimental activation energies, the nature of buffering during oxygen diffusion, key mechanisms, the ratio of cation and anion diffusion in the bulk and grain boundaries.

Aschauer *et al.* [325] have applied a combination of metadynamics and KMC approaches to oxygen vacancy diffusion in alumina. In metadynamics, a number of collective variables such as interatomic distances, angles, co-ordination numbers or other properties definable in atomic positions are used. Transitions between deep local minima are possible within the simulation timescale through a history-dependent bias potential applied to all atoms, providing them with additional energy to overcome the free energy barriers. A bulk supercell ($6 \times 6 \times 2$) of hexagonal alumina unit cells was heated in steps of 100 K using NPT ensemble in the unmodified Dl_POLY 2.0 code [326]. The distance between the jumping and the position previously occupied by the ion was chosen as the collective variable for these runs; structural relaxation associated with the vacancy creation was also taken into account.

KMC simulations were carried out by placing an oxygen vacancy randomly in the unit cell and then identifying all possible transitions with nearest neighbors. The transition i to be carried out was determined by a random number chosen uniformly between 0 and 1; the simulation time for each transition was advanced by $\Delta t = -\log \nu / R_n$ where ν

is another random number and $R_n = \sum_{j=1}^{n} r_j$ is a cumulative function of transition probabilities. Simulations were carried out for 50,000 jumps and 100 runs per temperature. The mean square displacement was calculated from the positions of vacancies at time t and diffusion constant D was computed as

$$D = \underset{t\to\infty}{\text{Lim}} \frac{\left\langle (r(t) - r(o))^2 \right\rangle}{6t} \tag{2.3.77}$$

Three classes of diffusive jumps were identified with the resulting diffusion constant best fitted by Arrhenius equation with a pre-exponential factor of 7.88×10^{-2} m^2/s with an activation energy of 510.83 kJ mol^{-1}(experimental activation energy: 531 kJ mol^{-1}). The lowest energy jumps did not form a continuous network and did not contribute significantly to the bulk diffusion. The next higher energy class formed such a network and was a diffusion-dominant class. Vacancy migration was found to be the dominant atomic-scale diffusion mechanism in alumina.

2.3.6.5.4 Diffusion in Fluids

NEMD can be used to calculate transport properties in multi-component solutions; the simulated system is perturbed away from equilibrium and the subsequent response of the system is measured. The perturbation can either be a steady state or a transient one and can be implemented as an external field, boundary or nonuniform initial condition. Assuming linear transport laws, the system's response is used to measure a transport property [327]. Multi-component diffusion can be described using a form of Stefan–Maxwell equation [328]

$$c_a \nabla \mu_a = \sum_{b \neq a} K_{ab}(v_b - v_a) \tag{2.3.78}$$

where a and b subscripts represent n species, c their molar concentration, μ their electrochemical potential and v the species velocity vector and K the binary interaction between two species. In the inhomogeneous boundary-driven NEMD, spatial inhomogeneity in species concentration is used to drive transport; additional mass needs to be injected from one end and removed from the other end. In the field-driven homogeneous NEMD, an external field is applied to the simulation cell and couples to some system property such as charge/mass and exerts a force with particles undergoing a net movement in the direction of force. Wheeler and Newman [327] used this approach to simulate diffusion in KCl and NaCl electrolytes over a wide concentration range; their results were in a semi-quantitative agreement with experiments and previous simulations on the system.

Masaki *et al.* [329] investigated self-diffusion in molten tin. The temperature dependence of diffusion in liquids is very difficult to simulate from microscopic as well as macroscopic points of view as one needs to take into account the temperature

dependence of interaction potentials as well. For simple liquid metals such as Na and K, interaction potentials can be well-modeled using the pseudo-potential theory [330]; and the transport properties of these metals can be predicted fairly well. For group IVB metals such as Pb, Sn, Ge and Si, there are inherent uncertainties in the determination of diffusion constant due to complex interatomic forces and liquid structures. Masaki *et al.* developed effective interaction potentials for liquid tin using inverse scheme from experimental structure factors obtained from neutron and X-ray scattering measurements for temperatures up to 1873 K. These were followed by MD simulations to compute the self-diffusion coefficient which was found to be in good agreement with experimental results over a wide temperature range.

The computation of self-diffusion in ionic liquids first requires the construction of a force model that can faithfully reproduce the geometric and energetic features of a real system. Self-diffusivity of a single component system is determined from the slope of the mean square displacement of molecules versus time over an extended period. The key challenge with ionic systems is that the "sufficiently long" time depends on the dynamics of the system. For a liquid to show a diffusive behavior, molecules should exhibit random walk with no residual correlation with initial positions or velocities; this is a tough criterion for ionic liquids (typical diffusivity $\sim 10^{-11}$ m^2/s at room temperature). Typical mean square displacement over 1 ns is ~ 1 $Å^2$which is much smaller than the ionic size. Simulations therefore need to be carried out for long periods or at high temperatures.

2.3.6.5.5 Diffusion in Dilute Al–Fe Alloys

Iron is a common impurity present in Al and is known to strongly affect the kinetic phenomena associated with grain boundaries [331]. Iron is known to have a very low solubility in Al and tends to retard recrystallization, forms precipitates or segregates to grain boundaries; all these processes are limited by the bulk diffusivity. Some of the experimental diffusivity data in Al for transition and nontransition metals are shown in Table 2.3.6.

It can be seen from the table that there is significant difference between the transition and nontransition metals; the activation energy for transition metals was found to be considerably higher. In addition, higher the melting temperature, lower the diffusivity and higher the activation energy for diffusion. Differences in melting temperatures and enthalpy for sublimation are a measure of chemical interaction of elements. All transition metals showed a low solubility in Al and had a tendency to make compounds.

The Fe–Al potential developed by Mendelev *et al.* [338] was used to investigate Fe diffusion in fcc Al. The vacancy formation energy in Al was determined to be 0.69 eV/atom at 0 K, and the migration energy for Fe has been determined to be 0.75 eV/atom; this makes the activation energy for the diffusion of Fe atom to be 1.44 eV/atom at 0 K, a value quite close to the energy of Al self-diffusion. KMC simulations were carried out on the system [339]. Two diffusion rate regimes were observed. At low temperatures, Fe vacancy complexes were observed that raised the migration energy to 1.39 eV/atom.

Table 2.3.6 Activation energy for diffusion (E_d), enthalpy of sublimation (ΔH_{sub}), melting temperature (T_m), and solubility in Al (C_0) for a range of transition and nontransition metals [332–337]

Element	E_d (eV/atom)	ΔH_{sub} (kJ/mol)	T_m (K)	C_0 (wt%)
V	3.13	445	2008	<1.5
Cr	2.92	338	2173	<2
Ti	2.69	410	1941	<2
Fe	2.29	350	1811	ppm
Mn	2.16	227	1523	<2
Co	1.75	376	1767	<0.5
Ni	1.51	370	1728	ppm
Cu	1.41	302	1357	<5
Ga	1.28	256	302	20
Ge	1.26	334	1210	5.2
Zn	1.25	115	693	83.1
Al	1.28	293	933	–

At high temperatures, there was no complex formation and energies corresponded to the exchange of single Fe atoms with a vacancy. MD investigations were also carried out on the system taking into account the temperature dependence of vacancy formation energy. Vacancies were introduced in the simulation cell initially with their concentration determined according to the equilibrium values expected. Up to 2% Fe atoms were distributed randomly in the system. Effective diffusivity was seen to increase linearly with vacancy concentration thereby indicating the absence of complex formation. The migration energies of Fe and Al were determined; the addition of Fe was found to slow down the overall diffusion as compared to pure Al.

2.3.6.5.6 Surface Diffusion in Semiconductors

Surface diffusion of atoms deposited on substrate surfaces is of great importance in semiconductors. Atomic diffusion on Si(100) surface was determined by Mo *et al.* [340,341] using scanning tunneling microscopy and a link was established between the surface reconstruction and dynamics of atoms; the rate of diffusion in two in-equivalent directions was found to differ by three orders of magnitude. The effects of the substrate on the hetero-epitaxial Ge islands grown on Si (100) substrates remain one of the poorly understood phenomena of atomistic processes. Williams *et al.* [342,343] demonstrated effects of surface diffusion, step motion and the interplay between the surface structure and dynamic phenomena on Si (111) surfaces; the reconstruction of this isotropic surface is based on features such as adatoms, dimerization, corner holes and stacking faults. Ordering phenomena have also been the subject of extensive theoretical and experimental research on compound semi-conductor surfaces [344,345]. Surface reconstruction is seen to introduce a pattern of strain to substrate sites which in turn affects the observed ordering of various patterns.

Kaxiras has reviewed atomistic simulations of surface diffusion and growth on semiconductors [346]; basic features of theoretical approaches were discussed along with their advantages and limitations. In the classical treatment of Si, two-body interactions are generally inadequate to represent interactions between two ions bonded by covalent interactions with directional preferences; a three- or higher-body interaction is generally required to represent complex local environment and inherently quantum mechanical phenomena. Two most popular Si interatomic potentials, the Stillinger and Weber potential and the Tersoff potential, have already been presented in Section 2.3.5.4.1. The next level of complexity uses tight-binding approximation wherein the electronic degrees of freedom are specifically taken into account but electron wave functions are not determined self-consistently [347]. In the third approach based on first-principles quantum mechanical calculations, true many-body Schrodinger equation for a system of electrons and ions is solved self-consistently [348]. Once the electronic density has been calculated for a given ionic configuration, the forces on ions can be obtained for MD simulations of ionic motions [349]. The computational efficiency was highest for classical potentials, simulations based on the tight binding approximation were slower by a factor of 60 and first principle computations were slower by another factor of 60.

Several mechanisms of self-diffusion have been discussed for Si; these involve defects such as vacancies and interstitials and a third approach based on complex atomic motion that allows two atoms to exchange position without involving defects [350]. Based on concerted exchange mechanism, a wide variety of local structures are created in which two atoms exchanging positions have three- or fourfold co-ordination during the breaking and the formation of covalent bonds. There were serious discrepancies between the classical potential results and first-principles calculations. There were large differences in the activation energy and the existence of deep metastable minima in classical potential results that was absent in other computations. This disagreement was explained in terms of extensive rehybridization that can only be captured through a quantum mechanical treatment of electronic degrees of freedom.

These studies have shown that simulations based on classical/empirical potentials give reasonable results for generic/order of magnitude type questions but may have limited accuracy while addressing very specific quantitative questions. A generic question could be the order of magnitude of the energy barrier, anisotropy in diffusion, average properties in statistical ensembles, etc., but these would not be able to provide exact energy barrier for the concerted exchange mechanism. A certain degree of caution is however warranted for first-principles investigations on real systems as well. Here two different calculations with exactly same methodology can give qualitatively different answers; exhaustive work is required to understand the microscopic details of physical phenomena [351].

Bulnes *et al.* [352] have carried out atomistic computer simulation investigations on collective surface diffusion for strongly interacting particles on an adsorbent surface.

The *n*-fold way KMC simulation was used to infer equilibrium and dynamical properties of the system, especially at low temperatures and on heterogeneous substrates. Critical slowing down of density fluctuations can significantly increase the computation time to drive collective dynamical relaxation at low temperatures, significantly affecting the local dynamics and kinetic behavior in the nonequilibrium regime. This knowledge plays an important role in developing a fundamental understanding of surface phenomena such as domain growth, surface aggregation, thermal desorption, catalysis, etc.

2.3.6.5.7 Computer Simulations of Chemical Vapor Deposition

The process of chemical vapor deposition (CVD) involves adsorption, desorption, evolution, and the incorporation of vapor species on the surface of a thin film. CVD involves a large number of competing chemical reactions that may occur on vastly different time scales [353]. MC methods have been used to investigate kinetic and nonequilibrium phenomena by exploring the phase space along a Markov chain. For example, the motion of an interstitial in a close-packed system can occur through the vibration of the atom about the center of the interstitial hole and hopping to nearest-neighbor interstitial sites. If preceded by a large number of vibrations, the individual hops/jumps of the interstitial atom can become uncorrelated thereby executing a random walk in the phase space. Two key requirements for a KMC are the identification of all possible events that can occur and their individual rates.

Two of the most challenging problems are capturing the surface morphology as a function of operating conditions and predicting the rate of film growth; both of these are determined by kinetic conditions. With typical growth rates approximately few microns/hour, MD simulations are very slow and KMC simulations is the technique of choice. The quality of KMC simulations depends strongly on the reaction rate data, generally determined fairly accurately from experimental results. A number of reactor-scale models of CVD have been developed focusing on reactive hydrodynamics and vapor-surface chemistry to predict composition and temperature profiles of film growth as necessary input for atomistic/molecular simulations [354–357]. Both MD and off-lattice MC studies have been carried out in one, two and three dimensions to provide a molecular view of the growing surface [358,359]. Garrison *et al.* [360] investigated the adsorption of gaseous species (H, H_2, CH_3) on diamond surfaces to determine various reaction rates.

All molecular models of CVD need to include details regarding adsorption, desorption and chemical reaction processes occurring during film growth; surface diffusion and transport of species on the surface may also be required. Two types of KMC models involving fixed or variable time steps have been used in these simulations. In most cases, a large number of reaction steps may be operating at a given time; these might be lumped together as KMC parameters; or alternatively, sticking coefficients or reaction probabilities are defined to predict a microscopic description of a kinetic process. Many of the

KMC simulations were focused on the general features of film growth including surface roughness and the role of surface diffusivity on vapor deposition [361].

A set of chemical reactions relevant to the growth process and associated reaction mechanisms form the basis of CVD simulations; these are used to define rates for various fundamental steps in the evolution of surface species during growth. As a description of the underlying structure involves chemical as well as spatial detail, these become the basic input for discrete computer simulation. A kinetic model requires quantitative information about the rates of all viable chemical processes. Most reactions are reversible and both forward and reverse reactions need to be considered. It is important to consider some of the limitations of KMC approach for CVD simulations. Firstly, it is very difficult to accurately estimate reaction rate parameters even using quantum mechanical approaches. A prior knowledge of all possible reactions may also not be available; simulations might represent a limited version of real chemistry. Although discrete KMC makes the problem tractable, a host of pertinent factors may get overlooked or be handled only approximately; stearic and other local effects are generally quite difficult to include. Other factors that are crucial to the overall growth include surface defects, relaxation, grain boundaries, and dislocations.

2.3.6.6. Defect Studies

The performance of materials is affected to a great extent by point defects, the influence of solutes, impurities, dislocations, grain boundaries, etc. A large number of atomistic computer simulations on defect interactions have been carried out. Some of these are presented in this section as representative examples.

2.3.6.6.1 Defect Interactions in Fe–Cr Alloys

High chromium (9–12 at.% Cr)–Fe alloys are candidate first-wall and breeder-blanket materials for future fusion reactors and for high temperature and aggressive environments [362]. These alloys have superior thermal, corrosion and radiation resistance compared to austenitic steels. The irradiation with high energy fusion neutrons can create a large number of point defects, defect clusters, displacement cascades, penetration by H (protons) and He (α particles) that can cause significant radiation damage and influence material characteristics/behavior. Using EAM potentials, Terentyev *et al.* [363] reported on the decreased diffusivity in Fe–12%Cr alloy. MD simulations have been reported on 10% Cr alloy to study the effect of Cr on the migration behavior of self-interstitials and small defect clusters [362]. Two different Fe–Cr potentials were used as these showed different size effect of Cr in the bcc iron lattice [364]. The Ackland potential was used to represent iron interactions [365] and Finnis–Sinclair potential was used for Cr interactions [152]. The simulation cell consisted of $50 \times 50 \times 50$ bcc unit cells with periodic boundary conditions; Cr was distributed randomly in the Fe lattice. Self-interstitials were

initially oriented in <111> direction; simulations were carried at temperatures ranging between 50 and 1000 K. Defect diffusivity was measured at intervals ranging from 10 to 200 ps. The MD results revealed that Cr tended to decrease the diffusivity of single, di- and tri-interstitials irrespective of the atomic size of Cr (whether oversized/undersized as compared to Fe atom as predicted by two different Fe–Cr potentials). Undersized Cr atoms led to the formation of mixed dumbbells and reduced diffusivity through a trapping mechanism. Oversized Cr atoms resulted in a significant enrichment/clustering of interstitial defects and a repulsive interaction between Cr and interstitial defects.

Olsson *et al.* [366] calculated the Cr–Cr and Cr–vacancy interaction energy in bulk Fe using interaction potentials and DFT. The DFT data showed that Cr–Cr repulsion was found to decrease rapidly with increasing distance. The Cr–V interaction was found to be negligible; this result is in good agreement with experimental results [367]. Vacancy migration barriers were also computed for both forward and backward movement; the barriers were found to be largest for both Cr and Fe exchange when there were three Cr atoms and three Fe atoms occupying six nearest-neighbor positions around a saddle point. Simulations also investigated the interaction between Cr precipitates and screw dislocations in Fe matrix. The dislocation core energy and radius, shear modulus, Poisson ratio, and Peirels stress were computed and compared with experimental results.

Neutron and proton irradiation effects in ferritic steels are important for nuclear reactors and operation of existing systems; the material response shows a strong dependence on the alloy composition. For doses below 15 DPA, the impact of generation of α particles on gas entrapment and surface swelling could be negligible for Cr contents of 2–6% as compared to pure Fe [368]. There is a minimum in ductile to brittle transition temperature for Cr concentration about 9%; the formation of Cr rich α' phase above 10% Cr is known to increase the hardening of steel [369]. MD simulations have been widely used in the simulation of defects, clusters and dislocation loops; however the validity of the interaction potential used could significantly influence defect behavior, especially in the absence of accurate experimental data.

Wallenius *et al.* [370] implemented a set of EAM potentials for the simulation of Fe–Cr system; functions for pure elements were fitted to elastic constants, vacancy formation energy and thermal expansion coefficients and mixing enthalpy was used for Fe–Cr potentials. The atomistic simulation of thermal aging was carried out at $T < 900$ K for Cr concentration ranging between 10% and 90% [371]. *Ab initio* calculations for low Cr (<6%) alloys determined the magnitude of the miscibility gap and indicated a negative mixing enthalpy for the ferromagnetic state of the random alloy [372]. The formation energy was found to be positive above these concentrations and provided a driving force for phase separation. At 700 K, the time needed for significant energy loss for 45%Cr alloy was determined to be of the order of several months; this result is consistent with experimental results [373]. At 800 K, the phase separation occurs in a few days and within few hours at 900 K.

2.3.6.6.2 Point Defect Interactions in Metals and Alloys

A number of atomistic simulations have been carried out on point defects such as vacancies, interstitials, impurity atoms and their complexes in fcc metals; studies include the computation of resulting energy/volume change, lattice distortions/relaxations in the immediate as well as distant neighborhood [374–376]. Studies have also been reported on point defect formation and lattice relaxation in bcc and hcp metals [377,378]. Johnson *et al.* have investigated the migration of carbon and nitrogen in bcc iron and vanadium [193]; the defect concentration was assumed to be low and defect–defect interaction was neglected. The defect was assumed to be surrounded by atoms treated as individual particles; the remainder lattice and more distant atoms were treated as elastic continuum. The activation volume for the migration of impurity atoms C/N, defined as the volume difference between a stable defect configuration and saddle point configuration, was found to be negligibly small for α-iron, a surprising result as the migration of impurity is associated with the squeezing of impurity through narrow gaps [379]. Vanadium on the other hand showed a significant amount of activation volume for the migration of nitrogen [380].

The experimental values of migration energy and activation volume of C in α-iron were used as important inputs in deriving optimal Fe–C interaction strengths. The octahedral interfacial configuration was found to be energetically more stable and the defect migration took place via octahedral to tetrahedral to octahedral sites. Due to attractive interaction between Fe–C over longer distances, carbon atoms had a small tendency to drag Fe atoms. These simulations however did not correctly predict the volume expansion per carbon atom; simulated values of 0.28 V (V = atomic volume of Fe) were much lower than the experimental value of ~1.0 V (although there is some experimental uncertainty regarding this value; recently more reliable experiments have quoted a value of 0.83 V). A carbon interstitial and iron interstitial formed a stable complex in a split configuration with a binding energy of 0.5 eV. The iron interstitial energy was computed as 0.3 eV and it migrated through forming complex with C interstitial and subsequent release [381]. This model also investigated the relaxation of nitrogen in vanadium. Nitrogen migration also occurred through the octahedral to tetrahedral to octahedral route; however it had an activation volume of 0.156 Ω (Ω: vanadium volume) which agreed well with the experimental values of 0.135 Ω [382].

One of the common problems in the power vessel steels in power reactors is hardening due to radiation-induced defect clusters in the iron lattice and the formation of copper precipitates even with low Cu concentrations [383]. It is important to specify reference states appropriately while defining the properties of defects in alloys; in this study, Fe atoms were present as a pure metal and Cu atoms were in a solid solution. The defect formation energy can be defined as

$$E_{\text{def}}^{f} = \left(E_{\text{block}}^{N} - E_{\text{block}}^{N^0}\right) - \left(N_A - N_A^0\right)\varepsilon_A \tag{2.3.79}$$

where E^{N}_{block} is the total energy of MD block containing N atoms at zero kelvin and $E^{N^0}_{\text{block}}$ is the energy of a defect free block of atoms; ε_A is the energy per atom in a pure metal [384]. The formation volume of the defect can also be defined as

$$V^{f}_{\text{def}} = \left(V^{N}_{\text{block}} - V^{N^0}_{\text{block}}\right) - \left(N_A - N^0_A\right)\Omega_A \tag{2.3.80}$$

where Ω_A is the volume per atom in a pure metal; these equations can be used for systems containing $(N - N^0)$ defects.

MD computer simulations on pure bcc iron determined the formation energy and formation volume of a vacancy to be 1.70 eV and $0.82\Omega_0$. The binding energy of the nearest-neighbor pair of vacancies was determined as 0.14 eV; the migration energy of single vacancy for the nearest neighbor was calculated to be 0.78 eV. Three stable self-interstitial configurations were the <110>, <111> dumbbell and <111> crowdion; their formation energies (and volumes in brackets) were determined as 4.87 eV ($0.76\Omega_0$), 5.00 eV ($0.63\Omega_0$) and 5.00 eV ($0.64\Omega_0$) respectively. These results are in good agreement with corresponding experimental results on the system [385]. Ackland *et al.* [384] determined the corresponding defect properties for pure Cu. The vacancy formation energy was determined as 1.19 eV with a formation volume of $0.77\Omega_0$. <100> dumbbell was found to be the stable configuration for interstitials with formation energy of 3.62 eV and a formation volume of $1.2\Omega_0$. When Cu atoms were introduced as impurities in various interstitial positions in iron lattice, these were generally found to be unstable; there was a marked preference for Cu to occupy a subsitutional site and for Fe to occupy an interstitial site. The binding energy of a vacancy to a copper solute atom was found to be 0.087 eV; the migration energy of a copper atom (0.6 eV) was lower than the migration energy of an iron atom (0.73 eV).

Osetsky *et al.* [386] investigated defect clusters in bcc iron and fcc Cu using atomistic computer simulations with different interatomic potentials including short-range Johnson type, many-body Finnis–Sinclair and pseudopotentials. Using a cubic crystallite of 4394 atoms, MD simulations were carried out on the diffusion of self-interstitials in iron; periodic boundary conditions were used. Simulation temperatures were in the range 300–1900 K; mean square displacements and jump frequencies were determined [387]. Planar defect clusters containing up to 50 interstitials were simulated in the form of rigid spheroid with initial habit planes {100}, {110} and {111}. Up to 19,000 atoms were used in the study with thermal aging and relaxation of the system to determine structural evolution of defect clusters. Vacancy clusters in Cu were found to be stable in the {111} plane; these could decay either into stacking faults or faulted vacancy loops. Interstitial clusters tended to be in a crowdion configuration along a closed packed direction as edge dislocation loops. Biborski *et al.* [388] have reported on canonical MC simulations on vacancy formation and ordering correlations in *A–B* intermetallics.

2.3.6.6.3 Hydrogen Embrittlement in Metals

Hydrogen is well known to significantly degrade the mechanical properties of metals [389]. In hydrogen-assisted cracking, the crack initiation and propagation are influenced by hydrogen and stress. While fracture may be a brittle or a plastic one, the presence of hydrogen can lower the failure stress. Due to complexities involved, there have been a few atomistic simulations of this phenomenon. The behavior of hydrogen in metals has been investigated using the quasi-atom theory [390,391]. Daw and Baskes [392] have reported on a semi-empirical, quantum mechanical calculation in Ni based on EAM potential approach wherein each atom is embedded in a host lattice of all other atoms. With the embedding energy depending only on the immediate environment, the impurity hydrogen experiences a locally uniform electron density. The potential for H–Ni was established by using the heat of solution and the migration energy of H in Ni.

Atomistic computer simulations were carried on a semi-infinite slab of Ni, 17 layers thick in [111] direction; periodic boundary conditions were used in $[1\bar{1}0]$ and $[11\bar{2}]$ directions. External stresses were applied along the [111] direction; the response of a perfect crystal to the applied stress is to expand according to symmetry considerations. However in the presence of point defects such as vacancies or local perturbation, the slab tended to break down after a critical stress was applied and resulted in the creation of new free surfaces in the central region. While a stress of 0.13 eV/Å^3 was required in the presence of four vacancies, the presence of a H atom that tended to occupy sites adjacent to the mid-plane near vacancies, the critical stress was reduced to 0.11 eV/Å^3. A higher concentration of H resulted in further reductions in stress values.

Zhong *et al.* [393] have reported on atomistic MD simulations of hydrogen embrittlement in palladium with an aim to clarify reaction mechanisms. According to "decohesion mechanism" embrittlement is caused by a decreased bond strength in the presence of H [394]; "hydrogen-related phase change mechanism" on the other hand suggests the stabilization of a metal hydride phase under stress [395] and "hydrogen-enhanced local plasticity" postulates a ductility enhancement at crack tips for the initiation/propagation of fracture [396]. Zhong *et al.* investigated the elastic response and mechanical stability of bulk Pd to uniaxial tensile stress for a range of temperatures and hydrogen concentrations. Extra degrees of freedom were introduced through coupling the system to an external heat bath or to a pressure reservoir to determine system deformations during the fracture process. A many-body alloy (MBA) potential based on *ab initio* calculations was used to investigate the structure and dynamics of the system [397]. The uniaxial stress was increased in small steps and the system was allowed to equilibrate after every pressure change; unit cell dimensions in the direction of force were found to increase substantially after reaching the critical stress. This structural change is associated with the development of long cracks leading to instability.

Critical stress showed a rapid linear increase with increasing temperature and a linear decrease with increasing hydrogen concentrations; both these factors tend to enhance

plasticity. Hydrogen atoms have a very small mass and size and are therefore expected to have a large diffusion constant. These atoms are most stable in an expanded lattice and tend to accumulate near fluctuations or stress-induced defects in the Pd matrix. These defects constitute mechanical weak points leading to locally enhanced plasticity and fracture under the application of tensile stresses. Bulk of the matrix will be relatively unaffected indicating minimal structural change outside the crack region. These atomistic computer simulations support the "hydrogen-enhanced local plasticity mechanism of fracture" [396,398].

Xu *et al*. [399] have carried out atomistic simulations on H embrittlement of Ni in the presence of significant amounts of plastic deformation. MD simulations were carried out using EAM potentials from Baskes *et al*. [400]. A 3D crack-tip model was designed with 16,632 Ni atoms and up to 653 H atoms. Computer simulations showed that H tended to localize plastic deformation so that elongation decreased near a fracture while the hydrogen-free region showed good ductility. The formation of nickel hydride is also known to cause brittle failure [401]. The macroscopic fracture occurred by the propagation of the crack tip into the notched area with considerable plasticity and was followed by the presence of micro-voids. With 653 H atoms in the simulation cell, a thin layer of hydrides was observed in front of the notched area in front of the crack tip which eventually led to brittle fracture.

2.3.6.7. Solidification Simulations

The basic problem of controlling the microstructure during solidification presents significant technological and scientific challenges. Recent developments in this field include the use of atomic level simulations to determine the equilibrium/nonequilibrium properties of the solid–liquid interfacial region, insights into nucleation, role of anisotropies, coupling of macroscopic fluid flow with microscopic temperature and solute fields. Some of the key developments are presented in the following section.

2.3.6.7.1 Atomistic Simulations of Dendritic Growth

Dendrites are the branched solid spikes generated during the solidification of supercooled systems and/or supersaturated alloys; their formation could significantly affect the mechanical integrity and characteristics of cast ingots of commercial alloys [402]. Dendrite type formation has been observed in diverse situations such as reaction diffusion systems, silica micelle structures, growth of bacterial colonies, etc. [403,404]. Key factors affecting dendrite formation involve diffusion and convective transport of heat/chemical constituents, capillary forces over diverse length scales. Atomic-scale processes that determine kinetics and energetics at the solid–liquid interface occur over nanometers; the dendrite tip radius typically ranges in microns with the thickness of diffusion boundary layer being two to three times larger. The modeling of such a process requires the

solution of complex free-boundary problem along with an accurate computation of surface tension. In addition to a steady-state growth under zero capillarity, the microscopic solvability theory incorporates interfacial free energy in the solidification theory [405,406]. Hoyt *et al.* [407] have provided an extensive review on atomistic and continuum modeling of dendritic solidification. Some of the atomistic features of crystallization are presented below.

During atomistic computer simulations of dendrite growth, the transport of heat away from the growing solid controls the rate of crystallization; the temperature at a given point along the moving crystal/melt interface depends on the curvature, normal velocity, melting point and the latent heat. Crystalline anisotropy in the thermodynamic and kinetic interfacial properties plays a crucial role in the growth direction and velocity. Crystal–melt interfacial free energy has been computed using MD simulations using two different approaches. A four-step cleaving process involves the reversible application and removal of external potential to form a crystal–melt interface from separate bulk solid and liquid systems [408]. A modification of this technique was used to compute the energy difference between solid Cu and molten Sn using modified EAM potentials [409]; the interatomic interactions between Cu and Sn were slowly switched off during extended simulations. Another technique uses MD computations of equilibrium fluctuations of the height of the solid–liquid boundary to extract interface stiffness [410]. This approach was used to investigate diverse problems such as Ising models, amorphous polymer films, surface step-edges, and liquid–vapor system using Lennard–Jones potentials [411,412].

The constant of proportionality between the velocity of a planar solid–liquid interface and its undercooling is known as the kinetic coefficient; the growth velocity of the interface is determined by the difference between the average transition rates of attachment/detachment of atoms from the melt to the crystal [413]. The temperature dependence of the interface velocity can be written as

$$V = V_0[1 - \exp(-\Delta\mu k_B T)] \tag{2.3.81}$$

where $\Delta\mu$, the difference in chemical potential between bulk solid and liquid phases, is the thermodynamic driving force; V_0 represents the maximum growth rate at infinite driving force. There are two main mechanisms of crystal growth. When V_0 is related to the diffusivity in the liquid phase, crystallization requires significant structural rearrangement which can become very slow at low temperatures [414]. However for pure metals, crystal growth occurs readily at low temperatures with crystallization determined by the frequency of collisions of liquid atoms rather than by time scales for diffusive motion [415]. MD simulations and *ab initio* approaches have been used for directly computing chemical potentials and associated crystalline anisotropy of dendritic growth in pure metals.

2.3.6.7.2 Phase Field Models

The phase-field method has emerged as a powerful computational approach for modeling mesoscale morphological and microstructural evolution in materials. Based on the concept of a diffuse interface, the origins of phase-field equations are based on the works of Cahn and Hilliard [416] and Allen and Cahn [417]. Microstructures are compositional/structural inhomogeneities that may consist of spatially distributed phases of different compositions/structures, grains of different orientations, structural defects; these features may have length scales ranging from microns to nanometers [418]. The system tends to lower its total free energy including the chemical free energy, interfacial energy, strain energy, magnetic and electrostatic energy, etc., through microstructural evolution with interfacial regions separating domains of different composition/structure. In the phase-field method, the interface between two phases is treated as a finite width diffuse region with a gradual variation of physical quantities; a phase field or an order parameter $\phi(x)$ is introduced to distinguish one phase from the other [419]. The phase-field method bridges the gap between the macroscopic and microscopic descriptions of solidifying structures during solidification in undercooled melts.

MD simulations have been carried out to determine parameters such as anisotropy of surface energy and kinetic coefficients that are difficult to measure experimentally [420,421]. The atomistic level solid–liquid interface is generally quite diffuse and can change over 5–8 atomic distances. During the solidification of microstructures, distances involved typically range from a few μm to few mm and associated time scales are in the range of msec to a few hours; these are much larger than typical distances (Å) and time scales (picoseconds to nanoseconds) during MD simulations. The phase-field method fills the gap between the microscopic and macroscopic descriptions by coarse-graining results from MD simulations and by combining them with macroscopic equations so that sharp interface equations are recovered for the case of a vanishing interface.

The phase-field model describes a micro-structure using a set of field variables that vary continuously across diffuse interfacial regions. The total energy of an inhomogeneous microstructure is described by a set of conserved and nonconserved variables. For example, local free-energy density could be represented by a field variable ϕ in a double-well form as

$$f(\phi) = 4\Delta f\left(-\frac{1}{2}\phi^2 + \frac{1}{4}\phi^4\right) \tag{2.3.82}$$

where Δf is the potential height between two states with the minimum free energy; states with $\phi = 1$ and -1 respectively represent the solid and liquid states. Another formulation uses a double-obstacle potential

$$f(\phi) = \Delta f\left(1 - \phi^2\right) + I(\phi) \tag{2.3.83}$$

with $I(\phi) = \infty$ for $|\phi| > 1$ and zero otherwise. Sometimes, more than one field variable is used or fields of one type are coupled with another, for example, phase field is coupled with a temperature or a concentration or an orientation field. The existence of interfaces is inherent to microstructural evolution; the excess free energy associated with interfacial inhomogeneities is the interfacial energy. The free energy of a microstructure can be represented in terms of bulk and interfacial energies:

$$F = F_{\text{Bulk}} + F_{\text{int}} = \int_v \left[f(\phi) + \frac{1}{2} k_\phi (\nabla \phi)^2 \right] \mathrm{d}V \tag{2.3.84}$$

where k_ϕ is the gradient energy coefficient, that can be expressed in terms of pair-wise interatomic interaction energies [422]. In solid-state phase transformations, the interfacial energy anisotropy can easily be introduced through gradient terms. The evolution of field variables can be obtained by solving the following Cahn–Hilliard and Allan–Cahn equations:

$$\frac{\partial c_i(r,t)}{\partial t} = \nabla M_{ij} \nabla \frac{\delta F}{\delta c_j(r,t)} \tag{2.3.85}$$

$$\frac{\partial n_p(r,t)}{\partial t} = -L_{pq} \frac{\delta F}{\delta n_q(r,t)} \tag{2.3.86}$$

where M_{ij} and L_{pq} represent mobility of atoms; field variables c's are conserved and η's are nonconserved. A number of phase-field simulations employ second-order difference equations on a uniform spatial grid and explicit time-stepping. Semi-explicit Fourier-spectral algorithms have also been used to solve these equations [423].

Provatas *et al.* [424] investigated the solidification microstructures on an adaptive finite element grid. The adaptive mesh significantly reduced the computational complexity of solving phase-boundary problems with the interface arclength; the usage of dynamic data structures also permitted the simulation of large sample sizes at very low undercooling. Dendrite tip velocities at intermediate and high undercoolings were found to agree well with the solvability theory. At low undercooling, the tip velocity in the presence of side branches was found to be different from that predicted by the solvability theory. Other applications of phase-field method include dendritic solidification with inherent separation of various length scales [425,426], solid state phase transformations [427–429], grain growth [430], phase transformations in thin films and surfaces [431,432], dislocation microstructures [433], crack propagation [434], electro-migration [435], etc.

2.3.6.7.3 Phase Field Crystal Models

Phase field crystal (PFC) method is one of the latest simulation approaches to investigate problems where atomic and micro-scales are tightly coupled [436]; the PFC method

operates on atomic length and diffusive time scales that are much longer than typical timescales accessible by MD simulations. The PFC model was initially developed to create a bridge between the atomic scale and phase field simulations. Some of the key phenomena in materials science that have been investigated using PFC techniques include liquid–solid transitions, colloid patterning, grain-boundary dynamics, crack propagation, Kirkendall effect, vacancy transport, foams, liquid crystals, etc. [437–446]. By resolving the crystal field, the PFC method is able to take into consideration the influence of defects, elastic interactions and large-scale distortions. Rational material design requires a fundamental understanding of evolution of properties while approaching mesoscale from collective assemblies of nanoscale objects. It then becomes important to provide a unified description of many scales being resolved. The basic idea in PFC is not to start with an MD description at nanoscale but with a DFT description whose equilibrium solutions are periodic density modulations. A system with underlying periodicity can be represented by a density wave with a slowly varying amplitude and uniform phase except in the vicinity of defects. The PFC can address the issue of nanoscale strains and their coupling from nanoscale to the continuum.

Both DFT and PFC approaches represent free energy through a functional of its density; both however use different functionals to achieve different goals [447]. Classical DFT creates a mean-field description of crystal density $n(r)$ to represent material properties; crystal density is sharply peaked around mean atomic positions and requires a large number of terms of reciprocal lattice density waves in the expansion of number density. The PFC approach uses much simplified functional that significantly limits the number of reciprocal vectors in the sum while extending both length and time scales as much as possible. The free energy PFC functional for an N-component mixture can be described by two contributions: a local free energy for N constituents and an excess free energy due to interactions. While the first term drives the density fields to become uniform, the second term drives density fields to become periodic by creating minima in free energy. The free energy functional can be written as

$$\frac{\Delta F}{k_B T} = \int \mathrm{d}r \left\{ \frac{\Delta F_{\mathrm{id}}}{k_B T} + \frac{\Delta F_{\mathrm{ex}}}{k_B T} \right\} \tag{2.3.87}$$

where F_{id} and F_{ex} respectively represent the ideal and excess energy due to correlative interactions. The ideal energy gives entropic contributions and exchange energy takes into account two particle inter-particle interactions. Let $F(\rho)$ represent the coarse-grained free energy functional of a d-dimensional system; a simple form of F that gives rise to triangular lattice equilibrium state [447] can be written as

$$F\{\rho(x)\} = \int d^d\tilde{x} \left| \rho \left(\alpha \Delta T + \lambda \left(q_0^2 + \nabla^2 \right)^2 \right) \frac{\rho}{2} + u \frac{\rho^4}{4} \right] \tag{2.3.88}$$

where α, λ, q_0, and u are related to material properties [448]. The dynamics of slowly varying amplitude and phase describes fluctuations about a given set of lattice vectors which must be covariant with respect to rotations of these lattice vectors. Equations of motion for the density n and each of the concentration field c_i follow conserved dissipative dynamics:

$$\frac{\partial n}{\partial t} = \nabla \cdot \left(M_n \nabla \frac{\delta F}{\delta n} \right) + \zeta_n \tag{2.3.89}$$

$$= \nabla \cdot \left(M_n \nabla \left\{ n - \eta \frac{n^2}{2} + \chi \frac{n^3}{3} + w \Delta F_{\text{mix}}(\{c_i\} - C_{\text{eff}} n) \right\} \right) + \zeta_n \tag{2.3.90}$$

where M_n and C_{eff} respectively represent the mobility of density and effective correlation function and ζ_n is the noise term representing thermal and concentration fluctuations. In a three-component ternary system, equilibrium is defined by the co-existence of bulk phases; the free energy minimization is defined by a common tangent to the free energy wells of co-existing phases. Detailed procedures have been developed for calculating phase diagrams for PFC models [449,450].

PFC models can currently take into account multi-component interactions between solute atoms and defects, atomic-scale effects of different solutes and their diffusion; it is possible to investigate solidification and precipitation from the computed phase diagrams. Dendritic solidification occurs when supercooled liquid is quenched into the solid/liquid coexistence region. With increasing time, the solidifying crystal develops the characteristic symmetry of the underlying lattice, with clear evidence for a discontinuous change in density across the solid/liquid interface. The simulation generally shows multiple diffusing species, density changes and anisotropy in surface tensions. PFC modeling of solute clustering and precipitation hardening during initial stages of heat treatment in Al–Cu–Mg alloys has also been reported [451].

Goldenfeld [452] has used a renormalization group approach for multi-scale simulation on PFC modeling of polycrystalline materials. The order parameter representing nanoscale density profile was constructed from slowly varying amplitude and phase that needed to satisfy rotationally covariant equations. The amplitude describes the maximum variations in the density through the unit cell and the phase describes uniform spatial translations. The phase of the density was used as a dynamic variable for describing spatially modulated nanoscale structure in a mesoscopic system. Through effective adaptive mesh refinement, it was possible to carry out realist modeling of large-scale materials processing and behavior.

2.3.6.7.4 Atomistic Simulations on Interfaces

A prerequisite of phase-field simulations is the accurate knowledge of material parameters such as interfacial energies (γ), kinetic parameters, and the velocity-dependent partition

function in terms of mole fractions of solid and liquid sides of the interface. It is important to understand the influence of impurities, symmetries, segregation, pressure and temperature on interfacial energies and mobilities in order to control microstructural evolution. The magnitude of interfacial free energy represents a critical term in the reversible work to form a solid nucleus; its structural variations can lead to nucleation of metastable phases in deeply undercooled melts. Atomistic simulations have been used extensively for the calculation of γ for a number of metals based on EAM potentials [453,454]. The average Turnbull coefficients α (slope of $\alpha\rho^{-2/3}$ vs. latent heat of melting plot) was determined to be 0.55 for fcc phases. A trend of lower average values of α was observed for bcc structure relative to fcc phase [455]. Laird and Davidchack carried out a direct calculation of crystal–melt interfacial free energies using MD simulations [456]. The value of γ was determined using thermodynamic integration technique using moving cleaving walls in order to resolve small anisotropy in γ that plays a crucial role determining the kinetics and morphology of dendritic growth [457]. Simulations were based on hard sphere and Lennard–Jones potentials and used specially constructed cleaving walls to reversibly cleave bulk liquid and crystal systems in cleaved planes. The value of γ for bcc melt was found to be 25% lower than for fcc melt, a result consistent with experimental/computational investigations on fcc-forming systems that show preferential formation of bcc nuclei in the initial stages of crystallization. The predicted results showed good agreement with computer simulation results based on *ab initio* and EAM potential approaches and experiments [458].

Due to their large surface/volume ratios, excess interfacial Gibbs energy and interfacial stress play an important role for nanophase and structured materials. Jiang *et al.* [459] have derived general equations for the size dependence of the solid–liquid interface energy, grain boundary energy, and interfacial stress. A compressible spherical particle with diameter D was immersed in a bulk liquid; all atoms on a low dimensional crystal were assumed to lie on its surface in contact with the bulk fluid and solid–liquid interface was assumed to be diffuse.

Grain boundaries are an important structural feature in processes such as recrystallization, grain growth and optimizing their population/orientation through suitable thermo-mechanical treatment is a key aspect of materials design. An important subclass, coherent interphase boundaries (CIPB), are characterized by the structural continuation of atomic planes of interfacing lattices; these constitute one of the most important approaches used to strengthen multiphase alloys through heat treatment [460]. The microstructural evolution and the kinetics of precipitate formation are currently not well understood due to significant difficulties in measuring interface boundaries [461].

A coherency stress is usually present in multiphase solids due to differences in lattice parameters of different phases and gives rise to elastic strain energy; with misfits up to 1%, interfacial energies and strain energies can become comparable. The elastic energy can be taken into account either through atomistic calculations or as a contribution to the energy

functional in the phase-field approach [462–464]. Using the homogeneous modulus approximation with an assumption of linear dependence of lattice parameter on solute concentration, the elastic energy functional can be written as

$$E_{\mathrm{el}} = \frac{1}{2}\int_{k} B[n]\cdot|\widetilde{c}(k)|^2 \frac{d^3k}{(2\pi)^2} \tag{2.3.91}$$

In 2D, the elasticity function $B(n)$ can be approximately written in terms of various elastic constants as

$$B_{\mathrm{el}} = \frac{4(C_{11}+2C_{12})^2}{C_{11}(C_{11}+C_{12}+2C_{44})}[C_{11}C_{12}-2C_{44}] \tag{2.3.92}$$

In the absence of stress, precipitating particles tend to be spherical in shape in an attempt to minimize the surface area; however cuboidal or elongated shapes may emerge in the presence of elastic stresses that may be anisotropic in nature. The ratio of interfacial and elastic energies and degree of elastic anisotropy are key factors affecting the shape of precipitates [465,466].

Grain boundaries (GB) represent a general class of interfaces in solid state; these break the continuation of lattice planes across the boundary. A number of parameters such as lattice orientation of a GB, boundary plane inclination are used to describe GB configuration and to compute GB formation energies. Slab/cluster calculations are used extensively during GB simulations: in the slab geometry, a single defect is placed in the center of the cell with periodic boundary conditions in the plane of GB. In the cluster geometry, a GB is imposed on a bulk crystal of finite size; periodic boundary conditions are not used. The effect of free surfaces on the electronic structure, geometrical configuration, and total energy needs to be carefully accounted for; these effects may also depend strongly on GB inclination or disorientation. An alternative approach is to use 3D supercells with periodic boundary conditions with a pair of compensating defects. GB energies constitute an important input for phase field simulations; but a consistent description in terms of five orientation parameters is still not available. First-principle GB simulations have been restricted to small system sizes and special GB orientations; these basically provide insights on atomistic mechanisms of various GB properties such as vacancy formation, impurity precipitates, GB sliding and migration, etc. [467,468]. Empirical potential computations have yielded large information of GB energies, boundary excess volumes and on the role of five degrees of freedom [469].

Bouar *et al.* [470] investigated the mechanism of formation of chessboard-like structure during coherent decomposition of alloys in the presence of orientation variants. The coherency strain was accommodated through spatial rearrangement of orientation variants of precipitates leading to formation of mesoscale microstructure, for example, in Co–Pt and (CuAu)–Pt systems [471]. Microstructures in both alloys were pseudo

two-dimensional; the microstructure in Co–Pt system consisted of cubic $L1_2$ and tetragonal $L1_0$ phases and a disordered fcc and ordered $L1_0$ phases were observed in the (CuAu)–Pt system. The computational model was based on the continuum stochastic field kinetic equations for the composition and long-range-order parameter profiles. No constraint was placed on the possible sequences of structural patterns evolving during simulations; strain-induced interaction between coherent precipitates of low symmetry phase and crystallographic transitions were key factors affecting microstructure evolution. The nucleation during the isothermal annealing produced a tweed pattern that later transformed into a microstructure with domains of irregular shapes.

2.3.7. CONCLUDING REMARKS

Nowadays, computer simulations are becoming just as important as experiments in developing a fundamental understanding of underlying physics and chemistry of a wide variety of systems. Simulations involving hundreds of millions of atoms have gone from being a computational curiosity to being a routine scientific tool to study diverse phenomena [472]. The need to understand the properties at atomic level and control the properties of solids with chemical specificity has increased tremendously; it is becoming essential to understand the effects of specific atomic-scale features on the properties of real solids. Describing equilibrium phenomena of solids at finite temperatures is very complex and seemingly intractable as it requires knowledge of all possible accessible configurations and total energies of the system; a variety of approaches are being developed to overcome these problems using fundamentals of theoretical physics. It is anticipated that atomistic simulations will continue to lead to new insights and provide a framework for numerical experiments to determine the role of chemical interactions, crystal structures, mechanisms, etc. The ability to observe the formation of metastable phases and heterogeneous nucleation in atomistic simulations opens several new directions for future work.

There is a growing body of literature on atomistic modeling and simulations that are generally focused on model validation based on comparisons between experimental and computed values. These are based either on empirical approaches using classical potentials or on first-principles quantum mechanical calculations. In order to have a real impact, computer simulation needs to go beyond the postprediction of experimental results and should start examining new systems. With peta-scale computing becoming widely available, computing power is no longer a limitation for studying larger systems, slow processes, complex behavior, etc. Due to tandem improvements in simulation techniques and computing power, more and more powerful tools are currently becoming available. It is important to harness these advances to help develop next-generation research to solve longstanding problems and pressing needs of coming years.

REFERENCES

[1] N. Metropolis, S. Ulam, J. Am. Stat. Assoc. 44 (1949) 335.
[2] N. Metropolis, A.W. Rosenbluth, M.N. Rosenbluth, A.H. Teller, E. Teller, J. Chem. Phys. 27 (1953) 1087.
[3] A. Papoulis, Probability, Random Variables, and Stochastic Processes, second ed., McGraw-Hill, New York, 1984p. 515.
[4] D. Frenkel, B. Smit, Understanding Molecular Simulation, From Algorithms to Applications, Academic Press2002.
[5] K. Binder, J.L. Lebowitz, M.K. Phani, M.H. Kalos, Acta Metall. 29 (1981) 1655.
[6] I.R. McDonald, Mol. Phys. 23 (1972) 41.
[7] D. Stauffer, An Introduction to Percolation Theory, Taylor and Francis, London, 1985.
[8] M.H. Calos, P.A. Whitlock, Monte Carlo Methods, Basics, vol. 1, John Wiley, New York, 1986.
[9] E.D. Cashwell, C.J. Evert, A Practical Manual of Monte Carlo Methods for Random Walk Problems, Pergamon, New York, 1959.
[10] K. Binder, Z. Phys. B 43 (1981) 119.
[11] R. Khanna, V. Sahajwalla, Scripta Metall. 40 (1999) 1289.
[12] R. Khanna, T.R. Welberry, Acta Cryst. A 46 (1990) 970.
[13] K. Kremer, K. Binder, Comput. Phys. Rep. 7 (1988) 259.
[14] D. Knuth, The Art of Computer Programming, vol. 2, Addison Wesley, Reading, MA, 1969.
[15] A. Compagner, Am. J. Phys. 59 (1991) 700.
[16] A.L. Garcia, W. Wagner, Phys. Fluids 12 (2000) 2621.
[17] L. Verlet, Phys. Rev. 198 (1967) 98.
[18] W.C. Swope, H.C. Anderson, P.H. Berens, K.R. Wilson, J. Chem. Phys. 76 (1972) 637.
[19] M. Parrinello, A. Rahman, Phys. Rev. Lett. 45 (1980) 1196.
[20] M. Parrinello, A. Rahman, J. Appl. Phys. 52 (1981) 1782.
[21] H.C. Anderson, J. Chem. Phys. 72 (1980) 2384.
[22] S. Nose, J. Chem. Phys. 81 (1984) 511.
[23] G.J. Martyna, D.J. Tobias, M.L. Klein, J. Chem. Phys. 101 (1994) 4177.
[24] J.M. Haile, H.W. Graben, J. Chem. Phys. 73 (1980) 2412.
[25] H. Tanaka, K. Nakanishi, N. Watanbe, J. Chem. Phys. 78 (1983) 2626.
[26] S.D. Bond, B.J. Leimkuhler, Acta Numer. 16 (2007) 1.
[27] P. Hohenberg, W. Kohn, Phys. Rev. B 136 (1964) 864.
[28] W. Kohn, L.J. Sham, Phys. Rev. A 140 (1965) 1133.
[29] J. Hafner, C. Wolverton, G. Ceder, MRS Bull. 31 (2006) 659.
[30] J.H.P. Perdew, M. Ernzernhof, K. Burke, J. Chem. Phys. 96 (1992) 1280.
[31] J. Andzelm, E. Wimmer, J. Chem. Phys. 78 (1983) 2626.
[32] R. Wu, A.J. Freeman, G.B. Olson, Science 265 (1994) 376.
[33] K. Nørskov, T. Bligaard, J. Rossmeis, C.H. Christensen, Nat. Chem. 1 (2009) 37.
[34] S.P. Tang, A.J. Freeman, Phys. Rev. B 47 (1993) 1460.
[35] S. Hao, W.K. Liu, B. Moran, F. Vernary, G.B. Olson, Comput. Methods A Mech. Engrg. 193 (2004) 1865.
[36] G. Casnyi, T. Albaret, M.C. Payne, A. de Vita, Phys. Rev. Lett. 93 (2004) 175503.
[37] T. Burkert, L. Nordstrom, O. Eriksson, O. Heinonen, Phys. Rev. Lett. 93 (2004) 27203.
[38] R. Wu, A.J. Freeman, J. Magn. Mater. 100 (1991) 497.
[39] J. Kudmovsky, V. Drchal, C. Blaas, P. Weiberger, I. Truek, P. Bruno, Phys. Rev. B 62 (2000) 15084.
[40] M. Sugihara, V. Buss, P. Entel, J. Hafner, J. Phys. Chem. B 108 (2004) 3673.
[41] S.H. Wei, L.G. Ferreira, J.E. Bernard, A. Zunger, Phys. Rev. B 42 (1990) 9622.
[42] C. Wolverton, X.Y. Tan, R. Vijayaraghavan, V. Ozolins, Acta Mater. 50 (2002) 2187.
[43] F.A. Reboredo, A.J. Williamson, Phys. Rev. B 71 (2005) 121105.
[44] J.R. Beeler, Phys. Rev. 150 (1966) 470.
[45] A. Chatterjee, D.G. Vlachos, J. Comput. Aided Mater. Des. 14 (2007) 253.
[46] T.P. Schulze, Phys. Rev. E 65 (2002) 036704.
[47] A.B. Bortz, M.H. Kalos, J.L. Labowitz, J. Comput. Phys. 17 (1975) 10.

[48] M.A. Snayer, A. Chatterjee, D.G. Vlachos, Comput. Chem. Eng. 29 (2004) 704.
[49] J.P. DeVita, L.M. Sander, P. Smereka, Phys. Rev. B 72 (2005) 205421.
[50] Y. Cao, D.T. Gillespie, L.R. Petzold, J. Chem. Phys. 122 (2005) 014116.
[51] M. Katsoulakis, A.J. Majda, D.G. Vlachos, Proc. Nat. Acad. Sci. U.S.A. 100 (2003) 782.
[52] R.L. McGreevy, L. Pusztai, Mol. Simul. 1 (1988) 359.
[53] R.L. McGreevy, M.A. Howe, Annu. Rev. Mater. Sci. 22 (1992) 217.
[54] D.R. Mckenzie, C.R. Davis, D.J.H. Cockayne, D.A. Muller, A.M. Cassallo, Nature 355 (1992) 622.
[55] R.L. McGreevy, L. Pusztai, Proc. R. Soc. A 430 (1990) 241.
[56] J.D. Wicks, R.L. McGreevy, Phase Transit. 61 (1997) 195.
[57] J.C. McLaughlin, J. Mol. Graphic Modell. 17 (1999) 275.
[58] R. Evans, Mol. Simul. 4 (1990) 409.
[59] S. Duane, A.D. Kennedy, B.J. Pendleton, D. Roweth, Phys. Lett. 195 (1987) 216.
[60] A.D. Kennedy, B. Pendleton, Nucl. Phys. B 607 (2001) 456.
[61] E. Akhmatskaya, S. Reich, Nucl. Sci. Technol. 2 (2011) 447.
[62] A.Z. Panagiotopoulos, Mol. Phys. 61 (1987) 813.
[63] A.Z. Panagiotopoulos, N. Quirke, M. Stapleton, D.J. Tildesley, Mol. Phys. 63 (1988) 527.
[64] F.W. Tavares, S.I. Sandler, J. AlChE 43 (1997) 218.
[65] J.I. Seipman, S. Karaborni, B. Smit, J. Am. Chem. Soc. 115 (1993) 6454.
[66] B. Chen, J.I. Seipman, J. Phys. Chem. B 103 (1999) 5370.
[67] M. Rao, B.J. Berne, J. Chem. Phys. 71 (1979) 129.
[68] R. Khanna, T.R. Welberry, Acta Cryst. A 46 (1990) 975.
[69] P.J. Rosky, J.D. Doll, H.L. Friedman, J. Chem. Phys. 69 (1978) 4628.
[70] M. Mezei, Mol. Simul. 5 (1991) 405.
[71] T.G.H. Vlugt, M.G. Martin, B. Smit, J.I. Siepman, R. Krishna, Mol. Phys. 94 (1998) 727.
[72] M.N. Rosenbluth, A.W. Rosenbluth, J. Chem. Phys. 23 (1955) 356.
[73] R.F. Cracknell, D. Nicholson, N.G. Parsonage, H. Evans, Mol. Phys. 71 (1990) 931.
[74] M. Mezei, Mol. Phys. 61 (1987) 565.
[75] F. Wang, D.P. Landau, Phys. Rev. Lett. 86 (2001) 2050.
[76] N. Rathore, J.J. de Pablo, J. Chem. Phys. 116 (2002) 7225.
[77] M. Troyer, S. Wessel, F. Alert, Phys. Rev. Lett. 90 (2003) 120201.
[78] C. Yamaguchi, Y. Okabe, J. Phys. A 34 (2001) 8781.
[79] B.J. Shulz, K. Binder, M. Muller, D.P. Landau, Phys. Rev. E 67 (2003) 067102.
[80] C. Zhou, R.N. Bhat, Phys. Rev. E 72 (2005) 025701.
[81] R.H. Swendson, J.S. Wang, Phys. Rev. Lett. 57 (1986) 2607.
[82] D.J. Earl, M.W. Doem, Phys. Chem. Chem. Phys. 7 (2005) 3910.
[83] U.H.E. Hansmann, Chem. Phys. Lett. 281 (1997) 140.
[84] D.A. Kofke, J. Chem. Phys. 120 (2004) 10852.
[85] Q.L. Yan, J.J. de Pablo, J. Chem. Phys. 113 (2000) 1276.
[86] E. Bittner, A. Nuβbaumer, W. Janke, Phys. Rev. Lett. 101 (2008) 130603.
[87] H.B. Cullen, Thermodynamics and an Introduction to Thermostatics, John Wiley & Sons, New York, 1985.
[88] P.A. Apte, I. Kusaka, Phys. Rev. E 73 (2006) 016704.
[89] J.Q. Broughton, G.H. Gilmer, J. Chem. Phys. 79 (1983) 5095.
[90] D.A. Kofke, Mol. Phys. 78 (1993) 1331.
[91] S. Habershon, D.E. Manopoulos, J. Chem. Phys. 135 (2011) 224111.
[92] S. Ono, S. Kondo, in: S. Flugge (Ed.), Encyclopaedia of Physics, Springer, Berlin, 1960, p. 10.
[93] J.G. Kirkwood, F. Buff, J. Chem. Phys. 17 (1949) 338.
[94] J. Rowlinson, B. Widom, Molecular Theory of Capillarity, Clarendon, Oxford, 1982.
[95] J. Rowlinson, J. Phys. Cond. Matt. 6A (1994) 1.
[96] K. Miyazaki, J.A. Barker, G.M. Pound, J. Chem. Phys. 64 (1976) 3364.
[97] O. Matsuoka, E. Clementi, M. Yoshimina, J. Chem. Phys. 64 (1976) 1351.
[98] M.G. Melchor, F. Bresme, J. Alejandre, J. Chem. Phys. 122 (2005) 104710.
[99] C.Y. Lee, H.L. Scott, J. Chem. Phys. 73 (1980) 4591.

[100] C.H. Bennet, J. Comput. Phys. 22 (1976) 245.
[101] G.M. Torrie, J.P. Valleau, Chem. Phys. Lett. 29 (1974) 578.
[102] G.J. Ackland, M.W. Finnis, Philos. Mag. A 54 (1986) 301.
[103] M.J. Norget, R. Flecher, J. Phys. C 17 (1970) L190.
[104] G.M. Finbow, R.M. Lyndon-Bell, I.R. McDonald, Mol. Phys. 92 (1997) 705.
[105] R. Khanna, V. Sahajwalla, Acta Mater. 53 (2005) 1205.
[106] J. Hautman, M.L. Klein, Phys. Rev. Lett. 67 (1991) 1763.
[107] G. Saville, J Chem. Soc. Farad. Trans. 11 (1977) 1122.
[108] J.D. Halverson, C. Maldarelli, A. Couzis, J. Koplik, R. Soc. Chem. 6 (2009) 1297.
[109] E.B. Webb, J.J. Hoyt, G.S. Grest, Curr. Opin. Sol. State Mater. Sci. 9 (2006) 174.
[110] H. Nakanishi, M.E. Fisher, J. Chem. Phys. 78 (1983) 3279.
[111] T. Kerle, J. Klein, K. Binder, Phys. Rev. Lett. 77 (1996) 1318.
[112] K. Binder (Ed.), Monte Carlo Methods in Statistical Physics, Springer, Berlin, 1979.
[113] D.W. Heerman, Phys. Rev. Lett. 52 (1984) 1126.
[114] M.J.L. Sangster, M. Dixon, Adv. Phys. 25 (1976) 247.
[115] K. Binder, J. Comput. Phys. 59 (1985) 1.
[116] J.E. Hillard, in: H.I. Aronson (Ed.), Phase Transformations, American Society of Metals, Metals Park, OH, 1970.
[117] R.V. Hockney, J.W. Eastwood, Computer Simulations Using Particles, McGraw Hill, New York, 1981.
[118] K. Binder, Phys. Rev. A 29 (1984) 341.
[119] R.F. Abraham, Phys. Rev. Lett. 50 (1983) 978.
[120] M. Parrinello, A. Rahman, Phys. Rev. Lett. 45 (1980) 1196.
[121] K. Binder, Z. Phys. B 43 (1981) 119.
[122] R. Khanna, V. Sahajwalla, Scripta Met. 40 (1999) 1289.
[123] J.M. Sanchez, D. de Fontaine, Phys. Rev. B 21 (1980) 216.
[124] D.W. Wood, J. Phys. C 5 (1972) L 181.
[125] P.G. Shewman, Diffusion in Solids, McGraw Hill, New York, 1963.
[126] M.I. Mendelev, Y. Mishin, Phys. Rev. B 80 (2009) 144111.
[127] D.R. Wheeler, J. Newman, J. Chem. Phys. 108 (2004) 18362.
[128] D. Paschek, R. Krishna, Langmuir 17 (2001) 247.
[129] R.Q. Snurr, J. Karger, J. Phys. Chem. B 101 (1997) 6469.
[130] S.J. Goodbody, K. Watambe, D. MacGowan, J.P.R. Walton, N. Quirke, J. Chem. Soc. Farad. Trans. 87 (1991) 1951.
[131] A.E. Carlsson, Solid State Physics, vol. 43, Academic Press1990p. 1.
[132] W.A. Harrison, Electronic Structure and the Properties of Solids, W.H. Freeman, San Francisco, 1980p. 253.
[133] R.G. Gordon, Y.S. Kim, J. Chem. Phys. 56 (1972) 3122.
[134] A. Dalgarno, W.D. Davison, Adv. At. Mol. Phys. 2 (1966) 1.
[135] E.S. Machlin, Interatomic Potentials and Lattice Defects, AIME, Warrendale, PA, 1981p. 33.
[136] U. Lundman, W.D. Luedke, Atomistic Simulation of Materials—Beyond Pair Potentials, Plenum Press, New York, 1989p. 443.
[137] G.C. Maitland, M. Rigby, E.B. Smith, W.A. Wakeham, Intermolecular Forces, Clarendon Press, Oxford, 1981.
[138] M.J. Sangster, M. Dixon, Adv. Phys. 25 (1976) 247.
[139] M.P. Allen, T.J. Tildesley, Computer Simulation of Liquids, second ed., Clarendon Press, Oxford, 1990.
[140] F.H. Stillinger, T.A. Weber, Phys. Rev. B 31 (1985) 5262.
[141] K. Maeda, V. Vitek, A.P. Sutton, Acta Metall. 30 (1982) 2001.
[142] K. Fuchs, Proc. R. Soc. Lond. A 153 (1936) 622.
[143] K.W. Jacobsen, J.K. Norskov, M.J. Puska, Phys. Rev. B 35 (1987) 7423.
[144] M. Basklas, M. Daw, B. Dodson, S. Foils, MRS Bull. XIII (2) (1988) 28.
[145] M.S. Daw, M.I. Baskes, Phys. Rev. B 29 (1984) 6433.

[146] F. Ercolessi, J.B. Adams, Europhys. Lett. 26 (1994) 583.
[147] M.I. Mendelev, S. Han, D.J. Srolovitz, G.J. Ackland, D.Y. Sun, M. Asta, Philos. Mag. 83 (2003) 3977.
[148] D.J. Tildesley, P.A. Madden, Mol. Phys. 42 (1981) 1137.
[149] S. Murad, K.E. Gubbins, in: ACS Symposium, Computer Modelling of Matter, vol. 86, American Chemical Society, Washington, 1978, p. 62.
[150] Reference [134], p. 21.
[151] D.J. Evans, R.O. Watts, Mol. Phys. 32 (1976) 93.
[152] M.W. Finnis, J.E. Sinclair, Philos. Mag. 50 (1984) 45.
[153] M.I. Mendelev, D.J. Srolovitz, Phys. Rev. B 66 (2002) 014205.
[154] K. Binder, J.L. Lebowitz, M.K. Phani, M.H. Kalos, Acta Metall. 29 (1981) 1655.
[155] V. Sahajwalla, R. Khanna, Acta Metall. 50 (2000) 663.
[156] A. Biborski, L. Zosiak, R. Kozubski, R. Sot, V. Pierron-Bohnes, Intermetallics 18 (2010) 2343.
[157] R.A. Johnson, Phys. Rev. A 134 (1964) 1329.
[158] Y.N. Osetsky, A.G. Mikhin, A. Serra, Philos. Mag. A 72 (1995) 361.
[159] P. Ehrhart, Landolt-Bornstein Numerical Data and Functional Relationships in Science and Technology, vol. III, Springer, Heidelberg, 1991.
[160] H. Hasegawa, D.G. Pettifor, Phys. Rev. Lett. 50 (1983) 130.
[161] J.A. Rayne, B.S. Chandrasekhar, Phys. Rev. 122 (1961) 1714.
[162] M.B. Gordon, F. Cyrot-Lackmanna, M.C. Desjonqueres, Surf. Sci. 80 (1979) 159.
[163] K. Masuda, A. Sato, Philos. Mag. A 44 (1981) 799.
[164] S.M. Foiles, J.B. Adams, Phys. Rev. B 40 (1989) 5909.
[165] G.J. Ackland, D.J. Bacon, A.F. Calder, T. Harry, Philos. Mag. A 75 (1997) 713.
[166] F. Cleri, V. Rosato, Phys. Rev. B 48 (1993) 22.
[167] M.I. Baskes, Phys. Rev. B 46 (1992) 2727.
[168] M. Muller, M. Ehrhart, K. Albe, J. Phys. Cond. Matt. 9 (2007) 326220.
[169] F. Birch, J. Geophys. Res. 57 (1952) 227.
[170] A.M. Dziewonski, D.L. Anderson, Phys. Earth Plan. Inter. 25 (1981) 297.
[171] L. Koci, A.B. Belonoshoko, R. Ahuja, Geophys. J. Int. 168 (2007) 890.
[172] S.M. Foiles, Phys. Rev. B 32 (1985) 3409.
[173] M.S. Daw, M.I. Baskes, Phys. Rev. Lett. 50 (1983) 1285.
[174] F. Ercolessi, J.B. Adams, Europhys. Lett. 26 (1994) 583.
[175] B.D. Todd, R.M. Lynden-Bell, Surf. Sci. 281 (1993) 191.
[176] Y. Mishin, D. Farkas, M.J. Mehl, D.A. Papaconstantopoulos, Phys. Rev. B 59 (1999) 3393.
[177] A.P. Sutton, J. Chen, Philos. Mag. Lett. 61 (1990) 6442.
[178] G.C. Abell, Phys. Rev. B 31 (1985) 6184.
[179] H. Balamane, T. Halicioglu, W.A. Tiller, Phys. Rev. B 46 (1992) 2250.
[180] R. Biswas, D.R. Hamann, Phys. Rev. Lett. 55 (1985) 2001.
[181] R. Biswas, D.R. Hamann, Phys. Rev. B 36 (1987) 6434.
[182] M.T. Yin, M.L. Cohen, Phys. Rev. Lett. 45 (1980) 1004.
[183] J. Tersoff, Phys. Rev. Lett. 56 (1986) 632.
[184] J. Tersoff, Phys. Rev. B 37 (1988) 6991.
[185] J. Tersoff, Phys. Rev. B 38 (1988) 9902.
[186] S.J. Cook, P. Clancy, Phys. Rev. B 47 (1993) 7686.
[187] B. Bolding, H.C. Anderson, Phys. Rev. B 41 (1990) 10568.
[188] J.F. Justo, M.Z. Bazant, E. Kaxiras, V.V. Bulatov, S. Yip, Phys. Rev. B 58 (1998) 2539.
[189] B.J. Lee, Comp. Coupl. Phase Diag. ThermoChem. 31 (2007) 95.
[190] J. Tersoff, Phys. Rev. Lett. 61 (1988) 2879.
[191] D.W. Brenner, Phys. Rev. B 42 (1990) 9458.
[192] J.H. Lee, N.L. Allinger, J. Am. Chem. Soc. 111 (1989) 8576.
[193] R.A. Johnson, G.J. Dienes, A.C. Damask, Acta Metall. 12 (1964) 1215.
[194] V. Rosato, Acta Metall. 37 (1989) 2759.
[195] T.L. Lau, C.J. Forst, X. Lin, J.D. Gale, S. Yip, K.J. van Vilet, Phys. Rev. Lett. 98 (2007) 215501.
[196] M. Ruda, D. Farkas, G. Garcia, Comput. Mater. Sci. 45 (2009) 550.

[197] D.J. Hepburn, G.J. Ackland, Phys. Rev. B 78 (2008) 165115.
[198] K.O.E. Hendriksson, K. Nordlund, Phys. Rev. B 79 (2009) 144107.
[199] R. Khanna, V. Sahajwalla, Phys. Status Solid B 213 (1999) 47.
[200] R. Khanna, V. Sahajwalla, Met. Trans B 31 (2000) 2000.
[201] N.H. de Leeuw, S.C. Parker, H.M. Sithole, P.E. Ngoepe, J. Phys. Chem. B 104 (2000) 7969.
[202] A.F. Guillermet, M. Hiller, B. Jansson, B. Sundman, Met. Trans B 12 (1981) 745.
[203] H. Ohtani, T. Nishizawa, ISIJ Int. 26 (1986) 655.
[204] V. Sahajwalla, R. Khanna, Acta Mater. 47 (1999) 793.
[205] K.T. Jacob, C.B. Alcock, Acta metal. 20 (1972) 221.
[206] V. Sahajwalla, R. Khanna, Acta Mater. 50 (2002) 663.
[207] J.A. Kitchener, O.M. Bockris, D. Libermann, Faraday Soc. Dis. 4 (1948) 49.
[208] T. Konishi, K. Ohsawa, T. Abe, E. Kuramoto, Comput. Mater. Sci. 14 (1999) 108.
[209] F. Hori, Y. Kamimura, T. Tsutsumi, E. Kuramoto, J. Nucl. Mater. 228 (1996) 215.
[210] J.H. Shim, H.J. Lee, B.D. Wirth, J. Nucl. Mater. 351 (2006) 56.
[211] D. Farkas, C.G. Schon, M.S.F. De Lima, H. Goldstein, Acta Metall. 44 (1995) 409.
[212] R. Pasionot, D. Farkas, E.J. Savino, Phys. Rev. B 43 (1991) 6952.
[213] P. Olsson, I. Abrikosov, L. Vitos, J. Wallenius, J. Nucl. Mater. 321 (2003) 84.
[214] P. Olsson, I. Abrikosov, J. Wallenius, Phys. Rev. B 75 (2007) 014110.
[215] G. Bonny, R.C. Pasionot, D. Terentyev, L. Maleba, Philos. Mag. A 91 (2011) 1724.
[216] P. Olsson, J. Wallenius, K. Domain, K. Nordlund, L. Malerba, Phys. Rev. B 74 (2006) 1.
[217] M. Grujicic, Mater. Sci. Engg. A 183 (1994) 223.
[218] M. Grujicic, P. Dang, Mater. Sci. Engg. A 201 (1995) 194.
[219] R.A. Johnson, Phys. Rev. B 39 (1989) 12554.
[220] R.A. Johnson, Phys. Rev. B 41 (1990) 9717.
[221] D. Bartocha, K. Janerka, Arch. Foundary Eng. 10 (2010) 7.
[222] P. Kula, R. Pietrasik, K. Dybowski, in: 13th Int. Conf. on Achievements in Mech. and Mater. Engg., Gliwise-Wista, Poland, 2005.
[223] J.I. Goldstein, A.E. Moren, Metall. Trans. A 9 (1978) 1515.
[224] R.W. Gurry, Trans. AIME 188 (1950) 671.
[225] F.J. Harvey, Met. Trans. A 9 (1978) 1507.
[226] C. Wells, R.F. Mehl, Trans. AIME 140 (1940) 279.
[227] V. Sahajwalla, R. Khanna, Metall. Mater. Trans. 31B (2000) 1517.
[228] V. Sahajwalla, R. Khanna, Scand. J. Metall 29 (2000) 114.
[229] H. Ohtani, T. Nishizawa, Trans. ISIJ 26 (1986) 655.
[230] C. Wu, R. Wiblen, V. Sahajwalla, Metall. Mater. Trans. 31B (2000) 1099.
[231] W.W. Dunn, R.B. McLellan, Metall. Trans. 1 (1970) 1263.
[232] A. McLean, Metall. Mater. Trans. 37B (2006) 319.
[233] D.R. Sain, G.R. Belton, Metall. Mater. Trans. 9 (1978) 403.
[234] P.G. Roddis, J. Iron Steel Inst. 211 (1973) 53.
[235] K. Gao, V. Sahajwalla, H. Sun, C. Wheatley, R. Dry, ISIJ Int. 40 (2000) 301.
[236] D.R. Sain, G.R. Belton, Metall. Mater. Trans. 7 (1976) 235.
[237] R. Khanna, V. Sahajwalla, N. Simento, S. Seetharaman, Acta Mater. 58 (2010) 2225.
[238] N.A.I. Andersson, A. Tillinder, L.T.I. Jonsson, P.G. Jonsson, Steel Res. Int. 83 (12) (2012) 1039.
[239] S. Asai, J. Szekely, Metall. Mater. Trans. 5B (1974) 651.
[240] R.J. Fruehan, Ironmak. Steelmak. 3 (1976) 153.
[241] T. Ohno, T. Nisida, Tetsu-tu-Hagane 63 (1977) 2094.
[242] J. Reichel, J. Szekely, Ironmak. Steelmak. 22 (1995) 41.
[243] J.O. Andersson, T. Helander, L. Hoglund, P. Shi, B. Sundman, Calphad 26 (2) (2002) 273.
[244] Z.H. Jiang, W. Gong, W.Z. Wang, Dev. Chem. Eng. Miner. Proc. 14 (2006) 429.
[245] A.K. Shukla, B. Deo, S. Millman, B. Snoeijer, A. Overbosch, A. Kapilashrami, Steel Res. Int. 81 (2010) 940.
[246] R.D. Walker, D. Anderson, Iron Steel 8 (1972) 403.
[247] L. Zhao, V. Sahajwalla, ISIJ Int. 43 (2003) 1.
[248] R. Khanna, V. Sahajwalla, Acta Mater. 53 (2005) 1205.
[249] V. Sahajwalla, R. Khanna, E. Kapilashrami, S. Seetharaman, Can. Met. Q. 46 (2007) 25.

[250] C. Holcomb, P. Clancy, J. Jollweg, Mol. Phys. 78 (1993) 437.
[251] G. Orkoulas, A.Z. Panagiotopoulos, J. Chem. Phys. 101 (1994) 1452.
[252] E. de Miguel, Phys. Rev. E 55 (1997) 1347.
[253] P.R. Ten Wolde, D. Frenkel, J. Chem. Phys. 109 (1998) 9901.
[254] Y.V. Kalyuzhnyi, P.T. Cummings, Mol. Phys. 87 (1996) 1459.
[255] F.W. Tavares, S.I. Sandler, Mol. Phys. 87 (1996) 1471.
[256] R.J. Sadhus, Fluid Phase Equil. 151 (1998) 63.
[257] P.G. Bolhuis, A. Stroobants, D. Frenkel, H.N.W. Lekkerkerker, J. Chem. Phys. 109 (1998) 9901.
[258] M.J. Blair, G.N. Patey, Phys. Rev. E 57 (1998) 5682.
[259] J.R. Errington, A.Z. Panagiotopoulos, J. Chem. Phys. B 102 (1998) 7470.
[260] D.P. Visco, D.A. Kofke, Fluid Phase Equil. 160 (1999) 67.
[261] J.A. Anta, E. Lomba, M. Lombardero, Phys. Rev. E 55 (1997) 2707.
[262] C. Caccamo, D. Costa, A. Fucile, J. Chem. Phys. B 106 (1997) 255.
[263] D.P. Visco, D.A. Kofke, Fluid Phase Equil. 109 (1998) 4015.
[264] T. Kristof, J. Liszi, J. Chem. Phys. B 101 (1997) 5480.
[265] P.B. Conrad, J.J. de Pablo, Fluid Phase Equil. 150 (1998) 51.
[266] Q.Y. Wang, J.K. Johnson, Fluid Phase Equil. 132 (1997) 93.
[267] D.W. Oxtoby, R. Evans, J. Chem. Phys. B 89 (1988) 7521.
[268] J.W. Cahn, J.E. Hilliard, J. Chem. Phys. B 31 (1959) 688.
[269] P. Tarazona, R. Evans, Rev. Mod. Phys. 48 (1983) 799.
[270] P.R. Swan, W.R. Duff, R.M. Fisher, Metal. Trans. 3 (1972) 409.
[271] R.D. Shull, H. Okamoto, P.A. Beck, Solid State Commun. 20 (1976) 863.
[272] M. Hasaka, Trans. Jpn. Inst. Met. 21 (1980) 660.
[273] N.S. Golosov, A.M. Tolstik, L.Y. Pudan, J. Phys. Chem. Solids 37 (1976) 273.
[274] B. Dunweg, K. Binder, Phys Rev. B 36 (1987) 6935.
[275] S.K. Bose, V. DrChal, J. Kudrnovsky, O. Jepson, O.K. Anderson, Phys Rev. B 55 (1997) 8184.
[276] D. Fuks, S. Dorfman, Solid State Commun. 90 (1994) 773.
[277] S. Dorfman, D. Fuks, V. Liubich, Int. J. Quantum Chem. 70 (1998) 1067.
[278] A.E. Carlsson, Phys Rev. B 40 (1989) 912.
[279] S.M. Allen, J.W. Cahn, Acta Metall. 24 (1976) 425.
[280] H. Sagane, K. Oki, Trans. Jpn. Inst. Met. 21 (1980) 811.
[281] D.A. Contreras-Solorio, F. Mejia-Lira, J.L. Moran-Lopez, Phys Rev. B 38 (1988) 11481.
[282] J.W. Cahn, J.E. Hilliard, J. Chem. Phys. B 31 (1959) 539.
[283] F.K. Legoues, Y.W. Lee, H.I. Aaronson, Acta Metall. 32 (1984) 1837.
[284] R. Poduri, L.Q. Chen, Acta Mater. 44 (1996) 4253.
[285] S. Hirosawa, T. Sato, Modell. Simul. Mater. Sci. Eng. 9 (2001) 129.
[286] A.G. Khachaturyan, T.F. Lindsay, J.W. Morris, Metal. Trans. A 19 (1988) 249.
[287] R. Poduri, L.Q. Chen, Acta Mater. 45 (1997) 245.
[288] L. Zhang, L.Q. Chen, Q. Du, Acta Mater. 56 (2008) 3568.
[289] G. Bonny, R.C. Pasianot, L. Malerba, Modell. Simul. Mater. Sci. Eng. 17 (2009) 025010.
[290] M. Grijicic, P. Dang, Mater. Sci. Engg. A 201 (1995) 194.
[291] E.E. Cech, D. Turnbull, Trans. AIME 206 (1956) 124.
[292] Z.Z. Yu, P.C. Clapp, Metal. Trans. A 20 (1989) 1617.
[293] K. Shibata, T. Fujita, Trans. ISIJ Int. 26 (1986) 1065.
[294] M. Grujicic, J. Du, Modell. Simul. Mater. Sci. Eng. 3 (1995) 811.
[295] C. Engin, H.M. Urbassek, Commun. Mater. Sci 41 (2008) 297.
[296] M. Bayerlein, H.J. Christ, H. Mughrabi, Mater. Sci. Eng. A 114 (1989) L11.
[297] I. Kaur, Y. Mishin, W. Gust, Fundamentals of Grain and Interface Boundary Diffusion, John Wiley & Sons, Chichester, NY, 1995.
[298] Y. Mishin, in: D. Gupta (Ed.), Diffusion Processes in Advanced Technological Materials, William Andrew, Norwich, NY, 2005, p. 113.
[299] M.I. Mendelev, S.W. Han, W.J. Son, G.J. Ackland, G.J. Srolowitz, Phys Rev. B 76 (2007) 214105.
[300] M.I. Mendelev, Y. Mishin, Phys Rev. B 80 (2009) 144111.
[301] S.M. Foiles, Phys Rev. B 49 (1994) 14930.
[302] A.H. Cottrell, B.A. Bilby, Proc. Phys. R. Soc. Lond. A 62 (1949) 49.

[303] A. Vehanen, P. Hautojorvi, J. Johansson, J. Yii-Kuappila, P. Moser, Phys. Rev. B 25 (1982) 762.
[304] R.A. Arndt, A.C. Damask, Acta Metall. 12 (1964) 341.
[305] C. Domain, C.S. Becquart, J. Foct, Phys. Rev. B 69 (2004) 144112.
[306] K. Tapasa, A.V. Barashev, D.J. Bacon, Y.N. Osetsky, Acta Mater. 55 (2007) 1.
[307] D.E. Jiang, E.A. Carter, Phys Rev. B 67 (2003) 214103.
[308] J.R.G. Da Silva, R.B. McLeillan, Mater. Sci. Eng. 26 (1976) 83.
[309] A. Ishii, S. Ogata, H. Kimizuka, Phys. Rev. B 85 (2012) 064303.
[310] T. Huber, A.E. Torda, W.F. Vangunsteren, J. Comput. Aided Mol. Des. 8 (1994) 695.
[311] S. Hara, J. Lee, Phys Rev. B 82 (2010) 184114.
[312] H. Grubmuller, Phys. Rev. E 52 (1995) 2893.
[313] R. Miron, F. Fichthorn, J. Chem. Phys. 119 (2003) 6210.
[314] A.F. Voter, Phys. Rev. Lett. 78 (1997) 3908.
[315] O. Engkwist, G. Karlstrom, Chem. Phys. 213 (1996) 63.
[316] A. Lord Jr., D. Beshers, Acta Metall. 14 (1966) 1659.
[317] A.V. Evteev, E.V. Levchenko, I.V. Belova, G.E. Burch, Philos. Mag. 87 (2007) 4335.
[318] R.H. Doremus, J. Appl. Phys. 100 (2006) 101301.
[319] A.H. Heuer, J. Eur. Ceram Soc. 28 (2008) 1495.
[320] A.H. Heuer, K.P.D. Lagerlof, Philos. Mag. Lett. 79 (1999) 619.
[321] P.W.M. Jacobs, E.A. Kotomin, Philos. Mag. A 68 (1993) 695.
[322] R.W. Grimes, J. Am. Ceram. Soc. 77 (1994) 378.
[323] K.P.D. Lagerlof, R.W. Grimes, Acta Mater. 46 (1998) 5689.
[324] J. Carrasco, N. Lopez, F. Illas, H.J. Freund, Phys. Rev. Lett. 93 (2004) 0268051.
[325] U. Aschauer, P. Bowen, S.C. Parker, Acta Mater. 57 (2009) 4765.
[326] W. Smith, T.R. Forrester, J. Mol. Graph. 14 (1996) 136.
[327] D.R. Wheeler, J. Newman, J. Chem. Phys. 108 (2004) 18362.
[328] J. Newman, Electrochemical Systems, second ed., Prentiss Hall, Englewood Cliffs, NJ, 1991.
[329] T. Masaki, H. Aoki, S. Munejiri, Y. Ishii, T. Itami, J. Non-Cryst. Sol. 312 (2012) 191.
[330] M. Shimozi, Liquid Metals, Academic Press, London, 1977.
[331] L.F. Mondolpho, Aluminium Alloys: Structure and Properties, Butterworths, London, 1976.
[332] M.I. Mendelev, A.O. Rodin, B.S. Bokstein, Defects Diff. Forum 289–292 (2009) 733.
[333] D. Bergner, N. Van Chi, Wissen Zeit. Padagog. 15 (1977) 15.
[334] N.L. Peterson, S.G. Rothman, Phys. Rev. B 1 (1970) 3264.
[335] S. Dais, R. Messer, A. Seeger, Mat. Sci. Forum 15–18 (1987) 419.
[336] S. Fujikawa, K. Hirano, Diffusion in Solid Metals and Alloys, vol. 26, Springer, Berlin, 1990.
[337] G. Erdélyi, D.L. Beke, F.J. Kedves, I. Gödény, Philos. Mag. B 38 (1978) 445.
[338] M.I. Mendelev, D.J. Srolovitz, G.J. Ackland, S. Han, J. Mater. Res. 20 (2005) 208.
[339] R. Krishnamurthy, D.J. Srolovitz, M.I. Mendelev, Acta Mater. 55 (2007) 5289.
[340] Y.W. Mo, B.S. Swartzentruber, R. Kariotis, M.W. Webb, M.G. Legally, Phys. Rev. Lett. 63 (1989) 2393.
[341] Y.W. Mo, J. Kleiner, M.W. Webb, M.G. Legally, Phys. Rev. Lett. 67 (1991) 1998.
[342] E.D. Williams, N.C. Bartlet, Science 251 (1991) 393.
[343] E.D. Williams, R.J. Phaneuf, J. Wei, N.C. Bartlet, T.L. Einstein, Surf. Sci. 294 (1993) 219.
[344] A. Madhukar, Thin Solid Films 231 (1993) 8.
[345] A. Zunger, S. Mahajan, in: S. Mahajan (Ed.), Atomic Ordering and Phase Separation in Epitaxial III-V Alloys, Handbook on Semiconductorsvol. 3, 1994.
[346] E. Kaxiras, Comput. Mater. Sci. 6 (1996) 158.
[347] D.J. Chadi, Phys. Rev. B 29 (1984) 785.
[348] E. Kaxiras, Z. Guo, Phys. Rev. B 49 (1994) 11822.
[349] R. Car, M. Parrinello, Phys. Rev. Lett. 55 (1985) 2471.
[350] K.C. Pandey, Phys. Rev. Lett. 57 (1986) 2287.
[351] A.P. Smith, J.K. Wiggs, H. Jonsson, H. Yan, L.R. Corrales, P. Nachtingall, K.D. Jordan, J. Chem. Phys. 102 (1995) 1044.
[352] F.M. Bulnes, V.D. Pereyra, J.L. Ricardo, Phys. Rev. E 58 (1998) 86.

[353] C.C. Battaile, D.L. Srolowitz, Annu. Rev. Mater. Res. 32 (2002) 297.
[354] D.J. Srolovitz, D.S. Dandy, J.E. Butler, C.C. Battaile, J. Min. Met. Mater. 49 (1997) 42.
[355] M. Masi, V. Bertani, C. Cavalloti, C. Carra, Mater. Chem. Phys. 66 (2000) 229.
[356] M. Grujicic, S.G. Lai, J. Mater. Sci. 35 (2000) 5359.
[357] S.K. Dew, T. Smy, M.J. Brett, J. Vac. Sci. Technol. B 10 (1992) 618.
[358] J.H. McCreery, G. Wolken, J. Chem. Phys. 63 (1975) 2340.
[359] K.A. Fichthorn, W.H. Weinberg, J. Phys. Chem. 95 (1991) 1090.
[360] B.J. Garrison, D. Srivastava, Annu. Rev. Phys. Chem. 46 (1995) 373.
[361] H.J. Leamy, G.H. Gilmer, K.A. Jackson, P. Bennema, Phys. Rev. Lett. 30 (1973) 601.
[362] K.L. Wong, J.H. Shim, B.D. Worth, J. Nucl. Mater. 367–370 (2007) 276.
[363] D. Terentyev, L. Malerba, J. Nucl. Mater. 329 (2004) 1161.
[364] J.H. Shim, H.J. Lee, B.D. Worth, J. Nucl. Mater. 351 (2006) 56.
[365] G.J. Ackland, D.J. Bacon, A.F. Calder, T. Harry, Philos. Mag. A 75 (1997) 713.
[366] P. Olsson, C. Domain, J. Wiiliams, Phys. Rev. B 75 (2007) 014110.
[367] A. Moslang, H. Graf, G. Balzer, E. Recknegal, A. Weidinger, T. Wichert, R.I. Grynszpan, Phys. Rev. B 27 (1983) 2674.
[368] F. Garner, M. Toloczko, B. Sencer, J. Nucl. Mater. 276 (2000) 123.
[369] M. Miller, J. Hyde, A. Cerezo, J. Smith, Appl. Surf. Sci. 87–88 (1995) 323.
[370] J. Wallenius, P. Olsson, C. Lagerstedt, N. Sandberg, R. Chakarova, V. Pontikis, Phys. Rev. B 69 (2004) 094103.
[371] H. Kuwano, Trans. JIM 26 (1985) 473.
[372] P. Olsson, I. Abrisokov, L. Vitos, J. Wallenius, J. Nucl. Mater. 321 (2003) 84.
[373] J. Hyde, M. Miller, A. Cerezo, G. Smith, Appl. Surf. Sci. 87–88 (1995) 311.
[374] A. Seeger, E. Mann, R.V. Jan, J. Phys. Chem. Sol. 23 (1962) 639.
[375] G.H. Vineyard, J. Phys. Soc. Jpn. 18 (Suppl. III) (1963).
[376] R.A. Johnson, E. Brown, Phys. Rev. B 127 (1962) 446.
[377] R.A. Johnson, Phys. Rev. A 134 (1964) 1329.
[378] R. Khanna, H.G. Haubold, Acta Cryst. A 38 (1982) 814.
[379] J. Bass, D. Lazarus, J. Phys. Chem. Sol. 23 (1962) 1820.
[380] G.W. Tichelaar, R.V. Coleman, D. Lazarus, Phys. Rev. 121 (1961) 748.
[381] R.A. Johnson, A.C. Damask, Acta Met. 12 (1964) 443.
[382] R.W. Powers, M.V. Doyle, J. Appl. Phys. 30 (1959) 514.
[383] J.T. Buswell, W.J. Pythian, R.J. McElroy, S. Dumbill, P.H.N. Ray, J. Macs, R.N. Sinclair, J. Nucl. Mater. 225 (1995) 196.
[384] G. Ackland, Philos. Mag. A 67 (1993) 285.
[385] W. Chambron, J. Verdone, P. Moser, in: M.T. Robinson, F.W. Young (Eds.), Fundamental aspects of Radiation damage in Metals, 1975, USERDA Report No. CONF 751006, 261.
[386] Y.N. Osetsky, M. Victoria, A. Sera, S.I. Golubov, V. Priego, J. Nucl. Mater. 251 (1997) 34.
[387] Y.N. Osetsky, A. Sera, Def. Diff. Forum 143–147 (1997) 155.
[388] A. Biborski, L. Zosiak, R. Kozubski, R. Sot, V.P. Bohnes, Intermetallics 18 (2010) 2343.
[389] C.D. Beachem (Ed.), Hydrogen Damage, American Society for Metals, Metals Park, OH, 1977.
[390] M.J. Stott, E. Zaremba, Phys Rev. B 26 (1980) 2875.
[391] J.K. Norskov, F. Besenbacher, J. Bottinger, B.B. Nielson, A.A. Pisarev, Phys. Rev. Lett. 49 (1982) 1420.
[392] M.S. Daw, M.I. Baskes, Phys. Rev. Lett. 50 (1983) 1285.
[393] W. Zhong, Y. Cai, D. Tomanek, Nature 362 (1993) 435.
[394] R.A. Oriani, P.H. Josephic, Acta Metall. (1974) 1065.
[395] D.G. Westlake, Trans. Am. Soc. Metals 62 (1969) 1000.
[396] T. Tabata, H.K. Birnbarn, Scripta Metall. 18 (1984) 231.
[397] W. Zhong, Y.S. Li, D. Tomanek, Phys Rev. B 44 (1991) 13053.
[398] C.D. Beecham, Metall. Trans. 3 (1972) 437.
[399] X. Xu, W. Mao, Z. Hu, S. Fukuyama, K. Yokogawa, Comput. Mater. Sci. 23 (2002) 131.
[400] M.I. Baskes, X. Sha, K.E. Angelo, N.R. Moody, Modell. Sim. Mater. Sci. Eng. 5 (1997) 651.

[401] T. Boniszewski, G.C. Smith, Acta Metall. 11 (1963) 165.
[402] W. Kurz, D.J. Fisher, Fundamentals of Solidification, Trans Tech, Switzerland, 1989.
[403] P.C. Fife, Mathematical Aspects of Reacting and Diffusing Systems, Springer, New York, 1979.
[404] E. Ben-Jacob, I. Cohen, H. Levine, Adv. Phys. 49 (2000) 395.
[405] G.P. Ivantsov, Dokl. Akad. Nauk SSSR 58 (1947) 567.
[406] D. Kessler, J. Koplik, H. Levine, Adv. Phys. 37 (1988) 255.
[407] J.J. Hoyt, M. Asta, A. Karma, Mater. Sci. Eng. R 41 (2003) 203.
[408] J.Q. Broughton, G.H. Gilmer, J. Chem. Phys. 84 (1986) 5759.
[409] R. Ravelo, M.I. Baskes, MRS Symp. Proc. (1996) 398.
[410] J.J. Hoyt, M. Asta, A. Karma, Phys. Rev. Lett. 86 (2001) 5530.
[411] T. Hapke, G. Patzold, D.W. Heerman, J. Chem. Phys. 109 (1998) 10075.
[412] M.P.A. Fisher, D.S. Fisher, J.D. Weeks, Phys. Rev. Lett. 48 (1982) 368.
[413] K.A. Jackson, B. Chalmers, Can. J. Phys. 34 (1956) 473.
[414] J. Frenkel, Phys. Z. Sowjetunion 1 (1932) 498.
[415] S.R. Corriell, D.H. Turnbull, Acta Metall. 30 (1982) 2135.
[416] J.W. Cahn, J.E. Hilliard, J. Chem. Phys. 28 (1958) 258.
[417] S.M. Allen, J.W. Cahn, Acta Metall. 27 (1979) 1085.
[418] L.Q. Chen, Annu. Rev. Mater. Res. 32 (2002) 113.
[419] I.S. Loginova, H.M. Singer, Rep. Prog. Phys. 71 (2008) 106501.
[420] J.J. Hoyt, M. Asta, A. Karama, Phys. Rev. Lett. 86 (2001) 5530.
[421] M. Amini, B.B. Laird, Phys. Rev. Lett. 97 (2006) 216102.
[422] R. Kobayashi, Phys. D 63 (1993) 410.
[423] L.Q. Chen, J. Shen, Comput. Phys. Commun. 108 (1998) 147.
[424] N. Provotas, N. Goldenfeld, J.A. Dantzig, Phys. Rev. Lett. 80 (1998) 3308.
[425] J.B. Collins, H. Levine, Phys. Rev. B 31 (1985) 6119.
[426] M. Ode, S.G. Kim, T. Suzuki, ISIJ Int. 41 (2001) 1076.
[427] Y.M. Jin, A. Artemev, A.G. Khachaturyan, Acta Mater. 49 (2001) 2309.
[428] D.Y. Li, L.Q. Chen, Acta Mater. 46 (1998) 639.
[429] A. Artemev, Y. Wang, A.G. Khachaturyan, Acta Mater. 48 (2000) 2503.
[430] L.Q. Chen, W. Wang, Phys. Rev. B 50 (1994) 15752.
[431] P.H. Leo, W.C. Johnson, Acta Mater. 49 (2001) 1771.
[432] Y.L. Li, S.Y. Hu, Z.K. Liu, L.Q. Chen, Acta Mater. 50 (2002) 393.
[433] J.W. Cahn, Acta Metall. 5 (1957) 169.
[434] I.S. Aranson, V.A. Kalatsky, V.M. Vinokur, Phys. Rev. Lett. 85 (2000) 118.
[435] M. Mahadevan, R.M. Bradley, Phys. Rev. B 59 (1999) 11037.
[436] H. Emmerich, H. Lowen, R. Wittkowski, T. Gruhn, G.I. Toth, G. Tegze, L. Granasy, Adv. Phys. 61 (2012) 665.
[437] K.R. Elder, N. Provotas, J. Berry, P. Stefnovic, M. Grant, Phys. Rev. B 75 (2007) 064107.
[438] G.I. Toth, G. Tegze, T. Pusztai, G. Toth, L. Granasy, J. Phys. Cond. Matter 22 (2010) 364101.
[439] G. Tegze, G.I. Toth, L. Granasy, Phys. Rev. Lett. 106 (2011) 195502.
[440] J. Berry, K.R. Elder, M. Grant, Phys. Rev. E 77 (2008) 061506.
[441] K.R. Elder, M. Grant, Phys. Rev. E 70 (2004) 051605.
[442] P.Y. Chan, N. Goldenfeld, H.R. Brand, Phys. Rev. E 79 (2009) 035701R.
[443] N. Guttenbirg, G. Goldenfeld, J. Dantzig, Phys. Rev. E 81 (2010) 065301.
[444] R. Spataschek, A. Karma, Phys. Rev. B 81 (2010) 214201.
[445] R. Wittowski, H. Lowen, H.R. Brand, Phys. Rev. E 82 (2010) 031708.
[446] S. Muralidharan, M. Haataza, Phys. Rev. Lett. 105 (2010) 126101.
[447] K.A. Wu, A. Adland, A. Karma, Phys. Rev. E 81 (2010) 061601.
[448] S.A. Brazovskii, Zh. Eksp. Teor. Fiz 68 (1975) 175.
[449] K.R. Elder, M. Katakowski, M. Haataza, M. Grant, Phys. Rev. Lett. 88 (2002) 245701.
[450] M. Greenwood, N. Provotas, J. Rottler, Phys. Rev. Lett. 105 (2010) 045702.
[451] M. Greenwood, N.O. Opoku, J. Rottler, N. Provotas, Phys. Rev. B 84 (2011) 064104.
[452] N. Goldenfeld, B.P. Athreya, J.A. Dantzig, Phys. Rev. E 72 (2005) 020601.

[453] J.J. Hoyt, M. Asta, T. Haxhimali, A. Karma, R.E. Napolitano, R. Trivedi, MRS Bull. 29 (2004) 935.
[454] J.J. Hoyt, M. Asta, D.Y. Sun, Philos. Mag. 86 (2006) 8651.
[455] D.Y. Sun, M. Asta, J.J. Hoyt, M.I. Mendelev, D.J. Srolovitz, Phys. Rev. B 69 (2004) 020102.
[456] B.B. Laird, R.L. Davidchack, J. Phys. Chem. B 109 (2005) 17802.
[457] B.B. Laird, R.L. Davidchack, Phys. Rev. Lett. 85 (2000) 4751.
[458] T.G. Germann, P.S. Lomdahl, Comput. Sci. Eng. 10 (1999) 10.
[459] Q. Jiang, D.S. Zhao, M. Zhao, Acta Mater. 49 (2001) 3143.
[460] V. Vaithyanathan, L.Q. Chen, Acta Mater. 50 (2002) 4031.
[461] L. Lymperakis, M. Friak, J. Neugebauer, Eur. Phys. J. Special Topics 177 (2009) 41.
[462] H. Emmerich, Cont. Mech. Therm. 15 (2003) 197.
[463] R. Folch, M. Plapp, Phys. Rev. E 72 (2005) 1.
[464] M. Doi, Mater. Trans. JIM 33 (1992) 637.
[465] P.W. Voorhees, Annu. Rev. Mater. Sci. 22 (1992) 197.
[466] T.A. Arias, J.D. Joannopoulos, Phys. Rev. B 49 (1994) 4525.
[467] R. Schweinfest, A.T. Paxton, M.W. Finnis, Nature 432 (2004) 1008.
[468] B.J. Lee, S.H. Choi, Modell. Sim. Mater. Sci. Eng. 12 (2004) 621.
[469] D.L. Olmsted, S.M. Foiles, E.A. Holm, Acta Mater. 57 (2009) 3694.
[470] Y.L. Bouar, A. Loiseau, A.G. Khachaturyan, Acta Mater. 46 (1998) 2777.
[471] K.I. Udoh, A.M. Araby, Y. Tanaka, K. Hisatsune, K. Yasuda, G. van Tandeloo, G. van Landuyt, J. Mater. Sci. Eng. A 203 (1995) 164.
[472] H.W. King, in: R.W. Cahn (Ed.), Physical Metallurgy, North Holland, Amsterdam, 1970, p. 60.

CHAPTER 3

Thermodynamic Aspects of Process Metallurgy

Introduction to Thermodynamics of Metallurgical Processes

Kazuki Morita, Nobuo Sano and Seshadri Seetharaman

Contents

3.1. First, Second and Third Laws of Thermochemistry 399
3.2. Phase Rule 495
3.3. Ellingham Diagram 507
3.4. Solution Thermochemistry 517
3.5. Thermodynamic Basis for Phase Diagrams 527
3.6. Dilute Solutions 557
3.7. Thermodynamics of Slags 587
3.8. Examples of Steelmaking Thermochemistry 617
3.9. Thermodynamics of Aqueous Phases 641
3.10. Thermodynamic Basis of Electrolysis and Electrochemistry 653

It is customary to classify natural science into Physics, Chemistry, and Mathematics. During the seventeenth, eighteenth, and nineteenth centuries, science has marked the evolution of three important subjects, which formed the foundation for the development of modern technology. These are mechanics, electromagnetism, and thermodynamics. The special feature of these three subjects is that they all start with basic logical reasoning which would lead to advanced development of theories of science and technology. Of these, the subject of Thermodynamics combines the reasonings from physics and chemistry and uses the mathematical tools in substantiating the outcoming deductions. The word "thermodynamics" is derived by a combination of the Greek terms "Thermos" meaning "heat" and "Dynamis" meaning "Power." This subject is taught to students in materials science and engineering, chemistry, physics, and mechanical engineering, often with variations in the applications while the basis is common.

One of the earliest reasonings in thermodynamics starts with the steam engine, viz., how to get the maximum efficiency with minimum input of heat to the engine. The conversion of one form of energy, in this case, the heat energy, to mechanical energy was the focal point. Some of the important names to be remembered with regard to thermodynamics are Black, Rumford, Hess, Carnot, Mayer, Joule, Clausius, Kelvin,

Treatise on Process Metallurgy, Volume 1
http://dx.doi.org/10.1016/B978-0-08-096986-2.00025-4
© 2014 Elsevier Ltd.
All rights reserved.

Helmholtz, and Gibbs. The observation of the evolution of heat by Col. Rumford when he was getting canon barrel bored had stimulated the thinking of conversion of heat energy out of mechanical working. Early in the 1900s, the famous scientist Joule determined the equivalent heat for mechanical work carried out. He defined 1 cal as the heat energy needed to increase the temperature of 1 g water by 1 °C (between 14.5 and 15.5 °C). Enligt Joule, 1 J (1 N m) mechanical energy would correspond to 0.241 cal. It is astonishing to compare this value to the accurate measurements in modern times which is reported as 0.2389 cal/N m.

Among the early publications on Thermodynamics found in the literature, a few that can be mentioned are:

Sainte-Claire Deville, Lecons sur la dissociation, Lecons Chim. 1864–1865, sid. 255.

A. Horstmann, Ber. deut. chem. Ges. m 1 (1869).

F. Haber, Thermodyn. Tech. Gas Reaktionen.

R. Oldenbourg Verlag, München, 1905.

Most important among them, in the opinion of the present authors, is the unique publication by J.W. Gibbs, The equilibrium of heterogeneous substances, Trans. Conn. Acad. Sci. 3 (1876), sid. 228.

Thermodynamics is very often considered as tangenting philosophy. This is well brought out in the early publications where a significant thought process was resorted to in order to define the terms involved as accurately as possible and discuss the "abstract" principles of order and disorder as well as the balance between these two primordial "forces," reminding of ancient eastern philosophies. The concept of "enthalpy," which often represents the order in systems and entropy, based on disorder are kept in equilibrium depending upon the conditions prevailing by the famous equation,

$$\Delta G = \Delta H - T\Delta S \tag{3.1}$$

where G stands for Gibbs energy, while the terms H and S stand for enthalpy and entropy respectively and T stands for temperature in Kelvin. One of the interesting aspects to note is that both H and S are functions of the specific heat, viz.

$$\mathrm{d}H = \int Cp \; \mathrm{d}T \tag{3.2}$$

and

$$\mathrm{d}S = \int (Cp/T) \; \mathrm{d}T \tag{3.3}$$

(Cp stands for specific heat) once again pointing to the commonness between order and disorder, based on structural principles. By the way, it is interesting to note that students of thermodynamics who get fascinated by these concepts often start applying these to human behavior and even economics.

The beauty of the subject of Thermodynamics is its expansivity from micro/atomic level (often by combining the principles of statistical mechanics) to macrosystems. The latter deals with metallurgical processes for producing millions of tons of steel. These processes are indeed based on thermodynamic principles and calculations. In this chapter, we focus on the applications to metallurgical processes, while the atomistic and structural aspects have been dealt with partly in Chapter 2.

It is important to keep in mind that the subject of thermodynamics provides the knowledge base for finding out whether a process is possible or not. It also gives information as to the heat effects accompanying such a process. While thermodynamics is very clear regarding the differences between two states of existence, as, for example, two temperatures of a defined system or two different pressures, it does not give any clue as to the rate at which the system moves from one state to the other. In this treatise, this kinetics part is dealt with in the chapter that follows, viz., Chapter 4.

In modern days, the development in the field of thermodynamics is twofold:

(a) Development of applications of thermodynamic principles to metallurgical processes and

(b) Measurement of modeling of thermodynamic data for the applications.

In the first case, commercial softwares have been developed for applications both in the industrial laboratories and in the universities. In the area of the measurement of thermodynamic data, with the improvements in modern instrumentations, very significant advances have been made with respect to the accuracy of the data obtained.

One of the effects of the modern developments in the field of Thermodynamics education is the emphasis that is being slightly shifted from an understanding of the principles of thermodynamics, which is the key to the evolution of new concepts and ideas, toward applications, especially of the softwares commercially available. The prime objective of the present chapter is to provide a basic knowledge of the thermodynamics of metallurgical processes so that the reader is acquainted well with them before proceeding to the applications. The commercial softwares available are presented in Chapter 9.

CHAPTER 3.1

First, Second, and Third Laws of Thermochemistry

Masanori Iwase*
Graduate School of Energy Science, Kyoto University

3.1.1. THERMODYNAMIC DATA COMPILATIONS

Representative data compilations are from Kubaschewski *et al.* [1] (hereafter expressed as *KAS*), Barin [2], Chase [3], Hultgren *et al.* [4,5], Elliott and Gleiser [6], Elliott *et al.* [7], and Turkdogan [8]. In addition, web site also provides thermodynamic data; http://kinetics.nist.gov/janaf/. Among these compilations, Ref. [1] would be most recommendable. Indeed, Table 3.1.A6 in Appendix of this chapter was reproduced from Ref. [1], while Table 3.1.A7 is from Ref. [8].

3.1.2. IDEAL GAS

Ideal gas is defined as a gas that satisfies the following relation

$$PV = nRT \tag{3.1.1}$$

where P, V, n, R, and T are pressure, volume, number of moles, gas constant, and absolute temperature, respectively. Single atom gases such as inert gases (He, Ne, Ar, Xe) and vapors of metals almost satisfy this equation. Since one mole of an ideal gas at 273.15 K and 1 atm pressure ($101{,}325\ \mathrm{Pa} = 101{,}325\ \mathrm{N\,m^{-2}} = 101{,}325\ \mathrm{J\,m^{-3}}$) has a volume of $22.414\ \mathrm{l}$ ($22.414 \times 10^{-3}\ \mathrm{m^3}$), the values of the molar gas constant, R, is given as

$$\begin{aligned} R &= \frac{1(\mathrm{atm}) \times 22.414(\mathrm{l})}{1(\mathrm{mol}) \times 273.15(\mathrm{K})} && = 0.08205\left(\mathrm{l\,atm\,mol^{-1}\,K^{-1}}\right) \\ &= \frac{101{,}325(\mathrm{Pa}) \times 22.414 \times 10^{-3}(\mathrm{m^3})}{1(\mathrm{mol}) \times 273.15(\mathrm{K})} && = 8.314\left(\mathrm{Pa\,m^3\,mol^{-1}\,K^{-1}}\right) \\ & && = 8.314\left(\mathrm{J\,mol^{-1}\,K^{-1}}\right) \end{aligned} \tag{3.1.2}$$

3.1.3. THE FIRST LAW OF THERMODYNAMICS

The First Law of Thermodynamics is often stated as "Energy can neither be created nor destroyed in a system of constant mass, although it may be converted from one form

*Late.

Treatise on Process Metallurgy, Volume 1
http://dx.doi.org/10.1016/B978-0-08-096986-2.00030-8
© 2014 Elsevier Ltd.
All rights reserved.

to another." Consider a mass of gas contained within a cylinder fitted with frictionless piston at constant temperature, and heat q supplied to the system. By absorbing this heat, the gas performs the amount of work w by expansion. Following to the first law, we have

$$\Delta U = q - w \tag{3.1.3}$$

where ΔU is the increase in the *internal energy* of the system. This equation can be regarded as the mathematical expression of the *First Law of Thermodynamics*. The internal energy U is a state function or state property and does not depend upon the path by which that state was reached. The individual quantities q and w may depend upon paths, while the difference $(q - w)$ always yields the same value of $\Delta U = U_2 - U_1$.

3.1.4. ENTHALPY AND HEAT CAPACITY

3.1.4.1. Enthalpy

For an infinitesimal change of state, Equation (3.1.3) becomes

$$\mathrm{d}U = \delta q - \delta w \tag{3.1.4}$$

The use of δ instead of d arises from that q and w are not state properties.

If the volume of the system, which consists of ideal gas, as an example, is maintained constant, then the system does not work, and Equation (3.1.4) becomes,

$$\Delta U = \delta q (\text{at constant volume}) \tag{3.1.5}$$

When the system expands against the constant pressure P, the work done by the system against the surroundings is given as

$$w = P(V_\mathrm{B} - V_\mathrm{A}) \,(\text{at constant pressure}) \tag{3.1.6}$$

where $(V_\mathrm{B} - V_\mathrm{A})$ is the change in volume by passing from state A to state B. Through such work w, the system absorbs a quantity of heat q. The increase in internal energy ΔU is then given by

$$\Delta U = U_\mathrm{B} - U_\mathrm{A} = q - P(V_\mathrm{B} - V_\mathrm{A}) \tag{3.1.7}$$

By rearranging Equation (3.1.7), we have

$$q = (U_\mathrm{B} + PV_\mathrm{B}) - (U_\mathrm{A} + PV_\mathrm{A}) \tag{3.1.8}$$

The quantity $U + PV$ is represented by a single symbol, H.

$$H = U + PV \tag{3.1.9}$$

Thus, it follows:

$$\Delta H = q = (U_\mathrm{B} + PV_\mathrm{B}) - (U_\mathrm{A} + PV_\mathrm{A}) \tag{3.1.10}$$

Table 3.1.1 Standard States

Solid	Pure substance at the most stable form at 1 atm pressure (101,325 Pa)
Liquid	Pure substance at the most stable form at 1 atm pressure
Gas	One atmospheric pressure

This function H is known as *enthalpy* or heat content. Like many other thermodynamic functions, the absolute values of enthalpy are not measurable: only changes in enthalpy can be obtained. Hence, reference or standard is required so that quantities can be given in terms of the difference between the state under consideration and the reference or standard state. The most commonly used standard state for solid, liquid, and gas at the temperature of interest are listed in Table 3.1.1.

3.1.4.2. Heat Capacity

The *heat capacity* C of a substance is defined as the quantity of heat q required to raise the temperature by 1 °C:

$$C = \left(\frac{\partial q}{\partial T}\right) \tag{3.1.11}$$

The heat capacity is an *extensive quantity*, which depends upon the amount of substance. It is more convenient to use molar heat capacity, which is an *intensive quantity*.

At constant volume, and at constant pressure, respectively, we have:

$$C_{\mathrm{V}} = \left(\frac{\partial q}{\partial T}\right)_V = \left(\frac{\partial U}{\partial T}\right)_V \tag{3.1.12}$$

$$C_{\mathrm{P}} = \left(\frac{\partial q}{\partial T}\right)_P = \left(\frac{\partial H}{\partial T}\right)_P, \tag{3.1.13}$$

respectively.

For ideal gas, we have:

$$C_{\mathrm{P}} - C_{\mathrm{V}} = R^* \tag{3.1.14}$$

$$C_{\mathrm{V}} = (3/2)R = 12.47\,\mathrm{J\,mol^{-1}\,K^{-1}} \tag{3.1.15}$$

$$C_{\mathrm{P}} = (5/2)R = 20.79\,\mathrm{J\,mol^{-1}\,K^{-1}} \tag{3.1.16}$$

Heat capacity measurements are normally conducted at ambient pressure (one atmospheric pressure). Hence, available heat capacity data are very often for C_{P} rather than C_{V}.

**Note*: In deriving Eqs. (3.1.14)–(3.1.16), reference can be made on any standard text book for thermodynamics.

3.1.4.3. Temperature Dependence of Heat Capacity

The temperature dependence of C_P is often represented by

$$C_P = A + B \times 10^{-3} T + C \times 10^5 / T^2 + D \times 10^{-6} T^2 \quad (3.1.17)$$

where A, B, C, and D are constants. Equation (3.1.17) is valid for temperatures above 298 K only. Compilations of heat capacity data for pure substances at standard states are available from Kubaschewski, Alcock and Spencer [1], Barin [2], and Chase [3]. Table 3.1.2 is taken from *KAS* for Al, O_2, and Al_2O_3, as examples.

From Table 3.1.2, we have:

$$\langle \mathrm{Al} \rangle \quad C_P/\mathrm{J\,mol\,K^{-1}} = 31.38 - 16.40 \times 10^{-3} T - 3.60 \times 10^5 / T^2 + 20.75 \times 10^{-6} T^2 \quad (298 < T < 934\mathrm{K}) \quad (3.1.18)$$

$$\{\mathrm{Al}\} \quad C_P/\mathrm{J\,mol\,K^{-1}} = 31.76 \quad (T > 934\mathrm{K}) \quad (3.1.19)$$

$$(\mathrm{Al}) \quad C_P/\mathrm{J\,mol\,K^{-1}} = 20.75 + 0.54 \times 10^5 / T^2 \quad (T > 298\mathrm{K}) \quad (3.1.20)$$

$$\langle \mathrm{Al_2O_3} \rangle \quad C_P/\mathrm{J\,mol\,K^{-1}} = 117.49 + 10.38 \times 10^{-3} T - 37.11 \times 10^5 / T^2 \quad (298\mathrm{K} < T < 2325\mathrm{K}) \quad (3.1.21)$$

$$\{\mathrm{Al_2O_3}\} \quad C_P/\mathrm{J\,mol\,K^{-1}} = 184.10 \quad (T > 2325\mathrm{K}) \quad (3.1.22)$$

$$(\mathrm{O_2}) \quad C_P/\mathrm{J\,mol\,K^{-1}} = 29.96 + 4.18 \times 10^{-3} T - 1.67 \times 10^5 / T^2 \quad (T > 298\mathrm{K}) \quad (3.1.23)$$

Equations (3.1.18) through (3.1.23) are valid for assigned temperature ranges only. By using these equations, heat capacities of Al, O_2, and Al_2O_3 are calculated and tabulated at an interval of 100 K in Tables 3.1.3–3.1.5, respectively, and are shown graphically in Figure 3.1.1. It is noteworthy that Tables 3.1.3–3.1.5 can easily be constructed by using *Microsoft Excel*. The C_P values at $T < 298$ K expressed by dotted lines were taken from Chase [3]. As shown in this figure, the C_P values for (Al) are very close to (5/2) $R = (5/2) \times 8.314 = 20.79$ J mol^{-1} K^{-1}, in conforming to Equation (3.1.16). Namely, monatomic metallic vapor would behave like ideal gas.

Table 3.1.2 Thermodynamic Data for Al, O_2, and Al_2O_3 Given in *KAS*

	$S_{298} \pm \delta S$ (J deg mol^{-1})	$-\Delta H_{298} \pm \delta H$ (kJ mol^{-1})	Phase	T (K)	$C_P = A + B \times 10^{-3} T + C \times 10^5 / T^2 + D \times 10^{-6} T^2$				H_T (kJ mol^{-1})
					A	B	C	D	
					(J deg mol^{-1})				
Al	28.3	0.0	fcc	298	31.38	−16.40	−3.60	20.75	–
			liq	**934**	31.76	–	–	–	10.7
Al(g)	164.4	−330	gas	298	20.75	–	0.54	–	–
Al_2O_3	50.9	1675.7 ± 1.3	hex	298	117.49	10.38	−37.11		–
			liq	**2325**	184.10	–	–	–	
O_2(g)	206.1	0.0	gas	298	29.96	4.18	−1.67	–	107.0

Table 3.1.3 Heat Capacities, Enthalpies, Entropies, Gibbs Energies, and Vapor Pressures of ⟨Al⟩, {Al}, (Al)

T (K)	C_P (J mol^{-1} K^{-1})			H (J mol^{-1})			S (J mol^{-1} K^{-1})			G (J mol^{-1})			G(Al) − G{Al} (J mol^{-1})	G(Al) − G⟨Al⟩ (J mol^{-1})	log P (atm)
	⟨Al⟩	{Al}	(Al)	⟨Al⟩	{Al}	(Al)	⟨Al⟩	{Al}	(Al)	⟨Al⟩	{Al}	(Al)			
298	24.28		21.36	0		330,000	28.300		164.400	−8433		281,009		289,442	−114
300	24.33		21.35	49		330,043	28.463		164.543	−8490		280,680		289,170	−113
400	25.89		21.09	2569		332,163	35.701		170.643	−11,712		263,905		275,617	−81
500	26.93		20.97	5210		334,265	41.592		175.334	−15,586		246,597		262,183	−62
600	28.01		20.90	7956		336,358	46.595		179.151	−20,001		228,867		248,868	−49
700	29.33		20.86	10,821		338,446	51.008		182.369	−24,885		210,787		235,672	−40
800	30.98		20.83	13,833		340,530	55.028		185.153	−30,190		192,408		222,598	−33
900	32.98		20.82	17,028		342,613	58.789		187.606	−35,882		173,768		209,650	−28
934	33.75		20.81	18,162	28,862	343,320	60.026	71.482	188.378	−37,902	−37,902	167,376	205,278	205,278	−26
1000		31.76	20.80		30,959	344,694		73.651	189.798		−42,692	154,895	197,588		−24
1100		31.76	20.79		34,135	346,774		76.678	191.781		−50,211	135,815	186,026		−20
1200		31.76	20.79		37,311	348,853		79.442	193.590		−58,019	116,545	174,564		−17
1300		31.76	20.78		40,487	350,931		81.984	195.253		−66,092	97,102	163,194		−15
1400		31.76	20.78		43,663	353,009		84.337	196.793		−74,410	77,499	151,908		−13
1500		31.76	20.77		46,839	355,087		86.529	198.227		−82,954	57,747	140,701		−11
1600		31.76	20.77		50,015	357,164		88.578	199.567		−91,711	37,856	129,567		−9.7
1700		31.76	20.77		53,191	359,241		90.504	200.826		−100,666	17,836	118,502		−8.4
1800		31.76	20.77		56,367	361,318		92.319	202.014		−109,808	−2,307	107,501		−7.2
1900		31.76	20.76		59,543	363,394		94.036	203.136		−119,126	−22,565	96,562		−6.1
2000		31.76	20.76		62,719	365,471		95.665	204.201		−128,612	−42,932	85,680		−5.2
2100		31.76	20.76		65,895	367,547		97.215	205.214		−138,257	−63,403	74,854		−4.3
2200		31.76	20.76		69,071	369,623		98.692	206.180		−148,053	−83,973	64,079		−3.5
2300		31.76	20.76		72,247	371,699		100.104	207.103		−157,993	−104,638	53,355		−2.8
2400		31.76	20.76		75,423	373,775		101.456	207.987		−168,071	−125,393	42,679		−2.1
2500		31.76	20.76		78,599	375,851		102.752	208.834		−178,282	−146,234	32,048		−1.5

Continued

Table 3.1.3 Heat Capacities, Enthalpies, Entropies, Gibbs Energies, and Vapor Pressures of ⟨Al⟩, {Al}, (Al)—cont'd

T (K)	C_P (J mol^{-1} K^{-1})			H (J mol^{-1})			S (J mol^{-1} K^{-1})			G (J mol^{-1})			G(Al) − G{Al} (J mol^{-1})	G(Al) − G⟨Al⟩ (J mol^{-1})	log P (atm)
	⟨Al⟩	{Al}	(Al)	⟨Al⟩	{Al}	(Al)	⟨Al⟩	{Al}	(Al)	⟨Al⟩	{Al}	(Al)			
2600		31.76	20.76		81,775	377,927		103.998	209.648		−188,620	−167,158	21,462		−0.99
2700		31.76	20.76		84,951	380,003		105.197	210.432		−199,080	−188,162	10,918		−0.49
2800		31.76	20.76		88,127	382,078		106.352	211.186		−209,658	−209,244	415		−0.02
2804		31.76	20.76		88,254	382,161		106.397	211.216		−210,084	−210,088	0		0.00
2900		31.76	20.76		91,303	384,154		107.466	211.915		−220,349	−230,399	−10,050		0.42
3000		31.76	20.76		94,479	386,230		108.543	212.618		−231,150	−251,626	−20,476		0.82

$H_F = 28{,}862 - 18{,}162 = 10{,}700\ \text{J mol}^{-1}$

$\Delta H_V = 328{,}161 - 88{,}254 = 293907\ \text{J mol}^{-1}\ \text{K}^{-1}$

$\Delta S_F = 71.482 - 60.026 = 11.45\ \text{J mol}^{-1}\text{K}^{-1}$

$\Delta S_V = 211.216 - 106.397 = 104.8\ \text{J mol}^{-1}\text{K}^{-1}$

Table 3.1.4 Heat Capacities, Enthalpies, Entropies, and Gibbs Energies of (O_2)

T (K)	C_P (J mol^{-1} K^{-1})	H (J mol^{-1})	S (J mol^{-1} K^{-1})	G (J mol^{-1})
	(O_2)	(O_2)	(O_2)	(O_2)
298	29.33	0	206.100	−61,418
300	29.36	59	206.296	−61,830
400	30.59	3,062	214.927	−82,909
500	31.38	6162	221.843	−104,759
600	32.00	9333	227.621	−127,240
700	32.55	12,561	232.596	−150,257
800	33.04	15,840	236.975	−173,739
900	33.52	19,168	240.894	−197,636
1000	33.97	22,543	244.449	−221,906
1100	34.42	25,963	247.708	−246,516
1200	34.86	29,427	250.722	−271,440
1300	35.30	32,934	253.529	−296,654
1400	35.73	36,486	256.161	−322,140
1500	36.16	40,080	258.640	−347,881
1600	36.58	43,717	260.987	−373,863
1700	37.01	47,396	263.218	−400,074
1800	37.43	51,118	265.345	−426,503
1900	37.86	54,883	267.381	−453,140
2000	38.28	58,689	269.333	−479,977
2100	38.70	62,538	271.211	−507,005
2200	39.12	66,429	273.021	−534,217
2300	39.54	70,363	274.769	−561,607
2325	39.65	71,353	275.197	−568,481
2400	39.96	74,338	276.461	−589,169
2500	40.38	78,355	278.101	−616,897
2600	40.80	82,415	279.693	−644,787
2700	41.22	86,516	281.241	−672,834
2800	41.64	90,659	282.748	−701,034
2804	41.67	90,826	282.807	−702,165
2900	42.06	94,844	284.216	−729,383
3000	42.48	99,072	285.649	−757,876

Table 3.1.5 Heat Capacities, Enthalpies, Entropies, and Gibbs Energies of $\langle Al_2O_3 \rangle$ and $\{Al_2O_3\}$

T (K)	C_P (J mol^{-1} K^{-1})		H (J mol^{-1})		S (J mol^{-1} K^{-1})		G (J mol^{-1})	
	$\langle Al_2O_3 \rangle$	$\{Al_2O_3\}$	$\langle Al_2O_3 \rangle$	$\{Al_2O_3\}$	$\langle Al_2O_3 \rangle$	$\{Al_2O_3\}$	$\langle Al_2O_3 \rangle$	$\{Al_2O_3\}$
298	78.80		−1,675,700		50.900		−1,690,868	
300	79.37		−1,675,542		51.429		−1,690,971	
400	98.45		−1,666,522		77.247		−1,697,421	
500	107.84		−1,656,161		100.327		−1,706,325	
600	113.41		−1,645,079		120.518		−1,717,390	
700	117.18		−1,633,538		138.300		−1,730,348	
800	120.00		−1,621,674		154.139		−1,744,985	
900	122.25		−1,609,558		168.407		−1,761,124	
1000	124.16		−1,597,235		181.389		−1,778,624	
1100	125.84		−1,584,733		193.303		−1,797,366	
1200	127.37		−1,572,072		204.319		−1,817,254	
1300	128.79		−1,559,263		214.570		−1,838,204	
1400	130.13		−1,546,317		224.164		−1,860,146	
1500	131.41		−1,533,239		233.186		−1,883,018	
1600	132.65		−1,520,036		241.707		−1,906,767	
1700	133.85		−1,506,711		249.785		−1,931,345	
1800	135.03		−1,493,267		257.469		−1,956,711	
1900	136.18		−1,479,706		264.800		−1,982,827	
2000	137.32		−1,466,030		271.815		−2,009,660	

2100	138.45		−1,452,242		278.542		−2,037,180	
2200	139.56		−1,438,342		285.008		−2,065,360	
2300	140.66		−1,424,330		291.236		−2,094,174	
2325	140.94	184.10	−1,420,810	−1,313,810	292.759	338.780	−2,101,474	−2,101,474
2400		184.10		−1,300,003		344.625		−2,127,103
2500		184.10		−1,281,593		352.140		−2,161,944
2600		184.10		−1,263,183		359.361		−2,197,521
2700		184.10		−1,244,773		366.309		−2,233,807
2800		184.10		−1,235,568		369.687		−2,270,774
2804		184.10		−1,225,626		373.267		−2,272,267
2900		184.10		−1,226,363		373.004		−2,308,400
3000		184.10		−1,207,953		379.464		−2,346,660
	$\Delta H_F = (-1{,}313{,}810) - (-1{,}420{,}810) = 107{,}000\ \text{J mol}^{-1}$				$\Delta S_F = 338.780 - 292.759 = 46.021\ \text{J mol}^{-1}\ \text{K}^{-1}$			

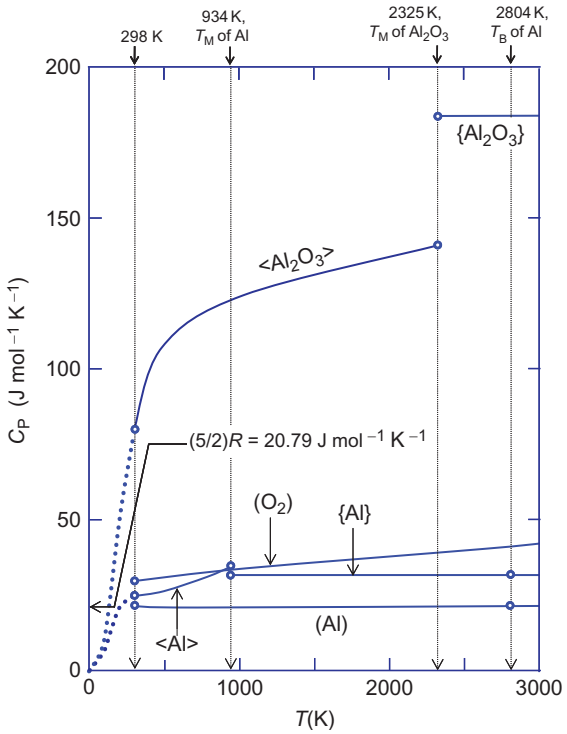


Figure 3.1.1 Heat capacities of Al, O_2, and Al_2O_3.

3.1.4.4. Temperature Dependence of Enthalpy

The enthalpy change due to changes in temperature from 298 K to T K is obtainable by integrating Equation (3.1.13):

$$H_T - H_{298} = \int_{298}^{T} C_P \mathrm{d}T \tag{3.1.24}$$

By convention, enthalpies of elements in the most stable form at 298 K are assigned to be zero.

$$H_{298} = 0 \,(\text{for elements of most stable form}) \tag{3.1.25}$$

The zero values of H_{298} given in Table 3.1.2[1], for Al and O_2, respectively, are based upon this convention rather than measurements. Thus, for elements, Equation (3.1.25) becomes:

[1] In *KAS*, symbol ΔH_{298} rather than H_{298} is used.

$$H_T = \int_{298}^{T} C_P \mathrm{d}T \tag{3.1.26}$$

For $\langle Al \rangle$ and (O_2), as examples, by putting Equations (3.1.18) and (3.1.23), respectively, into (3.1.26), we have

$$\begin{aligned} H_T\langle Al\rangle/\mathrm{J\,mol^{-1}} &= \int_{298}^{T} \left(31.38 - 16.40\times10^{-3}T - 3.60\times10^{5}/T^2 + 20.75\times10^{-6}T^2\right)\mathrm{d}T \\ &= 31.38\times(T-298) - (16.40/2)\times10^{-3}\times(T^2-298^2) \\ &\quad + 3.60\times10^{5}\{(1/T)-(1/298)\} + (20.75\times10^{-6}/3)\times(T^3-298^3) \\ &\quad \text{for } 298\,\mathrm{K} < T < 934\,\mathrm{K} \end{aligned} \tag{3.1.27}$$

$$\begin{aligned} H_T(O_2)/\mathrm{J\,mol^{-1}} &= \int_{298}^{T} \left(29.96 - 4.18\times10^{-3}T - 1.67\times10^{5}/T^2\right)\mathrm{d}T \\ &= 29.96\times(T-298) - (4.18/2)\times10^{-3}\times(T^2-298^2) \\ &\quad + 1.67\times10^{5}\{(1/T)-(1/298)\} \\ &\quad \text{for } T > 298\,\mathrm{K} \end{aligned} \tag{3.1.28}$$

For (Al), $H_{298}(Al) = +330$ kJ mol^{-1}, hence, we have

$$\begin{aligned} H_T(Al)\left(\mathrm{J\,mol^{-1}}\right) &= +330{,}000 + \int_{298}^{T} \left(20.75 + 0.54\times10^{5}/T^2\right)\mathrm{d}T \\ &= +330{,}000 + 20.75\times(T-298) - 0.54\times10^{5}\times\{(1/T)-(1/298)\} \end{aligned} \tag{3.1.29}$$

It is noted that H_{298} for (Al) is not zero, as gaseous monatomic aluminum is not the most stable form of Al at 298 K.

In contrast to elements, enthalpy values given in *KAS* for compounds at 298 K H_{298} are not based upon convention. For Al_2O_3, as an example, values for H_{298} are obtainable by determining calorimetrically the amounts of heat generated through reaction:

$$2\langle Al\rangle + (3/2)(O_2) = \langle Al_2O_3\rangle \tag{3.1.30}$$

$$\Delta H_{298}(3.1.30) = H_{298}\langle Al_2O_3\rangle - 2H_{298}\langle Al\rangle - (3/2)H_{298}(O_2) \tag{3.1.31}$$

By convention made on elements, $H_{298}\langle Al\rangle = H_{298}(O_2) = 0$. Hence, Equation (3.1.31) becomes

$$\Delta H_{298}\,(3.1.30) = H_{298}\langle Al_2O_3\rangle \tag{3.1.32}$$

The H_{298} value of -1675.7 ± 1.3 kJ mol^{-1} given in Table 3.1.2 for $\langle Al_2O_3\rangle$ is based upon such measurements. Thus, for $\langle Al_2O_3\rangle$, we have:

$$H_T\langle \mathrm{Al_2O_3}\rangle/\mathrm{J\,mol^{-1}} = -1{,}675{,}700 + \int_{298}^{T} \left(117.49 + 10.38 \times 10^{-3} T - 37.11 \times 10^5 / T^2\right) \mathrm{d}T \tag{3.1.33}$$

At temperatures greater than the melting point T_M, heat of fusion ΔH_F must be taken into account:

$$H_T\{\mathrm{liquid}\} = H_{298}\langle \mathrm{solid}\rangle + \int_{298}^{T_\mathrm{M}} C_\mathrm{P}\langle \mathrm{solid}\rangle \mathrm{d}T + \Delta H_\mathrm{F} + \int_{T_\mathrm{M}}^{T} C_\mathrm{P}\{\mathrm{liquid}\} \mathrm{d}T \tag{3.1.34}$$

From Table 3.1.2, for {Al}, we have $T_\mathrm{M} = 934$ K and $\Delta H_\mathrm{F} = +10{,}700$ J mol^{-1}, while for $\{\mathrm{Al_2O_3}\}$, $T_\mathrm{M} = 2325$ K and $\Delta H_\mathrm{F} = +107{,}000$ J mol^{-1}. Thus, we have:

$$\begin{aligned} H_T\{\mathrm{Al}\}/\mathrm{J\,mol^{-1}} &= \int_{298}^{934} \left(31.38 - 16.40 \times 10^{-3} T - 3.60 \times 10^5 / T^2 + 20.75 \times 10^{-6} T^2\right) \mathrm{d}T \\ &\quad + 10{,}700 + \int_{934}^{T} (31.76) dT \\ &= 31.38 \times (934 - 298) - (16.40/2) \times 10^{-3} \times (934^2 - 298^2) \\ &\quad + 3.60 \times 10^5 \times \{(1/934 - (1/298)\} + (20.75 \times 10^{-6}/3) \times (T^3 - 934^3) \\ &\quad + 10{,}700 + 31.76 \times (T - 934) \\ &\quad (\text{for } T > 934K) \end{aligned} \tag{3.1.35}$$

$$\begin{aligned} H_T\{\mathrm{Al_2O_3}\}(\mathrm{J\,mol^{-1}}) &= -1{,}675{,}700 \\ &\quad + \int_{298}^{2325} \left(117.49 + 10.38 \times 10^{-3} T - 37.11 \times 10^5 / T^2\right) \mathrm{d}T \\ &\quad + 107{,}000 + \int_{2325}^{T} (184.10) \mathrm{d}T \\ &= -1{,}675{,}700 + 117.49 \times (2325 - 298) + (10.38/2) \times 10^{-3} \\ &\quad \times (2325^2 - 298^2) \\ &\quad + (37.11 \times 10^{-5}/3) \times (2325^3 - 298^3) + 107{,}000 + 184.10 \\ &\quad \times (T - 2325) \\ &\quad (\text{for } T > 2325\mathrm{K}) \end{aligned} \tag{3.1.36}$$

The enthalpies of Al, O_2, and Al_2O_3 are shown graphically in Figure 3.1.2, where the boiling point of Al is given as 2804 K. Derivations of such values for boiling points will be described in a later section. As shown in Table 3.1.2, boiling point T_B and heat of vaporizations ΔH_V are not given in *KAS*.

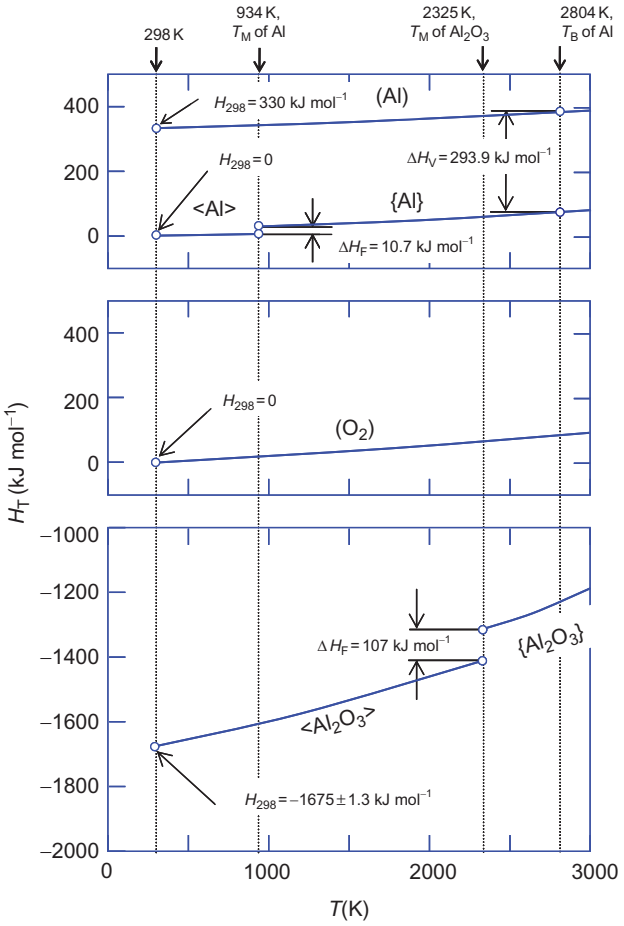


Figure 3.1.2 Enthalpies of Al, Al_2O_3, and O_2 as the function of temperature.

3.1.5. THE SECOND AND THIRD LAWS OF THERMODYNAMICS AND ENTROPY

The concept of entropy arises from the *Second Law of Thermodynamics*. Its derivation can be found in any textbook on thermodynamics. Hence, it will not be repeated here. The entropy of a substance at any temperature is defined as:

$$dS = \left(\frac{\partial q}{T}\right) \tag{3.1.37}$$

By combining Equation (3.1.13) with (3.1.37), for constant pressure, we have

$$dS = \left(\frac{\partial H}{T}\right)_p = \left(\frac{C_P}{T}\right) dT \tag{3.1.38}$$

By integrating this equation between 0 and T K,

$$S_T = S_0 + \int_0^T (C_P/T) dT \tag{3.1.39}$$

$$S_T = S_0 + \int_0^{298} (C_P/T) dT + \int_{298}^T (C_P/T) dT \tag{3.1.40}$$

Following to the *Third Law of Thermodynamics*, entropy of any ordered crystalline pure substances at 0 K S_0 should be zero:

$$S_0 = 0 \text{ (for ordered crystalline substances)} \tag{3.1.41}$$

Namely, in contrast to the values of enthalpy, which are related to arbitrary standards, those of entropies can be determined absolutely. Thus, Equation (3.1.40) becomes

$$S_T = \int_0^{298} (C_P/T) dT + \int_{298}^T (C_P/T) dT \tag{3.1.42}$$

For convenience in calculation, entropy values at 298.15 K, i.e., the first term of the right-hand side of Equation (3.1.42) is termed *standard entropies* and expressed by S_{298}:

$$S_{298} = \int_0^{298} (C_P/T) dT \tag{3.1.43}$$

Thus, Equation (3.1.42) becomes

$$S_T = S_{298} + \int_{298}^T (C_P/T) dT \tag{3.1.44}$$

Values for S_{298} are obtainable from low temperature C_P data. For ⟨Al⟩, plots of C_P/T against T are given in Figure 3.1.3. The area beneath C_P/T curves between 0 and 298 K corresponds to $S_{298}\langle Al\rangle = 28.3$ J mol^{-1} K^{-1}. Process metallurgists are rarely requested to evaluate S_{298} from C_P measurements, as this is usually done by those who measure the heat capacities.

By using heat capacity data for ⟨Al⟩, for example, we have:

$$\begin{aligned} S_T\langle Al\rangle/\text{Jmol}^{-1}K^{-1} &= 28.3 + \int_{298}^T \left(31.38/T - 16.40\times10^{-3} - 3.60\times10^5/T^3 + 20.75\times10^6 T\right) dT \\ &= 28.3 + 31.38\times\ln(T/298) - 16.40\times10^{-3}(T-298) \\ &\quad + (3.60/2)\times10^5(1/T^2 - 1/298^2) + (20.75/2)\times10^6(T^2 - 298^2) \end{aligned} \tag{3.1.45}$$

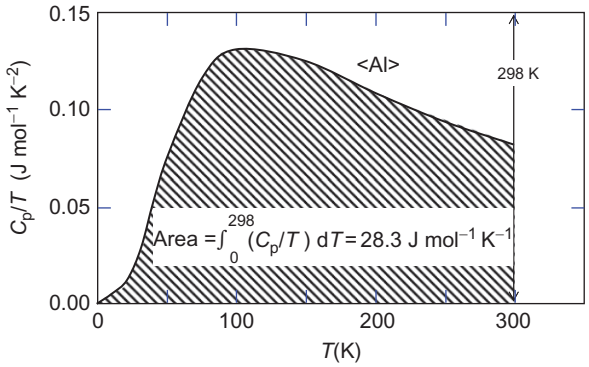


Figure 3.1.3 Relation between C_P/T and T for ⟨Al⟩.

At temperatures greater than melting temperature T_M, entropy of fusion ΔS_F has to be taken into account.

$$\Delta S_F = \frac{\Delta H_F}{T_M} \tag{3.1.46}$$

$$S_T = S_{298} + \int_{298}^{T_M} \langle C_P/T \rangle dT + \Delta S_F + \int_{T_M}^{T} \{C_P/T\} dT \tag{3.1.47}$$

For {Al}, $\Delta H_F = 10{,}700$ J mol^{-1} and $T_M = 934$ K. Hence $\Delta S_F = 10{,}700/934 = 11.456$ J mol^{-1} K^{-1}. Thus, we have

$$\begin{aligned} S_T\{\mathrm{Al}\}/\mathrm{Jmol}^{-1}K^{-1} = {} & 28.3 + 31.38 \times \ln(934/298) - 16.40 \times 10^{-3} \times (934 - 298) \\ & + (3.60/2) \times 10^5 \times (1/934^2 - 1/298^2) + (20.75/2) \\ & \times 10^{-6} \times (934^2 - 298^2) \\ & + 11.456 + 31.76 \times \ln(T/934) \end{aligned} \tag{3.1.48}$$

Figure 3.1.4 shows the entropies of Al, O_2, and Al_2O_3 as the function of temperature. As shown in this figure, entropies of pure substances are invariably positive.

3.1.6. GIBBS ENERGY

Gibbs energy is defined as

$$G \equiv H - TS \tag{3.1.49}$$

From this definition and that entropies of pure substances are invariably positive, Gibbs energies of pure substances decrease with an increase in temperature. Figure 3.1.5a shows schematically such decrease in Gibbs energy with increasing temperature for solid, liquid, and vapor of a substance at standard state. The most stable phase corresponds to the lowest Gibbs energy. Thus, the solid is most stable at low temperatures, then liquid and finally gas

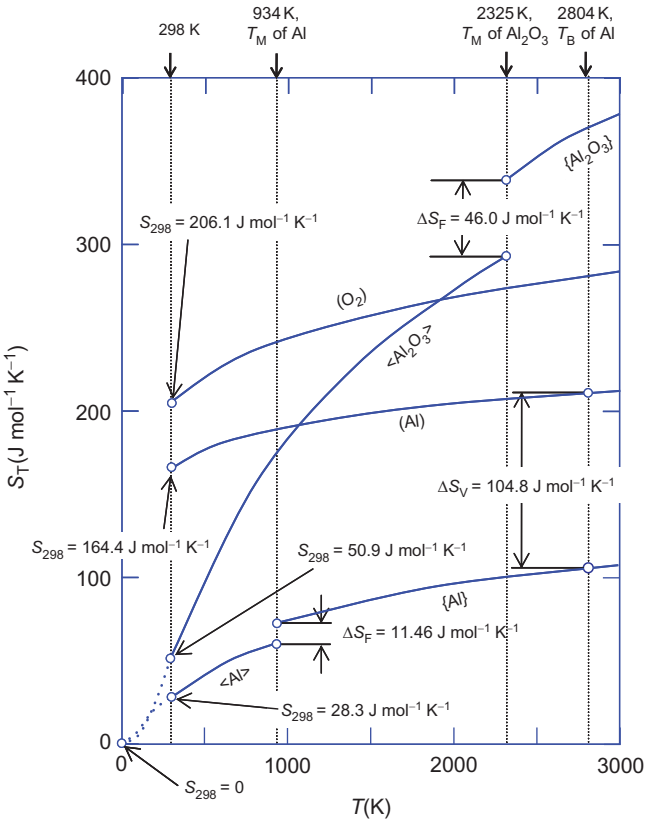


Figure 3.1.4 Entropies of Al, O_2, and Al_2O_3.

of 1 atm pressure. If the line for gas falls more steeply, as shown in Figure 3.1.5b, then it might intersect the line for solid before the line for liquid does. In such case, liquid is never the stable phase, and solid sublimes directly to a vapor.

Figure 3.1.6 shows Gibbs energies for Al, O_2, and Al_2O_3 as the function of temperature. It is noteworthy that Gibbs energies of pure substances are not linear functions of temperature.

At melting point T_M, solid phase should be in equilibrium with liquid. In conforming to this, as can be seen in Figure 3.1.6:

$$G_{934}\langle \mathrm{Al} \rangle = G_{934}\{\mathrm{Al}\} \tag{3.1.50}$$

$$G_{2325}\langle \mathrm{Al_2O_3} \rangle = G_{2325}\{\mathrm{Al_2O_3}\} \tag{3.1.51}$$

Although, *KAS* does not provide values for boiling points T_B, in Table 3.1.3 the T_B values for Al is given as 2804 K. This value of 2804 K was obtained through Gibbs energy calculations by using a manner described below.

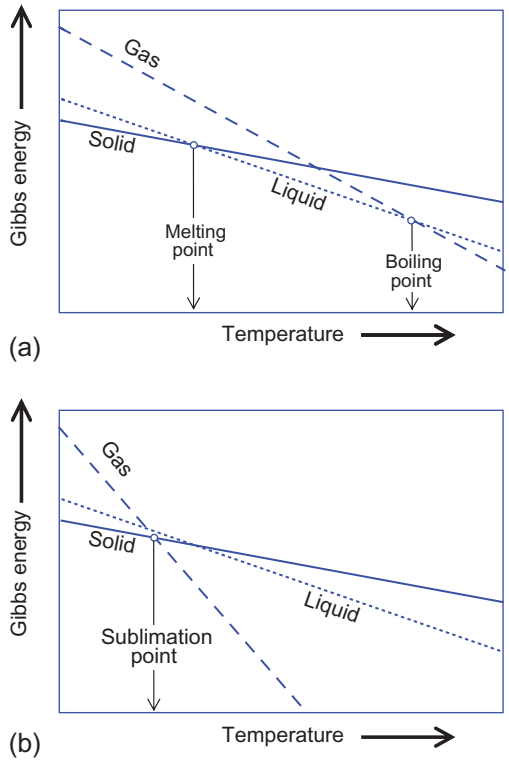


Figure 3.1.5 Schematic illustrations of Gibbs energies for solid, liquid, and gas. (a) With an increase in temperature, we have solid, liquid, and gas phases. (b) Phase equilibrium takes place between solid and gas phases (sublimation).

Tables 3.1.6–3.1.8, which were constructed through "*Microsoft Excel*," tabulate values for $G(\mathrm{Al}) - G\{\mathrm{Al}\}$ at an interval of 1, 0.1, and 0.01 K, respectively, near 2800 K. From Table 3.1.6, it can be seen that $2803\ \mathrm{K} < T_\mathrm{B} < 2804\ \mathrm{K}$, while Table 3.1.7 indicates $2803.9\ \mathrm{K} < T_\mathrm{B} < 2804.0\ \mathrm{K}$. Finally, Table 3.1.8 shows $2803.95\ \mathrm{K} < T_\mathrm{B} < 2803.96\ \mathrm{K}$. Thus, it is concluded that $T_\mathrm{B} = 2804\ \mathrm{K}$.

$$G_{2804}\{\mathrm{Al}\} = G_{2804}(\mathrm{Al}) \tag{3.1.52}$$

3.1.7. COMBINED STATEMENT OF THE FIRST AND SECOND LAWS OF THERMODYNAMICS

Let us refer to equations which reflect directly to the First and Second Law of thermodynamics, i.e., Equations (3.1.4) and (3.1.37), respectively.

$$\mathrm{d}U = \delta q - \delta w \tag{3.1.4}$$

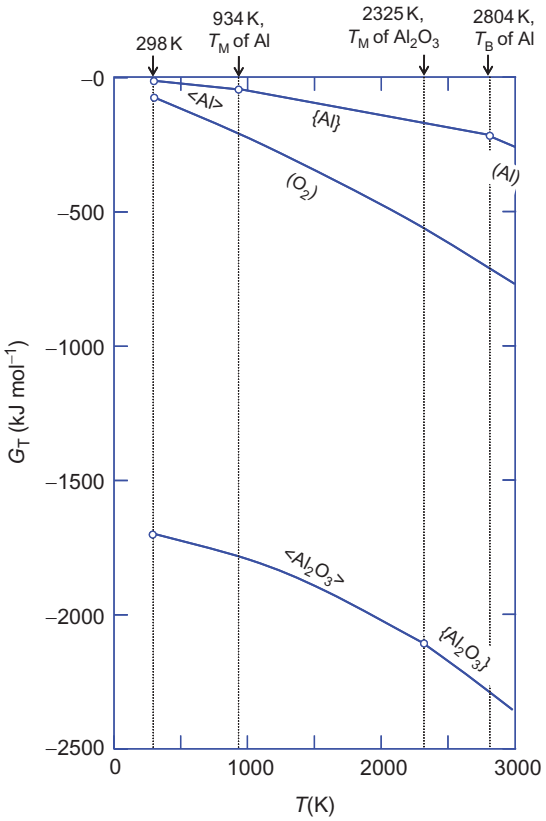


Figure 3.1.6 Gibbs energies of Al, O_2, and Al_2O_3.

Table 3.1.6 Values for *G*(Al) − G{Al} Between 2800 and 2806 K

T **(K)**	***G*(Al) − *G*{Al}** **(kJ mol^{-1})**
2800	415
2801	310
2802	205
2803	100
2804	−5
2805	−110
2806	−214

Table 3.1.7 Values for $G(\mathrm{Al}) - G\{\mathrm{Al}\}$ Between 2803.6 and 2804.2 K

T (K)	$G(\mathrm{Al}) - G\{\mathrm{Al}\}$ (kJ mol^{-1})
2803.6	37
2803.7	27
2803.8	16
2803.9	6
2804.0	−5
2804.1	−15
2804.2	−26

Table 3.1.8 Values for $G(\mathrm{Al}) - G\{\mathrm{Al}\}$ Between 2803.92 and 2803.98 K

T (K)	$G(\mathrm{Al}) - G\{\mathrm{Al}\}$ (kJ mol^{-1})
2803.92	3.58
2803.93	2.53
2803.94	1.48
2803.95	0.43
2803.96	−0.61
2803.97	−1.66
2803.98	−2.71

$$\mathrm{d}S = \left(\frac{\partial q}{T}\right) \tag{3.1.37}$$

If the only work done is that against pressure,

$$\delta w = P\mathrm{d}V \tag{3.1.53}$$

Hence, Equations (3.1.4) becomes

$$\mathrm{d}U = \delta q - P\mathrm{d}V \tag{3.1.54}$$

By combining Equations (3.1.37) and (3.1.54), then we have

$$dU = T\mathrm{d}S - P\mathrm{d}V \tag{3.1.55}$$

This expression applies only to a reversible process, since it is only for a reversible process that $\mathrm{d}S = \delta q/T$. On the other hand, G is defined by the relation

$$G = H - TS = U + PV - TS \tag{3.1.56}$$

By differentiating Equation (3.1.56) and combining with (3.1.55), we have

$$\begin{aligned} \mathrm{d}G &= \mathrm{d}U + P\mathrm{d}V + V\mathrm{d}P - T\mathrm{d}S - S\mathrm{d}T \\ \mathrm{d}U &= -P\mathrm{d}V + T\mathrm{d}S \\ \mathrm{d}G &= +V\mathrm{d}P - S\mathrm{d}T \end{aligned} \tag{3.1.57}$$

Equation (3.1.57) is the combined expression of the First and Second Laws of thermodynamics. At constant temperature, this equation becomes

$$\mathrm{d}G = V\mathrm{d}P \tag{3.1.58}$$

Since $PV = RT$, for ideal gas, we have

$$\mathrm{d}G = (RT/P)\mathrm{d}P = RT\mathrm{d}(\ln P) \tag{3.1.59}$$

By integration between $P = 1$ atm and $P = P$ atm, Equation (3.1.59) becomes

$$G_T(P) - G_T(1\,\mathrm{atm}) = RT\ln P \tag{3.1.60}$$

Hereafter, the Gibbs energy of a substance in the standard state is designated as G°_T. Hence, from Equation (3.1.60), the Gibbs energy of 1 mol of gas at any other pressure P is given as

$$G_T(P) = G^\circ_T + RT\ln P$$

or simply

$$G_T = G^\circ_T + RT\ln P \tag{3.1.61}$$

Next, consider equilibrium between liquid and its vapor. At boiling point, pure liquid phase is in equilibrium with its vapor of 1 atm.

$$G^\circ\{\mathrm{Liquid}\} = G^\circ(\mathrm{Gas}) \quad \text{at } T = T_\mathrm{B} \tag{3.1.62}$$

At temperatures lower than the boiling point, vapor of pressure P less than 1 atm is in equilibrium with pure condensed phase, thus

$$G^\circ\langle\mathrm{Solid}\rangle = G^\circ(\mathrm{Gas}) + RT\ \ln P \quad \text{at } T < T_\mathrm{M} \tag{3.1.63}$$

$$G^\circ\{\mathrm{Liquid}\} = G^\circ(\mathrm{Gas}) + RT\ \ln P \quad \text{at } T_\mathrm{M} < T < T_\mathrm{B} \tag{3.1.64}$$

Vapor pressures of Al calculated through Equation (3.1.63) and (3.1.64) are tabulated in Table 3.1.3, and shown graphically as the function of temperature in Figure 3.1.7.

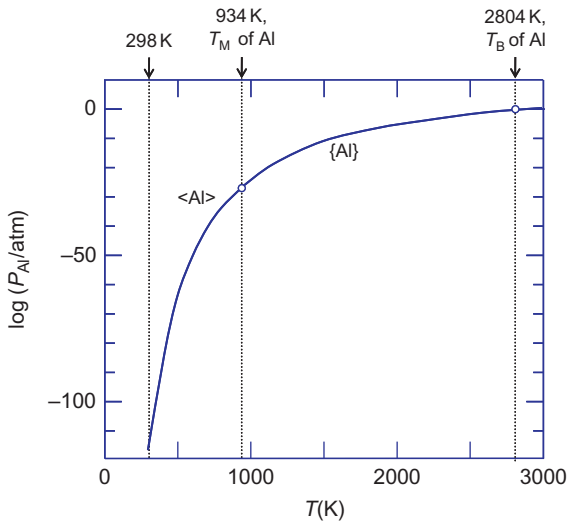


Figure 3.1.7 Vapor pressure of Al.

3.1.8. CHANGES IN GIBBS ENERGY, ENTHALPY, AND ENTROPY DUE TO REACTION

When all reactants and products are in their standard states, changes in Gibbs energy ΔG°, enthalpy ΔH° and entropy ΔS° due to chemical reaction can be calculated through

$$\Delta G^\circ = \sum G^\circ_{\text{products}} - \sum G^\circ_{\text{reactants}} \tag{3.1.65}$$

$$\Delta H^\circ = \sum H^\circ_{\text{products}} - \sum H^\circ_{\text{reactants}} \tag{3.1.66}$$

$$\Delta S^\circ = \sum S^\circ_{\text{products}} - \sum S^\circ_{\text{reactants}} \tag{3.1.67}$$

For the following reaction, as an example,

$$2\langle \text{Al} \rangle + (3/2)(\text{O}_2) = \langle \text{Al}_2\text{O}_3 \rangle \tag{3.1.68}$$

it follows

$$\Delta G^\circ_T(3.1.68) = G_T\langle \text{Al}_2\text{O}_3 \rangle - 2G_T\langle \text{Al} \rangle - (3/2)G_T(\text{O}_2) \tag{3.1.69}$$

$$\Delta H^\circ_T(3.1.68) = H_T\langle \text{Al}_2\text{O}_3 \rangle - 2H_T\langle \text{Al} \rangle - (3/2)H_T(\text{O}_2) \tag{3.1.70}$$

$$\Delta S^\circ_T(3.1.68) = S_T\langle \text{Al}_2\text{O}_3 \rangle - 2S_T\langle \text{Al} \rangle - (3/2)S_T(\text{O}_2) \tag{3.1.71}$$

Figure 3.1.8 shows values for ΔG°_T, ΔH°_T, and ΔS°_T for Reaction (3.1.68).

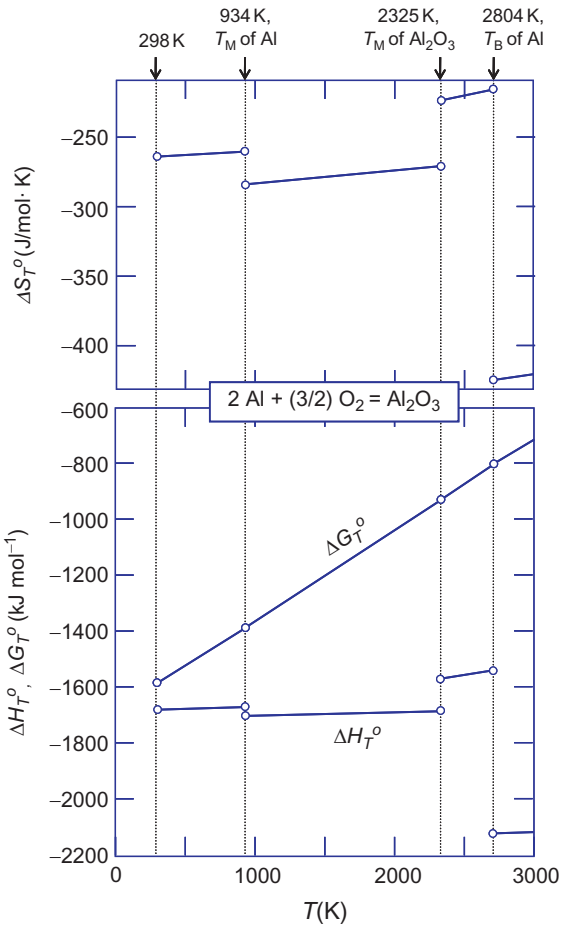


Figure 3.1.8 Changes in Gibbs energy, enthalpy, and entropy for reaction $2Al + (3/2)\ O_2 = Al_2O_3$ as the function of temperature.

As already described, Gibbs energies of pure substances are not linear functions of temperature. However, as shown in Figure 3.1.8, Gibbs energy changes due to chemical reactions can be expressed by the following formula:

$$\Delta G_T = \Delta H^\circ_{298} - T\Delta S^\circ_{298} \tag{3.1.72}$$

where ΔH°_{298} and ΔS°_{298} are constants[2]. By using thermochemical data compiled by JANAF [9–12], Barin and Knacke [13], Barin *et al.* [14], and Kubaschewski *et al.* [15],

[2] ΔH°_{298} and ΔS°_{298}, respectively, are termed second-law enthalpy and second-law entropy, respectively.

Turkdogan [8] computed values for ΔH°_{298} and ΔS°_{298} for selected chemical reactions, as shown in Table 3.1.A7 of Appendix.

3.1.9. GIBBS ENERGY FUNCTION

By combining Equations (3.1.35) and (3.1.48) with (3.1.49), values for $G_T\{\text{Al}\}$, for example, are expressed as

$$\begin{aligned} G_T\{\text{Al}\}/\text{Jmol}^{-1} = {} & 31.38 \times (934 - 298) - (16.40/2) \times 10^{-3} \times (934^2 - 298^2) \\ & + 3.60 \times 10^5 \times \{(1/934 - (1/298)\} + (20.75 \times 10^{-6}/3) \\ & \times (934^3 - 298^3) + 10{,}700 + 31.76 \times (T - 934) \\ & - T\{28.3 + 31.38 \times \ln(934/298) - 16.40 \times 10^{-3} \times (934 - 298) \\ & + (3.60/2) \times 10^5 \times (1/934^2 - 1/298^2) + (20.75/2) \\ & \times 10^{-6} \times (934^2 - 298^2) + 11.456 + 31.76 \\ & \times \ln(T/934)\} \end{aligned} \tag{3.1.73}$$

During the days when computer programs or even electric calculators were not common yet, calculations of G_T and ΔG_T for any reaction by virtue of this type of equation were time-consuming and tedious. It used to be convenient to tabulate Gibbs energy at even temperatures. Interpolations are, however, accurate only with tabulations at close intervals. The ideal function would vary slowly enough with temperature to allow accurate interpolation. The Gibbs energy function defined below meet these requirements:

$$\text{Gibbs energy function} = \frac{(G_T - H_{298})}{T} \tag{3.1.74}$$

With tabulated Gibbs energy functions available as exemplified in Table 3.1.9 which was taken from Ref. [6] published in 1960, it was easier to calculate ΔG_T at a variety of temperatures than it would be to use analytical equation of ΔG_T. Nowadays, however, computer software, e.g., *Microsoft Excel*, allows rapid calculations of G_T and ΔG_T at any desired temperature by using analytical equations. Thus, Gibbs energy function became less important than before. Gibbs energy function, however, would be still useful for evaluating thermochemical data obtained through chemical equilibrium.

Table 3.1.9 Tabulated Gibbs Energy Function for Al Given by Elliott and Gleiser [6]

	Al (gfw) 26.98 g				
	T (°K)	C_P° (cal/°/gfw)	$H_T^\circ - H_{298.15}^\circ$ (cal gfw^{-1})	S_T° (cal/°/gfw)	$-\left(F_T^\circ - H_{298.15}^\circ\right)/T$
Reference state: Solid from 298° to 932°; liquid from 932° to 2740°; ideal monatomic gas from 2740° to 3000°	298	5.82	0	6.77	6.77
	300	5.83	11	6.80	6.77
	400	6.12	600	8.49	6.99
	500	6.43	1230	9.91	7.45
	600	6.72	1890	11.11	7.96
	700	7.02	2580	12.17	8.49
$(H_{298.15}^\circ - H_0^\circ) =$ 1094 cal gfw^{-1}	800	7.31	3310	13.15	9.02
	900	7.61	4060	14.03	9.52
Phase changes	1000	7.00	7330	17.53	10.20
	1100	7.00	8030	18.19	10.89
m.p., 932 K	1200	7.00	8730	18.80	11.53
ΔH_m 2550 cal gfw^{-1}	1300	7.00	9430	19.36	12.11
	1400	7.00	10,130	19.88	12.65
b.p., 2740 K	1500	7.00	10,830	20.36	13.14
ΔH_e 70,700 cal gfw^{-1}	1600	7.00	11,530	20.81	13.61
	1700	7.00	12,230	21.24	14.05
	1800	7.00	12,930	21.64	14.46
	1900	7.00	13,630	22.02	14.85
	2000	7.00	14,330	22.38	15.22
	2100	7.00	15,030	22.72	15.57
	2200	7.00	15,730	23.04	15.89
	2300	7.00	16,430	23.35	16.21
	2400	7.00	17,130	23.65	16.52
	2500	7.00	17,830	23.94	16.81
	2600	7.00	18,530	24.21	17.09
	2700	7.00	19,230	24.48	17.36
	2800	4.97	90,510	50.50	18.18
	2900	4.97	91,010	50.67	19.29
	3000	4.97	91,500	50.84	20.34

APPENDIX

With respect to data compilations given in *KAS*, a few words seem to be pertinent. First of all, it is to be mentioned that *KAS* is the sixth edition of "*Metallurgical Thermochemistry*" with a new title "*Materials Thermochemistry*." In the five editions of *Metallurgical Thermochemistry* coauthored by Kubaschewski and Alcock [16], data compilations consisted of five tables as follows:

Table 3.1.A1	Heat of formation, standard entropies, structure, and temperatures of solid-phase transformation, melting, and boiling
Table 3.1.A2	Heats and temperatures of transformation
Table 3.1.A3	Heat capacities C_P of pure substances in an analytical formula $C_P = a + bT + cT^{-2} + dT^2$ (a, b, c, d; constants)
Table 3.1.A4	Vapor pressures P and evaporation constants (heats of evaporation and sublimation) in an analytical formula: $\log P\,(\text{mmHg}) = A/T + B \log T + CT + D$ (A, B, C, D; constants)
Table 3.1.A5	Standard Gibbs energies of reactions in an analytical formula $\Delta G_T = A + B\,T \log T + CT$ (A, B, C, D; constants)

Tables 3.1.A1–3.1.A5 for Al, O_2, and Al_2O_3, for examples, are as follows:

Table 3.1.A1 Heat of Formation, Standard Entropies, and Structures

Substances	H°_{298}(kcal mol^{-1})	S°_{298} (cal deg^{-1} mol^{-1})	tr.p. (°C)	m.p. (°C)	b.p. (°C)	Structure	Remark
⟨Al⟩	0	6.77 ± 0.05	–	660	2520	Cubic face centered	
(O_2)	0	49.0 ± 0.01	−250	−219	−183	–	
⟨Al_2O_3⟩	-400.9 ± 1.5	12.2 ± 0.1	1000	2050	–	Rhombohedral	

Table 3.1.A2 Heat and Temperatures of Transformation

Substance	θ_t (°C)	λ_t (kcal mol^{-1})	θ_f (°C)	λ_f (kcal mol^{-1})
⟨Al⟩	–	–	659	2.5 ± 0.03
(O_2)	−250; −229	0.0224; 0.178	−219	0.106
⟨Al_2O_3⟩	2051	25.7	2051	25.7

Table 3.1.A3 Heat Capacities

Substances	C_P (cal deg mol^{-1})				Remarks	Range (K)
	a	$b \times 10^3$	$c \times 10^{-5}$	$d \times 10^6$		
⟨Al⟩	4.94	2.96	–	–	–	298–m.p.
{Al}	7.6	–	–	–	–	m.p.–2400
(O_2)	7.16	1.0	−0.40	–	–	298–3000
⟨Al_2O_3⟩	25.48	4.25	−6.82	–	–	298–1800

Table 3.1.A4 Vapor Pressures and Evaporation Constant log P(mmHg) = $A/T + B \log T + CT + D$

Substance	log P(mmHg)				Temp. Range (K)
	A	B	$C \times 10^3$	D	
{Al}	−16,380	−1.0	–	12.32	m.p.–b.p.
(O_2)					
⟨Al_2O_3⟩					

Substance	b.p. (°C)	L_e at b.p. (kcal mol^{-1})	sb.p. (°C)	L_s at m.p. or sb.p. (kcal mol^{-1})	L_e at 25 °C (kcal mol^{-1})	L_s at 25 °C (kcal mol^{-1})
Al	2450	69.5 ± 2.0	–	75.6 ± 2.0	76.9 ± 3.0	–
O_2	−183	1.63 ± 0.01	–	–	–	–
Al_2O_3						

Table 3.1.A5 Standard Gibbs Energies of Reaction

Reaction	ΔG° (cal)			±kcal	Temp. Range (K)
	A	B	C		
⟨Al_2O_3⟩ = 2 ⟨Al⟩ + 3/2(O_2)	400,810	3.98	−87.64	3	298–923
⟨Al_2O_3⟩ = 2 {Al} + 3/2(O_2)	405,760	3.75	−92.22	4	923−1800

Thermochemical data given in Tables 3.1.A1–3.1.A5 have been utilized for many years by process metallurgists. Since nowadays vapor pressures and Gibbs energies can be computed by simple program as described in Chapter 3.1.7, Tables 3.1.A4 and

Table 3.1.A6 Data for the Thermodynamic Properties of Inorganic Compounds Reproduced from *KAS* [1]

Substance	$S_{298} \pm \delta S$ (J K^{-1} mol^{-1})	$-\Delta H_{298} \pm \delta H$ (kJ mol^{-1})	Phase	T (K)	$C_P = A + B\times10^{-3}T + C\times10^{5}T^{-2} + D\times10^{-6}T^{2}$ (J K^{-1} mol^{-1})				H_T (kJ mol^{-1})
					A	*B*	*C*	*D*	
Ag	42.6	0.0	fcc	298	21.30	8.54	1.51	–	–
			liq	1235	33.47	–	–	–	11.3
Ag(g)	172.9	-284.9	gas	298	20.79	–	–	–	–
AgCl	96.2	127.0	cubic	298	62.26	4.18	-11.30	–	–
			liq	728	66.94	–	–	–	13.2
AgCl(g)	246.1 ± 0.2	-92.6	gas	298	37.24	–	-1.42	–	–
Ag_2O	120.9 ± 0.4	31.1 ± 0.6	cubic	298	59.33	40.79	-4.60	–	–
Ag_2CO_3	167.4 ± 4.2	505.8 ± 2.5	cryst	298	79.37	108.16	–	–	–
Ag_2S	143.5 ± 1.3	31.8 ± 0.8	monocl	298	64.60	39.96	–	–	–
			cubic	449	81.34	2.93	–	–	3.9
			cubic	859	82.72	–	–	–	0.5
			liq	1103	93.09	–	–	–	7.9
Al	28.3	0.0	fcc	298	31.38	-16.40	-3.60	20.75	–
			liq	934	31.76	–	–	–	10.7
Al(g)	164.4	-330.0	gas	298	20.75	–	0.54	–	–
AlCl(g)	227.9 ± 0.2	51.5 ± 9.2	gas	298	36.59	1.26	-2.06	–	–
			gas	800	37.38	0.46	-3.05	–	–
$AlCl_2$(g)	287.9	288.7	gas	298	57.78	0.22	-4.95	–	–
$AlCl_3$	109.3 ± 0.8	705.6 ± 1.7	monocl	298	64.94	87.86	–	–	–

Continued

Table 3.1.A6 Data for the Thermodynamic Properties of Inorganic Compounds Reproduced from *KAS* [1]—cont'd

Substance	$S_{298} \pm \delta S$ (J K^{-1} mol^{-1})	$-\Delta H_{298} \pm \delta H$ (kJ mol^{-1})	Phase	T (K)	$C_P = A + B\times10^{-3}T + C\times10^{5}T^{-2} + D\times10^{-6}T^{2}$ (J K^{-1} mol^{-1})				H_T (kJ mol^{-1})
					A	*B*	*C*	*D*	
$AlCl_3$(g)	314.3 ± 1.3	584.5 ± 2.5	gas	298	81.96	0.63	-9.92	–	–
Al_2Cl_6(g)	475.5	1295.4 ± 3.3	gas	298	180.92	1.05	-20.42	–	–
Al_2O_3	50.9 ± 0.2	1675.7 ± 1.3	hex	298	117.49	10.38	-37.11	–	–
			liq	2325	184.10	–	–	–	107.0
Al_2O(g)	256.9 ± 6.7	130.5 ± 16.7	gas	298	50.84	3.97	-8.70	-2.38	–
AlS(g)	230.5 ± 0.4	-238.9	gas	298	36.84	0.69	-3.26	–	–
Al_2S_3	123.4	723.4	hex	298	102.17	36.07	–	–	–
			liq	1370	156.90	–	–	–	56.5
As	35.7 ± 0.4	0.0	rhomb	298	23.03	5.74	–	–	–
As_2(g)	239.3 ± 1.3	-190.8 ± 6.3	gas	298	37.20	0.15	-2.02	–	–
As_4(g)	328.4 ± 5.0	-156.1 ± 2.5	gas	298	82.94	0.13	-5.13	–	–
$AsCl_3$	212.5	315.5	liq	298	133.89	–	–	–	–
$AsCl_3$(g)	326.2 ± 0.8	271.1	gas	298	82.09	1.00	-5.94	–	–
As_2O_3	122.6	665.8 ± 2.1	monocl	298	59.83	171.96	–	–	–
			liq	587	152.72	–	–	–	22.6
As_2O_5	105.4 ± 2.5	920.1 ± 5.0	cryst	298	42.47	246.86	–	–	–
As_2S_3	163.6 ± 5.0	167.4 ± 16.7	monocl	298	105.65	36.44	–	–	–
			liq	585	177.86	16.86	–	–	28.7
AsS	63.4 ± 1.7	71.1 ± 10.5	monocl	298	41.46	18.66	–	–	–

			liq	580	73.22	–	–	–	6.1
AsS(g)	232.2 ± 4.2	-202.9	gas	298	34.94	1.63	–	–	–
Au	47.5	0.0	fcc	298	31.46	-13.47	-2.89	10.96	–
			liq	1338	50.33	-12.69	–	–	12.6
			liq	1500	30.96	–	–	–	–
Au(g)	180.4	-368.2	gas	298	20.79	–	–	–	–
			gas	1000	22.26	-3.01	–	1.51	–
AuCl	85.8 ± 4.2	36.4 ± 2.1	rhomb	298	48.53	5.44	-1.26	–	–
$AuCl_3$	164.4 ± 6.3	118.4 ± 4.2	monocl	298	97.91	5.44	-4.18	–	–
Au_2O_3	130.3	3.4	cubic	298	107.53	21.76	–	–	–
AuS(g)	267.6 ± 4.2	-230.5 ± 25.1	gas	298	37.32	0.05	-1.62	–	–
B	5.9	0.0	hex	298	17.91	9.64	-8.58	-1.80	–
			liq	2350	30.54	–	–	–	50.2
B(a)	6.5	-4.2 ± 1.3	amorph	298	16.05	10.00	-6.28	–	–
B(g)	153.3 ± 0.2	-560.7 ± 12.6	gas	298	20.79	–	–	–	–
BCl_3(g)	290.1 ± 0.8	403.3 ± 0.8	gas	298	78.41	2.41	-15.48	–	–
B_2O_3	54.0 ± 0.4	1273.5 ± 1.7	hex	298	57.03	73.01	-14.06	–	–
			liq	723	129.70	–	–	–	24.1
B_2O_3(a)	78.4 ± 0.8	1253.5 ± 2.5	amorph	298	23.72	131.29	–	–	–
			amorph	500	845.59	-741.82	-963.99	–	–
B_2O_3(g)	283.7 ± 4.2	836.4 ± 4.2	gas	298	78.78	22.18	-16.78	-4.44	–

Continued

Table 3.1.A6 Data for the Thermodynamic Properties of Inorganic Compounds Reproduced from *KAS* [1]—cont'd

Substance	$S_{298} \pm \delta S$ (J K^{-1} mol^{-1})	$-\Delta H_{298} \pm \delta H$ (kJ mol^{-1})	Phase	T (K)	$C_P = A + B\times10^{-3}T + C\times10^{5}T^{-2} + D\times10^{-6}T^{2}$ (J K^{-1} mol^{-1})				H_T (kJ mol^{-1})
					A	*B*	*C*	*D*	
B_2S_3	92.0 ± 20.9	252.3 ± 8.4	monocl	298	98.03	64.02	–	–	–
			liq	836	151.67	–	–	–	48.1
Ba	62.4	0.0	bcc	298	-473.21	1586.99	128.16	–	–
			bcc	648	0.67	-975.71	-710.02	-428.44	–
			liq	1003	22.84	7.82	126.78	–	7.7
			liq	1300	40.58	–	–	–	–
Ba(g)	170.1	-179.1	gas	298	20.79	–	–	–	–
			gas	900	48.66	-36.32	-49.04	13.43	–
$BaCl_2$	123.7 ± 0.2	858.6 ± 12.6	cubic	298	69.45	19.16	–	–	–
			ß	1198	123.85	–	–	–	16.9
			liq	1245	108.78	–	–	–	16.0
$BaCl_2$(g)	325.6 ± 5.0	498.7 ± 16.7	gas	298	58.20	–	-1.80	–	–
BaO	72.1 ± 0.4	548.1 ± 2.1	cubic	298	50.29	7.20	-4.60	–	–
			liq	2286	66.94	–	–	–	58.6
BaO(g)	235.4 ± 0.8	123.4 ± 8.4	gas	298	39.54	-3.85	-5.27	1.61	–
BaO_2	93.1 ± 9.6	634.3 ± 11.7	cubic	298	62.34	28.03	–	–	–
$BaCO_3$	107.5 ± 1.3	1217.5 ± 12.6	orth	298	86.90	48.95	-11.97	–	–
			tetrag	1079	154.81	–	–	–	18.8
			cubic	1241	163.18	–	–	–	2.9

BaS	78.2 ± 1.3	463.6 ± 3.3	cubic	298	51.17	7.87	-3.68	–	–
Be	9.5	0.0	hcp	298	21.21	5.69	-5.86	0.96	–
			bcc	1543	32.22	–	–	–	2.5
			liq	1562	29.46	–	–	–	12.6
Be(g)	136.1	-324.0	gas	298	20.92	–	–	–	–
			gas	1900	18.95	0.59	27.24	–	–
$BeCl_2$	82.7 ± 0.4	490.8 ± 3.3	orth	298	76.61	12.34	-13.77	–	–
			liq	688	121.42	–	–	–	8.7
$BeCl_2$(b)	75.8 ± 0.2	496.2 ± 3.3	orth.ß	298	65.65	20.88	-8.41	–	–
$BeCl_2$(g)	251.0 ± 4.2	360.2 ± 10.5	gas	298	58.12	3.47	-0.75	-6.99	–
Be_2Cl_4(g)	387.0 ± 8.4	821.3	gas	298	131.38	0.63	-14.98	–	–
BeO	13.8 ± 0.4	609.4 ± 3.3	hex	298	41.59	10.21	-17.24	-1.34	–
			cubic	2370	46.86	4.60	–	–	6.7
			liq	2780	64.85	–	–	–	84.9
BeS	33.5 ± 6.3	233.5 ± 4.2	cubic	298	41.71	8.12	-9.62	–	–
Bi	56.7	0.0	rhomb	298	11.84	30.46	4.10	–	–
			liq	545	19.04	10.38	20.75	-3.97	11.3
			liq	1200	27.20	–	–	–	–
Bi(g)	186.9	-209.6	gas	298	20.92	–	–	–	–
Bi_2(g)	273.2	-220.1	gas	298	37.24	–	–	–	–
BiCl(g)	255.0 ± 0.4	-25.1 ± 8.4	gas	298	37.32	0.84	-1.17	–	–

Continued

Table 3.1.A6 Data for the Thermodynamic Properties of Inorganic Compounds Reproduced from *KAS* [1]—cont'd

Substance	$S_{298} \pm \delta S$ (J K^{-1} mol^{-1})	$-\Delta H_{298} \pm \delta H$ (kJ mol^{-1})	Phase	T (K)	$C_P = A + B\times10^{-3}T + C\times10^{5}T^{-2} + D\times10^{-6}T^{2}$ (J K^{-1} mol^{-1})				H_T (kJ mol^{-1})
					A	*B*	*C*	*D*	
$BiCl_3$	171.5 ± 8.4	378.7 ± 5.0	cubic	298	68.83	133.89	–	–	–
			liq	507	127.61	–	–	–	23.6
Bi_2O_3	151.5 ± 2.9	570.7 ± 3.3	monocl	298	103.51	33.47	–	–	–
			cubic	978	146.44	–	–	–	56.9
			liq	1097	152.72	–	–	–	59.8
Bi_2S_3	200.4 ± 6.3	201.7	orth	298	114.47	27.70	–	–	–
			liq	1036	188.28	–	–	–	79.5
Br_2	152.2	0.0	liq	298	75.73	–	–	–	–
Br_2(g)	245.3	-30.9	gas	298	37.36	0.46	-1.30	–	–
Br(g)	174.9	-111.9	gas	298	19.87	1.49	0.42	–	–
C	5.7	0.0	graph	298	0.11	38.94	-1.48	-17.38	–
				1100	24.43	0.44	-31.63	–	–
C(d)	2.4 ± 0.1	-1.5 ± 0.1	diam	298	9.12	13.22	-6.19	–	–
C(g)	158.0	-716.7	gas	298	20.77	0.05	–	–	–
			gas	2000	19.49	0.72	–	–	–
C_2(g)	199.3 ± 0.1	-832.6 ± 5.9	gas	298	30.69	4.75	10.18	-0.43	–
C_3(g)	237.2	-820.1 ± 12.6	gas	298	31.84	14.98	1.21	-2.62	–
CCl_4	214.4 ± 1.3	135.4 ± 2.1	liq	298	133.89	–	–	–	–
CCl_4(g)	309.8 ± 0.4	102.9 ± 2.1	gas	298	104.18	2.01	-19.82	–	–

CH_4(g)	186.3 ± 0.2	74.8 ± 0.4	gas	298	12.45	76.69	1.45	-17.99	–
CO(g)	197.5	110.5	gas	298	28.41	4.10	-0.46	–	–
CO_2(g)	213.7	393.5	gas	298	44.14	9.04	-8.54	–	–
CS(g)	210.5 ± 0.2	-280.3 ± 25.1	gas	298	29.37	8.66	-1.86	-2.38	–
CS_2	151.3 ± 0.8	-89.1 ± 1.0	liq	298	76.99	–	–	–	–
CS_2(g)	237.9 ± 0.2	-116.9 ± 1.3	gas	298	49.58	13.68	-6.99	-3.77	–
Ca	41.6	0.0	fcc	298	16.02	21.51	2.55	–	–
			bcc	716	-0.45	41.35	–	–	0.9
			liq	1115	33.47	–	–	–	8.5
Ca(g)	154.8	-177.8	gas	298	20.79	–	–	–	–
$CaCl_2$	108.4	795.0 ± 3.3	tetrag	298	69.83	15.40	-1.59	–	–
			liq	1045	122.26	-14.90	0.71	–	28.2
$CaCl_2$(g)	287.4	481.6	gas	298	62.13	0.14	-2.55	–	–
CaO	38.1 ± 0.3	634.9 ± 0.8	cubic	298	50.42	4.18	-8.49	–	–
			liq	2900	83.68	–	–	–	52.3
$CaCO_3$	92.7 ± 0.8	1206.9 ± 2.9	calcit	298	104.52	21.92	-25.94	–	–
CaS	56.5 ± 1.3	473.2 ± 3.8	cubic	298	50.63	3.70	-3.89	–	–
CaS(g)	232.4	-116.7 ± 20.9	gas	298	37.20	0.11	-2.28	–	–
Cd	51.8	0.0	hex	298	22.05	12.55	0.14	–	–
			liq	594	29.71	–	–	–	6.2
Cd(g)	167.7	111.8	gas	298	20.79	–	–	–	–

Continued

Table 3.1.A6 Data for the Thermodynamic Properties of Inorganic Compounds Reproduced from *KAS* [1]—cont'd

Substance	$S_{298} \pm \delta S$ (J K^{-1} mol^{-1})	$-\Delta H_{298} \pm \delta H$ (kJ mol^{-1})	Phase	T (K)	$C_P = A + B\times10^{-3}T + C\times10^{5}T^{-2} + D\times10^{-6}T^{2}$ (J K^{-1} mol^{-1})				H_T (kJ mol^{-1})
					A	*B*	*C*	*D*	
$CdCl_2$	115.3 ± 0.4	390.8 ± 1.3	hex	298	47.28	91.63	–	–	–
			liq	842	110.04	–	–	–	30.5
$CdCl_2$(g)	285.8 ± 2.9	194.6 ± 6.3	gas	298	63.30	–	-4.60	–	–
CdO	54.8 ± 1.7	258.4 ± 0.8	cubic	298	48.24	6.36	-5.31	–	–
$CdCO_3$	92.5 ± 5.0	751.9 ± 8.4	hex	298	43.10	131.80	–	–	–
CdS	69.0 ± 2.1	149.4 ± 2.9	hex	298	44.56	13.81	–	–	–
Ce	56.9	0.0	fcc	298	22.38	15.06	–	–	–
			bcc	998	37.66	–	–	–	3.0
			liq	1071	37.66	–	–	–	5.2
Ce(g)	191.6	417.1	gas	298	24.89	15.02	-6.69	-3.77	–
$CeCl_3$	149.8 ± 7.5	1058.1 ± 1.7	hex	298	97.49	13.60	-5.02	–	–
			liq	1095	145.18	–	–	–	54.0
Ce_2O_3	148.1 ± 0.4	1799.7 ± 1.3	cubic	298	139.33	11.63	-24.23	–	–
				1050	126.78	32.30	-9.29	–	—
				1800	154.81	–	–	–	–
CeO_2	62.3 ± 0.3	1090.4 ± 0.8	cubic	298	64.81	17.70	-7.61	–	–
CeS	78.2 ± 1.3	456.5 ± 8.4	cubic	298	52.54	13.55	-5.89	–	–
Ce_3S_4	255.2 ± 12.6	1652.7 ± 20.9	cubic	298	167.82	39.66	–	–	–
Ce_2S_3	180.3 ± 1.7	1188.3 ± 12.6	cubic	298	124.93	12.72	–	–	–

Cl_2	223.0	0.0	gas	298	36.99	0.71	-2.93	–	–
Cl(g)	165.1	-121.3	gas	298	23.79	-1.28	-1.40	–	–
Co	30.0	0.0	hcp	298	18.12	23.14	-0.42	-0.08	–
			fcc	700	18.12	23.14	-0.42	-0.08	0.5
			fcc	1390	18.12	23.14	-0.42	-0.08	5.1
			liq	1768	40.50	–	–	–	16.2
Co(g)	179.4	-424.7	gas	298	27.03	-0.21	-3.59	–	–
$CoCl_2$	109.3 ± 0.4	312.5 ± 1.7	hex	298	82.09	6.74	-4.98	–	–
			liq	1013	99.16	–	–	–	44.8
$CoCl_2$(g)	298.3 ± 8.4	93.7 ± 8.4	gas	298	58.41	7.49	-0.73	-2.13	–
CoO	53.0 ± 0.4	237.7 ± 0.6	cubic	298	55.40	-6.44	–	7.11	–
Co_3O_4	114.3 ± 8.4	910.0 ± 4.6	cubic	298	140.75	17.28	-24.35	53.97	–
$CoCO_3$	87.9 ± 0.4	702.5 ± 12.6	hex	298	88.28	38.91	-17.99	–	–
$CoS_{0.89}$	51.5 ± 3.3	94.6 ± 4.2	cubic	298	40.25	15.52	–	–	–
Co_3S_4	184.1 ± 20.9	359.0 ± 25.1	cubic	298	143.30	76.57	–	–	–
CoS_2	69.0 ± 6.3	153.1 ± 8.4	cubic	298	60.67	25.31	–	–	–
Cr	23.6	0.0	bcc	298	21.76	8.98	-0.96	2.26	–
			liq	2130	39.33	–	–	–	17.2
Cr(g)	174.2	-397.5	gas	298	20.79	–	–	–	–
			gas	900	9.58	6.95	41.34	–	–
$CrCl_2$	115.3 ± 0.4	395.4 ± 10.5	orth	298	63.81	24.94	–	–	–

Continued

Table 3.1.A6 Data for the Thermodynamic Properties of Inorganic Compounds Reproduced from *KAS* [1]—cont'd

Substance	$S_{298} \pm \delta S$ (J K^{-1} mol^{-1})	$-\Delta H_{298} \pm \delta H$ (kJ mol^{-1})	Phase	T (K)	$C_P = A + B\times10^{-3}T + C\times10^{5}T^{-2} + D\times10^{-6}T^{2}$ (J K^{-1} mol^{-1})				H_T (kJ mol^{-1})
					A	*B*	*C*	*D*	
$CrCl_3$	124.7 ± 0.4	570.3 ± 10.9	monocl	298	79.50	41.21	–	–	–
Cr_2O_3	81.2 ± 1.3	1134.7 ± 7.5	rhomb	298	119.37	9.20	-15.65	–	–
CrO_3	73.2	587.0 ± 10.9	orth	298	71.76	87.86	-16.74	–	–
CrO_3(g)	270.7 ± 12.6	292.0	gas	298	82.55	-	-21.97	–	–
CrS	64.0 ± 6.3	155.6 ± 9.6	monocl	298	32.84	46.74	–	–	–
				450	51.64	4.90	–	–	0.3
Cs	85.2	0.0	bcc	298	32.34	–	–	–	–
			liq	302	29.89	0.90	2.03	–	2.1
			liq	700	30.94	–	–	–	–
Cs(g)	175.5	-76.5	gas	298	20.79	–	–	–	–
Cs_2(g)	284.5	-113.8	gas	298	37.18	2.82	–	–	–
CsCl	101.2 ± 0.2	442.7 ± 0.4	cubic	298	53.35	5.15	-2.09	–	–
				743	3.35	73.64	-3.77	–	3.8
			liq	918	57.99	17.91	–	–	20.3
CsCl(g)	256.0 ± 0.2	242.3 ± 4.2	gas	298	36.82	1.05	–	–	–
Cs_2O	146.9 ± 0.8	346.0 ± 2.9	hex	298	66.36	32.01	–	–	–
CsO_2	142.3 ± 12.6	286.2 ± 2.1	tetrag	298	72.38	30.96	–	–	–
Cs_2CO_3	204.0 ± 0.8	1136.4 ± 2.1	cryst	298	115.44	69.33	-10.96	–	–
Cu	33.1	0.0	fcc	298	30.29	-10.71	-3.22	9.47	–

			liq	1358	32.84	–	–	–	13.3
Cu(g)	166.3	-337.4	gas	298	20.79	–	–	–	–
			gas	1300	23.97	-4.60	–	1.67	–
CuCl	87.0 ± 2.9	137.2 ± 2.1	cubic	298	38.28	34.98	–	–	–
			liq	700	66.94	–	–	–	10.3
$CuCl_2$	108.1 ± 0.4	215.5 ± 4.2	monocl	298	67.03	17.57	–	–	–
Cu_2O	92.9 ± 0.3	173.2 ± 2.1	cubic	298	58.20	23.97	-1.59	–	–
			liq	1515	100.42	–	–	–	64.0
CuO	42.6 ± 0.4	161.9 ± 1.7	monocl	298	46.44	11.55	-7.11	2.59	–
$CuCO_3$	87.9	596.2 ± 9.2		298	92.05	38.91	-17.99	–	–
Cu_2S	120.9 ± 1.7	79.5 ± 1.7	orth	298	52.84	78.74	–	–	–
			hex	376	112.05	-30.75	–	–	3.8
			cubic	717	84.64	–	–	–	1.2
			liq	1402	89.12	–	–	–	9.6
CuS	66.5 ± 2.1	52.3 ± 4.2	hex	298	44.35	11.05	–	–	–
Dy	74.9	0.0	hcp	298	35.35	-21.88	-2.13	18.70	–
			bcc	1654	28.03	–	–	–	4.2
			liq	1685	49.92	–	–	–	11.0
Dy(g)	195.8	-290.4	gas	298	21.40	-2.12	-0.14	2.04	–
			gas	700	21.18	-1.99	–	2.29	–
			gas	1400	11.64	9.16	21.55	-1.37	–

Continued

Table 3.1.A6 Data for the Thermodynamic Properties of Inorganic Compounds Reproduced from *KAS* [1]—cont'd

Substance	$S_{298} \pm \delta S$ (J K^{-1} mol^{-1})	$-\Delta H_{298} \pm \delta H$ (kJ mol^{-1})	Phase	T (K)	$C_P = A + B\times10^{-3}T + C\times10^{5}T^{-2} + D\times10^{-6}T^{2}$ (J K^{-1} mol^{-1})				H_T (kJ mol^{-1})
					A	*B*	*C*	*D*	
$DyCl_3$	147.7 ± 11.3	995.8 ± 9.2	monocl	298	94.56	17.99	-1.42	–	–
			liq	924	144.77	–	–	–	25.5
$DyCl_3$(g)	383.3 ± 6.7	714.2 ± 11.3	gas	298	79.91	–	–	–	–
Dy_2O_3	149.8 ± 12.6	1862.7 ± 3.8	cubic	298	122.59	13.22	-8.49	–	–
			monocl	1590	148.11	–	–	–	0.9
			hex	2343	155.23	–	–	–	8.4
Er	73.1	0.0	hcp	298	28.37	-2.05	–	5.73	–
			bcc	1750	42.68	–	–	–	–
			liq	1795	38.70	–	–	–	19.9
Er(g)	193.9	-317.1	gas	298	20.79	–	–	–	–
			gas	500	22.12	-3.28	-0.64	2.27	–
			gas	1500	8.76	9.49	44.33	-1.20	–
$ErCl_3$	146.9 ± 4.2	992.4 ± 2.9	monocl	298	95.56	17.57	-1.05	–	–
			liq	1050	148.53	–	-	–	32.6
Er_2O_3	154.4 ± 0.6	1897.9 ± 4.2	cubic	298	115.27	29.29	-13.81	–	–
Eu	77.8	0.0	cubic	298	33.81	-19.33	-2.22	23.85	–
			liq	765	33.81	-19.33	-2.22	23.85	0.2
			liq	1096	38.07	–	–	–	9.2
Eu(g)	188.7	-175.3	gas	298	20.79	–	–	–	–

			gas	1200	22.42	-2.52	–	0.96	–
$EuCl_3$	125.5 ± 12.6	939.3 ± 4.6	hex	298	90.50	26.15	–	–	–
			liq	897	142.26	–	–	–	33.1
EuO	81.6 ± 4.2	589.9 ± 5.4	cubic	298	54.39	4.18	-6.15	–	–
Eu_2O_3	146.4	1662.7 ± 3.8	cubic	298	123.85	27.11	-8.70	–	–
			monocl	895	129.96	17.41	–	–	0.5
EuS	95.4 ± 0.8	451.9 ± 16.7	cubic	298	48.74	4.81	–	–	–
EuS(g)	272.0	-88.3 ± 16.7	gas	298	37.24	0.07	-1.91	–	–
F_2(g)	202.7	0.0	gas	298	35.90	1.34	-4.48	–	–
F(g)	158.6	-79.4	gas	298	21.69	-0.44	1.16	–	–
Fe	27.3	0.0	bcc	298	28.18	-7.32	-2.90	25.04	–
			bcc	800	-263.45	255.81	619.23	–	–
			bcc	1000	-641.91	696.34	–	–	–
			bcc	1042	1946.25	-1787.50	–	–	–
			bcc	1060	-561.95	334.13	2912.11	–	–
			fcc	1184	23.99	8.36	–	–	0.9
			bcc	1665	24.64	9.90	–	–	0.8
			liq	1809	46.02	–	–	–	13.8
Fe(g)	180.8	-415.9	gas	298	26.09	-1.40	–	–	–
			gas	400	30.93	-14.31	-0.99	5.95	–
			gas	1100	22.07	0.13	–	–	–

Continued

Table 3.1.A6 Data for the Thermodynamic Properties of Inorganic Compounds Reproduced from *KAS* [1]—cont'd

Substance	$S_{298} \pm \delta S$ (J K^{-1} mol^{-1})	$-\Delta H_{298} \pm \delta H$ (kJ mol^{-1})	Phase	T (K)	$C_P = A + B\times10^{-3}T + C\times10^{5}T^{-2} + D\times10^{-6}T^{2}$ (J K^{-1} mol^{-1})				H_T (kJ mol^{-1})
					A	*B*	*C*	*D*	
			gas	1600	24.83	-2.68	-26.61	1.11	–
			gas	3135	2.33	6.53	530.95	-0.14	–
$FeCl_2$	76.1 ± 2.5	341.8 ± 0.8	hex	298	79.24	8.70	-4.77	–	–
			liq	950	102.17	–	–	–	43.0
$FeCl_2$(g)	299.2 ± 4.2	141.0 ± 2.1	gas	298	59.50	3.31	-2.59	–	–
Fe_2Cl_4(g)	464.4 ± 12.6	431.4 ± 4.2	gas	298	130.21	3.26	-4.73	–	–
$FeCl_3$	142.3 ± 1.7	399.4 ± 1.0	hex	298	62.34	115.06	–	–	–
			liq	580	133.89	–	–	–	43.1
$FeCl_3$(g)	344.1	253.6 ± 4.2	gas	298	82.97	0.08	-4.73	–	–
Fe_2Cl_6(g)	537.0	654.8 ± 8.4	gas	298	182.67	0.13	-8.08	–	–
$Fe_{0.945}O$	60.1 ± 0.8	263.0 ± 2.5	cubic	298	48.79	8.37	-2.80	–	–
Fe_2O_3	87.4 ± 1.3	823.4 ± 3.3	hemat	298	98.28	77.82	-14.85	–	–
				950	150.60	–	–	–	–
				1050	132.67	7.36	–	–	–
Fe_3O_4	150.9 ± 1.7	1108.8 ± 4.2	magnet	298	91.55	202.00	–	–	–
				900	213.40	–	–	–	–
$FeCO_3$	92.9 ± 2.5	740.6 ± 3.3	sider	298	48.66	112.09	–	–	–
FeS	60.3 ± 0.4	100.4 ± 1.7	hex	298	-0.50	170.71	–	–	–
				411	72.80	–	–	–	2.4

				598	51.04	9.96	–	–	0.5
			liq	1461	71.13	–	–	–	32.3
FeS_2	52.9 ± 0.4	171.5 ± 2.1	pyrite	298	68.95	14.10	-9.87	–	–
Ga	40.8	0.0	orth	298	26.78	–	–	–	–
			liq	303	26.78	–	–	–	5.6
Ga(g)	168.9	-272.0	gas	298	31.76	-9.62	-3.05	2.18	–
GaCl(g)	240.0 ± 0.2	81.8 ± 15.1	gas	298	37.99	–	-2.01	–	–
$GaCl_3$	135.1 ± 13.8	524.7 ± 4.6	cryst	298	118.41	–	–	–	–
			liq	351	128.03	–	–	–	11.5
Ga_2O_3	84.9 ± 0.4	1089.1 ± 4.6	monocl	298	112.55	15.48	-21.67	–	–
Ga_2S(g)	290.0 ± 8.4	-20.9 ± 33.5	gas	298	56.00	1.15	-9.25	–	–
GaS	57.7 ± 6.3	209.2 ± 18.8	hex	298	41.34	15.69	–	–	–
Ga_2S_3	142.3 ± 16.7	516.3 ± 12.6	cubic	298	90.50	47.28	–	–	–
Gd	67.9	0.0	hcp	298	6.69	32.64	18.41	-8.37	–
			bcc	1533	28.45	–	–	–	3.9
			liq	1586	37.15	–	–	–	10.0
Gd(g)	194.2	-397.5	gas	298	30.91	-8.35	-0.95	2.15	–
			gas	1000	23.73	-4.00	23.20	2.55	–
			gas	2000	7.26	10.66	67.98	-0.94	–
$GdCl_3$	151.5 ± 2.5	1008.3 ± 3.3	orth	298	93.09	25.10	-2.47	–	–
			liq	875	139.33	–	–	–	40.7

Continued

Table 3.1.A6 Data for the Thermodynamic Properties of Inorganic Compounds Reproduced from *KAS* [1]—cont'd

Substance	$S_{298} \pm \delta S$ (J K^{-1} mol^{-1})	$-\Delta H_{298} \pm \delta H$ (kJ mol^{-1})	Phase	T (K)	$C_P = A + B\times10^{-3}T + C\times10^{5}T^{-2} + D\times10^{-6}T^{2}$ (J K^{-1} mol^{-1})				H_T (kJ mol^{-1})
					A	*B*	*C*	*D*	
Gd_2O_3	150.6 ± 0.4	1826.7 ± 3.3	cubic	298	119.20	12.95	-15.82	–	–
			monocl	1550	114.50	14.47	-10.84	–	1.7
Ge	31.1	0.0	cubic	298	21.55	5.86	–	–	–
			liq	1210	27.61	–	–	–	36.9
Ge(g)	167.8	-372.0	gas	298	39.90	-15.95	-3.93	–	–
$GeCl_4$(g)	347.7 ± 1.3	494.8 ± 10.5	gas	298	106.86	0.92	-10.00	–	–
GeO(g)	223.8 ± 0.4	30.7	gas	298	37.03	–	-5.65	–	–
GeO_2	39.7 ± 1.3	580.0 ± 1.5	tetrag	298	66.61	11.59	-17.74	–	–
			hex	1322	68.91	9.83	-17.70	–	21.1
GeS	66.0 ± 0.8	76.1 ± 4.6	orth	298	41.80	20.13	–	–	–
			liq	938	60.67	–	–	–	20.9
GeS(g)	235.6 ± 0.4	-99.4 ± 5.9	gas	298	36.74	0.42	-2.85	–	–
GeS_2	87.4 ± 2.1	156.9 ± 12.6	orth	298	56.44	31.05	–	–	–
H(g)	114.6 ± 0.0	-218.0 ± 0.0	gas	298	20.79	–	–	–	–
H_2(g)	130.6 ± 0.0	0.0	gas	298	27.37	3.33	–	–	–
HCl(g)	186.8	92.3	gas	298	24.80	7.99	1.88	-1.30	–
H_2O(l)	69.9	285.8	liq	298	75.44	–	–	–	–
H_2O(g)	188.7	241.8	gas	298	30.0	10.71	0.33	–	–
H_2O_2(l)	109.5 ± 0.5	187.8 ± 0.4	liq	298	89.33	–	–	–	–

H_2O_2(g)	232.9 ± 0.6	136.4 ± 0.8	gas	298	52.30	11.88	-11.88	–	–
H_2S(g)	205.6 ± 0.4	20.5 ± 0.8	gas	298	28.54	20.61	-0.37	-3.70	–
H_2S_2(l)	200.8 ± 12.6	18.0 ± 0.8	liq	298	92.26	–	–	–	–
H_2S_2(g)	266.4	-15.7 ± 0.8	gas	298	51.38	16.19	-4.18	–	–
Hf	43.5	0.0	hex	298	23.44	7.63	–	–	–
			bcc	2016	10.29	10.77	–	–	5.9
			liq	2504	33.47	–	–	–	27.2
Hf(g)	186.8	-620.1	gas	298	13.24	15.78	2.85	-3.47	–
			gas	2500	16.23	3.90	315.93	–	–
$HfCl_4$	190.8 ± 2.5	990.4 ± 2.1	cubic	298	131.67	–	-9.96	–	–
$HfCl_4$(g)	377.2 ± 6.3	882.8 ± 6.3	gas	298	108.44	0.21	-8.54	–	–
HfO_2	59.4 ± 0.4	1117.5 ± 1.7	monocl	298	72.11	9.05	-12.94	–	–
			tetrag	1973	108.78	–	–	–	9.3
Hg	75.9	0.0	liq	298	30.38	-11.46	–	10.15	–
Hg(g)	174.8	-61.4	gas	298	27.66	–	–	–	–
HgCl	95.8 ± 0.8	132.6 ± 0.8	tetrag	298	49.37	11.51	-1.80	–	–
$HgCl_2$	144.5 ± 0.4	230.1 ± 2.3	orth	298	70.00	20.29	-1.88	–	–
			liq	550	102.09	–	–	–	19.2
$HgCl_2$(g)	288.7 ± 1.7	149.0 ± 2.7	gas	298	62.13	0.13	-3.64	–	–
HgO	70.2 ± 0.4	90.8 ± 0.8	orth	298	35.56	30.12	–	–	–
HgS	82.4 ± 2.1	53.3 ± 4.2	hex	298	43.76	15.56	–	–	–

Continued

Table 3.1.A6 Data for the Thermodynamic Properties of Inorganic Compounds Reproduced from *KAS* [1]—cont'd

Substance	$S_{298} \pm \delta S$ (J K^{-1} mol^{-1})	$-\Delta H_{298} \pm \delta H$ (kJ mol^{-1})	Phase	T (K)	$C_P = A + B\times10^{-3}T + C\times10^{5}T^{-2} + D\times10^{-6}T^{2}$ (J K^{-1} mol^{-1})				H_T (kJ mol^{-1})
					A	*B*	*C*	*D*	
			cubic	618	44.02	15.19	–	–	4.0
Ho	75.0	0.0	hcp	298	35.46	-22.07	-2.96	18.83	–
			bcc	1713	28.03	–	–	–	4.7
			liq	1745	43.93	–	–	–	12.1
Ho(g)	195.5	-300.8	gas	298	20.79	–	–	–	–
			gas	500	22.05	-2.95	-0.67	1.95	–
			gas	1500	7.88	9.72	54.75	-1.30	–
$HoCl_3$	147.7 ± 14.6	1006.3 ± 2.9	monocl	298	95.56	12.97	-0.96	–	–
			liq	993	148.66	–	–	–	30.5
Ho_2O_3	158.2 ± 0.4	1881.1 ± 5.4	cubic	298	125.85	6.95	-11.51	–	–
I_2	116.1	0.0	orth	298	-50.65	246.91	27.97	–	–
			liq	387	80.67	–	–	–	15.8
I_2(g)	260.6	-62.4	gas	298	37.40	0.57	-0.62	–	–
I(g)	180.7	-106.8	gas	298	20.39	0.40	0.28	–	–
In	57.8	0.0		298	24.31	10.46	–	–	–
			liq	430	30.29	-1.38	–	–	3.3
In(g)	173.7	-240.4	gas	298	13.10	17.24	2.55	-2.97	–
				800	36.40	-5.23	-44.39	–	–
				1500	33.01	-5.15	–	0.59	–

				1900	23.81	–	85.23	-0.21	–
InCl	95.0 ± 6.3	186.2 ± 8.4	cubic	298	35.15	41.84	–	–	–
			ß	393	58.58	–	–	–	6.9
			liq	498	62.76	–	–	–	9.2
$InCl_2$	122.2 ± 6.3	362.8 ± 16.7	orth	298	58.58	50.21	–	–	–
$InCl_3$	141.0 ± 8.4	537.2 ± 8.4	monocl	298	78.66	55.65	–	–	–
In_2O_3	107.9 ± 3.3	925.9 ± 1.7	cubic	298	121.34	13.39	-30.12	–	–
InS	71.0 ± 0.8	133.9 ± 10.5	orth	298	42.51	18.83	–	–	–
			liq	965	60.67	–	–	–	36.0
In_2S_3	163.6 ± 2.5	355.6 ± 20.9	cubic	298	128.95	3.26	-10.63	–	–
			tetrag	660	97.78	55.40	–	–	1.1
			gamma	1100	159.41	–	–	–	4.0
Ir	35.5	0.0	fcc	298	22.89	7.03	–	–	–
			liq	2720	41.84	–	–	–	26.1
Ir(g)	193.5	-669.4	gas	298	15.42	9.56	2.48	-1.54	–
$IrCl_3$	114.6	245.2	cryst	298	84.94	18.83	-4.18	–	–
IrO_2	51.0	249.4	tetrag	298	61.88	20.42	-10.96	–	–
Ir_2S_3	51.0	249.4	orth	298	110.29	32.97	-9.62	–	–
IrS_2	69.0	133.1	orth	298	68.58	15.77	-6.57	–	–
K	64.7	0.0	bcc	298	25.27	13.05	–	–	–
			liq	337	37.18	-19.12	–	12.30	2.4

Continued

Table 3.1.A6 Data for the Thermodynamic Properties of Inorganic Compounds Reproduced from *KAS* [1]—cont'd

Substance	$S_{298} \pm \delta S$ (J K^{-1} mol^{-1})	$-\Delta H_{298} \pm \delta H$ (kJ mol^{-1})	Phase	T (K)	$C_P = A + B\times10^{-3}T + C\times10^{5}T^{-2} + D\times10^{-6}T^{2}$ (J K^{-1} mol^{-1})				H_T (kJ mol^{-1})
					A	*B*	*C*	*D*	
K(g)	160.2	-89.0	gas	298	20.79	–	–	–	–
K_2(g)	249.6	-127.1	gas	298	37.41	2.06	-0.12	–	–
KCl	82.6 ± 0.2	436.6 ± 0.4	cubic	298	40.02	25.47	3.64	–	–
			liq	1045	73.60	–	–	–	26.3
KCl(g)	239.0 ± 0.2	214.6	gas	298	37.15	0.96	-0.84	–	–
K_2O	94.1	363.2 ± 2.9	cubic	298	95.65	-4.94	-11.05	23.68	–
K_2O_2	113.0	495.0	rhomb	298	79.75	69.08	–	–	–
KO_2	122.6 ± 4.2	284.5 ± 2.5	tetrag	298	87.65	10.67	-11.97	–	–
K_2CO_3	155.5 ± 0.4	1153.1 ± 4.2	monocl	298	97.95	92.09	-9.87	–	–
			liq	1173	209.20	–	–	–	27.9
K_2S	115.1 ± 14.6	376.6 ± 12.6	cubic	298	66.94	25.94	–	–	–
			cubic	1050	142.34	–	–	–	10.5
			liq	1221	100.96	–	–	–	16.2
La	56.9	0.0	hex	298	26.44	2.33	–	–	–
			fcc	583	17.66	15.02	3.89	–	0.4
			bcc	1138	39.54	–	–	–	3.1
			liq	1191	34.31	–	–	–	6.2
La(g)	182.3	-430.0	gas	298	18.91	16.48	–	-5.15	–
				1400	32.51	–	-12.05	–	–

				1800	28.28	–	71.42	0.50	–
$LaCl_3$	137.7 ± 0.8	1070.7 ± 1.3	hex	298	86.19	39.75	–	–	–
			liq	1131	125.52	–	–	–	54.4
$LaCl_3$(g)	364.4 ± 6.7	740.6 ± 6.7	gas	298	80.75	0.25	-2.93	–	–
La_2O_3	127.3 ± 0.4	1794.9 ± 2.9	cubic	298	120.71	12.89	-13.72	–	–
La_2S_3	165.0 ± 0.8	1184.1 ± 12.6	rhomb	298	116.52	14.64	–	–	–
LaS	73.2	472.4 ± 5.0	cubic	298	46.48	5.44	–	–	–
LaS(g)	252.5 ± 0.4	-129.7	gas	298	37.07	0.17	-2.38	–	–
Li	29.1	0.0	bcc	298	1.30	56.27	6.02	–	–
			liq	454	31.21	-5.27	2.05	2.64	3.0
Li(g)	138.7	-159.3	gas	298	20.79	–	–	–	–
			gas	1700	22.64	-2.09	–	0.59	–
Li_2(g)	196.9	-211.3	gas	298	37.03	1.72	-1.34	0.59	–
			gas	1200	51.13	-4.94	-77.61	–	–
			gas	2000	61.09	-18.16	–	3.64	–
LiCl	59.3 ± 0.4	408.4 ± 0.4	cubic	298	41.42	23.39	–	–	–
			liq	883	73.39	-9.46	–	–	19.7
LiCl(g)	212.8 ± 0.4	195.4 ± 1.7	gas	298	36.80	0.89	-3.49	–	–
Li_2O	37.7 ± 0.2	597.9 ± 1.0	cubic	298	69.79	17.66	-18.49	–	–
			liq	1726	97.07	–	–	–	43.1
Li_2O(g)	232.6 ± 4.6	165.7 ± 5.4	gas	298	60.46	0.84	-9.33	–	–

Continued

Table 3.1.A6 Data for the Thermodynamic Properties of Inorganic Compounds Reproduced from *KAS* [1]—cont'd

Substance	$S_{298} \pm \delta S$ (J K^{-1} mol^{-1})	$-\Delta H_{298} \pm \delta H$ (kJ mol^{-1})	Phase	T (K)	$C_P = A + B\times10^{-3}T + C\times10^{5}T^{-2} + D\times10^{-6}T^{2}$ (J K^{-1} mol^{-1})				H_T (kJ mol^{-1})
					A	*B*	*C*	*D*	
Li_2O_2	58.2 ± 6.3	633.9 ± 8.4	hex	298	52.22	76.15	–	–	–
Li_2CO_3	90.2 ± 0.4	1215.5 ± 4.2	monocl	298	56.82	138.07	–	–	–
			ß	623	132.38	–	–	–	–
			gamma	683	14.35	180.75	–	–	2.5
			liq	1000	185.43	–	–	–	44.8
Li_2S	60.7 ± 8.4	446.9 ± 2.1	cubic	298	66.32	20.17	–	–	–
Lu	51.0	0.0	hex	298	27.41	-5.40	0.25	8.28	–
			liq	1936	47.91	–	–	–	19.2
Lu(g)	184.7	-427.6	gas	298	12.47	20.93	2.48	-7.15	–
			gas	800	30.63	-1.59	-26.41	-0.32	–
			gas	1700	28.24	-1.26	–	–	–
			gas	1936	38.64	-8.18	-72.20	1.32	–
Lu_2O_3	110.0 ± 0.4	1878.2 ± 7.5	cubic	298	112.63	23.01	-15.69	–	–
Mg	32.7	0.0	hcp	298	21.13	11.92	0.15	–	–
			liq	923	34.31	–	–	–	8.5
Mg(g)	148.5	-147.1	gas	298	20.79	–	–	–	–
$MgCl_2$	89.6 ± 0.8	641.4 ± 0.8	rhomb	298	79.08	5.94	-8.62	–	–
			liq	987	92.47	–	–	–	43.1
MgO	26.9 ± 0.4	601.6 ± 0.4	cubic	298	48.99	3.43	-11.34	–	–

			liq	3105	60.67	–	–	–	77.8
$MgCO_3$	65.9 ± 0.8	1095.8 ± 12.6	magnes	298	77.91	57.74	-17.41	–	–
MgS	50.3 ± 0.4	345.6 ± 4.2	cubic	298	48.74	3.64	-3.79	–	–
Mn	32.0	0.0	alpha	298	23.85	14.14	-1.57	–	–
			beta	990	34.85	2.76	–	–	2.2
			gamma	1360	25.23	14.90	-1.85	–	2.2
			delta	1410	46.44	–	–	–	1.8
			liq	1517	46.02	–	–	–	14.6
Mn(g)	173.6	-280.7	gas	298	20.79	–	–	–	–
			gas	1600	18.70	0.79	21.21	–	–
$MnCl_2$	118.2 ± 0.4	481.2 ± 0.8	hex	298	75.48	13.22	-5.73	–	–
			liq	923	94.56	–	–	–	37.7
$MnCl_2$(g)	295.4 ± 6.3	263.6 ± 2.1	gas	298	64.98	–	-6.15	–	–
MnO	59.8 ± 0.8	384.9 ± 1.3	cubic	298	46.48	8.12	-3.68	–	–
			liq	2058	60.67	–	–	–	54.4
Mn_3O_4	154.8 ± 6.3	1387.4 ± 1.7	tetrag	298	144.77	45.44	-12.97	–	–
			cubic	1440	210.04			–	20.9
Mn_2O_3	110.5 ± 2.1	958.1 ± 2.1	orth	298	112.26	35.06	-13.71	–	–
MnO_2	53.1 ± 0.4	520.9 ± 1.3	tetrag	298	69.45	10.21	-16.23	–	–
$MnCO_3$	109.6 ± 1.3	881.6 ± 4.6	hex	298	79.83	50.21	–	–	–
MnS	80.3 ± 0.8	214.2 ± 2.1	cubic	298	47.70	7.53	–	–	–

Continued

Table 3.1.A6 Data for the Thermodynamic Properties of Inorganic Compounds Reproduced from *KAS* [1]—cont'd

Substance	$S_{298} \pm \delta S$ (J K^{-1} mol^{-1})	$-\Delta H_{298} \pm \delta H$ (kJ mol^{-1})	Phase	T (K)	$C_P = A + B\times10^{-3}T + C\times10^{5}T^{-2} + D\times10^{-6}T^{2}$ (J K^{-1} mol^{-1})				H_T (kJ mol^{-1})
					A	*B*	*C*	*D*	
			liq	1803	66.94	–	–	–	26.4
MnS(g)	238.9	-265.7 ± 12.6	gas	298	36.36	–	-3.01	–	–
MnS_2	99.9 ± 0.4	207.1	cubic	298	69.71	17.66	-4.35	–	–
Mo	28.6	0.0	bcc	298	28.52	-4.42	-3.62	4.28	–
			liq	2896	40.33	–	–	–	39.1
Mo(g)	181.8	-658.1	gas	298	20.79	–	–	–	–
			gas	1200	35.40	-13.68	-49.54	3.68	–
$MoCl_4$	159.0 ± 2.5	504.2 ± 20.9	monocl	298	120.50	–	–	–	–
			ß	350	107.95	58.58	–	–	4.6
			liq	600	149.79	–	–	–	21.6
$MoCl_4$(g)	371.7	383.7 ± 16.7	gas	298	107.86	-0.42	-9.04	2.76	–
$MoCl_5$	238.5 ± 12.6	526.8 ± 9.2	monocl	298	165.69	–	–	–	–
			liq	470	88.28	–	–	–	18.8
$MoCl_5$(g)	398.1 ± 12.6	446.9 ± 9.2	gas	298	136.11	-0.75	-13.26	0.05	–
$MoCl_6$(g)	419.7 ± 16.7	460.2 ± 41.8	gas	298	157.53	0.01	-12.13	–	–
MoO_2	46.4 ± 0.4	587.9 ± 1.7	monocl	298	65.61	11.55	-12.13	–	–
MoO_2(g)	277.0 ± 8.4	8.4 ± 12.6	gas	298	55.65	0.44	-10.46	0.30	–
MoO_3	77.8 ± 0.8	745.2 ± 0.8	orth	298	75.19	32.64	-8.79	–	–
			liq	1074	126.90	–	–	–	48.5

MoO_3(g)	283.8 ± 4.2	345.2 ± 20.9	gas	298	74.89	6.95	-15.44	-1.46	–
Mo_2S_3	115.0 ± 8.4	406.7 ± 8.4	monocl	298	110.29	32.97	-9.62	–	–
MoS_2	62.6 ± 0.4	275.7 ± 2.5	hex	298	71.65	7.45	-9.20	–	–
N_2(g)	191.5	0.0	gas	298	30.42	2.54	-2.37	–	–
N(g)	153.2	-472.7	gas	298	20.79	–	–	–	–
			gas	1800	20.68	0.05			
NH_3(g)	192.7	45.9	gas	298	37.32	18.66	-6.49	–	–
NH_4Cl	95.0 ± 2.1	314.6 ± 0.4	cubic	298	38.87	160.25	–	–	–
				458	34.64	111.71	–	–	3.9
N_2O(g)	219.9 ± 0.2	-82.0 ± 0.6	gas	298	46.11	11.38	-10.04	-2.13	–
NO(g)	210.7 ± 0.2	-90.3 ± 0.4	gas	298	29.41	3.85	-0.59	–	–
N_2O_3(g)	309.2 ± 0.8	-82.8 ± 1.0	gas	298	80.10	17.82	-18.24	-3.51	–
NO_2(g)	239.9 ± 0.4	-33.1 ± 0.8	gas	298	35.69	22.91	-4.70	-6.33	–
				1500	53.76	1.28	–	–	–
N_2O_4(g)	304.0 ± 0.8	-9.4 ± 1.7	gas	298	101.11	24.31	-28.58	-4.85	–
N_2O_5(g)	355.6 ± 10.5	-11.7 ± 1.7	gas	298	118.66	35.48	-29.20	-10.50	–
NO_3(g)	252.7	-71.1	gas	298	67.78	12.55	-22.51	-2.64	–
Na	51.3	0.0	bcc	298	82.47	-369.32	–	627.60	–
			liq	371	37.51	-19.22	–	10.64	2.6
Na(g)	153.6	-107.5	gas	298	20.79	–	–	–	–
Na_2(g)	230.1	-142.3	gas	298	32.55	14.35	1.30	-7.74	–

Continued

Table 3.1.A6 Data for the Thermodynamic Properties of Inorganic Compounds Reproduced from *KAS* [1]—cont'd

Substance	$S_{298} \pm \delta S$ (J K^{-1} mol^{-1})	$-\Delta H_{298} \pm \delta H$ (kJ mol^{-1})	Phase	T (K)	$C_p = A + B\times10^{-3}T + C\times10^{5}T^{-2} + D\times10^{-6}T^{2}$ (J K^{-1} mol^{-1})				H_T (kJ mol^{-1})
					A	*B*	*C*	*D*	
			gas	1200	51.76	-9.58	-22.09	–	–
			gas	1900	69.83	-30.88	–	6.07	–
NaCl	72.1 ± 0.4	411.3 ± 0.4	cubic	298	45.94	16.32	–	–	–
			liq	1074	77.78	-7.53	–	–	28.2
			liq	1500	66.94	–	–	–	–
NaCl(g)	229.7 ± 0.4	182.0 ± 0.8	gas	298	37.33	0.74	-1.59	–	–
Na_2O	75.1 ± 0.4	415.1 ± 0.8	cubic	298	55.48	70.21	-4.14	-30.54	—
			ß	1023	82.30	12.76	–	–	1.8
			gamma	1243	84.85	10.71	–	–	11.9
			liq	1405	104.60	–	–	–	47.7
Na_2O_2	94.8 ± 1.3	513.0 ± 6.3	hex	298	85.48	42.68	-8.03	–	–
			ß	785	113.60	–	–	–	5.6
NaO_2	115.9 ± 1.3	260.7 ± 3.3	cubic	298	59.96	40.84	–	–	–
NaO(g)	228.4 ± 1.7	-102.5 ± 20.9	gas	298	37.24	0.92	-2.13	–	–
Na_2CO_3	135.0 ± 0.8	1129.7 ± 0.8	monocl	298	11.00	244.05	24.48	–	–
			hex	723	50.08	129.08	–	–	0.7
			liq	1130	189.54	–	–	–	29.7
Na_2S	96.2 ± 14.6	366.1 ± 12.6	cubic	298	83.16	13.81	-0.25	–	–
Nb	36.6	0.0	bcc	298	27.78	-3.84	-2.55	3.60	–

			liq	2745	41.78	–	–	–	30.5
Nb(g)	186.1	-722.6	gas	298	32.13	-8.79	0.50	2.59	–
$NbCl_4$	179.9 ± 10.5	694.5 ± 6.3	orth	298	133.47	–	-12.13	–	–
$NbCl_5$	214.2 ± 4.2	797.5 ± 4.2	monocl	298	148.53	–	–	–	–
			liq	479	184.10	–	–	–	33.9
$NbCl_5$(g)	404.0 ± 3.3	703.3 ± 8.4	gas	298	131.13	–	-12.55	–	–
NbO	46.0 ± 8.4	419.7 ± 12.6	hex	298	42.97	8.87	-4.02	–	–
			liq	2210	62.76	–	–	–	85.4
NbO(g)	238.9 ± 3.8	-198.7 ± 20.9	gas	298	35.52	1.09	-4.56	–	–
NbO_2	54.5 ± 0.4	795.0 ± 8.4	tetrag	298	61.30	25.77	-10.21	–	–
			tetrag	1090	89.04	–	–	–	3.4
			tetrag	1200	83.05	–	–	–	–
			liq	2175	94.14	–	–	–	42.3
NbO_2(g)	272.0 ± 8.4	200.0 ± 20.9	gas	298	54.77	1.59	-10.17	–	–
Nb_2O_5	137.3 ± 1.3	1899.5 ± 4.2	orth	298	162.17	14.81	-30.63	–	–
			liq	1785	242.25	–	–	–	104.2
Nd	71.1	0.0	hcp	298	14.66	26.92	4.48	–	–
			bcc	1128	44.56	–	–	–	3.0
			liq	1289	48.79	–	–	–	7.1
Nd(g)	189.3	-327.6	gas	298	17.95	19.29	-0.79	-8.45	–
			gas	1000	28.79	1.42	-14.81	–	–

Continued

Table 3.1.A6 Data for the Thermodynamic Properties of Inorganic Compounds Reproduced from *KAS* [1]—cont'd

Substance	$S_{298} \pm \delta S$ (J K^{-1} mol^{-1})	$-\Delta H_{298} \pm \delta H$ (kJ mol^{-1})	Phase	T (K)	$C_P = A + B\times10^{-3}T + C\times10^{5}T^{-2} + D\times10^{-6}T^{2}$ (J K^{-1} mol^{-1})				H_T (kJ mol^{-1})
					A	*B*	*C*	*D*	
$NdCl_3$	153.0 ± 0.8	1040.6 ± 2.1	hex	298	82.84	55.06	–	–	–
			liq	1032	146.44	–	–	–	48.5
Nd_2O_3	158.6 ± 0.4	1808.3 ± 3.3	cubic	298	115.77	29.79	-11.88	–	–
			hex	1395	155.64	–	–	–	0.6
NdS	74.1 ± 4.2	464.8 ± 5.0	tetrag	298	46.19	8.37	–	–	–
Nd_2S_3	185.4 ± 0.8	1125.5 ± 14.6	orth	298	118.53	13.35	–	–	–
Ni	29.9	0.0	fcc	298	11.17	37.78	3.18	–	–
			fcc	631	20.54	10.08	15.40	–	–
			liq	1728	38.91	–	–	–	17.2
Ni(g)	182.1	-430.1	gas	298	26.11	-1.30	-2.18	–	–
$NiCl_2$	98.1 ± 0.4	304.6 ± 2.1	hex	298	73.22	13.22	-4.98	–	–
NiCl(g)	251.3	-179.9	gas	298	39.66	0.84	-4.10	–	–
NiO	38.0 ± 0.4	239.7 ± 1.3	cubic	298	-20.88	157.23	16.28	–	–
			ß	525	58.07	–	–	–	–
			gamma	565	46.78	8.45	–	–	–
NiO(g)	241.2	-309.6	gas	298	42.33	-0.51	-0.78	–	–
$NiCO_3$	86.2 ± 0.4	696.2 ± 12.6	hex	298	88.70	38.91	-12.34	–	–
Ni_3S_2	133.9 ± 0.8	216.3 ± 5.0	hex	298	110.79	51.67	-7.53	–	–
			ß	829	188.61	–	–	–	56.2

			liq	1062	191.79	–	–	–	19.7
NiS	53.0 ± 0.4	87.9 ± 6.3	rhomb	298	44.69	19.04	-2.89	–	–
			hex	652	34.39	28.66	–	–	6.4
			liq	1249	76.78	–	–	–	30.1
Ni_3S_4	186.6	301.2 ± 25.1	cubic	298	121.96	143.68	–	–	–
O_2(g)	205.1	0.0	gas	298	29.96	4.18	-1.67	–	–
O_3(g)	238.8 ± 0.4	-142.3 ± 2.1	gas	298	44.35	15.61	-8.62	-4.35	–
O(g)	161.0	-249.2	gas	298	20.88	-0.05	0.97	–	–
Os	32.6	0.0	hcp	298	23.56	3.85	–	–	–
Os(g)	192.5	-788.0	gas	298	13.22	11.13	5.48	-1.59	–
			gas	3200	33.18	–	-229.83	0.21	–
OsO_2	51.9 ± 10.9	294.6 ± 9.6	tetrag	298	69.96	10.38	-14.18	–	–
OsO_4	136.8 ± 8.4	393.7 ± 8.4	monocl	298	151.46	–	–	–	–
			liq	314	157.74	–	–	–	14.3
OsO_4(g)	293.6 ± 0.4	336.2 ± 8.8	gas	298	85.98	20.42	-15.98	–	–
OsS_2	54.8 ± 8.4	146.9 ± 16.7	cubic	298	68.53	11.84	-8.79	–	–
P	41.1	0.0	white	298	19.12	15.82	–	–	–
			liq	317	26.32	–	–	–	0.7
P(r)	22.8 ± 0.2	17.4 ± 0.2	red	298	16.74	14.90	–	–	–
P(g)	163.1 ± 0.0	-316.5 ± 1.0	gas	298	20.79	–	–	–	–
P_2(g)	218 ± 0.2	-144.0 ± 0.4	gas	298	36.32	0.79	-4.14	–	–

Continued

Table 3.1.A6 Data for the Thermodynamic Properties of Inorganic Compounds Reproduced from *KAS* [1]—cont'd

Substance	$S_{298} \pm \delta S$ (J K^{-1} mol^{-1})	$-\Delta H_{298} \pm \delta H$ (kJ mol^{-1})	Phase	T (K)	$C_P = A + B\times10^{-3}T + C\times10^{5}T^{-2} + D\times10^{-6}T^{2}$ (J K^{-1} mol^{-1})				H_T (kJ mol^{-1})
					A	*B*	*C*	*D*	
P_4(g)	279.9 ± 0.3	-58.9 ± 0.3	gas	298	82.11	0.68	-13.44	–	–
PCl_3	218.5 ± 1.0	320.9 ± 9.2	liq	298	131.38	–	–	–	–
PCl_3(g)	311.7 ± 0.5	288.7 ± 4.2	gas	298	82.37	0.41	-9.41	–	–
PCl_5(g)	364.0 ± 1.7	360.2 ± 9.6	gas	298	131.46	0.84	-17.78	–	–
P_4O_6(g)	345.6 ± 1.3	2214.2	gas	298	182.42	48.12	-47.03	–	–
P_2O_5	114.4 ± 0.8	1505.0 ± 7.5	hex	298	74.89	162.34	-15.61	–	–
P_4O_{10}(g)	403.8	2834.2	gas	298	278.78	33.51	-9.12	–	–
P_4S_3	203.3 ± 0.4	154.4	orth	298	165.27	–	–	–	–
			hex	314	162.88	56.90	–	–	10.3
			liq	446	230.12	–	–	–	20.2
PS(g)	235.1 ± 0.8	-238.5 ± 9.6	gas	298	37.03	0.50	-1.80	–	–
P_2S_3	140.8 ± 8.4	121.3 ± 10.5	cryst	298	79.41	108.37	–	–	–
Pb	64.8	0.0	fcc	298	24.23	8.70	–	–	–
			liq	601	32.49	-3.10	–	–	4.8
			liq	1300	28.62	–	–	–	–
Pb(g)	175.3	-195.2	gas	298	20.79	–	–	–	–
			gas	900	17.70	-1.13	19.25	2.22	–
$PbCl_2$	136.0 ± 2.1	359.4 ± 0.8	orth	298	68.49	29.04	–	–	–
			liq	774	111.50	–	–	–	21.9

$PbCl_2$(g)	317.1 ± 2.9	174.1 ± 1.3	gas	298	58.03	0.33	-2.64	–	–
PbO	66.3 ± 0.8	219.4 ± 0.8	r.tet	298	52.38	8.66	-8.20	–	–
			y.orth	762	45.27	12.80	-2.99	–	0.2
PbO(g)	239.9 ± 0.2	-70.3 ± 7.1	gas	298	36.53	0.77	-3.91	–	–
Pb_3O_4	212.0 ± 6.7	718.8 ± 6.3	tetrag	298	187.19	14.48	-33.39	9.37	–
PbO_2	71.8 ± 0.4	274.5 ± 2.9	tetrag	298	63.22	31.00	-8.95	13.97	–
$PbCO_3$	131.0 ± 3.3	699.6 ± 5.4	orth	298	51.84	119.66	–	–	–
PbS	91.3 ± 1.7	98.3 ± 2.1	cubic	298	46.74	9.41	–	–	–
			liq	1387	66.94	–	–	–	18.8
PbS(g)	251.3 ± 0.2	-131.8 ± 6.3	gas	298	37.32	0.38	-2.05		–
Pd	37.9	0.0	fcc	298	23.78	7.39	–		–
			fcc	400	24.61	5.30	–	–	–
			fcc	1400	20.72	8.08	–	–	–
			liq	1825	34.73	–	–	–	17.6
Pd(g)	166.9	-377.0	gas	298	20.79	–	–	–	–
			gas	800	-6.74	20.17	74.81	–	–
			gas	2100	44.56	16.19	-949.01	-4.31	–
$PdCl_2$	103.8 ± 12.6	173.2 ± 12.6	hex	298	69.04	20.92	–	–	–
			liq	952	94.14	–	–	–	18.4
PdO	38.9 ± 4.2	115.5 ± 3.3	tetrag	298	45.31	7.03	-1.26	0.38	–
Pd_4S	180.7 ± 0.4	69.0 ± 2.1	tetrag	298	100.42	48.53	–	–	–

Continued

Table 3.1.A6 Data for the Thermodynamic Properties of Inorganic Compounds Reproduced from *KAS* [1]—cont'd

Substance	$S_{298} \pm \delta S$ (J K^{-1} mol^{-1})	$-\Delta H_{298} \pm \delta H$ (kJ mol^{-1})	Phase	T (K)	$C_P = A + B\times10^{-3}T + C\times10^{5}T^{-2} + D\times10^{-6}T^{2}$ (J K^{-1} mol^{-1})				H_T (kJ mol^{-1})
					A	*B*	*C*	*D*	
PdS	56.5 ± 6.3	70.7 ± 6.3	tetrag	298	41.71	17.20	-3.05	–	–
PdS_2	87.9 ± 12.6	78.2 ± 12.6	orth	298	68.58	15.77	-6.57	–	–
Pr	73.6	0.0	hcp	298	18.83	17.07	3.05	3.97	–
			bcc	1065	38.49	–	–	–	3.2
			liq	1191	42.97	–	–	–	6.9
Pr(g)	189.7	-355.6	gas	298	13.89	24.35	1.00	-10.42	–
			gas	1100	31.42	–	-27.15	-0.88	–
			gas	1600	30.46	-1.84	7.61	0.17	–
$PrCl_3$	153.3 ± 0.8	1057.7 ± 2.1	hex	298	88.37	45.61	-2.76	–	–
			liq	1059	133.89	–	–	–	50.6
$PrCl_3$(g)	379.5 ± 6.7	730.1 ± 5.0	gas	298	86.19	–	-3.35	–	–
Pr_2O_3	155.6 ± 2.1	1809.6	hex	298	119.66	17.78	-7.41	–	–
			cubic	2150	154.81	–	–	–	–
			liq	2570	152.30	–	–	–	92.0
Pt	41.5	0.0	fcc	298	24.69	5.02	-0.50	–	–
			fcc	1000	24.43	5.23	-0.75	–	–
			liq	2042	34.69	–	–	–	19.7
Pt(g)	192.3	-565.0	gas	298	36.32	-14.02	-5.86	–	–
			gas	500	31.21	-11.34	1.34	3.56	–

			gas	1700	18.66	1.38	33.64	–	–
$PtCl_4$	205.0 ± 20.9	236.8 ± 16.7	cubic	298	146.44	–	–	–	–
PtO_2(g)	255.9 ± 10.5	-168.6 ± 10.5	gas	298	55.44	2.09	-11.51	–	–
PtS	55.1 ± 0.4	83.1 ± 2.5	tetrag	298	41.71	17.20	-3.05	–	–
PtS_2	74.7 ± 0.4	110.9 ± 2.5	hex	298	68.58	15.77	-6.57	–	–
Rb	76.8	0.0	bcc	298	31.71	–	–	–	–
			liq	313	40.88	-26.21	0.33	14.14	2.2
Rb(g)	170.0	-80.9	gas	298	20.79	–	–	–	–
Rb_2(g)	270.7	-118.4	gas	298	37.28	2.00	–	–	–
RbCl	95.2 ± 0.4	435.1 ± 0.8	cubic	298	48.24	10.46	–	–	–
			liq	996	64.02	–	–	–	23.7
Rb_2O	125.5 ± 4.2	338.9 ± 8.4	cubic	298	60.25	46.02	–	–	–
			hex	613	89.96	–	–	–	4.6
			liq	778	95.81	–	–	–	20.9
Rb_2CO_3	181.3 ± 0.4	1133.0 ± 13.8	monocl	298	105.86	80.75	-10.88	–	–
Rb_2S	133.1 ± 12.6	361.1 ± 20.9	cubic	298	77.40	20.92	–	–	–
Re	36.5	0.0	hcp	298	23.68	5.44	–	–	–
Re(g)	188.8	-775.0	gas	298	20.79	–	–	–	–
			gas	1400	29.75	-10.84	–	3.26	–
$ReCl_3$	123.8 ± 0.4	263.6 ± 10.5	hex	298	105.48	27.61	-19.08	–	–
ReO_2	62.8 ± 4.6	432.6 ± 5.0	monocl	298	67.36	12.68	-12.93	–	–

Continued

Table 3.1.A6 Data for the Thermodynamic Properties of Inorganic Compounds Reproduced from *KAS* [1]—cont'd

Substance	$S_{298} \pm \delta S$ (J K^{-1} mol^{-1})	$-\Delta H_{298} \pm \delta H$ (kJ mol^{-1})	Phase	T (K)	$C_P = A + B\times10^{-3}T + C\times10^{5}T^{-2} + D\times10^{-6}T^{2}$ (J K^{-1} mol^{-1})				H_T (kJ mol^{-1})
					A	*B*	*C*	*D*	
ReO_3	80.8 ± 8.4	610.9 ± 12.6	cubic	298	108.78	–	–	–	–
Re_2O_7	207.1 ± 0.8	1248.5 ± 10.5	orth	298	121.96	184.10	-9.41	–	–
			liq	570	297.48	–	–	–	62.8
ReS_2	60.7 ± 8.4	178.7 ± 12.6	hex	298	68.58	15.77	-6.57	–	–
Re_2S_7	167.4 ± 20.9	451.5 ± 16.7	tetrag	298	184.10	50.21	–	–	–
Rh	31.5	0.0	fcc	298	20.79	13.43	0.33	-2.26	–
			liq	2236	41.84	–	–	–	21.5
Rh(g)	185.7	-553.1	gas	298	21.17	6.40	-2.13	-1.46	–
$RhCl_3$	126.8 ± 14.6	280.3 ± 12.6	monocl	298	105.44	27.61	-19.08	–	–
Rh_2O_3	106.3 ± 8.4	355.6	rhomb	298	86.78	57.74	–	–	–
RhO(g)	229.7 ± 10.5	-410.0 ± 50.2	gas	298	37.87	–	-5.44	–	–
Rh_3S_4	182.0 ± 25.1	357.7	cryst	298	145.60	60.25	-10.67	–	–
Rh_2S_3	125.5 ± 20.9	262.8	cryst	298	110.25	32.97	-9.62	–	–
Ru	28.5	0.0	hcp	298	18.58	9.29	2.80	–	–
			liq	2523	41.84	–	–	–	24.3
Ru(g)	186.4	-651.4	gas	298	23.93	2.01	-2.72	–	–
$RuCl_3$	127.6 ± 10.5	253.1 ± 14.6	hex	298	115.06	–	–	–	–
$RuCl_3$(g)	397.5 ± 20.9	-56.1 ± 18.8	gas	298	56.90	7.66	-3.01	–	–
$RuCl_4$(g)	374.5 ± 20.9	93.3 ± 16.7	gas	298	95.81	–	-10.46	–	–

RuO_2	58.6 ± 4.6	305.0 ± 6.3	tetrag	298	69.87	10.46	-14.85	–	–
RuO_4(g)	290.7 ± 0.4	184.1 ± 5.0	gas	298	101.80	3.05	-24.02	–	–
RuS_2	54.4 ± 12.6	205.9 ± 20.9	cubic	298	68.53	11.84	-8.79	–	–
S	32.0 ± 0.1	0.0	orth	298	23.51	–	–	–	–
			monocl	368	24.73	–	–	–	0.4
			liq	388	35.19	–	–	–	1.7
S(g)	167.7	-277.2 ± 0.4	gas	298	22.01	-0.42	1.51	–	–
			gas	2400	20.75	0.42	2.51	–	–
S_2(g)	228.1	-128.6	gas	298	33.53	6.02	-2.37	-2.09	–
			gas	1000	34.62	3.67	-6.07	-0.43	–
S_3(g)	276.0	-146.4	gas	298	57.60	0.32	-6.33	–	–
S_4(g)	325.9	-188.3	gas	298	82.55	3.14	-7.11	–	–
			gas	718	82.42	3.14	-7.11	–	–
S_5(g)	320.9	-111.0	gas	298	106.48	0.85	-16.45	–	–
S_6(g)	353.9	-98.7	gas	298	131.75	0.67	-17.20	–	–
S_7(g)	394.1	-102.9	gas	298	155.91	1.09	-23.34	–	–
			gas	718	155.91	1.09	-23.34	–	–
S_8(g)	423.1	-96.8	gas	298	181.18	0.92	-22.79	–	–
S_2Cl_2	223.8 ± 4.2	58.2 ± 2.1	liq	298	124.26	–	–	–	–
S_2Cl_2(g)	327.2 ± 0.4	16.7 ± 4.2	gas	298	80.79	3.04	-7.76	–	–
SCl_2(g)	281.5 ± 0.4	17.6 ± 3.3	gas	298	57.53	0.36	-6.00		

Continued

Table 3.1.A6 Data for the Thermodynamic Properties of Inorganic Compounds Reproduced from *KAS* [1]—cont'd

Substance	$S_{298} \pm \delta S$ (J K^{-1} mol^{-1})	$-\Delta H_{298} \pm \delta H$ (kJ mol^{-1})	Phase	T (K)	$C_P = A + B\times10^{-3}T + C\times10^{5}T^{-2} + D\times10^{-6}T^{2}$ (J K^{-1} mol^{-1})				H_T (kJ mol^{-1})
					A	*B*	*C*	*D*	
SO(g)	221.8 ± 0.2	-5.0 ± 2.1	gas	298	33.35	2.85	-3.60	–	–
SO_2(g)	248.1	296.8	gas	298	49.96	4.77	-10.46	–	–
SO_3	122.6 ± 8.4	438.5 ± 0.8	liq	298	179.91	–	–	–	–
SO_3(g)	256.7 ± 0.2	395.8 ± 0.8	gas	298	70.00	6.61	-19.35	–	–
Sb	45.5	0.0	rhomb	298	23.05	7.28	–	–	–
			liq	904	31.38	–	–	–	19.9
Sb(g)	180.2	-264.6	gas	298	20.79	–	–	–	–
			gas	800	17.83	1.91	9.68	–	–
Sb_2(g)	254.8	-231.2	gas	298	37.36	0.04	-0.91	–	–
			gas	1300	37.28	0.06	–	–	–
			gas	1860	37.39	–	–	–	–
Sb_4(g)	350.0	-206.5	gas	298	82.91	0.17	-1.80	–	–
			gas	1300	82.81	0.14	–	–	–
			gas	1860	62.14	–	–	–	–
$SbCl_3$	183.3 ± 3.8	381.2 ± 1.7	orth	298	43.10	225.94	–	–	–
			liq	346	123.85	–	–	–	13.0
$SbCl_3$(g)	338.5 ± 1.3	312.1 ± 3.3	gas	298	83.01	–	-4.98	–	–
$SbCl_5$(g)	401.7 ± 1.0	389.1 ± 5.4	gas	298	132.21	-9.83	–	–	–
Sb_2O_3	132.7 ± 4.2	716.1 ± 3.3	cubic	298	75.31	97.49	–	–	–

			orth	845	92.05	66.11	–	–	8.1
			liq	929	156.90	–	–	–	54.8
SbO_2	63.6 ± 4.2	453.5 ± 2.5	cubic	298	47.28	33.89	–	–	–
Sb_2O_5	125.1 ± 8.4	1007.5 ± 4.6	cubic	298	69.04	230.12	–	–	–
Sb_2S_3	107.53 ± 3.3	205.0	orth	298	101.84	60.54	–	–	–
			liq	823	167.36	–	–	–	47.9
Sc	34.8	0.0	hex	298	24.74	1.33	0.35	5.10	–
			cubic	1610	44.22	–	–	–	4.0
			liq	1814	44.35	–	–	–	14.1
Sc(g)	300.2	-379.1	gas	298	20.92	–	–	–	–
			gas	1600	28.12	-8.74	–	2.68	–
$ScCl_3$	121.3	918.8 ± 3.3	rhomb	298	95.65	15.40	-7.28	–	–
			liq	1240	143.43	–	–	–	67.4
Sc_2O_3	77.0 ± 0.4	1908.3 ± 3.3	cubic	298	99.79	22.22	-11.09	–	–
Se	42.3	0.0	hex	298	17.89	25.10	–	–	–
			liq	493	35.15	–	–	–	5.9
Se(g)	176.6	-235.4	gas	298	21.46	1.51	-0.92	–	–
Se_2(g)	246.9	-138.2	gas	298	44.60	-2.66	-2.50	–	–
Se_3(g)	314.9	-176.1	gas	298	58.15	3.04	-2.21	–	–
Se_4(g)	379.1	-183.3	gas	298	83.16	0.03	-2.51	–	–
Se_5(g)	385.3	-138.1	gas	298	107.93	0.09	-5.91	–	–

Continued

Table 3.1.A6 Data for the Thermodynamic Properties of Inorganic Compounds Reproduced from *KAS* [1]—cont'd

Substance	$S_{298} \pm \delta S$ (J K^{-1} mol^{-1})	$-\Delta H_{298} \pm \delta H$ (kJ mol^{-1})	Phase	T (K)	$C_P = A + B\times10^{-3}T + C\times10^{5}T^{-2} + D\times10^{-6}T^{2}$ (J K^{-1} mol^{-1})				H_T (kJ mol^{-1})
					A	*B*	*C*	*D*	
Se_6(g)	433.5	-135.1	gas	298	132.90	0.07	-5.92	–	–
Se_2Cl_2(g)	353.8	21.8 ± 8.4	gas	298	82.42	1.55	-4.52	–	–
$SeCl_2$(g)	295.6	33.5 ± 12.6	gas	298	57.95	0.13	-3.95	–	–
$SeCl_4$	194.6 ± 16.7	188.7 ± 6.3	monocl	298	133.89	–	–	–	–
SeO(g)	233.9	-62.3 ± 20.9	gas	298	34.94	1.51	-3.68	–	–
SeO_2	66.7 ± 1.7	225.1 ± 2.1	tetrag	298	69.58	3.89	-11.05	–	–
SeO_2(g)	264.8	107.9 ± 8.4	gas	298	52.84	3.10	-9.90	–	–
Si	18.8	0.0	diam	298	23.93	2.22	-4.14	–	–
			liq	1685	27.20	–	–	–	50.2
Si(g)	167.9	-450.0	gas	298	19.82	1.00	2.01	–	–
Si_2(g)	229.7	-585.8	gas	298	37.25	0.46	-0.28	–	–
Si_3(g)	267.8	-636.0	gas	298	61.99	0.13	-0.73	–	–
$SiCl_2$(g)	281.8 ± 4.2	167.4 ± 4.2	gas	298	57.57	0.38	-5.65	–	–
$SiCl_4$(g)	330.8 ± 0.4	662.7 ± 1.3	gas	298	106.52	0.75	-14.73	–	–
SiO(g)	211.5 ± 0.4	98.3 ± 8.4	gas	298	29.83	8.24	-2.05	-2.28	–
SiO_2	41.5 ± 0.4	910.9 ± 1.7	a–qtz	298	43.93	38.83	-9.69	–	–
			ß–qtz	847	58.91	10.04	–	–	0.7
SiO_2(cr)	43.4 ± 0.8	908.3 ± 1.7	a–cris	298	46.90	31.51	-10.08	–	–
			ß–cris	540	71.63	1.88	-39.06	–	1.3

			liq	2000	86.19	–	–	–	9.6
SiS(g)	223.7 ± 2.1	-105.9 ± 12.6	gas	298	36.42	0.74	-4.04	–	–
SiS_2	80.3 ± 4.2	213.4 ± 20.9	orth	298	74.14	12.38	–	–	–
			liq	1363	91.00	–	–	–	20.9
Sm	69.5	0.0	hcp	298	27.57	29.58	-5.61	-10.46	–
			bcc	1191	46.94	–	–	–	3.1
			liq	1346	50.21	–	–	–	8.6
Sm(g)	182.9	-206.7	gas	298	30.33	–	–	–	–
$SmCl_2$	127.6 ± 6.3	816.3 ± 8.4	cryst	298	77.40	16.74	–	–	–
$SmCl_2$(g)	315.5	500.4 ± 17.6	gas	298	65.19	-8.58	–	–	–
$SmCl_3$	113.0 ± 12.6	1028.4 ± 3.3	hex	298	82.26	47.70	0.75	–	–
Sm_2O_3	151.0 ± 0.4	1822.6 ± 3.3	monocl	298	128.66	19.41	-17.99	–	–
			monocl	1195	154.39	–	–	–	1.0
SmS	81.2 ± 4.2	431.0 ± 41.8	cubic	298	59.33	3.18	-1.92	–	–
Sn	51.2	0.0	tetrag	298	21.59	18.16	–	–	–
			liq	505	32.84	-6.28	–	–	7.2
			liq	700	28.45	–	–	–	–
Sn(g)	168.4	-301.2	gas	298	8.31	31.51	3.16	–	–
			gas	500	-1.49	66.33	4.21	-32.18	–
			gas	1000	50.14	-10.73	-63.12	–	–
			gas	1400	29.20	-1.36	91.76	–	–

Continued

Table 3.1.A6 Data for the Thermodynamic Properties of Inorganic Compounds Reproduced from *KAS* [1]—cont'd

Substance	$S_{298} \pm \delta S$ (J K^{-1} mol^{-1})	$-\Delta H_{298} \pm \delta H$ (kJ mol^{-1})	Phase	T (K)	$C_P = A + B\times10^{-3}T + C\times10^{5}T^{-2} + D\times10^{-6}T^{2}$ (J K^{-1} mol^{-1})				H_T (kJ mol^{-1})
					A	*B*	*C*	*D*	
$SnCl_2$	131.8	331.0	rhomb	298	50.63	83.68	–	–	–
			liq	520	96.23	–	–	–	12.6
$SnCl_4$	259.0 ± 3.3	528.9 ± 14.6	liq	298	164.85	–	–	–	–
$SnCl_4$(g)	364.8 ± 1.3	489.1	gas	298	106.98	0.84	-7.82	–	–
SnO	57.2 ± 0.4	280.7 ± 0.8	tetrag	298	39.96	14.64	–	–	–
SnO(g)	232.0 ± 0.2	-20.9 ± 9.6	gas	298	35.23	1.34	-3.51	–	–
SnO_2	52.3 ± 1.3	577.6 ± 0.4	tetrag	298	73.89	10.04	-21.59	–	–
SnS	77.0 ± 0.8	107.9 ± 2.1	orth	298	35.69	31.30	-3.77	–	–
			orth	875	32.55	15.65	–	–	0.7
			liq	1153	74.89	–	–	–	31.6
SnS(g)	242.3 ± 0.8	-112.5 ± 4.2	gas	298	36.94	0.33	-2.30	–	–
Sn_3S_4	243.5 ± 16.7	370.3 ± 20.9	tetrag	298	150.96	62.34	–	–	–
Sn_2S_3	164.4	263.6 ± 20.9	orth	298	107.03	43.93	–	–	–
SnS_2	87.4 ± 0.8	153.6	hex	298	64.89	17.57	–	–	–
Sr	52.3	0.0	fcc	298	27.70	-3.68	-1.38	19.20	–
			bcc	820	37.66	–	–	–	0.8
			liq	1042	35.15	–	–	–	8.2
Sr(g)	164.5	-164.0	gas	298	20.79	–	–	–	–
$SrCl_2$	114.8 ± 0.2	828.9 ± 2.5	cubic	298	113.72	-99.70	-14.90	92.88	–

			ß	1000	123.01	–	–	–	6.0
			liq	1147	104.60	–	–	–	16.2
$SrCl_2$(g)	316.2 ± 5.0	473.2 ± 6.3	gas	298	58.16	20.04	-2.13	-0.21	–
SrO	55.5 ± 0.4	592.0 ± 3.8	cubic	298	50.75	6.07	-6.28	–	–
SrO(g)	230.0 ± 0.4	13.4 ± 16.7	gas	298	36.40	0.67	-3.10	–	–
SrO_2	59.0 ± 10.0	633.5 ± 15.1	tetrag	298	73.97	18.41	–	–	–
$SrCO_3$	97.1 ± 1.7	1220.1 ± 8.4	orth	298	88.78	35.90	-15.48	–	–
			hex	1197	142.26	–	–	–	19.7
SrS	68.2 ± 2.9	452.7 ± 16.3	cubic	298	54.31	5.27	-6.49	–	–
Ta	41.5	0.0	bcc	298	23.77	7.41	-0.42	-2.72	–
			bcc	1400	47.82	-22.34	–	6.57	
			liq	3293	41.84	–	–	–	33.9
Ta(g)	185.1	-781.6	gas	298	17.95	11.21	-0.56	-1.72	–
$TaCl_3$	154.8 ± 8.4	552.3 ± 3.8	cubic	298	96.23	16.32	-7.11	–	–
$TaCl_4$	192.5 ± 8.4	705.0 ± 4.6	monocl	298	133.47	–	-12.13	–	–
$TaCl_4$(g)	382.8 ± 10.5	566.9 ± 8.8	gas	298	107.95	–	-8.37	–	–
$TaCl_5$	221.8 ± 6.3	859.0 ± 4.2	monocl	298	147.90	–	–	–	–
			liq	490	180.75	–	–	–	35.1
$TaCl_5$(g)	412.9 ± 3.3	764.8 ± 8.4	gas	298	132.51	0.27	-11.09	–	–
TaO_2(g)	279.5 ± 1.7	184.1 ± 20.9	gas	298	54.81	0.17	-10.13	–	–
Ta_2O_5	143.1 ± 1.3	2046.4 ± 4.2	orth	298	161.29	21.42	-29.20	–	–

Continued

Table 3.1.A6 Data for the Thermodynamic Properties of Inorganic Compounds Reproduced from *KAS* [1]—cont'd

Substance	$S_{298} \pm \delta S$ (J K^{-1} mol^{-1})	$-\Delta H_{298} \pm \delta H$ (kJ mol^{-1})	Phase	T (K)	$C_P = A + B\times10^{-3}T + C\times10^{5}T^{-2} + D\times10^{-6}T^{2}$ (J K^{-1} mol^{-1})				H_T (kJ mol^{-1})
					A	*B*	*C*	*D*	
			liq	2058	242.67	–	–	–	120.1
TaS_2	75.3	354.0 ± 16.7	hex	298	69.87	–	–	–	–
Tb	73.3	0.0	hcp	298	16.78	18.70	6.02	–	–
			bcc	1591	27.74	–	–	–	5.0
			liq	1633	46.44	–	–	–	10.8
Tb(g)	203.1	-388.7	gas	298	25.46	-2.85	–	–	–
			gas	500	19.50	5.87	4.15	–	–
			gas	1000	21.23	6.50	-9.08	-1.07	–
$TbCl_3$	147.7 ± 7.5	998.7 ± 3.3	orth	298	94.10	25.75	-3.10	–	–
			orth	783	123.93	–	–	–	14.2
			liq	855	144.47	–	–	–	19.5
Tb_2O_3	156.9 ± 8.4	1865.2 ± 7.5	cubic	298	108.78	41.42	-8.37	–	–
TbO_2	82.8	971.5 ± 3.8	cubic	298	64.81	17.70	-7.59	–	–
Te	49.5	0.0	hex	298	19.16	21.97	–	–	–
			liq	723	37.66	–	–	–	17.5
Te(g)	182.6	-211.7	gas	298	19.41	1.84	0.75	–	–
Te_2(g)	260.6	-159.1	gas	298	34.64	6.61	-0.26	–	–
$TeCl_4$	200.8 ± 20.9	323.8	cryst	298	138.49	–	–	–	–
			liq	497	230.12	–	–	–	18.9

$TeCl_4$(g)	376.6 ± 20.9	205.9 ± 20.9	gas	298	96.71	0.15	-5.49	–	–
TeO(g)	240.6 ± 0.8	-74.5	gas	298	35.31	1.34	-34.73	–	–
TeO_2	70.1 ± 0.8	316.3 ± 2.1	tetrag	298	65.19	15.06	-7.95	–	–
			liq	1004	112.63	2.18	–	–	29.1
TeO_2(g)	274.9 ± 4.2	52.3 ± 8.4	gas	298	54.77	2.43	-11.84	–	–
Th	53.4	0.0	fcc	298	25.10	8.37	-0.23	-0.22	–
			bcc	1633	15.69	11.97	–	–	3.6
			liq	2028	46.02	–	–	–	13.8
Th(g)	190.0	-597.1	gas	298	8.62	21.21	5.86	-3.20	–
$ThCl_4$	190.4 ± 5.0	1186.6 ± 2.9	orth	298	120.29	23.26	-6.15	–	–
			tetrag	679	120.29	23.26	-6.15	–	5.0
			liq	1043	163.18	–	–	–	61.5
$ThCl_4$(g)	390.8 ± 8.4	974.9 ± 9.2	gas	298	108.07	–	-6.15	–	–
ThO(g)	240.0 ± 0.4	28.5 ± 2.1	gas	298	37.91	–	-5.98	–	–
ThO_2	65.2 ± 0.4	1226.7 ± 1.3	cubic	298	69.29	9.33	-9.18	–	–
ThS	69.8 ± 0.4	399.6 ± 6.3	cubic	298	50.12	5.46	-3.59	–	–
Th_2S_3	171.5 ± 11.7	1083.2 ± 12.6	orth	298	121.96	15.06	-3.77	–	–
ThS_2	96.2 ± 0.8	627.6 ± 33.5	orth	298	67.03	11.00	–	–	–
Ti	30.7	0.0	hex	298	24.94	6.57	-1.63	1.34	–
			bcc	1155	30.84	-8.87	–	6.44	4.2
			liq	1943	41.84	–	–	–	16.7

Continued

Table 3.1.A6 Data for the Thermodynamic Properties of Inorganic Compounds Reproduced from *KAS* [1]—cont'd

Substance	$S_{298} \pm \delta S$ (J K^{-1} mol^{-1})	$-\Delta H_{298} \pm \delta H$ (kJ mol^{-1})	Phase	T (K)	$C_P = A + B\times10^{-3}T + C\times10^{5}T^{-2} + D\times10^{-6}T^{2}$ (J K^{-1} mol^{-1})				H_T (kJ mol^{-1})
					A	*B*	*C*	*D*	
Ti(g)	180.2	-473.6	gas	298	22.26	-3.26	2.76	2.13	–
$TiCl_2$(g)	87.4 ± 12.6	515.5 ± 16.7	gas	298	60.12	2.22	-2.76	–	–
$TiCl_3$	139.7 ± 1.3	721.7 ± 5.0	trigon	298	95.81	11.05	-1.80	–	–
$TiCl_3$(g)	316.7 ± 4.2	539.3 ± 6.3	gas	298	87.24	-0.71	-12.93	–	–
Ti_2Cl_6(g)	482.0 ± 16.7	1248.1 ± 16.7	gas	298	182.59	0.21	-11.55	–	–
$TiCl_4$	252.4 ± 0.8	804.2 ± 1.3	liq	298	142.80	8.70	-0.17	–	–
$TiCl_4$(g)	353.1 ± 4.2	763.2 ± 3.8	gas	298	107.19	0.47	-10.54	–	–
TiO	34.7 ± 2.1	542.7 ± 12.6	monocl	298	44.22	15.06	-7.78	–	–
			cubic	1265	49.58	12.55	–	–	3.4
Ti_2O_3	77.2 ± 0.4	1520.9 ± 8.4	trigon	298	31.80	213.38	–	–	–
			ß	470	147.70	3.43	-47.51	–	1.1
Ti_3O_5	129.4 ± 1.7	2459.1 ± 4.2	monocl	298	231.04	-24.77	-61.25	–	–
			orth	450	158.99	50.21	–	–	13.1
TiO_2	50.6 ± 0.4	944.0 ± 0.8	rutile	298	73.35	3.05	-17.03	–	–
TiO_2(a)	49.9 ± 0.4	941.4 ± 2.9	anatas	298	76.36	0.84	-20.08	–	–
TiS	56.5 ± 8.4	272.0 ± 29.3	hex	298	45.90	7.36	–	–	–
TiS(g)	246.4 ± 2.1	-330.5	gas	298	36.99	0.22	-2.95	–	–
TiS_2	78.2 ± 6.3	407.1 ± 33.5	hex	298	33.81	114.39	–	–	–
			hex	420	62.72	21.51	–	–	–

Tl	64.2	0.0	hcp	298	15.65	25.27	2.80	–	–
			ß	507	20.92	20.92	–	–	0.4
			liq	577	30.12	–	–	–	4.3
Tl(g)	180.8	-181.0	gas	298	20.79	–	–	–	–
			gas	700	23.60	-4.56	-3.17	2.08	–
TlCl	111.5 ± 0.4	204.2 ± 1.7	cubic	298	46.02	16.74	–	–	–
			liq	702	59.41	–	–	–	15.9
Tl_2O	134.3 ± 11.3	167.4 ± 7.5	hex	298	56.07	41.84	–	–	–
			liq	852	94.98	–	–	–	30.3
Tl_2O_3	137.2 ± 13.8	390.4 ± 5.9	cubic	298	131.88	3.56	-22.26	–	–
Tl_2S	159.0 ± 12.6	95.0 ± 4.6	hex	298	71.55	29.29	–	–	–
			liq	730	99.58	–	–	–	23.0
Tm	74.0	0.0	hcp	298	19.83	13.01	3.22	-1.88	–
			bcc	1780	37.24	–	–	–	–
			liq	1818	41.42	–	–	–	16.9
Tm(g)	190.0	-232.2	gas	298	20.79	–	–	–	–
			gas	900	22.52	-2.24	-3.18	0.83	–
$TmCl_3$	147.3 ± 11.7	988.3 ± 2.5	monocl	298	95.60	11.72	-1.26	–	–
			liq	1101	148.53	–	–	–	34.9
Tm_2O_3	139.7 ± 0.4	1888.7 ± 5.9	cubic	298	129.70	3.26	-14.31	–	–
			cubic	1680	133.89	–	–	–	1.3

Continued

Table 3.1.A6 Data for the Thermodynamic Properties of Inorganic Compounds Reproduced from *KAS* [1]—cont'd

Substance	$S_{298} \pm \delta S$ (J K^{-1} mol^{-1})	$-\Delta H_{298} \pm \delta H$ (kJ mol^{-1})	Phase	T (K)	$C_P = A + B\times10^{-3}T + C\times10^{5}T^{-2} + D\times10^{-6}T^{2}$ (J K^{-1} mol^{-1})				H_T (kJ mol^{-1})
					A	*B*	*C*	*D*	
U	50.2	0.0	orth	298	25.10	2.38	–	23.68	–
			tetrag	941	42.93	–	–	–	2.8
			cubic	1049	38.28	–	–	–	4.8
			liq	1408	48.66	–	–	–	9.2
U(g)	199.7	-531.4	gas	298	16.74	6.32	4.98	1.55	–
UCl_3	159.0 ± 0.8	861.9 ± 3.3	hex	298	87.03	32.43	4.39	–	–
			liq	1114	129.70	–	–	–	46.4
UCl_3(g)	356.9	569.0 ± 16.7	gas	298	91.00	–	-9.62	–	–
UCl_4	197.3 ± 0.8	1018.8 ± 2.1	tetrag	298	113.80	35.86	-3.31	–	–
			liq	863	162.34	–	–	–	50.0
UCl_4(g)	389.9 ± 6.3	828.4 ± 7.1	gas	298	112.97	–	-9.04	–	–
U_2Cl_8	623.8 ± 25.1	1778.6 ± 25.1	gas	298	248.53	–	-19.87	–	–
UCl_5	246.9 ± 10.5	1041.4 ± 2.1	monocl	298	140.04	35.44	-5.36	–	–
			liq	600	186.69	–	–	–	35.6
U_2Cl_{10}(g)	633.0 ± 10.5	1960.2	gas	298	287.44	–	-28.87	–	–
UCl_6	285.8 ± 1.7	1068.2 ± 2.1	hex	298	173.43	35.06	-7.41	–	–
			liq	451	213.97	–	–	–	20.9
UCl_6(g)	432.6	987.8 ± 8.4	gas	298	158.03	–	-12.34	–	–
UO_2	77.0	1085.0	cubic	298	80.33	6.78	-16.57	–	–

U_4O_9	334.1 ± 0.6	4510.4 ± 7.1	cubic	298	356.27	35.44	-66.40	–	–
U_3O_8	282.5 ± 0.5	3574.8 ± 2.5	orth	298	282.42	36.94	-49.96	–	–
UO_3	96.2 ± 0.4	1223.8 ± 1.3	monocl	298	93.30	10.88	-10.88	–	–
US	78.0 ± 0.4	318.0 ± 6.7	cubic	298	52.84	6.53	-3.79	–	–
US_2	110.4 ± 0.4	526.3 ± 6.3	hex	298	71.80	9.62	–	–	–
US_3	138.5 ± 0.4	548.1 ± 33.5	monocl	298	95.60	–	–	–	–
V	30.9	0.0	bcc	298	24.14	6.19	-1.38	-0.71	–
			bcc	900	25.90	-0.13	–	4.08	–
			liq	2183	47.28	–	–	–	23.0
V(g)	182.2	-514.2	gas	298	25.10	–	–	–	–
VCl_2	97.1 ± 1.3	461.5 ± 8.4	hex	298	72.17	11.38	-2.97	–	–
VCl_3	131.0 ± 1.7	581.2 ± 2.1	hex	298	96.23	16.40	-7.03	–	–
VCl_4	257.4 ± 2.1	569.9 ± 2.5	liq	298	161.71	–	–	–	–
VCl_4(g)	366.1	525.9	gas	298	99.16	8.37	-5.44	–	–
VO	33.1 ± 0.4	431.8 ± 2.1	cubic	298	50.21	11.84	-13.51	–	–
V_2O_3	92.9 ± 2.9	1218.8 ± 1.7	hex	298	112.97	19.29	-14.98	–	–
VO_2	47.1 ± 1.0	713.8 ± 1.0	monocl	298	73.01	2.43	-14.98	–	–
			tetrag	341	74.68	7.11	-16.53	–	4.3
			liq	1818	106.69	–	–	–	56.9
V_2O_5	130.5 ± 0.4	1550.2 ± 1.7	orth	298	141.00	42.68	-23.43	–	–
			liq	952	190.37	–	–	–	66.9

Continued

Table 3.1.A6 Data for the Thermodynamic Properties of Inorganic Compounds Reproduced from *KAS* [1]—cont'd

Substance	$S_{298} \pm \delta S$ (J K^{-1} mol^{-1})	$-\Delta H_{298} \pm \delta H$ (kJ mol^{-1})	Phase	T (K)	$C_P = A + B\times10^{-3}T + C\times10^{5}T^{-2} + D\times10^{-6}T^{2}$ (J K^{-1} mol^{-1})				H_T (kJ mol^{-1})
					A	*B*	*C*	*D*	
W	32.6	0.0	bcc	298	23.68	4.06	-0.47	-0.33	–
			bcc	1000	29.41	-2.95	-12.40	2.13	–
			bcc	2000	126.40	-58.68	-879.21	11.17	–
			liq	3693	54.02	–	–	–	50.0
W(g)	173.8	-851	gas	298	10.26	17.54	3.28	24.02	–
			gas	600	-46.25	157.86	29.82	-73.35	–
			gas	1000	116.14	-65.43	-227.29	13.25	–
			gas	2000	25.46	-3.52	370.70	1.24	–
WCl_4	198.3	443.5	rhomb	298	106.48	77.86	1.38	-18.62	–
WCl_4(g)	379.1	336.0	gas	298	107.40	0.46	-7.78	–	–
WCl_5	217.6	514.2 ± 37.7	monocl	298	124.43	109.91	-1.38	–	–
WCl_5(g)	405.4	412.5	gas	298	131.38	1.42	-10.29	–	–
W_2Cl_{10}(g)	711.3	868.6	gas	298	281.71	0.52	-16.53	–	–
WCl_6	238.5	594.1	rhomb	298	125.52	167.36	–	–	–
			ß	450	209.20	–	–	–	4.2
			gamma	503	188.28	–	–	–	15.5
			liq	555	200.83	–	–	–	6.7
WCl_6(g)	419.2	493.7	gas	298	157.53	0.21	-12.26	–	–
WO_3	75.9 ± 1.3	842.7 ± 2.9	monocl	298	91.29	10.46	-19.00	–	–

			orth	603	77.40	25.10	–	–	1.4
			tetrag	1013	99.79	–	–	–	1.9
			tet2	1173	105.86	–	–	–	1.2
			tet3	1490	112.97	–	–	–	0.5
			liq	1745	131.80	–	–	–	73.4
WO_3(g)	286.2 ± 12.6	292.9 ± 25.1	gas	298	70.92	13.39	-12.30	-3.89	–
WO_2	50.5 ± 1.7	589.5 ± 6.3	monocl	298	77.40	-7.03	-18.49	8.87	–
WO_2(g)	285.3	-76.6	gas	298	49.08	10.00	-7.32	-2.89	–
WS_2	64.9 ± 6.3	259.4 ± 16.7	hex	298	68.62	15.61	-8.66	–	–
Y	44.4	0.0	hcp	298	23.39	7.95	1.21	–	–
			bcc	1751	35.02	–	–	–	5.0
			liq	1795	39.79	–	–	–	11.4
Y(g)	179.4	-423.0	gas	298	26.15	-6.74	2.34	2.30	–
YCl_3	140.2	1000.0 ± 3.8	monocl	298	104.73	3.22	-12.13	–	–
			liq	994	177.57	–	–	–	31.5
YCl_3(g)	351.5 ± 6.7	702.9 ± 8.8	gas	298	83.68	–	-5.23	–	–
Y_2O_3	99.2 ± 0.4	1905.0 ± 5.0	cubic	298	109.62	20.08	-11.30	–	–
Yb	59.8	0.0	ß	298	22.84	14.52	–	-5.44	–
			gamma	1068	36.11	–	–	–	1.8
			liq	1092	36.82	–	–	–	7.7
Yb(g)	172.8	-152.0	gas	298	20.79	–	–	–	–

Continued

Table 3.1.A6 Data for the Thermodynamic Properties of Inorganic Compounds Reproduced from *KAS* [1]—cont'd

Substance	$S_{298} \pm \delta S$ (J K^{-1} mol^{-1})	$-\Delta H_{298} \pm \delta H$ (kJ mol^{-1})	Phase	T (K)	$C_P = A + B\times10^{-3}T + C\times10^{5}T^{-2} + D\times10^{-6}T^{2}$ (J K^{-1} mol^{-1})				H_T (kJ mol^{-1})
					A	*B*	*C*	*D*	
$YbCl_2$	122.6 ± 2.1	799.1 ± 8.4	ortho	298	67.99	20.92	–	–	–
$YbCl_3$	135.1 ± 12.6	961.1 ± 3.3	monocl	298	94.68	9.33	-1.88	–	–
			liq	1148	121.34	–	–	–	–
Yb_2O_3	133.1 ± 0.4	1814.6 ± 3.3	cubic	298	128.66	19.46	-17.15	–	–
Zn	41.6	0.0	hcp	298	22.38	10.04	–	–	–
			liq	693	31.38	–	–	–	7.3
Zn(g)	160.9	-130.4	gas	298	20.79	–	–	–	–
$ZnCl_2$	111.5 ± 0.4	415.1 ± 0.8	tetrag	298	59.83	37.66	–	–	–
			liq	591	100.83	–	–	–	16.1
$ZnCl_2$(g)	276.6 ± 2.1	265.7 ± 2.5	gas	298	61.71	–	-4.31	–	–
ZnO	43.6 ± 0.4	350.5 ± 0.6	hex	298	48.99	5.10	-9.12	–	–
$ZnCO_3$	82.4 ± 1.3	818.0 ± 1.3	hex	298	38.91	138.07	–	–	–
ZnS	57.7 ± 0.4	205.2 ± 2.5	cubic	298	49.25	5.27	-4.85	–	–
			hex	1293	49.45	4.44	-4.35	–	13.4
ZnS(g)	238.1 ± 2.1	-202.1 ± 16.7	gas	298	37.45	0.08	-1.67	–	–
Zr	39.0	0.0	hcp	298	22.84	8.95	-0.67	–	–
			bcc	1136	21.51	6.57	36.69	–	3.9
			liq	2128	33.47	–	–	–	18.8
Zr(g)	181.3	-601.2	gas	298	23.00	3.05	3.64	–	–

$ZrCl_4$	181.4 ± 2.5	980.3 ± 1.7	cubic	298	124.98	14.14	-8.37	–	–
$ZrCl_4$(g)	367.7 ± 0.4	868.6 ± 2.1	gas	298	107.45	0.29	-8.26	–	–
ZrO(g)	227.3	-58.6	gas	298	26.28	14.90	–	–	–
ZrO_2	50.4 ± 0.4	1100.8 ± 2.1	monocl	298	69.62	7.53	-14.06	–	–
			tetrag	1450	74.48	–	–	–	5.9
			liq	2950	87.86	–	–	–	87.0
ZrS_2	78.2 ± 12.6	577.4 ± 20.9	hex	298	64.27	15.06	–	–	–

Table 3.1.A7 Standard Gibbs Energy Changes for Reactions Reproduced from Ref. [8]

Reaction[a]	$\Delta G^\circ = A + B\,T$ (J mol^{-1})		Error (±kJ)	Temperature range[b] (K)
	A	*B*		
$\langle Ag\rangle = \{Ag\}$	11,300	−9.16	0.4	1234 m
$\{Ag\} = (Ag)$	258,300	−106.3	0.8	1234–2436 b
$\langle AgCl\rangle = \{AgCl\}$	13,000	−17.82	0.4	728 m
$\{AgCl\} = (AgCl)$	177,800	−96.7	20	1837 b
$\{AgCl\} = \{Ag\} + (1/2)(Cl_2)$	104,500	−23.0	4	1234–1837 b
$\langle Ag_2O\rangle = 2\langle Ag\rangle + (1/2)(O_2)$	30,500	−66.1	0.8	298
$\langle Ag_2S\rangle = \{Ag_2S\}$	7900	−7.1	2	1103 m
$\langle Ag_2S\rangle = 2\langle Ag\rangle + (1/2)(S_2)$	161,300	−168.6	8	298–1103 m
$\langle Al\rangle = \{Al\}$	10,790	−11.55	0.2	933 m
$\{Al\} = (Al)$	304,600	−109.5	2	933–2793 b
$(AlCl) = \{Al\} + (1/2)(Cl_2)$	77,400	58.2	4	933–2273
$(AlCl_3) = \{Al\} + (3/2)(Cl_2)$	602,100	−67.9	8	933–2273
$(Al_2Cl_6) = 2\langle Al\rangle + 3(Cl_2)$	1,292,000	−242.2	8	298–933
$\langle Al_2O_3\rangle = 2\{Al\} + (3/2)(O_2)$	1,687,200	−326.8	2	933–2327 m
$(Al_2O) = 2\{Al\} + (1/2)(O_2)$	170,700	49.4	20	933–2273
$(Al_2O_2) = 2\{Al\} + (O_2)$	470,700	−28.9	30	933–2273
$\langle As\rangle = (1/4)(As_4)$	36,570	−41.92	0.4	298–876 s
$\langle Au\rangle = \{Au\}$	12,550	−9.41	0.4	1336 m
$\{Au\} = (Au)$	340,600	−109.0	1	1336–3130 b
$\langle B\rangle = \{B\}$	50,200	−21.8	3	2303 m
$\langle B\rangle = (B)$	570,200	−147.8	3	298–2303 m
$\{B\} = (B)$	499,700	−117.3	3	2303–4275 b
$(BCl_3) = \langle B\rangle + (3/2)(Cl_2)$	404,000	−51.7	0.8	298–2303
$\langle B_2O_3\rangle = \{B_2O_3\}$	24,060	−33.26	0.4	723 m
$\{B_2O_3\} = 2\langle B\rangle + (3/2)(O_2)$	1,228,800	−210.0	4	723–2316 b
$(BO) = \langle B\rangle + (1/2)(O_2)$	3800	88.8	8	298–2303
$\langle Ba\rangle = \{Ba\}$	7700	−7.74	2	1002 m

Table 3.1.A7 Standard Gibbs Energy Changes for Reactions Reproduced from Ref. [8]—cont'd

Reaction	$\Delta G^\circ = A + B\,T$ (J mol^{-1})		Error (±kJ)	Temperature range (K)
	A	*B*		
$\{Ba\} = (Ba)$	150,000	−79.2	10	1002–1895 b
$\langle BaCl_2\rangle = \{BaCl_2\}$	15,980	−12.93	0.4	1235 m
$\{BaCl_2\} = \{Ba\} + (Cl_2)$	811,300	−121.5	8	1235–1895
$\langle BaO\rangle = \{Ba\} + (1/2)(O_2)$	557,180	−102.7	4	1002–1895
$\langle BaS\rangle = \{Ba\} + (1/2)(S_2)$	544,000	−123.4	20	1002–1895
$\langle BaCO_3\rangle = \langle BaO\rangle + (CO_2)$	250,700	−147.1	1	1073–1333 m
$\langle Be\rangle = \{Be\}$	11,700	−7.53	–	1560 m
$\{Be\} = (Be)$	299,900	−108.6	8	1560–2745 b
$(BeCl_2) = \{Be\} + (Cl_2)$	379,600	5.9	20	1560–2273
$\langle BeO\rangle = \langle Be\rangle + (1/2)(O_2)$	608,200	−97.7	4	298–1560
$\langle BeO\rangle = \{Be\} + (1/2)(O_2)$	613,600	−100.9	4	1560–2273
$\langle BeS\rangle = \langle Be\rangle + (1/2)(S_2)$	297,000	−86.6	20	298–1560
$\langle Bi\rangle = \{Bi\}$	11,300	−20.75	0.4	545 m
$\{Bi\} = (Bi)$	191,800	−99.4	2	545–1837 b
$\langle BiCl_3\rangle = \{BiCl_3\}$	23,600	−46.7	0.8	507 m
$\{BiCl_3\} = \{Bi\} + (3/2)(Cl_2)$	351,100	−160.5	10	545–712 b
$\langle Bi_2O_3\rangle = \{Bi_2O_3\}$	59,800	−54.6	4	1097 m
$\{Bi_2O_3\} = 2\{Bi\} + (3/2)(O_2)$	445,200	−159.6	10	1097–1773
$\langle Bi_2S_3\rangle = \{Bi_2S_3\}$	78,200	−74.5	10	1050 m
$\langle Bi_2S_3\rangle = 2\{Bi\} + (3/2)(S_2)$	360,000	−274.1	20	545–1050 m
graphite = diamond	1440	4.48	0.04	298–1173
$\langle C\rangle = (C)$	713,500	−155.5	4	2023–4073 s
$(CH_4) = \langle C\rangle + 2(H_2)$	91,040	−110.7	0.4	773–2273
$(CCl_4) = \langle C\rangle + 2(Cl_2)$	89,100	−129.2	2	298–2273
$(CO) = \langle C\rangle + (1/2)(O_2)$	114,390	85.8	0.4	773–2273
$(CO_2) = \langle C\rangle + (O_2)$	395,350	0.54	0.1	773–2273
$(CS) = \langle C\rangle + (1/2)(S_2)$	−163,000	87.9	20	298–2273

Continued

Table 3.1.A7 Standard Gibbs Energy Changes for Reactions Reproduced from Ref. [8]—cont'd

Reaction	$\Delta G^\circ = A + B\,T$ (J mol^{-1})		Error (±kJ)	Temperature range (K)
	A	*B*		
$(CS_2) = \langle C \rangle + (S_2)$	11,400	6.49	1	298–2273
$\langle Ca \rangle = \{Ca\}$	8540	−7.70	0.4	1112 m
$\{Ca\} = (Ca)$	157,820	−87.11	0.4	1112–1764 b
$\langle CaCl_2 \rangle = \{CaCl_2\}$	28,500	−27.3	1	1045 m
$\{CaCl_2\} = (CaCl_2)$	235,100	−106.4	4	2209 b
$\{CaCl_2\} = \{Ca\} + (Cl_2)$	798,600	−146.0	8	1112–1757
$\langle CaO \rangle = \{CaO\}$	79,500	−24.7	–	3200 m
$\langle CaO \rangle = \{Ca\} + (1/2)(O_2)$	640,200	−108.6	1	1112–1757
$\langle CaS \rangle = \{Ca\} + (1/2)(S_2)$	548,100	−103.8	4	1112–1757
$\langle CaCO_3 \rangle = \langle CaO \rangle + (CO_2)$	161,300	−137.2	1	973–1473
$\langle Cd \rangle = \{Cd\}$	6190	−10.42	0.2	594 m
$\{Cd\} = (Cd)$	101,700	−97.9	1	594–1040 b
$\langle CdCl_2 \rangle = \{CdCl_2\}$	30,100	−35.8	1	841 m
$\langle CdCl_2 \rangle = \{Cd\} + (Cl_2)$	389,600	−153.0	10	594–841 m
$\langle CdO \rangle = \{Cd\} + (1/2)(O_2)$	263,200	−104.9	10	594–1040
$\langle CdS \rangle = \{Cd\} + (1/2)(S_2)$	215,500	−97.2	10	594–1040
$\langle Ce \rangle = \{Ce\}$	5480	−5.10	0.2	1071 m
$\{Ce\} = (Ce)$	413,700	−111.8	4	1071–3699 b
$\langle CeCl_3 \rangle = \{CeCl_3\}$	53,600	−49.12	–	1090 m
$\langle CeCl_3 \rangle = \langle Ce \rangle + (3/2)(Cl_2)$	1,050,000	−239.7	20	298–1071
$\langle Ce_2O_3 \rangle = 2\langle Ce \rangle + (3/2)(O_2)$	1,788,000	−286.6	4	298–1071
$\langle CeO_{1.72} \rangle = \langle Ce \rangle + 0.86(O_2)$	992,000	−169.9	20	298–1071
$\langle CeO_{1.83} \rangle = \langle Ce \rangle + 0.915(O_2)$	1,029,000	−182.0	20	298–1071
$\langle CeO_2 \rangle = \langle Ce \rangle + (O_2)$	1,083,700	−211.8	4	298–1071
$\langle CeS \rangle = \langle Ce \rangle + (1/2)(S_2)$	534,900	−91.0	6	1071–2723 m
$\langle Co \rangle = \{Co\}$	16,190	−9.16	0.4	1768 m
$\{Co\} = (Co)$	387,200	−121.2	4	1768–3101 b

Table 3.1.A7 Standard Gibbs Energy Changes for Reactions Reproduced from Ref. [8]—cont'd

Reaction	$\Delta G^\circ = A + B\,T$ (J mol^{-1})		Error (±kJ)	Temperature range (K)
	A	*B*		
$\langle CoCl_2\rangle = \{CoCl_2\}$	44,800	−44.2	8	1013 m
$\langle CoCl_2\rangle = \langle Co\rangle + (Cl_2)$	307,100	−130	2	298–1013 m
$\langle CoO\rangle = \langle Co\rangle + (1/2)(O_2)$	245,600	−78.7	10	298–1768
$\langle Co_3O_4\rangle = 3\langle Co\rangle + 2(O_2)$	957,300	−456.9	10	298–973
$\langle Co_9S_8\rangle = 9\langle Co\rangle + 4(S_2)$	1,326,200	−666.3	10	298–1061
$\langle Co_4S_3\rangle = 4\langle Co\rangle + (3/2)(S_2)$	388,500	−146.2	4	1061–1150
$\langle CoS_2\rangle = \langle Co\rangle + (S_2)$	280,000	−182.4	20	298–873
$\langle Cr\rangle = \{Cr\}$	16,950	−7.9	–	2130 m
$\{Cr\} = (Cr)$	348,500	−118.4	4	2130–2945 b
$\langle CrCl_2\rangle = \{CrCl_2\}$	32,200	−29.6	6	1088 m
$\langle CrCl_2\rangle = \langle Cr\rangle + (Cl_2)$	389,000	−119.7	20	298–1088 m
$\langle CrCl_3\rangle = \langle Cr\rangle + (3/2)(Cl_2)$	548,000	−215.5	20	298–1218 s
$\langle Cr_2O_3\rangle = 2\langle Cr\rangle + (3/2)(O_2)$	1,110,100	−247.3	1	1173–1923
$\langle Cr_3O_4\rangle = 3\langle Cr\rangle + 2(O_2)$	1,355,200	−264.6	1	1923–1938 m
$\{CrO\} = \langle Cr\rangle + (1/2)(O_2)$	334,200	−63.8	1	1938–2023
$\langle CrS\rangle = \langle Cr\rangle + (1/2)(S_2)$	202,500	−56.1	8	1373–1573
$\langle Cs\rangle = \{Cs\}$	2090	−6.95	0.1	302 m
$\{Cs\} = (Cs)$	71,710	−76.19	0.4	302–1044 b
$\langle Cu\rangle = \{Cu\}$	13,100	−9.6	2	1356 m
$\{Cu\} = (Cu)$	308,200	−108.9	2	1356–2836 b
$(CuCl) = \{Cu\} + (1/2)(Cl_2)$	−63,300	66.8	4	1356–2273
$(Cu_3Cl_3) = 3\{Cu\} + (3/2)(Cl_2)$	313,800	−47.0	4	1356–2273
$\langle Cu_2O\rangle = 2\langle Cu\rangle + (1/2)(O_2)$	168,400	−71.3	4	298–1356
$\langle Cu_2O\rangle = \{Cu_2O\}$	56,800	−38	8	1509 m
$\{Cu_2O\} = 2\{Cu\} + (1/2)(O_2)$	118,700	−39.5	4	1509–2273
$\langle CuO\rangle = \langle Cu\rangle + (1/2)(O_2)$	152,300	−85.4	4	298–1356
$\langle Cu_2S\rangle_\gamma = 2\langle Cu\rangle + (1/2)(S_2)$	140,700	−43.3	1	298–708

Continued

Table 3.1.A7 Standard Gibbs Energy Changes for Reactions Reproduced from Ref. [8]—cont'd

Reaction	$\Delta G^\circ = A + B\,T$ (J mol^{-1})		Error (±kJ)	Temperature range (K)
	A	*B*		
$\langle Cu_2S\rangle_\mu = 2\langle Cu\rangle + (1/2)(S_2)$	131,800	−30.8	1	708–1402 m
$\langle Cu_2S\rangle = \{Cu_2S\}$	9000	−6.40	1	1402 m
$\langle Cu_{1.738}S\rangle_\mu = 1.738\langle Cu\rangle + (1/2)(S_2)$	113,600	−26.6	1	708–893
$\langle CuS\rangle = \langle Cu\rangle + (1/2)(S_2)$	115,600	−76.1	2	298–703
$\langle Fe\rangle_\delta = \{Fe\}$	13,800	−7.61	1	1809 m
$\{Fe\} = (Fe)$	363,600	−116.2	1	1809–3135 b
$\langle FeCl_2\rangle = \{FeCl_2\}$	43,010	−45.27	0.2	950 m
$\{FeCl_2\} = (FeCl_2)$	109,900	−84.7	8	1347 b
$(FeCl_2) = \langle Fe\rangle + (Cl_2)$	167,200	25	4	1347–2273
$(FeCl_3) = \langle Fe\rangle + (3/2)(Cl_2)$	259,900	−26.4	4	605–2273
$(Fe_2Cl_6) = 2\langle Fe\rangle + 3(Cl_2)$	655,200	−181.8	10	605–2273
$\langle Fe_{0.947}O\rangle = 0.947\langle Fe\rangle + (1/2)(O_2)$	263,700	−64.3	1	298–1644 m
$\langle Fe_{0.947}O\rangle = \{Fe_{0.947}O\}$	31,300	−19.0	1	1644 m
$\{FeO\} = \{Fe\} + (1/2)(O_2)$	256,100	−53.7	4	1644–2273
$\langle Fe_3O_4\rangle = 3\langle Fe\rangle + 2(O_2)$	1,102,200	−307.4	2	298–1870 m
$\langle Fe_2O_3\rangle = 2\langle Fe\rangle + (3/2)(O_2)$	814,100	−250.7	2	298–1773
$\langle FeS\rangle = \langle Fe\rangle_\gamma + (1/2)(S_2)$	154,900	−56.9	2	1179–1261
$\langle FeS\rangle = \{Fe\} + (1/2)(S_2)$	164,000	−61.1	2	1261–1468 m
$\langle FeS_2\rangle = \langle FeS\rangle + (1/2)(S_2)$	182,000	−187.7	4	903–1033
$\langle Ga\rangle = \{Ga\}$	5610	−17.20	0.2	303 m
$\{Ga\} = (Ga)$	264,100	−106.9	4	303–2478 b
$\langle Ga_2O_3\rangle = 2\{Ga\} + (3/2)(O_2)$	1,089,900	−323.6	10	303–2068 m
$\langle GaS\rangle = \{Ga\} + (1/2)(S_2)$	276,000	−110.9	20	303–1233 m
$\langle Ga_2S_3\rangle = 2\{Ga\} + (3/2)(S_2)$	720,000	−318.4	20	303–1363 m
$\langle Ge\rangle = \{Ge\}$	36,900	−30.5	2	1210 m
$\{Ge\} = (Ge)$	335,000	−107.9	2	1211–3107 b
$\langle GeO_2\rangle = \langle Ge\rangle + (O_2)$	574,900	−187.8	10	298–1211

Table 3.1.A7 Standard Gibbs Energy Changes for Reactions Reproduced from Ref. [8]—cont'd

Reaction	$\Delta G^\circ = A + B\,T$ (J mol^{-1})		Error (±kJ)	Temperature range (K)
	A	*B*		
$(HCl) = (1/2)(H_2) + (1/2)(Cl_2)$	94,100	6.40	1	298–2273
$\{H_2O\} = (H_2O)$	41,090	−110.1	0.1	373 b
$(H_2O) = (H_2) + (1/2)(O_2)$	247,500	−55.9	1	298–2273
$(H_2S) = (H_2) + (1/2)(S_2)$	91,600	−50.6	1	298–2273
$\langle Hf\rangle = \{Hf\}$	24,300	−9.6	–	2503 m
$\{Hf\} = (Hf)$	574,200	−117.7	4	2503–4873 b
$\langle HfO_2\rangle_\alpha = \langle Hf\rangle + (O_2)$	1,063,000	−174.1	20	298–1973
$\langle HfO_2\rangle_\alpha = \langle HfO_2\rangle_\beta$	10,460	−5.31	–	1973
$\{Hg\} = (Hg)$	60,800	−96.78	0.3	234–630
$\langle In\rangle = \{In\}$	3260	−7.61	0.1	273–430 m
$\{In\} = (In)$	234,900	−100.3	1	430–2346 b
$\langle In_2O_3\rangle = 2\{In\} + (3/2)(O_2)$	918,800	−309.4	10	430–2183 m
$\langle InS\rangle = \{InS\}$	35,980	−37.28	–	965 m
$\{InS\} = \{In\} + (1/2)(S_2)$	155,000	−60.7	20	965–1773
$\langle In_2S_3\rangle = 2\{In\} + (3/2)(S_2)$	544,000	−286.2	20	430–1173
$\langle Ir\rangle = \{Ir\}$	26,150	−9.6	–	2716 m
$\{Ir\} = (Ir)$	614,800	−130.9	8	2716–4701 b
$(IrO_3) = \langle Ir\rangle + (3/2)(O_2)$	−17,000	−45.2	20	298–1773
$\langle IrO_2\rangle = \langle Ir\rangle + (O_2)$	234,000	−169.5	20	298–1273
$\langle Ir_2S_3\rangle = 2\langle Ir\rangle + (3/2)(S_2)$	429,300	−298.7	20	298–1273
$\langle IrS_2\rangle = \langle Ir\rangle + (S_2)$	268,000	−190.4	20	298–1273
$\langle K\rangle = \{K\}$	2330	−6.95	0.3	336 m
$\{K\} = (K)$	84,470	−82.0	0.4	336–1032 b
$\langle KCl\rangle = \{KCl\}$	26,280	−25.19	0.4	1044 m
$\{KCl\} = (K) + (1/2)(Cl_2)$	474,050	−131.8	0.4	1044–1710 b
$(KCl) = (K) + (1/2)(Cl_2)$	306,300	−35.5	1	1710–2273
$\langle K_2O\rangle = 2\{K\} + (1/2)(O_2)$	361,900	−138	2	336–1154 d

Continued

Table 3.1.A7 Standard Gibbs Energy Changes for Reactions Reproduced from Ref. [8]—cont'd

Reaction	$\Delta G^\circ = A + B\,T$ (J mol^{-1})		Error (±kJ)	Temperature range (K)
	A	*B*		
$\langle K_2O_2\rangle = 2\{K\} + (O_2)$	496,200	−225.4	4	336–763 m
$\langle KO_2\rangle = \{K\} + (O_2)$	281,600	−150.0	10	336–675 m
$\langle K_2CO_3\rangle = \{K_2CO_3\}$	27,600	−23.51	–	1174 m
$\{K_2CO_3\} = 2(K) + \langle C\rangle + (3/2)(O_2)$	1,218,900	−363.5	4	1174–1973
$\langle K_2S\rangle = \{K_2S\}$	16,150	−13.22	–	1221 m
$\langle K_2S\rangle = 2\{K\} + (1/2)(S_2)$	481,000	−143.5	30	298–1032
$\langle La\rangle = \{La\}$	6190	−5.19	0.4	1193 m
$\{La\} = (La)$	416,300	−112.8	4	1193–3730 b
$\langle LaCl_3\rangle = \{LaCl_3\}$	54,400	−48.24	–	1128 m
$\langle LaCl_3\rangle = \langle La\rangle + (3/2)(Cl_2)$	1,063,000	−225.5	20	298–1128 m
$\langle La_2O_3\rangle = 2\langle La\rangle + (3/2)(O_2)$	1,786,600	−278.3	10	298–1193
$\langle LaS\rangle = \{La\} + (1/2)(S_2)$	527,000	−104.2	40	1193–1773
$\langle La_2S_3\rangle = 2\{La\} + (3/2)(S_2)$	1,418,000	−285.8	40	1193–1773
$\langle Li\rangle = \{Li\}$	3000	−6.61	0.1	454 m
$\{Li\} = (Li)$	151,300	−93.8	1	454–1615 b
$\langle LiCl\rangle = \{LiCl\}$	19,830	−22.97	0.4	883 m
$\{LiCl\} = \{Li\} + (1/2)(Cl_2)$	382,040	−52.38	0.4	883–1656 b
$(LiCl) = (Li) + (1/2)(Cl_2)$	360,200	−42.2	10	1656–2273
$\langle Li_2O\rangle = \{Li_2O\}$	58,600	−31.8	–	1843 m
$\langle Li_2O\rangle = 2\{Li\} + (1/2)(O_2)$	602,700	−135.1	2	454–1615
$\langle Li_2S\rangle = 2\{Li\} + (1/2)(S_2)$	515,000	−121	20	454–1273
$\langle Li_2CO_3\rangle = \{Li_2CO_3\}$	44,770	−45.06	0.4	993 m
$\{Li_2CO_3\} = \langle Li_2O\rangle + (CO_2)$	147,900	−78.7	1	993–1843
$\langle Mg\rangle = \{Mg\}$	8950	−9.71	0.4	922 m
$\{Mg\} = (Mg)$	129,600	−95.1	2	922–1363 b
$\langle MgCl_2\rangle = \{MgCl_2\}$	43,100	−43.68	0.4	987 m
$\langle MgCl_2\rangle = \langle Mg\rangle + (Cl_2)$	637,300	−155.4	2	298–922

Table 3.1.A7 Standard Gibbs Energy Changes for Reactions Reproduced from Ref. [8]—cont'd

Reaction	$\Delta G^\circ = A + B\,T$ (J mol^{-1})		Error (±kJ)	Temperature range (K)
	A	*B*		
$\{MgCl_2\} = (Mg) + (Cl_2)$	649,200	−157.7	2	987–1710 b
$\langle MgO\rangle = \langle Mg\rangle + (1/2)(O_2)$	600,900	−107.6	1	298–922
$\langle MgO\rangle = (Mg) + (1/2)(O_2)$	729,600	−204.1	1	1363–2273
$\langle MgS\rangle = \langle Mg\rangle + (1/2)(S_2)$	409,600	−94.4	10	298–922
$\langle MgS\rangle = (Mg) + (1/2)(S_2)$	539,700	−193.0	10	1363–1973
$\langle MgCO_3\rangle = \langle MgO\rangle + (CO_2)$	116,300	−173.4	8	298–675 d
$\langle Mn\rangle = \{Mn\}$	12,100	−7.9	–	1517 m
$\{Mn\} = (Mn)$	235,800	−101.2	4	1517–2335 b
$\langle MnCl_2\rangle = \{MnCl_2\}$	37,700	−40.8	1	923 m
$\langle MnCl_2\rangle = \langle Mn\rangle + (Cl_2)$	478,200	−127.7	10	298–923 m
$(MnCl_2) = \{Mn\} + (Cl_2)$	301,700	−9.8	8	1517–2335
$\langle MnO\rangle = \langle Mn\rangle + (1/2)(O_2)$	388,900	−76.3	2	298–1517
$\langle Mn_3O_4\rangle = 3\langle Mn\rangle + 2(O_2)$	1,385,000	−344.4	20	298–1517
$\langle Mn_3O_4\rangle = 3\langle MnO\rangle + (1/2)(O_2)$	232,200	−117.0	1	1198–1813 m
$\langle Mn_2O_3\rangle = 2\langle Mn\rangle + (3/2)(O_2)$	954,000	−255	20	298–1517
$\langle Mn_2O_3\rangle = (2/3)\langle Mn_3O_4\rangle + (1/6)(O_2)$	35,100	−28.1	2	1073–1273
$\langle MnO_2\rangle = \langle Mn\rangle + (O_2)$	518,800	−181.0	10	298–783 d
$\langle MnS\rangle = \{MnS\}$	26,110	−14.48	–	1803 m
$\langle MnS\rangle = \langle Mn\rangle + (1/2)(S_2)$	296,500	−76.7	1	973–1473
$\langle Mo\rangle = \{Mo\}$	27,800	−9.6	6	2893 m
$\{Mo\} = (Mo)$	590,800	−120.2	4	2893–4913 b
$\langle MoO_2\rangle = \langle Mo\rangle + (O_2)$	578,200	−166.5	10	298–2273
$(MoO_2) = \langle Mo\rangle + (O_2)$	18,400	−33.9	20	298–2273
$\langle MoO_3\rangle = \{MoO_3\}$	47,700	−45.2	–	1068 m
$\langle MoO_3\rangle = \langle Mo\rangle + (3/2)(O_2)$	740,100	−246.7	10	298–1068 m
$(MoO_3) = \langle Mo\rangle + (3/2)(O_2)$	360,000	−59.4	20	298–2273

Continued

Table 3.1.A7 Standard Gibbs Energy Changes for Reactions Reproduced from Ref. [8]—cont'd

Reaction	$\Delta G^\circ = A + B\,T$ (J mol^{-1})		Error (±kJ)	Temperature range (K)
	A	*B*		
$\langle Mo_2S_3\rangle = 2\langle Mo\rangle + (3/2)(S_2)$	594,000	−265.3	20	298–1473
$\langle MoS_2\rangle = \{MoS_2\}$	45,600	−31.3	–	1458 m
$\langle MoS_2\rangle = \langle Mo\rangle + (S_2)$	397,000	−182.0	20	298–1458 m
$(NH_3) = (1/2)(N_2) + (3/2)(H_2)$	53,720	−116.5	0.4	298–2273
$(NO) = (1/2)(N_2) + (1/2)(O_2)$	−90,420	12.68	0.4	298–2273
$(NO_2) = (1/2)(N_2) + (O_2)$	−32,300	−63.3	1	298–2273
$\langle Na\rangle = \{Na\}$	2590	−6.99	0.2	371 m
$\{Na\} = (Na)$	101,300	−87.9	1	371–1156 b
$\langle NaCl\rangle = \{NaCl\}$	28,160	−26.23	0.2	1074 m
$\langle NaCl\rangle = \{Na\} + (1/2)(Cl_2)$	411,620	−93.09	0.4	371–1074 m
$\{NaCl\} = (Na) + (1/2)(Cl_2)$	464,400	−134	8	1074–1738 b
$\langle Na_2O\rangle = \{Na_2O\}$	47,700	−33.9	4	1405 m
$\langle Na_2O\rangle = 2\{Na\} + (1/2)(O_2)$	421,600	−141.3	8	371–1405 m
$\{Na_2O\} = 2(Na) + (1/2)(O_2)$	518,800	−234.7	10	1405–2223 d
$\langle Na_2O_2\rangle = 2\{Na\} + (O_2)$	514,600	−218.8	10	371–948 m
$\langle Na_2S\rangle = \{Na_2S\}$	26,400	−21.1	–	1251 m
$\langle Na_2S\rangle = 2\{Na\} + (1/2)(S_2)$	439,000	−143.9	20	371–1251 m
$\langle Na_2CO_3\rangle = \langle Na_2O\rangle + (CO_2)$	297,100	−118.2	2	298–1123 m
$\{Na_2CO_3\} = \{Na_2O\} + (CO_2)$	316,400	−130.8	2	1405–2273
$\langle Nb\rangle = \{Nb\}$	26,900	−9.79	1	2750 m
$\{Nb\} = (Nb)$	689,900	−134.3	4	2750–5136 b
$\langle NbO\rangle = \{NbO\}$	84,000	−38.5	20	2210 m
$\langle NbO\rangle = \langle Nb\rangle + (1/2)(O_2)$	414,000	−86.6	20	298–2210 m
$\langle Nb_2O_5\rangle = \{Nb_2O_5\}$	104,300	−58.4	2	1785 m
$\langle Nb_2O_5\rangle = 2\langle Nb\rangle + (5/2)(O_2)$	1,888,200	−419.7	10	298–1785 m
$\langle NbO_2\rangle = \{NbO_2\}$	92,000	−42.3	20	2423 m
$\langle NbO_2\rangle = \langle Nb\rangle + (O_2)$	783,700	−166.9	10	298–2423 m

Table 3.1.A7 Standard Gibbs Energy Changes for Reactions Reproduced from Ref. [8]—cont'd

Reaction	$\Delta G^\circ = A + B\,T$ (J mol^{-1})		Error (±kJ)	Temperature range (K)
	A	*B*		
$\langle Ni\rangle = \{Ni\}$	17,500	−10.1	1	1726 m
$\{Ni\} = (Ni)$	386,000	−121.4	2	1726–3187 b
$\langle NiCl_2\rangle = (NiCl_2)$	225,100	−178.7	–	1260 s
$\langle NiCl_2\rangle = \langle Ni\rangle + (Cl_2)$	305,000	−146	20	298–1260 s
$\langle NiO\rangle = \langle Ni\rangle + (1/2)(O_2)$	235,600	−86.1	1	298–2257 m
$\langle Ni_3S_2\rangle = 3\langle Ni\rangle + (S_2)$	331,500	−163.2	8	298–1063 m
$\langle NiS\rangle = \langle Ni\rangle + (1/2)(S_2)$	146,400	−72.0	6	298–773
$\langle Os\rangle = \{Os\}$	31,800	−9.6	–	3303 m
$\{Os\} = (Os)$	744,800	−141.2	4	3303–5283 b
$\langle OsO_2\rangle = \langle Os\rangle + (O_2)$	289,800	−175.1	10	298–1173
$(OsO_4) = \langle Os\rangle + 2(O_2)$	333,900	−145.3	10	404 b
$\langle OsS_2\rangle = \langle Os\rangle + (S_2)$	271,100	−195.3	10	298–1373
$\langle P\rangle_{white} = \{P\}$	657	−2.05	0	317 m
$\langle P\rangle_{red} = (1/4)(P_4)$	32,100	−45.6	1	298–704 s
$(P_4) = 2(P_2)$	217,100	−139.0	2	298–1973
$(PCl_3) = (1/2)(P_2) + (3/2)(Cl_2)$	474,500	−209.2	10	298–1573
$(PCl_5) = (1/2)(P_2) + (5/2)(Cl_2)$	419,700	−279.3	10	298–1973
$(PO) = (1/2)(P_2) + (1/2)(O_2)$	77,800	11.59	–	298–1973
$(PO_2) = (1/2)(P_2) + (O_2)$	385,800	−60.2	–	298–1973
$(P_4O_{10}) = 2(P_2) + 5(O_2)$	3,156,000	−1011	–	631–1973
$\langle Pb\rangle = \{Pb\}$	4810	−7.99	0.4	601 m
$\{Pb\} = (Pb)$	181,960	−90.12	0.4	601–2023 b
$\langle PbCl_2\rangle = \{PbCl_2\}$	21,900	−28.2	1	774 m
$\{PbCl_2\} = \{Pb\} + (Cl_2)$	324,600	−103.5	2	774–1226 b
$(PbCl_2) = \{Pb\} + (Cl_2)$	188,000	7.5	40	1226–2023
$\langle PbO\rangle = \{PbO\}$	27,500	−23.7	1	1158 m
$\{PbO\} = \{Pb\} + (1/2)(O_2)$	181,200	−68.0	3	1158–1808 b

Continued

Table 3.1.A7 Standard Gibbs Energy Changes for Reactions Reproduced from Ref. [8]—cont'd

Reaction	$\Delta G^\circ = A + B\,T$ (J mol^{-1})		Error (±kJ)	Temperature range (K)
	A	*B*		
$\langle Pb_3O_4\rangle = 3\{Pb\} + 2(O_2)$	702,500	−368.9	10	601–1473
$\langle PbO_2\rangle = \{Pb\} + (O_2)$	272,400	−193.7	10	601–1173
$\langle PbS\rangle = \{PbS\}$	18,800	−15.9	6	1386 m
$\langle PbS\rangle = \{Pb\} + (1/2)(S_2)$	163,200	−88.0	4	601–1386 m
$\langle Pd\rangle = \{Pd\}$	17,600	−9.6	–	–1825 m
$\{Pd\} = (Pd)$	351,800	−108.6	2	1825–3237 b
$\langle PdO\rangle = \langle Pd\rangle + (1/2)(O_2)$	110,900	−96.7	–	298–1143 m
$\langle Pd_4S\rangle = 4\langle Pd\rangle + (1/2)(S_2)$	133,900	−86.1	10	298–1034 m
$\langle PdS\rangle = \langle Pd\rangle + (1/2)(S_2)$	134,000	−91.2	20	298–1243 m
$\langle PdS_2\rangle = \langle Pd\rangle + (S_2)$	201,000	−167	20	298–1245 m
$\langle Pt\rangle = \{Pt\}$	19,700	−9.6	–	2042 m
$\{Pt\} = (Pt)$	521,000	−127.3	1	2042–4103 b
$(PtO_2) = \langle Pt\rangle + (O_2)$	164,400	0	10	298–1973
$\langle PtS\rangle = \langle Pt\rangle + (1/2)(S_2)$	148,500	−101.5	10	298–1473
$\langle PtS_2\rangle = \langle Pt\rangle + (S_2)$	233,500	−182.3	10	298–1473
$\langle Pu\rangle = \{Pu\}$	2850	−3.10	1	913 m
$\{Pu\} = (Pu)$	335,000	−95.8	20	913–3503 b
$\langle PuCl_3\rangle = \{PuCl_3\}$	63,600	−61.17	–	1040 m
$\{PuCl_3\} = \{Pu\} + (3/2)(Cl_2)$	874,000	−141.8	20	1040–2063 b
$\langle PuO_2\rangle = \{Pu\} + (O_2)$	1,046,000	−177.9	10	913–2663 m
$\langle PuS\rangle = \{Pu\} + (1/2)(S_2)$	510,000	−101.3	40	913–1773
$\langle Pu_2S_3\rangle = 2\{Pu\} + (3/2)(S_2)$	1,188,000	−270.7	40	913–1473
$\langle Rb\rangle = \{Rb\}$	2190	−7.03	0.4	313 m
$\{Rb\} = (Rb)$	76,320	−79.66	0.4	313–961 b
$\langle RbCl\rangle = \{RbCl\}$	18,410	−18.62	–	988 m
$\{RbCl\} = (Rb) + (1/2)(Cl_2)$	477,000	−147.3	–	988–1654 b
$\langle Rb_2O\rangle = 2\{Rb\} + (1/2)(O_2)$	335,000	−154.0	20	298–961

Table 3.1.A7 Standard Gibbs Energy Changes for Reactions Reproduced from Ref. [8]—cont'd

Reaction	$\Delta G^\circ = A + B\,T$ (J mol^{-1})		Error (±kJ)	Temperature range (K)
	A	*B*		
$\langle Rb_2CO_3\rangle = \langle Rb_2O\rangle + (CO_2)$	402,000	−145.6	20	298–873
$\langle Re\rangle = \{Re\}$	33,200	−9.6	–	3453 m
$\{Re\} = (Re)$	705,300	−120.1	8	3453–5873 b
$\langle ReO_2\rangle = \langle Re\rangle + (O_2)$	428,400	−169.7	10	298–1473
$\langle ReS_2\rangle = \langle Re\rangle + (S_2)$	301,000	−190.8	20	298–1473
$\langle Rh\rangle = \{Rh\}$	21,500	−9.6	–	2233 m
$\{Rh\} = (Rh)$	505,000	−127.4	6	2233–3973 b
$\langle Rh_2O_3\rangle = 2\langle Rh\rangle + (3/2)(O_2)$	376,600	−266.0	10	298–1273
$(RhO_2) = \langle Rh\rangle + (O_2)$	199,200	19.6	10	298–1473
$\langle Ru\rangle = \{Ru\}$	24,300	−9.6	–	2523 m
$\{Ru\} = (Ru)$	604,600	−136.8	6	2523–4423 b
$\langle RuO_2\rangle = \langle Ru\rangle + (O_2)$	301,000	−162.3	20	298–1473
$(RuO_3) = \langle Ru\rangle + (3/2)(O_2)$	79,000	−60.7	20	298–1873
$(RuO_4) = \langle Ru\rangle + 2(O_2)$	180,000	−142.7	20	298–1973
$\langle RuS_2\rangle = \langle Ru\rangle + (S_2)$	331,000	−190.8	20	298–1473
$\langle S\rangle = \{S\}$	1715	−4.44	0	388 m
$\{S\} = (1/2)(S_2)$	58,600	−68.3	2	388–718 b
$(S_2) = 2(S)$	469,300	−161.3	2	298–1973
$(S_4) = 2(S_2)$	63,000	−115.5	20	298–1973
$(S_6) = 3(S_2)$	276,000	−305.0	20	298–1973
$(S_8) = 4(S_2)$	397,000	−448.1	20	298–1973
$(SO) = (1/2)(S_2) + (1/2)(O_2)$	57,800	5.0	1	718–2273
$(SO_2) = (1/2)(S_2) + (O_2)$	361,660	−72.7	0.4	718–2273
$(SO_3) = (1/2)(S_2) + (3/2)(O_2)$	457,900	−163.3	1	718–2273
$\langle Sb\rangle = \{Sb\}$	19,900	−22.0	1	904 m
$\{Sb\} = (Sb)$	85,300	−45.6	2	904–1860 b
$\langle Sb_2O_3\rangle = \{Sb_2O_3\}$	55,020	−59.25	–	929 m

Continued

Table 3.1.A7 Standard Gibbs Energy Changes for Reactions Reproduced from Ref. [8]—cont'd

Reaction	$\Delta G^\circ = A + B\,T$ (J mol^{-1})		Error (±kJ)	Temperature range (K)
	A	*B*		
$\{Sb_2O_3\} = 2\{Sb\} + (3/2)(O_2)$	660,700	−198.1	10	929–1729 b
$\langle Sc\rangle = \{Sc\}$	14,100	−7.78	–	1812 m
$\{Sc\} = (Sc)$	327,200	−105.6	4	1812–3103 b
$\langle ScCl_3\rangle = \{ScCl_3\}$	67,360	−54.31	–	1240 m
$\langle ScCl_3\rangle = \langle Sc\rangle + (3/2)(Cl_2)$	891,000	−229.7	40	298–1240 m
$\langle Sc_2O_3\rangle = 2\langle Sc\rangle + (3/2)(O_2)$	1,902,000	−290.9	10	298–1812
$\langle Se\rangle = \{Se\}$	5400	−11.0	1	494 m
$\{Se\} = (1/2)(Se_2)$	59,300	−61.2	4	494–958 b
$(SeO) = (1/2)(Se_2) + (1/2)(O_2)$	9200	4	–	958–1973
$(SeO_2) = (1/2)(Se_2) + (O_2)$	177,800	−66.1	10	958–1973
$\langle Si\rangle = \{Si\}$	50,500	−30.0	2	1685 m
$\{Si\} = (Si)$	395,400	−111.4	4	1685–3553 b
$(SiCl_4) = \langle Si\rangle + 2(Cl_2)$	660,200	−128.8	4	334–1685
$(SiO) = \langle Si\rangle + (1/2)(O_2)$	104,200	82.5	10	298–1685
$\langle SiO_2\rangle_{quartz} = \{SiO_2\}$	7700	−4.52	1	1696 m
$\langle SiO_2\rangle_{quartz} = \langle Si\rangle + (O_2)$	907,100	−175.7	10	298–1685
$\langle SiO_2\rangle_{cristobalite} = \{SiO_2\}$	9600	−4.8	2	1996 m
$\langle SiO_2\rangle_{cristobalite} = \langle Si\rangle + (O_2)$	905,800	−175.5	10	298–1685
$(SiS) = \langle Si\rangle + (1/2)(S_2)$	−51,800	81.6	2	973–1685
$\langle SiS_2\rangle = \{SiS_2\}$	8400	−6.15	4	1363 m
$\langle SiS_2\rangle = \langle Si\rangle + (S_2)$	326,000	−139.0	20	298–1363 m
$\langle Sn\rangle = \{Sn\}$	7030	−13.93	0.4	505 m
$\{Sn\} = (Sn)$	296,000	−102.9	3	505–2876 b
$\{SnCl_2\} = (SnCl_2)$	81,600	−88.2	–	925 b
$(SnCl_2) = \{Sn\} + (Cl_2)$	226,000	−13.0	20	925–1473
$(SnO) = \{Sn\} + (1/2)(O_2)$	−6300	50.9	10	505–1973
$\langle SnO_2\rangle = \{Sn\} + (O_2)$	574,900	−198.4	10	505–1903 m

Table 3.1.A7 Standard Gibbs Energy Changes for Reactions Reproduced from Ref. [8]—cont'd

Reaction	$\Delta G^\circ = A + B\,T$ (J mol^{-1})		Error (±kJ)	Temperature range (K)
	A	*B*		
$(SnS) = \{Sn\} + (1/2)(S_2)$	−25,900	49.4	10	505–1973
$\langle SnS_2\rangle = \{Sn\} + (S_2)$	285,000	−195.8	20	505–1038 m
$\langle Sr\rangle = \{Sr\}$	8400	−7.9	1	1041 m
$\{Sr\} = (Sr)$	141,500	−85.7	4	1041–1654 b
$\langle SrCl_2\rangle = \{SrCl_2\}$	16,200	−14.1	1	1147
$\langle SrCl_2\rangle = \langle Sr\rangle + (Cl_2)$	823,700	−148.0	4	298–1041
$\langle SrO\rangle = \{Sr\} + (1/2)(O_2)$	597,100	−102.4	4	1041–1650
$\langle SrS\rangle = \{Sr\} + (1/2)(S_2)$	519,000	−96	20	1041–1650
$\langle SrCO_3\rangle = \langle SrO\rangle + (CO_2)$	214,600	−141.6	4	973–1516 d
$\langle Ta\rangle = \{Ta\}$	31,600	−9.6	4	3287 m
$\{Ta\} = (Ta)$	739,800	−127.9	3	3273–5786 b
$\{TaCl_5\} = (TaCl_5)$	53,000	−105	4	507 b
$(TaCl_5) = \langle Ta\rangle + (5/2)(Cl_2)$	754,000	−169.4	8	507–2273
$(TaO) = \langle Ta\rangle + (1/2)(O_2)$	−188,000	86.6	60	298–2273
$(TaO_2) = \langle Ta\rangle + (O_2)$	209,000	20.5	60	298–2273
$\langle Ta_2O_5\rangle = \{Ta_2O_5\}$	151,000	−70.3	–	2150 m
$\langle Ta_2O_5\rangle = 2\langle Ta\rangle + (5/2)(O_2)$	2,025,000	−412.5	20	298–2150 m
$\langle Te\rangle = \{Te\}$	17,500	−24.2	1	773 m
$\{Te\} = (1/2)(Te_2)$	57,900	−45.9	4	773–1282 b
$(TeO) = (1/2)(Te_2) + (1/2)(O_2)$	7100	6.02	–	1282–1973
$\langle Th\rangle = \{Th\}$	16,300	−7.9	–	2028 m
$\{Th\} = (Th)$	527,200	−104.3	2	2028–5063 b
$\langle ThCl_4\rangle = \{ThCl_4\}$	43,900	−42.1	–	1043 m
$\langle ThCl_4\rangle = \langle Th\rangle + 2(Cl_2)$	1,178,600	−288.1	10	298–1043 m
$(ThO) = \langle Th\rangle + (1/2)(O_2)$	66,900	52.7	4	1873–2273
$\langle ThO_2\rangle = \langle Th\rangle + (O_2)$	1,221,700	−183.3	4	298–2273
$\langle ThS\rangle = \langle Th\rangle + (1/2)(S_2)$	462,800	−94.6	10	298–2273

Continued

Table 3.1.A7 Standard Gibbs Energy Changes for Reactions Reproduced from Ref. [8]—cont'd

Reaction	$\Delta G^\circ = A + B\,T$ (J mol^{-1})		Error (±kJ)	Temperature range (K)
	A	*B*		
$\langle Th_2S_3\rangle = 2\langle Th\rangle + (3/2)(S_2)$	1,268,000	−256.5	20	298–2273
$\langle ThS_2\rangle = \langle Th\rangle + (S_2)$	749,000	−172	20	298–2188 m
$\langle Ti\rangle = \{Ti\}$	15,500	−7.9	–	1943 m
$\{Ti\} = (Ti)$	426,800	−120.0	–	1943–3563 b
$(TiCl_4) = \langle Ti\rangle + 2(Cl_2)$	764,000	−121.5	10	298–1943
$\langle TiO\rangle_\beta = \langle Ti\rangle + (1/2)(O_2)$	515,000	−74.1	20	298–1943
$\langle TiO_2\rangle_{rutile} = \langle Ti\rangle + (O_2)$	941,000	−177.6	2	298–1943
$\langle Ti_2O_3\rangle = 2\langle Ti\rangle + (3/2)(O_2)$	1,502,100	−258.1	10	298–1943
$\langle Ti_3O_5\rangle = 3\langle Ti\rangle + (5/2)(O_2)$	2,435,000	−420.5	20	298–1943
$\langle Tl\rangle = \{Tl\}$	4140	−7.20	0.4	577 m
$\{Tl\} = (Tl)$	169,700	−97.6	3	577–1746 b
$\langle U\rangle = \{U\}$	8500	−6.07	3	1405 m
$\{U\} = (U)$	477,000	−105.4	20	1405–4403 b
$\langle UCl_3\rangle = \{UCl_3\}$	46,400	−42	–	1110 m
$\langle UCl_3\rangle = \langle U\rangle + (3/2)(Cl_2)$	887,000	−210.0	–	298–1110 m
$\{UCl_4\} = (UCl_4)$	141,400	−133.2	–	1062 b
$(UCl_4) = \{U\} + 2(Cl_2)$	848,500	−82.4	10	1405–1973
$\{UCl_5\} = (UCl_5)$	75,300	−94.1	–	800 b
$(UCl_5) = \{U\} + (5/2)(Cl_2)$	962,300	−172.8	–	1405–1973
$\{UCl_6\} = (UCl_6)$	50,200	−75.5	–	665 b
$(UCl_6) = \{U\} + 3(Cl_2)$	1,031,000	−259.0	20	1405–1973
$\langle UO_2\rangle = \{U\} + (O_2)$	1,086,600	−172.3	10	1405–2273
$\langle U_4O_9\rangle = 4\langle U\rangle + (9/2)(O_2)$	4,491,900	−740.2	10	298–873
$\langle U_3O_8\rangle = 3\langle U\rangle + 4(O_2)$	3,560,600	−652.5	10	298–873
$\langle UO_3\rangle = \langle U\rangle + (3/2)(O_2)$	1,226,700	−250.5	10	298–873
$\langle US\rangle = \{U\} + (1/2)(S_2)$	392,500	−103.8	10	1405–2733 m
$\langle U_2S_3\rangle = 2\{U\} + (3/2)(S_2)$	1,038,000	−266.1	40	1405–2303 m

Table 3.1.A7 Standard Gibbs Energy Changes for Reactions Reproduced from Ref. [8]—cont'd

Reaction	$\Delta G^\circ = A + B\,T$ (J mol^{-1})		Error (±kJ)	Temperature range (K)
	A	*B*		
$\langle US_2\rangle = \{U\} + (S_2)$	598,000	−169.9	40	1405–1973
$\langle V\rangle = \{V\}$	22,800	−10.4	–	2193 m
$\{V\} = (V)$	463,300	−125.8	10	2193–3693 b
$\langle VO\rangle = \langle V\rangle + (1/2)(O_2)$	424,700	−80.0	8	298–2073
$\langle V_2O_3\rangle = 2\langle V\rangle + (3/2)(O_2)$	1,202,900	−237.5	8	298–2343 m
$\langle VO_2\rangle = \langle V\rangle + (O_2)$	706,300	−155.3	10	298–1633 m
$\langle V_2O_5\rangle = \{V_2O_5\}$	64,400	−68.3	3	943 m
$\{V_2O_5\} = 2\langle V\rangle + (5/2)(O_2)$	1,447,400	−321.6	8	943–2273
$\langle W\rangle = \{W\}$	35,600	−9.6	–	3673 m
$\{W\} = (W)$	821,100	−140.8	4	3673–5823 b
$\langle WO_2\rangle = \langle W\rangle + (O_2)$	581,200	−171.8	10	298–2273 d
$\langle WO_3\rangle = \{WO_3\}$	73,400	−42.09	–	1745 m
$\langle WO_3\rangle = \langle W\rangle + (3/2)(O_2)$	833,500	−245.4	10	298–1745 m
$\langle Y\rangle = \{Y\}$	11,380	−6.32	0.2	1799 m
$\{Y\} = (Y)$	379,000	−105.4	4	1799–3613 b
$\langle YCl_3\rangle = \{YCl_3\}$	31,400	−31.6	–	994 m
$\langle YCl_3\rangle = \langle Y\rangle + (3/2)(Cl_2)$	967,800	−227.2	10	298–994 m
$\langle Y_2O_3\rangle = 2\langle Y\rangle + (3/2)(O_2)$	1,897,900	−282.0	10	298–1799
$\langle Zn\rangle = \{Zn\}$	7320	−10.6	0.2	693 m
$\{Zn\} = (Zn)$	118,100	−100.2	1	693–1180 b
$\{ZnCl_2\} = (ZnCl_2)$	119,200	−118.7	–	1005 b
$\{ZnCl_2\} = \{Zn\} + (Cl_2)$	403,000	−131.4	20	693–1005 b
$(ZnCl_2) = (Zn) + (Cl_2)$	393,000	−105.0	20	1180–1973
$\langle ZnO\rangle = (Zn) + (1/2)(O_2)$	460,200	−198.3	–	1180–1973
$\langle ZnS\rangle = \{Zn\} + (1/2)(S_2)$	277,800	−107.9	–	693–1180
$(ZnS) = (Zn) + (1/2)(S_2)$	−5000	−30.5	–	1455–1973
$\langle Zr\rangle = \{Zr\}$	20,900	−9.83	–	2125 m

Continued

Table 3.1.A7 Standard Gibbs Energy Changes for Reactions Reproduced from Ref. [8]—cont'd

Reaction	$\Delta G^\circ = A + B\,T$ (J mol^{-1})		Error (±kJ)	Temperature range (K)
	A	*B*		
$\{Zr\} = (Zr)$	579,700	−123.8	4	2125–4683 b
$\langle ZrCl_4\rangle = (ZrCl_4)$	110,500	−181.5	1	609 s
$(ZrCl_4) = \langle Zr\rangle + 2(Cl_2)$	871,100	−116.3	2	609–2273
$(ZrO) = \langle Zr\rangle + (1/2)(O_2)$	−54,600	67.1	4	1573–2123
$\langle ZrO_2\rangle = \{ZrO_2\}$	87,000	−29.5	–	2953 m
$\langle ZrO_2\rangle = \langle Zr\rangle + (O_2)$	1,092,000	−183.7	20	298–2123
$(ZrS) = \langle Zr\rangle + (1/2)(S_2)$	−237,000	78.2	20	298–2123
$\langle ZrS_2\rangle = \langle Zr\rangle + (S_2)$	699,000	−178.2	20	298–1823 m

[a] ⟨Solid⟩, {liquid}, (gas).
[b] m, melting; b, boiling; s, sublimation; d, decomposition temperature.

3.1.A5 were omitted in *KAS*. However, it is believed that analytical formula for Gibbs energies would be still convenient for process metallurgists. Hence, this book provides Table 3.1.A7, which was essentially taken from Ref. [8] with some modifications.

REFERENCES

[1] O. Kubaschewski, C.B. Alcock, P.J. Spencer, Materials Thermochemistry, sixth ed., Pergamon Press, Oxford, 1993.
[2] I. Barin, Thermochemical Data of Pure Substances, VCH Verlaggeselschaft, Weinheim, Germany, 1991.
[3] W. Chase Jr., NIST-JANAF Thermochemical Tables, fourth ed., American Chemical Society, National Institute of Standards and Technology, Washington, DC, 1998.
[4] R. Hultgren, P. Desai, D. Hawkins, M. Gleiser, K.K. Kelley, D.D. Wagman, Selected Values of the Thermodynamic Properties of the Elements, American Society for Metals, Metals Park, OH, 1973.
[5] R. Hultgren, P. Desai, D. Hawkins, M. Gleiser, K.K. Kelley, D.D. Wagman, Selected Values of the Thermodynamic Properties of Binary Alloys, American Society for Metals, Metals Park, OH, 1973.
[6] F. Elliott, M. Gleiser, Thermochemistry for Steelmaking, vol. 1, Addison-Wesley Publishing Co. Inc., Reading, MA, 1960.
[7] F. Elliott, M. Gleiser, V. Ramakrishna, Thermochemistry for Steelmaking, vol. 2, Addison-Wesley Publishing Co. Inc., Reading, MA, 1960.
[8] T. Turkdogan, Physical Chemistry of High Temperature Technology, Academic Press, Inc., New York, 1980.
[9] R. Stull, H. Prohet, JANAF thermochemical tables, NSRDS-NBS37, U. S. Dept. Commer., Washington, D. C., 1971.
[10] W. Chase Jr., J.L. Curnutt, A.T. Hu, H. Prohet, A.N. Syverud, L.C. Walker, J. Phys. Chem. Ref. Data 7 (1974) 311.

[11] W. Chase Jr., J.L. Curnutt, H. Prohet, R.A. McDonald, A.N. Syverud, J. Phys. Chem. Ref. Data 7 (1975) 1.
[12] W. Chase Jr., J.L. Curnutt, R.A. McDonald, A.N. Syverud, J. Phys. Chem. Ref. Data 7 (1978) 793.
[13] I. Barin, O. Knacke, Thermochemical Properties of Inorganic Compounds, Springer Verlag, Berlin, Germany, 1973, Metall. Trans. (5) (1974) 1769.
[14] I. Barin, O. Knacke, O. Kubaschewski, Thermochemical Properties of Inorganic Compounds, Supplement, Springer Verlag, Berlin, Germany, 1977.
[15] O. Kubaschewki, E.L. Evans, C.B. Alcock, Metallurgical Thermochemistry, fourth ed., Pergamon Press, Oxford, 1967.
[16] O. Kubaschewki, C.B. Alcock, Metallurgical Thermochemistry, fifth ed., Pergamon Press, Oxford, 1979.

CHAPTER 3.2

Phase Rule

Masanori Iwase*
Graduate School of Energy Science, Kyoto University

Following Prigogine and Defay [1], Gibbs' phase rule is given as:

$$F = (c' - r) + 2 - P \tag{3.2.1}$$

where

F is the degree of freedom, c' is the number of species involved within a system under consideration. The choice of species is optional provided the correct number of restriction is applied.

r is the number of restrictions on the system and often equals to the minimum number of reactions to express equilibrium reactions within the system under consideration. $(c'-r)$ is the number of independent species.[1]

P is the number of phases.

If system does not involve gas phase, and hence pressure cannot be chosen as an intensive property of the system under consideration, then Equation (3.2.1) becomes

$$F = (c' - r) + 1 - P \tag{3.2.2}$$

3.2.1. INTENSIVE AND EXTENSIVE PROPERTIES

An extensive property of matter is a property that depends upon the amount of substance, while intensive property is a property that is independent of the amount of substance. Thus, as examples, volume, Gibbs energies, and mass are extensive, while temperature, pressure, composition, molar Gibbs energy, activity, density, surface tension, and viscosity are intensive. Among intensive quantities, so far as we concern phase equilibrium, attention should be first focused on temperature, pressure, and composition.

3.2.2. DEGREE OF FREEDOM

When the state of a system cannot be completely determined until at least F intensive properties are given, we say it possesses F degree of freedom. In other words, F means

* Late.

[1] Older statements of the phase rule employ the term *number of independent components c*, which is given as $c = c' - r$. Thus phase rule often expressed as $F = c + 2 - P$.

Treatise on Process Metallurgy, Volume 1
http://dx.doi.org/10.1016/B978-0-08-096986-2.00031-X

© 2014 Elsevier Ltd.
All rights reserved.

the minimum number of intensive properties to determine completely the intensive quantities of all the species involved within the system under considerations without creation of new phase or disappearance of existing phase while equilibrium is maintained.

3.2.3. PHASE

A phase is a form of matter that is macroscopically uniform throughout in chemical composition and physical state. Thus we speak of solid, liquid, and gas phases of a substance. A gas or gas mixture is a single phase ($P=1$). A solid metal is a single phase so far as chemical composition and physical state are macroscopically uniform, in spite of the presence of grain boundaries, dislocations, vacancies, or microsegregation. Different allotropic forms constitute different phases.

3.2.4. SYSTEM

For the purpose of thermochemistry, the universe is divided into two parts, the system and its surroundings divided by boundary. The system is the part of the world in which we have a special interest and can be chosen arbitrarily.

3.2.5. CONDENSED PHASE-VAPOR EQUILIBRIUM

Consider water and water vapor contained in a sealed metal container. First, we choose system as shown in Figure 3.2.1a; sealed metal container is not involved in the system.

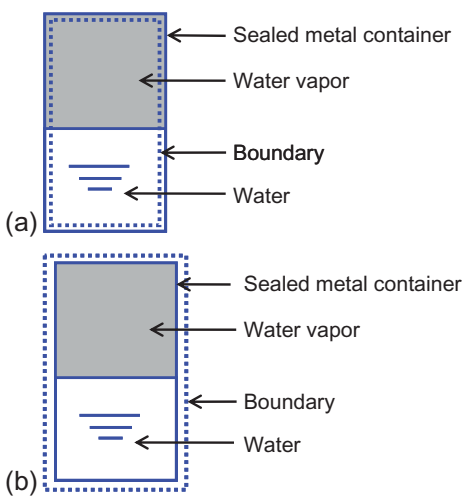


Figure 3.2.1 Water and water vapor contained within a sealed metal container: (a) metal container is not involved within system; (b) system contains water, water vapor, and metal container.

Table 3.2.1 Water Vapor Pressures p_{H_2O}

Temperature T		Pressure p_{H_2O} (atm.)	
°C	K		
0.01	273.16	0.006	Triple point
10	283.15	0.012	
20	293.15	0.023	
40	313.15	0.073	
60	333.15	0.197	
80	353.15	0.468	
100	373.15	1.00	
200	473.15	15.346	
300	573.15	84.756	
373.95	647.1	217.755	Critical point

Data are taken from *CRC Handbook of Chemistry and Physics* [2]

Then, we have

$$\begin{aligned} c' &= 2, \ \{H_2O\},(H_2O) \\ r &= 1, \ \{H_2O\} = (H_2O) \\ P &= 2, \ \text{liquid, gas} \\ F &= (2-1)+2-2=1 \end{aligned}$$

Unit freedom degree ($F=1$) means that we may arbitrarily fix, within limits, either the temperature or the pressure, after which all the other intensive properties of each phase of the system become determinate. In other words, once a temperature is selected, pressure cannot freely be selected. In order to know water vapor pressure at a given temperature, we need thermochemical data. For this purpose, reference can be made on *CRC Handbook of Chemistry and Physics* [2], from which Table 3.2.1 was cited.

3.2.6. ARBITRARY CHOICE OF SYSTEM

Next, one may choose boundary as shown in Figure 3.2.1b; system contains water, water vapor, and metal container. Then we have;

$$\begin{aligned} c' &= 3, \ \{H_2O\}, \ (H_2O), \ \text{metal} \\ r &= 1, \ \{H_2O\} = (H_2O) \\ P &= 3, \ \text{liquid, gas, solid} \\ F &= (3-1)+2-3=1 \end{aligned}$$

Thus, $F=1$ was obtained regardless of the choice of system.

3.2.7. CLAPEYRON EQUATION—LIQUID VAPOR EQUILIBRIUM

It is possible to maintain equilibrium between two phases, *phases 1* and *2*, by simultaneously varying temperature and pressure. For any infinitesimal changes in T and p,

$$\mathrm{d}G_{\mathrm{phase}\,1} = \mathrm{d}G_{\mathrm{phase}\,2} \tag{3.2.3}$$

From Equation (3.1.57),

$$\mathrm{d}G_{\mathrm{phase}\,1} = -S_{\mathrm{phase}\,1}\mathrm{d}T + V_{\mathrm{phase}\,1}\mathrm{d}p \tag{3.2.4}$$

and

$$\mathrm{d}G_{\mathrm{phase}\,2} = -S_{\mathrm{phase}\,2}\mathrm{d}T + V_{\mathrm{phase}\,2}\mathrm{d}p \tag{3.2.5}$$

By inserting Equations (3.2.4) and (3.2.5) into Equation (3.2.3), we have

$$-S_{\mathrm{phase}\,1}\mathrm{d}T + V_{\mathrm{phase}\,1}\mathrm{d}p = -S_{\mathrm{phase}\,2}\mathrm{d}T + V_{\mathrm{phase}\,2}\mathrm{d}p \tag{3.2.6}$$

$$\frac{\mathrm{d}p}{\mathrm{d}T} = \frac{\Delta S_{\mathrm{phase}\,1\to\mathrm{phase}\,2}}{\Delta V_{\mathrm{phase}\,1\to\mathrm{phase}\,2}} = \frac{\Delta H_{\mathrm{phase}\,1\to\mathrm{phase}\,2}}{T\Delta V_{\mathrm{phase}\,1\to\mathrm{phase}\,2}} \tag{3.2.7}$$

It should be noted here that at equilibrium $\Delta G = 0$, and hence $\Delta H = T\Delta S$. Equation (3.2.7) is known as the Clapeyron equation and gives the relationships between the variations of temperature and pressure, which are required for the maintenance of equilibrium between the two phases.

Figure 3.2.2 shows general regions of pressure and temperature where solid, liquid, and gas are stable. Liquid–gas equilibrium, e.g., water–water vapor, corresponds to line *bc* of this diagram. By rewriting the Clapeyron equation (3.2.7), the relation between p and T along this line, i.e., for liquid–vapor equilibrium, is given as

$$\frac{\mathrm{d}p}{\mathrm{d}T} = \frac{\Delta H_{\mathrm{V}}}{T\Delta V_{\mathrm{V}}} \tag{3.2.8}$$

where ΔH_{V} is the change in enthalpy due to vaporization, i.e., $\Delta H_{\mathrm{V}} = H(\mathrm{gas}) - H(\mathrm{liquid})$, and ΔV_{V} is the change in molar volume that occurs on vaporization, i.e., $\Delta V_{\mathrm{V}} = V(\mathrm{gas}) - V(\mathrm{liquid}) \approx V(\mathrm{gas})$. Both the vaporization enthalpy ΔH_V and the molar volume change ΔV_V are positive; hence $\mathrm{d}p/\mathrm{d}T$ is positive, corresponding to positive slope of line *bc*.

For solid–vapor equilibrium, the Clapeyron equation is given as

$$\frac{\mathrm{d}p}{\mathrm{d}T} = \frac{\Delta H_{\mathrm{S}}}{T\Delta V_{\mathrm{S}}} \tag{3.2.9}$$

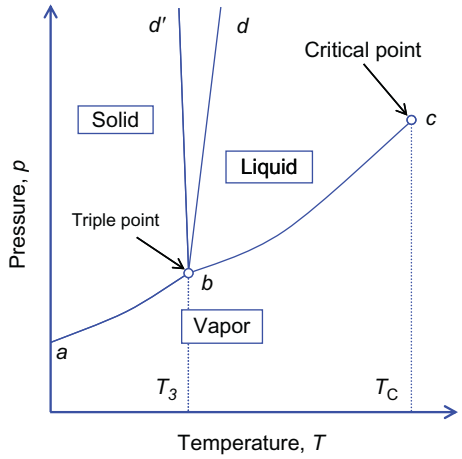


Figure 3.2.2 General regions of pressure and temperature where solid, liquid, and gas, respectively, are stable. Boundary between liquid and solid is expressed by either line *bd* or *bd′* respectively, for $\Delta V_F > 0$ and $\Delta V_F < 0$.

where ΔH_S is the change in enthalpy due to sublimation, i.e., $\Delta H_S = H(\text{gas}) - H(\text{solid})$, and ΔV_S is the change in molar volume that occurs on sublimation, i.e., $\Delta V_S = V(\text{gas}) - V(\text{solid})$. In the case of vapor, $V(\text{gas})$ is much larger than $V(\text{solid})$, and hence $\Delta V_S \approx V(\text{gas})$.

3.2.8. TEMPERATURE DEPENDENCE OF VAPOR PRESSURE

If the vapor is ideal gas, $\Delta V_V = V(\text{gas}) = RT/p$. Then, Equation (3.2.8) becomes

$$\frac{dp}{p} = \frac{\Delta H_V}{RT^2} dT \tag{3.2.10}$$

This is known as the Clausius–Clapeyron equation.
If ΔH_V is independent of temperature, then we have

$$\ln p = -\frac{\Delta H_V}{RT} + (\text{constant}) \tag{3.2.11}$$

With an assumption of $\Delta H_V = a + bT$ (where a and b are constants), Equation (3.2.11) becomes

$$\ln p = -\frac{A}{T} + B \ln T + C, \quad \text{where } A, B, \text{ and } C \text{ are constants} \tag{3.2.12}$$

Vapor pressures of substances are often expressed with this formula.

3.2.9. SOLID–LIQUID EQUILIBRIUM

Consider s system contains water and ice under an external pressure, as shown in Figure 3.2.3.

We have,

$$\begin{aligned} c' &= 2, \ \{H_2O\}, \langle H_2O\rangle \\ r &= 1, \ \{H_2O\} = \langle H_2O\rangle \\ P &= 2, \ \text{liquid, solid} \\ F &= (2-1)+2-2=1 \end{aligned}$$

Although system does not contain gas phase, pressure is to be considered so far as we concern the effect of pressure on liquid–solid equilibrium.

For solid-liquid equilibrium, the Clapeyron equation (3.2.7) can also be applied:

$$\frac{dp}{dT} = \frac{\Delta H_F}{T\Delta V_F} \tag{3.2.13}$$

where ΔV_F is change in molar volume $\Delta V_F = V(\text{liquid}) - V(\text{solid})$, and ΔH_F is enthalpy changes due to fusion $\Delta H_F = H(\text{liquid}) - H(\text{solid}) > 0$. Line bd or bd' of Figure 3.2.2 corresponds to Equation (3.2.13), depending upon the sign of ΔV_F. Table 3.2.2 shows changes in molar volume of H_2O and some metallic elements. As shown in this table, the ΔV_F value for H_2O is negative; hence dp/dT is negative. Thus line bd' of Figure 3.2.2 would correspond to H_2O.

Metallic elements, which have closed-packed structures in the solid state, are termed *true metal* and have positive values for ΔV_F. On the other hand, for *semimetals*, e.g., Ga and Bi, ΔV_F is negative.

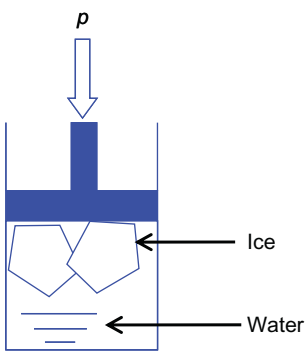


Figure 3.2.3 Ice and water under an external pressure, *p*.

Table 3.2.2 Molar Volume of H_2O and Some Metallic Elements at Melting Temperature

	Atomic Weight	T_m (K)	V(Solid)[a] (cm^3/mol)	V(Liquid) (cm^3/mol)	ΔV_F (cm^3/mol)
H_2O	18.00	273	19.64	18.00	−1.630
Na	23.0	371	24.1	24.8	0.73
K	39.1	337	44.4	47.2	2.87
Mg	24.3	923	14.6	15.3	0.72
Al	27.0	934	10.4	11.3	0.87
Ga	69.7	303	11.8	11.4	−0.350
Sn	118.7	505	16.6	17.0	0.41
Pb	207.2	601	18.8	19.4	0.62
Sb	121.8	904	18.59	18.64	0.05
Bi	209.0	545	21.6	20.8	−0.760
Cu	63.6	1358	7.5	7.9	0.45
Ag	107.9	1235	10.8	11.6	0.75
Au	197.0	1338	10.7	11.4	0.71
Fe	55.84	1809	7.5	8.0	0.52
Ni	58.7	1728	7.0	7.5	0.53

[a]Values for V(solid) at the melting temperature for metallic elements would contain uncertainties to some extents.

3.2.10. TRIPLE POINT

Consider ice, water, and water vapor contained in a sealed metal container. Since the choice of system is optional, the system of interest here contains water, ice, and water vapor but container. Then we have

$$\begin{aligned} c' &= 3, && \langle H_2O\rangle,\ \{H_2O\},\ (H_2O) \\ r &= 2^*, && \text{(i) } \langle H_2O\rangle = \{H_2O\} \\ & && \text{(ii) } \langle H_2O\rangle = (H_2O) \\ P &= 3, && \text{solid, liquid, gas} \\ F &= && (3-2)+2-3=0 \end{aligned}$$

Zero freedom degree means that we have no choice for intensive quantities in order to equilibrate water, water vapor, and ice. This corresponds to *triple point* at which three different phases (typically solid, liquid, and vapor) simultaneously coexist in equilibrium. In other words, temperature and pressure must be at specific values. For water $T = 273.16$ K (0.01 °C) and $p_{H_2O} = 611.73$ Pa (6.037×10^{-3} atm.) [3]. The triple point of pure substance is outside our control. If temperature of the system was raised up to 283 K (10 °C), then solid phase (ice) will disappear.

* Reaction $\{H_2O\} = \langle H_2O\rangle$ can be derived from the others; hence the minimum number of reactions is 2.

3.2.11. ARBITRARY CHOICE OF SYSTEM—IONIC SPECIES

Consider a system which contains water and water vapor. Since the choice of species is optional, in addition to $\{H_2O\}$, one may consider H^+ and OH^- ions within water. Thus,[2]

$$\begin{aligned} c' &= 4, \quad \{H_2O\},\ (H_2O),\ H^+,\ OH^- \\ & \quad\ \ (\mathrm{i})\ \{H_2O\} = (H_2O) \\ r &= 3 \quad (\mathrm{ii})\ \{H_2O\} = H^+ + OH^- \\ & \quad\ \ (\mathrm{iii})\ [H^+] = [OH^-]^* \\ P &= 2, \quad \text{liquid, gas} \\ F &= \quad (4-3)+2-2=1 \end{aligned}$$

As we saw already for liquid–vapor equilibrium, unit freedom degree means that by fixing temperature, all other intensive properties become determinate. For water, $[H^+] = [OH^-] = 10^{-7}$ (mol/l), corresponding to $-\log [H^+] \equiv \mathrm{pH} = 7$.

3.2.12. CRITICAL TEMPERATURE AND PRESSURE

Consider a liquid and its vapor contained in a rigid, closed container. At low vapor pressure or low temperatures, there is a significant difference in density between liquid and its vapor. Because of such difference in density, a surface is clearly observed. With an increase in temperature, the density of the vapor increases. At the same time, density of liquid would decrease slightly because of its expansion. Vaporization enthalpy ΔH_V decreases with an increase in temperature as shown in Figure 3.2.4. Eventually, there comes a stage when the density of the vapor is equal to that of the liquid, and surface between the two phases disappears. In conforming to such disappearance of surface, surface tension becomes zero. The temperature at which the surface disappears, and both ΔH_V and surface tension become zero, is called *critical temperature* T_C of the substance. At $T \geq T_C$, a single uniform phase termed *supercritical fluid* fills the container and the interface no longer exists: liquid phase does not exist.

3.2.13. FREEDOM DEGREE AND THERMOCHEMICAL DATA—1

Consider $\langle Ni \rangle$, $\langle NiO \rangle$, and (O_2) in a sealed container. As indicated already, we may neglect container. Then we have

[2] The concentrations of H^+ and OH^-, respectively, are expressed by $[H^+]$ and $[OH^-]$, respectively.
* This is to maintain electrical neutrality.

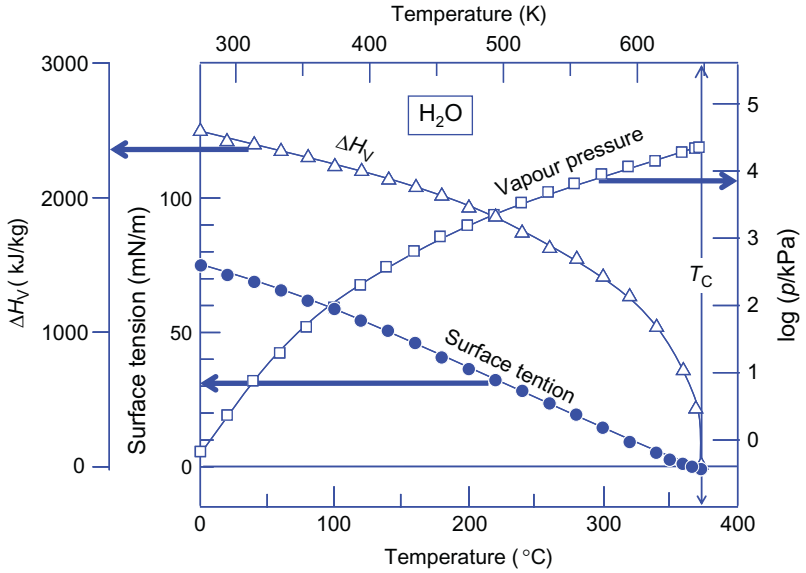


Figure 3.2.4 Surface tension, enthalpy of vaporization, and vapor pressure of water as a function of temperature, indicating that surface tension and evaporation enthalpy become zero at a critical temperature. *Data are taken from* CRC Handbook of Chemistry and Physics *[2]*.

$$
\begin{aligned}
&c' = 3, \ \ \langle \mathrm{Ni} \rangle, \ \langle \mathrm{NiO} \rangle, \ (\mathrm{O_2}) \\
&r = 1, \ \ 2\langle \mathrm{Ni} \rangle + (\mathrm{O_2}) = 2\langle \mathrm{NiO} \rangle \\
&P = 3, \ \ 2 \text{ solid phases and gas} \\
&F = (3-1) + 2 - 3 = 1
\end{aligned}
$$

Namely, by fixing temperature, oxygen pressure $p_{\mathrm{O_2}}$ is fixed through the reaction:

$$2\langle \mathrm{Ni} \rangle + (\mathrm{O_2}) = 2\langle \mathrm{NiO} \rangle \tag{3.2.14}$$

$$\Delta G^{\circ}(3.2.14) = RT \ \ln \ p_{\mathrm{O_2}} \tag{3.2.15}$$

As shown in Section 8 of Chapter 3.1, standard Gibbs energy change ΔG° (Equation 3.2.14) is the function of temperature only. Thus, $p_{\mathrm{O_2}}$ is fixed by giving temperature into Equation (3.2.15), in conforming to $F = 1$.

3.2.14. FREEDOM DEGREE AND THERMOCHEMICAL DATA—2

Consider (CO), (CO_2), and (O_2). We have

$$\begin{aligned} c' &= 3, \ \ (\mathrm{CO}), (\mathrm{CO_2}), (\mathrm{O_2}) \\ r &= 1, \ \ (\mathrm{CO}) + (1/2)\mathrm{O_2} = (\mathrm{CO_2}) \\ P &= 1, \ \ \text{gas} \\ F &= (3-1) + 2 - 1 = 3 \end{aligned}$$

Thus, $F=3$ indicates that, by fixing three intensive quantities, (i) temperature, (ii) total pressure, and (iii) p_{CO}/p_{CO_2} ratio, oxygen partial pressure p_{O_2} is fixed. In order to know the values for p_{O_2}, we need Gibbs energy data for the reaction:

$$(\mathrm{CO}) + (1/2)\mathrm{O_2} = (\mathrm{CO_2}) \tag{3.2.16}$$

$$\Delta G^{\circ}(3.2.16) = -RT\ln\frac{p_{CO_2}}{p_{CO}{p_{O_2}}^{1/2}} \tag{3.2.17}$$

Equation (3.2.17) indicates, however, that equilibrium oxygen partial pressures depend upon two intensive properties, (i) temperature and (ii) p_{CO}/p_{CO_2} ratio. Thus, one would be puzzled because it looks $F=2$ rather than $F=3$. It is to be noted, however, that F means "the minimum number of intensive quantities to determine *completely* the intensive quantities of *all the species* involved within the system under considerations without creation of new phase or disappearance of existing phase while equilibrium is maintained." In other words, the oxygen partial pressure p_{O_2} can be fixed by fixing two intensive properties, T and p_{CO}/p_{CO_2}, while, in order to fix the partial pressures of CO and CO_2, we have to fix three intensive properties, (i) temperature, (ii) total pressure, and (iii) p_{CO}/p_{CO_2} ratio, in conforming to $F=3$.

3.2.15. SINGLE-PHASE COMPOSITION AND BULK COMPOSITION

Figure 3.2.5 shows the phase diagram of the system Sn–Zn. Consider two mixtures of Sn + Zn, with Zn concentrations of 20- and 30-atomic pct, respectively. When these mixtures are heated to 573 K (300 °C), homogeneous liquid alloys are formed:

$$\begin{aligned} c' &= 2, \ \ \text{Sn in alloy, Zn in alloy} \\ r &= 0, \\ P &= 1, \ \ \text{liquid} \\ F &= (2-0) + 1 - 1 = 2 \end{aligned}$$

Namely after choosing this temperature of 573 K, we still have a choice of composition: homogeneous liquid alloys are indeed obtainable with Zn concentrations of 20- and 30-atomic pct.

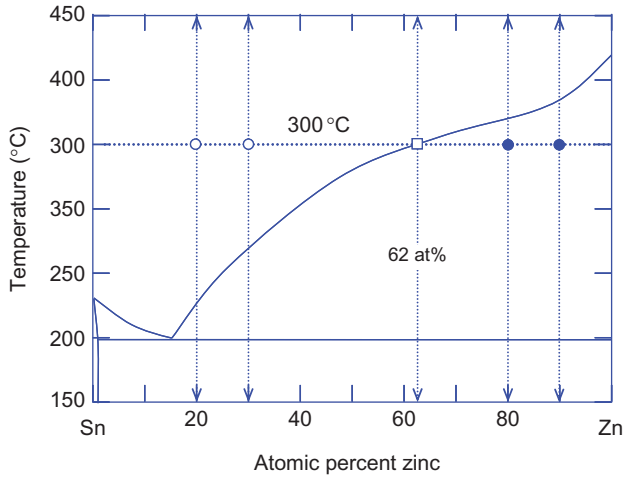


Figure 3.2.5 Phase diagram of the system Sn–Zn.

Next, consider two mixtures of Sn + Zn, with Zn concentrations of 80- and 90-atomic pct, respectively. For both mixtures, as can be seen from Figure 3.2.5, we have

$$\begin{aligned} c' &= 3, \ \text{Sn(in alloy)}, \ \text{Zn(in alloy)}, \ \text{solid Zn} \\ r &= 1, \ \text{Zn(in alloy)} = \langle \text{Zn} \rangle \\ P &= 2, \ \text{liquid, solid} \\ F &= (3-1)+1-2=1 \end{aligned}$$

Thus $F = 1$ means that at 573 K we have no choice for composition. The Zn concentrations in liquid and solid phases should be 62- and 100-atomic pct Zn, respectively, although the initial mixtures had different compositions.

From these examples, it is evident that composition falls into two categories, single-phase composition and bulk composition.[3] If the system consists of a single phase, both are identical, while for the system containing a number of phases, bulk composition is not equal to single-phase composition.

3.2.16. COMPOSITION OF INDUSTRIAL SLAG

In industry, composition normally means bulk composition.

Consider experiments to study the equilibrium partition of phosphorous between liquid metal and molten slag. The reaction underlying such experiments can be expressed as

$$[\text{P}]_{\text{Fe}} + (5/2)(\text{FeO})_{\text{slag}} = (5/2)\{\text{Fe}\} + (\text{PO}_{2.5})_{\text{slag}} \qquad (3.2.18)$$

[3] Bulk composition would also be termed *total composition*.

$$K'(3.2.18) = \frac{(\%\mathrm{P})}{[\%\mathrm{P}](\%\mathrm{FeO})^{5/2}} \tag{3.2.19}$$

Particular care has to be taken for discussing compositions of industrial slags in the case of processes, which would consist of two to three phases. Consider phosphorous, as an example, in slags used for hot metal processing. In such slags, dispersed fine or coarse particles of solid CaO and/or Ca_2SiO_4–$Ca_3P_2O_8$ solid solutions would often be detected. Chemical analysis of slags is usually made on samples taken by spoon sampler. Habitually, care is not taken to distinguish one phase from another existing within such samples. Hence, the chemical analysis of slags provides inevitably bulk compositions. Nevertheless, one would often speak of partition ratios of phosphorous by using phosphorous concentrations $(\%\mathrm{P})_{\mathrm{bulk}}$ thus determined and phosphorous content $[\%\mathrm{P}]_{\mathrm{metal}}$ in liquid iron.

On the other hand, experimental studies on equilibrium partition of phosphorous between slag and metal phases are normally conducted with homogeneous liquid slags and molten iron. The phosphorous partial ratios thus determined would often be different from those based upon $(\%\mathrm{P})_{\mathrm{bulk}}$.

REFERENCES

[1] I. Prigogine, R. Defay, Chemical Thermodynamics, Longman Green and Co., London, 1954, p. 172.
[2] R. Lide editor-in-chief, CRC Handbook of Chemistry and Physics, 90th ed., CRC Press, Boca Raton, 2009–2010, p. 6-5.
[3] *bid*, pp. 6–9.

CHAPTER 3.3

Ellingham Diagram

Masakatsu Hasegawa
Graduate School of Energy Science, Kyoto University

3.3.1. STANDARD GIBBS ENERGY CHANGE OF FORMATION OF COMPOUNDS

The standard Gibbs energy change of formation of a compound, ΔG_f°, is defined as the Gibbs energy change when one mole of a compound is formed from elements at 1 atmospheric pressure and can be calculated as

$$\begin{aligned}\Delta G_f^\circ &= \Delta H_f^\circ - T\Delta S_f^\circ \\ &= \left[\Delta H_{298}^\circ + \int_{298}^{T} \Delta Cp\,\mathrm{d}T\right] - T\left[\Delta S_{298}^\circ + \int_{298}^{T} (\Delta Cp/T)\,\mathrm{d}T\right]\end{aligned} \tag{3.3.1}$$

Ellingham [1] plotted the experimentally determined variation with temperature of ΔG_f° for oxides and sulfides and found that the relationship approximated to straight line over the temperature ranges in which no phase transformations occurred. Thus, within the limits of accuracy of the available thermodynamic data, the variation of ΔG_f° could be formulated as

$$\Delta G_f^\circ = A + BT \tag{3.3.2}$$

where A and B were constants. Figure 3.3.1 shows the $\Delta G_f^\circ - T$ relations for oxidation reactions involving one mole of gaseous oxygen; such a figure is called the Ellingham diagram. The thermodynamic data used in this figure are cited from the compilation by Kubaschewski *et al.* [2]. For example, they gave the following expression for oxidation of manganese:

$$2\mathrm{Mn(solid)} + \mathrm{O_2(gas)} = 2\mathrm{MnO(solid)} \tag{3.3.3}$$

$$\Delta G_f^\circ(3.3)/\mathrm{J\ mol^{-1}} = -769{,}440 + 145.6T \tag{3.3.4}$$

Based on $\Delta S = -[\partial \Delta G/\partial T]_p$, the values of constants A and B in Equation (3.3.2), respectively, correspond to the enthalpy change, ΔH_f°, and the negative of the entropy change, $-\Delta S_f^\circ$. As seen in Figure 3.3.1, the intercepts of all the representative lines at 0 K are negative; $A = \Delta H_f^\circ < 0$. These imply that oxidation reactions are exothermic. On the

Treatise on Process Metallurgy, Volume 1
http://dx.doi.org/10.1016/B978-0-08-096986-2.00032-1
© 2014 Elsevier Ltd.
All rights reserved.

other hand, the standard entropy of a gaseous species is generally greater than that of a condensed component, e.g., $S^{\circ}_{298}(O_2) = 205.1\ J\ K^{-1}\ mol^{-1}$, $S^{\circ}_{298}(\text{solid Mn}) = 32.0\ J\ K^{-1}\ mol^{-1}$ and $S^{\circ}_{298}(\text{solid MnO}) = 59.8\ J\ K^{-1}\ mol^{-1}$ [3]. Thus the values for ΔS°_f for oxidation reactions involving one mole of gaseous oxygen are very close to $S^{\circ}(O_2)$; $B = -\Delta S^{\circ}_f \approx S^{\circ}(O_2)$. Therefore, all the lines in Figure 3.3.1 are almost parallel to each other over the temperature ranges in which both of the metals and the oxides are condensed phases. In approximated formula (3.3.2), the ΔH°_f and ΔS°_f terms are assumed to be constant in a specified range. This does not take into account the small

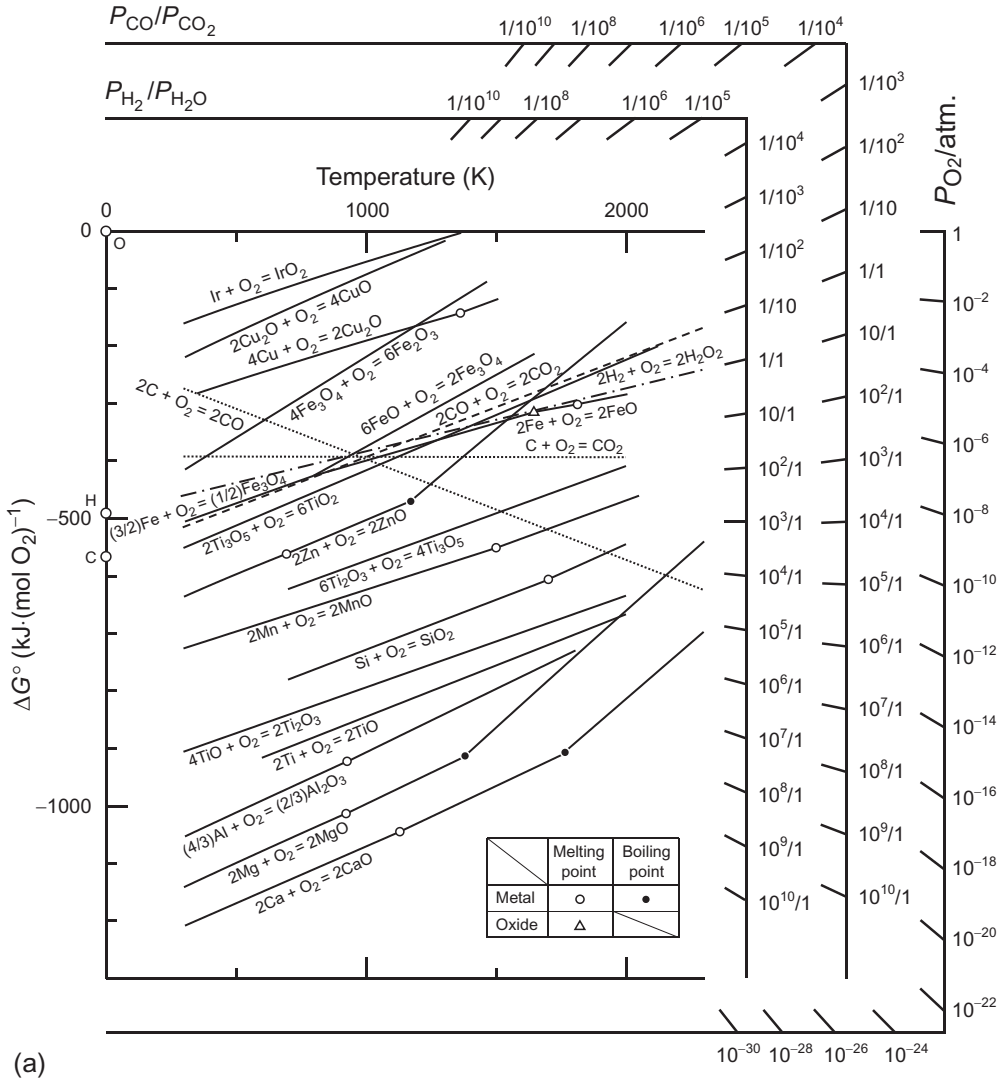


Figure 3.3.1 Ellingham diagram for some oxides; Richardson nomographic scales are included: (a) Al, Ca, Cu, Fe, Ir, Mg, Mn, Si, Ti, and Zn.

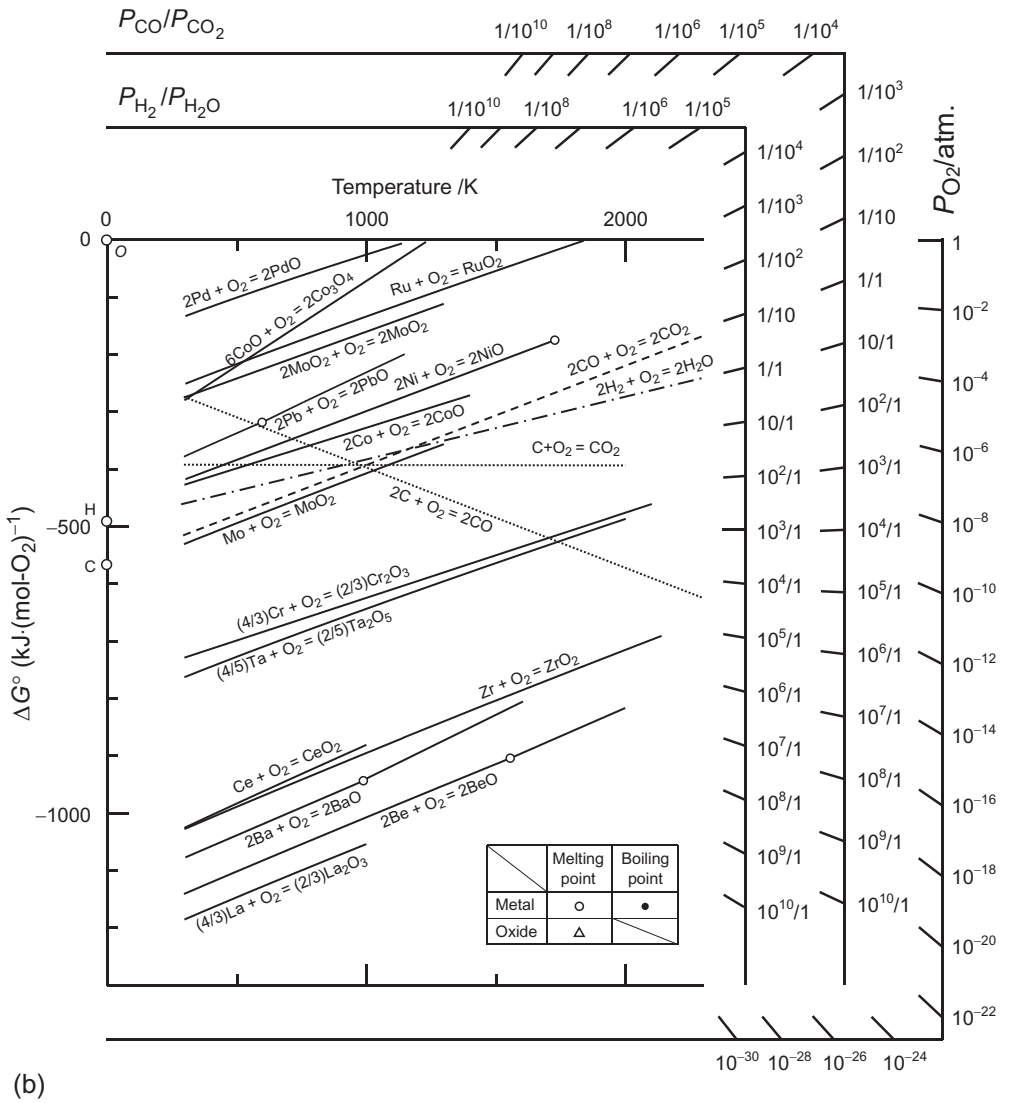


Figure 3.3.1, cont'd (b) Ba, Be, Ce, Co, Cr, La, Mo, Ni, Pb, Pd, Ru, Ta, and Zr.

Cp changes, ΔCp, in Equation (3.3.1). Thus, it should be pointed out here that the linearity of Ellingham plots is a slight approximation.

The open and solid circles in Figure 3.3.1 identify the melting and boiling points of the metals, while the open triangles represent the melting points of the oxides. As seen in Figure 3.3.1, the slopes of the lines representing ΔG_f°–T relations change at temperatures in which the phase transformations of reactants or products occur. Consider the fusion of manganese:

$$\mathrm{Mn(solid)} = \mathrm{Mn(liquid)} \tag{3.3.5}$$

The thermal data on manganese, i.e., heat capacity, Cp, heat of fusion, $\Delta H_{\mathrm{F}}^{\circ}$, and melting temperature, T_{M}, have been reported as follows [3] (see Table 3.1.A7 of Chapter 3.1):

$$Cp(\mathrm{solid\,Mn})/\mathrm{J\ K^{-1}\ mol^{-1}} = 46.44 \tag{3.3.6}$$

$$Cp(\mathrm{liquid\,Mn})/\mathrm{J\ k^{-1}\ mol^{-1}} = 46.02 \tag{3.3.7}$$

$$\Delta H_{\mathrm{F}}{}^{\circ}/\mathrm{J\ mol^{-1}} = 14{,}600 \tag{3.3.8}$$

$$T_{\mathrm{M}}/\mathrm{K} = 1517 \tag{3.3.9}$$

Figure 3.3.2 indicates that, at a given temperature below the melting point 1517 K, the enthalpy change from solid Mn to liquid Mn, $\Delta H_{\mathrm{F}}^{\circ}(T)$, is not equal strictly to the heat of fusion, $\Delta H_{\mathrm{F}}^{\circ}$, and can be calculated by extrapolating the heat capacity of liquid Mn:

$$\begin{aligned}\Delta H_{\mathrm{F}}^{\circ}(T) &= H^{\circ}(\text{liquid Mn}) - H^{\circ}(\text{solid Mn}) \\ &= \Delta H_{\mathrm{F}}^{\circ} + \int_{1517}^{T} \{Cp(\text{liquid Mn}) - Cp(\text{solid Mn})\}\mathrm{d}T\end{aligned} \tag{3.3.10}$$

Equation (3.3.10) is also available at temperature over the melting point when Cp (solid Mn) is extrapolated. From the thermal data, the integration term in Equation (3.3.10) at 1600 K can be calculated as

$$\begin{aligned}\int_{1517}^{1600} \{Cp(\text{liquid Mn}) - Cp(\text{solid Mn})\mathrm{d}T\} &= (46.02 - 46.44) \times (1600 - 1517) \\ &= -34.86\ \mathrm{J\ mol^{-1}}\end{aligned} \tag{3.3.11}$$

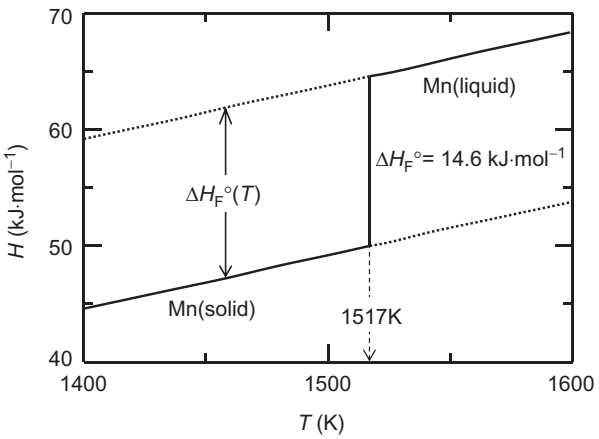


Figure 3.3.2 Standard enthalpy change of the fusion of manganese.

Comparing Equations (3.3.8) and (3.3.11), it can be concluded that the integration term is negligible. Thus $\Delta H_F^\circ(T)$ can be considered to be independent of temperature and equal to ΔH_F°. In analogy with the enthalpy change, the entropy change, $\Delta S_F^\circ(T)$, can be given as

$$\begin{aligned}\Delta S_F^\circ(T) &= S^\circ(\text{liquid Mn}) - S^\circ(\text{solid Mn}) \\ &= \Delta S_F^\circ + \int_{1517}^{T} [\{Cp(\text{liquid Mn}) - Cp(\text{solid Mn})\}/T]\mathrm{d}T \\ &\approx \Delta S_F^\circ = \Delta H_F^\circ / T_M\end{aligned} \tag{3.3.12}$$

Based on the considerations above, the standard free energy change of Reaction (3.3.5), $\Delta G_F^\circ(T)$, is expressed as

$$\begin{aligned}\Delta G_F^\circ(T)/\text{J mol}^{-1} &= \Delta H_F^\circ(T) - T\Delta S_F^\circ(T) \approx \Delta H_F^\circ - T\left(\Delta H_F^\circ / T_M\right) \\ &= 14{,}600 - 9.6T\end{aligned} \tag{3.3.13}$$

Combining Equations (3.3.4) and (3.3.13), we obtain

$$2\text{Mn(liquid)} + \text{O}_2\text{(gas)} = 2\text{MnO(solid)} \tag{3.3.14}$$

$$\Delta G_f^\circ(3.14)/\text{J mol}^{-1} = \Delta G_f^\circ(3.3) - 2\Delta G_F^\circ(T) = -798{,}640 + 164.8T \tag{3.3.15}$$

The slope of Mn(liquid)–MnO(solid) line in Equation (3.3.15) is greater than that of Mn(solid)–MnO(solid) line in Equation (3.3.4). As seen in Figure 3.3.1, the slopes increase slightly at the melting points of the metals and increase drastically at the boiling points of the metals because the entropy change of vaporization is generally much greater than that of fusion. Based on the analogical consideration, it can be understood that the ΔG_f°–T plot has a smaller slope at higher temperature owing to the opposite effect of fusion of the oxides.

3.3.2. EQUILIBRIUM OXYGEN PARTIAL PRESSURE

Consider the equilibrium among a metal M, its oxide M_xO_y and gaseous oxygen of partial pressure PO_2.

$$(2x/y)\text{M} + \text{O}_2\text{(gas)} = (2/y)\text{M}_x\text{O}_y \tag{3.3.16}$$

When both of M and M_xO_y are in their standard states, the equilibrium constant, K, corresponding to this reaction can be expressed as

$$K = 1/PO_2 \tag{3.3.17}$$

Strictly equilibrium constants should be expressed in terms of fugacity instead of partial pressure for gaseous species, but the difference between fugacity and partial

pressure is not significant at high temperature and low pressure. The equilibrium oxygen partial pressure of Reaction (3.3.16) at a given temperature can be fixed as

$$\Delta G_f^\circ = -RT \ln K = RT \ln PO_2 \tag{3.3.18}$$

If, at any temperature, the actual partial pressure of oxygen is greater than the calculated value from Equation (3.3.18), spontaneous oxidation of metal M occurs, while oxide M_xO_y decomposes to metal M and gaseous oxygen at the oxygen partial pressure less than the equilibrium value. In other words, an element is unstable and its oxide is stable at higher oxygen potentials than its ΔG_f°–T line on the Ellingham diagram. Therefore, the larger negative value for ΔG_f° an oxide has, the more stable it is. It can be visualized clearly in Figure 3.3.1 that aluminum has a stronger affinity for oxygen than iron and can reduce iron monoxide because Al–Al_2O_3 line lies lower than Fe–FeO line.

Richardson and Jeffes [4] improved the Ellingham diagram by adding a nomographic scale, which is designed so that the equilibrium oxygen partial pressure between metal and its oxide can be read off directly at a given temperature. As mentioned above, the equilibrium oxygen partial pressure can be calculated from Equation (3.3.18). The left-hand side of this equation, ΔG_f°, has been already illustrated for the selected oxides on the diagram, while, based on the right-hand side, the PO_2 scale is constructed. Namely, a particular PO_2 scale corresponds to a line which passes through point O, i.e., $RT \ln PO_2 = 0$ at 0 K, and has a slope of $R \ln PO_2$. Figure 3.3.3b shows how to read off the value for the equilibrium oxygen partial pressure between pure liquid Mn and pure solid MnO at 1750 K. The procedure consists of drawing the line which passes through point O and point *a* representing the value for Mn(liquid)–MnO(solid) line at 1750 K, and extending the line until it intersects the PO_2 scale; we can obtain $PO_2 = 6 \times 10^{-16}$ atm.

3.3.3. EQUILIBRIUM CO/CO_2 RATIO AND THE BOUDOUARD REACTION

Consider the equilibrium among gaseous species of CO, CO_2, and O_2.

$$2CO(gas) + O_2(gas) = 2CO_2(gas) \tag{3.3.19}$$

$$\Delta G_f^\circ(3.19)/\text{J mol}^{-1} = -RT \ln \left[PCO_2{}^2/PCO^2 \cdot PO_2\right] = -564{,}830 + 173.7T \text{ [2]} \tag{3.3.20}$$

According to the Gibbs Phase Rule, when one gas phase exists in a two-component system (C and O), there are three degrees of freedom, which give the number of independent intensive variables in the system under consideration. A paricular variable, PO_2, however, can be fixed by giving the two intensive properties, i.e., temperature and PCO/PCO_2 ratio, as shown in Equation (3.3.21):

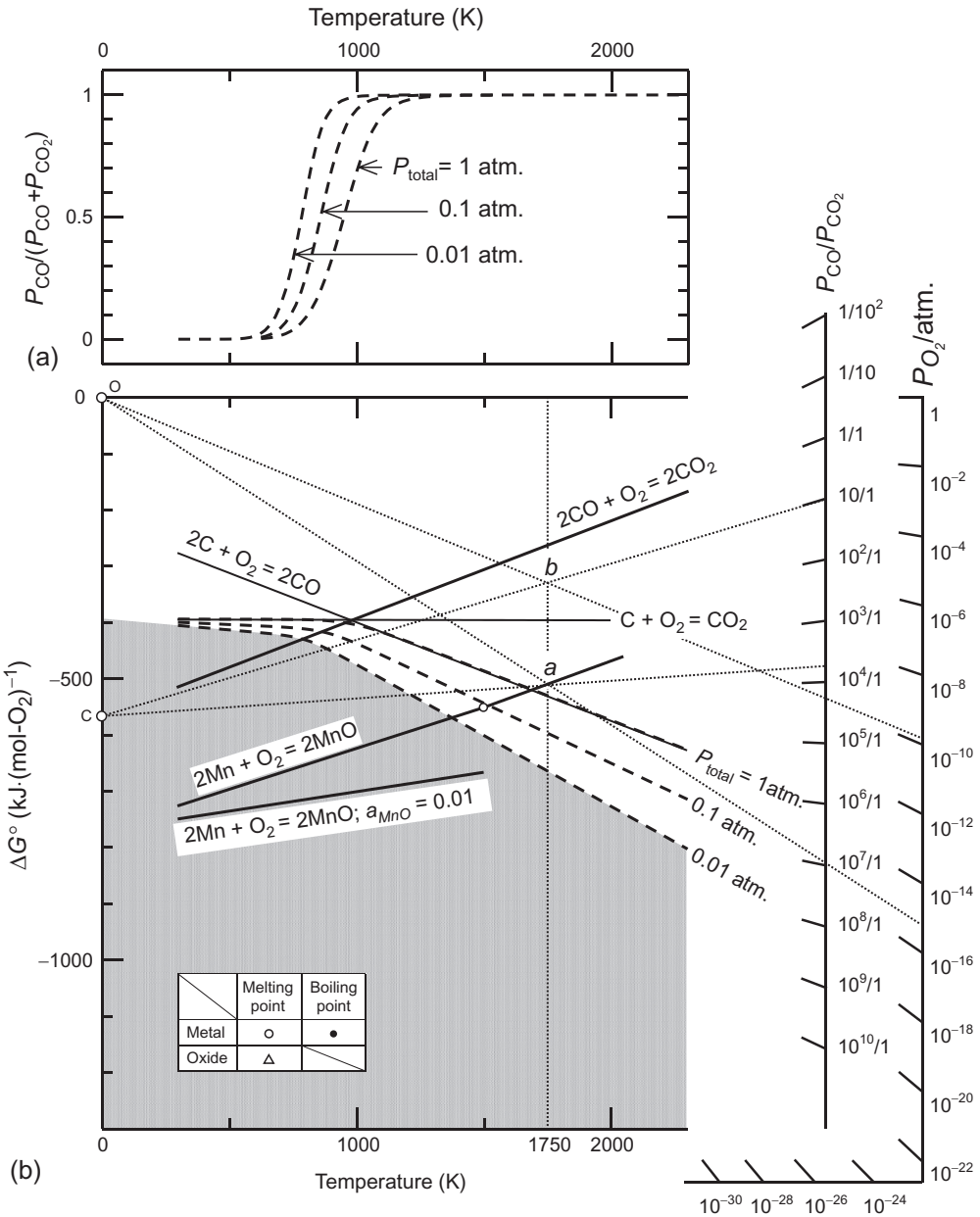


Figure 3.3.3 (a) The variation with temperature of $PCO/[PCO + PCO_2]$ in the $CO + CO_2 + O_2$ gaseous phase in equilibrium with solid carbon at $P_{total} = 0.01$, 0.1, and 1 atm. (b) Procedures to read off the equilibrium values for oxygen partial pressure and CO/CO_2 ratio by using the Richardson nomographic scales.

$$RT\ \ln P\mathrm{O}_2 = -564{,}830 + 173.7T - 2RT\ \ln[P\mathrm{CO}/P\mathrm{CO}_2]\ \left(\mathrm{J\,mol^{-1}}\right) \tag{3.3.21}$$

By using this equation, for instance, the equilibrium $P\mathrm{O}_2$ in the gas phase at 1750 K and $P\mathrm{CO}/P\mathrm{CO}_2 = 10/1$ can be calculated to be 1.6×10^{-10} atm.

Equation (3.3.21) also indicates the relation between the scale of $P\mathrm{O}_2$ (the left-hand side) and that of $P\mathrm{CO}/P\mathrm{CO}_2$ ratio (the right-hand side) in Figure 3.3.1; the latter can be constructed as follows. The $\Delta G_\mathrm{f}^\circ$–$T$ line for Reaction (3.3.19) is extrapolated to lower and higher temperatures until it intersects the ordinate at $T = 0$ K and the scale of $P\mathrm{CO}/P\mathrm{CO}_2$ ratio; these intersects are marked C and 1/1, respectively. A particular scale of $P\mathrm{CO}/P\mathrm{CO}_2$ ratio corresponds to a line which passes through point C and has a slope of $\{173.7 - 2R\ \ln\ [P\mathrm{CO}/P\mathrm{CO}_2]\}$. Figure 3.3.3b shows how to read off the equilibrium $P\mathrm{O}_2$ at 1750 K and $P\mathrm{CO}/P\mathrm{CO}_2 = 10/1$. Point *b* represents the value at 1750 K on the line connecting point C and a scale of $P\mathrm{CO}/P\mathrm{CO}_2$ ratio = 10/1. Then, by drawing the line which passes through point O and point *b*, and extending the line until it intersects the $P\mathrm{O}_2$ scale, we can obtain $P\mathrm{O}_2 = 1.6 \times 10^{-10}$ atm.

Gaseous species of CO and CO_2 are formed by oxidation of pure solid carbon, which represented by the following reactions, respectively:

$$2\mathrm{C(solid)} + \mathrm{O_2(gas)} = 2\mathrm{CO(gas)} \tag{3.3.22}$$

$$\begin{aligned}\Delta G_\mathrm{f}^\circ(3.3.22)/\mathrm{J\,mol^{-1}} &= -RT\ \ln K(3.3.22)\\ &= -RT\ \ln\left[P\mathrm{CO}^2/P\mathrm{O}_2\right] = -223{,}430 - 175.3T^{[2]}\end{aligned} \tag{3.3.23}$$

$$\mathrm{C(solid)} + \mathrm{O_2(gas)} = \mathrm{CO_2(gas)} \tag{3.3.24}$$

$$\begin{aligned}\Delta G_\mathrm{f}^\circ(3.3.24)/\mathrm{J\,mol^{-1}} &= -RT\ \ln K(3.3.24)\\ &= -RT\ \ln\left[P\mathrm{CO}_2/P\mathrm{O}_2\right] = -39{,}4130 - 0.8T^{[2]}\end{aligned} \tag{3.3.25}$$

It is noted here that Equation (3.3.20) is given by combining Equations (3.3.23) and (3.3.25). Figure 3.3.1 shows the $\Delta G_\mathrm{f}^\circ$–$T$ plots for Reactions (3.3.22) and (3.3.24) and indicates that, at low temperatures, CO_2 formation predominates, whereas at higher temperatures, CO formation predominates. Now, consider the equilibrium of the system consisting of solid carbon and gaseous phase consisting of CO, CO_2, and O_2. According to the Phase Rule, there are two degrees of freedom in this system. This means that the equilibrium partial pressures are to be fixed by giving two intensive properties, e.g., temperature and total pressure, P_total, defined as

$$P_\mathrm{total} = P\mathrm{CO} + P\mathrm{CO}_2 + P\mathrm{O}_2 \tag{3.3.26}$$

Equations (3.3.23), (3.3.25), and (3.3.26) involve three unknown quantities, $P\mathrm{CO}$, $P\mathrm{CO}_2$, and $P\mathrm{O}_2$. Hence, values for $P\mathrm{CO}$, $P\mathrm{CO}_2$, and $P\mathrm{O}_2$ can be obtained by solving these three equations simultaneously for a given temperature, T, and total pressure, P_total:

$$PO_2 = \left[\left\{K(3.3.22)^{1/2} + (K(3.3.22) + 4P_{\text{total}}(K(3.3.24) + 1))^{1/2}\right\}/2(K(3.3.24) + 1)\right]^2 \quad (3.3.27)$$

$$PCO = K(3.3.22)^{1/2} PO_2{}^{1/2} \quad (3.3.28)$$

$$PCO_2 = K(3.3.24) PO_2 \quad (3.3.29)$$

The results are illustrated in Figure 3.3.3a as relations between $PCO/[PCO + PCO_2]$ and temperature at $P_{\text{total}} = 0.01$, 0.1, and 1 atm. The proportion of CO increases at higher temperature and lower total pressure. These behaviors can be explained easily by applying Le Chatelier's principle, which states that "when subjected to an external influence, the state of a system at equilibrium shifts in the direction which tends to nullify the effect of the external influence," to the Boudouard reaction expressed in Equation (3.3.30), since this reaction is endothermic and the volume change is positive.

$$CO_2(\text{gas}) + C(\text{solid}) = 2CO(\text{gas}) \quad (3.3.30)$$

$$\Delta G^\circ(3.3.30)/\text{J mol}^{-1} = \Delta G_f^\circ(3.3.22) - \Delta G_f^\circ(3.3.24) = 170{,}700 - 174.5T \quad (3.3.31)$$

The Boudouard curves shown in Figure 3.3.3a can be also illustrated on the Ellingham diagram. The broken curves in Figure 3.3.3b, which represent the Boudouard reaction, are obtained by plotting Equation (3.3.27) as the $RT \ln PO_2$–T relations. It is noteworthy that, at $P_{\text{total}} = 0.01$ atm., solid carbon is stable and then the scale of PCO/PCO_2 ratio is unavailable within the corresponding hatched area in Figure 3.3.3b.

By using the scale added to the Ellingham diagram, the PCO/PCO_2 ratio can be read off directly which is in equilibrium with any metal + oxide systems. Figure 3.3.3b shows the procedure to obtain equilibrium ratio for the following reaction at 1750 K:

$$2Mn(\text{liquid}) + 2CO_2(\text{gas}) = 2MnO(\text{solid}) + 2CO(\text{gas}) \quad (3.3.32)$$

The procedure consists of drawing the line which passes through point C and point *a* representing the value for Mn(liquid) − MnO(solid) line at 1750 K, and extending the line until it intersects the scale of PCO/PCO_2 ratio; we can obtain $PCO/PCO_2 = 5 \times 10^3$. The scale of PH_2/PH_2O ratio in Figure 3.3.1 is used in exactly the same manner as that of PCO/PCO_2 ratio, except that the point H on the ordinate at $T = 0$ K is used instead of point C.

3.3.4. INFLUENCE OF ACTIVITY OF CONDENSED PHASES ON GIBBS ENERGY CHANGE

It should be noted that the Ellingham diagram (Figure 3.3.1) gives the Gibbs energy changes when the reactants and products are in their standard states. Now consider the

oxidation reaction of pure solid manganese when the MnO activity is 0.01. The Gibbs free energy change for this reaction can be expressed as

$$2\mathrm{Mn(solid)} + \mathrm{O_2(gas)} = 2\mathrm{MnO(solid,}\ a\mathrm{MnO} = 0.01) \tag{3.3.33}$$

$$\begin{aligned}\Delta G_\mathrm{f}(3.3.33)/\mathrm{J\ mol^{-1}} &= \Delta G_\mathrm{f}^\circ(3.3.3) + 2RT\ \ln\ a\mathrm{MnO} \\ &= -769{,}440 + 145.6T + 2 \times 8.314 \times T \times \ln(0.01) \qquad (3.3.34) \\ &= -769{,}440 + 69.0T\end{aligned}$$

The Gibbs energy change of Reaction (3.3.33) is also illustrated in Figure 3.3.3b.

REFERENCES

[1] H.J.T. Ellingham, J. Soc. Chem. Ind. 63 (1944) 125.
[2] O. Kubaschewski, C.B. Alcock, Metallurgical Thermochemistry, fifth ed., Pergamon Press, Oxford, 1979, p. 378.
[3] O. Kubaschewski, C.B. Alcock, P.J. Spencer, Materials Thermochemistry, sixth ed., Pergamon Press, Oxford, 1993, p. 258.
[4] F.D. Richardson, J.H.E. Jeffes, J. Iron Steel Inst. 160 (1948) 261.

CHAPTER 3.4

Solution Thermochemistry

Takahiro Miki
Associate Professor, Tohoku University, Japan

3.4.1. PARTIAL MOLAR QUANTITIES

Extensive thermodynamic properties such as volume, V, internal energy, E, enthalpy, H, entropy, S, the Helmholtz energy, F, and the Gibbs energy, G, can be expressed by Equation (3.4.1) by using Y to represent forgoing extensive properties:

$$Y = f(T, p, n_1, n_2, \ldots, n_i, \ldots) \tag{3.4.1}$$

Here, $n_1, n_2, \ldots, n_i, \ldots$ denotes the number of moles of component 1, 2, …, n, present in multicomponent solution in the system. If we consider an infinitesimal change in the value of Y, the following relation can be obtained:

$$\mathrm{d}Y = \left(\frac{\partial Y}{\partial T}\right)_{p,n_1,n_2,\ldots} \mathrm{d}T + \left(\frac{\partial Y}{\partial p}\right)_{T,n_1,n_2,\ldots} \mathrm{d}p + \left(\frac{\partial Y}{\partial n_1}\right)_{p,T,n_2,\ldots} \mathrm{d}n_1 + \cdots \tag{3.4.2}$$

At constant temperature and pressure, Equation (3.4.2) will be Equation (3.4.3).

$$\mathrm{d}Y = \left(\frac{\partial Y}{\partial n_1}\right)_{p,T,n_2,\ldots} \mathrm{d}n_1 + \left(\frac{\partial Y}{\partial n_2}\right)_{p,T,n_1,\ldots} \mathrm{d}n_2 + \cdots \tag{3.4.3}$$

Now we will introduce a new quantity, $\overline{Y}_i$, called the partial molar quantity defined as Equation (3.4.4):

$$\overline{Y}_i = \left(\frac{\partial Y}{\partial n_1}\right)_{p,T,n_j} \tag{3.4.4}$$

Here, $j \neq i$. From substitution of Equation (3.4.4) into Equation (3.4.3), the following will be derived:

$$\mathrm{d}Y = \overline{Y}_1 \mathrm{d}n_1 + \overline{Y}_2 \mathrm{d}n_2 + \overline{Y}_3 \mathrm{d}n_3 + \cdots \tag{3.4.5}$$

From integration Equation (3.4.6) can be obtained:

$$Y = \overline{Y}_1 n_1 + \overline{Y}_2 n_2 + \cdots \tag{3.4.6}$$

Treatise on Process Metallurgy, Volume 1
http://dx.doi.org/10.1016/B978-0-08-096986-2.00033-3
© 2014 Elsevier Ltd.
All rights reserved.

If the Gibbs energy is used in Equation (3.4.6), then we will have Equation (3.4.7):

$$G = \overline{G}_1 n_1 + \overline{G}_2 n_2 + \cdots = \sum \overline{G}_i n_i \tag{3.4.7}$$

The quantity $\overline{G}_i$ will be the change in the Gibbs energy when 1 mole of i is added to infinitely large quantity of solution.

Differentiating Equation (3.4.6) will deduce Equation (3.4.8).

$$\mathrm{d}Y = n_1 \mathrm{d}\overline{Y}_1 + n_2 \mathrm{d}\overline{Y}_2 + \cdots + \overline{Y}_1 \mathrm{d}n_1 + \overline{Y}_2 \mathrm{d}n_2 + \cdots \tag{3.4.8}$$

Subtracting Equation (3.4.5) from Equation (3.4.8) will give Equation (3.4.9):

$$n_1 \mathrm{d}\overline{Y}_1 + n_2 \mathrm{d}\overline{Y}_2 + \cdots = 0 \tag{3.4.9}$$

Division with $\mathrm{d}n_1$ gives the following equation:

$$n_1 \left(\frac{\partial \overline{Y}_1}{\partial n_1}\right)_{p,T,n_2,\ldots} + n_2 \left(\frac{\partial \overline{Y}_2}{\partial n_1}\right)_{p,T,n_2,\ldots} + \cdots = 0 \tag{3.4.10}$$

From the relation $\frac{n_1}{\mathrm{d}n_1} = \frac{X_1}{\mathrm{d}X_1}$, etc., and Equation (3.4.10), we will have Equation (3.4.11):

$$X_1 \left(\frac{\partial \overline{Y}_1}{\partial X_1}\right)_{p,T,X_2,\ldots} + X_2 \left(\frac{\partial \overline{Y}_2}{\partial X_1}\right)_{p,T,X_2,\ldots} + \cdots = 0 \tag{3.4.11}$$

The corresponding equation for the Gibbs energy is as follows:

$$X_1 \left(\frac{\partial \overline{G}_1}{\partial X_1}\right)_{p,T,X_2,\ldots} + X_2 \left(\frac{\partial \overline{G}_2}{\partial X_1}\right)_{p,T,X_2,\ldots} + \cdots = 0 \tag{3.4.12}$$

This equation is generally known as the Gibbs–Duhem equation. This equation is useful to derive the unknown activity of one component when the others are known. Another form of the Gibbs–Duhem equation can be deduced from Equation (3.4.9) by substituting the Gibbs energy as Y and dividing both sides by n:

$$X_1 \mathrm{d}\overline{G}_1 + X_2 \mathrm{d}\overline{G}_2 + \cdots = 0 \tag{3.4.13}$$

3.4.2. INTEGRAL MOLAR QUANTITIES

For multicomponent solution composed of n_1 moles of component 1, n_2 moles of component 2, and so forth, the Gibbs energy will be Equation (3.4.7). The total number of moles present in the solution is $n(=\sum n_i)$. The integral molar Gibbs energy of the solution can be defined as follows:

$$G = \frac{G}{\sum n_i} \tag{3.4.14}$$

From $\left(\frac{n_1}{\sum n_i}\right) = x_1$, $\left(\frac{n_2}{\sum n_i}\right) = x_2$, etc., Equation (3.4.14) will be as follows:

$$G = x_1\overline{G}_1 + x_2\overline{G}_2 + \cdots \tag{3.4.15}$$

where G is the Gibbs energy of 1 mole of a multicomponent solution.

3.4.3. RELATIONSHIP BETWEEN PARTIAL MOLAR QUANTITIES AND INTEGRAL MOLAR QUANTITIES

Differentiating Equation (3.4.15) will give the following equation:

$$dG = X_1 d\overline{G_1} + X_2 d\overline{G}_2 + \cdots + \overline{G}_1 dX_1 + \overline{G} dX_2 + \cdots \tag{3.4.16}$$

Combining Equations (3.4.13) and (3.4.16) gives Equation (3.4.17):

$$dG = \overline{G}_1 dX_1 + \overline{G} dX_2 + \cdots \tag{3.4.17}$$

For a two-component solution Equation (3.4.17) will be Equation (3.4.18).

$$dG = \overline{G}_1 dX_1 + \overline{G} dX_2 \tag{3.4.18}$$

Multiply both sides of Equation (3.4.18) by $\frac{X_1}{dX_2}$ gives Equation (3.4.19):

$$X_1\left(\frac{\partial G}{\partial X_2}\right)_{T,p} = X_1\overline{G}_1\left(\frac{\partial X_1}{\partial X_2}\right)_{T,p} + X_1\overline{G}_2\left(\frac{\partial X_2}{\partial X_2}\right)_{T,p} \tag{3.4.19}$$

From $X_1 + X_2 = 1$, Equation (3.4.19) will be Equation (3.4.20):

$$X_1\left(\frac{\partial G}{\partial X_2}\right)_{T,p} = -X_1\overline{G}_1 +_1 \overline{G}_2 \tag{3.4.20}$$

Combining Equation (3.4.20) with $G = X_1\overline{G}_1 + X_2\overline{G}_2$ will have Equation (3.4.21):

$$\overline{G}_2 = G + X_1\left(\frac{\partial G}{\partial X_2}\right)_{T,p} \tag{3.4.21}$$

Similarly, following can be obtained:

$$\overline{G}_1 = G + X_2\left(\frac{\partial G}{\partial X_1}\right)_{T,p} \tag{3.4.22}$$

For a multicomponent solution, the partial molar energy is given by Equation (3.4.23):

$$\overline{G}_1 = G + (1 - X_1)\left(\frac{\partial G}{\partial X_1}\right)_{T,p.X_2,X_3,\ldots} \tag{3.4.23}$$

3.4.4. RELATIVE PARTIAL MOLAR QUANTITIES AND INTEGRAL MOLAR QUANTITIES

The partial molar quantities refer to absolute values. However, for enthalpy, internal energy, and Gibbs energy, it is not possible to determine absolute values. Therefore, it is necessary to select some state as a reference and express the relative partial molar quantity. The most common reference is the pure-substance standard state. The relative partial molar quantity of component i is defined as follows:

$$\overline{Y}_i^{\mathrm{M}} = \overline{Y}_i - Y_i^{\circ} \tag{3.4.24}$$

Here, $\overline{Y}_i$ is defined by Equation (3.4.4) and Y_i° is the molar quantity for the component i in the reference state. For Gibbs energy it will be Equation (3.4.25):

$$\overline{G}_i^{\mathrm{M}} = \overline{G}_i - G_i^{\circ} = RT \ \ln \ a_i \tag{3.4.25}$$

Relative integral molar quantities can be expressed as follows. If we consider the formation of multicomponent solution consisting of n_1 moles of component 1, n_2 moles of component 2, and so on, for unmixed components that are in their reference states will be Equation (3.4.26):

$$Y^{\circ} = n_1 Y_1^{\circ} + n_2 Y_2^{\circ} + \cdots \tag{3.4.26}$$

If we combine Equations (3.4.9) and (3.4.26) and divide by total number of moles n, we will have relative integral molar property as Equation (3.4.27):

$$Y^{\mathrm{M}} = X_1 \overline{Y}_1^{\mathrm{M}} + X_2 \overline{Y}_2^{\mathrm{M}} + \cdots \tag{3.4.27}$$

For the Gibbs energy Equation (3.4.27) will be Equation (3.4.28):

$$G^{\mathrm{M}} = X_1 \overline{G}_1^{\mathrm{M}} + X_2 \overline{G}_2^{\mathrm{M}} + \cdots \tag{3.4.28}$$

From Equation(3.4.25) it can be expressed as follows:

$$G^{\mathrm{M}} = RT(X_1 \ \ln \ a_1 + X_2 \ \ln \ a_2 + \cdots) \tag{3.4.29}$$

Here, G^{M} is the relative integral molar Gibbs energy of mixing.

The relationship between molar quantities and relative for the Gibbs energy is shown in Figures 3.4.1 and 3.4.2.

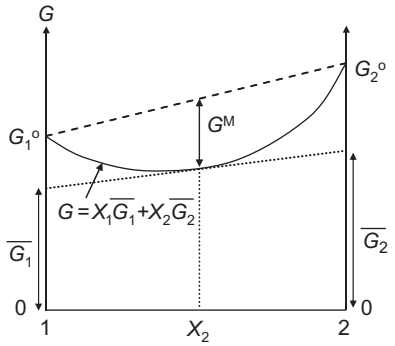


Figure 3.4.1 The relationship between molar quantities for the Gibbs energy.

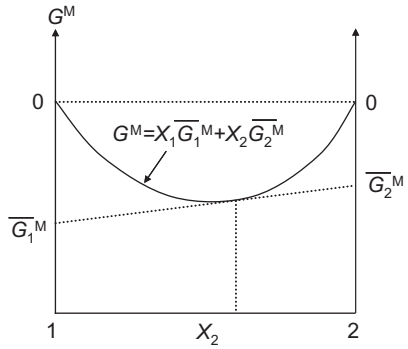


Figure 3.4.2 The relationship between relative molar quantities for the Gibbs energy.

3.4.5. RAOULT'S LAW AND IDEAL SOLUTIONS

If components in the solution are physically and chemically similar, it is sometimes possible to describe the behavior of solution by Raoult's law as shown in Equation (3.4.30):

$$a_i = X_i \tag{3.4.30}$$

Solutions that confirm to Raoult's law at all temperatures and pressures are known as ideal solutions. Most solutions deviate from ideal solution behavior. In general, deviation from Raoult's law will decrease as the mole fraction of the component approaches unity.

For ideal solution, Equation (3.4.30) will stand for all conditions. Combining with Equation (3.4.25) will give Equation (3.4.31) as the relative integral molar Gibbs energy of an ideal solution:

$$\overline{G}_i^{M,id} = RT \ln X_i \tag{3.4.31}$$

Also, the relative integral molar Gibbs energy or the Gibbs energy of formation of an ideal solution can be expressed as Equation (3.4.32):

$$\overline{G}^{\mathrm{M},id} = RT(X_1 \ \ln X_1 + X_2 \ \ln X_2 + \cdots) \tag{3.4.32}$$

The relative partial molar entropies can be determined as follows:

$$\overline{S}_i^{\mathrm{M,id}} = -\left(\frac{\partial \overline{G}_i^{\mathrm{M,id}}}{\partial T}\right)_p = -R \ \ln X_i \tag{3.4.33}$$

The relative integral molar entropy of an ideal solution can be expressed as Equation (3.4.34):

$$\overline{S}^{\mathrm{M,id}} = -R(X_1 \ \ln X_1 + X_2 \ \ln X_2 + \cdots) \tag{3.4.34}$$

The relative partial molar enthalpies can be determined as follows:

$$\overline{H}_i^{\mathrm{M,id}} = \overline{G}_i^{\mathrm{M,id}} + T\overline{S}_i^{\mathrm{M,id}} = RT \ \ln X_i - RT \ \ln X_i = 0 \tag{3.4.35}$$

The enthalpy or the heat of formation of an ideal solution is obtained as follows:

$$H^{\mathrm{M,id}} = \sum\nolimits_i X_i \overline{H}_i^{\mathrm{M,id}} = 0 \tag{3.4.36}$$

From Equation (3.4.36) heat of formation of an ideal solution is zero.

3.4.6. EXCESS THERMODYNAMIC QUANTITIES

Behavior of real solution deviates from that of ideal solution. To express the deviation from the ideal, it is useful to use excess functions:

$$\overline{G}_i^{\mathrm{E}} = \overline{G}_i^{\mathrm{M}} - \overline{G}_i^{\mathrm{M,id}} \tag{3.4.37}$$

Here, $\overline{G}_i^{\mathrm{E}}$ is known as the excess partial molar Gibbs energy of component *i*. Also, the following relation can be obtained:

$$\overline{G}_i^{\mathrm{E}} = \overline{G}_i^{\mathrm{M}} - \overline{G}_i^{\mathrm{M,id}} = RT \ \ln a_i - RT \ \ln X_i = RT \ \ln \gamma_i \tag{3.4.38}$$

The excess integral molar Gibbs energy of binary solution will be Equation (3.4.39):

$$G^{\mathrm{E}} = G^{\mathrm{M}} - G^{\mathrm{M,id}} = RT(X_1 \ \ln \gamma_1 + X_2 \ \ln \gamma_2) \tag{3.4.39}$$

Also, from Equation (3.4.36) the excess integral molar enthalpy will be as follows:

$$H^{\mathrm{E}} = H^{\mathrm{M}} - H^{\mathrm{M,id}} = H^{\mathrm{M}} \tag{3.4.40}$$

3.4.7. INTEGRATION OF THE GIBBS–DUHEM EQUATION

For a binary solution, if the activity of one component is known over a range of composition, the activity of the other component can be determined by Gibbs–Duhem equation. The form of Equation (3.4.41) can be applied for binary solution from Equation (3.4.13):

$$X_1 \mathrm{d}\overline{G}_1 + X_2 \mathrm{d}\overline{G}_2 = 0 \tag{3.4.41}$$

At a given temperature, Equations (3.4.42) and (3.4.43) can be utilized:

$$\mathrm{d}\overline{G}_1 = \mathrm{d}\overline{G}_1^{\mathrm{M}} = RT\mathrm{d}\ \ln\ a_1 \tag{3.4.42}$$

$$\mathrm{d}\overline{G}_2 = \mathrm{d}\overline{G}_2^{\mathrm{M}} = RT\mathrm{d}\ \ln\ a_2 \tag{3.4.43}$$

Hence, Equation (3.4.44) can be deduced:

$$X_1 \mathrm{d}\ \ln\ a_1 + X_2 \mathrm{d}\ \ln\ a_2 = 0 \tag{3.4.44}$$

For an ideal solution, Equation (3.4.44) will be Equation (3.4.45)

$$X_1 \mathrm{d}\ \ln\ X_1 + X_2 \mathrm{d}\ \ln\ X_2 = 0 \tag{3.4.45}$$

Subtraction will give Equation (3.4.46):

$$X_1 \mathrm{d}\ \ln\ \gamma_1 + X_2 \mathrm{d}\ \ln\ \gamma_2 = 0 \tag{3.4.46}$$

Rearranging and integration will deduce Equation (3.4.47):

$$\ln\ \gamma'_1 = -\int_{X_2=0}^{X_2=X'_2} \left(\frac{X_2}{X_1}\right) \mathrm{d}\ \ln\ \gamma_2 \tag{3.4.47}$$

When $X_1 = 1$, then $\gamma_1 = 1$ can be obtained and $\gamma_1 = \gamma'_1$ can be determined at $X_1 = X'_1 = 1 - X'_2$ from Equation (3.4.47).

3.4.8. REGULAR SOLUTIONS

Regular solution [1] may be introduced to express some nonideal solutions. This is defined as the solution that the entropy of mixing is the same as that for ideal solution. For a regular solution with components 1 and 2, Equations (3.4.48)–(3.4.50) will stand:

$$S^{\mathrm{M,r}} = S^{\mathrm{M,id}} = -R(X_1\ \ln\ X_1 + X_2\ \ln\ X_2 + \cdots) \tag{3.4.48}$$

$$G^{\mathrm{M,r}} = RT(X_1\ \ln\ a_1 + X_2\ \ln\ a_2 + \cdots) \tag{3.4.49}$$

$$H^{\mathrm{M,r}} = RT(X_1\ \ln\ \gamma_1 + X_2\ \ln\ \gamma_2 + \cdots) \tag{3.4.50}$$

The relative partial molar enthalpies are given by the following equations:

$$\overline{H}_1^{M,r} = RT \ln \gamma_1 \tag{3.4.51}$$

$$\overline{H}_2^{M,r} = RT \ln \gamma_2 \tag{3.4.52}$$

From statistical analysis using Margules equation [2], the relative partial molar enthalpies can be expressed as follows for binary 1–2 system:

$$RT \ln \gamma_1 = \Omega X_2^2 \tag{3.4.53}$$

$$RT \ln \gamma_2 = \Omega X_1^2 \tag{3.4.54}$$

Here, Ω is the interaction parameter independent of composition and temperature. The relative integral molar enthalpy and the excess integral molar Gibbs energy of solution can be determined as follows:

$$H^{M,r} = G^{E,r} = X_1 \Omega {X_2}^2 + X_2 \Omega {X_1}^2 = \Omega X_1 X_2 \tag{3.4.55}$$

It should be pointed out that regular solution is an approximation. For all solutions, the system approaches regular behavior at higher temperatures due to no ordering and segregation and entropy of mixing will be ideal.

3.4.9. DARKEN'S QUADRATIC FORMALISM

Darken [3] suggested that the activity coefficient of binary system can be expressed using quadratic formalism at high concentration range of component 1 or 2 as Equations (3.4.56)–(3.4.59):

$$\log \gamma_1 = \alpha_{12} X_2^2 \quad (\text{high concentration range of } 1) \tag{3.4.56}$$

$$\log\left(\frac{\gamma_2}{\overset{\circ}{\gamma}_2}\right) = \alpha_{12}\left(X_1^2 - 1\right) \quad (\text{high concentration range of } 1) \tag{3.4.57}$$

$$\log \gamma_2 = \alpha_{21} X_1^2 \quad (\text{high concentration range of } 2) \tag{3.4.58}$$

$$\log\left(\frac{\gamma_1}{\overset{\circ}{\gamma}_1}\right) = \alpha_{21}\left(X_2^2 - 1\right) \quad (\text{high concentration range of } 2) \tag{3.4.59}$$

If $\alpha_{12} = \alpha_{21}$, 1–2 binary solution will be regular solution. However, in general α_{12} will not be equal to α_{21}.

The activity coefficient of X in liquid Fe–X alloys [3] is shown in Figure 3.4.3. This figure shows that Equation (3.4.56) is valid for wide composition range.

Darken [3] also introduced the concept of excess stability for analysis of the binary solutions. The excess stability function, ψ, is defined as follows:

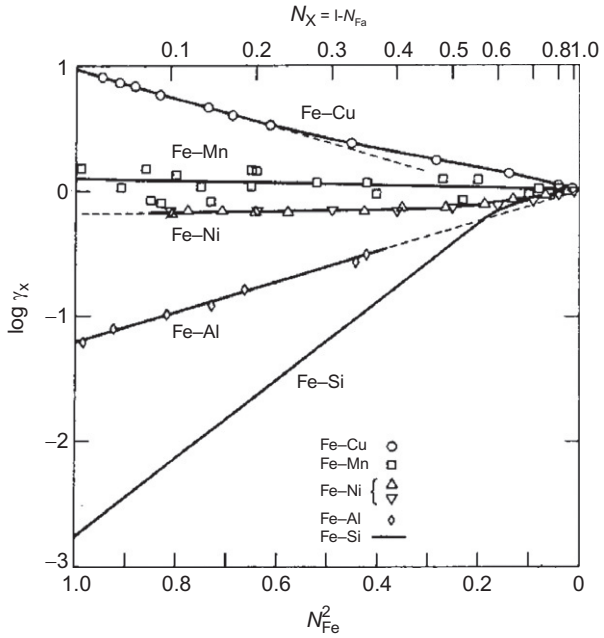


Figure 3.4.3 The activity coefficient of X in liquid Fe–X alloys [3].

$$\psi = \frac{\mathrm{d}^2 G^E}{\mathrm{d}X_1^2} = \frac{\mathrm{d}^2 G^E}{\mathrm{d}X_2^2} = -2\frac{\mathrm{d}G_1^E}{\mathrm{d}(X_2^2)} = -2\frac{\mathrm{d}G_2^E}{\mathrm{d}(X_1^2)}$$
$$= -4.605RT\frac{\mathrm{d}\log\gamma_1}{\mathrm{d}(X_2^2)} = -4.605RT\frac{\mathrm{d}\log\gamma_2}{\mathrm{d}(X_1^2)} \qquad (3.4.60)$$

For the systems having strong interaction, the excess stability has large values and exhibits a maximum close to the composition corresponding to intermetallic compound.

REFERENCES

[1] J.H. Hildebrand, J. Am. Chem. Soc. 51 (1929) 66.
[2] M. Margules, Sitzungber. Kaiser. Akadem. Wissenschaft. Wien. Mathmatisch- Naturwiss. Class. 104 (1895) 1243.
[3] L.S. Darken, Trans. Met. Soc. AIME 239 (1967) 80.

CHAPTER 3.5

Thermodynamic Basis for Phase Diagrams

Masakatsu Hasegawa
Graduate School of Energy Science, Kyoto University

3.5.1. GIBBS ENERGY OF BINARY SOLUTIONS

The Gibbs energy of a binary solution consisting of n_A moles of A and n_B moles of B can be expressed as:

$$G^* = n_A G_A + n_B G_B \tag{3.5.1}$$

where G_i is called the partial molar Gibbs energy of component i, and is defined by

$$G_i = (\partial G^*/\partial n_i)_{T,P,nj\,(j\neq i)} \tag{3.5.2}$$

Since this solution contains $(n_A + n_B)$ moles of the components, the Gibbs energy of 1 mol of this solution, G, is given by the following equation:

$$G = \frac{G^*}{(n_A + n_B)} = X_A G_A + X_B G_B \tag{3.5.3}$$

The change of the Gibbs energy between a mechanical mixture and a solution of an identical composition is called the integral Gibbs energy of mixing, G^M:

$$\begin{aligned} G^M &= G - \left(X_A G_A^\circ + X_B G_B^\circ\right) = X_A\left(G_A - G_A^\circ\right) + X_B\left(G_B - G_B^\circ\right) \\ &= H^M - TS^M \end{aligned} \tag{3.5.4}$$

where G_i° represents the Gibbs energy of component i in the standard state. Figure 3.5.1 shows the schematic dependences of the Gibbs energy, enthalpy and entropy of mixing on the composition at constant temperature and external pressure, when A–B binary solutions form from pure substances of A and B without any phase transformations. For such mixing, S^M should be positive and the value for H^M is negative (Figure 3.5.1a) when the interatomic interaction increases during mixing, while it is positive (Figure 3.5.1b) if the interaction decreases. For solutions which form spontaneously, the values for G^M should be negative. Based on the considerations above, the conditions in which solutions can form are illustrated by the hatched areas in Figure 3.5.2.

Treatise on Process Metallurgy, Volume 1
http://dx.doi.org/10.1016/B978-0-08-096986-2.00003-5
© 2014 Elsevier Ltd.
All rights reserved.

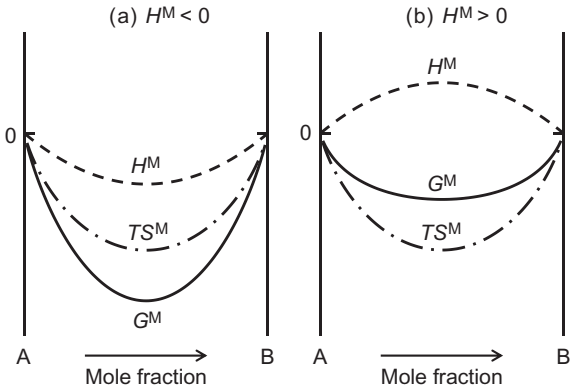


Figure 3.5.1 Schematic variation of the Gibbs energy, enthalpy and entropy of mixing with composition in a binary system at constant temperature and external pressure.

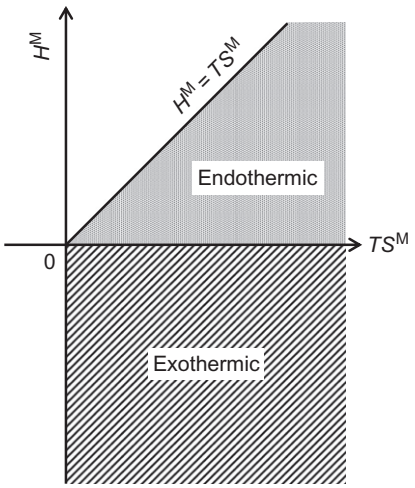


Figure 3.5.2 Illustration of the conditions in which solutions can form spontaneously.

The integral Gibbs energy of mixing can be also expressed by using the relative partial molar Gibbs energy of component i, $\overline{G}_i$:

$$G^M = X_A \overline{G}_A + X_B \overline{G}_B \tag{3.5.5}$$

For a binary solution consisting of n_A moles of A and n_B moles of B, $\overline{G}_B$ can be given by:

$$\begin{aligned}\overline{G}_{\mathrm{B}} &= G_{\mathrm{B}} - G_{\mathrm{B}}^{\circ} \\ &= \left(\frac{\partial[(n_{\mathrm{A}}+n_{\mathrm{B}})G^{\mathrm{M}}]}{\partial n_{\mathrm{B}}}\right)_{T,p,n_{\mathrm{A}}} \\ &= G^{\mathrm{M}} + (n_{\mathrm{A}}+n_{\mathrm{B}}) \times \left(\frac{\partial G^{\mathrm{M}}}{\partial X_{\mathrm{B}}}\right)_{T,p} \times \left(\frac{\partial X_{\mathrm{B}}}{\partial n_{\mathrm{B}}}\right)_{n_{\mathrm{A}}} \\ &= G^{\mathrm{M}} + (1-X_{\mathrm{B}})\left(\frac{\partial G^{\mathrm{M}}}{\partial X_{\mathrm{B}}}\right)_{T,p}\end{aligned} \tag{3.5.6}$$

In analogy with $\overline{G}_{\mathrm{B}}$, $\overline{G}_{\mathrm{A}}$ can be expressed as:

$$\begin{aligned}\overline{G}_{\mathrm{A}} &= G_{\mathrm{A}} - G_{\mathrm{A}}^{\circ} \\ &= \left(\frac{\partial[(n_{\mathrm{A}}+n_{\mathrm{B}})G^{\mathrm{M}}]}{\partial n_{\mathrm{A}}}\right)_{T,p,n_{\mathrm{B}}} \\ &= G^{\mathrm{M}} + (n_{\mathrm{A}}+n_{\mathrm{B}}) \times \left(\frac{\partial G^{\mathrm{M}}}{\partial X_{\mathrm{B}}}\right)_{T,p} \times \left(\frac{\partial X_{\mathrm{B}}}{\partial n_{\mathrm{B}}}\right)_{n_{\mathrm{B}}} \\ &= G^{\mathrm{M}} - X_{\mathrm{B}}\left(\frac{\partial G^{\mathrm{M}}}{\partial X_{\mathrm{B}}}\right)_{T,p}\end{aligned} \tag{3.5.7}$$

Equations (3.5.6) and (3.5.7) imply that the relative partial molar Gibbs energies can be obtained from the integral Gibbs energy of mixing by illustrating the tangent, as shown in Figure 3.5.3. The intercepts of the tangent at $X_{\mathrm{B}} = 0$ and 1 correspond to $\overline{G}_{\mathrm{A}}$ and $\overline{G}_{\mathrm{B}}$,

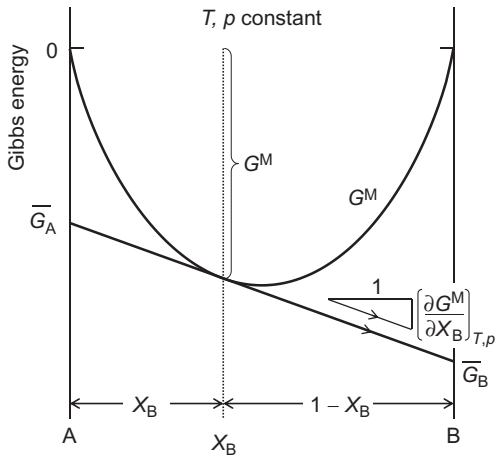


Figure 3.5.3 Correlation of the integral Gibbs energy of mixing and the relative partial molar Gibbs energies of the components.

respectively, for the solution of the composition corresponding to the contact point of the tangent. Then, the activities of components in the solution can be calculated by:

$$a_{\mathrm{A}} = \exp\left(\frac{\overline{G}_{\mathrm{A}}}{RT}\right) \tag{3.5.8}$$

$$a_{\mathrm{B}} = \exp\left(\frac{\overline{G}_{\mathrm{B}}}{RT}\right) \tag{3.5.9}$$

Phase diagrams show graphically thermochemical properties of solutions, and they are helpful in predicting phase transformations and resulting microstructures. Since external pressure remains constant in most applications, the relationships between phase diagrams and Gibbs energies at a constant pressure will be discussed in the following sections.

3.5.2. BINARY ISOMORPHOUS SYSTEM

Figure 3.5.4a shows a schematic phase diagram of a binary isomorphous system, which is characterized by complete solubilities in both liquid and solid phases. At temperatures below the melting point of B, T_{B}, A and B form substitutional solid solutions at all compositions. Complete solid solubility requires that components A and B have the same crystal structure, similar atomic size, electronegativity, and valency. If any of these conditions are not met, a miscibility gap will occur in the solid state. As shown in this figure, the solid solution of composition X_{SS} is in equilibrium with the liquid phase of composition X_{L} at temperature T_1.

Figure 3.5.4b illustrates the integral Gibbs energies of mixing and the relative partial molar Gibbs energies as functions of composition at T_1, which is lower than the melting point of A, T_{A}, while higher than the melting point of B, T_{B}. So, at T_1, the most stable states of components A and B are solid and liquid, respectively, and they are taken as the standard states. Complete solid solubility implies that the integral Gibbs energy of mixing for solid solutions, $G^{\mathrm{M}}_{(\mathrm{SS})}$, could be drawn by a curve connecting pure solid A and super-heated pure solid B. Similarly, the integral Gibbs energy of mixing of liquid phase, $G^{\mathrm{M}}_{(\mathrm{L})}$, starts from super-cooled pure liquid A and pure liquid B. In the two-phase coexistence of solid and liquid solutions, the relative partial molar Gibbs energies should be equal in both phases:

$$\overline{G}_{\mathrm{A}}(\text{in solid phase of } X_{\mathrm{SS}}) = \overline{G}_{\mathrm{A}}(\text{in liquid phase of } X_{\mathrm{L}}) \tag{3.5.10}$$

$$\overline{G}_{\mathrm{B}}(\text{in solid phase of } X_{\mathrm{SS}}) = \overline{G}_{\mathrm{B}}(\text{in liquid phase of } X_{\mathrm{L}}) \tag{3.5.11}$$

These requirements are equivalent to the condition of the common tangent; as shown in Figure 3.5.4b, point *a* on $G^{\mathrm{M}}_{(\mathrm{SS})}$ and point *b* on $G^{\mathrm{M}}_{(\mathrm{L})}$ correspond to the contact points of the common tangent. Solutions with $0 < X_{\mathrm{B}} < X_{\mathrm{SS}}$ are solid because $G^{\mathrm{M}}_{(\mathrm{SS})} < G^{\mathrm{M}}_{(\mathrm{L})}$ in this composition range. Similarly, solutions with $X_{\mathrm{L}} < X_{\mathrm{B}} < 1$ are liquid as $G^{\mathrm{M}}_{(\mathrm{L})} < G^{\mathrm{M}}_{(\mathrm{SS})}$. In the

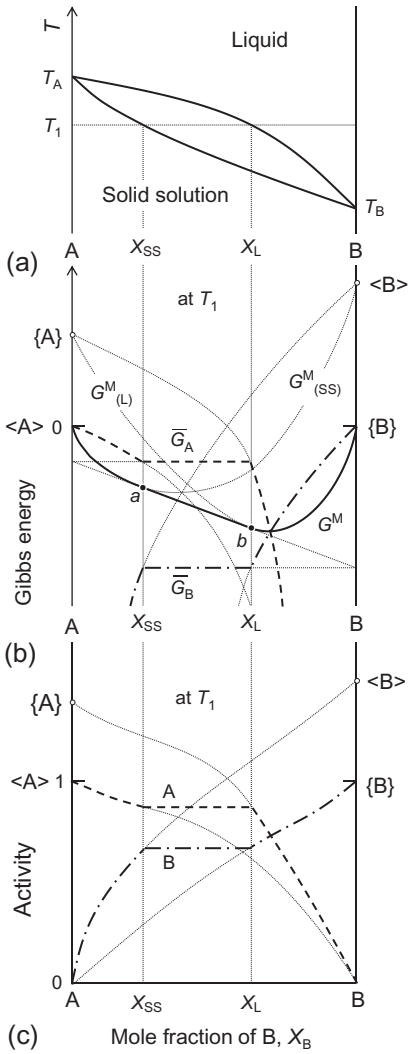


Figure 3.5.4 (a) Schematic phase diagram of a binary isomorphous system. (b) The molar Gibbs energies as functions of composition at T_1. (c) Activity-composition curves at T_1.

region $X_{SS} < X_B < X_L$, the two-phase assemblage of solid and liquid solutions have a lower Gibbs energy than the solid or liquid phase of an identical composition. Therefore, the integral Gibbs energies of mixing at T_1 lay on the solid line <A>–*a*–*b*–{B}. The relative partial molar Gibbs energies of components A and B are shown by the broken and dash-dotted lines, respectively.

Figure 3.5.4c gives the activity–composition curves at T_1. The activities are constant in the two-phase region. It could be noted here that the value obtained by extrapolating

the activity curve of A in the liquid phase to $X_B = 0$ corresponds to the activity of the super-cooled pure liquid A at T_1, which can be calculated by the following equation:

$$RT_1 \ln a_A = G\{A\}^\circ - G\langle A\rangle^\circ = \Delta H_{FA}\left(1 - \frac{T_1}{T_A}\right) \tag{3.5.12}$$

where ΔH_{FA} represents the heat of fusion of A, and in this equation, the difference between the heat capacity of pure solid A and that of pure liquid A is considered to be negligible. Similarly, the activity of the super-heated pure solid B at T_1 is graphically given by extrapolating the activity curve of B in the solid phase to $X_B = 1$, and it can be evaluated by:

$$RT_1 \ln a_B = G\langle B\rangle^\circ - G\{B\}^\circ = -\Delta H_{FB}\left(1 - \frac{T_1}{T_B}\right) \tag{3.5.13}$$

Figure 3.5.5 shows schematically the integral Gibbs energy, enthalpy and entropy of mixing for this binary isomorphous system at T_1. The subscripts of (SS) and (L) mean the quantities of solid and liquid solutions, respectively, and the solid lines represent the values of all solutions in equilibrium at T_1. Assuming that both solid and liquid solutions are ideal, Equations (3.5.10) and (3.5.11) can be rewritten as:

$$G\langle A\rangle^\circ + RT_1 \ln(1 - X_{SS}) = G\{A\}^\circ + RT_1 \ln(1 - X_L) \tag{3.5.14}$$

$$G\langle B\rangle^\circ + RT_1 \ln X_{SS} = G\{B\}^\circ + RT_1 \ln X_L \tag{3.5.15}$$

Combining Equations (3.5.12)–(3.5.15), we have

$$X_L = \frac{\left[1 - \exp\left\{\frac{\Delta H_{FA}\left(1 - \frac{T_1}{T_A}\right)}{RT_1}\right\}\right]}{\left[\exp\left\{\frac{\Delta H_{FB}\left(1 - \frac{T_1}{T_B}\right)}{RT_1}\right\} - \exp\left\{\frac{\Delta H_{FA}\left(1 - \frac{T_1}{T_A}\right)}{RT_1}\right\}\right]} \tag{3.5.16}$$

$$X_{SS} = X_L \exp\left[\frac{\Delta H_{FB}\left(1 - \frac{T_1}{T_B}\right)}{RT_1}\right] \tag{3.5.17}$$

Based on these results, the solidus and liquidus lines in isomorphous systems can be calculated when the ideal solution models can be applied to both the solid and liquid solutions.

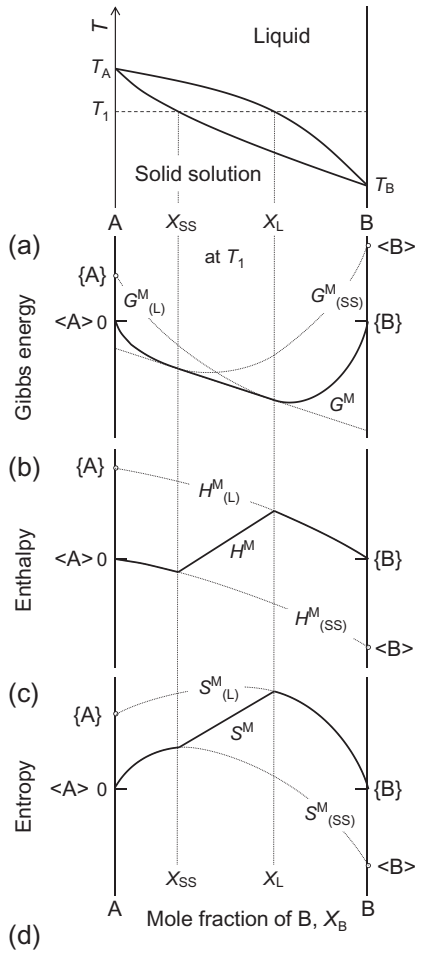


Figure 3.5.5 (a) Schematic phase diagram of a binary isomorphous system. (b) Relation between the integral Gibbs energy of mixing and composition at T_1. (c) Relation between the integral enthalpy of mixing and composition at T_1. (d) Relation between the integral entropy of mixing and composition at T_1.

3.5.3. BINARY EUTECTIC SYSTEM

Figure 3.5.6a shows a phase diagram for a binary eutectic system. Consider the situation that the homogeneous liquid phase of composition Y is cooled very slowly and phase equilibria are continuously maintained. Precipitation of solid phase α begins when the temperature reaches the liquidus line at T_1, and the liquid phase is enriched in B during crystallization. With continued cooling, the compositions of the solid and liquid phases follow the solidus and liquidus lines, respectively. At T_2, the composition

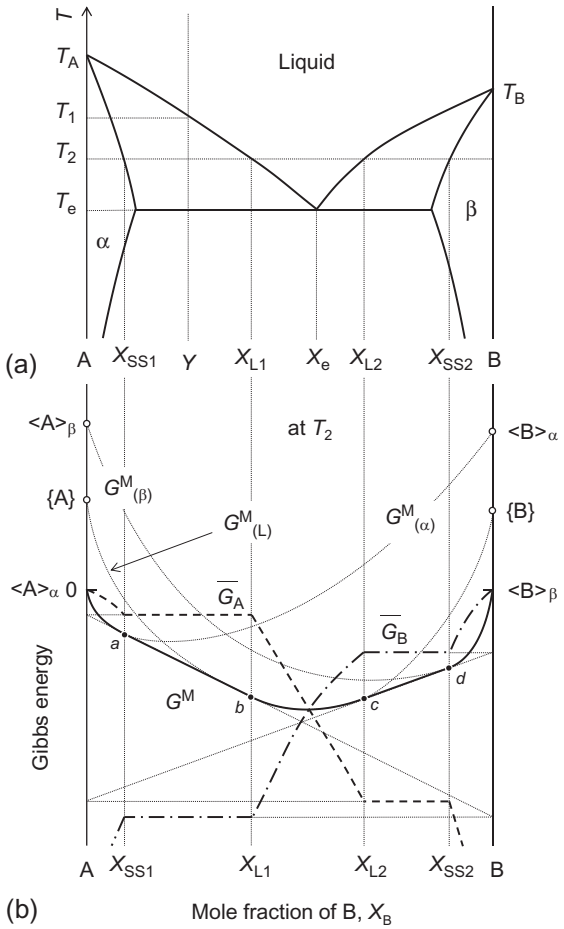


Figure 3.5.6 (a) Schematic phase diagram of a binary eutectic system. (b) The molar Gibbs energies as functions of composition at T_2 based on the assumption that solid phases α and β have different crystal structures.

of solid α in equilibrium with the liquid of X_{L1} is X_{SS1}, which is given by the tie line, and the fractions of the phases can be determined according to the lever rule:

$$\text{Fraction of}\,\alpha = \frac{(X_{L1} - Y)}{(X_{L1} - X_{SS1})} \tag{3.5.18}$$

$$\text{Fraction of Liquid} = \frac{(Y - X_{SS1})}{(X_{L1} - X_{SS1})} \tag{3.5.19}$$

As temperature is lowered to the eutectic temperature, T_e, the liquid phase is of the eutectic composition, X_e, and then is transformed into two-solid phases α and β simultaneously. This eutectic reaction proceeds to completion at the constant

temperature T_e. The resulting microstructure consisting of alternating layers of α and β phases is called eutectic structure.

Figure 3.5.6b shows the integral Gibbs energies of mixing and the relative partial molar Gibbs energies as functions of composition at T_2. As seen in Figure 3.5.6a, the liquid phase of X_{L1} coexists with the solid phase α of X_{SS1}, while the liquid phase of X_{L2} is in equilibrium with the solid phase β of X_{SS2}:

$$\overline{G}_A(\text{in}\,\alpha\,\text{of}\,X_{SS1}) = \overline{G}_A(\text{in Liquid of}\,X_{L1}) \tag{3.5.20}$$

$$\overline{G}_B(\text{in}\,\alpha\,\text{of}\,X_{SS1}) = \overline{G}_B(\text{in Liquid of}\,X_{L1}) \tag{3.5.21}$$

$$\overline{G}_A(\text{in}\,\beta\,\text{of}\,X_{SS2}) = \overline{G}_A(\text{in Liquid of}\,X_{L2}) \tag{3.5.22}$$

$$\overline{G}_B(\text{in}\,\beta\,\text{of}\,X_{SS2}) = \overline{G}_B(\text{in Liquid of}\,X_{L2}) \tag{3.5.23}$$

Figure 3.5.6b is based on the assumption that solid phases α and β have different crystal structures. The integral Gibbs energy of mixing for α, $G^M_{(\alpha)}$, could be drawn by a curve connecting stable pure solid A, $<A>_\alpha$, and hypothetical pure solid B having the same crystal structure as α, $<B>_\alpha$. Similarly, the integral Gibbs energy of mixing for β, $G^M_{(\beta)}$, starts from stable pure solid B, $<B>_\beta$, and hypothetical pure solid A of the same crystal structure as β, $<A>_\beta$. The integral Gibbs energies of mixing of all phases in equilibrium at T_2 lie on the solid line $<A>_\alpha$–*a*–*b*–*c*–*d*–$<B>_\beta$, and the broken and dash-dotted lines represent $\overline{G}_A$ and $\overline{G}_B$, respectively.

On the other hand, Figure 3.5.7b is based on the assumption that solid phases α and β have the same crystal structure. In this case, the integral Gibbs energy of mixing for the solid solutions, $G^M_{(SS)}$, is given by one curve connecting $<A>_\alpha$ and $<B>_\beta$. When regular solution models can be applied to both of the solid and liquid solutions, Equations (3.5.20)–(3.5.23) can be replaced by the following two expressions:

$$G\langle A\rangle^\circ + RT_2\ln(1-X_{SS}) + \Omega_{SS}X_{SS}^2 = G\{A\}^\circ + RT_2\ln(1-X_L) + \Omega_L X_L^2 \tag{3.5.24}$$

$$G\langle B\rangle^\circ + RT_2\ln X_{SS} + \Omega_{SS}(1-X_{SS})^2 = G\{B\}^\circ + RT_2\ln X_L + \Omega_L(1-X_L)^2 \tag{3.5.25}$$

In these equations, Ω_{SS} and Ω_L represent the interaction parameters of the regular solution models applied to the solid and liquid solutions, respectively, and are independent of temperature and composition. When the values for these parameters are given, the solidus and liquidus lines, which indicate the relationships between temperature and composition, can be calculated by solving Equations (3.5.24) and (3.5.25) simultaneously.

3.5.4. BINARY MONOTECTIC AND PERITECTIC SYSTEMS

Figure 3.5.8a gives a schematic phase diagram for a binary monotectic system, which is characterized by a liquid miscibility gap. When the homogeneous liquid of

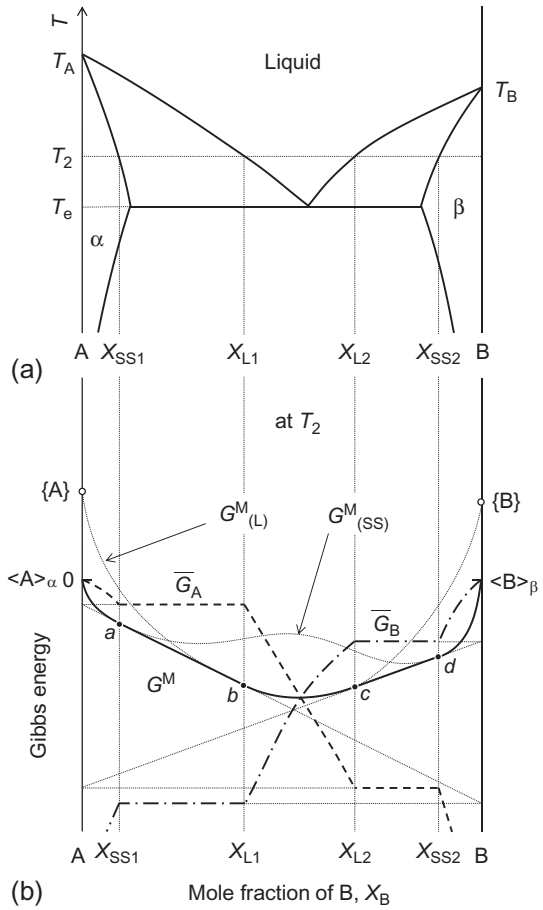


Figure 3.5.7 (a) Schematic phase diagram of a binary eutectic system. (b) The molar Gibbs energies as functions of composition at T_2 based on the assumption that solid phases α and β have the same crystal structures.

composition X_{L2} is cooled, phase separation into two immiscible liquids of compositions X_{L2} and X_{L3} occurs at temperature T_1. In this diagram, the highest temperature at which such phase separations occur is called the critical temperature and is represented by T_C in Figure 3.5.8a. When liquid solutions exhibit regular solution behavior, the integral Gibbs energy of mixing, $G^M_{(L)}$, is given by:

$$G^M_{(L)} = RT[(1-X_B)\ln(1-X_B) + X_B \ln X_B] + \Omega X_B(1-X_B) \tag{3.5.26}$$

and the relation between the interaction parameter Ω and T_C can be derived as follows. The second derivative of $G^M_{(L)}$ by X_B is:

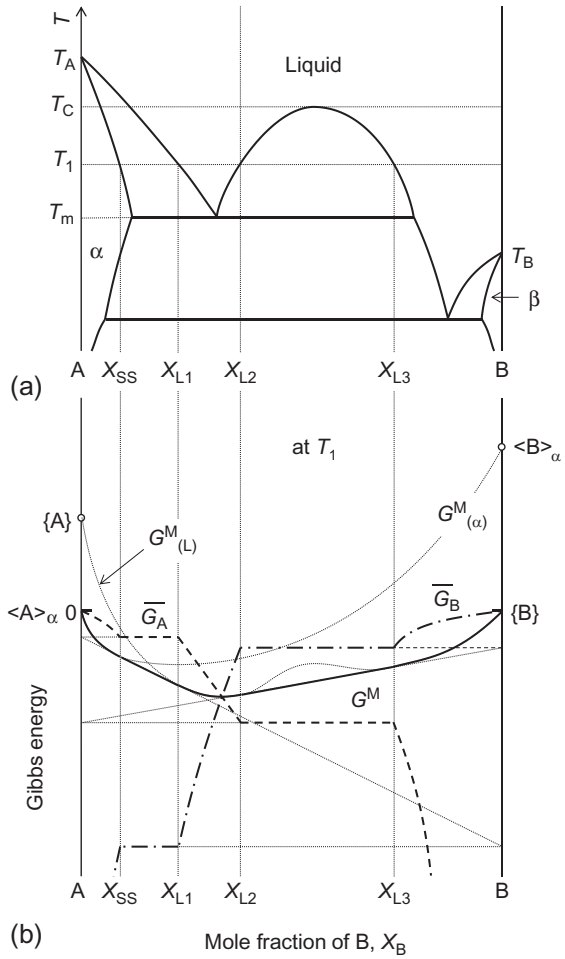


Figure 3.5.8 (a) Schematic phase diagram of a binary monotectic system. (b) The molar Gibbs energies as functions of composition at T_1.

$$\frac{\mathrm{d}^2 G^{\mathrm{M}}_{(\mathrm{L})}}{\mathrm{d}X_{\mathrm{B}}^2} = RT\left[\frac{1}{X_{\mathrm{B}}} + \frac{1}{(1-X_{\mathrm{B}})}\right] - 2\Omega \tag{3.5.27}$$

At T_C, $\frac{\mathrm{d}^2 G^{\mathrm{M}}_{(\mathrm{L})}}{\mathrm{d}X_{\mathrm{B}}^2} = 0$ has only one real root:

$$\frac{\mathrm{d}^2 G^{\mathrm{M}}_{(\mathrm{L})}}{\mathrm{d}X_{\mathrm{B}}^2} = 0 \tag{3.5.28}$$

$$X_{\mathrm{B}}^2 - X_{\mathrm{B}} + \frac{RT_{\mathrm{C}}}{(2\Omega)} = 0 \tag{3.5.29}$$

Thus, the discriminant of this quadratic equation, D, should be zero:

$$D = 1 - \frac{2RT_C}{\Omega} = 0 \tag{3.5.30}$$

and

$$T_C = \frac{\Omega}{(2R)} \tag{3.5.31}$$

Figure 3.5.8b shows G^M, $\overline{G}_A$, and $\overline{G}_B$ as functions of composition at T_1, which is located between T_C and the monotectic temperature, T_m.

Figure 3.5.9 shows a phase diagram of a binary peritectic system and the Gibbs energies at T_1, which is lower than the peritectic temperature, T_p.

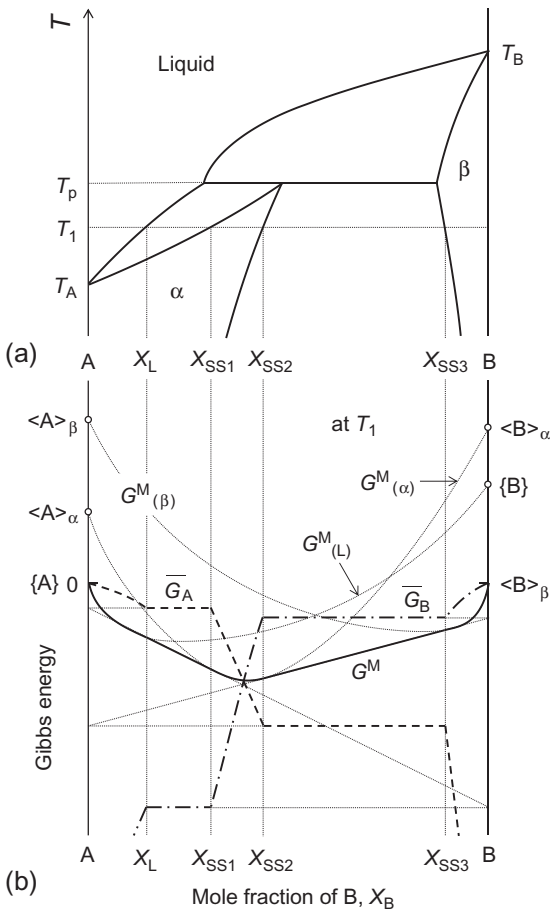


Figure 3.5.9 (a) Schematic phase diagram of a binary peritectic system. (b) The molar Gibbs energies as functions of composition at T_1.

3.5.5. BINARY SYSTEM INCLUDING AN INTERMEDIATE COMPOUND

The standard Gibbs energy change during the formation of 1 mol of the stoichiometric compound A_mB_n from pure solid A and B, $\Delta G^\circ_{A_mB_n}$, can be given as follows:

$$mA + nB = A_mB_n \tag{3.5.32}$$

$$\Delta G^\circ_{A_mB_n} = G\langle A_mB_n\rangle^\circ - mG\langle A\rangle^\circ - nG\langle B\rangle^\circ \tag{3.5.33}$$

When the intermediate compound A_mB_n is regarded as the binary solid solution of the identical composition, there are $(m+n)$ moles of the components in 1 mol of A_mB_n. Therefore, the integral Gibbs energy of mixing for A_mB_n is considered to be $\Delta G^\circ_{A_mB_n}/(m+n)$.

A schematic phase diagram including one congruently melting compound and negligible solubilities in the solid phases is shown in Figure 3.5.10b. Figure 3.5.10a and c illustrate the relations between the Gibbs energies of 1 mol of solutions and composition at temperatures T_1 and T_2, respectively. If the temperature under consideration is higher than the melting point of the compound, for example, T_1, the liquid phase is more stable than the compound. In this case, the value for $\Delta G^\circ_{A_mB_n}/(m+n)$ represented by point *a* must be higher than the G^M for the liquid phase of the same composition (point *b*). On the other hand, at T_2, which is lower than the melting point of the compound, the compound is stable relative to the liquid phase; $\Delta G^\circ_{A_mB_n}/(m+n)$ should be lower than the G^M of the liquid. Then, the compositions of the liquid phase in equilibrium with this intermediate compound can be determined by constructing the tangents through point *a*, as seen in Figure 3.5.10c. This figure also shows that the values for $\overline{G}_A$ and $\overline{G}_B$ change drastically within the extremely narrow composition range of the stoichiometric compound.

Figure 3.5.11b gives a schematic phase diagram including one incongruent melting compound, which decomposes into solid A and the liquid at T_d. In analogy with Figure 3.5.10, Figure 3.5.11a shows the Gibbs energies as functions of the compounds at T_1 higher than T_d, while Figure 3.5.11c presents them at T_2 lower than T_d. The melting points of the components, interatomic interactions of the components in the liquid phase and the standard Gibbs energy change of the formation of the compound decide whether the compound melts congruently or incongruently.

3.5.6. CONSISTENCY OF PHASE DIAGRAM AND THERMOCHEMICAL DATA OF THE BINARY SYSTEM CaO–SiO_2

Figure 3.5.12a shows the currently accepted phase diagram for the binary system CaO–SiO_2 [1]. As can be seen in this diagram, this system has the following double oxides:

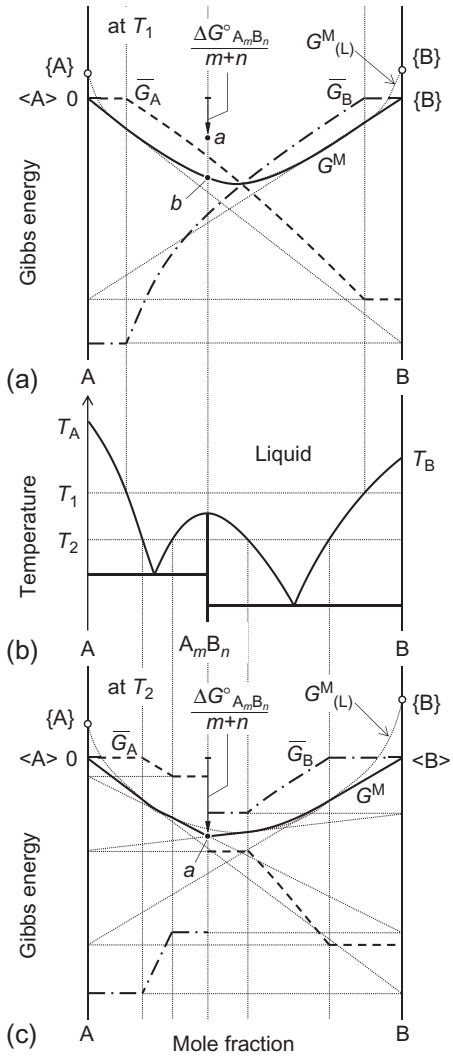


Figure 3.5.10 (a) The molar Gibbs energies as functions of composition at T_1. (b) Schematic phase diagram including one congruently melting compound. (c) The molar Gibbs energies as functions of composition at T_2.

$Ca_3SiO_5 = 3CaO{\cdot}SiO_2 = C_3S$
$Ca_2SiO_4 = 2CaO{\cdot}SiO_2 = C_2S$
$Ca_3Si_2O_7 = 3CaO{\cdot}2SiO_2 = C_3S_2$
$CaSiO_3 = CaO{\cdot}SiO_2 = CS$

For example, the SiO_2 activity within the two-phase assemblage of $CaO + Ca_3SiO_5$ at temperature T can be calculated by using thermal data.

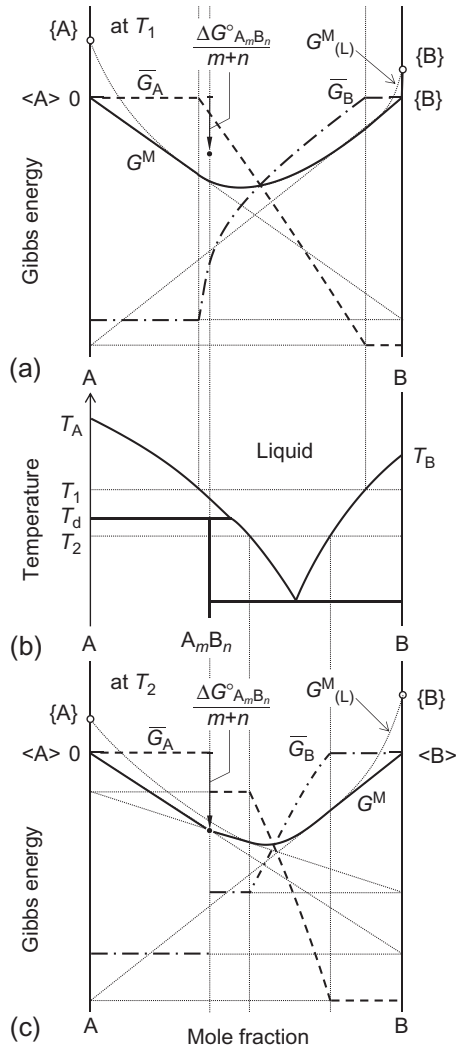


Figure 3.5.11 (a) The molar Gibbs energies as functions of composition at T_1. (b) Schematic phase diagram including one incongruently melting compound. (c) The molar Gibbs energies as functions of composition at T_2.

$$3\mathrm{CaO} + \mathrm{SiO_2} = \mathrm{Ca_3SiO_5} \tag{3.5.34}$$

$$\begin{aligned} \mathrm{RT}\ln[a_{\mathrm{SiO_2}}(\mathrm{CaO}+C_3S)] &= \Delta G^\circ(3.5.34,T) = G^\circ(C_3S) - 3G^\circ(\mathrm{CaO}) - G^\circ(\mathrm{SiO_2}) \\ &= \{H_{298}(C_3S) + \Delta H(C_3S) - 3H_{298}(\mathrm{CaO}) - 3\Delta H(\mathrm{CaO}) - H_{298}(\mathrm{SiO_2}) - \Delta H(\mathrm{SiO_2})\} \\ &\quad - T\{S_{298}(C_3S) + \Delta S(C_3S) - 3S_{298}(\mathrm{CaO}) - 3\Delta S(\mathrm{CaO}) - S_{298}(\mathrm{SiO_2}) - \Delta S(\mathrm{SiO_2})\} \end{aligned} \tag{3.5.35}$$

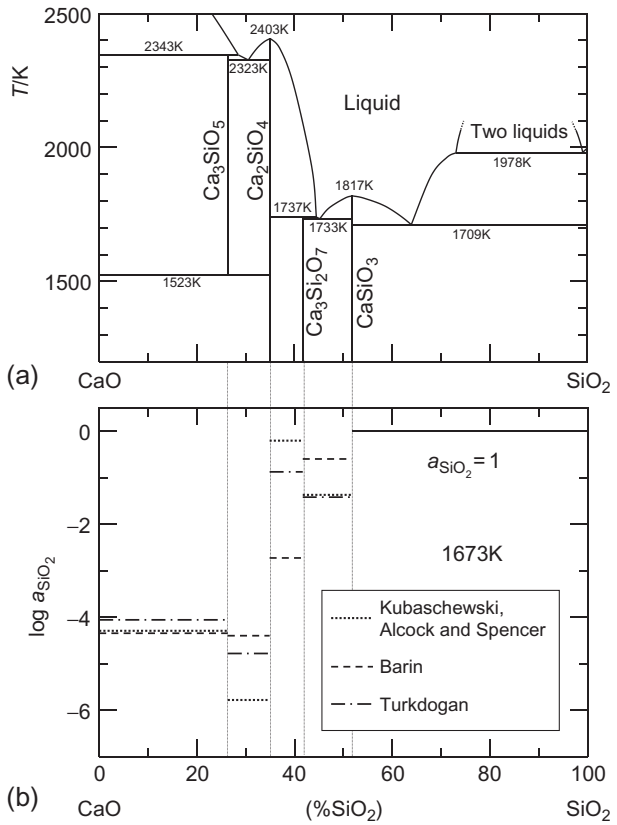


Figure 3.5.12 (a) Phase diagram of the binary system CaO–SiO_2. (b) Activities of SiO_2 in two-phase regions calculated by using the literature data.

where $\Delta G^\circ(i,\ T)$ is the standard Gibbs energy change of reaction i at temperature T, and $G^\circ(j)$ is the standard Gibbs energy of pure substance j. In this section, the standard state of the pure substance j is always taken to be the most stable phase at the temperature under consideration. The symbols of $H_{298}(j)$ and $S_{298}(j)$ represent the standard enthalpy and entropy of pure substance j at 298 K, respectively, and $\Delta H(j)$ and $\Delta S(j)$ denote the changes of standard enthalpy and entropy between 298 K and temperature T. The values for $\Delta H(j)$ and $\Delta S(j)$ can be calculated by using heat capacities, and heats and temperatures of phase transformations. Values for a_{SiO_2} within the two-phase regions at 1673 K can be calculated by using thermal and thermodynamic data taken from Kubaschewski, Alcock, and Spencer [2], Barin [3] and Turkdogan [4], as shown in Figure 3.5.12b. From thermodynamic point of view, the following inequality should hold:

$$a_{SiO_2}(CaO + C_3S) < a_{SiO_2}(C_3S + C_2S) \tag{3.5.36}$$

Nevertheless, calculated values for $a_{SiO_2}(CaO + C_3S)$and $a_{SiO_2}(C_3S + C_2S)$ do not satisfy this inequality; this could be due to errors in the thermal data.

Table 3.5.1 gives the compilation of thermal data cited from Kubaschewski *et al.* [2] By using these data, the CaO and SiO_2 activities can be calculated for the two-phase regions in the binary system CaO–SiO_2, and Figure 3.5.13 shows the median values and uncertainty ranges by dotted lines and error bars, respectively. In this figure, the compositions are illustrated schematically. As seen in Figure 3.5.13d, the median values for activities represented by dotted lines did not satisfy Inequality (3.5.36), while there was a possibility of deriving thermodynamically consistent values within the uncertainty ranges. Therefore, in this section, the thermal data by Kubaschewski *et al.* [2] were accepted on heat and temperature of phase transformation, and heat capacity. On the other hand, values for enthalpy and entropy at 298 K were adapted within their accuracies reported by Kubaschewski *et al.* [2] to the phase diagram.

The phase diagram of the CaO–SiO_2 binary system [1], shown in Figure 3.5.12a, indicates that Ca_3SiO_5 decomposes to CaO and Ca_2SiO_4, at temperatures below 1523 K. Then, thermodynamic consideration of the phase relations requires that Inequalities (3.5.37) through (3.5.42) should hold.

$$\begin{aligned} &a_{CaO}(CaO + C_2S) = 1 > a_{CaO}(C_2S + C_3S_2) \\ &> a_{CaO}(C_3S_2 + CS) > a_{CaO}(CS + SiO_2) \quad T < 1523\,K \end{aligned} \tag{3.5.37}$$

$$\begin{aligned} &a_{CaO}(CaO + C_3S) = a_{CaO}(C_3S + C_2S) = a_{CaO}(CaO + C_2S) = 1 > a_{CaO}(C_2S + C_3S_2) \\ &> a_{CaO}(C_3S_2 + CS) > a_{CaO}(CS + SiO_2) \quad T = 1523\,K \end{aligned} \tag{3.5.38}$$

$$\begin{aligned} &a_{CaO}(CaO + C_3S) = 1 > a_{CaO}(C_3S + C_2S) > a_{CaO}(C_2S + C_3S_2) \\ &> a_{CaO}(C_3S_2 + CS) > a_{CaO}(CS + SiO_2) \quad T > 1523\,K \end{aligned} \tag{3.5.39}$$

$$\begin{aligned} &a_{SiO_2}(CaO + C_2S) < a_{SiO_2}(C_2S + C_3S_2) \\ &< a_{SiO_2}(C_3S_2 + CS) < a_{SiO_2}(CS + SiO_2) = 1 \quad T < 1523\,K \end{aligned} \tag{3.5.40}$$

$$\begin{aligned} &a_{SiO_2}(CaO + C_3S) = a_{SiO_2}(C_3S + C_2S) = a_{SiO_2}(CaO + C_2S) < a_{SiO_2}(C_2S + C_3S_2) \\ &< a_{SiO_2}(C_3S_2 + CS) < a_{SiO_2}(CS + SiO_2) = 1 \quad T = 1523\,K \end{aligned} \tag{3.5.41}$$

$$\begin{aligned} &a_{SiO_2}(CaO + C_3S) < a_{SiO_2}(C_3S + C_2S) < a_{SiO_2}(C_2S + C_3S_2) \\ &< a_{SiO_2}(C_3S_2 + CS) < a_{SiO_2}(CS + SiO_2) = 1 \quad T > 1523\,K \end{aligned} \tag{3.5.42}$$

Table 3.5.1 gives the result of the present modification [5], and Figure 3.5.13 shows the modified values of the CaO and SiO_2 activities at 1673, 1523, and 1273 K by solid lines, and the hatched areas represent the ranges of uncertainties. As seen in this figure, the modified results for all of the two-phase regions were consistent thermodynamically with each other. This figure also indicates that the CaO and SiO_2 activities change drastically at the CaO/SiO_2 molar ratio of 2, that is, Ca_2SiO_4. This is in accord with the view that, in

Table 3.5.1 Thermal Data for Pure Substances in the Binary System $CaO–SiO_2$

Substance	H_{298} (kJ mol^{-1})		S_{298} (J K^{-1} mol^{-1})		Phase	Temperature Range (K)	Cp = A + BT + CT^{-2} + DT^2 (J K^{-1} mol^{-1})				ΔH_{Tr} (kJ mol^{-1})
	Modified Value	Kubaschewski, Alcock and Spencer	Modified Value	Kubaschewski, Alcock and Spencer			A	B × 10^3	C × 10^{-5}	D × 10^6	
CaO	−634.2	−634.9 ± 0.8	38.4	38.1 ± 0.3	Cubic	298–2900	50.42	4.18	−8.49	–	–
Ca_3SiO_5	−2936.7	−2928.8 ± 7.9	169.9	168.6 ± 1.3		298–	208.57	36.07	−42.47	–	–
Ca_2SiO_4	−2323.0	−2328.4 ± 5.4	119.7	120.5 ± 0.8	Olivin	298–970	133.30	51.80	−19.41	–	–
					Larnit	970–1710	134.56	46.11	–	–	10.9
						1710–	205.02	–	–	–	14.2
$Ca_3Si_2O_7$	−3952.3 ± 2.9	−3942.6 ± 12.6	210.9 ± 1.3	210.9 ± 1.3	Rankin	298–	257.36	55.81	−53.64	–	–
$CaSiO_3$	−1634.0 ± 0.3	−1635.1 ± 2.1	82.6 ± 0.2	83.1 ± 0.8	Wollas	298–1463	111.46	15.06	−27.28	–	–
					ps.wol	1463–1817	108.16	16.48	−23.64	–	5.7
SiO_2 (cristobalite)	−910.0	−908.3 ± 1.7	44.2	43.4 ± 0.8	α-Cris	298–540	46.90	31.51	−10.08	–	–
					β-Cirs	540–2000	71.63	1.88	−39.06	–	1.3
					Liq	2000–	86.19	–	–	–	9.6
SiO_2 (quartz)	–	−910.9 ± 1.7	–	41.5 ± 0.4	α-Qtz	298–847	43.93	38.83	−9.69	–	–
					β-Qtz	847–	58.91	10.04	–	–	0.7

H_{298}, standard enthalpy at 298 K; S_{298}, standard entropy at 298 K; Cp, heat capacity; ΔH_{Tr}, heat of phase transformation.

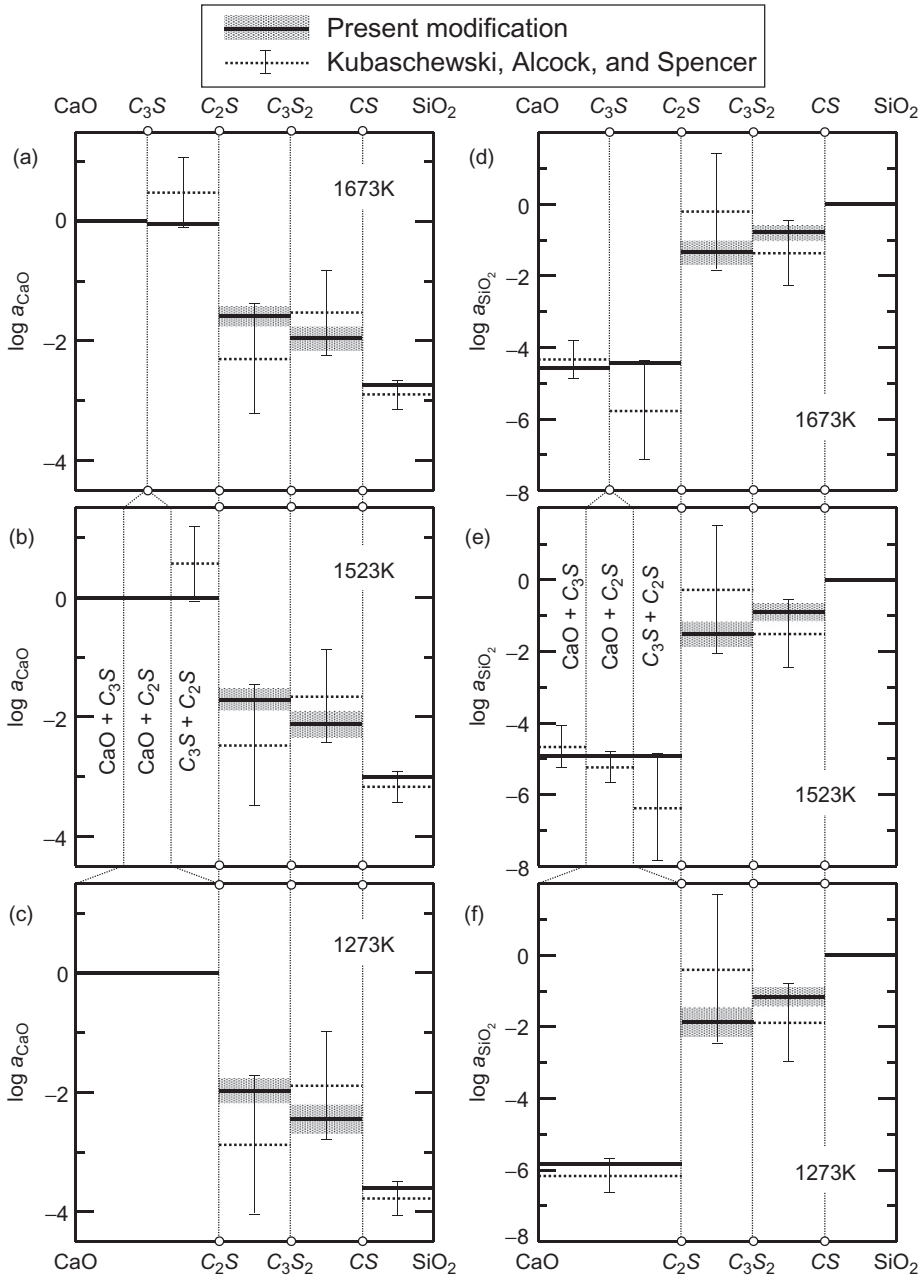


Figure 3.5.13 Activities of CaO and SiO_2 in the binary system CaO–SiO_2.

basic oxide melts with molar ratio $CaO/SiO_2 > 2$, the silicate would exist as SiO_4^{4-} monomers with a low SiO_2 activity relative to that in $Si_2O_7^{6-}$ dimers [6].

Equation (3.5.35) is a very complicated function of temperature. For convenience, the least-squares method applied to $\Delta G^\circ(3.5.34,\ T)$ yielded the following simple equation:

$$\Delta G^\circ(3.5.34,T)/\mathrm{J\,mol^{-1}} = -161{,}900 - 68.88T\log T + 231.1T \quad (1523\,\mathrm{K} - 2000\,\mathrm{K}) \tag{3.5.43}$$

Table 3.5.2 summarizes such regressive formulae and activities of CaO and SiO_2 for the two-phase regions in the binary system CaO–SiO_2 [5]. In this table, $<j>$ and $\{j\}$ denote solid and liquid j, respectively. By using the present regressive formulae in Table 3.5.2, the activities consistent with the phase relations could be obtained at temperatures above 1273 K.

3.5.7. TERNARY PHASE DIAGRAM

In ternary systems, there are four independent state variables, that is, temperature, external pressure, and two compositions. If the external pressure is assumed to be constant, phase relations in a ternary system can be represented three-dimensionally. Figure 3.5.14 shows an example of the three-dimensional phase diagram drawn using the composition triangle–temperature coordinates. This is a simple system with a ternary eutectic point (point d) and complete immiscibilities in the solid state. The three lateral surfaces represent the phase diagrams of the binary systems A–B, B–C, and C–A, and points e, f, and g denote the binary eutectic points. T_i denotes the melting temperature of the component i. Although such three-dimensional representations are helpful to understand phase relationships, it is difficult to obtain quantitative information. For this purpose, a ternary phase diagram is often expressed two-dimensionally by projecting the liquidus surfaces onto the base composition triangle, as given in Figure 3.5.15a.

When a liquid of composition h is cooled very slowly, Figures 3.5.14 and 3.5.15a, precipitation of solid A begins when the temperature reaches the liquidus surface at 1100 K (point h'). The surface T_A–e–d–g–T_A in Figure 3.5.14 represents the temperature and composition of the liquid phase that is in equilibrium with solid A, and the region A–e–d–g–A in Figure 3.5.15a is called the primary crystallization field of A. As the temperature decreases further, solid A continues to precipitate, the liquid solution is therefore depleted in A and the liquid composition changes along the line h'–i. At temperatures below 800 K (point i), both solid A and solid C crystallize together as a binary eutectic mixture, and the liquid composition moves along the curve i–d. Finally, at the ternary eutectic point (point d), solid phases A, B, and C crystallize together and the temperature remains constant until all the liquid has solidified. The boundary curve g–d, which corresponds to the intersection of the two liquidus surfaces (the primary

Table 3.5.2 Regressive Formulae and Activities in the Two-Phase Regions

Reaction	Temperature range (K)	$\Delta G^\circ = A + BT\log T + CT = RT \ln ai$ (J mol^{-1})			log *ai*					
		A	B	C	*i*	1273 K	1473 K	1523 K	1673 K	1873 K
$<CaO> + <Ca_2SiO_4> = <Ca_3SiO_5>$	1523–1710	−10,860	−37.54	+126.5	CaO	–	–	0.00	−0.05	–
	1710–2323	−22,390	−32.54	+117.1	CaO	–	–	–	–	−0.07
$<SiO_2> + 2<CaO> = <Ca_2SiO_4>$	1273–1523	−151,000	−31.34	+104.6	SiO_2	−5.82	−5.08	−4.93	–	–
$<SiO_2> + 3<CaO> = <Ca_3SiO_5>$	1523–2000	−161,900	−68.88	+231.1	SiO_2	–	–	−4.93	−4.58	−4.22
$\{SiO_2\} + 3<CaO> = <Ca_3SiO_5>$	2000–2343	−144,100	−37.42	+118.4	SiO_2	–	–	–	–	–
$<SiO_2> + 2<Ca_3SiO_5> = 3<Ca_2SiO_4>$	1523–1710	−129,300	+43.74	−148.5	SiO_2	–	–	−4.93	−4.43	–
	1710–2000	−94,690	+28.75	−120.3	SiO_2	–	–	–	–	−4.01
$\{SiO_2\} + 2<Ca_3SiO_5> = 3<Ca_2SiO_4>$	2000–2323	−76,890	+60.21	−233.1	SiO_2	–	–	–	–	–
$<CaO> + <Ca_3Si_2O_7> = 2<Ca_2SiO_4>$	1273–1710	−50,810 (±2940)	−19.38	+62.42 (±1.30)	CaO	−1.97 (±0.19)	−1.75 (±0.17)	−1.70 (±0.17)	−1.59 (±0.16)	–
	1710–1737	−27,750 (±2940)	−29.37	+81.22 (±1.30)	CaO	–	–	–	–	–
$<SiO_2> + 3<Ca_2SiO_4> = 2<Ca_3Si_2O_7>$	1273–1710	−49,390 (±5880)	+7.409	−20.28 (±2.60)	SiO_2	−1.88 (±0.38)	−1.58 (±0.34)	−1.52 (±0.34)	−1.35 (±0.32)	–
	1710–1737	−83,970 (±5880)	+22.40	−48.47 (±2.60)	SiO_2	–	–	–	–	–

Continued

Table 3.5.2 Regressive Formulae and Activities in the Two-Phase Regions—cont'd

Reaction	Temperature range (K)	$\Delta G^\circ = A + BT \log T + CT = RT \ln ai$ (J mol^{-1})			log *ai*					
		A	B	C	*i*	1273 K	1473 K	1523 K	1673 K	1873 K
$<CaO> + 2<CaSiO_3> = <Ca_3Si_2O_7>$	1273–1463	−76,310 (±3500)	−51.99	+174.6 (±1.6)	CaO	−2.44 (±0.23)	–	–	–	–
	1463–1733	−66,540 (±3500)	−19.67	+65.58 (±1.62)	CaO	–	−2.19 (±0.21)	−2.13 (±0.20)	−1.96 (±0.19)	–
$<SiO_2> + <Ca_3Si_2O_7> = 3<CaSiO_3>$	1273–1463	−11,130 (±3790)	+56.33	−188.5 (±1.8)	SiO_2	−1.17 (±0.25)	–	–	–	–
	1463–1733	−25,790 (±3790)	+7.856	−25.02 (±1.78)	SiO_2	–	−0.92 (±0.23)	−0.89 (±0.22)	−0.79 (±0.21)	–
$<CaO> + <SiO_2> = <CaSiO_3>$	1273–1463	−87,440 (±280)	+4.341	−13.93 (±0.16)	CaO	−3.61 (±0.02)	–	–	–	–
	1463–1709	−92,330 (±280)	−11.82	+40.56 (±0.16)	CaO	–	−3.11 (±0.02)	−3.01 (±0.02)	−2.75 (±0.02)	–

< >: solid; { }: liquid.

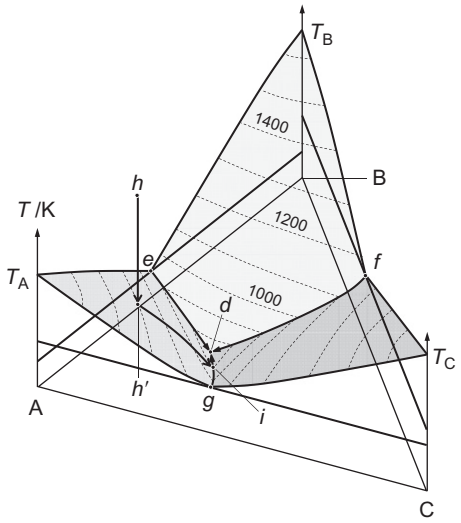


Figure 3.5.14 Schematic three-dimensional representation of liquidus surfaces of a ternary eutectic system.

crystallization fields) of A and C, denotes the relation between temperature and composition of the A–B–C ternary liquid phase that simultaneously coexists with the two solid phases A and C.

Figure 3.5.15b gives the vertical section of the schematic A–B–C ternary phase diagram along the trace A–*j* in Figure 3.5.15a. As seen in Figure 3.5.15b, the phase changes during the cooling of the liquid *h* mentioned above can be illustrated directly. However, attention should be paid to the fact that the compositions and fractions of the phases cannot be read from the vertical section.

In order to determine the compositions and fractions of the phases, the isothermal sections should be used. Figure 3.5.16a shows the isothermal section of the schematic A–B–C ternary system at 1000 K. Dash-dotted lines in this figure represent tie lines in the two-phase regions. The equilibrium phases of the mixture *h* at 1000 K are solid A and the liquid solution of composition *k*. The fractions of the phases can be determined according to the lever rule:

$$\text{Fraction of A} = \frac{(k-h)}{(k-\text{A})} \tag{3.5.44}$$

$$\text{Fraction of Liquid} = \frac{(h-\text{A})}{(k-\text{A})} \tag{3.5.45}$$

On the other hand, the mixture of *l* occurs at the three-phase assemblage of solid B, solid C and the liquid solution of composition *m*. The fraction of the liquid phase can be

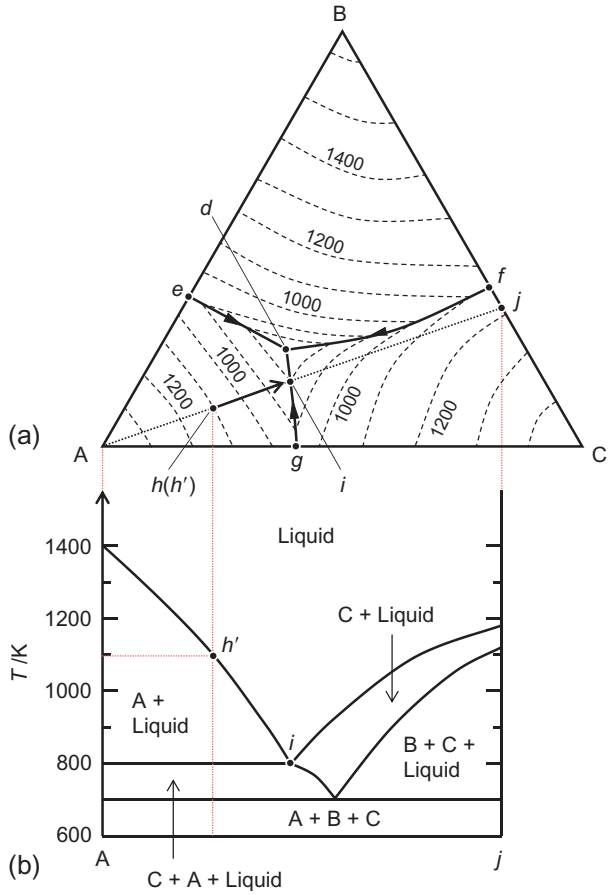


Figure 3.5.15 (a) Schematic phase diagram of a ternary eutectic system expressed two-dimensionally by projecting the liquidus surfaces onto the base composition triangle. (b) Vertical section of the ternary phase diagram along the line A–*j*.

obtained by dividing the area of the triangle B–C–*l* by that of the compatibility triangle B–C–*m*:

$$\text{Fraction of Liquid} = \frac{\Delta \text{BC}l}{\Delta \text{BC}m} \tag{3.5.46}$$

where Δxyz represents the area of the triangle x–y–z. Similarly, the fractions of solid B and solid C are given by:

$$\text{Fraction of solid B} = \frac{\Delta \text{C}ml}{\Delta \text{BC}m} \tag{3.5.47}$$

$$\text{Fraction of solid C} = \frac{\Delta \text{B}ml}{\Delta \text{BC}m} \tag{3.5.48}$$

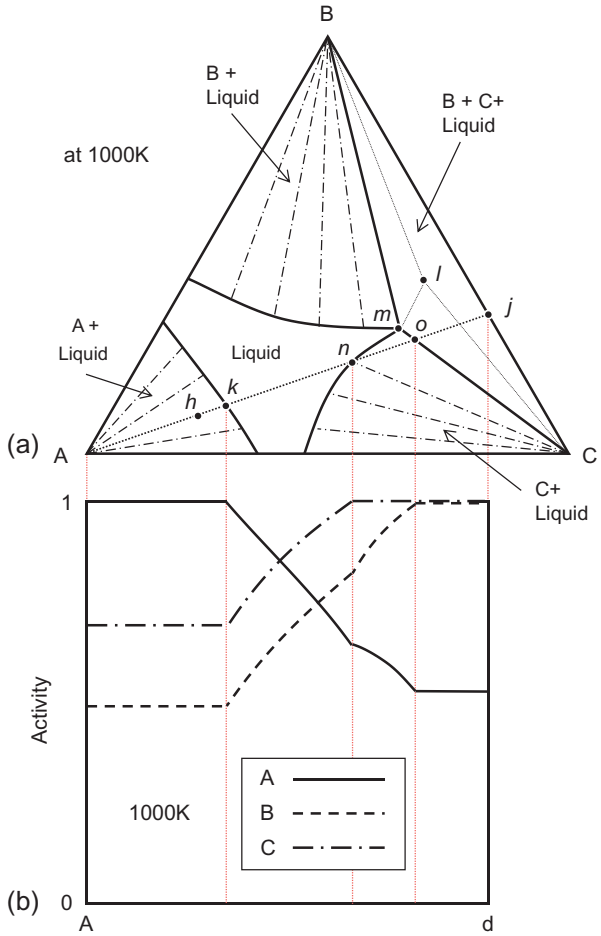


Figure 3.5.16 (a) Isothermal section of the ternary phase diagram at 1000 K. (b) Variation of the activities of the components along the line A–*j* at 1000 K.

According to the mass balances, the values for the compositions and fractions of the phases should be consistent with the following equations:

$$X_{\mathrm{A}}(\text{point } l) = (\text{Fraction of Liquid}) \times X_{\mathrm{A}}(\text{point } m) \tag{3.5.49}$$

$$X_{\mathrm{B}}(\text{point } l) = (\text{Fraction of solid B}) + (\text{Fraction of Liquid}) \times X_{\mathrm{B}}(\text{point } m) \tag{3.5.50}$$

$$X_{\mathrm{C}}(\text{point } l) = (\text{Fraction of solid C}) + (\text{Fraction of Liquid}) \times X_{\mathrm{C}}(\text{point } m) \tag{3.5.51}$$

Figure 3.5.16b shows the activities of the components A, B, and C at 1000 K along the line A–*j*. When the bulk compositions are located between the apex A and point *k*,

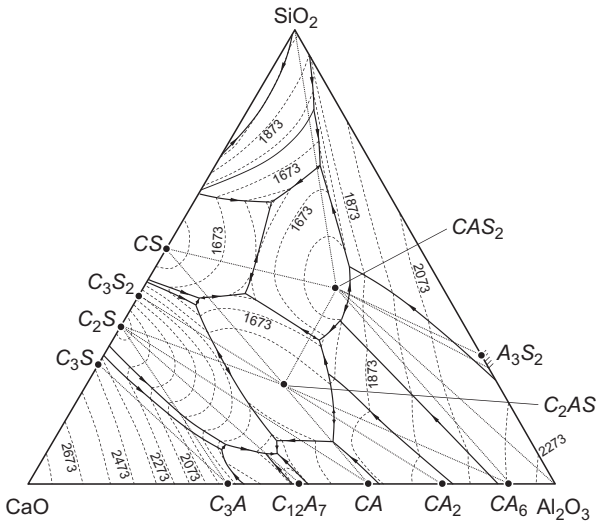


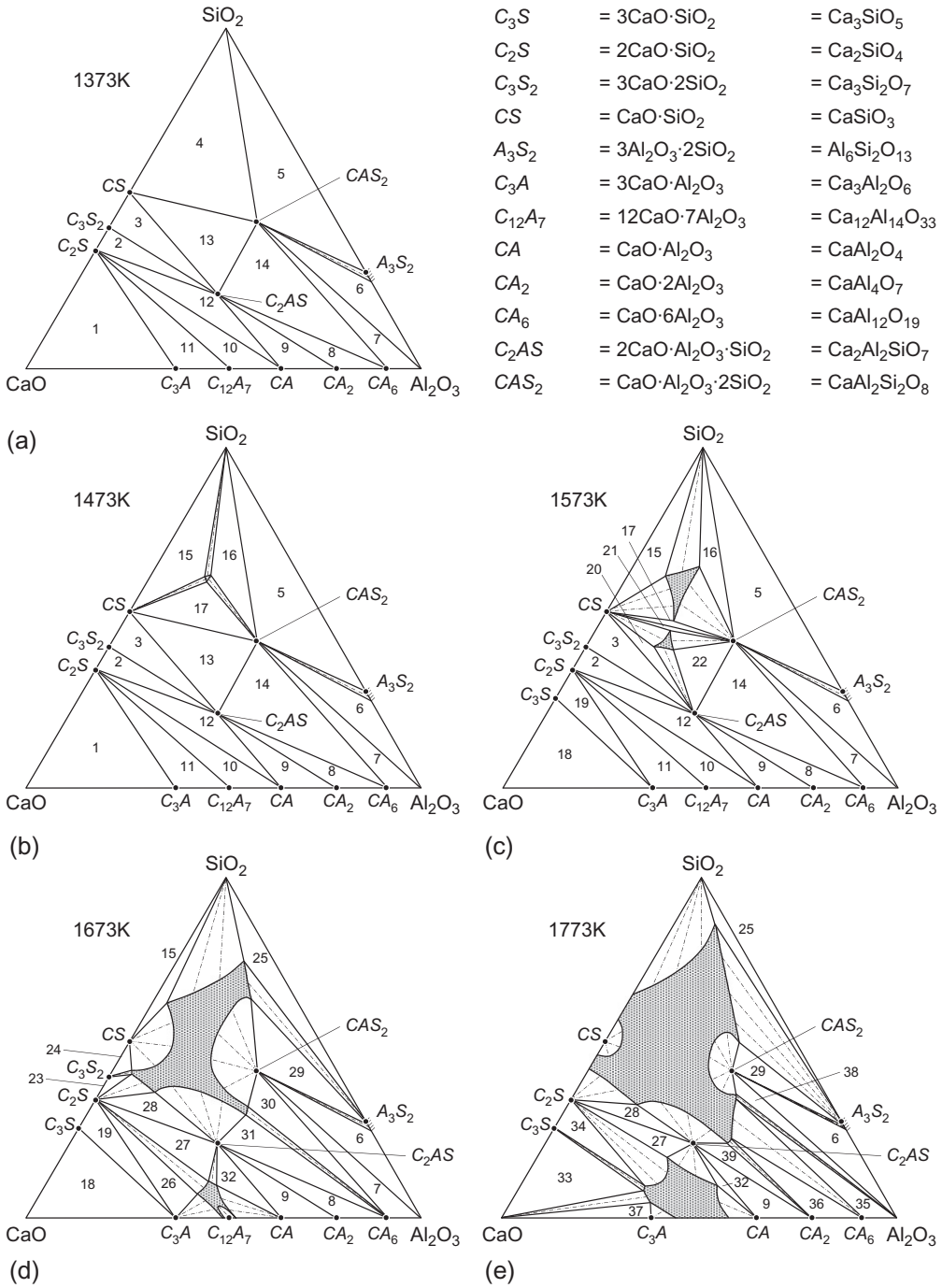
Figure 3.5.17 Phase diagram of the ternary system $CaO–SiO_2–Al_2O_3$. $C_3S = Ca_3SiO_5$, $C_2S = Ca_2SiO_4$, $C_3S_2 = Ca_3Si_2O_7$, $CS = CaSiO_3$, $A_3S_2 = Al_6Si_4O_{13}$, $CA_6 = CaAl_{12}O_{19}$, $CA_2 = CaAl_4O_7$, $CA = CaAl_2O_4$, $C_{12}A_7 = Ca_{12}Al_{14}O_{33}$, $C_3A = Ca_3Al_2O_6$, $CAS_2 = CaAl_2Si_2O_8$, and $C_2AS = Ca_2Al_2SiO_7$.

the mixtures exist in the two-phase region A + Liquid, and the liquid composition is fixed at point *k*. Therefore, the activities are constant here, and it can be noted especially that a_A is unity because the liquid coexists with solid A. From point *k* to point *n*, the homogeneous liquid phase exists, and then the activity of A decreases with a decrease in the concentration of A, while those of B and C increase. When the bulk composition moves from point *n* to point *o*, the liquid composition in equilibrium with solid C changes along the liquidus curve *n*–*m*. During this change, a_A decreases and a_B increases, while a_C remains constant with a value of unity. Finally, the mixtures between point *o* and point *j* consist of the three-phase assemblage of B + C + Liquid (point *m*). According to the Gibbs phase rule, the activities of all the components are constant in this region at a fixed temperature 1000 K.

The $CaO–SiO_2–Al_2O_3$ system provides a fundamental foundation for understanding the industrial behavior of metallurgical slags, fluxes, and cements. Figure 3.5.17 shows the phase diagram for this important ternary system [7]. Based on this figure, isothermal sections can be drawn and examples are shown in Figure 3.5.18. The hatched areas represent the homogeneous liquid region. The isothermal sections shown in Figure 3.5.18 include the following three-phase assemblages:

Region 1: $CaO + Ca_2SiO_4 + Ca_3Al_2O_6$
Region 2: $Ca_2SiO_4 + Ca_3Si_2O_7 + Ca_2Al_2SiO_7$
Region 3: $Ca_3Si_2O_7 + CaSiO_3 + Ca_2Al_2SiO_7$
Region 4: $CaSiO_3 + SiO_2 + CaAl_2Si_2O_8$
Region 5: $SiO_2 + Al_6Si_2O_{13} + CaAl_2Si_2O_8$
Region 6: $Al_6Si_2O_{13} + Al_2O_3 + CaAl_2Si_2O_8$
Region 7: $Al_2O_3 + CaAl_{12}O_{19} + CaAl_2Si_2O_8$
Region 8: $CaAl_{12}O_{19} + CaAl_4O_7 + Ca_2Al_2SiO_7$
Region 9: $CaAl_4O_7 + CaAl_2O_4 + Ca_2Al_2SiO_7$
Region 10: $Ca_2SiO_4 + CaAl_2O_4 + Ca_{12}Al_{14}O_{33}$
Region 11: $Ca_2SiO_4 + Ca_{12}Al_{14}O_{33} + Ca_3Al_2O_6$
Region 12: $Ca_2SiO_4 + CaAl_2O_4 + Ca_2Al_2SiO_7$
Region 13: $CaSiO_3 + Ca_2Al_2SiO_7 + CaAl_2Si_2O_8$
Region 14: $CaAl_{12}O_{19} + Ca_2Al_2SiO_7 + CaAl_2Si_2O_8$
Region 15: $CaSiO_3 + SiO_2 +$ Liquid
Region 16: $SiO_2 + CaAl_2Si_2O_8 +$ Liquid
Region 17: $CaSiO_3 + CaAl_2Si_2O_8 +$ Liquid
Region 18: $CaO + Ca_3SiO_5 + Ca_3Al_2O_6$
Region 19: $Ca_3SiO_5 + Ca_2SiO_4 + Ca_3Al_2O_6$
Region 20: $CaSiO_3 + Ca_2Al_2SiO_7 +$ Liquid
Region 21: $CaSiO_3 + CaAl_2Si_2O_8 +$ Liquid
Region 22: $Ca_2Al_2SiO_7 + CaAl_2Si_2O_8 +$ Liquid
Region 23: $Ca_2SiO_4 + Ca_3Si_2O_7 +$ Liquid
Region 24: $Ca_3Si_2O_7 + CaSiO_3 +$ Liquid
Region 25: $SiO_2 + Al_6Si_2O_{13} +$ Liquid
Region 26: $Ca_2SiO_4 + Ca_3Al_2O_6 +$ Liquid
Region 27: $Ca_2SiO_4 + Ca_2Al_2SiO_7 +$ Liquid
Region 28: $Ca_2SiO_4 + Ca_2Al_2SiO_7 +$ Liquid
Region 29: $Al_6Si_2O_{13} + CaAl_2Si_2O_8 +$ Liquid
Region 30: $CaAl_{12}O_{19} + CaAl_2Si_2O_8 +$ Liquid
Region 31: $CaAl_{12}O_{19} + Ca_2Al_2SiO_7 +$ Liquid
Region 32: $CaAl_2O_4 + Ca_2Al_2SiO_7 +$ Liquid
Region 33: $CaO + Ca_3SiO_5 +$ Liquid
Region 34: $Ca_3SiO_5 + Ca_2SiO_4 +$ Liquid
Region 35: $Al_2O_3 + CaAl_{12}O_{19} +$ Liquid
Region 36: $CaAl_{12}O_{19} + CaAl_4O_7 +$ Liquid
Region 37: $CaO + Ca_3Al_2O_6 +$ Liquid
Region 38: $Al_2O_3 + CaAl_2Si_2O_8 +$ Liquid
Region 39: $CaAl_4O_7 + Ca_2Al_2SiO_7 +$ Liquid
Region 40: $Al_6Si_2O_{13} + Al_2O_3 +$ Liquid
Region 41: $SiO_2 +$ Two liquids

Figure 3.5.19 shows the vertical section through the CaO apex and the triple oxide $CaAl_2Si_2O_8$.



C_3S	= $3CaO{\cdot}SiO_2$	= Ca_3SiO_5
C_2S	= $2CaO{\cdot}SiO_2$	= Ca_2SiO_4
C_3S_2	= $3CaO{\cdot}2SiO_2$	= $Ca_3Si_2O_7$
CS	= $CaO{\cdot}SiO_2$	= $CaSiO_3$
A_3S_2	= $3Al_2O_3{\cdot}2SiO_2$	= $Al_6Si_2O_{13}$
C_3A	= $3CaO{\cdot}Al_2O_3$	= $Ca_3Al_2O_6$
$C_{12}A_7$	= $12CaO{\cdot}7Al_2O_3$	= $Ca_{12}Al_{14}O_{33}$
CA	= $CaO{\cdot}Al_2O_3$	= $CaAl_2O_4$
CA_2	= $CaO{\cdot}2Al_2O_3$	= $CaAl_4O_7$
CA_6	= $CaO{\cdot}6Al_2O_3$	= $CaAl_{12}O_{19}$
C_2AS	= $2CaO{\cdot}Al_2O_3{\cdot}SiO_2$	= $Ca_2Al_2SiO_7$
CAS_2	= $CaO{\cdot}Al_2O_3{\cdot}2SiO_2$	= $CaAl_2Si_2O_8$

Figure 3.5.18 Isothermal sections of the $CaO–SiO_2–Al_2O_3$ ternary system. (a) 1373 K, (b) 1473 K, (c) 1573 K, (d) 1673 K, (e) 1773 K,

(Continued)

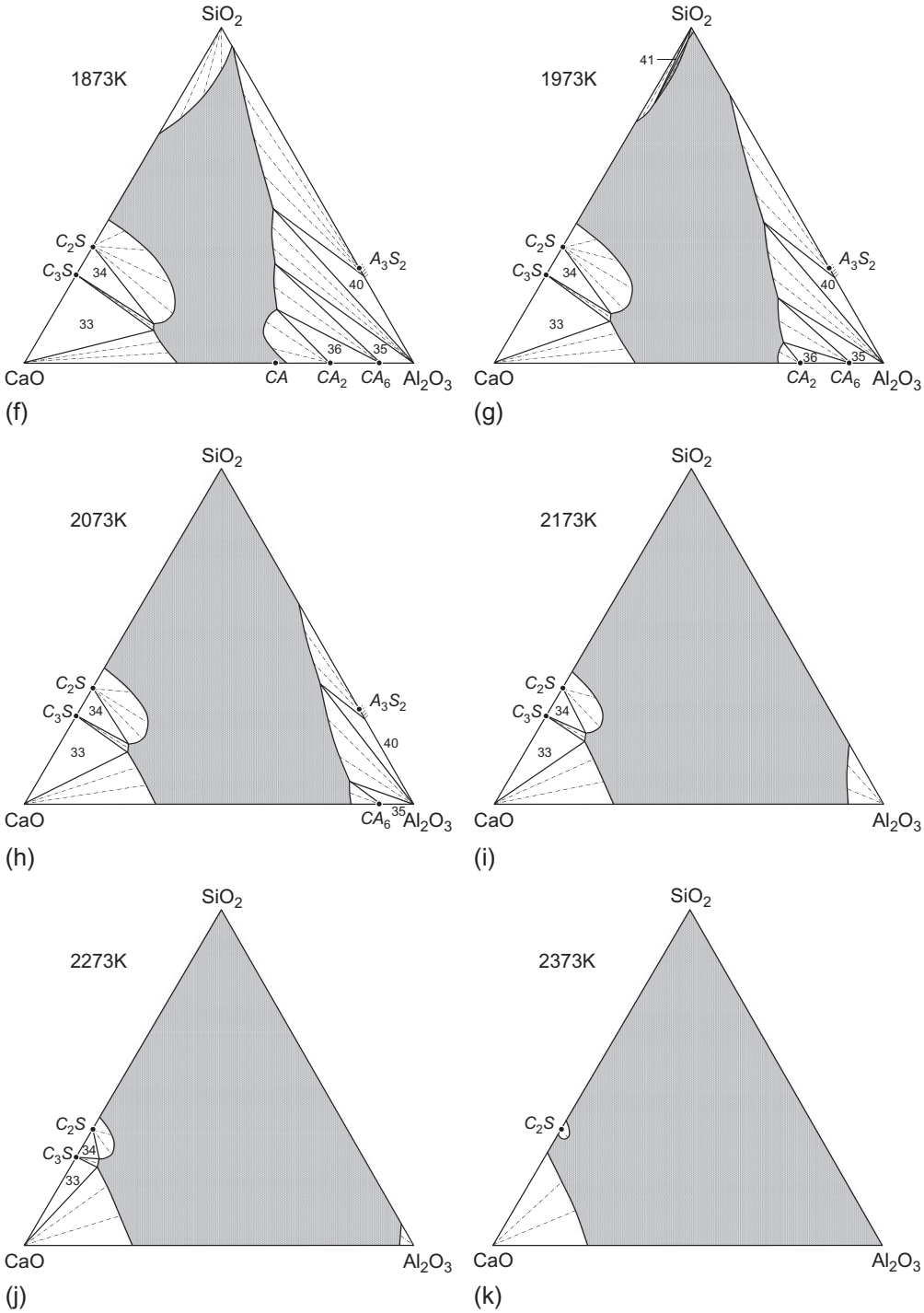


Figure 3.5.18, cont'd (f) 1873 K, (g) 1973 K, (h) 2073 K, (i) 2173 K, (j) 2273 K, and (k) 2373 K.

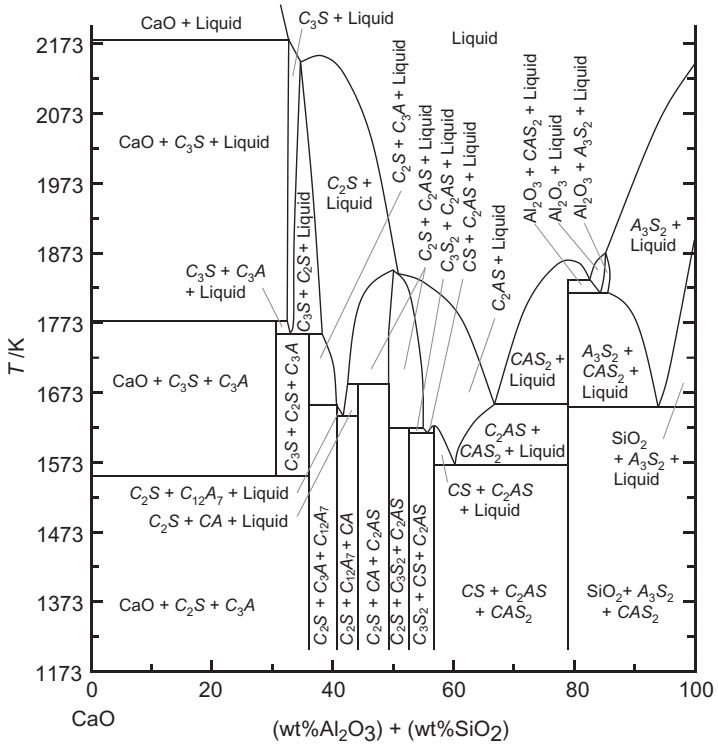


Figure 3.5.19 Vertical section of the $CaO–SiO_2–Al_2O_3$ ternary phase diagram through the CaO apex and the triple oxide $CaAl_2Si_2O_8$. $C_3S = Ca_3SiO_5$, $C_2S = Ca_2SiO_4$, $C_3S_2 = Ca_3Si_2O_7$, $CS = CaSiO_3$, $A_3S_2 = Al_6Si_4O_{13}$, $CA_6 = CaAl_{12}O_{19}$, $CA_2 = CaAl_4O_7$, $CA = CaAl_2O_4$, $C_{12}A_7 = Ca_{12}Al_{14}O_{33}$, $C_3A = Ca_3Al_2O_6$, $CAS_2 = CaAl_2Si_2O_8$, and $C_2AS = Ca_2Al_2SiO_7$.

REFERENCES

[1] B. Phillips, A. Muan, J. Am. Ceram. Soc. 42 (9) (1959) 413, Cited from *ACerS-Nist Phase Equilibrium Diagrams, CD-ROM database, Version* 3.1, Figure 237.

[2] O. Kubaschewski, C.B. Alcock, P.J. Spencer, Materials Thermochemistry, sixth ed., Pergamon Press, Oxford, 1993, p. 258.

[3] I. Barin (Ed.), Thermochemical Data of Pure Substances, VCH Publishers, Weinheim, 1989.

[4] E.T. Turkdogan, Physical Chemistry of High Temperature Technology, Academic Press, New York, 1980, p. 5.

[5] M. Hasegawa, M. Iwase, Kyoto University, Unpublished Research, 2012.

[6] E.T. Turkdogan, Fundamentals of Steelmaking, The Institute of Materials, London, 1996, p. 138.

[7] E.F. Osborn, A. Muan, Phase Equilibrium Diagrams of Oxide Systems, Plate 1, American Ceramic Society and the Edward Orton, Jr., Ceramic Foundation, 1960, Revised and redrawn. Cited from ACerS-Nist Phase Equilibrium Diagrams, CD-ROM database, Version 3.1, Figure 630.

CHAPTER 3.6

Dilute Solutions

Takahiro Miki
Associate Professor, Tohoku University, Japan

3.6.1. HENRY'S LAW AND SIEVERTS' LAW

The activity–composition diagram for a binary solution that exhibits negative deviation from Raoult's law is shown in Figure 3.6.1. The Raoultian standard state for component i is located at point **A** where the activity of i is unity. The deviations from Raoult's law by the actual solution is described in terms of the activity coefficient γ_I, where γ_i is given by the ratio: a_i/X_i. The activity coefficient is less than 1 when the interaction between solute and solvent is attractive and is greater than 1 for the case of repulsive interaction between solute and solvent. In infinitely dilute solutions, the Raoultian activity of component i, a_i, is directly proportional to its mole fraction, X_i, this is known as Henry's law:

$$a_i = \gamma^\circ X_i \tag{3.6.1}$$

Here, γ° is the activity coefficient of component i in the infinitely dilute solution, and at any given temperature has a constant value given by the slope of the Henry's law line, Figure 3.6.1. For this reason it is known as the Henrian coefficient and the value is independent of composition.

The dissolution of a diatomic gas A_2 into a molten metal can be expressed by the following reaction:

$$A_2(\text{gas}) = 2[A]_{\text{in metal}} \tag{3.6.2}$$

$$K = \frac{a_A^2}{p_{A_2}} \tag{3.6.3}$$

Here, K is the equilibrium constant and p_{A_2} is the partial pressure of A_2 gas. For the condition that the concentration of A in molten metal is sufficiently low to satisfy Henry's law, the activity coefficient will be constant. Therefore, the solubility of A in the molten metal is proportional to the square root of the partial pressure of A_2:

$$x_A \propto \sqrt{p_{A_2}} \tag{3.6.4}$$

This is known as Sieverts' law.

Treatise on Process Metallurgy, Volume 1
http://dx.doi.org/10.1016/B978-0-08-096986-2.00034-5
© 2014 Elsevier Ltd.
All rights reserved.

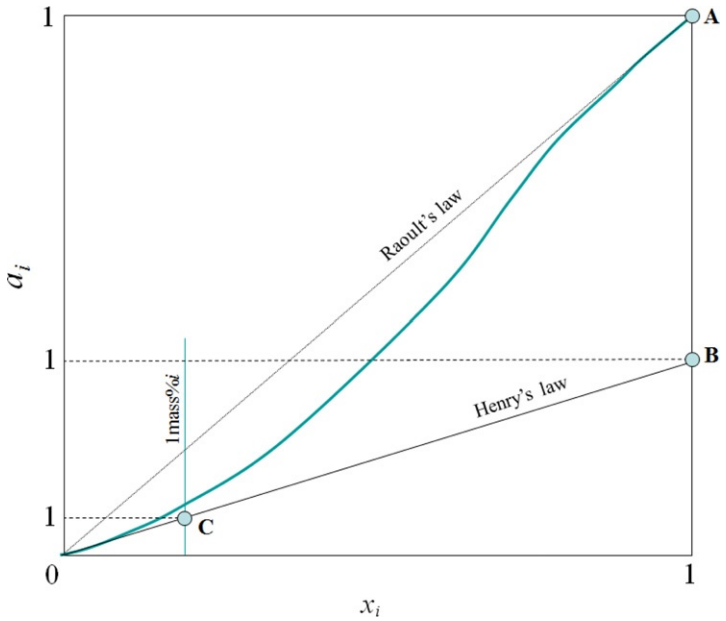


Figure 3.6.1 Illustration of the Raoultian, Henrian and 1 mass% standard states.

3.6.2. HENRIAN ACTIVITIES AND THE CONVERSION OF STANDARD STATES

During refining processes, solutes or impurities at relatively low concentrations are usually considered. In these circumstances, it is often convenient to use a scale of activities defined with respect to Henry's law rather than Raoult's law. The Henrian standard state is located at $X_i = 1$ on the Henry's law line, point **B** in Figure 3.6.1. This point represents pure i in the hypothetical nonphysical state in which its activity is defined as unity. The activity of i in a solution with respect to the Henrian standard state is given by Equation (3.6.5), where superscript H denotes the Henrian standard state. If solute i obeys Henry's law, the activity coefficient γ_i^{H} which represents the deviation from Henry's law is unity.

$$a_i^{\mathrm{H}} = \gamma_i^{\mathrm{H}} x_i \tag{3.6.5}$$

As the mole fraction of i is virtually proportional to the mass% of i in a dilute solution, a third standard state can be defined, which is located at the point on Henry's law line corresponding to 1 mass% of i, shown as point **C** in Figure 3.6.1. The activity of i in a solution with respect to the 1 mass% standard state is given by Equation (3.6.6), where $a_i^{\%}$, f_i, and [%i] represent the activity based on the 1 mass% standard state, the

corresponding activity coefficient for the deviation from Henry's law on a mass% basis, and the concentration of i in mass%, respectively,

$$a_i^{\%} = f_i[\%i] \tag{3.6.6}$$

The standard Gibbs energy change for a reaction will depend on the selected standard states of the components. The conversion from one standard state to another can be calculated from the difference between the Gibbs energy of the two standard states. For example, the conversion of the standard state from Raoultian (point **A**) to Henrian (point **B**) can be obtained as follows:

$$i(\text{Raoult; pure liquid}) = i(\text{Henry}) \tag{3.6.7}$$

$$\mu_i = \mu_i^0(\text{Raoult}) + RT\ln a_i \tag{3.6.8}$$

$$\mu_i = \mu_i^0(\text{Henry}) + RT\ln a_i^{\text{H}} \tag{3.6.9}$$

Here, μ_i, R, and T are the chemical potential of component i, gas constant, and absolute temperature, respectively. Subtracting Equation (3.6.8) from (3.6.9), the following equation is obtained:

$$\Delta G_i^0(\text{Raoult} \rightarrow \text{Henry}) = \mu_i^0(\text{Henry}) - \mu_i^0(\text{Raoult}) = RT\ln\frac{a_i}{a_i^{\text{H}}} = RT\ln\frac{\gamma_i}{\gamma_i^{\text{H}}} \tag{3.6.10}$$

For infinite dilute solution, γ_i and γ_i^{H} will be γ_i^0 and 1.

$$\Delta G_i^0(\text{Raoult} \rightarrow \text{Henry}) = \mu_i^0(\text{Henry}) - \mu_i^0(\text{Raoult}) = RT\ln\,\gamma_i^0 \tag{3.6.11}$$

This is the Gibbs energy change accompanying the change in the standard state.

The conversion of the standard state from Henrian (point **B**) to mass% (point **C**) is given as follows:

$$i(\text{Henry}) = i(\text{Henry;1 mass\%}) \tag{3.6.12}$$

$$\mu_i = \mu_i^0(\text{Henry}) + RT\ln a_i^{\text{H}} \tag{3.6.13}$$

$$\mu_i = \mu_i^0(\text{mass\%}) + RT\ln a_{\%i} \tag{3.6.14}$$

$$\mu_i^0(\text{mass\%}) - \mu_i^0(\text{Henry}) = RT\ln\frac{a_i^{\text{H}}}{a_{\%i}} = RT\ln\frac{\gamma_i^{\text{H}}}{f_i} + RT\ln\frac{x_i}{[\%i]}. \tag{3.6.15}$$

For infinite dilute solution, γ_i^H, f_i, and $\frac{x_i}{[\%i]}$ will be 1, 1, and $\frac{M}{100\cdot M_i}$, respectively, where M is the molecular weight of the solvent and M_i is that of solute i. The Gibbs energy change accompanying this change in standard state is given by:

$$\Delta G_i^0(\text{Henry} \rightarrow \text{mass\%}) = \mu_i^0(\text{mass\%}) - \mu_i^0(\text{Henry}) = RT\ln\frac{M}{100\cdot M_i} \tag{3.6.16}$$

The conversion of the standard state from Raoultian (point **A**) to mass% (point **C**) is given by Equation (3.6.18):

$$i(\text{Raoult;pure liquid}) = i(\text{Henry;1 mass\%}) \tag{3.6.17}$$

$$\Delta G_i^0(\text{Raoult} \rightarrow \text{Henry}) = RT\ln\frac{\gamma_i^0 M}{100 \cdot M_i} \tag{3.6.18}$$

3.6.3. DESCRIPTION OF ACTIVITIES OF MINOR SOLUTE ELEMENTS IN METALLIC SOLUTION (WAGNER'S EQUATION)

The presence of other solutes may have effects in changing the activity coefficient of a solute in a dilute solution. If solute 2,3, ..., c are dissolved in solvent 1, a Taylor's expansion of $\ln \gamma_2$ as a function of the mole fractions of the solutes is given by Equation (3.6.19):

$$\begin{aligned}\ln\gamma_2 = \ln\gamma_2^0 &+ X_2\frac{\partial\ln\gamma_2}{\partial X_2} + X_3\frac{\partial\ln\gamma_2}{\partial X_3} + X_4\frac{\partial\ln\gamma_2}{\partial X_4} + \cdots + X_c\frac{\partial\ln\gamma_2}{\partial X_c} \\ &+ \sum_{i=2}^{c}\left(\frac{1}{2}\frac{\partial^2\ln\gamma_2}{\partial X_i^2}X_i^2 + \frac{1}{6}\frac{\partial^3\ln\gamma_2}{\partial X_i^3}X_i^3 + \cdots\right) \\ &+ \sum_{\substack{i=2\\ j=3}}^{c}\left(\frac{\partial^2\ln\gamma_2}{\partial X_i \partial X_j}X_i X_j\right) + \cdots\end{aligned} \tag{3.6.19}$$

The interaction parameter for the effect of j on i, ε_i^j, is defined by Equation (3.6.20):

$$\lim_{x_1 \rightarrow 1}\left(\frac{\partial\ln\gamma_i}{\partial X_j}\right)_{T,p,X_{k\neq j}} = \varepsilon_i^j \tag{3.6.20}$$

Also, the following relation is valid:

$$\varepsilon_i^j = \varepsilon_j^i \tag{3.6.21}$$

If the activity coefficient of solute 2 is influenced by various solutes, it can be expressed by Equation (3.6.22) as a first approximation:

$$\ln\gamma_2 = \ln\gamma_2^0 + \varepsilon_2^2 X_2 + \varepsilon_2^3 X_3 + \varepsilon_2^4 X_4 + \cdots + \varepsilon_2^c X_c \tag{3.6.22}$$

When the solute becomes more concentrated or the interactions between the solutes are strong, the cross terms defined by Equations (3.6.23) and (3.6.24) should be considered

$$\frac{1}{2}\lim_{X_1\to 1}\left(\frac{\partial^2 \ln\gamma_i}{\partial X_j^2}\right)_{T,p,X_{k\neq j}} = \rho_i^j \tag{3.6.23}$$

$$\lim_{X_1\to 1}\left(\frac{\partial^2 \ln\gamma_i}{\partial X_j \partial X_k}\right)_{T,p,X_{l\neq j,k}} = \rho_i^{j,k} \tag{3.6.24}$$

The activity coefficient of solute 2 is expressed by Equation (3.6.25) by considering the cross terms:

$$\ln\gamma_2 = \ln\gamma_2^0 + \varepsilon_2^2 X_2 + \rho_2^2 X_2^2 + \varepsilon_2^3 X_3 + \rho_2^3 X_3^2 + \rho_2^{2,3} X_2 X_3 \cdots \tag{3.6.25}$$

For practical purposes, it is convenient to define an interaction parameter e_i^j in terms of the concentration in mass% and logarithms to the base 10:

$$\lim_{[\%1]\to 100}\left(\frac{\partial \log f_i}{\partial [\%j]}\right)_{T,p,X_{k\neq j}} = e_i^j \tag{3.6.26}$$

The activity of solute 2 in a solution with respect to the 1 mass% standard state is expressed by Equation (3.6.27) as a first approximation:

$$\log f_2 = e_2^2[\%2] + e_2^3[\%3] + e_2^4[\%4] + \cdots + e_2^c[\%c] \tag{3.6.27}$$

The relation between ε_i^j and e_i^j is given by Equation (3.6.28), M is the molecular weight of the solvent and M_i is that of solute i:

$$\varepsilon_i^j = 230\frac{M_j}{M}e_i^j + \left(1 - \frac{M_j}{M}\right) \tag{3.6.28}$$

Also, the cross terms are defined by Equations (3.6.29) and (3.6.30)

$$\frac{1}{2}\lim_{X_1\to 1}\left(\frac{\partial^2 \log f_i}{\partial [\%j]^2}\right)_{T,p,X_{k\neq j}} = r_i^j \tag{3.6.29}$$

$$\lim_{X_1\to 1}\left(\frac{\partial^2 \log f_i}{\partial [\%j]\partial [\%k]}\right)_{T,p,X_{l\neq j,k}} = r_i^{j,k} \tag{3.6.30}$$

The activity of solute 2 in a solution with respect to the 1 mass% standard state is expressed by Equation (3.6.31) by considering the cross terms.

$$\log f_2 = e_2^2[\%2] + r_2^2[\%2]^2 + e_2^3[\%3] + r_2^3[\%3]^2 + r_2^{2,3}[\%2][\%3] \cdots \tag{3.6.31}$$

3.6.4. EXAMPLES FOR THE CALCULATION OF HENRIAN ACTIVITIES

To determine the equilibrium state for a chemical reaction, the equilibrium constant, K, must be defined:

$$aA + bB = cC + dD \tag{3.6.32}$$

$$K = \frac{a_C^c a_D^d}{a_A^a a_B^b} \tag{3.6.33}$$

Partial pressure, P, will be used instead of activity, a, in Equation (3.6.33) if a gas phase is involved in the reaction. At equilibrium, the free energy change for the reaction, ΔG°, can be expressed by the following equation:

$$\Delta G^\circ = -RT \ln K \tag{3.6.34}$$

The following example is presented to illustrate the calculation process.

Molten Fe was held in a SiO_2 crucible at 1800 K and the equilibrium Si content in Fe was 0.5 mass%. Calculate the equilibrium oxygen partial pressure. The activity coefficient of component Si in dilute solution, molar weight of Fe and Si are $\overset{\circ}{\gamma}_{Si} = 0.0008$, $M_{Fe} = 56$, and $M_{Si} = 28$, respectively. Also, the free energy change for SiO_2 formation at 1800 K is shown below.

$$Si(l) + O_2(g) = SiO_2(s) \tag{3.6.35}$$

$$\Delta G^\circ = -557800(J/mol) \tag{3.6.36}$$

Interaction between solutes in molten Fe is neglected.

From Equations (3.6.17) and (3.6.18), the free energy of Si dissolution into molten Fe can be expressed as follows:

$$Si(l) = \underline{Si}(mass\%, in\,Fe) \tag{3.6.37}$$

$$\begin{aligned}\Delta G^\circ(R \rightarrow H, \%) &= RT \ln \frac{\overset{\circ}{\gamma}_{Si} M_{Fe}}{100 M_{Si}} \\ &= 8.314 \cdot 1800 \cdot \ln \frac{0.0008 \cdot 56}{100 \cdot 28} = -165{,}300(J/mol)\end{aligned} \tag{3.6.38}$$

From Equations (3.6.35)–(3.6.38), the following can be obtained:

$$\underline{Si}(mass\%, in\,Fe) + O_2(g) = SiO_2(s) \tag{3.6.39}$$

$$\Delta G^\circ = -557800 - (-165300) = -392500(J/mol) \tag{3.6.40}$$

The activity of SiO_2 is unity and also activity coefficient f_{Si} is unity because interaction between solutes can be neglected. Hence, the free energy change can be expressed as follows:

$$\Delta G^\circ = -RT\ln\frac{a_{SiO_2}}{f_{Si}[\text{mass\%Si}]P_{O_2}} = -RT\ln\frac{1}{[\text{mass\%Si}]P_{O_2}} \tag{3.6.41}$$

Finally, equilibrium oxygen partial pressure can be determined as follows:

$$\begin{aligned} P_{O_2} &= \frac{1}{[\text{mass\%Si}]}\exp\left(\frac{\Delta G^\circ}{RT}\right) \\ &= \frac{1}{0.5}\exp\left(\frac{-392500}{8.314\cdot 1800}\right) = 8.14\times 10^{-12}(\text{atm}) \end{aligned} \tag{3.6.42}$$

3.6.5. DATA COMPILATIONS FOR DILUTE LIQUID ALLOYS

Considerable data on the thermodynamic behavior of elements in liquid alloys have been reported. Sigworth and Elliott [1–4] have summarized the available data on the thermodynamic behavior of elements in Fe-, Cu-, Ni-, and Co-based alloys. Also, thermodynamic data for Fe-based alloys have been summarized by The Japan Society for Promotion of Science [5].

3.6.5.1. The Thermodynamics of Liquid Iron Alloys

Interaction parameters of elements in iron alloys (e_i^j) at1873 K

i	j								
	Ag	**Al**	**As**	**Au**	**B**	**Be**	**C**	**Ca**	**Ce**
Ag	−0.04	−0.08					0.22		
Al	−0.017	0.043					0.091	−0.047	
As							0.25		
Au									
B					0.038		0.22		
Be									
C	0.028	0.043	0.043		0.244		0.243 (0.14)	−0.097	−0.0026

Continued

i	j								
	Ag	**Al**	**As**	**Au**	**B**	**Be**	**C**	**Ca**	**Ce**
Ca		−0.072					−0.34	−0.002	
Ce							−0.077		0.0039
Co							0.02		
Cr	−0.0024						−0.114		
Cu							0.066		
Ge							0.03		
H		0.013			0.058(0.05)		0.06		0
Hf									
La							0.03		
Mg							0.15		
Mn					−0.0236		−0.0538 (−0.07)		0.054
Mo							−0.14 (−0.097)		
N		0.01 (−0.028)	0.018		0.094		0.13		
Nb							−0.486		
Ni							0.032 (0.042)	−0.066	
O	−0.011	−1.17 (−3.9)		−0.007 (−0.005)	−0.31 (−2.6)	−2.4	−0.421 (−0.45)	−515	−64
P		0.037			0.015		0.126		
Pb		0.021					0.1 (0.066)		
Pd									
Pt									
Rh									
S		0.041 (0.035)	0.0041	0.0028 (0.0042)	0.134		0.111	−110	−9.1
Sb							0.11		
Sc									
Se									
Si		0.058			0.2		0.18	−0.066	

i \ j	Ag	Al	As	Au	B	Be	C	Ca	Ce
Sn							0.18 (0.37)		
Ta							−3.5 (−0.37)		
Te									
Ti									
U		0.059							
V							−0.14 (−0.34)		
W							−0.15		
Y									
Zr									

Values in ( ) are from Sigworth and Elliott. Others are from The Japan Society for Promotion of Science.

i \ j	Co	Cr	Cu	Ge	H	Hf	La	Mg
Ag		−0.0097						
Al					0.24			
As								
Au								
B					0.58(0.49)			
Be								
C	0.0075 (0.0009) {0.0002}	−0.023	0.016	0.008	0.67		0.0066	0.07
Ca								
Ce					−0.6			
Co	0.00509 (0.0022) −0.000024	−0.022			−0.14			
Cr	−0.019	−0.0003	0.016		−0.34 (−0.33)			
Cu		0.018	−0.02 (0.023) −0.00013		−0.19 (−0.24)			

Continued

i	j							
	Co	Cr	Cu	Ge	H	Hf	La	Mg
Ge				0.007	0.41			
H	0.0018	−0.0024 (−0.0022)	0.0013 (0.0005)	0.01	0		−0.027	
Hf						0.007		
La					−4.3		−0.0078	
Mg								
Mn	−0.0036	0.0039			−0.34 (−0.31)		0.11	
Mo		−0.0003			−0.13 (−0.20)			
N	0.012	−0.046 (1.56/ $T-0.00053$)	0.009					
Nb					−0.7 (−0.61)			
Ni		−0.0003			−0.36 (−0.25)			
O	0.008	−0.055 (−0.04) [Cr < 3] −380/ $T+0.151$ (10.2/ $T-0.00487$) [3 < Cr < 30]	−0.013		0.73(−3.1)	−0.28	−5	−1.98
P	0.004	−0.018 (−0.03)	−0.035 (0.024)		0.33(0.21)			
Pb	0	0.02	−0.028					
Pd					−0.021 (0.20)			
Pt								
Rh					0.13(0.37)			
S	0.0026	−0.0105	−0.0084	0.014	0.41(0.12)	−0.045	−18.3	
Sb								
Sc								

i	j							
	Co	**Cr**	**Cu**	**Ge**	**H**	**Hf**	**La**	**Mg**
Se								
Si		−0.0003	0.0144		0.64			
Sn		0.015	−0.024		0.16(0.12)			
Ta					−0.47 (−4.4)			
Te								
Ti					−1.1			
U								
V		0.0119			−0.59			
W					0.088			
Y								
Zr					−1.2			

i	j					
	Mn	**Mo**	**N**	**Nb**	**Nd**	**Ni**
Ag						
Al			0.015 (−0.058)			
As			0.077			
Au						
B	−0.00086		−0.73(0.074)			
Be						
C	−0.0084 (−0.012)	−0.0137 (−0.0083)	0.11	−0.059		0.01
Ca						−0.044
Ce	0.13					
Co	−0.0042		0.037(0.032)			
Cr	0.0039	0.0018	−0.182			0.0002
Cu			0.025			
Ge						
H	−0.002 (−0.0014)	0.0029(0.0022)		−0.0033 (−0.0023)	−0.038	−0.0019(0)

Continued

i	j					
	Mn	**Mo**	**N**	**Nb**	**Nd**	**Ni**
Hf						
La	0.28					
Mg						
Mn	0	0.0046	−0.091	0.0073		−0.0072
Mo	0.0048	0.0121	−0.1			
N	−0.02	−0.011	0	−0.068		0.007(0.01)
Nb	0.0093		−0.0475 (−0.42)	0		
Ni	−0.008		0.015(0.028)			0.0007 (0.0009)
O	−0.021	0.005(0.0035)	−0.14(0.057)	−0.12(−0.14)		0.006
P	−0.032(0)	0.001	0.13(0.094)	−0.012		0.003 (0.0002)
Pb	−0.023	0				−0.019
Pd						
Pt						
Rh						
S	−0.026	0.0027	0.01	−0.013		0
Sb			0.043			
Sc						
Se			0.014			
Si	−0.0146 (0.002)	2.36	0.092	0		0.005
Sn			0.027			
Ta	0.0016		−0.685 (−0.47)			
Te			0.6			
Ti	−0.043		−2.06(−1.8)			
U						
V	0.0056		−0.455 (−0.35)			

i	j					
	Mn	**Mo**	**N**	**Nb**	**Nd**	**Ni**
W	0.0136		−0.079 (−0.072)			
Y						
Zr			−4.13			

i	j					
	O	**P**	**Pb**	**Pd**	**Pt**	**Rh**	**S**
Ag	−0.099						
Al	−1.98 (−6.6)	0.033	0.0065				0.035(0.030)
As							0.0037
Au	−0.14 (−0.11)						−0.0051 (0.0037)
B	−0.21 (−1.8)	0.008					0.048
Be	−1.3						
C	−0.32 (−0.34)	0.051	0.0099 (0.0079)				0.044(0.046)
Ca	−580						−140
Ce	−560						−40
Co	0.018	0.0037	0.0031				0.0011
Cr	−0.16 (−0.14)	−0.033 (−0.053)	0.0083				−0.17 (−0.020)
Cu	−0.065	−0.076 (0.044)	−0.0056				−0.021
Ge							0.026(0.027)
H	0.05(−0.19)	0.015(0.011)		0.0041 (0.0062)		0.0056 (0.0063)	0.017(0.008)
Hf	−3.2						−0.27
La	−43						−79
Mg	−3						
Mn	−0.083	−0.06 (−0.0035)	−0.0029				−0.048

Continued

i	j						
	O	P	Pb	Pd	Pt	Rh	S
Mo	0.0083 (−0.0007)	−0.006	0.0023				−0.0006 (−0.0005)
N	−0.12(0.05)	0.059(0.045)					0.007
Nb	−0.72 (−0.83)	−0.045					−0.046 (−0.047)
Ni	0.01	0.0018 (−0.0035)	−0.0023				−0.0036 (−0.0037)
O	−0.17 (−0.20)	0.07		−0.009	0.0045	0.0136	−0.133
P	0.13	0.054(0.062)	0.011				0.034()
Pb		0.048					−0.32
Pd	−0.084			0.002			
Pt	0.0063						0.032
Rh	0.064(0.11)						
S	−0.27	0.035(0.29)	−0.046		0.0089		−0.046 (−0.028)
Sb	−0.2						0.0019
Sc	−3.7						
Se							
Si	−0.119 (−0.23)	0.09(0.11)	−0.01 (0.01)				0.066(0.056)
Sn	−0.11	0.036	0.035				−0.028
Ta	−1.2						−0.13 (−0.021)
Te							
Ti	−3.4(−1.8)	−0.06					−0.27(−0.11)
U	−6.6						−0.53
V	−0.46 (−0.97)	−0.042					−0.033 (−0.028)
W	0.052 (−0.052)	−0.16	0.0005				0.043(0.035)
Y	−2.6						−0.77
Zr	−23						−0.61(−0.16)

i	j						
	Sb	**Sc**	**Se**	**Si**	**Sn**	**Ta**	**Te**
Ag							
Al				0.056			
As							
Au							
B				0.078			
Be							
C	0.015			0.08	0.022	−0.23(−0.021)	
Ca				−0.096			
Ce							
Co							
Cr				−0.004	0.009		
Cu				0.027	−0.011		
Ge							
H				0.027	0.0057	0.0017(−0.02)	
Hf							
La							
Mg							
Mn				−0.0327(0)		0.0035	
Mo				8.05			
N	0.0088		0.006	0.048	0.007	−0.049(−0.032)	0.07
Nb				−0.01			
Ni				0.006			
O	−0.023	−1.3		−0.066(−0.131)	−0.0111	−0.1	
P				0.099(0.12)	0.013		
Pb				0.048	0.057		
Pd							
Pt							
Rh							
S	0.0037			0.075(0.063)	−0.0044	−0.019(−0.0002)	
Sb							

Continued

i	j						
	Sb	Sc	Se	Si	Sn	Ta	Te
Sc							
Se							
Si				0.103	0.017	0.04	
Sn				0.057	0.0017		
Ta				0.23		0.11	
Te							
Ti				2.1			
U							
V				0.042			
W							
Y							
Zr							

i	j					
	Ti	U	V	W	Y	Zr
Ag						
Al		0.011				
As						
Au						
B						
Be						
C			−0.03(−0.077)	−0.0056		
Ca						
Ce						
Co						
Cr	−0.059		0.012			
Cu						
Ge						
H	−0.019		−0.0074	0.0048		−0.0088

i	j					
	Ti	U	V	W	Y	Zr
Hf						
La						
Mg						
Mn	−0.05		0.0057	0.0071		
Mo						
N	−0.6(−0.53)		−0.123(−0.093)	−0.002(−0.0015)		−0.63
Nb						
Ni						
O	−1.12(−0.6)	−0.44	−0.14(−0.3)	0.0085(−0.0085)	−0.46	−4
P	−0.04		−0.024	−0.023		
Pb				0		
Pd						
Pt						
Rh						
S	−0.18(−0.072)	−0.067	−0.019(−0.016)	0.011(0.0097)	−0.275	−0.21(−0.052)
Sb						
Sc						
Se						
Si	1.23		0.025			
Sn						
Ta						
Te						
Ti	0.042(0.013)					
U		0.013				
V			0.0309(0.015)			
W						
Y					0.03	
Zr						0.032

Behavior of elements at infinite dilution in liquid iron

Element	Sigworth and Elliott		JSPS	
	γ° (1873 K)	ΔG° $M(\text{pure}) = \underline{M}(\text{mass\%,in Fe})$ (J/mol)	γ° (1873 K)	ΔG° $M(\text{pure}) = \underline{M}(\text{mass\%,in Fe})$ (J/mol)
Ag(l)	200	$82400 - 43.8T$	200	$82400 - 43.76T$
Al(l)	0.029	$-63200 - 27.9T$	0.049	$-71100 - 19.4T$
B(s)	0.022	$-65300 - 21.5T$	0.022	$-65300 - 21.55T$
C(gr)	0.57	$22600 - 42.3T$	0.538	$17230 - 39.87T$
Ca(v)	2240	$-39500 + 49.4T$		
Ce(l)			0.322	$-16700 - 46.44T$
Co(l)	1.07	$1000 - 38.7T$	0.55	
Cr(l)	1.0	$-37.7T$	1.0	$-37.70T$
Cr(s)	1.14	$19200 - 46.9T$	1.14	$19200 - 46.86T$
Cu(l)	8.6	$33500 - 39.4T$	8.58	$33500 - 39.37T$
$1/2H_2(g)$		$36500 + 30.5T$		$36500 + 30.46T$
La(l)			9.3	$125900 - 94.6T$
Mn(l)	1.3	$4080 - 38.2T$	1.44	
Mo(l)	1	$-42.8T$	1.0	
Mo(s)	1.86	$27600 - 52.4T$	2.2	
$1/2N_2(g)$		$3600 + 23.9T$		$9916 + 20.17T$
Nb(l)	1.0	$-42.7T$	0.2	
Nb(s)	1.4	$23000 - 52.3T$	1.4	$23000 - 52.3T$
Ni(l)	0.66	$-20900 - 31.0T$	0.66	$-20900 - 31.1T$
$1/2O_2(g)$		$-117000 - 2.89T$		$-117110 - 3.39T$
$1/2P_2(g)$		$-122000 - 19.2T$		$-157700 + 5.4T$
Pb(l)	1400	$213000 - 106T$	837	
$1/2S_2(g)$		$-135000 + 23.4T$		$-125100 + 18.5T$
Si(l)	0.0013	$-132000 - 17.2T$	0.0013	$-131500 - 17.24T$
Sn(l)	2.8	$16000 - 44.4T$	2.58	
Ta(l)			0.04	

Ti(l)	0.037	$-46000-37.0T$	0.004	
Ti(s)	0.038	$-31100-45.0T$	0.009	
U(l)	0.027	$-56100-50.2T$	0.027	$-56100-50.3T$
V(l)	0.08	$-42300-36.0T$	0.08	$-42300-36.0T$
V(s)	0.1	$-20700-45.6T$	0.1	$-20700-45.6T$
W(l)	1	$-48.1T$	1	$-48.1T$
W(s)	1.2	$31400-63.6T$	7.6	
Zr(l)	0.037	$-51000-42.4T$	0.037	$-51000-42.38T$
Zr(s)	0.043	$-34700-50.0T$	0.043	$-34700-50.00T$

3.6.5.2. The Thermodynamics of Liquid Copper Alloys

Interaction parameters of elements in copper alloys (e_i^j) at $1373-1823$ K

i	j														
	Ag	**Al**	**Au**	**Bi**	**Ca**	**Co**	**Cr**	**Fe**	**Ga**	**Ge**	**H**	**Mg**	**Mn**	**O**	
Ag	−0.005														
Al		0.14													
Au			0.008												
Bi				$-9.0/T+0.0052$											
Ca					0.14										
Fe								−0.029							
Ga									0.028						
Ge										0.051					
H	0.0006	0.0058	0.0003			0.015	0.0092	−0.015			0		−0.006		
Mg												0.1			
Mn													0.03		
O	0		0.015			−0.32		$-20000/T+10.8$						$-414/T+0.122$	
Pb															
S			0.012			−0.023		$-125/T+0.042$							
Sb															
Sn															
Tl															
Zn															

i	j										
	Ni	**P**	**Pb**	**Pt**	**S**	**Sb**	**Si**	**Sn**	**Te**	**Tl**	**Zn**
Ag											
Al											
Au											
Bi											
Ca											
Fe											
Ga											
Ge											
H	-0.026	0.088	0.031	-0.0084	0.073	0.031	0.042	0.016	-0.012		0.029
Mg											
Mn											
O	$-169/T+0.079$	$6230/T+3.43$	-0.007	0.057	-0.164		-62	-0.009			
Pb			-0.0006								
S	$-159/T+0.069$			0.019	$-179/T-0.004$		0.062				
Sb						0.04					
Sn								0.025			
Tl										-0.008	
Zn											0.017

Behavior of elements at infinite dilution in liquid copper

Element	γ° (1473 K)	ΔG° $M(\text{pure}) = \underline{M}(\text{mass\%,in Cu})(\text{J/mol})$
Ag(l)	3.23	$16300 - 44.0T$
Al(l)	0.0028	$-36100 - 57.9T$
As(v)	$4.8 \times {}^{\circ}10^{-4}$	$-93500 - 39.5T$
Au(l)	0.14	$-19400 - 50.6T$
Bi(l)	1.25	$24900 - 63.2T$
C(gr)	$1.4 \times {}^{\circ}10^{5}$	$35800 + 50.2T$
Ca(l)	$5.1 \times {}^{\circ}10^{-4}$	$-92900 - 34.3T$
Cd(v)	15.6	$-108000 + 53.1T$
Cd(l)	0.53	$-7780 - 42.7T$
Co(s)	15.4	$33500 - 37.7T$
Cr(s)	43	$46000 - 36.5T$
Fe(s)	24.1	$54300 - 47.4T$
Fe(l)	19.5	$38900 - 38.8T$
Ga(l)	0.034	$-45200 - 36.3T$
Ge(l)	0.009	$-66900 - 32.9T$
$1/2H_2$(g)		$43500 + 31.4T$
In(l)	0.41	$-40000 - 23.3T$
Mg(v)	0.08	$-168000 + 63.2T$
Mg(l)	0.044	$-36300 - 31.5T$
Mn(l)	0.51	$-8160 - 36.9T$
Mn(s)	0.53	$6490 - 46.6T$
Ni(l)	2.22	$9790 - 37.7T$
Ni(s)	2.66	$27400 - 48.1T$
$1/2O_2$(g)		$-85400 + 18.5T$
Pb(l)	5.27	$36100 - 58.6T$
Pd(s)	1.3	$3350 - 42.3T$
Pt(s)	0.05	$-42700 - 43.8T$
$1/2S_2$(g)		$-120000 + 25.2T$

Sb(l)	0.014	$-52300-43.5T$
Se(v)	0.002	$-76200-40.1T$
Si(l)	0.006	$-62800-31.4T$
Si(s)	0.01	$-12100-61.4T$
Sn(l)	0.048	$-37200-43.5T$
Te(v)	0.0328	$-41800-44.1T$
Tl(l)	8.5	$28200-49.1T$
V(s)	130	$118000-75.7T$
Zn(l)	0.146	$-23600-38.4T$

3.6.5.3. The Thermodynamics of Liquid Cobalt Alloys

Interaction parameters of elements in cobalt alloys (e_i^j) at 1873 K

i	j															
	Al	**As**	**Au**	**B**	**Ce**	**Cr**	**Cu**	**Fe**	**Ge**	**H**	**Mn**	**Mo**	**N**	**Nb**	**Ni**	**O**
Al	0.076															
C	0.017	0.017	0.006	0.068	−0.008	−0.015	0.007	−0.0013	0.0083		−0.0035	−0.0053			0.0009	−0.54
Fe								−0.0062								
Ge									0.033							
H	0.014			0.09		0	−0.003	0.0014		0	−0.0035	0.0041		0	−0.002	
N	0.04					−0.043	−0.009	−0.01				−0.008	0	−0.042	0.024	
O			0.0026			−0.07	−0.009	−0.019			−0.2				−0.0011	0
Pd																
S							−0.016	−0.0034							−0.007	
Si						0.05										
Ti						0.035										

i	j													
	P	Pb	Pd	Rh	Ru	S	Si	Sn	Ta	Te	Ti	U	V	W
Al														
C	0.029	0.0018	0.0044	0.0019	−0.0008	0.034	0.024	0.01	−0.0023	0.014		−0.0019	−0.021	−0.0006
Fe														
Ge														
H							0.021	0.006	0.0054					0.0064
N							0.12		−0.029		−0.45		−0.1	−0.007
O						−0.133							−0.28	
Pd			0.002											
S						−0.0036								
Si							0.05							
Ti														

Behavior of elements at infinite dilution in liquid cobalt

Element	γ° (1873 K)	ΔG° $M(\text{pure}) = \underline{M}(\text{mass\%, in Co})$ (J/mol)
Al(l)	0.005	$-91200 - 27.2T$
Au(l)	3.3	$18400 - 48.1T$
C(gr)	6.7	$20900 - 20.4T$
Cr(s)	0.6	$6990 - 45.6T$
Cr(l)	0.53	$-9960 - 37.2T$
Fe(l)	1.6	$-12100 - 27.5T$
Ge(l)	0.12	$-33100 - 40.0T$
$1/2H_2$(g)		$35600 + 31.5T$
Mn(l)	1.0	$-37.7T$
$1/2N_2$(g)		$41800 + 21.9T$
Ni(l)	0.53	$1260 - 44.1T$
Ni(s)	0.47	$18800 - 54.4T$
$1/2O_2$(g)		$-61600 - 9.71T$
Pb(l)	370	$92100 - 48.7T$
Pd(l)	1.9	$29300 - 53.6T$
Pt(s)	0.03	$-54400 - 48.1T$
$1/2S_2$(g)		$-135000 + 30.3T$
Si(l)	0.0017	$-146000 - 7.03T$
Sn(l)	0.34	$-16700 - 43.9T$
Ti(l)	0.0009	$-109000 - 36.6T$
Ti(s)	0.00091	$-94100 - 44.4T$
V(l)	0.048	$-47200 - 37.0T$
V(s)	0.06	$-25700 - 46.6T$
W(l)	1.4	$5400 - 47.6T$
W(s)	4.3	$40800 - 57.2T$

3.6.5.4. The Thermodynamics of Liquid Nickel Alloys

Interaction parameters of elements in nickel alloys (e_i^j) at 1873 K

i	j															
	Al	**As**	**Au**	**B**	**C**	**Ca**	**Ce**	**Co**	**Cr**	**Cu**	**Fe**	**Ga**	**Ge**	**H**	**In**	**Mn**
Al	0.08															
Au			0.003													
C	0.027	0.017	0.004	0.064			−0.006	−0.001	−0.013	0.004	0	0.012	0.021		0.009	0.0017
Ca						0.004			0.059		0.035					0.04
Co								0								
Cr									0.0083		0.01					
Cu										0.0076						
Fe											0.013					
H	0.014		0.0076					0.0031	0.0036	0.0017	0.0024			0		−0.0096
Mg											0.03					
N	0						−0.55	−0.0054	−0.11		−0.02					
O			0		−0.57			−0.006	−0.2	−0.008	−0.029					−0.45
S	0.133							0.007	0.03	0.0003	0.005					
Si																

i	j															
	Mo	**N**	**O**	**P**	**Pd**	**Pt**	**S**	**Sb**	**Se**	**Si**	**Sn**	**Te**	**Ti**	**V**	**W**	**Zn**
Al																
Au																
C	−0.005			0.04	0.002	0.003		0.012	0.011	0.031	0.01	0.008	−0.022	−0.015	−0.001	0.008
Ca	0.086															
Co																
Cr										0.09			0.06			
Cu																
Fe																
H	0.011									0.033				0.013	0.011	
Mg																
N	−0.04	0											−0.2		−0.26	−0.24
O			0	0			−0.089	−0.137					−0.46	−0.4		
S	0.053						−0.028			0.048			0.16			
Si										0.11						

Behavior of elements at infinite dilution in liquid nickel

Element	γ° (1873K)	ΔG° $M(\text{pure}) = \underline{M}(\text{mass\%,in Ni})(\text{J/mol})$
Al(l)	0.0002	$-155000 - 19.3T$
Au(l)	1.62	$7530 - 48.3T$
B(s)	0.0016	$-59400 - 46.0T$
B(l)	0.009	$-110000 - 24.2T$
C(gr)	0.31	$20800 - 46.0T$
Ca(l)	0.6	$-8030 - 35.0T$
Ca(v)	1.27	$-186000 + 66.4T$
Co(l)	0.45	$1260 - 45.5T$
Cr(s)	0.46	$10500 - 49.6T$
Cr(l)	0.39	$-9210 - 40.1T$
Cu(l)	2.18	$12100 - 38.9T$
Fe(l)	0.36	$-41800 - 24.1T$
Ge(l)	0.13	$-31300 - 40.0T$
$1/2H_2(g)$		$20100 + 35.0T$
Mg(l)	0.32	$-17600 - 30.9T$
Mg(v)	2.2	$-163000 + 62.6T$
Mn(l)	1	$-37.7T$
Mo(s)	2.1	$32600 - 53.5T$
Mo(l)	1	$-42.3T$
$1/2N_2(g)$		$27900 + 39.7T$
$1/2O_2(g)$		$-71000 + 1.41T$
Pb(l)	1.4	$5020 - 48.7T$
Pd(s)	1.35	$4690 - 43.1T$
$1/2S_2(g)$		$-119000 + 15.1T$
Si(l)	0.000015	$-176000 - 30.3T$
Sn(l)	0.14	$-105000 - 4.48T$
Ti(s)	0.00019	$-118000 - 44.6T$
V(s)	0.011	$-52100 - 46.7T$

V(l)	0.009	$-73600-37.0T$
W(s)	13.5	$69000-62.9T$
W(l)	11.3	$37700-47.7T$
Zr(s)	0.00007	$-289000+32.9T$

REFERENCES

[1] G.K. Sigworth, J.F. Elliott, Metal Sci. 8 (1974) 298.
[2] G.K. Sigworth, J.F. Elliott, Can. Met. Q. 13 (1974) 455.
[3] G.K. Sigworth, J.F. Elliott, Can. Met. Q. 15 (1976) 123.
[4] G.K. Sigworth, J.F. Elliott, G. Vaughn, G.H. Geiger, Can. Met. Q. 16–17 (1977–1978) 104.
[5] The Japan Society for Promotion of Science, The 19th Committee in Steelmaking: Steelmaking Data Sourcebook, Gordon and Breach Science Publishers, New York, 1988.

CHAPTER 3.7

Thermodynamics of Slags

Kazuki Morita
Department of Materials Engineering, Graduate School of Engineering, The University of Tokyo

3.7.1. PHASE DIAGRAMS AND ACTIVITIES

Slags consist of a mixture of various kinds of oxide and are encountered in almost all high temperature metallurgical processes as by-products of smelting and refining of materials. They are mostly in a uniform liquid phase, but also exist as mixtures of solid–liquid multi phases. When slags are a mixture of only two oxides, their states are expressed with binary phase diagrams as functions of composition and temperature, but in most cases they are composed of three or more components and are represented in Gibbs triangles as ternary or pseudoternary systems. Fundamental aspects are summarized in Chapter 3.5.

Regarding the thermodynamic properties of slags, a representative indicator is the activity of each component of the system, which provides quantitative information regarding slag–metal reactions of any pyrometallurgical process as well as the formation of solid compounds in the multicomponent slag system. In the case of a binary system, each activity can be shown as an activity-composition curve at a certain temperature. As an example, the activity curves of CaO in the CaO–SiO_2 system are summarized in Figure 3.7.1 [1–7].

The standard state for the CaO activity is pure solid CaO as adopted in most oxide systems. These activity curves for CaO, as well as those for SiO_2 should conform to the Gibbs–Duhem relationship. When the number of components is three or more, each activity is often drawn as an iso-activity contour in the Gibbs triangle, namely the isothermal cross section of the ternary phase diagram. As typical examples, iso-activity contours of SiO_2 [8], CaO [1], and $AlO_{1.5}$ [1] at 1823 K are shown on the isothermal section of the CaO–SiO_2–$AlO_{1.5}$ ternary system in Figure 3.7.2 [1,2,8].

In the present system, aluminum oxide is defined as $AlO_{1.5}$ instead of the molecular form of Al_2O_3 which may be more widely used. In fact, both standard states can be acceptable since the following relation holds regardless of the slag composition. However it should be noted that there is a difference in the composition when described on a molar fraction basis.

$$a^2_{AlO_{1.5}} = a_{Al_2O_3} \tag{3.7.1}$$

This ternary system is often used to show the composition of blast furnace slag although about 8–10 mass% of MgO is contained in the practical slags and each activity

Treatise on Process Metallurgy, Volume 1
http://dx.doi.org/10.1016/B978-0-08-096986-2.00035-7
© 2014 Elsevier Ltd.
All rights reserved.

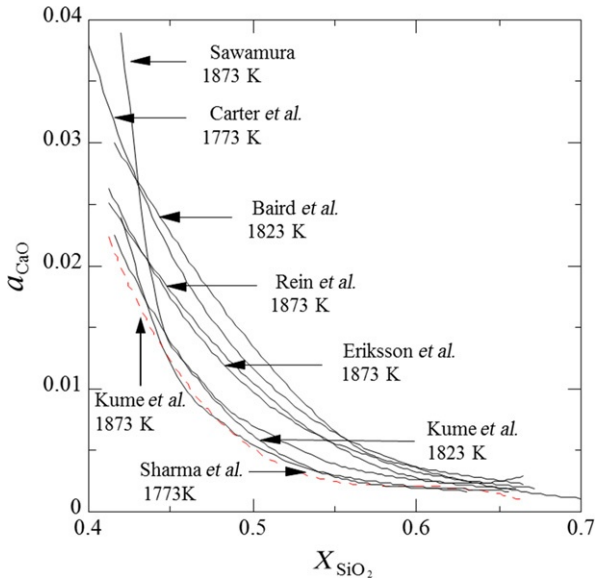


Figure 3.7.1 Comparison of the CaO activities for the CaO–SiO_2 system at 1773, 1823, and 1873 K reported by several researchers [1–7].

value can be roughly estimated from the respective contour. The activities can be evaluated more precisely from the data obtained at a constant MgO content of 10 mol%, as shown in Figure 3.7.3 [8].

On the other hand, refining slags are often composed of multi phases and the evaluation of each activity in such systems is quite important. In the case of ternary systems, two or three phases often coexist at a certain average composition. A two phase region can be shown as an area between liquidus and/or solidus curves and any point in that area is composed of each phase at the composition on each curve. Although composition can be specified only when the tie lines are available, the solidus often can be shown as a point due to the limited solid solubility in case of oxide systems so that any point can be clearly specified with the composition and the amount of each coexisting phase. In the case of three-phase coexistence, the three-phase region is represented by the Gibbs triangle in an isothermal cross section of the phase diagram.

As an example, the CaO activity in the CaO–SiO_2–$AlO_{1.5}$ system can be estimated when the composition varies along the line of constant ratio $X_{CaO}/X_{AlO_{1.5}} = 4$ from $\%SiO_2 = 0$ to 100 as shown in Figure 3.7.4.

In the first two phase region of CaO + L, CaO activity remains at unity in spite of the change in slag composition. On the line *a*–*b*, average composition exists in the Gibbs triangle CaO + Ca_3SiO_5 + L, hence the CaO activity is still constant at unity. On the line *b*–*c*, the composition exists in the two phase region of Ca_3SiO_5 + L, where CaO activity

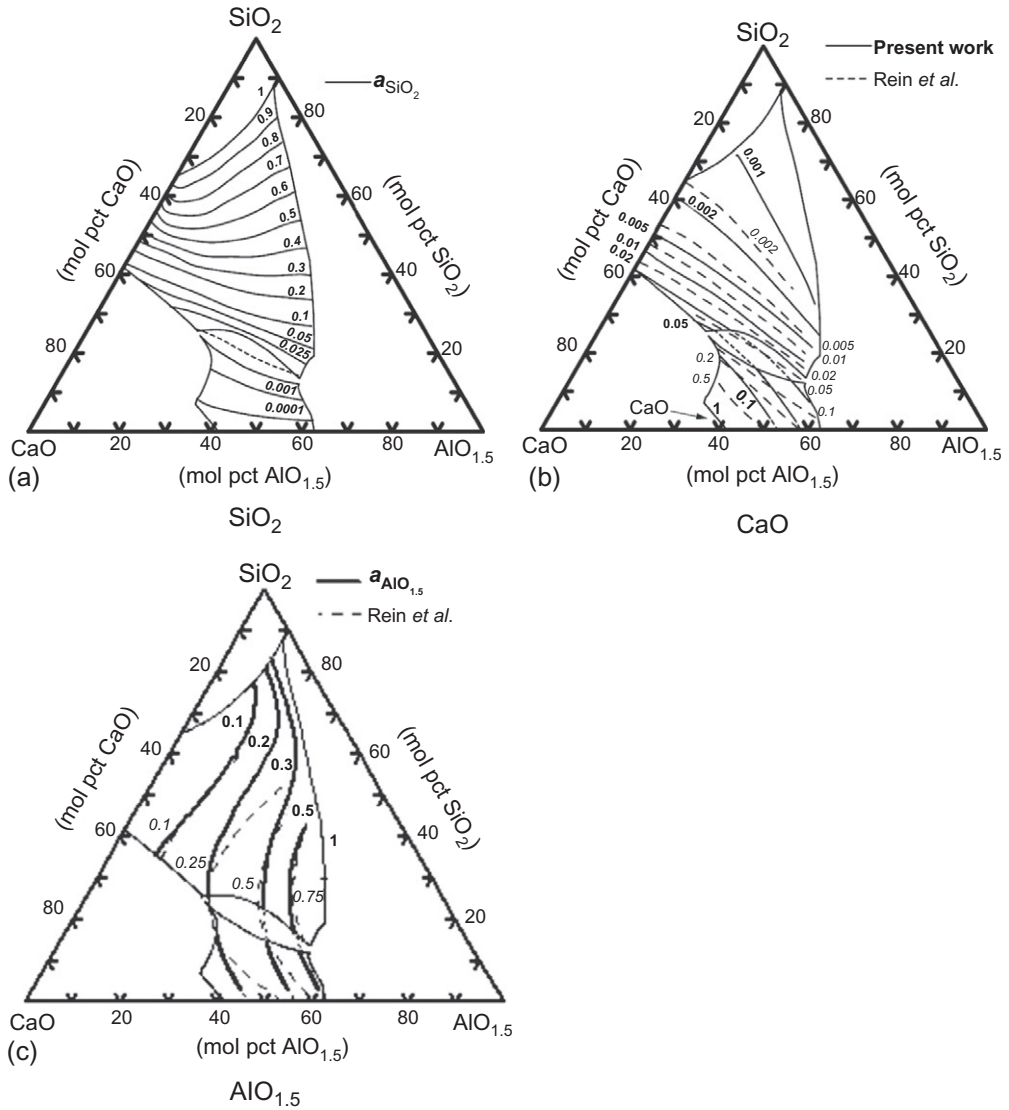


Figure 3.7.2 Iso-activity contours of each constituent for the $CaO–SiO_2–AlO_{1.5}$ system at 1823 K; (a) SiO_2, (b) CaO, and (c) $AlO_{1.5}$ [1,2,8].

decreases with increasing SiO_2 content. On the line *c–d*, CaO activity remains constant again in the Gibbs triangle $Ca_3SiO_5 + Ca_2SiO_4 + L$, then decreases along the line *d–e* in the two phase region of $Ca_2SiO_4 + L$. The short line *e–g*, is divided at point f into two separate three-phase regions of $Ca_2SiO_4 + Ca_2Al_2SiO_7 + L$. Although CaO activity remains constant within each three-phase region it abruptly drops at point f. Along the line *g–h* in the other two phase region of $Ca_2SiO_4 + L$, it decreases and also does

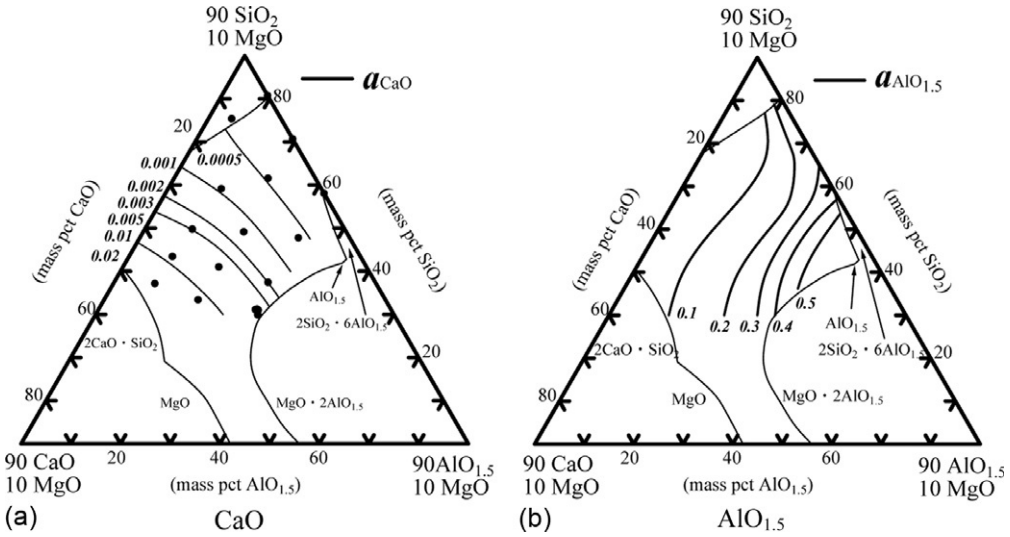


Figure 3.7.3 Iso-activity contours of (a) CaO and (b) $AlO_{1.5}$ for the CaO–SiO_2–$AlO_{1.5}$–MgO system at 1823 K [8].

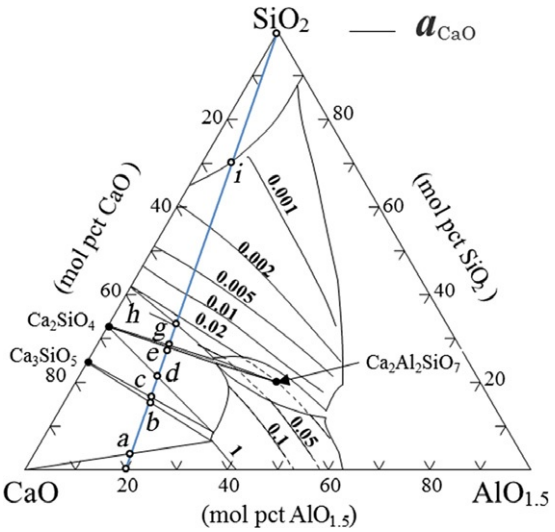


Figure 3.7.4 Iso-activity contours of CaO and the line for $X_{CaO}/X_{AlO1.5} = 4$ in the isothermal section of the CaO–SiO_2–$AlO_{1.5}$ system at 1823 K.

the same along the line *h*–*i* within the single phase liquid region. After point *i*, the CaO activity remains constant since the liquid composition is saturated with SiO_2 and does not change all the way to SiO_2. The variation of CaO activity is shown in Figure 3.7.5.

On the other hand, by measuring the chemical potential (activity) of a component of the system, phase relations can be confirmed. Hoshino and Iwase [9] have measured the

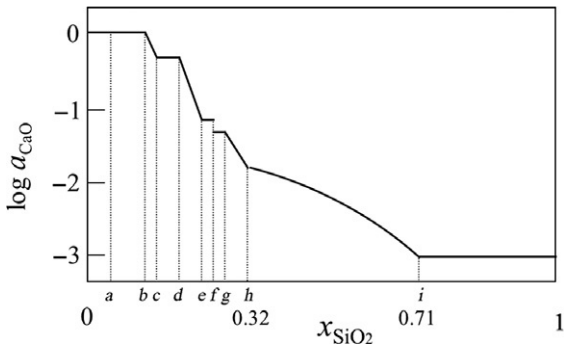


Figure 3.7.5 The variation of CaO activity at $X_{CaO}/X_{AlO1.5} = 4$ in the isothermal section of the $CaO–SiO_2–AlO_{1.5}$ system at 1823 K.

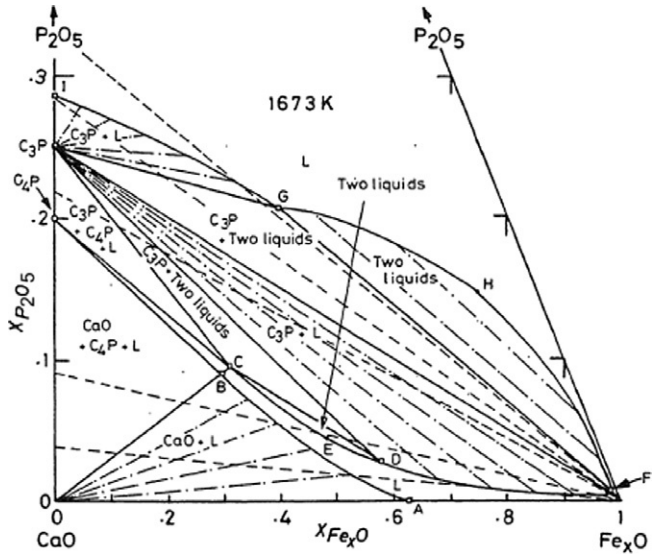


Figure 3.7.6 Isothermal section of the phase diagram of the system $CaO + P_2O_5 + Fe_xO$ at 1673 K [10,11]. $C_4P = Ca_4P_2O_9$, $C_3P = Ca_3P_2O_8$, and L = liquid [9].

chemical potentials of oxygen for the multiphase $CaO–P_2O_5$-Fe_xO slag in equilibrium with iron, namely the activity of Fe_xO followed by obtaining those of P_2O_5 and CaO. They were consistent with the ternary phase diagram (Figure 3.7.6) [10,11] as shown in Figures 3.7.7–3.7.10 [9].

Figure 3.7.7b shows the Fe_xO activity at the various compositions with $X_{CaO}/X_{P2O5} = 96/4$ and 10/1, where the bending points of the activity curves agree well with the phase boundaries shown in Figure 3.7.7a. In the three-phase regions surrounded by the Gibbs triangle, the activity value remains constant as shown by the lines 1–2, 5–6, and 9–10, although it continuously changes within the single phase region (L) and the two phase regions.

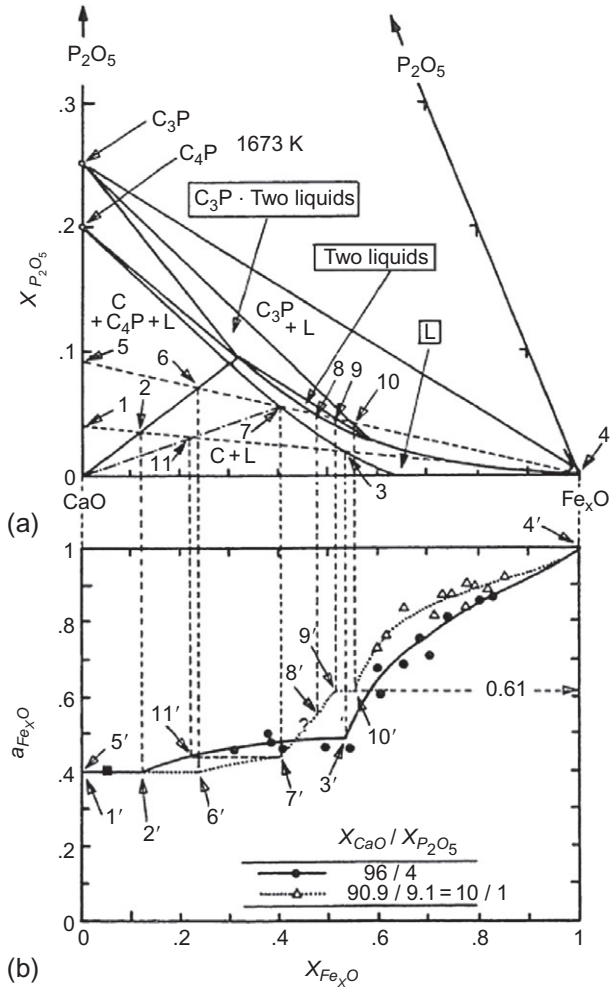


Figure 3.7.7 (a) and (b) Activities of Fe_xO for slags of CaO/P_2O_5 mole ratios of 96/4 and 90.9/9.1 (=10/1). C = CaO, $C_4P = Ca_4P_2O_9$, $C_3P = Ca_3P_2O_8$, and L = liquid [9].

3.7.2. BASICITY AND REFINING ABILITY OF SLAGS

Chemical composition of molten slags often becomes the key in the optimization of each refining process. Among others, basicity is known to be a major factor in the redox reactions during metal refining.

3.7.2.1. Basicity of the Slags

In the refining and alloying processes of metals, the distribution ratios of the impurity or additive elements between slags and metals will naturally control their removal fractions

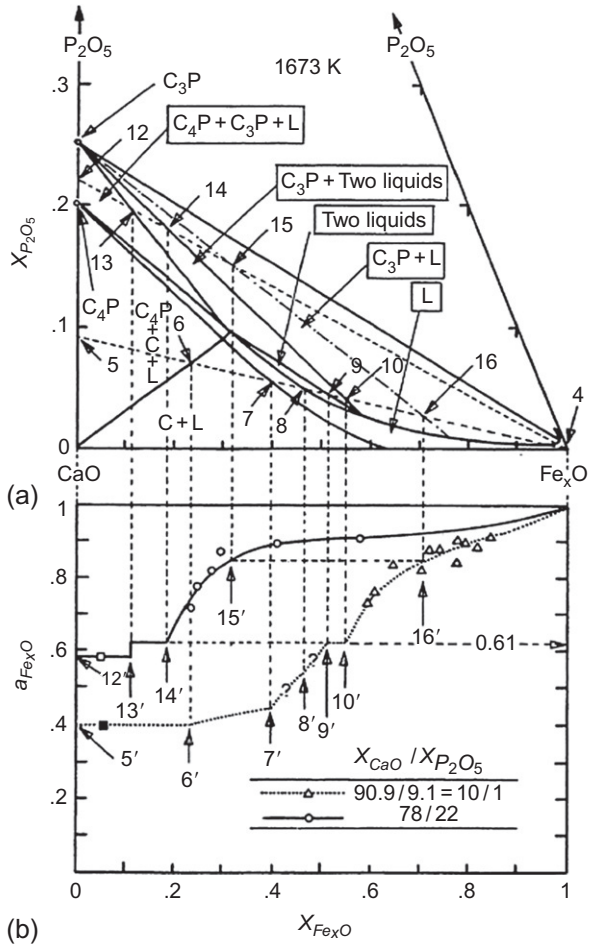


Figure 3.7.8 (a) and (b) Activities of Fe_xO for slags of CaO/P_2O_5 mole ratios of 90.9/9.1 (=10/1) and 78/22. C = CaO, $C_4P = Ca_4P_2O_9$, $C_3P = Ca_3P_2O_8$, and L = liquid [9].

or alloying yields. Distribution of the element M between slags and metals can be categorized into the following three types of reactions (3.7.2)–(3.7.4) depending on the form of M in the slag phase:

$$\underline{\mathrm{M}} + 2n\mathrm{O}^{2-} = \mathrm{M}^{4n-} + n\mathrm{O}_2 \tag{3.7.2}$$

$$\underline{\mathrm{M}} + m\mathrm{O}_2 = \mathrm{M}^{4m+} + 2m\mathrm{O}^{2-} \tag{3.7.3}$$

$$\underline{\mathrm{M}} + m\mathrm{O}_2 + n\mathrm{O}^{2-} = \mathrm{MO}_{2m+n}^{2n-} \tag{3.7.4}$$

When M exists in the slag phase as M^{4n-}, Equation (3.7.2), M in the metal phase will be removed via a reducing reaction. Sulfur is a typical impurity in hot metal which is generally removed into slags as the S^{2-} ion while in the blast furnace and during hot metal

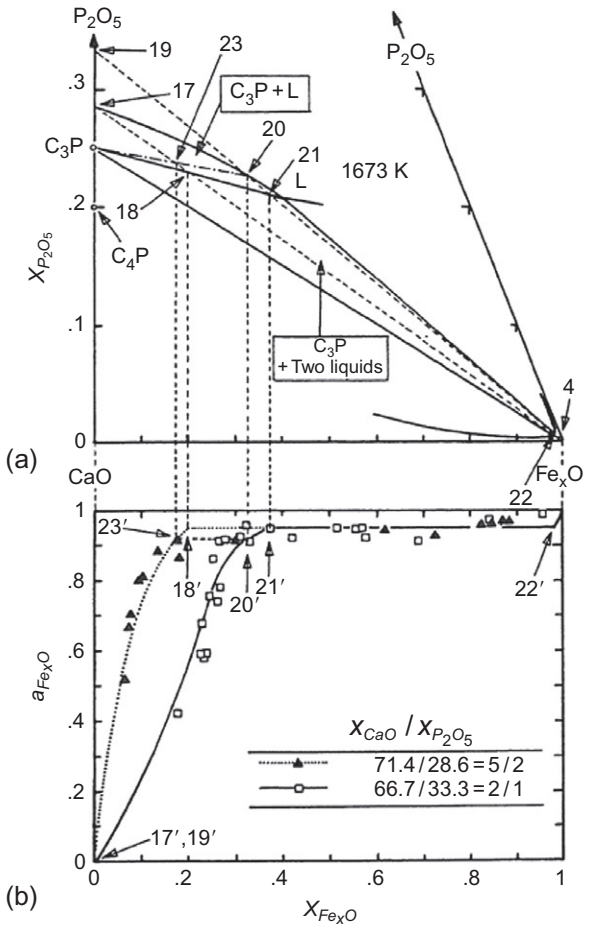


Figure 3.7.9 (a) and (b) Activities of Fe_xO for slags of CaO/P_2O_5 mole ratios of 71.4/28.6 (=5/2) and 66.7/33.3 (=2/1). $C_4P = Ca_4P_2O_9$, $C_3P = Ca_3P_2O_8$, and L = liquid [9].

treatment processes. On the other hand, M can be removed by oxidation and exist as either M^{4m+} or MO_{2m+n}^{2n-} in slags, Equations (3.7.3) and (3.7.4), respectively. Typical examples are the removal of Mn and P from hot metal by the respective slag–metal reactions.

As can be seen from the effect of O^{2-} ion in each reaction, more basic slags are preferable for the removal of M, such as S and P, by the reactions (3.7.2) and (3.7.4), while also preferable for lower loss of M, such as Mn, by reaction (3.7.3). Accordingly, basicity is a very important factor for most of the slag refining reactions in metallurgical processes. Although the conceptual definition of basicity should be expressed in terms of oxygen ion activity, the measurement of O^{2-} activity is practically impossible and a ratio of basic oxide content to that of acidic oxide, such as mass% CaO/mass% SiO_2, is widely used

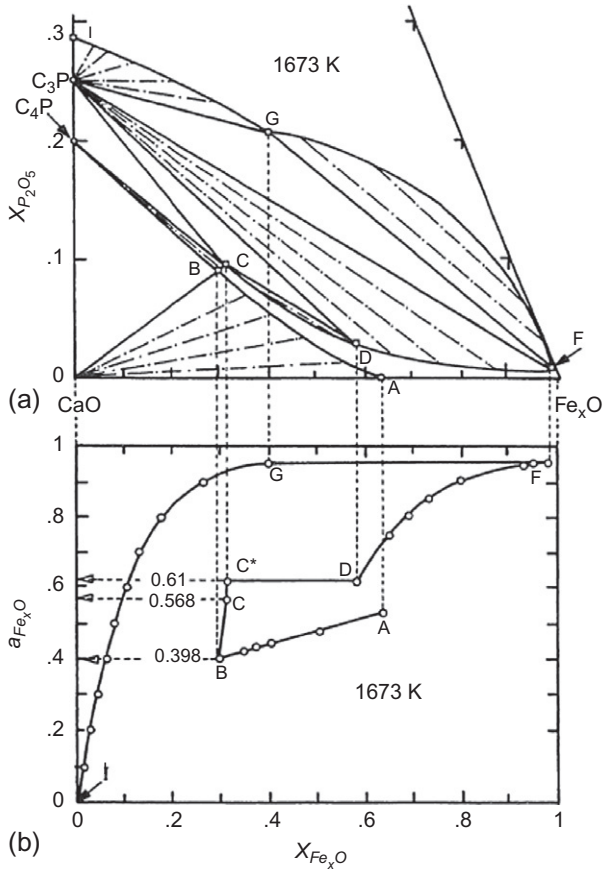


Figure 3.7.10 (a) and (b) Activities of Fe_xO along the phase boundary line A–B–C–D–F–G–I. $C_4P = Ca_4P_2O_9$, $C_3P = Ca_3P_2O_8$, and L = liquid [9].

as an index for slag basicity. For more exact evaluation, optical basicity and capacities are often used as shown in the following sections.

3.7.2.2. Optical Basicity

According to the definition of Lewis [12], an acid is a substance that can employ an electron lone pair from another molecule in completing the stable group of one of its own atoms, and a base is any species that donates a pair of electrons to the acid. In the case of molten oxides, the O^{2-} ion is a base and cations, such as Ca^{2+} and Si^{4+}, are acids. For instance, when alkaline or alkaline earth ions exist around the O^{2-} ion, they do not attract the pair electrons around the O^{2-} ion, and therefore do not change the electron density around the O^{2-} ion. Hence, they are considered to be strongly basic. On the other hand, when Si^{4+} ions exist around the O^{2-} ion, Si^{4+} ion will attract those pair

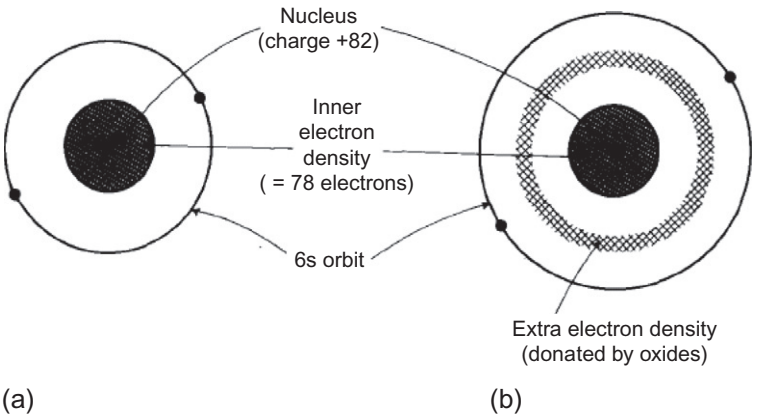


Figure 3.7.11 Schematic diagram of nephelauxetic effect for defining the optical basicity using the lead ion as an example. (a) Free Pb^{2+} ion and (b) Pb^{2+} ion after receiving negative charge from neighboring oxide ion [14].

electrons, which will form bonds such as Si–O^-, Si–O–Si, etc. Accordingly, the electron density around the O^{2-} ion will shift toward the Si^{4+} ion, forming a covalent bond, and the basicity will decrease.

Duffy and Ingram [13] have defined the optical basicity of molten oxides and glasses by applying the fact that the UV absorptions of 6s → 6p of Pb^{2+}, Tl^+, and Bi^{3+} ions will shift to higher frequency with increasing basicity of the matrix. This is known as the Nephelauxetic effect, Figure 3.7.11. For example, the absorption frequency of 60,700 cm^{-1} for an isolated Pb^{2+} ion in vacuum will shift to 29,700 cm^{-1} when a very small amount of Pb^{2+} is added to CaO. Accordingly, the optical basicity, Λ, was defined as Equation (3.7.5):

$$\Lambda_{Pb^{2+}} = \frac{\nu_{\text{free ion}} - \nu_{\text{glass}}}{\nu_{\text{free ion}} - \nu_{O^{2-}}} = \frac{60{,}700 - \nu_{\text{glass}}}{31{,}000} \tag{3.7.5}$$

Similarly, those for Tl^+ and Bi^{3+} were defined as Equations (3.7.6) and (3.7.7), respectively:

$$\Lambda_{Tl^+} = \frac{\nu_{\text{free ion}} - \nu_{\text{glass}}}{\nu_{\text{free ion}} - \nu_{O^{2-}}} = \frac{55{,}300 - \nu_{\text{glass}}}{18{,}300} \tag{3.7.6}$$

$$\Lambda_{Bi^{3+}} = \frac{\nu_{\text{free ion}} - \nu_{\text{glass}}}{\nu_{\text{free ion}} - \nu_{O^{2-}}} = \frac{56{,}000 - \nu_{\text{glass}}}{28{,}800} \tag{3.7.7}$$

Figure 3.7.12 shows the relationship between optical basicity values measured for the three ions and Na_2O content of the Na_2O–B_2O_3 glass together with that theoretically derived from the composition. Although the theoretical optical basicity is introduced in the following chapter, there is a similar composition dependency. The introduction of optical basicity enabled comparisons to be made of the basicity for various compositions of glasses.

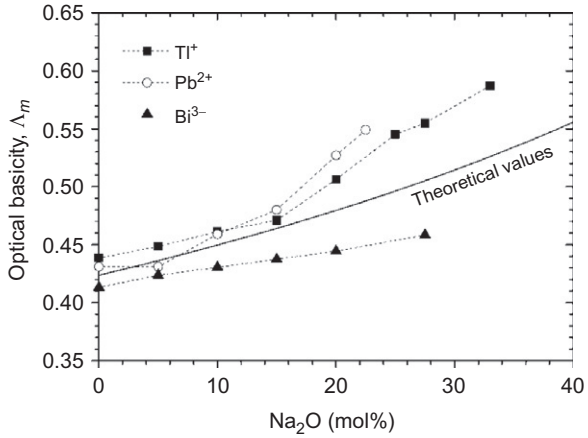


Figure 3.7.12 Experimentally determined optical basicities in the Na_2O–B_2O_3 glass system. Solid line indicates theoretically calculated optical basicity [14].

3.7.2.3. Theoretical Optical Basicity

From the optical basicity measured experimentally, Duffy and Ingram [14,15] introduced the new indicative, basicity moderating power, γ_i, which is the reciprocal of the optical basicity of each pure oxide. Also, γ_i has a relationship with Pauling's electronegativity for cations, χ, as shown by Equation (3.7.8). These derived values are summarized in Table 3.7.1.

$$\gamma_i = 1.36(\chi_i - 0.26) \tag{3.7.8}$$

Furthermore, they proposed the theoretical optical basicity of multicomponent systems by Equations (3.7.9) and (3.7.10)

$$\Lambda_{\text{th}} = \sum_i \frac{z_i r}{2\gamma_i} \tag{3.7.9}$$

$$\Lambda_{\text{th}} = \frac{\sum_i n_i \cdot X_i \cdot \Lambda_{\text{th},i}}{\sum_i n_i \cdot X_i} \tag{3.7.10}$$

Here, z_i, r_i, and γ_i are the valence, the number per one oxygen atom and the basicity moderating power of species i, respectively. X_i and n_i are the molar fraction of the oxide and number of oxygen per unit, respectively. In case of SiO_2, n_i is 2. Figure 3.7.13 shows the relationship between optical basicity values experimentally measured by the chemical shift of Pb^{2+} and those theoretically derived from the above equations. They mostly show very good agreement, indicating that the theoretical optical basicity can be utilized as a general basicity index.

Table 3.7.1 Basicity Moderating Power and Theoretical Basicity of Each Element Oxide [15]

Element	Basicity Moderating Power, γ_i	Theoretical Optical Basicity of Each Element Oxide, $\Lambda_{th,i}$
Chlorine	3.73	0.27
Nitrogen	3.73	0.27
Sulfur	3.04	0.33
Carbon	3.04	0.33
Phosphorus	2.50	0.40
Hydrogen	2.50	0.40
Boron	2.36	0.42
Silicon	2.09	0.48
Aluminum	1.65	0.61
Magnesium	1.28	0.78
Calcium	1.00	1.00
Lithium	1.00	1.00
Sodium	0.87	1.15
Potassium	0.73	1.37

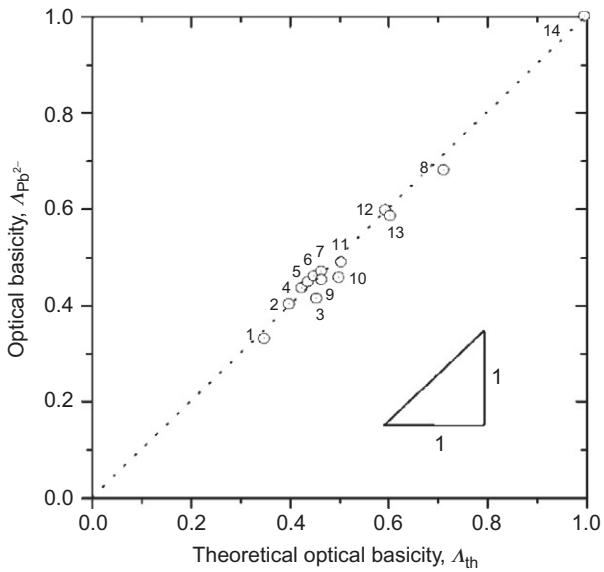


Figure 3.7.13 Graph of theoretical Λ_{th} versus practically determined Λ_{Pb}^{2+}. The media consist of (1) 100% H_2SO_4, (2) 100% H_3PO_4, (3) $NaHSO_4$–$KHSO_4$, (4) B_2O_3 glass, (5)–(8) Na_2O–B_2O_3 glasses containing (5) 5% (6) 10% (7) 15% (8) 67% Na_2O, (9) K_2SO_4–$ZnSO_4$ (2:3) glass, (10) $Ca(PO_3)_2$ glass, (11) K_2O–Al_2O_3–B_2O_3 (15.4:15.4:69.2) glass, (12) Al_2O_3, (13) Na_2O–SiO_2 (3:7), and (14) CaO [15].

3.7.2.4. Capacity and Dissolution

In the evaluation of refining reactions with slag treatments, distribution ratios are often used. However, such data often conform only to a specific process, which may not be applicable to other cases with different operating conditions. In order to provide a more widely applicable indicator of the distribution of elements between slag and metal phases, the concept of slag capacity was introduced by Carl Wagner [16]. This slag capacity indicator has been widely used to quantify the ability of a molten slag to absorb species such as sulfur, phosphorus, nitrogen, and carbon dioxide. These capacities indicate the solubilities of various gas species in molten slag when the slag is equilibrated with the appropriate gas species at unit partial pressure. The capacity of a slag for a particular species is a physicochemical property of the slag that depends only on temperature and slag composition.

3.7.2.4.1 Sulfide, Phosphate, and Carbonate Capacities [16]

As typical examples, desulfurization and dephosphorization reactions between metal and slag can be expressed in ionic form by Equations (3.7.11) and (3.7.12). Each reaction can be converted to the dissolution of sulfur and phosphorus from the gas phase into the molten slag as shown by Equations (3.7.13) and (3.7.14). The sulfide and phosphate capacities of the slag, i.e., the ability of the slag to absorb the respective gases, are defined in terms of measurable parameters as shown in Equations (3.7.15) and (3.7.16), respectively. These capacities have been measured for various slag systems and results are summarized in Figures 3.7.14 [17] and 3.7.15 [18], respectively.

$$\mathrm{S(in\,metal)} + \left(\mathrm{O^{2-}}\right) = \left(\mathrm{S^{2-}}\right) + \frac{1}{2}\mathrm{O_2(g)} \tag{3.7.11}$$

$$\mathrm{P(in\,metal)} + \frac{5}{4}\mathrm{O_2(g)} + \frac{3}{2}\left(\mathrm{O^{2-}}\right) = \left(\mathrm{PO_4^{3-}}\right) \tag{3.7.12}$$

$$\frac{1}{2}\mathrm{S_2(g)} + \left(\mathrm{O^{2-}}\right) = \left(\mathrm{S^{2-}}\right) + \frac{1}{2}\mathrm{O_2(g)} \tag{3.7.13}$$

$$\frac{1}{2}\mathrm{P_2(g)} + \frac{5}{4}\mathrm{O_2(g)} + \frac{3}{2}\left(\mathrm{O^{2-}}\right) = \left(\mathrm{PO_4^{3-}}\right) \tag{3.7.14}$$

$$C_{\mathrm{S^{2-}}} = \left(\mathrm{mass\%S^{2-}}\right)\frac{p_{\mathrm{O_2}}^{1/2}}{p_{\mathrm{S_2}}^{1/2}} = \frac{K_{7.13}a_{\mathrm{O^{2-}}}}{f_{\mathrm{S}}{}^{2-}} \tag{3.7.15}$$

$$C_{\mathrm{PO_4^{3-}}} = \frac{\left(\mathrm{mass\%PO_4^{3-}}\right)}{p_{\mathrm{P2}}^{1/2}\cdot p_{\mathrm{O_2}}^{5/4}} = \frac{K_{7.14}\left(a_{\mathrm{O^{2-}}}\right)^{3/2}}{f_{\mathrm{PO_4^{3-}}}} \tag{3.7.16}$$

Both capacities can also be expressed in terms of the collection of nonmeasureable parameters shown after the last equality sign in each of the Equations (3.7.15) and (3.7.16). Assuming that the variations of activity coefficients of sulfide ions and phosphate ions are small, the capacity approximately depends on basicity, $a_{\mathrm{O^{2-}}}$, which implies that

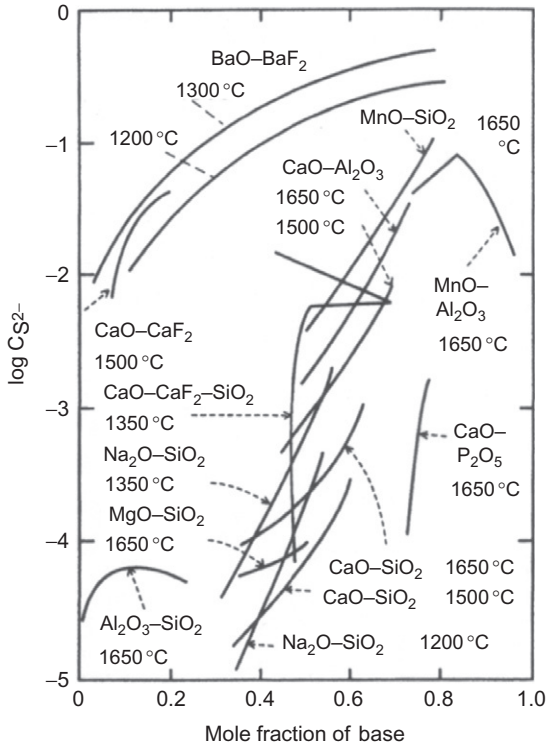


Figure 3.7.14 $C_{S^{2-}}$ for various slag systems [17].

capacity could be a semiquantitative index of the basicity of slags. Sosinski and Sommerville [19] have reported a very good correlation between sulfide capacity and optical basicity for various slag systems as shown in Figure 3.7.16.

Carbonate capacity, $C_{CO_3^{2-}}$, which is derived from the solubility of carbon dioxide gas into molten slags (Equation 3.7.17) and defined as Equation (3.7.18), can be another such indicator of slag basicity:

$$CO_2(g) + \left(O^{2-}\right) = \left(CO_3^{2-}\right) \tag{3.7.17}$$

$$C_{CO_3^{2-}} = \frac{\left(\text{mass\%}CO_3^{2-}\right)}{p_{CO_2}} = \frac{K_{7.17}a_{O^{2-}}}{f_{CO_3^{2-}}} \tag{3.7.18}$$

For practical applications, each capacity can be converted to a distribution ratio of a particular element between slag and metal, when the thermodynamic property of the element dissolved in the metal is of interest. For example, in the case of sulfur and phosphorus, their dissolution reactions from the gas phase into molten iron can be expressed by Equations (3.7.19) and (3.7.20) and the corresponding Gibbs energies of reaction can

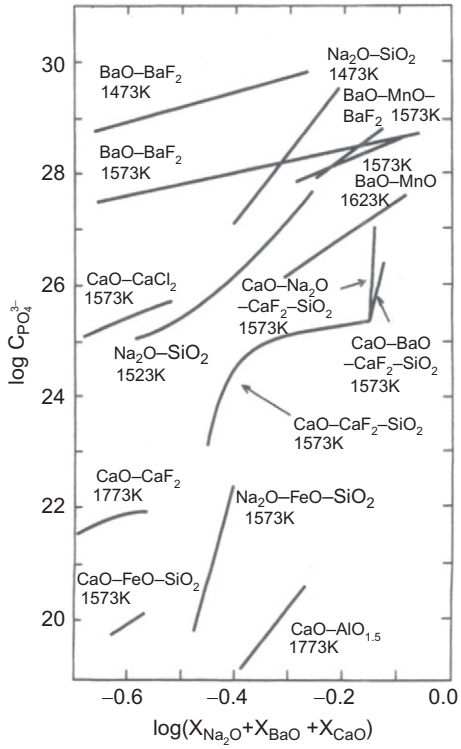


Figure 3.7.15 $C_{PO_4^{3-}}$ for various slag systems [18].

be expressed by Equations (3.7.21) and (3.7.22) where the standard state for the solutes is located on the Henry's law line corresponding to the hypothetical 1 mass% of the respective elements in molten iron:

$$\frac{1}{2}S_2(g) = S(1\,\text{mass\%}) \tag{3.7.19}$$

$$\frac{1}{2}P_2(g) = P(1\,\text{mass\%}) \tag{3.7.20}$$

$$\Delta G^\circ = -131{,}900 + 22.05T\,(\text{J/mol})\,[20] \tag{3.7.21}$$

$$\Delta G^\circ = -122{,}200 - 19.25T\,(\text{J/mol})\,[20] \tag{3.7.22}$$

The distribution ratios of sulfur and phosphorus between slag and molten iron, L_S and L_P, can be derived from Equations (3.7.23) and (3.7.24), respectively:

$$L_S = \frac{(\text{mass\%}\,S^{2-})}{[\text{mass\%}\,S]} = \frac{f_S C_{S^{2-}}}{K_{7.19} p_{O_2}^{1/2}} \tag{3.7.23}$$

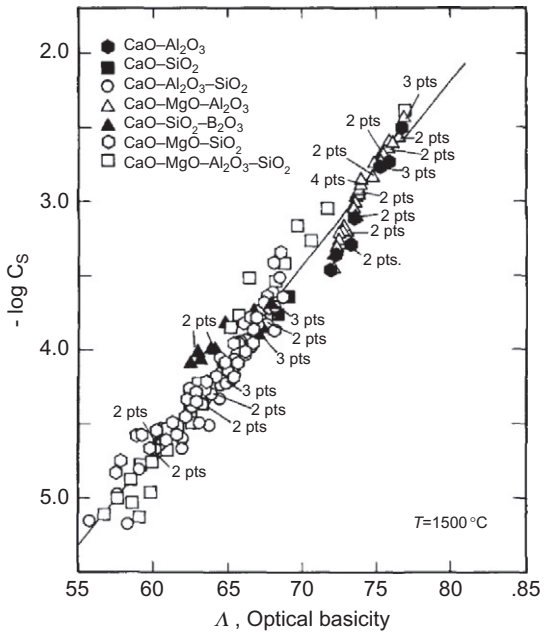


Figure 3.7.16 Correlation of sulfide capacity data with the calculated optical basicity of slags at 1773 K [19].

$$L_P = \frac{0.326\left(\text{mass\%}PO_4^{3-}\right)}{[\text{mass\%}\,P]} = \frac{0.326 f_P C_{PO_4^{3-}} p_{O_2}^{5/4}}{K_{7.20}} \tag{3.7.24}$$

3.7.2.4.2 Phosphide and Nitride Capacities

Under reducing conditions, some elements tend to ionize by accepting electrons instead of donating them, thus indicating they would rather exist as anions than as cations. In steelmaking processes, phosphorus is mostly removed to the slag phase as phosphate by oxidation. On the other hand, dephosphorization can be performed by reduction under extremely reducing conditions as shown in Equation (3.7.25). The phosphide capacity is then defined as Equation (3.7.26):

$$\frac{1}{2}P_2(g) + \frac{3}{2}\left(O^{2-}\right) = \left(P^{3-}\right) + \frac{3}{4}O_2(g) \tag{3.7.25}$$

$$C_P{}^{3-} = \frac{(\text{mass\%}P^{3-})p_{O_2}^{3/4}}{p_{P_2}^{1/2}} = \frac{K_{7.25}\left(a_{O^{2-}}\right)^{3/2}}{f_P^{3-}} \tag{3.7.26}$$

Tabuchi and Sano [21,22] have reported the phosphide capacity for the $CaO–CaF_2$ and the $BaO–BaF_2$ systems as shown in Figures 3.7.17 and 3.7.18.

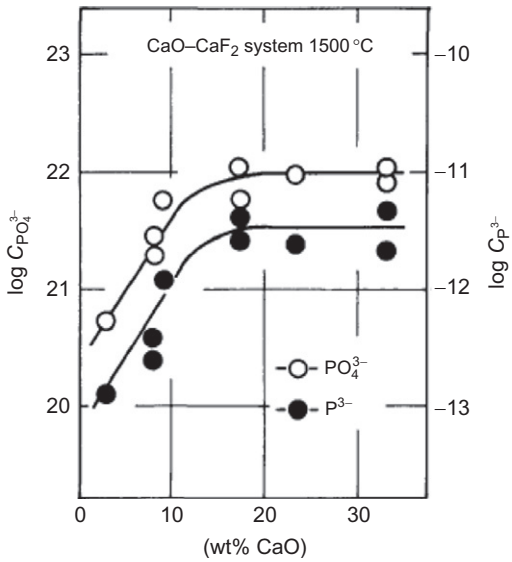


Figure 3.7.17 Phosphate and phosphide capacities for the $CaO–CaF_2$ system at 1500 °C [21].

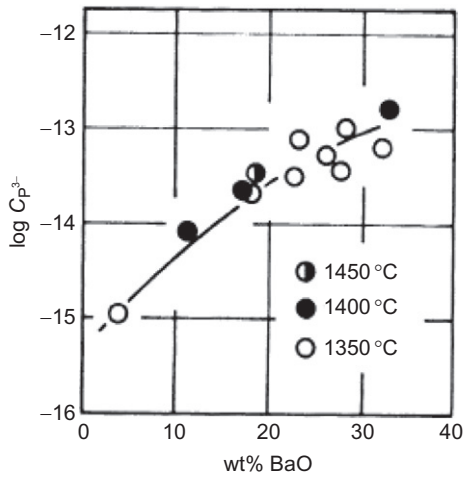


Figure 3.7.18 Phosphide capacities for the $BaO–BaF_2$ system [22].

Nitride capacity has been used to evaluate the possibility of nitrogen removal from molten metals during slag treatment. It is basically similar to phosphide capacity and defined as follows:

$$\frac{1}{2}N_2(g)+\frac{3}{2}\left(O^{2-}\right)=\left(N^{3-}\right)+\frac{3}{4}O_2(g) \tag{3.7.27}$$

$$C_N^{3-} = \frac{(\text{mass\%}N^{3-})p_{O_2}^{3/4}}{p_{N_2}^{1/2}} = \frac{K_{7.27}(a_{O^{2-}})^{3/2}}{f_{N^{3-}}} \tag{3.7.28}$$

In silicate slags, however, due to the nature of the covalent bond between silicon and nitrogen, nitrogen tends to exist in a silicate network structure by replacing oxygen in acidic compositions. Hence, the slag composition dependence of nitrogen is somewhat complicated compared with other capacities. Some reported values were summarized by Martinez and Sano [23,24] as shown in Figure 3.7.19.

3.7.2.4.3 Other Capacities

Morita *et al.* [31–34] defined chloride capacity to evaluate chlorine dissolution when chlorine was involved in slag treatment processes, borate capacity in slag treatment during silicon refining, and ruthenate and rhodate capacities in recycling platinum group metals.

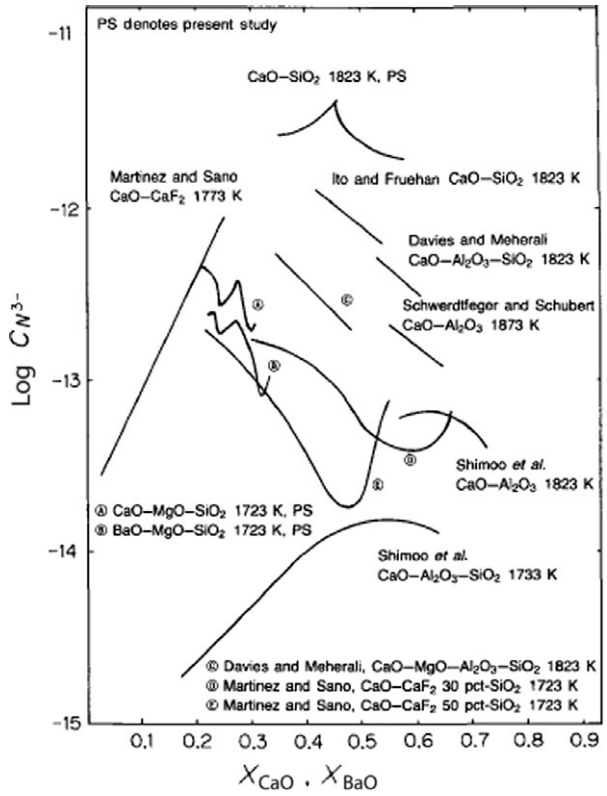


Figure 3.7.19 Nitride capacities of a variety of slag systems as a function of CaO or BaO mole fraction [23–30].

These capacities are defined according to the following reactions:
Chloride capacity (Figure 3.7.20) [31]

$$\frac{1}{2}\mathrm{Cl_2(g)}+\frac{1}{2}\left(\mathrm{O^{2-}}\right)=\left(\mathrm{Cl^-}\right)+\frac{1}{4}\mathrm{O_2(g)} \tag{3.7.29}$$

$$C_{\mathrm{Cl}^-}=\frac{(\mathrm{mass\%Cl^-})p_{\mathrm{O_2}}^{1/4}}{p_{\mathrm{Cl_2}}^{1/2}}=\frac{K_{7.29}(a_{\mathrm{O}}{}^{2-})^{1/2}}{f_{\mathrm{Cl}^-}} \tag{3.7.30}$$

Borate capacity (Figure 3.7.21) [32]

$$\mathrm{B(s)}+\frac{3}{4}\mathrm{O_2(g)}+\frac{3}{2}\left(\mathrm{O^{2-}}\right)=\left(\mathrm{BO_3^{3-}}\right) \tag{3.7.31}$$

$$C_{\mathrm{BO_3}}^{3-}=\frac{\left(\mathrm{mass\%BO_3^{3-}}\right)}{\left(a_{\mathrm{B}}\cdot p_{\mathrm{O_2}}^{3/4}\right)}=\frac{K_{7.31}(a_{\mathrm{O}}{}^{2-})^{3/2}}{f_{\mathrm{BO_3}}^{3-}} \tag{3.7.32}$$

Ruthenate capacity (Figure 3.7.22) [33]

$$\mathrm{Ru(s)}+\frac{3}{4}\mathrm{O_2(g)}+\frac{1}{2}\left(\mathrm{O^{2-}}\right)=\left(\mathrm{RuO_2^-}\right) \tag{3.7.33}$$

$$C_{\mathrm{RuO_2}^-}=\frac{\left(\mathrm{mass\%RuO_2^-}\right)}{a_{\mathrm{Ru}}\cdot p_{\mathrm{O_2}}^{3/4}}=\frac{K_{7.33}(a_{\mathrm{O}}{}^{2-})^{1/2}}{f_{\mathrm{RuO_2}^-}} \tag{3.7.34}$$

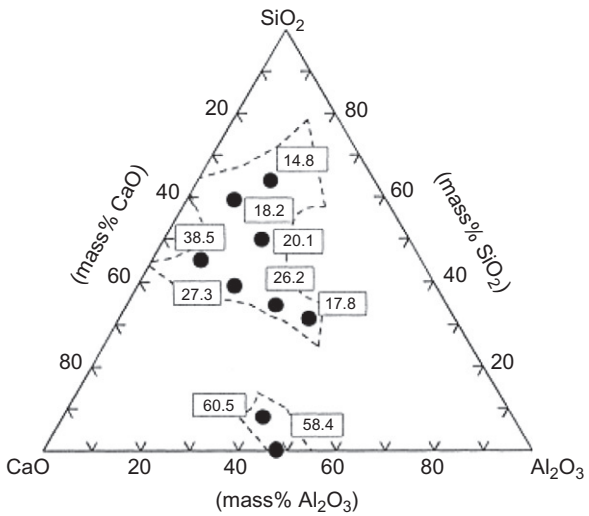


Figure 3.7.20 Chloride capacities for the CaO–SiO_2–Al_2O_3 system at 1748 K [31].

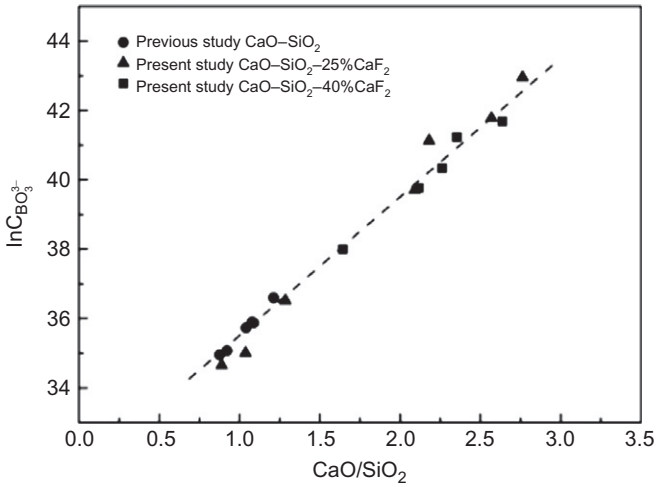


Figure 3.7.21 Logarithmic relation between the basicity and the borate capacity of silicate slags at 1823 K [32].

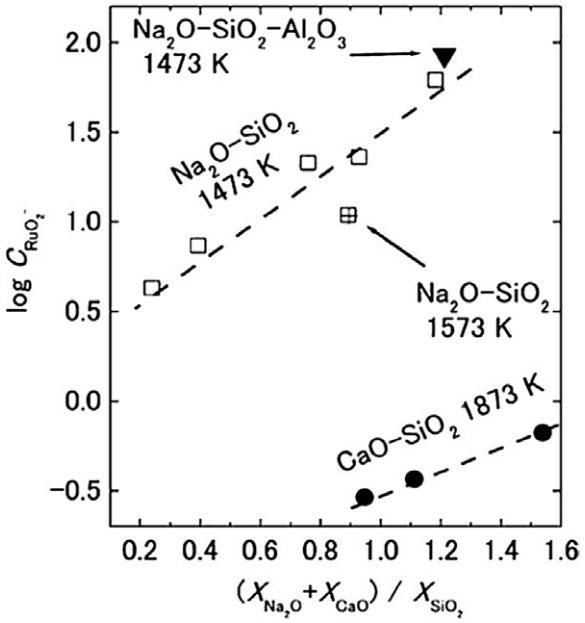


Figure 3.7.22 Slag composition dependence of ruthenate capacity [33].

Rhodate capacity (Figure 3.7.23) [34]

$$\mathrm{Rh(s)}+\frac{3}{4}\mathrm{O_2(g)}+\frac{1}{2}\left(\mathrm{O^{2-}}\right)=\left(\mathrm{RhO_2^-}\right) \tag{3.7.35}$$

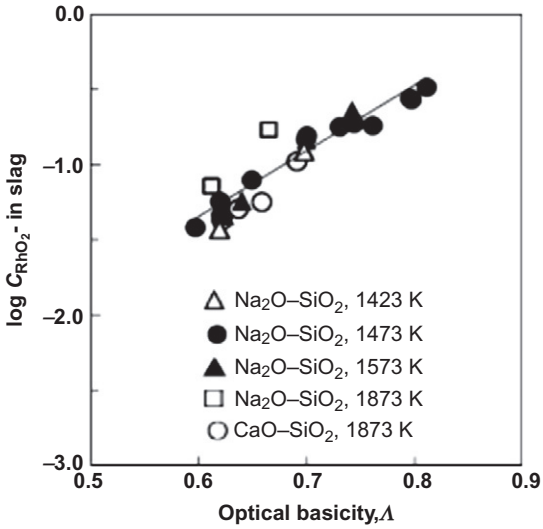


Figure 3.7.23 Correlation between the rhodate capacity and the theoretical optical basicity [34].

$$C_{RuO_2^-} = \frac{(\text{mass\%}RhO_2^-)}{\left(a_{Rh} \cdot p_{O_2}^{3/4}\right)} = \frac{K_{7.35}(a_O{}^{2-})^{1/2}}{f_{RhO_2^-}} \tag{3.7.36}$$

3.7.3. STRUCTURE AND THERMOCHEMICAL MODELS FOR SLAGS

As described by many authors, oxides can be categorized in terms of the fraction of ionic/covalent bonds that exist between the element and the oxygen atoms. The tendency to become a cation by releasing an oxide ion, is related to the electronegativity, and represents the ability to break the network forming covalent bond, and vice versa. Hence oxides can be categorized into either a network forming group or a network modifying group and are called acidic or basic oxides, respectively. Certain oxides, known as amphoteric oxides, can exhibit either an acidic character when present in a basic melt, or a basic character when present in an acidic melt. Representative network forming oxides are SiO_2, P_2O_5, and B_2O_3, and examples of network modifying oxides are Na_2O, CaO, and MgO. Amphoteric behavior is exhibited by Al_2O_3 and Cr_2O_3. During the mixing of oxides to form a solution, the different types of oxides, basic and acidic, have a strong affinity for each other due to their respective ability to provide and accept oxide ions, hence forming a very stable configuration in the liquid state. For this reason, when basic and acidic oxides form liquid solutions, there is significant negative deviation from ideality and this is reflected by the high negative Gibbs energies of mixing. The resultant oxide melt or molten slag, can be simply considered as a mixture of cations and complex

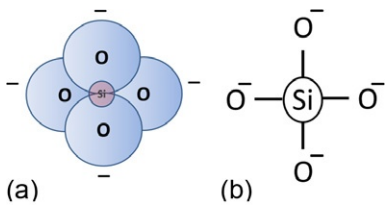


Figure 3.7.24 Tetrahedral unit of the silicate structure.

anions, such as Ca^{2+} and SiO_4^{4-} in case of the CaO–SiO_2 system based on the reaction shown in Equation (3.7.37):

$$SiO_2 + 2CaO = SiO_4^{4-} + 2Ca^{2+} \tag{3.7.37}$$

Silicate structures can be categorized into 5 types denoted by Q^n ($n = 0$, 1, 2, 3, 4), where n represents the number of bridging oxygens connected to the silicon atoms. When the silicon atom connects to 4 oxygen atoms forming a tetrahedral unit as shown in Figure 3.7.24a, it can be represented as indicated in Figure 3.7.24b. The local structures of Si for various Q^n ($n = 1$, 2, 3, 4) are shown in Figure 3.7.25a–d. However, at the composition of CaO:$SiO_2 = 2{:}1$, there exists a significantly stable solid compound of Ca_2SiO_4 and the liquid is practically formed at higher SiO_2 contents as can be seen in the phase diagram of the CaO–SiO_2 binary system (Figure 3.5.12a). Since the amount of CaO is not enough to dissociate all the SiO_2 network into SiO_4^{4-} tetrahedra, various kinds of silicate complex anions are formed. The addition of CaO to the SiO_2 network structure will introduce negative charges on the unshared oxygen at the corners where the covalent bonds with other silicon atoms are broken. Accordingly, Ca^{2+} ions locate near these negatively charged oxygens.

The structure of silicate melts significantly affects the thermochemical properties as well as physical properties, such as viscosity, thermal conductivity, etc. The thermodynamic description of ionic liquids is complicated as the entropy of mixing is affected by the mixing of cations among themselves and anions in a similar fashion. The characteristic features of oxide melts have been well reviewed in text books, such as those written by Richardson [35], Rao [36], Turkdogan [37] and more recently by Seetharaman [38]. Aspects of some of the classical models are outlined in the following sections.

3.7.3.1. Temkin's and Flood *et al.*'s Description of Ionic Melts [38]

For ionic melts, Temkin [39] suggested that anions and cations should be grouped separately and that the entropies of mixing should be calculated separately for each subgrouping. On this basis, he suggested that the activity of a component, MA_2, in a salt melt, is given by

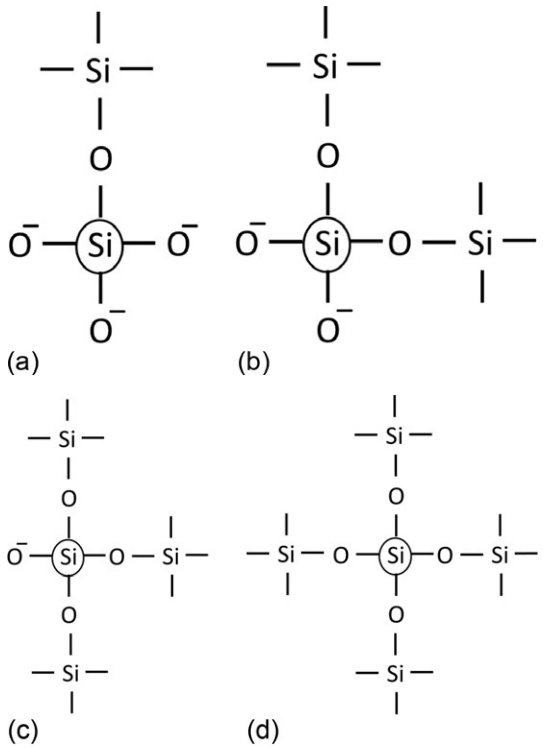


Figure 3.7.25 Local structure of Si atom for Q^n. (a) $n=1$, (b) $n=2$, (c) $n=3$, and (d) $n=4$.

$$a_{MA_2} = N_M^{2+} \cdot N_{A-}^2 \tag{3.7.38}$$

where N_M^{2+} is the cation fraction of M^{2+} ions and N_{A-} the anion fraction of $A-$ ions. Later Flood *et al.* [40], introduced the concept of equivalent ion fractions. For example, in the case of the salt melt NaCl–$CaCl_2$, the activity of NaCl is given by:

$$a_{NaCl} = N'_{Na^+} \cdot N'_{Cl^-} \tag{3.7.39}$$

where N′ terms are the equivalent ionic fractions. N'_{Na^+} can be defined as:

$$N'_{Na^+} = \left(\frac{n_{Na^+}}{n_{Na^+} + n_V + n_{Ca^{2+}}}\right) = \left(\frac{n_{Na^+}}{n_{Na^+} + 2n_{Ca^{2+}}}\right) \tag{3.7.40}$$

The second equality can be assumed because a cation vacancy is formed when Ca^{2+} ion is replaced by Na^+ ion. The choice of Temkin's or Flood *et al.*'s ion activity concept, according to Sridhar and Jeffes [41], should be based on the extent of deviation of the system from ideality. For low values of ΔH^M, Temkin activities can be used while, for systems with high values of ΔH^M it is more appropriate to use the concept of Flood *et al.*

3.7.3.2. Richardson's Theory of Ideal Mixing of Silicates [38]

Richardson [42] proposed that binary silicates of equal silica mole fraction (such as $FeSiO_3 + CaSiO_3$) mix ideally with one another. This would mean that the enthalpy of mixing is zero and the entropy of mixing, which is the same as the configurational entropy arising from the mixing of cations only, will be ideal.

This is given by:

$$\Delta S^{M} = -R\left[\left(X_{MO}\ln\left(\frac{X_{MO}}{(X_{MO}+X_{YO})}\right)\right)+\left(X_{YO}\ln\left(\frac{X_{YO}}{(X_{MO}+X_{YO})}\right)\right)\right] \quad (3.7.41)$$

The Gibbs energy of mixing is:

$$\Delta G^{M} = -T\Delta S^{M} \quad (3.7.42)$$

The theory of ideal mixing is very useful in estimating the ternary activities from the binary values. The validity of the theory is somewhat uncertain when the cation sizes differ widely.

3.7.3.3. Lumsden's Description of Silicates [38,43]

Lumsden proposed that the silicate melts can be considered as melts consisting of O^{2-} ions and cations like Ca^{2+}, Fe^{2+} and even Si^{4+}, the latter by considering the SiO_4^{4-} tetrahedral as dissociating into Si^{4+} and O^{2-} ions. Lumsden's consideration demanded the visualization of pure covalent liquid silica in contrast to the fully ionized silica in the silicate. Lumsden introduced a change of the standard state in order to account for this. While the Lumsden description is contrary to the structure of silicates, it is found to be a very useful tool in empirical modeling of slags.

3.7.3.4. Slag Models [38]

A number of models have been developed for providing an adequate thermodynamic description of slags. These can be classified into structural models and semiempirical motels. Structural models are based on the polymer theory as applied to silicate melts, the pioneering work being that of Masson [44]. The weight fractions of the various anionic species can be calculated by the polymeric model. Although they are successful for simple silicates, a great deal of further work is necessary for multicomponent slags.

Kapoor *et al.* [45] presented a statistical thermodynamic treatment of silicate melts where units of one oxygen and two cations are visualized. The model was later expanded to more complex systems and is referred to as the IRSID model. Models based on silicate structure and quasichemical approach have been developed by Pelton and his group [46]. These form the basis for silicate descriptions for the Factsage system as introduced in Chapter 9.

3.7.4. OXIDATION–REDUCTION EQUILIBRIUM IN SLAGS

Many transition metal cations exist in molten slags in various oxidation states. Their ratios depend on oxygen partial pressure, temperature, and slag composition, particularly the basicity. When metallic elements are oxidized to a valence state of m, some exist as single cations, M^{m+}, while others as complex anions, $MO_{(m+p)/2}^{p-}$. The equilibria can be expressed by the following reactions:

$$M + \frac{m}{4}O_2 = M^{m+} + \frac{m}{2}O^{2-} \tag{3.7.43}$$

$$M + \frac{m}{4}O_2 + \frac{p}{2}O^{2-} = MO_{(m+p)/2}^{p-} \tag{3.7.44}$$

Hence, any equilibria between two ionic species of transition metals can be expressed as a combination of two different equilibria of Equations (3.7.43) and/or (3.7.44). They are categorized into three types as follows:

(i) Redox between cations

Redox equilibrium between two cations, M^{m+} and $M^{n+}(m<n)$, can be expressed by Equation (3.7.45).

$$M^{m+} + \frac{n-m}{4}O_2 = M^{n+} + \frac{n-m}{2}O^{2-} \tag{3.7.45}$$

(ii) Redox between cation and anion

Redox equilibria between a cation and an anion, M^{m+} and $MO_{(n+p)/2}^{p-}(m<n)$, can be expressed by Equation (3.7.46).

$$M^{m+} + \frac{n-m}{4}O_2 + \frac{m+p}{2}O^{2-} = MO_{(n+p)/2}^{p-} \tag{3.7.46}$$

(iii) Redox between anions

Redox equilibria between two anions, $MO_{(m+p)/2}^{p-}$ and $MO_{(n+q)/2}^{q-}(m<n, p<q)$, can be expressed by Equation (3.7.47).

$$MO_{(m+p)/2}^{p-} + \frac{n-m}{4}O_2 + \frac{q-p}{2}O^{2-} = MO_{(n+q)/2}^{q-} \tag{3.7.47}$$

When the contents of such ionic species in slags are small enough, the existence ratio r_M, of ions with different valence states of m and n, explicitly depends on oxygen partial pressure as shown by Equation (3.7.48) regardless of the formula, M^{m+} or $MO_{(m+p)/2}^{p-}$:

Table 3.7.2 Temperature Dependence of the Redox Equilibrium Constants for Sodium Disilicate Melts Containing Less than 2% of Variable-Valence Ions [37,47,48]

$\log\left(\frac{Ti^{4+}}{Ti^{3+}}\right)^2 p_{O_2}^{-1/2} = \frac{12{,}565}{T} + 2.00$
$\log\left(\frac{Mn^{3+}}{Mn^{2+}}\right)^2 p_{O_2}^{-1/2} = \frac{6010}{T} - 5.92$
$\log\left(\frac{Fe^{3+}}{Fe^{2+}}\right)^2 p_{O_2}^{-1/2} = \frac{11{,}980}{T} - 4.75$
$\log\left(\frac{Co^{3+}}{Co^{2+}}\right)^2 p_{O_2}^{-1/2} = \frac{2185}{T} - 3.97$
$\log\frac{Sn^{4+}}{Sn^{2+}} p_{O_2}^{-1/2} = \frac{18{,}575}{T} - 9.18$
$\log\frac{Sb^{5+}}{Sb^{3+}} p_{O_2}^{-1/2} = \frac{11{,}475}{T} - 7.50$
$\log\left(\frac{Ce^{4+}}{Ce^{3+}}\right)^2 p_{O_2}^{-1/2} = \frac{3280}{T} - 1.44$

$$r_M = \left(\frac{{X_M}^{n+}}{{X_M}^{m+}}\right) = k p_{O_2}^{(n-m)/4} \tag{3.7.48}$$

where k denotes a constant depending on slag composition and temperature.

As Turkdogan [37] summarized in Table 3.7.2, redox equilibrium constants of various elements for sodium disilicate melts in the temperature range 1085–1300 °C are expressed as a function of temperature.

Morita and Sano *et al.* [49,50] have clarified the behavior of chromium redox equilibria among divalent, trivalent, and hexavalent chromium ions in molten slags, which contain typical examples of above cases. Chromium tends to exist in the hexavalent state rather than the trivalent state when slags are more basic and when the oxygen partial pressure is higher, while divalent chromium is more stable when slags are acidic and conditions are strongly reducing. Figures 3.7.26 and 3.7.27 show the basicity dependences of Cr^{6+}/Cr^{3+} and Cr^{2+}/Cr^{3+} ratios for the $MgO–SiO_2–CaO–CrO_X$ system in air and under reducing conditions, respectively. Figure 3.7.28 shows the oxygen partial pressure dependence of Cr^{2+}/Cr^{3+} ratios for the $MgO–SiO_2–CaO–CrO_X$ system.

According to the following redox equilibria of chromium, each ratio varies with oxygen partial pressure and basicity in typical molten slags at 1600 °C.

$$CrO_2^- + \frac{3}{4}O_2 + \frac{1}{2}O^{2-} = CrO_4^{2-} \tag{3.7.49}$$

$$Cr^{2+} + \frac{1}{4}O_2 + \frac{3}{2}O^{2-} = CrO_2^- \tag{3.7.50}$$

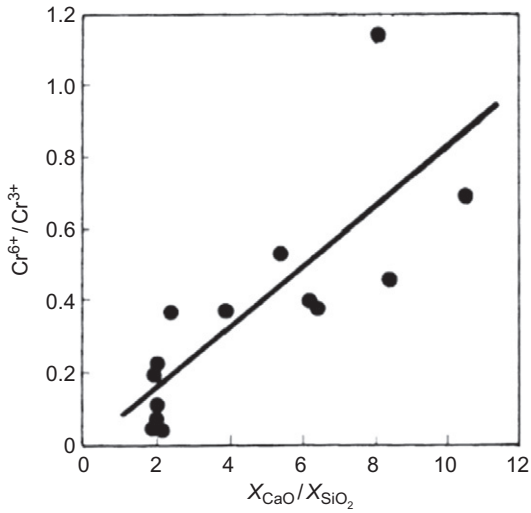


Figure 3.7.26 Basicity dependence of Cr^{6+}/Cr^{3+} ratio in $MgO–SiO_2–CaO–CrO_X$ melts at 1600 °C in air [49].

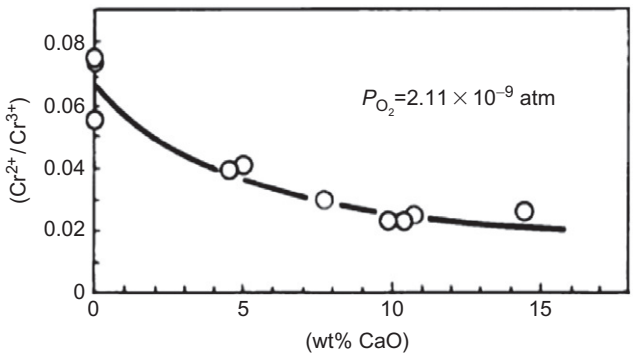


Figure 3.7.27 Effect of CaO content on the Cr^{2+}/Cr^{3+} ratio in $MgO–SiO_2–CaO–CrO_X$ melts ($2MgO \cdot SiO_{2satd}$) at 1600 °C and $P_{O_2} = 2.11 \times 10^{-9}$ atm [50].

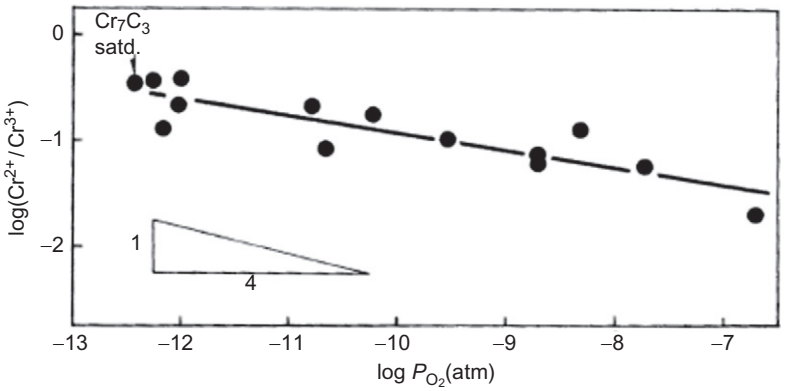


Figure 3.7.28 Oxygen partial pressure dependence of the Cr^{2+}/Cr^{3+} ratio in $MgO–SiO_2–CrO_X$ melts ($2MgO \cdot SiO_{2satd.}$) at 1600 °C [50].

Accordingly, basic slag compositions would make hexavalent chromium more stable in air, while divalent chromium is more stable in acidic slags under reducing conditions. These facts are important not only in optimizing slag compositions for the smelting and refining of stainless steels, but also in the prevention of hexavalent chromium dissolution from waste slags.

REFERENCES

[1] K. Kume, K. Morita, T. Miki, N. Sano, ISIJ Int. 40 (2000) 561.
[2] R.H. Rein, J. Chipman, Trans. AIME 233 (1965) 415.
[3] K. Sawamura, Tetsu-to-Hagané Overseas 2 (1962) 219.
[4] R.A. Sharma, F.D. Richardson, J. Iron Steel Inst. 200 (1962) 373.
[5] P.T. Carter, T.G. Macfarlane, J. Iron Steel Inst. 185 (1957) 54.
[6] J.D. Baird, J. Taylor, Trans. Faraday Soc. 54 (1958) 527.
[7] G. Eriksson, P. Wu, M. Blander, A.D. Pelton, Can. Metall. Q. 33 (1994) 13.
[8] K. Morita, K. Kume, N. Sano, ISIJ Int. 40 (2000) 554.
[9] H. Hoshino, M. Iwase, Metall. Mater. Trans. B. 27B (1996) 595.
[10] G. Tromel, H.W. Fritze, Arch. Eisenhüttenwes. 30 (1959) 461.
[11] G. Tromel, W. Fix, Arch. Eisenhüttenwes. 33 (1962) 755.
[12] G.N. Lewis, Valence and the Structure of Atoms and Molecules, The Chemical Catalog Co. Inc., New York, 1923, p. 142.
[13] J. Duffy, M. Ingram, J. Am. Chem. Soc. 93 (1971) 6448.
[14] J. Duffy, M. Ingram, J. Non-Cryst. Solids 21 (1976) 373.
[15] J. Duffy, M. Ingram, J. Inorg. Nucl. Chem. 37 (1975) 1203.
[16] C. Wagner, Metall. Trans. B 6B (1975) 405.
[17] I.P. Rachev, F. Tsukihashi, N. Sano, Metall. Trans. B 22B (1991) 333.
[18] T. Hara, F. Tsukihashi, N. Sano, Tetsu-to-Hagané 76 (1990) 352.
[19] D.J. Sosinsky, I.D. Sommerville, Metall. Trans. B 17B (1986) 331.
[20] J.F. Elliot, M. Gleiser, V. Ramakrishna, Thermochemistry for Steelmaking II, Addison-Wesley Publishing Co. Ltd, Reading, MA, 1960.
[21] S. Tabuchi, N. Sano, Metall. Trans. B 15B (1984) 351.
[22] S. Tabuchi, N. Sano, Metall. Trans. B, Tetsu-to-Hagané 71 (1985) 687.
[23] E.R. Martinez, N. Sano, Metall. Trans. B 21B (1990) 97.
[24] E. Martinez, N. Sano, Steel Res. 58 (1987) 485.
[25] T. Shimoo, H. Kimura, M. Kawai, J. Jpn. Inst. Met. 35 (1971) 1103.
[26] K. Schwerdtfeger, H.G. Schubert, Metall. Trans. B 8B (1977) 535.
[27] T. Shimoo, H. Kimura, M. Kawai, J. Jpn. Inst. Met. 36 (1972) 723.
[28] E. Martinez, N. Sano, CAMP-ISIJ 1 (1988) 256.
[29] K. Ito, R.J. Fruehan, Metall. Trans. B 19B (1988) 419.
[30] M.W. Davies, S.G. Meherali, Metall. Trans. 2 (1971) 2729.
[31] T. Hirosumi, K. Morita, ISIJ Int. 40 (2000) 943.
[32] L.A.V. Teixeira, Y. Tokuda, T. Yoko, K. Morita, ISIJ Int. 49 (2009) 777.
[33] H. Shuto, T.H. Okabe, K. Morita, Mater. Trans. 52 (2011) 1899.
[34] C. Wiraseranee, T.H. Okabe, K. Morita, Metall. Mater. Trans. B 44B (2013) 584.
[35] F.D. Richardson, Physical Chemistry of Melts in Metallurgy, Academic Press, New York, 1974.
[36] Y.K. Rao, Stoichiometry and Thermodynamics of Metallurgical Processes, Cambridge University Press, Cambridge, England, 1985.
[37] E.T. Turkdogan, Physiochemical Properties of Molten Slags and Glasses, Metals Society, London, 1983, p. 252.
[38] S. Seetharaman, Fundamentals of Metallurgy, Woodhead Publishing Ltd., Cambridge England, 2005, p. 72.
[39] M. Temkin, Acta Phys. Chim URSS 20 (1945) p. 411.

[40] H. Flood, T. Førland, K. Grjotheim, Inst. Min. Metall., London (1953) 47.
[41] R. Sridhar, J.H.E. Jeffes, Trans. Inst. Min. Metall. 76 (1967) C44.
[42] F.D. Richardson, Trans. Faraday 52 (1956) 1312.
[43] R.A. Swalin, Thermodynamics of Solids, John Wiley & Sons, Toronto, 1972, p. 214.
[44] C.R. Masson, Proc. R. Soc. A 28 (1965) 201.
[45] M.L. Kapoor, G.M. Mehrotra, M.G. Frohberg, Archiv. Eisenhüttenw. 45 (1974) 213, p. 663.
[46] M. Blander, A. Pelton, Metall. Trans. B 17B (1986) 805.
[47] W.D. Johnston, J. Am. Chem. Soc. 47 (1964) 198.
[48] W.D. Johnston, J. Am. Chem. Soc. 48 (1965) 184.
[49] K. Morita, T. Shibuya, N. Sano, Tetsu-to-Hagané 74 (1988) 632.
[50] K. Morita, A. Inoue, N. Takayama, N. Sano, Tetsu-to-Hagané 74 (1988) 999.

CHAPTER 3.8

Examples of Steelmaking Thermochemistry

Hideki Ono[a], Takahiro Miki[b] and Masakatsu Hasegawa[c]

[a]Division of Materials and Manufacturing Science, Graduate School of Engineering, Osaka University, Japan
[b]Metallurgical Process Engineering, Department of Mettallurgy, Graduate School of Engineering, Tohoku University, Japan
[c]Graduate School of Energy Science, Kyoto University, Japan

3.8.1. FUNDAMENTAL CONSIDERATIONS PERTAINING TO REMOVAL OF IMPURITIES FROM MOLTEN STEEL

The amount of iron and steel production will continuously increase all over the world, and the generation rate of ferrous scrap will also increase. For this reason, it is important to recycle ferrous scrap and establish methods for removal of impurities. The removal of impurities from molten iron is achieved by transporting the impurities to other phases as shown in Figure 3.8.1. Possible routes for the removal of impurities include (a) removal to the slag phase, (b) removal to the gas phase, (c) formation of inclusions, (d) absorption of inclusions, and (e) reaction with refractory. In this section, the possibilities for impurity removal by the first two routes are discussed since these are usually considered to be the most important.

Elements that are easily oxidized tend to be removed by the slag phase, while elements that have high vapor pressure tend to be removed in the gas phase. In order to evaluate the possibility of impurity' removal by these methods, it is necessary to quantify the two different types of behavior. An important indicator of the oxidation behavior of an element is the oxygen partial pressure, which is in equilibrium with the pure element and the corresponding oxide at any particular temperature. Elements that are oxidized at relatively low oxygen partial pressure tend to be easily oxidized and are then removed by the slag phase. In contrast, elements that are only oxidized at higher oxygen partial pressures are more difficult to be removed by the slag phase. As mentioned above, a measure that shows the tendency of an element to be removed in the gas phase is the vapor pressure of the pure element at any particular temperature. Elements with high vapor pressure are relatively easy to remove in the gas phase, while those with lower vapor pressure are more difficult to remove by evaporation. The oxygen partial pressure for oxidation of each pure element is calculated from thermodynamic data [1] at the steelmaking temperature of 1873 K. Figure 3.8.2 shows the relation between the vapor pressure of pure elements

Treatise on Process Metallurgy, Volume 1
http://dx.doi.org/10.1016/B978-0-08-096986-2.00005-9
© 2014 Elsevier Ltd.
All rights reserved.

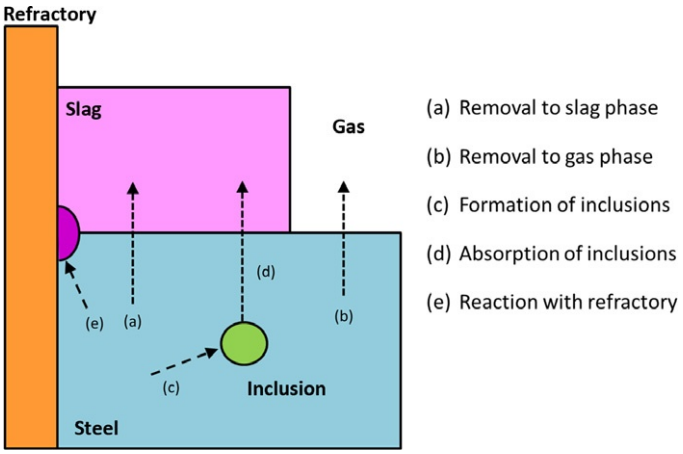


Figure 3.8.1 Possible routes for the removal of impurities from molten steel.

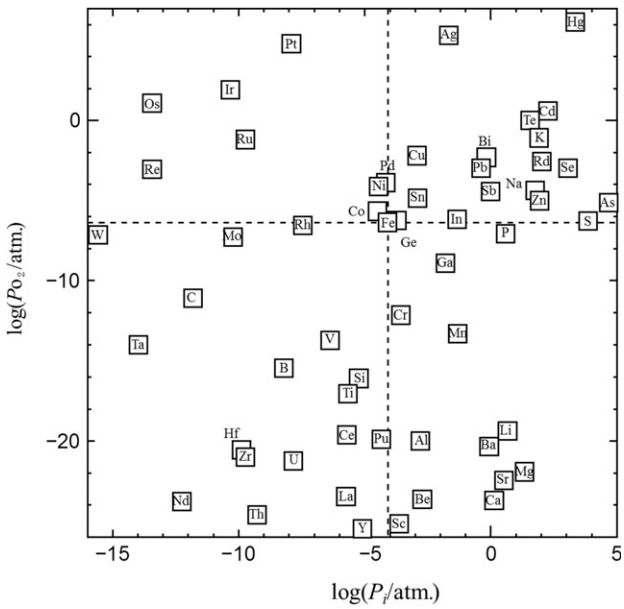


Figure 3.8.2 Relationship between vapor pressure of pure elements and oxygen partial pressure for metal/oxide equilibrium at 1873 K.

and the oxygen partial pressure at the metal/oxide equilibrium at 1873 K. In Figure 3.8.2, iron is located in the upper right area of the diagram. Elements that are located in the lower region of the diagram are more easily oxidized and can then be removed by the slag phase. Elements that are located to the right of the diagram are more easily vaporized and can be removed in the gas phase. Elements that are located in the upper-left side

of the diagram are more difficult to remove from molten iron. Fortunately, there are not so many elements in this zone that are found as impurities in steel scrap.

In Figure 3.8.2, the tendencies for oxidation and evaporation are compared for each pure element. However, when considering the removal of small amounts of impurities from molten iron, it must be remembered that the activities of these solute elements are much smaller than unity, and it is therefore more difficult to oxidize or evaporate then the pure elements. Taking this fact into consideration, W, Mo, Rh, Ge, Sn, and Cu are particularly difficult to remove in addition to Pt, Os, Ir, Re, Ru, Co, Ni, and Pd. In recycling ferrous scrap, the elements difficult to remove include W, Mo, and Ni, which are found in high alloyed steels, such as stainless steels, and Sn and Cu, which are usually found mixed in ferrous scrap. It is therefore important to develop appropriate methods to remove these elements in order to effectively recycle ferrous scrap.

3.8.2. EFFECT OF SOLUTE ELEMENTS ON SILICON DEOXIDATION OF FERROUS ALLOYS

Silicon is widely used for the deoxidation of molten ferrous alloys, and it is important to know the effect of solute elements on the silicon deoxidation reaction which is expressed by:

$$\underline{\mathrm{Si}}(\text{in Fe}) + 2\underline{\mathrm{O}}(\text{in Fe}) = \mathrm{SiO_2(s)} \tag{3.8.1}$$

The equilibrium constant for Equation (3.8.1), $K_{(3.8.1)}$, is represented by:

$$\log K_{(3.8.1)} = \log \frac{a_{\mathrm{SiO_2}}}{a_{\mathrm{Si}} {a_{\mathrm{O}}}^2} = \log a_{\mathrm{SiO_2}} - \log a_{\mathrm{Si}} - 2\log a_{\mathrm{O}} \tag{3.8.2}$$

where $a_{\mathrm{SiO_2}}$ denotes the activity of SiO_2 relative to the pure solid, and a_{O} and a_{Si} are the activities of oxygen and silicon, respectively, relative to the hypothetical 1 mass% dilute solution. The activities of oxygen and silicon in molten iron are defined by:

$$a_{\mathrm{O}} = f_{\mathrm{O}}[\text{mass\%O}] \tag{3.8.3}$$

$$a_{\mathrm{Si}} = f_{\mathrm{Si}}[\text{mass\%Si}] \tag{3.8.4}$$

The activity coefficients of oxygen and silicon relative to the infinitely dilute solution, f_{O} and f_{Si}, are given as follows:

$$\log f_{\mathrm{O}} = e_{\mathrm{O}}^{\mathrm{Si}}[\text{mass\%Si}] + e_{\mathrm{O}}^{\mathrm{O}}[\text{mass\%O}] + e_{\mathrm{O}}^{\mathrm{M}}[\text{mass\%M}] \tag{3.8.5}$$

$$\log f_{\mathrm{Si}} = e_{\mathrm{Si}}^{\mathrm{Si}}[\text{mass\%Si}] + e_{\mathrm{Si}}^{\mathrm{O}}[\text{mass\%O}] + e_{\mathrm{Si}}^{\mathrm{M}}[\text{mass\%M}] \tag{3.8.6}$$

where M is a third solute element in molten iron, and e_i^j denotes the first-order interaction parameter which describes the effect of j on i. From the viewpoint of deoxidation, it

Table 3.8.1 Interaction Parameters for Oxygen and Silicon with Oxygen, Silicon, and Molybdenum at 1873 K

j	O	Si	Mo
e^j_O	−0.17 [2]	−0.06 [2]	0.005 [2]
e^j_{Si}	−0.119 [2]	0.103 [2]	2.36 [3]
			0.11 [4]

is desirable to have larger values for f_O and f_{Si}. According to Equations (3.8.5) and (3.8.6), taking into account the effect of the third element, M, on the deoxidation reaction, it is desirable to have larger positive values for e^M_O and e^M_{Si}. Molybdenum is an example of one element that fulfils this requirement; both e^{Mo}_O and e^{Mo}_{Si} are positive. The interaction parameters for oxygen and silicon with oxygen, silicon, and molybdenum at 1873 K are summarized in Table 3.8.1.

Two values are reported for the interaction parameter e^{Mo}_{Si} for the effect of molybdenum on the behavior of silicon, and both values are shown in Table 3.8.1. The equilibrium constant for Reaction (3.8.1), $K_{(3.8.1)}$, is given by [2]:

$$\log K_{(3.8.1)} = 30{,}110/T - 11.40 \tag{3.8.7}$$

The silicon deoxidation equilibria of Fe-0, 0.5, and 1.0% Mo–Si–O alloys are calculated at 1873 K using Equations (3.8.2) through (3.8.7) and the interaction parameters in Table 3.8.1 under the condition of $a_{SiO_2} = 1$. The relationships between silicon and oxygen contents are shown in Figure 3.8.3. The silicon deoxidation equilibria of

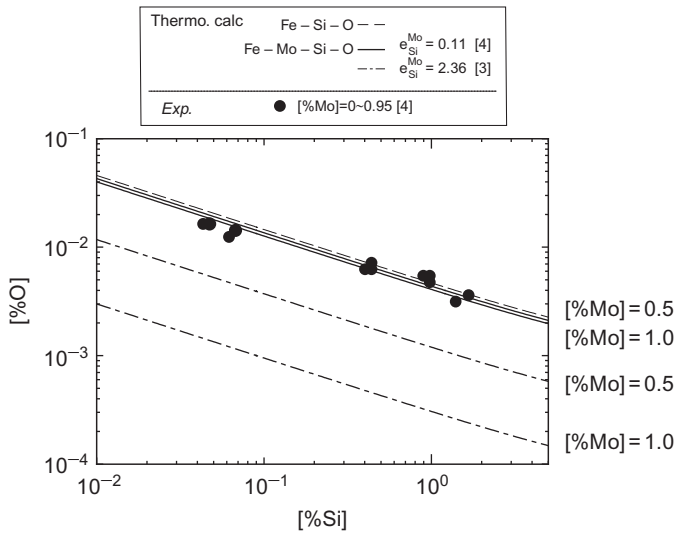


Figure 3.8.3 Effect of Mo on Si deoxidation of molten iron at 1873 K and $a_{SiO_2} = 1$.

Fe-0–0.95%Mo–Si–O alloys under the condition of $a_{SiO_2} = 1$ at 1873 K were investigated, and the experimental results are also plotted in Figure 3.8.3 [4]. The equilibrated oxygen content rapidly decreases with an increasing molybdenum content at the same silicon content when using $e_{Si}^{Mo} = 2.36$ [3]. The oxygen content also decreases with an increasing molybdenum content when using $e_{Si}^{Mo} = 0.11$ [4] although the effect of the molybdenum is clearly much less.

The oxygen contents of seven different steels are shown in Table 3.8.2. The values for steels containing molybdenum (SUS316, SUH3, SKD61, and SKH51) were calculated by using the interaction parameter $e_{Si}^{Mo} = 0.11$.

The activity coefficients of oxygen and silicon in the different steels relative to the infinitely dilute solution, f_O and f_{Si}, are as follows:

$$\log f_O = e_O^{Si}[\text{mass\%Si}] + e_O^{Mo}[\text{mass\%Mo}] + e_O^{C}[\text{mass\%C}] + e_O^{Mn}[\text{mass\%Mn}] + e_O^{Cr}[\text{mass\%Cr}] + e_O^{X}[\text{mass\%X}] + e_O^{O}[\text{mass\%O}] \quad (3.8.8)$$

$$\log f_{Si} = e_{Si}^{Si}[\text{mass\%Si}] + e_{Si}^{Mo}[\text{mass\%Mo}] + e_{Si}^{C}[\text{mass\%C}] + e_{Si}^{Mn}[\text{mass\%Mn}] e_{Si}^{Cr}[\text{mass\%Cr}] + e_{Si}^{X}[\text{mass\%X}] + e_{Si}^{O}[\text{mass\%O}] \quad (3.8.9)$$

The interaction parameters with respect to oxygen and silicon at 1873 K are summarized in Table 3.8.3. The silicon deoxidation equilibria for the various steels are calculated by using Equations (3.8.2) through (3.8.4), Equations (3.8.7) through (3.8.9), and the interaction parameters shown in Table 3.8.3 under the conditions of $a_{SiO_2} = 1$ and 0.1 at 1873 K. The derived oxygen contents are shown in Table 3.8.2.

Table 3.8.2 Composition of Seven Different Steel Grades and the Corresponding Equilibrium Oxygen Contents at 1873 K Under the Conditions $a_{SiO_2} = 1$ and 0.1

Type	(Mass%)							
	Si	Mo	C	Mn	Cr	X	O	
							$a_{SiO_2} = 1$	$a_{SiO_2} = 0.1$
SUS316	0.6	2.5	0.03	1	17	Ni = 35	0.019	0.0060
SUH3	2	1	0.4	0.4	11		0.014	0.0042
SKD61	1	1.5	0.35	0.4	5	V = 1.0	0.012	0.0039
SKH51	0.25	6.5	0.85	0.35	4.1	W = 5.0 V = 2.0	0.019	0.0061
SKS93	0.2	–	1.05	0.5	0.3	–	0.025	0.0078
SUS403	0.25	–	0.12	0.4	12	–	0.037	0.012
SUS430	0.5	–	0.1	0.8	17	–	0.040	0.013

Table 3.8.3 Interaction Parameters of Oxygen and Silicon in Molten Iron at 1873 K

j	O	Si	Mo	C	Mn	Cr	Ni	V	W
e_O^j (r_O^j)	−0.17 [2]	−0.066 [2]	0.005 [2]	−0.421 [2]	−0.021 [2]	−0.052 (0.00058) [2]	0.006 [2]	−0.14 [2]	−0.0085 [2]
e_{Si}^j	−0.119 [2]	0.103 [2]	0.11 [4]	0.18 [2]	−0.0146 [2]	−0.0003 [2]	0.005 [2]	0.025 [2]	–

It is found from Table 3.8.2 that the calculated oxygen contents under the condition of $a_{SiO_2} = 0.1$ are in the range of 39–61 mass ppm of the four steels containing molybdenum. On the other hand, the oxygen contents for the three molybdenum-free steels are in the range of 78–130 mass ppm. Accordingly, it is concluded that the oxygen content is more easily decreased for steels containing molybdenum.

3.8.3. THERMODYNAMICS OF CALCIUM TREATMENT OF AL-KILLED STEEL

Calcium treatment of Al-killed steel is carried out during secondary refining as part of the steelmaking process for the purpose of desulfurization, controlling the morphology of sulfide and oxide inclusions, and preventing nozzle blockage. With Ca/Al deoxidation, under controlled conditions, a small amount of calcium in steel can form liquid rather than solid calcium aluminate inclusions that do not cause nozzle blockage. Therefore, it is very important to study the conditions that influence the formation of solid and liquid calcium aluminates. The phase stability of calcium aluminate inclusions can be predicted based on the thermodynamic knowledge of Al and Ca deoxidation equilibria and the $CaO–Al_2O_3$ oxide system as follows:

The deoxidation reactions of Al and Ca in liquid steel are given by Equations (3.8.10) and (3.8.11) [5,6]:

$$Al_2O_3(s) = 2\underline{Al} + 3\underline{O} \quad \log K_{(3.8.10)} = -45{,}300/T + 11.62 \tag{3.8.10}$$

$$CaO(s) = \underline{Ca} + \underline{O} \quad \log K_{(3.8.11)} = -7220/T - 3.29 \tag{3.8.11}$$

where $K_{(3.8.i)}$ denotes the equilibrium constant of Equation (3.8.i). The interaction parameters related to Equations (3.8.10) and (3.8.11) are listed in Table 3.8.4.

In calculating the deoxidation equilibria, information on activities of CaO and Al_2O_3 are necessary. Figure 3.8.4 shows the activities of CaO and Al_2O_3 in liquid calcium–aluminate in equilibrium with molten iron at 1873 K [10] calculated from their Gibbs energies of formation [11].

Using these thermodynamic data, the composition of liquid steel, which satisfies the Al and Ca deoxidation equilibria of Equations (3.8.10) and (3.8.11) at the same time, is solved numerically as follows:

Table 3.8.4 Interaction Parameters at 1873 K

i	j	k	e_i^j	r_i^j	$r_i^{(j,k)}$	References
Al	Al		0.043			[5]
	Ca	O	−0.047		5.24	[7,8]
	Mg	O	−0.019		−260	[8]
	O	Al	−6.9	7.6	9.05	[5]
Ca	Al	O	−0.072		5.58	[7,8]
	Ca		0			[7]
	Mg	O	0		7.06	[8]
	O	Ca	−779	650,000	−90,000	[7]
Mg	Al	O	−0.017		−230	[8]
	Ca	O	0		4.71	[8]
	Mg		0			[9]
	O	Mg	−430	350,000	−61,000	[9]
O	Al	O	−4.09	2.67	9.05	[5]
	Ca	Al	−313	−18,000	0	[8]
		Mg			0	[8]
		O			520,000	[7]
	Mg	Al	−280	−20,000	−150	[8]
		O			462,000	[9]
	O		−0.17	0		[7]

(1) The activity of Al_2O_3 at the aimed composition of CaO–Al_2O_3 slag or inclusion is first determined from Figure 3.8.4, and Ca and Al concentrations which satisfy Al deoxidation equilibrium of Equation (3.8.10) are solved numerically at the assumed dissolved oxygen concentration.

(2) In a similar manner to step (1), the Ca and Al concentrations, which satisfy Ca deoxidation equilibrium of Equation (3.8.11), are solved numerically at the CaO activity determined by the same slag or inclusion composition and the assumed oxygen concentration.

(3) The relation between [%Al] and [%Ca] obtained by the above procedures (1) and (2) is drawn. The composition ([%Al], [%Ca], and assumed [%O]) at the intersection of each line gives the composition of molten steel in equilibrium with the CaO–Al_2O_3 inclusion.

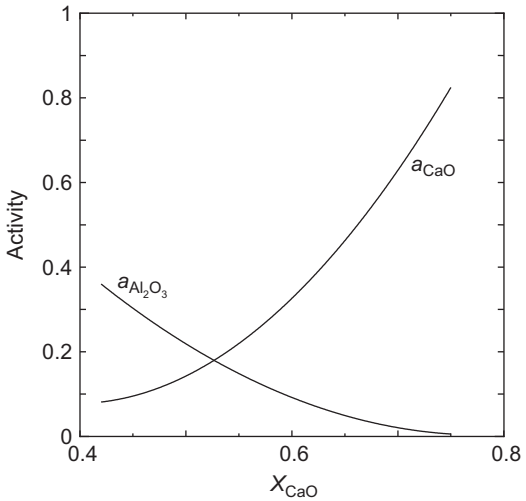


Figure 3.8.4 Activities of CaO and Al_2O_3 in CaO–Al_2O_3 melts at 1873 K.

(4) The above procedure is repeated within the oxygen concentration range from 10^{-5} to 10^{-2} mass%.

Based on this approach, the phase stability diagram for Al–Ca deoxidation equilibria of molten iron can be drawn as shown in Figure 3.8.5. The phase stability of the calcium aluminate inclusions can be predicted from this figure.

Subsequently, we would like to consider CaO–Al_2O_3–MgO system. Aluminum deoxidation is one of the most important refining technologies in the secondary refining process. In most cases, Al is added into molten steel held in a vessel with a MgO refractory lining, where the surface of molten steel is usually covered with slag. Calcium- or magnesium-alloy is sometimes added together with Al depending on the specification of the steel product. In such cases, Al in the steel could react with MgO (or CaO) in the refractory or slag to generate Mg or Ca dissolved in the steel. The Al deoxidation product could then be possibly transformed to inclusions within the CaO–Al_2O_3–MgO system. Among such CaO–Al_2O_3–MgO inclusions, $MgO{\cdot}Al_2O_3$ is one of the most harmful compounds due to its high melting point and hard deformability and can cause defects such as cracking. In order to minimize such harmful effects, the reforming of the inclusions into deformable ones is necessary. For such purpose, information on the phase stability such as liquid phase or deformable compound is very important to control the composition of the deoxidation product. For this calculation, consideration of the equilibrium involving the deoxidation reaction of Mg in liquid steel is necessary in addition to reactions (3.8.10) and (3.8.11). This is given by Equation (3.8.12) [9]:

$$\mathrm{MgO(s)} = \underline{\mathrm{Mg}} + \underline{\mathrm{O}} \quad \log K_{(3.8.12)} = -4700/T - 4.28 \tag{3.8.12}$$

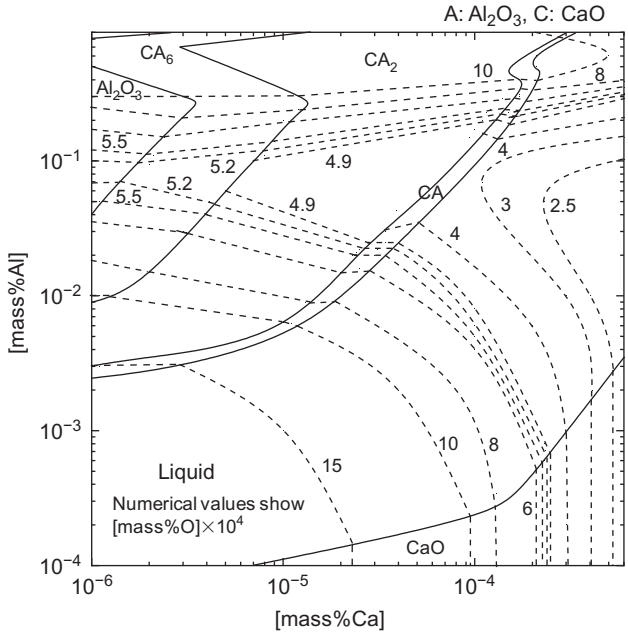


Figure 3.8.5 Complex deoxidation equilibria of molten iron by Al and Ca at 1873 K.

The interaction parameters related to Equations (3.8.10–3.8.12) are listed in Table 3.8.4. Figure 3.8.6 shows the activities in CaO–Al_2O_3–MgO melts at 1873 K [12].

The composition of liquid steel, which satisfies the Al, Ca, and Mg deoxidation equilibria of Equations (3.8.10–3.8.12) at the same time, is solved numerically by assuming the equilibrium of liquid steel with CaO–Al_2O_3–MgO slag or inclusions. The following example at 1873 K and 0.03 mass% of Al concentration in liquid steel is shown below:

(1) The activity of Al_2O_3 at the aimed composition of CaO-Al_2O_3-MgO inclusion is first determined from Figure 3.8.6, and Ca and Mg concentrations, which satisfy Al

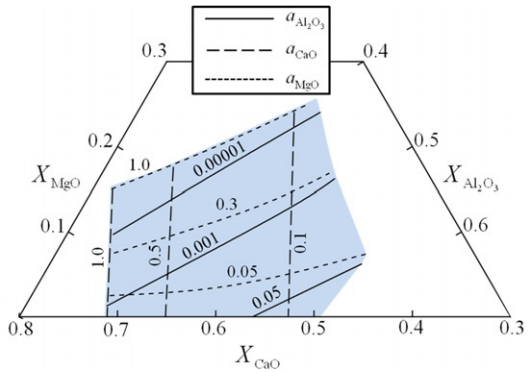


Figure 3.8.6 Activity of CaO, Al_2O_3, and MgO in CaO–Al_2O_3–MgO melts at 1873 K.

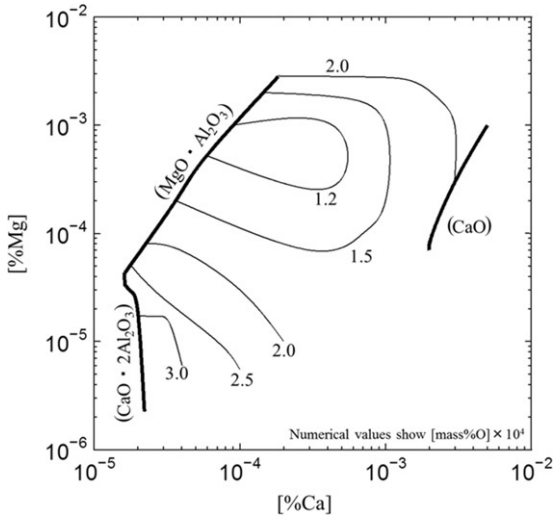


Figure 3.8.7 Complex deoxidation equilibria of molten iron by Al, Ca, and Mg at 1873 K with a [mass% Al] = 0.03.

deoxidation equilibrium of Equation (3.8.10), are solved numerically at the assumed dissolved oxygen concentration.

(2) The Ca and Mg concentrations, which satisfy Ca deoxidation equilibrium of Equation (3.8.11), are solved numerically at the CaO activity given by the same inclusion composition and the assumed oxygen concentration.

(3) The relation between [%Ca] and [%Mg] obtained in the above procedures (1) and (2) is drawn. At the composition ([%Al] = 0.03, [%Ca], [%Mg], and assumed [%O]) on the intersection of each line, the satisfaction of Mg deoxidation equilibrium is confirmed at MgO activity of the given inclusion composition. If Equation (3.8.12) is satisfied, the $CaO–Al_2O_3–MgO$ inclusion is in equilibrium with the liquid steel. If not, the above procedure is repeated at an other oxygen concentration until Equations (3.8.10–3.8.12) are satisfied.

In this way, the phase stability diagram for Al–Ca–Mg complex deoxidation equilibria can be drawn as shown in Figure 3.8.7.

The phase stability such as liquid phase and deformable compound can be obtained from Figure 3.8.7. In this way, the composition of the deoxidation product in the $CaO–Al_2O_3–MgO$ system can be determined.

3.8.4. EQUILIBRIUM BETWEEN SOLID OXIDES AND HIGHLY ALLOYED STEELS

High concentration of alloying elements in steel may have a large influence on equilibrium between solid oxides and steels. The case of Fe–Mn alloy will be considered here.

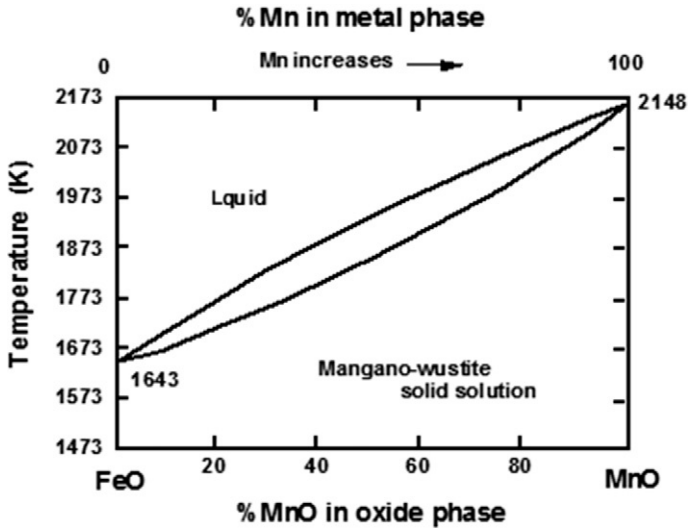


Figure 3.8.8 Phase diagram of MnO–FeO system.

It is well known that MnO and FeO form an ideal solid solution as shown in Figure 3.8.8 [13]. According to this figure, liquid Fe–Mn–O alloy is in equilibrium with molten MnO–FeO slag or MnO–FeO solid solution depending on the manganese content of the metal at steelmaking temperature.

The thermodynamic behavior of MnO–FeO slag or MnO–FeO solid solution is very close to ideality. The chemical reaction between solid MnO and Fe_tO and the equilibrium constant are represented by Equations (3.8.13) and (3.8.14):

$$\mathrm{FeO(s)} + \mathrm{Mn(l)} = \mathrm{MnO(s)} + \mathrm{Fe(l)} \tag{3.8.13}$$

$$K_{(3.8.13)} = \left\{a_{\mathrm{MnO(s)}}a_{\mathrm{Fe(l)}}\right\} / \left\{a_{\mathrm{FeO(s)}}a_{\mathrm{Mn(l)}}\right\} \tag{3.8.14}$$

Since both FeO–MnO solid solution and molten Fe–Mn alloy exhibit almost ideal behavior, Equations (3.8.15) and (3.8.16) are satisfied and the equilibrium constant, $K_{(3.8.13)}$, is expressed by Equation (3.8.17) if all standard states for the activities are taken as the pure substances:

$$N_{\mathrm{MnO(s)}} + N_{\mathrm{FeO(s)}} = 1 \quad (\text{in FeO} - \text{MnO solid solution}) \tag{3.8.15}$$

$$N_{\mathrm{Mn(l)}} + N_{\mathrm{Fe(l)}} = 1 \quad (\text{in molten Fe} - \text{Mn alloy}) \tag{3.8.16}$$

$$\begin{aligned} K_{(3.8.13)} &= \left\{N_{\mathrm{MnO(s)}}N_{\mathrm{Fe(l)}}\right\} / \left\{N_{\mathrm{FeO(s)}}N_{\mathrm{Mn(l)}}\right\} \\ &= \left\{N_{\mathrm{MnO(s)}}\left(1 - N_{\mathrm{Mn(l)}}\right)\right\} / \left\{\left(1 - N_{\mathrm{MnO(s)}}\right)N_{\mathrm{Mn(l)}}\right\} \end{aligned} \tag{3.8.17}$$

The activity of MnO can be expressed as a function of manganese content in liquid iron as shown in Equation (3.8.18):

$$a_{\mathrm{MnO(s)}} = N_{\mathrm{MnO(s)}} = K_{(3.8.13)}N_{\mathrm{Mn(l)}} / \left\{1 - N_{\mathrm{Mn(l)}} + K_{(3.8.13)}N_{\mathrm{Mn(l)}}\right\} \tag{3.8.18}$$

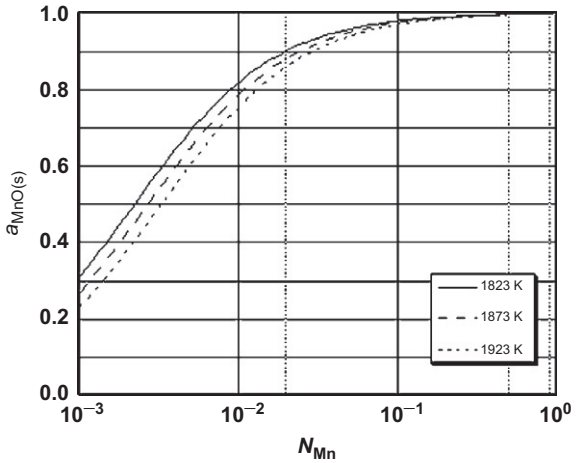


Figure 3.8.9 Activity of MnO(s) in FeO–MnO solid solution and the mole fraction of Mn in liquid iron.

The value of $K_{(3.8.13)}$ is calculated from the standard free energy change of Equation (3.8.13) which can be obtained from the data recommended by Turkdogan [1]:

$$\Delta G^{\circ}_{(3.8.13)} = -RT\ln K_{(3.8.13)} = -113{,}600 + 11.59T(\mathrm{J}) \tag{3.8.19}$$

The relation between the activity of MnO in Fe_tO–MnO solid solution and the mole fraction of Mn dissolved in liquid iron is shown in Figure 3.8.9.

The relation between Mn and O dissolved in liquid iron and in equilibrium with MnO(l) is expressed by Equation (3.8.20). The equilibrium constant is calculated from Equation (3.8.21) based on the work of Takahashi and Hino [14] together with the free energy of fusion of MnO(s) [15]:

$$\mathrm{MnO(l)} = \underline{\mathrm{Mn}} + \underline{\mathrm{O}} \tag{3.8.20}$$

$$\log K_{(3.8.20)} = \log\left\{h_{\mathrm{Mn}}h_{\mathrm{O}}/a_{\mathrm{MnO(l)}}\right\} = -9610/T + 3.97 \tag{3.8.21}$$

$$\mathrm{MnO(s)} = \mathrm{MnO(l)} \tag{3.8.22}$$

$$\Delta G^{\circ}_{(3.8.22)} = -RT\ln\left(a_{\mathrm{MnO(l)}}/a_{\mathrm{MnO(s)}}\right) = 43{,}920 - 21.64T(\mathrm{J}) \tag{3.8.23}$$

Since the activity of MnO(l) will also deviate from unity, it is estimated as follows:

$$\mathrm{FeO(l)} + \underline{\mathrm{Mn}} = \mathrm{MnO(l)} + \mathrm{Fe(l)} \tag{3.8.24}$$

$$\log K_{(3.8.24)} = \log\left(a_{\mathrm{MnO(l)}}a_{\mathrm{Fe(l)}}/a_{\mathrm{FeO(l)}}h_{\mathrm{Mn}}\right) = 3290/T - 1.23 \tag{3.8.25}$$

$$a_{\mathrm{MnO(l)}} = N_{\mathrm{MnO(l)}} = 1 - 1/\left\{1 + K_{(3.8.24)}f_{\mathrm{Mn}}[\%\,\mathrm{Mn}]\right\} \tag{3.8.26}$$

The calculated relation between $\underline{\mathrm{Mn}}$ and $\underline{\mathrm{O}}$ in liquid iron equilibrated with solid and liquid FeO–MnO slag is shown in Figure 3.8.10 [16]. From this figure, it is evident that

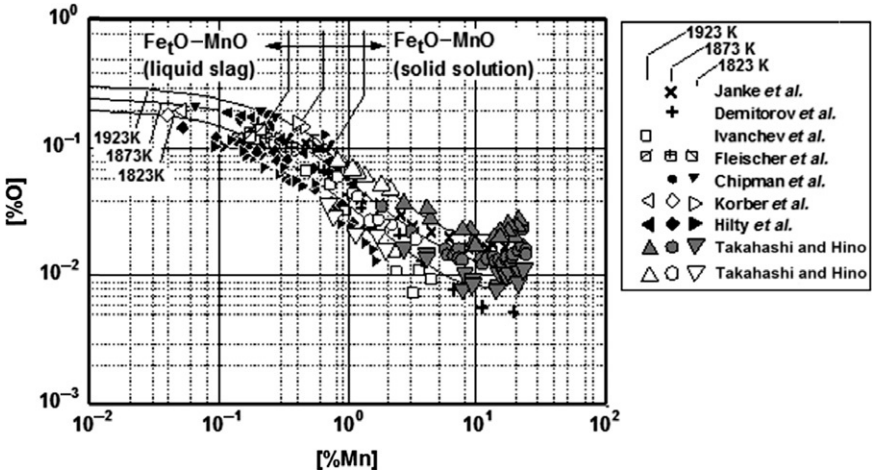


Figure 3.8.10 Equilibrium relation between [%Mn] and [%O] with FeO–MnO slags or solid solutions.

the equilibrium oxide phase changes from liquid to solid in the vicinity of 0.2–0.7 mass% Mn at steelmaking temperatures. For comparison, some literature values [13,14,16–22] are also shown in Figure 3.8.10. These experimental results, except for some cases, are in good accord with the calculated relation between Mn and O, when the change of MnO activity is taken into account.

3.8.5. THERMODYNAMICS OF CALCIUM TREATMENT OF MOLTEN IRON

With the increase in demand for clean steel, it becomes necessary to control the sulfur content of steel to less than a few ppm. Decrease of the oxygen potential is important to lower the sulfur content of steel, and the addition of a strong deoxidizing agent, such as calcium, is most effective. Calcium in liquid iron has strong thermodynamic affinities for both oxygen and sulfur. Therefore, the interaction between Ca and O or Ca and S cannot be ignored even at the low oxygen or sulfur contents of a few mass ppm that are considered to be the lower limits after deoxidation and desulfurization by calcium. Accordingly, it is important to know the deoxidation and the desulfurization equilibria of liquid iron by calcium in order to control the oxygen and the sulfur contents of steel.

The reactions for the deoxidation and the desulfurization of liquid iron by calcium are, respectively, expressed as follows:

$$\mathrm{CaO(s)} = \underline{\mathrm{Ca}}(\text{mass\%, in Fe}) + \underline{\mathrm{O}}(\text{mass\%, in Fe}) \tag{3.8.27}$$

$$\mathrm{CaS(s)} = \underline{\mathrm{Ca}}(\text{mass\%, in Fe}) + \underline{\mathrm{S}}(\text{mass\%, in Fe}) \tag{3.8.28}$$

The equilibrium constants for Equations (3.8.27) and (3.8.28) are, respectively, represented as follows [6,23]:

$$\log K_{(3.8.27)} = \log(a_{Ca} a_O / a_{CaO}) = -9.08(\text{at } 1873\text{K}) \quad (3.8.29)$$
$$\log K_{(3.8.28)} = \log(a_{Ca} a_S / a_{CaS}) = -6.23(\text{at } 1873\text{K}) \quad (3.8.30)$$

where a_{CaO} and a_{CaS} are the activities of CaO and CaS relative to the pure solids, respectively. a_i (i: Ca, O, or S) denotes the activity of component i relative to the infinite dilute solution and is defined by the following equation:

$$a_i = f_i[\text{mass\%i}] (i : \text{Ca, O, or S}) \quad (3.8.31)$$

The activity coefficient relative to the infinite dilute solution, f_i, is given by [24]:

$$\log f_i = \sum_j e_i^j [\text{mass\%}j] + \sum_i \sum_j r_i^{(j,k)} [\text{mass\%}j][\text{mass\%}k] \; (j \le k) \quad (3.8.32)$$

where e_i^j and $r_i^{(j,k)}$ denote the first-order interaction coefficient for the effect of j on i and the second-order interaction coefficient for the combined effects of j and k on i, respectively. The deoxidation and the desulfurization equilibria of liquid iron by calcium can be derived by investigating the relationship among the Ca, O, and S contents, which simultaneously satisfy the equilibria of Equations (3.8.27) and (3.8.28). The interaction parameters needed for the calculation are shown in Table 3.8.5.

Table 3.8.5 The Interaction Parameters for Ca, O, S, and Al in Molten Iron at 1873 K

i	j				References
Ca	Ca	−0.002			[6]
	O	−780	650,000	−90,000	[6]
	S	−28.0			[23]
	Al	−0.072			[2]
O	Ca	−313	−18,000	520,000	[6]
	O	−0.17			[2]
	S	−0.133			[2]
	Al	−1.17	−0.01	47.4	[5]
S	Ca	−22.4			[23]
	O	−0.27			[2]
	S	−0.046			[2]
	Al	−0.035			[2]
Al	Ca	−0.047			[2]
	O	−1.98	40	−0.0284	[5]
	S	0.035			[2]
	Al	0.043			[2]

Reference [5]: Applicable range of 0.3–200 mass ppm Ca.

The calculation was conducted using Equations (3.8.29) through (3.8.32) under the condition of $a_{CaO} = a_{CaS} = 1$ at 1873 K.

The calculated results are described by the solid curves in Figure 3.8.11. Several studies are reported on the deoxidation and the desulfurization of liquid iron by calcium, and the experimental conditions are shown in Table 3.8.6 [25–27].

The experimental results are also plotted in Figure 3.8.11. It is found that the oxygen and sulfur contents of liquid iron are minimized at specified calcium contents, respectively. The lower limits of oxygen and sulfur contents are calculated to be 1.6 mass

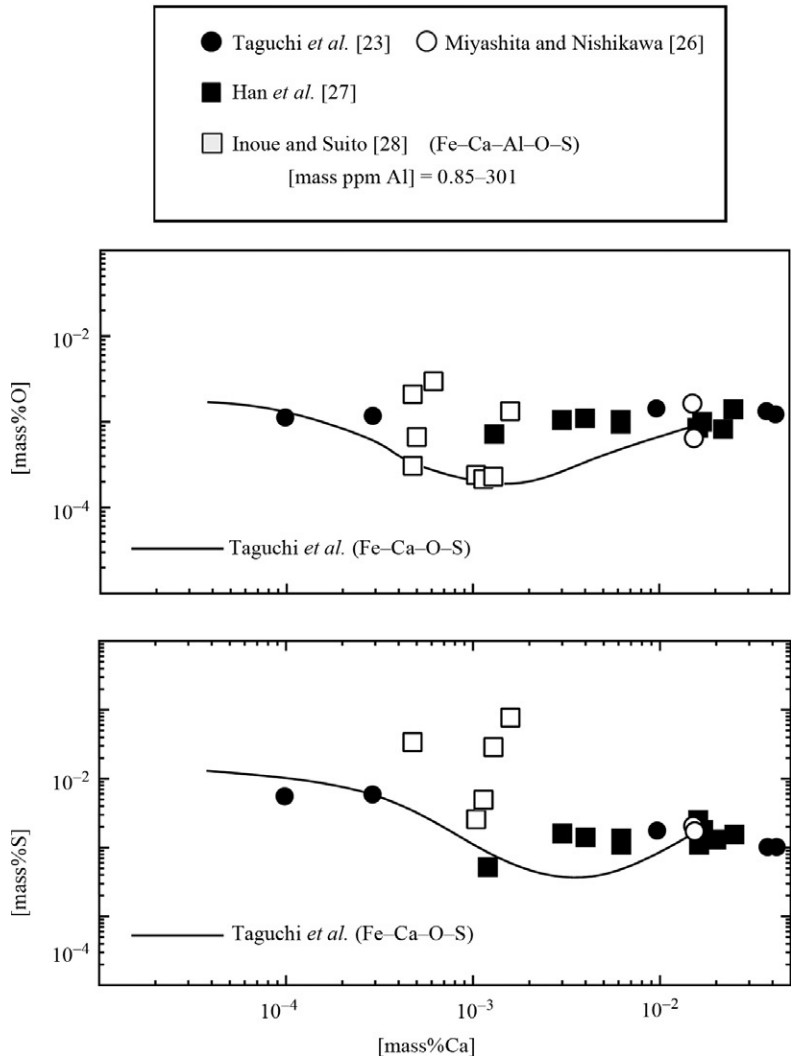


Figure 3.8.11 Effect of calcium content on the equilibrated oxygen and sulfur contents in Fe–Ca–O–S alloy for $a_{CaO} = a_{CaS} = 1$ at 1873 K.

Table 3.8.6 Experimental Conditions for Calcium Desulfurization of Liquid Iron Reported by Several Investigators

	System	Temperature (K)	Impurity Content
Miyashita *et al.* [25]	Fe–Ca–C–O–S	1873	C: 40–100 mass ppm
Han *et al.* [26]	Fe–Ca–O–S	1873	–
Inoue *et al.* [27]	Fe–Ca–Al–O–S	1873	Al: 0.85–301 mass ppm
Taguchi *et al.* [23]	Fe-Ca-O-S	1873	–

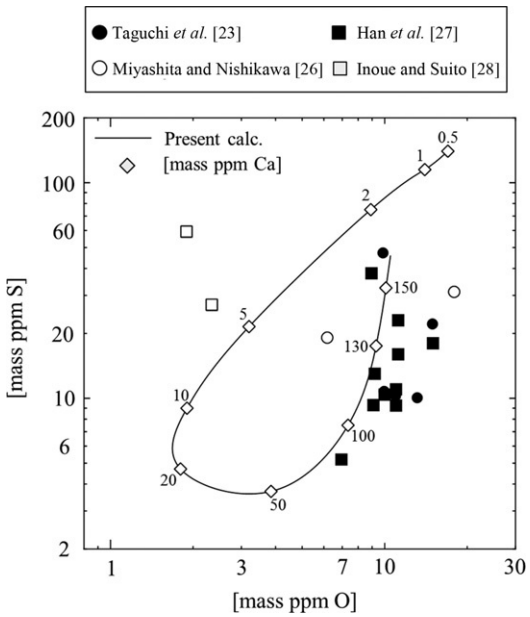


Figure 3.8.12 Deoxidation and desulfurization equilibria of liquid iron by calcium with $a_{CaO} = a_{CaS} = 1$ at 1873 K.

ppm O (at 15 mass ppm Ca) and 3.5 mass ppm S (at 40 mass ppm Ca), respectively, at 1873 K. The deoxidation and the desulfurization equilibria of liquid iron by calcium are described as the relationship between the O and the S contents in Figure 3.8.12 under the condition of $a_{CaO} = a_{CaS} = 1$ at 1873 K. It is found that the oxygen and sulfur contents decrease with increasing calcium contents up to 20–30 mass ppm and then increase with further increasing calcium contents above 20–30 mass ppm.

Thus, it is necessary to precisely control the calcium content in order to effectively lower the O and S contents of steel.

3.8.6. CHEMICAL POTENTIAL CONTROL BY GAS EQUILIBRIA

When studying reaction kinetics or equilibria between gaseous and condensed phases, the chemical potentials of one or more elements in the gas phase can be controlled readily by using appropriate gas mixtures, e.g., H_2+H_2O, $CO+CO_2$, $CO+CO_2+SO_2+Ar$, and H_2+CO_2 [28].

The oxygen potential can be fixed with H_2+H_2O or $CO+CO_2$ gas mixtures. Since the equilibrium oxygen partial pressures at elevated temperatures are many orders of magnitude lower than those of H_2 and H_2O or CO and CO_2, the ratios of P_{H_2}/P_{H_2O} and P_{CO}/P_{CO_2} in the equilibrium states at elevated temperatures could be considered practically to be the same as the initial ratios. Hence, the calculation of the equilibrium oxygen potentials in these gas mixtures is a simple procedure as mentioned in Chapter 3.3 on the Ellingham diagram.

On the other hand, the dissociation and formation of molecular gaseous species occur inevitably in the case of $CO+CO_2+SO_2+Ar$ or H_2+CO_2 gas mixtures. The calculation method for such multicomponent systems will be described in this section.

3.8.6.1. $CO+CO_2+SO_2+Ar$ Gas Mixture

A great number of investigations have been conducted on the equilibrium between desulphurization slags and the gaseous phase. At oxygen partial pressures less than 10^{-6} atm., sulfur can dissolve into molten slag by replacing oxygen ions [29]. This reaction can be expressed by Equation (3.8.33):

$$(1/2)S_2(\text{gas})+\left(O^{2-}\right)=(1/2)O_2(\text{gas})+\left(S^{2-}\right) \tag{3.8.33}$$

where (O^{2-}) and (S^{2-}) represent O^{2-} and S^{2-} ions in slag, respectively. Sulfide capacity [29], C_S, is the fundamental thermochemical property of a slag to hold sulfur as sulfide and is defined as Equation (3.8.34), where the mass concentration of sulfur in molten slag, $(\%S^{2-})$, the oxygen partial pressure, P_{O_2}, and the sulfur partial pressure, P_{S_2}, are all values that can be measured:

$$C_S\equiv\left(\%S^{2-}\right)\left(P_{O_2}/P_{S_2}\right)^{1/2}=K_{(3.8.33)}aO^{2-}/fS^{2-} \tag{3.8.34}$$

where $K_{(3.8.33)}$ is the apparent equilibrium constant of Equation (3.8.33), aO^{2-} is the activity of O^{2-} and fS^{2-} is the activity coefficient of S^{2-} in molten slag. The value for sulfide capacity can be determined by bringing the oxide melt into equilibrium with the gaseous phase of fixed P_{O_2} and P_{S_2} at elevated temperature. The system of $CO+CO_2+SO_2+Ar$ is one of the typical gas mixtures used for this purpose.

At high temperatures, the gaseous species of CO_2 and SO_2 are partially dissociated and then O_2, S_2, S, SO, and COS are formed. The chemical reactions between the gaseous species can be expressed as follows [30]:

$$CO + (1/2)O_2 = CO_2 \tag{3.8.35}$$

$$\log K_{(3.8.35)} = \log\left(P_{CO_2}/\left[P_{CO}\cdot P_{O_2}^{(1/2)}\right]\right) = -4.534 + 1.475\times 10^4/T \tag{3.8.36}$$

$$(1/2)S_2 + O_2 = SO_2 \tag{3.8.37}$$

$$\log K_{(3.8.37)} = \log\left(P_{SO_2}/\left[P_{S_2}^{(1/2)}\cdot P_{O_2}\right]\right) = -3.783 + 1.893\times 10^4/T \tag{3.8.38}$$

$$(1/2)S_2 = S \tag{3.8.39}$$

$$\log K_{(3.8.39)} = \log\left(P_S/P_{S_2}^{(1/2)}\right) = 3.245 - 8.440\times 10^3/T \tag{3.8.40}$$

$$(1/2)S_2 + (1/2)O_2 = SO \tag{3.8.41}$$

$$\log K_{(3.8.41)} = \log\left(P_{SO}/\left[P_{S_2}^{(1/2)}\cdot P_{O_2}\right]\right) = 3.059\times 10^{-1} + 3.365\times 10^3/T \tag{3.8.42}$$

$$CO + (1/2)S_2 = COS \tag{3.8.43}$$

$$\log K_{(3.8.43)} = \log\left(P_{COS}/\left[P_{CO}\cdot P_{S_2}^{(1/2)}\right]\right) = -4.086 + 4.996\times 10^3/T \tag{3.8.44}$$

With respect to the material balances, the total numbers of the molecules of gaseous species should change through the reactions above, while the mole ratios of n_C/n_O, n_S/n_O, and n_{Ar}/n_O remain constant. Hence, we have

$$\begin{aligned} n_C/n_O &= \left([P_{CO} + P_{CO_2}]/[P_{CO} + 2P_{CO_2} + 2P_{SO_2}]\right)_{initial} \\ &= [P_{CO} + P_{CO_2} + P_{COS}]/[P_{CO} + 2P_{CO_2} + 2P_{SO_2} + 2P_{O_2} + P_{SO} + P_{COS}] \end{aligned} \tag{3.8.45}$$

$$\begin{aligned} n_S/n_O &= \left(P_{SO_2}/[P_{CO} + 2P_{CO_2} + 2P_{SO_2}]\right)_{initial} \\ &= [P_{SO_2} + 2P_{S_2} + P_S + P_{SO} + P_{COS}]/[P_{CO} + 2P_{CO_2} + 2P_{SO_2} + 2P_{O_2} + P_{SO} + P_{COS}] \end{aligned} \tag{3.8.46}$$

$$\begin{aligned} n_{Ar}/n_O &= \left(P_{Ar}/[P_{CO} + 2P_{CO_2} + 2P_{SO_2}]\right)_{initial} \\ &= P_{Ar}/[P_{CO} + 2P_{CO_2} + 2P_{SO_2} + 2P_{O_2} + P_{SO} + P_{COS}] \end{aligned} \tag{3.8.47}$$

where the subscript "$_{initial}$" indicates the values in the initial mixture, and the partial pressures without the subscript correspond to those in the equilibrium state.

When the gas phase is present at one atmospheric pressure:

$$P_{CO} + P_{CO_2} + P_{SO_2} + P_{O_2} + P_{S_2} + P_S + P_{SO} + P_{COS} + P_{Ar} = 1 \tag{3.8.48}$$

Attention is now focused on Equations (3.8.36), (3.8.38), (3.8.40), (3.8.42), and (3.8.44)–(3.8.48). These nine equations involve nine unknowns, i.e., P_{CO}, P_{CO_2}, P_{S_2}, P_{O_2}, P_{S_2}, P_S, P_{SO}, P_{COS}, and P_{Ar}. Hence, values for these unknowns can be obtained

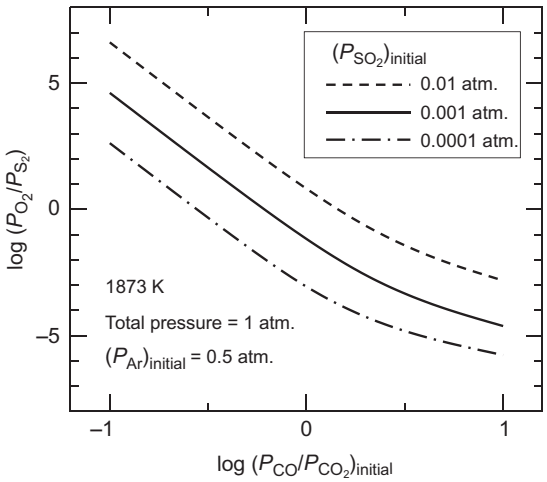


Figure 3.8.13 Equilibrium values for P_{O_2}/P_{S_2} in the C–S–O–Ar gaseous system at 1873 K.

by solving these equations simultaneously for a given temperature and known initial values for P_{CO}, P_{CO_2}, P_{SO_2}, and P_{Ar}. Figure 3.8.13 shows the relationships between the equilibrium value for P_{O_2}/P_{S_2} at 1873 K and the initial value for P_{CO}/P_{CO_2} under the initial conditions that P_{SO_2} is 0.01, 0.001, or 0.0001 atm. and P_{Ar} is 0.5 atm.

3.8.6.2. $H_2 + CO_2$ Gas Mixture

The oxygen potential can also be controlled in the $H_2 + CO_2$ gas mixture. The reactions between the gaseous species can be expressed as [30]:

$$CO + (1/2)O_2 = CO_2 \tag{3.8.35}$$

$$\log K_{(3.8.35)} = \log\left(P_{CO_2}/\left[P_{CO}\cdot P_{O_2}^{(1/2)}\right]\right) = -4.534 + 1.475\times 10^4/T \tag{3.8.36}$$

$$H_2 + (1/2)O_2 = H_2O \tag{3.8.49}$$

$$\begin{aligned}\log K_{(3.8.49)} &= \log\left(P_{H_2O}/\left[P_{H_2}\cdot P_{O_2}^{(1/2)}\right]\right)\\ &= 4.829\times 10^{-1} - 9.790\times 10^{-1}\log T + 1.251\times 10^4/T\end{aligned} \tag{3.8.50}$$

$$CO + 2H_2 = CH_4 + (1/2)O_2 \tag{3.8.51}$$

$$\begin{aligned}\log K_{(3.8.51)} &= \log\left(\left[P_{CH_4}\cdot P_{O_2}^{(1/2)}\right]/\left[P_{CO}\cdot P_{H_2}^2\right]\right)\\ &= -1.165 - 2.677\log T - 2.225\times 10^3/T\end{aligned} \tag{3.8.52}$$

Since the mole ratios of n_H/n_C and n_O/n_C remain constant through the reactions:

$$\begin{aligned}n_H/n_C &= (2P_{H_2}/P_{CO_2})_{initial}\\ &= [2P_{H_2} + 2P_{H_2O} + 4P_{CH_4}]/[P_{CO} + P_{CO_2} + P_{CH_4}]\end{aligned} \tag{3.8.53}$$

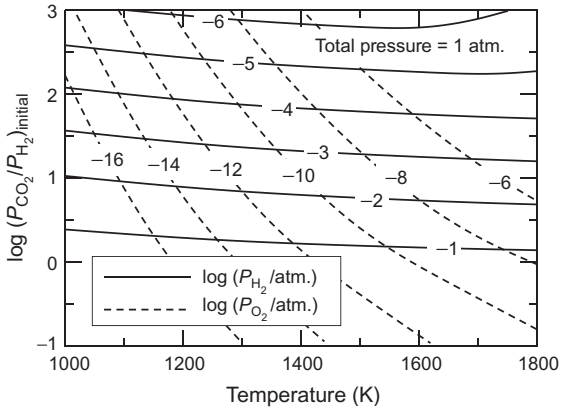


Figure 3.8.14 Equilibrium iso-pressure curves for oxygen and hydrogen in the C–H–O gaseous system.

$$\begin{aligned} n_O/n_C &= (2P_{CO_2}/P_{CO_2})_{initial} = 2 \\ &= [P_{CO} + 2P_{CO_2} + P_{H_2O} + 2P_{O_2}]/[P_{CO} + P_{CO_2} + P_{CH_4}] \end{aligned} \tag{3.8.54}$$

With the gas phase present at one atmospheric pressure:

$$P_{CO} + P_{CO_2} + P_{H_2} + P_{H_2O} + P_{O_2} + P_{CH_4} = 1 \tag{3.8.55}$$

These six equations (3.8.36), (3.8.50), (3.8.52), (3.8.53), (3.8.54), and (3.8.55) involve six unknowns, i.e., P_{CO}, P_{CO_2}, P_{H_2}, P_{H_2O}, P_{O_2}, and P_{CH_4}. Hence values for these unknowns can be calculated by solving these equations simultaneously for a given temperature and a known initial ratio of P_{CO_2}/P_{H_2}. Figure 3.8.14 shows the iso-pressure curves for oxygen and hydrogen in the equilibrium state. It should be noted here that solid carbon precipitates at lower temperature and lower initial values for P_{CO_2}/P_{H_2} than those ranges where the iso-pressure curves are illustrated in Figure 3.8.14.

Now consider the reaction equilibrium between solid carbon and the C–H–O ternary gaseous phase; the mixture consists of n_C moles of carbon, n_H moles of atomic hydrogen, and n_O moles of atomic oxygen. Let the mixture generate $n_{\langle C\rangle}$ moles of solid carbon and gas of volume, V, containing n_{CO}, n_{CO_2}, n_{H_2}, n_{H_2O}, n_{O_2}, and n_{CH_4} moles of gaseous species at a given temperature. This calculation method can be applied not only to the determination of oxygen potential but also to the discussion on thermal decomposition of organic materials [31].

At high temperatures, reactions between the various species can be expressed as [30]:

$$\langle C\rangle + (1/2)O_2 = CO \tag{3.8.56}$$

$$\log K_{(3.8.56)} = \log\left(P_{CO}/P_{O_2}^{(1/2)}\right) = 4.578 + 5.835 \times 10^3/T \tag{3.8.57}$$

$$\langle C\rangle + O_2 = CO_2 \tag{3.8.58}$$

$$\log K_{(3.8.58)} = \log\left(P_{CO_2}/P_{O_2}\right) = 4.371 \times 10^{-2} + 2.059 \times 10^{4}/T \tag{3.8.59}$$

$$H_2 + (1/2)O_2 = H_2O \tag{3.8.49}$$

$$\begin{aligned}\log K_{(3.8.49)} &= \log\left(P_{H_2O}/\left[P_{H_2} \cdot P_{O_2}^{(1/2)}\right]\right) \\ &= 4.829 \times 10^{-1} - 9.790 \times 10^{-1} \log T + 1.251 \times 10^{4}/T\end{aligned} \tag{3.8.50}$$

$$\langle C \rangle + 2H_2 = CH_4 \tag{3.8.60}$$

$$\log K_{(3.8.60)} = \log\left(P_{CH_4}/P_{H_2}^2\right) = 3.413 - 2.677 \log T + 3.610 \times 10^{3}/T \tag{3.8.61}$$

The mass balances for carbon, hydrogen, and oxygen, respectively, are given as follows:

$$n_C = n_{\langle C \rangle} + n_{CO} + n_{CO_2} + n_{CH_4} \tag{3.8.62}$$

$$n_H = 2n_{H_2} + 2n_{H_2O} + 4n_{CH_4} \tag{3.8.63}$$

$$n_O = n_{CO} + 2n_{CO_2} + n_{H_2O} + 2n_{O_2} \tag{3.8.64}$$

Assuming ideal behavior of the gaseous species, the partial pressures, P_j, of gaseous components, j, (j = CO, CO_2, H_2, H_2O, O_2, and CH_4) are related to n_j and V through the following relationship:

$$P_j V = n_j RT \tag{3.8.65}$$

By combining Equation (3.8.65) with Equations (3.8.62)–(3.8.64), respectively:

$$n_C = n_{\langle C \rangle} + (V/RT)(P_{CO} + P_{CO_2} + P_{CH_4}) \tag{3.8.66}$$

$$n_H = (V/RT)(2P_{H_2} + 2P_{H_2O} + 4P_{CH_4}) \tag{3.8.67}$$

$$n_O = (V/RT)(P_{CO} + 2P_{CO_2} + P_{H_2O} + 2P_{O_2}) \tag{3.8.68}$$

Since the gas phase is present at one atmospheric pressure:

$$P_{CO} + P_{CO_2} + P_{H_2} + P_{H_2O} + P_{O_2} + P_{CH_4} = 1 \tag{3.8.55}$$

These eight Equations (3.8.50), (3.8.55), (3.8.57), (3.8.59), (3.8.61), (3.8.66), (3.8.67), and (3.8.68) involve eight unknowns, i.e., V, $n_{\langle C \rangle}$, P_{CO}, P_{CO_2}, P_{H_2}, P_{H_2O}, P_{O_2}, and P_{CH_4}. Hence, values for these unknowns can be calculated by solving these equations simultaneously for a given temperature and known values for n_C, n_H, and n_O.

Figure 3.8.15 shows the equilibrium partial pressures of gaseous species at 1500 K as a function of n_O/n_C. According to Gibbs phase rule, there are three degrees of thermodynamic freedom when the C–H–O ternary gaseous phase coexists with solid carbon; $F = 3$ (components) $+ 2 - 2$(phases) $= 3$. As seen in Figure 3.8.15, the partial pressures are constant in the regions where the gaseous phase coexists with solid carbon. This is consistent with the consideration that there are no degrees of freedom at a fixed temperature, a fixed total pressure and a fixed n_O/n_H mole ratio in the gaseous phase. Figure 3.8.15 also

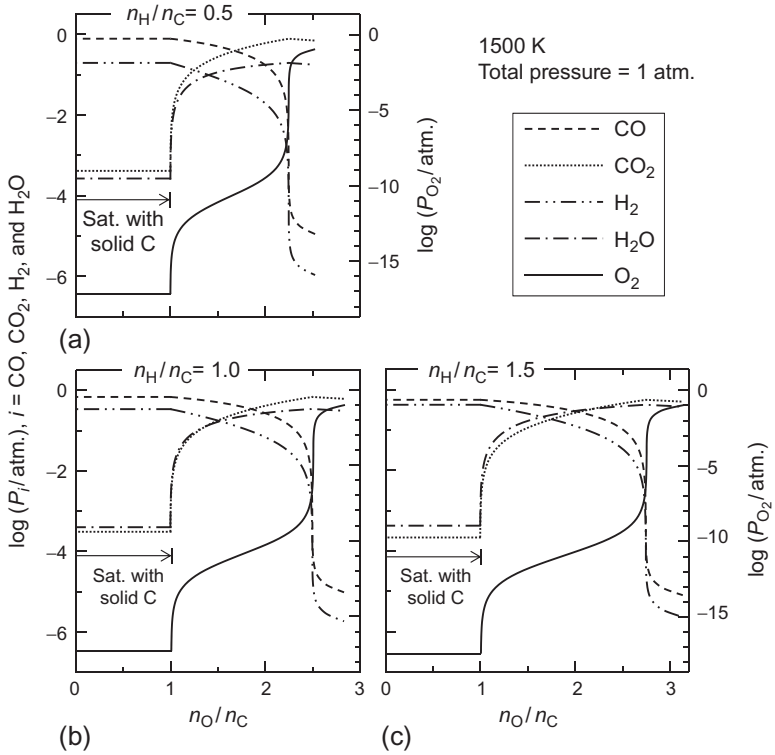


Figure 3.8.15 Equilibrium partial pressures of gaseous species in the C–H–O system at 1500 K as functions of O/C molar ratio.

illustrates that the equilibrium oxygen partial pressures change drastically at n_O/n_C mole ratios close to 1 and $[2+(1/2)(n_H/n_C)]$; these values correspond to the compositions of the major gaseous species generated, i.e., CO and CO_2+H_2O, respectively.

REFERENCES

[1] E.T. Turkdogan, Physical Chemistry of High Temperature Technology, Academic Press, New York, 1980.
[2] The 19th Committee on Steelmaking Data Sourcebook, The Japan Society for the Promotion of Science: Gordon and Breach Science Publishers, New York, 1988.
[3] G.I. Batalin, V.S. Sudavstova, Sov. Prog. Chem. 42 (1976) 33.
[4] H. Ono-Nakazato, R. Maruo, K. Taguchi, T. Usui, ISIJ Int. 47 (2007) 365.
[5] H. Itoh, M. Hino, S. Ban-ya, Tetsu-to-Hagane 83 (1997) 773.
[6] H. Itoh, M. Hino, S. Ban-ya, Tetsu-to-Hagane 83 (1997) 695.
[7] The Japan Society for the Promotion of Science, in: The 19th Committee on Steelmaking: Steelmaking Date Sourcebook, Gordon and Breach Science Publishers, New York, 1988, 280, 282, 288.
[8] H. Itoh, M. Hino, S. Ban-ya, Tetsu-to-Hagane 84 (1998) 85.
[9] H. Itoh, M. Hino, S. Ban-ya, Tetsu-to-Hagane 83 (1997) 623.
[10] T. Fujisawa, M. Yamauchi, H. Sakao, CAMP-ISIJ 1 (1988) 1115.

[11] B. Hallstedt, J. Am. Ceram. Soc. 73 (1990) 15.
[12] Y. Ehara, M. Hino, S. Ban-Ya, CAMP-ISIJ 7 (1997) 883.
[13] W.A. Fischer, H.J. Fleischer, Arch. Eisenhüttenw. 32 (1961) 1.
[14] K. Takahashi, M. Hino, High Temp. Mater. Proc. 19 (2000) 1.
[15] H. Schenck, N.G. Schmahl, A.K. Biswas, Arch. Eisenhüttenw. 28 (1957) 517.
[16] M. Hino, K. Takhashi, T. Itoh, I. Kikuchi, T. Nagasaka, Scand. J. Metall. 31 (2002) 169.
[17] D. Janke, W.A. Fischer, Arch. Eisenhüttenw. 47 (1976) 147.
[18] S. Dimitrov, H. Wenz, K. Koch, D. Janke, Steel Res. 66 (1995) 39.
[19] I. Ivanchev, H.B. Bell, J. Iron Steel Inst. 210 (1972) 543.
[20] J. Chipman, J.B. Gero, T.B. Winkler, J. Met. Trans. AIME 188 (1950) 341.
[21] F. Korber, W. Oelsen, Mitt. K. W. Inst. 14 (1932) 181.
[22] D.C. Hilty, W. Crafts, J. Met. Trans. AIME 188 (1950) 425.
[23] K. Taguchi, H. Ono, D. Nakai, T. Usui, K. Marukawa, ISIJ Int. 43 (2003) 1705.
[24] C.H.P. Lupis, Chemical Thermodynamics of Materials, Elsevier Science Publishing Co., Inc., New York, 1983, 255.
[25] Y. Miyashita, K. Nishikawa, Tetsu-to-Hagané 57 (1971) 1969.
[26] Q. Han, X. Zhang, D. Chen, P. Wang, Metall. Trans. B 19B (1988) 617.
[27] R. Inoue, H. Suito, Steel Res. 65 (1994) 403.
[28] R.A. Rapp (Ed.), In: Physicochemical Measurements in Metals Research Part 1, Techniques of Metals Research, vol.IV, Interscience Publishers, a Division of Wiley & Sons, Inc., New York, 1970, p. 328.
[29] C.J.B. Fincham, F.D. Richardson, Proc. R. Soc. A223 (1954) 40.
[30] O. Kubaschewski, C.B. Alcock, Metallurgical Thermochemistry, fifth ed., Pergamon Press, Oxford, 1979, p. 378.
[31] M. Takekawa, K. Wakimoto, M. Matsu-ura, M. Hasegawa, M. Iwase, A. McLean, Steel Res. Int. 74 (6) (2003) 347.

CHAPTER 3.9

Thermodynamics of Aqueous Phases

Tetsuji Hirato
Department of Energy Science and Technology, Kyoto University, Kyoto, Japan

3.9.1. CHEMICAL POTENTIALS AND ELECTROCHEMICAL POTENTIALS

The chemical potential of an electrolyte A is given as the partial molar Gibbs energy, G, as follows

$$\mu_A = \left(\frac{\partial G}{\partial n_A}\right)_{n_s,T,P} \tag{3.9.1}$$

where s refers to the solvent. Electrolytes dissociate into ions (particles with electrical charges) when they are dissolved in water. For ion species i, the chemical potential may be defined by

$$\mu_i = \left(\frac{\partial G}{\partial n_i}\right)_{n_j,n_s,T,P} \tag{3.9.2}$$

where j refers to all ionic species other than i. However, Equation (3.9.2) does not represent a physically realizable process. It is impossible to add ions of species i only into solutions, since equal amounts of positive charge on cations and negative charge on anions are only allowable in water. The energy state of ionic species depends on the chemical environment. In addition, free energy is required to build up the charge of the ions. The second energy is clearly proportional to the internal electrical potential, ϕ, at the phase in question, which can be calculated from electrostatic theory. Although one cannot experimentally separate these two components for a single species, Guggenheim [1] separated them conceptually and introduced the electrochemical potential, $\widetilde{\mu}_i$, for individual ionic species:

$$\widetilde{\mu}_i = \mu_i + z_i F \phi_i \tag{3.9.3}$$

where z_i is the charge number (signed) of the ion and F is the Faraday constant. For reactions in a single conducting phase, ϕ_i is constant everywhere in the phase and thus shows no effect on a chemical equilibrium. The chemical potentials of ions defined by

Treatise on Process Metallurgy, Volume 1
http://dx.doi.org/10.1016/B978-0-08-096986-2.00036-9
© 2014 Elsevier Ltd.
All rights reserved.

Equation (3.9.2) can be used to calculate chemical equilibriums in aqueous solutions, although they cannot be measured experimentally. Examples will be shown later in this chapter.

3.9.2. ACTIVITY AND ACTIVITY COEFFICIENTS

Accepting the use of the chemical potential of a solute in real solutions, the chemical potentials of individual ionic species can be related to their activities, a_i:

$$\mu_i = \mu_i^0 + RT \ln a_i \tag{3.9.4}$$

Since the composition of the solution is described commonly in terms of the molality scale, usually the hypothetical one-molal solution of the ion is chosen as the standard state. The standard state is an imaginary solution with molality m^0=1 mol/kg in which the ions behave ideally. The activity is related to the molality, m_i, by

$$a_i = \gamma_i \frac{m_i}{m^0} \tag{3.9.5}$$

where γ_i is the molal activity coefficient. The activity and activity coefficient have no dimensions. As the molality approaches zero, obeying Henry's law, γ_i tends to 1:

$$\gamma_i \to 1 \text{ and } a_i \to m_i \to 0 \tag{3.9.6}$$

The chemical potential can be written as follows:

$$\mu_i = \mu_i^0 + RT \ln m_i + RT \ln \gamma_i = \mu_i^{\text{ideal}} + RT \ln \gamma_i \tag{3.9.7}$$

where μ_i^{ideal} is the chemical potential of the ideal-dilute solution of the same molality. Thus, all deviations from ideality are carried in the activity coefficient. The molality scale can be converted to the mole fraction scale, which is often used in theoretical treatment, because the mole amount of solvent can be calculated using its formula weight.

For the molarity scale, the hypothetical one-molar solution ($c^0 = 1$ mol/L) is chosen as the standard state. The chemical potential can be written using the molarity, c_i, and the molar activity coefficient, γ_i:

$$\mu_i = \mu_{i(c)}^0 + RT \ln c_i + RT \ln \gamma_i \tag{3.9.8}$$

$$\gamma_i \to 1 \text{ and } a_i \to c_i \text{ as } c_i \to 0. \tag{3.9.9}$$

The molarity can be related to the molality by measuring the density of the solution.

3.9.3. MEAN ACTIVITY COEFFICIENTS

The chemical potential of electrolytes as a whole can be measured experimentally. If the general formula of an electrolyte A is expressed by $M_{\nu_1}X_{\nu_2}$, where the cation M and

the anion X have charges z_1e and z_2e, respectively, the following equation is obtained for electrical neutrality:

$$\nu_1 z_1 + \nu_2 z_2 = 0 \tag{3.9.10}$$

The molar Gibbs energy for a real solution of $M_{\nu_1}X_{\nu_2}$ is as follows:

$$\begin{aligned}\mu_{M_{\nu_1}X_{\nu_2}} &= \nu_1\mu_{M^{z_1}} + \nu_2\mu_{X^{z_2}} \\ &= \nu_1\mu^0_{M^{z_1}} + \nu_1 RT\ \ln\ m_{M^{z_1}} + \nu_1 RT\ \ln\ \gamma_{M^{z_1}} + \nu_2\mu^0_{X^{z_2}} \\ &\quad + \nu_2 RT\ \ln\ m_{X^{z_2}} + \nu_2 RT\ \ln\ \gamma_{X^{z_2}}\end{aligned} \tag{3.9.11}$$

More simply, taking A for the formula of the electrolyte and denoting the cation by 1 and the anion by 2:

$$\mu_A = \mu^0_A + RT\ \ln\ (m_1^{\nu_1} m_2^{\nu_2}) + RT\ \ln\ (\gamma_1^{\nu_1}\gamma_2^{\nu_2}) \tag{3.9.12}$$

$$\mu^0_A = \nu_1\,\mu^0_{M^{z_1}} + \nu_2\mu^0_{X^{z_2}} \tag{3.9.13}$$

The mean molarity and mean activity coefficient are defined as follows:

$$m_\pm = (m_1^{\nu_1} m_2^{\nu_2})^{1/\nu} \tag{3.9.14}$$

$$\gamma_\pm = (\gamma_1^{\nu_1}\gamma_2^{\nu_2})^{1/\nu} \tag{3.9.15}$$

and where $\nu = \nu_1 + \nu_2$, Equation (3.9.12) becomes

$$\mu_A = \mu^0_A + \nu RT\ \ln\ (m_\pm\gamma_\pm) \tag{3.9.16}$$

Thermodynamic data of electrolytes are often reported and tabulated as the mean activity coefficient.

3.9.4. THE DEBYE–HÜCKEL LAW [2]

Electrolyte solutions generally consist of solvated ions and solvent molecules. The departures from ideality in ionic solutions are dominantly caused by the Coulombic interaction between ions. The contribution of the ion–ion interaction is estimated on the basis of the Debye–Hückel theory. Detailed descriptions of the calculation can be found in specialized books on electrochemistry.

Ions that are oppositely charged attract one another. As a result, anions are more likely to be found near cations in solution, and vice versa. Near any given ions, there is an excess of counter ions (ions of opposite charge), even though the overall solution is electrically neutral. The Debye–Hückel theory relates the activity coefficient of the central ion to its ionic atmosphere, which is a spherical haze with a net charge equal in magnitude but opposite in sign to that of the central ion. The electrostatic interaction between the central ion and its ionic atmosphere decreases the energy of the central ion. This energy

change appears as the difference between the chemical potential and the ideal value of the solute, and hence can be identified as $RT \ln \gamma_{\pm}$.

In very dilute solutions, the activity coefficient can be calculated from the Debye–Hückel limiting law:

$$\log\gamma_{\pm} = -|z_{+}z_{-}|AI^{1/2} \tag{3.9.17}$$

where $A = 0.509$ for an aqueous solution at 298 K and I is the ionic strength of the solution:

$$I = \frac{1}{2}\sum_{i} m_i z_i^2 \tag{3.9.18}$$

The ionic strength is used widely where ionic solutions are discussed.

For more concentrated solutions, where the ionic strength of the solution is too high ($I > 0.2$) for the limiting law to be valid, the activity coefficient may be estimated from the extended Debye–Hückel law:

$$\log\gamma_{\pm} = \frac{-|z_{+}z_{-}|AI^{1/2}}{1 + BI^{1/2}} + CI \tag{3.9.19}$$

where B and C are other dimensionless constants. Although B can be related to effective ion radius, it is better considered as an adjustable empirical parameter.

3.9.5. CHEMICAL EQUILIBRIUM AND GIBBS ENERGY OF FORMATION OF IONS

Consider the following reaction:

$$a\mathrm{A} + b\mathrm{B} = c\mathrm{C} + d\mathrm{D} \tag{3.9.20}$$

The reaction Gibbs energy, ΔG_r, is expressed by using chemical potentials of the species, A, B, C, and D:

$$\Delta G_r = c\mu_C + d\mu_D - a\mu_A - b\mu_B \tag{3.9.21}$$

By considering Equation (3.9.4), the following formula is obtained:

$$\Delta G_r = c\mu_C^0 + d\mu_D^0 - a\mu_A^0 - b\mu_B^0 + RT\ln\frac{a_C^c a_D^d}{a_A^a a_B^b} = \Delta G^0 + RT\ln\frac{a_C^c a_D^d}{a_A^a a_B^b} \tag{3.9.22}$$

where $\Delta G^0 = c\mu_C^0 + d\mu_D^0 - a\mu_A^0 - b\mu_B^0$.

Since ΔG_r is zero at equilibrium, one obtains

$$\Delta G^0 = -RT \ln K \tag{3.9.23}$$

where K is the equilibrium constant.

The value of ΔG^0 can be calculated by using Gibbs energy of formation, ΔG_f^0, instead of chemical potentials, as in the following equation:

$$\Delta G^0 = c\Delta G_f^0(\mathrm{C}) + d\Delta G_f^0(\mathrm{D}) - a\Delta G_f^0(\mathrm{A}) - b\Delta G_f^0(\mathrm{B}) \tag{3.9.24}$$

In aqueous solution, by taking the standard free energy of formation of $H^+(aq)$ as zero, the standard free energy of formation of individual ionic species can be obtained. For example, consider the following reaction:

$$\mathrm{HCl(g)} = \mathrm{H^+(aq)} + \mathrm{Cl^-(aq)} \tag{3.9.25}$$

Here, $\Delta G_r{}^0 = -35.9\,\mathrm{kJ/mol}$ and $\Delta G_f^0(\mathrm{HCl,g}) = -95.3\,\mathrm{kJ/mol}$; thus, the standard free energy of formation of $Cl^-(aq)$ can be calculated as follows:

$$\Delta G_f^0(\mathrm{Cl^-,aq}) = -131.2\,\mathrm{kJ/mol}$$

In the same way, by taking the standard enthalpy of formation and entropy of $H^+(aq)$ as zero:

$$\Delta H_f^0(\mathrm{H^+,aq}) = 0 \tag{3.9.26}$$

$$\Delta S^0(\mathrm{H^+,aq}) = 0 \tag{3.9.27}$$

the standard enthalpy of formation and entropy of individual ionic species can be obtained.

The data of the standard free energy and enthalpy of formation and entropy of individual ionic species were tabulated by Latimer [3].

The standard free energy of formation at temperature T, ΔG_T^0, is given as follows:

$$\Delta G_T^0 = \Delta H_T^0 - T\Delta S_T^0 \tag{3.9.28}$$

$$\Delta G_T^0 = \Delta H_{298}^0 + \int_{298}^{T} \Delta C_p^0 \mathrm{d}T - T\Delta S_{298}^0 - T\int_{298}^{T} \frac{\Delta C_p^0}{T}\mathrm{d}T \tag{3.9.29}$$

where $\Delta H^0, \Delta S^0$, and ΔC_p^0 are changes of enthalpy, entropy and specific heat at 1 atm., respectively. Knowledge is limited about the specific heat of ionic species in aqueous solution, so we have to calculate the value of ΔC_p^0 approximately. First, ΔC_p^0 is approximated to be zero in the considered temperature range.

$$\Delta G_T^0 = \Delta H_{298}^0 - T\Delta S_{298}^0 = \Delta G_{298}^0 - \Delta S_{298}^0(T - 298) \tag{3.9.30}$$

Second, if ΔC_p^0 is approximated to be constant between 298 K and the temperature of interest, the extrapolation is straightforward.

$$\Delta G_T^0 = \Delta H_{298}^0 - T\Delta S_{298}^0 + \Delta C_p^0 \int_{298}^{T} \mathrm{d}T - T\Delta C_p^0 \int_{298}^{T} \frac{1}{T}\mathrm{d}T \tag{3.9.31}$$

If ΔH_T^0 is measured at a temperature other than 298 K, the value of ΔC_p^0 can be calculated.

As the third approximation, the Criss–Cobble correspondence principle [4] is commonly applied for simple cations and anions, oxyanions (XO_n^{z-}), and acid oxyanions (HXO_n^{z-}). The relationship between ionic entropies at 298 K and those at elevated temperatures can be expressed as follows:

$$S_T^{\cdot} = \alpha_T + \beta_T S_{298}^{\cdot} \tag{3.9.32}$$

where $S_T^{\cdot}$ and $S_{298}^{\cdot}$ are absolute entropies at the temperature and at 298 K, respectively, and α_T and β_T are constants dependent on the temperature and type of ion. The absolute entropy is related to the conventional entropy (based on $S_{298}^0 = 0$ for $H^+(aq)$) as in the following equation:

$$S_{298}^{\cdot}(i) = S_{298}^0(i) + zS_{298}^{\cdot}(H^+) \tag{3.9.33}$$

where z is the ionic charge (signed) and $S_{298}^0(i)$ is the conventional entropy for ion species, i.

3.9.6. CHEMICAL EQUILIBRIUM IN AQUEOUS SOLUTIONS

3.9.6.1. Acid–Base Reaction

According to the definition by Brønsted and Lowly, acid–base reactions are characterized as proton transfer reactions. In this system, Brønsted acids donate a proton and Brønsted bases accept a proton. Here a proton means a hydrogen cation, H^+:

$$HA(aq) + H_2O(l) = A^-(aq) + H_3O^+(aq) \tag{3.9.34}$$

Here, HA(aq) is an acid and $H_2O(l)$ is a base, and $A^-(aq)$ is a conjugate base and $H_3O^+(aq)$ is a conjugate acid:

$$B(aq) + H_2O = HB^+(aq) + OH^-(aq) \tag{3.9.35}$$

Here, B(aq) is a base and $H_2O(l)$ is an acid, $HB^+(aq)$ is a conjugate acid, and $OH^-(aq)$ is a conjugate base.

Although free protons do not exist in aqueous solutions, $H^+(aq)$ or H^+ is used as a representation of the state of the proton in this section for simplicity. Accordingly, the equilibrium constants for reactions (3.9.34) and (3.9.35) are expressed as follows:

$$K_a = \frac{a(H^+)a(A^-)}{a(HA)} \tag{3.9.36a}$$

$$K_b = \frac{a(HB^+)a(OH^-)}{a(B)} \tag{3.9.36b}$$

where K_a is the acidity constant and K_b is the basicity constant.

The equilibrium constant, K_W, for dissociation of water is:

$$H_2O(l) = H^+(aq) + OH^-(aq) \tag{3.9.37}$$

$$K_W = a(H^+)a(OH^-) \tag{3.9.38}$$

It is common to use the negative common logarithm of equilibrium constants:

$$pK = -\log K \tag{3.9.39}$$

Since acid–base reaction is a proton transfer reaction, pH is one of the most important factors to describe reactions in aqueous solutions, where

$$pH = -\log a(H^+) \tag{3.9.40}$$

In weak acid solutions, pH can be expressed as follows:

$$pH = pK_a - \frac{a(A^-)}{a(HA)} \tag{3.9.41}$$

where the pH value is determined by the ratio of $a(A^-)/a(HA)$

$$pH = pK_a - \frac{a(A^-)}{a(HA)} \tag{3.9.42}$$

In aqueous solutions containing metallic ions, hydrolysis reactions must be considered:

$$M^{n+}(aq) + nH_2O(l) = M(OH)_n(s) + nH^+(aq) \tag{3.9.43}$$

According to this reaction, the relationship between $a(M^{n+})$ and pH is determined as follows:

$$pH = \frac{1}{n}\{pK_{MOH} - \log a(M^{n+})\} \tag{3.9.44}$$

where K_{MOH} is the equilibrium constant of the reaction (3.9.43).

In Lewis acid–base reactions, an acid can accept an electron lone pair from another molecule (Lewis base). Complex formation reaction is one of the Lewis acid–base reactions:

$$M^{n+}(aq) + mL(aq) = ML_m^{n+}(aq) \tag{3.9.45}$$

where L represents a ligand. Here the metal ion, $M^{n+}(aq)$, is a Lewis acid and the ligand is a Lewis base. The equilibrium constants of complex formation reactions have been tabulated by Martell and Smith [5]. The standard free energy of formation for a complex species, $ML_m^{n+}(aq)$ can be calculated by using its equilibrium constant.

3.9.6.2. Redox Reactions

Redox reactions (oxidation–reduction reactions) are characterized as electron transfer reactions. Like acid–base reactions, oxidants accept protons and reductants donate electrons. An oxidation reaction does not occur without a reduction reaction. Each reaction is called a "half reaction." In general, a half reaction is presented as follows:

$$\mathrm{Ox} + z\mathrm{e}^- = \mathrm{Red} \tag{3.9.46}$$

where Ox and Red represent an oxidant and a reductant, respectively.

Although the chemical potential of ions cannot be determined as described in Section 3.9.1, the value of ΔG^0 can be calculated by defining Gibbs energy of formation of ions. Although the chemical potential of electrons cannot be determined, the equilibrium of reaction (3.9.46) can be considered in the same way, by defining the chemical potential of electrons as follows:

$$\mu_\mathrm{e} = -FE \tag{3.9.47}$$

where F is the Faraday constant, and E is potential, the potential, E, is the potential based on the hydrogen standard electrode as described later.

The potential can be obtained on the basis of Equations (3.9.21) and (3.9.22):

$$E = -\frac{\Delta G^0}{zF} - \frac{RT}{zF}\ln\frac{a(\mathrm{Red})}{a(\mathrm{Ox})} \tag{3.9.48}$$

where $\Delta G^0 = \Delta G_\mathrm{f}^0(\mathrm{Red}) - \Delta G_\mathrm{f}^0(\mathrm{Ox})$.

The standard potential, E^0, is calculated as follows:

$$E^0 = -\frac{\Delta G^0}{zF} \tag{3.9.49}$$

By using this Equation (3.9.48) can be expressed as follows:

$$E = E^0 - \frac{RT}{zF}\ln\frac{a(\mathrm{Red})}{a(\mathrm{Ox})} \tag{3.9.50}$$

This equation is called the Nernst equation for half-reactions.

Consider the reduction of hydrogen ions:

$$2\mathrm{H}^+(\mathrm{aq}) + 2\mathrm{e}^- = \mathrm{H}_2(\mathrm{g}) \tag{3.9.51}$$

where

$$E^0 = -\frac{\Delta G_\mathrm{f}^0(\mathrm{H}_2) - 2\Delta G_\mathrm{f}^0(\mathrm{H}^+)}{2F} = 0 \tag{3.9.52}$$

Thus, it is understood that the potential determined by Equation (3.9.47) is the potential based on the hydrogen standard electrode.

For example, in the Daniell cell,

$$(\text{anode})\text{Zn}|\text{ZnSO}_4(\text{aq})||\text{CuSO}_4(\text{aq})|\text{Cu}(\text{cathode})$$

at the anode, zinc is oxidized as the following half-reaction:

$$\text{Zn}^{2+}(\text{aq}) + 2\text{e}^- = \text{Zn}(\text{s}) \tag{3.9.53}$$

At the cathode, copper ions are reduced as the following half-reaction:

$$\text{Cu}^2(\text{aq}) + 2\text{e}^- = \text{Cu}(\text{s}) \tag{3.9.54}$$

The total reaction is as follows:

$$\text{Zn}(\text{s}) + \text{Cu}^2(\text{aq})^+ = \text{Zn}^{2+}(\text{aq}) + \text{Cu}(\text{s}) \tag{3.9.55}$$

One can obtain the anode and cathode potentials:

$$E_{\text{Zn}^{2+}/\text{Zn}} = E^0{}_{\text{Zn}^{2+}/\text{Zn}} - \frac{RT}{2F}\ln\frac{a(\text{Zn})}{a(\text{Zn}^{2+})} \tag{3.9.56}$$

$$E_{\text{Cu}^{2+}/\text{Cu}} = E^0{}_{\text{Cu}^{2+}/\text{Cu}} - \frac{RT}{2F}\ln\frac{a(\text{Cu})}{a(\text{Cu}^{2+})} \tag{3.9.57}$$

where

$$E^0{}_{\text{Zn}^{2+}/\text{Zn}} = -\frac{\Delta G_\text{f}^0(\text{Zn}) - \Delta G_\text{f}^0(\text{Zn}^{2+})}{2F} = -0.76\text{V} \tag{3.9.58}$$

$$E^0{}_{\text{Cu}^{2+}/\text{Cu}} = -\frac{\Delta G_\text{f}^0(\text{Cu}) - \Delta G_\text{f}^0(\text{Cu}^{2+})}{2F} = +0.34\text{V} \tag{3.9.59}$$

and the electromotive force (emf) of the total reaction can be obtained as follows:

$$\text{emf} = E_{\text{Cu}^{2+}/\text{Cu}} - E_{\text{Zn}^{2+}/\text{Zn}} = 1.10 - \frac{RT}{zF}\ln\frac{a(\text{Zn}^{2+})}{a(\text{Cu}^{2+})} \tag{3.9.60}$$

3.9.7. POTENTIAL–pH DIAGRAMS (POURBAIX DIAGRAMS) [6]

Many reactions in aqueous solutions involve the transfer of electrons and/or protons, which means that redox potentials and the pH of solutions are very important measures of the tendency of reactions. Therefore, potential–pH diagrams, which was invented by Marcel Pourbaix (1904–1998) are useful tools for understanding reactions in electrolyte solutions. The diagrams are also known as Pourbaix diagrams or *E*h–pH diagrams.

In general, reactions in aqueous solutions are represented by the following equation:

$$m\mathrm{Ox} + n\mathrm{H}^+ + z\mathrm{e} = s\mathrm{Red} + t\mathrm{H_2O} \tag{3.9.61}$$

and when $z \neq 0$, one can obtain the potential as a function of pH and activities of species in aqueous solutions, on the basis of the above discussion.

$$E = -\frac{\Delta G^0}{zF} - \frac{2.303RT}{zF}\left\{\log\frac{a(\mathrm{R})^s}{a(\mathrm{O})^m} - n\mathrm{pH}\right\} \tag{3.9.62}$$

When $n = 0$, the reaction is a simple redox reaction.
At 298 K,

$$E = -\frac{\Delta G^0}{zF} - \frac{0.0591}{z}\left\{\log\frac{a(\mathrm{R})^s}{a(\mathrm{O})^m} - n\mathrm{pH}\right\} \tag{3.9.63}$$

When $z = 0$, the reaction is an acid–base reaction and we can obtain the following relationship:

$$\Delta G^0 = -2.303RT\left\{\log\frac{a(\mathrm{R})^s}{a(\mathrm{O})^m} - n\mathrm{pH}\right\} \tag{3.9.64}$$

As $\Delta G^0 = -2.303RT\log K$, the following equation is obtained:

$$\mathrm{pH} = \frac{1}{n}\log\frac{a(\mathrm{R})^s}{a(\mathrm{O})^m} + \frac{1}{n}\log K \tag{3.9.65}$$

The stability of water is important in aqueous solutions. Water is decomposed to $H_2(g)$ and $O_2(g)$.

$$2\mathrm{H}^+(\mathrm{aq}) + 2\mathrm{e} = \mathrm{H_2(g)} \tag{3.9.66}$$

$$E = -0.059\mathrm{pH} - 0.03\log p_{\mathrm{H_2}} \tag{3.9.67}$$

$$\mathrm{O_2(g)} + 4\mathrm{H}^+(\mathrm{aq}) + 4\mathrm{e} = 2\mathrm{H_2O} \tag{3.9.68}$$

$$E = 1.23 - 0.059\mathrm{pH} - 0.015\log p_{\mathrm{O_2}} \tag{3.9.69}$$

To obtain Equation (3.9.69), the standard free energy changes of formation of H_2O shown in Table 3.9.1 are used. At potentials higher than Equation (3.9.67) and lower than Equation (3.9.69), water is stable.

The potential–pH diagram for the Zn–H_2O system is constructed by using the standard free energy changes of formation shown in Table 3.9.1, as shown in Figure 3.9.1.

The numbered lines in Figure 3.9.1 represent the following reactions:

1,2: $\mathrm{Zn}^{2+} + 2\mathrm{e} = \mathrm{Zn}$ $E = -0.761 + 0.0295\log a(\mathrm{Zn_{2+}})$

3,4: $\mathrm{Zn}^{2+} + 2\mathrm{H_2O} = \mathrm{Zn(OH)_2} + 2\mathrm{H}^+$, $\mathrm{pH} = 5.86 - 0.5\log a(\mathrm{Zn}^{2+})$

5: $\mathrm{Zn(OH)_2} = \mathrm{HZnO_2}^- + \mathrm{H}^+$, $\mathrm{pH} = 15.7\log a(\mathrm{HZnO_2}^-)$

Table 3.9.1 Standard Free Energy Change of Formation

Formula	State	ΔG_f^0 (kJ/mol)
Zn	c	0
Zn^{2+}	aq	−147.03
$Zn(OH)_2$	c	−553.58
$HZnO_2^-$	aq	−464.0
ZnO_2^{2-}	aq	−389.2
H^+	aq	0
H_2O	l	−237.2

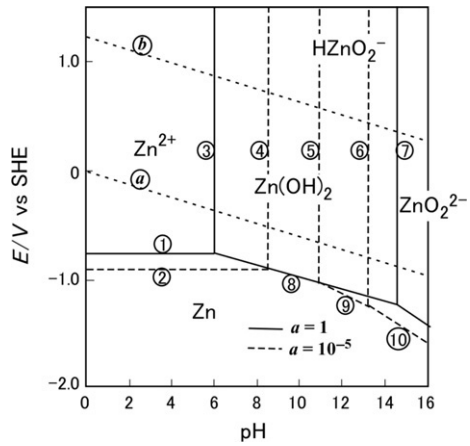


Figure 3.9.1 Potential–pH diagram for the Zn–H_2O system at 298 K.

6: $HZnO_2^- = ZnO_2^{2-} + H^+,\ \ pH = 13.1 + \log a(ZnO^-)/a(HZnO^-)$

7: $Zn(OH)_2 = ZnO_2^{2-} + 2H^+,\ \ pH = 14.6 + 0.5\log a(ZnO^-)$

8: $Zn(OH)_2 + 2H^+ + 2e = Zn + 2H_2O,\quad E = -0.416 - 0.0591pH$

9: $HZnO_2^- + 3H^+ + 2e = Zn + 2H_2O,\ \ E = 0.05 - 0.089,pH - 0.295\log a(HZnO^-)$

10: $ZnO_2^{2-} + 4H^+ + 2e = Zn + 2H_2O,\ \ E = 0.44 - 0.118pH + 0.295\log a(ZnO^{2-})$

Some may think it strange that reactions concerning Zn^{2+}(aq) are considered at potentials lower than line *a*, where water is not stable. Strictly speaking, potential–pH diagrams are not equilibrium phase diagrams. It is, however, useful to consider these reactions in aqueous solutions, since Zn deposition from an aqueous solution actually happens due to kinetics.

REFERENCES

[1] E.A. Guggenheim, J. Phys. Chem. 33 (1929) 842, 34, 1540(1930).
[2] P. Atkins, J. de Paula, Atkins' Physical Chemistry, eighth ed., Oxford University Press, Oxford, 2006, pp. 163–165.
[3] W.M. Latimer, The Oxidation States of the Elements and Their Potentials in Aqueous Solutions, second ed., Prentice-Hall, Inc., Englewood Cliffs, N.J., 1952.
[4] J.W. Cobble, et al., J. Am. Chem. Soc. 86 (1964) 5385, 5390, 5396.
[5] A.E. Martell, R.M. Smith, Critical Stability Constants, Plenum Press, New York, NY, 1974.
[6] M. Pourbaix, Atlas of Electrochemical Equilibria in Aqueous Solutions, Pergamon Press, Oxford, 1966.

CHAPTER 3.10

Thermodynamic Basis of Electrolysis and Electrochemistry

Tetsuji Hirato
Department of Energy Science and Technology, Kyoto University, Kyoto, Japan

3.10.1. ZINC ELECTROWINNING

The thermodynamic basis of zinc electrowinning can be understood from the potential–pH diagram shown in Figure 1 of Chapter 3.9. In the process, the anode reaction is oxygen evolution, which is shown as line *b* in the potential–pH diagram. The reaction proceeds at potentials higher than line *b*. The cathode reaction is deposition of metal zinc, which is shown as line 1 in the potential–pH diagram because the concentration of Zn^{2+}(aq) is relatively high in solutions used in this process.

The reaction proceeds at potentials lower than line 1. Since this potential region is lower than line *a*, it is easily understood that hydrogen evolution cannot be avoided in this process.

The voltage required in this process is the difference between lines *b* and 1. The voltage increases with decreasing pH value, and at pH 0, a voltage of at least 1.99 V is required for progression of the zinc electrowinning process. Of course, more voltage is required to operate the real process, including overpotential of zinc deposition, and an IR drop in a circuit with an electric current.

This diagram can also be used to consider the removal of Zn^{2+} from waste solutions as $Zn(OH)_2$. In the pH area between lines 4 and 5, the concentration of zinc in the solution can be reduced to less than 10^{-5}.

3.10.2. COPPER ELECTROWINNING

The thermodynamic basis of copper electrorefining can be understood from the potential–pH diagram shown in Figure 3.10.1. In this process, the anode reaction is oxygen evolution, which is shown as line *b* in the potential–pH diagram. The reaction proceeds at potentials higher than line *b*. The cathode reaction is deposition of metal copper shown as line 1 in Figure 3.10.1. The reaction proceeds at potentials lower than line 1. The potential indicated by line 1 is higher than line *a*, and thus hydrogen evolution does not need to be considered in this process. The voltage required in this process is the

Treatise on Process Metallurgy, Volume 1
http://dx.doi.org/10.1016/B978-0-08-096986-2.00037-0
© 2014 Elsevier Ltd.
All rights reserved.

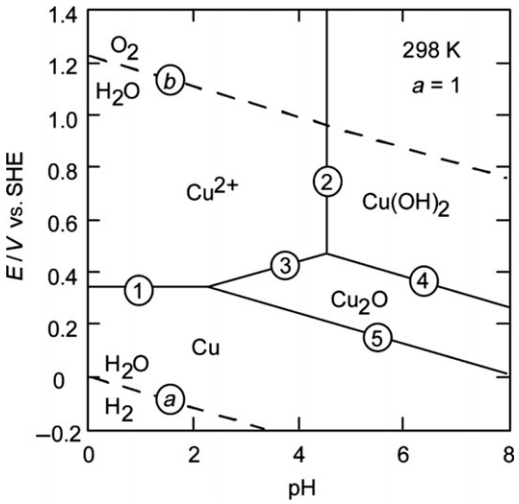


Figure 3.10.1 Potential–pH diagram for the Cu–H_2O system at 298 K.

difference between lines b and 1. The voltage increases with decreasing pH value, and at pH 0, a voltage of at least 0.899 V is required for progression of the copper electrowinning process, which is much lower than that in zinc electrowinning process.

3.10.3. COPPER ELECTROREFINING

The thermodynamic basis of copper electrorefining can also be understood from the potential–pH diagram shown in Figure 3.10.1. In this process, anode and cathode reactions are expressed as follows:

$$\text{at anode}: \quad \mathrm{Cu} = \mathrm{Cu}^{2+} + 2\mathrm{e}$$
$$\text{at cathode}: \quad \mathrm{Cu}^{2+} + 2\mathrm{e} = \mathrm{Cu}$$

Both reactions are indicated by line 1 in Figure 3.10.1 and the required voltage is 0 from a thermodynamic understanding. More strictly, the activity of anode copper is less than 1 because of impurities, so the voltage is a little bit more than 0.

3.10.4. ELECTROCHEMISTRY IN LEACHING

The electrochemistry in acid leaching or dissolution of copper oxides and hydroxides can also be understood by the potential–pH diagram shown in Figure 3.10.1. The dissolution reactions of copper oxides and hydroxides are as follows:

$$\mathrm{Cu(OH)_2(s)} + 2\mathrm{H}^+ = \mathrm{Cu}^{2+}\mathrm{(aq)} + 2\mathrm{H_2O(l)} \qquad (3.10.1)$$

$$Cu_2O(s) + 2H^+(aq) = 2Cu^{2+}(aq) + H_2O(l) + 2e \qquad (3.10.2)$$

Reactions (3.10.1) and (3.10.2) are indicated by lines 2 and 3 in the diagram, respectively. Reaction (3.10.2) is a redox reaction as well as an acid–base reaction. For the dissolution of Cu_2O to proceed, oxidant is required. When powders of Cu_2O are put into an aqueous sulfuric acid solution from which oxygen is purged, the following disproportionation reaction occurs:

$$Cu_2O(s) + 2H^+(aq) = Cu(s) + Cu^{2+}(aq) + H_2O(l) \qquad (3.10.3)$$

The thermodynamic properties of sulfide minerals in an aqueous environment can also be described by means of potential–pH diagrams. Such diagrams are as useful to hydrometallurgists as are Ellingham diagrams to pyrometallurgists [1]. For example, Figure 3.10.2 shows the potential–pH diagram for the Zn–S–H_2O system. This diagram is constructed by considering that zinc in zinc sulfide is decomposed to Zn^{2+}, Zn, and Zn $(OH)_2$ and sulfur to H_2S, S, HSO_4^-, or HS^-. As can be seen from this figure, zinc sulfide can be decomposed by oxidation, acidification, or reduction. The decomposition of zinc sulfide is represented by the following reactions:

Oxidation

$$ZnS = Zn^{2+} + S + 2e^-$$
$$ZnS + 4H_2O = Zn^{2+} + HSO_4^- + 7H^+ + 8e^-$$
$$ZnS + 4H_2O = Zn^{2+} + SO_4^{2-} + 8H^+ + 8e^-$$

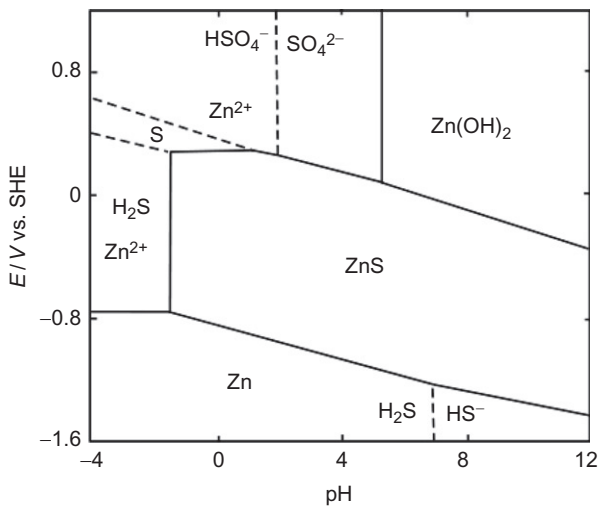


Figure 3.10.2 Potential–pH diagram for the Zn–S–H_2O system at 298 K.

Acidification

$$ZnS + 2H^+ = Zn^{2+} + H_2S$$

Reduction

$$ZnS + 2H^+ + 2e^- = Zn + H_2S$$
$$ZnS + 2e^- = Zn + S^{2-}$$

In oxidative leaching, oxygen or Fe^{3+} is used as an oxidant. In real oxidative leaching of sulfides, the stable area of elemental sulfur seems larger than shown in Figure 3.10.2. This is caused by the slow reaction of oxidation from elemental sulfur to sulfate. This diagram can also be used to consider the removal of Zn^{2+} from waste solutions as ZnS. In this case, the activity of Zn^{2+}(aq) should be set at 10^{-6}.

REFERENCES

[1] E. Peters, Metall. Trans. B 7B (1976) 505–517.

CHAPTER 4.1

Rate Phenomena in Process Metallurgy

Viswanathan N. Nurni[a] **and Bharath N. Ballal**[b]

[a]Minerals and Metals Research Laboratory (MiMeR), Luleå University of Technology, Luleå, Sweden
[b]Centre of Excellence in Steel Technology (COEST), Department of Metallurgical Engineering and Materials Science, Indian Institute of Technology Bombay, Mumbai, India

NOMENCLATURE

$\vec{a}$ acceleration, m s^{-2}
A area, m^2
c sonic velocity, m s^{-1}
C concentration, mol m^{-3}
C specific heat capacity for condensed phases, J kg^{-1} K^{-1}
C_1, C_2 integration constants
C_D discharge coefficient
C_p specific heat capacity at constant pressure, J kg^{-1} K^{-1}
d diameter or distance, m
$\mathbb{D}$ mass diffusivity, m^2 s^{-1}
D diameter, m
D_b size of bubble, m
D_e equivalent diameter, m
D_p size of particles, m
D_{sph} diameter of sphere having equivalent volume, m
$\dot{E}$ rate of energy or power, W
$\hat{E}_f$ friction loss, J kg^{-1}
E emissive power, W m^{-2}
E energy, J
E_b emissive power of black surface at temperature T_b, W m^{-2}
E^s energy in a system, J
F force, N
f_D D'Arcy's friction factor
f_F Fanning friction factor
F_{ij} view factor from surface "i" to "j"
g acceleration due to gravity, m s^{-2}
$\dot{G}'''$ molar generation rate per unit volume, mol s^{-1} m^{-3}
G mass flux, kg m^{-2} s^{-1}
G total irradiation, W m^{-2}
Gr Grashof number
Gz Graetz number
h height, m
h heat transfer coefficient, W m^{-2} K^{-1}
h_{loc} local heat transfer coefficient, W m^{-2} K^{-1}
$\hat{H}$ enthalpy per unit mass, J kg^{-1}

Treatise on Process Metallurgy, Volume 1
http://dx.doi.org/10.1016/B978-0-08-096986-2.00004-7
© 2014 Elsevier Ltd.
All rights reserved.

$\boldsymbol{H}$ enthalpy, J
$\boldsymbol{I}$ intensity of radiation, W m^{-2} m^{-1} sr^{-1}
$\boldsymbol{j}$ diffusive mass flux in the mixture velocity frame, kg
$\boldsymbol{J}$ radiosity irradiation, W m^{-2}
$\boldsymbol{J}^*$ diffusive molar flux in the mixture velocity frame, kg
$\boldsymbol{k}$ D'Arcy's permeability, m^{-2}
$\boldsymbol{k_f}$ energy loss factor (friction loss)
$\boldsymbol{k_m}$ mass transfer coefficient, m s^{-1}
$\widehat{\text{K.E}}$ kinetic energy per unit mass, J kg^{-1}
$\boldsymbol{L}$ length, m
$\boldsymbol{L_e}$ equivalent length, m
$\boldsymbol{L_{mf}}$ length or height of fluidized bed at minimum fluidization, m
$\dot{\boldsymbol{m}}$ mass flow rate, kg s^{-1}
$\boldsymbol{m}$ mass, kg
$\boldsymbol{m_i}$ mass fraction of species "i"
$\boldsymbol{m^s}$ mass in the system, kg
$\boldsymbol{M}$ molecular weight, kg mol^{-1}
$\boldsymbol{Ma}$ Mach number
$\boldsymbol{n''}$ mass flux in the laboratory frame, kg
$\boldsymbol{N''}$ molar flux in the laboratory frame, kg
$\boldsymbol{Nu}$ Nusselt number
$\mathbb{P}$ modified pressure, $\mathbb{P} = P + \rho g h$, where h is distance upward from a reference, Pa
$\boldsymbol{P}$ perimeter, m
$\boldsymbol{P}$ pressure, Pa
$\widehat{\text{P.E}}$ potential energy per unit mass, J kg^{-1}
$\boldsymbol{Pr}$ Prandtl number ν/α
$\dot{\boldsymbol{q}}$ rate of heat transfer, W
$\dot{\boldsymbol{q}}_f$ rate of heat transfer through fin, W
$\dot{\boldsymbol{q}}''$ heat flux, W m^{-2}
$\dot{\boldsymbol{q}}''_x$ heat flux along x-coordinate, W m^{-2}
$\dot{\boldsymbol{Q}}$ rate of heat (power), W
$\dot{\boldsymbol{Q}}'''$ rate of thermal energy generation per unit volume, W m^{-3}
$\hat{\boldsymbol{Q}}$ heat per unit mass, J kg^{-1}
$\boldsymbol{r}$ radial coordinate, m
$\boldsymbol{r}^*$ dimensionless radial coordinate
$\boldsymbol{R}$ radius, m
$\boldsymbol{R}$ thermal resistance, K W^{-1}
$\boldsymbol{R}$ universal gas constant, J mol K^{-1}
$\boldsymbol{Ra}$ Raleigh number
$\boldsymbol{Re}$ Reynolds number
$\boldsymbol{Sc}$ Schmidt number ν/D
$\boldsymbol{Sh}$ Sherwood number
$\boldsymbol{St}$ Stanton number
$\boldsymbol{t}$ time, s
$\boldsymbol{T}$ temperature, K
$\boldsymbol{T_0}$ initial temperature, K
$\boldsymbol{T_\infty}$ bulk temperature or temperature of approaching fluid, K
$\boldsymbol{T_b}$ bulk temperature, K
$\boldsymbol{T_f}$ film temperature, K

$\boldsymbol{T_M}$ melting temperature, K
$\boldsymbol{T_s}$ temperature at surface, K
$\boldsymbol{\hat{U}}$ specific internal energy, J kg^{-1}
$\boldsymbol{\bar{v}}$ average velocity, m s^{-1}
$\boldsymbol{v}$ velocity, m s^{-1}
$\boldsymbol{v'}$ fluctuating component of velocity in a turbulent flow, m s^{-1}
$\boldsymbol{v^*}$ mixture velocity, m s^{-1}
$\boldsymbol{v_0}$ superficial velocity, m s^{-1}
$\boldsymbol{v_\infty}$ velocity of the approaching fluid, terminal velocity, m s^{-1}
$\boldsymbol{v_b}$ bubble velocity, m s^{-1}
$\boldsymbol{v_{mf}}$ superficial velocity at minimum fluidization, m s^{-1}
$\boldsymbol{v_x}$ velocity in x-direction, m s^{-1}
$\boldsymbol{v_y}$ y-component of velocity, m s^{-1}
$\boldsymbol{v_z}$ z-component of velocity, m s^{-1}
$\hat{\mathbf{v}}_0$ unit vector along v_0, m s^{-1}
$\vec{\boldsymbol{v}}_0$ superficial velocity vector, m s^{-1}
$\boldsymbol{\dot{V}}$ volumetric flow rate, m
$\boldsymbol{\hat{V}}$ specific volume, m^3 kg^{-1}
$\boldsymbol{V}$ volume, m^3
$\boldsymbol{\dot{W}}$ rate of work, W
$\boldsymbol{\hat{W}}$ work per unit mass, J kg^{-1}
$\boldsymbol{x}$ x-coordinate, m
$\boldsymbol{x_i}$ mole fraction of species "i"
$\boldsymbol{y}$ y-coordinate, m
$\boldsymbol{z}$ axial or z-coordinate, m

GREEK SYMBOLS

$\boldsymbol{\alpha}$ radiation absorptivity
$\boldsymbol{\alpha}$ thermal diffusivity, m^2 s^{-1}
$\boldsymbol{\beta}$ correction factor for kinetic energy in mechanical energy balance
$\boldsymbol{\gamma}$ adiabatic gas constant or heat capacity ratio
$\boldsymbol{\Delta H_M}$ enthalpy of melting per unit mass, J kg^{-1}
$\boldsymbol{\Delta r}$ infinitesimal distance in r-coordinate, m
$\boldsymbol{\Delta x}$ infinitesimal distance in x-coordinate, m
$\boldsymbol{\Delta y}$ infinitesimal distance in y-coordinate, m
$\boldsymbol{\Delta z}$ infinitesimal distance in z-coordinate, m
$\boldsymbol{\delta}$ boundary layer or film thickness, m
$\boldsymbol{\varepsilon}$ voidage in packed or fluidized bed
$\boldsymbol{\varepsilon_b}$ volume fraction of bubble phase in bubbling fluidized bed
$\boldsymbol{\varepsilon_f}$ effectiveness of a fin
$\boldsymbol{\varepsilon_{mf}}$ voidage at minimum fluidization
$\in$ emissivity
$\in$ mean roughness, m
$\in$ radiation: emissivity, m
$\boldsymbol{\kappa}$ thermal conductivity, W m^{-1} K^{-1}
$\boldsymbol{\kappa_f}$ film thermal conductivity, W m^{-1} K^{-1}
$\boldsymbol{\eta_f}$ efficiency of a fin

$\boldsymbol{\theta}$ dimensionless temperature difference
$\boldsymbol{\theta}$ polar angle in spherical coordinates
$\boldsymbol{\theta_0}$ dimensionless temperature difference at the center
$\boldsymbol{\mu}$ viscosity, Pa s
$\boldsymbol{\nu}$ kinematic viscosity, $m^2\ s^{-1}$
$\boldsymbol{\nu_T}$ turbulent kinematic viscosity, $m^2\ s^{-1}$
$\boldsymbol{\rho}$ density, $kg\ m^{-3}$
$\boldsymbol{\rho_s}$ density of solid, $kg\ m^{-3}$
$\boldsymbol{\rho_{solute}}$ mass concentration of solute, $kg\ m^{-3}$
$\boldsymbol{\sigma}$ Stefan–Boltzmann constant, $W\ m^{-2}\ K^{-4}$
$\boldsymbol{\tau_{rz}}$ shear stress or z-momentum flux transferred in r direction, $N\ m^{-2}$
$\boldsymbol{\tau_{yx}}$ shear stress or x-momentum flux transferred in y direction, $N\ m^{-2}$
$\dot{\phi}$ rate of conservable entity, ϕ, entity s^{-1}
$\boldsymbol{\phi}$ any conservable entity or material property, entity
$\boldsymbol{\phi}$ azimuthal angle in spherical coordinates
$\boldsymbol{\phi}$ sphericity of particles
$\boldsymbol{\phi'''}$ any material property per unit volume, property m^{-3}
$\boldsymbol{\omega}$ solid angle, sr

4.1.1. INTRODUCTION

Process metallurgy is all about change: changing primary and secondary raw materials into valuable new materials, improving the quality of material products and process efficiencies, and reducing/eliminating the environment's impacts resulting from these changes. To bring about such desirable changes, it is necessary to understand what drives these processes as well as the rates at which these processes occur. This knowledge can be applied directly to control physical and chemical processes, or indirectly through improved design of equipment and technologies.

A process can be defined as that which brings about a change in the state of the system. The state of a system is defined using measurable properties that describe the system, such as density, pressure, temperature, and composition. An isolated system left to itself would eventually attain equilibrium, wherein the state of the system remains constant. A system at equilibrium can be altered through external factors imposed through the system boundary, such as work and/or transfer of mass and energy, so that the system seeks a new state of equilibrium. Therefore, a process can be viewed as the system response toward attaining equilibrium either left to itself (isolated systems) or being continuously altered through external means (closed and open systems). Using the principles of thermodynamics, which deal extensively with the definition of the state variables and equilibrium, the driving force for a process can be deduced by knowing how far away the current state of the system is from the state of equilibrium.

Thermodynamics does not, however, deal with rates at which processes occur. Rates are determined not only by the driving forces but also by the mechanisms of change and

resistances offered to change. To describe the rates of processes there is a need to understand and define how mass, work as well as energy are being exchanged through the system boundary with time as well as the rate at which the state of the system evolves toward equilibrium. Transport phenomena in conjunction with reaction kinetics deal with these aspects of processes. Through the system boundary, mass can be transferred by bulk flow or molecular mechanisms. Similarly, energy in the form of work, heat, or other forms can be exchanged through the system boundary. These aspects of transport of mass, momentum, and heat are dealt with together in this section as transport phenomena. The rates of processes involving chemical reactions are dealt in a separate section on reaction kinetics.

4.1.1.1. Importance of Transport Phenomena in Metallurgical Processing

Transport phenomena is an engineering science subject and are essential for understanding, designing, and operating most engineering processes. Therefore, it is an essential part of core curriculum of several engineering disciplines such as mechanical, civil, chemical, and materials engineering. The subject is dealt with in each case with a different emphasis in keeping the focus of the particular discipline. In this section, the importance of the subject for process metallurgy will be illustrated through a typical example of a packed bed reactor.

Consider a simple packed bed reactor shown in Figure 4.1.1. Hot gas is fed from the bottom of the reactor and is allowed to rise through the packed bed of particles, heating the bed. Gas flowing tortuously through the voids exerts a force on the particles, which in turn exerts an opposite force on the gas. To keep the gas flowing at a desired rate of throughput, therefore, a net force has to be exerted on the gas in the form of a pressure

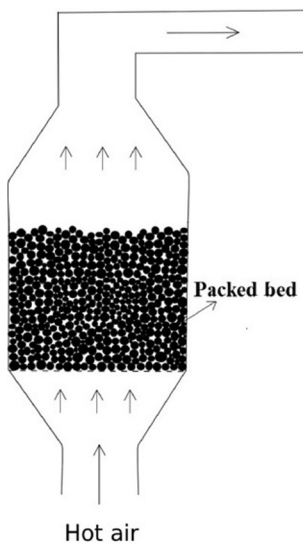


Figure 4.1.1 Example of a simple packed bed reactor.

difference across the bed. To estimate the required pressure difference, the forces acting on individual particles or an ensemble of them should be understood and quantified. Numerous detailed investigations have been carried out; the results of such investigations are rationalized through the principles of momentum transport.

As the hot gas flows up through the bed, the difference in temperature between the gas and the solid phases leads to thermal interactions, heat being transferred from the hot gases to the colder solids. This interaction, brought about at the basic level, by molecular phenomena, is dependent on the materials properties of the gas and the solid, on one hand, and the process conditions such as fluid flow, particle size and shape, and so on, on the other. The gas continuously cools as it moves up through the bed and the solid heats up. At the scale of the reactor, temperatures of the solids and the gas are seen to vary with time and position. Energy conservation principles have to be used to develop a methodology for predicting these changes in the context of heat transfers at the particle level. This understanding and these methodologies are rationalized into the principles of heat transfer.

In a reactor such as the blast furnace, the gases and the solids react chemically. Hot gas generated in front of the tuyeres located near the bottom of the furnace consists primarily of CO, H_2, and N_2. A mixture mainly of iron ores and coke forms the slowly descending packed bed of solids. Gas moves at great velocities covering a height of 25 m in 4–5 s. CO and H_2 in the gas chemically react with the solids resulting in the overall reduction of the ore to lower oxides and eventually in the formation of iron metal. The rates of the reduction processes determine evolution of the compositions of the solids and the gases. Since the ore exists as particles of considerable size (10–40 mm), the reductant specie, CO and H_2 have to be transferred from the flowing gas to the oxides deep within the particles. The rates of this transfer are determined by material properties and the process conditions such as flow velocities, particle size and shape, and the pore structure. The results of experimental and theoretical studies of all such phenomena are organized into the area of mass transfer. The rates of the chemical reactions at the reaction interface, between iron and its oxide, for example, are the subject matter of reaction kinetics.

In the blast furnace, there are many other processes taking place. For example, the reduced iron would ultimately melt lower down in the furnace due to the high temperatures in this region. Gangue materials from the ore and ash from coke, along with the added flux also melt down forming a slag. These two immiscible liquids trickle down the coke bed as drops and rivulets to collect at the bottom of the furnace to be taken out periodically/continuously. The rates of trickle flow of the liquid phases are important, since inadequate rates of trickling at high rates of production can lead to liquid accumulation in the bed and process break-down. To understand all these phenomena it is necessary to study transport phenomena.

Another example of a packed bed reactor is the iron ore-sintering machine, wherein air is made to flow down through a packed bed made of a mixture of ore, coke, and

limestone fines, by applying suction at the bottom. Once the coke at the top is ignited, the complex interchange of heat and mass between the gases and the solids results in the progressive movement of the flame front down through the bed. The high temperatures generated from combustion lead to incipient fusion in the solid particles and agglomeration to larger lumps, accompanied by complex reactions of reduction, oxidation, and slag formation. Though the process itself looks substantially different from the blast furnace process, the underlying phenomena have much similarity and are described by similar principles of transport phenomena and reaction kinetics.

Thus the principles of transport phenomena are integral to the design, operation, and control of engineering processes, and metallurgical processes are no exception.

4.1.1.2. Basic Methodologies in Transport Phenomena

Transport phenomena consist of broadly three important topics: momentum transfer or fluid dynamics, heat transfer, and mass transfer. The methodology used to describe transport phenomena consists of conservation equations, especially applied to open systems, coupled with constitutive relations describing the physics of specific phenomena. As these methodologies are nearly the same for fluid flow, heat transfer, or mass transfer, Bird *et al.* [1] integrated these topics and formulated a unified approach, which they termed transport phenomena. Since then, chemical engineers have preferred to treat these topics together in this fashion. Mechanical and civil engineers, however, regard these as three separate topics. Process metallurgists, along the lines of chemical engineers, have preferred the unified approach. In this section, the important concepts and methodologies generic to transport phenomena are discussed.

The concept of a continuum is the fundamental basis on which much of the subject of transport phenomena is developed. All materials, including fluids, are made of discrete atoms or molecules with large amount of void space between them. The continuum hypothesis, however, treats materials as continuous media and correspondingly properties are defined as varying spatially in a continuous manner. The hypothesis is valid only when a derivative of any material property, say ϕ, can be defined as

$$\phi''' = \frac{\mathrm{d}\phi}{\mathrm{d}V} = \lim_{\Delta V \to \lambda^3} \frac{\Delta \Phi}{\Delta V}$$

and that λ is small enough for this derivative to be meaningful in the scale of the macroscopic system under study, but is still large enough that the discreteness at the molecular level is averaged into a continuum. This approximation is almost always valid for the flow of liquids since the molecular dimensions are very small (the exception to this occurs for flow of liquids through channels of nanometer scale and below). In gases, the mean free path, i.e., the average distance traversed by a molecule between two consecutive collisions, should be small compared to the system dimensions, for example, the diameter of the pipe

through which the gas flows. If the mean free path is comparable to the scale of the system of interest, then the frequency of collisions of molecules with the walls of the system will be comparable to those among molecules themselves. Continuous variation of a property such as density across the cross section of the pipe then becomes meaningless. This phenomenon is characterized by Knudsen number (named in honor of the scientist Knudsen, for his contributions in this field). The Knudsen number is defined as the ratio of the mean free path of the gas molecules at a particular state of the system under study to the characteristic dimension of the system. In many engineering situations, the Knudsen number is very low and hence the system can be treated as a continuum. However, the Knudsen number can become significant, especially when considering the flow of gases under vacuum or in fine pores. In this chapter, only the continuum approach has been used. The reader may refer elsewhere [2] for other approaches.

The principle used to describe the conservation of mass, energy, momentum, etc., can be illustrated using the example of filling and draining of water in a tank. The variation of water level in the tank with time when both inlet and outlet valves are open can be calculated using the following simple equation of volume conservation.

$$\text{The rate of change volume of water in the tank} = \text{Volume flow rate in} - \text{Volume flow rate out}$$

This principle can be extended to any generic conservable entity say, ϕ, as

$$\begin{aligned}\text{Rate of accumulation of } \phi \; = {} & \text{Rate at which } \phi \text{ comes into the system} - \\ & \text{Rate at which } \phi \text{ goes out of the system} + \\ & \text{Rate at which } \phi \text{ is generated within the system}\end{aligned} \tag{4.1.1}$$

The example below illustrates the use of the principle for predicting changes in composition during change of ladle and grade in the continuous casting of steel.

Example 4.1.1

Figure 4.1.2 is a schematic of a continuous steel casting machine showing the ladle, the tundish, and the mold. The hot liquid steel is delivered in batches to the casting machine by the ladle. The tundish, the intermediate reservoir primarily for flow control, supplies liquid steel continuously to the mold through a nozzle. The continuous casting machine is operated without interruption even when an empty ladle is replaced by a newer ladle. If the steel in this new ladle is of different grade from the previous one, intermediate cast slabs have composition deviating significantly from both the desired grades.

Let a thin slab-casting machine operate at 5 m min^{-1} to produce slabs of cross section 1500 mm × 50 mm. The machine has a tundish with a capacity of 5 tonnes. Estimate the amount of slab to be discarded, if the operator accepts a variation of 20% in grade. Assume as a first approximation that the amount of metal in the tundish as well as the casting speed remains the same during the transition from one grade to the other. Additionally, assume

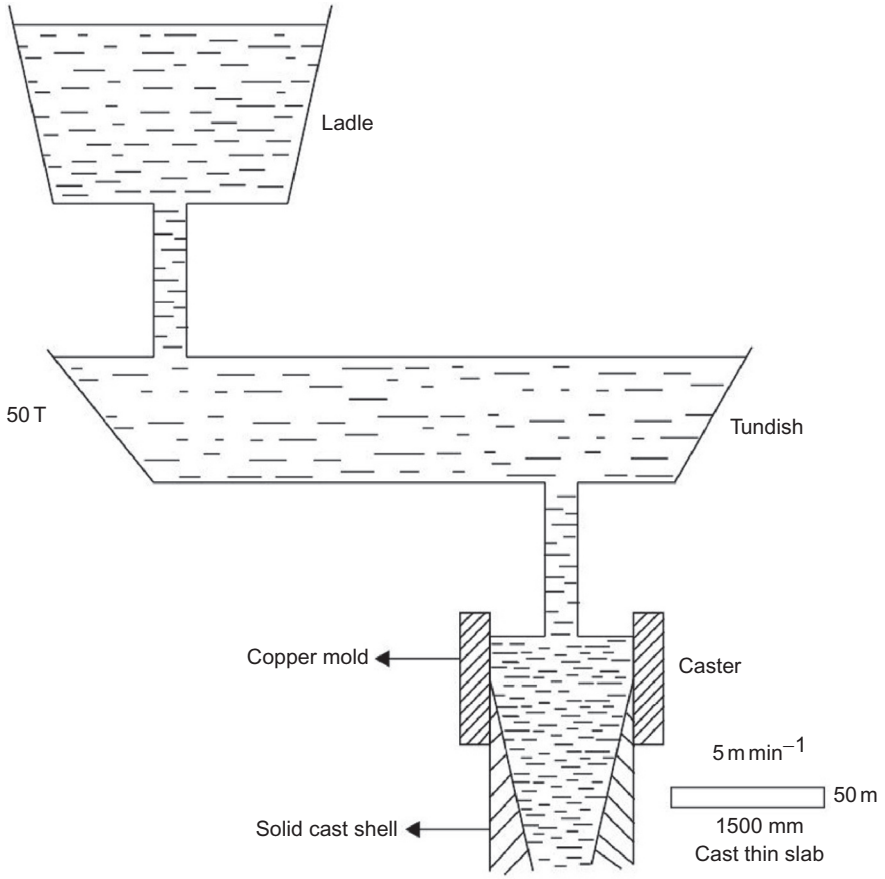


Figure 4.1.2 Schematic of a continuous metal caster.

that the tundish is well stirred and that the composition of the steel is uniform throughout the tundish at any instant of time.

Solution

Let us denote the composition of any particular solute in the steel by $\rho_{\text{solute},1}$ and $\rho_{\text{solute},2}$ (expressed as mass per unit volume of liquid steel) for grades 1 and 2, respectively. To find the mass of slab to be discarded, the variation of composition in the tundish, ρ_{solute}, with time should be examined. Since the composition in the tundish is uniform, the composition of steel that exits to the mold from the tundish at any instant of time would be the same as that in the tundish. If V is the volume of the liquid steel in the tundish and $\dot{V}$ the volumetric flow rate of steel flowing into as well as out of the tundish (both V and $\dot{V}$ are assumed to remain constant during ladle exchange), the conservation principle to the solute in the tundish yields,

$$V\frac{\mathrm{d}\rho_{\text{solute}}}{\mathrm{d}t} = \dot{V} \times \rho_{\text{solute,inlet}} - \dot{V} \times \rho_{\text{solute}}$$

$$\text{Rate of accumulation of solute} = \text{Rate in : solute} - \text{Rate out : solute}$$

The composition of the solute in the tundish changes as soon as the transition to grade 2 starts. At $t=0$, the composition of the solute in the tundish would be that corresponding to grade 1, i.e., $\rho_{\text{solute},1}$. The composition of the liquid steel reaching the inlet of the tundish will remain that corresponding to grade 2, i.e., $t \geq 0$, $\rho_{\text{solute,inlet}} = \rho_{\text{solute},2}$. Solution of the differential equation with the initial condition is

$$\frac{\rho_{\text{solute}} - \rho_{\text{solute},2}}{\rho_{\text{solute},1} - \rho_{\text{solute},2}} = \exp\left(-\frac{V}{V}t\right)$$

As per the problem posed, a composition (C) variation up to $0.8\rho_{\text{solute},1} + 0.2\rho_{\text{solute},2}$ is accepted as grade 1 and correspondingly $0.2\rho_{\text{solute},1} + 0.8\rho_{\text{solute},2}$ is accepted as grade 2. These correspond to $\frac{\rho_{\text{solute}} - \rho_{\text{solute},2}}{\rho_{\text{solute},1} - \rho_{\text{solute},2}}$ being 0.8 and 0.2, respectively. Hence, from the solution of the differential equation, the time duration when $\frac{\rho_{\text{solute}} - \rho_{\text{solute},2}}{\rho_{\text{solute},1} - \rho_{\text{solute},2}}$ changes from 0.8 to 0.2 can be calculated knowing the volume of the steel in the tundish and the volumetric flow rate of steel through the tundish. For a liquid steel of 5 tonnes, the volume will be approximately 7.1 m^3 and flow rate of liquid steel can be estimated from the casting speed and cross section of slab as 0.00625 $m^3\ s^{-1}$. Thus, the time period over which the composition of liquid steel in the tundish will be unacceptable is about 1570 s and the corresponding weight of slab to be discarded is 69 tonnes.

The generic conservation Equation (4.1.1) is now examined more closely for a system with a finite volume and definite boundaries. Boundaries are those through which the system interacts with the surroundings. The term on the left-hand side represents the accumulation of the conservable entity, ϕ, in the system. Generally, the entity to be conserved is expressed as a quantity per unit volume of the system. For example, in case of mass conservation, the mass per unit volume, density (ρ), can be used in the conservation expression. Similarly, momentum per unit volume (ρv), enthalpy per unit volume (ρH), and species density of any species "i" (ρ_i) can be used in the conservation equations for momentum, heat, and species "i," respectively, in a system. The first two terms together on the right-hand side of Equation (4.1.1) denote the net amount of entity ϕ entering the system. Conservable entity is transported through the system boundary generally by two mechanisms. One, by virtue of the bulk movement of material through the boundary, the associated momentum, enthalpy, or species in the material are transported along with it. This is termed as advective transport. Second, there can be transfer of conservable entity, even in the absence of the macroscopic transport because of molecular or atomic interactions in the material. For example, heat

can be transported through the system boundary without having any bulk movement of materials through the boundary. Such transport is termed as diffusive transport. This transport originating from molecular or atomic interactions is specific to a particular material as well as to the entity being transported. Therefore, this diffusive transport is defined using constitutive laws, such as, Fourier's law of heat conduction. The last term in the conservation Equation (4.1.1) denotes the bulk generation term, generally expressed as the rate of generation per unit volume of the system. In case of conservation of heat, it may denote heat liberated due to bulk reaction, or dissipation of mechanical energy to internal energy. Similarly, there may be body forces acting on the system due to gravity, electromagnetic field, etc., leading to generation of momentum according to Newton's second law of motion. Physics specific to these interactions are described quantitatively by the generation terms.

The principle of conservation can be applied at various scales depending on the information required. The simple example from continuous casting discussed above illustrates the conservation principle being applied in a macroscopic scale. For a flow of fluid through a pipe, if only the pressure drop required to maintain a particular flow rate is desired, the mechanical energy conservation principle is applied at the scale of pipe. The effect of finer details of flows is accounted for through empirical correlations, permitting fast and cost-effective solution to engineering design problems. However, if the details of the flow profile in the system are required, the conservation equations need to be applied at an infinitesimal or differential scale. Such formulations for real systems often lead to nonlinear partial differential equations, which necessitate sophisticated numerical techniques to obtain solutions.

4.1.2. MOMENTUM TRANSFER

A large number of transport processes involve fluids: liquids and gases. In comparison to rigid solids, fluids can flow, i.e., velocity variations can occur within the body of the fluid. Flow of the fluid has large influence on transport of heat and mass. In transport phenomena, therefore, description of flow becomes an integral part of analysis of most processes.

A packet of fluid in a flow field can be viewed as that carrying momentum or as being characterized by its kinetic energy. Flow takes place under the influence of forces acting on it. The fluid flow can be analyzed either by performing momentum balances, considering forces as those that generate momentum according to Newton's second law of motion or by performing energy balances according to first law of thermodynamics considering the work done by the forces on the system. Apart from forces due to external factors, such as pressure and gravity, internal forces resisting flow variations develop within the body of the fluid due to "viscous" phenomena. The Laws of motion and the relationships describing the viscous phenomena are the constitutive equations needed for fluid flow descriptions.

4.1.3. FLOW DESCRIPTION

Elastic solids resist a shear force by a shear deformation, i.e., a shear stress resisting the external force is developed within the body due to the deformation, till a stable equilibrium is reached. A simple fluid cannot resist a shear force by a static deformation; it continues to deform. The fluid develops a resisting shear stress by the rate of deformation and comes to a dynamic equilibrium (there are complex fluids that can resist shear elastically up to some limiting value). This implies that a static fluid cannot have any shear stresses present in it; only normal stresses are present. It can be proved using simple force balance that this normal stress is the same irrespective of direction and hence is described by a scalar entity called pressure (the reader can find the proof in any text book on fluid mechanics). The normal force on any surface is calculated by the product of pressure and surface area, the latter being a vector.

Some of the terminologies used to describe fluid flow are given below.

4.1.3.1. Steady and Unsteady Flows

A system is at steady state when all the properties at any point (some of these such as velocity to be defined with respect to a frame of reference) in the system remain constant with respect to time. If this condition is not satisfied, the system is said to be unsteady or in a transient state. In general, a property is a function of space and time, i.e., $\phi(x,y,z,t)$. For a steady-state process, the partial derivative $\frac{\partial \phi}{\partial t}$ remains constant everywhere in the system.

4.1.3.2. Uniform and Nonuniform Flows

Flow is uniform if properties associated with flow, such as velocity, momentum, and density, are the same everywhere, at any instant of time. That is, partial derivatives with respect to spatial coordinates are zero. Evidently, uniform flows can be unsteady, and steady flows can be nonuniform.

A flow that is uniform with respect to all the three coordinates gives a rigid body motion. More often, the definition refers to uniformity with respect to one or two coordinates, as for example, "uniform across the cross section."

4.1.3.3. Streak Lines, Particle Paths, and Stream Lines

Flows are often visualized, experimentally or in graphical descriptions, through lines of flow. These lines are dependent on the view point or the experimental method of visualization. One can visualize a flow by continuous release of a visual trace into the flowing fluid from a point fixed in space. Each packet of tracer emanating from the point at successive times forms a continuous line. If an "instantaneous" photograph of this

is taken, a streak line is obtained. A thin smoke trail from a chimney top in slowly moving air is an example.

Another way of visualization is to release a single neutrally buoyant tracer particle into the flow from any point at a given instant of time. The particle will move along with the fluid tracing a path in the flow field. This can be captured experimentally with time-lapse photography, i.e., by keeping the aperture of the camera open for a length of time. These lines are called particle paths. In a steady flow, streak lines and particle paths superimpose on each other. This need not be the case for unsteady flows.

In contrast to these two observable lines, the streamline is a mathematical construction: it is a continuous line for which tangent at every point gives the direction of velocity. Evidently there is no flow across a streamline (in two-dimensional (2D) view) or across a stream surface formed by series of stream lines. Streamlines cannot be visualized, except in the case of steady flows where it is identical to the streak lines and particle paths.

4.1.3.4. Eulerian and Lagrangian Points of View

Since properties at a point depend on the coordinates of the point, and coordinates depend on the frame of reference, expressions of flow descriptions can be different in different frames of reference. Frames of reference can be arbitrary. Two types are of specific interest.

A Eulerian frame is one that is fixed with respect to the laboratory and the fluid flows relative to it. This is the familiar frame of reference. Fluid flow past a given fixed point, and therefore a property at that point refers to different fluid elements at different times. In the Lagrangian view point, the frame of reference moves along with the fluid element. A property at a point with respect to this frame of reference refers to the same fluid particle over time.

These two view points are equivalent and are related to each other through the fluid velocity vector. Selection of either of them depends on convenience. Take the example of a bubble rising up steadily in a fluid. The flow around the bubble can be described from a Eulerian frame of reference fixed with respect to the container, or a Lagrangian frame fixed to the leading point on the bubble. The former view point will describe the flow as unsteady, whereas the Lagrangian frame depicts steady flow in the neighborhood of the bubble.

4.1.3.5. Laminar and Turbulent Flows

One of the most influential scientific papers on fluid dynamics is by Reynolds [3,4]. In his classic experiment (the experimental set up is still preserved at the Manchester University, United Kingdom), he injected dye into a stream of water flowing through a pipe. His observations have been reproduced from his original paper in Figure 4.1.3.

Below a critical velocity, he observed laminar flow where the dye streak remained straight. Above the critical velocity, the flow exhibited a transition state where the

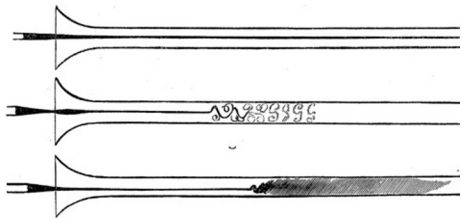


Figure 4.1.3 Reynolds' experimental observations [3].

dye streak became wavy. At high flow velocities, the dye mixed significantly with the water within a short distance and this is termed as turbulent flow.

Thus, flow of a fluid can take place in two distinct regimes depending on the intensity of flow and system geometry: laminar and turbulent. At low velocities, the flow seems to be "orderly": tracer particles traveling along smooth lines seem to indicate the flow consists of layers (lamella) sliding past each other. This is laminar flow. As the flow rate is increased, however, the flow becomes "turbulent": the particles seem to travel in random paths, though the overall direction of travel is in the direction of mean flow. The flow consists of "eddies," fluid packets of various sizes making circular motion; it is difficult to visualize the flow using streak lines, since the tracer quickly dissipates due to the eddies. Whether the flow is laminar, turbulent, or in a transition regime between the two is determined by a characteristic dimensionless number called the Reynolds number, Re (see Section 4.1.8 for further discussion).

$$Re = \frac{\rho V L}{\mu}$$

where V is the characteristic velocity, L is a dimension characterizing the system size, ρ and μ are the fluid density and viscosity, respectively. Over a small range of Re values, the flow changes from laminar flow (low Re) to turbulent flow.

Reynolds in his experiments of flow through tubes found that the critical velocity beyond which flow changes from laminar to turbulent corresponds to a Reynolds number of approximately 2000. Most flows of engineering interest are turbulent. More discussions on these aspects are presented in later sections (Section 4.1.15.1).

4.1.3.6. Incompressible and Compressible Flows

The densities of fluids change with pressure, i.e., all real fluids are compressible. However, for many engineering flows, the change in density due to change in pressure during flow is small enough to be neglected. Such flows are classified as incompressible flows. The incompressible flow approximation leads to large simplifications. Using some simple reasoning, the conditions where a flow can be considered incompressible can be determined.

In a flowing fluid with velocity varying between 0 and V, the pressure variation is of the order of $\frac{\rho V^2}{2}$ (description on this term derived from energy balance is presented in Section 4.1.4). The relative density change expected in ideal gases under isothermal conditions is therefore:

$$\frac{|\Delta\rho|}{\rho} = \frac{|\Delta P|}{P} \approx \frac{1}{2}\frac{\rho v^2}{P} = \frac{1}{2}\frac{\rho v^2}{\rho RT/M} \tag{4.1.2}$$

The velocity of sound under isothermal conditions is given by $c = \sqrt{\frac{RT}{M}}$ and hence,

$$\frac{\Delta P}{P} \approx \frac{1}{2}\frac{v^2}{c^2} = \frac{1}{2}Ma^2 \tag{4.1.3}$$

where the ratio of the velocity of the fluid to the speed of sound is termed the Mach number, Ma. For a $\frac{\Delta\rho}{\rho}$ of 0.05, i.e., for a 5% change in density, the value of Mach number is approximately 0.3. Thus, for speeds where $Ma < 0.3$, the change in density will be <5%, and assuming the fluid to be incompressible is a reasonable engineering approximation. The orders of magnitude of the associated errors remain the same in non-isothermal flows too. Once fluid velocities reach values beyond that corresponding to Mach number of 0.3, the change in density due to pressure difference becomes significant. In such flows, the equation of state, which relates the density with pressure and temperature, must be considered. Generally in such flows, a change in density results in significant change in temperature and it is necessary to examine both flow and heat transfer together to arrive at a better understanding. If the velocities are less than that of sound in the fluid, $Ma < 1$, they are termed as subsonic flows and those beyond the velocity of sound are classified as supersonic flows. In process metallurgy, most of the flows are incompressible. However, in some processes, such as basic oxygen furnace (BOF) wherein supersonic nozzles are used to inject oxygen into the liquid steel, the gas flows are compressible. Throughout this section, most of the flows discussed are incompressible; a separate section has been devoted to compressible flows with specific focus on the supersonic nozzle for oxygen injection in BOF.

4.1.4. OVERALL ENERGY BALANCE

In order to perform the overall energy balance in a flowing fluid system, it is generally necessary to consider the following energies associated with the fluid: (1) the kinetic energy arising out of flow velocities, (2) the potential energy due to the gravitational field, and (3) the internal energy. In addition, the system can exchange energies with the surroundings through the boundary as work done against pressure, other forms of work through pumps and turbines, or as heat. Other forms of energies, such as

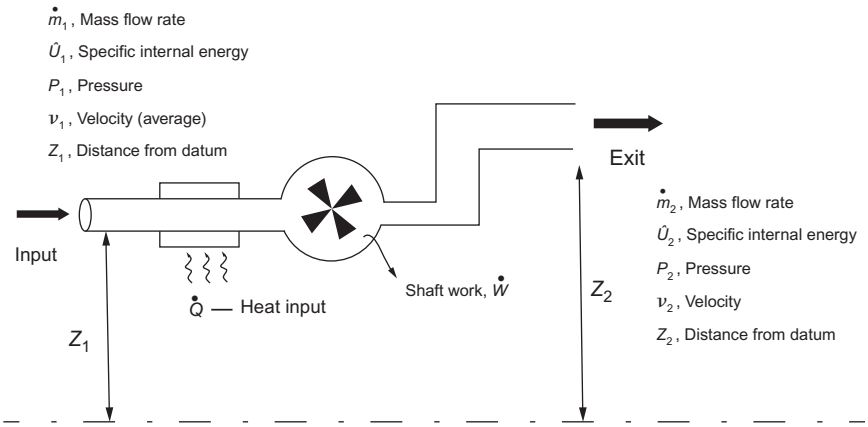


Figure 4.1.4 Schematic of a flowing system performing shaft work using a heat source.

chemical, electrical, and magnetic, can be further added depending on the system; for brevity, these additional terms are not considered in the present discussions.

Let us consider a general system shown in Figure 4.1.4, wherein a fluid enters and leaves the system at mass flow rates of $\dot{m}_1$ and $\dot{m}_2$, respectively (there can be multiple inlets and outlets, without loss of generality). The fluid carries with it internal energy, kinetic energy, and potential energy. At the inlet and the outlet P–V kind of work needs to be done to push the fluid through the boundaries. The fluid also performs shaft work continuously at the rate of $\dot{W}$ on the surroundings (for example, in driving a turbine). During its transit through the system, the fluid receives heat at the rate of $\dot{Q}$ from the surroundings. Let P_i, $\hat{U}_i$, v_i, and ρ_i represent pressure, specific internal energy (internal energy per unit mass), velocity, and density at any point "i." Let z represent the height.

If E_T represents the total energy of the system at any instant of time, then conservation equation gives,

$$\frac{dE_T}{dt} = \overbrace{\dot{m}_1\left(\hat{U}_1 + \frac{1}{2}\frac{v_1^2}{\beta_1} + gz_1\right) - \dot{m}_2\left(\hat{U}_2 + \frac{1}{2}\frac{v_2^2}{\beta_2} + gz_2\right)}^{\text{Net advective energy input}} + \overbrace{\frac{P_1\dot{m}_1}{\rho_1} - \frac{P_2\dot{m}_2}{\rho_2}}^{P-V\text{ work}} + \overbrace{\dot{Q}}^{\text{Heat input}} - \overbrace{\dot{W}_S}^{\text{Shaft work}} \tag{4.1.4}$$

If the system is at steady state, LHS is zero, and $\dot{m}_1 = \dot{m}_2 = \dot{m}$. Then, after dividing by $\dot{m}$,

$$\left(\hat{U}_2 - \hat{U}_1\right) + \left(\frac{1}{2}\frac{v_2^2}{\beta_2} - \frac{1}{2}\frac{v_1^2}{\beta_1}\right) + \left(gz_2 - gz_1\right) + \left(\frac{P_2}{\rho_2} - \frac{P_1}{\rho_1}\right) - \hat{Q} + \hat{W}_S = 0 \tag{4.1.5}$$

where $\hat{Q} = \frac{\dot{Q}}{\dot{m}}$ and $\hat{W}_S = \frac{\dot{W}_S}{\dot{m}}$. The terms in the above equation have units of J kg^{-1}. Let us look at some of these terms closely.

Internal energy is the energy associated with a mass of fluid excluding its kinetic and potential energies. Normally internal energy change manifests itself in the form of temperature change and is calculated as sensible heat using specific heat C_v. Energy can also be stored in the system by phase change and chemical reactions.

Potential energy per unit mass with respect to a datum is gz.

Kinetic energy per unit mass is $\frac{1}{2}v^2$. If the velocity across a cross section is uniform at $\overline{v}$, the total kinetic energy flow across the cross section is $\frac{\dot{m}\overline{v}^2}{2}$. If the flow, however, is nonuniform with the velocity averaged over the area of cross section A being $\overline{v}$, then the total kinetic energy crossing the section is $\int_A \frac{v^2}{2}(v\rho dA)$. This term is represented as $\frac{1}{2\beta}\dot{m}\overline{v}^2$, where β is the correction factor that accounts for nonuniformity in flow. Most engineering flows in conduits are turbulent and the flow is nearly uniform except very close to the boundaries, and therefore $\beta \approx 1$. In laminar flow, β is significantly lower than 1; for steady flow through circular pipes $\beta = 0.5$.

Equation (4.1.5) describes the conservation principle from an Eulerian view point, i.e., the system is fixed with respect to the laboratory, and counting is done at the boundary. One would like to use such an equation for design purposes: to estimate, for example, the pressure drop that needs to be applied across a length of piping to maintain a desired flow rate of water. The presence of an internal energy term here, however, is inconvenient. In most engineering situations, one is neither interested in specifying the internal energy changes and the associated temperature changes, nor in tracking them; these are often very small anyway. Neglecting the term, however, can give meaningless solutions, as the following example illustrates.

Consider flow of an incompressible fluid such as water through a horizontal pipe of constant cross section (see Figure 4.1.5). Let the wall be adiabatic $\left(\widehat{Q} = 0\right)$ and no shaft work is done inside the pipe between sections 1 and 2 ($\hat{W}_S = 0$). Since the fluid is incompressible ($\rho_1 = \rho_2$), flow rate and average velocities are constant ($\dot{m}_1 = \dot{m}_2 = \dot{m}, \overline{v}_1 = \overline{v}_2$). Then Equation (4.1.5) gives

$$\left(\frac{P_2}{\rho_2} - \frac{P_1}{\rho_1}\right) = \left(\hat{U}_2 - \hat{U}_1\right)$$

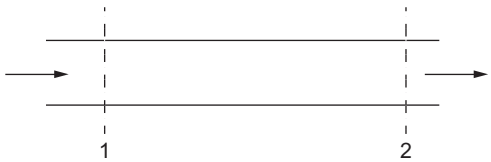


Figure 4.1.5 Flow through a straight pipe.

It is known that a pressure difference must be applied to maintain a flow in a pipe to counter the viscous resistances. This work done against the pressure difference is converted irreversibly into an increase in the internal energy, which manifests itself as a barely perceptible rise in temperature. Unless this rise in temperature is measured, it is not possible to estimate the pressure difference needed to maintain a desired flow rate.

The increase in internal energy arises from the irreversible conversion of mechanical energy to internal energy, due to the viscous phenomena. The viscous phenomena, as discussed later, are related to the details of the flow field inside the system, and an equation developed by measurements at the boundary cannot capture this phenomenon. To do this, a Lagrangian approach must be used: consider a packet of fluid as a "closed system" and perform an energy balance on it as it travels from the inlet to the outlet.

Let the packet of fluid be of unit mass, having internal energy $\hat{U}_1$ and $\hat{U}_2$, and density ρ_1 and ρ_2, at the inlet and outlet, respectively. Due to change in density, this packet would have changed its volume and therefore performed P–V work on its surroundings. If the heat input $\dot{Q}$ in the system has been distributed uniformly, the packet would have received a heat of $\hat{Q}$.

Though the first law of thermodynamics is about conservation of total energy, scientists concerned with material behavior often restrict themselves to internal energy alone, ignoring the contributions from kinetic and potential energies as follows

$$\hat{U}_2 - \hat{U}_1 = \hat{Q} - \hat{W}_{P-V} = \hat{Q} - \int_1^2 P \, \mathrm{d}\hat{V} = \hat{Q} - \int_1^2 P \, \mathrm{d}\left(\frac{1}{\rho}\right) \tag{4.1.6}$$

where, $\hat{V}$ is the specific volume or reciprocal of the density, ρ, and the P–V work has been assumed to be reversible.

This assumption works fine in cases where the mechanical energies are only associated with the position and movement of the system as a whole, and remain uncoupled with the internal energy of the material. If there are relative movements within the system itself, however, there is dissipation of mechanical energy to internal energy, and in a balance written for internal energy alone this should appear as a generation term. If the rate of conversion of mechanical energy into internal energy (per unit mass) within the body of the fluid is $\hat{E}_\mathrm{f}$, Equation (4.1.6) is modified as:

$$\hat{U}_2 - \hat{U}_1 = \hat{Q} - \int_1^2 P \, \mathrm{d}\left(\frac{1}{\rho}\right) + \hat{E}_\mathrm{f} \tag{4.1.7}$$

Substituting Equation (4.1.7) into Equation (4.1.5), and noting that $\frac{P_2}{\rho_2} - \frac{P_1}{\rho_1} = \int_1^2 \mathrm{d}\left(\frac{P}{\rho}\right)$, the following expression is obtained.

$$\frac{1}{2}\frac{v_2^2}{\beta_2}-\frac{1}{2}\frac{v_1^2}{\beta_1}+g(z_2-z_1)+\int_1^2\left(\frac{1}{\rho}\right)\mathrm{d}P+\hat{W}+\hat{E}_\mathrm{f}=0 \tag{4.1.8}$$

If $\hat{E}_\mathrm{f}$ can be estimated from the details of the flow, Equation (4.1.8) is an extremely useful equation for design and analysis. This is the generalized form of the overall or the integral energy balance equation.

For laminar flows, depending on the system geometry and the fluid, flow details (flow structures) can be predicted from first principles. However, as the velocities become larger, these structures become quite complex and manifest as turbulence. Prediction of these turbulent flow structures from first principles is still an ongoing active research topic for the scientific community. For many systems of engineering interest, however, a large body of experimental data exists, and these have been coded into empirical equations for $\hat{E}_\mathrm{f}$, using the principles of dimensional analysis and similarity.

In addition, a few remarks need to be made regarding the term, $\int_1^2\frac{1}{\rho}\mathrm{d}P$ in Equation (4.1.8). This term, generally termed as flow work, is path dependent. For incompressible fluids, the density does not change during flow, and hence this term becomes $\frac{\Delta P}{\rho}$. However, for compressible flows, the path by which the compression–expansion takes place needs to be defined. Idealized paths, such as isothermal or adiabatic, are frequently used to describe many compressible flows. In a later section, design of a supersonic nozzle for steel-making operations is discussed using such a simplified analysis.

As a first approximation, many systems can be analyzed by neglecting the friction loss term, i.e., $\hat{E}_\mathrm{f}$ in Equation (4.1.8). In thermodynamic terminology, friction loss is an irreversible phenomenon. Hence, a flowing system without having friction losses is an idealized system and can be termed as a reversible system. For an incompressible fluid flowing without having any friction loss and shaft work, Equation (4.1.8) can be rewritten as

$$\frac{1}{2}v_2^2+gz_2+\frac{P_2}{\rho}=\frac{1}{2}v_1^2+gz_1+\frac{P_1}{\rho} \tag{4.1.9}$$

This equation is the well-known Bernoulli's equation, named after the famous scientist Bernoulli.

The mechanical energy balance equation can also be written in differential form as

$$v\frac{\mathrm{d}v}{\beta}+g\,\mathrm{d}z+\frac{1}{\rho}\mathrm{d}P+\mathrm{d}\hat{W}+\mathrm{d}\hat{E}_\mathrm{f}=0 \tag{4.1.10}$$

Let us look at a simple application of this equation in a continuous caster. In order to make clean steel, it is essential that oxygen pick-up into the liquid steel is minimized. Any dissolved oxygen in steel can result in inclusions or porosity in the cast product that can have adverse effect on further processing of solid steel as well as on the mechanical properties of the end product.

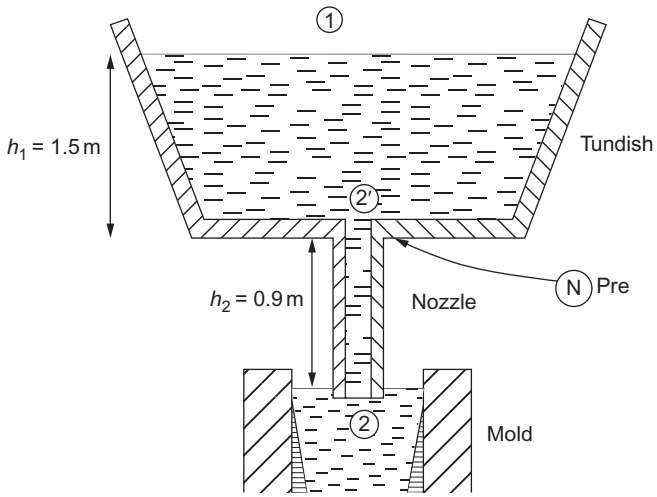


Figure 4.1.6 Schematic showing flow of liquid steel through a nozzle from a tundish to a caster.

Example 4.1.2

Figure 4.1.6 shows a schematic of flow of liquid steel from a tundish to a mold through a submerged entry nozzle. Estimate the velocity of the liquid steel at the exit of the nozzle and the pressure at the neck where the tundish meets the nozzle (shown as N in the figure). Neglect friction losses. Comment on the results [5].

Solution

In order to estimate the exit velocity of liquid steel at the tip of the nozzle, we need to apply Bernoulli's equation between the levels of liquid steel in the tundish and the tip of the nozzle. Let us denote them by 1 and 2, respectively. The pressure at location 1 is atmospheric. If only a negligible length of the nozzle (compared to its total length) is dipped into the liquid metal in the mold, one can assume pressure at 2 also to be atmospheric. Since the tundish area is large compared to the nozzle area, the kinetic energy contribution at 1 compared to that at 2 can be neglected. If frictional losses are also neglected ($\hat{E}_f = 0$), Equation (4.1.9) gives,

$$\frac{1}{2}v_2^2 + g(-(h_1 + h_2) - 0) = 0,$$

$$\text{i.e.,} v_2 = \sqrt{2g(h_1 + h_2)}$$

(It may be noted that the velocity at the exit corresponds to the free fall velocity from a height of $h_1 + h_2$. This is the consequence of neglecting friction). Let us denote the section at the neck by 2′. From mass balance, the velocity of liquid steel just below the neck should be the same as that at the exit (location 2). Applying Bernoulli's equation between location 2′ and 2 will therefore give

$$0+\frac{P_2-P_{2'}}{\rho}+g(-h_2-0)=0$$

$$P_{2'}=P_2-\rho g h_2$$

P_2 being atmospheric pressure, the pressure $P_{2'}$ is below the atmospheric pressure.

Comment: The neck area, sometimes with slide gates, consists of joints. Further, the nozzle components are refractory materials that are often porous. A negative pressure at the neck therefore can lead to aspiration of air leading to inclusions in the product. In Al-killed steel, the residual aluminum can react with this air depositing Al_2O_3 on the nozzle, progressively narrowing down the opening, which ultimately leads to choking.

The Bernoulli equation has been used in designing many flow-measuring devices such as the Venturi meter, orifice meter, and Pitot tube. The Venturi meter (Figure 4.1.7) works on the principle that on flow through a pipe, a change in fluid velocity due to change in cross section of the tube leads to a corresponding change in pressure.

The meter consists of converging, straight, and diverging sections. Pressure taps are placed just before the converging section and at the throat, where the area of cross section for the flow is the least. Applying mass balance and energy balance (Bernoulli's equation) between these two sections for turbulent flow of an incompressible fluid will give

$$\frac{\pi D^2}{4}\rho v_A=\frac{\pi d^2}{4}\rho v_B \tag{4.1.11}$$

$$\frac{P_A}{\rho}+\frac{1}{2}v_A^2=\frac{P_B}{\rho}+\frac{1}{2}v_B^2 \tag{4.1.12}$$

where v_A and v_B refer to fluid velocities at the initial and throat sections, respectively. From the above two equations, volume flow rate $\left(\dot{V}\right)$ can be deduced as

$$\dot{V}=\frac{\pi d^2}{4}v_B=C_D\frac{\pi d^2}{4}\sqrt{\frac{2\left(P_A-P_B\right)}{\rho}\Big/\left[1-\frac{d^4}{D^4}\right]} \tag{4.1.13}$$

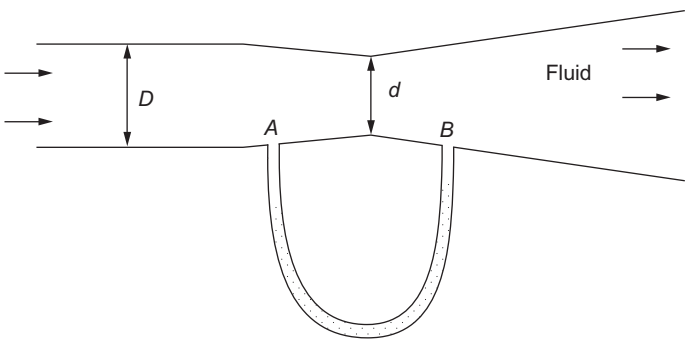


Figure 4.1.7 Schematic of a Venturi meter.

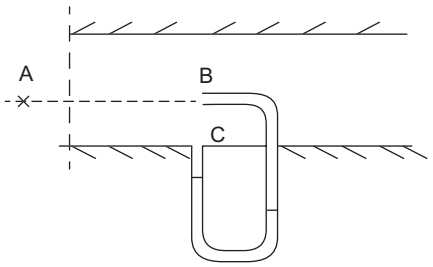


Figure 4.1.8 Schematic of a Pitot tube.

where a factor C_D, discharge coefficient, is introduced to account for the assumption of zero frictional effects. For making accurate measurements, the Venturi should be calibrated against known flows and C_D determined. Fortunately, experiments have shown [6] that the calibration factor generally ranges between 0.95 for cast venturies and almost 1 for well-designed machined venturies. To minimize friction losses arising from recirculating zones in the diverging section, the diverging angle should be kept small.

The Pitot tube is another relatively simple measuring device that can measure velocity in a flowing fluid. A schematic of a Pitot tube (named after French scientist from seventeenth century) measuring the velocity at a point B in a pipe is shown in Figure 4.1.8.

In the absence of the Pitot tube, velocity at the point of interest, B, is the same as at a point A upstream. When the Pitot tube is placed with its opening normal to the flow direction, the fluid is brought to rest at B along the centerline (note that the fluid inside the Pitot tube is static). On an infinitesimal stream tube, enveloping the centerline between points A and B, the Bernoulli equation is applied:

$$P_B = P_A + \frac{1}{2}\rho v^2 \tag{4.1.14}$$

The pressure at A and pressure at B away from the tube (or the pressure in the absence of the Pitot tube) are nearly the same, if the pipe is large enough compared to the Pitot tube. This pressure can then be measured at C, and is called the static pressure at B. The pressure at the opening at B is the combined effect of the static pressure and the effect of bringing the fluid to rest. It is called the total pressure. The difference $P_B - P_A = P_B - P_C = \frac{1}{2}\rho v^2$, called the dynamic pressure, is measured by the manometer.

Pitot tube is an absolute velocity-measuring device. This can be used without calibration to a maximum accuracy of $\pm 2\%$, unless the flow is compressible. Care should be taken to see that the total pressure opening is normal to the flow and the static pressure opening is parallel to the flow.

The static and total pressure openings can be combined to a single device called the Pitot-static tube as shown in Figure 4.1.9. Due to its geometry and large size, disturbance to the flow is large; Pitot-static tube should be calibrated before use as a measurement device.

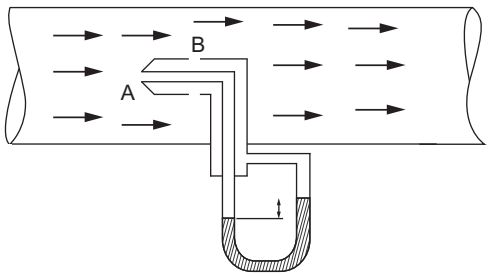


Figure 4.1.9 Schematic of a Pitot static tube.

4.1.5. THE CONCEPT OF VISCOSITY

In general, scientific methodology for explaining any new phenomenon is to seek a "law" that can give a generalized description of experimental observations, especially when carried out on simple systems where a particular phenomenon of interest is isolated from the rest. Subsequently, the law is applied in conjunction with other existing laws to describe the observations in complex systems. In the last section, we saw that in order to obtain the energy term corresponding to friction losses (conversion of mechanical energy to internal energy), it is necessary to look at the internal structure of the flow itself.

The irreversible process is a consequence of the work that needs to be done against forces developed within the fluid resisting relative motion between adjoining regions. Consider, for example, a fluid between two large parallel plates at a distance "d" apart (see Figure 4.1.10). To maintain the velocity, v, of the top plate constant with respect to the stationary bottom plate, a constant force, F, must be applied. Work done by this force does not result in any acceleration (increase in momentum); it is dissipated as internal energy. The analogous situation is the constant motion of a book dragged along the table top, leading to heating of the two surfaces that are touching each other.

The law that relates the force needed to keep the fluid in relative motion is called the Newton's law of viscosity, named after Sir Issac Newton. Using this law, a unique

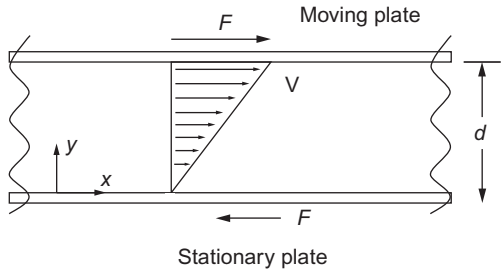


Figure 4.1.10 Flow profile of a fluid between two plates, one stationary and the other moving with a constant velocity, v.

property of the fluid called the coefficient of viscosity or simply viscosity is defined. Newton's law of viscosity can be described in simple terms using the system shown in Figure 4.1.10.

The area of each plate in contact with the fluid is A. Then the force, F, needed to maintain the upper plate in steady motion is:

$$F \propto A\frac{v}{d}$$

If the plates and the fluid are in steady motion, and the bottom plate needs to be held with an opposite force $-F$ to keep it from moving, a steady force should have been exerted by the fluid on the plates. How does this come about?

One of the fundamental properties of fluid is that it does not slip past a solid surface or an adjoining fluid packet (this is called the no-slip condition). Hence, when the top plate is set suddenly in motion at a velocity, v, the fluid next to it is also set into motion at the same velocity. The relative motion of this fluid layer with the adjoining layer below leads to an internal stress within the fluid, leading to dragging of the next layer, and so on. Finally, the fluid would develop a velocity gradient as shown, leading to the opposite force applied to the bottom plate.

The internal shear stress is opposite to the applied force pair as shown in Figure 4.1.11 and this can be expressed as

$$\begin{aligned}\tau_{yx} &\propto -\frac{F}{A}\\ &\propto -\frac{v}{d}\\ &= -\mu\frac{v}{d}\end{aligned}$$

In a general case where the velocity gradient is not constant, the shear stress at any point is defined as

$$\tau_{yx} = -\mu\frac{\mathrm{d}v_x}{\mathrm{d}y} \tag{4.1.15}$$

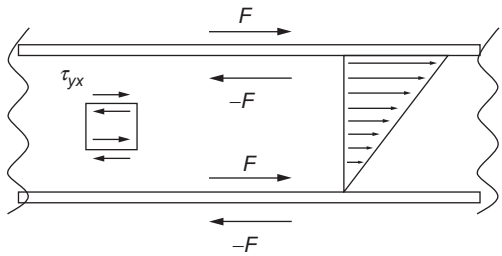


Figure 4.1.11 Forces acting on the plate and the fluid layers: flow of a fluid between two plates, one stationary and the other moving with a constant velocity, *v*.

This is the Newton's law of viscosity. The proportionality constant μ is called the coefficient of absolute viscosity, or simply viscosity, and is the property of the fluid.

τ_{yx}, the internal shear stress, when +ve can be interpreted as a force in the +ve x-direction being applied by a fluid layer normal to the xy plane at lesser y to the one above or as a force in the −ve x-direction being applied by a fluid layer at larger y to the one below. In solid mechanics, opposite sign convention is often used. Bird *et al.* [1], in their unified approach toward momentum, mass, and heat transfer, interpreted τ_{yx} as momentum flux. The force acting on the fluid at the top surface can be viewed as generating momentum (Newton's second law of motion). Since momentum cannot be accommodated at a surface (it has no volume), it has to be transported away. So the x-momentum generated at the top surface is transported down the velocity gradient. Finally, at the bottom, the momentum flux is neutralized by the negative momentum generated by a negative force on the bottom plate. For the case in Figure 4.1.11, the velocity gradient is +ve, and therefore τ_{yx} is negative: a +ve x-momentum transported in the −ve y-direction. A +ve value of τ_{yx} can indicate either flux of +ve x-momentum flux in the +ve direction or −ve x-momentum transported in the −ve y direction.

In the SI system, the units of viscosity are Pa s, and in CGS, it is poise. The ratio of viscosity to density is termed as kinematic viscosity. In the CGS system, the unit of kinematic viscosity is Stokes, in honor of a great scientist during Newton's era. In the SI system, unit is m^2/s.

The viscosities of condensed fluids such as liquids, slurries, and pastes are determined experimentally. The viscosities of gases and gas mixtures can be estimated to a reasonable degree of accuracy using kinetic theory of gases [1]. Study of kinetic theory also gives an insight to the molecular origin of the viscous phenomena.

Gases generally obey Newton's law of viscosity. Experiments have shown that only simple fluids obey Newton's law of viscosity. For complex fluids, such as slurries, polymeric solutions, gum, pastes, and metallic mixtures consisting both liquid and solid phases in the freezing range, the line correlating the shear stress and the velocity gradient (shear rate) is either not a straight line or does not pass through the origin. The flow behavior of such fluids is termed as rheology and is not discussed here. The reader may refer other sources for more information [7].

In Section 4.1.1.2, it was stated that a full description of a phenomenon needs a conservation equation, for example, conservation of momentum as well as constitutive equations describing the physics behind the underlying flow phenomena. Newton's law of viscosity forms one of the prime constitutive relationships for momentum transfer. The approach of Bird *et al.* [1] in viewing τ_{yx} as momentum flux due to a velocity gradient (and therefore a gradient of momentum) makes Equation 4.1.15 analogous to the constitutive equations in the other two-rate phenomena: Fourier's law of heat conduction in heat transfer and Fick's law of diffusion in mass transfer. This permits the three-rate processes to be treated in a unified fashion.

4.1.6. STEADY-STATE FULLY DEVELOPED LAMINAR FLOW THROUGH A STRAIGHT PIPE

Flow of fluids through pipes and conduits are quite common not only in engineering applications, but also in many natural systems. In fact the famous eighteenth century French scientist Jean Léonard Marie Poiseuille performed extensive experiments on the flow of distilled water through capillaries to understand the flow of blood. He discovered a functional relationship between the volumetric flow rate, the length and the diameter of the tube, and the pressure differential. Later, in 1860, Eduard Hagenbach derived Poiseuille's relation. The relation is therefore named Hagen–Poiseuille's law [8]. The derivation of this relationship is discussed below.

Consider a steady flow of liquid through a pipe as shown in Figure 4.1.12a. The fluid enters the pipe from a larger reservoir as illustrated in the figure. Let us also assume that just outside the inlet of the smaller pipe, the flow is almost uniform. As soon as the fluid layer reaches the inner wall of the pipe, its velocity becomes zero (no-slip condition). As the fluid moves farther into the pipe, more and more layers closer to the walls start decelerating due to viscous momentum transport. In other words, as the fluid moves farther into the pipe, the fluid layers starting from the wall are progressively affected by the presence of the wall. Since the volumetric flow rate of the incompressible fluid is being maintained (steady state), the velocity of fluid layers in the vicinity of the axis of the pipe progressively

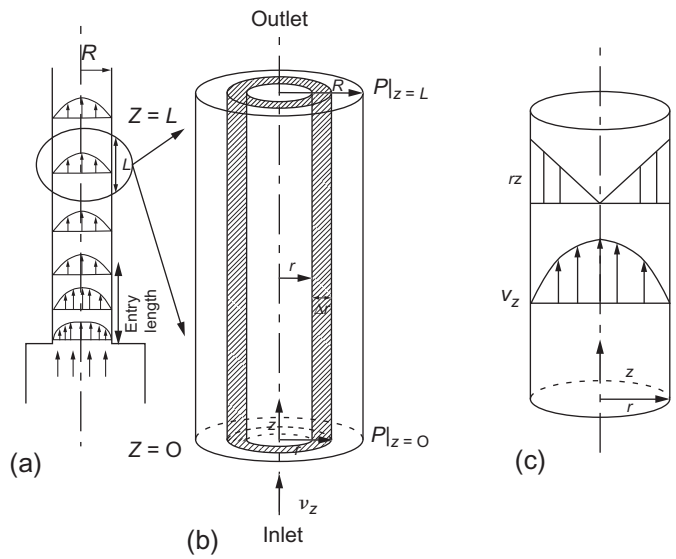


Figure 4.1.12 Steady laminar compressible flow through a vertical pipe: schematic of the (a) flow profiles, (b) shell or infinitesimal control volume, and (c) velocity and viscous momentum flux profiles.

increases. The schematic of the velocity profiles at different locations along the length of the pipe from the entry point are shown in Figure 4.1.12a. Further downstream, the affected region of the flow reaches the center and does not change further downstream. Flow in this region is termed as fully developed: the velocity is no longer a function of axial distance. Very close to the exit, the profile again relaxes: it changes to suit the exit conditions. The distance the fluid needs to travel before it attains a fully developed profile is termed as the entry length. Similarly, the length near the exit where the profile changes axially is the exit length. The region in between is the fully developed flow region. In the fully developed region, the velocity at any point is a function of radial position alone. The streamlines are therefore parallel to the axis. Mass balance would then demand the radial and azimuthal velocities (v_r and v_θ) be zero. The flow is said to be one dimensional (1D): only one component of the velocity is nonzero, and it changes in one direction only.

As already stated earlier, the flow is steady, laminar, and fully developed. In order to obtain the detailed description of the flow, mass and momentum balances are undertaken on a differential control volume and subsequently the appropriate differential equation is obtained. Since the problem is axi-symmetric, i.e., there is no variation of flow parameters along the circumferential direction. Let us consider a small annular shell of radius, r, length, Δz, and thickness, Δr as illustrated in Figure 4.1.12b.

To perform the mass balance for the fluid flowing through this shell (at steady state, the fluid entering the shell must be equal to that leaving the shell). The curved surfaces are parallel to the streamlines and there is no flow through them, and therefore:

$$(2\pi r\Delta r v_z \rho)\big|_{z=z} = (2\pi r\Delta r v_z \rho)\big|_{z=z+\Delta z}$$

Thus, v_z is independent of z for constant ρ and depends only on r, i.e., $v_z = f(r)$ as was already known.

Let us perform a momentum balance. As the flow is in the z-direction, it is only necessary to perform the balance of the z-component of momentum. The z-momentum balance will have the following terms.

The advective momentum entering the control volume from the bottom by virtue of fluid motion is the product of mass flow rate and velocity: $(2\pi r\Delta r)\rho(v_z v_z)\big|_{z=z,r=r+\Delta r/2}$ at $z=z, r=r+\Delta r/2$. Similarly, the advective momentum leaving the control volume from the top at $z=z+\Delta z, r=r+\Delta r/2$ is $2\pi r\Delta r\rho(v_z v_z)\big|_{z=z,r=r+\Delta r/2}$.

At the curved surfaces at r and $r+\Delta r$, there are no advective fluxes. Since there are velocity gradients across these surfaces, z-momentum fluxes across the surfaces, or equivalently viscous forces in the z-direction act on these surfaces. τ_{rz} represents the z-viscous momentum flux transferred along the r direction. Therefore, the viscous momentum enters the shell at $r=r$ at the rate of $\tau_{rz}\big|_{z=z+\Delta z/2, r=r}\ 2\pi r\Delta z$. This can also be seen as the force that fluid at lesser r exerts on the shell along z-direction because of viscous friction. Similarly, the rate at which viscous momentum leaves the shell at $r=r+\Delta r$ is

$\tau_{rz}|_{z+\Delta z/2,r=r+\Delta r}\ 2\pi(r+\Delta r)\Delta z$. This is the force that fluid at r more than $r+\Delta r$ exerts on the shell along negative z-direction.

The force due to pressure at the inlet is $P|_{z=z,r=r+\Delta r/2}\ 2\pi r\Delta r$, and at the outlet is $-P|_{z=z+\Delta z,r=r+\Delta r/2}\ 2\pi r\Delta r$.

The gravitational body force is $2\pi r\Delta r\Delta z\rho(-g)$. In the general case of an inclined tube, g_z is used (z-component of gravity in place of $-g$).

As the system is at steady state, by conservation of momentum (refer to Section 4.1.1.2):

$$\begin{aligned}&2\pi r\Delta r\rho\left\{(v_z v_z)|_{z=z,r=r+\Delta r/2}-(v_z v_z)|_{z=z+\Delta z,r=r+\Delta r/2}\right\}\\&+\tau_{rz}|_{z+\Delta z/2,r=r}2\pi r\Delta z-\tau_{rz}|_{z+\Delta z/2,r=r+\Delta r}2\pi(r+\Delta r)\Delta z\\&+2\pi r\Delta r\left(P|_{z=z,r=r+\Delta r/2}-P|_{z=z+\Delta z,r=r+\Delta r/2}\right)-2\pi r\Delta r\Delta z\rho g=0\end{aligned}$$

By mass conservation, $v_z|_z=v_z|_{z+\Delta z}$, and therefore the first term is zero. Dividing the above equation by the volume of the shell, $2\pi r\Delta r\Delta z$ and taking the limit as $\Delta r\to 0$,

$$-\frac{1}{r}\frac{\rho}{\partial r}(r\tau_{rz})-\frac{\mathrm{d}P}{\mathrm{d}z}-\rho g=0 \tag{4.1.16}$$

There is no component of velocity in the radial direction and hence, by performing radial momentum balance, we obtain

$$-\frac{\partial P}{\partial r}=0 \tag{4.1.17}$$

Similarly there is no variation of pressure in the θ-direction. Pressure P is a function of z alone.

Substituting Newton's law of viscosity, Equation (4.1.15), into Equation (4.1.16),

$$\frac{1}{r}\frac{\partial}{\partial r}\left(r\mu\frac{\partial v_z}{\partial r}\right)-\frac{\mathrm{d}P}{\mathrm{d}z}-\rho g=0 \tag{4.1.18}$$

Since the flow under consideration is fully developed, flow in a region between two sections at z_1 and z_2, and that between z_2 and z_3 are exactly identical and therefore $\frac{\mathrm{d}P}{\mathrm{d}z}$ should be independent of z and can be written as $\frac{P_{z=L}-P_{z=0}}{L}$. If so Equation (4.1.18) can be considered as an ordinary differential equation and can be written as,

$$\frac{1}{r}\frac{\mathrm{d}}{\mathrm{d}r}\left(r\mu\frac{\mathrm{d}v_z}{\mathrm{d}r}\right)+\frac{P_{z=0}-P_{z=L}}{L}-\rho g=0 \tag{4.1.19}$$

Integrating the above equation,

$$v_z=-\left(\frac{P_{z=0}-P_{z=L}}{L}-\rho g\right)\frac{r^2}{4\mu}+C_1\ln(r)+C_2 \tag{4.1.20}$$

where C_1 and C_2 are the integration constants that need to be determined using appropriate boundary conditions.

Boundary condition 1: Since velocities have to be finite anywhere inside the tube including the center, $r=0$, the constant C_1 has to be zero.

Boundary condition 2: As mentioned earlier, there is no slip between the solid surface and the fluid adjacent to it and therefore at $r=R$, $v_z=0$

Using the boundary conditions,

$$v_z = \frac{P_{z=0} - P_{z=L} - \rho g L}{4\mu L}\left(R^2 - r^2\right) \tag{4.1.21}$$

Defining a new quantity called the modified pressure, $\mathbb{P} = P - \rho g_z z$, where g_z is the component of gravity in the z-direction. In the present case, $g_z = -g$, and therefore $P + \rho g z$ (see footnote[1]), then, Equation (4.1.21) can be written as

$$v_z = \frac{\mathbb{P}_{z=0} - \mathbb{P}_{z=L}}{4\mu L} R^2 \left(1 - \frac{r^2}{R^2}\right) \tag{4.1.22}$$

The schematic profiles of the velocity and the viscous momentum flux (shear stress) are shown in Figure 4.1.12c. The velocity profile is parabolic with the maximum at the center and the viscous momentum flux is linear having the maximum at the wall.

From the velocity profiles, the volumetric flow rate is determined by integration:

$$\dot{V} = \int_0^R v_z(r) 2\pi r \, \mathrm{d}r = \frac{(\mathbb{P}_{z=0} - \mathbb{P}_{z=L})\pi R^4}{8\mu L} \tag{4.1.23}$$

This is the famous Hagen–Poiseuille's equation. The average velocity of the fluid, denoted by $\overline{v}$, is easily obtained by dividing the volumetric flow rate by the area of cross section.

$$\overline{v} = \frac{(\mathbb{P}_{z=0} - \mathbb{P}_{z=L})R^2}{8\mu L} \tag{4.1.24}$$

Application of overall energy balance equation (Equation 4.1.8) for fully developed incompressible flow ($\overline{v}_1 = \overline{v}_2$), in a tube,

$$\begin{aligned} g(z_2 - z_1) + \frac{P_2 - P_1}{\rho} + \hat{E}_\mathrm{f} = 0, \\ \text{i.e.,} \frac{\mathbb{P}_1 - \mathbb{P}_2}{\rho} = \hat{E}_\mathrm{f} \end{aligned} \tag{4.1.25}$$

[1] Pressure varies in a static fluid as $P = P|_{z=0} + \rho g_z z$ (Pascal's law). Hence, $\mathbb{P} = P - \rho g_z z = P|_{z=0}$, everywhere. Variation in $\mathbb{P}$ therefore is the variation of pressure beyond the static fluid pressure variation, and this is the driving force for flow.

Substituting for $(\mathbb{P}_1 - \mathbb{P}_2)$ from Equation (4.1.24)

$$\hat{E}_f = \frac{8\mu v L}{\rho R^2} \tag{4.1.26}$$

Hence, the total work done per unit time in the section is $\dot{m}\cdot\hat{E}_f = \rho\cdot\pi R^2\cdot\overline{v}\cdot\hat{E}_f = 8\pi\mu\overline{v}^2 L$. Interestingly, it can be shown that:

$$\left(\tau_{rz}\big|_{r=R}\cdot 2\pi RL\right)\overline{v} = -\mu\frac{dv_z}{dr}\bigg|_{r=R}\cdot 2\pi RL\cdot\overline{v} = 8\pi\mu\overline{v}^2 L \tag{4.1.27}$$

The energy loss due to friction can be seen as the work done to move the fluid at a velocity $\overline{v}$ against the viscous forces at the pipe walls. This, however, should not be interpreted to mean that all dissipation takes place at the pipe/fluid interface. Dissipation is due to work against the shear force in the bulk and is given as $\mu\left(\frac{\partial v_z}{\partial r}\right)^2$ per unit volume. Integration of this term over the volume would give Equation (4.1.27).

It is now possible to calculate the kinetic energy per unit mass in the mechanical energy balance equation (Equation 4.1.8) for laminar flow through pipe. The kinetic energy flow through an infinitesimal area formed by a ring with radii r and $r+\Delta r$:

$$\text{K.E. per unit mass} = \frac{\int_0^R (2\pi r dr)(\rho v_z(r))\left(\frac{1}{2}v_z^2(r)\right)}{\rho\dot{V}} = \frac{\overline{v}^2}{2\beta} \tag{4.1.28}$$

The above equation gives $\beta = \frac{1}{2}$ for fully developed laminar flow through circular tubes.

From the above example, it can be seen that for laminar flows, the *first principle approach*, i.e., the basic constitutive equation for flow in conjunction with mass and momentum conservation, can be used to arrive at the detailed flow structure and then to deduce the energy loss due to friction in the system. When the flow becomes unstable and subsequently manifests as turbulent flow, however, predicting the flow structures from *first principles* is not possible for most engineering systems. An empirical approach is therefore necessary. Experiments are performed on each system of interest. Experimental effort as well as data organization is optimized using the similarity approach, based on the Buckingham Π theorem as described in the next section.

4.1.7. BUCKINGHAM Π THEOREM AND ITS APPLICATION TO TRANSPORT PHENOMENA

The Buckingham Π theorem is a theorem in dimensional analysis. A process or a phenomenon can be described by a set of variables based on its physics. The nature of

these variables is captured in their dimensional representations in terms of a few independent dimensions. These dimensional representations indicate the interrelationships between the variables. Due to these interrelationships, the degrees of freedom of a process are phenomenon constrained by the principle of dimensional homogeneity: each term in a function relating several variables should have the same dimension for it to be physically meaningful.

Let a process be described by n variables; $X_1, X-2, \ldots X_n$. A general polynomial representation would be

$$X_n = \sum_i C_i X_1^{m_{1,i}} X_2^{m_{2,i}} \ldots X_{n-1}^{m_{n-1,i}}$$

C_is are arbitrary constants and $m_{1,i}, m_{2,i} \ldots m_{n-1,i}$ are arbitrary exponents. One may obtain these exponents as well as the constants C_i using regression analysis of the data obtained through experiments. The principle of dimensional homogeneity stipulates that each of the terms on both sides of the equations should have the same dimensions. In other words, if all the variables $(X_1, X_2, \ldots X_n)$ are expressed in their fundamental dimensions and substituted in the proposed power law, the exponents of each of the fundamental dimension should be the same in all terms.

This constraint is expressed formally in the Buckingham Π theorem: if there are "n" variables identified to describe a particular phenomenon in a system and if all these "n" variables can be expressed using "k" fundamental dimensions such as mass, length, time, and charge, then one can form "$n-k$" independent dimensionless numbers. Further, suppose these dimensionless numbers are denoted as $\Pi_1, \Pi_2 \ldots \Pi_{n-k}$, then one can write a mathematical relation $f(\Pi_1, \Pi_2 \ldots \Pi_{n-k}) = 0$ to describe the phenomena in the system.

The dimensionless numbers can be obtained using power law relation,

$$\Pi_p = X_1^{p_1} X_2^{p_2} \ldots X_n^{p_n}$$

Though the choice of these exponents is arbitrary, generally, one would like to choose these exponents as integers and in such a way that the dimensionless numbers represent some physically meaningful entity. Please note that the dimensionless numbers need to be independent of each other. With a given set of variables one may be able to form a large number of dimensionless variables (product of two or more dimensionless numbers would also be dimensionless). Which set of mutually independent Πs are to be selected depends on the phenomenon under study.

The Buckingham Π theorem reduces the number of experiments to be conducted for studying a particular phenomenon in a system substantially. Let us say, one has identified "n" variables that describe the phenomena of interest and decides to choose 10 levels for each of the "n" variables for experimentation. Then, one needs to perform 10^n experiments to cover the whole spectrum of planned experiments. However, if k is the number of fundamental

dimensions, experiments need to be conducted only with $n-k$ dimensionless numbers as dictated by the theorem, and thereby, the number of experiments reduces to 10^{n-k}. Additionally, the amount of information needed to report the experimental data and correlations developed on that data through tables, charts, or equations also reduce substantially. In transport phenomena, therefore, the numerous experimental data as well as correlations developed based on experimental data are reported using dimensionless numbers.

Another consequence of this theorem is that in two geometrically similar systems, if all the dimensionless numbers corresponding to a particular phenomenon of interest are identical, then the systems are similar as far as that phenomenon is concerned. In other words, in both systems, identical mathematical relations among the dimensionless variables hold good in describing the phenomenon of interest. This has been used extensively in studying many process metallurgical systems using, what is termed as, physical models, which are built on a laboratory scale to study a particular phenomenon. For example, water models at the laboratory scale have been used to understand mixing of steel in Basic Oxygen Furnace (BOF), Electric Arc Furnace (EAF), and ladles and to understand flow phenomena and subsequent to control liquid steel flow in tundish and continuous casting molds.

4.1.8. REYNOLDS NUMBER

In Section 4.1.3, the experiment by Reynolds was discussed. In a given flow system, laminar flow is maintained only at low velocities. Beyond some critical velocity, which is characteristic of a particular system, the flow becomes unstable and with further increase, manifests as turbulent flow. The dimensionless number that is used to characterize the transitions from laminar to unstable and further to turbulent flow is the Reynolds number:

$$Re_L = \frac{\rho \overline{v} L}{\mu} \tag{4.1.29}$$

where $\overline{v}$ is the characteristic velocity that characterizes the strength of the flow and L is the characteristic length for the system. One can interpret the Reynolds number as the ratio of advective momentum flux or inertial force to the viscous momentum flux or viscous force. The advective momentum flux is the product of the mass flux and the velocity and is given by $(\rho\overline{v})\overline{v}$. Similarly, the viscous momentum flux or stress is given by $\tau = \mu\dfrac{\overline{v}}{L}$. It must be noted that the characteristic length is used to characterize the velocity gradients. For flow through pipes, the characteristic velocity chosen is the average velocity of the fluid through the pipe and as the velocity gradients are primarily along the radial direction, the characteristic length chosen is the diameter of the tube. Similarly, for flow around a sphere, the velocity of the approaching fluid far away from the sphere and the diameter of the sphere are chosen as characteristic velocity and length, respectively. Experiments in numerous systems have shown that for geometrically similar systems, the

Reynolds number characterizes the nature of the flow. For flow through pipes, one can maintain laminar flow under normal circumstances for Reynolds number up to approximately 2000. At Re values above 5000–10,000, the flow becomes fully turbulent. In the intermediate region, the flow is said to be in transition: flow keeps alternating between laminar and turbulent states. The transitions depend on disturbances. If the inner surface of the pipe is smooth and if one maintains experimental conditions with extreme care so as to minimize the vibrations and disturbances in the incoming flow to the pipe, the transition from laminar flow can be delayed till the Reynolds number reaches values much beyond 2000.

4.1.9. FRICTION FACTOR FOR FLOW THROUGH PIPES

As has been said earlier in Section 4.1.6, the energy term corresponding to friction in flowing fluids through pipes can be deduced from first principles only for laminar flows. Once the flow becomes unstable, one needs to rely on empirical correlations developed using experimental data. So, let us look at the application of the Buckingham Π theorem in understanding flow through a pipe.

The first step is to identify the variables that would affect the flow phenomenon through the pipe. They are:

(1) Diameter of the pipe, D
(2) Length of the pipe, L
(3) Surface roughness of the pipe. This is characterized by the average height of the asperities, and let it be denoted as ϵ
(4) The density of the fluid, ρ
(5) The viscosity of the fluid, μ
(6) The pressure difference one needs to maintain across the length of the pipe, $\Delta\mathbb{P}$. (The modified pressure has been used so that the pressure difference accounts only for the frictional losses eliminating the gravitational term)
(7) The average velocity of the fluid through the pipe, v.

There are seven variables and these can be expressed using three fundamental dimensions, namely, mass, length, and time. Therefore, as per the theorem, one can have four independent dimensionless numbers. The dimensionless numbers that specify the geometry of the system are $\frac{L}{D}$ and $\frac{\epsilon}{D}$. As mentioned earlier, the Reynolds number for the system can be defined as $\frac{\rho v D}{\mu}$. The pressure difference, $\Delta\mathbb{P}$ can be made dimensionless by the characteristic dynamic pressure, namely, $\frac{1}{2}\rho v^2$. Thus, the flow phenomena through the pipe can be described using the following equation

$$f\left(\frac{\Delta\mathbb{P}}{\frac{1}{2}\rho v^2}, Re_D, \frac{L}{D}, \frac{\epsilon}{D}\right) = 0 \tag{4.1.30}$$

The dimensionless number $\frac{\Delta\mathbb{P}}{\rho v^2}$ is referred to as the Euler number.

The relationship for flow through pipes can then be written as:

$$\frac{\Delta\mathbb{P}}{\rho v^2} = f\left(\frac{L}{D}, \frac{\epsilon}{D}, Re_D\right) \tag{4.1.31}$$

For fully developed flow, the pressure drop is linearly dependent on length, since any two sections of equal length should show equal pressure drop. One can therefore write

$$\frac{\frac{\Delta\mathbb{P}}{\rho v^2}}{\frac{L}{D}} = f\left(\frac{\epsilon}{D}, Re_D\right) \tag{4.1.32}$$

The function f in the above equation is also dimensionless and can be used to characterize the flow in place of the Euler number.

$$f_D\left(\frac{\epsilon}{D}, Re_D\right) = \frac{\frac{\Delta\mathbb{P}}{(1/2)\rho v^2}}{\frac{L}{D}} \tag{4.1.33}$$

is called the D'Arcy–Weisbach's or simply D'Arcy's friction factor popular among mechanical engineers. Chemical engineers use a slightly different form and call it the Fanning friction factor f_F:

$$f_F = \frac{\frac{\Delta\mathbb{P}}{\rho v^2}}{\frac{2L}{D}} \tag{4.1.34}$$

Evidently, $4f_F = f_D$.[2]

The above dimensional analysis has been made without the assumption of the nature of the flow. It is therefore valid for both flows, i.e., the friction factor for incompressible fully developed flow in circular tubes is dependent only on the Reynolds number, Re, and the relative roughness $\frac{\epsilon}{D}$. In the case of the entrance or exit regime where the flow changes along the axial direction, the friction factor is dependent on $\frac{L}{D}$ too. Extensive experimental data have been compiled into dimensionless forms and have been presented in graphical or equation forms. Figure 4.1.13 gives a graph of the Fanning friction factor, f_F, as a function of Reynolds number and relative roughness [9,10]. One may note that the friction factor is independent of roughness in the laminar regions and can be obtained from Equation (4.1.24) as:

[2] Fanning friction factor is normally defined with respect to force of friction:

$$F_{\text{friction}} = \frac{\pi D^2}{4} \cdot \Delta\mathbb{P} = (\pi DL)\left(\frac{1}{2}\rho v^2\right) f_F$$

where πDL represents the wetted area on which the friction force, F_{friction} acts and $\frac{1}{2}\rho v^2$ gives the characteristic kinetic energy (or dynamic pressure).

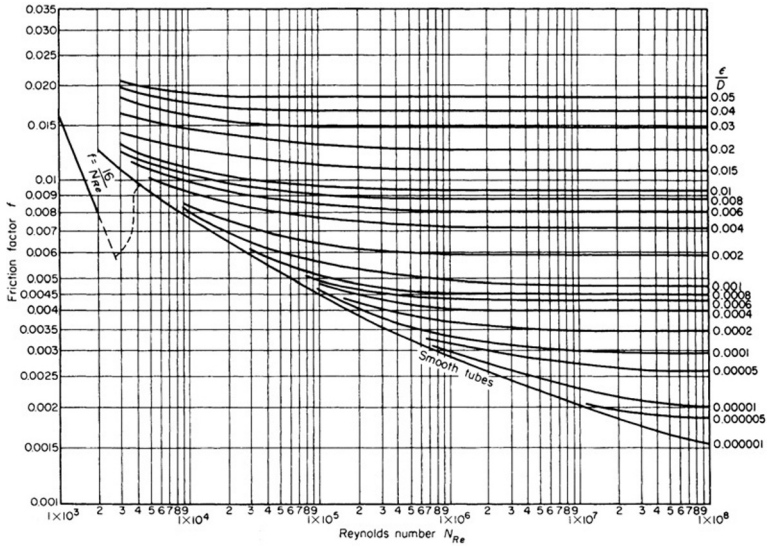


Figure 4.1.13 Fanning friction factor chart for pipe flow [9].

$$f_F = \frac{16}{Re_D} \tag{4.1.35}$$

This corresponds to $\hat{E}_f = \dfrac{\Delta \mathbb{P}}{\rho} = \dfrac{8\mu v^2}{\rho R^2}$ given by Equation (4.1.26).

In the transition region, it has been observed that the pressure drop does not remain stable; it keeps fluctuating. This is marked with dotted lines and generally is not suitable for engineering applications due to its unpredictability. In the turbulent region, the friction factor values are stable and vary depending on the Reynolds number and the relative roughness. One can clearly see that the dependence of Reynolds number on friction factor decreases with increasing Reynolds number. Dependence also decreases with increasing roughness.

Instead of graphical representation, correlations in the form of algebraic equations are also available to estimate the friction factor through pipes in the turbulent region. The most widely used correlation is by Colebrook [11]

$$\frac{1}{\sqrt{f_F}} = -4\log\left(\frac{1}{3.7}\frac{\epsilon}{D} + \frac{1.255}{Re_D\sqrt{f_F}}\right) \quad \text{Turbulent flow, for } Re_D > 4000 \tag{4.1.36}$$

There is also a more recent correlation by Churchill [12], which has the advantage of estimating the friction factor directly as the equation is explicit unlike the previous one

$$\frac{1}{\sqrt{f_F}} = -4\log\left(0.27\frac{\epsilon}{D} + \left(\frac{7}{Re_D}\right)^{0.9}\right) \quad \text{Turbulent flow, for } Re_D > 4000 \tag{4.1.37}$$

Table 4.1.1 Values of Surface Roughness for Various Materials [9]

Material Surface Roughness	mm
Drawn tubing (brass, lead, glass, and the like)	0.00152
Commercial steel or wrought iron	0.0457
Asphalted cast iron	0.122
Galvanized iron	0.152
Cast iron	0.259
Wood stove	0.183–0.914
Concrete	0.305–3.05
Riveted steel	0.914–9.14

For turbulent flow through hydraulically smooth pipes ($\epsilon \to 0$), up to Re_D of 10^5, one can also use the simpler expression by Blasius [13]

$$f_F = \frac{0.0791}{Re_D^{0.25}} \quad \text{Turbulent flow, smooth pipes, for } Re_D < 10^5 \tag{4.1.38}$$

Typical, surface roughness values of materials of commercial pipes are shown in Table 4.1.1. The roughness values shown in the table correspond to newly manufactured pipes. Colebrook [11] found that a simple linear relation can reasonably represent the increase in roughness because of corrosion and scale deposition.

The energy term corresponding to friction losses, $\hat{E}_f$, in a pipe is related to the friction factor as follows

$$\hat{E}_f = 2\frac{L}{D}v^2 f_F \tag{4.1.39}$$

4.1.9.1. Friction Losses from Pipe Fittings

In a piping system, there are always pipe fittings such as bends, valves, and couplings besides straight sections. One needs to account for the additional friction losses due to these fittings. Friction losses are also associated with entry lengths and exit conditions. One of the ways of quantifying these additional friction losses is through an equivalent length of a straight pipe giving the same friction loss as that with the pipe fitting. For geometrically similar pipe fittings, irrespective of their actual dimensions, the friction losses can be expressed using an equivalent length to diameter ratio ($\frac{L_e}{D}$). Some typical values obtained from experimental measurements are tabulated in Table 4.1.2 for common pipe fittings.

Table 4.1.2 Equivalent Pipe Length to Diameter Ratio for Some Common Pipe Fittings (Turbulent Flow) [14]

Pipe Fitting	$\frac{L_e}{D}$
Globe valve, wide open	~300
Angle valve, wide open	~170
Gate valve, wide open	~7
3/4 Open	~40
1/2 Open	~200
1/4 Open	~900
90° Elbow, standard	30
Long radius	20
45° Elbow, standard	15
Tee, used as elbow, entering the stem	90
Tee, used as elbow, entering one of two side arms	60
Tee, straight through	20
180° Close return bend	75
Ordinary entrance (pipe flush with the wall of the vessel)	16
Borda entrance (pipe protruding into vessel)	30
Rounded entrance, union, coupling	Negligible
Sudden enlargement from d to D	
Turbulent flow in d	$\frac{1}{4f_{F,ind}}\left[1-\frac{d^2}{D^2}\right]^2$
Sudden contraction from D to d	
Turbulent flow in d	$\frac{1}{10f_{F,ind}}\left[1.25-\frac{d^2}{D^2}\right]$

Often in flow systems, there may be elements for which defining an equivalent length is not convenient. A chamber in the flow line filled with pebbles for mixing of fluids or a water-cooled mold with complex geometry are examples. These need experimental determinations of pressure drop. The data are then stored as an energy loss factor k_f using the following equation:

$$\Delta P = \frac{1}{2}\rho v^2 k_f \tag{4.1.40}$$

In highly turbulent flows, k_f remains relatively independent of Re.

4.1.9.2. Estimation of Friction Factor for Flow Through Conduits Having Noncircular Cross Section

For turbulent flow through conduits having noncircular cross sections, one can approximate the friction loss by representing the conduit as a circular pipe having an equivalent diameter, D_e defined as:

$$D_e = 4(\text{Hydraulic radius}) = 4\left(\frac{\text{Area of cross section}}{\text{Wetted perimeter}}\right) \tag{4.1.41}$$

For example, for a conduit having a square cross section with side a, the equivalent diameter, D_e, for calculating the friction loss will be a.

Example 4.1.3

Oxygen is being delivered to a steel melt shop (SMS) at the rate of 400 $Nm^3\,min^{-1}$ through a 50 m long, 100-mm piping from a reservoir at the oxygen plant. The piping has five 90° bends of standard radius. In addition, one gate valve and one globe valve are placed in the pipeline. If the delivery pressure at the SMS should be 10^6 Pa (gauge pressure), what should be the minimum pressure at the reservoir with the valves fully open? Pipes are made of galvanized iron. The viscosity of oxygen at room temperature (300 K) is 20.2×10^{-6} Pa s. Density of oxygen at STP is 1.4 kg m^{-3}.

Solution

First one needs to identify whether the flow can be approximated as being incompressible. For that, let us find the Mach number (Ma). The pressure will be minimum at the exit and therefore the velocity is maximum at this section. For a temperature of 300 K and pressure of 10^6 Pa, the volumetric flow rate is

$$\dot{V} = \frac{400\left(\frac{300}{273}\right)\left(\frac{1.013}{11}\right)}{60} = 0.67\,\text{m}^3\,\text{s}^{-1}$$

the velocity, v, is

$$v = \frac{\dot{V}}{\pi\frac{D^2}{4}} = 85\,\text{m}\,\text{s}^{-1}$$

The velocity of sound under adiabatic condition is given by $c = \sqrt{\frac{\gamma RT}{M}}$, which for oxygen gives 330 m s^{-1}. Thus the Mach number is $\frac{85}{330} = 0.26$. As the Mach number is <0.3, one can approximate the flow as incompressible.

The Reynolds number for the flow is independent of pressure for isothermal flow:

$$Re_D = \frac{\rho v D}{\mu} = \frac{14.11 \times 85 \times 0.1}{20.2 \times 10^{-6}} = 5.8 \times 10^6$$

From Table 4.1.1, the relative roughness for the pipe is $\frac{0.152}{100} = 0.00152$. For this roughness, the flow is completely turbulent and the friction factor is independent of Reynolds number (see Figure 4.1.13). The Fanning friction factor, f_F, is approximately as 0.0055.

Though the flow is considered incompressible, one needs to estimate the density and velocity at some mean pressure for the entire tube. Let us assume that the upstream pressure is 1.4×10^6 Pa (absolute), and the average pressure is 1.2×10^6 Pa (absolute). Thus, the average density and the average velocity for the flow are 16.6 kg m^{-1} and 78 m s^{-1}, respectively.

The equivalent length for the piping system can be calculated using values given in Table 4.1.2:

$$\sum \frac{L}{D} = \left(\frac{L}{D}\right)_{\text{Straight pipe}} + 5\left(\frac{L_e}{D}\right)_{\text{Elbow}} + \left(\frac{L_e}{D}\right)_{\text{Gate value}} + \left(\frac{L_e}{D}\right)_{\text{Globe value}}$$

$$\sum \frac{L}{D} = 500 + 5 \times 30 + 7 + 300 = 957$$

Applying mechanical energy balance, Equation (4.1.8)

$$\frac{v^2}{2} + \frac{P_2 - P_1}{\rho} + 2 \times 0.0055 \times 957 v^2 = 0$$

$$\therefore P_1 - P_2 = \Delta P = 0.95 \times 10^6 \text{ Pa}$$

Here ΔP is comparable to P. Our assumption of the average pressure being 1.2×10^6 Pa is erroneous. One needs to iteratively improve the solution by trial and error. This leads to the value of P_1 to be 1.88×10^6 pa.

Example 4.1.4

A schematic of a continuous casting mold is shown in Figure 4.1.14. One side of the continuous casting mold face has the dimensions of 1 m height and 2 m width. The hot face made of copper is backed by a steel plate with a gap of 20 mm in between. The designer specifies that cooling water should be passed in the gap between the two plates at a velocity of at least 10 m s^{-1}, from the bottom to the top.

- What is the pressure drop across the mold?
- What is the theoretical pump rating for supplying water to this mold, discounting losses in supply pipes, entrance, exit, etc.? Assume the surfaces to be hydraulically smooth.

Solution

In the above problem, the flow of water is through a rectangular duct. As the flow rate is quite large, the flow is expected to be turbulent. Therefore, one can conveniently represent the conduit by a circular pipe having equivalent diameter given by Equation (4.1.41)

$$D_e = 4 \times \frac{2 \times 20 \times 10^{-3}}{2 \times (2 + 20 \times 10^{-3})} = 0.0396 \text{m}$$

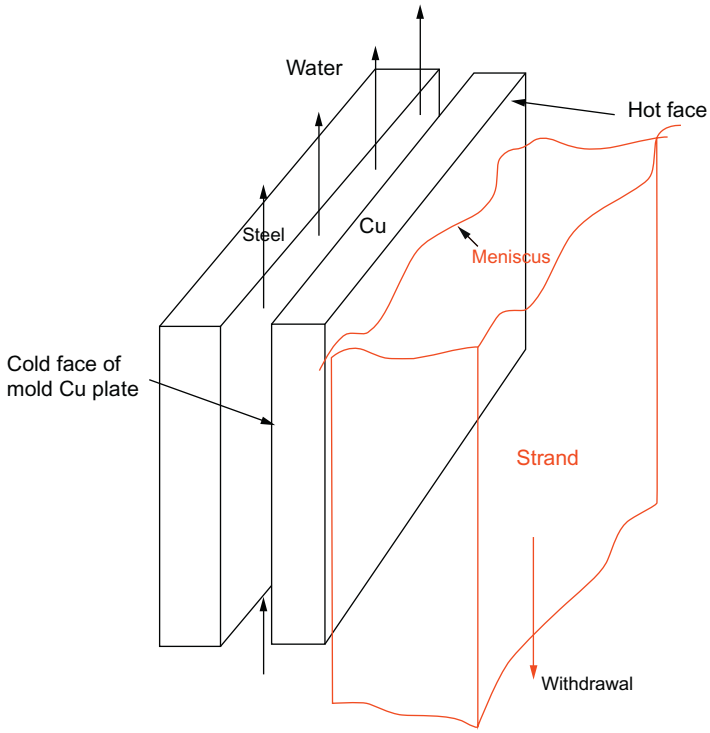


Figure 4.1.14 Continuous casting mold: water flow.

The viscosity of water at room temperature is approximately 0.001 Pa s. Hence, the Reynolds number for the flow is

$$Re_D = \frac{1000 \times 10 \times 0.0396}{0.001} = 3.96 \times 10^5$$

Using Churchill's (refer to Equation 4.1.37) relation for friction factor,

$$f_F = 6.3 \times 10^{-4}$$

Applying the mechanical energy balance equation (Equation 4.1.8) between inlet of water at the bottom of the mold and the exit at the top,

$$\frac{P_2 - P_1}{\rho} + g(z_2 - z_1) + 2 f_F \frac{L}{D} v^2 = 0$$

$$\frac{P_2 - P_1}{1000} + g(1) + 2 \times 6.3 \times 10^{-4} \frac{1}{0.0396} 10^2 = 0$$

$$P_1 - P_2 = 13\,\text{kPa}$$

The work done per unit time to maintain the pressure drop and the flow on both sides of the mold

$$(P_1 - P_2)(Av) = 13 \times 2 \times 2 \times 20 \times 10^{-3} \times 10 = 10.4\text{kW}$$

Comment: Molds used in practice normally have a series of slits along its width, with water distributor at the top and bottom. Supply pipes are connected to these distributors. The overall geometry is fairly complex, and one may have to generate data for equivalent lengths or energy loss factors. Pressure drop through the overall system may be substantially higher.

4.1.10. FLOW THROUGH PACKED BEDS

As mentioned in the introductory section, understanding flow through packed beds is very important for design and operation of numerous metallurgical processes. Simple examples of packed beds include rock piles, sand filters, and a soil bed. A predominant part of the interior of a working blast furnace consists of a packed bed of iron ore and coke at the top with gas flowing through it and a packed bed of coke at the bottom with gas and liquids flowing through it. Similarly, a sinter bed for iron ore sintering or a bed of pellets for induration are packed beds. Leaching operations can also be performed in a reactor where the leachant is allowed to flow through a packed bed of mineral particles.

While designing a packed bed reactor, a process engineer desires to calculate the pressure difference that needs to be applied to maintain a desired flow rate through the bed. One would also like to know how this relation between the pressure drop and the flow rate changes depending on the properties of the packed bed. While describing flow through packed beds, a term called "superficial velocity" is often used. This refers to the flow rate per unit area of cross section of the reactor (in the absence of the particles). Please note that the fluid flows only through the voids between particles in the bed and the actual area available for the fluid to flow is a fraction of the cross-sectional area of the reactor.

The methodology commonly adopted in developing relationships for complex systems like flow through packed beds is to approximate the system by a comparatively simpler system that is amenable to analysis. The hypothesis is that the functional relationship developed for the simple systems is applicable to the complex system under consideration with a few empirical corrections. In the case of packed beds, two approaches have been adopted: (1) considering the flow of fluid through the voids in the packed bed as flow through a bundle of tubes and (2) considering the system as flow around particles submerged in a fluid. The tube-bundle theory has been adopted here for developing the governing equation.

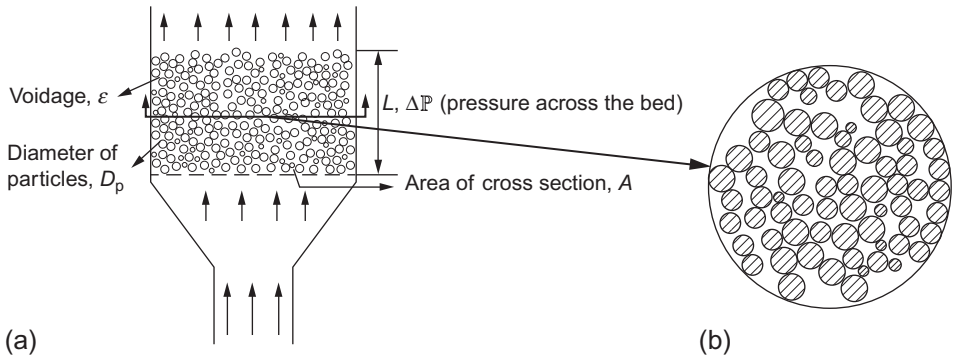


Figure 4.1.15 (a) A simple packed column or bed and (b) cross section of the bed.

Consider the simple case of a packed bed made from randomly packed uniform-sized spherical particles in a container as shown in Figure 4.1.15. The two important bulk characteristics of such a packed bed are the average volume fraction of voids, ε, and the diameter of the particles, D_p. The voidage in a randomly packed bed is reasonably uniform, except near the wall where it is higher. Experiments have shown that this wall region extends to a distance of $3D_p - 5D_p$ from the wall [15]. Let us, therefore, consider a case where the cross-sectional dimension of the reactor is much larger than the diameter of the particle, so that the effect of the wall is negligible.

The basic idea behind the tube-bundle theory is to estimate an equivalent diameter for the bundle of tubes that gives the same pressure drop for the desired flow rate, i.e., the tube that gives the same friction loss as that for the flow through the bed. The equivalent diameter for noncircular conduit cross sections is given by

$$D_e = 4 \times \frac{\text{Area of cross section for the flow}}{\text{Wetted perimeter for the flow}}$$

Figure 4.1.15b shows a schematic cross-section of the bed. The nonhatched area is the area available for flow. The sum of the boundaries of the particles is the wetted perimeter. When bed diameter is large enough, the length along the wall can be neglected.

Let us multiply the denominator and numerator of the RHS of this equation by an infinitesimal bed height dL.

$$\begin{aligned} D_e &= 4 \times \frac{\text{Area of cross section for the flow} \times dL}{\text{Wetted perimeter for the flow} \times dL} \\ &= 4 \times \frac{\text{Volume of the voids in height } dL \text{ of this bed}}{\text{Surface of area of particle in height } dL \text{ of this bed}} \end{aligned}$$

Since the bed is macroscopically uniform, the above relationship should hold for any thin slice of the bed. Hence the equation can be rewritten as

$$D_e = 4 \times \frac{\text{Volume of the voids in height } L \text{ of this bed}}{\text{Surface of area of particle in height } L \text{ of this bed}}$$

Suppose, ε denotes the average fraction of voidage in the bed and D_p denotes the diameter of the particles that constitute the packed bed, and A denotes the cross-sectional area of the packed bed column as shown in the figure, then

$$\begin{aligned}
\text{Volume of the voids in the bed} &= \varepsilon AL \\
\text{Number of particles in the bed} &= \frac{(1-\varepsilon)AL}{\frac{1}{6}\pi D_p^3} \\
\text{Surface of area of particle in the bed} &= \text{Number of particles in the bed} \\
&\quad \times \text{Surface area of one particle} \\
&= \frac{(1-\varepsilon)AL}{\frac{1}{6}\pi D_p^3}\left(\pi D_p^2\right) = \frac{6(1-\varepsilon)}{D_p}AL \\
\therefore D_e &= 4\frac{\varepsilon AL}{\frac{6(1-\varepsilon)}{D_p}AL} = 4\frac{\varepsilon D_p}{6(1-\varepsilon)}
\end{aligned} \tag{4.1.42}$$

The actual average velocity $\overline{v}$ through the voids is related to the superficial velocity, v_0:

$$\overline{v} = \frac{v_0}{\varepsilon} \tag{4.1.43}$$

Using Equations (4.1.42) and (4.1.43) in the equation for flow through a tube (Equation 4.1.34):

$$\frac{\Delta \mathbb{P}}{\rho} = \frac{4L}{D_e} \cdot \frac{\overline{v}^2}{2} \cdot f_F = \frac{2L}{D_e} \cdot \frac{{v_0}^2}{\varepsilon^2} \cdot f_F \tag{4.1.44}$$

The value of f_F is dependent on Re for the flow and the "roughness" of the tube. The Reynolds number for tubes is given by

$$Re = \frac{\rho \overline{v} D_e}{\mu} = \frac{\rho v_0 D_e}{\varepsilon \mu} = \frac{4}{6}\frac{\rho v_0 D_p}{(1-\varepsilon)\mu}$$

For laminar flow in tubes, $f_F = \frac{16}{Re}$. From Equation (4.1.44), one obtains

$$\frac{\Delta \mathbb{P}}{L} = \frac{72\mu(1-\varepsilon)^2}{D_p^2 \varepsilon^3} v_0$$

This equation is now empirically corrected for the assumption of a straight tube and fully developed flow by replacing the constant 72 to 150 to obtain,

$$\frac{\Delta \mathbb{P}}{L} = \frac{150\mu(1-\varepsilon)^2}{D_p^2 \varepsilon^3} v_0 \tag{4.1.45}$$

In his paper on packed beds, Ergun [16] attributes the above equation to Blake and Kozeny and calls it the Blake–Kozeny equation. Much earlier, in the 1850s, the French scientist D'Arcy had observed, in flow through sand beds, a linear dependence of the pressure drop on v_0 and μ and proposed what is now known as D'Arcy's equation:

$$\frac{\Delta \mathbb{P}}{L} = k\mu v_0 \tag{4.1.46}$$

where k is called the specific permeability of the bed.

Reynolds number for packed beds is defined as [3]

$$Re_E = \frac{\rho v_0 D_p}{(1-\varepsilon)\mu} \tag{4.1.47}$$

Equation (4.1.45) for the pressure drop is valid for $Re_E \lesssim 10$.

At much larger values of Re_E, the flow becomes fully turbulent. For flow through tubes, f_F becomes independent of Re_E if the roughness of the tube is very high (see Figure 4.1.13). Flow channels in a packed bed of particles can reasonably be viewed as a very rough tube. Therefore, the pressure equation becomes

$$\frac{\Delta \mathbb{P}}{L} = \frac{2}{D_e} \cdot \frac{\rho v_0^2}{\varepsilon^2} \cdot f_F = 3 f_F \frac{(1-\varepsilon)}{D_p \varepsilon^3} \rho v_0^2$$

The constant $(3f_F)$ is now empirically determined and is found to be 1.75 giving

$$\frac{\Delta \mathbb{P}}{L} = 1.75 \frac{(1-\varepsilon)}{D_p \varepsilon^3} \rho v_0^2 \tag{4.1.48}$$

Ergun [16] calls it the Burke–Plummer equation. The above equation is valid for $Re_E \gtrsim 1000$, when flow everywhere in the bed is expected to be turbulent.

In the range of $10 < Re_E < 1000$, the flow can be mixed. Since flow through a packed bed involves several openings of different sizes between particles, the flow can be laminar, turbulent, or in transition simultaneously at different places in the bed, in this intermediate range of Reynolds numbers. Ergun [16] found empirically that summing the terms on the RHS of Equation (4.1.45) and Equation (4.1.48) predicts the pressure drop to a reasonable accuracy:

$$\frac{\Delta \mathbb{P}}{L} = \frac{150\mu(1-\varepsilon)^2}{D_p^2 \varepsilon^3} v_0 + \frac{1.75\rho(1-\varepsilon)}{\varepsilon^3 D_p} v_0^2 \tag{4.1.49}$$

This equation is called the Ergun equation and is used extensively for packed bed flow analysis over the entire Re range. One can rewrite this equation as:

[3] Note that the constant $\frac{4}{6}$ that occurred in the definition earlier is dropped since transition values for Re are anyway determined experimentally for each geometric system.

$$\frac{\Delta\mathbb{P}}{\rho v_0^2}\frac{D}{L}\frac{\varepsilon^3}{1-\varepsilon}=\frac{150\mu(1-\varepsilon)}{D_p\rho v_0}+1.75=\frac{150}{Re_E}+1.75 \tag{4.1.50}$$

The first term on the left is the definition of a friction factor for packed beds. Hence:

$$f_{F,\text{packed bed}}=\frac{150}{Re_E}+1.75 \tag{4.1.51}$$

Data from experiments plotted as $\log(f_{F,\text{packed bed}})$ versus $\log(Re_E)$ show a straight line with a slope of -1 for $Re \lesssim 10$, and a constant value for $Re \gtrsim 1000$ and a smooth curve connecting these two straight lines in between [1].

The above expression has been deduced for a packed bed having spherical particles with uniform size. However, in reality, the industrial packed beds are made of particles having different shapes and sizes and even completely different materials, such as iron ore and coke in blast furnace. Thus, detailed characterization of the packed bed is required. For nonspherical particles, there may be different ways of defining particle sizes. However, one needs to adopt an appropriate one as far as flow through packed bed is concerned. Two important measures of a particle that affect the flow are its volume and surface area. Thus, the size and shape of particles in a packed bed are characterized using these measures.

The size of the particle is defined by the size of equivalent sphere having the same volume of that of the particle, i.e.,

$$D_{sph} = \text{Diameter of sphere having the same volume as that of the particle} \tag{4.1.52}$$

In order to account for the surface area of the particle, a parameter called sphericity, ϕ, is defined as

$$\phi=\frac{\text{Surface area of the sphere having equivalent volume of the particle}}{\text{Surface area of the particle}} \tag{4.1.53}$$

Sphericity of some of the commonly shaped particles is listed in Table 4.1.3.

The particle size, D_p, used in Ergun equation (Equation 4.1.49) is, then, given by

$$D_p=\phi\times D_{sph} \tag{4.1.54}$$

For the estimation of D_p from standard screen size, the reader may refer to Ref. [14].

If there is a size distribution of particles, the average size that can be used for flow through packed bed is

$$\overline{D}_p=\frac{1}{\sum_i\left(\frac{\xi_i}{D_{p,i}}\right)} \tag{4.1.55}$$

Table 4.1.3 Sphericity of Particles [14,17]

Particle Shape	Sphericity, ϕ
Sphere	1.00
Cube	0.81
Cylinder	
$h = d$	0.87
$5h = d$	0.70
$10h =$ d	0.58
Disks	
$3h = d$	0.76
$6h = d$	0.60
$10h = d$	0.47
Old beach sand	As high as 0.86
Young river sand	As low as 0.53
Average for various types of sand	0.75
Crushed solids	0.5–0.7
Granular particles	0.7–0.8
Wheat	0.85
Raschig rings	0.26–0.53

where ξ_i is the volume fraction of particles of size $D_{p,i}$.

In many metallurgical processes, the bed characteristics change spatially. In a blast furnace, for example, the packed bed consists of layers of ore and coke. Further, due to softening of iron-bearing layers at the bottom part of the furnace, the voidage in this layer reduces to very small values and the gas flows only through the coke layer. There can also be variation in the bed characteristic due to particle breakage, physico-chemical changes, size-segregation, etc. In such situations, the Ergun equation (Equation 4.1.49) can be written in a differential form and bed characteristics are allowed to change spatially so that detailed flow behavior can be obtained. Please note the word detailed in the current context refers only to a flow behavior averaged over several particles in the bed, not to the scale of each single particle. This also implies that the macroscopic bed characteristics such as bed voidage and particle size are also averaged over several particles locally to represent their spatial distribution.

When the flow in a packed bed is three-dimensional (3D), the Ergun equation (Equation 4.49) can be interpreted as a relationship between the local pressure drop per unit length and the superficial velocity aligned along the flow direction. For an arbitrarily selected coordinate system, velocity needs to be defined as a vector, $\vec{v_0}$ and the Ergun equation in vector form can be written as

$$\nabla \mathbb{P} = -\left(\frac{150.0\mu(1-\varepsilon)^2}{D_p^2\varepsilon^3} + \frac{1.75\rho(1-\varepsilon)}{\varepsilon^3 D_p}|\vec{v_0}|\right)\vec{v_0} \tag{4.1.56}$$

Example 4.1.5

In a pellet-hardening unit, the flow rate of air at 1000 K is 5×10^{-3} m^3 s^{-1} and the size of the spherically shaped pellets is 4 mm. Pellets are filled to a depth of 250 mm. The cross-sectional area is 0.185 m^2. If the void fraction is 0.4, calculate the pressure drop needed to maintain the flow in mm of water. The density of air at 1000 K is 0.43 kg m^{-3} and its viscosity is 30×10^{-6} Pa s.

Solution

Ergun equation (Equation 4.1.49) needs to be used to find the pressure drop across the bed:

$$\frac{\Delta \mathbb{P}}{L} = \frac{150\mu(1-\varepsilon)^2}{D_p^2\varepsilon^3}v_0 + \frac{1.75\rho(1-\varepsilon)}{\varepsilon^3 D_p}v_0^2$$

The superficial velocity, $v_0 = 5 \times 10^{-3}/0.185 = 0.027$ m s^{-1}. Substituting this in the Ergun equation yields $\frac{\Delta \mathbb{P}}{L} = 44.00$ and hence $\Delta \mathbb{P} = 11$ Pa $= 1.1$ mm of water.

It can be easily verified that only the first term in the Ergun equation is significant, since the superficial velocity is so small.

Example 4.1.6

The quality of cement greatly depends on the surface area of particles per unit mass of cement (specific surface area). Since the pressure drop in packed beds primarily depends on this property, one can design a simple packed-bed apparatus for determining the quality of cement powder. Figure 4.1.16 shows a schematic of such an apparatus. The apparatus consists of a glass bulb, valves to control air flow, manometer, and an appropriately designed container wherein desired amount of cement can be placed to make a packed bed.

Initially by opening the valve A, air is filled in the glass bulb to a predetermined pressure that can be measured using the manometer. Subsequently, valve A is closed and valve B is opened to allow the air to pass through the packed bed. As the air is removed from the bulb, the pressure decreases. Therefore, the pressure drop across the bed progressively decreases with a corresponding decrease in the flow rate through the cement bed and hence the rate of depletion of pressure in the bulb. This rate of depletion depends on

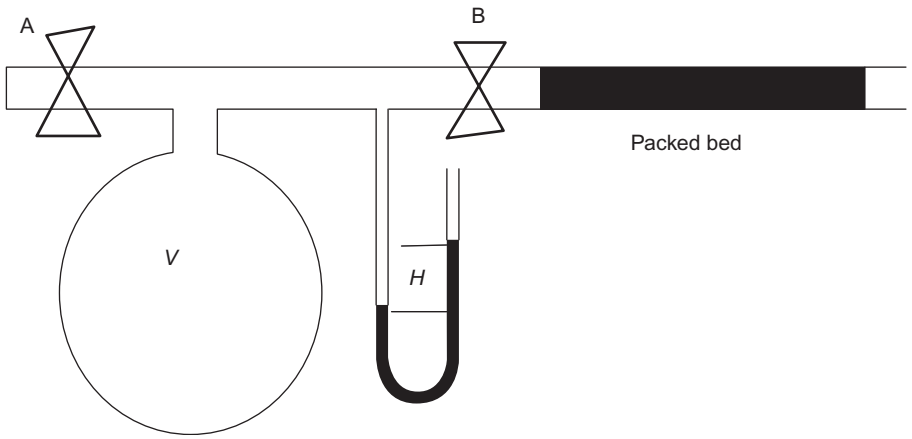


Figure 4.1.16 A schematic of a cement testing apparatus.

the resistance that the packed bed offers, which in turn depends on the bed characteristics. Flow rate through the cement bed is small enough to consider only the first term in the Ergun's equation. We need to obtain a relationship for the pressure in the bed as a function of time, from which the bed characteristics may be estimated.

Solution

According to the Ergun equation at low flow rates, the superficial velocity through the bed is proportional to the pressure drop across the bed. As the bed is expected to offer much more resistance than pipe and fittings, it is reasonable to assume that difference in pressure between that inside the bulb and that at the exit can be attributed completely to the packed bed. If $F_1 v_0$ represents the first term in the Ergun Equation (4.1.49), then,

$$P_{\text{bulb}} - P_0 = \Delta P_{\text{bulb}} = F_1 v_0 L \tag{4.1.57}$$

Please note that it has been assumed that any small change in pressure drop across the cement bed would result in instantaneous change in superficial velocity as well. This is quite reasonable as the characteristic time to attain steady-state velocity is much shorter than the characteristic time for the depletion of pressure inside the bulb.

The unsteady mass balance from the bulb can be written as

$$V_{\text{bulb}} \frac{\mathrm{d}(\rho_{\text{bulb}})}{\mathrm{d}t} = -\rho_{\text{average}} \times A_{\text{bed}} v_0 \tag{4.1.58}$$

where V_{bulb} denotes the volume of the bulb, ρ_{bulb} the density of air inside the bulb, and ρ_{average} the average density of the air while flowing through the cement bed. Applying ideal gas law, the above equation becomes,

$$V_{\text{bulb}} \frac{\mathrm{d}(P_0 + \Delta P_{\text{bulb}}) M/(RT)}{\mathrm{d}t} = -(P_0 + \Delta P_{\text{bulb}}/2) M/(RT) \times A_{\text{bed}} v_0 \tag{4.1.59}$$

$$V_{\text{bulb}}\frac{\mathrm{d}(\Delta P_{\text{bulb}})}{\mathrm{d}t} = -(P_0 + \Delta P_{\text{bulb}}/2)^* A_{\text{bed}} v_0 \tag{4.1.60}$$

Substituting from Equation (4.1.57) for v_0,

$$V_{\text{bulb}}\frac{\mathrm{d}(\Delta P_{\text{bulb}})}{\mathrm{d}t} = -(P_0 + \Delta P_{\text{bulb}}/2)^* A_{\text{bed}}\frac{\Delta P_{\text{bulb}}}{F_1} \tag{4.1.61}$$

If $\Delta P_{\text{bulb}} \ll P_0$, the second-order term on the right-hand side of the above equation can be neglected and hence,

$$V_{\text{bulb}}\frac{\mathrm{d}(\Delta P_{\text{bulb}})}{\mathrm{d}t} = -P_0 A_{\text{bed}}\frac{\Delta P_{\text{bulb}}}{F_1} \tag{4.1.62}$$

The solution of this equation for an initial pressure difference ΔP^0_{bulb} will be

$$\Delta P_{\text{bulb}} = \Delta P^0_{\text{bulb}} \exp\left(-\frac{P_0 A_{\text{bed}}}{F_1 V_{\text{bulb}}} t\right) \tag{4.1.63}$$

The slope of the line in the graph $\log(\Delta P)$ vs. time permits the calculation of F_1, which is equal to $\dfrac{150.0\mu(1-\varepsilon)^2}{D_{\text{p}}^2\varepsilon^3}$. Knowing μ_{air} and ε, one can estimate the particle size, D_{p}

4.1.11. FLUIDIZED BEDS

As upward flow rate of a fluid through a packed bed is increased, there is an increase in the pressure drop across the bed too. Eventually, the net force due to the pressure drop would equal that of the weight of the bed. Beyond this point, the particles that were static in the bed start moving and eventually with further increase in gas flow rate become suspended in the fluid; this is termed fluidization. Once fluidized, the suspension behaves like a fluid. For example, if the bed is tilted, the top surface remains horizontal. Further, the suspension can be transferred from one container to another in a manner similar to that with fluids. This suspension is named as fluidized bed. In case of liquid–solid systems, once fluidized, increase in superficial velocity results in a uniform increase in suspension volume as the voidage in the bed increases. This is termed particulate fluidization. In case of gas–solid systems, once fluidized, increase in superficial velocity can result in non-uniform expansion of the suspension containing bubble-like regions devoid of any particles. This state is termed bubbling fluidization and the bed is called a bubbling bed. The superficial velocity at the point of change from a packed bed to a fluidized bed is termed the minimum fluidization velocity, v_{mf}. These fluidization phenomena are illustrated in the schematics in Figure 4.1.17.

The change in pressure drop as well as the bed voidage with increase in superficial velocity is illustrated in Figure 4.1.18. When the bed is static, the pressure drop increases

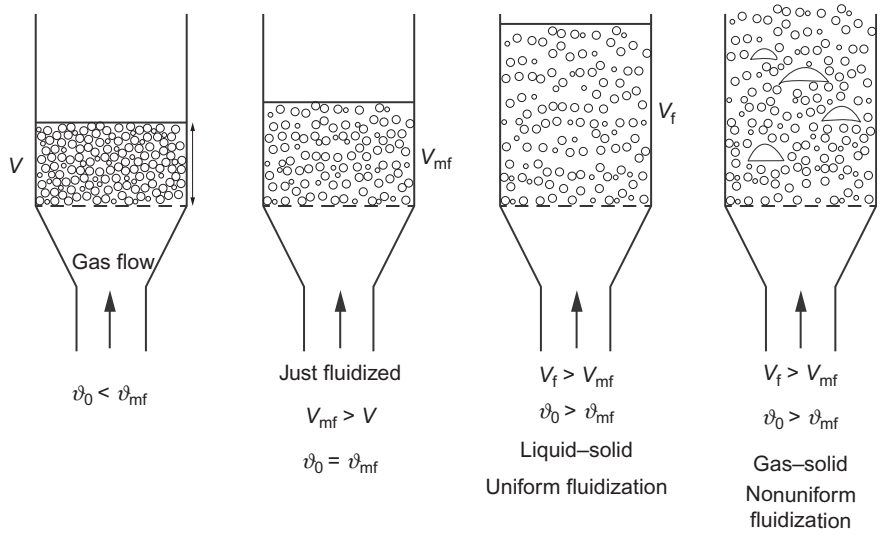


Figure 4.1.17 A schematic of fluidization phenomena.

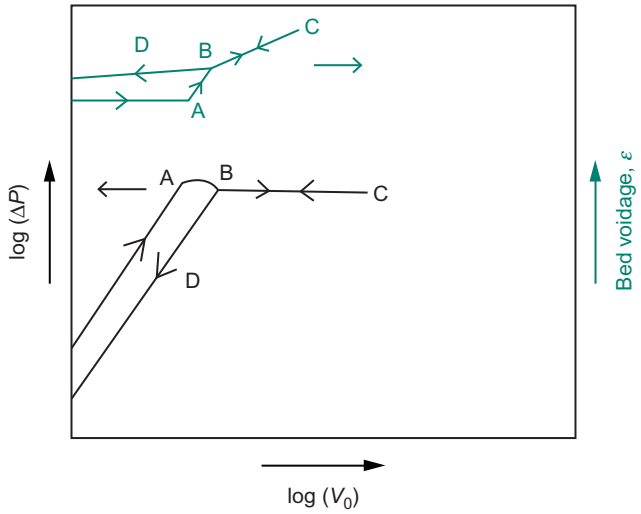


Figure 4.1.18 A schematic of variation of pressure and bed voidage during fluidization.

with increase in superficial velocity in a manner predicted by the Ergun equation. Increase in superficial velocity beyond the point where the pressure drop counterbalances the weight of the bed results in fluidization. In the fluidization region, the pressure across the bed remains constant, just balancing the weight of the bed in the fluid. The void fraction and, therefore, the height of the bed should correspondingly increase (Figure 4.1.17).

In real systems, the bed might have been initially packed tightly interlocking the particles. Hence, the pressure in this packed condition may rise initially to a point A before the particles become free to move. As soon as the particles are released, the pressure drop settles back to the steady value corresponding to the fluidized bed (point B). If the superficial velocity is reduced from C, the bed settles down to a packed bed at point B with higher voidage than that when it was formed while filling. The pressure drop follows the path CBD. This difference in voidage often arises due to higher impact forces during bed formation or due to vibratory compaction.

4.1.11.1. Minimum Fluidization Velocity, v_{mf}

The minimum fluidization velocity can be estimated, since at this point the bed still remains packed, but the force arising from the pressure drop just balances the weight of the bed. As the pressure drop across the bed is given by the Ergun equation (4.1.49), the force balance at v_{mf} can be written as

$$\begin{aligned} AL(1-\varepsilon_{mf})(\rho_s-\rho)g &= \Delta\mathbb{P}A \\ &= AL\left(\frac{150.0\mu(1-\varepsilon_{mf})^2}{D_p^2\varepsilon_{mf}^3}v_{mf}+\frac{1.75\rho(1-\varepsilon_{mf})}{\varepsilon_{mf}^3 D_p}v_{mf}^2\right) \end{aligned} \tag{4.1.64}$$

As mentioned before, the voidage corresponding to the minimum fluidization (ε_{mf}) needs to be determined experimentally by slowly allowing the bed to settle from a fluidized state to a static one. Wen and Yu [18] found empirically that for a variety of systems, ε_{mf} can be correlated with sphericity, ϕ, using the following equations

$$\frac{1}{\phi\varepsilon_{mf}^3}\approx 14 \quad \text{and} \quad \frac{1-\varepsilon_{mf}}{\phi^2\varepsilon_{mf}^3}\approx 11 \tag{4.1.65}$$

Substituting the above equations along with Equation (4.1.54) in Equation (4.1.65), the expression for estimating the minimum fluidization velocity can be written as,

$$\frac{D_{sph}v_{mf}\rho}{\mu}=\left(33.7^2+\frac{0.0408D_{sph}^3\rho(\rho_s-\rho)g}{\mu^2}\right)^{0.5}-33.7 \tag{4.1.66}$$

4.1.11.2. Voidage in Particulate Fluidized Bed

As illustrated in Figure 4.1.18, the pressure drop across the bed remains more or less constant in the fluidization regime. One can assume that the Ergun's equation is still valid in the fluidized bed, but with varying voidage (ε) in the bed. In other words, the voidage is dependent on the superficial velocity. Since the pressure drop across the bed is equal to the apparent bed weight, one can write:

$$(1-\varepsilon)(\rho_s-\rho)g=\frac{150.0\mu(1-\varepsilon)^2}{D_p^2\varepsilon^3}v_0+\frac{1.75\rho(1-\varepsilon)}{\varepsilon^3 D_p}v_0^2 \tag{4.1.67}$$

In principle, the voidage in the fluidized bed (ε) can be determined by solving the above implicit nonlinear equation for a given superficial velocity, v_0. However, experimental investigations have indicated that the voidage measured in the bed is less than that predicted by the above equation. This may be due to the fact that the resistance offered by the bed on the gas flow changes with changing voidage in the bed.

Attempts have therefore been made for obtaining empirical correlations to predict the voidage in particulate fluidized beds with increasing superficial velocity. One such correlation based on a simple power law is proposed by Lewis *et al.* [19]:

$$v_0=\varepsilon^m \tag{4.1.68}$$

where the exponent m is obtained from a plot of m vs. Re_{D_p} as given in Figure 4.1.19 [20].

4.1.11.3. Voidage in Bubbling Fluidized Bed [21]

The bubbling fluidized bed also expands with increasing superficial velocity through the bed. Interestingly, experiments have shown that the primary contribution to this expansion comes from the bubble phase rather than relatively dense particulate–fluid phase. In other words, the voidage in the dense phase can be assumed as not increasing significantly with increasing superficial velocity, and the volume of gas flowing through this dense phase remains almost the same.

If ε_b represents the volume fraction of the bubble, v_b the bubble velocity, and v_{mf} is superficial velocity at the minimum fluidization point, then in a bubbling fluidized bed

$$v_0=\varepsilon_b v_b+(1-\varepsilon_b)v_{mf} \tag{4.1.69}$$

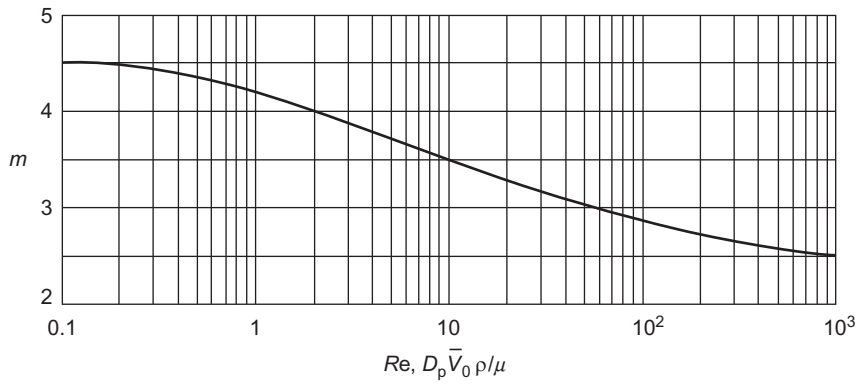


Figure 4.1.19 Exponent m in correlation for bed voidage in particulate fluidized bed [20].

The average velocity of the bubble, v_b, has been empirically correlated to the bubble size, D_b, as [21]

$$v_b = 0.711\sqrt{gD_b} \tag{4.1.70}$$

Experiments have also shown that large bubbles are generally mushroom shaped rather than spherical and for such cases D_b calculated based on bubble volume holds quite well.

Since the volume of the dense phase in a bubbling fluidized bed remains the same, the height of the fluidized bed, L, can be related to that at the minimum fluidization, L_{mf} as

$$L_{mf} = L(1 - \varepsilon_b) \tag{4.1.71}$$

4.1.12. FLOW AROUND PARTICLES

In many metallurgical processing systems, solid particles, liquid droplets, or gas bubbles dispersed in a fluid medium are common, e.g., solid particles in a liquid medium in sedimentation processes, solid particles in a gas medium in pneumatic screening processes and pneumatic transport of granular materials, solid or liquid inclusions in liquid metal, solid particles or liquid droplets in a spray-forming process, and gas bubbles in gas-stirred liquid metals. In all such systems where there is a relative movement between the dispersed phase and the continuous fluid medium, the movement of the particle is governed by the drag force arising from the viscosity of the fluid, the buoyancy force, and the gravitational force. Additional forces may also exist in the system such as those arising from electrostatic, magnetic, or electromagnetic phenomena. Even though these additional forces are not considered in the current section, these can be easily added to the governing equation.

In general, the governing equation for a dispersed phase of mass, m, moving in a fluid medium can be described using Newton's law of motion as

$$m\vec{a} = \vec{F}_{Drag} + \vec{F}_{Buoyancy} + m\vec{g} \tag{4.1.72}$$

where $\vec{a}$ is the acceleration of the dispersed phase.

For the case wherein the movement of the particle as well as the net force acting on the dispersed phase is either along the gravitational direction or against it, the above vectorial equation reduces to a simple scalar equation. When the dispersed phase has an axis of symmetry or a plane of symmetry parallel to the direction of its movement and has no rotational motion, the drag force acts exactly opposite to the direction of the movement of the particle. If not, the drag force need not be in line with its direction of movement resulting in what is termed as lift forces in addition to the drag forces. In many

metallurgical systems, the shape of the second phase may be approximated to a spherical shape using an appropriate sphericity factor discussed earlier and its motion as well as forces acting on it can be considered to be acting opposite to the flow direction. In the current section, only such cases are discussed.

For the case where the movement of the dispersed phase is along the gravitational direction (example: sedimentation of an ore particle in a liquid media), the force balance equation reduces to

$$ma = -F_{\text{Drag}} - F_{\text{Buoyancy}} + m\vec{g} \tag{4.1.73}$$

and for the case where the movement of the dispersed phase is opposite to the gravitational direction (example: bubble rising in a fluid),

$$ma = -F_{\text{Drag}} + F_{\text{Buoyancy}} - m\vec{g} \tag{4.1.74}$$

In both these cases, as the velocity of particle increases, the drag force opposing the motion increases as well. Eventually, the dispersed phase may reach a point where the net force acting on it becomes zero. Then, the dispersed phase attains a constant velocity, termed the terminal velocity. The concept of terminal velocity has been found to be quite useful in designing sedimentation systems, pneumatic screening processes, flotation of inclusions in liquid steel, etc.

In order to determine the net drag force acting on an object submerged in a flowing fluid, the concept of the friction factor is used. The definition of Fanning friction factor developed for flow through conduits using forces is extended to flows around submerged objects, also termed as external flows:

$$F_{\text{Drag}} = A\left(\frac{1}{2}\rho v_\infty^2\right) f_{\text{F}} \tag{4.1.75}$$

where A is the characteristic area, typically taken as the projected area of the solid on a plane perpendicular to the velocity of the approaching fluid, v_∞, ρ is the density of the fluid and f_{F} is the Fanning friction factor. For a spherical object of diameter D_{p}, the above equation becomes

$$F_{\text{Drag}} = \left(\frac{\pi D_{\text{p}}^2}{4}\right)\left(\frac{1}{2}\rho v_\infty^2\right) f_{\text{F}} \tag{4.1.76}$$

Using Buckingham's Π theorem, it can be easily proved that the friction factor, f_{F}, will be a function of the Reynolds number, Re_D. The Reynolds number Re_D is defined using the characteristic velocity v_∞ and the characteristic dimension, D_{p}.

Numerous studies, especially on the flow of fluids around spheres, have been carried out by many researchers. The important flow features from these studies are illustrated in Figure 4.1.20. Please note that a situation in which a spherical particle is seen to be

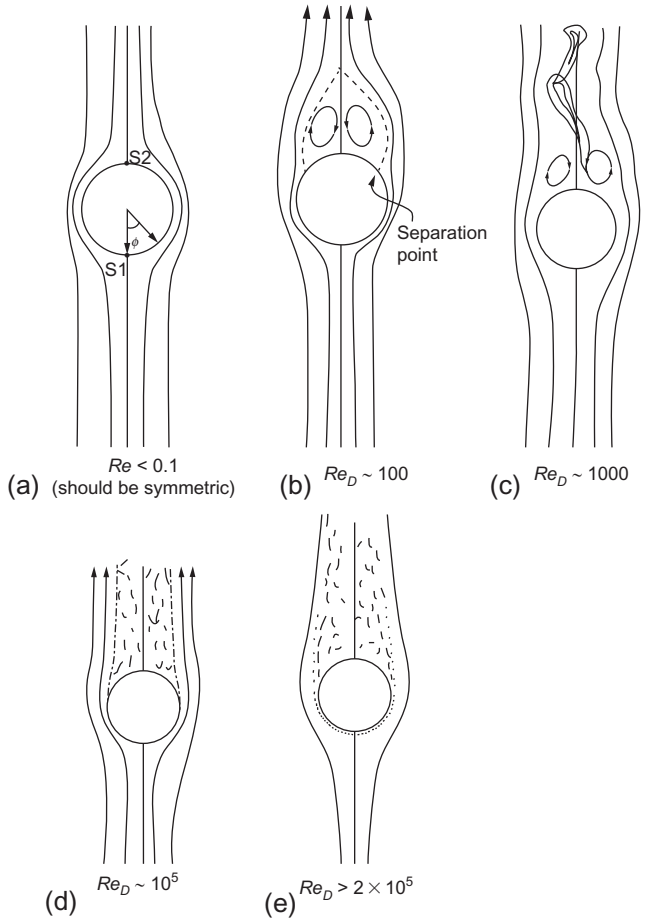


Figure 4.1.20 Schematic illustration of flow around a sphere.

moving in a fluid medium in the laboratory frame of reference can also be viewed as fluid moving around a stationary spherical particle if the frame of reference is attached to the moving particle.

At very low velocities ($Re_D < 0.1$), the viscous forces dominate over the inertial forces. As illustrated in the schematic (see Figure 4.1.20a), the flow lines are almost symmetrical on the front and the back side of the sphere. Stokes [22] obtained an analytical solution for the differential momentum balance equations along with the equation of continuity, for the asymptotic limit wherein the velocity is so small that one can neglect the advective momentum term (the differential momentum balance equations and the continuity equation are described in Section 4.1.14.2). Flows at such low velocities are termed as creeping flows. From the analytical expression, Stokes [22] found that

the net drag force acting on the sphere in the direction opposite to the flow direction has contributions both from the pressure and the tangential force (arising from the fluid velocity gradients at the surface of the sphere) acting on the surface of the sphere. The net force acting on the particle arising from the pressure is given by $\pi\mu D_p v_\infty$ and that from the tangential force is given by $2\pi\mu D_p v_\infty$. The first term is termed as the form drag and the latter as viscous drag or friction drag.

Thus the total drag force on the spherical particle is

$$F_{\text{Drag}} = 3\pi\mu D_p v_\infty \tag{4.1.77}$$

This is the Stokes law. Based on the definition used to describe the Fanning friction factor for external flows (refer to Equation 4.1.75), the Fanning friction factor for creeping flow around a sphere can be determined as:

$$f_F = \frac{24}{Re_D} \tag{4.1.78}$$

Experiments have shown that the Stokes law can be used to estimate the drag force with reasonable accuracy up to Re_{D_p} of 0.1. The law is useful for small particles moving in low viscosity gases and liquids as well as larger particles moving through viscous liquids.

Beyond the Stokes regime, it has not been possible to determine the drag force from theory alone; instead it needs to be estimated using dimensionless correlations developed using data obtained through experiments conducted by numerous researchers. The variation of Fanning friction factor, f_F, with the Reynolds number, Re_{D_p}, for spherical particles (sphericity $\phi = 1.0$, see Equation 4.1.53) is depicted in Figure 4.1.21. The figure gives the friction factor for some irregular particles too, where the particle size is defined based on the size of the sphere having equivalent volume (Equation 4.1.52).

Beyond the Stokes regime, the plot becomes nonlinear. Interestingly, the friction factor remains relatively constant at about 0.44 in the range of Reynolds numbers between 500 and 100,000; the drag force in this range is proportional to square of the velocity. This region is the Newton's regime. At Re_D greater than about 2×10^5, the flow all around the sphere becomes turbulent.

The variation in friction factor with Reynolds number can be correlated to some of the features observed in such flows. The region near the sphere where the velocity is significantly different from the undisturbed velocity in the free stream far away from the sphere is normally called the boundary layer. Any fluid packet flowing through the boundary layer undergoes accelerations and decelerations as it flows past the sphere. The packet approaching the sphere at a constant speed of v_∞ from far away decelerates as it comes close to the front of the sphere. It then accelerates as it flows past the sphere up to an angle of $\theta = 90°$, and then decelerates till it reaches the region near the rear. It again accelerates away downstream to reach the free stream value of v_∞. Bernoulli's equation

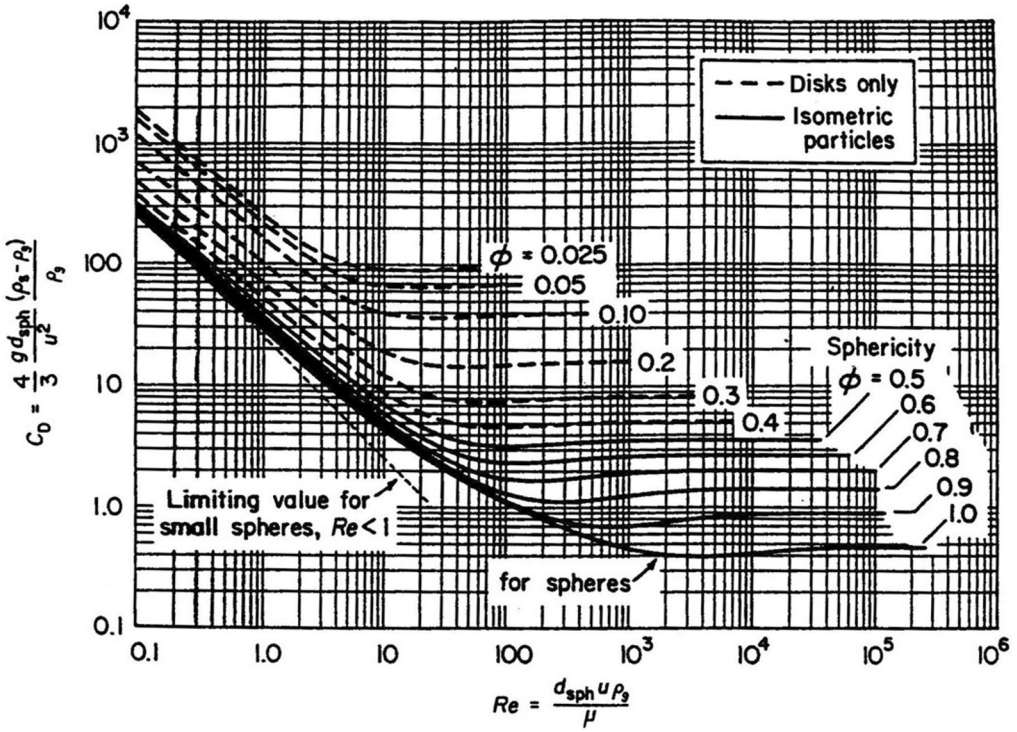


Figure 4.1.21 Fanning friction factor for flow across particles [1].

applied along a streamline helps understanding the pressure variations near the sphere. A fluid element reaching the surface of the sphere along the streamline normal to the sphere loses all its kinetic energy, which results in a corresponding increase in pressure. This high pressure point, called the front stagnation point, is shown as point S1 in Figure 4.1.20a. A second stagnation point, S2, is at the rear of the particle, diametrically opposite to S1. For an ideal fluid, the pressures at both S1 and S2 would be the same. Due to viscous dissipations in real fluids, however, the pressure at S2 is lower than that at S1. This asymmetry leads to a net force, called the form drag, along the flow direction. Additionally there is a viscous force, called the friction drag, due to transverse velocity gradients at the sphere surface. These two forces together form the total drag on the sphere (given by the Stokes law at low Reynolds numbers). Please note that the buoyancy force exists on the sphere irrespective of whether the fluid flows or not.

Due to the acceleration and deceleration in flow around the sphere, pressure decreases first (till $\theta = 90°$, Figure 4.1.20a) and then increases as the fluid flows toward the rear stagnation point. In the latter region, the flow is against a pressure gradient (uphill). The higher the velocity, the higher is the adverse pressure gradient. To avoid this uphill

pressure gradient, the flow *separates* at Re_D of about 20: the fluid moving towards the sphere moves away much earlier than the rear stagnation point. The fluid near the rear now remains attached to the sphere and recirculates in a toroidal fashion, as shown in Figure 4.1.20b. The point on the sphere that delineates the main flow from the recirculating region is called the separation point. The toroidal recirculating flow region is called the wake.

The size of the recirculating zone increases with increasing Reynolds number. It starts to oscillate at higher Reynolds numbers, and at Re_D of around 200, parts of it are *periodically* shed, i.e., they disengage from the sphere and move downstream as illustrated in Figure 4.1.20c. These recirculating flow formations traveling downstream are referred as vortices. A similar phenomenon of shedding of vortices is also observed in flows across long cylinders and other blunt shapes. In the case of cylinders, the shedding of vortices occurs alternately from each side of the cylinder. Interestingly, the frequency of vortex shedding in the case of cylinders correlates well with the free stream velocity and can be used as a measurement technique.

With further increase in Reynolds number, the flow in the wake region becomes more and more chaotic even as the flow before the separation point remains laminar. The separation point slowly moves upstream till the Reynolds number reaches a value of about 2×10^5 when it is positioned at an angle of approximately 85° (Figure 4.1.20d). Once this critical Reynolds number is exceeded, the boundary layer in the front of the particle itself turns turbulent. This delays separation (Figure 4.1.20e) and the separation point shifts to a point behind the sphere at an angle of approximately 140°. This shift results in a sharp drop in friction factor. Experiments have shown that the transition occurs at lower Reynolds numbers for spheres having rough surfaces. Many phenomena are manifestations of the interesting flow dynamics in the wake region: the spiral paths that some bubbles take, the flutter of a flag behind the flag pole, swing of a cricket ball, singing of overhead wires, etc.

4.1.13. COMPRESSIBLE FLOW

Flow of gases with velocities less than that corresponding to a Mach number of 0.3 can be treated as incompressible flows as discussed in Section 4.1.3. For incompressible flows, the term $\int \frac{dP}{\rho}$ in the mechanical energy balance (Equation 4.1.8) simplifies to $\frac{1}{\rho}\int dP$. For compressible flows, however, the integral needs to be evaluated with density varying as the fluid flows through the system. This, in turn, is governed by local temperature and pressure. Thus for rigorous evaluations, one needs to solve the heat transfer equation along with the equations governing the motion. In undertaking simple analyses, the flow can be considered under two extreme conditions, namely, (1) adiabatic and (2)

isothermal. If the flow is through a short conduit or nozzle, it can be approximated as adiabatic. For long conduits, where the surface area available for heat transfer per unit volume of gas flowing through the system is large, the flow is expected to be closer to isothermal conditions. In reality, the system would be somewhere between these two extreme cases, depending on heat transfer.

4.1.13.1. Compressible Flow Through a Pipe of Constant Cross Section

First, let us look at an adiabatic steady-state flow of an ideal gas from a reservoir through a straight pipe of length L and diameter D, as shown in Figure 4.1.22.

In this system, it is expected that both the velocity as well as the density of the gas changes as it flows through the pipe. However, from mass conservation it can be easily inferred that the average mass flux of gas through the pipe remains constant along the length of the pipe. Let us denote this mass flux by G and let $\hat{V}$ denote the specific volume of the gas. Then

$$\hat{V} = \frac{1}{\rho} \quad \text{and} \quad \nu = \frac{G}{\rho} = G\hat{V}$$

The differential mechanical energy balance given by Equation (4.1.10) can then be written in terms of G as,

$$G^2 \hat{V}\, \mathrm{d}\hat{V} + \hat{V}\, \mathrm{d}P + \frac{2 f_F}{D} G^2 \hat{V}^2\, \mathrm{d}L = 0 \tag{4.1.79}$$

Dividing the above equation by V^2, we obtain

$$G^2 \frac{\mathrm{d}\hat{V}}{\hat{V}} + \frac{\mathrm{d}P}{\hat{V}} + \frac{2 f_F}{D} G^2\, \mathrm{d}L = 0 \tag{4.1.80}$$

The above equation can be integrated from location 1 near the entrance to the exit point 2, assuming adiabatic flow, i.e.,

$$P\hat{V}^{\gamma} = \text{constant} \quad \text{where } \gamma = \frac{c_P}{c_{\hat{V}}} \tag{4.1.81}$$

Since at large Reynolds numbers the friction factor for pipe flow remains relatively constant, it is reasonable to assume that f_F remains the same throughout the length of the pipe. If so, integration of Equation (4.1.80) and substitution of Equation (4.1.81) gives:

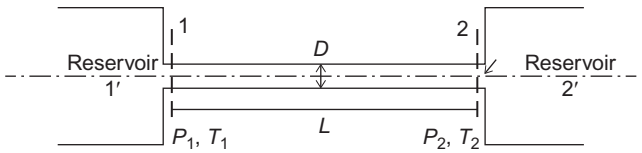


Figure 4.1.22 Schematic of a compressible flow through a straight pipe.

$$G^2 = \frac{\frac{\gamma}{\gamma+1}\frac{P_1}{V_1}\left[1-\left(\frac{P_2}{P_1}\right)^{(\gamma+1/\gamma)}\right]}{\left[2f_F\frac{L}{D}-\frac{1}{\gamma}\ln\frac{P_2}{P_1}\right]} \tag{4.1.82}$$

The above equation shows a very interesting trend. If G^2 is plotted as a function of P_2 keeping P_1 constant, it can be easily observed that G^2 goes through a maximum. By differentiating Equation (4.1.82) with respect to P_2 and equating it to zero, the maximum value of the mass flux and the corresponding velocity, v_{max}, can be obtained. This velocity is:

$$v_{max} = \sqrt{\frac{\gamma R T_2}{M}} = \sqrt{\left(\frac{\partial P}{\partial \rho}\right)_S} = c \tag{4.1.83}$$

where c corresponds to the sonic velocity under constant entropy (S).

Equation (4.1.82) suggests that beyond the maximum, decreasing the exit pressure P_2 (keeping P_1 constant) decreases the mass flux, which is nonphysical. This can only mean that this equation is not valid when P_2 is lowered below that corresponding to the maximum. In order to understand this, let us have a re-look at the experiment. Imagine initially the pressure at point 2 are equal to P_1. There will not be any flow of gas through the pipe. Now suppose the pressure at the reservoir at the exit end is decreased a little. The information of pressure decrease traverses at the speed of sound (speed of sound is the speed at which pressure disturbance travels through the medium) in the direction opposing the flow, a pressure profile develops in the tube and thus a steady flow is established. Once the velocity of the fluid reaches the sonic velocity, however, the information that the pressure has been decreased at reservoir 2 cannot reach the reservoir 1. In other words, the pressure at exit end (at point 2) of the pipe does not decrease beyond the critical value corresponding to the maximum mass flux. From the exit end of the pipe (point 2) to the reservoir 2 (point 2′), the pressure changes abruptly through a series of shock waves.

Once the maximum mass flux through the pipe is achieved, the mass flux cannot be altered by changing conditions at the exit end; the pipe is said to be choked. Further change in mass flux can be only achieved by changing the conditions at the upstream reservoir.

Similarly, the integration of Equation (4.1.80) can be undertaken under isothermal conditions for an ideal gas. The resulting expression for the mass flux, G, is:

$$G^2 = \frac{\frac{M}{2RT_1}\left(P_1^2 - P_2^2\right)}{2f_F\frac{L}{D} - \ln\frac{P_2}{P_1}} \tag{4.1.84}$$

Similar to the adiabatic flow, the velocity corresponding to the maximum mass flux (choked flow) is given by

$$v_{\max} = \sqrt{\frac{RT}{M}}$$

This corresponds to the speed of sound or sonic velocity under the isothermal assumption.

Example 4.1.7

Let us revisit the example problem 4.1.3 relaxing the assumption of flow being incompressible.

Solution

Let us use the same friction factor, f_F, of 0.0055.

Knowing the gas volumetric flow rate at STP, gas density at STP and the area of cross section of the pipe, the mass flux, G, can be determined and is equal to 1197 kg m^{-2}. As the pipe is very long, let us estimate the pressure drop assuming isothermal condition. If so, using the expression given in Equation (4.1.84), the value of P_1 can be calculated iteratively for a known value of P_2 (1.1×10^6 Pa) and T (300 K). The value of P_1 is equal to 1.92×10^6 Pa. The difference between this and the one calculated using incompressible flow is only 2%.

The pressure, P_1, can be estimated using adiabatic assumption as well using Equation (4.1.82) and its value is equal to 1.67×10^6 Pa. The difference between this value and the one calculated using incompressible flow assumption is 19%. This indicates that the assumption of isothermal conditions for this problem gives values close to that obtained for incompressible flow. For long tubes, the assumption of the isothermal flow may be more reasonable for the reasons mentioned earlier.

4.1.13.2. Compressible Flow Through Convergent–Divergent (de Laval) Nozzle

In the last section, we saw that for a compressible fluid, the exit velocity through a pipe of constant cross section cannot exceed the sonic velocity. To achieve velocities beyond sonic velocities, i.e., supersonic velocities, a convergent–divergent nozzle, otherwise called de Laval (named after a Swedish scientist who invented it in 1888) nozzle is used. In BOF, these nozzles are used to generate supersonic flow of oxygen that penetrates the liquid metal and slag and aids in achieving the rapid refining of steel.

A schematic of a convergent–divergent nozzle is shown in Figure 4.1.23. The diverging section is long compared to the converging section. The area of cross section changes slowly in the diverging section in order to suppress boundary layer separation. However, the converging section is short as the boundary layer separation does not occur in this section. The location where the cross-sectional area is the minimum is termed as the throat of the nozzle. As the total length of the nozzle is small, a simple analysis can be made by considering the flow to be adiabatic with negligible friction losses.

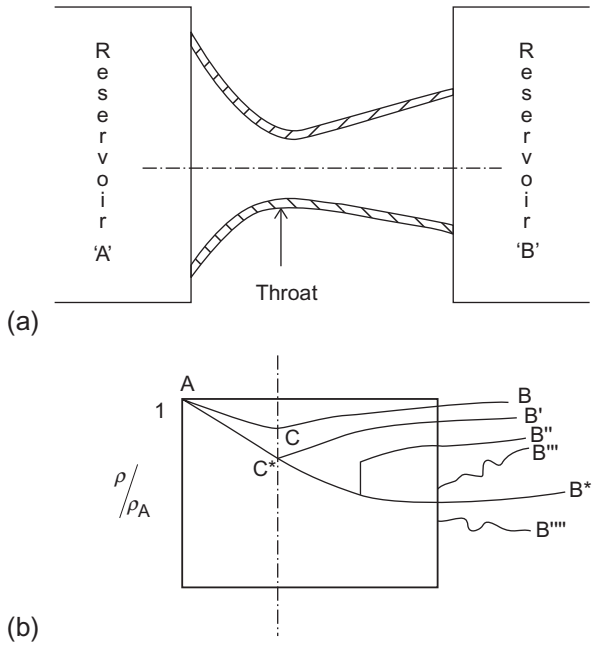


Figure 4.1.23 (a) Schematic of a convergent–divergent (de Laval) nozzle and (b) schematic of the pressure profiles under various flow regimes.

At steady state, the mass flow rate of gas through the nozzle remains constant along the length of the nozzle, i.e.,

$$A\rho v = \dot{m} = \text{constant}$$

$$\text{Thus } \frac{dA}{A} + \frac{d\rho}{\rho} + \frac{dv}{v} = 0 \tag{4.1.85}$$

The mechanical energy balance equation (Equation 4.1.10), neglecting the friction loss term, reduces to

$$\frac{dP}{\rho} + v\,dv = 0 \tag{4.1.86}$$

Using the above equation and Equation (4.1.83) in Equation (4.1.85), we obtain

$$\frac{dv}{v}\left(1 - \frac{v^2}{c^2}\right) + \frac{dA}{A} = 0$$

$$\frac{dv}{v}\left(1 - Ma^2\right) + \frac{dA}{A} = 0 \tag{4.1.87}$$

From this equation, it can be inferred that through the converging section $\left(\frac{dA}{A} < 0\right)$, for subsonic flows ($Ma < 1$), the velocity of the flowing gas increases $\left(\frac{dv}{v} > 0\right)$. Similarly, through a diverging nozzle $\left(\frac{dA}{A} > 0\right)$, for subsonic flows ($Ma < 1$), the velocity of the

flowing gas decreases along the direction of the flow. This trend is the same as that for flow of incompressible fluids through converging or diverging sections. For supersonic flows ($Ma > 1$), on the other hand, the trend reverses, i.e., the velocity decreases through a converging section and increases through a diverging section. This implies that supersonic flows can only be obtained if at the throat $\left(\frac{dA}{A} = 0\right)$ the velocity is sonic.

Before deriving the design equations for a supersonic nozzle, it is instructive to understand the flow regimes that are obtained when operating a convergent–divergent nozzle under different pressure differences. In Figure 4.1.23, a schematic of a converging–diverging nozzle connected across two gas reservoirs is shown. Keeping the pressure and temperature at reservoir A constant and by progressively reducing the pressure at reservoir B, various flow regimes are obtained. Figure 4.1.23b gives the profiles of pressure ratio, $\frac{P}{P_A}$ (P_A is the pressure at reservoir A or stagnation pressure) corresponding to each flow regime. The regimes are as follows:

Subsonic flow: Suppose the pressure at reservoir B (placed at the exit end of the nozzle) is decreased slowly starting from a value equal to P_A. In the beginning, the flow would be subsonic throughout the nozzle; the velocity increases and reaches a maximum at the throat and beyond the throat it decreases. The pressure would correspondingly decrease in the converging section reaching a minimum at the throat (point C) and increase in the diverging section. This is similar to a flow of incompressible fluid through a venturi. The pressure profile is shown in the figure 4.1.23b as ACB.

Flow is just choked: As the flow rate through the nozzle is increased, a situation arises when the velocity at the throat is sonic and the nozzle is choked. Two situations can take place: the flow can become subsonic in the diverging portion and the pressure can reach B′ along AC*B′. The flow can instead become supersonic, in which case the pressure follows the path PC*B* and the exit pressure would be at B*. This latter is the designed operation, the flow transitioning from subsonic to supersonic smoothly and reversibly.

Flow with a normal shock in the nozzle: Since flow cannot have a reversible transition from subsonic to supersonic state, or vice versa, in a diverging region, pressure between B′ and B* is not reachable by reversible expansions. If an exit pressure is maintained at a value between B′ and B*, the flow has to become irreversible somewhere in the diverging section. In the diverging section, the pressure suddenly jumps from a low value to a higher value through what is termed as a normal shock, as illustrated in the figure (see curve AC*B″). Across the shock the flow changes suddenly from supersonic to subsonic. The shock wave moves toward the exit end of the nozzle decreasing in intensity as the pressure at B is progressively decreased and eventually, the shock wave would reach the exit end and disappear at the designed exit pressure of B*.

Under expanded flow: Decreasing the pressure in reservoir B below B* cannot change the flow inside the nozzle. Pressure at the exit remains at B*, and decreases outside the nozzle to the reservoir pressure B"" through a series of oblique shock waves. This jet is said to be under-expanded in the nozzle.

Irreversible phenomena such as shock waves dissipate mechanical energy into internal energy of the gas. A supersonic nozzle is designed for a given exit Mach number and pressure drop and should therefore be operated at design conditions.

Analytical expressions for pressure and velocity distribution along the length of the nozzle can easily be obtained for idealized conditions, wherein the gas flow through the de Laval nozzle can be approximated as adiabatic frictionless flow of an ideal gas (isentropic flow).

Equation (4.1.86) can be integrated using Equation (4.1.81). If the gas velocity in the supply tube is small compared to the sonic velocity, the contribution to kinetic energy can be neglected. Then we obtain at any section

$$v^2 = \frac{2}{(\gamma-1)}\frac{\gamma P}{\rho}\left[\left(\frac{P_A}{P}\right)^{(\gamma-1/\gamma)} - 1\right] \tag{4.1.88}$$

In terms of Mach number, Ma (sonic velocity, $v_s = \sqrt{\frac{\gamma P}{\rho}}$):

$$Ma^2 = \frac{2}{(\gamma-1)}\left[\left(\frac{P_A}{P}\right)^{(\gamma-1/\gamma)} - 1\right] \tag{4.1.89}$$

For a choked nozzle, the Mach number at the throat has to be 1, hence,

$$\frac{P_{C^*}}{P_A} = \left(\frac{2}{\gamma+1}\right)^{(\gamma/\gamma-1)} \tag{4.1.90}$$

Similarly for a given Mach number at the exit, $\frac{P_B}{P_A}$ can be determined as

$$Ma_B^2 = \frac{2}{(\gamma-1)}\left[\left(\frac{P_A}{P_B}\right)^{\gamma-1/\gamma} - 1\right] \tag{4.1.91}$$

It should be noted that adiabatic flow results in continuous change in temperature of the gas and therefore the sonic velocity. The Mach number at any location is defined with respect to the sonic velocity at that point. Sonic velocities at A, B, and C are therefore different. From the pressures, the temperatures, the densities, and the velocities can be calculated at various locations throughout the length of the nozzle. Using these values, one can determine the dimensions of the nozzle.

4.1.14. MOMENTUM BALANCE AT DIFFERENTIAL SCALE

In Section 4.1.1.2, it was stated that the conservation equations can be applied at a macroscopic scale or at a differential scale depending on the objective. To this point in the discussion, the conservation principle has been applied at a macroscopic scale in most of the situations. For example, an overall energy balance pertaining to flow (see Section 4.1.4) is developed at a macroscopic scale to relate the net flow rate and the pressure drop, wherein the interest was not really to capture the detailed flow profiles in a system. For obtaining a

detailed flow profile in the fully developed flow region in a pipe, momentum balances were indeed made at a differential scale; this, however, was for a simple 1D steady-state flow. For 3D flows, this approach needs to be generalized.

In a generic case of a flowing fluid, it is desirable to know the spatial and temporal variation of velocities as well as the pressure in the system. Velocity being a vector needs to be described using three of its components according to the coordinate system. Thus, including pressure, the number variables add up to four; therefore four equations are required to obtain the flow profiles in any system. These four equations correspond to one of mass conservation and three momentum conservation equations corresponding to each component of velocity. The mass conservation equation (for an incompressible fluid this would lead to volume conservation) at the differential scale this is termed the equation of continuity. The momentum conservation at a differential scale for an incompressible Newtonian fluid having constant viscosity leads to one of the celebrated equations in fluid dynamics, the Navier–Stokes equation. In the following sections, the equation of continuity and the Navier–Stokes equation are described in detail. These equations are derived in Cartesian coordinates and these equations can also be transformed to other coordinate systems of interest such as cylindrical, spherical coordinates.

4.1.14.1. Equation of Continuity

Consider an infinitesimal control volume in a flowing fluid as shown in Figure 4.1.24. The control volume is located at (x,y,z) with respect to a chosen Cartesian coordinate system. The shape of the control volume corresponds with that of the coordinate system and its dimensions are Δx, Δy, and Δz.

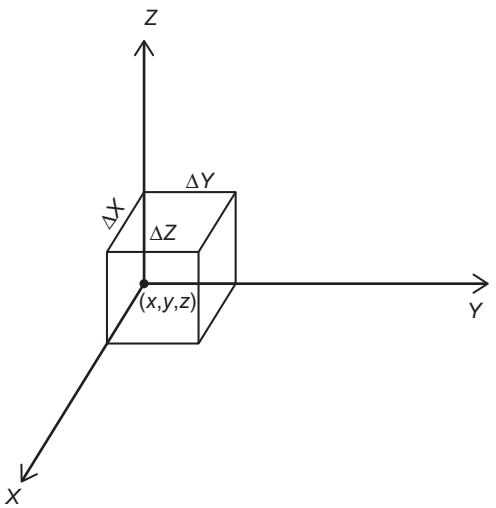


Figure 4.1.24 Infinitesimal control volume in Cartesian coordinates.

Let $v_x(x,y,z)$, $v_y(x,y,z)$, and $v_z(x,y,z)$ denote the x-, y-, and z-velocity components, respectively, and $\rho(x,y,z)$ denote density of the fluid at the location (x,y,z). Considering the conservation of mass in the control volume,

$$\begin{aligned}\frac{\partial\rho}{\partial t}_{\left(x+\frac{\Delta x}{2},y+\frac{\Delta y}{2},z+\frac{\Delta z}{2}\right)}\Delta x\Delta y\Delta z = &\left(\rho v_x\right)\big|_{x,y+\frac{\Delta y}{2},z+\frac{\Delta z}{2}} - \left(\rho v_x\right)\big|_{(x+\Delta x,y+\frac{\Delta y}{2},z+\frac{\Delta z}{2})}\\ &\left(\rho v_y\right)\big|_{x+\frac{\Delta x}{2},y,z+\frac{\Delta z}{2}} - \left(\rho v_y\right)\big|_{(x+\frac{\Delta x}{2},y+\Delta y,z+\frac{\Delta z}{2})}\\ &\left(\rho v_z\right)\big|_{x+\frac{\Delta x}{2},y+\frac{\Delta y}{2},z} - \left(\rho v_y\right)\big|_{(x+\frac{\Delta x}{2},y+\frac{\Delta y}{2},z+\Delta z)}\end{aligned} \tag{4.1.92}$$

Dividing the above equation by $\Delta x\Delta y\Delta z$ and taking the limit as the control volume is reduced to zero, the Equation (4.1.92) reduces to

$$\frac{\partial\rho}{\partial t} + \nabla\cdot\left(\rho\,\vec{v}\right) = 0 \tag{4.1.93}$$

This is the equation of continuity for any fluid. Here $\rho\vec{v}$ is the mass flux vector and $\nabla\cdot(\rho\vec{v})$ gives the net rate of mass flowing out of a unit volume fixed in space. Since $\nabla\cdot(\rho\vec{v}) = \rho(\nabla\cdot\vec{v}) + \vec{v}\cdot\nabla\rho$, it can be shown that

$$\frac{\mathrm{D}\rho}{\mathrm{D}t} = \frac{\partial\rho}{\partial t} + \vec{v}\cdot\nabla\rho = -\rho\left(\nabla\cdot\vec{v}\right)$$

$\frac{\mathrm{D}\rho}{\mathrm{D}t}$ is the material or substantial derivative and gives the change in density of fluid packet as it travels (Lagrangian frame of reference). $\nabla\cdot\vec{v}$ is the rate of change of volume for the fluid packet.

If the flow is steady, then

$$\nabla\cdot\left(\rho\,\vec{v}\right) = 0 \tag{4.1.94}$$

If the flow is also incompressible, then

$$\nabla\cdot\left(\vec{v}\right) = 0 \tag{4.1.95}$$

4.1.14.2. Navier–Stokes Equation

In the control volume considered in Section 4.1.14.1, let us perform an x-momentum balance, i.e., balancing the x component of the momentum. For momentum conservation, the accumulation of momentum in the control volume, the rate at which the momentum enters and leaves the control volume, and the forces acting on the control volume need to be considered. As far as momentum being transported in and out of the control volume is concerned, there are basically two modes of transport, one by advection and another by momentum diffusion or viscous transport. Let us denote the diffusive momentum flux by τ_{ij}, where "i" denotes the direction in which the "j" component of momentum is transported. The reader may refer to Section 4.1.5 where the diffusive momentum flux has been elaborated.

It should be noted that the diffusive momentum flux, τ_{ii}, arises as the velocity component, v_i, changes in the "i" direction.

Let us look at each term in the x-momentum conservation one by one

Rate of accumulation:

$$\frac{\partial(\rho v_x)}{\partial t}\Big|_{\left(x+\frac{\Delta x}{2},\,y+\frac{\Delta y}{2},\,z+\frac{\Delta z}{2}\right)}\cdot\Delta x\cdot\Delta y\cdot\Delta z$$

Advective momentum transfer:

Rate of advective x-momentum entering through surface $x=x$ in the control volume

$$(\rho v_x v_x)\big|_{\left(x,\,y+\frac{\Delta y}{2},\,z+\frac{\Delta z}{2}\right)}\cdot\Delta y\cdot\Delta z$$

and the rate leaving the control volume at $x=x+\Delta x$ is

$$(\rho v_x v_x)\big|_{\left(x+\Delta x,\,y+\frac{\Delta y}{2},\,z+\frac{\Delta z}{2}\right)}\cdot\Delta y\cdot\Delta z$$

Advective x-momentum entering through surface $y=y$ in the control volume

$$\left(\rho v_y v_x\right)\big|_{\left(x+\frac{\Delta y}{2},\,y,\,z+\frac{\Delta z}{2}\right)}\Delta x\Delta y$$

Please note that the net mass entering through the surface $y=y$ is

$$\left(\rho v_y\right)\big|_{\left(x+\frac{\Delta y}{2},\,y,\,z+\frac{\Delta z}{2}\right)}\Delta x\Delta y$$

and this fluid's x component of velocity is v_x

Similarly, advective momentum entering through surfaces $z=z$ as well as leaving through surfaces $y=y+\Delta y$ and $z=z+\Delta z$ can be written.

Viscous or diffusive momentum:

Rate of viscous momentum entering through face $x=x$ is

$$\tau_{xx}\big|_{\left(x,\,y+\frac{\Delta y}{2},\,z+\frac{\Delta z}{2}\right)}\Delta y\cdot\Delta z$$

and the viscous momentum entering through face $y=y$ is

$$\tau_{yx}\big|_{\left(x+\frac{\Delta x}{2},\,y,\,z+\frac{\Delta z}{2}\right)}\cdot\Delta y\cdot\Delta z$$

Similarly, viscous momentum entering through surfaces $z=z$ as well as leaving through surfaces $x=x+\Delta x$, $y=y+\Delta y$, and $z=z+\Delta z$ can be written.

Forces acting on the control volume along the x-direction

Due to pressure

$$\left(P|_{(x,y+\frac{\Delta y}{2},z+\frac{\Delta z}{2})} - P\Big|_{(x+\Delta x,y\frac{\Delta y}{2},z+\frac{\Delta z}{2})}\right)\Delta y\Delta z$$

Due to gravity

$$\rho\Delta x\Delta y\Delta z g_x$$

where g_x is a component of acceleration due to gravity (g), along the x-direction.
It may be noted that if there are additional forces acting on the fluid, such as those arising from electromagnetic interaction, they can be appropriately incorporated as source terms in the conservation equation.

All these terms are put together using the conservation equation (Equation 4.1.1) and dividing by $\Delta x\Delta y\Delta z$ and taking the limit as the control volume is reduced to zero, the following expression is obtained

$$\begin{aligned}\frac{\partial \rho v_x}{\partial t} = &-\frac{\partial \rho v_x v_x}{\partial x} - \frac{\partial \rho v_y v_x}{\partial y} - \frac{\partial \rho v_z v_x}{\partial z} \\ &-\frac{\partial \tau_{xx}}{\partial x} - \frac{\partial \tau_{yx}}{\partial y} - \frac{\partial \tau_{zx}}{\partial z} \\ &-\frac{\partial P}{\partial x} + g_x\end{aligned} \tag{4.1.96}$$

Similar equations can be written for y- and z-momentum.

In deriving Equation (4.1.96), no assumptions have been made regarding the nature of the fluid (Newtonian or non-Newtonian) or the nature of the flow (laminar, transition, turbulent). In this form, these equations are therefore applicable for all types of fluids and flows, and are therefore termed generalized, differential momentum balance equations. These equations contain five unknowns: ρ, P, v_x, v_y, and v_z. These equations along with the continuity equations, Equation (4.1.93), and the equation of state for the fluid, which relates ρ to P and T, should be solved. If, in addition, temperatures are varying, the heat transfer equation should be solved simultaneously.

Before attempting to solve these equations, the constitutive equations for the fluid under consideration relating τ_{ij} with the velocity gradients should be written. For 1D flow of simple fluids it is the Newton's law of viscosity presented earlier in Equation (4.1.15). Even for these Newtonian fluids, the relationships in 3D flows are elaborate and are given by Stokes' relationships discussed below. For non-Newtonian fluids, such relationships can be even more elaborate.

Evidently, solutions of these equations are difficult. Analytical solutions do not exist, except for a few, very simple cases. For most systems of engineering interest, solutions need to be obtained numerically. Though several computational fluid dynamics (CFD) software codes are available, the effort involved in obtaining solutions is still very

large, even for laminar flows. Turbulent flows present further difficulties. Spatial variation of velocity is now at a very fine scale (inside eddies), and there is a certain stochasticity in the temporal variations. Direct numerical simulation (DNS) of these flows has to be at these fine scales of space and time, making computation intractable except for small regions. These turbulent flows are therefore "modeled" in terms of some new parameters that are smoother functions but still capture the effects of fine-scale variations. Turbulence models are briefly presented in Section 4.1.15. However, more elaborate description can be found in *Chapter 4, Treatise on Process Metallurgy, Volume 2: Process Phenomena.*

For a generalized flow of a Newtonian fluid, Stokes developed expressions for viscous momentum flux based on the primary assumption that the fluids are isotropic. Details regarding the development of Stokes relations can be found elsewhere [1]. The relationships valid for constant ρ and μ are:

$$\text{Normal components}: \tau_{ii} = -2\mu\frac{\partial v_i}{\partial i} \tag{4.1.97}$$

$$\text{Shear components}: \tau_{ij} = \tau_{ji} = -\mu\left(\frac{\partial v_i}{\partial j} + \frac{\partial v_j}{\partial i}\right)$$

Substituting these relationships into the momentum conservation equation, Equation (4.1.96), and using the equation of continuity, the following expression is obtained after rearrangement

$$\rho\left(\frac{\partial v_x}{\partial t} + v_x\frac{\partial v_x}{\partial x} + v_y\frac{\partial v_x}{\partial y} + v_z\frac{\partial v_x}{\partial z}\right) = \mu\left(\frac{\partial^2 v_x}{\partial x^2} + \frac{\partial^2 v_x}{\partial y^2} + \frac{\partial^2 v_x}{\partial z^2}\right) - \frac{\partial P}{\partial x} + \rho g_x \tag{4.1.98}$$

Similar equations can be written for the y- and z-momentum balances.

These are the Navier–Stokes equations valid for Newtonian fluids with constant ρ and μ. The expression on the left-hand side of Equation (4.1.98) denotes the x component of the acceleration of a particular fluid packet, i.e., in a Lagrangian frame of reference where the frame is moving with the fluid packet. In terms of the substantial or material derivative, the equation is:

$$\rho\frac{\mathrm{D}v_x}{\mathrm{D}t} = \mu\nabla^2 v_x - \frac{\partial P}{\partial x} + \rho g_x \tag{4.1.99}$$

Thus the Navier–Stokes equation can be interpreted as

$$\rho\frac{\mathrm{D}v_x}{\mathrm{D}t} = \rho a_x = \text{Viscous forces} + \text{Force due to pressure} + \text{Force due to gravity} \tag{4.1.100}$$

which describes Newton's first law of motion for a unit volume fluid packet.

In vector form, the equation can be written as

$$\rho\frac{\mathrm{D}\vec{v}}{\mathrm{D}t}=\mu\left(\nabla\cdot\nabla\vec{v}\right)-\nabla P+\rho\vec{g} \tag{4.1.101}$$

The generalized equations are solved for particular systems by removing those terms that are either zero or insignificant and with appropriate boundary conditions, as the example below will demonstrate.

Example 4.1.8

Consider a Newtonian fluid such as water flowing steadily down an inclined plane as shown in Figure 4.1.25a. In the region of this plane away from entrance at the top, exit from the bottom, and the side plates, the flow may be considered to be fully developed: the velocity is unidirectional and varies only in the x-direction. We need to develop a relationship for the velocity profile.

Since $v_x=v_y=0$, the equation of continuity (Equation 4.1.95) for an incompressible fluid gives

$$\frac{\partial v_z}{\partial z}=0$$

which is to be expected in a fully developed region. The z-component Navier–Stokes equation is:

$$\rho\frac{\partial v_z}{\partial t}+v_x\frac{\partial v_z}{\partial x}+v_y\frac{\partial v_z}{\partial y}+v_z\frac{\partial v_z}{\partial z}=+\mu\left(\frac{\partial^2 v_z}{\partial x^2}+\frac{\partial^2 v_z}{\partial y^2}+\frac{\partial^2 v_z}{\partial z^2}\right)-\frac{\partial P}{\partial z}+\rho g_z$$

This equation can be simplified as follows:

LHS is zero, since $\frac{\partial v_z}{\partial t}=0$ (steady state), $v_x=v_y=0$ (fully developed), and $\frac{\partial v_z}{\partial z}=0$ (continuity)

On the RHS, $\frac{\partial^2 v_z}{\partial z^2}=0$ (continuity) and $\frac{\partial^2 v_z}{\partial y^2}=0$ (far away from the side plates)

The equation is reduced to:

$$\mu\frac{\partial^2 v_z}{\partial x^2}=\frac{\partial P}{\partial z}=-\rho g_z \tag{4.1.102}$$

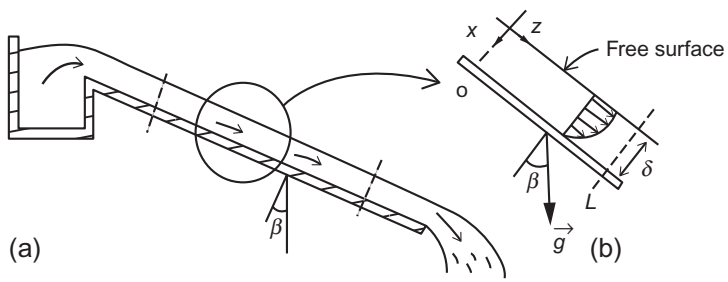


Figure 4.1.25 (a) Laminar flow over an inclined plane (b) Zoomed view of the circled section in (a).

An examination of the x- and y-component momentum equations will reveal (since $v_x = v_y = 0$)

$$\frac{\partial P}{\partial x} = \rho g_x \quad \text{and} \quad \frac{\partial P}{\partial y} = \rho g_y$$

Since $x = 0$ is a free surface, pressure is atmospheric and may be assumed as a constant for all z. Therefore for any x, the pressure $P = P_0 + \rho g_x x$ is independent of z. Therefore, $\frac{\partial P}{\partial z} = 0$.

Hence Equation (4.1.102) simplifies to

$$\mu \frac{\partial^2 v_z}{\partial x^2} = -\rho g_z = -\rho g \sin \beta \tag{4.1.103}$$

Integrating the above equation,

$$v_z = -\frac{\rho g \sin \beta x^2}{2\mu} + C_1 x + C_2$$

where C_1 and C_2 are constants of integration to be evaluated with the boundary conditions.

Boundary condition 1: At the water–air interface ($x = 0$), air offers negligible resistance for the water flow. Therefore

$$\tau_{xz}|_{x=0} = -\mu \frac{\partial v_z}{\partial x}|_{x=0} = 0 \Rightarrow C_1 = 0$$

Boundary condition 2: At $x = \delta$, $v_z = 0$ (no-slip boundary condition)

$$C_2 = \frac{\rho g \sin \beta \delta^2}{2\mu}$$

Hence the velocity profile is

$$v_z = \frac{\rho g \sin \beta \delta^2}{2\mu} \left[1 - \left(\frac{x}{\delta}\right)^2\right]$$

The average velocity of the flowing film is:

$$\overline{v}_z = \frac{\rho g \sin \beta \delta^2}{3\mu}$$

4.1.15. MODELS OF TURBULENCE

In Section 4.1.4, the need to account for the friction losses was discussed. These friction losses result from work against frictional forces associated with velocity gradients. If the velocity field is fully known, these friction losses can be estimated, as shown for laminar flow through circular pipes in Section 4.1.6. Even fairly involved

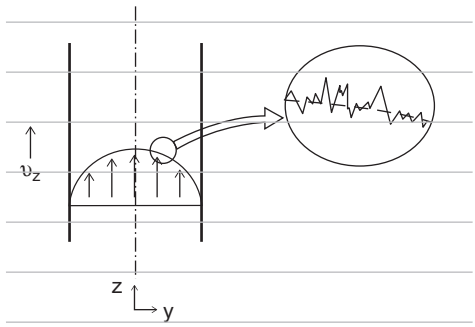


Figure 4.1.26 Schematic of the average velocity flow profile in a turbulent flow through a pipe.

2D and 3D laminar flow profiles can in principle be obtained from the continuity and the momentum balance equations within reasonable computational cost. Once the flow becomes turbulent, however, the velocity profiles develop a fine structure both spatially and temporally. Though a macroscopic representation of a velocity profile for turbulent flow may seem to be smooth, as for example, flow through a tube (Figure 4.1.26), at a much finer scale the velocity changes sharply over very small distances (inset in the figure). Further, these profiles change significantly in short time spans, even when the average flow shows the flow to be steady or changing slowly. Very fine space-wise grids and small time steps need to be employed (as in direct numerical simulation, DNS) to capture these phenomena, making it computationally unviable except for very simple flows over small regions.

Two approaches are employed to handle the turbulent flow in systems of interest in engineering. The expedient approach is to rely on empirical correlations to estimate the losses developed through dimensional analysis and experiments and perform conservation at the macroscopic scale as was done in the case of pipes earlier. In many systems, including those pertaining to process metallurgy, one may further be interested in investigating the flow characteristics in detail, i.e., the velocity variations within the system, and this can help in improving system performance and control through modification in design and operation. Experimental studies can be designed through similarity criteria, as has been done to understand flow in many process vessels such as ladles, BOF vessels, continuous casting tundish, and mold.

The second approach is to model the fine-scale turbulent characteristics in terms of a few parameters that are smooth functions over system dimensions and process time. These parameters, for example, the local rate of dissipation of mechanical energy, capture the effect of the fine-scale variations without performing calculations at the microscopic level. The parameters themselves are related to the microscopic flow characteristics that are being estimated through semi-empirical correlations. Such an approach is computationally more viable than the DNS, and at the same time gives more information

about the process than the purely empirical approach. Examples of these approaches are briefly discussed in the following section. Readers can find more detailed description of all these topics in *Chapter 4, Treatise on Process Metallurgy, Volume 2: Process Phenomena*.

4.1.15.1. Generic Flow Features in Turbulent Flows

Leonardo da Vinci (sixteenth century) was possibly the earliest to recognize and record the distinct features of turbulent flows, a copy of which can be found in Professor J. M. McDonough's lecture notes on turbulence [23]. In his lecture notes, Professor J. M. McDonough also gives the modern description of da Vinci's rendition, as is reproduced below

> *. . .the smallest eddies are almost numberless, and large things are rotated only by large eddies and not by small ones, and small things are turned by small eddies and large.*

da Vinci termed the phenomena as "turbolenza," which corresponds to the modern word turbulence.

Reynolds' experiments on laminar and turbulent flows have already been presented in Section 4.1.3. With developments in flow visualization and measurement techniques, numerous investigations have been carried out to understand turbulent flows subsequent to Reynolds' experiments. Hinze, in his book on turbulence [24], summarizes turbulence based on these observations as "an irregular condition of the flow in which various quantities show a random variation with time and space coordinates, so that statistically distinct averages can be discerned."

With growing super computing power, it is widely accepted that the flow in the finest temporal and spatial scales can be deterministically predicted by equations such as the Navier–Stokes equation, and the randomness that is observed is due to high levels of sensitivity to initial conditions and boundary conditions at these finest scales. However, solutions by direct numerical simulations (DNS) at these fine time and length scales at present are restricted only to simple flows and are not amenable for large systems with the available computing resources.

Chapman and Tobak [25] summarized the evolution of the understanding of turbulence as three overlapping areas of (i) statistical (because of random variations with distinct averages), (ii) structural (because of eddies), and (iii) deterministic (in principle, turbulent flow can be obtained from Navier–Stokes equations). Turbulence models can also be classified along the same lines.

The models that are based on statistical methodologies applied to Navier–Stokes equations are addressed in a generic fashion, as Reynolds-averaged Navier–Stokes (RANS) equations. RANS models, especially, the κ–ϵ model, have been extensively used to understand flows in metallurgical systems (see *Chapter 4, Treatise on Process Metallurgy, Volume 2: Process Phenomena*). DNS techniques, on the other hand, are at present

largely restricted to understanding the nature of turbulence, due to high computational costs [23]. Large eddy simulations (LES), first proposed by Deardorff [26], lie somewhere between RANS and DNS and have been used to study some of the metallurgical flows in the recent past. In the following sections, a brief introduction to RANS and LES models are presented; details can be found elsewhere [23].

4.1.15.2. RANS Models

One of the important characteristic features of turbulent flow is mixing at the macroscopic level due to advective transport at the microscopic level from the random movements. This can be visualized macroscopically as enhanced diffusive transport. Many models simulate turbulent flow using an enhanced viscosity referred to as turbulent viscosity or eddy viscosity. Unlike molecular viscosity, turbulent viscosity is not just a fluid property, it is a property of the flow including geometry, and it is not constant in the flow domain.

RANS models of turbulence aim to determine this turbulent or eddy viscosity based on the statistical analysis of Navier–Stokes equations. The first step in such an analysis is to perform time smoothening of the Navier–Stokes equation; this is briefly described below.

Any instantaneous velocity in a turbulent flow can be split into a mean value, $\overline{v}$, and a fluctuating component, v'. This is referred to as Reynolds decomposition and can be written as

$$\mathbf{v} = \overline{\mathbf{v}} + \mathbf{v}'$$

The average here refers to an "ensemble average": averaged over several identical systems, measurements being made at a corresponding space point and time. Here, average of $\mathbf{v}'$, i.e., $\overline{\mathbf{v}}'$, is zero, since the fluctuations are truly random.

Substituting the above in Navier–Stokes equation and subsequently performing the smoothening (mean operation) result in the following equation (for x-momentum)

$$\rho\left(\frac{\partial \overline{v}_x}{\partial t}+\frac{\partial \overline{v}_x\overline{v}_x}{\partial x}+\frac{\partial \overline{v}_x\overline{v}_y}{\partial y}+\frac{\partial \overline{v}_x\overline{v}_z}{\partial z}\right) = -\frac{\partial \overline{\rho v_x' v_x'}}{\partial x}-\frac{\partial \overline{\rho v_x' v_y'}}{\partial y}-\frac{\partial \overline{\rho v_x' v_z'}}{\partial z} + \mu\left(\frac{\partial^2 \overline{v}_x}{\partial x^2}+\frac{\partial^2 \overline{v}_x}{\partial y^2}+\frac{\partial^2 \overline{v}_x}{\partial z^2}\right)-\frac{\partial \overline{P}}{\partial x}+\rho g_x \quad (4.1.104)$$

As the inertial terms or advective terms in the Navier–Stokes equations are nonlinear, smoothening of these terms gives rise to additional terms, namely, $\overline{\rho v_x' v_x'}$, $\overline{\rho v_x' v_y'}$, and $\overline{\rho v_x' v_z'}$. There will be also six more additional terms arising from y- and z-momentum equations. These terms together are called Reynolds stresses or turbulent momentum fluxes. Analogous to molecular viscosity, these turbulent momentum fluxes are modeled using "turbulent viscosity" and the gradient of averaged velocity field. This is expressed as

$$\overline{v_x' v_z'} = -v_T \left(\frac{\partial \overline{v}_x}{\partial z} + \frac{\partial \overline{v}_z}{\partial x} \right) \tag{4.1.105}$$

where v_T is turbulent kinematic viscosity. This concept was originally proposed by Boussinesq [27].

4.1.15.2.1 Mixing-Length Theory

This is one of the earliest turbulent models introduced by Prandtl [28]. Analogous to the kinetic theory of gases, Prandtl visualized fluid parcels (eddies) moving randomly with some characteristic velocity (v_{mix}) and a characteristic length (l_{mix}). The characteristic length can be interpreted as distance over which eddies retain their identities. Based on dimensional analysis, Prandtl proposed that

$$v_T = l_{mix}^2 \left| \frac{d\overline{v}_x}{dz} \right| \tag{4.1.106}$$

Further the mixing length l_{mix} has been experimentally correlated with the characteristic length of the system as $l_{mix} = C\delta(x)$. Here $\delta(x)$ is a characteristic length and C is a correlation constant. The correlation constant C needs to be determined for different flow geometries. Mixing-length theory has been applied fairly successfully to flows near the wall where there has been no flow separation. There have been many modifications to the basic mixing-length models. The success of the model has been limited in predicting engineering flows.

4.1.15.2.2 κ–ϵ Model [29]

The κ–ϵ model is one of the most widely used models in engineering for the investigation of fluid flows. This belongs to a family of two-equation models; κ denotes the turbulent kinetic energy and the ε denotes the dissipation rate of turbulent kinetic energy. The turbulent kinetic energy is expressed as

$$\kappa = \frac{1}{2}\left(\overline{v_x' v_x'} + \overline{v_y' v_y'} + \overline{v_z' v_z'} \right) \tag{4.1.107}$$

The turbulent kinetic energy does not distinguish between small and large eddies. The experimentally observed fact that the dissipation rate of smaller eddies is faster compared to the larger ones is accounted through a dissipation rate (ϵ) in the model, which is expressed in tensorial notation as

$$s_{i,j}' = \frac{1}{2}\left(\frac{\partial v_i'}{\partial j} + \frac{\partial v_j'}{\partial i} \right) \tag{4.1.108}$$

$$\epsilon = 2\nu \overline{s_{i,j}' s_{i,j}'} \tag{4.1.109}$$

where i and j stand for the coordinates x, y, and z.

The governing equations for the standard κ–ϵ model proposed by Launder and Spalding [29] in the vectorial form are

$$\nabla\cdot\overline{\mathbf{V}} = 0 \tag{4.1.110}$$

$$\frac{\partial\overline{\mathbf{V}}}{\partial t} + \overline{\mathbf{V}}\cdot\nabla\overline{\mathbf{V}} = \nabla\overline{P} + \nabla\cdot((\nu+\nu_{\mathrm{T}})\nabla\overline{\mathbf{V}}) \tag{4.1.111}$$

$$\frac{\partial\kappa}{\partial t} + \overline{\mathbf{V}}\cdot\nabla\kappa = \mathcal{P} - \varepsilon + \nabla\cdot((\nu+\nu_{\mathrm{T}}/\sigma_{\kappa})\nabla\kappa) \tag{4.1.112}$$

$$\frac{\partial\epsilon}{\partial t} + \overline{\mathbf{V}}\cdot\nabla\epsilon = C_{\epsilon 1}\frac{\epsilon}{\kappa}\mathcal{P} - C_{\epsilon 2}\frac{\epsilon^2}{\kappa} + \nabla\cdot((\nu+\nu_{\mathrm{T}}/\sigma_{\epsilon})\nabla\epsilon) \tag{4.1.113}$$

where $\mathcal{P}$ is the rate of production of eddies (in Cartesian coordinate system) and is given by

$$\mathcal{P} = 2\nu_{\mathrm{T}}\overline{s_{i,j}}\frac{\partial\overline{v}_i}{\partial j} \quad \text{(for incompressible flow)} \tag{4.1.114}$$

The turbulent viscosity, ν_{T}, is determined from κ and ϵ as

$$\nu_{\mathrm{T}} = C_{\nu}\frac{\kappa^2}{\epsilon} \tag{4.1.115}$$

The constants in the standard κ–ϵ model are

$$C_{\nu} = 0.09, \quad C_{\epsilon 1} = 1.44, \quad C_{\epsilon 2} = 1.92, \quad \sigma_{\kappa} = 1.0, \quad \text{and} \quad \sigma_{\epsilon} = 1.3 \tag{4.1.116}$$

These are empirical model constants whose values were found through data fitting for a wide range of flows.

One of the drawbacks of these models is that they cannot be applied near the solid boundary; special formalisms are needed near the walls. It is generally hypothesized that the flow near the wall can be viewed as consisting of three layers, namely an innermost viscous layer, a middle buffer layer, and outer turbulent layer and the velocity profile near the wall can be reasonably represented by a logarithmic profile [30]. This wall function term has been extensively used to specify boundary conditions near the wall for turbulent flows. There are also more rigorous approaches wherein special low *Re* κ–ϵ formalisms have been applied at the vicinity of the wall, the details of which can be found elsewhere [31].

Other than the standard κ–ϵ model, there are other two-equation models, such as RNG κ–ϵ models [32], κ–ω models [31], and Reynolds stress models [29]. Many of these models are available for use in commercial CFD codes such as FLUENT, PHOENICS, and CFX.

4.1.15.3. LES Models

As mentioned in the beginning of this section, one of the important features of turbulence is continuous formation and dissipation of eddies in a large spectrum of both spatial and temporal scales. A schematic representation of the size of the eddies (represented as wave number, k, inverse of size) and their corresponding turbulent energy, $E(k)$, is shown in Figure 4.1.27.

According to Kolmogorov [33], most of the turbulent kinetic energy is carried by the larger eddies and they are not affected by the molecular viscosity. The larger eddies dissipate their energy to smaller eddies. He also postulated that in the intermediate scale, known as inertial scale, the eddies pass on the energy from larger eddies to the smaller ones at the same rate. The eddies at the lowest scales are the ones that actually dissipate the energy through molecular viscosity. Based on dimensional analysis, the size of the smallest eddy was estimated as $\eta = \frac{1}{4}\left(\frac{\nu^3}{\epsilon}\right)$, known as the Kolmogorov scale. The spectrum widens with increasing Reynolds number. Thus, in principle, to obtain turbulent flow directly by solving the Navier–Stokes equations using numerical methods (DNS approach), the phenomena in the smallest of these scales need to be captured, which in turn are determine the grid spacing. For example, for channel flow the approximate number of nodes needed is $0.088Re^{9/4}$ [31], which for a Re of 10^6 corresponds to 100 billion nodes. Thus, with the current computing power, DNS simulations at present cannot be used anything other than small and simple geometries. It has also been observed that there is a tendency toward more universal behavior as lower scales are approached; in other words, they are more amenable for modeling. Thus, in LES methodology, the lower scales of turbulence (part of inertial subrange and into the beginning of dissipation scales) are modeled. The principle idea behind LES methodology is presented here; readers are urged to refer elsewhere [31] for a much more detailed description.

As in Reynolds decomposition, any generic variable such as velocity can be represented as two parts, i.e.,

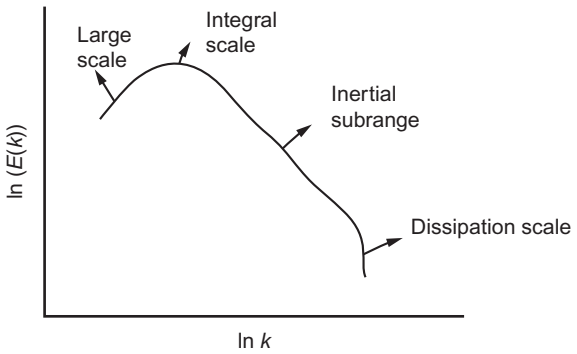


Figure 4.1.27 Schematic of the turbulence energy wave number spectrum.

$$\mathbf{v} = \widetilde{\mathbf{v}} + \mathbf{v}' \tag{4.1.117}$$

In this case, however, the decomposition is based on a low-pass spatial filter where $\widetilde{\mathbf{v}}$ is the filtered velocity and the $\mathbf{v}'$ is the residual part. A low-pass filter is a smoothening filter that attenuates the high frequencies (corresponding to sharp peaks) retaining the small frequencies unchanged. It should be noted that unlike Reynolds decomposition, the time average of $\mathbf{v}'$ need not be zero. The filtering can be performed by representing the variable in Fourier space and choosing a filter kernel, for example, a Gaussian filter.

The filtering of the continuity equation for an incompressible fluid is similar to that corresponding to Reynolds decomposition and can be written as

$$\nabla\cdot\widetilde{\mathbf{v}} = 0 \quad \text{and} \quad \nabla\cdot\mathbf{v}' = 0 \tag{4.1.118}$$

Filtering of the Navier–Stokes equation, i.e.,

$$\frac{\partial \mathbf{v}}{\partial t} + \nabla\cdot(\mathbf{v}\mathbf{v}) = -\nabla P + \nu\nabla^2\mathbf{v} \tag{4.1.119}$$

gives the nonlinear term $\nabla\cdot\mathbf{v}\mathbf{v}$ that contains the residual part, $\mathbf{v}'$; the time average of which is not zero. Unlike Reynolds decomposition, therefore, the filtering gives rise to cross terms in addition to Reynolds' stress terms (4.1.105). That is

$$\widetilde{\left(\widetilde{\nu}+\nu'\right)\left(\widetilde{\nu}+\nu'\right)} = \left\{ \begin{array}{l} \left(\widetilde{\nu}_x+\nu'_x\right)\widetilde{\left(\widetilde{\nu}_x+\nu'_x\right)\left(\widetilde{\nu}_y+\nu'_y\right)}\left(\widetilde{\nu}_x+\nu'_x\right)\widetilde{\left(\widetilde{\nu}_z+\nu'_z\right)} \\ \left(\widetilde{\nu}_x+\nu'_x\right)\widetilde{\left(\widetilde{\nu}_y+\nu'_y\right)}\left(\widetilde{\nu}_y+\nu'_y\right)\widetilde{\left(\widetilde{\nu}_y+\nu'_y\right)\left(\widetilde{\nu}_z+\nu'_z\right)} \\ \left(\widetilde{\nu}_x+\nu'_x\right)\widetilde{\left(\widetilde{\nu}_z+\nu'_z\right)}\left(\widetilde{\nu}_z+\nu'_z\right)\widetilde{\left(\widetilde{\nu}_y+\nu'_y\right)\left(\widetilde{\nu}_z+\nu'_z\right)} \end{array} \right\} \tag{4.1.120}$$

Looking at one of the terms

$$\widetilde{\left(\widetilde{\nu}_x+\nu'_x\right)\left(\widetilde{\nu}_y+\nu'_y\right)} = \left(\widetilde{\widetilde{\nu}_x\nu_y}\right) + \left(\widetilde{\widetilde{\nu}_x\nu'_y}\right) + \left(\widetilde{\widetilde{\nu}_y\nu'_x}\right) + \left(\widetilde{\nu'_x\nu'_y}\right) \tag{4.1.121}$$

The last term $\nu'_x\nu'_y$ is also referred to as the Reynolds stress in the LES formalism.

To obtain the filtered momentum equation in a useful form, this can be written as

$$\widetilde{\widetilde{\mathbf{v}}\widetilde{\mathbf{v}}} + \left(\widetilde{\left(\widetilde{\mathbf{v}}+\mathbf{v}'\right)\left(\widetilde{\mathbf{v}}+\mathbf{v}'\right)} - \widetilde{\widetilde{\mathbf{v}}\widetilde{\mathbf{v}}}\right) = \widetilde{\widetilde{\mathbf{v}}\widetilde{\mathbf{v}}} + \tau_{\mathrm{SGS}} \tag{4.1.122}$$

where τ_{SGS} contains the lower scale part (higher frequency) of the LES equation. Thus, the momentum equation for solving the filtered part of the (large scale) of the velocity vectors can be written as

$$\frac{\partial \widetilde{\mathbf{v}}}{\partial t} + \nabla\cdot(\widetilde{\mathbf{v}}\widetilde{\mathbf{v}}) = -\nabla\widetilde{P} + \nu\nabla^2\widetilde{\mathbf{v}} - \widetilde{\nabla}\cdot\tau_{\mathrm{SGS}} \tag{4.1.123}$$

It is interesting to note that the numerical discretization of the Navier–Stokes equation can be interpreted as a filtering operation and the width of the filter is directly related to the discrete step size of the numerical approximation. Thus eddies whose sizes are of order of the scale corresponding to the step size and greater are captured by the filtered momentum equation. However, the scales below that of the step size need to be modeled and hence they are referred to as τ_{SGS}, where SGS stands for subgrid scale. In principle, as the step size becomes smaller and smaller, the LES scheme should converge to the DNS scheme and correspondingly the τ_{SGS} should go toward zero. In other words, the τ_{SGS} should depend on the grid size of the numerical scheme.

A number of models are proposed for τ_{SGS}. Among them, one of the oldest is by Smagorinsky [34] and is based on the Boussinesq hypothesis [27]. The equations for the Smagorinsky model are

$$\tau_{SGS} = -2\nu_{SGS}\widetilde{\mathbf{S}} \tag{4.1.124}$$

$$\nu_{SGS} = (C_s\Delta)^2\left|\widetilde{\mathbf{S}}\right| \quad \text{(Analogous to mixing length model, Equation 4.106)} \tag{4.1.125}$$

Here, $\mathbf{S}$ refers to the strain rate tensor (see Equation 4.1.108), Δ is the filter width, which is proportional to grid size, and C_s is the Smagorinsky constant. The typical values of C_s are of the order of 10^{-1}. In the recent past, many new methodologies have been constructed for LES wherein the constant C_s is determined by performing two or more filtering operations using different filter widths (multigrid). Detailed description of the formulation as well as implementation of LES can be found elsewhere [35].

4.1.16. INTRODUCTION TO HEAT TRANSFER

Heat transfer, in simple terms, is energy transfer arising from differences in temperature. In a static system, where there is a medium, the primary mode of heat transfer is by conduction. This mode of transfer is also termed as diffusive transfer and is caused by molecular interactions within the medium. Hence, the quantity of heat being transferred depends on the material of the medium. If there is a net flow in the medium, then, in addition to the conduction mode, there is also the advective transfer of heat that arises from the bulk motion and that occurs simultaneously with conduction. This is termed as convection. In a multiphase system, wherein there is a net relative motion between any two phases, there can be large gradients in velocity and temperature at the interface between the phases. Quantifying this heat transfer through the interface is essential in most engineering systems. Heat can be transferred even without a medium as electromagnetic waves or photons. This mode of heat transfer is termed as radiative heat transfer. Most condensed media absorb electromagnetic waves so heat transfer through such media cannot occur by this mechanism. Radiative heat transfer is, however, significant through gaseous media. The gas molecules can absorb, scatter as well as emit photons. The radiative exchange through gases depends on the characteristics of the gas molecules,

which constitute the gaseous media. The constitutive relations describing all these modes of heat transfer and their application in engineering problems through the conservation principle make up the subject of heat transfer and are described in the following sections.

4.1.17. CONSERVATION EQUATION AS APPLIED TO THERMAL SYSTEMS

The overall energy balance for a steady-state system has been discussed earlier in Section 4.1.4. This can be generalized for an unsteady state or a transient system as

$$\frac{\mathrm{d}E^{\mathrm{s}}}{\mathrm{d}t} = -\dot{E}^{\text{net out}} - \dot{Q}^{\text{net out}} - \dot{W}^{\text{net out}} \tag{4.1.126}$$

Here, E^{s} denotes the energy in the system, $\dot{E}^{\text{net out}}$ is the net rate of energy advected out from the system with the flowing mass, $\dot{Q}^{\text{net out}}$ is the net rate of heat transfer out from the system by other mechanisms, and $\dot{W}^{\text{net out}}$ the net rate of work done by the system on the surroundings. Please note that the "net out" term for any conservative entity, say ϕ is defined by

$$\dot{\phi}^{\text{net out}} = \left(\dot{\phi}^{\text{out}} - \dot{\phi}^{\text{in}}\right)$$

The net energy that is advected out from the system with the flowing mass as well as that getting accumulated in the system, includes kinetic energy, potential energy arising from gravitation field, and the internal energy as explained in Section 4.1.4. In addition to this, there can be net flow of heat energy out from the system through the system boundaries by conduction and interface heat transfer by convection and radiation. The term 'work', in general, involves two important components, the flow work (as explained in Section 4.1.4) and the shaft work. Thus, the overall energy balance can be written in a more rigorous form as,

$$\frac{\mathrm{d}E^{\mathrm{s}}}{\mathrm{d}t} = -\int_B \left(\hat{U} + \widehat{K.E.} + \widehat{P.E.}\right)\mathrm{d}\dot{m} - \dot{Q}^{\text{net out}} - \int_B P\hat{V}\,\mathrm{d}\dot{m} - \dot{W}_{\text{shaft}}^{\text{net out}} \tag{4.1.127}$$

Here, B refers to the system boundary, $\hat{U}$ the internal energy per unit mass, $\widehat{K.E.}$ the kinetic energy per unit mass, $\widehat{P.E.}$ the potential energy per unit mass, P the pressure, and $\hat{V}$ the specific volume. In thermodynamics, the term $\widehat{U} + P\hat{V}$ is defined as enthalpy, $\hat{H}$. Thus, the above equation can be written as,

$$\frac{\mathrm{d}E^{\mathrm{s}}}{\mathrm{d}t} = -\int_B \left(\hat{H} + \widehat{K.E.} + \widehat{P.E.}\right)\mathrm{d}\dot{m} - \dot{Q}^{\text{net out}} - \dot{W}_{\text{shaft}}^{\text{net out}} \tag{4.1.128}$$

In general, most problems of interest to a process engineer can be considered as constant pressure processes. Besides, the potential and kinetic energies are generally much smaller than changes in enthalpy and are often neglected.

Hence, for constant pressure processes, the energy conservation equation can be written as

$$\frac{\mathrm{d}\left(m^{\mathrm{s}}\hat{H}\right)}{\mathrm{d}t} = -\int_{B} \hat{H}\,\mathrm{d}\dot{m} - \dot{Q}^{\text{net out}} - \dot{W}^{\text{net out}}_{\text{shaft}} \tag{4.1.129}$$

Here, m^{s} refers to the mass in the system. Depending on the system, there can be other forms of energies such as magnetic, electric, chemical, interfacial, and nuclear, which may need to be included in the conservation equation. Detailed information on these aspects can be found in books on thermodynamics. In heat transfer, the focus is on the sensible part of the enthalpy, which results in a change in temperature. The other forms of energies such as those associated with phase changes, chemical reactions, electrical, magnetic, and nuclear phenomena are incorporated through generation terms. These conversions to sensible enthalpy are treated as volumetric phenomena. It is to be noted that the degradation of mechanical energy into internal energy also needs to be accounted for. This term, however, is often neglected as being small in comparison to changes in sensible enthalpy. Thus, the equation becomes

$$\frac{\mathrm{d}\left(m^{\mathrm{s}}\hat{H}\right)}{\mathrm{d}t} = -\int_{B} \hat{H}\,\mathrm{d}\dot{m} - \dot{Q}^{\text{net out}} - \dot{W}^{\text{net out}}_{\text{shaft}} + \int_{V} \dot{Q}'''\,\mathrm{d}V \tag{4.1.130}$$

where $\dot{Q}'''$ denotes the rate of conversion of other forms of energies to thermal energy per unit volume.

The sensible enthalpy for a material is quantified using specific heat capacity at constant pressure, denoted by C_{p}

$$\hat{H} = \int_{T_{\text{ref}}}^{T} C_{\mathrm{p}}\,\mathrm{d}T \tag{4.1.131}$$

where T_{ref} is an arbitrary reference temperature, usually taken as 298 K.

Using the above, the heat balance equation can be written as

$$m^{\mathrm{s}} C_{\mathrm{p}} \frac{\mathrm{d}T}{\mathrm{d}t} = -\int_{B} \hat{H}\,\mathrm{d}\dot{m} - \dot{Q}^{\text{net out}} - \dot{W}^{\text{net out}}_{\text{shaft}} + \int_{V} \dot{Q}'''\,\mathrm{d}V \tag{4.1.132}$$

Here onward, the symbol C will be used to denote C_{p} as most of the cases one deals with in process metallurgy are at constant pressure. Exceptions to this will be clearly spelt out.

4.1.18. CONDUCTION

Heat transfer resulting from atomic or molecular interactions in a medium is termed conduction. Consequently, conductive heat transfer is dependent on the constitution of the medium. Conductive transfer is characterized by the material property called thermal conductivity. The primary constitutive equation for conduction is named after Fourier, a great mathematician and a physicist. The law as stated is phenomenological and was based on experimental observations.

To demonstrate this form of heat transfer, consider a solid rod of cross section "A" and length "L" as shown in Figure 4.1.28. The curved side of the rod is insulated.

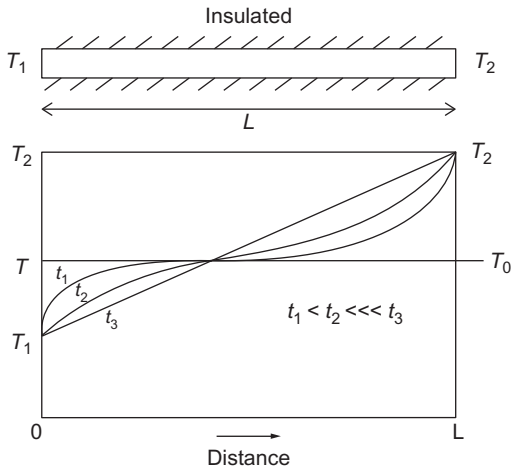


Figure 4.1.28 Schematic showing heat conduction through a rod of constant cross section.

The rod is initially at a uniform temperature, T_0. At time $t=0$, the two ends of the rod are brought to temperatures of T_1 and T_2, respectively, and are maintained at these values. The temperature profile along the length of the rod will change continuously over time as shown schematically in Figure 4.1.28. The system will attain steady state, after sufficiently long time; the profile would be nearly a straight line if temperature differences are small. Experimentally, the amount of heat transferred can be measured, for example, by keeping the cold side of the rod under an ice–water mixture and measuring the amount of ice melted. Fourier's law states that the heat transferred per unit time at steady state, $(\dot{q})$, is proportional to the difference in temperature of the two ends of the rod, $T_1 - T_2$ and the area of cross section "A" and is inversely proportional to the length of the rod, "L." That is

$$\dot{q} = \kappa \frac{(T_1 - T_2)A}{L}$$

The proportionality constant, κ, is the thermal conductivity of the material of the rod. In differential form in one dimension, the law is stated as:

$$\dot{q}''_x = -\kappa \frac{\mathrm{d}T}{\mathrm{d}x} \tag{4.1.133}$$

where $\dot{q}''_x$ is the heat flux, the rate of heat transfer per unit area [4]. The direction x is along the length of the rod.

[4] Fourier's law of heat conduction is analogous to Newton's law of viscosity when viewed as equation of momentum flux. Under the condition of constant ρ and C_p, Equations (4.1.133) and (4.1.15) can be written as:

$$\tau_{yx} = -\frac{\mu}{\rho}\frac{\partial \rho v_x}{\partial y} = -\nu \frac{\partial \rho v_x}{\partial y} \quad \text{and} \quad \dot{q}'' = -\frac{\kappa}{\rho C_p}\frac{\partial \left(\rho C_p (T - T_{ref})\right)}{\partial \infty} = -\alpha \frac{\partial \left(\rho C_p (T - T_{ref})\right)}{\partial \infty}$$

(ρv_x) and $\rho C_p(T - T_{ref})$ are conserved quantities, namely, momentum and enthalpy densities: (kg m s^{-1} m^{-3}) and (J m^{-3}). The laws can be viewed as when there is a gradient in a conserved quantity, there is a flux of that quantity down the gradient. These two laws are further analogous to Fick's law of mass diffusion as discussed later in Section 4.1.21. The dimension of all the proportionality constants is m^2 s^{-1}.

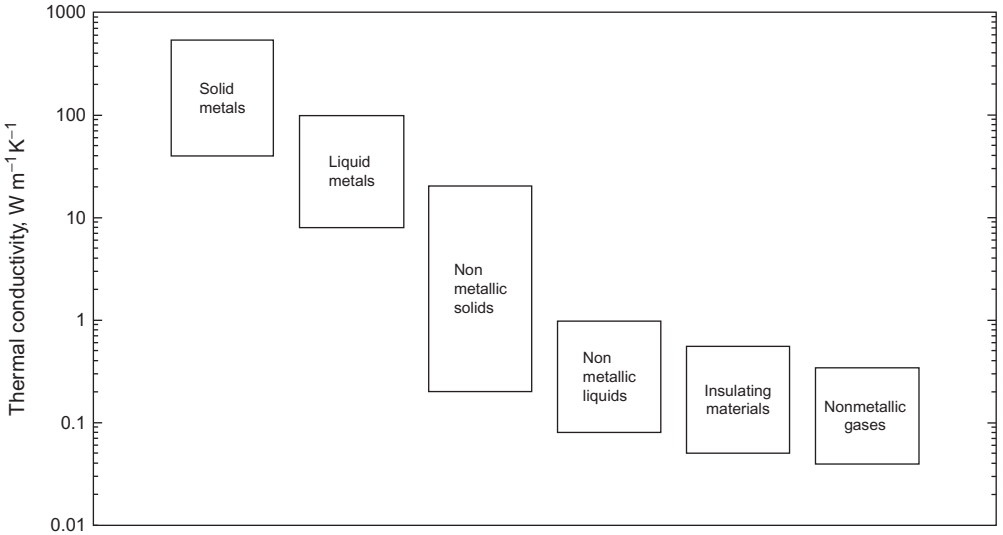


Figure 4.1.29 Ranges of thermal conductivities of different materials [36].

In a general 3D scenario, for an isotropic medium, Fourier's law of conduction can be written as

$$\dot{q}'' = -\kappa \nabla T \tag{4.1.134}$$

It is to be noted that the heat flux vector, $\dot{q}''$, is orthogonal to an isothermal surface. In most engineering situations encountered in process metallurgy, the conductive medium can be considered to be isotropic. Readers may refer elsewhere for conductive heat transfer through anisotropic media [36].

Typical ranges of thermal conductivities of materials, are shown in Figure 4.1.29 adopted from Ref. [36]. Solid metals normally have high thermal conductivities, since both lattice vibrations and free electrons contribute to thermal conduction. With increasing temperature, the mean free path of electrons decreases resulting generally in a decrease in thermal conductivities with increasing temperature. In nonmetallic solids, on the other hand, only the lattice vibrations contribute to the thermal conductivity and their thermal conductivities generally increase with increasing temperature. Many insulating materials are made intentionally porous to serve as inhibitors for heat transfer. Hence their conductivities are closer to those of the gases.

As with viscosity, the thermal conductivities of gases and gas mixtures can be estimated with reasonable accuracy from the kinetic theory of gases [1]. For solids and liquids, these data must be obtained by experimental measurements, and data have been tabulated for a large number of materials [37,38].

4.1.18.1. Conduction Equation

The conservation equation given by Equation (4.1.132) is applied to a differential element in conjunction with Fourier's law (the constitutive relation for conduction) to deduce the generalized conductive heat transport equation. Consider a differential element in Cartesian coordinate system as shown in Figure 4.1.30.

The medium is static and hence there is only conductive heat transfer. There is no advective mass transport, and no radiative transfer through the medium. The conservation of heat in this control volume is written as

$$\begin{aligned}\rho C\frac{\partial T}{\partial t}(\Delta x\Delta y\Delta z) = {} & \Delta y\Delta z\left(-\kappa\frac{\partial T}{\partial x}\bigg|_{abcd}+\kappa\frac{\partial T}{\partial x}\bigg|_{efgh}\right)\\ & +\Delta x\Delta z\left(-\kappa\frac{\partial T}{\partial y}\bigg|_{adhe}+\kappa\frac{\partial T}{\partial y}\bigg|_{bcgf}\right)\\ & +\Delta x\Delta z\left(-\kappa\frac{\partial T}{\partial z}\bigg|_{adfe}+\kappa\frac{\partial T}{\partial z}\bigg|_{hgcd}\right)\\ & +\dot{Q}'''(\Delta x\Delta y\Delta z)\end{aligned} \tag{4.1.135}$$

Taking the limit as Δx, Δy, and $\Delta z \longrightarrow 0$, then

$$\rho C\frac{\partial T}{\partial t}=\frac{\partial}{\partial x}\left(\kappa\frac{\partial T}{\partial x}\right)+\frac{\partial}{\partial y}\left(\kappa\frac{\partial T}{\partial y}\right)+\frac{\partial}{\partial z}\left(\kappa\frac{\partial T}{\partial z}\right)+\dot{Q}''' \tag{4.1.136}$$

In vectorial form, this equation can be written as

$$\rho C\frac{\partial T}{\partial t}=-\nabla\cdot(\kappa\nabla T)+\dot{Q}''' \tag{4.1.137}$$

If the thermophysical properties, namely ρ, C, and κ, are assumed to be constant within the temperature range of interest, the equation can be simplified to

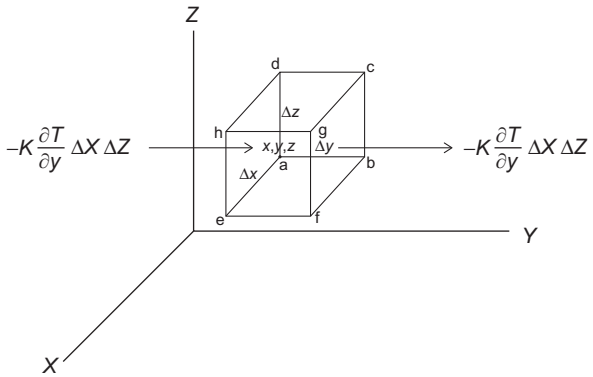


Figure 4.1.30 Differential element in Cartesian coordinates.

$$\frac{\partial T}{\partial t} = \alpha \nabla^2 T + \frac{1}{\rho C} \dot{Q}''' \tag{4.1.138}$$

The material property, α, termed thermal diffusivity, is given by $\frac{\kappa}{\rho C}$ the dimension of which is $m^2\,s^{-1}$, as also for kinematic viscosity, ν, and mass diffusion coefficient, $\mathbb{D}$.

Equation (4.1.137) is often termed as the heat equation or the diffusion equation belonging to the class of parabolic partial differential equations. Even though the heat equation was derived using the Cartesian coordinate system, the vectorial form can be easily expanded for any curvilinear coordinate system. The equation can be solved for any particular system, by specifying the temperature distribution in space at any given time (initial condition) and specifying conditions at the boundaries for the entire time duration of interest (boundary conditions). Some of the common boundary conditions encountered in conductive heat transfer are discussed below.

4.1.18.2. Boundary Conditions

4.1.18.2.1 Prescribed Surface Temperature

The temperature at the boundary is known for all times of interest (Figure 4.1.31):

$$\text{At } x = 0, \quad T = T_s(t).$$

This boundary condition is also known as the Dirichlet condition, after the famous mathematician. Such a condition can be imposed by keeping the boundary at a phase-transition temperature.

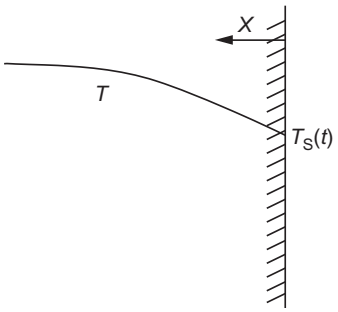


Figure 4.1.31 Illustration of the Dirichlet boundary condition.

4.1.18.2.2 Prescribed Heat Flux

The heat flux through the boundary is known as a function of time (Figure 4.1.32):

$$\text{At } x = 0, \quad -\kappa \frac{\partial T}{\partial x} = \dot{q}''_s(t).$$

This condition is named after the mathematician Neumann. Such a condition can be obtained, for example, by having an electric heater at the boundary, which is insulated perfectly on the other side.

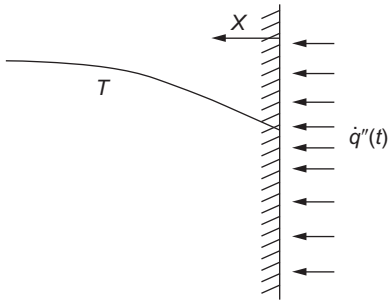


Figure 4.1.32 Illustration of the Neumann boundary condition.

A special case of the Neumann condition is an adiabatic surface, where the heat flux and, therefore, the temperature gradient at the surface are zero.

$$\text{At } x = 0, \quad \frac{\partial T}{\partial x} = 0.$$

A perfectly insulated boundary is adiabatic. Such a condition is obtained at symmetry planes, in perfectly symmetrical systems.

4.1.18.2.3 Convective Boundary Condition

The most common boundary condition specified is the one at a boundary between the stationary medium for which the conduction problem is being solved and a moving fluid. The stationary medium may be a solid, or a liquid that is relatively stagnant. Continuity of heat flux across the interface demands that the conductive heat flux on one side be equal to the convective heat flux on the other as shown in Figure 4.1.33.

Convective heat transfer at the interface is a function of fluid and flow properties, and is given by a phenomenological equation.

$$\dot{q}''_{x,\text{conv}} = h(T_\text{b} - T_\text{s}).$$

where T_s and T_b are the surface and bulk temperature in the moving fluid, respectively, and h is called the heat transfer coefficient, which is related to fluid and flow properties, often through empirical correlations (see Section 4.1.19). The boundary condition therefore becomes

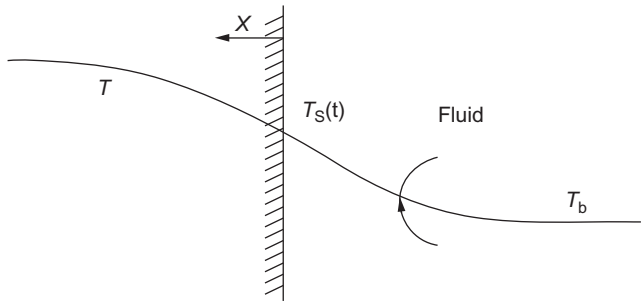


Figure 4.1.33 Illustration of the Convective boundary condition.

$$\text{At } x=0, \quad -\kappa\frac{\partial T}{\partial x}=h(T_b-T_s).$$

or

$$x=0, \quad -\kappa\frac{\partial T}{\partial x}+hT_s=hT_b.$$

This condition neither specifies the surface temperature nor the temperature gradient at the surface; it specifies a linear combination of the two. It is therefore called the mixed condition; T_s adjusts itself to satisfy this condition.

Examination of the above equation tells us that, for any finite heat flux at the interface, $T_s \to T_b$ as $h \to \infty$. That is, the prescribed surface temperature condition is difficult to be practically achieved, except by having a high enough heat transfer coefficient for a given κ_s value. Phase changes, as when steam condenses on a surface, can provide such high heat-transfer coefficients.

4.1.18.2.4 A Boundary Between Two Conducting Media

If two conducting media are in perfect thermal contact, the heat flux as well as temperature at the interface should be continuous, since there can be no accumulation at a surface, $\kappa^{I}\frac{\partial T}{\partial x}\Big|^{-}=\kappa^{II}\frac{\partial T}{\partial x}\Big|^{+}$ (Figure 4.1.34).

If the two media are both solids, pressed together, the contact is never perfect and there is always a third medium in between, which is normally a gas such as air or a liquid. This thin layer, of indeterminate thickness, offers a further resistance to heat flow. Though the heat flux can still be assumed to be continuous (even in an unsteady heat flow situation), since the thermal capacity of these interface layers is very small, there can be a sharp temperature drop across this layer. The mechanisms of heat transport across the layer are conduction and radiation (if the medium in the layer is transparent); a theoretical treatment is, however, difficult, due to the uncertain geometry of the interface. An empirical approach is therefore adopted, and a heat transfer coefficient across this interface is defined (Figure 4.1.35).

$$\dot{q}''=-\kappa^{I}\frac{\partial T}{\partial x}\Big|^{-}=h\left(T_s^{I}-T_s^{II}\right)=\kappa^{II}\frac{\partial T}{\partial x}\Big|^{+}$$

In a mixed condition, the heat flow away from the surface may have a radiative component superimposed on the convective: At $x=0, -\kappa_s\frac{\partial T}{\partial x}=h(T_b-T_s)+\varepsilon\sigma\left(T_a^4-T_s^4\right)$,

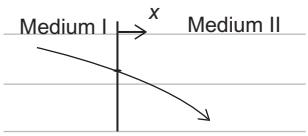


Figure 4.1.34 Illustration of the boundary condition between two conductive media in perfect thermal contact.

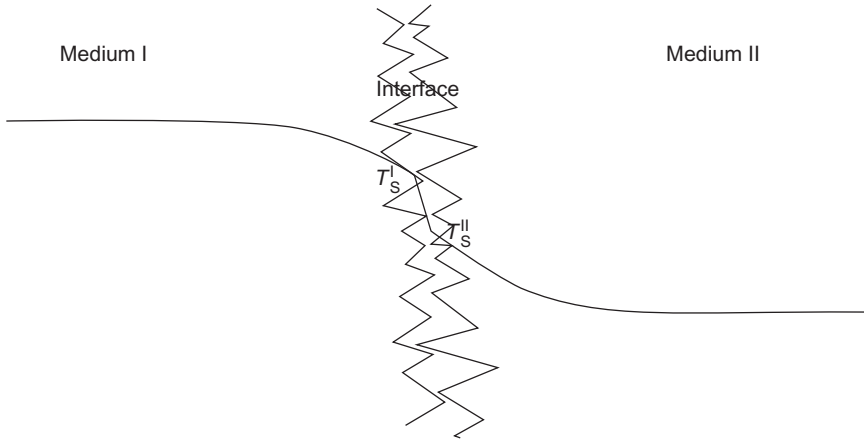


Figure 4.1.35 Illustration of the boundary condition between two conductive media in contact.

where T_a is the ambient temperature from which the radiation is received and σ is the Stefan–Boltzmann constant. This boundary condition is highly nonlinear in T_s and can give difficulties in computation. If the difference between T_a and T_s is small, a linearized form of the equation can be used,

$$\text{at } x=0, \quad -\kappa_s \frac{\partial T}{\partial x} = h(T_b - T_s) + \varepsilon\sigma\left(T_a^4 - T_s^4\right) = h(T_b - T_s) + h_{rad}(T_a - T_s)$$
$$\text{where } h_{rad} = \varepsilon\sigma\left(T_s^2 + T_s^2\right)(T_s + T_a) \approx \varepsilon\sigma 4 T_{avg}^3 \quad \text{where } T_{avg} = (T_s + T_a)/2.$$

4.1.18.3. 1D Steady-State Conduction

The heat transfer process is at a steady state condition when temperature at any location remains constant over a long period of time. This can be achieved by maintaining a constant heat transfer condition at the boundary over a long period of time. For example, if a furnace or an oven is maintained at a constant temperature for a long time, then the walls of the furnace can attain a steady temperature profile. Similarly, when a hot fluid having a fixed inlet temperature flows at a constant rate through a pipe maintained in a steady environment, the walls of the pipe will attain a steady temperature profile. In many metallurgical processes, simple analyses can often be performed by approximating the heat transfer as a 1D steady-state heat transfer either in Cartesian or cylindrical coordinates. Quite often, in such simple systems, an electrical analogue can also be constructed to describe heat transfer, which can help in the analysis.

4.1.18.3.1 Conduction Through a Plane Wall

When the length and width of a wall are much larger than the thickness of a wall, steady-state heat transfer through the wall can often be approximated as 1D steady-state conduction in the Cartesian coordinate system. Heat transfer through plane walls of a large furnace is one such typical example.

The heat conduction equation (Equation 4.1.137) for steady-state conduction through a plane wall of thickness L with no generation of heat inside the wall reduces to

$$\frac{\partial}{\partial x}\left(\kappa\frac{\partial T}{\partial x}\right)=0 \tag{4.1.139}$$

If the thermal conductivity of material of the wall is taken to be independent of temperature, the solution of the differential equation results in a linear temperature profile across the wall. In many engineering systems, it is reasonable to assume constant thermal conductivity (at the average temperature). The temperature profile and the heat flux through the wall can be written as

$$T(x)=T_0-\frac{T_0-T_L}{L}x$$
$$\dot{q}''_x=\kappa\frac{T_0-T_L}{L}$$

where T_0 and T_L refer to the temperature on the wall at location $x=0$ and $x=L$, respectively. These two temperatures when not specified can be deduced from the corresponding boundary conditions at $x=0$ and $x=L$.

Consider a case where convective boundary conditions are imposed with heat transfer coefficients h_0 and h_L and fluid temperatures of $T_{\infty,0}$ and $T_{\infty,L}$ at $x=0$ and $x=L$, respectively. Balancing the convective heat flux flowing from fluid at $x=0$, the conductive heat flux across the wall, and the convective flux flowing out to the fluid at $x=L$, the following equations can be written.

$$\dot{q}=A\dot{q}''_x=Ah_0\left(T_{\infty,0}-T_0\right)=A\kappa\frac{T_0-T_L}{L}=Ah_L\left(T_L-T_{\infty,L}\right) \tag{4.1.140}$$

A schematic temperature profile for the system is depicted in Figure 4.1.36a.

The temperature profile within the wall is linear. The convective heat transfer through the fluid on both sides of the wall is represented as a curved profile with a steep gradient near the fluid–solid interface. This is to depict the temperature profile resulting from the flow of liquid having a steep gradient in velocity at the solid–liquid interface. More discussions on this convective heat transfer can be found in later sections. The rate of heat transfer can be written after eliminating the unknown surface temperatures as:

$$\dot{q}=A\dot{q}''_x\frac{\left(T_{\infty,0}-T_{\infty,L}\right)}{\frac{1}{h_0A}+\frac{L}{AK}+\frac{1}{h_LA}} \tag{4.1.141}$$

The overall resistance to heat flow is the sum of the conductive and convective resistances (Fig 4.1.36b). The analogy can be extended to multiple conducting walls as shown in Figure 4.1.37.

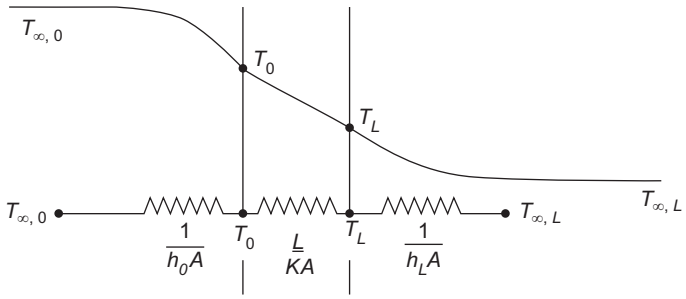


Figure 4.1.36 Steady-state conduction through a plane wall: schematic temperature profile and equivalent electrical analogue.

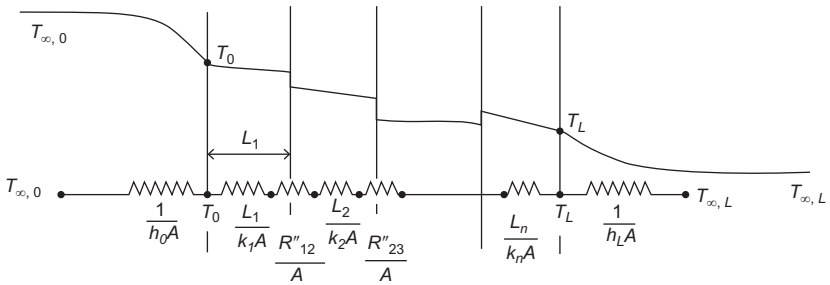


Figure 4.1.37 Steady-state conduction through a plane composite wall: schematic temperature profile and equivalent electrical analogue.

The heat transfer through the wall can be represented using an electrical analogue wherein the heat flowing through the system is equivalent to the current in the analogous electrical circuit, and the temperature difference is the driving force or the potential difference. The convective heat transfer on either side as well as the conductive heat transfer through the wall is represented using equivalent resistance terms as shown in Figures 4.1.36b and 4.1.37b. The intermediate temperatures at any intermediate point can also be determined as that corresponding to electric potential in the electrical analogue.

When designing walls for insulation of furnaces, many layers of different materials are laid to form a composite wall. Not only should the thermal conductivity of the insulation material be considered but its service temperature should also be taken into account. For example, refractory bricks can be used at the inner layers of the furnace where temperatures are high; for the outer layers, having lower temperatures, ceramic wools having relatively much lower thermal conductivities can be used.

In many systems, it is desirable to enhance the heat transfer so that the system can be maintained at lower temperatures. In such systems, the resistance offered by the interface between two different materials can significantly alter the heat transfer rates. These

interface resistances depend on the quality of the physical contact as well as the filling materials, if any, at the interface boundary. By selecting an interfacial medium with high thermal conductivity, the interface resistance can be decreased. A typical example of this application is the use of heat-conducting silver paste to bond heat sinks to the top of IC chips.

4.1.18.3.2 Conduction Through Radial Systems

Steady-state heat transfer through the walls of long cylindrical furnaces or pipes of circular cross section can be analyzed using the 1D heat transfer equation in the radial direction (refer to Equation 4.1.137).

$$\frac{1}{r}\frac{\partial}{\partial r}\left(r\kappa\frac{\partial T}{\partial r}\right)=0 \tag{4.1.142}$$

Integration, with temperatures specified at the inner and the outer wall, will give a situation similar to that obtained for the plane wall. The solution for the above equation can be expressed by an electrical equivalent as shown in Figure 4.1.38. The equation for the heat flow is

$$\dot{q}=\frac{T_0-T_1}{\frac{\ln(R_1/R_0)}{2\pi L\kappa}} \tag{4.1.143}$$

Here, L is length of the cylinder.

This approach can be extended with several concentric layers of different materials, and convective heat transfers at the inner and the outer surfaces.

$$\dot{q}=\frac{T_{\infty,0}-T_{\infty,n}}{R_{\text{total}}} \tag{4.1.144}$$

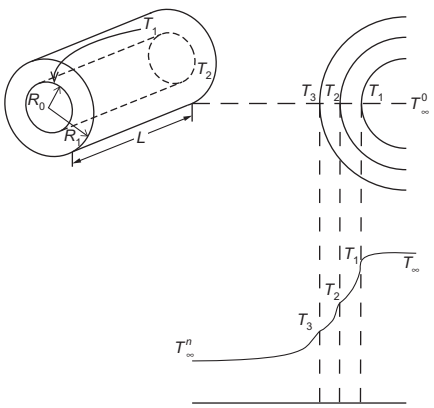


Figure 4.1.38 Illustration of Steady-state heat conduction through a cylindrical wall.

$$R_{\text{total}} = \frac{1}{2\pi R_0 L h_0} + \frac{\ln(R_1/R_0)}{2\pi L \kappa_1} + \frac{R''_{1,2}}{2\pi R_1 L} + \cdots + \frac{\ln(R_i/R_{i-1})}{2\pi L \kappa_i} + \frac{R''_{i,i+1}}{2\pi R_i L} + \cdots + \frac{\ln(R_n/R_{n-1})}{2\pi L \kappa_n} + \frac{1}{2\pi R_n L h_n} \tag{4.1.145}$$

where $R''_{i,i+1}$ are interfacial resistances between layers i and $i+1$.

Heat transfer through a spherical shell can be similarly analyzed. The conduction resistance through a spherical wall is $\frac{1}{4\pi\kappa}\cdot\left(\frac{1}{R_i} - \frac{1}{R_o}\right)$, where R_i and R_o are inner and outer radii, respectively.

4.1.18.3.3 Heat Transfer Through Extended Surfaces

Extended surfaces are used in thermal systems to enhance the heat transfer rates. For example, electronic components, such as a processor chip in a computer, need to be maintained below a critical temperature. When the processor is on, the electric circuits generate thermal energy, which needs to be efficiently dissipated to avoid overheating of the chip. These extended surfaces, also known as fins, are also used in many electrical, electronic, and thermal systems, where thermal energy needs to be dissipated efficiently. In addition, extended surfaces are used in heat exchangers where one is interested in transferring heat efficiently from one medium to another. Heat transfer analysis through extended surfaces is also important when designing temperature-measuring probes using thermocouples. The thermocouple lead wires, or the tube in which the thermocouple is placed, can themselves act as heat dissipaters, giving rise to significant errors in measurements.

The basic purpose of using fins is to enhance the convective heat transfer at solid–fluid interface when the solid is a good conductor and the resistance due to conduction is minimal. The increase of surface area enables increase in heat dissipation to the surroundings. When designing these fins, care needs to be taken to ensure that the advantage of enhancing the heat transfer by increasing the convective surface area is not offset by the additional conductive resistance and, in cases where a separate heat sink is attached, an additional contact resistance.

Consider a simple pin fin of constant cross section of length L as shown in Figure 4.1.39.

The thickness of fins is generally small so that the convective heat transfer resistance can be considered dominant, and the temperature variation across the thickness is negligible. Along the length of the fin, on the other hand, conductive resistance is important. Performing a steady-state heat balance for an infinitesimal length of Δx of the fin as shown in the figure, one can write,

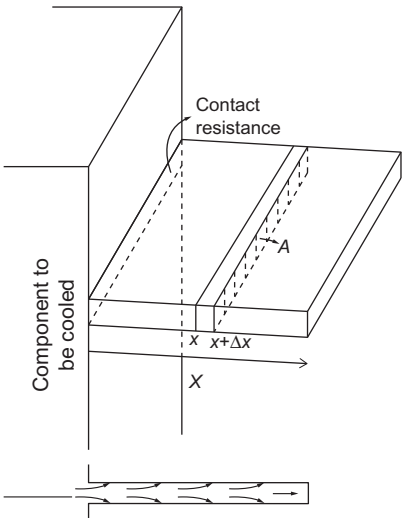


Figure 4.1.39 Schematic of a heat transfer fin having constant area and cross section.

$$\left(-A\kappa\frac{dT}{dx}\right)\Bigg|_{x} - \left(-A\kappa\frac{dT}{dx}\right)\Bigg|_{x+\Delta x} - h(P\Delta x)\left(T|_{x+\Delta x/2} - T_\infty\right) = 0$$

where, A is the area of cross section of the fin, P the perimeter of the fin, h the heat transfer coefficient, and T_∞ the temperature of the surrounding fluid. One can then obtain the differential equation:

$$\frac{\mathrm{d}}{\mathrm{d}x}\left(\kappa A\frac{\mathrm{d}T}{\mathrm{d}x}\right) - hP(T - T_\infty) = 0 \tag{4.1.146}$$

At the base of the fin ($x = 0$), the boundary condition is

$$T|_{x=0} = T_\mathrm{B}$$

The general boundary condition at the tip is

$$x = L, \quad -\kappa\frac{dT}{dx}\Bigg|_{x=L} = h\left(T|_{x=L} - T_\infty\right)$$

Using these boundary conditions, the solution to Equation (4.1.146) is:

$$\frac{T - T_\infty}{T_\mathrm{B} - T_\infty} = \frac{\cosh(m(L-x)) + \frac{h}{m\kappa}\sinh(m(L-x))}{\cosh(mL) + \frac{h}{m\kappa}\sinh(mL)} \tag{4.1.147}$$

where

$$m = \sqrt{\frac{hP}{\kappa A}} \tag{4.1.148}$$

and the corresponding total heat transfer rate through the fin ($\dot{q}_f$) is given by

$$\dot{q}_f = \sqrt{hP\kappa A}(T_B - T_\infty)\frac{\sinh(mL) + \frac{h}{m\kappa}\cosh(mL)}{\cosh(mL) + \frac{h}{m\kappa}\sinh(mL)} \tag{4.1.149}$$

In most cases, the heat transfer surface would contain an array of fins, analysis for which can be easily obtained from the above. The expression for heat transfer would be different if the boundary condition at the tip of the film is different, as for example, an insulated tip.

The analysis described above is for fins of constant cross section (constant A). Fins can also have varying area cross sections along their length. Generally, all these fins are characterized by two parameters, namely (1) effectiveness and (2) efficiency. The effectiveness of a fin is defined as the ratio of heat transferred with the fin to that without the fin for a specified base temperature. Thus, for a fin of constant cross section, the effectiveness can be obtained from Equation (4.1.149) as

$$\varepsilon_f = \frac{\dot{q}_f}{\dot{q}_{\text{without fin}}} = \frac{\dot{q}_f}{hA(T_B - T_\infty)} = \sqrt{\frac{P\kappa}{Ah}}\frac{\sinh(mL) + \frac{h}{m\kappa}\cosh(mL)}{\cosh(mL) + \frac{h}{m\kappa}\sinh(mL)} \tag{4.1.150}$$

The efficiency of a fin is defined by comparing the heat transfer from the fin to that from an ideal one. An ideal fin is that which offers no conductive resistance. For an ideal fin, therefore, the entire fin would be at the base temperature T_B. The equation for the efficiency of a fin would be:

$$\eta_f = \frac{\dot{q}_f}{A_f h(T_B - T_\infty)} \tag{4.1.151}$$

where A_f is the total exposed surface area of the fin. For a given fin geometry, fin material and a convective heat transfer coefficient (h), one can obtain the efficiency, η_f, by solving the appropriate heat transfer equation similar to the one given in Equation (4.1.146). For commonly used fin geometries (radial, fins with varying cross sections, etc.), the efficiency of the fin is given in the form of charts, from which one can directly obtain q_f. If f is the fraction of the surfaces of the wall covered by fins, the heat transfer at the wall can be written as: $\dot{q}'' = \big((1-f) + A_{f,t}\eta_f\big)h(T_B - T_\infty)$, where $A_{f,t}$ is the total surface area of the array of fins on a wall of unit area. The net effect of the fins is therefore to enhance the effective heat transfer coefficient at a plane wall by a factor of $(1-f) + A_f\eta_f$. One

can solve multiwall problems using this enhanced heat transfer coefficient for the convective resistance.

4.1.18.4. 1D Transient Conduction

Transient systems where temperature varies with time are common in metallurgical processes starting from primary metal production from ore, followed by casting of liquid metal and finally to achieve microstructural control through thermomechanical treatments. In this section, analysis of transient heat transfer in bodies submerged in a fluid phase is presented.

The heat transfer process depends on one hand on the transfer within the solid and the size and the shape of the component, and material properties such as heat capacity and thermal conductivity. It also possible for the rate to depends principally on the flow and the fluid properties outside the component, i.e. the rate is determined convective transfer. At the one extreme, the conductive resistance can be much smaller than the convective resistance, as when the component is made of high conductivity materials and is of small size in relation to this conductivity. In this case it is expected that the temperature gradients within the body are small in comparison to gradients outside. These are called thermally thin bodies and can be approximated as having uniform temperatures within the body. If the gradients within the body are not insignificant, it is a thick body problem. If the heat transfer coefficient and the mass of the body to be heated are relatively large the difference between the surface temperature and the bulk fluid temperature is small; the temperature gradients are primarily within the body. It should be emphasized that the definitions of "thin" and "thick" are relative terms dependent not only on the component itself but also on the convective conditions.

Thermally thin and thick systems can be characterized using a simple analysis. Consider a slab of thickness $2L$ with other dimensions much larger than L as shown in Figure 4.1.40. This slab, starting with uniform initial temperature, T_0, is immersed in a fluid of temperature T_∞. The figure illustrates the two cases of thermally thin and thermally thick systems. The heat transfer is primarily in the direction of the slab thickness. The two resistances for the heat transfer are conduction resistance within the slab and the external convective heat transfer resistance from the slab surface to the fluid bulk.

For the slab, the conduction resistance can be written as $R_{\text{conduction}} \approx \frac{L}{A\kappa_S}$ and the external convective resistance on one side as $R_{\text{convection}} = \frac{1}{hA}$. Here, A denotes the area perpendicular to the slab thickness. The ratio of these two resistances is denoted as the Biot number

$$Bi = \frac{R_{\text{conduction}}}{R_{\text{convection}}} = \frac{L}{A\kappa_S} \Big/ \frac{1}{hA} = \frac{hL}{\kappa_S} \tag{4.1.152}$$

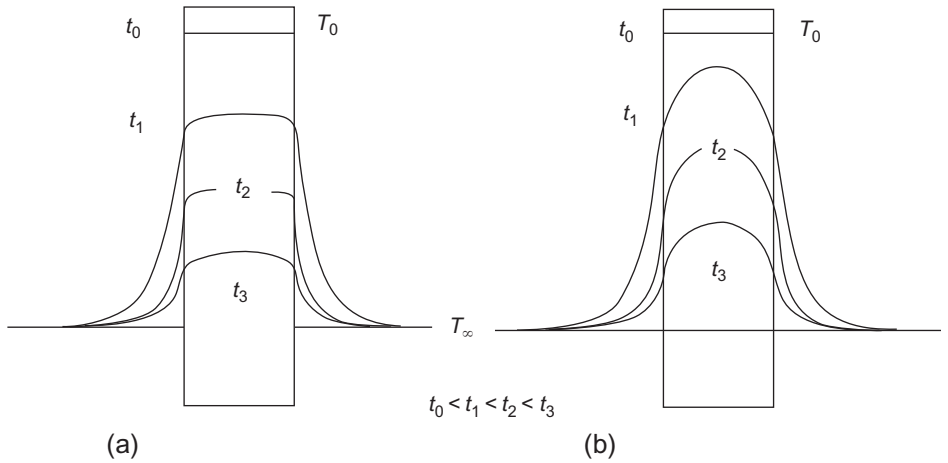


Figure 4.1.40 Schematic temperature profiles in (a) thermally thin and (b) thermally thick bodies.

In the above equation, L is the characteristic dimension for the slab, which can be generalized for irregular-shaped bodies as $\frac{V}{A_S}$, where V is volume of the component and A_S is the external surface area through which convection occurs. If the Biot number is very small, one can consider the component to be thermally thin, such that the temperature within the body is nearly uniform, spatially, at any instant of time. In general, a Biot number <0.1 can be considered to be a thermally thin system for common engineering heat transfer analysis. Such systems are also referred to as lumped parameter systems.

4.1.18.4.1 Thermally Thin Bodies

Transient heat transfer analysis in thin bodies is quite simple. Consider a solid body of volume V, surface area A_s, density ρ_s, and thermal conductivity κ_s initially at temperature T_0. It is immersed into a large volume of fluid at temperature T_∞, at time $t=0$. The amount of fluid is large enough for its bulk temperature to remain constant at T_∞. The convective heat transfer coefficient between the fluid and body is denoted by h. As discussed earlier, the Bi number, given by $\frac{hV}{A_s\kappa_s}$, is so small that the solid body can be considered to be at uniform temperature, T, at any instant of time. Thus, the heat balance gives:

$$V_s\rho_s C\frac{dT}{dt} = -A_s h(T - T_\infty) \tag{4.1.153}$$

The solution of the equation 4.1.153 with the initial condition of $t=0$, $T=T_0$ is

$$\frac{T(t) - T_\infty}{T_0 - T_\infty} = \exp\left(-\frac{A_s h}{V_s\rho_s C}t\right) = \exp\left(-\frac{t}{\tau}\right) \tag{4.1.154}$$

$\tau = \frac{V\rho_s C}{A_s h}$ has the dimension of time and can be termed as the characteristic response time for the system, which is quite useful in comparing transient responses of different systems. Since at large times the body will reach the temperature of the fluid, the LHS of the equation represents the unaccomplished temperature change. The equation can also be written as:

$$\theta^* = \frac{T(t) - T_\infty}{T_0 - T_\infty} = \exp\left(-\frac{hV/A_s}{\kappa_s} \cdot \frac{\kappa_s/\rho C}{(V/A_s)^2} t\right) = \exp(-Bi \cdot Fo) \tag{4.1.155}$$

Fo, the Fourier number, is the dimensionless time and θ^* is the dimensionless temperature difference.

Example 4.1.9

A thermocouple junction, which may be approximated as a sphere, is to be used for temperature measurement in a gas stream. The convection coefficient between the junction surface and the gas is known to be $h = 400\ \mathrm{W\ m^{-2}\ K^{-1}}$ and the junction thermophysical properties are $\kappa = 200\ \mathrm{W\ m^{-1}\ K^{-1}}$, $C = 400\ \mathrm{kg^{-1}\ K^{-1}}$, and $\rho = 8500\ \mathrm{kg\ m^{-3}}$. Determine the junction diameter needed for the thermocouple to have a time constant of 1 s. If the junction is initially at 298 K and is placed in a gas stream that is at 573 K, how long will it take for the junction to reach 572 K?

Solution

The time constant, as discussed earlier, is given by $\frac{V\rho_s C}{A_s h}$. For a sphere, this reduces to $\frac{D\rho_s C}{6h}$, where D is the diameter of the sphere. For the desired time constant of 1 s, D should be 0.7 mm.

The *Bi* number for the thermocouple tip-fluid system is given by

$$Bi = \frac{hV}{A_s \kappa} = \frac{hD}{6\kappa} = 0.0023$$

and is very small so that the thermally thin approximation is valid.

Using Equation (4.1.154), the time for the thermocouple junction to reach 572 K when immersed in a gas stream of 573 K can be calculated as

$$\frac{572 - 573}{298 - 573} = \exp(-t/1)$$

Thus, $t = 5.6$ s.

4.1.18.4.2 Thermally Thick Bodies

When the Biot number (*Bi*) is significantly large (>0.1), the difference between the center and surface temperature within the component is comparable to or larger than the difference between the surface temperature and the bulk temperature of the fluid. In such

cases, one needs to solve the transient heat conduction equation (Equation 4.1.137) with appropriate boundary conditions.

4.1.18.4.3 Conduction in 1D

For simple geometries such as a slab with finite thickness with the other two dimensions being larger, a long cylinder whose radius is much smaller in comparison to its length or a sphere, one can obtain approximate analytical solutions from a 1D analysis. Further, there are special cases wherein the system can be considered as a semi-infinite system as explained later in this section. These cases are primarily analyzed using the 1D transient heat conduction equation.

4.1.18.4.4 Slab

Consider a thermally thick slab shown in Figure 4.1.40. Here, a slab of thickness $2L$ initially at T_0 is being cooled for all $t>0$ by a fluid that is at T_∞. Because of symmetry, one needs to consider only one half of the slab (see Figure 4.1.40). The 1D heat equation in Cartesian coordinates, with thermal properties being independent of temperature, is:

$$\frac{\partial T}{\partial t} = \alpha_s \frac{\partial^2 T}{\partial x^2} \tag{4.1.156}$$

The initial and boundary conditions are:

$$t=0;\ \text{and for } 0 \le x \le L : T = T_0 \quad \text{(Initial condition)} \tag{4.1.157}$$

$$t>0;\ \text{and for } x=0 : \frac{\partial T}{\partial x} = 0 \quad \text{(Boundary condition : symmetry at the center)}$$

$$t>0;\ \text{and for } x=L : -\kappa_s \frac{\partial T}{\partial x} = h\left(T|_{x=L} - T_\infty\right)$$

(Boundary condition : surface heat balance)

The governing equations can be nondimensionalized so that the number of parameters needed to express the solution can be reduced. The equation is nondimensionalized using the following:

$$x^* = \frac{x}{L} \quad \text{(Dimensionless space coordinate)}$$

$$Fo = \frac{\alpha_s t}{(L^2)} \quad \text{(Dimensionless time or Fourier number)}$$

$$\theta^* = \frac{T(x,t) - T_\infty}{T_0 - T_\infty} \quad \text{(Dimensionless temperature difference)}$$

to give,

$$\frac{\partial \theta^*}{\partial Fo} = \frac{\partial^2 \theta^*}{\partial x^{*2}} \tag{4.1.158}$$

with the initial and boundary conditions,

$$\begin{aligned} &Fo = 0;\ 0 \le x^* \le 1; \quad \theta^* = 1 \\ &Fo > 0;\ x^* = 0; \quad \frac{\partial \theta^*}{\partial x^*} = 0 \\ &Fo > 0;\ x^* = 1; \quad \frac{\partial \theta^*}{\partial x^*} = -\mathrm{Bi}\theta^*|_{x^*=1} \end{aligned} \tag{4.1.159}$$

Here Biot number (Bi) is $\frac{hL}{\kappa_s}$.

An analytical series solution is obtained for the above equation using variable separable method (see Ref. [39] for details) and is given as

$$\theta^* = \sum_{i=1}^{\infty} C_i \exp\left(-\lambda_i^2 Fo\right) \cos\left(\lambda_i x^*\right) \tag{4.1.160}$$

$$\text{where } C_i = \frac{4\sin\left(\lambda_i\right)}{2\lambda_i + \sin\left(2\lambda_i\right)}$$

and

$$\lambda_i \tan\left(\lambda_i\right) = Bi$$

Please note that the parameter λ_i denotes the roots of the transcendental equation. In the above infinite series, the first term dominates over other terms, especially for $Fo > 0.2$. Therefore, in many engineering applications, the approximate solution containing only the first term is used, i.e.,

$$\theta^* = C_1 \exp\left(-\lambda_1^2 Fo\right) \cos\left(\lambda_1 x^*\right)$$

The parameter λ_1, which denotes the first root of the transcendental equation, and the corresponding C_1 are tabulated in Table 4.1.4 as given in Ref. [38]. It can also be computed using standard computing software such as MATLAB and OCTAVE; Equation (4.1.161) can be split into two as follows:

$$\theta^* = \theta_0^* \cos\left(\lambda_1 x^*\right) \quad \text{and} \quad \theta_0^* = C_1 \exp\left(\lambda_1^2 Fo\right)$$

Here θ_0^* represents the temperature at the center of the slab ($x^* = 0$). Thus the Equation (4.1.161) can be presented as a set of two charts: one showing the dimensionless center temperature (θ_0^*) as a function of Bi and Fo and the other giving θ^* (for $0 < x^* \le 1$) as a function of θ_0^* and Bi. These charts are named after Heisler, who drew them for the first time [40]. From the approximate solution, one can determine the amount of heat transferred from the beginning to any time t as

Table 4.1.4 Values of the Parameters in the Approximate Analytical Solution of 1D Transient Conduction in a Long Slab, Long Cylinder, and a Sphere [38]

Bi	Long Slab		Long Cylinder		Sphere	
	λ_1	C_1	λ_1	C_1	λ_1	C_1
0.01	0.0998	1.0017	0.1412	1.0025	0.1730	1.0030
0.02	0.1410	1.0033	0.1995	1.0050	0.2445	1.0060
0.04	0.1987	1.0066	0.2814	1.0099	0.3450	1.0120
0.06	0.2425	1.0098	0.3438	1.0148	0.4217	1.0179
0.08	0.2791	1.0130	0.3960	1.0197	0.4860	1.0239
0.1	0.3111	1.0161	0.4417	1.0246	0.5423	1.0298
0.2	0.4328	1.0311	0.6170	1.0483	0.7593	1.0592
0.3	0.5218	1.0450	0.7465	1.0712	0.9208	1.0880
0.4	0.5932	1.0580	0.8516	1.0931	1.0528	1.1164
0.5	0.6533	1.0701	0.9408	1.1143	1.1656	1.1441
0.6	0.7051	1.0814	1.0184	1.1345	1.2644	1.1713
0.7	0.7506	1.0918	1.0873	1.1539	1.3525	1.1978
0.8	0.7910	1.1016	1.1490	1.1724	1.4320	1.2236
0.9	0.8274	1.1107	1.2048	1.1902	1.5044	1.2488
1.0	0.8603	1.1191	1.2558	1.2071	1.5708	1.2732
2.0	1.0769	1.1785	1.5995	1.3384	2.0288	1.4793
3.0	1.1925	1.2102	1.7887	1.4191	2.2889	1.6227
4.0	1.2646	1.2287	1.9081	1.4698	2.4556	1.7202
5.0	1.3138	1.2403	1.9898	1.5029	2.5704	1.7870
6.0	1.3496	1.2479	2.0490	1.5253	2.6537	1.8338
7.0	1.3766	1.2532	2.0937	1.5411	2.7165	1.8673
8.0	1.3978	1.2570	2.1286	1.5526	2.7654	1.8920
9.0	1.4149	1.2598	2.1566	1.5611	2.8044	1.9106
10.0	1.4289	1.2620	2.1795	1.5677	2.8363	1.9249
20.0	1.4961	1.2699	2.2880	1.5919	2.9857	1.9781
30.0	1.5202	1.2717	2.3261	1.5973	3.0372	1.9898

Continued

Table 4.1.4 Values of the Parameters in the Approximate Analytical Solution of 1D Transient Conduction in a Long Slab, Long Cylinder, and a Sphere [38]—cont'd

Bi	Long Slab		Long Cylinder		Sphere	
	λ_1	C_1	λ_1	C_1	λ_1	C_1
40.0	1.5325	1.2723	2.3455	1.5993	3.0632	1.9942
50.0	1.5400	1.2727	2.3572	1.6002	3.0788	1.9962
100.0	1.5552	1.2731	2.3809	1.6015	3.1102	1.9990
∞	1.5708	1.2732	2.4048	1.6021	3.1416	2.0000

$$\frac{Q}{Q_0} = 1 - \frac{\sin\lambda_1}{\lambda_1}\theta_0^*,$$

where $Q_0 = \rho CV(T_i - T_\infty)$, the maximum heat transferred at $t \to \infty$.

4.1.18.4.5 Long Cylinder and Sphere

Using the same methodology, approximate solutions for long cylinders and spheres are also obtained [38]. For both cases, the characteristic dimension used for defining the dimensionless radius (r^*), *Bi* and *Fo* is the radius, *R*.

For a long cylinder of radius *R*,

$$\theta^* = C_1 \exp\left(-\lambda_1^2 Fo\right) J_0(\lambda_1 r^*) \tag{4.1.161}$$

where

$$C_1 = \frac{2}{\lambda_1} \frac{J_1(\lambda_1)}{J_0^2(\lambda_1) + J_1^2(\lambda_1)}$$

and

$$\lambda_1 \frac{J_1(\lambda_1)}{J_0(\lambda_1)} = Bi$$

$$\frac{Q}{Q_0} = 1 - \frac{2\theta_0^*}{\lambda_1} J_1(\lambda_1)$$

Here, J_0 and J_1 are the Bessel functions of the first kind.

For a sphere of radius *R*,

$$\theta^* = C_1 \exp\left(-\lambda_1^2 Fo\right) \frac{1}{\lambda_1 r^*} \sin\left(\lambda_1 r^*\right) \tag{4.1.162}$$

where

$$C_1 = \frac{4(\sin(\lambda_1) - \lambda_1 \cos(\lambda_1))}{2\lambda_1 - \sin(2\lambda_1)}$$

and

$$1 - \lambda_1 \cot(\lambda_1) = B_i$$

$$\frac{Q}{Q_0} = 1 - \frac{3\theta_0^*}{\lambda_1^3}(\sin(\lambda_1) - \lambda_1 \cos(\lambda_1))$$

The parameters λ_1 and C_1 for long cylinders as well as spheres are also tabulated in Table 4.1.4.

Analytical solutions given above are valid only for specific cases having an initial condition of spatially uniform temperature and a convective boundary condition with a constant heat transfer coefficient and a constant fluid temperature. For other cases, numerical methods have to be used. Readers may refer to books on numerical heat transfer [41] for further information.

Example 4.1.10

A 0.314 diameter stainless steel billet ($\rho_s = 7900\ \text{kg m}^{-3}$, $k_s = 25\ \text{W m}^{-1}\ \text{K}^{-1}$, $C = 600\ \text{J kg}^{-1}\ \text{K}^{-1}$) is passing through a 6.1-m long heat-treating furnace. The initial billet temperature is 298 K. The temperature of the billet must be raised to a minimum of 1090 K before working. The heat transfer coefficient between the furnace gases and the billet surface is 85.2 $\text{W m}^{-2}\ \text{K}^{-1}$, and the furnace gases are at 1530 K. At what minimum velocity must the billet travel through the furnace to satisfy these conditions? What will be temperature difference between the center and the surface of the billet when it exits the furnace?

Solution

First verify whether the billet is a thermally thin or a thick system by computing the Biot number. When verifying this, the characteristic length for Bi should be $\frac{V}{A} = \frac{\pi R^2 L}{2\pi R L} = \frac{R}{2}$.

$$Bi = \frac{hR/2}{k_s} = \frac{85 \times 0.152/2}{25} = 0.258 > 0.1$$

The system needs to be treated as thermally thick.

As the minimum temperature that needs to be achieved is 1090 K, it is needed to make sure that the center temperature reaches this temperature as all other temperatures would be higher than this. Being a cylindrical body, the solution given in Equation (4.1.161) needs to be applied. The dimensionless time Fo has to be computed knowing $\theta^*(r^* = 0)$ and Bi. Here, Bi is calculated using characteristic length R.

$$\theta^*(r^*=0)=\frac{T(r=0)-T_\infty}{T(t=0)-T_\infty}=\frac{1090-1530}{298-1530}=0.357$$

$$\frac{hR}{k_s}=Bi=0.516$$

From Table 4.1.4, the values of λ_1 and C_1 are 0.941 and 1.115, respectively. From Equation (4.1.161), the dimensionless time Fo is 1.28. Therefore, the residence time for the billet in the furnace should be

$$Fo=1.28=\frac{\alpha_s t}{R^2}=\frac{\kappa_s t}{\rho_s C R^2}=\frac{25\times t}{7900\times 600\times 0.152^2}$$

$$\therefore\ t=5610\text{s}$$

Corresponding to this time, the velocity of the billet through 6-m long furnace would be 3.85 m h^{-1}. Using Equation (4.1.161) again, the dimensionless temperature at the surface of the billet is calculated as $\theta^*(r^*=1)=\theta^*(r^*=0)J_0(\lambda_1)=0.2822$ which gives the temperature at the surface of the billet as 1182 K, which is 92 K more than the billet center temperature.

4.1.18.4.6 Semi-infinite System

Semi-infinite systems are those that span from $x=0$ to $x=\infty$, the primary boundary condition being applied at the surface at $x=0$. Practically, a slab can be treated as a semi-infinite solid if it has a thickness large enough such that changes applied on one surface ($x=0$) do not, in the time period of interest, result in any noticeable change at the centre line of the material.

Consider a slab that is initially at temperature T_0 stretching from $x=0$ to $x\to\infty$ (Figure 4.1.41). At $t=0$, the temperature at the surface at $x=0$ is raised to T_s and maintained thereafter. A schematic of the evolution of the temperature profile with time ($t_3>t_2>t_1>0$) is shown in the figure. The governing heat equation and the initial and boundary conditions are:

$$\frac{\partial T}{\partial t}=\alpha_s\frac{\partial^2 T}{\partial x^2};\quad t>0;\ 0<x<\infty; \tag{4.1.163}$$

$$\text{Initial condition at}\,(t=0,\ 0<=x<=\infty)\ T=T_0$$

$$\text{Boundary condition 1 at}\,(t>0,\ x=0)\ T=T_s$$

$$\text{Boundary condition 2 at}\,(t>0,\ x\to\infty)\ T=T_0$$

The solution to the equation is obtained by making use of the fact that the temperature profiles at different times have the same shape, i.e., one would get the profile at, say, $t=t_3$ from the profile at $t=t_2$ by appropriately stretching the time axis. In that case, it should be possible to transform the above partial differential equation with the initial

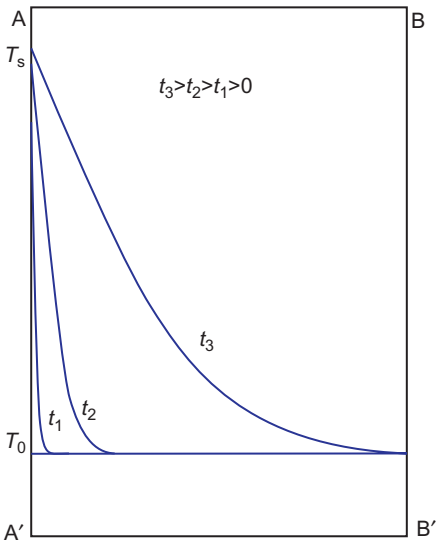


Figure 4.1.41 Schematic of heat conduction in a semi-infinite system.

and the boundary conditions to an ordinary differential equation by appropriately scaling the distance, x, using the time t. This is accomplished by introducing a new variable, called the similarity variable, $\eta = \frac{x}{2\sqrt{(\alpha_s t)}}$:

$$\frac{d^2T}{d\eta^2} = -2\eta\frac{dT}{d\eta};\ \ 0<\eta<\infty; \tag{4.1.164}$$

$$\text{Boundary condition 1}\ \ T(\eta=0)=T_s$$

$$\text{Boundary condition 2}\ \ T(\eta\to\infty)=T_0$$

One may note that the initial condition and boundary condition 2 merge into a single boundary condition. The solution of the above equation is

$$\frac{T(x,t)-T_s}{T_0-T_s} = \text{erf}\left(\frac{x}{2\sqrt{\alpha_s t}}\right) \tag{4.1.165}$$

and the flux at $x=0$ (surface AA')

$$\dot{q}''(x=0) = \frac{\kappa_s(T_s-T_0)}{\sqrt{\pi\alpha_s t}} \tag{4.1.166}$$

Similar analytical solutions for the semi-infinite system with other boundary conditions, either convective heat transfer or a constant heat flux at the surface, have also been obtained [38].

Example 4.1.11

Rate of solidification of a liquid metal poured into a mold depends on the rate of heat that can be extracted through the mold. Hence, understanding the heat transfer through the mold and the metal is of great importance in casting designs. One of the most widely used and simple rule to estimate the solidification time for castings is Chvorinov's rule, named after Nicolas Chvorinov [42]. This rule states that

$$t_{\text{solidification}} = C\left(\frac{V}{A_s}\right)^n$$

Here V and A_s denote the volume and surface area of the casting, respectively. C and n are constants, the value of n being close to 2. The parameter C depends on the properties of metal as well as the mold. Using a 1D heat transfer analysis through a sand mold, the scientific rationale behind this rule can be appreciated (Figure 4.1.42).

Consider a long slab casting of thickness $2L$ being cast in a sand mold as illustrated in the figure. Initially the mold is at room temperature. Consider the hypothetical case where liquid metal is poured just at its melting point T_M. Let us assume that the time for filling the mold is very small compared to the solidification time. Initially the solidification rate will be very high as the mold starts out being cold. As regions in the mold closer to the hot metal are heated, the rate of heat transfer and correspondingly the rate of solidification decrease. If the casting is small and the mold is comparatively thick and is made of low conducting materials such as porous sand, the outer side of the mold can remain at room temperature till the solidification is complete. If the resistance for heat

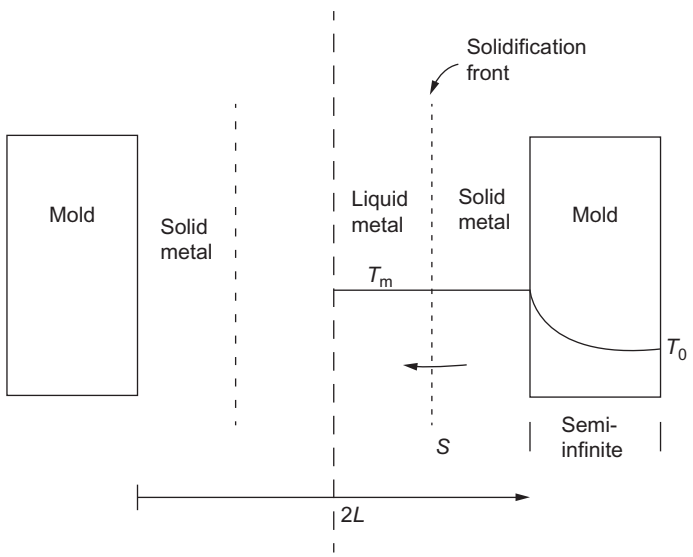


Figure 4.1.42 Solidification of a slab in sand mold.

transfer through the solidified metal is much lower than that through the sand mold, one may further assume that the solidified metal remains close to T_M till the end of solidification. The time–temperature profiles through the mold can then be considered to be those corresponding to a semi-infinite system. Equating the heat flux given by equation for a semi-infinite system to rate at which heat of fusion is released by the solidifying metal gives:

$$\dot{q}'' = \frac{\kappa_{mold}(T_M - T_0)}{\sqrt{\pi \alpha_{mold} t}} = \rho_{metal} \frac{dS}{dt} \Delta H_M \tag{4.1.167}$$

where $\frac{dS}{dt}$ is velocity of the solidification front or the rate of solidification. Integration of the above equation from $x=0$ corresponding to the mold–metal interface to $x=L$ corresponding to the center of the casting gives

$$t_{solidification} = \left(\frac{\rho_{metal} \Delta H_M \sqrt{\pi \alpha_{mold}} L}{2\kappa_{mold}(T_M - T_0)} \right)^2 \tag{4.1.168}$$

That is, the time for solidification is proportional to the square of the slab thickness, L, which agrees with the Chvorinov's law. One needs to note that many assumptions are made in the above analysis.

For the analysis of solidification of castings of shapes other than long slabs, ideally, heat transfer analysis in 2D or 3D needs to be performed. However, as a first approximation, for such cases, the ratio of volume of the casting to its external surface area, $\frac{V}{A_s}$ can be used in place of L in the above equation. Further, the exponent, n and C in the Chvorinov rule can be empirically estimated for castings of specific shape cast in a specific mold. For molds having higher thermal conductivities, such as metallic molds, the heat transfer analysis becomes more elaborate with both the conductive heat transfer resistance through the mold and the external convective and radiative heat transfer resistances becoming significant.

More often than not, numerical methods are needed for solving such problems in two and three dimensions. More details on these methodologies can be found elsewhere [41].

4.1.19. CONVECTION

Convective heat transfer refers to the transfer phenomena in the presence of flow of a fluid. In addition to transfer of heat by conduction discussed above, sensible energy can also be transferred when a fluid particle itself moves from one place to another (advection). The sum of these two processes is the total energy transferred and is termed convective transfer.

There are two kinds of engineering situations where convective transfers are important:

- Temperature variations within a flowing fluid. Examples of this type of problem are temperature profiles in liquid metal bath in a stirred ladle, tundish used in continuous casting, liquid in the mold that is electromagnetically stirred, or variation of temperature within a gas-fired furnace (here radiation is also important since the gas is not transparent). Temperature redistribution takes place when packets of fluids are carried from one place to another dissipating heat along the way by conduction. The flow equations for predicting the flow (continuity and momentum balance equations) in addition to the convective–diffusive heat transport equations must be solved. The generalized heat transport equation is derived by performing a differential heat balance on an infinitesimal volume element, as was done in the case of momentum. In this, both advective and conduction fluxes in and out of the control volume need to be considered. A simplified approach would be to apply the conduction equation developed in an Eulerian frame of reference (fixed with respect to the laboratory frame of reference) in a Lagrangian frame: a fluid particle advecting with the fluid. The partial derivative $\partial/\partial t$ in Equation (4.1.137) is replaced by the substantial derivative $\mathrm{D}/\mathrm{D}t$. The same equation is obtained in both approaches for the cases of constant density, and specific heat, C, i.e.,

$$\rho C\frac{DT}{Dt} = \nabla\cdot(\kappa\nabla T) + \dot{Q}''' \tag{4.1.169}$$

  Here, the term $\dot{Q}'''$ should also include viscous dissipation of mechanical energy into thermal energy; however, in most problems, this term is small enough to be neglected. The heat generation, however, from other sources, such as electromagnetic interactions and chemical reactions, needs to be accounted through the term $\dot{Q}'''$. For most realistic systems of importance, one needs to spend considerable computational effort to obtain solutions to these equations.
- The second situation, which is quite frequently encountered, is where interest is in determining the rate of heat transferred to/from an interface between two media, one which is flowing past the interface. The medium on the other side of the interface can either be a solid or a liquid. Heat transferred from the surface of a piece made of steel when quenched in water during heat treatment is one example. Heat getting lost to air from the liquid metal surface in an open ladle is another.

In the case of a fluid flowing past the surface of solid (or a stagnant liquid), the fluid at the surface is at rest with respect to the solid. The heat transfer mechanism at the surface is by conduction and is proportional to the temperature gradient at the surface. In the liquid away from the surface, the heat transfer and thereby the surface temperature gradient are influenced by fluid flow. To estimate this temperature gradient, a knowledge of the flow is required and estimating this from first principles would involve solving flow and heat transfer equations simultaneously.

Interface heat transfer fluxes are normally represented phenomenologically using the Newton's law of cooling through a quantity called the "heat transfer coefficient," h:

$$\dot{q}'' = h(T_s - T_\infty) = -\kappa_f \left.\frac{\partial T}{\partial s}\right|_{s=0} \tag{4.1.170}$$

where T_s and T_∞ are temperatures at the interface and the bulk of the flowing fluid, respectively; κ_f is the fluid conductivity, and the temperature gradient is that in the fluid at the interface.

Over a finite surface, the heat transfer condition may be different at different locations; one can define a local heat transfer coefficient, h_{loc} as:

$$d\dot{q} = h_{loc}(T_s - T_\infty)dA \tag{4.1.171}$$

where $d\dot{q}$ is the infinitesimal heat transferred over a differential area dA.

In many engineering systems, the average heat transfer across the interface is of more interest than the detailed spatial distribution of it. In such cases, a mean heat transfer coefficient is defined to characterize the net heat across the interface. Mathematically this can be expressed as

$$\overline{h} = \frac{1}{A}\int_A h(dA_{interface}) \tag{4.1.172}$$

For most problems dealt with in this section only the average heat transfer coefficient $\overline{h}$ is required. For brevity, the symbol h has been used to denote average heat transfer coefficient. Exceptions from this notation have been specifically mentioned for those special cases.

Convective transport is generally classified into two categories: forced convection and free convection. In the case of forced convection, the flow is generated by external means, such as blowing a fan around a solid object or making a hot fluid flow through a cold tube. On the other hand, in the absence of any external force, gradients in density assisted by gravity can give rise to flow within the system, which ultimately results in heat transfer. A hot object kept in a still fluid is a typical example. These are free convection or natural convection situations. Additionally, systems operate at high enough temperatures where one of the phases undergoes a phase change at the interface. Cooling water jets falling on hot rolled steel sheets at a temperature of approximately 1200 K in a run-out table is one such example. Readers may refer books on heat transfer [38] for these additional topics.

Heat transfer coefficients have been obtained for various situations of engineering importance, either by solving the generalized equations for flow and heat transfer or more commonly through empirical methods. When presenting these correlations, for both forced and natural convection situations, the flow is classified into external and internal flows.

In internal flows, the flowing fluid is confined with an external boundary through which heat transfer is taking place. The amount of fluid is limited and heat transfer leads

to accumulation/depletion of the total energy contained in the fluid. Heat transfer from/to the walls of a pipe to water flowing through it, wall heat transfer in a gas-fired furnace, and heat loss through the walls of a ladle are some examples.

In external flows, a large body of fluid flows relative to the body on the surface of which heat transfer takes place. When the body of the fluid is large enough, temperature of the fluid far away from the body remains unaffected by the heat transfer. Flow over a cylinder or a sphere and flow over a plate such as a wing of an aeroplane are some examples. Flow around a bubble or an inclusion rising in a large ladle, flow around a rising aluminum droplet shot as a bullet into liquid steel bath for deoxidation, and flow around a temperature probe dipped into the stream of pig iron flowing in the blast furnace runner can be viewed as external flows.

Since in external flows, properties such as velocity and temperature are disturbed only near the boundary of the submerged object, only this boundary region, called the boundary layer, needs to be analyzed. Transfer process in a boundary layer is treated as a separate section called the boundary layer phenomena, and the book by Schlichting and Gersten [30] is a classic reference. Though extensive treatment of this subject is beyond the scope of this chapter, a simple analysis is illuminating since most of the correlations are built around this idea.

4.1.19.1. Boundary Layer Theory

At the beginning of the twentieth century, Prandtl proposed [43] the boundary layer concept. It is considered to be one of the revolutionary concepts in fluid dynamics worth the Nobel Prize [44]. He conceptualized a thin layer of fluid flowing around a body, which ultimately governs the resistance and other consequent heat and mass transfer characteristics.

Consider a flat stationary solid plate and a fluid that moves parallel to this plate as shown in Figure 4.1.43. The fluid approaching the plate has a uniform flow parallel to the length of the plate with a velocity V_∞ (approach velocity). As soon as the fluid layer reaches the plate, the fluid layer adjacent to the plate would come to rest because of the no-slip condition. Subsequently, due to viscous transport, the adjacent fluid layers also start decelerating. As the fluid moves farther along the length of the plate in direction x, more and more fluid layers are decelerated. Thus a velocity profile develops in the neighborhood of the plate as shown in Figure 4.1.43. Moving away from the plate in the y direction, the velocity asymptotically approaches the bulk fluid velocity, v_∞. The large gradients in velocity are restricted to the neighborhood of the plate. By convention, the locus of the points where the velocity is 99% of the approach velocity, v_∞ (also called free stream velocity) is defined as the velocity boundary layer. The thickness of the boundary layer at any cross section increases as x increases. The boundary layer thickness is smaller at higher fluid flow velocities.

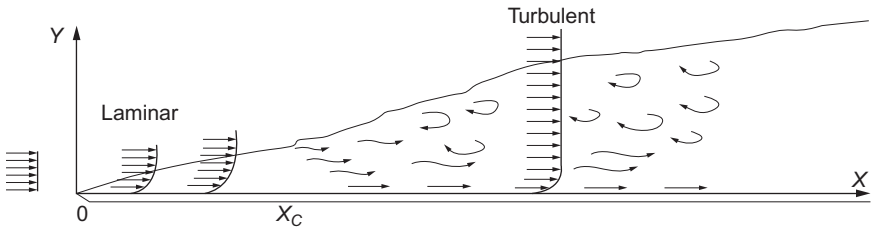


Figure 4.1.43 Schematic of a velocity boundary layer for a parallel flow over a flat plate.

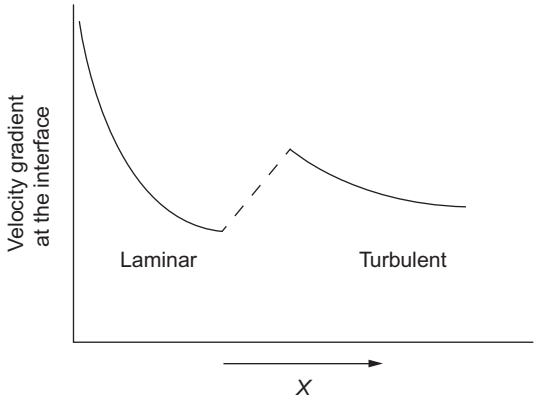


Figure 4.1.44 Illustration of variation of the velocity gradient at the interface in the boundary layer for flow parallel to a flat plate.

The transition from laminar to turbulent flow also occurs for boundary layer flows. For a flat plate, at $Re_x = \frac{\rho V_\infty x}{\mu}$ of about 5×10^5, the flow changes from laminar to turbulent with a transition layer in between. Here x is distance from the leading edge as shown in Figure 4.1.44. Observations have shown that the boundary layer thickness increases significantly during transition from laminar to turbulent flow. The flow structure is streamlined in the laminar region. The turbulent region predominantly consists of eddies; however, close to the plate, eddy strengths become so low that they almost die down and researchers identify a thin fluid layer close to the surface in which the flow is nearly laminar; this is referred to as the laminar sublayer.

Figure 4.1.44 illustrates the variation of velocity gradient for the fluid layer adjacent to the plate along the length of the plate. Ideally for a plate with sharp leading edge, the velocity gradient should approach infinity at $x = 0$ (singularity). Further along the length of the plate the gradient drops. During transition from laminar to turbulent, the velocity gradient shows a sharp increase. In the turbulent regime, the velocity gradient again starts decreasing along the length of the plate.

Since the flow variations are primarily restricted to the boundary layer, it is necessary to solve the flow equations only in this layer. These equations, called the boundary layer equations, are deduced from the Navier–Stokes equations using the order of magnitude approximation [43], which makes the problem considerably simpler. The main basis for this approximation is the observation that for high Reynolds number flows, the boundary layer thickness δ_x at any x is much smaller than x ($\delta_x \ll x$), making gradients in y direction predominant compared to those in the x-direction. The details of these approximations are not presented here; readers can find them in Schlichting's book [30]. The boundary layer equations for flow of an incompressible fluid over a flat plate at zero incidence (plate is parallel to the approach velocity) are:

$$\frac{\partial v_x}{\partial x} + \frac{\partial v_y}{\partial y} = 0 \tag{4.1.173}$$

$$v_x \frac{\partial v_x}{\partial x} + v_y \frac{\partial v_x}{\partial y} = \nu \frac{\partial^2 v_x}{\partial x^2} \tag{4.1.174}$$

For a uniform flow, the gradient in pressure is zero and this is impressed on the boundary layer too.

These equations can be nondimensionalized using a characteristic length L (length of the plate) and the characteristic velocity v_∞ (approach velocity), which yields

$$\frac{\partial v_x^*}{\partial x^*} + \frac{\partial v_y^*}{\partial y^*} = 0 \tag{4.1.175}$$

$$v_x^* \frac{\partial v_x^*}{\partial x^*} + v_y^* \frac{\partial v_x^*}{\partial y^*} = \frac{1}{Re_L} \frac{\partial^2 v_x^*}{\partial x^{*2}} \tag{4.1.176}$$

From the above equation, the dimensionless velocity parallel to the plate can be written as

$$v_x^* = f(x^*, y^*, Re_L) \tag{4.1.177}$$

The expression for a friction factor (also termed as drag coefficient), f, from the friction factor definition for external flows (see Equation 4.1.75) can be written as

$$f = \frac{\tau_{yx}\big|_{y=0}}{\frac{1}{2}\rho V_\infty^2} = \frac{-\mu \frac{\partial v_x}{\partial y}\big|_{y=0}}{\frac{1}{2}\rho V_\infty^2} = \frac{-2}{Re_L} \frac{\partial v_x^*}{\partial y^*}\bigg|_{y^*=0} \tag{4.1.178}$$

From the above equation, the friction factor can be interpreted as the dimensionless velocity gradient at the fluid–solid interface. From Equation (4.1.177), it is evident that the friction factor at any location x^* is given by

$$f_{\text{loc}} = f(x^*, Re_L)$$

and mean friction factor, f,

$$\overline{f} = f(Re_L)$$

A dimensional analysis (see Section 4.1.9) produces the same results, and therefore the above dimensionless relations are valid for turbulent flows as well.

The above example can be extended to heat transfer by considering the plate being maintained at a constant temperature T_s and the approaching fluid at a uniform temperature of T_∞. The temperature of the fluid adjacent to the plate should be the same as that of the plate, T_s, which is different from the free stream fluid temperature. Note the similarity of this condition to the flow situation arising out of the no-slip condition. Very far away from the plate, along the y direction, the temperature asymptotically approaches the free stream temperature of T_∞. Analogous to the velocity boundary layer, a thermal boundary layer then can be defined as the locus of points where the temperature difference $(T_s - T)$ is 99% of the maximum temperature difference $(T_s - T_\infty)$. The thermal boundary layer depends on both flow and thermal characteristics and can have thickness different from the velocity boundary layer. From Equation (4.1.169), the heat transport equation for the boundary layer can be deduced using the order of magnitude analysis:

$$v_x \frac{\partial T}{\partial x} + v_y \frac{\partial T}{\partial y} = \alpha \frac{\partial^2 T}{\partial x^2} \tag{4.1.179}$$

A dimensionless temperature difference $\theta^* = \frac{T_s - T}{T_s - T_\infty}$ can be defined and the heat transport equation can also be made dimensionless:

$$v_x^* \frac{\partial \theta^*}{\partial x^*} + v_y^* \frac{\partial \theta^*}{\partial y^*} = \frac{1}{Re_L Pr} \frac{\partial^2 \theta^*}{\partial x^{*2}} \tag{4.1.180}$$

Here, Pr is the dimensionless number in honor of Prandtl and is defined as $\frac{\nu}{\alpha} = \frac{\mu C}{\kappa}$.

The dimensionless temperature profile can be obtained from Equation (4.1.180) using velocities deduced through the velocity boundary layer equation (Equation 4.1.176). The dimensionless temperature difference would be

$$\theta^* = f(x^*, y^*, Re_L, Pr) \tag{4.1.181}$$

The heat transfer at the solid–fluid interface is related to the definition of heat transfer coefficient as

$$-\kappa_f \left.\frac{\partial T}{\partial y}\right|_{y=0} = h(T_s - T_\infty) \tag{4.1.182}$$

Here, κ_f is thermal conductivity of the fluid; the subscript f is used to distinguish that from the solid. The above equation is made dimensionless as

$$\left.\frac{\partial\theta^*}{\partial y^*}\right|_{y^*=0} = \frac{hL}{\kappa_f} = Nu_L \tag{4.1.183}$$

The LHS of the above equation denotes the dimensionless temperature gradient at the interface similar to the friction factor denoting the dimensionless velocity gradient at the interface. Thus, this dimensionless temperature gradient, termed as Nusselt Number, Nu, can be used to characterize the heat transfer at the interface for different flow and thermal conditions for a given system.

In fact, when $Pr=1$, boundary layer equations for velocity, heat transfer, and mass transfer become identical. If so, Equations (4.1.178) and (4.1.183) yield,

$$f\frac{Re_L}{2} = Nu \quad \text{or} \quad \frac{f}{2} = \frac{Nu}{Re_L} \tag{4.1.184}$$

The above equation demonstrates the equivalence of friction factor and a corresponding dimensionless number for heat transfer. In other words, knowing the friction factor, the heat transfer coefficient can be estimated from the above equation. This is known as the Reynolds analogy. For Prandtl numbers other than 1, this analogy is further modified as,

$$\frac{f}{2} = St\,Pr^{2/3} = \frac{Nu}{Re\,Pr^{1/3}} \tag{4.1.185}$$

where St is the Stanton number given by $\frac{Nu}{Re\cdot Pr}$. This is known as modified Reynolds analogy or Chilton–Colburn analogy [38].

From the expression for the dimensionless temperature difference given by Equation (4.1.181), the expression for a local Nu_{loc} can be written as

$$Nu_{loc} = \left.\frac{\partial\theta^*}{\partial y^*}\right|_{y^*=0} = f_{loc}(x^*, Re_L, Pr) \tag{4.1.186}$$

A mean Nusselt number ($\overline{N}u$) using mean heat transfer coefficient ($\overline{h}$), hence, can be written as

$$\overline{N}u = f(Re_L, Pr) \tag{4.1.187}$$

which is obtained by integrating over the entire surface.

For laminar flow, the boundary layer equations can be solved using similarity principles [30] to obtain the velocity boundary layer thickness as well as the friction factor. Flow remains laminar up to a distance from the leading edge where local Reynolds number, defined as $Re_x = \frac{\rho V_\infty x}{\mu}$, remains less than 5×10^5.

$$\delta(x) = \frac{5x}{\sqrt{Re_x}} \tag{4.1.188}$$

$$f_{\text{loc}} = \frac{0.664}{\sqrt{Re_x}} \tag{4.1.189}$$

$$\overline{f} = \frac{1.328}{\sqrt{Re_x}} \tag{4.1.190}$$

At distances where Re_x is greater than 5×10^5, transitions to turbulent flow take place. For turbulent flows, the following correlations have been obtained empirically

$$\delta(x) = 0.37 x Re_x^{-(1/5)} \tag{4.1.191}$$

$$f_{\text{loc}} = 0.0592 (Re_x)^{-(1/5)} \tag{4.1.192}$$

$$\overline{f} = 0.074 (Re_x)^{-(1/5)} - \frac{1742}{Re_x} \tag{4.1.193}$$

Please note that in case of turbulent flows, the mean friction factor, $\overline{f}$, includes the initial laminar flow region as well.

In general for laminar flows, the thickness of the thermal boundary layer (δ_t) and the velocity boundary layer (δ) are related as

$$\frac{\delta}{\delta_t} \approx Pr^{1/3} \tag{4.1.194}$$

For gases, the Prandtl number is of the order of 1 and consequently the thickness of velocity boundary layer and thermal boundary layers is comparable. For oils, whose viscosities are high and thermal conductivities are low, the Prandtl number is high. Hence, their velocity boundary layers are relatively thicker compared to thermal boundary layer. The converse is true for the liquid metals.

Similar to the friction factor, the correlations for Nu for a flow parallel to an isothermal flat plate are developed either analytically (for laminar flows) or empirically (for turbulent flows) and these are [38]:

For laminar flows

$$Nu_{\text{loc}} = 0.332 Re_x^{1/2} Pr^{1/3} \quad Re < 5 \times 10^5 \; \overline{N}u_L = 2Nu_{\text{loc}} \quad Pr \gtrsim 0.6 \tag{4.1.195}$$

Liquid metals have relatively low viscosities compared to their thermal diffusivities, i.e., Pr is small

$$Nu_{\text{loc}} = 0.564 Re_x^{1/2} Pr^{1/2} \quad Pr \leq 0.05,\ Re_x \cdot Pr \lesssim 100 \tag{4.1.196}$$

$$\overline{N}u_x = 2Nu_{\text{loc}} \tag{4.1.197}$$

For turbulent flows (obtained using Chilton–Colburn analogy)

$$Nu_{\text{loc}} = 0.0296 Re_x^{4/5} Pr^{1/3} \quad 0.6 \lesssim Pr \lesssim 60 \tag{4.1.198}$$

$$\overline{N}u_x = \left(0.037 Re_x^{4/5} - 871\right) Pr^{1/3} \quad 0.6 \lesssim Pr \lesssim 60 \tag{4.1.199}$$

4.1.19.2. Forced Convection: Heat Transfer Coefficient Correlations

For geometrically similar systems, numerous experimental data on heat transfer coefficient with forced convection are correlated using the generic relation $Nu = f(Re, Pr)$. In the following sections, some important correlations relevant for a metallurgical process engineer are presented. Even though these correlations are suitable for engineering calculations, caution needs to be exercised as far as accuracy of these correlations are concerned. Depending on the uncertainties associated with heat transfer experiments, errors as large as 25% are expected. It should be noted that these correlations can be highly sensitive to changes in geometry.

Often correlations are built on some theoretical framework; depending on these, a number of correlations are possible for identical geometric systems. With more sophistication in experimental techniques, existing correlations are often modified with greater accuracy. In the following sections, some popular correlations for selected systems are presented. It is always recommended, however, to refer to recent literature specific to the system under consideration for improved correlations.

Since heat transfer essentially results from temperature variations and materials properties depend on temperature, there is a degree of uncertainty about which representative temperature should be chosen for estimating the properties used in the nondimensionless numbers. Since the correlations are empirical, the procedure followed during the development of the correlation should be adopted. Correlations should therefore prescribe the temperatures at which the material properties need to be evaluated.

4.1.19.3. External Flow

Complex flow patterns such as the boundary layer, its separation, and wake region are developed in external flows, as was discussed earlier. Correspondingly, the local heat transfer also shows complex variations along the surface of an object. These variations in detail can be quite challenging to determine either through experiments or CFD

techniques. Detailed investigations have been carried out especially for simple shapes such as flat plates, long cylinders, and spheres. However, one can make a relatively simpler analysis of these systems by estimating the average heat transfer coefficient using empirical correlations developed specifically for these purposes. These are prescribed below:

4.1.19.3.1 Flow over a Flat Plate

The correlations for laminar flow obtained from the boundary layer analysis were presented earlier in Section 4.1.19.1.

4.1.19.3.2 Flow Across Cylinder

Empirical correlation recommended by Hilpert [45] is one of the most widely used correlations to estimate average heat transfer coefficient for flow around sphere and is given by

$$\overline{Nu}_D = \frac{\overline{h}D}{\kappa_f} = CRe_D^m Pr^{1/3} \quad \text{for } Pr \gtrsim 0.7 \tag{4.1.200}$$

The empirical constants C and m have been tabulated in Table 4.1.5. The fluid properties need to be evaluated at the film temperature, which is the average of the temperature of the approaching fluid, T_∞, and the temperature at the surface of the cylinder, T_s, i.e., $T_f = (T_\infty + T_s)/2$. This correlation has also been extended to cross flow across noncircular cylinders by modifying the values of empirical constants C and m; details can be found elsewhere [38].

Churchill and Bernstien [46] have proposed a single comprehensive correlation for Nusselt number that can be used for the entire range of Re_D as

$$\overline{Nu}_D = 0.3 + \frac{0.62 Re_D^{1/2} Pr^{1/3}}{\left[1 + (0.4/Pr)^{2/3}\right]^{1/4}} \left(1 + \left\{\frac{Re_d}{282{,}000}\right)^{5/8}\right\}^{4/5} \quad \text{for } Re_D Pr \gtrsim 0.2. \tag{4.1.201}$$

Table 4.1.5 Constants of Equation (4.1.200) to estimate average, $\overline{h}$ for flow across circular cylinder [45]

Re_D	C	m
0.4–4	0.989	0.330
4–40	0.911	0.385
40–4000	0.683	0.466
4000–40,000	0.193	0.618
40,000–400,000	0.027	0.805

The properties are evaluated at the film temperature $T_f = (T_\infty + T_s)/2$.

4.1.19.3.3 Flow Around Sphere

Whitaker recommends the following expression to estimate the average heat transfer coefficient for flow around spheres [47]

$$\overline{Nu_D} = 2 + \left(0.4Re_D^{1/2} + 0.06Re_D^{2/3}\right) Pr^{0.4} \left(\frac{\mu}{\mu_s}\right)^{1/4} \quad (4.1.202)$$

$$\text{for} \quad 0.71 \leq Pr \lesssim 380;$$
$$3.5 \lesssim Re_D \lesssim 7.6 \times 10^4;$$
$$1.0 \lesssim \frac{\mu}{\mu_s} \leq 3.2$$

Here, all properties are evaluated at the temperature of the approaching fluid, T_∞, except μ_s which is evaluated at T_s.

Ranz and Marshall's [48] correlation for freely falling liquid drops is relatively a simple expression to evaluate heat transfer around particles

$$\overline{Nu_D} = 2 + 0.6Re_D^{1/2} Pr^{1/3} \quad (4.1.203)$$

It may be noted that in both of these expressions, when $Re_D \to 0$,

$$Nu_D = 2 \quad (4.1.204)$$

This corresponds to heat transfer by pure conduction from spherical surface to a stationary, infinite medium around the surface.

4.1.19.4. Internal Flow: Flow Through Conduits

In many metallurgical plants, hot flue gases from furnaces flowing through ducts, heat exchangers, and gas-cleaning systems are finally dispersed in the atmosphere through a stack. In order to attain high thermal efficiencies, process gases, blast air, etc., are preheated using heat exchangers such as Cooper stoves and recuperators before feeding them into reactors or furnaces. Large amounts of water are made to flow through channels to achieve cooling in continuous casting, walls of blast furnace and EAF, supersonic nozzle tip in BOF, etc. The extent of heat transfer achieved through such internal flow systems affects the productivity, product quality, and component life. Therefore, heat transfer to/from flowing fluids through conduits is of prime importance.

The definition of a bulk fluid temperature away from the surface is nonobvious in the case of internal flows, since the heat transfer process keeps changing the total heat content as the fluid flows downstream. The definition of the heat transfer coefficient, h, for flow through conduits is therefore modified as follows

$$\dot{q}''(z) = h(T_s(z) - T_m(z)) \quad (4.1.205)$$

where $\dot{q}''$ is the heat flux from the inner surface of the conduit to the fluid flowing through it, T_s is the inner surface temperature of the conduit, and T_m is the mean temperature of the fluid. Here z stands for the location along the length of the conduit. The expression for the mean temperature T_m is given by

$$T_m(z) = \frac{\int_{A_c} \rho v_z C_p T dA_c}{\dot{m} C_p} \tag{4.1.206}$$

The mean temperature $T_m(z)$ at an axial location, z, can be physically interpreted as the mean temperature of the fluid collected at the cross section at z. $T_m(z)$ is also referred to as the end mixing temperature.

Consider a simple case of cold fluid flowing through a tube (Figure 4.1.45). By some external means, the wall of the tube is maintained at a constant temperature. Let us consider the case where the temperature at the wall of the pipe is more than that of the mean temperature of the fluid. A schematic of the temperature profile of the fluid as it traverses through the pipe is shown in Figure 4.1.45. If the length of the pipe is much larger than its diameter, the velocity attains a constant profile along the axial direction (fully developed velocity profile, as discussed in Section 4.1.6). The temperature profile, however, changes both along with the radial and axial directions of the pipe. The analogy with the velocity profile is the fact that after some entrance length, the shapes of the profiles become self-similar, and can be scaled to make a constant profile. A dimensionless temperature difference can be defined as follows

$$\theta^* = \frac{T(r,z) - T_s}{T_m(z) - T_s} \tag{4.1.207}$$

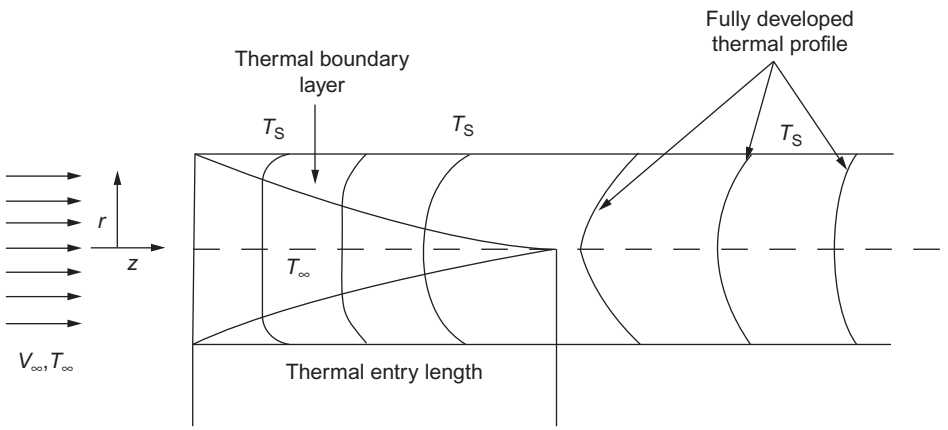


Figure 4.1.45 Schematic temperature profile of a cold fluid flowing through a tube maintained at constant temperature.

where, $T(r, z)$ denotes the temperature of fluid at any location in the pipe, T_s is the temperature at the surface of the pipe, and T_m is the mean temperature of the fluid.

The fluid attains a fully developed temperature profile if the dimensionless temperature, θ^*, becomes independent of z $\left(\frac{\partial \theta^*}{\partial z} = 0\right)$. It can be proven theoretically that fully developed temperature profiles can be attained for two cases: (1) when the surface temperature of pipe is maintained constant and (2) when a constant heat flux is maintained at the pipe surface. The former case is more common and needs detailed analysis. The latter case is simpler, since rate of heat transfer is constant and specified.

Figure 4.1.46 illustrates the variation of the heat transfer coefficient, h, along the length of a pipe. The local heat transfer coefficient near the entrance decreases with increasing z and attains a constant value once the temperature profile is fully developed. The distance from the entrance to the location where the temperature profile becomes fully developed is termed as the thermal entry length. For laminar flows, the thermal entrance effects would prevail up to a distance z, such that $\frac{z/D}{Re_D Pr} = \frac{1}{Gz_D} \approx 0.05$. Gz_D is the Graetz number [38].

The heat transfer correlation for laminar flow through conduits of circular cross section [49,50] is given by

$$\overline{Nu_D} = \frac{hD}{\kappa_f} = 3.66 + \frac{0.0668 Gz_D}{1 + 0.04 Gz_D^{2/3}} \text{ Laminar flow, } T_s = \text{constant} \qquad (4.1.208)$$

For long pipes $\left(\frac{1}{Gz_D} \gg 0.05\right)$, the second term on the RHS becomes negligible. For laminar flows through conduits other than circular cross sections, readers may refer to the monograph by Shah and London [51].

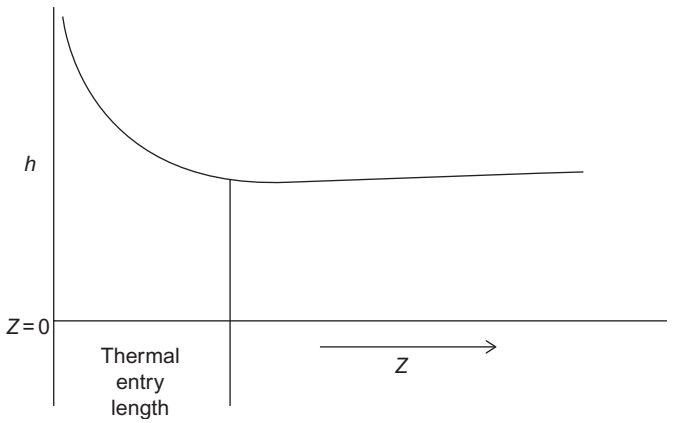


Figure 4.1.46 Schematic temperature profile of a cold fluid flowing through a tube maintained at constant temperature.

Most engineering flows through conduits are turbulent. For fully developed turbulent flow through smooth tubes, the heat transfer coefficient can be estimated using the Dittus–Boelter equation [52]

$$\overline{Nu}_D = \frac{hD}{\kappa_f} = 0.023 Re_D^{4/5} Pr^n \tag{4.1.209}$$

$$\text{with } n = 0.4 \text{ for heating } (T_s > T_m) \quad \text{and} \quad n = 0.3 \text{ for cooling } (T_s < T_m)$$

$$Re_D \gtrsim 10{,}000; \quad 0.6 \lesssim Pr \lesssim 160; \quad \frac{L}{D} \gtrsim 10$$

In the above equation, all the properties need to be evaluated at T_m.

For flows where T_s is significantly different from T_m, the following equation due to Sieder and Tate [53] is recommended

$$\overline{Nu}_D = \frac{hD}{\kappa_f} = 0.023 Re_D^{4/5} Pr^{1/3} \left(\frac{\mu}{\mu_s}\right) \tag{4.1.210}$$

$$Re_D \gtrsim 10{,}000; \quad 0.7 \lesssim Pr \lesssim 16{,}700; \quad \frac{L}{D} \gtrsim 10$$

In the above equation, all properties except μ_s are evaluated at T_m. μ_s denotes the viscosity at T_s.

Entry lengths for turbulent flow are typically small, $10 \lesssim \frac{z}{D} \lesssim 60$. For long tubes, it is reasonable to assume the average Nusselt number for the entire length. For short tubes, the following equation is recommended

$$\frac{\overline{Nu}_{D,\text{short}}}{\overline{Nu}_D} = 1 + \frac{C}{(z/D)^m} \tag{4.1.211}$$

The values of C and m depend on the nature of the inlet such as sharp-edged and nozzle. More details on these can be found in Refs. [54,55].

Liquid metals have small Prandtl numbers. Seban and Shimazaki [56] recommend the following correlation

$$Nu_D = 5.0 + 0.025 Pe_D^{0.8} \quad T_s = \text{constant} \quad Pe_D = Re_D Pr \gtrsim 100 \tag{4.1.212}$$

For turbulent flow through noncircular conduits, the above correlations can be used applying the concept of equivalent diameter or hydraulic radius (see Section 4.1.9.2) with reasonable accuracy.

Knowing the heat transfer coefficient, h, the variation of the mean temperature of a fluid flowing through a conduit with the inner walls of the conduit maintained at a constant temperature, T_s, can be developed performing an overall heat balance. Consider a fluid at $T_{m,in}$ entering a conduit at a mass flow rate of $\dot{m}$. Considering an infinitesimal length, Δz, and performing a heat balance (as shown in Figure 4.1.47a)

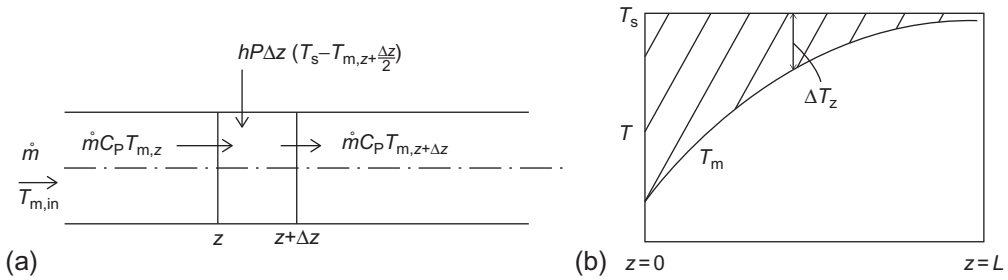


Figure 4.1.47 Heat balance for a fluid flowing through a pipe at constant surface temperature: (a) control volume and (b) schematic temperature profile of the fluid.

$$\dot{m}C_{\mathrm{p}}\left(T_{\mathrm{m},z}-T_{\mathrm{m},z+\Delta z}\right)+hP\Delta z\left(T_{\mathrm{s}}-T_{\mathrm{m},z+\Delta z/2}\right)=0 \tag{4.1.213}$$

Here, P is the perimeter of the conduit. From the above, the following differential equation can be deduced

$$\dot{m}C_{\mathrm{p}}\frac{\mathrm{d}T_m}{\mathrm{d}z}=hP\left(T_{\mathrm{s}}-T_{\mathrm{m}}\right) \tag{4.1.214}$$

For a constant h, C_{p}, and T_{s} this equation can be integrated for a length of pipe, L of the conduit as

$$\ln\left(\frac{T_{\mathrm{s}}-T_{\mathrm{m}}(L)}{T_{\mathrm{s}}-T_{\mathrm{m,in}}}\right)=-\frac{hP}{\dot{m}C_{\mathrm{p}}}L \tag{4.1.215}$$

A schematic of the evolution of the mean temperature is shown in Figure 4.1.47b. Here $\Delta T_z=T_{\mathrm{s}}-T_{\mathrm{m},z}$ is the temperature difference at location z and is the driving force for the convective heat transfer. As the temperature profile is logarithmic, it is possible to define a logarithmic mean temperature difference (LMTD) given by the shaded area divided by the axial length z. The expression for the LMTD is

$$\Delta T_{\mathrm{LM}}=\frac{\Delta T_L-\Delta T_{\mathrm{in}}}{\ln(\Delta T_L/\Delta T_{\mathrm{in}})} \tag{4.1.216}$$

Thus, the heat balance equation can also be written as

$$\dot{m}C_{\mathrm{p}}\left(T_{\mathrm{m},L}-T_{\mathrm{m,in}}\right)=h(PL)\Delta T_{\mathrm{LM}} \tag{4.1.217}$$

Under conditions of varying rates of heat transfer along the axis, it is difficult to maintain a constant surface temperature. In many practical applications, the temperature of the external fluid, which surrounds the pipe, is constant rather than the inner surface temperature of the conduit as illustrated in Figure 4.1.48. Convective heat transfer takes place both externally and internally. In cases where the length of the pipe is much larger than its diameter, the conductive heat transfer through the pipe is predominantly in the direction

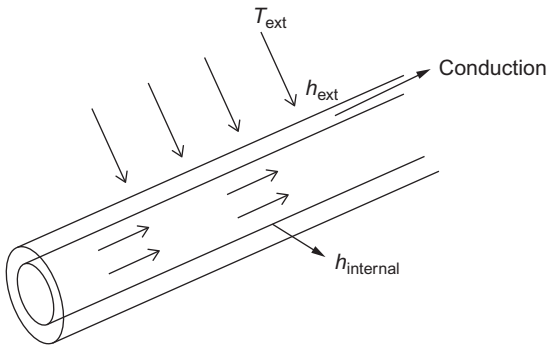


Figure 4.1.48 Schematic showing the heat transfer from a hot/cold fluid flowing through a thick pipe.

normal to the axis of the conduit. The problem therefore becomes that of radial conduction with convective boundary conditions discussed in Section 4.1.18.3. It is possible to define an overall heat transfer coefficient, $h_{overall}$ by considering the internal convective heat transfer, the conduction through the pipe, and the external convective (also radiation if significant) heat transfer. The expression for $h_{overall}$ can be deduced by considering all the heat transfer resistances in series and is given by

$$\frac{1}{A_{external}h_{overall,ext}} = \frac{1}{A_{internal}h_{overall,int}} = \frac{1}{A_{internal}h_{internal}} + \text{Conduction resistance} + \frac{1}{A_{external}h_{external}} \quad (4.1.218)$$

The heat transfer rate is given by

$$\dot{Q} = A_{external}h_{overall,ext}\Delta T_{LM} = A_{internal}h_{overall,int}\Delta T_{LM} \quad (4.1.219)$$

where ΔT_{LM} is given by Equation (4.1.217).

Example 4.1.12

In a continuous slab caster, the wide face mold consists of a copper plate of 20 mm thickness and 1.25 m wide (exposed surface), backed by a steel plate, with slots for the water to flow as shown in Figure 4.1.49a. The typical heat flux profile in the mold for different casting speeds is given in Figure 4.1.49b [57]. Design engineers need to determine the minimum velocity needed to maintain a rate of heat transfer such that the cooling water that is in contact with the copper mold (cold face) does not boil, which otherwise can come in the way of heat transfer that could result in mold damage. Consider a casting speed of 1.2 m min^{-1}. The heat transfer coefficients for the slots may be approximated by the use of correlation for tube heat transfers, with appropriate equivalent diameters (hydraulic radius concept). Calculate the minimum velocity of water flow in the mold,

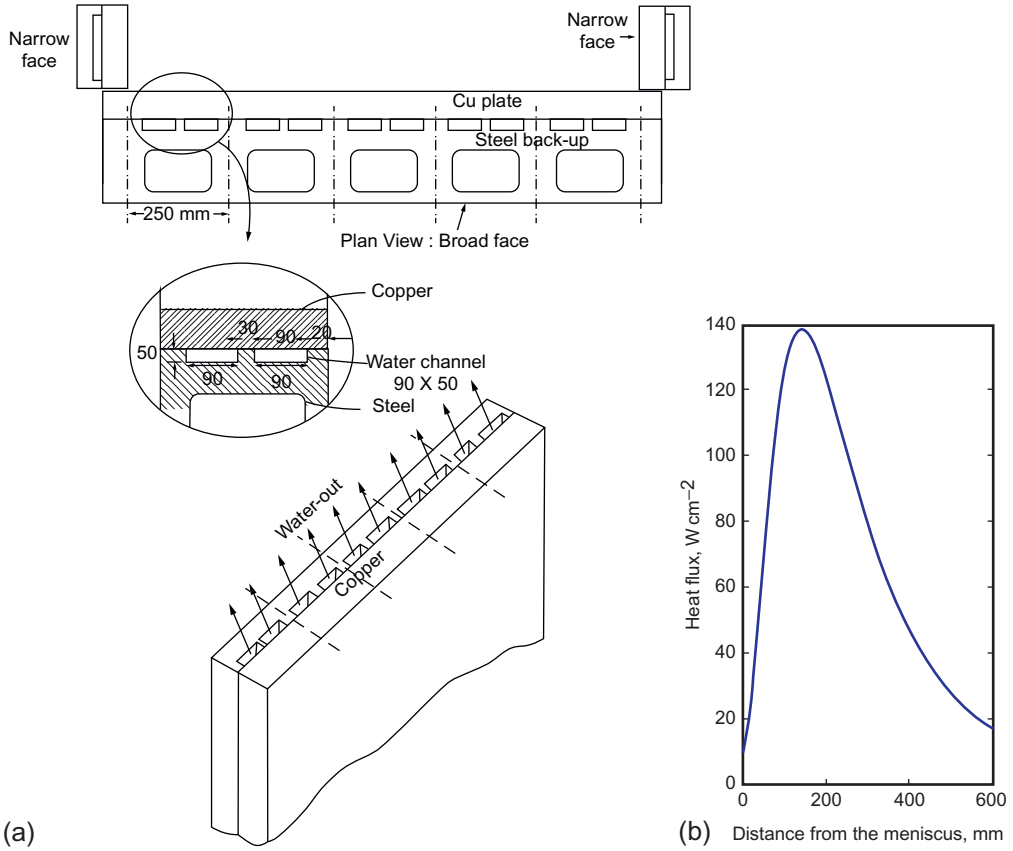


Figure 4.1.49 (a) Schematic of a continuous casting mold with cooling channel and (b) heat flux through a continuous casting mold.

so that at no place in the cold surface of copper plate the temperature exceeds 100 °C, if the bulk water temperature is 20 °C.

Data: water: density = 950 kg m^{-3}, viscosity = 0.37×10^{-3} Pa s, $C_p = 4195$ J kg^{-1}, $\kappa = 0.67$ Wm^{-1} K^{-1}, and $Pr = 2.29$.

Solution

The heat transfer through the cooling channel needs to be high enough so that the temperature at the hot face (mold face in contact with the liquid/solid steel) is kept well below the melting point of copper. This is maintained through high heat transfer coefficients in the cooling channels. It is to be noted that the slots are in the steel plate and this is in contact with the cold surface of the copper mold. Only some part of the cold face of the copper mold is in contact with the cooling water. The conductive resistance of the steel plate is significantly larger than that of the copper mold; heat flux through the steel plate is neglected.

From the measured heat flux profile given in Figure 4.1.49b,

- Maximum heat flux at the hot face $= 1.40 \times 10^6\ \mathrm{Wm^{-2}}$
- Maximum heat flux in cooling channels $= 1.40 \times 10^6 \times 250/(2 \times 90) = 1.94 \times 10^6\ \mathrm{Wm^{-2}}$ (only part of cold face of the copper mold is in contact with the cooling water)

The minimum heat transfer coefficient, $h_{\min}$, needed for the cooling channel $= 1.94 \times 10^6\ \mathrm{Wm^{-2}} = h_{\min}(100 - 20)$. Here, 100 °C is the boiling of water at a pressure 1 atm.; the cold face of the copper mold needs to be below the boiling point of water to avoid any formation of steam bubbles. The boiling point of water increases with increasing pressure; the static pressure in the channel is kept at a pressure much higher than the atmospheric pressure to keep the surface temperature well below the boiling point.

$h_{\min} = 2.43 \times 10^4\ \mathrm{Wm^{-2}\,K^{-1}}$. Flow rate needed to maintain $h_{\min}$ of $2.43 \times 10^4\ \mathrm{Wm^{-2}\,K^{-1}}$ can be back calculated using correlation for internal flow (Equation 4.1.210)

$$Nu = 0.023 Re_D^{4/5} Pr^{0.4}$$

Equivalent diameter for the cooling channel (see Section 4.1.9.2)

$$D_{\text{equivalent}} = \frac{4A}{P} = \frac{4 \times 90 \times 50}{2 \times (90 + 50)} = 64.3\,\mathrm{mm}$$

$$Nu = \frac{h_{\min} D_{\text{equivalent}}}{\kappa_f} = \frac{3.038 \times 10^4 \times 64.3 \times 10^{-3}}{0.67} = 2332 = 0.023 Re_D^{4/5} Pr^{0.4}$$

From the above, $Re = \rho v D_{\text{equivalent}}/\mu = 1.19 \times 10^6$, which yields a minimum velocity of $\overline{v} = 7.24\,\mathrm{ms^{-1}}$.

4.1.19.5. Heat Transfer in Packed Beds

Incropera and Dewitt [38] recommend the following correlation developed based on the modified Reynolds or Chilton–Colburn analogy (see Section 4.1.19.1), for estimating heat transfer coefficients in packed beds

$$\varepsilon \bar{j}_H = StPr^{2/3} = 2.06 Re_D^{-0.575} \psi \quad \text{for } Pr \approx 0.7 \text{ and } 90 \lesssim Re_D \lesssim 4000 \tag{4.1.220}$$

where

$$Re_D = \frac{\rho v_0 D_p}{\mu}$$

$$St\,(\text{Stanton number}) = \frac{Nu}{Re_D Pr}$$

$$\psi = \text{Correction factor for particle shape}$$

Here D_p is the particle diameter and V_0 is the superficial velocity. ψ is 0.79 for cylindrical particles with aspect ratio 1 and 0.71 for cubes. The properties should be evaluated at the arithmetic mean of the fluid inlet and outlet temperatures.

4.1.19.6. Natural Convection or Free Convection

Natural or free convection is one of the common modes of heat transfer that is encountered in many engineering processes. A pipe carrying a hot fluid and a furnace kept in a common plant environment are some typical examples. The surface at the exterior of the pipe or the furnace wall is cooled by the still air in the plant environment. Adjacent to the exterior surface where temperature is different from the surroundings, results in density gradient which due to gravity results in fluid to flow close to the surface. Free convective velocity boundary layer close to vertical hot flat plate is illustrated in the Figure 4.1.50.

As can be readily seen from Figure 4.1.50, the flow characteristic depends on the orientation of the surface with respect to the gravitational direction and therefore the heat transfer characteristics also would change depending on the orientation. Unlike forced convection, a Reynolds number for free convection cannot be defined as there is no characteristic velocity that is known *a priori*. The velocity profile in the boundary layer depends on the variation of density with respect to temperature, decided by a property called volumetric thermal expansion coefficient $\beta = -\frac{1}{\rho}\left(\frac{\partial \rho}{\partial T}\right)_P$. For relatively small differences in temperatures in the boundary layer and in the surrounding fluid, a linear relation can be assumed

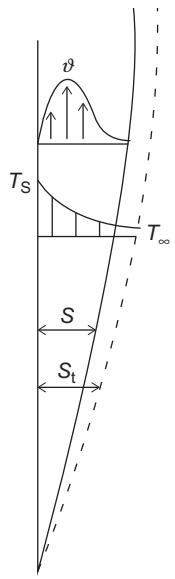


Figure 4.1.50 Schematic of free convective velocity and thermal boundary layer from hot vertical plate.

$$\beta \approx -\frac{1}{\rho}\left(\frac{\Delta\rho}{\Delta \mathrm{T}}\right) = -\frac{1}{\rho}\left(\frac{\rho-\rho_\infty}{T-T_\infty}\right) \tag{4.1.221}$$

to yield

$$\rho - \rho_\infty \approx \rho\beta(T - T_\infty) \tag{4.1.222}$$

This simplification is known as the Boussinesq approximation [58]. The driving force for the natural convection is evident in the above equation. The boundary layer analysis presented earlier can be extended for natural convection using the Boussinesq approximation. In this analysis, the Reynolds number is defined using a characteristic velocity v_0. Buoyant force being origin of flow, v_0 is chosen such that $v_0^2 = g\beta(T_s - T_\infty)L$. Then, the Reynolds number becomes $\sqrt{g\beta(T_s - T_\infty)L^3/v^2}$. In place of this Reynolds number, another number called Grashof number, *Gr*, is defined as the square of the Reynolds number given by

$$Gr_L = \frac{g\beta(T_s - T_\infty)L^3}{v^2} \tag{4.1.223}$$

For free convective flows without any forced convection, the Nusselt number, *Nu*, will be a function of *Gr* and *Pr*, $Nu = f(Gr, Pr)$. Since in most correlations *Gr* and *Pr* occur as a product, another number called Rayleigh number, $Ra = GrPr$, is also used in many free convection correlations. In principle, most forced convection flows will have associated free convective flows as well, hence $Nu = f(Re, Gr, Pr)$. However, the forced convection encountered in engineering is generally where $Re_{\text{forcedconvection}}$ is much larger than $\sqrt{Gr}$ and contribution due to free convection is often neglected.

4.1.19.6.1 Flat Plates

As mentioned earlier, the correlations for free convective flows around flat plates depend on the orientation of the plate with respect to the gravitational direction.

For vertical plates, Churchill and Chu [59] recommend the correlation,

$$\overline{Nu}_L = \left[0.825 + \frac{0.387 Ra_L^{1/6}}{\left[1 + (0.492/Pr)^{9/16}\right]^{8/27}}\right]^2 \tag{4.1.224}$$

Here *L* is the length of the plate in the vertical direction. All the properties need to be evaluated at the film temperature, $T_f = (T_s + T_\infty)/2$. This correlation can also be used for vertical cylinders as long as the diameter of the cylinder is much higher than the boundary layer thickness, i.e., $\frac{D}{L} \gtrsim \frac{35}{Gr^{1/4}}$.

For horizontal plates, the characteristic length *L* is defined as the ratio of surface area to the perimeter, $\frac{A_s}{P}$. The correlations are

Upper surface of hot plate or lower surface of cold plate [60]

$$\overline{Nu}_L = 0.54 Ra_L^{1/4} \quad \text{for} \left(10^4 \lesssim Ra_L \lesssim 10^7, Pr \gtrsim 0.7\right)$$

$$\overline{Nu}_L = 0.15 Ra_L^{1/3} \quad \text{for} \left(10^7 \lesssim Ra_L \lesssim 10^{11}, \text{ for all } Pr\right)$$

Lower surface of hot plate or upper surface of cold plate [61]

$$\overline{Nu}_L = 0.52 Ra_L^{1/5} \quad \text{for} \left(10^4 \lesssim Ra_L \lesssim 10^9, Pr \gtrsim 0.7\right)$$

For inclined surfaces with top and bottom surfaces cold and hot, respectively, the correlation for the vertical surface can be used, except that in calculating Gr, g should be replaced by $g \cos\theta$. Here, θ is the angle the surfaces makes with the vertical. Unfortunately, for an inclined surface with top and bottom surfaces being hot and cold, respectively, the flow has three-dimensionality and no generalized correlation can be recommended [38].

4.1.19.6.2 Cylinders

For horizontal cylinders, Churchill and Chu [62] recommend the correlation

$$\overline{Nu}_D = \left[0.6 + \frac{0.387 Ra_D^{1/6}}{\left[1 + (0.559/Pr)^{9/16}\right]^{8/27}}\right]^2 \quad \text{for } Ra_D \lesssim 10^{12} \tag{4.1.225}$$

4.1.19.6.3 Spheres

For free convection around spheres, Churchill [63] recommends the following correlation

$$\overline{Nu}_D = 2.0 + \frac{0.589 Ra_D^{1/4}}{\left[1 + (0.469/Pr)^{9/16}\right]^{4/9}} \quad \text{for } Ra_D \lesssim 10^{11},\ Pr \gtrsim 0.7 \tag{4.1.226}$$

For other specific systems, readers may refer other sources [38].

4.1.20. RADIATION

Unlike momentum and mass transport, heat can be transported without the presence of a medium as electromagnetic waves or photons; this is termed radiative transport. All materials emit and absorb radiation. For gases and semitransparent materials, this is a volumetric phenomenon. In most solids and liquids, radiation emitted by interior molecules is absorbed by the neighboring molecules; surface emission originates from volume within a distance of approximately 1 μm. Hence, such emission and absorption of radiation can be viewed as surface phenomena. Radiative heat exchange between such opaque surfaces is often encountered in engineering. Additionally, the gaseous medium present between these opaque surfaces may participate in the radiative exchange. In this section, methodologies to estimate the heat exchange between opaque surfaces are discussed in detail. At the end of the section, a brief description of a methodology to estimate radiative exchange in the presence of participating gaseous medium is presented.

4.1.20.1. Definitions

Before, describing these methodologies, some of the important terminologies used to describe radiative exchange need to be defined.

4.1.20.1.1 Radiation Intensity

Radiation originating from a point source travels at the speed of light in all directions. Hence, by its very nature, spherical coordinates are needed to describe radiation. Consider a surface with an infinitesimal area, dA, emitting radiation in a direction θ with respect to the normal, as shown in Figure 4.1.51. In the spherical coordinate system with its origin, O, located at the surface dA and z-coordinate aligned with the normal to the surface, (r,θ,ϕ) denotes the coordinates of a point P. The intensity of radiation at point P, $I_{\lambda,e}$, for the radiation emanating from surface dA at a wavelength, λ, is defined based on the energy that reaches the point P. This is written as

$$d\dot{q}_{\lambda,e} = I_{\lambda,e}(\lambda,\theta,\phi)dA\cos(\theta)\cdot d\omega\cdot d\lambda \tag{4.1.227}$$

$d\dot{q}_{\lambda,e}$ is the rate of radiative energy that reaches an area dA_1 around point P subtending solid angle $d\omega$ along the direction OP from surface dA having wavelength between λ and $\lambda + d\lambda$. It may be noted that the term $dA\cos\theta$ denotes the component of area dA along the direction OP.

In a nonparticipating medium, the intensity of radiation does not change along its direction of travel; this can be easily comprehended from the concept of solid angle and the fact that radiation travels along straight lines. Further, using spherical coordinates,

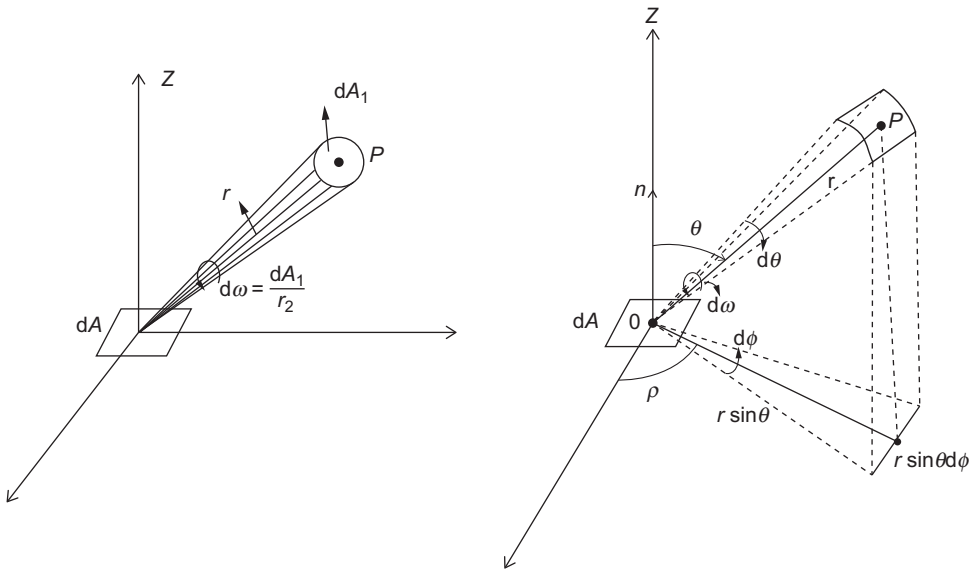


Figure 4.1.51 Radiation intensity definition illustrated in spherical coordinate system.

it can be easily shown that $d\omega = \sin(\theta)d\theta\, d\phi$. Thus, the spectral (with respect to wavelength), directional (with respect to θ and ϕ) intensity for emission is defined as

$$I_{\lambda,e}(\lambda,\theta,\phi) = \frac{d\dot{q}_{\lambda,e}}{dA\cos(\theta)\cdot d\omega\cdot d\lambda} \tag{4.1.228}$$

Equation (4.1.228) can be integrated for all the wavelengths from 0 to ∞ to obtain directional intensity, I_e given by

$$I_e(\theta,\phi) = \int_0^\infty I_{\lambda,e}(\lambda,\theta,\phi)d\lambda \tag{4.1.229}$$

If the intensity of radiation emitted is same in all directions, then such a surface is termed as a diffuse emitter, i.e., for a diffuse emitter, $I_e(\theta,\phi)$ is a constant.

4.1.20.1.2 Emissive Power

If all the radiations per unit time per unit area of the emitted by the surface dA in all directions at all wavelengths are accounted for, this yields the emissive power, E of the surface.

$$E = \int_0^{2\pi}\int_0^{\frac{\pi}{2}}\int_0^\infty I_{\lambda,e}(\lambda,\theta,\phi)\cos(\theta)\sin(\theta)d\lambda\; d\theta\; d\phi \tag{4.1.230}$$

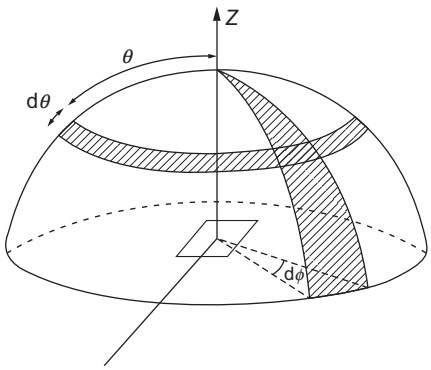


Figure 4.1.52 Illustration of the emissive power of radiant heat source as a function of geometry.

This is illustrated in Figure 4.1.52. Please note that from an opaque surface, the emissions are only in one half of sphere and hence in Equation (4.1.230) the θ varies from 0 to $\frac{\pi}{2}$ (see Figure 4.1.52). For a diffuse emitter, the Equation (4.1.230) yields

$$E = \int_0^{2\pi} \int_0^{\frac{\pi}{2}} I_e \cos(\theta) \sin(\theta) d\theta d\phi = \pi I_e \tag{4.1.231}$$

4.1.20.1.3 Black Body

A black body is characterized by the following

- It absorbs all the incident radiations at all wavelengths coming from all directions.
- For a given temperature, no surface can emit more energy than a black body at all wavelengths.
- The intensity of radiation from a black body is the same in all directions; in other words a black body is a diffuse emitter.

Planck [64] derived the expression for intensity of emission from a black body as

$$I_{\lambda,T} = \frac{2hc_o^2}{\lambda^5(\exp(hc_o/\lambda k_B T) - 1)} \tag{4.1.232}$$

Integrating the above expression for all wavelengths for all directions, the emissive power, E_b, for black body is given by

$$E_b = \sigma T^4 \tag{4.1.233}$$

where σ is the Stefan–Boltzmann constant, a universal constant whose value is given by 5.67×10^{-8} W m^{-2} K^{-4}. Being a diffuse emitter, the direction intensity, I_b for a black surface would be E_b/π.

It can be proven that radiation inside a closed isothermal cavity or enclosure is that corresponding to a black surface even if the emitting surface is not black owing to infinite multiple reflections. This argument can be extended to show that the radiation from isothermal surroundings falling on a surface can be approximated to that from a black surface at the temperature of the surrounding.

4.1.20.1.4 Irradiation

Definitions described earlier for emission can be extended for incident radiation or irradiation, namely, for spectral, directional intensity of irradiation, $I_{\lambda,\mathrm{i}}(\lambda,\theta,\phi)$, directional intensity of irradiation, $I_{\mathrm{i}}(\theta,\phi)$, and total irradiation, G.

If the incident radiation is diffuse, then the intensity of irradiation is the same from all directions and hence $I_{\mathrm{i}} = G/\pi$. A black body would absorb all the incident radiation. When a real surface is irradiated, the radiation may be neglected, absorbed, or transmitted. For opaque bodies, transmission would be zero.

4.1.20.1.5 Emission from Real Surfaces

Radiation emanating from real opaque surfaces consists of two parts: (a) that emitted by the surface by virtue of its temperature (emission) and (b) that from incident radiation reflected by the surface. Similar to E and G, radiosity J is defined as the rate of energy emanating (emitted + reflected) from a unit area of surface. It is to be noted that for a black surface, $J_{\mathrm{b}} = E_{\mathrm{b}}$, as all incident radiations are absorbed by the surface.

Figure 4.1.53 shows a schematic of intensity of radiation, $I_{\lambda,\mathrm{e}}$ for a real surface. The intensity of emission from a real surface is always less than that from a black surface. The deviation in intensity of emission for real surfaces from that of black surfaces can vary with wavelength and direction of emission, as illustrated in Figure 4.1.53. In order to characterize the radiations emitted by real surfaces, a term called emissivity, ϵ, is used by comparing its intensity of emission with that from a black surface and is given by

$$\epsilon(\lambda,\theta,\phi,T) = \frac{I_{\lambda,\mathrm{e}}(\lambda,\theta,\phi,T)}{I_{\lambda,\mathrm{b}}(T)} \tag{4.1.234}$$

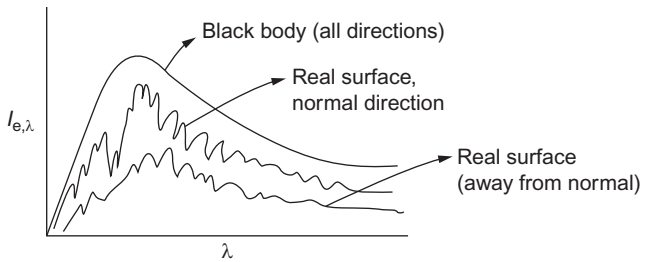


Figure 4.1.53 Illustration of intensity of emission from real surfaces.

By integrating the denominator and numerator for all directions and wavelengths, the total emissivity ϵ is defined as

$$\epsilon(T) = \frac{\int_0^{\frac{\pi}{2}} \int_0^{2\pi} \int_0^{\infty} I_{\lambda,\mathrm{e}}(\lambda,\theta,\phi,T) \sin\theta \cos\theta \, \mathrm{d}\lambda \, \mathrm{d}\phi \, \mathrm{d}\theta}{\pi I_{\lambda,\mathrm{b}}(T)} = \frac{E(T)}{E_{\mathrm{b}}(T)} \tag{4.1.235}$$

Metallic surfaces have low emissivity; highly polished surfaces can reach ϵ as low as 0.02 and in presence of oxide layer emissivity can go beyond 0.6. Emissivities of nonconductors generally exceed 0.6. The emissivity also varies with direction (θ) for both metals and nonconductors. Starting from the normal direction, the emissivity remains almost constant with increasing θ and significant variations occur only when θ reaches close to $\pi/2$ (tangential direction). Hence, for engineering calculations, the total emissivity of real surfaces is approximated as emissivity in the normal direction. Further, as the emissivity remains almost constant with θ, real surfaces can be approximated as diffused emitters for engineering calculations. Real surfaces for which emissivity is independent of both directions and wavelengths are termed as gray surfaces.

4.1.20.1.6 Absorptivity and Reflectivity for Opaque Surfaces

For incident radiations on an opaque surface, a part of the radiation is absorbed and the rest is reflected. The fraction of the incident radiation that is absorbed by the surface is defined as the absorptivity, α, of a surface. Like, emissivity, the absorptivity can be defined for wavelength and direction of the incident radiation and is given by,

$$\alpha_\lambda(\alpha,\theta,\phi) = \frac{I_{\lambda,\mathrm{i,abs}}(\lambda,\theta,\phi)}{I_{\lambda,\mathrm{i}}(\lambda,\theta,\phi)} \tag{4.1.236}$$

Similarly, total absorptivity α is defined as

$$\alpha = \frac{G_{\mathrm{abs}}}{G} \tag{4.1.237}$$

It is to be noted that unlike emissivity, which depends only on the surface and its temperature, absorptivity depends also on the spectral, directional characteristics of incident radiation. Absorptivity of a black surface is 1.

For an opaque surface, the reflectivity $\rho = 1 - \alpha$. Ideally for a smooth surface the reflections are specular (which obeys Snell's law of the angle of incidence being equal to the angle of reflection). Rough surfaces encountered in practical applications reflect diffusely.

4.1.20.1.7 Kirchoff's Law

Emission occurs from a material when transitions of electrons from excited states to ground states occur and are quantized. The reverse transition of electrons from ground

states to excited states occurs during absorption. In others words, emission and absorption are complementary phenomena. The consequence of this is that the spectral directional emissivity and spectral directional absorptivity are equal to each other, i.e.,

$$\epsilon(\lambda,\theta,\phi,T) = \alpha(\lambda,\theta,\phi,T) \tag{4.1.238}$$

This is not so, however, for the directional absorptivity, $\alpha(\theta,\phi,T)$, and the total absorptivity, α, whose values depend on the spectral directional intensity distribution of the incident radiation. Kirchoff's law states that only under special circumstances is the total emissivity, ϵ, equal to the total absorptivity, α, i.e., $\epsilon = \alpha$. These special conditions are:

- the surface kept in an isothermal enclosure whose temperature is the same as that of the enclosure. This corresponds to irradiation from black body at the same temperature as the surface.
- the surface is diffuse and gray.

For practical applications of estimating the radiation exchange between opaque surfaces, the surfaces are normally approximated as diffuse, gray surfaces, as this allows relatively simple formulation and computation of radiative heat exchange. Caution needs to be exercised as this approximation is reasonable only when the spectral distribution of irradiation and emission are close. In the following section, radiative exchange between diffuse–gray surfaces is presented. For more advanced formulations, the reader may refer elsewhere [65].

4.1.20.2. Radiation Exchange Between Opaque–Diffuse–Gray Surfaces

Radiative exchange between any two surfaces depends on the proportion of radiation emanating from one surface that is intercepted by the second one. This depends on the geometrical configuration of the surfaces. For determining the radiation exchange between opaque–diffuse–gray surfaces, it is necessary to define a view factor or a configuration factor.

4.1.20.2.1 View Factor or Configuration Factor

Consider two gray surfaces "i" and "j" having surface areas A_i and A_j, respectively, as shown in Figure 4.1.54. Let $I_{e+r,i}$ be the intensity of emission and radiation from surface "i."

Based on the definition of intensity, the amount of this radiation from surface "i" intercepting surface "j" can be written as

$$\dot{q}_{i\to j} = \int \mathrm{d}\dot{q}_{i\to j} = \int\int I_{e+r,i}\mathrm{d}A_i \cos(\theta_i)\mathrm{d}\omega_{j\to i} = \int_{A_j}\int_{A_i} I_{e+r,i}\mathrm{d}A_i \cos\theta_i \frac{\mathrm{d}A_j \cos\theta_j}{(r_{ij})^2} \tag{4.1.239}$$

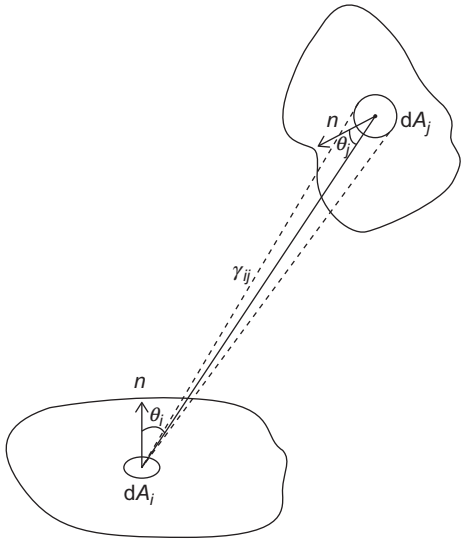


Figure 4.1.54 Illustration for the definition of view factor.

If the radiosity, J_i is uniform throughout the surface "i," then,

$$\dot{q}_{i\to j} = \int_{A_j}\int_{A_i} \frac{J_i}{\pi} \mathrm{d}A_i \cos(\theta_i) \frac{\mathrm{d}A_j \cos\theta_j}{(r_{ij})^2} \tag{4.1.240}$$

Let F_{ij} be the view factor, that is, the fraction of radiations from "i" being intercepted by "j," then,

$$\dot{q}_{i\to j} = A_i J_i F_{ij} = \int_{A_j}\int_{A_i} \frac{J_i}{\pi} \mathrm{d}A_i \cos\theta_i \frac{\mathrm{d}A_j \cos\theta_j}{r_{ij}^2} \tag{4.1.241}$$

Therefore,

$$F_{ij} = \frac{1}{A_i}\int_{A_j}\int_{A_i} \frac{\mathrm{d}A_i \cos\theta_i \mathrm{d}A_j \cos\theta_j}{\pi r_{ij}^2} \tag{4.1.242}$$

Conversely, the view factor from $j \to i$, i.e., the fraction of radiation from surface "j" being intercepted by surface "i" is given by

$$F_{ji} = \frac{1}{A_j}\int_{A_j}\int_{A_i} \frac{\mathrm{d}A_i \cos\theta_i \mathrm{d}A_j \cos\theta_j}{\pi r_{ij}^2} \tag{4.1.243}$$

Therefore,

$$A_i F_{ij} = A_j F_{ji} \tag{4.1.244}$$

This relation is known as the reciprocity relation. From the expression for the view factor, it can be clearly seen that it is a geometrical factor that depends only the configuration of the surfaces. For some of the common configurations encountered engineering, for example, circular discs separated by a distance, two rectangular walls facing each other or at 90° angle, two parallel cylinders, cylinder and a flat plate, etc., the view factor has been computed analytically and is available in the form of charts or expressions. A few of these expressions are presented in Table 4.1.6. Readers can find these charts or expressions in books on heat transfer and radiation [38,65]. Radiation from a concave surface will be intercepted by the surface itself, but not for flat or convex surface. Hence for a flat or convex surface, "*i*," the self view factor $F_{ii}=0$ and for a concave surface $F_{ii}>0$. For n number of surfaces, there would be n^2 view factors including the self view factors (F_{ii}). If those n surfaces form an enclosure, then the radiation from a surface "*i*" will be intercepted completely by all surfaces together. Therefore,

$$\sum_{j=1}^{n} F_{ij} = 1 \tag{4.1.245}$$

These relations for each surface will make n relations. The reciprocity relation between any two surfaces will form nC_2 relations. Therefore, $n^2 - n - nC_2 = n(n-1)/2$ view factors need to be calculated directly using the expressions for configuration factors.

Example 4.1.13

Find the view factors corresponding to an annular enclosure formed by two long pipes as illustrated in Figure 4.1.55. The radii of inner and outer cylinders are R_1 and R_2, respectively.

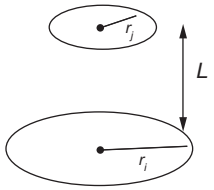
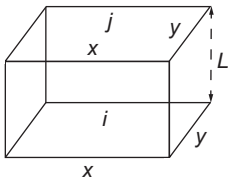
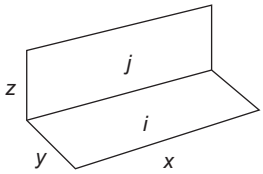
Solution

The exchange is between the outer surface of inner pipe and the inner surface of the outer pipe. As the outer surface of the inner pipe is convex, its self view factor (fraction radiation from the surface being intercepted by the same surface) $F_{11}=0$. In other words, all the radiation from 1 is intercepted by surface 2, $F_{12}=1$. Using the reciprocity relation $F_{21}=A_1F_{12}/A_2=R_1F_{12}/R_2=R_1/R_2$. Therefore, $F_{22}=1-F_{21}=R_1/R_2$.

4.1.20.2.2 Heat Balance at an Opaque–Diffuse–Gray Surface

Consider an opaque–diffuse–gray surface, "*i*" kept at a temperature T_i. This surface exchanges heat with other surfaces through radiation. Thus, in order to maintain the surface "*i*" at a constant temperature other means such as a heat source (if the surface loses energy by net radiative exchange) or a heat sink (if the surface gains energy by net radiative exchange) need to be adopted. This is schematically shown in Figure 4.1.56.

Table 4.1.6 View Factors for Selected Geometrical Configurations

Configuration	View Factor
	$R_i = r_i/L, \quad R_j = r_j/L$ $S = 1 + \dfrac{1 + R_j^2}{R_i^2}$ $F_{ij} = \dfrac{1}{2}\left(S - \left[S^2 - 4\left(r_i/r_j\right)^2 \right]^{\frac{1}{2}} \right)$
	$\overline{X} = X/L, \quad \overline{Y} = Y/L$ $F_{ij} = \dfrac{2}{\pi \overline{X}\,\overline{Y}} \left\{ \ln \left[\dfrac{\left(1+\overline{X}^2\right)\left(1+\overline{Y}^2\right)}{1+\overline{X}^2+\overline{Y}^2} \right]^{1/2} \right.$ $+\overline{X}\left(1+\overline{Y}^2\right)^{1/2} \tan^{-1} \dfrac{\overline{X}}{\left(1+\overline{Y}^2\right)^{1/2}}$ $+\overline{Y}\left(1+\overline{X}^2\right)^{1/2} \tan^{-1} \dfrac{\overline{Y}}{\left(1+\overline{X}^2\right)^{1/2}}$ $\left. -\overline{X} \tan^{-1} \overline{X} - \overline{Y} \tan^{-1} \overline{Y} \right\}$
	$H = Z/X, \quad W = Y/X$ $F_{ij} = \dfrac{1}{\pi W} \left\{ W \tan^{-1} \dfrac{1}{W} + H \tan^{-1} \dfrac{1}{H} \right.$ $-(H^2+W^2)^{1/2} \tan^{-1} \dfrac{1}{(H^2+W^2)^{1/2}}$ $\dfrac{1}{4} \ln \left[\dfrac{(1+W^2)(1+H^2)}{1+W^2+H^2} \right.$ $\left(\dfrac{W^2(1+W^2+H^2)}{(1+W^2)(W^2+H^2)} \right)^{W^2}$ $\left. \left. \times \left(\dfrac{H^2(1+W^2+H^2)}{(1+H^2)(W^2+H^2)} \right)^{H^2} \right] \right\}$

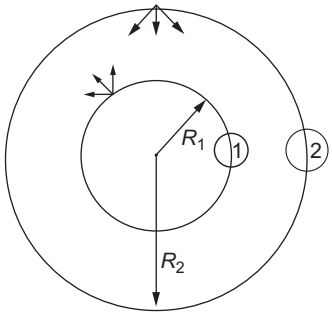


Figure 4.1.55 View factor for an annular enclosure.

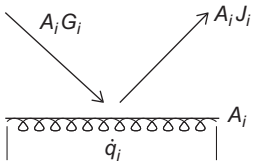


Figure 4.1.56 Heat balance at an opaque surface for radiative exchange.

If G_i denotes the uniform irradiation the surface "i" receives and J_i the uniform radiosity, then balancing the net energy yields

$$\dot{q}_i + A_i G_i = A_i J_i \tag{4.1.246}$$

Radiosity being the sum of emission and reflection and for an opaque–diffuse–gray surface, $\epsilon = \alpha$, it can be written

$$J_i = (1-\alpha) G_i + E_i = (1-\epsilon_i) G_i + \varepsilon_i E_{\mathrm{b},i} \tag{4.1.247}$$

Here, $E_{\mathrm{b},i}$ is emissive power of a black surface at the temperature corresponding to surface "i" (T_i). Substituting this in Equation (4.1.246) yields

$$\dot{q}_i = \frac{E_{\mathrm{b},i} - J_i}{(1-\epsilon_i)/\epsilon_i A_i} \tag{4.1.248}$$

If the surface is black, $\varepsilon_i = 1$. Since, $\dot{q}_i$ is not zero, $E_{\mathrm{b},i} = J_i$. This is as expected, since a black surface does not reflect any incident radiation. Equation (4.1.248) can be interpreted as an electrical analogue, where there is a resistance R_s at a gray surface: $R_s = (1-\varepsilon_i)/(\varepsilon_i A_i)$.

4.1.20.2.3 Radiation Exchange at a Surface in an Enclosure Consisting of Opaque–Diffuse–Gray Surfaces

Consider an enclosure formed by opaque–diffuse–gray surfaces as illustrated in Figure 4.1.57. Each of these surfaces is isothermal having a distinct temperature. Consider one such opaque–diffuse–gray surface, "i" at temperature T_i. Let us determine the total

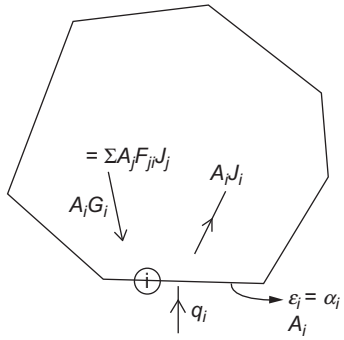


Figure 4.1.57 Illustration of heat balance in an enclosure formed by opaque–diffuse–gray surfaces.

irradiation reaching the surface "i"; this consists of the summation of the emitted and reflected radiations from all the surfaces forming the enclosure. This can be written as

$$A_i G_i = \sum_{j=1}^{n} A_j F_{ji} J_j = \sum_{j=1}^{n} A_i F_{ij} J_j \quad \text{(Reciprocity relation)} \tag{4.1.249}$$

Combining Equations (4.1.246) and (4.1.249), the radiation exchange at an opaque–diffuse–gray surface, "i" for the enclosure shown in Figure 4.1.57 can be written as

$$\dot{q}_i = A_i J_i - A_i G_i = A_i J_i - \sum_{j=1}^{n} A_i F_{ij} J_j = \sum_{j=1}^{n} A_i F_{ij} \left(J_i - J_j \right) \tag{4.1.250}$$

Equations (4.1.248) and (4.1.250) can be written for each surface resulting in $2n$ equations for an enclosure formed by n opaque–diffuse–gray surfaces. These equations can be represented using the electrical analogue as follows

$$\dot{q}_i = \frac{E_{\mathrm{b},i} - J_i}{(1-\varepsilon_i)/\varepsilon_i A_i} = \frac{E_{\mathrm{b},i} - J_i}{R_{\mathrm{s},i}}$$

$$\dot{q}_i = \sum_{j=1}^{n} \frac{J_i - J_j}{\left(A_i F_{ij} \right)^{-1}} = \sum_{j=1}^{n} \frac{J_i - J_j}{R_{ij}}$$

Here $\dot{q}_i$ is equivalent to the current and E_b and J represent the potentials. $R_{\mathrm{s},i}$ can be denoted as surface resistance and R_{ij} as view factor resistance. A pictorial representation of the electrical analogue for any surface "i" is shown in Figure 4.1.58.

If a surface is adiabatic or completely insulated from the other side (no heat sink or heat source), then $\dot{q}$ for the surface is zero. All the irradiations on to this surface are radiated back to the enclosure through emission and reflection. Such surfaces are referred to as re-radiating surfaces.

Example 4.1.14

250-tonnes ladle has inner diameter of 3.4 m and depth of 4.0 m. It is filled with 250 tonnes of liquid steel at 1800 K. The thickness of the slag layer over the liquid

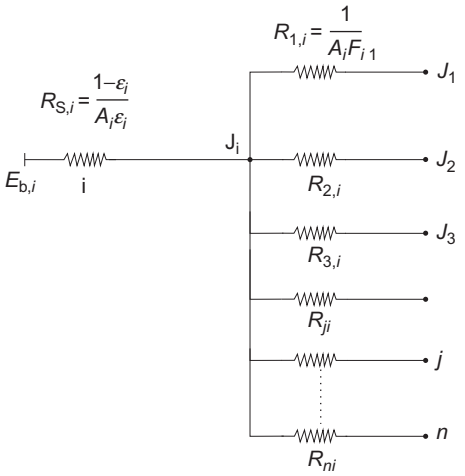


Figure 4.1.58 Electrical analogue for radiation exchange.

steel can be neglected. The free board at the top of the ladle is 0.5 m in height. The emissivity of the slag layer is 0.8. Assuming the walls to be adiabatic, estimate the radiative heat loss from the open ladle. The temperature of the surroundings is 300 K.

Solution

The radiative heat transfer from the top of the slag surface is illustrated in Figure 4.1.59a. The slag layer is denoted by 1 (diffuse–gray surface), the side walls by 2 (re-radiating surface), and the opening by surface 3 (black surface).

The electrical analogue depicting the radiative heat transfer is shown in Figure 4.1.59b. Net heat flow from surface 2, $\dot{q}_2$, is zero as it is a re-radiating surface.

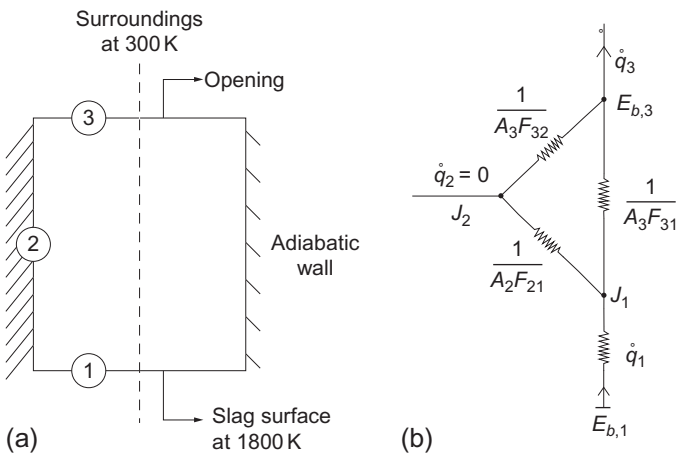


Figure 4.1.59 Radiation loss from a ladle: (a) illustration of the radiation enclosure and (b) electrical analogue.

The net heat flow can be written as

$$\dot{q}_1 = -\dot{q}_3 = \frac{E_{b,1} - E_{b,3}}{(1-\epsilon_1)/(A_1\epsilon) + ([1/A_1F_{12} + 1/A_3F_{32}]||1/A_1F_{13})}$$

The view factor, F_{13}, is 0.764 (using the expression for view factor for two coaxial circular discs facing each other in Table 4.1.6). Hence, $F_{12} = 1 - F_{13} = 0.236$. Therefore,

$$\dot{q}_1 = -\dot{q}_3 = \frac{\sigma 1800^4 - \sigma 300^4}{0.0275 + ([0.4667 + 0.4667]||0.1442)} = \frac{\sigma 1800^4 - \sigma 300^4}{0.1524} = 3.903\,\text{MW}$$

This corresponds to a drop in temperature at a rate of 1.13 K min^{-1}. In addition to this, there would be conduction losses through the walls of the ladle.

In the above treatment of enclosures, each surface was considered to be isothermal. In large furnaces, the surface temperatures can vary along the surface of a wall or a component. In such cases, both the wall surfaces and component surfaces can be divided into a number of subsurfaces having distinct temperatures. This would result in a large number of simultaneous equations to be solved to determine the radiative heat transfer. For such cases, J_is can be eliminated from Equations (4.1.246) and (4.1.249) to obtain equations in terms of qs and E_bs alone. In all these problems, either the q or E_b would be unknown for each surface and hence the following equation can be accordingly rearranged for the unknowns to compute the radiative exchange and temperatures.

$$\frac{\dot{q}_i}{A_i\epsilon_i} - \sum_{j=1}^{n} \frac{1-\epsilon_j}{\epsilon_j} F_{ij} \frac{\dot{q}_j}{A_j} = \sum_{j=1}^{n} F_{ij}\left(E_{b,i} - E_{b,j}\right) \quad \text{for } i = 1 \ldots n \tag{4.1.251}$$

Conductive losses through the walls can also be incorporated as current sinks, and heat inputs as current sources.

4.1.20.3. Gas Radiation

Nonpolar gases such as N_2 and O_2 do not emit thermal radiations and are transparent to thermal radiations. However, polar molecules especially CO_2 and H_2O present in combustion products on the other hand can emit and absorb radiation. Unlike condensed phases wherein the radiation spectra are continuous, for gases the spectra are banded; the emission and absorption take place over specific wavelength intervals. Additionally, gaseous radiation is a volumetric phenomenon.

The absorption and radiation for a gaseous medium is defined through a linear absorption coefficient, k_g, as

$$\mathrm{d}I_\lambda = -k_g I_\lambda \,\mathrm{d}s \tag{4.1.252}$$

where $\mathrm{d}I_\lambda$ is the change in intensity of radiation as it travels a distance of $\mathrm{d}s$ through a gas medium. Thus, integrating this expression along the direction $\vec{s}$,

$$I_\lambda(s) = I_{\lambda,s=0}\exp\left(-k_g s\right) \tag{4.1.253}$$

The spectral directional absorptivity of a gas is defined as

$$\alpha_{\lambda,g} = \frac{\text{Radiation absorbed}}{\text{Incident radiation}} = \frac{\left(I_{\lambda,s=0} - I_{\lambda,s=0}\exp\left(-k_g s\right)\right)}{I_{\lambda,s=0}} = 1 - \exp\left(-k_g s\right) \tag{4.1.254}$$

The directional, spectral emissivity, $\epsilon_{\lambda,g}$, of a gas is defined by comparing the emission to that from a black surface. For the reasons mentioned earlier (Kirchoff's law), the spectral direction absorptivity, $\alpha_{\lambda,g}$ of a gas is equal to the spectral directional emissivity, $\epsilon_{\lambda,g}$. Please note that both these definitions are for a radiation traveling along a direction, $\vec{s}$, for a distance traveled $\left|\vec{s}\right|$.

In order to determine the radiation exchange in a system where volume of gas and opaque surfaces are involved, a radiation energy balance needs to be performed for all the directions. This would result in complex integro-differential equations [65] that need sophisticated numerical techniques to solve and are also computationally very expensive. Instead, relatively easier but approximate methodologies have been developed. In this section, the simplest approach proposed by Hottel and Sarofim [66], which can be used for engineering calculation with reasonable accuracy, is presented. For more sophisticated methods, readers may refer other sources [65].

Analogous to the total emissivity for a surface, Hottel and Sarofim [66] defined emissivity from a gas temperature T_g contained in a hemisphere of radius L to a surface element located at the center of hemispherical base (see Figure 4.1.60).

$$\epsilon_g(L) = \frac{\int_{\text{hemisphere}}\int_0^\infty \epsilon_{\lambda,g}(L) I_{\lambda,b}\left(T_g\right) d\lambda\, dA\cos(\theta) d\omega}{\int_{\text{hemisphere}}\int_0^\infty I_{\lambda,b}\left(T_g\right) d\lambda\, dA\cos(\theta) d\omega} \tag{4.1.255}$$

$$\epsilon_g(L) = \frac{\int_{\text{hemisphere}}\int_0^\infty \epsilon_{\lambda,g}(L) I_{\lambda,b}\left(T_g\right) d\lambda\cos(\theta) d\omega}{\sigma T^4}$$

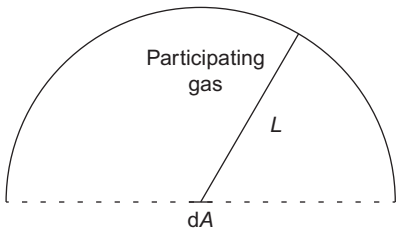


Figure 4.1.60 Illustration for defining total emissivity/absorptivity for a gaseous medium.

In other words, emission from a gas at temperature T_g contained in a hemisphere of radius L to a surface having unit area placed at the base of the hemisphere is $\epsilon_g \sigma T_g^4$. ϵ_g is a function of gas temperature T_g, total pressure p, the partial pressure p of the participating species, and the radius of the hemisphere L.

The emissivities in the form of charts were first proposed by Hottel and Sarofim [66] and later were refined by Leckner [67]. Modest [65] recommends the following empirical expression by Leckner to estimate the total emissivities for H_2O and CO_2.

$$\epsilon_0\left(p_a L(\text{bar cm}), p = 1\,\text{bar}, T_g(\text{K})\right) = \exp\left[\sum_{i=0}^{M}\sum_{j=0}^{N} C_{ji}\left(\frac{T_g}{1000}\right)^j \left(\log_{10}(p_a L)\right)^i\right] \tag{4.1.256}$$

Here ϵ_0 is the emissivity for the limiting case when partial pressure of the absorbing species (H_2O, CO_2) goes to zero. The emissivities at other pressures and partial pressure of absorbing species are then found from

$$\frac{\epsilon\left(p_a L, p, T_g\right)}{\epsilon_0\left(p_a L, 1\,\text{bar}, T_g\right)} = 1 - \frac{(a-1)(1-P_E)}{a+b-1+P_E}\exp\left(-\left[\log_{10}\frac{(p_a L)_m}{p_a L}\right]^2\right) \tag{4.1.257}$$

The empirical parameters for the above two equations for H_2O and CO_2 are tabulated in Tables 4.1.7 and 4.1.8.

In a gas where both H_2O and CO_2 are present, additionally a correction factor needs to be introduced, as the radiation bands of these two gases partially overlap. These corrections are given as

$$\epsilon_{CO_2+H_2O} = \epsilon_{CO_2} + \epsilon_{H_2O} - \Delta\epsilon\left(p_{H_2O}L,\, p_{CO_2}L\right) \tag{4.1.258}$$

$$\Delta\epsilon\left(p_{H_2O}L,\, p_{CO_2}L\right) = \left\{\frac{x_{H_2O}}{10.7+101x_{H_2O}}0.0089x_{H_2O}^{1}0.4\right\}\left(\log_{10}\left(\left(p_{H_2O}+p_{CO_2}\right)L\right)\right)^{2.76}$$

where x_{H_2O} is the mole fraction of water vapor in the gas.

The total absorptivity α_g is equal to the total emissivity ϵ_g for a given temperature T_g. In real systems, the source of radiation can be at temperature T_s and gas may be at another temperature T_g; the absorptivity depends on both the temperature of the radiating source T_s as well as the temperature of the gas T_g.

The absorptivity of gases at temperature T_g from gray surface at temperature T_s can be calculated from

$$\alpha\left(p_i, L, p, T_g, T_s\right) = \left(\frac{T_g}{T_s}\right)^{1/2}\epsilon\left(p_i, L, \frac{T_s}{T_g}, p, T_s\right) \tag{4.1.259}$$

Table 4.1.7 Correlation constants for the determination of the total emissivity for water vapor using equations (4.1.256) and (4.1.257)

M,N			**2,2**		
C_{00}	C_{01}	C_{02}	-2.2118	-1.1987	0.035596
C_{10}	C_{11}	$C_{12}4$	0.85667	0.93048	-0.14391
C_{20}	C_{21}	C_{22}	-0.10838	-0.17156	0.045915
P_E			$\left(p+2.56p_a/\sqrt{T_g/1000}\right)$		
$(p_aL)_m$			$13.2(T_g/T)^2$		
a			$2.144\left(T_g<750\right)$ $1.888-2.053\log_{10}\left(T_g/1000\right),\quad T_g>750$		
b			$1.10/(T_g/100)^{1.4}$		
c			0.5		

Table 4.1.8 Correlation constants for the determination of the total emissivity for CO_2 using equations (4.1.256) and (4.1.257)

M,N				**2,3**			
C_{00}	C_{01}	C_{02}	C_{03}	-3.9893	2.7669	-2.1081	0.39163
C_{10}	C_{11}	$C_{12}4$	C_{13}	1.2710	-1.090	1.0195	-0.21897
C_{20}	C_{21}	C_{22}	C_{23}	-0.23678	0.19731	-0.19544	0.044644
P_E				$(p+0.28p_a)$			
$(p_aL)_m$				$0.054/\left(T_g/T\right)^2,\quad T_g<700$ $0.225\left(T_g/T\right)^2,\quad T_g>700$			
a				$1.0+0.1/(T_g/1000)^{1.45}$			
b				0.23			
c				1.47			

Emissivities and absorptivities of gas mass of shapes other than hemispheres are extended using a concept of mean beam length, L_e, where L_e is the equivalent radius of the hemispherical gas mass whose emissivity or absorptivity is the same as that of the gas mass of interest. The mean beam lengths for various gas geometries are given in Table 4.1.9.

The radiation heat rate from a gas mass to an adjoining surface of area A

$$\dot{q}=A\epsilon_g\sigma T_g^4 \tag{4.1.260}$$

Table 4.1.9 Mean beam lengths, L_e, for various gas geometries [38]

Geometry	Characteristic Length	L_e
Sphere (radiation to the surface)	Diameter (D)	0.65 D
Infinite circular cylinder (radiation to the curved surface)	Diameter (D)	0.95 D
Semi-infinite circular cylinder (radiation to base)	Diameter (D)	0.65 D
Circular cylinder of equal height and diameter (radiation to entire surface)	Diameter (D)	0.60 D
Infinite parallel planes (radiation to planes)	Spacing between planes (L)	1.80 L
Cube (radiation to any surface)	Side (L)	0.66 L
Arbitrary shape of volume V (radiation to surface area A)	V/A	3.6 V/A

4.1.21. MASS TRANSFER

Engineering materials, more often than not, are multiphase materials; each phase is a solution of many chemical constituents present as different atomic, molecular, or ionic species. Properties of materials depend on size, shape, and distribution of phases, as well as composition of chemical constituents and their distribution in each phase. Process metallurgists aim at designing processes to achieve desired distributions of phases in terms of size and shape, as well as the constitution of each phase, so that materials with desired properties can be produced consistently. Hence, understanding transport of chemical constituents within a phase and across different phases is of great importance for a process engineer. The subject of mass transport addresses the transport of chemical constituents within a phase as well as across phases. Often associated with these transports of chemical constituents are chemical reactions and phase transitions. Thus, for analyzing engineering processes, a knowledge of the principles of chemical kinetics and phase transformations is needed, together with the principles of mass transport. In this section, the primary focus is on the transport of chemical constituents. A separate section with a focus on chemical kinetics is presented at the end of this chapter.

Sugar added to a cup of tea is a common example of mass transfer. The dissolution of sugar in tea can be enhanced by stirring the tea with a spoon. The time for dissolution also depends on the size and shape of the sugar crystals being added. Deoxidation of liquid steel using aluminum is an example from steel making. In this process, the added solid aluminum melts and dissolves in the steel bath and is then distributed in the bath. The dissolved aluminum chemically reacts with the dissolved oxygen in steel to produce billions of nonmetallic alumina particles as a second phase. The efficiency of the

deoxidization process depends on ensuring proper delivery of aluminum by maintaining adequate flow in the bath by Ar purging, and on controlling the temperature of the bath, metal, and slag chemistry. The mechanism of sugar dissolution or aluminum being distributed in the liquid occurs through both bulk flow of the fluid (advection) as well as molecular interactions (diffusion). These mechanisms are similar to the mechanisms of heat and momentum transfer discussed earlier. However, the diffusive mass transfer is in one aspect distinct from diffusive heat and momentum transport. This arises from the fact that different chemical species travel at different velocities. These differences in velocities of chemical species can result in a net bulk flow, even in the absence of any mechanical driving force.

The driving force for diffusive transport of chemical species arises from difference in thermodynamic chemical potential. Therefore, anything that can bring about a change in chemical potential can result in mass transfer driving the system toward equilibrium. Differences in concentration of species are the obvious source of potential difference leading to what is termed as ordinary diffusion. Driving forces can also be due to differences in pressure (pressure diffusion), temperature (thermal diffusion), electric field in case of ions (forced diffusion), etc. This section deals with only the ordinary diffusion—that which is driven by concentration differences.

4.1.21.1. Fick's Law of Diffusion

As the mechanism of diffusive transport of mass is similar to that of heat, the rate equation of mass transport is also similar to that of Fourier's law of conduction. The rate equation, known as Fick's law, is stated for a binary solution containing species "A" and "B" as

$$j_A = \rho \mathbb{D}_{AB} \nabla m_A \tag{4.1.261}$$

or

$$J_A^* = -C \mathbb{D}_{AB} \nabla x_A \tag{4.1.262}$$

Here, j_A is the mass flux in kg s^{-1} m^{-2}, ρ is density, and m_A is the mass fraction of species "A" in the solution. $\mathbb{D}_{AB}$ is the phenomenological constant, analogous to thermal conductivity, and is called the binary diffusion coefficient. The law can be also written in terms of molar transport where J_A^* is molar flux, C denotes the molar density or total molar concentration, and x_A denotes the mole fraction of "A" in the binary solution. The value of $\mathbb{D}_{AB}$, with the units of m^2 s^{-1}, is the same in both the equations. Unlike conduction, however, mass diffusion often involves simultaneous transport of two or more species in a solution. Fluxes of each species can be different in a solution. This can lead to seemingly paradoxical situations, unless Equations (4.1.261) and (4.1.262) are interpreted correctly.

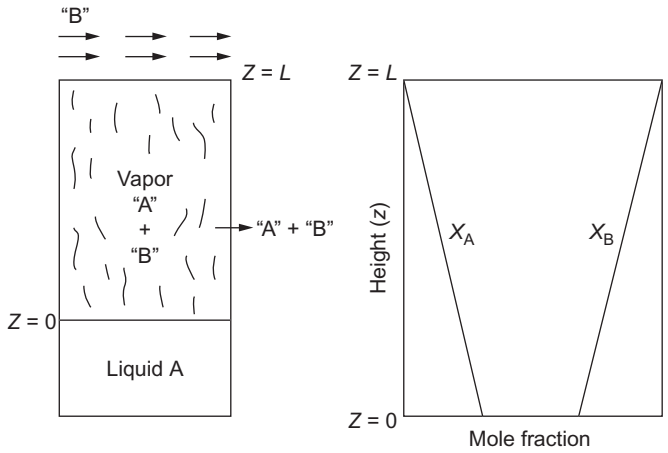


Figure 4.1.61 Stefan experiment on evaporation through a gas column: (a) experimental set up and (b) incorrect composition profile.

An experiment on evaporation of a liquid and the consequent diffusion of the vapor through a seemingly stagnant gas, referred to as Stefan's experiment [5], elucidates the above observation.

Consider a jar containing a liquid "A" up to a height $z=0$ as shown in Figure 4.1.61a. The top of the jar is open; a pure gas "B" flows across the entrance, so that any vapor of species A reaching the top is swept away, so that the concentration of "A" at the top ($z=L$) remains close to zero. Evaporation of "A" is slow, and the level of the liquid is kept at $z=0$ (say by connecting it to a larger reservoir). The liquid would evaporate, and the vapor would diffuse through the "apparently" stagnant gas column of B to escape at the top. Since the pressure everywhere is the same as the atmospheric pressure and the gas mixture is ideal, the total molar concentration of gas in the column is constant. The concentration of "A" at $z=0$ is near saturation value, and is zero at $z=L$, leading to a gradient in x_A as shown in Figure 4.1.61b. Since $x_A+x_B=1$ (or $C_A+C_B=C=\frac{p}{RT}$), there is an inverse gradient in x_B.

Equation (4.1.262) would indicate that there is an inward flux of "B." But if "B" is insoluble in the liquid, this is impossible! Hence the contradiction. A careful examination of the physical situation would reveal that there is a nonzero flux of "A" outward, and a stagnant "B," leading to a net molar flux of gas outward. A careful measurement with a Pitot tube should reveal an outward velocity of gas, however small. Molecular diffusion, as given by Equations (4.1.261) and (4.1.262), should be interpreted as the fluxes relative

[5] This experiment is named after famous Slovene physicist, mathematician, and poet, Joseph Stefan, who conducted a large number of experiments on evaporation.

to this gas mixture moving at this net velocity. In this experiment described above, the species "B" does not have a net inward flow with respect to the stationary coordinates.

Let us denote the molar flux of "A" and "B" with respect to the stationary frame of reference (in this case the tube) as N''_A and N''_B, respectively. Since the flux is equal to velocity times concentration, then

$$N''_A = Cx_A v_A \quad \text{and} \quad N''_B = Cx_B v_B$$

Then the average velocity of the gas mixture or simply the mixture velocity would be

$$Cv^* = Cx_A v_A + Cx_B v_B = \left(N''_A + N''_B\right)$$
$$v^* = \left(N''_A + N''_B\right)/C$$

The molar fluxes with respect to the frame moving with the mixture velocity can then be written as

$$J^*_A = Cx_A(v_A - v^*) \quad \text{and} \quad J^*_B = Cx_B(v_B - v^*)$$

Thus Fick's law can be applied to the fluxes in this frame of reference to give

$$J^*_A = Cx_A(v_A - v^*) = -C\mathbb{D}_{AB}\nabla x_A \tag{4.1.263}$$

Please note that in the frame moving with the mixture velocity, the flux of species "A" and "B" should be equal and opposite, i.e., $J^*_A + J^*_B = 0$. In a binary mixture, $x_A + x_B = 1$, therefore, $\mathbb{D}_{BA} = \mathbb{D}_{AB}$.

In terms of molar fluxes N''_A and N''_B, the above equation can be written as

$$N''_A - x_A\left(N''_A + N''_B\right) = -C\mathbb{D}_{AB}\nabla x_A \tag{4.1.264}$$

or

$$N''_A = -C\mathbb{D}_{AB}\nabla x_A + x_A\left(N''_A + N''_B\right)$$

In a similar way, Fick's law can also be defined in terms of mass flux instead of molar flux as

$$j_A = \rho m_A(v_A - v) = -\rho\mathbb{D}_{AB}\nabla m_A$$

where

$$v = m_A v_A + m_B v_B = \left(n''_A + n''_B\right)/\rho$$

and hence

$$n''_A = \rho\mathbb{D}_{AB}\nabla m_A + x_A\left(n''_A + n''_B\right) \tag{4.1.265}$$

Equations (4.1.264) and (4.1.265) are the general equations of binary diffusion with respect to stationary coordinates. The second term on the RHS is often determined by

the physical situation. Let us revisit the Stefan experiment with these formulations. Since "B" is insoluble in liquid "A," $N''_B = 0$. Applying this to Equation (4.1.264)

$$\begin{aligned} N''_A &= -C\mathbb{D}_{AB}\nabla x_A + x_A N''_B \\ (1-x_A)N''_A &= -C\mathbb{D}_{AB}\frac{dx_A}{dz} \\ N''_A &= -C\mathbb{D}_{AB}\frac{1}{1-x_A}\frac{dx_A}{dz} \end{aligned}$$

At steady state $\frac{dN''_A}{dz} = 0$ (the molar flux $N''_A = \text{constant}$).

$$\frac{d}{dz}\left(C\mathbb{D}_{AB}\frac{1}{1-x_A}\frac{dx_A}{dz}\right) = 0$$

The differential equation can be solved using boundary conditions at $z = 0$ and $z = L$. At $z = 0$, i.e., the liquid–gas interface, thermodynamic equilibrium can be assumed. Let us denote the equilibrium mole fraction at the interface as x^0_A.

At $z = L$, the composition of gas is imposed externally and let it be denoted as x^L_A. For example, if pure gas "B" is flowing at flow rates much larger than the evaporation rate, x^L_A can be taken to be zero.

Using the above two boundary conditions, the solution would be

$$\frac{1-x_A}{1-x^0_A} = \left(\frac{1-x^L_A}{1-x^0_A}\right)^{z/L} \tag{4.1.266}$$

$$N''_A = \frac{C\mathbb{D}_{AB}}{L}\ln\left(\frac{1-x^L_A}{1-x^0_A}\right) \tag{4.1.267}$$

The variation of the mole fraction along the gas column as illustrated in Figure 4.1.62b is nonlinear. Please note that in the frame moving with mixture velocity (v^*), the flux, J^*_B has to be equal and opposite to the flux J^*_A. Hence on the stationary frame, the flux, N''_B is given by

$$\begin{aligned} N''_B &= -C\mathbb{D}_{AB}\nabla x_B + x_B\left(N''_A + N''_B\right) \\ &= C\mathbb{D}_{AB}\nabla x_A + x_B\left(N''_A + N''_B\right) \\ N''_B(1-x_B) &= C\mathbb{D}_{AB}\nabla x_A + (1-x_A)N''_A = 0 \end{aligned}$$

An example of stagnant layer diffusive mass transfer is the evaporation of zinc from hot galvanized sheets in stagnant air.

A similar effect, of the overall flux on the flux of individual species, manifests itself as the "Kirkendall effect" in diffusion of substitutional elements in solid solutions. One may observe the overall flux as leading to marker movements in diffusion couples, or as leading to generation of pores. In view of the structure of solids, however, the phenomenon is treated differently for solids.

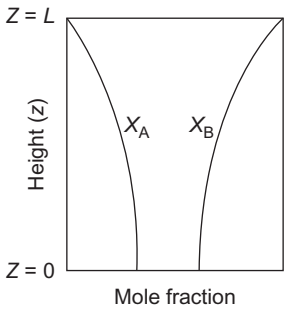


Figure 4.1.62 Stefan experiment on evaporation through a gas column: composition profile.

4.1.21.2. Binary Diffusivities

The mass diffusivities, $\mathbb{D}_{AB}$, for binary gas mixtures are functions of temperature and pressure. These can be estimated, especially for nonpolar gases using the kinetic theory of gases. Bird *et al.* [1] recommend the following correlations based on Lennard Jones parameters:

$$\mathbb{D}_{AB} = 1.8583 \times 10^{-7} \frac{\sqrt{T^3\left(\frac{1}{M_A} + \frac{1}{M_B}\right)}}{p\sigma_{AB}^2 \Omega_{\mathbb{D}_{AB}}} \tag{4.1.268}$$

where $\mathbb{D}_{AB}$ is in $m^2\ s^{-1}$, T is temperature in K, M_A and M_B are molecular weights of gas species A and B, p is pressure in atm., and σ_{AB} and $\Omega_{\mathbb{D}_{AB}}$ are the Lennard Jones parameters. For determining the Lennard Jones parameters, please refer to Ref. [1].

As the structure of liquids and solids are complex, there are no generic correlations available to estimate the binary diffusivities at present; experimental data for specific systems are the most reliable source. Unlike gases, the diffusivities in liquids and solids increase with increasing temperature; in general, these are found to be thermally activated processes and hence can be represented using Arrhenius-type relations.

4.1.21.3. Multicomponent Diffusion

Multicomponent diffusion in ideal gases is described by Stefan–Maxwell equations [1]

$$\nabla x_i = \sum_{j=1}^{n} \frac{1}{C\mathbb{D}_{ij}} \left(x_i N_j'' - x_j N_i'' \right) \tag{4.1.269}$$

For a binary system, this equation will simplify to Equation (4.1.264). For a multicomponent solution, analogous relations can be written as

$$N_j'' = -C\mathbb{D}_i \nabla x_i + x_i \sum_{j=1}^{n} N_j'' \tag{4.1.270}$$

where $\mathbb{D}_i$ is the diffusivity of species "i" in the multicomponent solution. From the above equations, the multicomponent diffusivity $\mathbb{D}_{im}$ can be related to the binary diffusivities as

$$\frac{1}{C\mathbb{D}_i} = \frac{\sum_{j=1}^{n} \left(1/C\mathbb{D}_{ij}\right)\left(x_i N_j'' - x_j N_i''\right)}{N_i'' - x_i \sum_{j=1}^{n} N_j''} \tag{4.1.271}$$

Please note that $\mathbb{D}_i$ is dependent on position as it changes with composition.

Special cases can be deduced for which the expression for $\mathbb{D}_i$ becomes simple:

For dilute solutions $(x_2, x_3, \ldots, x_n \to 0)$ in solvent $(x_1 \to 1)$:

$$\mathbb{D}_i = \mathbb{D}_{i1} \tag{4.1.272}$$

If all binary diffusivities are same ($\mathbb{D}_{ij}$s are same):

$$\mathbb{D}_i = \mathbb{D}_{ij} \tag{4.1.273}$$

For systems wherein species 2,3,. . .,n move with the same velocity or for a stationary system $\left(\sum_{j=1}^{n} N_j'' = 0\right)$:

$$\frac{1 - x_1}{C\mathbb{D}_1} = \sum_{j=2}^{n} \frac{x_i}{D_{1j}} \tag{4.1.274}$$

In systems where $\mathbb{D}_i$ varies significantly, a linear variation approximation with composition has given satisfactory results [1].

4.1.21.4. Diffusion Equation for Stationary Media: Steady and Transient

In dilute systems, where the solute concentrations are significantly small, the bulk flow arising out of diffusive mass transfer can be considered insignificant. Additionally, systems wherein the net sum of the fluxes of species is zero $\left(\sum_{j=1}^{n} N_j'' = 0\right)$, for example, equimolar counter current diffusion of CO and CO_2 through a porous product layer during the reduction of a solid metal oxide to metal, the medium is stationary. In such cases, the Equation (4.1.270) reduces to

$$N_i'' = -C\mathbb{D}_i \nabla x_i \tag{4.1.275}$$

This equation is analogous to the heat conduction equation, Equation (4.1.134). The molar conservation of species "i" in a stationary medium can be written as

$$C\frac{\partial x_i}{\partial t} = -\nabla\cdot N_i'' + \dot{G}_i''' \tag{4.1.276}$$

where $\dot{G}_i'''$ is the rate of generation of species "i" (in mol m^{-3} s^{-1}) that can occur through chemical reactions and nuclear processes. Substituting the diffusion equation into the conservation equation:

$$C\frac{x_i}{t} = C\nabla\cdot(\mathbb{D}_i\nabla x_i) + G_i''' \tag{4.1.277}$$

1D transient diffusion equations without a generation term in Cartesian, cylindrical, and spherical coordinates are

$$\frac{\partial x_i}{\partial t} = \frac{\partial}{\partial z}\left(\mathbb{D}_i\frac{\partial x_i}{\partial z}\right) \tag{4.1.278}$$

$$\frac{\partial x_i}{\partial t} = \frac{1}{r}\frac{\partial}{\partial r}\left(r\mathbb{D}_i\frac{\partial x_i}{\partial r}\right) \tag{4.1.279}$$

$$\frac{\partial x_i}{\partial t} = \frac{1}{r^2}\frac{\partial}{\partial r}\left(r^2\mathbb{D}_i\frac{\partial x_i}{\partial r}\right) \tag{4.1.280}$$

Equation (4.1.276) is analogous to the general conduction equation, Equation (4.1.138). Hence, the solutions for diffusion problems in stationary media are analogous to those in conduction problems.

For example, steady diffusion of a species "i" through a cylindrical wall, with no species generation is governed by

$$\frac{1}{r}\frac{\partial}{\partial r}\left(r\mathbb{D}_i\frac{\partial x_i}{\partial r}\right) = 0$$

with the boundary conditions:at $r = r_1, x_i = x_i^1$ and at $r = r_2, x_i = x_i^2$. The solution is

$$N_i = \frac{C\left(x_i^1 - x_i^2\right)}{\left(\ln(r_2/r_1)/(2\pi L\mathbb{D}_i)\right)}$$

Similarly, the transient diffusion through a semi-infinite wall with a constant $\mathbb{D}_i$ is analogous with Equation (4.1.164) governed by:

$$C\frac{\partial x}{\partial t} = C\mathbb{D}_i\frac{\partial^2 x_i}{\partial z^2};\quad t > 0; 0 < z < \infty;$$
Initial condition at $(t = 0, 0 <= z <= \infty) x_i = x_i^0$
Boundary condition 1 at $(t > 0, z = 0) x_i = x_i^s$
Boundary condition 2 at $(t > 0, z \to \infty) x_i = x_i^0$

The concentration profiles are given by (see Equation 4.1.165)

$$\frac{x_i(z,t)-x_i^s}{x_i^0-x_i^s}=\text{erf}\left(\frac{z}{2\sqrt{\mathbb{D}t}}\right) \tag{4.1.281}$$

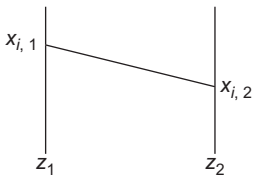
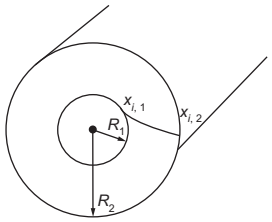
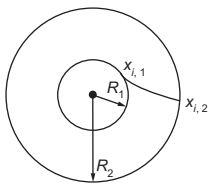
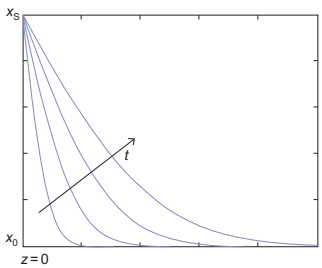
Other cases of transient diffusion through plane walls, cylindrical rods, and spheres can be similarly dealt with as given in Table 4.1.10.

When the overall molar concentration C is relatively constant, the diffusion equation can be written in terms of concentrations. For example, for 1D diffusion, one can write the flux as:

$$N''_{i,x}=-\mathbb{D}_i\frac{\partial C_i}{\partial x}+x_i\sum_{j=1}^{n}N''_{j,x} \tag{4.1.282}$$

In process metallurgy literature, this is the form in which the diffusion equation is often used.

Table 4.1.10 Concentration profiles for 1D diffusion: stationary media

Steady state	
$N_i=AN_i''=\dfrac{C\left(x_i^1-x_i^2\right)}{(z_2-z_1)/\mathbb{D}_iA}$ (Planar)	
$N_i=\dfrac{C\left(x_i^1-x_i^2\right)}{\dfrac{\ln(R_2/R_1)}{2\pi L\mathbb{D}_i}}$ (Cylindrical)	
$N_i=\dfrac{C\left(x_i^1-x_i^2\right)}{\dfrac{(1/R_1-1/R_2)}{4\pi\mathbb{D}_i}}$ (Spherical)	
Transient semi-infinite	
$\dfrac{x_i(z,t)-x_i^s}{x_i^0-x_i^s}=\text{erf}\left(\dfrac{z}{2\sqrt{\mathbb{D}_it}}\right)$ $N_i''(z=0)=\dfrac{C\mathbb{D}_i\left(x_i^s-x_i^0\right)}{\sqrt{\pi\mathbb{D}_it}}$ (Planar)	

4.1.21.5. Convective Mass Transfer

Convective mass transfer refers to transfer of a species, with respect to a solution of two or more species, in a flowing fluid. As in the case of heat transfer (Section 4.1.19), a species can be transported due to the movement of the fluid particle itself (advection) in addition to diffusion due to a concentration gradient. There are again, as in heat transfer, two situations of engineering interest:

- Concentration variations within a flowing fluid body, as in distributing alloying elements within a steel bath held in a ladle with argon stirring.
- Rate of transfer of species to/from an interface across which a fluid, containing the species of interest, is flowing, as in the case of the transfer of sulfur from the slag/metal interface to the bulk of the slag.

Rigorous treatment of both cases needs solutions of convective transport equations, along with the equations to describe fluid flow. The generalized convective species transport equation can be deduced from the diffusion equation by replacing the partial time derivative with a substantial or total derivative (Lagrangian in place of Eulerian view point)

$$\frac{DC_i}{Dt} = \frac{C_i}{t} + \overrightarrow{v} \cdot \nabla C_i = \nabla \cdot (\mathbb{D}_i \nabla C_i) + \dot{G}_i''' \tag{4.1.283}$$

This equation is analogous to Equation (4.1.169) for convective heat transfer. Application to complex systems needs computational techniques to be adopted.

Interface mass transfer is in general handled through correlations as was done in the case of heat transfer. One defines a mass transfer coefficient as:

$$N_i''|_s = Ck_{m,i}\left(x_i^s - x_i^{bulk}\right) \quad \text{or} \quad N_i''|_s = k_{m,i}\left(C_i^s - C_i^{bulk}\right) \tag{4.1.284}$$

where N'' is the molar flux and x_i^s and x_i^{bulk} are the mole fraction of species "i" at the interface and that in the bulk away from the interface. C_i's are the corresponding molar concentrations.

The mass transfer coefficient is nondimensionalized into the Sherwood number:

$$Sh = \frac{k_{m,i}L}{\mathbb{D}_i} \tag{4.1.285}$$

where L is the characteristic dimension for the system. The Sherwood number is analogous to the Nusselt number (some authors use the term Nu_m in place of Sh).

By dimensional analysis it can be shown that the Sherwood number is a function of Reynolds number, and the Schmidt number defined as

$$Sc = \frac{\mu/\rho}{\mathbb{D}_i} = \frac{\nu}{\mathbb{D}_i} \tag{4.1.286}$$

Schmidt number is the ratio of momentum diffusion to mass diffusion and is analogous to Prandtl number, $Pr = \frac{\nu}{\alpha}$.

The Chilton–Colburn analogy given in Equation (4.1.185) can be extended to mass transfer:

$$\frac{f}{2} = \frac{Nu}{Re \cdot Sc} Sc^{2/3} = \frac{Sh}{Re\, Sc^{1/3}} \tag{4.1.287}$$

The Chilton–Colburn analogy holds for many geometrically simple systems, especially between heat and mass transfer. For example, for flow of a fluid past a sphere, where mass transfer of a species takes place between the fluid and the sphere surfaces, the simple correlation commonly used is

$$\overline{Sh}_D = 2.0 + 0.6 Re_D^{1/2} Sc^{1/3} \quad (\text{see Equation } 4.1.204) \tag{4.1.288}$$

Note that correlations developed specifically for mass transfer should be preferred over those obtained using the analogy given in Equation (4.1.287). Detailed discussion on the empirical correlations for various situations is beyond the scope of this chapter, and readers may refer to books on mass transfer.

The following example of reaction of a porous solid with a gaseous species elucidates several of the concepts presented above.

Example 4.1.15
Topochemical Model for Gas–Solid Reaction

Consider a reducing gas, say a mixture of H_2 and H_2O, reacting with a spherical pellet of NiO (Figure 4.1.63a). Once the solid oxide at the surface is reduced, reaction can only proceed if H_2 diffuses into the pellet and the product H_2O diffuses out. Alternatively O

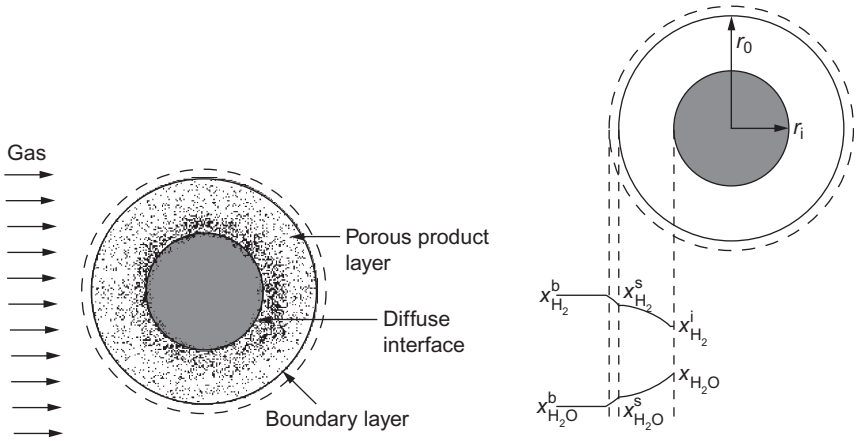


Figure 4.1.63 Gas–solid reaction in a spherical pellet. (a) General schematic showing a diffuse reaction interface and (b) schematic showing a sharp interface for the topochemical model.

has to diffuse out through the solid, which is extremely slow. Solid state diffusion of H_2/H_2O through solid product Ni is also extremely slow. If the initial pellet itself, or at least the product Ni, is porous, diffusion can take place through the gas in the pores, since gas phase diffusion coefficients are several orders of magnitude higher than those in the solid phase.

In porous pellets, therefore, reaction can proceed inside the pellet at reasonable rates. At any spherical cross section inside the pellet, H_2 arriving by diffusion from outside is partly consumed by the reduction reaction. The remaining hydrogen can diffuse further in. The reaction at any instant of time, in general, would be taking place over a diffuse region (Figure 4.1.63a).

Under certain conditions, the region of reaction can be thin enough to be approximated as being a sharp interface. This would happen primarily in either or both of the following conditions: (1) The starting oxide pellet is dense, i.e., the porosity is very low, and the product layer that forms is comparatively porous. The rate of diffusion through the unreacted core of the particle would then be negligibly low compared to that of the diffusion in the outer product layer and the chemical reaction. (2) The chemical reaction at the interphase is extremely fast compared to pore diffusion. The gas arriving at the interface by diffusion through the product layer is almost entirely consumed in a thin interface layer, leaving little H_2 to diffuse further in.

Under these conditions, one can approximate the interface layer to be a sharp surface, with a radius, r_i, which is continuously shrinking (Figure 4.1.63b). Various reaction models can be constructed to describe this process. A comparatively simple is the shrinking core model or the topochemical model. The model assumes that there is no overall change in the radius r_o of the pellet as the reaction proceeds, and the chemical reaction is of first order but reversible. This is described below.

There are five different rate processes that need to take place in series for the reaction to continue:

(1) Diffusion of H_2 from bulk gas to the pellet surface at $r = r_o$ by convective mass transfer.
(2) Diffusion of H_2 from the pellet surface at $r = r_o$ to the reaction interface at $r = r_i$.
(3) Chemical reaction at the interface: $NiO(s) + H_2(g) = Ni(s) + H_2O(g)$.
(4) Diffusion of H_2O from the reaction interface at $r = r_i$ to the pellet surface at $r = r_o$.
(5) Diffusion of H_2O from the pellet surface to the bulk gas by convective mass transfer.

The overall rate of reaction will be decided by the rates of the above steps. The process, as such, is in an unsteady state, since the interface radius r_i is continuously decreasing. The rate equations can, however, be written for each of the steps under the pseudosteady-state approximation: the rate of change of r_i is very slow and therefore each of the processes is very close to steady state that would be obtained for any given r_i.

Then the rate of reaction for a pellet at any instant of time is given by (refer to Figure 4.1.63c)

$$
\begin{aligned}
N_{H_2} &= \left(4\cdot\pi\cdot r_o^2\right)\cdot k_{m,H_2}\cdot C\cdot\left(x_{H_2}^{b} - x_{H_2}^{s}\right) \quad \text{(step a)} \\
&= \frac{C\cdot\left(x_{H_2}^{s} - x_{H_2}^{i}\right)}{\dfrac{1/r_i - 1/r_o}{4\cdot\pi\cdot\mathbb{D}_{H_2,\,\text{eff}}}} \quad \text{(step b)} \\
&= \left(4\cdot\pi\cdot r_i^2\right)\cdot k_r\cdot C\cdot\left(x_{H_2}^{i} - x_{H_2O}^{i}/K_{eq}\right) \quad \text{(step c)} \\
&= \frac{C\cdot\left(x_{H_2O}^{i} - x_{H_2O}^{s}\right)}{\dfrac{1/r_i - 1/r_o}{4\cdot\pi\cdot\mathbb{D}_{H_2O,\,\text{eff}}}} \quad \text{(step d)} \\
&= \left(4\cdot\pi\cdot r_o^2\right)\cdot k_{m,H_2O}\cdot C\cdot\left(x_{H_2O}^{s} - x_{H_2O}^{b}\right) \quad \text{(step e)}
\end{aligned}
$$

In the above, C is the total molar concentration ($=P_{total}/RT$), k_{m,H_2} and k_{m,H_2O} are convective mass transfer coefficients, k_r is the chemical reaction rate constant, and K_{eq} is the equilibrium constant for the reaction. $\mathbb{D}_{H_2,\,\text{eff}}$ and $\mathbb{D}_{H_2O,\,\text{eff}}$ are effective diffusivities in the porous product considering the product to be a homogeneous phase. Since the entire cross section of the pellet is not available for gaseous diffusion, and the path that hydrogen has to follow is tortuous, $\mathbb{D}_{i,\,\text{eff}}$ is less than the $\mathbb{D}_i$ defined for the homogeneous gas phase. $\mathbb{D}_{i,\,\text{eff}}$ is normally calculated as $\mathbb{D}_i\cdot\epsilon/\tau$, where ϵ is the porosity (<1) and τ is the tortuosity (>1).

Note that the pore diffusion as well as the gas phase mass transfer is equimolar counter diffusion, since 1 mol of H_2 generates 1 mol of H_2O. Further if the gas is a binary mixture, $\mathbb{D}_{H_2} = \mathbb{D}_{H_2O}$ and $k_{m,H_2} = k_{m,H_2O}$.

From the above series of equations, the intermediate mole fractions can be eliminated to give the instantaneous rates in terms of the bulk gas composition, which is measurable:

$$
\text{Rate} = N_{H_2} = -N_{H_2O} = \frac{\left(C\left(x_{H_2}^{b} - x_{H_2O}^{b}/K_{eq}\right)\right)}{\left(\frac{1}{4\cdot\pi\cdot r_o^2\cdot k_{m,H_2}}\cdot\left(1+\frac{1}{K_{eq}}\right) + \frac{1/r_i - 1/r_o}{4\cdot\pi\cdot\mathbb{D}_{H_2,\,\text{eff}}}\cdot\left(1+\frac{1}{K_{eq}}\right) + \frac{1}{4\cdot\pi\cdot r_i^2\cdot k_r}\right)} \tag{4.1.289}
$$

The mass transfer coefficients are estimated from correlations for flow past a sphere, or flow through a packed bed, etc., as the case may be.

The reduction rate any instant can be related to the rate of change of the interface radius:

$$
\text{Rate} = 4\cdot\pi\cdot r_i^2\cdot\frac{\partial r_i}{\partial t}\left(\rho_{NiO,\text{molar}}\right) \tag{4.1.290}
$$

where $\rho_{NiO,molar}$ is the apparent molar density of nickel oxide in the original pellet. Equation (4.1.289) when combined with Equation (4.1.290) is a first-order differential equation for r_i, with the initial condition: at $t=0, r_i=r_o$, and can be numerically integrated. At any instant of time, the extent of reaction $F(t)$ is given by:

$$F(t) = 1 - \left(\frac{r_i}{r_o}\right)^3$$

Kinetics of reduction of porous oxide particles is important in several metallurgical processes. In the iron blast furnace, for example, hematite, Fe_2O_3, particles charged at the top of the furnace get reduced to magnetite, Fe_3O_4, and then to wustite, Fe_xO, in the upper part of the furnace. In the middle region, the wustite particles further get reduced to metallic iron, all in solid state. The latter reaction is often treated in a manner similar to what is described in the above example. In the top region on the other hand, the two reactions, hematite-to-magnetite and magnetite-to-wustite, may take place simultaneously inside each pellet, resulting in two reaction fronts one inside the other. This would need more sophisticated treatment. Further, the temperatures of the pellets, and the gas surrounding them, change continuously as they descend in the furnace. A mathematical model describing the processes in the entire furnace, therefore, needs to combine the single pellet reduction rate equation (in differential form) with the overall enthalpy, mass, and species balance equations for complete description.

REFERENCES

[1] R. Bird, W. Stewart, E. Lightfoot, Transport Phenomena, John Wiley & Sons, New York, 1960.
[2] H. Struchtrup, Macroscopic Transport Equations for Gas Flows Approximate Methods in Kinetic Theory, first ed., Springer, Germany, 2005.
[3] O. Reynolds, Philos. Trans. R. Soc. Lond. A 174 (1883) 935.
[4] O. Reynolds, Philos. Trans. R. Soc. Lond. A 186 (1894) 123.
[5] R.I.L. Guthrie, Engineering in Process Metallurgy, Oxford University Press, USA, 1992.
[6] ISO Technical Committee ISP/TC30, I.O. of Standards (ISO 5167-1), Measurement of fluid flow by means of pressure differential devices part 1: orifice plates, nozzles, and venturi tubes inserted in circular cross-section conduits running full, ISO, Geneva, 2003.
[7] C.W. Macosko, Rheology: Principles, Measurements, and Applications (Advances in Interfacial Engineering), first ed., Wiley-VCH, USA, 1994.
[8] S.P. Sutera, R. Skalak, Annu. Rev. Fluid Mech. 25 (1993) 1.
[9] R. Perry, D. Green, Chemical Engineers Handbook, eighth ed., McGraw-Hill, New York, 2008.
[10] L. Moody, N. Princeton, Trans. ASME (Novermber 1944), 671–678.
[11] C.F. Colebrook, J. Inst, Civil Eng. London 11 (1939) 138–156.
[12] S.W. Churchill, Chem. Eng. 84 (1977) 891.
[13] P.R.H. Blasius, Das Aehnlichkeitsgesetz bei Reibungsvorgangen in Flüssigkeiten, Forschungsheft 131 (1913) 1–41.
[14] O. Levenspiel, Engineering Flow and Heat Exchange, Plenum Press, New York, 1984.
[15] E. Achenbach, Exp. Therm. Fluid Sci. 5 (1995) 17.
[16] S. Ergun, Chem. Eng. Prog. 48 (2) (1952) 89.
[17] G.G. Brown, Unit Operations, first ed., Wiley, USA, 1950.
[18] C.Y. Wen, Y.H. Yu, AIChE J. 12 (1966) 610.
[19] W.K. Lewis, E.R. Gilliland, W.C. Bauer, Ind. Eng. Chem. 41 (1949) 1104.

[20] M. Leva, Fluidization, McGraw-Hill, New York, 1959.
[21] D. Kunii, O. Levenspiel, Ind. Eng. Chem. Process Des. Dev. 7 (1968) 481.
[22] G.G. Stokes, Trans. Cambridge Philos. Soc. 9 (1851) 8–106.
[23] J.M. McDonough, Introductory Lectures on Turbulence, University of Kentucky, Lexington, KY, 2007.www.engr.uky.edu/acfd/lctr-notes634.pdf (June 4, 2012).
[24] J.O. Hinze, Turbulence, McGraw-Hill, New York, 1959.
[25] G.T. Chapman, M. Tobak, in: D.L. Dwoyer et al., (Ed.), Theoretical Approaches to Turbulence, Springer-Verlag, 1985, p. 19.
[26] J.W. Deardorff, J. Fluid Mech. 41 (1970) 453.
[27] T.V. Boussinesq, Mém. Prés. Acad. Sci., third ed., vol. XXIIII, Paris, 1877.
[28] L. Prandtl, Z. Angew. Math. Mech. 5 (1925) 136.
[29] B.E. Launder, D.B. Spalding, Mathematical Models of Turbulence, Academic Press, London, 1972.
[30] H. Schlichting, K. Gersten, Boundary Layer Theory, eighth ed., McGraw-Hill, New York, 2000.
[31] D.C. Wilcox, Turbulence Modeling for CFD, DCW Industries Inc., La Canada, 1993.
[32] V. Yakhot, S.A. Orszag, S. Thangam, T.B. Gatski, C.G. Speziale, Phys. Fluids A 4 (1992) 1510.
[33] A.N. Kolmogorov, J. Fluid Mech. 13 (1962) 82.
[34] J. Smagorinsky, Mon. Weather Rev. 91 (1963) 99.
[35] P. Sagaut, Large Eddy Simulation for Incompressible Flows, Springer, Berlin, 2001.
[36] M.N. Ozisik, Heat Conduction, John Wiley & Sons, New York, 1993.
[37] Y.S. Touloukian, Thermophysical Properties of Matter, vols. 1–2, IFI/Plenum, New York, 1970.
[38] F.P. Incropera, D. DeWitt, Fundamentals of Heat and Mass Transfer, fifth ed., Wiley, New York, 2002.
[39] E. Kreyszig, Advance Engineering Mathematics, John Wiley & Sons, New York, 2006.
[40] M.T. Heisler, Trans. ASME 69 (1947) 227.
[41] S. Patankar, Numerical Heat Transfer and Fluid Flow, Hemisphere Publishing Corporation, USA, 1980.
[42] N. Chvorinov, Giesserei 27 (1940) 177.
[43] L. Prandtl, in: A. Krazer (Ed.), Conference: Verhandlungen des dritten internationalen Mathematiker-Kongresses in Heidelberg 1904, Teubner, Leipzig, Germany, 1905, p. 484.
[44] J.D. Anderson, Phys. Today 58 (2005) 42.
[45] R. Hilpert, Forsch. Geb. Ingenieurwes. 4 (1933) 215.
[46] S.W. Churchill, M. Bernstien, J. Heat Transfer 99 (1977) 300.
[47] S. Whitaker, AIChE J. 18 (1972) 361.
[48] W. Ranz, W. Marshall, Chem. Eng. Prog. 48 (1922) 141.
[49] W.M. Kays, Trans. ASME 77 (1955) 1265.
[50] H.Z. Hausen, VDI Beih. Verfahrenstech. 4 (1943) 91.
[51] R.K. Shah, A.L. London, Laminar Flow Forced Convection in Ducts, Academic Press, New York, 1978.
[52] R.H.S. Winterton, Int. J. Heat Mass Transfer 41 (1998) 809.
[53] E.N. Sieder, G.E. Tate, Ind. Eng. Chem. 28 (1936) 1429.
[54] M.S. Bhatti, R.K. Shah, Handbook of Single-Phase Convective Transfer, Wiley-Interscience, Hoboken, NJ, 1987(Chapter 4).
[55] R.H. Norris, Augmentation of Convective Heat and Mass Transfer, ASME, New York, 1970.
[56] R.A. Seban, T.T. Shimazaki, Trans. ASME 73 (1951) 803.
[57] A. Cramb (Ed.), The Making, Shaping and Treating of Steel, 11th ed., Association for Iron & Steel Technology, 2003.
[58] L. Rayleigh, Philos. Mag. 1 (1876) 257.
[59] S.W. Churchill, H.H.S. Chu, Int. J. Heat Mass Transfer 18 (1975) 1323.
[60] J.R. Lloyd, W.R. Moran, J. Heat Transfer 96 (1974) 443.
[61] E. Radziemska, W.M. Lewandowski, Appl. Energy 68 (2002) 347.
[62] S.W. Churchill, H.H.S. Chu, Int. J. Heat Mass Transfer 18 (1975) 1049.
[63] S.W. Churchill, in: G.F. Hewitt (Exec. Ed.), Heat Exchanger Design Handbook, Section 2.5.7, Begell House, New York, 2002.
[64] M. Planck, The Theory of Heat Radiations, Dover Publications, New York, 1959.
[65] M.F. Modest, Radiative Heat Transfer, Academic Press, California, 2003.
[66] H.C. Hottel, A.F. Sarofim, Radiative Transfer, McGraw-Hill, New York, 1967.
[67] B. Leckner, Combust. Flame 19 (1972) 33.

CHAPTER 4.2

Reaction Kinetics

Peter Hayes
School of Chemical Engineering, The University of Queensland, Queensland, Brisbane, Australia

NOMENCLATURE

a (chemical) activity
A area m^2
$\boldsymbol{C_I}$ concentrations of the species (mol m^{-3})
D diffusion coefficient (m^2 s^{-1})
$\triangle \boldsymbol{E}$ apparent activation energy (J mol^{-1})
F activity coefficient
F Faraday's constant (C mol^{-1})
g acceleration due to gravity (m s^{-2})
$\triangle \boldsymbol{G}$ Gibbs free energy (J mol^{-1})
h Plank's constant (J s^{-1})
$\boldsymbol{\Delta H}$ enthalpy change (C mol^{-1})
I nucleation frequency (s^{-1})
j electrical current density (A m^{-2})
J molar flux (mol $m^{-2}s^{-1}$)
$\boldsymbol{k_1}$ chemical reaction rate constant for reaction (1 m s^{-1})
$\boldsymbol{k_m}$ mass transfer coefficient (m s^{-1})
$\boldsymbol{K_{eq}}$ equilibrium constant
M molecular weight (g mol^{-1})
n amount of material (mol)
N Avogadro's number (mol^{-1})
p partial pressure
Q volumetric flow (m^2 s^{-1})
r radius (m)
$\boldsymbol{\Delta S}$ entropy change (C mol^{-1} K^{-1})
t time (s)
V volume (m^3)
V velocity (m s^{-1})
z distance (m)

GREEK LETTERS

$\boldsymbol{\gamma}$ activity coefficient
$\boldsymbol{\sigma}$ surface tension (J m^{-2})
$\boldsymbol{\rho}$ density (kg m^{-3})
$\boldsymbol{\eta}$ overpotential (V)
$\boldsymbol{\gamma}$ activity coefficients
$\boldsymbol{\Phi}$ electrical potential (V)

Treatise on Process Metallurgy, Volume 1
http://dx.doi.org/10.1016/B978-0-08-096986-2.00014-X
© 2014 Elsevier Ltd.
All rights reserved.

$\boldsymbol{\phi^1}$ apparent chemical rate constant (mol m^{-2} s^{-1} atm^{-1})
$\boldsymbol{\theta}$ fractional surface coverage
$\boldsymbol{\mu}$ dynamic viscosity (N s m^{-2})
$\boldsymbol{\mu_i}$ chemical potential for species (I C mol^{-1})

4.2.1. REACTION KINETICS AND REACTION SYSTEMS

In its broadest sense, a "chemical reaction" is any change of state of a species; this includes changes to individual atoms or molecules as well as the chemical interactions of different species. The reactions can occur within a single phase, involve a phase transition of species or the transfer of species between phases, as can be clearly seen from inspection of the following examples of reactions encountered in metallurgical systems.

$$CO(gas) + O_2(gas) \rightarrow CO_2(gas) \quad (1\,phase)$$
$$Cu(solid) \rightarrow Cu(liquid) \quad (2\ phases)$$
$$S^{2-}(slag) \rightarrow S(in\ solution\ in\ mental) + 2e \quad (2\ phases)$$

Chemical reactions can also result in the loss of phases and the creation of new phases, for example,

$$H_2O(aqueous) \rightarrow 0.5O_2(gas) + 2H^+(aqueous) + 2e^- \quad (2\ phases)$$
$$2CaO(solid) + SiO_2(solid) \rightarrow 2CaO{\cdot}SiO_2(solid) \quad (3\ phases)$$
$$FeO(liquid) + C(solid) \rightarrow Fe(solid) + CO(gas) \quad (4\ phases)$$

It is clear that for the reactions to continue to take place new reactant species must be provided and products removed; so mass transfer of species must also be taking place at the same time as chemical reactions are occurring. It is also clear that in the examples of multi-phase reactions not all chemical reaction steps can occur at the same place in the reaction system at the same time. In the case of the reduction by solid carbon of FeO species dissolved in liquid slag to form solid iron and a gas phase, this would require all four phases to be simultaneously in contact with each other. This is the first clue that these reactions, although appearing to be simple from the balanced chemical equation, in fact involve some quite complex reaction mechanisms; a number of simultaneous physical and chemical processes are taking place. Each and every one of these process steps has the potential to influence the overall rate of a particular reaction, and, in the case of solid materials, the physical, and chemical properties of the reaction products.

So the question is where to start the analysis of these complex processes? The approach taken in the present chapter is to first identify different classes of chemical reactions that are encountered in metallurgical processes. This classification is based on consideration of the phases present, the reaction mechanisms, and the geometric

boundary conditions defining the reaction interfaces. The characteristics of each of these classes and the conditions under which they are formed are then systematically examined. This approach may help to clarify the relationships between experimentally determined rate data and the dominant reaction mechanisms in these systems, thereby making it easier to

(i) Identify the key process variables,
(ii) formulate descriptions the reaction rates as a function of these key variables, and
(iii) understand how design, control, and performance of metallurgical processes could potentially be improved.

We start the discussion by considering the phases involved in the reactions. There are two major classes of reactions namely homogeneous reactions and heterogeneous reactions.

4.2.1.1. Homogeneous Reactions

The term homogeneous reactions refers to reaction phenomena taking place within a single phase, such as might occur in gas, liquid, or solid solutions. In the gas phase, we readily recognize that different gas species can coexist and that at equilibrium the relative populations of these species are functions of bulk chemical composition, temperature, and pressure. The equilibrium populations of the different species can be described by chemical thermodynamic principles; any changes in these state properties will result in changes in the chemical characteristics of the system. Similarly, in aqueous solutions, a range of ionic solute species can coexist, the equilibrium populations of which are dependent on, for example, the bulk chemical composition, temperature, solution potential (E_h), and hydrogen ion concentration as reflected in the pH of the solutions. Molten oxides (slags) can contain transition metals that are present in a number of oxidation states, the relative concentrations of these ionic species may change with bulk composition, oxygen partial pressure, and temperature. In crystalline solids, defect populations within a given solid are also known to change with changes in bulk chemical composition and temperature. Clearly then differences in chemistry can be established by changes to thermodynamic state functions in single phase systems, these differences represent the driving forces for change.

The rates of these homogeneous reactions are largely dependent on the combined probabilities that (a) the reactant species will collide or closely approach each other, and (b) specific atomic rearrangement and electron transfer reaction steps will proceed. In very general terms, it can be said that the mobilities of atoms and molecules within gas and liquid solutions, that is fluid phases, in metallic and inorganic systems are relatively high, and the reactant species are relatively simple in structure. The result is that chemical reaction rates in these fluid systems are relatively fast and chemical equilibrium in these single phase solutions is rapidly approached. In solid phases, however, the rates of homogeneous reactions are largely limited by mass transfer of species within the condensed

phases. Since reactions in these solid solutions are dealt with extensively elsewhere in the materials science literature they will not be discussed further here. The point to make here is that we should be aware of this class of reactions; however, in general, the rates of homogeneous reactions do not represent the major concerns or limitations when considering reactions in metallurgical systems.

4.2.1.2. Heterogeneous Reactions

Central to the practice of chemical process metallurgy and materials engineering is the control of multi-phase processes and reactions. These *heterogeneous processes,* involving transfers of species between gas, liquid, and solid phases, necessarily include chemical reactions occurring at interfaces in addition to transport across and within individual phases. The overall rate of a reaction between the phases will be influenced by not only the chemical reactions themselves but also by the interfacial area available for transfer. In the example shown in Figure 4.2.1, the volume fractions of phases 1 and 2 are the same for case (a) and case (b); however, there is clearly a difference in the interfacial area between the two phases. The interfacial area available for reaction, and therefore reaction rate, is in all cases dependent on the relative proportions of the phases, the size distributions, and shapes of the dispersed phases.

For the purposes of describing and discussing these heterogeneous reactions in a systematic way, these chemical reaction systems have been further subdivided into *solute transfer reactions* and *phase formation reactions* (see Figure 4.2.2).

As is implied by the name, solute transfer reactions refer to solute species moving from one phase to another and in doing so taking on different chemical associations within the individual phases; the solvent phases 1 and 2 remain essentially unchanged. Solute transfer reactions involve both chemical reaction at the interface and mass transfer in the matrix phases; it is therefore necessary to define the bulk chemistries of the matrix phases and geometries of the interfaces formed by these phases in order to be able to quantitatively

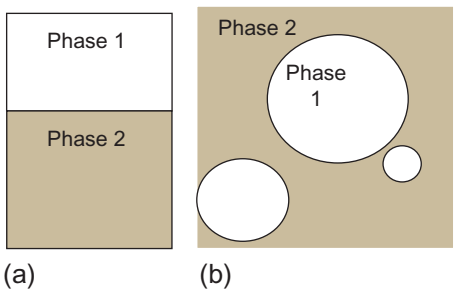


Figure 4.2.1 Examples of different dispersions of phases in a two phase system.

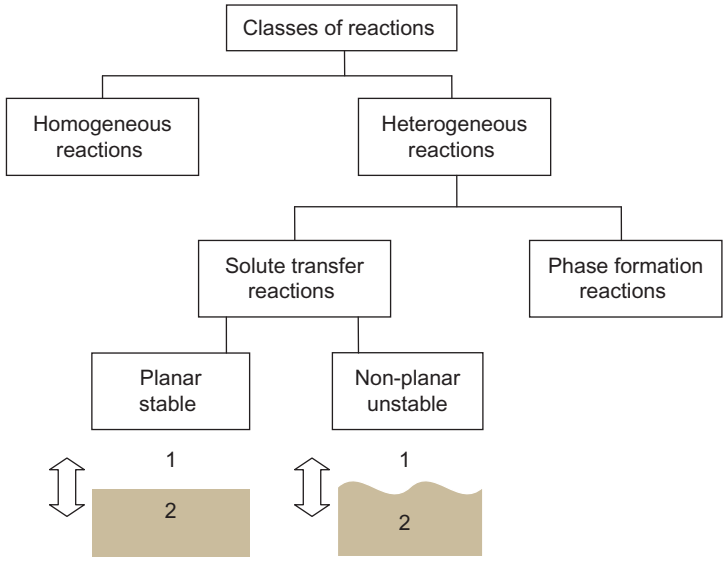


Figure 4.2.2 Classes of chemical reactions.

describe the overall rates of the reactions. The simplest case to describe in quantitative terms is that of a planar stable interface, this is defined as one in which the interfacial area is constant or moves to minimum value for the reaction system. These planar interfaces are observed when mass transfers at and along the interface itself are fast compared to chemical reactions at the interface.

There are situations in which the chemical reactions taking place at the interface are fast compared to local mass transfer processes; in these cases the interface can become unstable, the effective interfacial area increases with reaction time or extent time. An example of the later class includes liquid/liquid systems in which spontaneous emulsification, or dispersion of one phase in another, occurs as a result of the simultaneous chemical reaction and the transfer of species across the interface. The rates of reactions at these unstable interfaces are more complex and additional factors have to be taken into account. To be able to clearly distinguish these different cases, the classes of solute transfer reactions have been divided into those that involve *planar interfaces* and those exhibiting *unstable interfaces*; the conditions under which interfaces become unstable will be discussed in more detail later in Chapter 4.4.

As the name implies phase formation reactions are chemical reactions in which new phases are formed by the interaction of the reactant species. The reaction products can be gas, liquid, or solid phases. Where and how these new phases are formed can significantly impact on the overall reaction rates and reaction mechanisms taking place in any particular system. This class of reactions will be dealt with in separate sections in Chapters 4.5 and 4.6.

4.2.2. REACTION RATES AND RATE-LIMITING PROCESSES

Heterogeneous chemical reactions can be envisaged as consisting of a series of reaction steps involving,

(i) Mass transfer of the reactant species from the bulk phases to the reaction interface.
(ii) "Chemical reaction" between the reactive species at the reaction interface.
(iii) Mass transfer of products from the reaction interface to the original bulk phases or the formation of a new product phase.

In addition, accompanying all chemical and electrochemical reactions as they proceed are changes in enthalpy. The total quantity of heat released or absorbed by the reactions is directly proportional to the amount (mass or moles) of material that has been transformed by the reaction. So, if the process is proceeding under isothermal conditions, heat transfer between the reaction interface and the surroundings must also simultaneously take place.

To illustrate the issues that must be addressed in describing reaction rates in heterogeneous chemical reaction systems, the example of the transfer of a single solute species, molecular oxygen, from one solution phase (gas phase) to another (water) is considered. In undertaking this transfer, the species itself has not changed but the matrix in which it finds itself is different. As indicated in the introduction this transfer process from one phase to another can be considered as a chemical reaction and the overall process described by the equation,

$$O_2(\text{gas}) \rightarrow O_2(\text{aqueous solution}) \tag{4.2.1}$$

If there is little or no oxygen dissolved in the water at the start of the reaction there will be a net thermodynamic driving force for dissolution of oxygen species; contact of the water with the gas phase will result in the net transfer of oxygen from the gas to the water. This process will continue until the system comes to an equilibrium condition at which no more oxygen can dissolve in the aqueous solution under these process conditions.

Examining this process carefully it can be seen that a number of elementary process steps are occurring during the transfer of the solute species between the two phases; these steps involve (i) mass transfer of solute from the bulk phase to the interphase boundary, "the interface," (ii) chemical reaction at the interface associated with change in the local chemical environment experienced by the molecule on transferring from the gas phase to the aqueous solution, and (iii) mass transfer of the solute in aqueous phase from the interface into the bulk aqueous solution. This process is illustrated schematically in Figure 4.2.3.

In general terms, the overall transfer of a species from phase I to phase II can be described by an equation of the form

$$\text{solute(phase I)} \rightarrow \text{solute(phase II)} \tag{4.2.2}$$

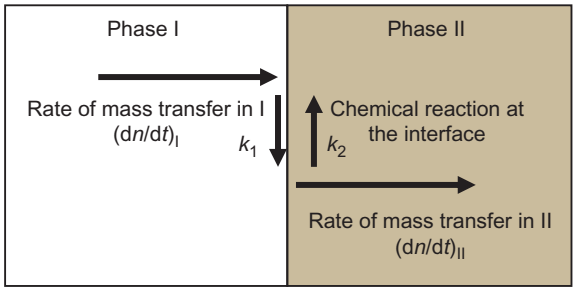


Figure 4.2.3 Schematic of the elementary process steps taking place during transfer of a solute species across an interface from phase I to phase II. Step (i) mass transfer of solute from the bulk phase I to the interface, step (ii) chemical reaction at the interface, and step (iii) mass transfer of the solute in phase II from the interface into the bulk phase II.

In order to determine the overall rate of the reaction, it is first necessary to establish the boundary conditions for the problem. By the way of illustration, consider the case in which there is steady-state transfer of a particular species in solution phase I across a fixed interface area, A, to solution phase II. To simplify the analysis, a first order chemical reaction involving the change in chemical environment of the solute species is assumed to occur at the interface. Considering the process to occur as a series of three steps, (i) to (iii), as outlined above, a number of scenarios can be envisaged for this process, and it is useful to start by examining the limiting conditions.

4.2.2.1. Case (a): Mass Transfer in Phase I is Rate Limiting

For the net mass transfer of the species from the bulk phase I to the reaction interface, there must be a net driving force; this is manifested in this present case in the form of a concentration gradient. The concentration of the species in the bulk phase is C_I and the concentration of the species at the interface is C_I^i.

The rate of mass transfer of the species from the bulk phase I to the interface, is given by

$$1/A\cdot(\mathrm{d}n/\mathrm{d}t)_I = k_{mI}\cdot\left[C_I - C_I^i\right] \quad \left(\mathrm{mol\ m^{-2}s^{-1}}\right) \tag{4.2.3}$$

where C_I and C_I^i are the concentrations of the species in the bulk phase and at the interface in phase I respectively (all concentrations in mol m^{-3}), k_{mI} is the mass transfer coefficient for the species in phase I ($\mathrm{m\ s}^{-1}$). The solute concentration profile across the interface for this limiting condition is illustrated schematically in Figure 4.2.4a [68]. It is not possible in practice to directly measure C_I^i, however, as will be demonstrated, this term can be expressed in an alternative and more useful form. For conditions in which the chemical reaction at the interface is fast, that is, when the chemical reaction constants, k_1 and k_2, for the forward and back reactions, respectively, at the interface are high, and mass

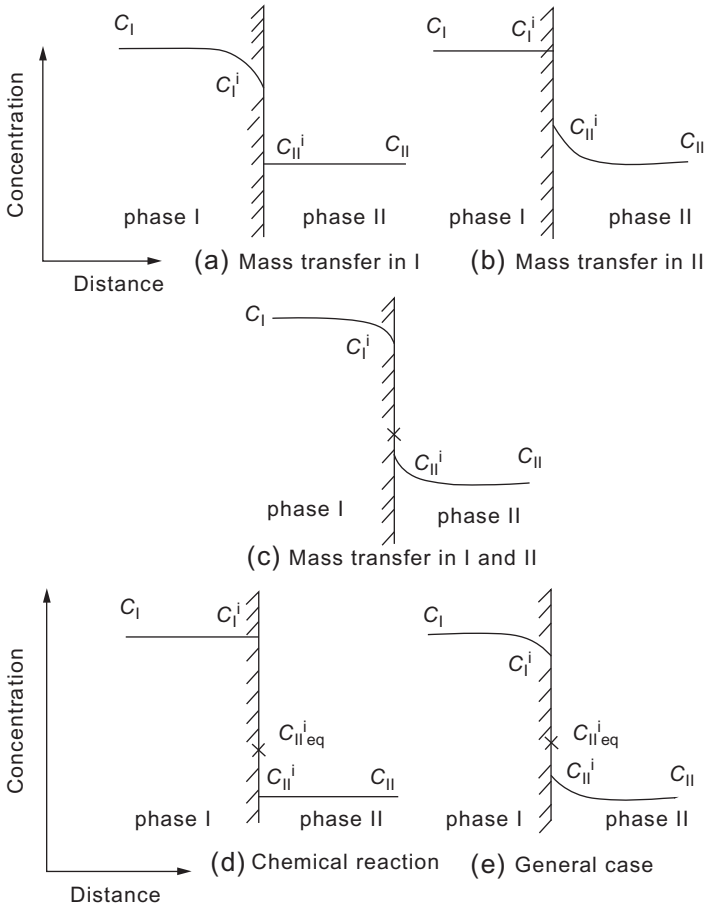


Figure 4.2.4 Schematic illustration of the solute concentration profiles across the interface between phases I and II; (a) mass transfer in phase I rate limiting; (b) mass transfer in phase II rate limiting; (c) mass transfer in phases I and II, both rate limiting; (d) chemical reaction at the interface between phases I and II rate limiting; and (e) general case. C_{IIeq}^i is the concentration at the interface in phase II that would be in equilibrium with phase I at concentration C_I. *Adapted from [68].*

transfer in phase II is rapid, it can be reasonably assumed that the chemical reaction step approaches local equilibrium at the interface. Then $[k_1 C_I{}^i = k_2 C_{II}{}^i]$ and, rearranging this equality,

$$C_I{}^i / C_{II}{}^i = k_2/k_1 = (\gamma_I/\gamma_{II}) \cdot 1/K_{eq} = 1/K \tag{4.2.4}$$

where K_{eq} is the equilibrium constant for reaction 1.1, γ_I and γ_{II} are the activity coefficients of the solute species in phases I and II respectively. Substituting $C_{II}{}^i/K$ for $C_I{}^i$ in Equation (4.2.3) then

$$1/A\cdot(\mathrm{d}n/\mathrm{d}t)_{\mathrm{I}} = k_{\mathrm{mI}}\cdot\left[C_{\mathrm{I}} - C_{\mathrm{II}}{}^{\mathrm{i}}/K\right] \quad \left(\mathrm{mol\,m^{-2}\,s^{-1}}\right) \tag{4.2.5}$$

and, since for these conditions, $C_{\mathrm{II}}{}^{\mathrm{i}} = C_{\mathrm{II}}$, then finally

$$1/A\cdot(\mathrm{d}n/\mathrm{d}t)_{\mathrm{I}} = k_{\mathrm{mI}}\cdot[C_{\mathrm{I}} - C_{\mathrm{II}}/K] \quad \left(\mathrm{mol\,m^{-2}\,s^{-1}}\right) \tag{4.2.6}$$

This is the rate equation in the limiting condition when the overall rate of the reaction is determined by the mass transfer in phase I.

4.2.2.2. Case (b): Mass Transfer in Phase II is Rate Limiting

The rate of mass transfer of the species from the interface to the bulk phase II,

$$1/A\cdot(\mathrm{d}n/\mathrm{d}t)_{\mathrm{II}} = k_{\mathrm{mII}}\cdot\left[C_{\mathrm{II}}{}^{\mathrm{i}} - C_{\mathrm{II}}\right] \quad \left(\mathrm{mol\,m^{-2}\,s^{-1}}\right) \tag{4.2.7}$$

where C_{II} and $C_{\mathrm{II}}{}^{\mathrm{i}}$ are the concentrations of the species in the bulk phase and at the interface in phase II respectively (all concentrations in mol $\mathrm{m^{-3}}$), k_{mII} is the mass transfer coefficient in phase II. The bulk concentration of the species in phase II, C_{II}, is assumed to remain constant throughout the process. The solute concentration profile across the interface for this limiting condition is illustrated schematically in Figure 4.2.4b [68]. Again assuming that the chemical reaction rate at the interface is fast, $C_{\mathrm{I}}{}^{\mathrm{i}}/C_{\mathrm{II}}{}^{\mathrm{i}} = k_2/k_1 = 1/K$, where K is the apparent equilibrium constant for the reaction 1.2. Substituting $C_{\mathrm{I}}{}^{\mathrm{i}}$ K for $C_{\mathrm{II}}{}^{\mathrm{i}}$ in Equation (4.2.7) and since for these conditions, $C_{\mathrm{I}}{}^{\mathrm{i}} = C_{\mathrm{I}}$, then

$$1/A\cdot(\mathrm{d}n/\mathrm{d}t)_{\mathrm{I}} = k_{\mathrm{mII}}\cdot(C_{\mathrm{I}}K - C_{\mathrm{II}}) \quad \left(\mathrm{mol\ m^{-2}\,s^{-1}}\right) \tag{4.2.8}$$

This is the rate equation in the limiting condition when the overall rate of the solute transfer is determined by the mass transfer in phase II.

4.2.2.3. Case (c): Mass Transfer in Both Phases I and II are Rate Limiting

If mass transfer in both phases is slow relative to the chemical reaction rate at the interface, and the process is occurring under steady-state conditions, then the rate of mass transfer of the species from the bulk phase I to phase II is described by the equation

$$1/A\cdot(\mathrm{d}n/\mathrm{d}t)_{\mathrm{I}} = k_{\mathrm{mI}}\cdot\left[C_{\mathrm{I}} - C_{\mathrm{I}}{}^{\mathrm{i}}\right] = k_{\mathrm{mII}}\cdot\left[C_{\mathrm{II}}{}^{\mathrm{i}} - C_{\mathrm{II}}\right] \quad \left(\mathrm{mol\ m^{-2}\,s^{-1}}\right) \tag{4.2.9}$$

The concentration profile across the interface for this condition, where mass transfer in both phase I and phase II are slow relative to the rates of the chemical reactions at the interface, is illustrated schematically in Figure 4.2.4c [68]. It follows from Equation (4.2.9) that, considering the transfer in phase II

$$C_{\mathrm{II}}{}^{\mathrm{i}} = C_{\mathrm{II}} + \left[1/Ak_{\mathrm{mII}}\cdot(\mathrm{d}n/\mathrm{d}t)_{\mathrm{II}}\right] \tag{4.2.10}$$

and since the chemical reaction rate is fast,

$$C_{\mathrm{I}}{}^{\mathrm{i}} = C_{\mathrm{II}}{}^{\mathrm{i}}/K = 1/K\left\{C_{\mathrm{II}} + \left[1/Ak_{\mathrm{mII}}\cdot(\mathrm{d}n/\mathrm{d}t)_{\mathrm{II}}\right]\right\} \tag{4.2.11a}$$

Considering the transfer in phase I

$$C_{\mathrm{I}}{}^{\mathrm{i}} = C_{\mathrm{I}} - 1/Ak_{\mathrm{mI}}\cdot(\mathrm{d}n/\mathrm{d}t)_{\mathrm{I}} \tag{4.2.11b}$$

Equating and rearranging Equations (4.2.11a) and (4.2.11b)

$$1/A\cdot(\mathrm{d}n/\mathrm{d}t) = \{1/\{1/k_{\mathrm{mI}} + K/k_{\mathrm{mII}}\}\cdot(C_{\mathrm{I}} - KC_{\mathrm{II}}) \tag{4.2.12}$$

If $k_{\mathrm{mII}} \gg k_{\mathrm{mI}}$ then the system approaches the limiting condition for mass transfer in phase I, that is,

$$1/A\cdot(\mathrm{d}n/dt) = k_{\mathrm{mI}}\cdot(C_{\mathrm{I}} - C_{\mathrm{II}}/K) \tag{4.2.13}$$

If $k_{\mathrm{mI}} \gg k_{\mathrm{mII}}$ then the system approaches the limiting condition for mass transfer in phase II, that is,

$$1/A\cdot(\mathrm{d}n/\mathrm{d}t) = (1/\{Kk_{\mathrm{mII}}\})\cdot(C_{\mathrm{I}} - C_{\mathrm{II}}/K) = k_{\mathrm{mII}}\cdot(C_{\mathrm{I}}K - C_{\mathrm{II}}) \tag{4.2.14}$$

4.2.2.4. Case (d): Chemical Reaction at the Interface is Rate Limiting

In the scenario where the rates of mass transfer in both phases I and II are rapid compared to the rate of the chemical reaction step at the interface, then $C_{\mathrm{I}}{}^{\mathrm{i}} = C_{\mathrm{I}}$ and $C_{\mathrm{II}}{}^{\mathrm{i}} = C_{\mathrm{II}}$

The rate of the forward chemical reaction at the interface,

$$\text{that is, transfer from phase I to phase II} = k_1 C_{\mathrm{I}}{}^{\mathrm{i}} = k_1 C_{\mathrm{I}} \tag{4.2.15}$$

The rate of the back reaction at the interface,

$$\text{that is, transfer from phase II to phase I} = k_2 C_{\mathrm{II}}{}^{\mathrm{i}} = k_2 C_{\mathrm{II}} \tag{4.2.16}$$

The concentration profile across the interface for this condition where mass transfer in both phase I and phase II are relatively fast and the chemical reaction is rate limiting is illustrated schematically in Figure 4.2.4d [68].

It has been shown previously (see Equation (4.2.4)) that the rate constants k_1 and k_2 are related to the equilibrium constant for the reaction, that is, $k_2/k_1 = 1/K$. Substituting for k_2 into Equation (4.2.16) the net rate of chemical reaction at the interface, is given by the equation

$$\begin{aligned} 1/A\cdot(\mathrm{d}n/\mathrm{d}t)_i &= \left[k_1 C_{\mathrm{I}}{}^{\mathrm{i}} - k_2 C_{\mathrm{II}}{}^{\mathrm{i}}\right] = [k_1 C_{\mathrm{I}} - k_2 C_{\mathrm{II}}] \\ &= k_1[C_{\mathrm{I}} - C_{\mathrm{II}}/K] \quad \left(\mathrm{mol\,m^{-2}\,s^{-1}}\right) \end{aligned} \tag{4.2.17}$$

4.2.2.5. Case (e): Overall Rate Equation

Following the same procedures as outlined above it can be shown that, for the general case at steady-state conditions,

$$1/A\cdot(\mathrm{d}n/\mathrm{d}t) = k_{\mathrm{mI}}\cdot[C_{\mathrm{I}} - C_{\mathrm{II}}/K] = \left[k_1 C_{\mathrm{I}}{}^{\mathrm{i}} - k_2 C_{\mathrm{II}}{}^{\mathrm{i}}\right] = k_{\mathrm{mII}}\cdot(C_{\mathrm{I}}\cdot K - C_{\mathrm{II}}) \qquad (4.2.18)$$

The expressions can be combined and rearranged, and so that the overall rate of transfer can be expressed in the form

$$1/A\cdot(\mathrm{d}n/\mathrm{d}t) = 1/[1/k_{\mathrm{mI}} + 1/k_1 + 1/Kk_{\mathrm{mII}}]\cdot[C_{\mathrm{I}} - C_{\mathrm{II}}/K] \quad \left(\mathrm{mol\,m^{-2}s^{-1}}\right) \qquad (4.2.19)$$

Equation (4.2.19) highlights not only the dependence of the overall rate of transfer on the rates of the individual steps but also demonstrates that, in the limit, it will be the slowest of these steps that will largely determine the overall reaction rate. The form of Equation (4.2.19) can also be viewed as

$$\text{Rate or flux} = \text{driving force/resistance} \qquad (4.2.20)$$

$1/A\cdot(dn/dt)$	$=1/[1/k_{\mathrm{mI}}$	$+1/k_1$	$+1/Kk_{\mathrm{mII}}]\cdot[C_I - C_{\mathrm{II}}/K]$	
Resistance due to	mass transfer in I	chemical reaction	mass transfer in II	(4.2.19)

In effect, there is a resistance associated with each reaction step in the process. The concentration profile across the interface for this general condition where mass transfer in both phase I and phase II and the chemical reaction provide significant resistance to solute transfer is illustrated schematically in Figure 4.2.4e [68]. It can be seen from Equation (4.2.19) that if the rate constant associated with one of the reaction steps is small compared to those of the other two steps then the equation for the overall reaction rate approaches the limiting rate defined by the rate equation for the slowest step, as given in Equations (4.2.6), (4.2.8), and (4.2.17).

It can also be seen from the rate expression that changing the interfacial area, A, does not directly change the relative rates of the mass transfer and chemical processes for this particular example. To change from, for example, a mass transfer limited reaction to one limited by the chemical reaction rate, the relative values of the rate constants k_{mI}, k_{mII}, and k_1 must be changed; these are the process variables that can be influenced by process design and operational practice.

Equation (4.2.19) describes the rate of the reaction at any instant in time; for the rate to remain constant it is necessary that

- A pseudo-steady state is maintained in the system, that is, the bulk compositions of the phases I and II should remain constant.
- There is no change in reaction geometry with time, that is, surface area and interface shape remains constant throughout the reaction.

- The same reaction mechanisms, and the same rate-limiting chemical reaction steps, are occurring for all conditions.
- The same relative contributions to the heat and mass transfer mechanisms are occurring for all conditions, for example, the relative contributions from thermal and mass diffusivity, natural and forced convection, radiation remain constant, and the system temperature is constant.

Clearly not all of these conditions apply to the real systems of interest to engineering practice. In reality, the boundary and system conditions, and the rates of individual reaction steps, invariably change with time and extent of reaction. In some cases, these changes in boundary conditions lead to step changes in actual reaction mechanism; these changes can be profound, and extrapolation and interpolation can lead to erroneous conclusions with significant implications for the process. It is for these reasons that it is necessary to carefully examine and understand the details of the reaction system to ensure the overall reaction rate is accurately described.

4.2.3. STRUCTURE OF THE CHAPTER

The examples given in Section 4.2.2 indicate that the study of reaction kinetics is not just about the rates of individual chemical reaction steps but is concerned with the overall rates of process, which necessarily include transport processes and other reaction mechanisms. Just as in any mathematical equation it is necessary to establish the boundary conditions to the problem in order to obtain a solution, in describing the kinetics of a particular reaction system it is necessary to define conditions, such as, the driving force for reaction, reaction geometries, and the chemical and physical characteristics of the species and the phases in the system. To assist in identifying and establishing these boundary conditions, the discussion is structured in the following Chapters 4.3–4.8.

To illustrate the concepts and the application of these ideas, examples of reaction phenomena observed in process metallurgy are provided in the text. Further examples of reaction kinetics in metallurgical systems can be found in a number of excellent books on this topic [68–80].

REFERENCES

[68] F.D. Richardson, Physical Chemistry of Melts in Metallurgy, Academic, London, 1974, p. 420.
[69] J. Szekely, J.W. Evans, H.Y. Sohn, Gas-Solid Reactions, Academic Press, Inc., New York, 1976.
[70] H.Y. Sohn, M.E. Wadsworth, Rate Processes in Extractive Metallurgy, Plenum, New York, 1978.
[71] E.T. Turkdogan, Physical Chemistry of High Temperature Technology, Academic, New York, 1980.
[72] K.J. Laidler, Chemical Kinetics, third ed., Harper Row, New York, 1987.
[73] H.Y. Sohn, P.C. Chaubal, G.R. St Pierre, in: Y. Sahai (Ed.), Transport Processes in Engineering 4: Advances in Transport Processes in Metallurgical Engineering, Elsevier, Amsterdam, 1992, pp. 1–52.
[74] O. Levenspiel, Chemical Reaction Engineering, third ed., John Wiley, New York, 1999.
[75] J.W. Christian, Theory of Phase Transformations in Metals and Alloys, third ed., Pergamon, Oxford, 2002.

[76] W. Kurz, D.J. Fischer, Fundamentals of Solidification, third ed., Trans Tech, Switzerland, 2004.
[77] A.R. Burkin, Chemical Hydrometallurgy—Theory and Practice, Imperial College Press, London, 2001.
[78] K.A. Jackson, Kinetic Processes—Crystal Growth, Diffusion and Phase Transitions in Materials, Wiley-VCH, Weinheim, 2004.
[79] S. Seetharaman (Ed.), Fundamentals of Metallurgy, Woodhead Publications, Cambridge, UK, 2005.
[80] Perry's Chemical Engineering Handbook, McGraw Hill, New York, 2008.

CHAPTER 4.3

Chemical Reaction Kinetics

Peter Hayes
School of Chemical Engineering, The University of Queensland, Queensland, Brisbane, Australia

4.3.1. CHEMICAL KINETICS

4.3.1.1. Empirical Rate Equations

Chemical reaction rates are frequently described by empirical mathematical relations in the form of "rate laws" [81–83], for example,

$$\mathcal{R} = kC_A{}^{\alpha}C_B{}^{\beta} \tag{4.3.1}$$

where $\mathcal{R}$ is the overall rate, k is the "apparent rate constant", C_A and C_B are the concentrations of species A and B in the system. The power to which the concentration of the species is raised in a rate law of this kind is referred to as the "order of the reaction", in this case α and β for species A and B, respectively.

There are several important points that need to be made here regarding these empirical rate laws.

These reaction orders are simply those that best describe the experimental data; they need not be integer values, and they do not necessarily reflect the stoichiometry as expressed in a balanced chemical reaction equation describing the overall reaction. The apparent rate constant is valid for a specific chemical reaction involving particular phases of a given bulk composition and reaction geometry and reaction temperature; in the case of heterogeneous reactions, the rate constant may include the interfacial reaction area. The rate equation given in the form of Equation (4.3.1) is valid only if all of these parameters remain constant throughout the complete process.

The apparent rate equations do not necessarily include all of the reactant species listed in the stoichiometric equation; this is very much dependent on the system under consideration. If, for example, species A and B react in equal molar proportions and there are comparable amounts of both phases present in the system, the concentrations of both will measurably change during the course of the reaction and the experimentally determined rate law would include both species. If, however, there is only a large amount of species B then, as a result of mass balance, there will be a significant change to the concentration of A but the concentration of B in the system may remain almost unchanged; thus the

Treatise on Process Metallurgy, Volume 1
http://dx.doi.org/10.1016/B978-0-08-096986-2.00015-1
© 2014 Elsevier Ltd.
All rights reserved.

empirical reaction order for component B would appear to be zero even though this component is participating in the reaction.

The temperature dependence of thermally activated processes is commonly explained in terms of rate laws, such as, the Arrhenius equation

$$k = k^{o} \exp(-\Delta E/RT) \tag{4.3.2}$$

where k^{o} is an experimentally determined preexponential factor, R is the gas constant (J mol^{-1} K^{-1}), T is the absolute temperature (K), and ΔE is referred to as the apparent activation energy for the reaction (J mol^{-1}). These thermally activated processes include both chemical and diffusional processes. The apparent activation energy is often used to provide an indication of the rate limiting reaction step in a process, for example, mass transfer or chemical reaction. However, careful analysis is required in interpreting the rate data especially for heterogeneous reactions approaching chemical equilibrium since these conditions can lead to misleading conclusions [84].

The final point is that the use of empirical rate equations is valid only as long as the governing reaction mechanism is unchanged over the range of conditions considered. Changes in reaction mechanism can lead to significant changes in the apparent law and sometimes counter intuitive trends in behavior, such as step changes in rate or decreases in rate with increasing temperature.

4.3.1.2. Reaction Rate Theory

One of the important insights into the kinetics of chemical reactions that has emerged from previous studies is the realization that the rates of chemical processes are not only dependent on the probability of bringing the species together, as described by collision theory, but also that many different ways or reaction pathways are possible to enable these reactions to occur. The basis for our current understanding of rate processes is provided by absolute reaction rate or transition state theory [81–83]; a simplified version of the theory is provided for convenience in the present context.

Transition state theory can be applied to any thermally activated, that is, temperature dependent process, these include all chemical reactions, and the transfer of species through thermally activated diffusional processes. The transition state model envisages the movement of species through a variety of reaction paths, or reaction coordinates, from the initial to the final state. The reaction coordinates here include not only the distances between species but also factors, such as, the relative orientation of atoms or molecules. The Gibbs free energy of the species is a function of the position on the reaction coordinate. Transition state theory assumes the formation of an activated complex that subsequently decomposes at a given rate into the reaction products. This transition from reactant to product is illustrated schematically in Figure 4.3.1. For a reaction involving reactants L and M, this activated complex or transition state may, for convenience, be

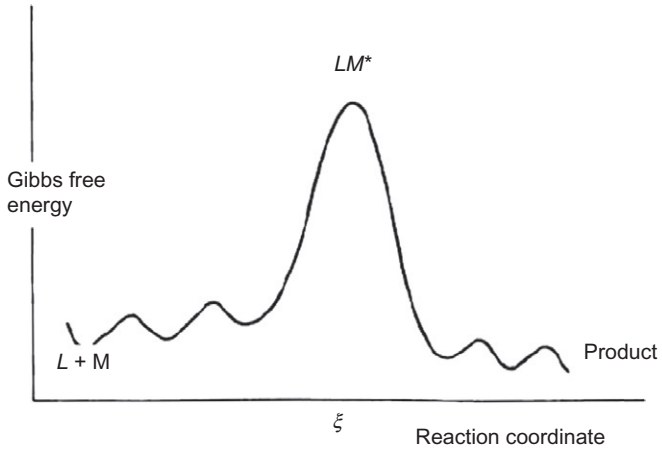


Figure 4.3.1 Schematic of the Gibbs free energy as a function of reaction coordinate for the formation of the activated complex, LM^*.

called LM^*. It is assumed that LM^* has a Gibbs free energy corresponding to the maximum on the reaction coordinate and that this complex is in equilibrium with the reactants. The assumption of equilibrium between the activated complex and the reactants comes about since the reaction steps prior to the formation of the complex are assumed to be rapid compared to the rate of decomposition of the complex. The formation of this transition state can be represented by the equation

$$L + M = LM^* \tag{4.3.3}$$

and the equilibrium constant, K^*_{eq} for the reaction is given by

$$K^*_{\text{eq}} = a_{LM^*}/(a_L \cdot a_M) \tag{4.3.4}$$

Assuming the rate of decomposition of the activated complex is $k^{\text{f}*}(\text{s}^{-1})$, is the same as the rate of formation of product

$$\text{d}C_{\text{prod}}/\text{d}t = -\text{d}C_{LM^*}/\text{d}t = k^{\text{f}*} c_{LM^*} \tag{4.3.5}$$

From Equation (4.3.4) $c_{LM^*} = a_{LM^*}.c^{\text{o}}/\gamma_{LM^*} = K^*_{\text{eq}}(a_L \cdot a_M)c^{\text{o}}/\gamma_{LM^*} = K_{\text{eq}}{}^*(c_L \cdot c_M)$ $(\gamma_L \cdot \gamma_M/\gamma_{LM^*})/c^{\text{o}}$ where c^{o} is the standard state and γ is the activity coefficient of the respective species. Then

$$\text{d}C_{\text{prod}}/\text{d}t = k^{\text{f}} \cdot c_L \cdot c_M \tag{4.3.6}$$

where k^{f} is the specific forward reaction rate constant for the reaction, that is, $k^{\text{f}} = k^{\text{f}*} \cdot K^*_{\text{eq}} \cdot (\gamma_L \cdot \gamma_M/\gamma_{LM^*})/c^{\text{o}}$. It can be shown [83] from transition state theory that the rate of decomposition of the activated complex, $k^{\text{f}*} = RT/Nh\ (\text{s}^{-1})$.

In any chemical or physical change, such as, the movement of an electron, atom, or molecule from one position to another in the system there will always be a number of transition states formed in the process. The stabilities of the activated complexes will be different in each of these cases and for this reaction path the resulting overall reaction rate law will be dependent on the reaction step that is the slowest in this sequence. Since the resulting reaction rate law for the overall reaction is determined by the slowest step it becomes clear why the apparent order of the reaction does not therefore necessarily correspond to the reaction stoichiometry indicated in the balanced chemical reaction. This point is illustrated in the following examples.

Example: Reaction of hydrogen gas with oxygen at a condensed phase surface
Consider the reaction

$$H_2(g) + O(\text{solid}) = H_2O(g)$$

This apparently simple reaction can involve a number of chemical reaction steps, for example, any one of the following reaction steps could be rate limiting.

$$H_2(g) = H_2(\text{ads}) \quad K_1 = a_{H_2}/p_{H_2} \tag{1}$$
$$H_2(\text{ads}) = 2H(\text{ads}) \quad K_2 = {a_H}^2/a_{H_2} \tag{2}$$
$$H_2(\text{ads}) + O(\text{solid}) = H_2O(\text{ads}) \quad K_3 = a_{H_2O}/a_{H_2}\cdot a_O \tag{3}$$
$$H(\text{ads}) + O(\text{solid}) = OH(\text{ads}) \quad K_4 = a_{OH}/a_H\cdot a_O \tag{4}$$
$$OH(\text{ads}) + H(\text{ads}) = H_2O(\text{ads}) \quad K_5 = a_{H_2O}/a_{OH}\cdot a_H \tag{5}$$
$$H_2O(\text{ads}) = H_2O(g) \quad K_6 = p_{H_2O}/a_{H_2O} \tag{6}$$

K_1 to K_6 are the equilibrium constants associated with each of these specific reaction steps.

If reaction (1) is the slowest step then

$$\text{Rate}_1 = k_1^f\cdot p_{H_2} \tag{7}$$

where k_1^f is the specific rate constant for reaction (1). If reaction (3) is the slowest step then

$$\text{Rate}_3 = k_3^f\cdot a_{H_2}\cdot a_O \tag{8}$$

In this latter case, since the previous reactions (1)–(3) are fast compared to (3) they can be assumed to be at equilibrium, so the activities of the intermediate species can be described in terms of these equilibria. In this case,

$$\text{Rate}_3 = k_3^f\cdot a_{H_2}\cdot a_O = k_3^f\cdot K_1\cdot p_{H_2}\cdot a_O \tag{9}$$

If reaction (4) is the slowest step then

$$\text{Rate}_4 = k_4^f\cdot a_H\cdot a_O = k_4^f\cdot(K_2\cdot a_{H_2})^{0.5}\cdot a_O = k_4^f\cdot(K_2\cdot K_1\cdot p_{H_2})^{0.5}\cdot a_O = k'\cdot {p_{H_2}}^{0.5}\cdot a_O \tag{10}$$

where k' is the apparent rate constant for the reaction.

The rate order with respect to hydrogen is then determined by which of the individual reaction steps is rate limiting [85,86].

4.3.1.3. Reactions at Interfaces

Transition state theory can also be applied to reactions occurring at interfaces. The activities of the individual reactant species, i, that are adsorbed at the interface can be directly related to their concentrations through the expression $a_i = \gamma_i^s \Gamma_i$, where γ_i^s is the surface activity coefficient for species, i, and Γ_i is the surface concentration of the species (mol m^{-2}). Γ_i can be further related to the fractional occupation of surface sites, θ_i, through the expression, $\Gamma_i = \Gamma^o \theta_i$, where Γ^o is the total moles of absorption sites on the surface when all sites are occupied [81–83].

In high temperature, metallurgical systems adsorbed species tend to be relatively simple in structure and are held at surfaces by chemisorption rather than being physically adsorbed. The result is that there are strong local bonds between the adsorbed species and the surfaces; physical and multilayer adsorption obtained in low temperature systems is not favored. As an example a relationship between the equilibrium surface coverage of an adsorbed species, i, and its partial pressure in the gas phase, p_i, can be derived as follows,

Rate of arrival of species at the interface $= J^+ = k^+ p_i (1 - \theta_i)$

Rate of desorption of species from the interface $= J^- = k^- \theta_i$

where k^+ and k^- are the forward and back reactions at the surface, and θ_i and $(1 - \theta_i)$ represent the fraction of sites occupied by species i and the vacant or unoccupied sites at the surface, respectively.

At equilibrium,

$$k^+ p_i (1 - \theta) = k^- \theta_I \tag{4.3.7}$$

Rearranging

$$K_s p_i = k^+ / k^- \cdot p_i = \theta_i / (1 - \theta_i) \tag{4.3.8}$$

where K_s is the equilibrium constant for the surface adsorption reaction. This relationship is commonly referred to as the Langmuir adsorption isotherm.

Alternatively, Equation (4.3.8) can be rearranged, so that the coverage of the surface by species, i, is given by

$$\theta_i = K_s p_i / (1 + K_s p_i) \tag{4.3.9}$$

The relationship between surface coverage and bulk composition for Langmuir adsorption is shown schematically in Figure 4.3.2.

The surface coverage increases approximately linearly at low concentrations, that is, $\theta_i = K p_i$, and then asymptotically approaches saturation at $\theta = 1$, where $(1 - \theta) = 1 / K_s p_i$. If multiple species are adsorbed

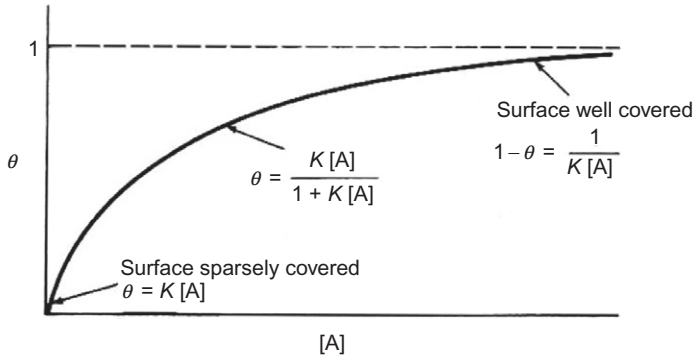


Figure 4.3.2 Langmuir adsorption; surface coverage, θ, as a function of activity of species A [82].

$$\theta_i = K_s p_i / \left(1 + \sum_j K_s p_j\right) \tag{4.3.10}$$

This Langmuir model is valid if the heat of adsorption at the surface is constant with surface coverage, in effect, there is no interaction between adsorbed species.

Adsorbed species that do not participate in the reaction of interest can, in some circumstances, inhibit the overall reaction rate by occupying reaction sites on the interface.

Example: Nitrogen transfer from liquid iron to gas

The removal of nitrogen from liquid iron into the gas phase is a problem that serves to illustrate the range of issues that should be addressed when considering transfer of solute species between phases. The overall reaction is described by the equation

$$2\mathrm{N(in\,Fe)} \rightarrow \mathrm{N_2(g)} \tag{11}$$

This process can be viewed as taking place through a series of elementary steps [87].

Step 1: Mass transfer in the liquid iron

The transport of nitrogen atoms in the liquid iron from the bulk liquid to the gas/liquid interface

$$\mathrm{N(bulk)} \rightarrow \mathrm{N(\ interface)} \tag{12}$$

The rate of transfer in the liquid phase, r_l is conveniently described by an equation of the form

$$r_{liq} = -V\cdot(\mathrm{d}C_b/\mathrm{d}t) = -k_m\cdot A\cdot(C_b - C_s)\,\mathrm{mol\,N\,s^{-1}} \tag{13}$$

where k_m is the liquid phase mass transfer coefficient (m s^{-1}), C_b, C_s are the concentrations of nitrogen dissolved in the iron in the bulk and at the liquid/gas interface, respectively (mol m^{-3}), and A is the interfacial area (m^2) across which nitrogen transfer is occurring, V is the volume of the liquid phase.

Step 2: Chemical reaction at the interface (which includes all adsorption, association, and desorption steps)

Assuming the rate of the chemical reactions at the interface, r_c, is described by an equation of the form

$$2\underline{N}(\text{in Fe}) \rightarrow N_2(\text{ interface}) \tag{14}$$

then

$$r_c = -V\cdot(dC_b/dt) = -k_c\cdot A\cdot\left(C_s{}^2 - p^s_{N_2}/K\right)\ \text{molN s}^{-1} \tag{15}$$

where k_c is the apparent chemical reaction rate constant, $p^s_{N_2}$ is the partial pressure of nitrogen in the gas phase at the gas/liquid interface, K is the equilibrium constant for reaction (11), that is, $K = p_{N_2}/C_b^2$.

Step 3: Mass transfer in the gas phase

The transport of nitrogen molecules in the gas phase from the interface to the bulk gas can be described by the equation

$$N_2(\text{gas,interface}) \rightarrow N_2(\text{gas,bulk}) \tag{16}$$

Mass transport in the gas phase can be described as

$$r_{gas} = -V\cdot(dC_b/dt) = -k_c\cdot A\cdot(P/RT)\ln\left\{\left(p - p^b_{N_2}\right)/\left(p - p^s_{N_2}\right)\right\}$$

For total pressure $P = 1$ atm and $p^b_{N_2}, p^s_{N_2} \ll 1$, the equation can be written approximately as

$$r_{gas} = -k_g\cdot A/RT\cdot\left(p^s_{N_2} - p^b_{N_2}\right)\ \text{molN s}^{-1} \tag{17}$$

where k_g is the gas phase mass transfer coefficient (m s^{-1}).

From these relations it can be seen that the overall rate will be first order with respect to nitrogen in iron if mass transfer in the liquid iron is rate limiting, and second order if the chemical reaction at the interface is rate limiting.

It has been shown that the presence of surface active elements that are not participating directly in the chemical reaction can influence the overall chemical reaction rates [88]. In the case of nitrogen transfer from iron to the gas phase, oxygen and sulfur dissolved in the metal are found to have a significant retarding effect on nitrogen removal. The adsorption of these surface active species at the reaction interface reduces the effective fraction of vacant sites, θ_v, on the surface that can be occupied by the nitrogen atoms and which can then participate in the chemical reaction step, that is, $\theta_v = (1 - \theta_S - \theta_O)$

If the chemical rate at the metal/gas interface is rate limiting, the forward rate is then given by

$$-(\mathrm{d}C_\mathrm{b}/\mathrm{d}t) = (A/V)\cdot k'_\mathrm{c}(C_\mathrm{N})^2 \tag{18}$$

Integrated over the reaction time, t,

$$[1/C_\mathrm{N} - 1/C_{\mathrm{N}_\mathrm{o}}] = (A/V)\cdot k'_\mathrm{c}\cdot t \tag{19}$$

where C_N, $C_{\mathrm{N}_\mathrm{o}}$ are the instantaneous and initial nitrogen concentrations in the metal.

Assuming the adsorption of species conform to Langmuir (ideal) adsorption model and the reaction involves a single adsorption site, then the apparent chemical reaction rate, k'_c, is described by [87,88]

$$k'_\mathrm{c} = k^\mathrm{o}_\mathrm{c} f^2_\mathrm{N}\theta_\mathrm{v} = k^\mathrm{o}_\mathrm{c} f^2_\mathrm{N}/(1 + K_\mathrm{S}a_\mathrm{S} + K_\mathrm{O}a_\mathrm{O}) \tag{20}$$

where f_N is the activity coefficient of nitrogen in iron.

In practice, it might be expected that there would be some departure from the Langmuir model, which assumes the formation of a monolayer of noninteracting, adsorbed species and independence on site coverage. In the case of multiple species adsorbed at the interface and high surface coverage by these "surface active" species, it is reasonable to anticipate (a) a variation in the heat of adsorption and (b) interaction between dissimilar, neighboring adsorbed species. Nevertheless, the behavior of high temperature systems appear to be much simpler than the multilayer interfacial adsorption isotherms observed at low temperatures and with complex molecules [82]. The recognition that surface active species can significantly influence the rates of interfacial chemical reaction has gone a long way to explaining the wide variation in apparent reaction rates reported in the literature for these types of reactions.

The overall transfer of solute between phases cannot by definition be completely limited by any one of the reaction and mass transfer steps; there must be a thermodynamic driving force for each reaction step to occur. While the limiting conditions represent the cases when one of these reaction steps is predominantly the slowest reaction step the reality that is that all reactions are mixed control, all reaction steps are occurring simultaneously.

4.3.2. ELECTROCHEMICAL REACTIONS

4.3.2.1. Rate Equations

The above discussion has focused on atomic and molecular reactions; however, there is another important class of reactions that requires further characterization, those involving electrical charge transfer through electrons or ionized species. The rates of transfer in these systems can also be described using transition state theory, and since electrical charge transfer takes place the rates are often more conveniently expressed in terms of electrical current flow rather than molar or mass units [89–92].

Applying the transition reaction rate approach to a simple electrochemical reaction involving the reduction of a cation, M^{z+}, from solution by electrons at an electrode surface, to form metal M^{o}; this reaction can be described by the equation

$$M^{z+}(\text{solution}) + ze = M^{o}(\text{electrode}) \tag{4.3.11}$$

In the absence of any applied potential difference between the solution and the electrode, the reaction will go to the right if there is a net decrease in Gibbs free energy, ΔG, associated with this reaction (see Figure 4.3.3a). The chemical rate constant for the forward reaction $k_c^f(s^{-1})$, is

$$k_c^f = (RT/Nh)K^* = (RT/Nh)\exp(-\Delta G^*/RT) \tag{4.3.12}$$

where ΔG^* is the Gibbs free energy for the formation of the activated complex. The chemical rate constant for the back, that is, reverse, reaction k_c^r, is

$$k_c^r = (RT/Nh)\exp(-\{\Delta G^* + \Delta G\}/RT) \tag{4.3.13}$$

When a potential difference, φ, is applied across the electrode interface this changes the Gibbs free energy difference between the two phases by an amount $zF\varphi$, where F is Faraday's constant. In addition, this applied potential also changes the potential of the transition state to ΔG^{**} and the physical position of the state of maximum energy on the reaction coordinate. The potential that is applied to the interface is assumed to act over a finite distance, referred to as the electric double layer. The transition state does not necessarily lie physically midway between across the double layer. For this reason, a symmetry factor, β, is introduced, which defines the position of the maximum energy state within the double layer.

In the presence of an applied potential difference across the interface, the forward rate constant, k^f, then becomes

$$k^f = (RT/Nh)\exp(-\{\Delta G^* + z\beta F\phi\}/RT) = k_c^f \exp(-z\beta F\phi/RT) \tag{4.3.14}$$

while for the reverse reaction,

$$\begin{aligned} k^r &= (RT/Nh)\exp(-\{\Delta G - zF\phi + \Delta G^* + z\beta F\phi\}/RT) \\ &= (RT/Nh)\exp((-\{\Delta G + \Delta G^*\} + z[1-\beta]F\phi)/RT) = k_c^r \exp(\{z[1-\beta]F\phi\}/RT) \end{aligned} \tag{4.3.15}$$

Now the rate of the reactions may be expressed in terms of the electrical current flowing across the interface. If each cation passing through a unit area of interface per unit time carries a charge z then the net current density, j_{net}, across the interface is given by

$$j_{net} = j^f - j^r = zF\left\{k^f\sigma(\text{solution}) - k^r\sigma(\text{electrode})\right\}\text{A m}^{-2} \tag{4.3.16}$$

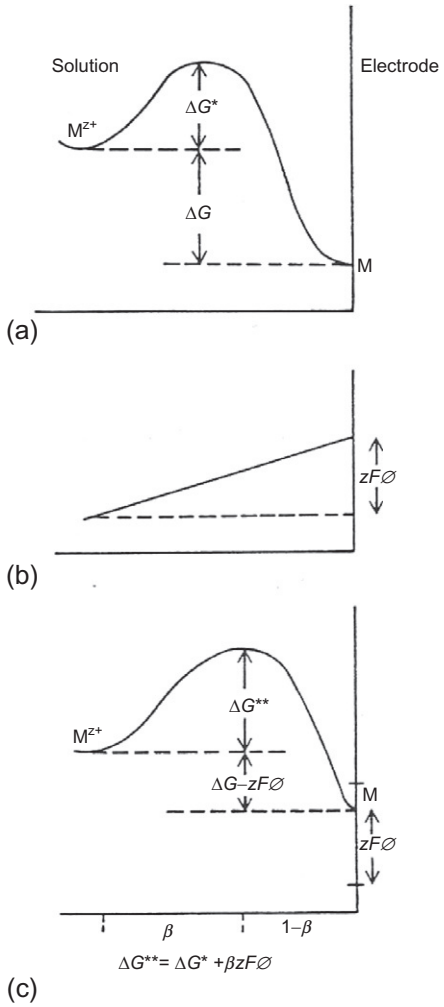


Figure 4.3.3 Schematic of the Gibbs free energy as a function of distance from the electrode in an electrochemical reaction; (a) no applied potential, (b) applied potential gradient, and (c) the net effect of applied potential [92].

where σ(solution) and σ(electrode) are the moles of cations per unit area of interface in the solution and the electrode respectively, F is Faraday's constant (coulomb mol^{-1} electrons).

$$j_e^f = zF\sigma(\text{solution})k_e^f \exp(-z\beta F\varphi_e/RT) \tag{4.3.17}$$

$$j_e^r = zF\sigma(\text{electrode})k_e^r \exp(-z[1-\beta]F\varphi_e/RT) \tag{4.3.18}$$

Defining the deviation of the actual potential difference from the equilibrium value, the overpotential, to be η, that is, $\eta = \varphi - \varphi_e$, then the net current under nonequilibrium conditions is related to the current densities at equilibrium by

$$j_{net} = j_e^f \exp(-z\beta F\eta/RT) - j_e^r \exp(z[1-\beta]F\eta)/RT)\text{Am}^{-2} \tag{4.3.19}$$

but since $j_e^j = j_e^r = j_o$, the exchange current density, then this equilibrium expression may be simplified to

$$j_{net} = j_o\{\exp(-z\beta F\eta/RT) - \exp(z[1-\beta]F\eta\}/RT)\}\text{Am}^{-2} \tag{4.3.20}$$

Thus when the overpotential, η, is negative there will be a net reduction and cations are deposited at the electrode, that is, $M^{z+} + ze \rightarrow M^o$.

When the overpotential, η, is positive the net reaction will be one of oxidation and the electrode will dissolve, that is, $M^o \rightarrow M^{z+} + ze$

Equation (4.3.20), known commonly as the Butler–Volmer equation is central to any discussion of the kinetics of electrochemical reactions. The relationship between the overpotential on the electrode and the net current flow is often presented in the form of a plot between overpotential and log current density (see Figure 4.3.4), also known commonly as a Tafel plot.

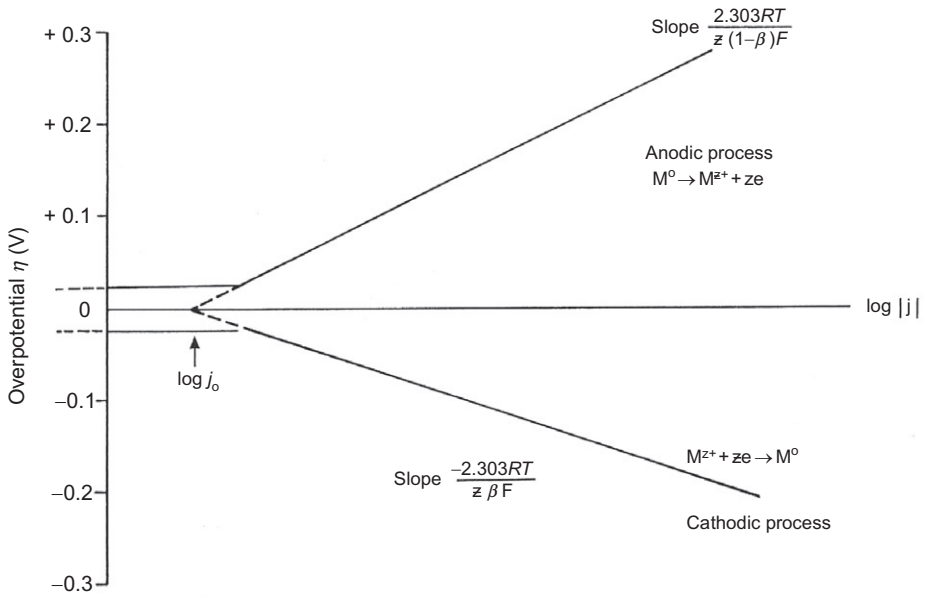


Figure 4.3.4 Schematic of the overpotential–current relationship for an electrochemical reaction at a single electrode [92].

4.3.2.2. Electrochemical Cells

Individual electrochemical reactions, such as described in Equation (4.3.11) above, do not occur in isolation there is a requirement to balance not only the moles of chemical species described in the electrochemical equation but also the electrical charge. The electrons produced or consumed as a result of the electrochemical reaction must be consumed or supplied by other parallel electrochemical reactions. In other words, there must be parallel electrochemical reactions occurring in the system; these however need not necessarily, and frequently do not, occur at the same interface as the other half-cell reactions. The situation is best considered as the establishment of an electrochemical cell (Figure 4.3.5). The electrochemical cell consists of different electrochemical sites at which cathodic (electron consumption) and anodic (electron addition) reactions are occurring. The sites must be connected electrically to enable electrical charge transfer. This occurs through simultaneous transfer of electrons in an electron conductor and charged species through an ion conductor (electrolyte).

Since each electrochemical reaction has its own electrochemical characteristics the appropriate Butler–Volmer equation must be applied to each different reaction. Considering two separate electrochemical reactions, the first point to note is that each will possess a different electrochemical potential at the outset of the reaction. This means that the overall difference in Gibbs free energy at the electrodes may lead to spontaneous current flow or not; the former is referred to as a *self-driven cell* and examples include fuel cells, charged batteries, leaching, and corrosion reactions. Electrochemical cells in which there is no spontaneous flow of electrons require an external driving force to be applied, these are referred to as *production cells*. The ability to apply a potential difference between two electrodes represents another method of changing the effective Gibbs free energy

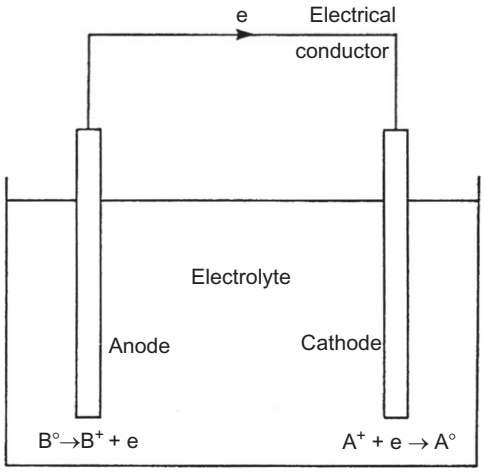


Figure 4.3.5 Schematic diagram of an electrochemical cell.

difference between the half-cell reactions in the cell and driving the reactions in directions they would not otherwise move.

The Butler–Volmer relationships between electrode potentials and current densities in self-driven electrochemical reactions and in reactions where an external potential is applied to the system are illustrated schematically in Figures 4.3.6–4.3.8 for electrodes of equal area.

For electrochemical cells to which an external potential must be applied to drive the reactions (Figure 4.3.6a) it can be seen that when the applied potential, V, is less or equal to the difference between the equilibrium reversible electrode potentials that is, $U=(E_{\mathrm{I}}-E_{\mathrm{II}})$, the net current flow at each electrode is minus infinity, that is, zero. The greater the overpotential, η, that is, the difference between the effective applied potential difference between the electrodes, V, and the equilibrium reversible electrode potentials, U, the greater the electron current flow.

In the case of a self-driving electrochemical cell reaction, it can be seen (Figure 4.3.6b) that when the electrodes are at their individual equilibrium potentials the current is zero, this situation can be sustained when there is a large electrical resistance, R, within the circuit, effectively preventing electron flow. Lowering this resistance through increased conductivity through the electrolyte or the external electron conductor, whichever has the highest resistance, results in electron flow. The voltage difference between the electrodes is IR, where I is the current flow through the cell. When no resistance to electron flow exists the net flow of electrons is a maximum $j_{\max}$.

In practice, it is necessary to also consider the transport of species to and from the electrochemical sites. At high current densities, the transfer of ions to or from these sites may become rate limiting; this has a dramatic effect on the relationship between potential and cell current as illustrated in Figures 4.3.7 and 4.3.8. It can be seen for an externally

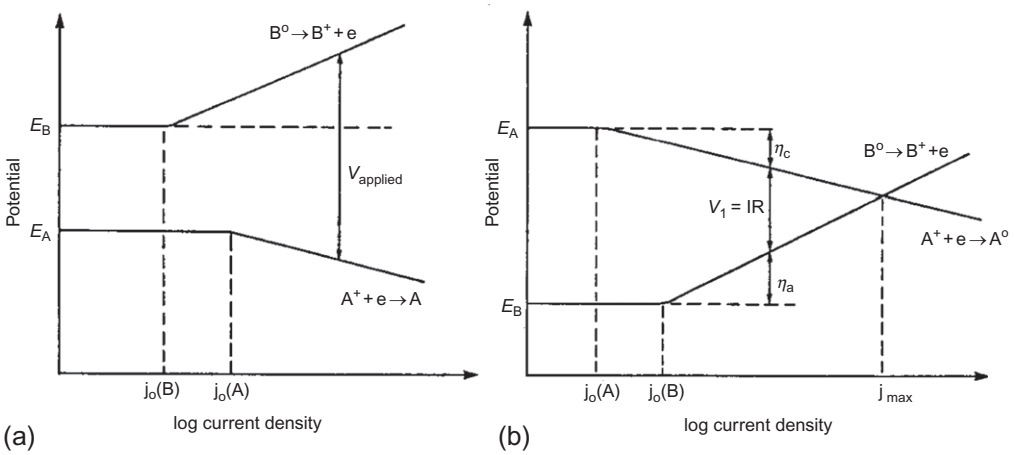


Figure 4.3.6 Potential–current plots for (a) externally driven and (b) self-driven cells [92].

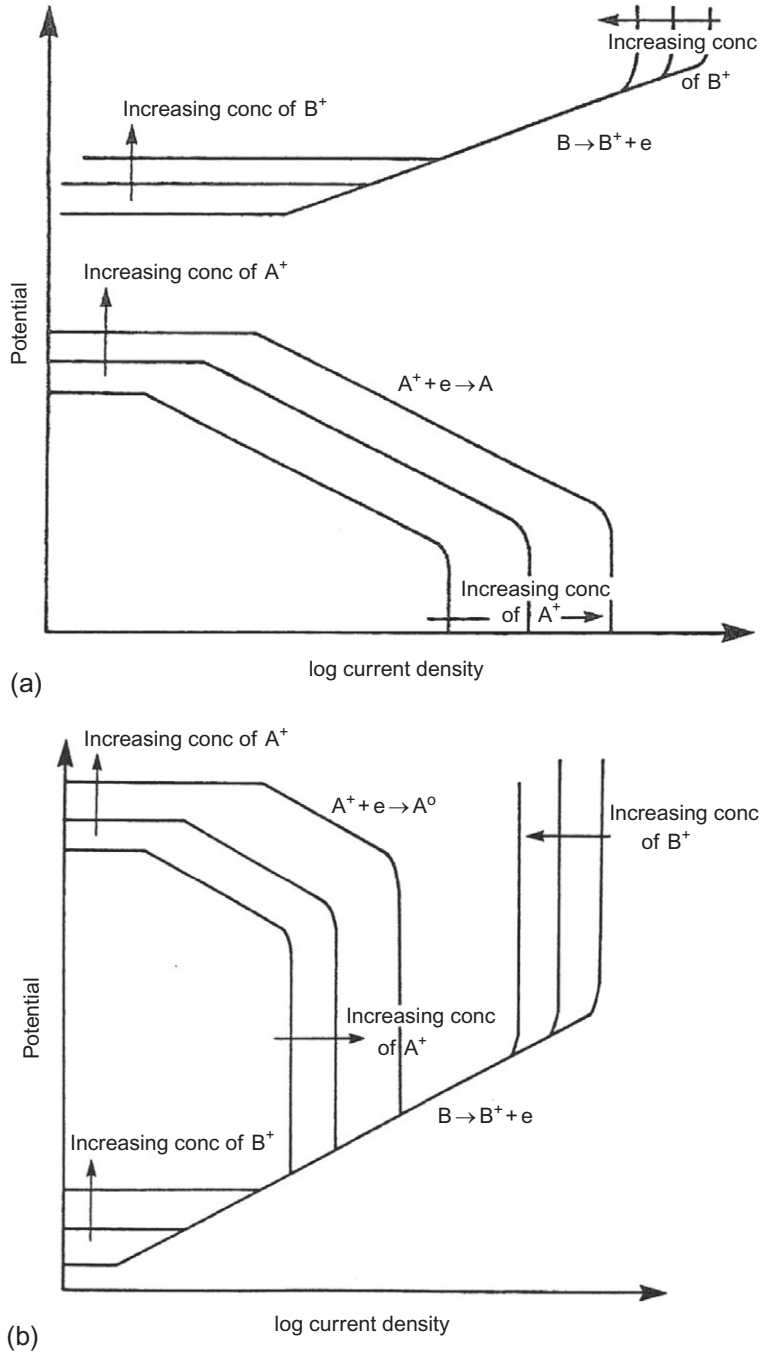


Figure 4.3.7 (a) A potential–current diagram illustrating the effect of increased solute concentration on cell characteristics for an externally driven cell [92]. (b) A potential–current diagram illustrating the effect of increased solute concentration on cell characteristics for a self-driven cell [92].

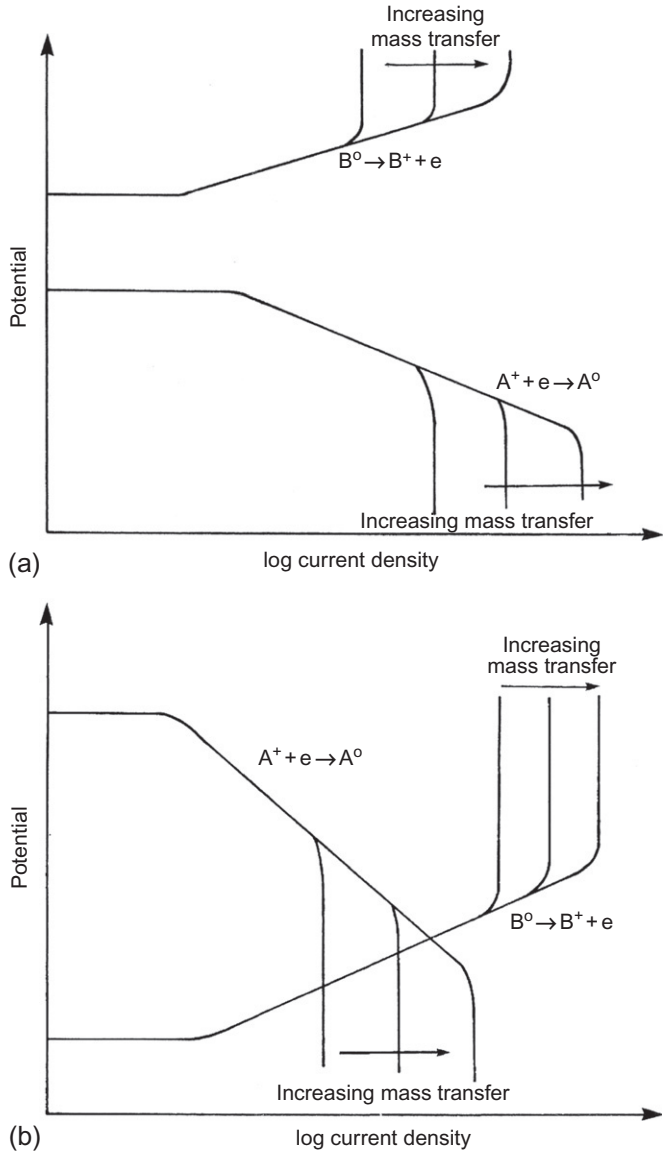


Figure 4.3.8 (a) A potential–current diagram illustrating the effect of increased mass transfer at the electrodes on cell characteristics for an externally driven cell [92]. (b) A potential–current diagram illustrating the effect of increased mass transfer at the electrodes on cell characteristics for a self-driven cell [92].

driven cell in reactions that are mass transfer limited the supply of ions to or the removal of ions from the electrodes becomes increasingly difficult with increasing applied potential until beyond a critical value the no further increase in current density is possible. Similar situations arise in self-driven cells, in these cases when the rates are limited by mass transfer the limiting current density is less than the values assuming only the electrochemical reactions are important.

The potential–current characteristics of electrochemical cells are then dependent on the reversible cell potentials, exchange current densities, limiting current densities, resistances to current flow within the cell.

The effects of mass transfer and solute concentrations on cell characteristics are illustrated in Figures 4.3.7 and 4.3.8. For externally driven cells, it can be seen that increasing the concentration of ions available for the cathodic reaction results not only in a decrease in the electrode potential that has to be applied to obtain a given current density but also an increase in the limiting current density at the electrode for a given applied potential. For a given cell current, the power (IV) required to run the cell is lower at higher solute concentrations and the maximum production rate is generally higher. Increasing the mass transfer rates to and from the electrodes affects only the limiting current densities.

At the anode of an externally driven cell, the greater the bulk solute concentration the lower the driving force for mass transfer from the electrode surface to the bulk solution; increasing the bulk solute concentration therefore decreases the limiting current density at the anode. In the limit, the solubility product of the salt may be exceeded and deposition of solids on the electrode may occur; the latter would obviously lead to a drastic decrease in mass transfer effectively halting the electrochemical reaction.

The effect of increasing mass transfer for a given set of solution concentrations is illustrated schematically for externally driven cells in Figure 4.3.8a and self-driven cells in Figure 4.3.8b.

4.3.2.3. Half-Cell Reactions

The previous discussion has focused on the formation of a single reaction product but in multicomponent systems it is possible for parallel electrochemical half-cell reactions to occur at the reaction interface. These electrochemical transfer reactions can involve different chemical species and can occur at different places on the interface. In these situations, while the total current density is unchanged the proportion of electrons that may, for example, form useful products will be affected. In effect, the current efficiency of the process depends on the products formed.

Example: Electrowinning of zinc

The recovery of zinc from aqueous acid sulfate solutions is currently the principle method of zinc metal production. From a purely thermodynamic perspective this reaction should be impossible since the standard electrode potential for zinc metal is -0.7 V.

Thermodynamics tells us that the application of applied voltage to this cell would result in the decomposition of the electrolyte with oxygen evolution at the anode through the reaction

$$2H_2O \rightarrow O_2(g) + 4H^+(aq) + 4e \quad E^o = 1.228\,V$$

At the cathode, it is to be expected that hydrogen gas would be produced

$$4H^+(aq) + 4e \rightarrow 2H_2(g) \quad E^o = 0\,V$$

In practice under carefully controlled solution conditions, the electrochemical reaction rates at the cathode for hydrogen gas evolution are low, and the alternative reaction

$$2Zn^{2+}(aq) + 4e \rightarrow 2Zn(s)k4 \quad E^o = -0.77\,V$$

takes place. Impurities such as nickel ions in solution must be removed before electrowinning [93] since these species are preferentially deposited at the cathode and significantly increase the exchange current density for the hydrogen evolution reaction; thus effectively catalyzing the release of hydrogen and drastically decreasing the proportion of electrons that are used in reducing the zinc ions from the solution. In practice, using purified solutions it is possible to recover zinc ions from aqueous solution although thermodynamically this is not the predicted outcome; the effect is illustrated in terms of the potential—current density relations in Figure 4.3.9.

Example: Electrowinning of aluminum

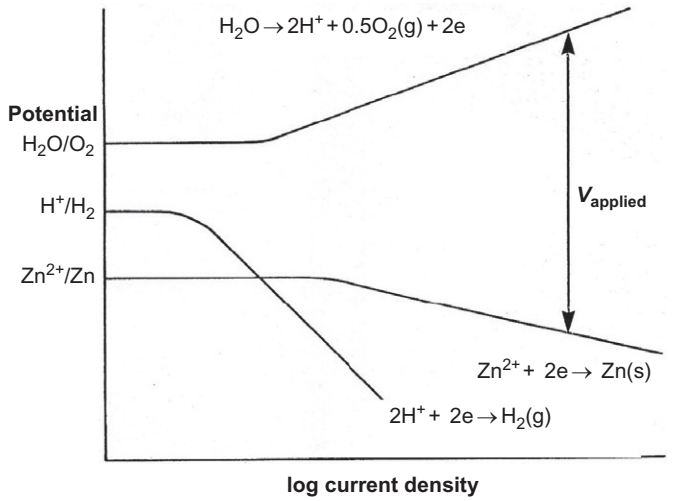


Figure 4.3.9 A schematic potential–current diagram illustrating the effect of parallel half-cell reactions involving $H_2(g)$ and zinc metal production taking place at the cathode in an externally driven cell [92].

In the Hall–Herault process for aluminum production, aluminum ions are reduced from a solution of $NaF–AlF_3$ molten salt at the cathode. Although complex aluminum species are present in the electrolyte this electrochemical reaction can be represented by the simplified equation

$$2Al^{3+}(\text{electrolyte}) + 6e \rightarrow 2Al(l)$$

At the anode, it is anticipated that as a result of reaction with the consumable carbon electrode, CO would be the predominant gas species produced through the reaction

$$3C(s) + 3O^{2-}(\text{electrolyte}) \rightarrow 3CO(g) + 6e$$

however, the kinetics of the electrochemical reactions are such that the rates of formation of CO_2 through the reaction

$$1.5C(s) + 3O^{2-}(\text{electrolyte}) \rightarrow 1.5CO_2(g) + 6e$$

under these applied potential conditions are faster than the rates of formation of CO [94]. In this case, significant benefit is obtained through the reduced consumption of carbon/mol aluminum produced through the formation of a nonequilibrium species.

It is common to assume that because no electrons appear in a balanced chemical reaction that there are therefore no reactions involving electron transfer or charged species occur during the reaction. A moment's reflection would indicate that this cannot be the case since our understanding of the nature of chemical bonding involves the transfer and sharing of electrons between neighboring atoms or molecules. Any rearrangement of these local electron associations at an atomic level implies some form of electrochemical change.

Example: Reaction rates of CO/CO_2 gas mixtures on iron oxide—Containing slags The chemical reaction of CO and CO_2 gas molecules with surfaces of molten slags containing iron oxide is described by the equation

$$CO_2(g) = CO(g) + O(\text{slag})$$

The measured rates of oxidation of the slags are described by the relation

$$v = k_{\text{app}}^{\text{for}}(p_{CO_2} - P_{CO}a_O)$$

where $k_{\text{app}}^{\text{for}}$ is the apparent forward rate constant of the oxidation reaction, a_O is the activity of oxygen in local equilibrium with the slag described in the form of the equivalent ratio of the CO_2/CO partial pressures in the gas phase. $k_{\text{app}}^{\text{for}}$ has been shown to be a complex function of the slag bulk composition, the oxygen activity in the slag and the reaction temperature and is empirically described by an equation of the form [88]

$$k_{\text{app}}^{\text{for}} = k_{\text{app}}^{\text{for}}(a_O)^{-\alpha}$$

where k_{app}^{for} and α are dependent on the iron oxide concentration and the other species present in the melt, for example, CaO. The overall reaction can be viewed alternatively as [95]

$$2Fe^{2+}(slag) + CO_2(g) = 2Fe^{3+}(slag) + CO(g) + O^{2-}(slag)$$

Again using the approach outlined above this can be broken down into a series of reaction steps. One reaction pathway involves the formation of an activated complex $CO_2^-(ads)$ through the reaction steps

$$\begin{aligned} CO_2(g) + v &= CO_2(ads) \\ CO_2(ads) + e^- &= CO_2^-(ads) \\ CO_2^-(ads) + e^- &= CO(ads) + O^{2-}(ads) \\ CO(ads) &= CO(g) \end{aligned}$$

where v is a vacant adsorption site on the interface

An alternate reaction pathway involves the formation of an activated complex $CO_2^{2-}(ads)$ through the reaction steps

$$\begin{aligned} CO_2(ads) + 2e^- &= CO_2^{2-}(ads) \\ CO_2^{2-}(ads) &= CO(ads) + O^{2-}(ads) \\ CO(ads) &= CO(g) \end{aligned}$$

The activity of the electrons on the slag is determined by the ferric/ferrous redox reaction

$$Fe^{2+}(slag) = Fe^{3+}(slag) + e^-$$

A detailed analysis of the data obtained from isotope exchange experiments [96] indicates that the rate limiting step involves the dissociation of the adsorbed species $CO_2^-(ads)$ at the gas/slag interface. This then explains the observed dependence of the rate constant on the bulk composition and the electrochemical properties of the slag phase.

4.3.2.4. Coupled Reactions

The transfer of electrons between phases means, in effect, there is a common reactant species and as a result the transfer reactions are coupled to each other rather than occurring independently. Overall charge neutrality must be maintained.

In any electrochemical reaction, there must be a charge balance as well as an elemental balance. The conservation of charge associated with the transfer of species between different phases is illustrated clearly in the case of sulfur transfer between metal and slag phases. As pointed out above the rates of individual electrochemical reactions are

governed by the rate (Tafel) equations for the individual reactions and these rates will be different for each species. The individual reactions are not however independent of the other species; the reactions are *coupled* or linked at any point in time. This can result in reactions moving initially in directions not anticipated from the final equilibrium, an elegant example of this process is given below.

Example: Rate of sulfurization iron silicate slags

The reaction of CO, CO_2, and SO_2 gases with a molten iron silicate that has previously been equilibrated at the same oxygen partial pressure results in the sulfurization of the melts through the reaction

$$0.5S_2(g) + O^{2-}(\text{slag}) = S^{2-}(\text{slag}) + 0.5O_2(g) \tag{21}$$

It can be seen from Figure 4.3.10 [96] that starting from zero sulfur in slag the sulfur concentration gradually and monotonically approaches the equilibrium sulfur value for this overall reaction.

If the same reactions are carried out on a slag that had been preequilibrated with iron metal, the simultaneous sulfurization and oxidation of the melt by reaction with the gas phase through

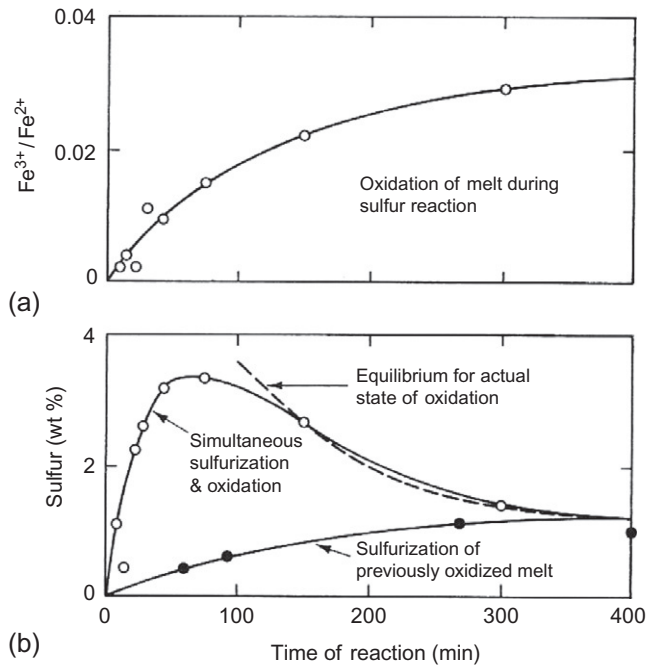


Figure 4.3.10 Sulfurization and oxidation of iron silicate melt in CO, CO_2, and SO_2 gas mixtures ($pCO/pCO_2 = 3.0$ and $pSO_2 = 0.028$, 1550 °C) [96].

$$2Fe^{2+}(slag) + 0.5O_2(g) = 2Fe^{3+}(slag) + O^{2-}(slag) \quad (22)$$

takes place, and a very different result is obtained. In this instance, the sulfur concentration first rapidly increases and then subsequently decreases towards the equilibrium value. The phenomenon can be explained if it assumed that the sulfurization reaction (21) occurs at a far greater rate than the oxidation reaction (22); this results in the initial reduction of the melt. The sulfur level in the slag continues to increase until local equilibrium described by the equation

$$0.5S_2(g) + 2Fe^{2+}(slag) = S^{2-}(slag) + 2Fe^{3+}(slag) \quad (23)$$

is achieved. At this stage, however, the system as a whole is not at equilibrium and oxidation of the melt through reaction (22) continues. As the Fe^{3+}/Fe^{2+} ratio increases the reaction moves from right to left and the sulfur concentration in the slag decreases towards the final equilibrium value given by reaction (21).

It has been shown [97] that the rates of transfer of species between liquid phases can be described using a general kinetic model for coupled electrochemical reactions. This takes into account both mass transfer and chemical reactions, and has been successfully applied to a range of metal refining processes.

4.3.3. REVERSIBLE PROCESSES

The discussion in the previous sections has assumed that the reactions are taking place irreversibly, in effect they are a long way from chemical equilibrium and only reactions in the forward direction need be considered. For reactions that do approach chemical equilibrium, the possibility of reaction products spontaneously decomposing and reverting to the reactant species must be considered.

Example: Reduction of "pure" FeO to iron in H_2/H_2O

$$FeO + H_2(g) = Fe + H_2O(g)$$

The rate of the forward reaction is given by

$$R_{for} = k^f \cdot p_{H_2}$$

The rate of the back reaction is given by

$$R_{back} = k^r \cdot p_{H_2O}$$

Assuming the reaction is reversible and at equilibrium,

$$K_{eq} = k^f / k^r = (p_{H_2O}/p_{H_2})_{eq}$$

$$\text{Net reaction rate } R_{nett} = R_{for} - R_{back} = k^f \cdot p_{H_2} - k^r \cdot p_{H_2O}$$

Substituting for k_b

$$\begin{aligned}\text{Net reaction rate} &= R_{for} - R_{back} = k^f \cdot p_{H_2} - k^f \cdot p_{H_2O} \cdot \left(p_{H_2}/p_{H_2O}\right)_{eq} \\ &= k^f \cdot \left(p_{H_2} - p_{H_2O}/K_{eq}\right)\end{aligned}$$

Other examples of heterogeneous chemical reactions occurring in metallurgical systems can be found in references [98–101].

REFERENCES

[81] S. Glasstone, K.J. Laidler, H. Eyring, Theory of Rate Processes, McGraw Hill, New York, 1941.
[82] K.J. Laidler, Chemical Kinetics, third ed., Harper Row, New York, 1987.
[83] P.W. Atkins, J. de Paula, Atkins' Physical Chemistry, ninth ed., Oxford University Press, Oxford, 2010.
[84] H.Y. Sohn, Metall. Mater. Trans. B 35 (2004) 121.
[85] A. Gala, H.J. Grabke, Archiv. Eisenhuttenw 43 (1972) 463.
[86] P.C. Glaws, G.R. Belton, Metall. Mater. Trans B 21B (1990) 511.
[87] S. Banya, F. Ishii, Y. Iguchi, Y. Nagasaka, Metall. Mater. Trans. B 19B (1988) 233.
[88] G.R. Belton, Metall. Mater. Trans. B 24B (1993) 241.
[89] J.O'.M. Bockris, D.M. Drazic, Electrochemical Science, Taylor and Francis, London, 1972.
[90] D.B. Hibbert, Introduction to Electrochemistry, MacMillan, England, 1993.
[91] H.Y. Sohn, M.E. Wadsworth, Rate Processes in Extractive Metallurgy, Plenum, New York, 1979.
[92] P.C. Hayes, Process Principles in Minerals and Materials Production, third ed., Hayes Publ., Co., Sherwood, Australia, 2004 (Chapter 7).
[93] D.J. McKinnon, J.M. Branner, P.L. Fenn, J. Appl. Electrochem. 17 (1987) 1129.
[94] K. Grjotheim, C. Krohn, M. Malinovsky, K. Matiasovsky, J. Thonstad, Aluminium Electrolysis: The Chemistry of the Hall Herault Process, Aluminium Verlag, Dusseldorf, Germany, 1977.
[95] M. Barati, K.S. Coley, Metall. Mater. Trans. B 36B (2005) 169. M. Barati, K.S. Coley, Metall. Mater. Trans. B 37B (2006) 61.
[96] E.T. Turkdogan, P.M. Bills, Trans. Metall. Soc. AIME 227 (1963) 940.
[97] D.G.C. Robertson, B. Deo, S. Ohguchi, Ironmak. Steelmak. 11 (1) (1984) 41.
[98] E.T. Turkdogan, Physical Chemistry of High Temperature Technology, Academic Press, New York, 1980.
[99] F.D. Richardson, Physical Chemistry of Melts in Metallurgy, Academic Press, London, 1974.
[100] F. Oeters, Metallurgy of Steelmaking, Verlag Stahleisen mbH, Dusseldorf, Germany, 1994.
[101] A.R. Burkin, Chemical Hydrometallurgy—Theory and Practice, Imperial College Press, London, 2001.

CHAPTER 4.4

Chemical Reactions at Moving Surfaces: Shape Change, No Phase Change

Peter Hayes
School of Chemical Engineering, The University of Queensland, Queensland, Brisbane, Australia

4.4.1. REACTION RATES ON FLUID/CONDENSED PHASES INTERFACES

4.4.1.1. Reactions with the Gas Phase

The maximum rate at which gas molecules can be removed from a condensed phase surface into the gas phase, or can arrive at a surface, can be derived from the kinetic theory of gases. The resulting Hertz-Knudsen equation is given by [102]

$$R_{\max} = {}^{1}\!/_{4} \cdot N A \nu_{\text{ave}} = {}^{1}\!/_{4} \cdot (p_i/RT) \cdot (8RT/\pi M)^{0.5} = p_i/(2\pi MRT)^{1/2} \qquad (4.4.1)$$

where p_i is the partial pressure of the gas species in the gas phase, M is the molecular weight of the vaporizing species, R is the gas constant, T the absolute temperature K, N_i is the concentration of species in the gas phase, A is the interfacial area, and ν_{ave} is the average velocity of gas molecules. This maximum, or free vaporization, rate is obtained under conditions when (i) the composition of the vaporizing species is the same as in the condensed phase, (ii) the surface of the condensed phase is not contaminated with species that may retard or impede the removal of the gas species, and (iii) the pressure of the system is sufficiently low that there is no back reaction, that is, the vaporizing species do not return to the surface.

In practice, this limiting rate is difficult to reach in a mechanically or physically generated vacuum system, the rates become limited by mass transfer at the reaction interface. Increases in rates of mass transfer can, however, be achieved in reactive gas systems through the formation of new chemical species.

Example Enhanced vaporization of metals [103]

At high temperatures, the rates of vaporization of metals can be increased by chemical reaction of species present in the gas phase. This increased rate occurs because of the counter diffusion of gaseous metal and reactive gas species in the region of the reaction interface. This mechanism is illustrated in Figure 4.4.1 for the case of iron vaporization in a system in which oxygen acts as the reactive gas. The iron vapor moves from the surface into the bulk gas; at the same time there is counter diffusion of oxygen toward the surface. At a short distance from the surface, the gas species meet and react to form fine particles of

Treatise on Process Metallurgy, Volume 1
http://dx.doi.org/10.1016/B978-0-08-096986-2.00016-3
© 2014 Elsevier Ltd.
All rights reserved.

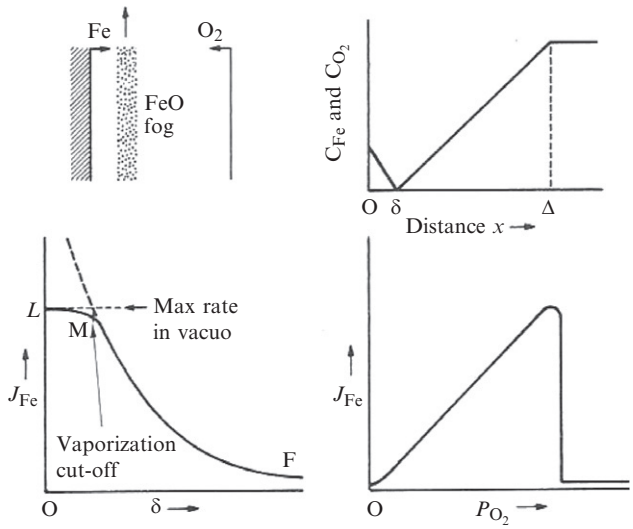


Figure 4.4.1 Schematic representation of enhanced vaporization of metals in a reactive gas mixture through counter flux of diffusing species [103].

iron oxide. This chemical reaction effectively reduces the diffusion distance from the surface to the bulk phase hence enhancing the diffusive flux of iron from the surface, J_{Fe}. As the pressure of oxygen increases, the effective boundary layer thickness, δ, decreases and the rate of iron vaporization is further increased. This trend of enhanced vaporization continues with increasing oxygen pressure until a critical pressure is reached when the oxygen flux exceeds that of the iron and oxidation of the iron surface occurs. Similar phenomena have been observed in other metal systems.

Example Vaporization in a reactive atmosphere

Whilst metals are predominantly present as atomic species, in the presence of reactive gas species the concentrations of more complex metal-containing molecules can be significant and these can influence the rates of vaporization. The relative concentrations of the different metal-containing species in metal–oxygen and metal–sulfur systems can depend critically on oxygen or sulfur partial pressures in the gas phase, respectively. These effects are clearly illustrated in the tin–oxygen system [104].

The individual reactions determining the equilibrium tin vapor pressure are as follows

$$\begin{aligned}
\mathrm{Sn(liq)} &= \mathrm{Sn(g)} \\
\mathrm{Sn(liq)} + 0.5\mathrm{O_2(g)} &= \mathrm{SnO(g)} \\
\mathrm{SnO_2(s)} &= \mathrm{Sn(g)} + \mathrm{O_2(g)} \\
\mathrm{SnO_2(s)} &= \mathrm{SnO(g)} + 0.5\mathrm{O_2(g)} \\
2\mathrm{SnO(g)} &= \mathrm{Sn_2O_2(g)} \\
3\mathrm{SnO(g)} &= \mathrm{Sn_3O_3(g)} \\
4\mathrm{SnO(g)} &= \mathrm{Sn_4O_4(g)}
\end{aligned}$$

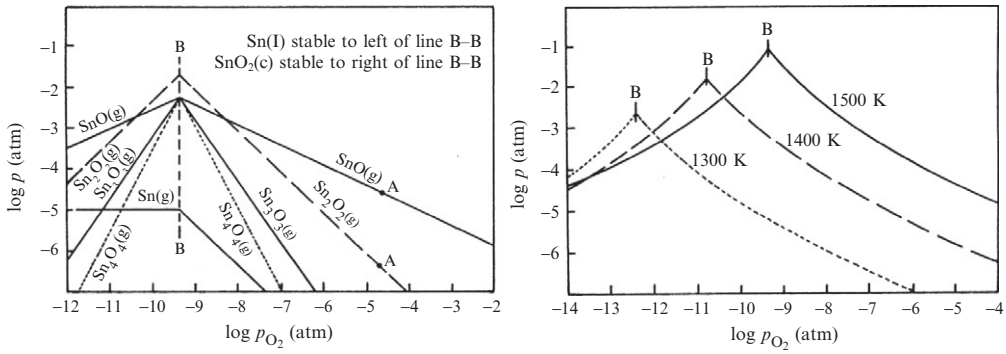


Figure 4.4.2 Vapor pressures in the Sn–O system as a function of oxygen partial pressure in the gas phase [104]. (a) Pressures of individual species at 1500 K, (b) total tin vapor pressures.

The partial pressures of these species as a function of oxygen partial pressure at 1500 K and the total vapor pressures of tin species as a function of temperature are shown in Figure 4.4.2a and b [104]. There is a maximum total vapor pressure at the oxygen partial pressures corresponding to the equilibrium between tin metal and tin oxide, marked by the line B–B in the figures. It can be seen that even in the presence of liquid tin metal the principle tin vapor species are tin oxides. The partial pressure of tin gas at metal saturation is constant with increasing oxygen pressure and is relatively low; the Sn(g) vapor pressure further decreases with increasing oxygen pressure for conditions at which tin oxide solid is stable. In contrast at metal saturation, the partial pressure of SnO(g) increases with increasing oxygen partial pressure up until the critical oxygen partial pressure for the formation of SnO_2 is reached. Beyond this critical condition the vapor pressures of SnO species decrease with increasing oxygen partial pressure. The total vapor pressure of tin in the system at equilibrium is given by

$$p_{\mathrm{Sn}}(\mathrm{total}) = P_{\mathrm{Sn}} + p_{\mathrm{SnO}} + p_{\mathrm{Sn_2O_2}} + p_{\mathrm{Sn_3O_3}} + p_{\mathrm{Sn_4O_4}}$$

and the anomalous variation in the vaporization of tin is thus explained by the reactive formation of vapor phase species.

In general, the vapor pressures of metal halides, sulfides are considerably greater than the corresponding metals. In some cases, even metal oxides have higher vapor pressures than the corresponding metals.

4.4.1.2. Thermodynamic Driving Force for the Reaction

In condensed phase, solid/liquid and solid/solid closed systems temperature is the key process variable used to generate the thermodynamic driving force for transformation. For example, in metal solidification the nonisothermal conditions lead to thermal and compositional/constitutional undercooling.

In solid/solid transformations, such as, precipitation, eutectoid and spinoidal decomposition, isothermal reactions are undertaken at temperatures below those necessary for the stability of the single phase, that is, at bulk compositions and temperatures at which multiphase systems are present at equilibrium.

In open systems in which there is chemical interaction between reactive gases and solids under isothermal conditions, the thermodynamic driving force is principally controlled through the composition of the gas phase.

The transfer of oxygen from a solid to a gas phase can be described by a general reaction of the form

$$O(s) \rightarrow O(g) \tag{4.4.2}$$

The difference in Gibbs free energy of these states, $\Delta G_{reaction}$, is given by the relation

$$\Delta G_{reaction} = RT \ln[(a_o(g)/a_o(s))] \tag{4.4.3}$$

where $a_o(g)$ and $a_o(s)$ are the oxygen activities of the gas and oxide phases, respectively.

In a reactive gas system, for example, H_2/H_2O gas mixture, the oxygen activity can be related to the reactant gas composition through the equation

$$0.5O_2(g) + H_2(g) \rightarrow H_2O(g) \tag{4.4.4}$$

$$\Delta G = \Delta G^o + RT \ln\left[\{(1/a_o(g)\}\cdot(P_{H_2O}/P_{H_2})\right]_{gas} \tag{4.4.5}$$

where $a_o(g) = {P_{O_2}}^{1/2}$, P_{H_2}, P_{H_2O} are the partial pressures of H_2 and H_2O in the reaction gas. At equilibrium $\Delta G = 0$ and rearranging gives for the gas

$$RT \ln a_o(g) = \Delta G^o + RT \ln(P_{H_2O}/P_{H_2})_{gas} \tag{4.4.6}$$

For chemical equilibrium between the oxide and the gas phase

$$RT \ln a_o(s) = \Delta G^o + RT \ln(P_{H_2O}/P_{H_2})_{ox} \tag{4.4.7}$$

On substitution of Equations (4.4.6) and (4.4.7) into Equation (4.4.3), the maximum thermodynamic driving force, $\Delta G_{reaction}$, available for the reaction is given by

$$\Delta G_{reaction} = RT \ln\left[(P_{H_2}/P_{H_2O})_{ox}\cdot(P_{H_2O}/P_{H_2})_{gas}\right] \left(\text{J mol}^{-1}\text{O}\right) \tag{4.4.8}$$

where $(P_{H_2}/P_{H_2O})_{ox}$ is the ratio of gas pressures for equilibrium with the oxide phase at the reaction temperature T(K).

4.4.1.3. Removal of Species from Solid Surfaces

In gas/liquid systems, it is assumed that the shape of the interface from which the species are being removed stays planar and constant with time. Mass transfer in the liquid phase is

relatively fast; gravitational/buoyancy and Marangoni (surface tension) forces ensure that the liquid surface remains atomically smooth and planar.

The same cannot be said for fluid/solid systems. In the case of solids, crystalline materials are characterized by differences in bond strengths depending on the crystal planes that are exposed to the fluid phase. This can result in a range of behaviors from, at the one extreme, a relatively uniform removal of species across the surface to highly selective removal from particular planes and directions. In the former case, an initially flat surface will remain flat as vaporization/dissolution occurs; in the latter the surface will become progressively faceted and angular in shape.

Example Gaseous reduction of solid ZnO

The reduction of ZnO solid with CO gas results in the removal of both zinc and oxygen in the gas phase, through the reaction

$$\mathrm{ZnO(s) + CO(g) = Zn(g) + CO_2(g)}$$

The relatively high vapor pressure of zinc gas at reducing conditions ensures that both oxygen and zinc metal are removed simultaneously from the solid surface. Starting with dense polycrystalline ZnO solid the resulting surface morphology is illustrated in Figure 4.4.3. It can be seen that the removal of oxygen and zinc takes place from selected planes in the hexagonal ZnO. The initial dense material also becomes increasingly porous as there is preferential removal of material from the grain boundaries.

The reasons for these differences are explored more fully in the following section. Assume the individual atoms in a solid are represented by cubes and that the crystal structure is constructed by placing these cubes face to face so that there are no gaps between. At the free surface of the crystal, we can anticipate that there will be a number of different types of sites, each having a different number of shared faces with neighboring cubes;

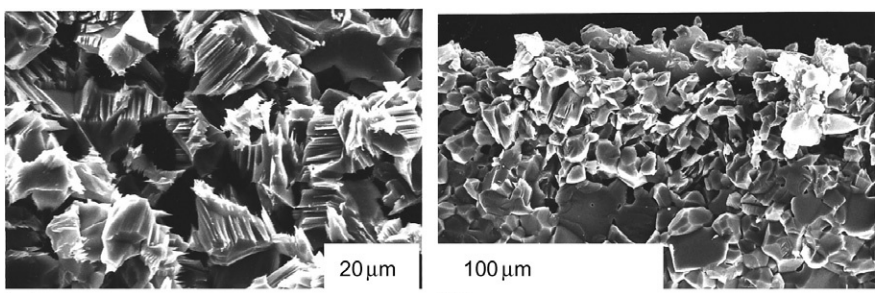


Figure 4.4.3 Surface of a ZnO crystal following reaction in CO gas atmosphere illustrating the faceted nature of the interface that has been generated from the original smooth polycrystalline material planar surface. (a) View of the faceted reaction surface, and (b) cross section of the interface illustrating the change from dense grain structure to faceted porous structure.

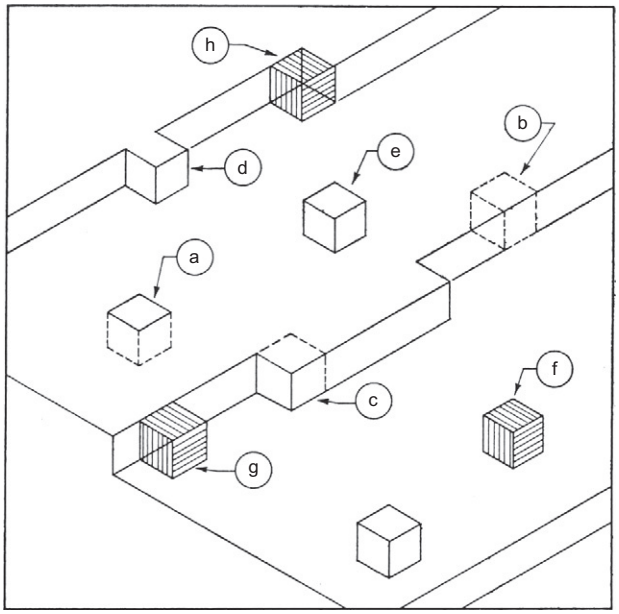


Figure 4.4.4 Schematic representation of a crystal surface demonstrating the relative bonding of atoms at different adsorption sites; maximum shared faces = 6, (a) 5, (b) 4, (c) 3, (d) 2, (e) 1; adsorbed species represented by sites (f), (g), and (h).

these possibilities are illustrated in Figure 4.4.4. The atoms most strongly bonded to the surface will be those having the most number of common faces; the atom most weakly bound is that with only one common face.

On atomically rough surfaces the atoms are relatively loosely bound to the surface and even at low thermodynamic driving forces the atoms from all sites are easily removed.

On atomically smooth surfaces the atoms are relatively strongly bound to the surface and ad atoms, such as, at site (e) are readily removed. The further removal of atoms takes place from atoms associated with the ledge or partially removed planes of atoms. The preferential removal from kink sites, such as (c), on specific atom planes results in the removal that is highly dependent on crystal structure and the formation of a facetted or angular surface, such as that shown in Figure 4.4.3.

Another important feature of the zinc oxide reduction example is that *there is no accumulation of metal species at the interface*, the transfer of metal into the gas phase ensures its rapid removal. Although interesting this example is not representative of most systems in which metal compounds react with the gas phase. At low temperatures, the metal vapor pressures are low and these components remain in the original condensed state. The situation is also different from the cases considered in Chapter 4.3 on Chemical Kinetics since here the matrix, or solvent phase, is decomposing and the reaction interface moving as the reaction proceeds rather than being of fixed geometry.

4.4.2. CHEMICAL REACTIONS ON MOVING SOLID SURFACES

4.4.2.1. Chemical Reaction Rates on Moving Surfaces

The problem of chemical reaction on moving surfaces is illustrated by considering the reaction of a dense solid oxide in a gas atmosphere. Here, the chemical reaction of the gas with oxygen in the condensed phase takes place only at the outer surface of the solid oxide. The removal of oxygen from the oxide surface by reaction with the gas phase then results in the progressive advance of this interface into the bulk of the material, that is, perpendicular to the reaction interface at a velocity, V_o. The reaction system is illustrated schematically in Figure 4.4.5 for reaction of a dense oxide, MeO_v, with H_2/H_2O gas mixtures at a fixed temperature.

Although there are many possible chemical reaction steps involved in removing oxygen from the system the general behavior is broadly reflected in the following treatment [105–107]. Consider the overall rate of oxygen removal from the surfaces of oxide, R, through the reaction

$$MeO_v(s) + vH_2(g) \rightarrow Me(s) + vH_2O(g) \tag{4.4.9}$$

to be described by the first order rate equation of the form

$$R_o = \phi^1 P_{H_2} a_{MeO_v} - \phi^{11} P_{H_2O} a_{Me} \left(\text{mol}\,H_2\,\text{m}^{-2}\,\text{s}^{-1}\right) \tag{4.4.10}$$

where ϕ^1, ϕ^{11} are the apparent chemical reaction rate constants for the forward and reverse reactions (mol m^{-2} s^{-1} atm^{-1}); P_{H_2}, P_{H_2O} are the partial pressures of H_2 and H_2O in the reaction gas (atm); and a_{MeO_v} and a_{Me} are the activities of the MeO_v

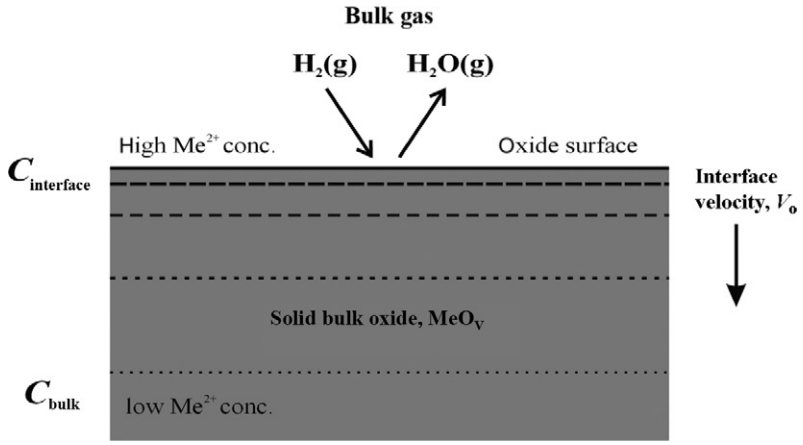


Figure 4.4.5 Schematic cross section of the reaction interface illustrating reactions between gas and a planar dense oxide surface [105].

and Me phases. For the reduction of pure metal oxides to pure metal and the condition when the gas is in equilibrium with the oxide,

$$0 = \phi^1 P_{H_2} - \phi^{11} P_{H_2O} \quad \text{or,} \quad \text{rearranging} K_T = \phi^{11}/\phi^1 = (P_{H_2}/P_{H_2O})_{eq} \tag{4.4.11}$$

where K_T is the equilibrium constant for reaction (4.4.9) at temperature T, $(P_{H_2}/P_{H_2O})_{eq}$ is the gas mixture for the condition where Me and MeO phases are in chemical equilibrium. Substituting in Equation (4.4.10) for ϕ^{11} gives

$$\begin{aligned} R_o &= \phi^1 P_{H_2} - \phi^1 (P_{H_2}/P_{H_2O})_{eq} P_{H_2O} \\ &= \phi^1 P_{H_2} \left[1 - (P_{H_2}/P_{H_2O})_{eq} (P_{H_2O}/P_{H_2})\right] \left(\text{mol} H_2 \text{m}^{-2} \text{s}^{-1}\right) \end{aligned} \tag{4.4.12}$$

It can be seen that the chemical rates are characterized by the apparent rate constants, the absolute pressures of the reactant gases, and a function $(P_{H_2}/P_{H_2O})_{eq}(P_{H_2O}/P_{H_2})$. The ratio $(P_{H_2}/P_{H_2O})_{eq}(P_{H_2O}/P_{H_2})$ represents the "undersaturation" of the gas relative to the oxide, and is directly related to the thermodynamic driving force for the reaction. From Equation (4.4.8)

$$\left[(P_{H_2}/P_{H_2O})_{eq}(P_{H_2O}/P_{H_2})\right] = \exp(\Delta G_{reaction}/RT) \tag{4.4.13}$$

and substitution into Equation (4.4.11) gives

$$V_o = R_o/\rho_o = \left\{\phi^1 P_{H_2}/\rho_o\right\} [1 - \exp(\Delta G_{reaction}/RT)] \left(\text{ms}^{-1}\right) \tag{4.4.14}$$

where V_o is the oxide interface velocity and ρ_o is the oxide density (mol O m^{-3}) for oxide MeO_ν.

The net chemical reaction rate, commonly given in the forms shown by Equation (4.4.12), can therefore be alternatively represented by the interface velocity, V_o, the partial pressure of the reactant gas and thermodynamic driving force for the reaction, $\Delta G_{reaction}$, as in Equation (4.4.14). The relationships between $\Delta G_{reaction}$ and V_o are shown schematically in Figure 4.4.6 for a range of values of P_{H_2}, assuming the values of ϕ^1 are constant and independent of reaction rate; these form a series of curves originating at $\Delta G_{reaction} = 0$, as $\Delta G_{reaction} \to -\infty$ then $V_o = R_{omax}/\rho_o = \phi^1 P_{H_2}/\rho_o$.

For highly unstable oxides, $\Delta G_{reaction}$ will be a large negative value and the chemical reaction rates and interface velocities will approach those for the forward reaction at a given p_{H_2}. For relatively stable solids, $\Delta G_{reaction}$ approaches zero and the back or reverse reaction becomes significant and must be taken into account. For the conditions, for $P_{H_2} + P_{H_2O} =$ constant, as the relative stabilities of oxide and gas approach each other, the interface velocities will be described, at each total pressure, by a locus of points across varying values of P_{H_2} that become progressively smaller as chemical equilibrium is approached (see Figure 4.4.7). Understanding the relationships between thermodynamic

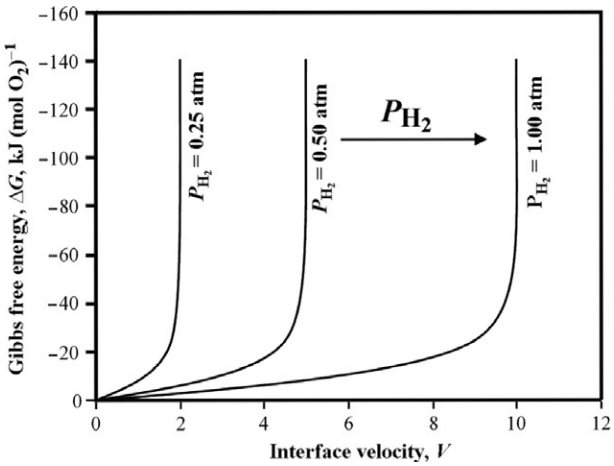


Figure 4.4.6 Schematic of the theoretical oxide interface velocities, V_o (driven by chemical reaction) as a function of thermodynamic driving force (ϕ = constant) for varying P_{H_2} [105].

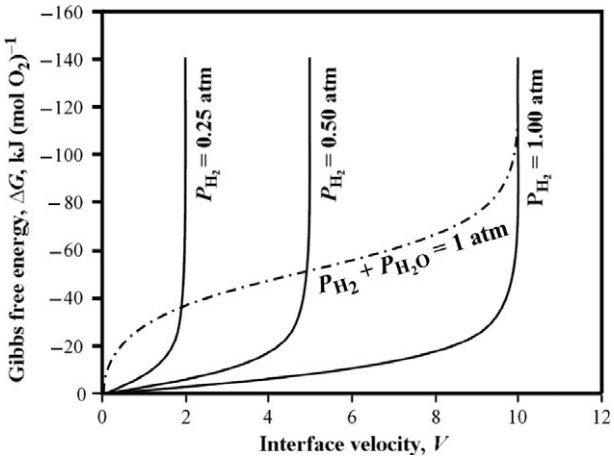


Figure 4.4.7 Schematic of the theoretical oxide interface velocities, V_o (driven by chemical reaction) as a function of thermodynamic driving force (ϕ = constant) for $P_{H_2} + P_{H_2O}$ = constant [105].

driving force, ΔG, and reaction rate is important in interpreting the phenomena occurring in these reaction systems, as will be described in a later section.

4.4.2.2. The Influence of Atomic Roughness on Chemical Reactions Rates

It is now well established [108,109] that solid phases having low entropy of formation, for example, metal alloys, will during transformation to liquid or gas, produce atomically rough surfaces that appear macroscopically to be smooth. In contrast, solids having high entropy of formation will form atomically smooth surfaces having faceted surfaces and

interfaces. The implications of these phenomena for chemical reaction rates on oxide surfaces are significant and are explored further below.

The surface roughness at an atomic level can be characterized by the parameters α and α_c. α, commonly referred to as the Jackson factor [108,109], $\alpha = \Delta S_f \eta_1 / RZ$, where ΔS_f is the entropy difference between the two phases at the interface, η_1 = number of nearest neighbors in the surface layer, Z is the maximum number of atom nearest neighbors for each atom in the crystal; α_c = critical α value for surface roughening transition, at which there is always a ledge/kink site present at the surface and there is no significant nucleation barrier to overcome to enable atom attachment or removal to take place. Metal oxides typically exhibit high entropy of formation, for example, for iron oxides [105], $\alpha \approx 15$. Values of α_c are typically in the range 2 for melt growth, to 8 for vapor phase growth [109].

On atomically rough surfaces all sites on the surface are potentially available as active reaction sites for chemical reaction on the surface. The relationship between thermodynamic driving force, ΔG and theoretical interface velocity due to chemical reaction, V_o (see Equation (4.4.14)) for $\alpha_c/\alpha = 1$, a fixed P_{H_2} and varying values of ϕ^1, is shown schematically in Figure 4.4.8.

Compounds having high entropy of formation, such as metal oxides, $\alpha_c/\alpha = 0.4$, tend to form surfaces and interfaces that are atomically smooth. In these cases, reaction of adsorbed species with the oxides preferentially occurs at selected sites, such as kink sites on ledges formed on the surface of the condensed phase [109]. As the reaction proceeds, these ledges are created and progressively move across the oxide surface. The atomic roughness of a surface is a function of the crystal structure, crystal plane, rate of removal

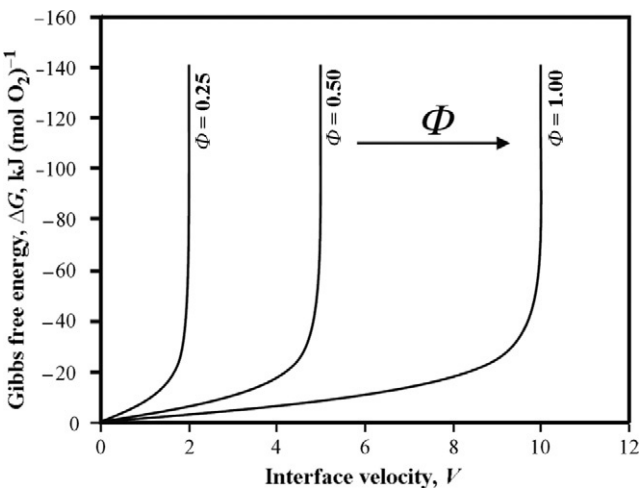


Figure 4.4.8 Schematic of the theoretical oxide interface velocities, V_o (driven by chemical reaction) as a function of thermodynamic driving force ($\alpha_c/\alpha = 1$, P_{H_2} = constant) for varying ϕ [105].

from individual sites, and rate of surface diffusion [109]. It has been argued [105] that the apparent chemical reaction rate constants on oxides surfaces are, therefore, not strictly constants but in fact are functions of the surface roughness. At low reaction rates and low thermodynamic driving forces for oxygen removal, and relatively high surface diffusion rates, the oxide surfaces are atomically smooth as the surface continuously rearranges itself to minimize the disorder in atomic structure at the surface. The apparent chemical reaction rate constants at any temperature for conditions in which there is no net oxygen removal then approach those measured using isotope exchange measurements [110–114] and smooth facetted surfaces are formed. On this basis the fraction of active sites on the iron oxide surfaces at chemical equilibrium have been calculated to be in the range 10^{-3} and 10^{-4} at temperatures between 1073 and 1273 K [115].

When there is net removal from or addition of species to facetted surfaces they will become increasingly atomically rough. As the surface roughness is a function of the dynamic reaction conditions at the interface, it is not possible to directly observe these structures; however, the structures of various crystal surfaces have been simulated using computer models for a range of materials and conditions [116–119]. Examples of these simulations generated using Monte Carlo techniques to demonstrate surface roughness for a range of values of α_c/α are shown in Figure 4.4.9. It is clear that the surface roughness decreases with decreasing α_c/α ratio. Calculated growth rates as a function of thermodynamic driving force for various surfaces are shown in Figure 4.4.10 [119]. For oxide

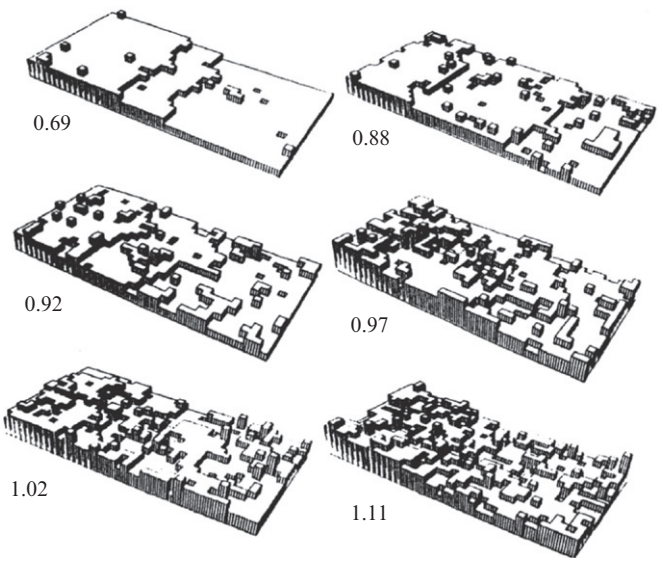


Figure 4.4.9 Calculated surface structures on facetted surfaces below and above the roughening transition, $\alpha_c/\alpha = 1$ [119].

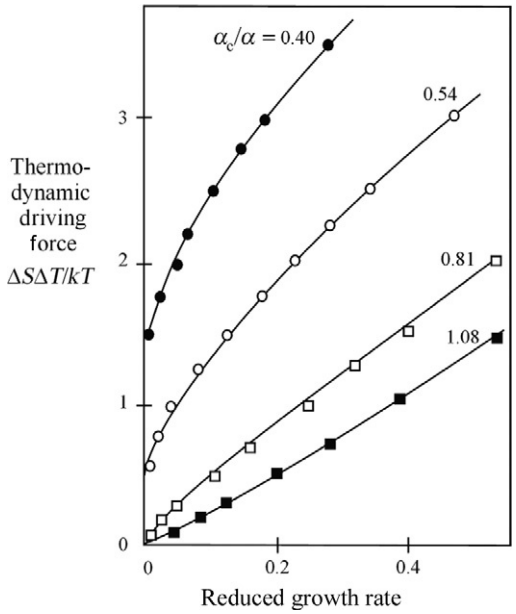


Figure 4.4.10 Calculated growth kinetics on facetted surfaces for various values of α_c/α ($\Delta S\Delta T = \Delta G$). *Adapted from [119].*

surfaces having low values of α_c/α, typically between 0.4 and 0.5 it can be seen that the observed growth rates are significantly lower than the maximum growth rate assuming all sites are active, that is, when $\alpha_c/\alpha = 1$; the differences in rates are most marked at low values of $\Delta G/RT$, and can differ by orders of magnitude as the net driving force $\Delta G/RT$ tends to zero. The surface roughness and the resultant growth rates only approach the "ideal" surface $\alpha_c/\alpha = 1$ at high thermodynamic driving forces. The relationship between ΔG and V_o for α_c/α less than unity, that is, high ΔS_f, for $P_{H_2} + P_{H_2O} =$ constant using α_c/α values from Figure 4.4.10, is shown schematically in Figure 4.4.11 [105]. It is clear from this evidence that the effects of surface roughness at the atomic level at moving interfaces must be taken into account in determining interface velocity.

In addition to atom movement at the reaction interface, the net removal of oxygen at the gas/oxide interface by chemical reaction with the gas produces changes in the oxide stoichiometry and creates local excess metal cations in the oxide in the interface region (see Figure 4.4.5). The principal means of mass transport of these excess metal cations in the oxide from and along the reaction interface are through volume and surface diffusion. The mass fluxes, J_i resulting from these transport mechanisms are determined by the concentration gradients and mass transport characteristics of the solid through Fick's laws, for example,

$$J_i = -D_i \cdot dC/dz \left(\text{mol m}^{-2}\text{s}^{-1}\right) \tag{4.4.15}$$

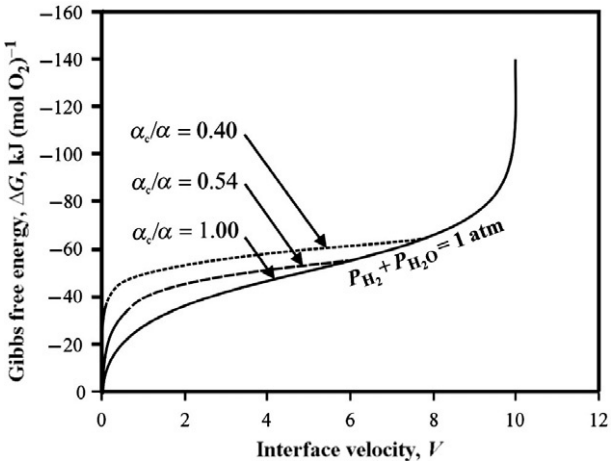


Figure 4.4.11 Schematic of the theoretical interface velocities, V_o (driven by chemical reaction) as a function of thermodynamic driving force for $P_{H_2} + P_{H_2O} =$ constant and for selected values of α_e/α [105].

where D_i is the diffusion coefficient of species i in the solid ($m^2\ s^{-1}$). The concentration gradients, which also directly reflect thermodynamic potential gradients, and the directions and magnitudes of the diffusive fluxes, vary with the interface geometry and the limiting chemical potentials associated with the various reactions gas/solid and solid/solid transformations taking place.

In the section the above, the chemical rate and mass transfer equations defining the rates of reactions at metal oxide surfaces have been established. These relationships will now be used in the analysis of reactions occurring at moving interfaces.

4.4.3. REACTIONS WITH ACCUMULATION AT THE INTERFACE

The overall decomposition of the oxides described by Equation (4.4.9) indicates that on completion of the reaction solid metal product is formed. To view the process only this way is to overlook the structural changes taking place in the oxide both before and during the production of the metal phase. To better understand the sequence of the structural changes and their implications for product, microstructure development reactions involving only the gas with oxide surface are considered first; the analysis and findings are then applied to the more complex systems in which both oxide and metal coexist.

4.4.3.1. Conditions for Instability Formation at Moving Interfaces

Reaction of the gas with the metal oxide surface (see Figure 4.4.5) creates an excess of metal cations at the surface of the oxide, $C_{interface}$, relative to the bulk, C_{bulk}; this

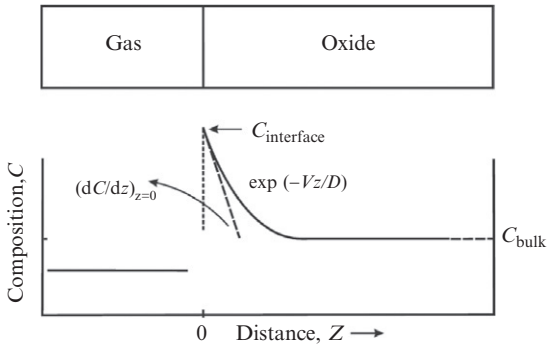


Figure 4.4.12 Schematic diagram of the gas/oxide interface illustrating the moving boundary problem for the decomposition of solid oxides.

concentration difference provides a net driving force for cation diffusion into the bulk oxide in the direction, z. At the same time, as indicated through Equation (4.4.14), the interface moves into the oxide in direction z at velocity, V_o. A plot of cation concentration as a function of distance from the reaction interface is illustrated in Figure 4.4.12. This planar interface moving boundary problem is analogous to the solute build up that occurs in metal alloy solidification [120] and diffusional solid/solid phase transformations [121]. It has been observed that in these situations the interface can either remain planar during decomposition, or become unstable such that perturbations in the surface profile can grow and the interface becomes increasingly uneven (see Figure 4.4.13). The conditions for instability formation at a moving interface, assuming there is no solubility of the solute in the new phase formed has been examined in detail and can be described by the equation [122–127]

$$(dC/dz)_{z=0} < (C_{interface} - C_{bulk}) \cdot V/D \tag{4.4.16}$$

where $(dC/dz)_{z=0}$ is the limiting concentration gradient in the oxide at the reaction interface, G_c, at $z=0$; $C_{interface}$ and C_{bulk} are the solute concentrations at the reaction interface and the bulk phase, respectively, V is the interface velocity, D is the solute diffusivity in the original liquid or solid phase.

The formation of instabilities in these transformations is favored under conditions of high interface velocity, V, low diffusivity D in the bulk phase, high differences in composition between the bulk and interface $(C_{interfac} - C_{bulk})$.

The mathematical solutions to the moving interface problem can also be used to describe gas/solid systems in which a solid decomposes in a reactive gas, for example, the gaseous reduction of a metal oxide. In the gas/solid systems involving the decomposition of metal oxide at the interface, the compositional gradient at the interface, $(dC/dz)_{z=0}$ can be shown [120], to be equivalent to $\Delta G/dz$, the thermodynamic potential gradient, thus the condition for instability formation is

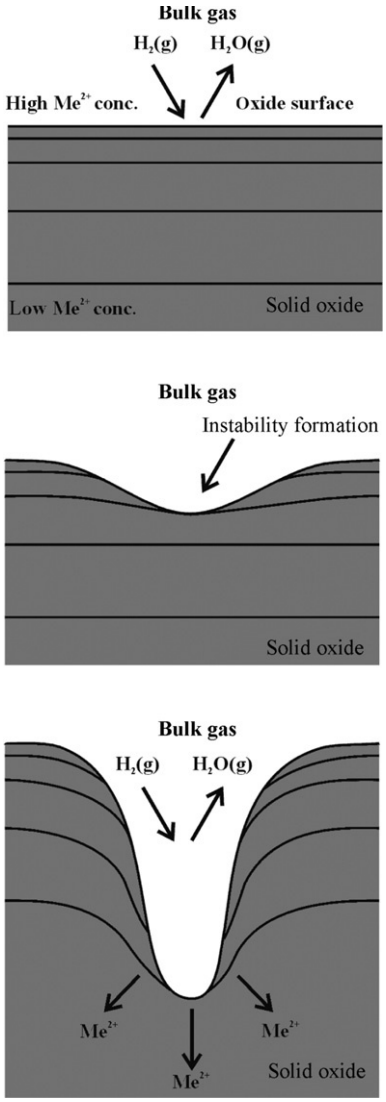


Figure 4.4.13 Schematic illustrations showing the progressive growth of an instability on a solid oxide surface during decomposition in a reactive gas mixture [105].

$$\Delta G/\mathrm{d}z < (C_{\text{interface}} - C_{\text{bulk}})\cdot V/D, \quad \text{or} \quad \Delta G/\mathrm{d}z < (\Delta C_{\text{ox}}/D)\cdot V \tag{4.4.17}$$

where ΔC_{ox} is the difference in solute concentration in the oxide between the gas/oxide interface and bulk oxide.

In nonisothermal conditions, systems in which alloy solidification is occurring in a temperature gradient at the interface, $G_{\text{T}} = (\mathrm{d}T/\mathrm{d}z)_{z=0}$, can be related [120] to the

concentration gradient, G_c, through the equation $G_T = mG_c$, where m is the liquidus slope $m = \left(T_{l(C_s)} - T_{l(C_l)}\right)/(C_s - C_l)$, $\Delta C = (C_s - C_l)$, where C_s and C_l are the solidus and liquidus compositions, respectively. The conditions for stability during crystal growth are described by the relation

$$G_T < (-m\Delta C/D)\cdot V \tag{4.4.18}$$

Instability formation in a positive temperature gradient is favored when there is a relatively low temperature gradient, G_T, or high compositional gradient, G_c, at the interface; this leads to the condition known commonly [109] as "constitutional undercooling" of the liquid ahead of the moving interface. In metal solidification, systems temperature gradient, G_T, and interface velocity, V, can be controlled independently by undertaking the transformations under directional solidification conditions. For a given material, progressive transition from planar growth, to cellular/columnar growth to dendritic structures has been shown [120] to occur for a given thermal gradient with increasing interface velocity, V. The cellular and dendritic pores in reactive gas/solid systems can be regarded as equivalent to primary phase cellular and dendritic crystal formation in alloy solidification. By analogy, the critical conditions for instability formation at the reacting oxide surface are established. *The important point to emerge from this initial analysis is that during decomposition of oxides the surface can remain as a stable planar surface, or it can become unstable and decompose into complex networks of tunnel-like pores depending on the material properties of the oxide and the process conditions.*

4.4.3.2. Oxide Surface Morphologies in Reactive Gas Atmospheres

Using the condition for interface stability given in Equation (4.4.17), and the expression for maximum interface velocity, V_o, given in Equation (4.4.14) it is now possible to demonstrate the range of conditions under which planar and unstable interfaces will be formed as a result of reaction with the gas phase. Both Equations (4.4.14) and (4.4.17) contain the term ΔG, the thermodynamic driving force for the reaction. Although ΔG and $\Delta G/dz$ are not the same numerically, the use of ΔG makes it possible to demonstrate schematically the trends in behavior with increasing thermodynamic driving forces and interface velocities.

Consider first systems in which the solid phase has low entropy of fusion, or entropy of formation. The relationship between thermodynamic driving force, ΔG and the maximum interface velocity, V_o, is illustrated schematically in Figure 4.4.14 for given values of $\Delta C_{ox}/D$ and $\phi^1 P_{H_2}$, $\alpha_c/\alpha = 1$, for the case when the value of ϕ^1 the chemical reaction rate constant is assumed to be independent of V and ΔG. It can be seen that at low values of ΔG the conditions generated by the chemical reaction with the gas mean that the interface is unstable, and the surface will decompose into a cellular pore growth morphology; with increasing thermodynamic driving force the cell pore walls themselves become

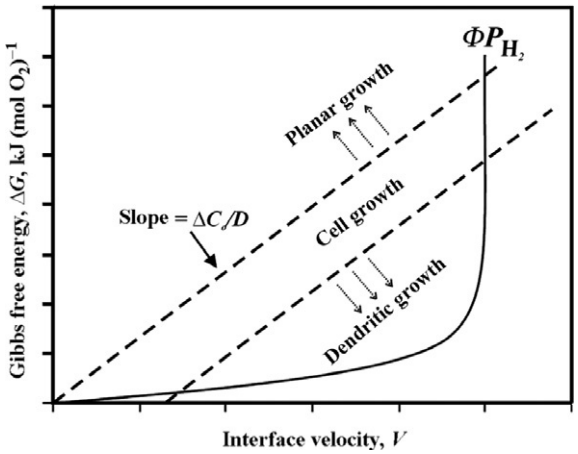


Figure 4.4.14 Schematic illustration of the conditions for planar, cellular, and dendritic growth morphologies in reactive gas systems ($\alpha_c/\alpha = 1$, $\phi =$ constant, $P_{H_2} =$ constant) [105].

unstable and the structure degenerates into dendritic pore growth morphologies. For cellular or dendritic pore growth, the shape and velocity of the growing pore tip is determined primarily by diffusion of excess metal solute into the bulk oxide ahead of the moving interface; the value of $C_{\text{interface}}$ is determined by the relative values of the thermodynamic driving force, chemical reaction rate on the oxide and the diffusive flux from the gas/oxide interface. For the conditions displayed in Figure 4.4.14, at high values of ΔG the interface velocity, V, tends toward its limiting value $\phi^1 P_{H_2}/\rho_o$ and theoretically the relative conditions at the interface change back progressively to those favoring cellular growth before reaching the conditions when the planar interface is again stable.

In systems exhibiting high entropy of formation, the variation in effective chemical reaction rate constant with undersaturation with respect to the gas phase (discussed in Section 4.4.2.2) has to be taken into account; this has significant implications for the conditions for interface stability in reactive gas systems. As pointed out previously, the tendency to form atomically smooth facetted surfaces at low net driving forces $\Delta G/RT$ results in a significant change in the ΔG versus V interface velocity relation as this limit is approached (see Figure 4.4.11), the interface velocities being significantly lower than for atomically rough surfaces. From the above considerations, it is predicted that a range of interface microstructures will be formed during the decomposition of oxides in reactive gas systems.

For reaction systems having high entropy of formation (low α_c/α), low values of $\Delta C_{ox}/D$ and $\phi^1 P_{H_2}$, it can be seen from Figure 4.4.15 that with increased driving force the interface velocity will always increase more slowly than the critical condition for interface instability. This means that the decomposing interface will always be planar

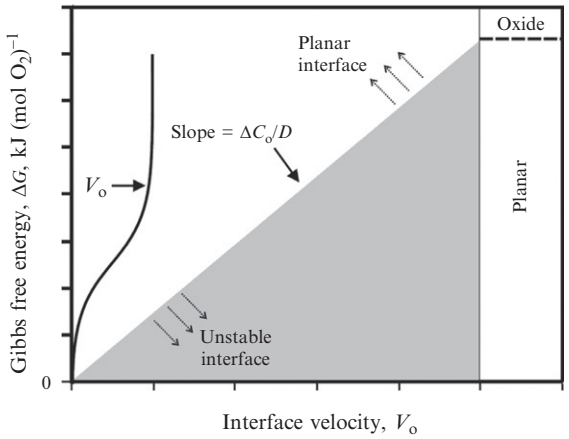


Figure 4.4.15 Schematic illustration of the conditions for planar, unstable growth morphologies in reactive gas systems ($\alpha_c/\alpha < 1$, $P_{H_2} + P_{H_2O}$ = constant, ϕ = constant (low), $\Delta C_o/D$ = low) [105].

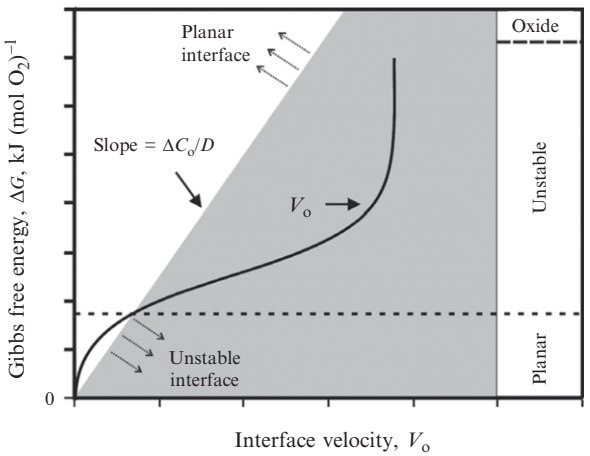


Figure 4.4.16 Schematic illustration of the conditions for planar, unstable growth morphologies in reactive gas systems ($\alpha_c/\alpha < 1$, $P_{H_2} + P_{H_2O}$ = constant, ϕ = constant (high), $\Delta C_o/D$ = high) [105].

and tend to form facetted surfaces. This is an important difference from atomically rough surfaces forming under the same conditions (Figure 4.4.14).

For reaction systems having high entropy of formation (low α_c/α), high values of $\Delta C_{ox}/D$ for intermediate values of $\phi^1 P_{H_2}$ a range of behaviors will be observed (Figure 4.4.16). Approaching chemical equilibrium conditions, the interface will be planar; with increasing driving force the chemical rates of reactions on the surfaces will exceed the critical limits for instability formation and will result in the formation of isolated pores or cellular/columnar-like growth of pores into the bulk oxide. As the thermodynamic driving force is progressively increased, the cellular pores transform to

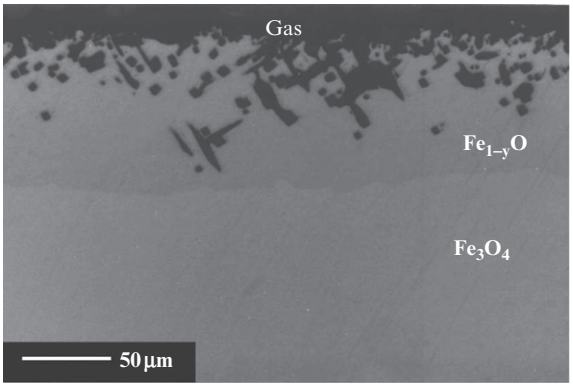


Figure 4.4.17 Optical micrograph showing gas pores (black) formed in wustite, $Fe_{1-y}O$, on reduction of dense magnetite, Fe_3O_4 (973 K, 76.1% H_2/23.9% H_2O, $P_{tot} = 1$ atm) [130].

increasingly dendritic structures. The critical conditions for instability formation will clearly depend on the chemical and physical characteristics of the reaction system.

The thermodynamic driving force, ΔG, and interface velocity, V, have been shown to be two of the factors influencing interface stability. Theoretically at all conditions when very high potential gradients are generated at the interface by reaction with the gas the planar interface is stable; whether these conditions can be achieved in practice depends on the chemical characteristics of individual systems.

High interface velocities, V, which are equivalent to high chemical reaction rate, for a given thermodynamic driving force, ΔG, favor the formation of dendritic pore structures (see example in Figure 4.4.17).

Through Equation (4.4.17), ΔG, and V are related by the factor $(\Delta C_{ox}/D)$, where ΔC_{ox} is the solute concentration difference between surface and bulk in the oxide and D is the effective diffusivity of the solute species. These material properties influence the extent to which metal solute build up ahead of the decomposing interface can occur. Each of these effects will now be examined in turn.

The maximum concentration difference that can be achieved between surface and bulk oxide is dependent on the particular material, the conditions under which it was prepared and the thermal history prior to contact with the reactive gas system. Oxide phases all contain some degree of nonstoichiometry as a result of intrinsic defects, for example, metal or oxygen vacancies, or interstitial atoms [128]. The defect concentrations depend on crystal structure, temperature and oxygen partial pressure. Many of the transition metals can exist in more than one oxidation state; this characteristic can influence the ranges of stoichiometries and the relative stabilities of the different crystal structures. The bulk oxide compositions will therefore depend on the conditions under which they have been prepared and the extents to which they have been exposed to other reaction conditions (temperature, oxygen pressure, time) before final reduction. In

industrial processes, it is often the case that the material is slowly heated to the reaction temperature possible changes to bulk oxide stoichiometry during these prereaction conditions should be taken into account when determining the maximum difference in metal ion concentration between surface and bulk phases.

In the presence of a single phase, as the planar reaction front advances, the limiting values of C_{bulk}, the bulk solute composition, will change as the diffusion front penetrates the sample section and, in these cases, decreases the value of $(C_{interface} - C_{bulk})$. For plate-shaped samples [129], the concentration at the center of the plate will be approximately 0.1 of that at the gas/solid interface when the reaction is only 30% complete ($Dt/L^2 = 0.07$), 0.2 when 50% complete ($Dt/L^2 = 0.20$), and 0.5 when 70% complete ($Dt/L^2 = 0.4$). Here, D is the solute diffusivity, L is the half thickness of the solid, and t is the reaction time. Clearly, the times to obtain the particular extents of reaction are larger for larger particle sizes and materials having lower diffusivities, and smaller for smaller particle sizes and oxides having high diffusivities. The concentration gradients generated in the solid at the gas/solid interface will also be influenced by any phase changes that may be simultaneously taking place in the solids. For example, the original solid may be transformed by solid state diffusion into a series of intermediate oxides. The proximity of these intermediate phases to the gas/oxide interface is important since the phase boundary will determine the limiting boundary conditions for the diffusion.

Chemical diffusivities in oxides are also related to material characteristics and are thermally activated processes. Through the Arrhenius equations of the form the diffusivity, D, is given by

$$D = D^{o} \exp(-\Delta E/RT) \left(m^{-1} s^{-1}\right) \tag{4.4.19}$$

where ΔE is the activation energy for diffusion, R = gas constant, T = absolute temperature (K).

Increases in temperature will lead to increases in diffusion coefficient in all cases. From Equation (4.4.17), clearly an increase in the value of temperature, and hence D, will tend to increase the geometric stability of the moving oxide surface favoring the formation of a planar reaction surface.

In reactive gas systems in which the rate of removal of the oxygen from the gas/oxide interface is dependent on the chemical reaction, the rate will be described by equations of the form given in Equation (4.4.14), and be influenced by the gas composition. If, however, the rate of pore growth is limited solely by solid state diffusion of solute in the oxide phase the growth rate will be independent of reactive gas partial pressures. This is a significant finding that has not been previously recognized for the class of reactions and should be taken into account in any detailed modeling of these reaction systems.

The presence of another metal cation, in solid solution in the oxide or as a stoichiometric oxide, adds to the complexity to the problem changing values of ΔG, ΔC_{ox} and D

for a given reactant gas mixture and temperature. The presence of a second cation solute species will, in cases in which there are large differences in the relative stabilities of the metal oxides in the original oxide material, enhance the probability of solute accumulation at the reaction interface and the formation of instabilities. Reaction of the gas with the original homogeneous metal oxide will then result initially in the accumulation of the more stable oxide at the interface, the development of dendritic pores and in nonuniform dispersions of the cation components in solid solution in the product. It is also possible that new oxide compounds may be formed as local compositions of the more stable component are increased as a result of the selective reduction of the oxide and the moving unstable interface.

4.4.4. SUMMARY

In this section, the general qualitative relationship between the chemical reaction with the fluid phase and the conditions for stability of solid surfaces has been established. The analysis shows that the reaction interface can remain stable and planar during the progress of the reaction, or the effective interfacial area and geometry may change as a direct result of the reaction at the interface. The analysis is valid for any fluid/solid reaction. It provides the basis for a deeper understanding of the parallel chemical and mass transfer processes occurring during reaction. This makes it possible to now identify and understand the key process variables that determine the conditions for pore growth during decomposition of metal compounds in reactive fluid mixtures.

REFERENCES

[102] E.T. Turkdogan, Physical Chemistry of High Temperature Technology, Academic, New York, 1980.
[103] E.T. Turkdogan, P. Grieveson, L.S. Darken, J. Phys. Chem. 67 (1963) 1647.
[104] H.H. Kellogg, Trans. Met. Soc. AIME, 236 (1966) 602.
[105] P.C. Hayes, Metall. Mater. Trans. B. 41B (2011) 19.
[106] C. Wagner, in: J.F. Elliott (Ed.), Proc. Chipman Conf, MIT Press, Dedham, MA, 1962, p. 19.
[107] E.T. Turkdogan, J.V. Vinters, Metall. Trans B. 3B (1972) 1561.
[108] K.A. Jackson, D.R. Uhlmann, J.D. Hunt, J. Cryst. Growth 1 (1967) 1.
[109] K.A. Jackson, Kinetic Processes—Crystal Growth, Diffusion and Phase Transitions in Materials, Wiley-VCH, Weinheim, 2004.
[110] H.J. Grabke, Ber. Bunsenges. Phys. Chem. 69 (1965) 48.
[111] S. Stotz, Ber. Bunsenges. Phys. Chem. 70 (1966) 37.
[112] E. Riecke, K. Bohnenkamp, Archiv. Eisenhuttenwes. 40 (1969) 717.
[113] A. Gala, H.J. Grabke, Archiv. Eisenhuttenwes. 43 (1972) 463.
[114] H.J. Grabke, Ann. N. Y. Acad. Sci. 213 (1973) 110.
[115] P.C. Hayes, Metall. Trans B. 10B (1979) 211.
[116] H.J. Leamy, G.H. Gilmer, J. Cryst. Growth 24/25 (1974) 499.
[117] G.H. Gilmer, J. Cryst. Growth 24/25 (1974) 499.
[118] K.A. Jackson, J. Cryst. Growth 42 (1977) 3.
[119] K.A. Jackson, J. Cryst. Growth 198 (1999) 1.
[120] W. Kurz, D.J. Fischer, Fundamentals of Solidification, third ed., Trans Tech, Switzerland, 2004, p. 74, 88, 151.

[121] J.W. Christian, Theory of Phase Trans formations in Metals and Alloys, Pergamon, Oxford, 1965.
[122] M.E. Glicksman, R.J. Schaefer, J.D. Ayers, Metall. Trans A. 7A (1976) 1747.
[123] J.S. Langer, H. Muller-Krumbhaar, J. Cryst. Growth 42 (1977) 11.
[124] J.S. Langer, H.J. Muller-Krumbhaar, Acta Metall. 26 (1978), p. 1681, 1689, 1697. J.S. Langer, H.J. Muller-Krumbhaar, Acta Metall. 29 (1981), p. 145.
[125] J.S. Langer, H.J. Muller-Krumbhaar, Acta Metall. 29 (1981) 145.
[126] W.W. Mullins, R.F. Sekerka, J. Appl. Phys. 35 (1964) 444.
[127] R.F. Sekerka, J. Cryst. Growth 3/4 (1968) 71.
[130] S.P. Matthew, P.C. Hayes, Metall. Trans B 21B (1990) 153.
[128] P. Kofstad, Nonstoichiometry, Diffusion, and Electrical Conductivity in Binary Metal Oxides, Wiley-Interscience, New York, 1972.
[129] R.W. Gurry, Trans. AIME 150 (1942) 172.

CHAPTER 4.5

Phase Formation Reactions

Peter Hayes
School of Chemical Engineering, The University of Queensland, Queensland, Brisbane, Australia

4.5.1. CLASSES OF PHASE FORMATION REACTIONS

In the introduction to the topic of reaction kinetics, two important classes of reactions were identified, homogeneous and heterogeneous reactions. Heterogeneous reactions include reactions that result in solute transfer across stable planar interfaces, solute transfer across unstable nonplanar interfaces and phase formation reactions. It is this latter class of reactions that is examined in more detail in the present section. In the context of the present discussion, the term new phase is taken to mean a gas, liquid, or solid phase that was not present at the start of the process. In these systems, new phases can appear when appropriate changes to the temperature, pressure, and bulk composition are made. From observations that have been made on a wide range of chemical systems, it is possible to distinguish different classes of phase formation reactions. Systematic analysis and classifications of solid/solid transformations encountered in physical metallurgy and materials science have already been published [131,132]. The new classification provided here is an attempt to encompass the range of phenomena that are encountered in fluid/solid reaction systems.

The classification that is used in this discussion is based on a hierarchy of criteria. At the highest level, the classification of fluid/solid transformation is based on thermodynamic conditions for transformation, this is then subdivided according to reaction mechanisms. The classification is summarized in Figure 4.5.1. The characteristics of each of these reactions and the conditions necessary for their formation will be discussed further in the following sections and Chapter 4.6.

The thermodynamics of the system not only determines whether a reaction can proceed and the driving force for change but also plays a key role in determining the mechanism of phase transformation that takes place; in this respect two classes of phase transformation have been identified, these can be are termed for convenience "*Continuum*" and "*Heterogeneous*" *Phase Formation Reactions*.

In the case of the continuum phase formation reactions, small fluctuations in chemical composition on an atomic scale spontaneously expand in magnitude and size until the new phases are formed having defined uniform compositions, there is no thermodynamic

Treatise on Process Metallurgy, Volume 1
http://dx.doi.org/10.1016/B978-0-08-096986-2.00017-5
© 2014 Elsevier Ltd.
All rights reserved.

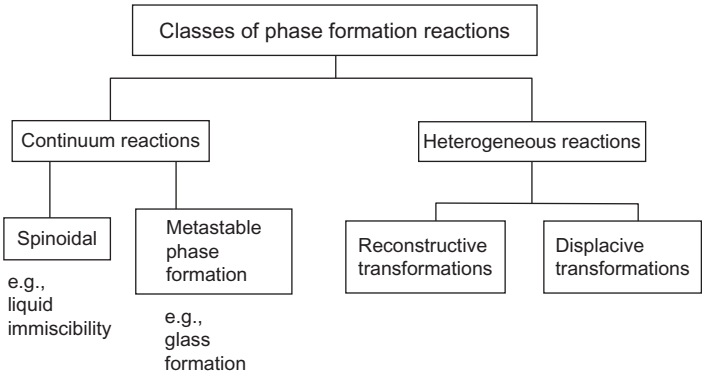


Figure 4.5.1 Classes of phase formation reactions.

barrier to the formation of the new phases. In heterogeneous phase formation reactions, the new phase takes on a defined chemical composition right from the initial stages of its formation and undergoes the classical nucleation and growth reaction steps, the system has to overcome an energy barrier for the process in order to proceed to new product formation [131–134].

Phase transformations in the solid state can occur through two principle mechanisms. Those involving the substantial rearrangement of individual atoms to form new crystalline phases are referred to as reconstructive transformations. In the case of reactant and product solids that have common structural features or symmetry elements, it is possible for transformations to occur by cooperative movement of many atoms. These displacive transformations are observed in modular materials [135]. The details of these types of transformations mechanisms and the potential implications for process control are discussed in the following sections.

4.5.2. ELEMENTARY REACTION PROCESSES

4.5.2.1. Continuum Phase Formation Reactions (Spinoidal)

This class of phase transformation is observed during gas/liquid transitions, liquid immiscibility, and spinoidal decomposition reactions in solids. From a thermodynamic viewpoint their behavior is analogous. The following example is given by way of illustration.

Consider the chemical thermodynamic stability of a given single phase to be described by the sum of contributions from the enthalpy, ΔH_m, and entropy of mixing, ΔS_m, that is,

$$\Delta G_m = \Delta H_m - T\Delta S_m \tag{4.5.1}$$

In this system which may be one of gas, liquid, or solid solutions, the enthalpy of solution is strongly positive. At high temperature, the dispersion of the components in the solution, be they atoms or molecules, tends to be random and there is little or no short range interaction between these components. Under these conditions the

entropy component $T\Delta S_m$ dominates the relationship. Across the range of solution compositions from pure A to pure B the stable state is that resulting in the lowest Gibbs free energy and so the single phase solution is stable for all bulk compositions in the range.

As the temperature of the system is lowered, the short range forces between atoms and molecules become relatively more important and the relative contributions to the enthalpy and entropy of solution change. As the entropy component is reduced with decreasing temperature, this may lead to inflection in the Gibbs free energy composition relationship.

This creates the potential for compositional instability in the system. If the bulk composition is between a' and a'' at temperature T_3 then it is possible for two compositions of the same phase to be in chemical equilibrium; the compositions of these phases are marked in the full line in Figure 4.5.2f. As the temperature of the system is further lowered below the critical transition temperature, the driving force for the separation of the single phase into two phases having different compositions but of similar crystal structure or arrangement of atoms and molecules increases.

Between compositions which are characterized by regions of negative curvature ($\delta^2 G/\delta C^2 < 0$), known as the spinoidal (marked in Figure 4.5.2f as a dashed line), there are no barriers to the movement of the various species in these systems beyond their random movements within the system, the rate of development of the separate phases by this mechanism is determined by diffusional processes. This has important implications as

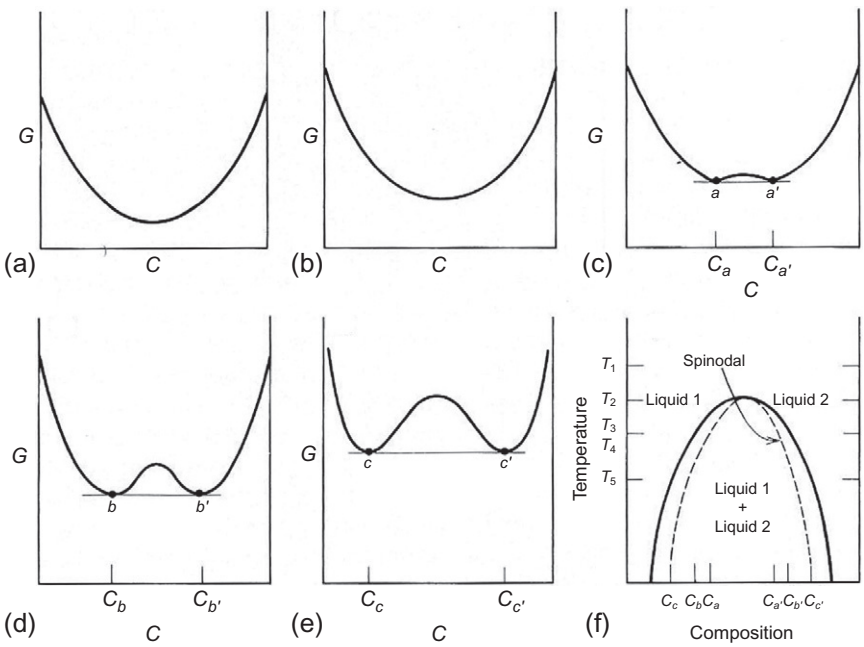


Figure 4.5.2 Thermodynamic conditions for the development of immiscibility and spinoidal reaction with decreasing temperature: (a) T_1, (b) T_2, (c) T_3, (d) T_4, (e)T_5 [134].

these instabilities can be triggered by random movement of atoms and molecules, and there is no additional barrier to their formation. The spontaneous decomposition of a single phase into a multiphase system in liquids leads to liquid/liquid immiscibility, in solids to spinoidal decomposition, and in gases this leads to condensation phase transitions with the formation of liquid/gas equilibria.

There is an important difference here between the spinoidal decomposition reactions and conditions, where $\delta^2 G/\delta C^2 > 0$; in these later conditions any small fluctuations in composition result in increases in Gibbs free energy. In order to attain the final lowest free energy condition, material substantial local compositional fluctuations must occur. This material can be retained in a metastable condition but requires a different transformation mechanism in order to achieve the equilibrium phase assemblage. This brings us to the second class of transformations.

4.5.2.2. Heterogeneous Phase Formation Reactions (Nucleation and Growth)

4.5.2.2.1 Nucleation

The formation of a new phase must necessarily result in a distinct phase boundary, either side of this boundary the material is of different characteristic structure or composition. It is the creation of this boundary that enables us to define the second class of phase transformations, that of nucleation and growth.

Additional energy is associated with the formation of an interface. In determining the net energy available for the transformation, this interface energy should be taken into account. It will be demonstrated in the section below that it is the very initial conditions for the formation of the new phase that are most affected by these considerations.

Consider a system in which a phase A is stable above a critical transition temperature, T_o, and phase B is the thermodynamically stable bulk phase below T_o; this can be any type of transition solidification, precipitation, condensation, or change in crystal structure. If a small region of A is transformed to B there are several contributions to the free energy of the system. ΔG_v is the Gibbs free energy per unit volume associated with the phase transition from A to B. There is the interfacial free energy associated with the new boundary between the two phases. Another component is the strain free energy associated with distortions in the atomic arrangements in the A and B phases associated with the formation of the new phase; this latter term in reality is only of significance in solid/solid transformations and is not included in the discussion further for sake of brevity and clarity.

Considering the formation of a spherical phase B in A, the net free energy change is given by

$$\Delta G_{net} = 4\pi r^2 \gamma + 4/3\pi r^3 \Delta G_v \tag{4.5.2}$$

where r is the radius of the new phase B and γ is the interfacial energy. By inspection, it can be seen that for ΔG_v approaching zero, that is, at low supersaturations, the first term

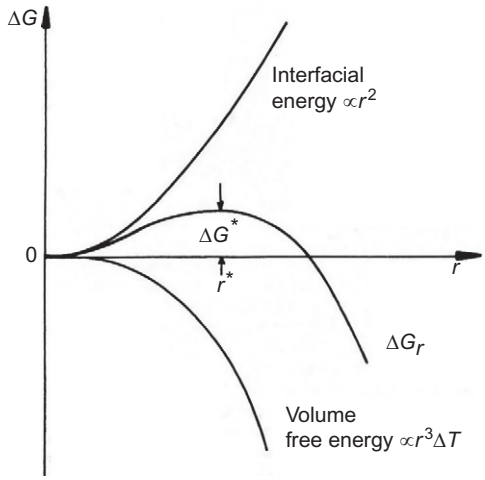


Figure 4.5.3 Gibbs free energy of a new phase as a function of size. Continued growth of the nucleus is favored above the critical nucleus size.

in this expression will be dominant and the net free energy change will be positive. As the size of the new phase, or nucleus, of B increases, the second term increases with the third power of the radius, while the magnitude of the surface energy term is dependent on r^2. At a critical radius, the change associated with the volume free energy becomes dominant. This situation is illustrated schematically in Figure 4.5.3.

An example of the heterogeneous nucleation of iron metal on the surface of iron oxide is given in Figure 4.5.4.

The critical radius of the nucleus that must be achieved for the phase to become stable as is grows, $\delta(\Delta G_v)/\delta r = 0$, is given by the condition

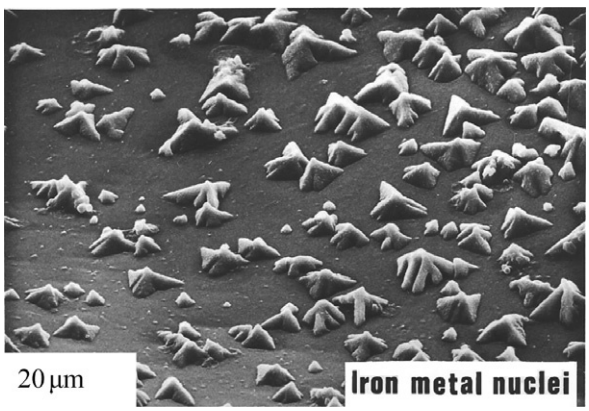


Figure 4.5.4 The formation of metallic iron nuclei on the surface of solid iron oxide (wustite) on reduction in a CO/CO_2 gas mixture.

$$r^* = -2\gamma/\Delta G_v \tag{4.5.3}$$

Clearly, the greater the thermodynamic driving force for the formation of the new phase B, the smaller the critical radius for a stable nucleus of phase B.

In any material at temperatures above absolute zero, there will be random motion of atoms or molecules. At any instant in time in the original material, this random motion will lead to local associations of species that at an atomic level will approximate to the composition and structure of phase B [134]. Assuming the concentration of these associations size, r, can be described by the relation

$$n_r = n_o \exp(-\Delta G/RT) \tag{4.5.4}$$

The concentration of critical sized nuclei n^* is given by

$$n^* = n_o \exp\left(-\Delta G^*/RT\right), \quad \text{where} \Delta G^* = 4\pi r^{*2} \quad \gamma = 16\pi\gamma^3/(\Delta G_v)^2 \tag{4.5.5}$$

From this conceptual understanding of the nucleation process, it is possible to derive expressions for nucleation frequency in the system. Assuming that the concentration of critically sized nuclei is that given by Equation (4.5.5), that the number can be increased by the addition of a single atom or molecule, and that all nuclei that reach this critical size continue to grow, the rate of nucleation per unit volume, I, is given by

$$I_v = \upsilon n_s n^*$$

where υ is the collision frequency of atoms or molecules with the surface, n_s is the number of atoms or molecules at the surface of a critically sized nucleus. That is, the nucleation rate per unit volume is the number of times single species contact the surface of critically sized nuclei. The collision frequency, υ, can be estimated in different ways depending on the nature of the interface. For impact of gas molecules from an ideal gas,

$$\upsilon = \alpha_c p_A / \left\{ n_A (2\pi MRT)^{0.5} \right\} \tag{4.5.6}$$

where α_c the condensation coefficient is the fraction of incident molecules that condense on the surface, p_A is the vapor pressure of A, n is the number of atoms per unit area, and M is the molecular weight of A. For condensed phases, involving diffusional processes, the collision frequency can be conveniently expressed in the form

$$\upsilon = \upsilon_o \exp(-\Delta G_m/RT) \tag{4.5.7}$$

where υ_o is the molecular or atomic jump frequency and ΔG_m is the activation energy for transport across the matrix/nucleus interface.

The rate of nucleation per unit volume, I_v, is then given by

$$I_v = \upsilon n_s n^* = \upsilon_o n_o n_s \exp(-\Delta G_m/RT) \exp\left(-\Delta G^*/RT\right) \tag{4.5.8}$$

This relationship provides important insights to the trends in nucleation behavior expected from changing process variables. Temperature is clearly important as it appears

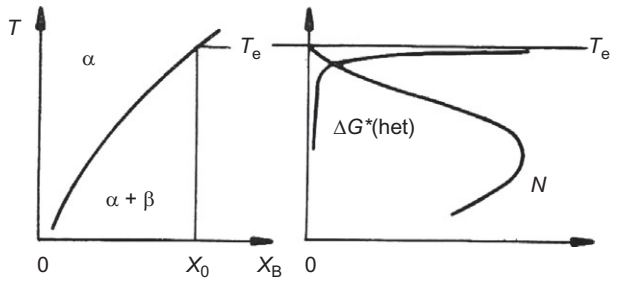


Figure 4.5.5 Nucleation frequency N of the β phase as a function of undercooling of material bulk composition X_o from the equilibrium or phase boundary at temperature T_e·ΔG^* is the critical Gibbs free energy for nucleation [133].

in two exponential terms in the expression involving transport of species and thermodynamic driving force.

These combined effects are expressed graphically in Figure 4.5.5 for the cooling of a phase of bulk composition, X_o, below the phase boundary temperature, T_e.

It can be seen that at low supersaturations the nucleation rate is dominated by the effects of thermodynamic driving force, while at high undercooling the rates are determined by the flux of species to the interface. Thus the nucleation frequency first increases then decreases with increasing undercooling; for any system there is a condition under which the nucleation frequency is a maximum; this is a general conclusion and applies to all phase transitions involving nucleation and growth.

The transport of species depends critically on the physical state of the original phase and the physicochemical properties of the phase. Clearly from earlier discussions in this chapter, gas phase mass transfer is rapid compared to condensed phases. The movement of species in fluid phases is intimately associated with the local bonding between atoms and molecules, in metals, molten salts, mattes, and aqueous solutions the mobility of individual atoms and molecules is relatively high. In slags and organic liquids, both of which can contain species having strong covalent bonds, mobility can be low. In either case, the collision frequency term decreases exponentially as the temperature decreases; this effect is most marked on systems that are rapidly cooled from reaction temperature. The most striking example of this is the retention of silicate slag as amorphous, or glassy state, on rapid cooling which takes place during water granulation of tapped slags. The rates of movement of species in solid phases is significantly lower than in fluids and the effect of the collision frequency term is most readily observed.

Although the thermodynamic driving force can be seen to change as a function of temperature the sensitivity of processes to this variable is not immediately apparent from the formulation given in Equation (4.5.8). For the nucleation of condensed phases, the ΔG_v is the Gibbs free energy per unit volume associated with the phase transition from A to B can be expressed as

$$\Delta G_v = \Delta H_v - T\Delta S_v \tag{4.5.9}$$

ΔH_v and ΔS_v are respectively the enthalpy and entropy changes per unit volume associated with the phase transition from A to B. At the critical, or equilibrium, temperature T_o, $\Delta G_v = 0$, and $\Delta H_v = T_o \Delta S_v$. At temperatures just below the critical temperature, the values of ΔH_v and ΔH_v can be assumed to be close to the values at T_o. Equation (4.5.9) can then be expressed as

$$\Delta G_v = \Delta H_v (T_o - T)/T_o \tag{4.5.10}$$

substitution for ΔG_v in Equation (4.5.8) the temperature dependence of nucleation becomes [134]

$$I_v = I_o \exp(-\Delta G_m/RT) \exp\left[-16\pi\gamma^3 {T_o}^2/{\Delta H_v}^2 (T_o - T)^2\right] \tag{4.5.11}$$

A similar expression is obtained for gas/condensed phase transformations. In this case, $\Delta G_v = (RT/V_\beta)\cdot\ln(p/p_o)$, where V_β is the molar volume of the B phase, p and p_o are the partial pressures of the species in the gas and at equilibrium.

$$I_v = I_o \exp(-\Delta G_m/RT) \exp\left[-16\pi\gamma^3/\left\{\left(RT/V_\beta\right)\cdot\ln(p/p_o)\right\}^2\right] \tag{4.5.12}$$

It is clear here that the thermodynamic during force increases dramatically with increased undercooling, in effect increased supersaturation.

In the discussion above, it was implicitly assumed that the formation of the new phase took place directly from the original phase; this is referred to as homogeneous nucleation. In most practical systems, interfaces already exist in some form or other whether in the form of walls of containment materials, existing second phase product materials, impurity particles, etc. The presence of these interfaces offers the opportunity for the nucleation of the new phase on these existing surfaces. This comes about through the fact that the interfacial energies present at the existing surfaces are lower than the energies required to create new interfaces through homogeneous nucleation. Putting this in context, the first term in equation

$$\Delta G_{net} = 4\pi r^2\gamma + 4/3\pi r^3 \Delta G_v \tag{4.5.13}$$

is lower and hence the critical nucleus size is commensurately reduced and the nucleation frequency for these conditions increased. The formation of critically sized nuclei on existing surfaces or interfaces is referred to as heterogeneous nucleation. This is the dominant mechanism of formation of new phases in most process metallurgy applications.

Heterogeneous nucleation is favored on those preexisting surfaces that are closest to the structure or properties of the new phase that is to be formed. As heterogeneous nucleation necessarily involves existing surfaces, these systems are sensitive to the presence of impurity elements that can significantly influence surface properties.

4.5.3. MECHANISMS OF GROWTH

4.5.3.1. Introduction

While the change in Gibbs free energy indicates that spontaneous change should occur, the kinetics of these structural changes can vary significantly depending on the mechanism of the transformation. In some cases in crystalline solids, only minor changes to the relative positions of atoms are required to achieve the required change in crystal structure; these are referred to as "displacive" transformations. These transformations occur relatively rapidly. In other cases, bond breakage and extensive rearrangement of atom positions, "reconstructive transformation," is necessary (see Figure 4.5.6). These major structural changes tend to be relatively slow and can be suppressed below the equilibrium transformation temperature by rapid cooling of materials.

An example of a displacive transformation is that of β to γ $2CaO{\cdot}SiO_2$ on cooling, this transformation results in a 14% volume change and the spontaneous breakage of the crystals due to the internal stresses generated by the structural change (see Figure 4.5.7) [136].

Multiple polymorphic transformations can occur in the case of silica [134]. Under 1 atm pressure the stable form of silica at room temperature is low quartz. On heating this transforms by a displacive mechanism at 573 °C (846 K). Further heating to 867 °C (1140 K) leads to the reconstructive transformation of this material into high tridymite; the Si—O covalent bond in silica is very strong so bond breakage and the reorganization of atoms within the lattice is extremely slow. Tridymite remains the stable phase on further heating until 1470 °C (1743 K) at which temperature cristobalite become the equilibrium phase; again this involves a reconstructive transformation. Both tridymite and cristobalite undergo displacive transformations that occur readily on cooling (Figure 4.5.8).

Phase changes involving a change in state, that is, gas, liquid, solid, all take place through reconstructive transformations. Solid state processes can, as shown in the above examples, involve both reconstructive and displacive processes.

4.5.3.2. Rates of Reconstructive Transformations

Reconstructive transformations by definition must include atom movement and diffusional processes. These have been studied and analyzed in detail for liquid/solid transformations (solidification) [137] and solid/solid transformations [131–134]. While these closed reaction systems are not usually regarded as relevant to reaction kinetic studies in process metallurgy there are analogies between reactions occurring in liquid/solid and solid/solid systems, and those observed in fluid/solid systems; this latter point is discussed in more detail in Chapter 4.6.

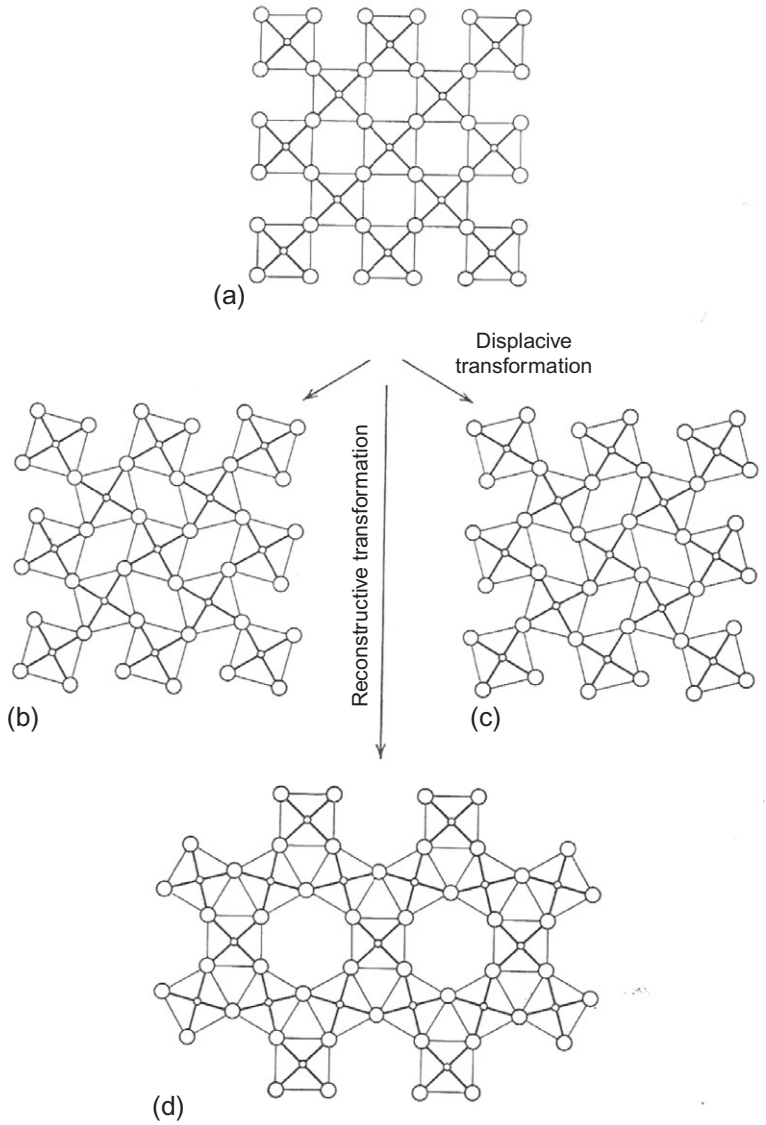


Figure 4.5.6 Schematic diagram illustrating displacive {(a) to (b), (a), and (c)} and reconstructive {(a) to (d)} crystalline phase transformations into different crystal structures [134].

4.5.3.2.1 Growth of New Phases

The growth of new phase in general requires the transport or redistribution of solute species ahead of the moving reaction front and the rearrangement of atoms at the interface. The key variables that can be used to control the thermodynamic driving force for growth of new phases in closed systems are the same as for nucleation, that is, bulk

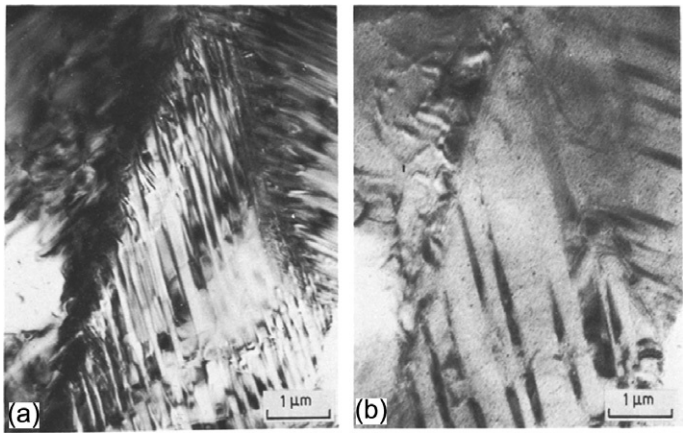


Figure 4.5.7 Transmission electron micrographs showing displacive transformation of β to γ $2CaO{\cdot}SiO_2$ [136].

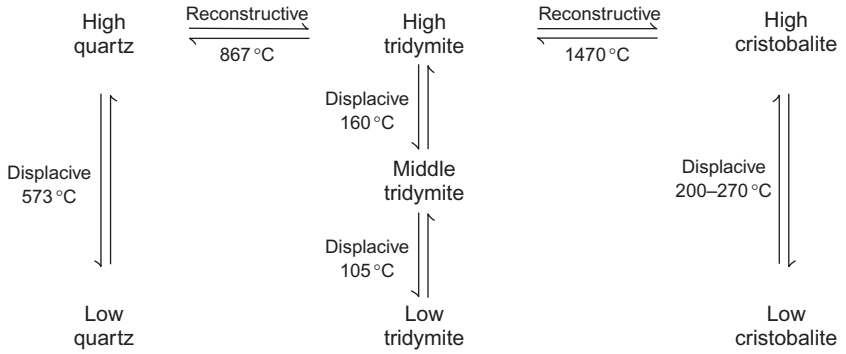


Figure 4.5.8 Polymorphic transformations and transformation mechanisms in pure silica [134].

composition and temperature. In open systems, the chemical potential of the reacting species in the second phase provides an additional opportunity to influence the thermodynamic driving force.

In cases in which the growth rates of new phase are dependent on the transport of species to the growing interface and the thermodynamic driving force for change. For example, the instantaneous diffusive flux across an interface is given by Fick's first law has the form

$$J_i = -D_i \cdot dC_i/dx \tag{4.5.14}$$

If the concentration of the species is expressed in terms of chemical potential

$$d\mu_i = RT \ln C_i \tag{4.5.15}$$

The first law may be rewritten in the more general form

$$J_i = -(C_i \cdot D_i / RT) \cdot \text{Grad}i \tag{4.5.16}$$

where Grad i is the driving force for diffusion. The ratio D_i/RT is alternatively referred to as the mobility [138]. Then,

$$\text{Rate} = \text{mobility} \times \text{driving force} \tag{4.5.17}$$

Provided the mobility, driving force and interface geometry remains constant a constant rate of transformation is obtained.

A similar form of expression is obtained if the chemical processes at the interface are rate limiting

$$\text{Rate} = \text{chemical rate constant} \times \text{driving force} \tag{4.5.18}$$

The following examples demonstrate the typical effect of changing temperature on the rates of isothermal phase formations.

Example: The isothermal growth of crystals from a melt or glass

The growth velocities of devitrite ($Na_2O{\cdot}3CaO{\cdot}6SiO_2$) crystals from silicate melts have been measured as a function of transformation temperature. This was achieved by supercooling the melts and holding them under isothermal conditions. The resulting crystal growth rates are shown in Figure 4.5.9.

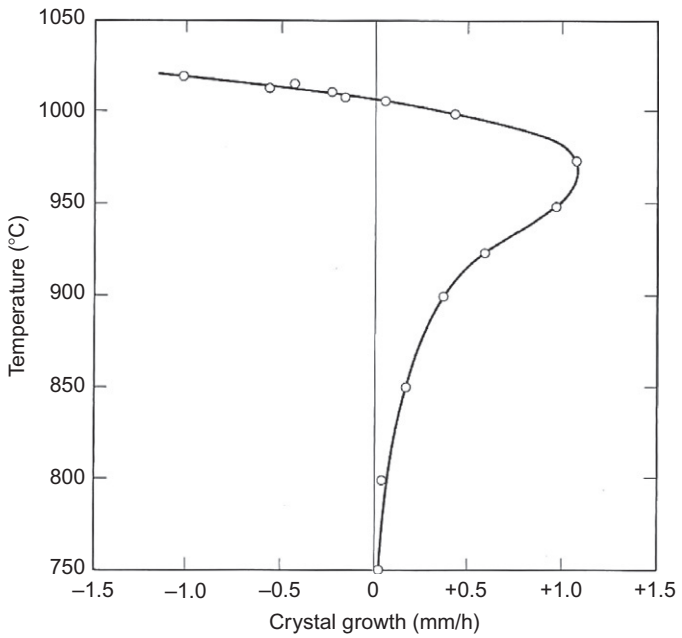


Figure 4.5.9 Initial growth rates of devitrite ($Na_2O{\cdot}3CaO{\cdot}6SiO_2$) crystals in oxide melts and glasses [134].

As the temperature of the transformation is lowered below the liquidus, in this case 100 °C, the growth rates of individual crystals at first increase with increased undercooling; at larger undercooling the rates decrease with increased undercooling. The system then is seen to exhibit a maximum in growth rate. At high temperatures, the mobility term is high relative to the thermodynamic driving force and an increase in the thermodynamic driving force results in an increased rate. The situation is reversed at low temperatures, the mobility term, which is largely determined by mass diffusivity in the bulk phase, decreases rapidly with decreasing temperature; hence the growth rates become limited by transport in the super-cooled liquid or glassy solvent phase. In effect, the rates of these transformations follow rate equations that are similar in form to those derived for nucleation phenomena.

Example: Precipitation of gibbsite from aqueous solutions (continuous planar stable growth)

In the Bayer process for alumina production, $Al(OH)_3$ aluminum trihydrate in the form of gibbsite crystals, is precipitated from supersaturated caustic solutions by undercooling the liquor. The growth rate of the trihydrate is controlled through the progressive cooling of the solution in a series of precipitation tanks. It has been shown [139] in experimental laboratory studies using a population balance model approach that the rate of growth of the gibbsite crystals is described by the empirical relation

$$\text{Rate} = 1.96 \times 10^{10}\left\{\left(A - A^*\right)/C\right\}^2 \cdot \exp\{-59{,}770/RT\}\,\mu\text{m s}^{-1}$$

where A and C are the Al_2O_3 and Na_2O concentrations in the solution in g l^{-1} respectively; A^* is the maximum Al_2O_3 solubility at any temperature. The observed rates of growth of the gibbsite crystals as a function of temperature for a range of initial Al_2O_3 concentrations in the liquor are shown in Figure 4.5.10. It is clear that for a given solution composition the maximum growth rate varies with solution temperature, as discussed previously in this section of the text, and that the maximum growth rates are dependent on the initial Al_2O_3 concentration in the solution.

The apparent second order rate law would indicate that the rate of growth of the gibbsite crystals are not limited by diffusion in the bulk fluid, nevertheless this system exhibits the maximum in growth rate as a function of temperature as a result of the changing driving force and chemical reaction kinetics at the crystal/solution interface.

The example given above involves the formation of a new phase at a defined reaction interface where there is direct contact between the solvent phases. This type of reaction can be undertaken in different conditions. In closed systems, the thermodynamic driving force for change and the growth rate will decrease as the solute concentration and activity changes with extent of reaction. In open systems, the process conditions and the chemical or thermodynamic driving force for reaction can be maintained throughout the reaction by continued supply of reactant materials.

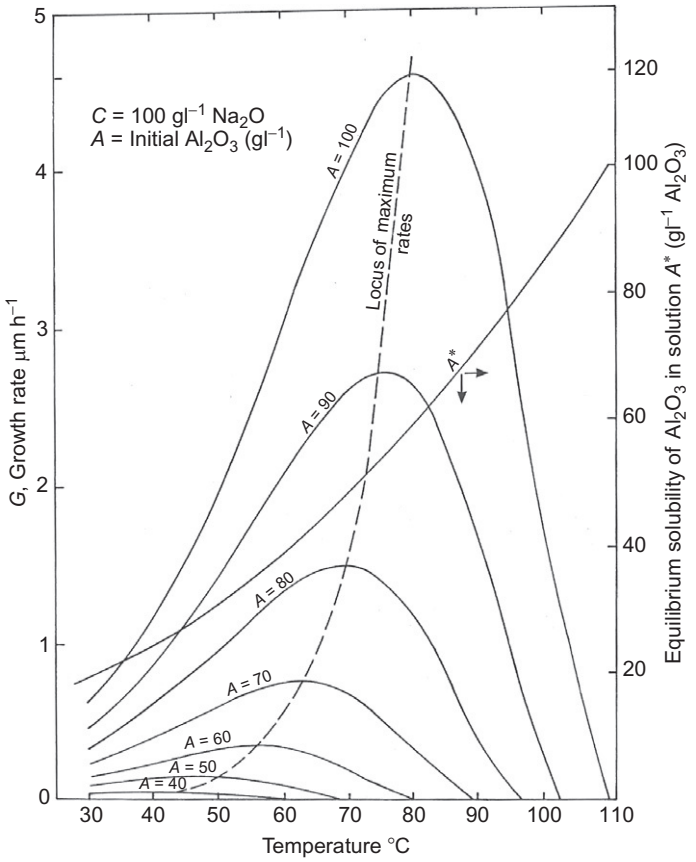


Figure 4.5.10 Growth rate of gibbsite, $Al(OOH)_3$, crystals from aqueous solutions as a function of temperature and *A*, the alumina concentration in the initial solution; *A** is the Al_2O_3 solubility at any temperature [139].

4.5.4. SUMMARY

Heterogeneous reactions involving the formation of new phases can take place through a number of different reaction mechanisms. To assist in understanding the origin of these differences and the implications for reaction kinetics, a system of classification has been introduced based on a hierarchy of criteria; at the highest level the reaction classification is based on the thermodynamic conditions for transformation, this is then subdivided into reconstructive and displacive changes. The reaction mechanisms observed with these different classes of reactions will be discussed further in Chapter 4.6.

REFERENCES

[131] J.W. Christian, Theory of Phase Transformations in Metals and Alloys, Pergamon, Oxford, 1965.
[132] J. Cahn, Trans. Met. Soc. AIME 242 (1968) 166.
[133] D.E. Porter, K.E. Easterling, Phase Transformations in Metals and Alloys, Van Nostrand Reinhold, New York, 1981.
[134] W.D. Kingery, H.K. Bowen, D.R. Uhlmann, Introduction to Ceramics, second ed., John Wiley, New York, 1975.
[135] R.J.D. Tilley, Defects in Solids, John Wiley, Hoboken, NJ, 2008.
[136] G.W. Groves, J. Mater. Sci. 18 (1983) 1615.
[137] W. Kurz, D.J. Fischer, Fundamentals of Solidification, third ed., Trans Tech, Switzerland, 2004.
[138] P. Kofstad, Non-Stoichiometry, Diffusion and Electrical conductivity in Binary Metal Oxides, Wiley-Interscience, New York, 1972.
[139] E.T. White, M. Steemson, D.J. Milne, Light Metals, TMS AIME, Warrendale, USA, 1984, p. 233.

CHAPTER 4.6

Chemical Kinetics + Phase Changes + Shape Changes

Peter Hayes
School of Chemical Engineering, The University of Queensland, Queensland, Brisbane, Australia

4.6.1. INTRODUCTION

The majority of reactions involving fluid/solid reactions encountered in metallurgical practice result in the formation of new phases or compounds. Common examples of these reaction systems include: the oxidation of metals and compounds, the reduction of metal oxides, and the decomposition of hydroxides, carbonates, and chlorides. Extensive experimental and theoretical studies have been carried out on the reactivity of these solids to measure, or to provide predictive models to determine, the rates of decomposition as a function of chemical and physical properties, such as, solids composition, particle size and sample porosity, and specific reaction conditions, such as, temperature and bulk gas composition. As demonstrated in many studies [140,141], a range of product microstructure types can be formed even in a single chemical system. Importantly, these product microstructures can significantly influence the overall reaction rates; hence, the need to better understand these complex chemical and solid state transformation processes.

In Chapter 4.5, two classes of phase formation reactions were identified, continuum reactions and heterogeneous reactions. In the present section, some further examples of heterogeneous reactions are now explored. The first examples considered are those in which only the solute species dissolved in the solid solvent or matrix take part in the phase formation reactions with species supplied by the fluid phase. The examples then move to considering process conditions under which the matrix material itself becomes unstable and reacts to form a new compound. A number of different reaction mechanisms and product morphologies are illustrated. These examples demonstrate that changes in process conditions can result in different products and product morphologies for a given starting material.

In Chapter 4.4 on "Reactions at Moving Oxide Interfaces," it was shown that, as a result of the chemical reactions occurring at the gas/solid oxide interface, the decomposing metal compound surfaces can change in shape from planar to unstable nonplanar geometries. In this chapter, the critical solid characteristics and process parameters for the formation of new product phases on these stable and unstable solid surfaces are

Treatise on Process Metallurgy, Volume 1
http://dx.doi.org/10.1016/B978-0-08-096986-2.00018-7
© 2014 Elsevier Ltd.
All rights reserved.

examined and defined; comparisons and analogies with microstructure formation in metal solidification systems and the crystallization of solids from supersaturated liquid solutions are made. It is argued that the cellular and dendritic pore structures formed in reactive gas/solid oxide systems are, from a theoretical perspective, directly analogous to the solid structures formed in solidification and solid/solid transformations, and as such similar mathematical treatments can be used to describe these phenomena.

Section 4.6.3 brings together the major findings of the theoretical analysis and demonstrates how the critical conditions for formation of the various product morphologies on metal production from metal compounds can be summarized and described graphically in the form of "*Morphology Maps*". These maps conveniently display the range of conditions under which selected morphologies are stable as functions of key process variables; the thermodynamic driving force for the reaction and the reaction temperature, for a given gas reaction system and initial oxide composition.

Section 4.6.4 summarizes the various elementary reaction processes that can occur during reactions at fluid/solid interfaces during phase formation reactions.

Throughout the following analysis of metal oxide reduction reactions it is assumed that the reaction rates at the oxide and metal surfaces are not limited by mass transfer in the gas phase, that is, gas film mass transfer and gas phase porous diffusion processes are rapid relative to the rates of the elementary chemical reactions occurring in the systems. Under these scenarios, the bulk gas composition is identical to that at the gas/solid reaction interface.

4.6.1.1. Chemical Reactions on Metal Surfaces

In the examples given in Chapters 4.2 and 4.4, solute species are transferred from one phase to another; no new phases were formed and these species were assumed to remain in solution in the original phases. The selective reaction of species in solution resulting in the formation of new compound can lead to several variants in behavior. These various phenomena can be illustrated through examination of the oxidation of alloys under a range of process conditions.

Example Oxidation of Fe Si alloys

The high temperature oxidation of solid iron–silicon alloys has been undertaken for a range of oxygen partial pressures at 1123 K [142]. In this case, the potential reactant species are the O, Si, and Fe. The microstructures formed as a result of these reactions are illustrated in Figure 4.6.1; the initial oxygen concentration in the metal at the start of the reaction is essentially zero. At very low partial pressures, there is no reaction between the O, Si, and Fe species; these coexist in solid solution in the iron matrix (Figure 4.6.1e).

As the oxygen partial pressure in the gas phase is increased the formation of stable SiO_2 phase becomes thermodynamically favorable. Following the initial adsorption of oxygen at the gas/metal interface concentration gradients are established in the gas and metal phases, which, in this situation, are behaving as solvents supporting the O and Si reactant

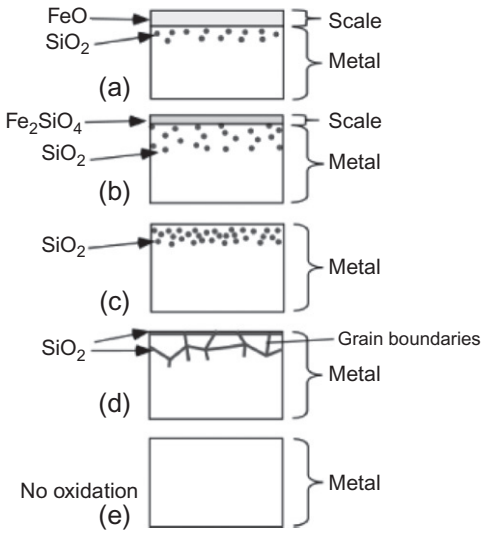


Figure 4.6.1 Schematic representation of the scale structures formed on oxidation of Fe–Si alloys. (a) Formation of FeO, (b) formation of internal oxide scale of SiO_2 and $2FeO{\cdot}SiO_2$ scale, (c) formation of internal oxide scale of SiO_2, (d) formation of external oxide scale of SiO_2, and (e) no oxidation [142].

species, respectively. The transport of oxygen in the gas phase to the gas/metal interface is rapid. The diffusivity of O atoms in the iron matrix is low and, at low oxygen partial pressures, so too is the oxygen solubility in the iron. The net result is that the oxygen flux from the gas/metal interface into the iron matrix is extremely low; so low that the counter diffusion of silicon atoms from the bulk metal to the interface is relatively faster. Silicon and oxygen atoms therefore meet at the external surface of the sample, and the grain boundaries near the surface, to form the SiO_2 scale layer (Figure 4.6.1d).

As the oxygen partial pressure in the gas phase is increased so too is the solubility of oxygen in iron, and the O concentration difference between the gas/metal and the bulk metal. The higher O flux from the gas/metal interface results in O diffusion into the bulk iron. At some critical level of supersaturation, the O and Si atoms in the matrix react to form and grow individual solid SiO_2 nuclei within the matrix; this process is commonly referred to as internal oxidation (Figure 4.6.1c). The limit of penetration of the internally oxidized layer in the alloy corresponds approximately to the position in the sample at which the critical condition for SiO_2 formation is achieved. The depth of penetration of the oxidized layer increases with time as further oxygen diffuses into the metal from the surface. The flux following Fick's first law, $J_o = -D_o \cdot dC_o/dx$, decreases as the depth of the internally oxidized layer increases; the thermodynamic limits determined by the gas phase and the critical conditions for the formation of the SiO_2 remain unchanged. As a consequence the rate of growth of the oxidized layer decreases with increasing reaction time.

Further increase in the oxygen partial pressure in the gas phase results in the critical condition for the formation of the phase, $2FeO{\cdot}SiO_2$, fayalite. As this thermodynamic limit is first reached at the gas/metal interface, where there is direct contact between gas and metal, this solid fayalite phase nucleates and grows across the surface of the solid alloy (Figure 4.6.1b). Although this cuts off direct contact between the gas phase and the underlying oxide there is still an oxygen potential generated at the metal/$2FeO{\cdot}SiO_2$ interface, so oxygen continues to penetrate into the bulk matrix and internal oxidation proceeds.

At still higher oxygen pressures, the iron oxide on its own becomes stable and a planar dense layer of FeO, wustite, scale, is formed at the gas/solid interface (Figure 4.6.1a). A summary of the experimentally determined critical combinations of oxygen pressure and silicon concentration in the alloy are shown in Figure 4.6.2.

The formation of *dense reaction product scales* is a common outcome of fluid/solid reactions. In these cases, the product phase is a dense solid that covers the interface. The formation of these dense scales means that the fluid phase is no longer in direct contact with the original solid phase; nevertheless the reaction product layer continues to increase in thickness with time albeit at a much reduced rate. The explanation for how this can occur, the reaction mechanism and the subsequent growth of the layers has been the subject of many studies. The oxidation of metals serves to illustrate the phenomena taking place during this class of reactions.

Example The oxidation of metals

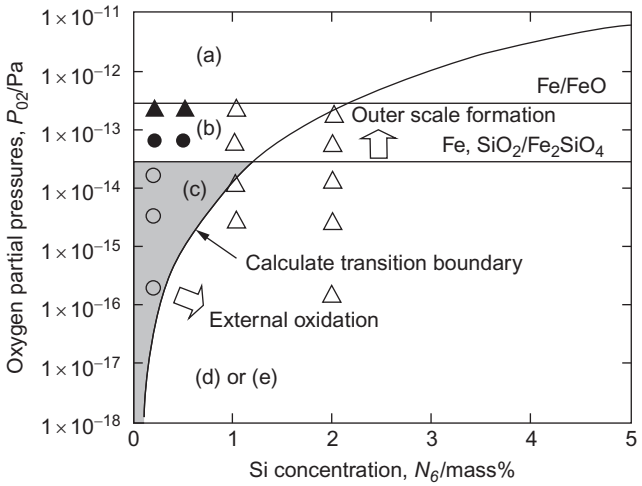


Figure 4.6.2 Transition in phase transition mechanism with increasing oxygen partial pressure and silicon concentration in Fe–Si alloys at 1123 K; open circles indicate internal oxidation, filled circles indicate internal and external oxidation, open triangles indicate external oxidation, and filled triangles exhibit outer scale formation [142].

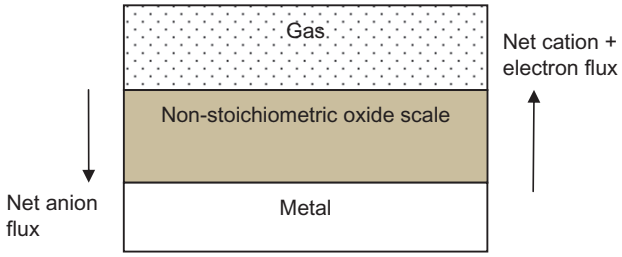


Figure 4.6.3 Schematic illustration of dense oxide scale formation on a metal surface.

The general case for the formation of dense oxide scale on the metal surface is illustrated in Figure 4.6.3. It can be seen that the initial single reaction interface between gas and metal is replaced by two interfaces: gas/oxide and oxide/metal. Chemical reaction can occur at either of these interfaces. Importantly it should be appreciated that oxides are never exactly stoichiometric, these compounds always contain defects in the crystal lattice [143,144]. These defects are in a number of forms, such as *intrinsic defects*, cation vacancies, cation interstitials, anion vacancies, anion interstitials, electron holes (electron deficient ions), and *extrinsic defects* that are induced by the presence of impurity elements. As a result of the chemical reactions at the interfaces concentration gradients are established across the reaction product thickness. The oxygen concentration is highest in contact with the oxidizing gas and is lowest in equilibrium with the metal phase. The cation concentration in the oxide scale is the reverse; it is highest in contact with the metal and lowest in contact with the gas.

The net direction of growth of the scale is determined by the relative fluxes of the cations and anions. In most oxides and sulfides, the fluxes of the smaller cations are significantly greater than that of oxygen or sulfur ions, the scale therefore grows by addition to the outer gas/oxide surface, that is, there is a net transfer of metal through the scale to the gas/oxide interfaces.

It has been shown that the rate of scale growth can be described by equation of the form [143,144]

$$\mathrm{d}n/\mathrm{d}t = (A/\xi)\left\{1/F^2\int_{\mu_x^{\mathrm{i}}}^{\mu_x^{\mathrm{o}}}(t_1+t_2)t_3\sigma\cdot\mathrm{d}\mu_x/\mathrm{d}z\right\}\text{equivalents s}^{-1}$$

where ξ is the instantaneous scale thickness, σ is the total electrical conductivity, t_1, t_2, and t_3 are the transference numbers for cation, anion, and electrons, respectively, $\mu_x{}^{\mathrm{o}}$ and $\mu_x{}^{\mathrm{i}}$ are the chemical potentials for the nonmetal species at the internal and external interfaces, z is the scale thickness.

The integrated form of the rate equation reduces to the well-known parabolic expression

$$\xi^2 = 2k_p t.$$

This expression has been shown to be valid for high temperature oxidation processes. The absolute values of the growth rates may depart from those predicted by bulk diffusivity of the ions as alternative pathways such as grain boundary diffusion may become significant at lower temperatures. These pathways and associated transport mechanisms are illustrated in Figure 4.6.4. As the transport of the ions through the scale is directly related to the diffusivity and conductivity, it can be shown that the rate constant, k_p, is also directly proportional to $PO_2^{1/n}$, where n is the oxidation state of the cation species.

At low temperatures and nonplanar geometries, the scale formation rate may depart from this parabolic relationship for a number of reasons, including spalling or breakdown of the product layer. This may lead to pseudolinear behavior if a porous scale is produced or discontinuous rate behavior if periodic mechanical breakdown of the scale occurs [146].

The above examples illustrate once more that by changing the relative rates of chemical reactions and mass transfer processes at the reaction interface it is possible to change the product morphologies formed and the rate limiting reactions in these processes.

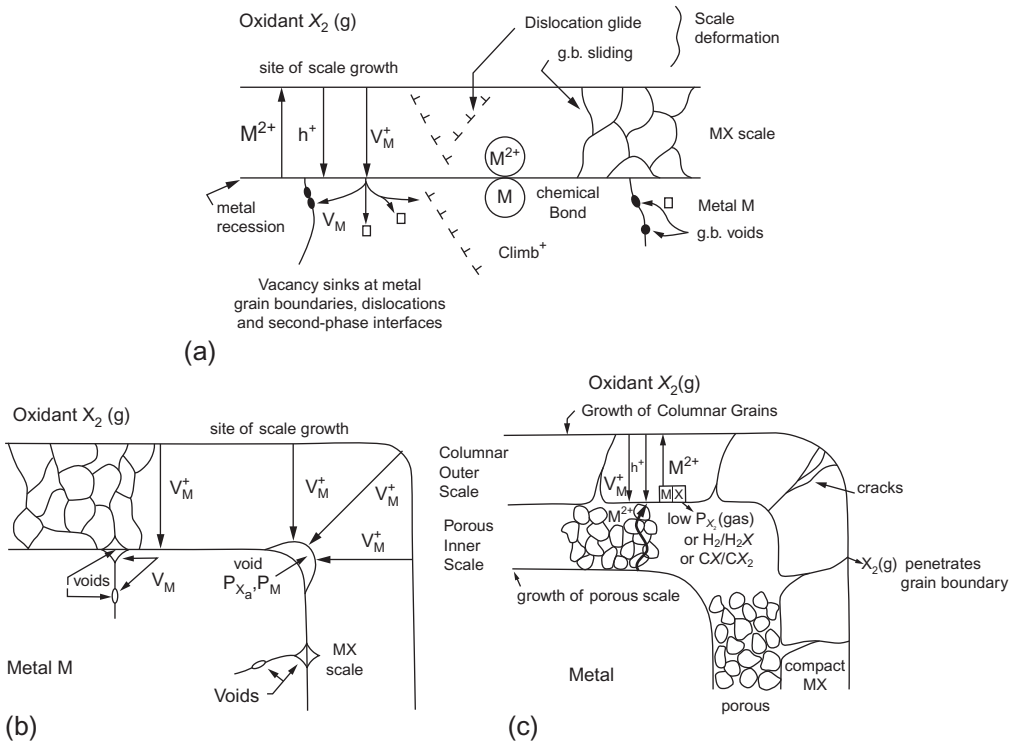


Figure 4.6.4 Schematic illustrations of the elementary reaction steps occurring during the growth of oxide scales by cation diffusion during the oxidation of metals [145].

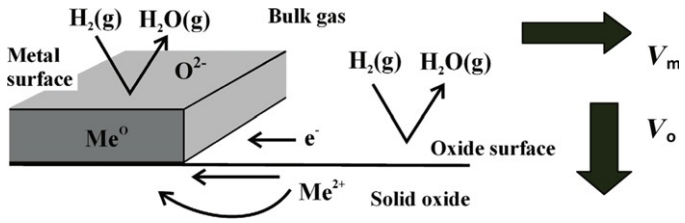


Figure 4.6.5 Illustration of the simultaneous decomposition of oxide and the growth of metal at the gas/solid interface in a reactive gas atmosphere [147]. The metal phase is shown as spreading across the interface at velocity, V_m, and the oxide surface in moving in a perpendicular direction at velocity, V_o.

This is an important concept now applied to consideration of systems in which the metal phase is formed on an oxide surface as a result of exposure to reactive gas mixtures. After the initial reaction of oxide with the gas, metal phase nucleation occurs at the gas/oxide interface. The simultaneous reactive decomposition of the oxide phase and the growth of the metal phase across the oxide surface is illustrated schematically in Figure 4.6.5.

The removal of oxygen from the system through reactions on the metal surface is thought to occur in a series of steps involving movement of oxygen from the oxide on to the surface of metal and then subsequent removal of this adsorbed oxygen by reaction with the gas [147]. The removal from the metal surface is described by reactions of the form

$$O^{2-}(\text{ads}) + 2H(\text{ads}) \rightarrow H_2O(\text{ads}) + 2e^- \tag{4.6.1}$$

The removal of oxygen from the metal and oxide surfaces leaves behind excess metal cations adjacent to the metal. These excess cations are readily incorporated into the periphery of the metal nucleus through the electrochemical reduction reaction,

$$Me^{2+}(\text{oxide}) + 2e^- \rightarrow Me^{o}(\text{metal}) \tag{4.6.2}$$

The addition of metal to the periphery of the metal leads directly to the growth of the metal across the surface of the oxide at velocity, V_m,

$$\begin{aligned} V_m &= R_m(b_m/\rho_m h_m) \\ &= (b_m/\rho_m h_m)\cdot\phi^1_m P_{H_2}\left[1 - (P_{H_2}/P_{H_2O})_{eq}\cdot(P_{H_2}/P_{H_2})\right] \left(ms^{-1}\right) \end{aligned} \tag{4.6.3}$$

where ρ_m is the density (mol m^{-3}) of metal Me, ϕ^1_m is the apparent chemical rate constant for the metal surface (mol m^{-2} s^{-1} atm^{-1}), h_m is the thickness of the metal layer (m), and b_m is the breadth of the reaction rim at the edge of the growing metal layer (m).

4.6.2. METAL GROWTH MORPHOLOGIES

The discussion in Section 4.4.3 has been focused on the stability of the oxide surface, as this is the material that is decomposing in the presence of the reactive gas under the various process conditions. Attention is now drawn to the secondary reaction: the formation and growth of the solid metal or metal oxide product phase. The decomposition of the original oxide into planar interface, or into tunnels or pores in the oxide, can take place before metal formation on the oxide surface has occurred, and after the metal/second oxide phase is present on the surface. It is at this point that some of the differences in the characteristics between liquid/solid and solid/solid transformations, and as a result of the gas/solid reactions start to become more apparent.

For clarity of the discussion, the focus will be on scenarios in which metal phase is present on the oxide surface and the relative movement of the gas/oxide and metal/oxide interfaces will be examined. As discussed in Chapter 4.4 the removal of oxygen from the oxide surface by reaction with the gas phase result in progressive advance of this interface into the bulk materials, that is, perpendicular to the reaction interface at a velocity, V_o. Removal of oxygen by chemical reaction on the metal surface results in the addition of metal to the periphery of the metal through Equation (4.6.2), and leads directly to the growth of the metal across the surface of the oxide parallel to the gas/oxide interface at a velocity, V_m. Based on this simple model the conditions for the formation of different metal product morphologies can be examined. All reaction systems involving oxide decomposition to metal in reactive gases can be divided to a first approximation into three classes depending on the ratio of the rates of the chemical reactions on the oxide and metal surfaces.

1. If $V_o > V_m$, that is, the rate of removal of oxygen from the surface of the oxide is greater than on the metal surface, then the oxide surface will always remain exposed to the reactive gas phase, that is, the oxide is predominant.
2. If $V_o < V_m$, that is, the rate of removal of oxygen from the surface of the oxide is less than on the metal surface, the oxide surface will become covered with a metal layer, that is, the metal is predominant.
3. If $V_o = V_m$, then both oxide and metal remain exposed to the gas throughout the reaction; this corresponds to the special case of coupled or cooperative growth of metal and pores.

4.6.2.1. Dendritic Pore Formation

Each of these cases is now considered in turn. If $V_o > V_m$, the movement of the interface into the bulk oxide will stay ahead of the metal. If $V_o \gg V_m$, the resultant product morphology development can be treated as separate sequential reaction steps, this is true whether planar or nonplanar oxide interface is created. In all of these scenarios, chemical

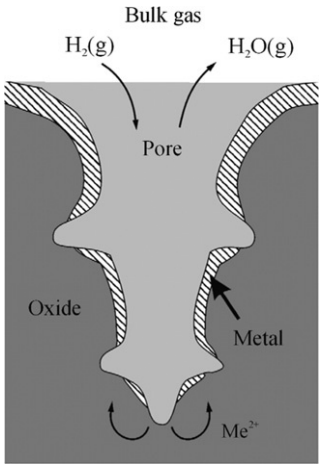


Figure 4.6.6 Schematic illustration of dendritic pore formation with trailing metal layer [147].

reactions are occurring on the oxide surface, and mass transfer is simultaneously occurring on the surface and into the bulk oxide. If the interface is planar, the steady state interface velocity is determined through solution of the moving boundary problem outlined in Section 4.4.3. For dendritic growth, the tip velocity is determined by the diffusion of solute away from the moving interface [148]. The formation of the 3D curved dendrite tip enables the rapid dispersion of the solute into the bulk such that the composition of the tip approaches that of the bulk oxide rather than equilibrium with the gas phase. The maintenance of the high thermodynamic driving force at the dendrite tip and the high surface roughness created by the local atomic rearrangement means that the movement of the oxide surface will always stay ahead of the growing metal layer formed on the pore wall. This dendritic pore structure with the trailing metal layer is illustrated in Figure 4.6.6.

4.6.2.2. Metal Whisker Growth

The condition for $V_o > V_m$ can also be achieved on planar oxide surfaces by effectively slowing down or stopping reaction on the metal surface, that is, $V_m = 0$. The reaction of adsorbed oxygen on the metal surface with CO/CO_2 and H_2/H_2O gases has been shown to be sensitive to the presence of impurity elements that poison the metal reaction surface, occupying reactive metal adsorption sites in preference to the oxygen. These poisons include commonly encountered surface active species on metals, for example, sulfur and phosphorus on iron [149]. In these situations in which although reduction takes place, the oxide surface remains planar, no or slow lateral metal growth takes place, metal whisker growth can occur on the oxide surface. In the case of iron oxide, reduction oxygen is then removed primarily from the oxide surface, as described by Equation (4.6.1).

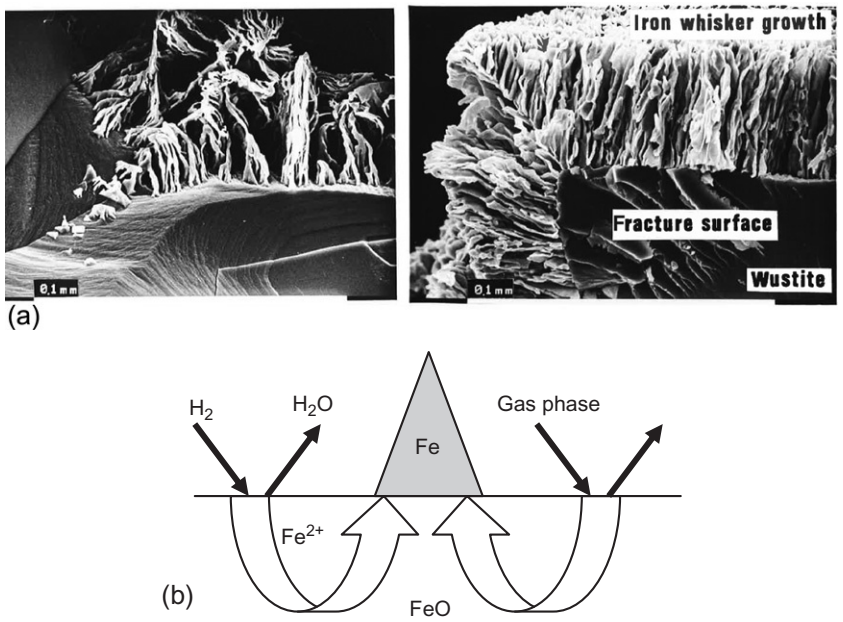


Figure 4.6.7 (a) Formation of iron metal whiskers on reduction of iron oxide [150]. (b) Mechanism of formation of iron metal whiskers on reduction of iron oxide [150].

The excess metal ions generated by the reduction reaction move through the bulk oxide and deposit at the *base* of the existing metal nuclei through the electrochemical reduction reaction (4.6.2). The result is the metal phase literally grows out from the surface and metal whiskers are formed (see Figure 4.6.7a and b) [150].

4.6.2.3. Continuous and Discontinuous Metal Layer Growth

Under conditions where $V_o < V_m$, the oxide surface will become covered with a metal layer. Importantly the formation of a dense solid product layer on the oxide surface has the immediate effect of cutting off direct contact between the reactive gas and the underlying oxide phase, resulting in a step change in rate limiting reaction mechanism.

If the dense metal product completely covers the oxide surface (Figure 4.6.8a) and remains as a solid layer covering the surface, then any subsequent removal of oxygen from the oxide can only occur by dissolution of oxygen in the metal phase transfer by diffusion through this dense metal layer, and reaction at the gas/metal surface. As the chemical reaction rates, at the gas/metal surface, are high relative to oxygen permeability in most metals the rates will be limited by oxygen diffusion in the solid state [151].

The next important point is the observation that the dense metal product covering the oxide surface can periodically break down (Figure 4.6.8b). In the case of iron oxides, it has been found [152–156] that in CO/CO_2, H_2/H_2O, and $CO/CO_2/H_2/H_2O$ gas

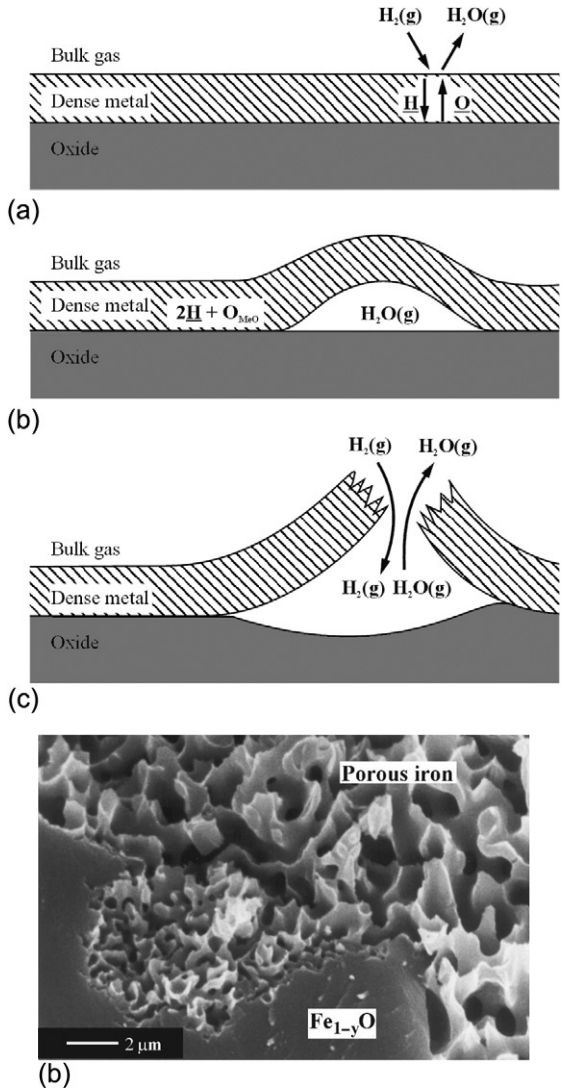


Figure 4.6.8 (a) Schematic illustrations of (a) dense metal layer on a planar oxide surface, (b) and (c) discontinuous pore growth through metal layer breakdown [147,152]. (b) Periodic breakdown of dense iron layers on wustite leading to discontinuous advance of the reaction interface and a porous iron product [156].

mixtures the breakdown of face centered cubic iron during reduction from wustite ($Fe_{1-y}O$) depends principally on thermodynamic driving force for reaction; at low thermodynamic driving forces a dense layer of metal product forms on the oxide surface; at high thermodynamic driving forces the breakdown of the metal layer occurs. A similar behavior has been observed in the $NiO/H_2/H_2O$ system [157–158]. The critical

thermodynamic driving force, ΔG, depends on the chemical system and the reaction temperature. Above the critical potential a dense metal product is formed initially at the reaction interface but the physical breakdown or rupture of the metal layer, exposing the gas once more to the oxide surface, enables further direct reaction between the gas and the bulk oxide and oxygen removal from the oxide surface to occur. The reaction cycle is repeated resulting in the discontinuous growth of the reaction interface, the interface velocity being principally dependent on the frequency of breakdown or bursting of the metal layer. An example of this cyclic sequence of events taking place during the reduction of iron oxide in reactive gas mixtures is shown in Figure 4.6.4, the smaller pores at the reaction interface are recently formed; the larger pores adjacent to this area indicate the interface has not moved forward and the dense metal layer still covers those portions of the interface.

The mechanism of breakdown is not totally characterized, however, it appears to be associated with the chemical reactions at the interface rather than simple mechanical failure. Experimental studies on iron and nickel oxide reduction point to the likely cause involving the decomposition of the gas phase on the covering metal surface, for example, H_2 decomposing and dissolving in the metal as H atoms, CO decomposing to form C in solution in metal. Solid state diffusion of the H and C solute species can then take place from the gas/metal interface to the metal/metal oxide interface. At the metal/metal oxide interface, reaction is delayed until the nucleation or formation of a void at the interface, at which time the H and C can continue to react and the gas pressure in the void increases until the pressure is sufficient to burst the metal layer. The critical condition for the transition from dense metal to periodic breakdown appears to be associated with the thermodynamic driving force for the reaction rather than the reactant gas species, that is, H_2/H_2O or CO/CO_2 themselves. The thermodynamic driving force may simply determine the nucleation frequency of the gas bubbles but there may be other explanations for the phenomenon [152].

A metal layer can form under conditions in which $V_o \gg V_m$, as in the dendritic pore structure but in this case the initial reaction front, the oxide surface at the pore tip, always remains exposed to the gas; the dense metal layer forms on the slower moving side walls of the pores in a subsequent reaction step. This may result in the pore surfaces being covered by dense or porous metal product depending on the thermodynamic potential in the gas phase.

4.6.2.4. Coupled Growth

The conditions for $V_o = V_m$, at which the velocities of the oxide and metal surface are equal and a planar reaction interface is formed, represents a special case. The cooperative or coupled growth of pores and metal in metal oxide reduction systems are shown schematically in Figure 4.6.9. In the case of gas/solid oxide reduction reactions, the metal moves from the oxide to metal phase, the oxygen partitions to the gas phase rather than

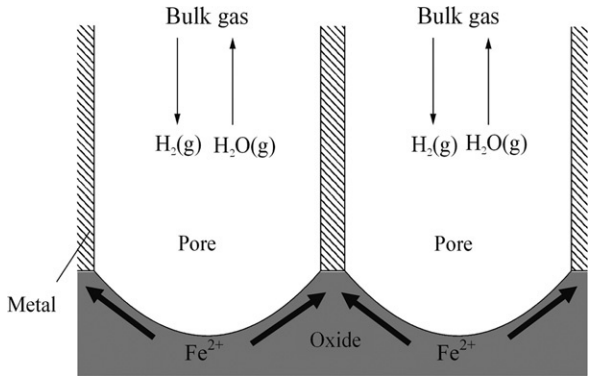


Figure 4.6.9 Schematic illustration of coupled growth of pores and metal during gaseous reduction of metal oxide [147,156].

to a second solid product phase. The coupled growth of pores and metal is of particular practical significance as in this situation both the original oxide and metal surfaces remain continuously exposed to the gas throughout the reaction. If this product morphology can be retained throughout the reaction over product layer thicknesses that are comparable with oxide particle sizes encountered in industrial processes, this offers the possibility of high reduction rates and high extent of reaction.

4.6.2.5. Analogies with Solid/Liquid and Solid/Solid Systems

The coupled growth morphology illustrated in Figure 4.6.10 can be viewed as a direct analogy of eutectic and eutectoid reactions that have been observed in liquid/solid [148] and solid/solid [160] transformations (Figure 4.6.11). Both involve the decomposition of a single phase into two phases. In the case of the reactive decomposition of wustite $Fe_{1-y}O$, this involves the formation of the solid iron phase and the gas phase, and the partitioning of elements Fe and O between these two phases. In the case of the eutectic reaction solute, species in the liquid phase, L, partition into two new phases, α and β. In both cases, a combination of mass transfer processes and phase formation are required.

Further analogies can be made for the complex reaction systems involving simultaneous multiphase transitions. Figure 4.6.12 shows microstructures obtained from a polished section of a partially reduced dense hematite, Fe_2O_3, sample, illustrating the Fe_2O_3/Fe_3O_4, $Fe_3O_4/Fe_{1-y}O$ and $Fe_{1-y}O/Fe$ interfaces, and the final porous iron product at the particle surface [161]. The initial reactions and phase transitions involve the formation of dense Fe_3O_4. and wustite ($Fe_{1-y}O$) layers on the surface of the magnetite. In the presence of the reactive gas, this magnetite and wustite becomes unstable, and decomposes into dendritic gas pores that approach in the hematite/magnetite interface. Subsequently the pore walls of the wustite are covered with a dense iron layer, and this layer breaks down by the mechanism described earlier in this section. This transformation

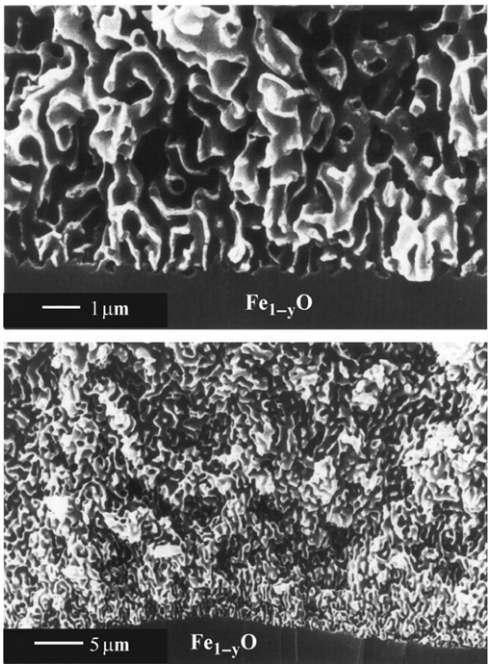


Figure 4.6.10 Coupled growth of metal and gas pores in the oxide [156].

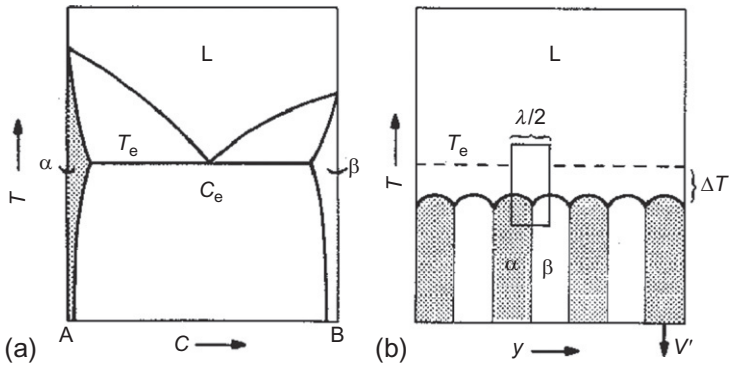


Figure 4.6.11 Schematic illustration of a eutectic reaction system; (a) phase equilibria of a simple eutectic system and (b) idealized nonfaceted eutectic structure.

can be viewed as analogous to a peritectic solidification reaction in a continuously cooled system (see Figure 4.6.13) in which for an initial liquid composition, C_o, a primary phase α is formed at temperature T_L, the surface of this phase is subsequently covered by the secondary phase, β, at T_p, the peritectic temperature.

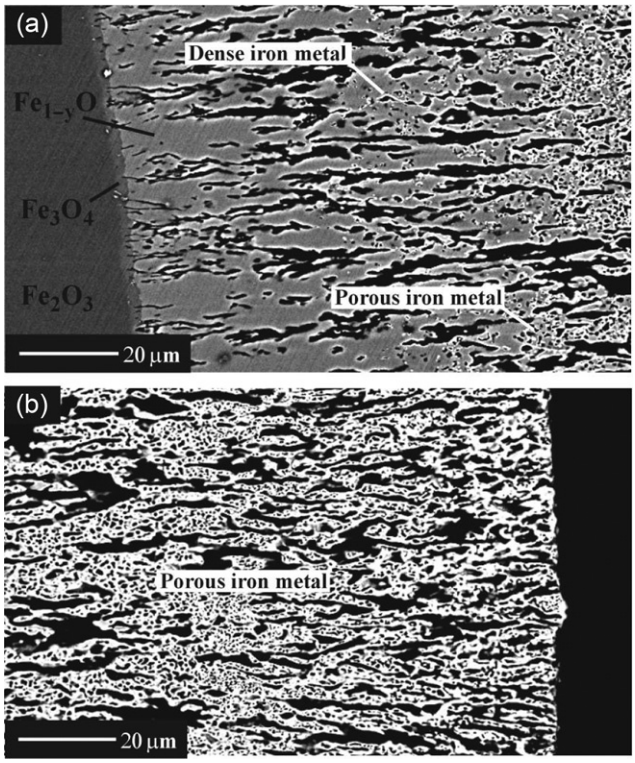


Figure 4.6.12 Typical microstructures obtained from a polished section of a partially reduced dense hematite sample (pure CO, 1 atm, 900 °C). (a) the Fe_2O_3/Fe_3O_4, $Fe_3O_4/Fe_{1-y}O$ and $Fe_{1-y}O/Fe$ interfaces, and (b) the final porous iron product at the particle surface [161].

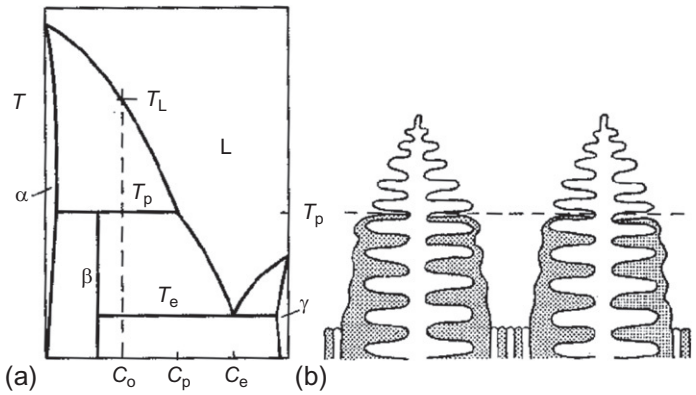


Figure 4.6.13 Schematic illustration of a nonisothermal solidification in a peritectic reaction system; (a) phase equilibria of a simple peritectic system, (b) idealized nonfaceted peritectic structure with the formation of primary phase, α, followed by a secondary β phase.

In Section 4.5.3, examples of phase transformations taking place through shear or displacive mechanisms were briefly mentioned in relation to polymorphic transformations. These changes in crystal structure are observed in cases where there are favorable crystallographic relationships between the structures in the original and the product materials. Although, in the case of solids, the Gibbs free energy change in ΔG with pressure is small, there are a few practical examples where the free energies of the structures are so close together that even these minor changes are sufficient to change the balance of stability. These examples include stress induced transformations, such as martensitic transformations in steels [162], and the tetragonal-monoclinic transformations in partially stabilized zirconia [163]. Despite the low driving forces for transformation the reactions occur rapidly because the mechanisms involve only minor adjustments to individual atom positions rather than reconstructive transformations.

The thermodynamic driving force for these displacive transformations can be induced by not only temperature and mechanical stress changes but also by chemical reactions occurring within the system. Typically these are chemical reactions occurring at the surfaces of solids; growth of the new phase through the parent solid phase occurs through shear or military transformations along specific crystal planes and in specific directions. The transformations are such that only minor movements of individual atoms are required to change the crystal structure. This enables these reactions to occur rapidly and selectively penetrate the material, potentially leading to macroscopic changes to physical properties of the materials.

Examples of these types of transformations in process metallurgy include the reversible reaction of hexagonal Fe_2O_3 to face-centered cubic Fe_3O_4 under reducing and oxidizing conditions [164], and the analogous chromite spinel/sesquioxide oxidation/reduction transformations [165]. These reactions appear to take place through nucleation of the product phase at the gas/solid interface and propagation through the bulk structures through a shear transformation on the close-packed oxygen planes in these crystal structures. The rates of these shear transformations are orders of magnitude faster than are observed for bulk diffusion processes. By way of illustration, depending on the temperature and driving force, these transformations can transverse several millimeters of solid in a matter of seconds. Examples of these structures in partially reduced rutile are shown in Figure 4.6.14.

These displacive reaction mechanisms appear to be operative under conditions of relatively low thermodynamic driving force for transformation. It has been shown [164], for example, in the case of gaseous reduction of Fe_2O_3 to Fe_3O_4 that there is a critical thermodynamic driving force that must be exceeded in order to obtain the transition from a displacive reaction mechanism, resulting in dense lath structures, to a reconstructive mechanism, involving the formation of gas pores in the magnetite. This condition is illustrated in Figure 4.6.15 and is shown to hold over a range of temperatures. Reduction of Fe_2O_3 at high thermodynamic driving forces results in a reconstructive transformation

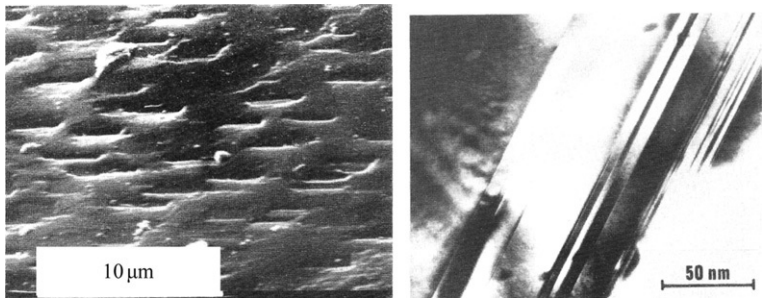


Figure 4.6.14 Electron micrographs showing the chemically induced phase transformations during the reduction of natural rutile, TiO_2 by H_2, (a) SEM micrograph showing reduced rutile nuclei formed at the surface of rutile, (b) transmission electron micrograph showing the shear planes penetrating the bulk structure [166].

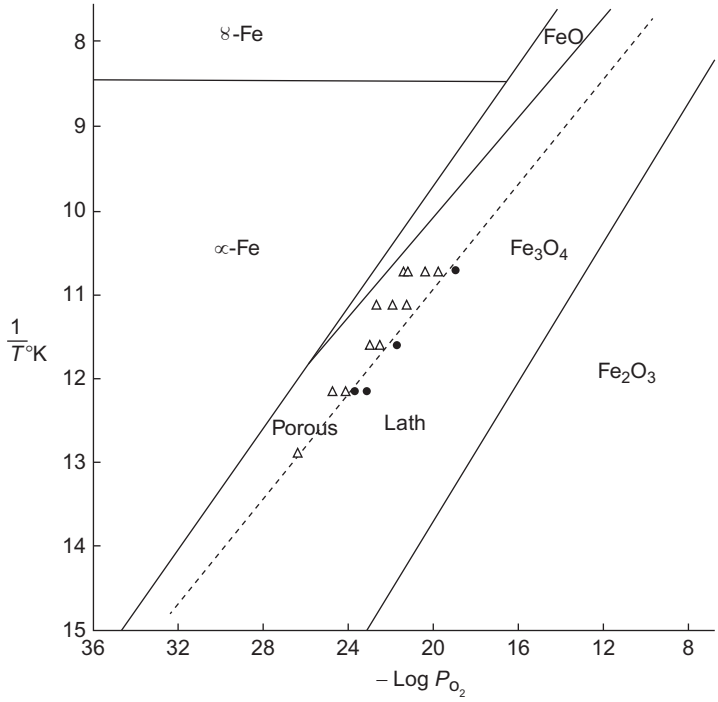


Figure 4.6.15 Critical conditions for the reconstructive/displacive formation Fe_3O_4 on reduction of Fe_2O_3 in CO/CO_2 gas mixtures [164].

mechanism involving the coupled growth of 10–20 nm sized gas pores and magnetite [167]; these structures appear to be analogous to those formed in eutectic and eutectoid reactions (Figure 4.6.16a). The lath type structures Figure 4.6.16b superficially resemble those formed as a result of martensitic transformations.

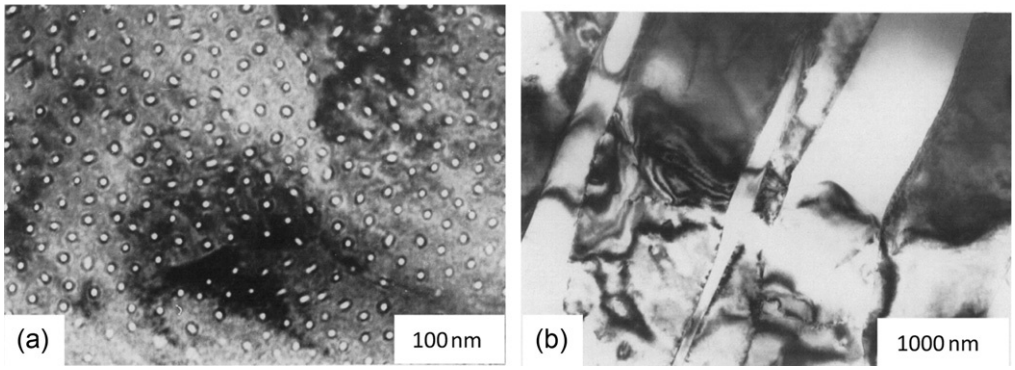


Figure 4.6.16 Transmission electron micrographs showing the formation of (a) gas pores and (b) dense lath Fe_3O_4 structures on reduction of Fe_2O_3 in H_2/H_2O gas mixtures [167].

From the above discussion, it is clear that a range of reaction product morphologies that result from decomposition of the oxide and the growth of the metal phase can be formed as the reaction with the gas phase goes to completion. The rate limiting reactions for the formation of each of these product morphologies will be different, and consequently, as will be the response of the overall rates of transformation to changes in key process variables. It is therefore quite conceivable that a range of reaction mechanisms and product morphologies can appear with changing process conditions, and that step changes to reaction rates may occur as changes in product morphology take place as the reactions progress.

4.6.3. MORPHOLOGY MAPS

It is convenient to summarize all of the conditions for the formation of the various interface structures discussed above in graphical form in "morphology maps," which can be constructed for each set of initial solids and process conditions [147]. These morphology maps can be plotted using the thermodynamic driving force, ΔG, the interface velocity, V, and reaction temperature as variables.

Figure 4.6.17 illustrates a ΔG versus V map for conditions in which $\phi^1 P_{H_2}$ and $\Delta C_{ox}/D$ are low. Starting at the equilibrium gas composition, the thermodynamic driving force, $\Delta G = 0$, and the interface velocity $V = 0$, following the curve representing the nominal chemical reaction rate on the oxide surface $0ij$, it can be seen that a planar oxide surface is stable under all conditions. For the thermodynamic driving forces between 0 and i, a planar dense metal layer morphology is formed, as $V_o < V_m$ and the metal phase is dominant on the planar oxide surface under these conditions. As indicated in the previous discussion, the overall reduction rate when a dense metal product layer is formed will be determined by oxygen permeability through the metal layer. Between i and j, the initial dense metal layer that forms on the oxide surface periodically breaks down and is

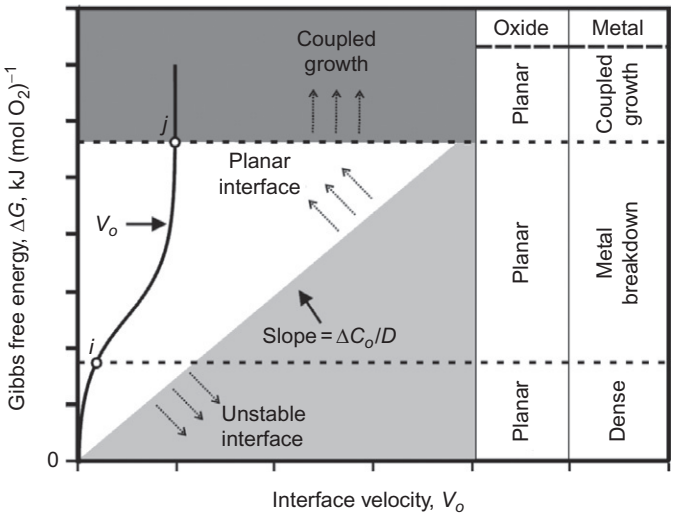


Figure 4.6.17 Predicted oxide and metal growth morphologies for ϕ low, $\Delta C_o/D$ low, $\alpha_c/\alpha < 1$, facetted oxide, $P_{H_2} + P_{H_2O} =$ constant [147].

subsequently reformed resulting in discontinuous movement of the interface, the rate of reduction being determined primarily by the frequency of the breakdown of the metal layer. The mean interface velocity is determined by considering both the time for which the interface is stationary due to the formation of the dense metal layer and the time over which the interface is actually moving forward into the bulk oxide. Above j a coupled growth morphology is formed at high thermodynamic driving forces, where $V_o = V_m$. This morphology results in continuous access of reactant gas to the oxide surface and the rates of reaction are determined by the chemical reaction rate between the gas and atomically rough oxide surfaces, and the gas and oxygen adsorbed on the metal surfaces.

Figure 4.6.18 illustrates a ΔG versus V map for conditions in which $\phi^1 P_{H_2}$ and $\Delta C_{ox}/D$ are high. Again starting at the equilibrium condition $\Delta G = 0$ and following the curve 0xyz; between 0 and x a planar dense metal layer is formed. Above x the oxide surface will be unstable and will evolve into cellular or dendritic pores. Between x and y the side walls of the pores in the oxide will be covered by a dense iron metal layer. Above y the dense metal layer on the pore walls will break down to form a porous metal product. At thermodynamic driving forces above z-coupled growth of pores and metal product is predicted.

The relative rates of the chemical reaction and the conditions for the formation of a range of product morphologies have been described in terms of the thermodynamic driving force, ΔG and interface velocity, V_o. All of these process characteristics, the thermodynamic and physicochemical properties of the solids and reactive gases, the ranges of solid stoichiometries, chemical reaction rates, and diffusivities are temperature dependent

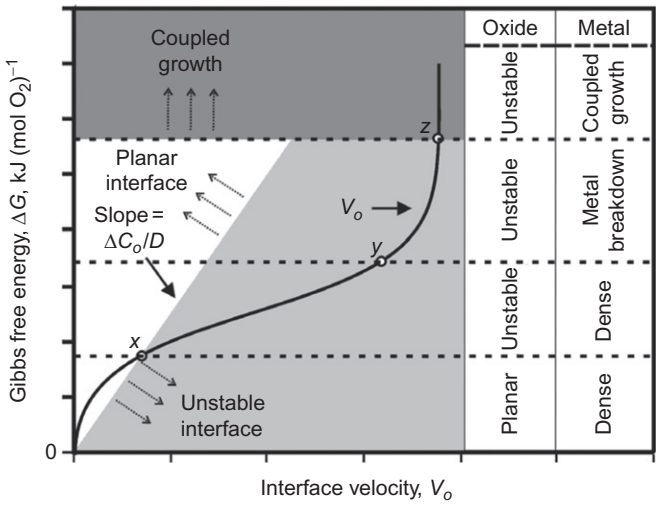


Figure 4.6.18 Predicted oxide and metal growth morphologies for ϕ high, $\Delta C_o/D$ high, $\alpha_c/\alpha < 1$, facetted oxide, $P_{H_2} + P_{H_2O} =$ constant [147].

quantities. For these reasons, the conditions for formation of the various morphologies can also be represented as a function of ΔG and temperature. In effect, this form of morphology map is constructed from the locii of points obtained by projection of the critical conditions for change in oxide and metal product morphology described previously (shown in Figures 4.6.17 and 4.6.18) on to the ΔG axis for each of the temperatures for the specified gas conditions.

Given the many factors influencing product morphology, at this stage of our understanding, these morphology maps must be determined by experiment studies rather than from first principles. Examples of morphology maps that have been determined include, magnetite (Fe_3O_4) and wustite ($Fe_{1-y}O$) reduction in H_2/H_2O and CO/CO_2 systems [152–156], and NiO reduction in H_2/H_2O systems [159].

The ΔG versus T morphology map shown in Figure 4.6.19 illustrates the product morphologies formed on isothermal reduction of magnetite to metallic iron [156]. At low temperatures, it is shown that the reaction proceeds by a continuous growth mechanism involving the formation of instabilities in the form of gas pores in the intermediate wustite product layer. At higher temperatures, the surfaces of the pores become isolated and covered with a dense iron layer; the rate of removal of the residual oxygen from the wustite becomes limited by solid state diffusion through this solid product layer. At high temperatures and above critical thermodynamic driving force it appears that the dense iron layer becomes unstable and the reaction proceeds through the discontinuous formation and breakdown of this product layer.

There is clearly scope to expand this form of analysis to other reaction systems to better understand the characteristics of these heterogeneous reactions. The analysis

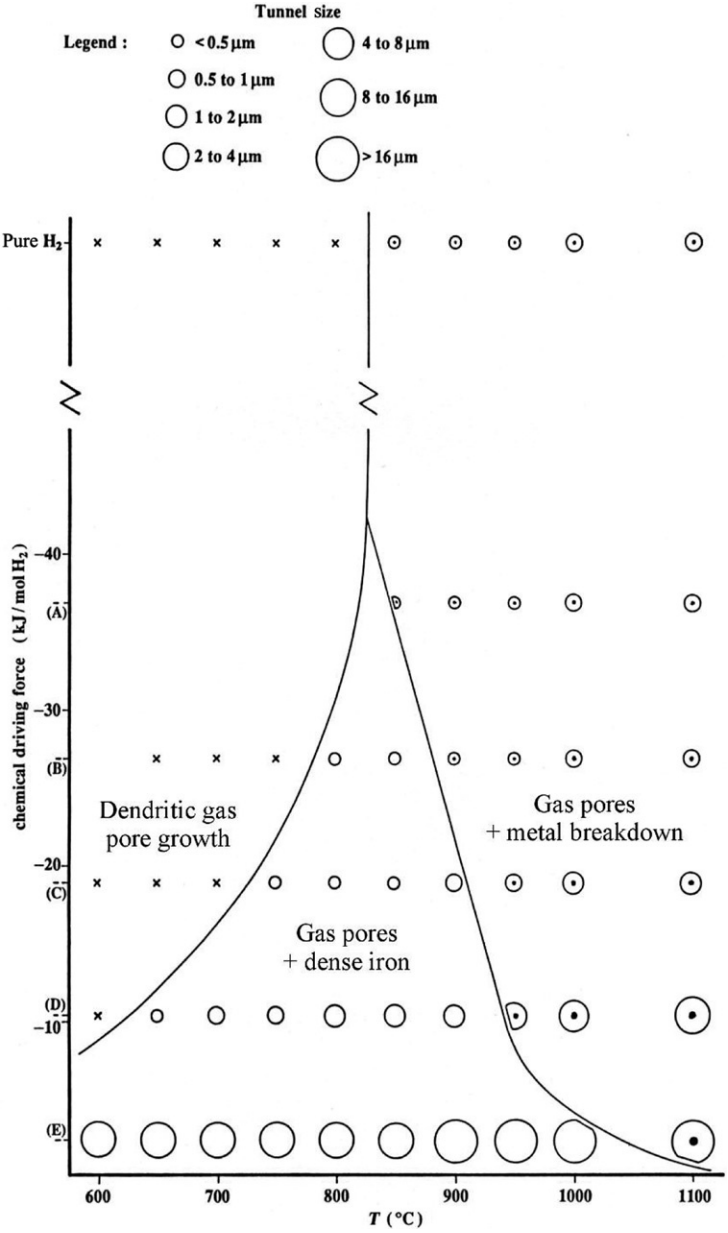


Figure 4.6.19 Morphology map or summary of product structures formed during the isothermal reduction of magnetite at temperatures above 843 K in H_2/H_2O gas mixtures ($H_2 + H_2O = 1$ atm) [156].

demonstrates the clear linkages between reaction mechanism and reaction rate, and the response to changes in key process variables.

4.6.4. SUMMARY

In the present section, a number of examples of phase formation reactions resulting from chemical reactions between fluid and solid phases have been discussed and the conditions under which these phases are formed identified. Schematic illustrations of the interface structures that can be formed during reaction between fluid and solid phases are summarized in Figure 4.6.20.

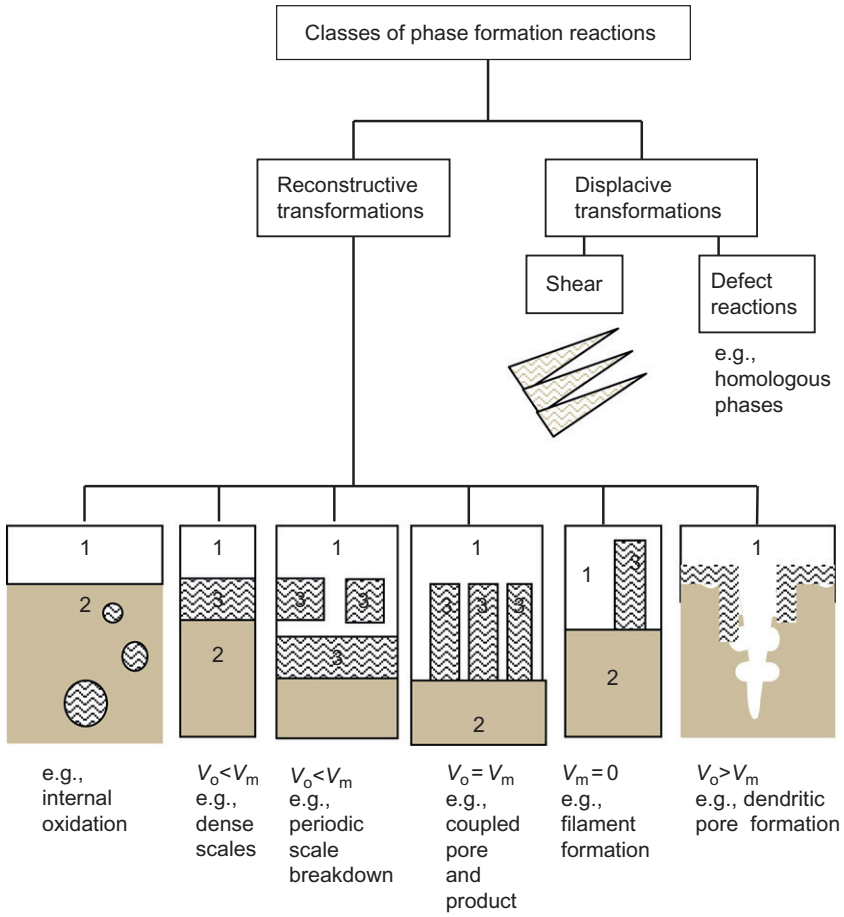


Figure 4.6.20 Reconstructive and displacive phase formation reactions, and schematic illustrations of the interface structures that can be formed during reaction between fluid (1) and solid (2) phases. Phase 3 is the new solid phase formed as a result of the chemical reaction.

A summary of elementary processes and process steps that have been identified as occurring during the decomposition of solids in reactive gas environments is provided in Table 4.6.1 [168]. Each of these elementary processes or steps has been categorized and assigned a number to assist in their identification in the subsequent text or in graphical representations of the processes occurring during the decomposition processes. For the purposes of present discussion, the focus will be on the decomposition of pure metal oxides, multimetallic compounds, or oxide solid solutions in the presence of the reactive gas mixtures, H_2/H_2O and CO/CO_2; however, the arguments can equally well be applied to other analogous reaction systems, such as the decomposition of other solids including sulfides, hydroxides, halides, etc. Many of these elementary processes are common to aqueous/solid reaction systems, and this indicates the potential to extend the analysis to these systems also.

To illustrate where and how all of these elementary processes can contribute to the overall decomposition process schematic diagrams of cross sections of the particle and the reaction interface (Figure 4.6.21) have been prepared.

In Figure 4.6.21, the elementary processes #8 and #9 represent the mass transport of reactant and product species in the gas phase to and from the outer surface of the particle. For the majority of metals, the reaction temperatures are well below the melting and boiling temperatures of the metal product, and the product will remain in the solid state throughout the reaction and will form a product layer on the original solid. The thickness of the product layer increases as the reaction proceeds. These are commonly referred to as exhibiting shrinking core geometries as the volume of reactant solid is progressively reduced but the external geometry of the particle defined by the outer product layer. To simplify the detailed description of the reaction interface distinction is made between the cases when the product forms a "dense metal layer" that covers the surface, cutting off direct access of the gas to the oxide surface; or when a "porous metal product" layer is formed that allows the bulk gas to penetrate through the product to the nominal reaction interface. Each of these cases, dense or porous product, leads to a different set of elementary processes steps that are predominant during the decomposition reaction.

The case in which the oxide surface is initially covered by a "dense metal product" is shown schematically on the left-hand side of Figure 4.6.21, that is, the metal phase is predominant. Here, there is no direct contact, or only intermittent contact, between bulk reactant gas and the original bulk oxide. The reactant gas species are supplied to the surface of the particle (#8) and are adsorbed onto the metal surface (#1) where they partially or fully dissociate, or take part in chemical reactions on this metal surface.

As there is no direct contact between reactant gas and bulk oxide, chemical reactions must take place at the metal surface (#1) or at the metal–metal oxide interface (#4). In order for reactions to take place at #1, oxygen must diffuse (#13) through the dense metal covering layer from the metal–metal oxide interface to the gas–metal interface. In metals in which the solubility and diffusivity of oxygen in the metal lattice is extremely low, the

Table 4.6.1 Elementary Processes and Process Steps Occurring During the Gaseous Reduction of Metal Oxides [168]

A. *Chemical reactions*:
1. Adsorption/chemical reaction/desorption at metal–gas interface.
2. Adsorption/chemical reaction/desorption at oxide–gas interface.
3. Adsorption/chemical reaction/desorption at the contact region between three phases (metal–oxide–gas).
4. Chemical reaction at metal–oxide interface.

B. *Nucleation and Growth*
5. Nucleation of metal product.
6. Growth of metal by attachment of ions on the base of the nucleus.
7. Growth of metal by attachment of ions on the perimeter of the nucleus.

C. *Mass transports of reactants:*
8. Mass transfer of gaseous reactant from the bulk gas to the outer solid surface.
9. Pore diffusion of gaseous reactant from the outer solid surface to the reaction interface through porous metal product.
10. Solid state diffusion of reactant from metal–gas interface to metal–oxide interface through dense metal product.
11. Diffusion of reactant along metal–oxide interface from the contact region between three phases (metal–oxide–gas) to the reaction interface.
12. Solid state diffusion of oxygen from solid bulk to metal oxide surface via lattice diffusion.
13. Solid state diffusion of oxygen from metal–oxide interface to metal–gas interface through dense metal product via lattice diffusion.
14. Surface diffusion of oxygen from oxide phase to metal phase.
15. Diffusion of oxygen along metal–oxide interface from metal–oxide interface to the contact region between three phases (metal–oxide–gas).

D. *Mass transports of products:*
16. Solid state diffusion of cation via bulk diffusion.
17. Surface diffusion of cation.
18. Solid state diffusion of nonmetallic product from metal–oxide interface to metal–gas interface through dense metal product via lattice diffusion.
19. Diffusion of nonmetallic product along metal–oxide interface from metal–oxide interface to the contact region between three phases (metal–oxide–gas).
20. Pore diffusion of gaseous product to the outer solid surface from the reaction interface through porous metal product.
21. Mass transfer of gaseous product from the outer solid surface to the bulk gas.

E. *Physical changes*
22. Sintering, swelling, softening, and cracking.
23. Bursting of dense metal product through the formation of gaseous reaction product at the metal–oxide interface.

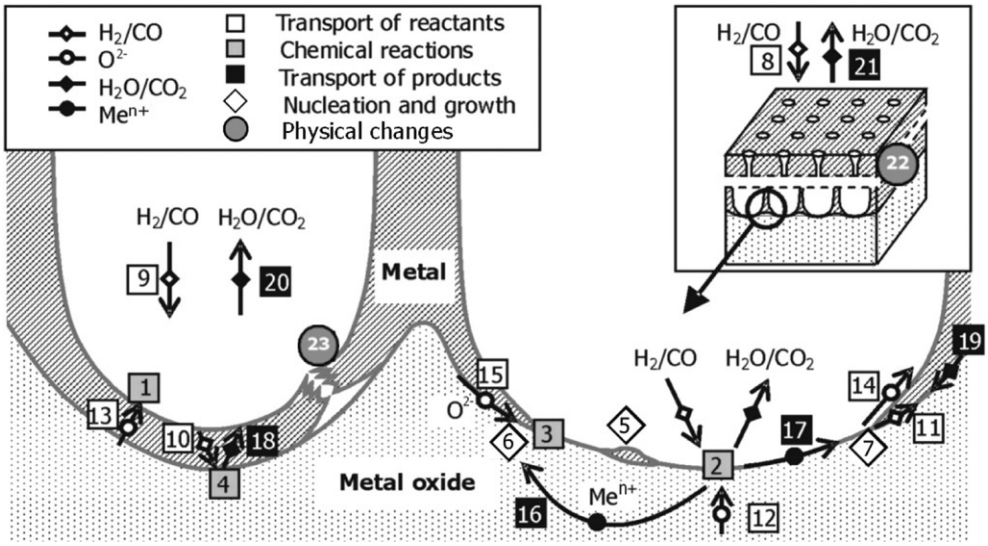


Figure 4.6.21 Elementary process steps that may take place during gaseous reduction of metal oxides [168].

oxygen permeability through this dense layer will be low. If this dense product morphology persists, very low overall reaction rates are observed. The rates of reduction progressively decrease with time as the product layer thickness increases and the diffusive flux decreases.

For the reactions to occur at the metal–metal oxide interface reactant species must diffuse through the dense metal covering layer from the gas–metal interface to this metal–metal oxide interface (#10). This scenario involves in the case of hydrogen or carbon monoxide the dissociation of H_2 gas to atomic H, or CO gas to C. Both H and C can exist in interstitial solid solutions in metals and their diffusion through the dense metal is the more likely scenario for the conditions in which the dense metal layer is formed. The chemical reaction of H and C species with O in the metal oxide can occur at the metal/metal oxide interface (#4); as this is a solid/solid interface the reaction products remain in the condensed state unless nucleation and growth of gas pores at the metal/metal oxide interface can occur. The solubility of H_2O and CO in metals as molecular species is very low because of the relatively large size of these molecules; the permeability of these products through the metal product (#18) is therefore low. It has been observed that H_2O and CO reaction products can form critically sized gas bubbles and pressures sufficient to burst or break down the metal product layer (#23). This has the effect of not only releasing the gaseous product species but also allowing subsequent access of the reactant gas to and reaction with (#2) freshly exposed bulk metal oxide. This raises the possibility of a cyclic, discontinuous reaction mechanism in which relatively fast

chemical reaction at the oxide and metal surfaces results in an initial product morphology consisting of metal oxide covered with dense metal product, this is followed by a second slow step limited by the diffusive flux of reactant species through the dense metal layer and the time required to nucleate critically sized gas bubbles, this dense layer then breaks down allowing fast chemical reaction between reactant gas and oxygen species, and so the cycle is continued.

The right-hand side of Figure 4.6.21 represents situations in which the oxide phase is predominant, there is a "porous metal product" and there is continuous contact between the reactant gas and the oxide phase throughout the course of the decomposition reaction. In these cases, mass transport of reactant and product species occurs in the gas phase to and from the bulk gas and the outer surface of the particle (#8, #21), to and from the outer surface of the particle through the porous product layer to and from the reaction interface (#9, #20). Mass transfer of oxygen reactant species on and in condensed phases can occur along the oxide surface from the oxide surface on to the metal surface (#14), along the metal–metal oxide phase boundary (#15) or in the bulk oxide phase (#12). Chemical reactions can occur and may take place on the metal surface (#1), on the oxide surface (#2), at the three phase metal/metal oxide/gas interface (#3), or at the metal/metal oxide interface (#4). In some cases, metastable or final oxide products are formed between the original metal oxide and the final metal product (#19).

The metal ions resulting from the chemical reactions may form new metal or oxide nuclei (#5) at the gas/oxide interface. The more likely scenario in the proximity of existing metal product is that these excess metal ions will join to the existing phase either at the metal bulk metal/oxide interface (#6) following diffusive mass transport through the bulk oxide (#16), or to the edge or periphery of existing metal or oxide phase (#7) through surface diffusion mechanisms (#17).

The present analysis demonstrates that there are many simultaneous processes and process steps occurring during the decomposition, or reactive reduction, of solid metal compounds. There is compelling evidence that these cannot be treated as simply "chemical reactions" in the strictest sense of the word; these involve synergistic chemical reactions and mass transport processes on atomic and microscopic levels.

In the case of gaseous reduction of metal oxides, the conditions for the formation of various product morphologies, and the links between these morphologies and the net rates of reactions, have been identified by considering

(i) established criteria for the stability of moving interfaces in a thermodynamic potential gradient,

(ii) the relative rates of chemical reactions on the oxide and metal surfaces, and

(iii) key process phenomena and physicochemical properties of the solid phases.

Further examples of these various reaction systems and product microstructures are to be found in the literature, some selected examples of different chemical reaction systems are to be found in [169–187].

REFERENCES

[140] L. Von Bogdandy, H.J. Engell, The Reduction of Iron Ores, Springer, Berlin, 1972.
[141] P.C. Hayes, Miner. Process. Extract. Metall. Rev. 8 (1992) 73.
[142] T. Onishi, S. Nakakuda, M. Takeda, Mater. Trans. JIM 51 (2010) 482.
[143] P. Kofstad, Non-Stoichiometry, Diffusion and Electrical Conductivity in Binary Metal Oxides, Wiley, New York, 1972.
[144] R.J.D. Tilley, Defects in Solids, John Wiley, Hoboken, NJ, 2008.
[145] R.A. Rapp, Metall. Trans. B 15B (1984) 195.
[146] N. Birks, G.H. Meirer, F.S. Petit, Introduction to the High Temperature Oxidation of Metals, Cambridge University Press, Cambridge, UK, 2006.
[147] P.C. Hayes, Metall. Mater. Trans. B 41B (2011) 19.
[148] W. Kurz, D.J. Fischer, Fundamentals of Solidification, third ed., Trans Tech, Switzerland, 2004, p. 74, 88, 151.
[149] G.R. Belton, Can. Met. Q. 21 (1982) 137.
[150] D.H. St John, F. Nakiboglu, P.C. Hayes, Metall. Trans. B 16B (1986) 383.
[151] E. Riecke, K. Bohnenkamp, H.J. Engell, Archiv. Eisenhuttenw. 38 (1967) 249.
[152] M. Farren, S.P. Matthew, P.C. Hayes, Metall. Trans. B 21B (1990) 135.
[153] D.H. St John, S.P. Matthew, P.C. Hayes, Metall. Trans. B 15B (1984) 701.
[154] D.H. St John, P.C. Hayes, Metall. Trans. B 13B (1982) 117.
[155] S.P. Matthew, P.C. Hayes, Metall. Trans. B 21B (1990) 153.
[156] S.P. Matthew, T.R. Cho, P.C. Hayes, Metall. Trans. B 21B (1990) 733.
[157] T. Hidayat, M.A. Rhamdhani, E. Jak, P.C. Hayes, Metall. Mater. Trans. B 40B (2009) 1.
[158] T. Hidayat, M.A. Rhamdhani, E. Jak, P.C. Hayes, Metall. Mater. Trans. B 40B (2009) 4462.
[159] T. Hidayat, M.A. Rhamdhani, E. Jak, P.C. Hayes, Metall. Mater. Trans. B 40B (2008) 474.
[160] J.W. Christian, Theory of Phase Transformations in Metals and Alloys, Pergamon, Oxford, UK, 1965.
[161] P.C. Hayes, Steel Res. Int. 82 (2011) 480.
[162] D.E. Porter, K.E. Easterling, Phase Transformations in Metals and Alloys, Van Nostrand Reinhold, New York, 1981.
[163] W.D. Kingery, H.K. Bowen, D.R. Uhlmann, Introduction to Ceramics, second ed., John Wiley, New York, 1975.
[164] P.C. Hayes, P. Grieveson, Metall. Trans. B 12B (1981) 579.
[165] B. Zhao, P.C. Hayes, in: 12th Intl. Ferroalloys Congress, INFACON XII, Helsinki, Outotec Oyj, vol. 2, 2010, p. 263.
[166] A.A. Struthers, P.C. Hayes, PhD., Metallurgical Engineering, University of Queensland, Brisbane, Australia, 2001.
[167] P.R. Swann, N.J. Tighe, Metall. Trans. B 8B (1977) 479.
[168] T. Hidayat, M.Phil., Metallurgical Engineering, University of Queensland, Brisbane, Australia, 2009.

General

[169] A.R. Burkin, Miner. Sci. Eng. 1 (1969) 4.
[170] S. Luidold, H. Antrekowitsch, JOM 59 (6) (2007) 20.

Dendritic

[171] J. Harkki, Helsinki Univ of Technology, Institution of Process Metallurgy, Finland, Report TKK-V-B11–13, 1980, ISBN 951 752 091 1-3.
[172] J. Porter, L.C. De Jonghe, Metall. Trans. 12B (1981) 299.
[173] S. Geva, M. Farren, D.H. St John, P.C. Hayes, Metall. Trans. B 21B (1990) 743.
[174] J.A. Bustnes, N.N. Viswanathan, D. Sichen, S. Seetharaman, Metall. Mater. Trans. B 31B (2000) 540.
[175] I. Arvanitidis, A. Kapilashrami, D. Sichen, S. Seetharaman, J. Mater. Res. 15 (2000) 338.
[176] L.D. Teng, S. Noguchi, S. Seetharaman, Metall. Mater. Trans. B 38B (2007) 55.

Coupled Growth

[177] K.R. Lilius, Acta Polytechnica Scand. Finnish Acad. Technol., Helsinki, (1974)(Chapters 117 to 120).
[178] J.R. Porter, P.R. Swann, Ironmak. Steelmak. 4 (1977) 300.
[179] Y.K. Rao, S.K. El Rahaiby, W.C. Taylor, Trans. Inst. Min. Metall. C 89 (1980) C186.
[180] S.J. Wilson, J.D.C. McConnell, M.H. Stacey, J. Mat. Sci 15 (1980) 3081.
[181] Y.K. Rao, Trans. Inst. Min. Metall. C 90 (1981) C47.

Filamentary Growth

[182] C. Wagner, in: J.F. Elliott (Ed.), Proc. Conf. Steelmaking: The Chipman Conference, MIT Press, Dedham, MA, 1962, p. 19.
[183] T. Chida, J.D. Ford, Can. J. Chem. Eng. 55 (1977) 313.
[184] M.A. Fahim, F.D. Ford, Can. J. Chem. Eng. 54 (1976) 578.
[185] R.E. Cech, T.D. Tiemann, Trans. AIME 245 (1969) 1727.
[186] M. Chang, L.C. de Jonghe, Metall. Trans. B 16B (1984) 685.

Shear Transformations

[187] M.L. De Vries, I.D. Grey, J. Fitzgerald, Metall. Mater. Trans. B 38B (2007) 267.

CHAPTER 4.7

Factors Influencing Reaction Area

Peter Hayes
School of Chemical Engineering, The University of Queensland, Queensland, Brisbane, Australia

4.7.1. INTRODUCTION

By now, the reader will be familiar with the general rate equation introduced in Chapter 4.2 to describe the instantaneous rate of heterogeneous reaction

$$\text{Overall rate} = \{1/[1/k_{\text{ml}} + 1/k_{\text{c}} + 1/Kk_{\text{mII}}]\}\cdot A\cdot[C_{\text{I}} - C_{\text{II}}/K] \tag{4.7.1}$$

where C_{I} and C_{I}^{i} are the concentrations of the species in the bulk phase and at the interface in phase I, respectively, K is the apparent equilibrium constant, and A is the interface area. The many factors influencing the rate constants k_{mI}, k_{c}, and k_{mII} have already been discussed in this chapter. Attention is now turned to the parameter A, the interfacial area. Clearly, this is also a key process parameter determining rates of these heterogeneous reactions. To emphasis its importance, this factor is explicitly addressed and discussed in the following section. The interfacial area available for chemical reaction in reaction system is determined by the

(i) Process conditions imposed on the system,
(ii) Reaction induced mechanisms, and
(iii) Time or extent of reaction.

These factors are summarized in Table 4.7.1 and examples of each are presented and discussed in more detail below.

The most common assumption made in describing reaction systems is that the shape of the reactant materials or system geometry does not change over time or extent of reaction, or if it does, it is in a well-defined way.

In reality, all materials are continuously changing their shape either at an atomic or macroscopic scale. The first thing to establish in the analysis is the extent of these changes and how fast they are occurring relative to other process that are taking place in the reaction system. If the shape changes do not influence the rate limiting reaction steps or are slow compared to other reaction steps then the assumption of constant shape or geometry may be valid, if not these changes must be taken into account in any quantitative analysis of the process kinetics.

Treatise on Process Metallurgy, Volume 1
http://dx.doi.org/10.1016/B978-0-08-096986-2.00019-9
© 2014 Elsevier Ltd.
All rights reserved.

Table 4.7.1 Summary of Factors Influencing Interfacial Area in Reaction Systems

Factor	System	Phenomena/Properties	Control Parameters
Process Conditions	Fluid/fluid	Viscosity, interfacial tension, density, volume fraction, physical dispersion	Composition, bulk flow
	Fluid/solid	Particle size, size distribution, porosity, pore size distribution, selective reaction	Pre-preparation through comminution and physical processing, liberation analysis
Reaction Induced Phenomena	Fluid/fluid	Emulsification, gas phase formation	Reactant composition, temperature, pressure
	Gas/solid	Product structure, changing geometry	Reactant composition, temperature, pressure
Reaction Time/Extent	Fluid/fluid	Coalescence/settling	Adjustment to interfacial chemistry
	Fluid/solid	Sintering, densification, recrystallization	Temperature

4.7.2. REACTANT CHARACTERISTICS

4.7.2.1. Fluid/Fluid Systems

4.7.2.1.1 Composition

There are essentially two types of liquid/liquid systems encountered in metallurgical processing, (i) chemically induced immiscibility, such as is found in metal smelting and refining processes, and (ii) systems in which separate liquids are added to the system, for example, aqueous/organic solvent extraction processes.

The compositions of the liquid phases created as a result of chemically induced immiscibility are dependent on the thermodynamic and phase equilibrium properties, which are principally functions of bulk chemical composition and temperature. This information can be used to determine the volume fractions of each of the phases. If the phase diagram is available then this information can be obtained using the lever rule construction, or alternatively directly from thermodynamic calculations.

In the case of systems in which the liquids are added to the process, there are no restrictions on the relative amounts of the phases present in the system.

The relative volumes of the liquid phases determine the dispersion of the phases and the ability of the phases to disengage from each other. In well-mixed or agitated liquid system, the phase having the higher volume fraction will become the continuous phase and the second phase the discontinuous or dispersed phase. As the bulk compositions of these phases are different then so too are the bulk densities. If there is no mixing or low turbulence in the system then the phases will separate out under gravitational forces into layers, the denser liquid moving to the bottom of the reactor vessel (see Figure 4.7.1).

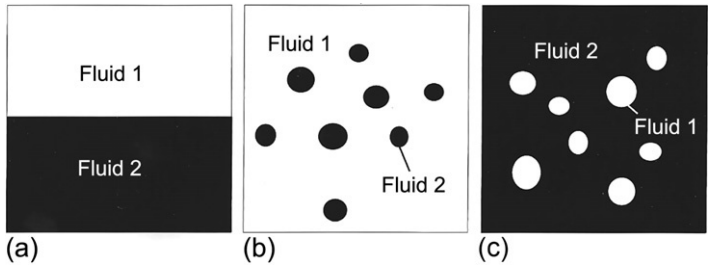


Figure 4.7.1 Phase contact and dispersion in a binary fluid/fluid system, (a) equilibrium distribution gravity separation with no mixing leads to minimum interfacial area, (b) fluid 1 is the continuous phase, and (c) fluid 2 is the continuous phase.

The existence of separate fluid is a direct result of the different chemical environments in these phases; the properties of the interface between these phases depend critically on the composition and arrangement of species at the atomic/molecular level. The network required to create a planar interface between the liquid and gas phases is defined as the surface tension, σ. For example, pure water 293 K has a surface tension of $0.073\ \mathrm{J\ m^{-2}}$ [188], pure molten iron $1.88\ \mathrm{J\ m^{-2}}$ at 1811 K [189], data on other liquids are to be found elsewhere [188–191]. The interfacial energies between liquid phases are in general less than the surface tensions of the individual liquids.

It follows that the total interfacial energy of a system is reduced if the interfacial area is lowered. A system containing a dispersion of liquids or gas bubbles in a liquid phase is thermodynamically less stable than the same system when the two phases exist as bulk fluids. There is then, in any system in which interfaces are present a driving force for the reduction of interfacial area.

As the surface tension is dependent on the interactions within a few monolayers of the surface these values can be very sensitive to the presence of small concentrations of impurity element. What constitutes an impurity species is critically dependent on the chemical environment of the host solution phase; in general, species that have low bulk solubility in the solution can be regarded as surface active and are expected to preferentially segregate to the interface [189]. The presence of these surface active species can also influence the dynamic processes occurring at the interface. For example, small differences in solute concentration can result in surface tension driven (Marangoni) flow at the gas/liquid interface and change the fluid flow and circulation patterns within the droplets.

Liquid/liquid systems are used primarily to transfer solute species between phases. In practice, this is undertaken in two stages, the first involving the creation of high interfacial area through agitation and second low agitation conditions to allow for separation of the dispersed liquids. This second stage involves the coalescence of droplets and leads to a smaller number of droplets of larger size; the denser droplets separate out under gravitational forces. For a given droplet size and assuming no effects from other droplets in the system, the separation velocity, v, to a first approximation is given by Stokes law

$$v = 2g(\rho_d - \rho_c)r^2/9\mu \tag{4.7.2}$$

where ρ_d and ρ_c are the densities of the discontinuous and continuous phase, respectively (kg m^{-3}), r is the droplet radius (m), μ is the dynamic viscosity (N s m^{-2}), and g is the acceleration due to gravity (9.61 m s^{-2}). This relation can be taken only as a first approximation as it is only valid for laminar flow conditions; these are approached only at low settling velocities in systems having low volume fractions of dispersed phase and small droplet sizes. The time at which the droplet remains dispersed in the continuous phase clearly depends on the depth of the reactor. Once these droplets are incorporated into the settled liquid phase the interfacial area available for transfer of species is clearly reduced.

4.7.2.1.2 Bulk Flow

Gas injection is widely used in metallurgical systems; the technique can be used in two principal roles, (a) to provide bulk mixing of fluids in the reactors and (b) as a means of providing reactant species to the system. In the former case, the increased flow and mixing of the continuous phase increases the effective mass transfer coefficients and enhances the probability of breakup and dispersion of multiple liquid phases. In the second case, the reactant species are consumed during passage through the reactor and either absorbed into the fluid or transformed into new chemical species.

In gas injection systems at low gas flows, isolated gas bubbles are formed. High gas fractions and injection velocities lead to the formation of bubble swarms or plumes and the hold up of gas in the liquid; at high gas fractions foams are formed. At very high gas velocities, continuous gas jets are formed on exiting the lance or tuyeres. This mass of gas then becomes unstable and breaks up into a dispersion of bubbles as it passes through the bath. Clearly, the available interfacial area for reaction in these systems and mass transfer characteristics vary dramatically. The complex phenomena and behavior of gas and bulk fluid in gas injection systems has been the topic of extensive research [192].

If the gas phase is contained within a spherical bubble in the liquid phase, the pressure within the bubble at equilibrium can be calculated by equating the work required to incrementally increase the bubble size with the increased surface energy. The work of expansion, $\Delta P\mathrm{d}v$, must be equal to $\sigma \mathrm{d}A$, where $\mathrm{d}v = 4\pi r^2 \mathrm{d}r$ and $\mathrm{d}A = 8\pi r\mathrm{d}r$ then it follows that,

$$\Delta P = \sigma \mathrm{d}A/\mathrm{d}v = 2\sigma/r \tag{4.7.3}$$

In this case, the pressure at all parts of the interface is equal. The radius of a bubble entrained in a fluid depends on the hydrostatic pressure P_H created by the fluid, this is; a function of fluid density, depth of immersion, and gravitational acceleration. Most gases have limited solubility in the liquid phases, so it can be assumed to a first approximation that the number of moles in the gas phase in the bubble remains constant. As a single bubble rises through a liquid phase the hydrostatic pressure decreases, and the bubble diameter and bubble rise velocity increases.

In real reaction systems, bubbles are rarely at rest and are subject to a number of additional forces [193], gravity forces, F_g (weight of fluid) $\rho g L^3$; viscous flow forces, F_μ (tangential shear stress × area) μUL; inertial forces, F_i (inertial mass × acceleration) $\rho U^2 L^2$; pressure forces, F_p (pressure × cross section) PL^2 where ρ_g, ρ_l are the densities of the gas and liquid phases, μ is the liquid viscosity (Pa s), and U is the bubble velocity (m s^{-1}).

These forces act unevenly, and of different magnitude, over the surface of the bubble resulting in changes to the bubble shape until local equilibrium is reached. A summary of the conditions for the formation of different bubble shapes is given in Figure 4.7.2 [194].

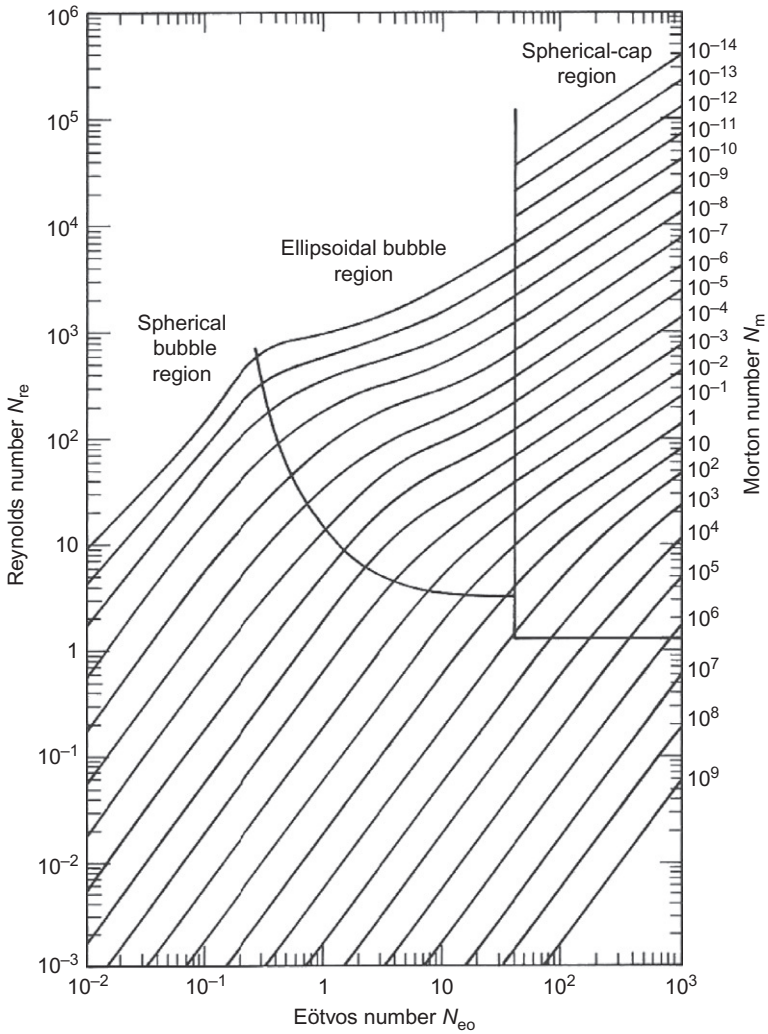


Figure 4.7.2 Relationships between bubble shape and size and the physicochemical properties of the fluids [194].

The variables used in Figure 4.7.2 are expressed in dimensionless numbers, Reynolds $N_{Re} = \rho d_e U/\mu$, Morton $N_{Mo} = g\mu^4 \Delta\rho/\rho^2\sigma^3$, Eötvos $N_{Eo} = g\Delta\rho d_e^2/\sigma$, where g = gravitational acceleration, d_e = equivalent drop diameter, U = drop velocity, μ = viscosity, ρ = density of the continuous phase, $\Delta\rho$ = density difference, and σ = interfacial tension.

The data describe a wide range of process conditions. Effectively at small bubble diameter and low rise velocities, the bubbles are spherical in shape; there is laminar or streamline flow around the bubbles. At high bubble volume, the bubbles take on a spherical cap shape; laminar or stream line flow occurs around the leading surface of the bubble, however, the trailing surface is characterized by the appearance of turbulent eddies. Clearly then the bubble shape has a marked effect on the local flow conditions in the surrounding liquid and at the bubble interface, and hence mass transfer to the bubble and across the liquid/bubble interface.

The presence of multiple bubbles creates local turbulence in the liquid phase and additional shear stresses in the liquid leads to local pressure differences on the bubble surface, this in turn results in differences in bubble surface geometry; the bubbles on rising follow these local differences in pressure, and follow unstable paths as they rise through the liquid phase. In multibubble systems, bubbles can be expected to collide, break up to form daughter bubble size distributions, and coalescence to form larger bubbles.

The description of the bubble size population within a given system is clearly a complex problem. It requires a description of the rate of creation of bubbles, their evolution with time and position in the system, breakage and coalescence. The population balance model methodology linked with the solution of fluid flow equations, that later becoming available through increased computing power and the development of improved computational fluid dynamic codes [195,196]. The mechanisms and models for the coalescence of immiscible fluids and the breakup of drops in turbulent dispersions are similar to those described in gas/liquid systems.

4.7.2.2. Fluid/Solid Systems

4.7.2.2.1 Particle Characteristics

The interfacial area available for reaction in fluid/solid reaction systems is frequently based on the geometric area of the mean particle size. The real value can be significantly different depending on the characteristics of the solids. In the case of a single phase dense material, the surface area of the solid is a function of particle size, shape, and size distribution. To be accurate in describing the kinetics of a reaction involving fluid/particles systems, the rates associated with each size should be determined and the overall rate will be the summation of these individual contributions. If the particle size distribution is narrow, the selection of a mean particle diameter may be an acceptable approximation

in calculations describing the behaviour of the system. If systems having a wide range of particle sizes then the contributions from each size fraction should be taken into account.

In single phase systems in which the solids possess open or connected porosity, the fluid phase can penetrate into the interior of the particle, thus the effective surface area available for reaction is greater than the external geometric surface area. The additional parameters that are important in these cases are the connected porosity, pore size, and pore size distribution [197].

In multiphase or composite particles, the physical surface area of solid available for contact with the fluid is not necessarily the same as the effective area relevant to the proposed reaction. There are two principle reasons for this. In the first instance, the solids may not consist solely of the component that will react with the fluid; there may be other inert phases present in the particles. In addition, these reactive phases may be dispersed within the particle rather than having exposed or free surfaces that are in direct contact with the reactant fluid. Examples of these composite particles, the effect of particle size on liberation and exposure to the reacting fluid are illustrated in Figure 4.7.3a and b in which the dissolution of the solid in the fluid phase occurs. It is clear that only the reactant solid phase that is exposed to the fluid is removed, the remaining reactant solid is encapsulated in the dense matrix material. The key parameters that should be determined then also include the extent to which the reactant solid phases are liberated, that is, consists solely of the reacting solid, the fraction of composite particles, and the extent to which the reactant solid is exposed to the surrounding fluid phase [198].

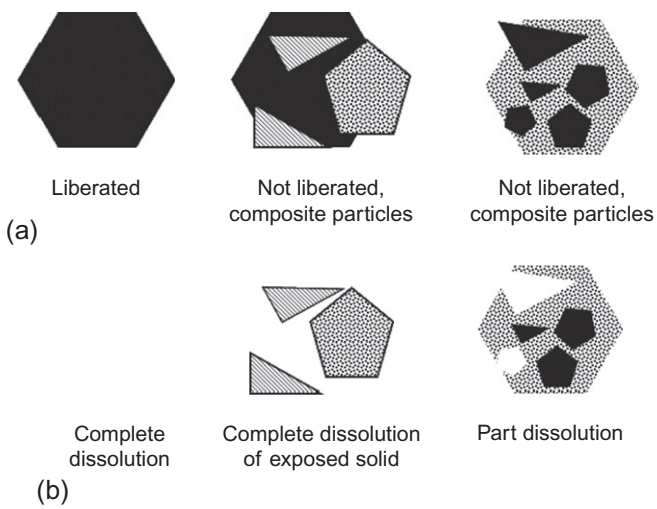


Figure 4.7.3 (a) Particles before reaction with fluid. (b) Particles following selective dissolution in the surrounding fluid phase.

4.7.3. REACTION INDUCED PHENOMENA

4.7.3.1. Fluid/Fluid Systems

4.7.3.1.1 Emulsification

Spontaneous formation of dispersed liquid phases or emulsions was first reported to occur in slag/metal reactions [199]. The reactions appear to be associated with lowering of interfacial energy, which takes place during solute transfer between the liquid phases. This leads to a large increase in the number of metal droplets dispersed in the slag phase and with it an increase in interfacial area. It has been shown [200] that the rates of reactions in these systems can be described by a first order relationship consistent with mass transfer in the liquid phase after the instantaneous surface area in the reactions is taken into account. Similar approaches appear to account for the transient kinetics between slag and metal during steelmaking [201].

4.7.3.1.2 Gas Phase Formation

Reactions between condensed (liquid/liquid, liquid/solid) phases can result in gaseous reaction products; in the main, the gas phase nucleation occurs at the reaction interface and as a result can influence not only the rate of the reaction but also the reaction mechanisms that are active at the new interfaces that are created.

Example Reduction of iron oxide in slag by iron–carbon melts

The overall reaction between carbon dissolved in iron and iron oxide dissolved in slag is represented by the equation

$$\mathrm{FeO(slag)} + \mathrm{C(in\,Fe-C\,alloy)} = \mathrm{Fe(liq)} + \mathrm{CO(g)}$$

The equation as written implies that the reaction takes place at a three-phase boundary involving liquid alloy/slag/gas phases. It has been shown [202] that in this slag system the interfacial forces are such that the gas bubbles cover most of the reaction interface. It therefore appears that the reaction actually occurs through a gas ferrying mechanism in which CO and CO_2 gases move in a countercurrent between the metal/gas and slag/gas interfaces (see Figure 4.7.4). The reactions at these interfaces are as follows

$$\text{metal/gas interface} \quad \mathrm{CO_2(g)} + \underline{\mathrm{C}} = 2\mathrm{CO(g)}$$

$$\text{slag/gas interface} \quad \mathrm{CO(g)} + \mathrm{O^{2-}(slag)} = \mathrm{CO_2(g)} + 2\mathrm{e}$$

The reduction of the iron from the bulk slag takes place through an electrochemical reduction reaction in the slag

$$\mathrm{Fe^{2+}(slag)} + 2\mathrm{e} = \mathrm{Fe(liq)}$$

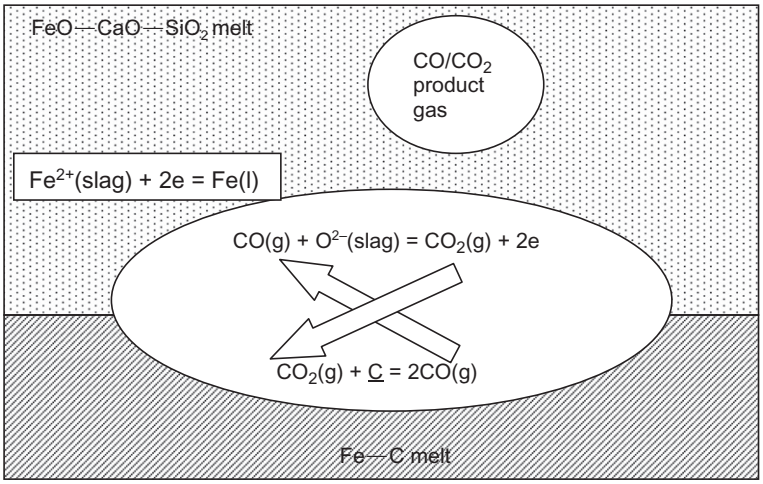


Figure 4.7.4 Schematic representation of gas phase formation at the liquid/liquid interface during reduction of iron oxide-containing melts with carbon in liquid iron demonstrating the gas ferrying mechanism between the metal/gas and slag/gas interfaces.

The rapid evolution of gas from the interface induces breakup of metal droplets and enhanced reaction rates with increasing FeO concentrations.

Similar reaction mechanisms have been shown to be operative during the reduction of iron from slag with solid carbon [203,204].

4.7.3.2. Fluid/Solid Systems

4.7.3.2.1 Product Structure

In the case of fluid/solid reactions, the effective reaction interface area can increase or decrease as reaction proceeds depending on the physical state and structure of the reaction products.

If the solid reaction interface proceeds in a nonplanar manner then the effective area can increase with the extent of reaction. An example of this was given in Section 4.4.3 for the reduction of zinc oxide with CO gas. The products of the reaction are zinc gas and CO gas and the resulting solid surface area on a microscopic scale is much greater than the geometric cross-section of the interface. A similar effect is observed with the gasification of carbon in an oxidizing gas atmosphere.

On the other hand the formation of a solid product can significantly reduce the effective area of contact between the reacting fluid and solid phases. If dense product layer is formed covering the surface then a dramatic change in reaction mechanism must occur as the reaction proceeds as the reacting fluid and solid phases are no longer in contact. This has been shown to be the case for the scale formation during the oxidation of metals

(see example in Section 4.6.1) and in the gaseous reduction of metal oxides (see example in Section 4.6.2).

4.7.3.2.2 Reaction Micromodels for Nonplanar Interfaces

To provide quantitative descriptions of changes taking place in individual particles, a number of mathematical process micromodels have been developed [205–208]. These models describe the reaction rates and extents of reaction in these heterogeneous systems as a function of time for given particle and reaction geometries and bulk gas compositions. These process micromodels, in general, assume the overall reaction takes place in a series of reaction steps involving,

(i) Mass transfer of reactant gas species from the bulk gas to the outer surfaces of the particles.

(ii) Mass transfer of reactants from the outer surface of the particle to the reaction interface through porous product layers.

(iii) "Chemical reaction" between the reactive gaseous species and the solid oxide material at the reaction interface.

(iv) Mass transfer of gaseous products from the reaction interface to the outer surface of the particle through porous product layers.

(v) Mass transfer of product gas species from the particle surface to the bulk gas.

Heat transfer between the solids and the surroundings also takes place in parallel to these mass transfer and chemical reaction processes (Figure 4.7.5).

These mathematical micromodels are routinely used, for defined boundary conditions and product characteristics, to describe reaction systems in initially dense or porous particles. In the case of complete removal of the products into the fluid phase will result in a decrease in the diameter of the particle with increasing reaction time, these systems are said to exhibit shrinking particle geometries (Figure 4.7.6).

For the majority of systems, product will remain in the solid state throughout the reaction and the external geometry of the particle remains unchanged, but the volume of the original material remaining and the interfacial area between fluid and solid is progressively decreased; these are commonly referred to as exhibiting shrinking core geometries.

For reaction of initially porous particles, the mass transfer of reactants through the pores in the solid are in general fast compared to the chemical reaction rates. In the limit, the effective surface area is that of the whole sample. A situation can be envisaged in which the reaction occurs uniformly throughout the whole particle (Figure 4.7.7c). The combination of the reaction leading to a shrinking particle and simultaneous internal reaction is illustrated in Figure 4.7.7d.

One method of describing this type of particulate system is through a grain model, which assumes that the larger particle is made up of a large number of smaller grains each of which exhibit shrinking core behavior [207]. This model is illustrated schematically in Figure 4.7.8.

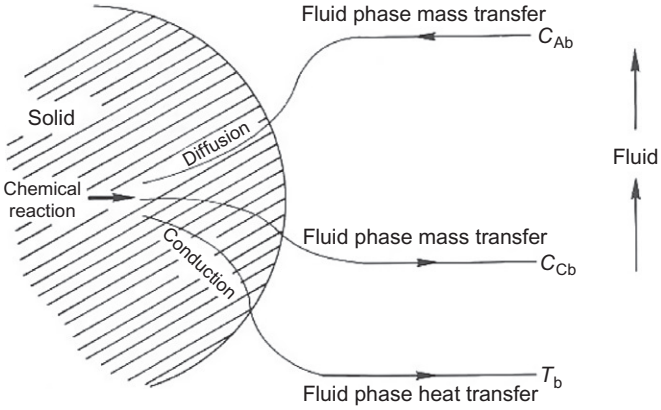


Figure 4.7.5 Schematic of mass and heat transfer and chemical reactions occurring in a fluid/solid reaction system [207].

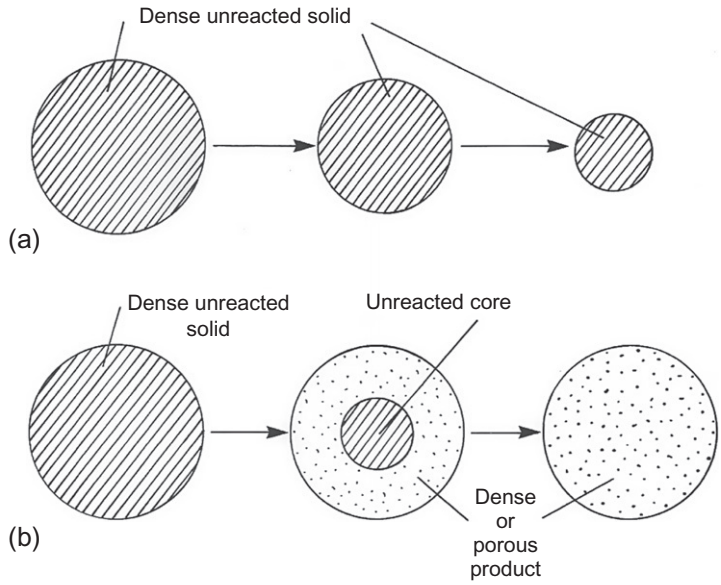


Figure 4.7.6 Reaction of an initially dense particle, (a) shrinking particle and (b) shrinking core reaction systems [207].

4.7.4. REACTION TIME/EXTENT

4.7.4.1. Fluid/Fluid Systems

The issues relating to the coalescence of liquid droplets and of gas bubbles in fluids were briefly discussed in Section 4.7.2.1.

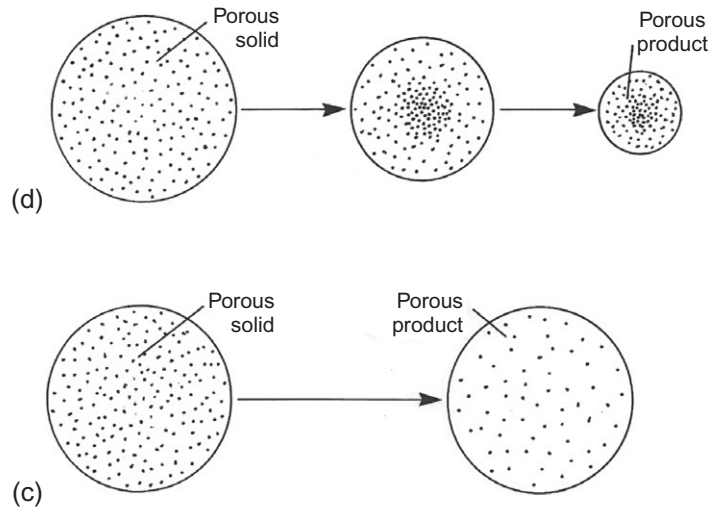


Figure 4.7.7 Reaction of an initially porous particle, (d) shrinking particle and (c) uniform internal reaction systems [207].

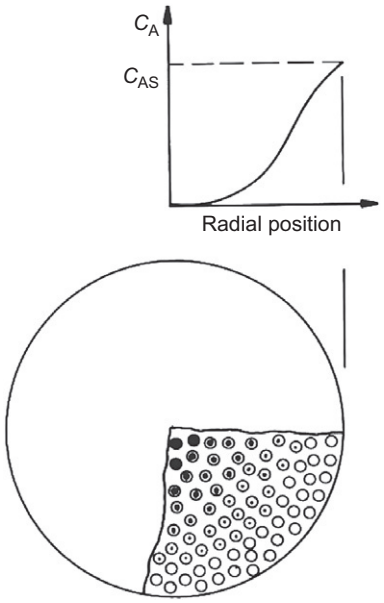


Figure 4.7.8 Schematic of the grain model for reaction of fluid with a porous solid, with the individual grains exhibiting shrinking core behavior. The notional concentration of the reactant species, A, is shown as a function of distance across the section of the particle [207].

4.7.4.2. Fluid/Solid Systems

When two grains of a given crystalline material are brought together, it is unlikely that the orientation of the crystal lattices will be exactly the same; the interface between the grains of different orientation but identical crystal structure is referred to as a grain boundary. Even if the adjacent crystals are perfect at the grain boundary the mismatch of the lattices and the local breakage of bonds between atoms at the interface represents an energy that is over and above that present in a single crystal. The degree of mismatch at the junction of the two crystals grain boundary will determine the grain boundary energy. The grain boundary energy in a given material arises from (i) difference in the orientations of the crystals, (ii) local differences in curvature of the boundaries, and (iii) the total area of boundaries.

In addition to grain boundaries, there are other internal defects in every crystal in the form of equilibrium and nonequilibrium point defects, line defects (dislocations), and planar defects that disturb the repeat pattern in the lattice and contribute to the excess energy of the system.

The greater the grain boundary surface area and the concentration of internal defects in the solids, the greater the internal energy of the material and the material becomes increasingly unstable relative to a defect-free single crystal. These forces lead to shape and microstructure changes within the solid through

(i) migration of existing grain boundaries,
(ii) grain size growth, and
(iii) recrystallization, the formation of new crystals of lower internal energy than the existing material.

Example Microstructural changes on heating porous nickel metal

An initial nickel metal produced from the reduction of nickel oxide with hydrogen at 350 °C (623 K) consists of 0.1–0.5 μm diameter grains containing 10–20 nm pores (see Figure 4.7.9) [209]. On heating to 600 °C (873 K) for 1 h the structure changes dramatically; the nanopores have disappeared and so have the microcracks present in the original structure (see Figure 4.7.9b). The pore volume is significantly reduced on heating at 700 °C (see Figure 4.7.9c). Treatment at 800 (1073 K) and 900 °C (1173 K) sees the significant growth in diameter of the nickel grains (see Figure 4.7.9d and e) with grains in the range 1–2 μm in diameter. At 1000 °C (1273 K), the surface of the nickel takes on a facetted structure in an attempt to further reduce the total surface energy of the curved surface structure.

The atomic arrangements of atoms are not the only factor that determines surface energy, the curvature of surface should also be taken into account. The difference in the energy, that is, the work done in transferring material from a flat to a spherical shape, $RT\ln(p/p_o)$, must be equal to the product of the surface energy and the change in area

$$RT\ln(p/p_o) = \gamma \mathrm{d}A = \gamma \cdot 8\pi r \mathrm{d}r \tag{4.7.4}$$

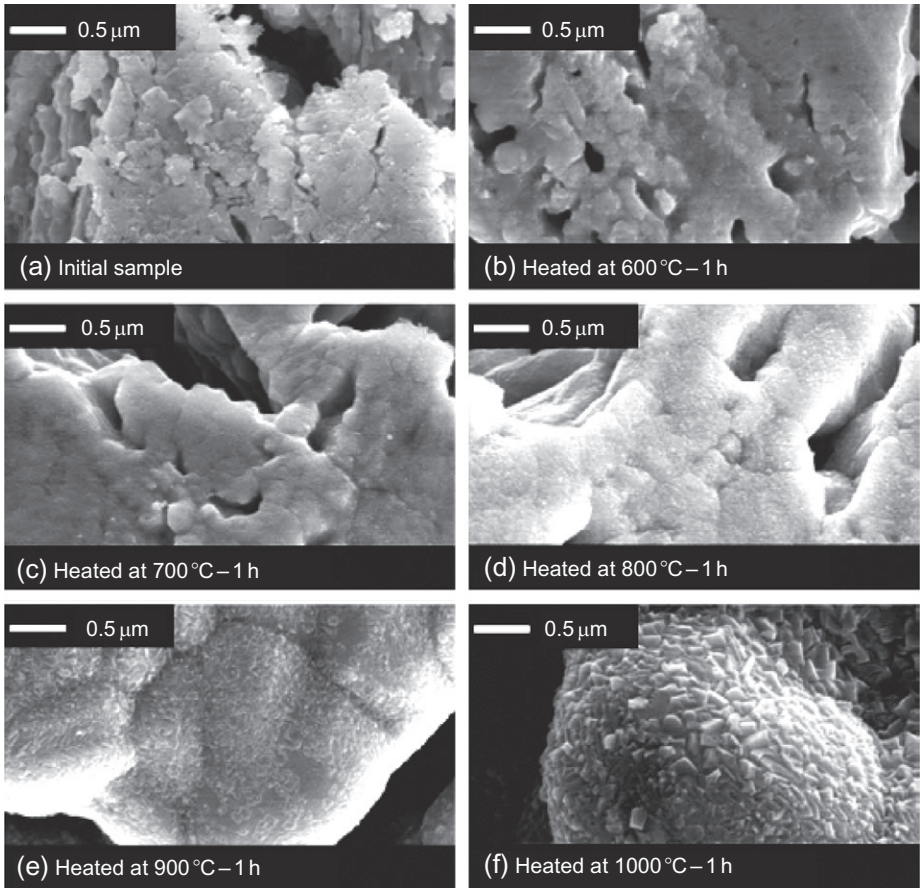


Figure 4.7.9 Effect of heating on the microstructures of nickel metal in N_2–H_2 gas for 1 h at the temperatures indicated showing (b) sintering, (c) densification, (d) and (e) grain growth, and (f) surface faceting. (a) Initial structure prepared from reduction of NiO with 100%H_2 at 350 °C (623 K) [209].

as the change in volume $dv = 4\pi r^2 dr$, $dr = V/4\pi r^2$, where V is the molar volume of the condensed phase, then

$$\ln(p/p_o) = (\gamma V/RT)(2/r) \tag{4.7.5}$$

This difference in equilibrium pressure above the curved surface becomes more pronounced as the radius of curvature of the surface becomes smaller and becomes significant when r is below micron scale.

There is also a difference between the net binding force of the solid material having a positive radius of curvature and that having a negative radius of curvature. Surfaces having a positive radius of curvature are less stable relative to those with negative radius of curvature. These effects become significant when considering shape changes in solids.

Initial rates at which material is transferred to the point of contact of the two solids are at their greatest at point contact; as the point of contact or neck between the two solids increases in size, the radius of curvature of the neck becomes larger and the driving force for change decreases.

A third factor influencing the change in shape of the solids material is stress, this becomes important only at high stresses, high temperatures, and high mobility of atoms.

The three principle-driving forces for change in shape a solid of uniform composition are

- reduction in surface area,
- elimination of curvature, and
- mechanical stress

The mechanisms of material transport in these fluid/solid systems include fluid phase transfer, surface, grain boundary, and volume diffusion, dislocation movement, these pathways are illustrated in Figure 4.7.10.

The above analysis applies to a single surface; however, these driving forces are also valid when there are multiple surfaces present, such as a single grain of complex initial shape or a multiparticle system. In all cases, it would appear that the lowest energy configuration at the gas/solid interface is dependent on crystal structure and orientation.

The changes occurring in solid materials over time are commonly referred to as sintering; there are, however, some important differences in reaction mechanism and outcomes that result (Figure 4.7.11).

Movement via surface diffusion, vapor phase, and liquid phase leads to decrease in surface and an increase in radius of curvature of neck surfaces, that is, a tendency for

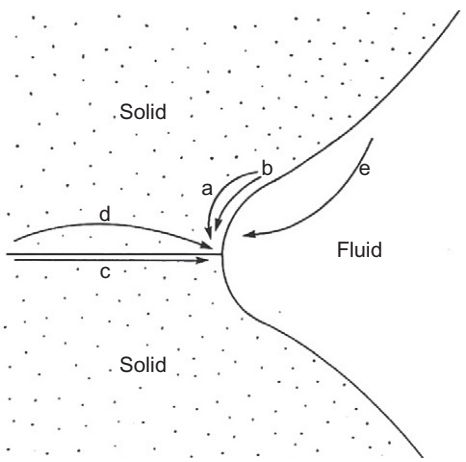


Figure 4.7.10 Alternate paths for matter transport to the neck joining two particles during sintering, (a) volume diffusion from surface, (b) surface diffusion, (c) grain boundary diffusion, (d) volume diffusion from bulk, and (e) fluid phase transfer.

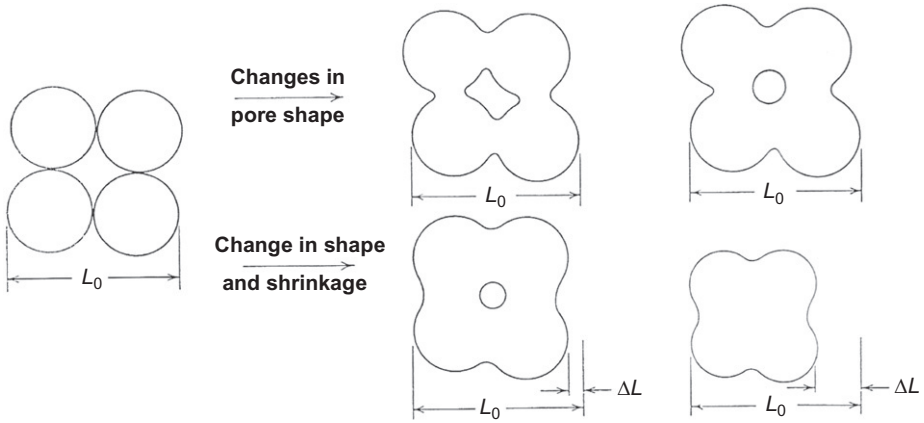


Figure 4.7.11 Sintering of solid particles involving changes in pore shape and shrinkage (densification).

surface to become "flat." Changing shape by these mechanisms the distance between the centers of two adjacent particles will remain constant. These are shape changes but do not lead to elimination of voidage or bring together adjacent particles.

The "densification" of the solid material, the elimination of the remaining voids in the material, and bringing the particles closer together occurs through mass transfer by grain boundary or bulk diffusion, or dislocation movement.

On the basis of differences in activation energies, it is expected that sintering by surface diffusion mechanisms will predominate at low temperatures while the rates of densification become significant at high temperatures when bulk diffusion rates increase.

An example of the change in mean pore size with time is given in Figure 4.7.12 for the sintering of porous nickel metal product. It can be clearly seen that the initial rates of

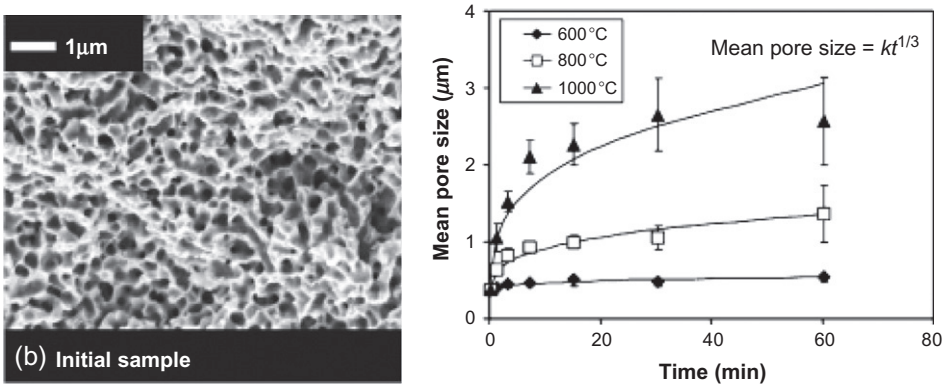


Figure 4.7.12 The increase in mean pore size with time for porous nickel (initial structure prepared by the reduction of dense NiO with 13% H_2, 87% N_2, total pressure 1 atm, at 600 °C for 15 min) [209].

change of the pore size at a given temperature are rapid—decreasing with time. Empirical rate equations are often used to describe these systems. Clearly, the changes in surface area and shapes within the structures with time are complex functions dependent on material properties, such as the composition of the solids, particle size, size distribution, and process conditions and such as temperature and oxygen partial pressure for oxide systems [210].

The presence of a liquid phase that wets the solid surfaces can enhance the rate of shape change in the system through increased rate of solid dissolution and transport from the convex to the concave surfaces [211]—mechanism (e) in Figure 4.7.10.

In addition with the presence of a liquid phase that wets the surface of the solid, that is, the contact angle is less than 90°, there will be an additional capillary force ($P=2\gamma/r$) that will tend to draw the particles together. This stress will favor the rearrangement of individual particles in packed solids—this phenomenon is illustrated in Figure 4.7.13.

Reaction sintering occurs when a new compound or compounds are formed from existing components. In general, the thermodynamic driving force created by compositional differences in the system leads to enhanced rates of mass transfer and increased sintering kinetics [211].

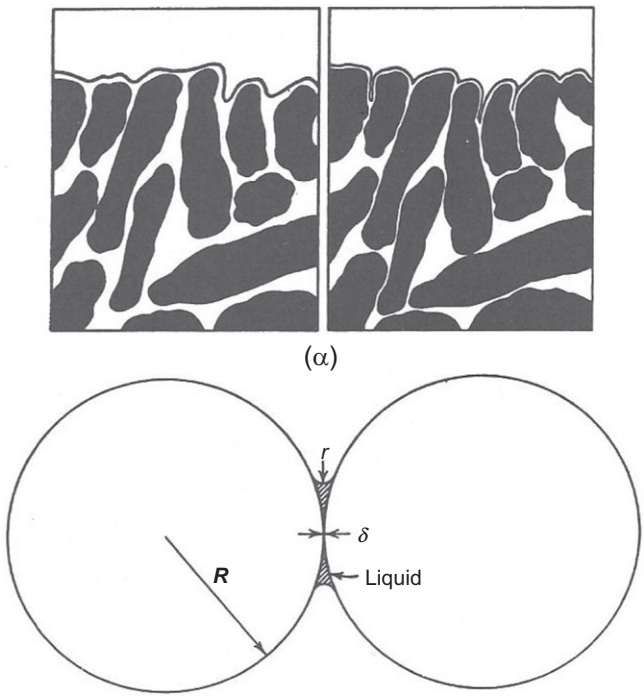


Figure 4.7.13 The effect of liquid phase in assisting liquid phase sintering and densification through particle rearrangement, capillary pressure, and enhanced mass transport through the liquid phase [211].

4.7.5. SUMMARY

It is clear that the shape changes in reaction systems take place on a range of scales from macroscopic dispersions through bulk flow of fluids, through microscopic scale with progressive exposure to reactant phases and changes to reaction mechanisms, and even on the atomic scale at which interfacial roughness can be very different from geometric cross-sections.

The interfacial area available for transfer of species between phases can be controlled by selection of appropriate process conditions; for example, composition, temperature, chemical potential, bulk mixing, and selection of appropriate particle characteristics. Changes to effective reaction area can and will take place as the reactions in these heterogeneous systems proceed, and any formulation of the overall process should take all of these factors into account.

REFERENCES

[188] P.W. Atkins, J. de Paulo, Physical Chemistry, ninth ed., Oxford University Press, Oxford, UK, 2010.
[189] K.C. Mills, Y.C. Su, Int. Mater. Rev. 51 (2006) 329.
[190] Y. Waseda, J.M. Toguri, The Structure and Properties of Oxide Melts, World Scientific, Singapore, 1988.
[191] Verein Deutscher Eisenhuttenleute (Ed.), Slag Atlas, second ed., Verlag Stahleisen, Dusseldorf, Germany, 1999.
[192] J.K. Brimacombe, K. Nakanishi, P.E. Anagbo, G.G. Richards, in: P.J. Koros, G.R. St Pierre (Eds.), Proceedings of the Elliot Symposium on Chemical Metallurgy, Iron and Steel Society, Warrendale, Cambridge, Mass, 1990, p. 343.
[193] R.I.L. Guthrie, Engineering in Process Metallurgy, Oxford University Press, Oxford, UK, 1989.
[194] R. Clift, J.R. Grace, M.E. Weber, Bubbles, Drops and Particles, Dover Publications, Mineola, NY, 2005.
[195] Y. Liao, D. Lucas, Chem. Eng. Sci. 65 (2010) 2851.
[196] Y. Liao, D. Lucas, Chem. Eng. Sci. 64 (2010) 3389.
[197] T. Allen, Particle Size Measurement, Chapman and Hall, London, 1997.
[198] P.C. Hayes, Process Principles in Minerals and Materials Production, Hayes Publ. Co., Sherwood, Australia, 2003.
[199] P. Kozakevitch, G. Urbain, M. Sage, Rev. Metall. 2 (1955) 161.
[200] M.A. Rhamdhani, G.A. Brooks, K.S. Coley, Metall. Mater. Trans. B 36B (2005) 219.
[201] G.A. Brooks, M.A. Rhamdhani, K.S. Coley, Subagyo, Y. Pan, Metall. Mater. Trans. B 40B (2009) 353.
[202] C.L. Molloseau, R.J. Fruehan, Metall. Mater. Trans. B 33B (2002) 335.
[203] S.R. Storey, B. Sarma, R.J. Fruehan, A. Cramb, G.R. Belton, Metall. Mater. Trans. B 29B (1998) 929.
[204] S.L. Teasdale, P.C. Hayes, ISIJ Int. 45 (2005) 642.
[205] J. Szekely, N.J. Themelis, Rate Phenomena in Process Metallurgy, Wiley-Interscience, New York, 1971.
[206] J. Szekely, J.W. Evans, H.Y. Sohn, Gas-Solid Reactions, Academic Press, Inc., New York, 1976.
[207] H.Y. Sohn, M.E. Wadsworth (Eds.), Rate Processes in Extractive Metallurgy, Plenum, New York, 1979.
[208] H.Y. Sohn, P.C. Chaubal, in: Y. Sahai, G.R. St Pierre (Eds.), Transport Processes in Engineering 4: Advances in Transport Processes in Metallurgical Engineering, Elsevier, Amsterdam, 1992, p. 1.

[209] T. Hidayat, M.A. Rhamdhani, E. Jak, P.C. Hayes, Metall. Mater. Trans. B 40B (2009) 462.
[210] R.M. German, Sintering Theory and Practice, John Wiley, New York, 1996.
[211] W.D. Kingery, H.K. Bowen, D.R. Uhlmann, Introduction to Ceramics, second ed., John Wiley, New York, 1975.

CHAPTER 4.8

Reaction System Performance

Peter Hayes
School of Chemical Engineering, The University of Queensland, Queensland, Brisbane, Australia

4.8.1. DRIVING FORCES FOR REACTION

The final parameter to consider in the heterogeneous rate equation,

$$\begin{aligned}\text{Overall instantaneous rate} &= 1/A(\mathrm{d}n/\mathrm{d}t)_{\mathrm{i}} \\ &= 1/[1/k_{\mathrm{mI}} + 1/k_{1} + 1/Kk_{\mathrm{mII}}]\cdot[C_{\mathrm{I}} - C_{\mathrm{II}}/K],\end{aligned} \tag{4.8.1}$$

is the driving force for reaction, given by the term $[C_{\mathrm{I}} - C_{\mathrm{II}}/K]$. Here, C_{I} and C_{II} are the concentrations of the species in bulk phase I and bulk phase II, respectively (all concentrations in mol m^{-3}), k_{mI} is the mass transfer coefficient for the species in phase I (m s^{-1}), and A is the interface area. There are several important observations to be made about this driving force term. The first follows from the nature of the reaction itself that reactants are being consumed and products generated during the course of the reaction. Unless specific steps are taken to replace these reactant species as they are consumed their concentration will decrease as the reaction progresses and so too will the driving force for reaction. In a closed system the reaction concentration decreases with time and in an open system reagent concentrations can be maintained at constant values.

It is often assumed for the sake of simplicity that reactions are irreversible and that only the forward reaction rate need be considered, effectively that $C_{\mathrm{II}}/K_{\mathrm{eq}}$ in this expression is zero. In the case of reversible reactions, the driving force for change will be reduced as the concentrations of the product species becomes significant relative to the equilibrium values.

Finally, the driving force may change in an irregular function of the reaction time during the course of the process as reagents are added or products removed.

4.8.2. REACTION ENGINEERING AND PROCESS MODELS

Mathematical descriptions of specific reaction systems describing bulk changes to reaction process conditions with time, composition, and temperature are classical reaction engineering problems [212–214]. These models do not take into account the

Treatise on Process Metallurgy, Volume 1
http://dx.doi.org/10.1016/B978-0-08-096986-2.00020-5
© 2014 Elsevier Ltd.
All rights reserved.

detailed reaction mechanisms that may be taking place but assume overall chemical reaction rate laws in relation to particular species.

4.8.2.1. Batch/Semibatch (Discontinuous) Reactors

Although perhaps the easiest type of reactor to visualize the batch reactor is perhaps the most difficult to describe and control from a reaction engineering perspective. In its simplest form, all reactants are charged into the batch reactor at the start of the reaction and the spontaneous reactions proceed to completion. The products of the reaction are discharged at a selected extent of reaction and the procedure is repeated. The concentration of reactants change with the extent of reaction and, it follows, the reaction time. The reaction rate will vary with time and as enthalpy change for the system is a function of the extent of reaction so too will the rate of enthalpy release or consumption. In addition to the heat that is transferred through the reactor walls, supplementary means of providing or removing this thermal energy is necessary to maintain isothermal conditions in the reactor.

In ideal operation, the reactors are perfectly mixed, that is, the concentrations of reactants and products, and temperatures are uniform throughout the reactor.

These, then, are discontinuous operations with varying thermal and possibly reactant additions as a function of time.

For a perfectly mixed batch reactor with first order reaction with respect to species A, in which the materials are added at time $t = t_o$, a material balance for the reactor [214] gives

$$\begin{aligned}&(\text{inflow of A}) - (\text{outflow of A}) + (\text{production rate of A})\\ &= (\text{rate of accumulation of A}) \qquad (4.8.2)\end{aligned}$$

$$0 - 0 + (-kCV) = \mathrm{d}/\mathrm{d}t(VC), \qquad (4.8.3)$$

where C is the concentration of species A, V is the volume of the reactor, and k is the first order rate constant. Rearranging and integrating between the limits $t = 0$, $C = C_o$ and $t = t$, $C = \mathrm{C}$

$$\int_{C_o}^{C} (\mathrm{d}C/C) = -k\int_{t_o}^{t} \mathrm{d}t \qquad (4.8.4)$$

$$\mathrm{In}(C/C_o) = -kt \quad \text{or} \quad (C/C_o) = \mathrm{e}^{-kt} \qquad (4.8.5)$$

The concentration of species A is expected to decrease in an exponential manner with reaction time.

4.8.2.2. Continuous Flow Reactors

In contrast, continuous flow reactors can be operated at steady state, that is, the composition of the discharge is constant with time if the feed composition, material flow rates, and the temperature remain invariant.

In *plug flow reactors* (PFRs), the material passes through the reactor without mixing with material that has previously entered or follows it into the reactor, that is, there is no back mixing. All species have the same residence time V/Q, where V is the reactor volume (m^3) and Q is the volumetric flow rate ($m^3\ s^{-1}$). The concentrations of species only vary along the length of the reactor.

For an ideal PFR with first order reaction with respect to species A, a material balance for the reactor gives

$$\begin{aligned}&(\text{inflow of A}) - (\text{outflow of A}) + (\text{production rate of A})\\ &= (\text{rate of accumulation of A})\end{aligned} \tag{4.8.6}$$

$$QC_x - QC_{x+\mathrm{d}x} + (-kC_x\mathrm{d}V) = \mathrm{d}/\mathrm{d}t(VC). \tag{4.8.7}$$

Noting that Q is the volumetric flow through the reactor ($m^2\ s^{-1}$), $U = Q/A$, $\mathrm{d}V = A\mathrm{d}x$, and $(C_x - C_{x+\mathrm{d}x}) = \mathrm{d}C_x$, where U is the flow velocity ($m\ s^{-1}$) and A is the cross section of the reactor (m^2), for steady state conditions with no accumulation, this reduces to

$$U(\mathrm{d}C_x/\mathrm{d}x) - kC_x = 0. \tag{4.8.8}$$

Rearranging and integrating between the limits $t = 0$, $C = C_o$, and $t = t$, $C = C$ along the reactor length, L,

$$\int_{C_o}^{C} (\mathrm{d}C/C) = \int_0^L \mathrm{d}x, \tag{4.8.9}$$

$$\mathrm{In}(C_f/C_o) = -kt \quad \text{or} \quad (C_f/C_o) = \mathrm{e}^{-kL/U} = \mathrm{e}^{-kV/Q} = \mathrm{e}^{-kt_R}, \tag{4.8.10}$$

where t_R is the mean residence time in the reactor. It can be seen that the performance of a plug flow reactor with respect to species A is equivalent to that of a batch reactor.

In a *continuous stirred tank reactor*, as a result of vigorous agitation, the reactor contents are well mixed so that the material discharged from the reactor is the mean composition of the whole reactor. For a perfectly mixed reactor with first order reaction with respect to species A, a material balance for the reactor gives

$$QC_o - QC - kVC = 0. \tag{4.8.11}$$

As $C = C_f$, then

$$C_f = [Q/(Q + kV)\}C_o \quad \text{or} \quad C_f/C_o = [Q/(Q + kV)\}. \tag{4.8.12}$$

Alternatively, as rate $R = kC$, then

$$R = (C_o - C)/(VQ). \tag{4.8.13}$$

In practice, reactors do not behave ideally and hence the need for more accurate descriptions of the processes.

4.8.2.3. Complex Reactor Models

To increase process productivity and efficiency, increasingly there is a need for more detailed descriptions of processes that incorporate the phenomena taking place at a range of scales, from reactor scale down to and including atomic scale processes.

The development in computing power and capacity is rapidly changing the face of process modeling. Classical reaction engineering relied on analytical solutions. The modern approach is the use of numerical solutions to these complex problems. This is already well advanced in the case of bulk flow of fluids with computational fluid dynamics (CFD). These approaches have been introduced briefly in Chapter 4.1. Further discussion of these reactor types and their application is given in Chapter 11.

The next level of complexity is to develop platforms that will incorporate CFD and subroutines that call on micromodels and elementary process models to describe the detailed reactions and process occurring in different regions within the reactor.

Macromodels: Describing bulk and multi-phase material flows, and heat flows into, out of and within the reactor, as a function of time.

Micromodels: Describing changes with time to local mass transport boundary and chemical reaction conditions as a result of the reactions.

Elementary process models: Describing the rates of physical and chemical heterogeneous reaction processes and process steps at given process conditions and geometry.

Providing solutions to these complex interactive problems requires an interactive solution approach since, as indicated in the present chapter, critical changes occurring at the elementary and micromodel levels can influence the overall outcomes of the larger process.

4.8.3. SUMMARY

From the examples given in this chapter on reaction kinetics, it is clear that each "chemical reaction", far from being a single reaction step, actually involves a number of elementary chemical and process steps. Improved understanding of these fundamental phenomena helps to:

- identify the reaction mechanisms and rate limiting processes or steps,
- define the key process variables,
- formulate appropriate reaction models, and
- maximize the reaction rates.

REFERENCES

[212] O. Levenspiel, Chemical Reaction Engineering, third ed., John Wiley, New York, 1999.
[213] R.I.L. Guthrie, Engineering in Process Metallurgy, Oxford University Press, Oxford, UK, 1989.
[214] H.Y. Sohn, P.C. Chaubal, in: Y. Sahai, G.R. St Pierre (Eds.), Transport Processes in Engineering 4: Advances in Transport Processes in Metallurgical Engineering, Elsevier, Amsterdam, 1992, p. 1.

INDEX

Note: Page numbers followed by "*f*" indicate figures, and "*t*" indicate tables.

A

Ab initio density functional theory, 296–298
Acid-base reaction, 646–647
Activity coefficients, 642
Adams-Gibb relation, 178
Aerodynamic levitation, 65–66, 66*f*
Agitated autoclaves, 30
Agitation leaching, 30–31, 31*f*
Alchemy and metal discovery
  alchemists, 3
  alkali metals, 8
  carbon, 5
  copper, 4–5
  Delhi iron pillar, 7*f*
  discovery, 9*t*
  Ellingham diagram, 4, 5*f*
  gold, 4–5
  human civilization, 3–4
  oxides, reduction, 5
  salt, 2
  symbols, 3, 3*f*
  Viking sword, 8*f*
Al-killed steel, 622–626
Al-Li system, 357–358
Alloyed steels, 626–629
Alloys, 80–86, 134–137, 135*t*
Aluminosilicates, 153–154, 164, 167–169, 178–179
Amphoteric oxides, 155–156
Analytic bond-order potential, 323–324
Aqueous phases
  activity and activity coefficients, 642
  chemical and electrochemical potentials, 641–642
  chemical equilibrium (*see* Chemical equilibrium)
  The Debye-Hückel law, 643–644
  formation, ions, 644–646
  mean activity coefficients, 642–643
  potential-pH diagrams, 649–651
Arbitrary choice of system, 497, 502
Asymmetric stretching, vibrations, 174, 174*f*
Atomistic computer modeling, decarburization, 347–350
Atomistic interaction potentials, 317–340
Atomistic simulations
  biased MC schemes, 303–304
  computer (*see* Computer simulation techniques)
  dendritic growth, 375–376
  Gibbs ensemble technique, 302–303
  high temperatures, 340–383
  hybrid MC methods, 301–302
  interaction potentials, 317–340
  interfaces, 380–383
  KMC method, 299–300
  parallel tempering method, 306–307
  physical properties determination (*see* Physical properties determination)
  RMC method, 300–301
  Wang-Landau formalism, 304–306

B

Basicity, slag structure, 155–156, 592–595
Batch/semibatch (discontinuous) reactors, 940
Bath refining processes, 34–35
Bath smelting processes, 33–34, 34*f*
Bayer process, 887
Bending, vibrations, 174
Beyond pair potentials, 317–318
Bhatia-Thornton Formalism, 73
Bhatia-Thornton partial pair-correlation factors, 85–86, 87*f*
Biased MC schemes, 303–304
Binary alloys phase behavior, 356–360
Binary and ternary systems interaction potentials, 331–340
Binary diffusivities, 806
Binary eutectic system, 533–535
Binary fluid/fluid system, 920, 921*f*
Binary isomorphous system, 530–532
Binary monotectic system, 535–538
Binary peritectic systems, 535–538
Binary system $CaO\text{-}SiO_2$ activities, 539–546, 545*f*
Blake-Kozeny equation, 701
Blast furnaces and counter current reactors, 36–37, 36*f*
Body-centered cubic (bcc) crystal structure, 49
Bolding-Anderson model, 329
Borate capacity, 604–607, 606*f*
Born-Fowler relation, 139
Born-Green's equation, 139
Boudouard reaction, 512–515
Boundary conditions, 292
Boundary layer theory, 766–772
Boussinesq approximation, 783
Bragg peaks, 69–70
Bragg-William (BW) treatment, free energy, 356–357
Brenner potential, 330
Bridging oxygens (BOs), 159
Bronze Age, 5–6
Brownian dynamic smart MC method, 303–304
Bubbling fluidized bed, 709–710
Buckingham Π theorem, 687–689
Bulk composition, 504–505
Burke-Plummer equation, 701

C

Calcium desulfurization, liquid iron, 632*t*
Calcium treatment
  Al-killed steel, 622–626
  molten iron, 629–632
Calvet calorimetry, 194
Calvet-type calorimeter, 194, 194*f*
Canonical ensemble for closed systems, 290
CaO activities
  $CaO\text{-}SiO_2$ system, 588*f*
  iso-activity contours, 589*f*, 590*f*
  phase boundary line A-B-C-D-F-G-I, 595*f*
  slags of CaO/P_2O_5 mole ratios, 592*f*, 593*f*, 594*f*
  at $X_{CaO}/X_{AlO1.5}$, 591*f*

CaO-Al_2O_3-MgO system, 624–625
CaO-SiO_2-$AlO_{1.5}$-MgO system, iso-activity contours, 590*f*
CaO-SiO_2-$AlO_{1.5}$ system
  iso-activity contours, 589*f*
  isothermal section, 590*f*, 591*f*
CaO-SiO_2-Al_2O_3 system, chloride capacities, 605*f*
CaO-SiO_2-Al_2O_3 ternary phase diagram, 556, 556*f*
CaO-SiO_2-Al_2O_3 ternary system, 552–553, 554*f*
Cape-Lehmann fit, 106*f*
Capillary dilatometers, 93
Capillary viscometer, 127–128
Capillary waves (ripplons), 200–201
Carbon, 329–331
Carbonate capacities, 599–602
Carbon depletion, alumina-carbon refractories, 352–354
Carbon diffusion, bcc iron, 362–364
Carburization, molten steel, 340–345
Cement testing apparatus, 704, 705*f*
CFD. *See* Computational fluid dynamics (CFD)
Chemical equilibrium
  in aqueous solutions, 646–649
  and Gibbs energy, 644–646
Chemical potential control, 633–638, 641–642
Chemical reaction kinetics
  electrochemical, 838–851
  interfaces, 835–838
  "rate laws", 831
  reaction rate theory, 832–834
  reversible processes, 851–852
Chemical reaction rates
  atomic roughness, 861–865, 862*f*, 863*f*, 864*f*, 865*f*
  metal surfaces, 892–897
  moving surfaces, 859–861, 859*f*, 861*f*
Chemical vapor deposition (CVD), 369–370
Chloride capacity, 604–607, 605*f*
C-H-O gaseous system, 636*f*, 638*f*
Clapeyron equation, 498–499
Clausius-Clapeyron equation, 499
Cleaner production, 17
Cluster variation method (CVM), 356–357
Cobalt alloys at 1873 K, interaction parameters, 579
CO+CO_2+SO_2+Ar gas mixture, 633–635
Collision theory, 832
Combined statement, First and Second Law of thermodynamics, 415–418
Commodity prices, 16
Compatibility triangle, 549–551
Complex deoxidation equilibria, 625*f*, 626*f*
Composition triangle, 546, 550*f*
Compressible flow, metallurgical processing, 715–721
Computational fluid dynamics (CFD), 942
Computer simulation techniques, 288–298, 369–370
Concentric cylinder method, 199
Condensed phases, 515–516
Conduction, metallurgical processing, 738–763
Configuration factor, 790–792
Conical nozzle levitator, 65–66
Constant pressure ensemble, 295
Constant temperature ensemble, 295
Constant temperature, Gibbs energy, enthalpy and entropy of mixing, 527, 528*f*
Continuity equation, 722–723
Continuous and discontinuous metal layer growth, 900–902, 901*f*
Continuous caster, 665, 666*f*
Continuous flow reactors, 940–941
Continuous processes, 17
Continuous stirred tank reactor, 941
Continuum phase formation reactions (spinoidal), 876–878, 877*f*
Convection, metallurgical processing, 763–784
Convective boundary condition, 743–744
Convective mass transfer, 810–814
Coordination number, 80*f*
  cations, 161–163
  and nearest neighbor distance, 74*f*, 75*f*
Copper alloys at 1373-1823 K, interaction parameters, 575
Copper electrorefining, 654
Copper electrowinning, 653–654
Copper production, 22*f*
Coupled growth, pores and metal, 902–903, 903*f*
Coupled reactions, 849–851
Covalently bonded group IV element interaction potentials, 326–331
Criss-Cobble correspondence principle, 646
Cristobalite, 883, 885*f*
Critical temperature, 502
Crystalline solids, 819
Crystallizers/precipitation reactors, 32
C-S-O-Ar gaseous system, 635*f*
Cubic invariant, 77, 77*f*
Cubic materials and impurities, 325
Cu-H_2O system, 654, 654*f*
Cummings correction, 122–123
CVD. *See* Chemical vapor deposition (CVD)
Cylinders, 784

D

D'Arcy-Weisbach's friction factor, 691
Darken equation, 111–112
Darken's quadratic formalism, 524–525
Dash-dotted lines, 549
The Debye-Hückel law, 643–644
Decarburization reactions, molten Fe-C-S system, 346–352
Decomposition, oxide and metal growth, 896–897, 897*f*
Defect studies, 370–375
Degree of freedom, 495–496, 502–503, 504
Degree of polymerization
  diffusion coefficient (D), 215–216
  flow and transport properties, 198
  nonideal solutions structural models, 277–279
Delhi iron pillar, 7*f*
Dendritic growth, 375–376
Dendritic pore formation, 898–899, 899*f*
Density
  effects, 91*f*
  measurements, levitated samples, 95*f*
  and thermal expansion, 130, 131*t*
Density and thermal expansion coefficient
  Archimedian (or Buoyancy) method, 225

data requirement, 223
dilatometry, 225
draining crucible, 225
factors affecting, 223–224
linear thermal expansion, 223
liquid slags, 225
maximum bubble pressure (MBP) method, 225
published models, 230*t*
Pyknometry (or weighing) method, 225
sessile drop method, 225
slags and glasses, 231*t*
Density functional theory (DFT), 296–298
Depletion of carbon, alumina-carbon refractories, 352–354
DFT. *See* Density functional theory (DFT)
Differential scanning calorimetry (DSC), 97–99, 192–193
Differential thermal analysis (DTA), 97–98
Diffusion, 113–114, 114*f*, 315–316, 360–370
Diffusion coefficient (D)
absolute rate theory approach, 219
anions size, 216–217
calculation, methods, 221–222
capillary reservoir (CR/Immersion) method, 220
cations number and valence, 217–218
chemical diffusion, 215
data for, 221
degree of polymerization, 215–216
determination, methods, 219
diffusion couple method, 220
electrochemical method, 221
factors affecting, 215
Fick's first and second laws, 212–214
friction coefficient approach, 219
instantaneous plane source, 220
inter-diffusion, 215
mean free path approach, 219
molecular dynamics calculations, 221
self-diffusion, 214
silicate melts, 221*t*, 222*t*
tracer diffusion, 214–215
Dilatometers, 92
Dilute Al-Fe alloys, 366–367
Dilute liquid alloys, 563–585
Dirichlet boundary condition, 742, 742*f*
Discard/unwanted materials, 17
Displacive reaction mechanisms, 906–907
Displacive transformations, 883, 884*f*, 885*f*
Disproportionation reaction, 159
Draining crucible (DrCru) method, 200
Drop calorimetry, 99–102, 101*f*, 193–194
DSC. *See* Differential scanning calorimetry (DSC)
1D steady-state conduction, 745–752
DTA. *See* Differential thermal analysis (DTA)
1D transient conduction, 752–763
Duffour effect, 97
Dulong-Petit rule, 95
Dynamic structure factor, 115*f*

E

EAM. *See* Embedded-atom method (EAM)
EDXRD. *See* Energy dispersive x-ray diffraction (EDXRD)
Electrical conductivity, 68, 107–111
Electrical conductivity and electrical resistivity
Arrhenius equation, 208
calculation models, slag, 212, 213*t*
cell arrangements, molten slags, 211*f*
"charge hopping", 206
data for, 211
determination methods, 211
double layer model, 206*f*
frequency, 211
Helmholtz model, 206
ionic and electronic conduction mechanisms, 209
ionic conductivity, 206, 207–209
logarithm, 208*f*
polarization, 211
Electrical resistivity, 131, 133*t*, 138*f*
Electrical steelmaking, 206
Electrochemical cells
Butler–Volmer relationships, 843, 843*f*, 844*f*, 845*f*
production, 842–843
Electrochemical potentials, 641–642
Electrochemical production reactors, 32–33, 32*f*
Electrochemical reactions, 838–851
Electrochemical reduction reaction, 897, 899–900
Electrolysis and electrochemistry
copper electrorefining, 654
copper electrowinning, 653–654
leaching, 654–656
zinc electrowinning, 653
Electromagnetic levitation (EML), 65, 68, 68*f*
Electron spin resonance (ESpRes), 175
Electro-slag remelting (ESR), 206
Electrostatic levitation, 66–68, 67*f*
Electrowinning
aluminum, 847
zinc, 846–849, 847*f*
Ellingham diagrams, 507, 508*f*, 512, 515, 655–656
Embedded-atom method (EAM), 322–323, 325
Emissivity, 130, 131*t*
Emulsification, 926
Energy dispersive x-ray diffraction (EDXRD), 78–79
Enhanced vaporization, metals, 853, 854*f*
Enthalpy, 400–401, 408–410
Entrained flow reactors, 26–28, 27*f*
Entropy catastrophe, 62–63
Entropy of fusion, 195–196
Equilibrium CO/CO_2 ratio, 512–515
Equilibrium iso-pressure curves, 636*f*
Equilibrium oxygen partial pressure, 511–512, 562, 563
Equilibrium partial pressures, gaseous species, 638*f*
ESR. *See* Electro-slag remelting (ESR)
Eulerian and Lagrangian view, 670
Eutectic system, 533–535
EXAFS. *See* Extended X-ray absorption fine structure (EXAFS)
Excess thermodynamic quantities, 522
Extended X-ray absorption fine structure (EXAFS), 72–73, 82–83, 84*f*, 175
Extensive property, 495

External equilibrium, 43
External flow
  across cylinder, 773–774
  around sphere, 774
  over flat plate, 773
Extraction processes, metallurgy, 10–13

F

Faber-Ziman distribution functions, 73
Face-centered cubic (fcc) crystal structure, 49, 63
Falling ball method, 200
Fe-Al system, 356–357
Fe-Cr alloys, 370–371
Fe-Cr system, 336–339
Fe-C-S system, 334–336, 346–352
Fe-C system, 331–333
Fe-Ni-Cr system, 339–340
Ferrous alloys, 619–622
Fe-S-O system, 333–334
Fick's first law, 885, 893
Fick's law of diffusion, 802–805
Finnis-Sinclair potential, 320–322, 325
First Law of Thermodynamics, 399–400
First sharp diffraction peak (FSDP), 69–70
Flash smelting processes, 38, 38*f*
Flat plates, 783–784
Flexibility, 17
Flow and transport properties
  capillary viscometry, 198
  concentric cylinder method, 199
  diffusion coefficient, 212–222
  electrical conductivity and electrical resistivity (*see* Electrical conductivity and electrical resistivity)
  falling ball method, 200
  inclined plane test, 201
  oscillating plate method, 199–200, 200*f*
  rotating bob (or cylinder) method, 199, 199*f*
  silicate structural units, 196–198
  slag, degree of polymerization, 198
  viscosity data, 198, 202, 203*t*
FLUENT, 733
Fluid and solid phases, 912, 912*f*
Fluid/condensed phases interfaces, 853–858
Fluid flow description, 669–672
Fluid/fluid systems
  bulk flow, 922–924, 923*f*
  composition, 920–922, 921*f*
  emulsification, 926
  gas phase formation, 926–927, 927*f*
  liquid droplets and gas bubbles, 929
Fluidized beds, 26, 27*f*, 706–710
Fluid phase
  equilibrium, schematic diagram, 44*f*
  gas, 47
  glass = amorphous solid, 47–48
  glass transition, 51–52
  liquid, 47
  metallic and oxide melts, structural features, 57–59
  phase transition, 48–51
  plasma, 46*t*, 48
  solid, 46–47
  state and equilibrium, 43–44
  state of matter, 45–46, 46*f*
  structural features, 52–57
Fluids, 355–356, 365–366
Fluid/solid reactions, 891
Fluid/solid systems
  microstructural changes, heating porous nickel metal, 931
  particle characteristics, 924–925, 925*f*
  product structure, 927–928
  reaction micromodels, nonplanar interfaces, 928
Fluid/solid transformation, 875, 876*f*
Forced convection, 772
Free convection, 782–784
Free energy determination, 307–309
Friction factor, 690–698
FSDP. *See* First sharp diffraction peak (FSDP)

G

Gas equilibria, 633–638
Gas injection systems, 922
Gas/liquid reactors, 33–35
Gas/liquid systems, 856–857
Gas/oxide interface, 866*f*
Gas phase formation, 926–927, 927*f*
Gas radiation, 797–800
Gas/solid reactors, 24–28
Generalized gradient approximation (GGA), 297
Gibbs-Duhem equation, 523
Gibbs energy, 644–646
  Al, O_2, and Al_2O_3, 414
  binary solutions, 527–530
  change, 559–560
  change of Reaction, 515–516
  changes, 419–421, 476*t*
  definition, 413
  function, 421–422, 422*t*
  of mixing, 610
  molar quantities, 521*f*
  relative molar quantities, 521*f*
  solid, liquid, and gas, 415*f*
Gibbs ensemble method, 302–303
Gibbs free energy, 832–833, 833*f*, 856, 878–879, 879*f*
Gibbsite precipitation, 887, 888*f*
Gibbs phase rule, 495, 637–638
Glass = amorphous solid, 47–48
Glass transition, 51–52, 62–63, 184*f*
Glassy samples, 152–153
Grain boundary, 931
Grand canonical ensemble for open systems, 290–291
Growth mechanisms, phase formation reactions, 883–887

H

Hagen-Poiseuille's law, 683, 686
Hagen-Rubens relation, 140
Half-cell reactions, 846–849
Halides, 19–20, 21*f*
H_2+CO_2 gas mixture, 635–638
Heap leaching, 29
Heat and temperatures of transformation, 423*t*
Heat capacity, 401, 402–407, 424*t*
Heat capacity, entropy and entropy of fusion
  calvet calorimetry, 194
  Cp and enthalpy data, 195
  differential scanning calorimetry (DSC), 192–193
  drop calorimetry, 193–194
  entropy of fusion, 195–196
  factors affecting, 191–192, 192*f*
  measurement methods, 192
  single pan (Smith) calorimetry, 194–195
Heat of formation, standard entropies, and structures, 423*t*
Heat transfer, 736–737, 781–782

Heat transfer and transport properties, silicate network
analysis of data, 256–257
convection, 252
lattice (or phonon) conductivity, 249–250
lattice waves, 245
liquid slags, thermal conductivity, 250*f*
LP method, 252–253, 253*f*
measurement problems, 252
measurements on silicate slags, 254*t*
mold flux, 250*f*
published models, 257*t*
radiation conductivity, 251–252, 251*f*
thermal conductivity data, 246–249, 254–255
THW method, 253–254
Heat transfer coefficient correlations, 772
Helmholtz configuration, 66
Henrian activities, 558–560, 562–563
Henry's law, 557
Hertz-Knudsen equation, 853
Heterogeneous nucleation, iron metal, 879, 879*f*
Heterogeneous phase formation reactions, 875, 878–882
Heterogeneous reactions, 819–820, 820*f*, 821*f*, 875
Hexagonally closed packing (hcp), 63
HEXRD. *See* High-energy X-ray diffraction (HEXRD)
High-energy X-ray diffraction (HEXRD), 82–83
High-speed agitators, 30
High temperatures applications, 340–383
Hirai equation, 125–126
Homogeneous liquid alloys, 504
Homogeneous nucleation, 882
Homogeneous reactions, 819–820, 875
Hybrid levitator, 66, 67*f*
Hybrid Monte Carlo (HMC) method, 301–302
Hydro and electrometallurgical reactors, 40
Hydrogen embrittlement, metals, 374–375
Hydrogen gas with oxygen reaction, 834

I

Icosahedral packing, 63, 63*f*
Ideal gas, 399
Ideal solution behavior, 521–522
Ideal solution model, 532
Incompressible and compressible flows, 671–672
Industrial slag composition, 505–506
Infrared, ultraviolet, and Raman spectroscopy, 174
Inorganic compounds, thermodynamic properties, 425*t*
In situ leaching, 29
Instability formation, moving interfaces, 865–868
Integral Gibbs energy of mixing, 527, 528, 529*f*, 530, 535
Integral molar quantities, 518–519, 520
Intensive property, 495
Interaction potentials, 317–340
Interatomic potentials, 318–320, 326
Interfaces, 380–383
Internal equilibrium, 43
Internal flow, 774–781
Internal oxidation, 893, 893*f*
Interproperty relations, 139–142
Ion exchange reactors, 33
Ionic melts, 608–609
Ionic species, 502
Ions formation, 644–646
Iron, 320–324
Iron Age, 6–8
Iron alloys at 1873 K, interaction parameters, 563
Iron interaction potentials, 320–324
Iron-smelting furnace, 10, 11*f*
Irreversible reactions, 939
Isobaric isothermic ensemble, 291
Isomorphous system, 530–532
Isothermal growth, crystals, 886, 886*f*

J

Jackson factor, 862

K

Kaptay equation, 125–126
Kauzmann temperature, 62–63
κ-ε Model, 732–733
Kinematic viscosity, 124
Kinetic Monte Carlo (KMC) method, 299–300
Kirchoff's law, 789–790
Knudsen number, 664–665
Kohn-Sham equations, 296–297
Kozlov-Romanov-Petrov model, 125–126

L

Laminar and turbulent flows, 670–671
Langmuir adsorption, 835, 836*f*
Laplace operator, 96, 112
Large eddy simulations (LES) models, 734–736
Laser flash apparatus (LFA), 104–105, 105*f*
Lattice gas models, 292
Leaching electrochemistry, 654–656
Lead metal production, 23*f*
Le Chatelier's principle, 515
LES. *See* Large eddy simulations (LES) models
Lever rule, 533–534, 549
Levitated drop (LD), 91–92, 94
Lewis acid-base reactions, 647
LFA. *See* Laser flash apparatus (LFA)
Lindemann melting criterion, 61–62
Liquid Al-Cu, viscosity, 137*f*
Liquid cobalt, behavior at infinite dilution, 581
Liquid copper, behavior at infinite dilution, 578
Liquid Fe-X alloys, activity coefficient, 525*f*
Liquid iron, behavior at infinite dilution, 574–575
Liquid/liquid reactions, 35–36, 35*f*
Liquid/liquid systems, 920
Liquid metal
pair-distribution function, 71, 71*f*
static structure factor, 69–70, 70*f*
Liquid nickel, behavior at infinite dilution, 584–585
Liquid-phase reactors, 33–36
Liquid slags, 185
Liquid/solid reactors, 28–33
Liquid transition metals, 325
Liquidus line, 532, 533–534, 535
Liquid vapor equilibrium, 498–499
Local density approximation (LDA), 297
Lorenz number, 140–141, 141*f*
Low-speed agitators, 30

M

Magnetite isothermal reduction, 910, 911*f*
Margules equation, 524
Martensitic transformations, Fe-Ni system, 358–360
Mass diffusion, 111–114
Mass transfer, 801–814
Materials science, DFT applications, 297–298
Maximum bubble pressure (MBP) method, 91–92, 119–120, 225
MEAM. *See* Modified embedded-atom method (MEAM)
Mean activity coefficients, 642–643
Mean molarity, 643
Mercury distillation still, 10, 10*f*
Metal alloys, recycling, 19
Metal container, 496, 496*f*, 497
Metal growth morphologies, 898–908
Metallic and oxide melts, structural features
  quartz glass, 58–59, 59*f*
  random network structure, 59
  RDFs, 57, 58*f*
Metallic solution, 560–561
Metallurgical plant, 10, 11*f*
Metallurgical processing
  alternative process routes, 19–23
  Buckingham Π theorem, 687–689
  compressible flow, 715–721
  conduction, 738–763
  conservation equation, thermal systems, 737–738
  convection, 763–784
  drivers for change, 15–17
  flow around particles, 710–715
  fluid flow description, 669–672
  fluidized beds, 706–710
  friction factor, 690–698
  heat transfer, 736–737
  laminar flow, straight pipe, 683–687
  mass transfer, 801–814
  momentum balance, 721–728
  momentum transfer, 668
  overall energy balance, 672–679
  packed beds, 698–706
  process stages and aims, 17–19
  process trends, 17
  radiation, 785–800
  reactor and process design methodologies, 40–42
  Reynolds number, 689–690
  transport phenomena, 662–668
  turbulence models, 728–736
  viscosity, 680–682
Metallurgical reactors
  characteristics, 39–40
  classification, 24–39
Metallurgy
  alchemy and metal discovery, 3–9
  chemical reactions, 3*f*
  concept of elements, 2*f*
  "destruction of metallic principle", 1–2
  elements in nature, 2*f*
  extraction processes, 10–13
Metal oxide gaseous reduction, 915*f*, 916
Metal oxide reduction reactions, 892
Metal oxides, 19–20, 20*f*
Metals and alloys, point defect interactions, 372–373
Metals production, 19, 19*f*
Metal whisker growth, 899–900, 900*f*
$MgO\text{-}SiO_2\text{-}CaO\text{-}CrO_X$ melts, 613*f*
Micro-canonical ensemble for isolated systems, 289–290
Microgravity, 105*f*
Minimum fluidization velocity, v_{mf}, 708
Miscibility gap, 530, 535–537
Mixer-settler reactor, 39, 39*f*
Mixing-length theory, 732
MnO-FeO system, 627*f*
Modified embedded-atom method (MEAM), 325, 329
Modulation calorimetry, 102, 103*f*
Moelwyn-Hughes model, 125–126
Molar Gibbs energy, 643
Molecular dynamics (MD) methods, 293–296
Molten iron, 562, 629–632
Molten metals
  experimental techniques, 87–130
  levitation methods, 65–68
  properties, 86–137
  structure, 61–86
  structure-property relations and interproperty relations, 138–142
  surface tension and viscosity, 140*f*
  x-ray and neutron diffraction, 69–74
Molten steel, 617–619
Momentum balance, 721–728
Momentum transfer, 668
Monochromatic neutrons, 114
Monotectic system, 535–538
Monte Carlo (MC) method, 289–293, 863–864, 863*f*
Morphology maps, 908–912, 909*f*, 910*f*, 911*f*
Mossbauer spectroscopy, 175
Moving and fixed grate reactors, 28, 28*f*
Multicomponent diffusion, 806–807
Multistage smelting processes, 38–39
Multistep reactors, 36–39

N

$Na_2O\text{-}B_2O_3$ glass system, 597*f*, 598*f*
National Physical Laboratory (NPL), 100
Natural convection, 782–784
Navier-Stokes equation, 723–728
NBOs. *See* Nonbridging oxygens (NBOs)
Nearest neighbor distance, 80*f*
NEMD methods. *See* Nonequilibrium molecular dynamics (NEMD) methods
Nephelauxetic effect, optical basicity, 596*f*
Nernst equation for half-reactions, 648
Neumann boundary condition, 742, 743*f*
Neumann-Kopp rule, 95
Neutron diffraction, 82–83, 173
Neutron scattering, 86*f*
Newton's law of viscosity, 682
Nickel alloys at 1873 K, interaction parameters, 581
Nickel production, 23*f*, 24*f*
Nitride capacities, 602–604, 604*f*
Nitrogen transfer, liquid iron to gas, 836
NMR spectroscopy, 174–175
Nonbonded macro-molecular potentials, 331
Nonbridging O/tetragonal O (NBO/T), 156
Nonbridging oxygens (NBOs), 161
Nonequilibrium molecular dynamics (NEMD) methods, 316

Nonrenewable materials, 16
NPT ensemble, 291
Nucleation, 878–882
Nucleation frequency, 881, 881*f*
Nusselt Number, 770

O

O/C molar ratio, 638*f*
Opaque-diffuse-gray surfaces, 790–797
Optical basicity, 157–158, 157*t*, 595–596
Optical properties, silicate network
  absorption coefficients, 260–262
  bulk sample, high-temperature measurement, 265
  composition effect, 258
  data, 258, 266
  electronic polarizability, 259*t*
  factors affecting, 258–260
  molten sample, high-temperature measurement, 265–266
  published models for calculation, 267, 268*t*
  reflectivity, transmissivity, and absorption coefficient, 262–263
  refractive index (n), 258, 259*f*, 263–265
  temperature dependence, 260
  wavelength effect, 259
Order-disorder transformations, Al-Li system, 357–358
Oscillating cup viscometer, 128–129, 129*f*
Oscillating drop, 122–124, 129–130
Oscillating plate method, 199–200, 200*f*
Oscillation spectrum, levitated spherical drop, 123, 123*f*
Oxidation, Fe Si alloys, 892, 893*f*, 894*f*
Oxidation, metals, 894, 895*f*, 896*f*, 897*f*
Oxidation-reduction equilibrium, slags, 611–614
Oxide surface morphologies, reactive gas atmospheres
  Arrhenius equations, diffusivity, 872
  condition, planar and unstable growth, 869–871, 870*f*
  interface velocities, 871, 871*f*
  planar, cellular and dendritic growth, 868–869, 869*f*
  plate shaped samples, 872
Oxygen vacancy diffusion, alumina, 364–365

P

Packed beds, 698–706, 781–782
Pair-correlation functions, 77
Parallel tempering method, 306–307
Partial molar Gibbs energy of component, 527, 528, 529*f*, 530–531
Partial molar quantities, 517–518, 520
Particle paths, 669–670
Particulate fluidized beds, 708–709
Percolation leaching, 29–30, 30*f*
Peritectic system, 535–538
PFRs. *See* Plug flow reactors (PFRs)
Phase, 496
Phase behavior, 355–360
Phase diagrams, 312–315
  and activities, 587–591
  binary system CaO-SiO_2, 539–546
Phase equilibria, fluids, 355–356
Phase field crystal models, 378–380
Phase field models, 377–378
Phase formation reactions
  continuum, 876–878
  growth mechanisms, 883–887
  heterogeneous, 878–882
Phase transition
  iron, allotropes, 49
  mechanism, 894, 894*f*
  solid, liquid, and gas, relations, 50*f*
  sublimation, 49
  temperature *vs.* energy, 50*f*
  vaporization, 49
Phase-vapor equilibrium, 496–497
PHOENICS, 733
Phosphate capacities, 599–602, 603*f*
Phosphide capacities, 602–604, 603*f*
Physical properties determination, 307–316
Pipe fittings, friction loss, 693–694
Pitot static tube, 679, 680*f*
Pitot tube, 679, 679*f*
Plug flow reactors (PFRs), 941
Point defect interactions, metals and alloys, 372–373
Population balance model approach, 887
Porous nickel metal, heating
  change, mean pore size with time, 934–935, 934*f*
  "densification," solid material, 934
  effect, liquid phase, 935, 935*f*
  mechanisms, material transport, 933, 933*f*
  microstructures, 931, 932*f*
  sintering, solid particles, 933, 934*f*
  solid of uniform composition, 933
Position-sensitive device (PSD), 128–129
Potential-pH diagram, 654, 654*f*, 655–656, 655*f*
Potential-pH diagrams, 649–651
Potentials. *See* Atomistic interaction potentials
Pourbaix diagrams, 649–651
Prepeak, 81
Prescribed heat flux, 742–743
Prescribed surface temperature, 742
Primary crystallization field, 546–549
Principal value metal, 17
Production cells, 842–843
Product preparation, 19
PSD. *See* Position-sensitive device (PSD)
Pulse-heating experiments, 109*f*
Pure elements, 74–79
Pure metals, 130–134
Push-rod technique, 93–94
Pyrometallurgy, 39–40
Pyrometry, 87–90

Q

Quasielastic neutron scattering, 64–65

R

Radial distribution function (RDF), 53, 173
Radial systems, 748–749
Radiation, metallurgical processing
  black body, 787–788
  emission from real surfaces, 788–789
  emissive power, 786–787
  gas radiation, 797–800
  intensity, 785–786
  irradiation, 788
  Kirchoff's law, 789–790
  opaque-diffuse-gray surfaces, 790–797
  opaque surfaces, 789

Random numbers and accuracy considerations, 292–293
Raoultian standard, 557, 558*f*, 559, 560
Raoult's law, 521–522, 557, 558*f*, 559
Rate equations, electrochemical reactions
  Gibbs free energy, 839, 840*f*
  overpotential–current relationship, 841, 841*f*
Rate laws, 831
Rate-limiting processes. *See* Reaction rates and rate-limiting processes
Ratio/two-color pyrometer, 89–90
RDF. *See* Radial distribution function (RDF)
Reactant characteristics, 920–925
Reaction engineering and process models, 939–942
Reaction induced phenomena, 926–928
Reaction kinetics
  rates and rate-limiting processes, 822–828
  structure, 828
  and systems, 818–821
Reaction micromodels, nonplanar interfaces, 928, 929*f*, 930*f*
Reaction rates
  CO/CO_2 gas mixtures, 848
  fluid/condensed phases interfaces, 853–858
  theory, 832–834
Reaction rates and rate-limiting processes
  chemical, interface, 826–827
  heterogeneous chemical, 822
  mass transfer, phase I, 823–825, 824*f*
  mass transfer, phases I and II, 825–826
  phase II, mass transfer, 825
  steady-state conditions, 827–828
  transfer, solute species, 822, 823*f*
Reactions
  gas phase, 853–855, 854*f*, 855*f*
  interfaces, 835–838
Reaction system performance
  "chemical reaction", 942
  engineering and process models, 939–942
  parameter, heterogeneous rate equation, 939
Reaction systems, 818–821
Reaction systems, interfacial area, 919, 920*t*
Reactive gas system, 856
Reactor models, 942
Real crystal, 61–62
Real gases, 61–62
Reconstructive transformations, 876, 883–887, 886*f*, 888*f*
Recycling processes, 18
Redox reactions, 611, 648–649
Refractive index
  ellipsometry, 264–265
  immersion method, 265
  minimum deviation method, 263–264
  optimal angle method, 263
Regular solution model, 535
Regular solutions, 523–524
Relationship, partial molar quantities and integral molar quantities, 519–520
Relative integral molar Gibbs energy
  binary solution, 522
  and excess, 524
  ideal solution, 521, 522
Relative partial molar Gibbs energy, 528
Removal of impurities, 617–619
Resin-in-leach (RIL) processes, 33
Reverberatory furnaces, 37–38
Reverse Monte Carlo (RMC) method, 78–79, 300–301
Reversible processes, 851–852
Reversible reactions, 939
Reynolds-averaged Navier-Stokes (RANS) models, 731–733
Reynolds number, 689–690
Richardson nomographic scales, 508*f*, 513*f*
Richardson's theory, 610
RMC method. *See* Reverse Monte Carlo (RMC) method
Roman shaft furnace, 10, 12*f*
Rotary kiln, 25–26, 25*f*
Rotating bob (or cylinder) method, 199, 199*f*
Rotating cup viscometer, 128
Ruthenate capacity, 604–607, 606*f*

S

Sampling procedures, 291–292
Scattering experiment, 69
Scattering geometries, 69*f*
SD. *See* Sessile drop (SD)
Second Law of Thermodynamics, 411–413
Self-diffusion, 111–112, 132–134, 133*f*, 134*t*, 361–362
Self-driven cell, 842–843
Semi-infinite system, 760–763
Separation stages, 18
Sessile drop (SD), 91–92, 120–122, 120*f*, 121*f*
Sessile liquid Al-Cu drop, 121*f*
Shaft furnaces, 10, 12*f*, 24–25, 25*f*
Sherwood number, 810
Sieverts' law, 557
Silicate network, slags properties
  density, thermal expansion coefficient and ultrasonic velocity, 223–237
  flow and transport properties (*see* Flow and transport properties)
  heat transfer and transport properties, 245–257
  optical properties, 257–267
  surface and interfacial tension, 237–244
  thermodynamic properties, 185–196
Silicates, 610
Silicate slags
  activation energy parameter, 179*f*
  aluminosilicates, 153–154, 178–179, 270
  CaF_2 addition, 171, 172*f*, 271
  CaF_2 and B_2O_3 effect, 155
  CaO-SiO2 composition, 162*t*
  cations effect, 180–182
  Centigrade scale, 151
  composition, 151
  concentrations, 158–159
  diffusion coefficient, 176–177
  electrical conductivity, 176–177
  Fe_2O_3 and Cr_2O_3 effect, 154, 271
  iron oxides, 170–171
  methods, structure determination, 171–175, 172*t*
  mixed alkali effect, 182
  parameters, 155–160
  Q^n values, 159
  structure, 151–153, 160–166, 167, 176–179, 267–270
  temperature effect, 182–185, 270

TiO_2 and ZrO_2 effect, 154
viscosity, 176–177
Silicates, structural characteristics
aluminosilicates, 164, 167–169
bond strength, 165
CaO-SiO_2 composition, 162*t*
cation radius values, 160*t*
cations, coordination number, 161–163
configurational entropy, 166
medium-range order, 160–161
sheet structure, 161*f*
short-range order, 160–161
silicate tetrahedra, 161*f*
Si-O-Si bond angles distribution, 165*f*
tetrahedral and inter-tetrahedral angles, 165*f*
topology, bond angles, bond energies, 163–166
two-dimensional structures, 164*f*
units nature, 161
viscosity, 162*f*
Silicon, 327–329
Silicon deoxidation, 619–622
Simple packed bed reactor, 662–663, 662*f*
Simulation. *See* Solidification simulations
Single pan (Smith) calorimetry, 194–195, 195*f*
Single-phase composition, 504–505
Sintering, 933, 934*f*
Slags
basicity, 592–595
capacity and dissolution, 599–607
ionic melts, 608–609
optical basicity, 595–596
oxidation-reduction equilibrium, 611–614
Richardson's theory, 610
silicates, 610
theoretical optical basicity, 597–598, 607*f*
SLLS. *See* Surface laser light scattering (SLLS)
Sn-Zn system, 504, 505*f*
Solid and molten iron carburization, 340–344
Solidification simulations, 375–383
Solid/liquid and solid/solid systems
chemically induced phase transformations, 906, 907*f*
coupled growth, metal and gas pores, 903, 904*f*
eutectic reaction system, 903, 904*f*
microstructures, reduced dense hematite sample, 903–904, 905*f*
nonisothermal solidification, peritectic reaction system, 903–904, 905*f*
reconstructive/displacive formation Fe_3O_4, 906–907, 907*f*
shear/displacive mechanisms, 906
transmission electron micrographs, 906–907, 908*f*
Solid-liquid equilibrium, 500
Solid oxides, 626–629
Solid oxide surface, 865–866, 867*f*
Solid slags, 183–185
Solid/solid systems. *See* Solid/liquid and solid/solid systems
Solid/solid transformations, 856
Solid surfaces, 856–858
Solidus line, 532, 535
Solid-vapor equilibrium, 498–499
Solid ZnO gaseous reduction, 857, 857*f*, 858*f*
Solute transfer and phase formation reactions, 820, 821*f*
Solvent extraction, 39
Specific heat, 130, 132*t*
Spheres, 784
Spinoidal reaction, 877–878, 877*f*
Standard enthalpy change of manganese, 510*f*
Standard free energy change of formation, 651*t*
Standard Gibbs energies of reactions, 424*t*
Standard Gibbs energy change, 507–511
Static concentration wave (SCW) theory, 357
Statistical ensembles, 289–291
Statistical errors, 293
Steady and transient diffusion, 807–809
Steady and unsteady flows, 669
Steelmaking thermochemistry
calcium treatment (*see* Calcium treatment)
gas equilibria, 633–638
removal of impurities, molten steel, 617–619
silicon deoxidation, ferrous alloys, 619–622
solid oxides and alloyed steels, 626–629
Stefan-Boltzmann constant, 99–100
Steric hindrance, viscosity, 160
Stillinger and Weber potential, 327–328
Stokes-Einstein (SE) relation, 141, 142*f*
Stokes law, 921–922
Streak lines, 669–670
Stream lines, 669–670
Structure factors, 75–76, 76*f*, 79*f*
Structure-property relations, 138–139
Submerged arc reactor, 37, 37*f*
Submerged injection reactor, 34, 35*f*
Substitutional solid solution
Sulfide, 19–20, 20*f*, 599–602
Sulfide capacity, 633
Sulfurization iron silicate slags, 850, 850*f*
Supercritical fluid, 62–63
Surface and interfacial tension
calculation methods, 244, 247*t*
data for, 237–240, 244, 246*t*
detachment methods, 243–244
factors affecting, 240–241
lens method, 244
MBP method, 242
pendent drop (PD) and drop weight method, 243
SD and big drop methods, 242–243
x-ray SD method, 244
Surface diffusion, semiconductors, 367–369
Surface laser light scattering (SLLS), 200
Surface segregation, 118*f*
Surface tension, 64, 115–124, 134, 135*t*, 136*f*, 310–311
Sutton-Chen potentials, 324, 326
Symmetric stretching, vibrations, 174, 174*f*
Systematic errors, 293
System contains, 496*f*, 497, 500

T

Taylor's expansion, 560
Temperature dependence, enthalpy, 408–410

Temperature dependence, heat capacity
Al, , (Al), 403*t*
Al, O_2, and Al_2O_3 thermodynamic data, 402, 402*t*
Al_2O_3 and, 406*t*
O_2, 405*t*
representation, 402
Ternary impurities, iron carburization, 344–345
Ternary phase diagram, 546–556
Tersoff potential, 328–330
Theoretical models, decarburization, 350–352
Theoretical optical basicity, 597–598, 607*f*
Thermal conductivity, 103–106, 131, 132*t*
Thermal diffusivity, 103–106
Thermal expansion and density, 90–94
Thermally thick bodies, 754–755
Thermally thin bodies, 753–754
Thermal systems, 737–738
Thermochemical data, 539–546
Thermochemical data-1, 502–503
Thermochemical data-2, 504
Thermodynamic data compilations, 399
Thermodynamic factor, 111–112
Thermodynamic properties, silicate network
activity coefficients and, 189–191
bond strengths, 185
heat capacity, entropy, entropy of fusion, 191–196
liquidus temperature, 186–189
phase equilibria and, 271–272
Thermodynamics, 622–626, 629–632
Gibbs energy, 396
literature, 396
macrosystems, 397
measurement, 397
principles, 397
steam engine, 395–396
Thermophoresis, 96–97
Thermophysical properties, silicate network
acoustic properties, 273–274
density, 273–274
flow and transport properties, 272–273
modeling, 275
molar volume, 273–274
optical properties, 274
phase equilibria and thermodynamic properties, 271–272
surface and interfacial tension, 274–275
thermal conductivity, 274
thermal expansion, 273–274
thermal properties, 274
Third Law of Thermodynamics, 411–413
THW. *See* Transient hot wire (THW)
Tie line, 533–534, 549
Titano-silicates, 169–170, 271
Top submerged lance (TSL) reactors, 34
Transient hot wire (THW), 97, 104
Transition metals, 325
Transition state theory, 832–833, 838
Trial moves, 292
Tridymite, 883, 885*f*
Triple point, 501
Turbulence models, 728–736
Two-phase regions, regressive formulae and activities, 546, 547*t*

U

Ultrasonic waves, velocity and absorption coefficient
acoustic property data, 226
compositional dependency, 229–232
data for, 234–237
frequency dependency, 226–229
molar volume, 232
published models, 237, 238*t*
pulse echo technique, 233, 233*f*
pulse transmission technique, 233*f*, 234
temperature dependency, 229
Undercooled liquids, 62–63, 78–79
Uniform and nonuniform flows, 669
Useful by-products, 17

V

Vaporization, reactive atmosphere, 854, 855*f*
Vapor pressures, 499
Vapor pressures and evaporation constant, 424*t*
Venturi meter, 678, 678*f*
"Verlet" algorithm, 294
View factor, 790–792
Viscometers, 127, 127*f*
Viscosity, metallurgical processing, 680–682

W

Wagner's equation, 560–561
Wang-Landau formalism, 304–306
Water vapor pressures, 497*t*
Wettability, 311–312
Wiedeman-Franz relation, 140–141
Wiedemann-Franz law, 108

X

XANES. *See* X-ray near-edge absorption spectroscopy (XANES)
X-ray absorption spectroscopy, 175
X-ray and Neutron Diffraction, 69–74
X-ray diffraction, 82–83
X-ray, electron, and neutron diffraction, 173
X-ray emission spectroscopy, 175
X-ray near-edge absorption spectroscopy (XANES), 175
X-ray photon spectroscopy, 175

Z

Zinc electrowinning, 653
Zn-H_2O system, 650, 651*f*
Zn-S-H_2O system, 655–656, 655*f*